Coastal and Hydraulics Laboratory

US Army Corps of Engineers®
Engineer Research and
Development Center

North Jetty Performance and Entrance Navigation Channel Maintenance, Grays Harbor, Washington

Volume II: Appendices

Nicholas C. Kraus and Hiram T. Arden, editors
With contributions by (in alphabetical order)
Jessica L. Baker, Mark R. Byrnes, Mary A. Cialone,
Julie A. Cohen, Michael H. Davies, David B. Hericks,
David Katzev, Neil J. McDonald, Philip D. Osborne,
Maria Timpano, Ty V. Wamsley, and Donald L. Ward

June 2004

North Jetty Performance and Entrance Navigation Channel Maintenance, Grays Harbor, Washington

Volume II: Appendices

Nicholas C. Kraus and Hiram T. Arden, editors
With contributions by (in alphabetical order)
Jessica L. Baker, Mark R. Byrnes, Mary A. Cialone,
Julie A. Cohen, Michael H. Davies, David B. Hericks,
David Katzev, Neil J. McDonald, Philip D. Osborne,
Maria Timpano, Ty V. Wamsley, and Donald L. Ward

Coastal and Hydraulics Laboratory
U.S. Army Engineer Research and Development Center
3909 Halls Ferry Road
Vicksburg, MS 39180-6199

Final report

Approved for public release; distribution is unlimited

Prepared for   U.S. Army Engineer District, Seattle
                   P.O. Box 3755, Seattle, WA 98124-3755

ABSTRACT:

This report documents a study performed for the U.S. Army Engineer District, Seattle, to identify and evaluate feasible methods for reducing annual maintenance dredging in the outer Federal navigation channel at Grays Harbor, WA, by modification of the north jetty. Main interest was in potential reduction of southward sand bypassing the north jetty and preservation of the jetty should the neighboring beach erode. Considerable information and predictive capability were generated concerning the behavior of the Federal navigation channel and adjacent coastal and inlet shorelines. The study was conducted as a coordinated multi-disciplinary approach involving field measurement, physical modeling of the hydrodynamics and potential sediment pathways, geomorphic analysis and sediment budget formulation, and numerical modeling of waves, circulation and sediment transport, including modeling of shoreline change and bypassing.

Numerous alternatives were considered and subjected to a screening process to identify feasible engineering and physically constructible alternatives within broad criteria. Six alternatives passed the screening and were evaluated. The alternatives concerned an innovative submerged spur that would be placed parallel to the shoreline along the north jetty, partial and full rehabilitation of the north jetty, and a combination of these alternatives with structures of different lengths.

The sediment-control alternatives were evaluated relative to the existing condition. The study revealed many wide-area processes controlling sedimentation in and around Grays Harbor. The scale of change in southward-directed bypassing of sediment expected to occur after construction of any of the evaluated alternatives was found to be small compared to the scale of transport at the Grays Harbor entrance from sources originating outside the entrance or by being reworked and redistributed within the entrance. Modification of the north jetty is one of relatively few options for controlling sedimentation in the outer navigation channel; others include channel realignment and modifications to the south jetty.

Contents

List of Figures

xlii

List of Tables

Conversion Factors, Non-SI to SI Units of Measurement

Non-SI units of measurement used in this report can be converted to SI units as follows:

Multiply	By	To Obtain
acres	4,046.873	square meters
cubic yards	0.7645549	cubic meters
feet	0.3048	meters
inches	25.4	millimeters
miles (U.S. statute)	1.609347	kilometers
pounds (mass)	0.4535924	kilograms
tons (2,000 pounds, mass)	907.1847	kilograms
square miles	2,589,998	square meters

Preface

This report describes a multidisciplinary study of the sediment retention and bypassing functioning of the north jetty at Grays Harbor, WA, and its relation to sediment shoaling in the federally authorized deep-draft navigation channel at Grays Harbor. The report consists of two volumes. Volume I contains the main text, references, and conclusions of the study. Volume II contains eight appendices providing further information in text, figures, photographs, and tables.

The study was conducted for the U.S. Army Engineer District, Seattle (NWS) by the U.S. Army Engineer Research and Development Center (ERDC), Coastal and Hydraulics Laboratory (CHL), Vicksburg, MS. Mr. Hiram T. Arden was the NWS project manager for this study, and Ms. Aimee T. Kinney, and Messrs. George A. Hart, Eric E. Nelson, and Robert M. Parry, provided NWS technical assistance and review of this report.

The ERDC study team was under the technical direction of Dr. Nicholas C. Kraus, Senior Scientists Group, CHL. Contributors to this report are identified on the first page of each chapter. Contributors were Mr. Arden, NWS, and Dr. Kraus, CHL, for engineering and dredging; Ms. Jessica L. Baker and Dr. Mark R. Byrnes, Applied Coastal Research and Engineering, Inc., Mashpee, MA, for morphologic analysis; Ms. Mary A. Cialone, Coastal Processes Branch (CPB), CHL, for wave and circulation numerical modeling; Ms. Julie A. Cohen and Dr. Donald L. Ward, Coastal Harbors and Structures Branch (CHSB), CHL, for physical modeling; Dr. Michael H. Davies, Mr. David Hericks, Dr. Neil J. McDonald, Dr. Philip D. Osborne, and Dr. Vladimir Shepsis, formerly Pacific International (PI) Engineering, PLLC, Edmonds, WA, presently Coast and Harbor Engineering, Inc., for field measurement, literature review, dredged volume analysis, and particle tracking modeling; and Mr. Ty V. Wamsley (CPB) for numerical modeling of shoreline change. Dr. Osborne was the project coordinator at PI Engineering. Mr. Terry Larson, captain of the vessel *Tricia Rae*, and Mr. Dave Mullins, Mullins Guide Service, provided support of field data collection. U.S. Coast Guard Station Astoria provided helicopter pilots and crews to assist with instrument deployment and recovery.

Dr. Kraus and Mr. Arden were the report technical editors. Mr. Dennis G. Markle, Chief, CHSB, assisted Dr. Kraus in administrative aspects of the study. Ms. J. Holley Messing, Coastal Engineering Branch, CHL, completed final report word processing and formatting for both volumes. The Information Technology Laboratory (ITL) technical editor was Mr. Bill Mullen.

The study was conducted from October 2000 through December 2002 under the administrative supervision of Mr. Thomas W. Richardson, Director of CHL, and Dr. William D. Martin, Deputy Director, CHL.

At the time of publication of this report, Dr. James R. Houston was Director of ERDC, and COL James R. Rowan, EN, was Commander and Executive Director.

Appendix A
Stability Analysis of a Submerged Spur, North Jetty, Grays Harbor, Washington[1]

Introduction

This appendix documents results of an independent investigation of stability of a submerged spur being considered as a sediment control structure at the north jetty at the entrance to Grays Harbor, WA. The study was funded by local interests (Coastal Communities of Southwest Washington) independent of the U.S. Army Corps of Engineers (USACE) north jetty Operation and Maintenance (O&M) study described in the main text of this report. The present study included development of design waves, analysis of existing published data on stone stability for submerged structures, and physical modeling in a large-scale two-dimensional (2-D) wave flume.

A reconnaissance study performed in year 2000 for the U.S. Army Engineer District, Seattle (NWS) by the U.S. Army Engineer Research and Development Center, Coastal and Hydraulics Laboratory (CHL) and Pacific International Engineering[PLLC] determined that a submerged spur could be constructed in the north jetty environment with a marine-based operation consisting of split-hull bottom dump barges and tugs. The constructability analysis concluded that rock size should be as small as possible for a marine hopper barge operation; barge openings up to 8 ft can dump rock up to approximately 3 ft in diameter. Furthermore, construction would be simplified greatly if a single rock gradation can be used due to the difficulties with trimming and dressing of the structure in the north jetty wave and current environment. A 3-ft diam maximum rock size is small relative to the size of stone normally used in North Pacific Ocean jetty construction. The small rock size and broad gradation raised concerns regarding rock stability in the energetic wave regime at the north jetty, Grays Harbor.

Existing formulae and experimental data for submerged structure stability were reviewed and evaluated. Calculations of crest stone sizes for the extreme

---

[1] Written by Philip D. Osborne, Nels Sultan, and Michael H. Davies, Pacific International Engineering, PLLC, Edmonds, WA.

depth-limited wave height and period conditions at north jetty following van der Meer and Pilarczyk (1990) and Vidal, Medina, and Martin (2000) suggest that a stone diameter of at least 7 to 8 ft might be required to achieve stability. Stones of this size could be impractical should the structure need to be constructed using split-hull dump barges. However, it was recognized that the north jetty environment and submerged spur geometry are generally close to or just beyond the limits of most laboratory investigations of stability and structure performance. Furthermore, even in the case of conventional rubble-mound breakwaters, information is lacking for depth-limited breaking waves (Melby and Kobayashi 1998). Therefore, conclusions based on previous empirical studies need to be considered with caution. A physical model study, as documented in the appendix, was deemed necessary to more fully evaluate structure stability.

A series of large-scale 2-D flume tests was undertaken at the Canadian Hydraulics Centre (CHC) in Ottawa, Canada, to evaluate the cross-sectional stability of a proposed spur constructed with a relatively small stone size. Tests were also undertaken for a structure composed of 4-cu yd geotextile bags (geobags). Conceptual rock armor and geobag cross-sections are shown in Figures A1 and A2. Structural stability and general performance were evaluated for the most severe combinations of wave height and period anticipated at the site. The interaction between the rock-armored structure and the sand seabed was also investigated. Design waves for the empirical analysis and physical modeling were determined from an analysis of wave measurements offshore of Grays Harbor. Results of the large-scale flume tests conducted by CHC are summarized in this appendix. Davies (2001) gives a more comprehensive presentation of the test results.

Development of Design Waves at North Jetty, Grays Harbor

Design wave heights and periods for the analytical and physical model investigations were developed by applying the following procedure:

 a. Review existing studies and available wave data for the Grays Harbor entrance.

 b. Analyze extremal statistics to determine the offshore wave heights for various return periods.

 c. Analyze joint occurrence of significant wave heights and associated peak periods at the project site. Extend to expected durations of significant wave heights and associated peak period combinations over an anticipated 25-year lifespan for a submerged spur.

 d. Select the 10 largest wave events measured at Grays Harbor since 1982. Determine the typical spectral shape for these extreme wave events.

 e. Select prototype design significant wave height, peak period and spectral shape for an offshore location.

 f. Develop scaled significant wave height, peak period, and spectrum for the wave tank. Adjust for shoaling to determine the correct wave spectrum given the water depth in the wave tank near the wave generation.
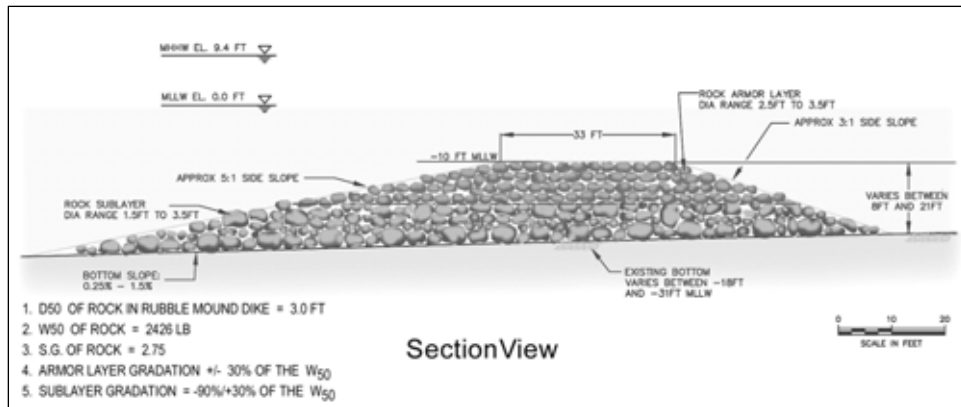
Figure A1.   Rock armor cross section for 2-D stability tests
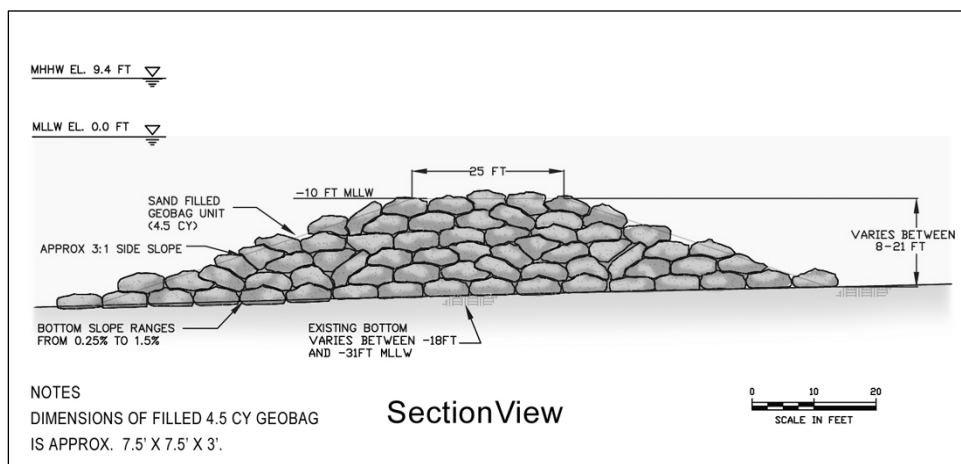
Figure A2.   Geobag cross section for 2-D stability tests

Existing data and wave climate studies

One source of design wave information is a memorandum recommending rehabilitation of the north jetty at the entrance to Grays Harbor (USAED, Seattle, 1974). The proposed design wave was 6.7 m (22 ft). This wave height was developed assuming depth-limited conditions over the submerged end of the jetty.

However, depth-limited breaking should not be assumed a priori for the proposed spur. Also, morphological surveys of the north jetty area reveal that the seabed elevation in proximity to the north jetty fluctuates as much as 5 to 10 ft annually. Therefore, an offshore non-depth limited design wave is developed based on the most recent available data. The design waves are transformed to the project site by applying shoaling factors and checked for depth-limited breaking. A range of water levels from mean lower low water (mllw) to mean higher high water (mhhw) plus storm surge is included in the analysis to account for potential variations in water depth and water level that are anticipated at the north jetty.

Wave data are available from a buoy seaward of Grays Harbor that has been operating since 1982 (Coastal Data Information Program 2000). The buoy is located approximately 1 km southwest from the entrance to Grays Harbor in a water depth of 41.5 m. Measurements from the buoy from 1993 to 2001 have been analyzed previously in an engineering report for nearby Willapa Bay (Kraus 2000; Kraus, Arden, and Simpson 2002). Also, PI Engineering has conducted an extremal analysis of the wave height data from 1982-2000 to document existing conditions for spur dike feasibility (PI Engineering 2000) and from 1982-2002 as part of the north jetty O&M study (Chapter 4).

The joint distribution of wave heights and periods measured at the CDIP buoy is summarized in Figure A3. The plot represents all measured wave heights and corresponding wave periods offshore of Grays Harbor (CDIP buoy 3601) over the period January 1994 through December 2001. The distribution shows a concentration of extreme waves with significant heights, H_s, larger than 6 m at peak periods, T_p, of 10-15 sec and also of waves longer than 15 sec at somewhat lower wave heights.
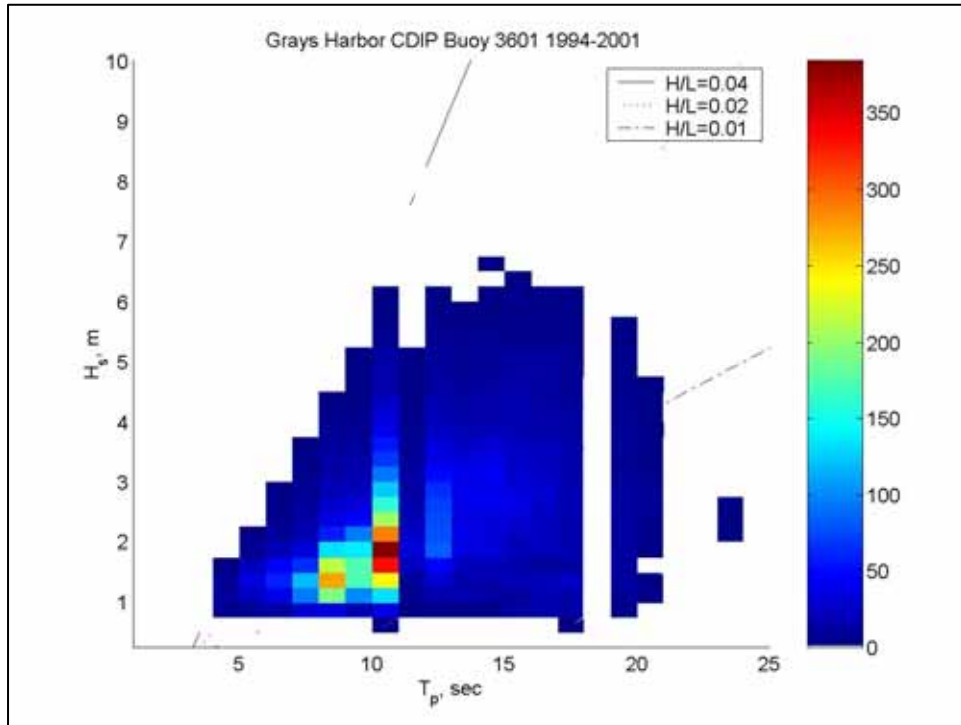
Figure A3. Joint distribution of H_s and T_p for measurements at Grays Harbor CDIP buoy 3601 between January 1994 and December 2001. Color scale represents number of hours per year. Diagonal lines represent lines of constant wave steepness (H/L), where L is local wavelength

The H_s-T_p occurrence presented in Figure A3 can be extended to an expected duration of given H_s-T_p combinations over an anticipated 25-year lifespan of the submerged structure. The resulting data set expressing the hours of occurrence for each H_s-T_p combination is presented in Figure A4. Figure A4 reveals that durations longer than 4 hr are associated with H_s greater than 7 m, and T_p of 16 to 18 sec. For T_p between 20 and 21 sec, the associated H_s decreases to between 5 m

to 7 m. Although waves with periods as long as 25 sec have been recorded at Grays Harbor, they are associated with wave heights of only 2 m. This inter-relationship between H_s and T_p is central to the design of a submerged structure such as the Grays Harbor spur because the potential for damage to the structure has been observed to be strongly influenced by wave period (e.g., Ahrens 1987, 1989).
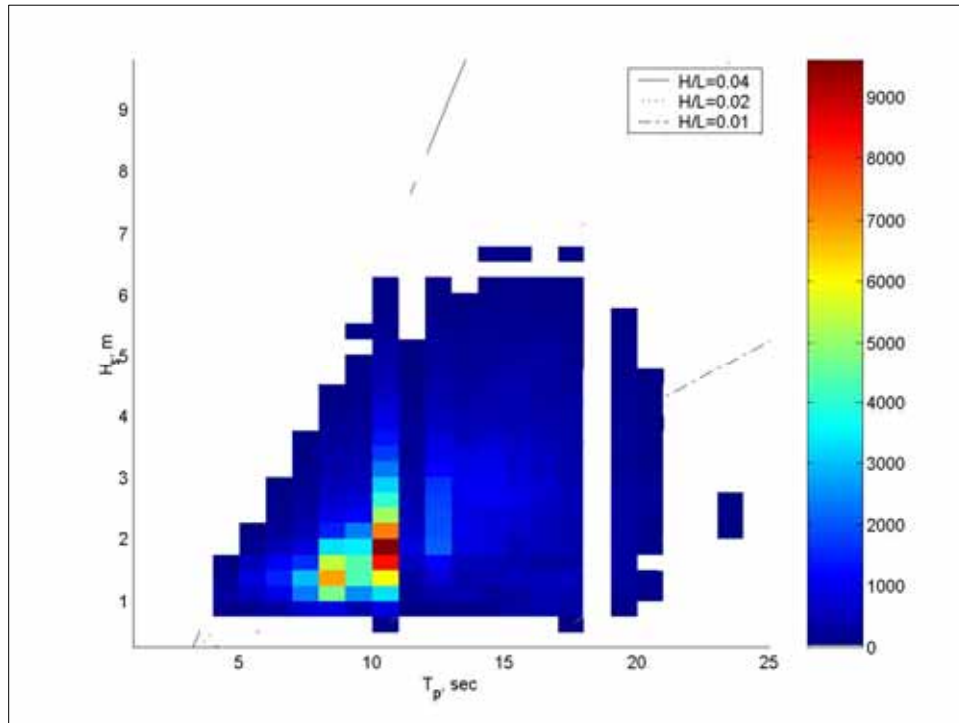
Figure A4.   25-year durations (hr) of H_s and T_p. based on measurements from Grays Harbor CDIP buoy 3601

Spectral shape

The surface elevation spectra for nine of the 10 largest significant wave heights measured at the Grays Harbor buoy are plotted in Figure A5. Modified JONSWAP spectra (Goda 1987) were fitted using the measured H_{m0}, T_p and $\gamma = 1.5$ and 3.3. Unfortunately, the spectral data excludes the storm with the largest wave height on record (H_s=9.74 m, T_p= 15.4 sec, 3 March 1999) because no spectral data are available for this event. The spectral shapes in Figure A5 are similar and suggest that the modified JONSWAP spectrum provides a reasonable approximation to spectral shape for extreme waves approaching the project site. A value of 3.3 was used for γ to generate irregular wave series for the flume tests at CHC as it appeared to give a qualitative best fit to the average spectrum.
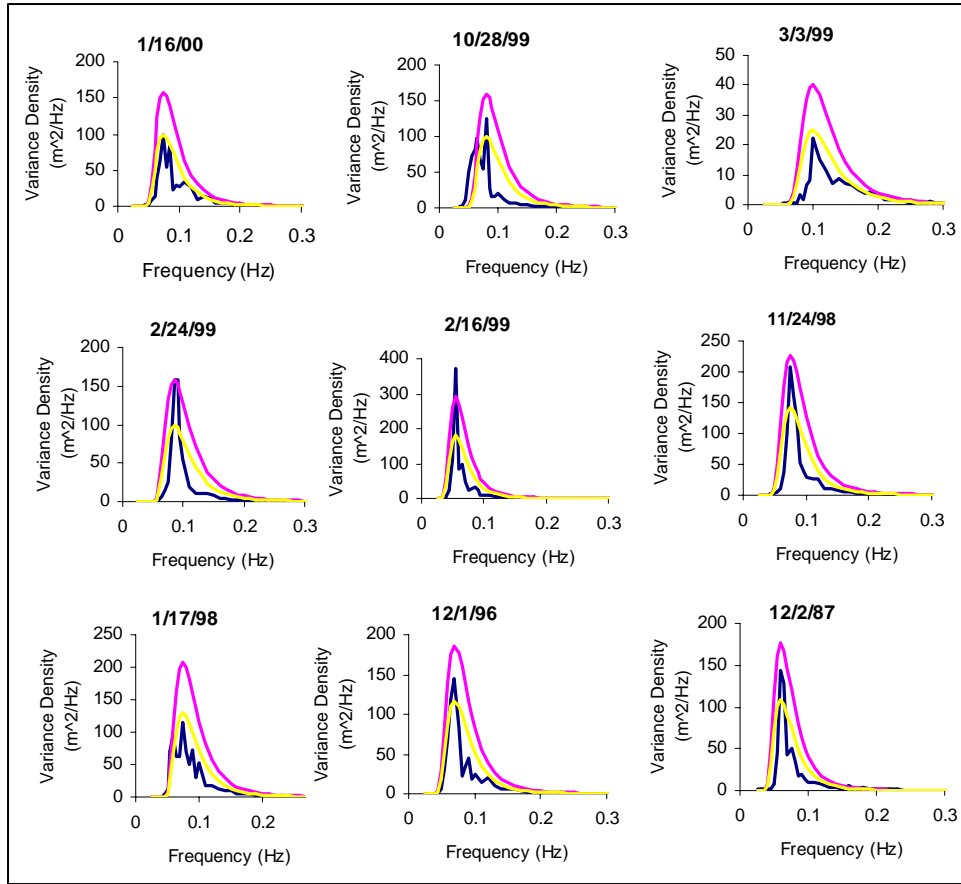
Figure A5.   Nine of 10 most extreme spectra measured at Grays Harbor CDIP buoy between 1982-2000. Note: blue line shows measured spectrum, yellow line is a JONSWAP spectrum with $\gamma = 1.5$ and magenta line is a JONSWAP spectrum with $\gamma = 3.3$

Application of Existing Design Equations for Structure Stability

Several studies have investigated rock stability for low-crested and submerged rubble-mound structures (e.g., van der Meer 1988, van der Meer and Pilarczyk 1990; Givler and Sørenson 1986; Vidal et al. 1992; Vidal, Losada, and Mansard 1995; Vidal, Medina, and Martin 2000; Rufin et al. 1994, 1996). Van der Meer (1988) describes of relevant fundamental parameters for inclusion in formulas for design of rubble-mound breakwaters and revetments: These include: side slope of the breakwater or revetment, significant wave height, H_s deepwater wave steepness, $2\pi H_s/gT_p^2$, wavelength, L_o, or period, permeability, P, damage criterion, S, storm duration, often defined in terms of the number of waves, and median mass of armor stones, M_{50}. According to van der Meer (1988), $S = A_e/D_{n50}$ where A_e is the area of cross-section eroded, as calculated from damaged and undamaged profiles, and D_{n50} is the nominal median armor stone diameter. The onset of damage is generally taken as between 1 and 3. The damage criterion, S, represents the number of stones of a nominal diameter, D_n, which are

removed from the cross section. Other parameters relevant to the case of submerged rubble-mound structures include the submergence, R, the crest width, B, spectral width, the stone gradation, bottom slope (tan α), and water depth at the toe of the structure, $\overline{h}_{toe}$. The Irribarren Number, defined according to Battjes (1974) in its deepwater, ξ_0, and inshore, ξ_h, forms as:

$$\xi_o = \tan \sqrt{\frac{H_o}{L_o}} \ , \ \ \xi_b = \frac{\tan}{\sqrt{H_b / L_o}} \tag{A1}$$

where tan α is the local bottom slope, and H_o and L_o are the deepwater wave height and wavelength, respectively, and H_b is the wave height at breaking. Representative values of the parameters used in analysis and evaluation of a submerged structure at the end of the north jetty are listed in Table A1. Relevant nomenclature is indicated in Figure A6.

Table A1 Representative Parameters for North Jetty, Grays Harbor Environment		
Parameter	**Minimum**	**Maximum**
h_t (m)	-7 (mllw)	-12 (mhhw)
h_c (m)	2.4	4.6
R (m)	-3 (mllw)	5.5 (mhhw)
B (m)	10	15
H_{so} (m)	1	10
T_p (sec)	8	25
tan α	0.015	0.035
ξ_0	0.047	1.09
*H_{50} is the incident significant was height measured in deep water; Tp is the peak period of the incident waves.		

The analyses of Ahrens (1987, 1989) and van der Meer (1988) were concerned with change in crest height in response to wave attack. Ahrens (1987, 1989) defined a number of dimensionless parameters that describe the behavior of reef type structures ($R > 0$). The main parameter is the relative crest height reduction factor ($h_c/ h_c^{'}$) defined as the ratio of crest height at the end of the test (h_c) to the crest height at the beginning of the test, $h_c^{'}$. The two authors apply a dimensionless stability number to describe the wave height relative to the stone size:
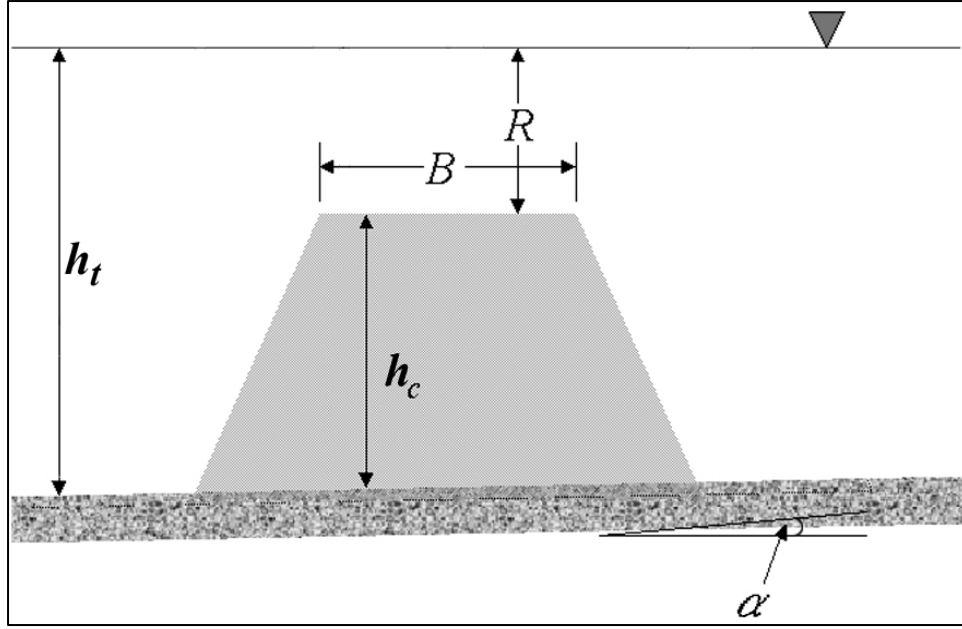
Figure A6.   Submerged breakwater nomenclature

$$N_s = \frac{H_s}{\Delta D_{n50}} \tag{A2}$$

where Δ = relative mass density (ρ_s/ρ -1), D_{n50} = nominal diameter of rock = $(M_{50}/\rho_s)^{1/3}$, and M_{50} median stone mass.

Ahrens (1987, 1989) also introduced the spectral stability number to account for the observation that longer period waves cause more displacement of material:

$$N_s^* = \frac{H^{2/3} L_p^{1/3}}{\Delta D_{n50}} \tag{A3}$$

where L_p is the linear theory wavelength calculated with T_p and the water depth at the toe of the structure.

For dynamically stable reef breakwaters (i.e., breakwaters of low crest elevation which will undergo significant reshaping during wave attack), van der Meer and Pilarczyk (1990) suggest the following equation to predict the equilibrium crest height, h_c:

$$h_c = \sqrt{A_t / \exp(aN_s^*)} \tag{A4}$$

where $a = -0.028 + 0.045C' + 0.034\, h_c'/h - 6 \times 10^{-9}\, B_n^2$ and A_t is the area of structure cross-section, $C' = \exp(aN_s^*)$, $B_n = A_t/D_{n50}^2$, and h is the water depth.

Van der Meer and Pilarczyk (1990) show that the previous equations are valid over a wider range of conditions than the Ahrens (1987, 1989) original equations for h_c. It is possible to draw design curves from these equations, which give the crest height as a function of either N_s^* or H_s.

The previous equations are for dynamically stable reef-type structures where $R > 0$. Van der Meer and Pilarczyk (1990) give a stability formula for statically stable submerged structures that includes the previous class:

$$\frac{h_c'}{h} = (2.1 + 0.1S)\exp\left(-0.14N_s^*\right) \tag{A5}$$

Thus, a functional relationship is provided between the relative crest height of a submerged breakwater, the damage level, S, and the spectral stability number, N_s^*. Stability of submerged breakwaters is a function of the relative crest height, the damage level, S, and the spectral stability number.

For fixed crest height, water level, damage level, and wave height and period, the required ΔD_{n50} can be calculated, giving finally the required stone weight (diameter). Also, wave height versus damage curves can be derived. The analysis conducted by van der Meer and Pilarczyk (1990) did not consider damage to different breakwater segments or the effects of structure side slopes on stability.

The previous analysis by van der Meer and Pilarczyk (1990) is based on the limited experimental data of van der Meer (1988) and Givler and Sørensen (1986) and is valid only for side slopes of 1.5 to 2.5. Van der Meer and Pilarczyk (1990) suggest that because wave attack is concentrated on the crest and less on the seaward slope of a submerged structure, it may be possible to exclude the effect of slope in the analysis. The stability formula (Equation A5) is based upon $0.5 < h_c/h < 1$ and $N_s^* < 12$. Van der Meer and Pilarczyk (1990) noted a large increase in the stability number as h_c/h decreases below 0.45.

Figure A7 shows stable crest stone size as a function of deepwater wave height calculated using the method of van der Meer and Pilarczyk (1990) for a structure with $0.4 < h_c/h < 0.6$. The calculations shown are made for the onset of damage ($S = 2$) for selected wave periods from 10 to 22 sec and for water levels between mllw and mhhw plus storm surge and including mean water level (mwl). Stone size increases with increasing wave height until depth-limited breaking criterion is reached for the north jetty environment. Depth-limited breaking wave heights were estimated assuming a constant nearshore slope of 0.0265 (1:38) and a breaking criterion of $H_b/h = 0.78$ and follows the methodology in the *Coastal Engineering Manual* (2003), Part II, Chapter 4.
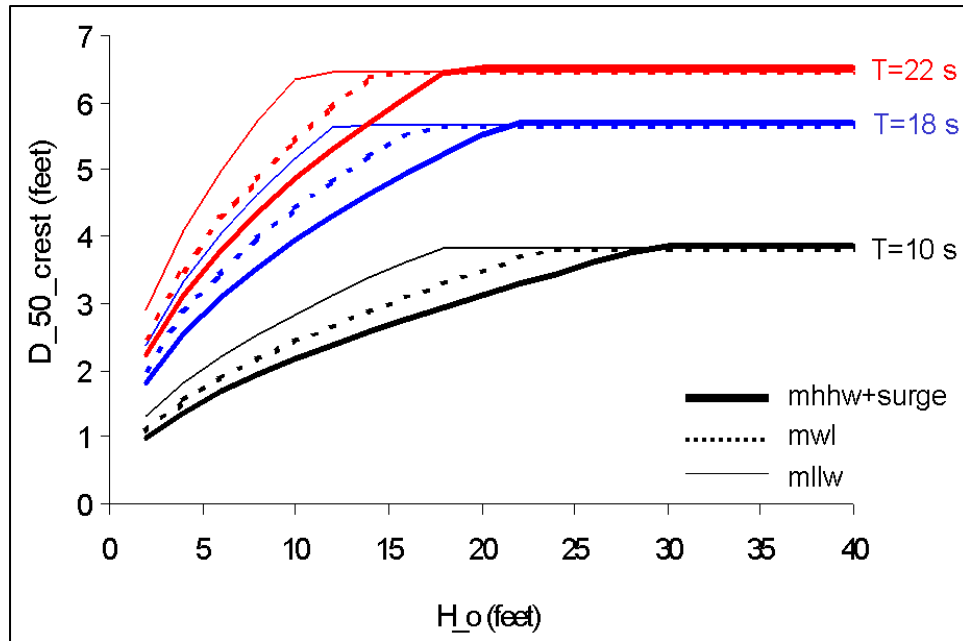
Figure A7.   Crest stone size for a submerged breakwater as a function of deep-
             water wave height for a range of wave periods and water levels for
             Ocean Shores (R=0.5, S=2) following van der Meer and Pilarczyk
             (1990)

Vidal et al. (1992) and Vidal, Losada, and Mansard (1995) conducted laboratory experiments to develop damage curves for various sectors of submerged structures (e.g., front slope, crest, back slope, front head, and back head). For each sector, damage curves relating the nondimensional freeboard, $R_d = R/D_{50}$, (where $R = h_c - h$), with the stability number, N_s, for a given damage level were obtained.

Vidal et al. (1992), Vidal, Losada, and Mansard (1995), Vidal, Medina, and Martin (2000), and Rufin et al. (1994, 1996) show that the most critical location for stability on submerged breakwaters is at the crown edge and backslope. Backslope stability increases significantly with increasing submergence.

Based on results of these and other physical model experiments, Vidal, Medina, and Martin (2000) developed a methodology and proposed a series of equations based on R_d and N_s to assess stability and damage of submerged structures. The procedure involves calculating the armor size, D_∞, of a conventional emergent rubble-mound breakwater with the same characteristics (e.g., core, layers, slope, and damage level) by means of any available formula. In this case, we have applied the well-known Hudson formula (SPM 1984) to calculate D_∞ for conventional emergent breakwater assuming a unit weight of armor stone unit of 165 lb/cu ft. A value of 2 for K_d was deemed appropriate for rough angular quarry stone, placed randomly and subject to breaking waves (*Shore Protection Manual* 1984, Table 7-8). D_∞ is then applied to scale the freeboard ($R_{d\infty} = R/D_\infty$). The front slope armor unit size can be determined from:

$$D_{fs} = D_{\infty} \frac{N_{s(\infty)}}{N_{fs}(R_{d\infty})} \tag{A6}$$

where $R_{s(\infty)}$ is the nonovertopped limit of the stability number. To calculate the size of the armor units of the crest, D_c, first the front-slope size of the units is calculated as Equation A6 and applied to rescale the nondimensional freeboard ($R_d = R/D_{fs}$). The size of the armor units is:

$$D_{cs} = D_{fs} \frac{N_{fs}(R_d)}{N_{sc}(R_d)} \tag{A7}$$

Figure A8 is based on this methodology (Vidal, Medina, and Martin 2000). The analysis extends the available knowledge on stone size for conventional, emergent, breakwaters to submerged breakwaters. In this case, the Hudson formula and values of the coefficients K_d found in the *Shore Protection Manual* (1984, Tables 7-8) are inserted to calculate the stable stone size needed for a submerged breakwater, (K_d=2 and freeboard = 3 m).

Stability formulae for conventional surface-piercing (emergent) rubble-mound structures are based on an extensive set of experimental and prototype data. However, the formulae and data applied in the previous section for submerged structures are based on a much more limited data set (e.g., Vidal et al. 1992; Vidal, Losada, and Mansard 1995; van der Meer 1988; Givler and Sørensen 1986). As a result only limited design formulae are available (e.g., van der Meer and Pilarczyk 1990; Vidal, Medina, and Martin 2000) with which to evaluate stability of a submerged spur in the north jetty environment. Further, the limited experimental data are more applicable to structures that have steeper slopes and are closer to the surface than the design concepts being evaluated for the north jetty. Also, much of the physical testing to date has been based on intermediate water depths and few, if any, are based on shallow water and breaking waves (Melby and Kobayashi 1998). Caution is appropriate in evaluating the results presented thus far. A physical model test is indicated given the scope of this project.
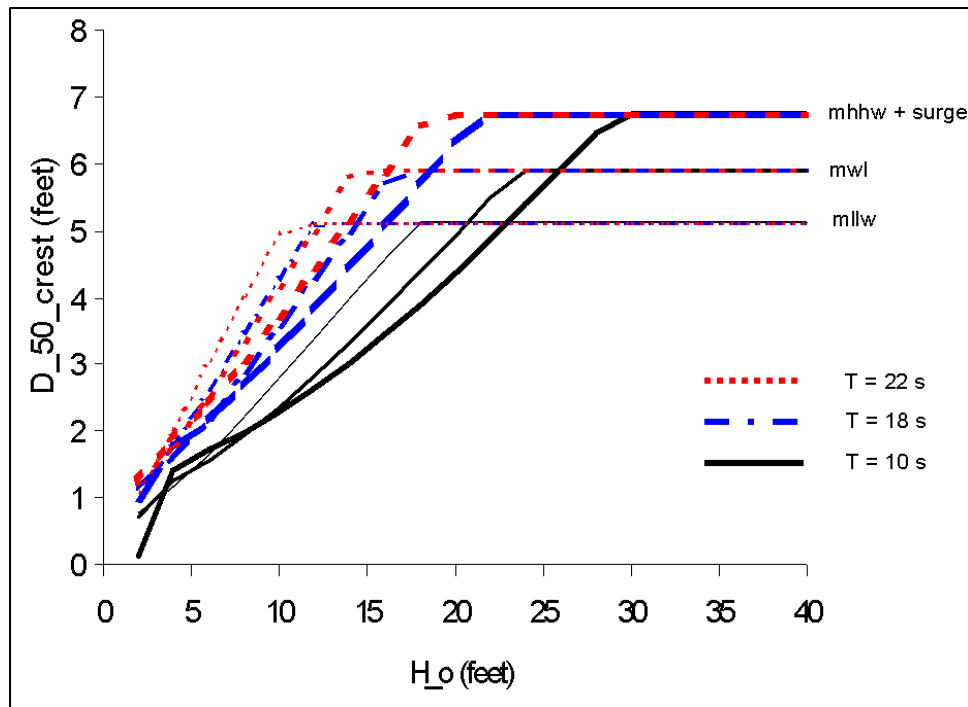
Figure A8.　Crest stone size required for a submerged breakwater as a function of deepwater wave height for a range of wave periods and water levels for case of Ocean Shores based on Vidal, Medina, and Martin (2000) (m = 0.0265; K_d = 2)

Waves in deep water offshore of Grays Harbor range in significant height between 1 and 10 m and have significant periods from less than 5 sec to almost 25 sec as confirmed by over 19 years of measurements at the CDIP wave buoy. Applying the equations of Vidal, Medina, and Martin (2000) and for these conditions suggests that the general range of stability numbers for submerged structures is typically between 1 to 3, whereas the value for the stability number for the proposed spur exceeds this range. Calculations of crest stone sizes for conditions at north jetty following van der Meer and Pilarczyk (1990) and Vidal, Medina, and Martin (2000) suggests stone diameter of at least 5-7 ft might be required to achieve stability (Figures A7 and A8). However, considering the high relative submergence at the end of the north jetty, and by considering a lower structure side slope than is conventionally used (e.g., 7:1 or 5:1 instead of 1.5: 1 or 2:1) and perhaps a broader crest width, it may be possible to achieve a stable structure using the smaller stone size. Furthermore, the north jetty environmental conditions and submerged spur geometry are generally close to or just beyond the limits of most experimental investigations of stability and structure performance. Therefore, the possibility of achieving stability with a relatively small stone size was the focus of a 2-D laboratory investigation at CHC.

Description of 2-D Physical Model

The 2-D physical model investigation is described in terms of experimental setup, test program and an assimilation of the results. More detail concerning the physical model test results may be found in Davies (2001).

Model scale

Physical model studies of breakwater armor stone at Froude-scales between 1:30 and 1:50 are typical and have been successfully used in the past for physical model studies of conventional rubble-mound structures (Hughes 1993). However, for a wholly submerged structure in a high-energy breaking wave environment, a larger scale model is indicated. The relatively small stone size and rock gradation indicated by the constructability analysis will result in smaller porosity and smaller transmissivity to fluid flow than for conventional structures. Therefore, interstitial viscosity may be significant in contrast with the situation of conventional rubble-mound structures. A larger scale model permits greater possibility of ensuring the correct scales of turbulence and Reynolds law scaling.

Also, the presence of large breaking waves at north jetty introduces significant amounts of breaking-generated turbulence that may be a decisive factor controlling stone stability. Therefore, because of the structure's submergence and the potential importance of breaking-generated turbulence and interstitial flow, a large model scale was required. The Wave Research Flume at the CHC was chosen for the study because it can handle large-scale models (the flume is 98 m long and 2.8 m deep, and can generate waves up to 1.5 m high). The flume also offers viewing windows at the test section to allow visual assessment of structure performance.

A 1:20 Froude-scaled model of the spur cross section was built in the Wave Research Flume (Figures A9 to A13).

Scaling of rock weight

The model scale factor of the armor stone must be carefully selected to ensure that the submerged stability of the stone is reproduced correctly. This is required in cases where the densities of the model stone and prototype stone differ, and where fresh water is used in the model to represent sea water.

The Hudson formula (*Shore Protection Manual* 1984) is a widely accepted equation for the stable weight of submerged armor material under wave attack. Scaling armor weights using this formula will yield a model stone or armor unit having the same stability as the prototype condition.
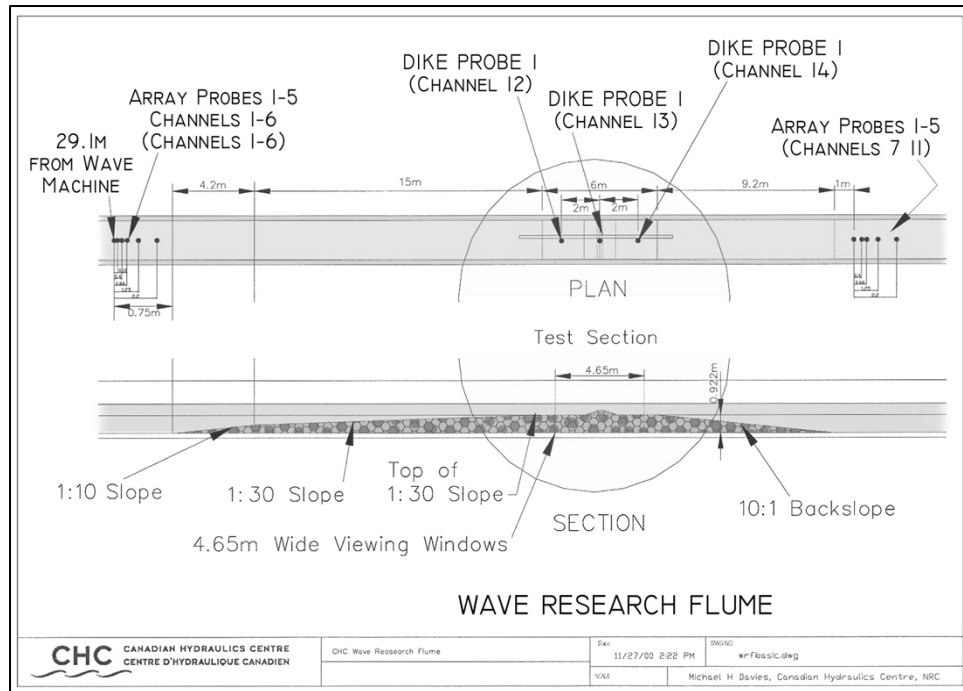
Figure A9.   Cross section and plan view of test setup in Wave Research Flume
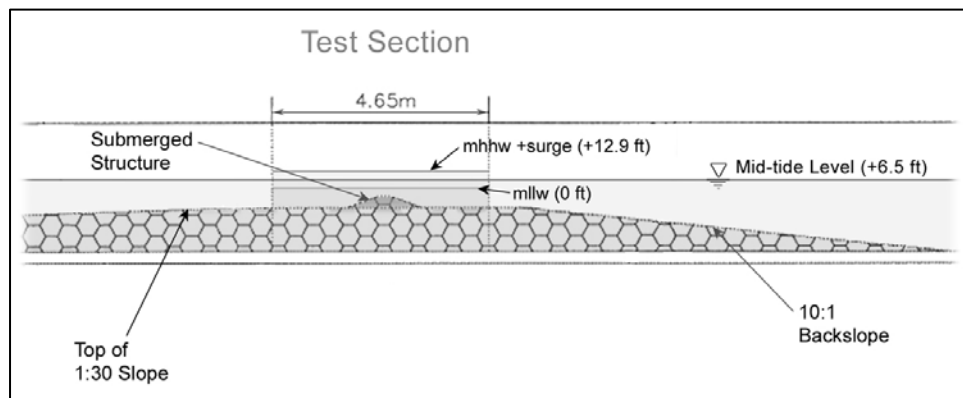
Figure A10. Close-up of test section showing water levels used in test program

Figure A11. Construction of spur showing templates

Figure A12. Construction of spur as seen through viewing windows at test section

Figure A13. Spur with templates removed

The Hudson formula is:

$$W = \frac{w_r H^3}{K_D \left(S_r - 1\right)^3 \cot\theta} \tag{A8}$$

where

W = weight of armor material (N)

w_r = unit weight of the armor material (N/cu m)

H = design wave height (m)

θ = angle of the structure

K_D = stability coefficient of the armor material

S_r = specific gravity of the armor material and can be written as
$S_r = w_r / w_w$, where w_w is the unit weight of the water (N/cu m)

To scale for physical modeling purposes, the relationship:

$$N_w = \frac{N_{wr} N_H{}^3}{N_{K_D} N_{(S_r-1)}{}^3 N_{\cot\theta}} \tag{A9}$$

where N represents the ratio of prototype to model values of a quantity, should be maintained. Assuming that the model stone has the same approximate shape ($\therefore N_{K_D} = 1$), and because the model is undistorted ($\therefore N_{\cot\theta} = 1$), the prior relationship can be reduced to:

$$N_W = \frac{N_{w_r} N_H{}^3}{N_{(S_r - 1)}{}^3} \tag{A10}$$

The rock placed in the model was limestone having a unit weight of approximately 2,710 kg/cu m. The prototype armor was assumed to have an identical unit weight of 2,710 kg/cu m. This is a conservative assumption because rock sources used in rubble-mound structures in the Pacific Northwest are typically igneous in origin with higher unit weights (2,850-3,000 kg/cu m). Therefore, the scale of the unit weight of rock becomes unity, $N_{w_r} = 1$.

Assuming a seawater density of 1,025 kg/cu m, the scale of the specific gravity term is:

$$N_{(S_r - 1)} \quad = \quad N_{\left(\frac{w_r}{w_w} - 1\right)} \quad = \quad \frac{\left(\dfrac{2710}{1025} - 1\right)}{\left(\dfrac{2710}{1000} - 1\right)} \quad = \quad 0.961 \tag{A11}$$

The scale of the wave height is the model length scale (i.e., $N_H = 20$); therefore, the weight scale for the armor stone is:

$$N_W = \frac{(20)^3}{(0.961)^3} = 9{,}014 \approx 20.81^3 \tag{A12}$$

To account for the fresh water used in the model, the weight of the stone used in the model was roughly 12.5 percent lighter than that given by standard Froude scaling. (According to standard Froude scaling, the scale for rock weight would be $20^3 = 8{,}000$.) The assumed specific gravity for the full-scale armor stone was $S_r = 2.71$.

All armor stone gradations used had a $W_{50} = 2{,}426$ lb. Select armor placed on the upper portion of the spur had a gradation of ± 30 percent of W_{50} (nominally 2.5 to 3.5 ft diam). The sublayer gradation was -90 to $+30$ percent of W_{50}. (nominally 1.5 to 3.5 ft diam).

The prior relationships and a model specific gravity of $S_r = 2.71$ were used to determine the model armor stone gradations as presented in Table A2 and Figure A14. For test series A, which was a preliminary evaluation of armor stability, a single gradation was used which was an initial approximation to the

target armor layer. The sublayer was modeled for the armor layer stones. For all subsequent tests, a closer match to the armor layer gradation was obtained using hand-picked stones, and the sublayer was modeled using a mechanically sorted gradation which provided a reasonably close match. These gradations are shown graphically (in full-scale units) in Figure A14.

Table A2 Armor Gradations Used in Model						
Armor Type	**Model M (grams)**			**Full-scale W (lb)**		
	M_{min}	M_{50}	M_{max}	W_{min}	W_{50}	W_{max}
Target from PI Engineering	104	138	166	1820	2426	3033
Armor layer for test series A	98	132	166	1630	2196	2761
Hand-picked upper armor (Tests B onward)	100	138	160	1664	2426	2828
Sublayer as specified by PI Engineering	14	138	180	243	2426	3154
Sublayer used in model (Tests B onward)	10	140	208	166	2329	3460
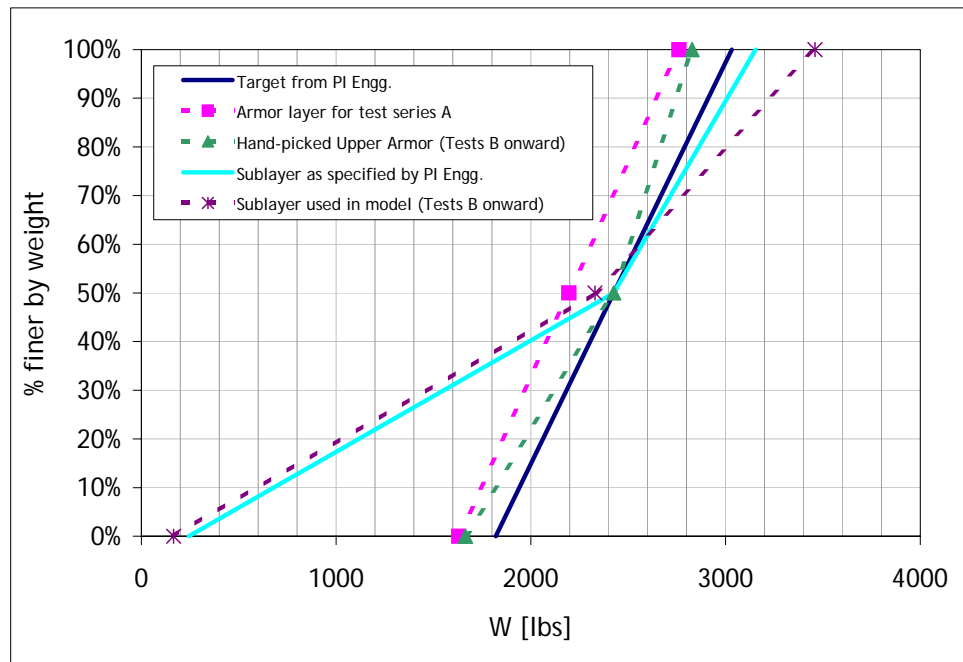
Figure A14. Stone gradations

Bathymetry

The bathymetry at the north jetty varies considerably. In cases where the wave height is large relative to the local water depth, depth-limited breaking can reduce wave height. Over a flat bottom, once wave breaking is initiated, energy will generally be lost through whitecapping and turbulence until the wave height is reduced to about half the water depth. The rate of energy dissipation varies considerably with offshore slope. In general, a steep offshore slope can create worse wave conditions than a mild one. For the Grays Harbor site, an analysis

was undertaken of the site bathymetry (1999) to select the offshore slope that resulted in the most severe waves at the project site. This occurred near the southerly limit of the spur where waves propagating from the west-southwest traveled up a slope of approximately 1:40.

A second consideration in setting the offshore bathymetry is that the physical model needed to be laid out such that a sufficient depth of water exists at the wave machine to allow generation of the required storm waves.

During the testing program, concerns were raised that the offshore slope in the physical model may not be in fact flat enough, thereby allowing larger wave heights at the test section than would exist in nature. To remedy this problem, sandbags were placed offshore of the test section to promote depth-limited breaking. This effectively reduced the nearshore slope to 1:60 from the test section out to the 33-ft contour (some 500 ft seaward of the test section). By comparison, the original slope was 1:30 from the test section, which positioned the 41-ft contour 500 ft seaward of the test section.

Three different offshore bathymetries were modeled over the course of the test program:

a. The initial bathymetry consisted of a 1:30 nearshore slope extending seaward to the 57.8-ft contour. From there, a 1:10 slope extended out to the floor of the flume, which is at the 110.5-ft contour. (The offshore slope used in the 2-D testing was composed of a 1:30 slope extending 15 m from the test section. This slope extended seaward 980 ft to a depth of 58 ft). The test section was built on a 6-m-wide flat section at the viewing windows as shown in Figure A9. This bathymetry was used for Tests A, B, C, and W.

b. The second bathymetry was a modification of the initial slope to allow for a sediment bed at the test section. Construction of a 15-cm-deep sand bed at the test section necessitated a slight steepening of the offshore region just in front of the test section. This bathymetry was used for Test D. To alleviate the steepening of the offshore slope sand bags and a concrete beam were placed offshore to match a 1:60 offshore slope.

c. Once the effect of the sand bed had been evaluated, the sand section was removed and the bed returned to initial conditions. With the return to the original water level in the flume, the sandbags were moved further offshore (but the concrete beams were removed) to try to maintain the milder 1:60 offshore slope. This bathymetry was used for Tests E, F, and G.

Instrumentation

Wave gauges. Water levels and waves were measured with CHC capacitance wave gauges. Tests of these probes show that they exhibit a highly linear water level to voltage response, with calibration errors of less that 0.5 percent model scale over the whole calibration range. This represents an accuracy of ±0.5 mm in

the model, or ±10 mm prototype. These probes are calibrated at the start of the test series and whenever the system is disconnected for modifications. Zero readings for each gauge are taken at the start of each test. All wave gauges are sampled at 20 Hz. A total of 14 wave gauges were used in the tests. The layout of the wave gauges in the model is shown in Figure A9.

Velocity measurement. Velocities in the flume were measured using two SonTek acoustic Doppler velocity gauges (ADV). The SonTek 16-MHz MicroADV (Figure A15) is a single-point, high-resolution, 3-D Doppler current meter. MicroADV Doppler processing techniques provide several important advantages: 3-D velocity measurements in a remote sampling volume; invariant factory calibration (no periodic recalibration required); simple operation; direct calculation of turbulent parameters such as Reynolds stress; and excellent low-flow performance. The two ADVs were mounted on a beam over the test section.

Video and still photography. Video and still photography was acquired during all tests. Still photographs were taken before and after each test to document any stone displacement. All photographs were taken with a digital camera and catalogued in the project files. The video records allow visual interpretation of interaction between the structure and the breaking waves. Selected video segments have been digitized and stored as MPEG movie clips.

Figure A15. SonTek 16 MHz ADV

Analysis

Waves were sampled during all tests. After completion of a test, the data files were analyzed for the time- and frequency-domain characteristics of the measured waves and velocities. Summary plots of wave and current time-series and tables of summary descriptive parameters were produced. Damage to the structure was monitored during testing. After each test, photos were taken and damage summaries compiled. The changes in profile of the sediment-control spur were measured intermittently.

Analysis of waves and currents

Standard Generalized Data Acquisition Package (GEDAP) spectral and time-domain analysis programs were used to analyze the waves measured in the model. Details are provided in Davies (2001, Section 6.1). Current measurements were made for Test Series D onwards. Data are summarized in Davies (2001, Appendix 3) in terms of mean, maximum, and minimum velocities measured at Gauge 1 (center of water column at center line of spur) and Gauge 2, 2 m landward of the spur.

Damage

Damage was measured by visual analysis of stone (or geobag) mobility, supported with both video and digital still photography. Stone counts were made in two ways:

   a. The number of stone movements observed during a 100-wave interval was recorded to provide an estimate of the average number of stones moving per wave. This was performed over the entire test section so the stone counts provided in this report represent stone movements that would occur over a 40-m-wide section of the sediment-control spur in nature.

   b. The total number of stones removed from the structure was counted at the end of each test segment. This number is reported as a total for the 40-m-wide section of the spur being tested in the flume.

Overview of Test Program

The test program started on 16 January 2001 and continued through 23 February 2001. Approximately 160 tests were run on seven test configurations (Davies 2001, Section 6.1). Configurations are identified by a letter, A through G. The test series are summarized in Table A3.

A sequential test log and detailed description of the tests and associated results are presented in Davies (2001). Results presented relate to stability and stone mobility, structure-seabed and structure-sand interactions, geobag stability, influence of offshore bathymetry on wave field and structural stability, and wave transformations and transmission.

Table A3
Summary of Model Test Series

Test Series	Structure	Waves	Tests
A	Single gradation rock	Hs 4 to 10 m Tp 12 to 22 sec	37
B	Two-layer rock (5H:1V seaward slope)	Hs 4 to 8 m Tp 18 to 22 sec	15
C	Two-layer rock (3H:1V seaward slope)	Hs 4 to 8 m Tp 18 to 20 sec	7
D	Two-layer rock (5H:1V seaward slope); 15 cm sand bed	Hs 4 to 8 m Tp 16 to 20 sec	14
E	Single outer layer rock (5H:1V seaward slope); sand core	Hs 4 to 10 m Tp 18 to 20 sec	7
F	Geobag	Hs 4 to 10 m Tp 18 to 22 sec	16
G	Two-layer rock (5H:1V seaward slope); sand slurry matrix	Hs 4 to 10 m Tp 18 to 20 sec	12
W	None	As in A	34

Damage Analysis

With respect to the rock-armored structure, the total stones displaced per storm segment can be used to develop an empirical damage function. The damage function expresses the total number of armor units displaced per hour of storm segment, N_d, as a function of H_s - T_p combinations. The expected duration of any given H_s - T_p combination is shown in Figure A16 and the damage function is shown in Figure A17. Multiplying the damage function by the expected wave durations yields the expected lifetime damage per 100 ft run of spur. Integrating the function over all H_s and T_p provides an estimate of the total stone damage expected in a 25-year life cycle (Figure A18). The results presented in Figure A18 indicate a total stone damage of 98 stones/100 ft over 25 years. This number is small in relation to the total number of stones composing the surface of the structure. Typically, there are about 2,000 stones on the surface of the spur per 100 m length. Therefore, the 98 stones/100 ft equates to about 5 percent of the stones on the surface of the structure.

Overview of Physical Model Tests

An overview of damage results from the test program is provided in this appendix. Detailed results are provided in Davies (2001).

Both the rock-armored structure and the geobag structure performed satisfactorily in the flume tests at CHC. Some stone movement was observed during the most severe wave and water levels tested. However, stone movements did not develop to an extent that would detract from the performance of the structure. No significant degradation of the spur crest was experienced during the testing.
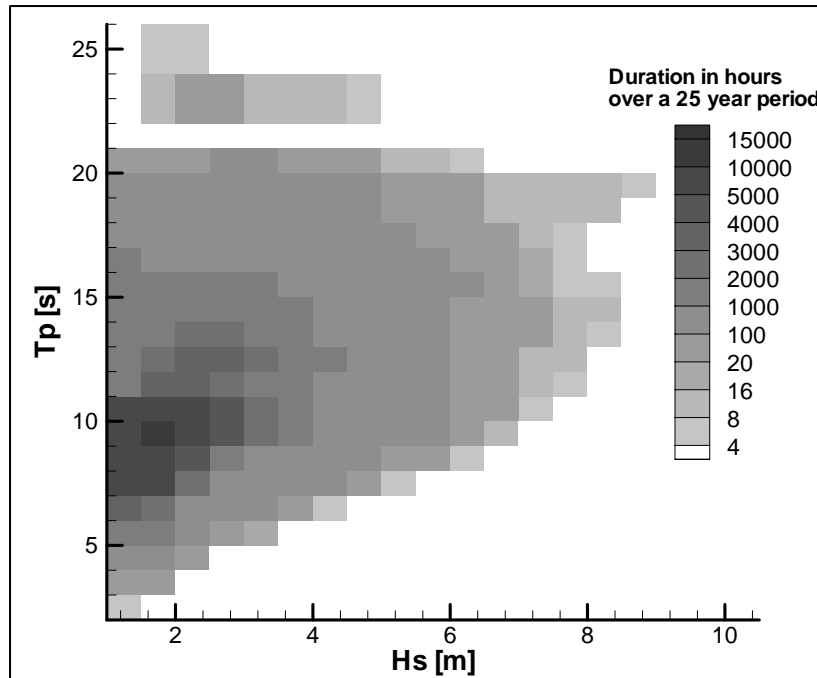
Figure A16. Expected $H_s - T_p$ durations (in hours) over a 25-year life cycle based on measured waves offshore of Grays Harbor
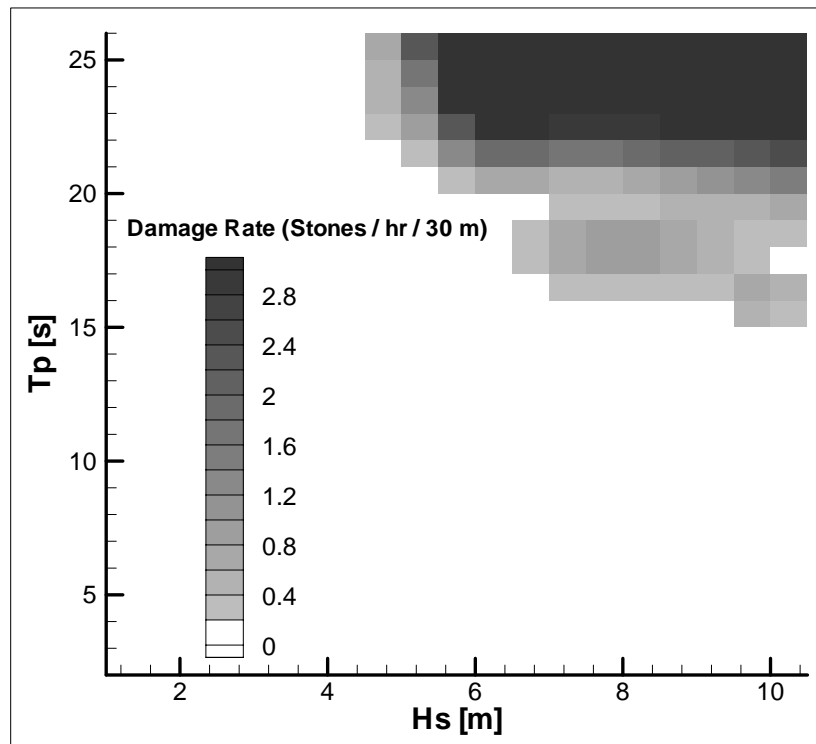
Figure A17. Empirical damage function expressing number of stones removed per 30 m of spur per hour of storm for each H_s - T_p combination
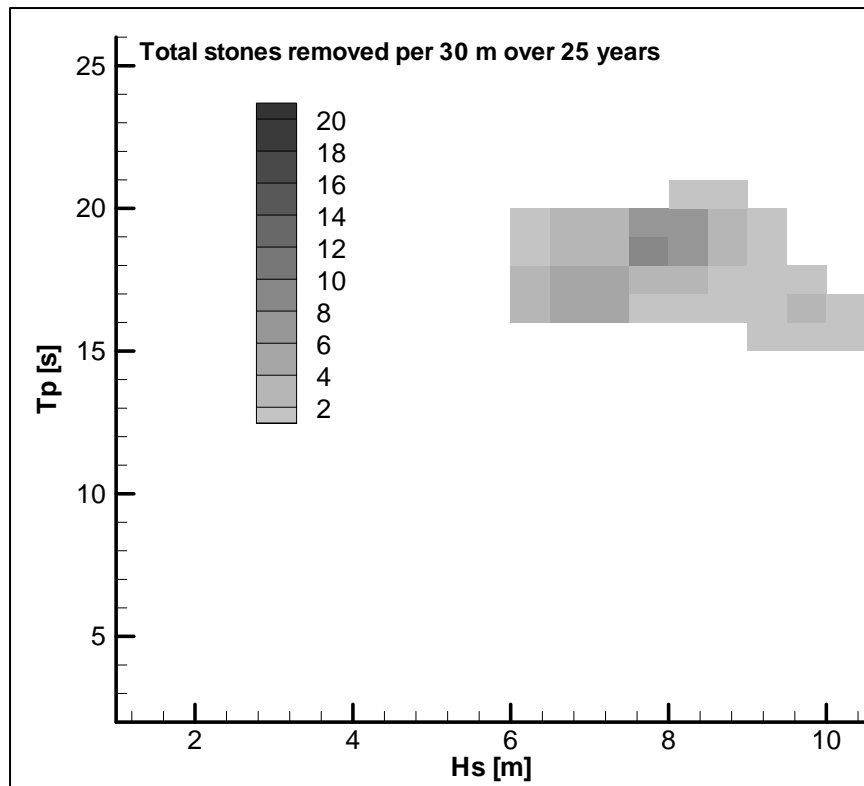
Figure A18. Expected damage levels over a 25-year period

The experimental program also examined interactions between the rock-armored structure and the sand seabed. Partial infilling of the voids of the sediment-controled spur was allowed to occur during some of the testing. This was not seen to adversely affect structure stability. Wave transmission measurements were also made during the test program, and these are included in Davies (2001).

References

Ahrens, J. P. (1987). "Characteristics of reef breakwaters," Technical Report CERC-87-17, Coastal Engineering Research Center, U.S. Army Engineer Waterways Experiment Station, Vicksburg, MS.

Ahrens, J. P. (1989). "Stability of reef breakwaters," *Journal of Waterway, Port, Coastal, and Ocean Engineering* 115(2), ASCE.

Battjes, J. A. (1974). "Surf similarity," *Proceedings 14th Coastal Engineering Conference*, ASCE, 466-479.

Coastal Data Information Program. (2000). "Grays Harbor Washington Buoy, Station No. 03601," CDIP Web page http://cdip.ucsd.edu/.

Davies, M. H. (2001). "Grays Harbor dike testing," Technical Report HYD-CTR-103 V0.1, Canadian Hydraulics Centre, National Research Council, Canada.

Givler, L. D., and Sørensen, R. M. (1986). "An investigation of the stability of submerged homogeneous rubble-mound structures under wave attack," Lehigh University, H.R. IMBT Hydraulics, Report No. IHL-110-86.

Goda, Y. (1987). "Statistical variability of sea state parameters as a function of wave spectrum," *Proceedings IAHR Seminar on Wave Analysis and Generation in Laboratory Basins*, Lausanne.

Headquarters, U.S. Army Corps of Engineers. (2003). "Surf zone hydrodynamics," *Coastal Engineering Manual*, Part II-4, Washington, DC.

Hughes, S. A. (1993). "Physical models and laboratory techniques in coastal engineering," *Advanced Series on Ocean Engineering* 7, 568, World Scientific, New Jersey.

Kraus, N. C. (editor). (2000). "Study of navigation channel feasibility Willapa Bay, Washington," Technical Report ERDC/CHL TR-00-6, U.S. Army Engineer Research and Development Center, Vicksburg, MS.

Kraus, N. C., Arden, H. T., and Simpson, D. P. (editors). (2002). "Study of navigation channel feasibility, Willapa Bay, Washington, Report 2: Entrance channel," ERDC/CHL TR-00-06, U.S. Army Engineer Research and Development Center, Vicksburg, MS.

Melby, J. A., and Kobayashi, N. (1998). "Progression and variability of damage on ruble mound breakwaters," *Journal of Waterway, Port, Coastal, and Ocean Engineering* 124(6), ASCE, 286-294.

Pacific International Engineering[PLLC]. (2000). "Documentation of existing conditions: Grays Harbor North Jetty Spur Dike feasibility study project," Pacific International Engineering[PLLC], for the Coastal and Hydraulics Laboratory, U.S. Army Engineer Research and Development Center.

Rufin, Jr., T. M., Mizutani, N., Totsuka, N., Kurata, K., and Iwata, K. (1994). "Wave forces acting on armor unit of a submerged wide-crown breakwater," *Proceedings 4th International Offshore and Polar Engineering Conference*, Osaka, Japan, 556-563.

Rufin Jr, T. M., Mizutani, N., and Iwata, K. (1996). "Estimation method of stable weight of spherical armor unit of a submerged wide-crown breakwater," *Coastal Engineering* 28(1-4), 183-228.

Shore protection manual. (1984). 4th ed., 2 Vol, U.S. Army Engineer Waterways Experiment Station, U.S. Government Printing Office, Washington, DC.

U.S. Army Engineer District, Seattle. (1974). "Design memorandum, north jetty rehabilitation," U.S. Army Corps of Engineers.

van der Meer, J. W. (1988) "Rock slopes and gravel beaches under wave attack," Ph.D diss., Delft University of Technology, also Delft Hydraulics Communication No. 396.

van der Meer, J. W., and Pilarczyk, K. W. (1990). "Stability of low-crested and reef breakwaters," *Proceedings 22ⁿᵈ Coastal Engineering Conference* 2, ASCE, 1,375-1,388.

Vidal, C., Medina, R., and Martin, F.L. (2000). "A methodology to assess the armor unit stability of low-crested and submerged rubble-mound breakwaters," *Proceedings Coastal Structures '99*, Balkema, Rotterdam, 721-725.

Vidal, C., Losada, M. A., and Mansard, E. P. D. (1995). "Stability of low-crested rubble-mound breakwater heads," *Journal of Waterway, Port, Coastal, and Ocean Engineering* 121(2), 114-122.

Vidal, C., Losada, M. A., Medina, R., Mansard, E. P. D., and Gomez-Pina, G. (1992). "A universal analysis for the stability of both low-crested and submerged breakwaters," *Proceedings, 23ʳᵈ Coastal Engineering Conference*, ASCE, 1,679-1,692.

Appendix B
Physical Modeling of North Beach and Jetty[1]

Introduction

Appendix B contains supplemental figures and tables to augment Chapter 5 of Volume I of this report. Figures include photographs taken during studies with coal tracer and dye, figures showing wave heights at each of the wave gauge locations, and plots showing differences in wave heights between structural alternatives for the same generated storm and water level. Tables summarize wave heights and wave periods calculated at each of the wave gauges, and velocities calculated at each of the velocimeters. Where available, figures of coal tracer studies and dye studies include a label indicating time from start of experiment. Times are given in model scale and should be multiplied by 8.66 to convert to prototype scale.

Figures B1 through B55 document results obtained with storms from the west-northwest. Figures B1 through B14 contain photographs taken during experiments with coal tracer, and Figures B15 through B46 show photographs taken during experiments with dye. Figures B47 through B55 show differences in calculated wave heights at each wave gauge with Alt 2A compared to wave heights calculated with Alt 1. The alternatives are described in Chapter 1 of Volume 1.

Figures B56 through B91 document results obtained with storms from the southwest. Figures B56 through B64 contain photographs taken during experiments with Alt 1 and Figures B65 through B73 contain photographs taken during experiments with Alt 2A. Differences in calculated wave heights at each wave gauge with Alt 2A compared to Alt 1 are shown in Figures B74 through B82; differences in calculated wave heights at each wave gauge with Alt 3B compared to Alt 1 are shown in Figures B83 through B91.

Figures B92 through B113 document results obtained during experiments with Alt 2A and the GENEralized model for SImulating Shoreline change

---

[1] Written by Donald L. Ward and Julie A. Cohen, Coastal and Hydraulics Laboratory, U.S. Army Engineer Research and Development Center, Vicksburg, MS.

(GENESIS) 5-year projected shoreline. Photographs from dye studies taken during runs with storms from the west-northwest are contained in Figures B92 though B97, and storms from the southwest are contained in Figures B98 though B106. Figures B107 through B113 show differences in wave heights at selected wave gauge locations between Alt 2A with the existing shoreline and Alt 2A with the GENESIS 5-year projected shoreline.

Wave heights calculated from displacements in water-surface elevation at each wave gauge for storms from the west-northwest are tabulated in Tables B1 through B9 for Alt 1 and Alt 2A. Velocities from each velocimeter are tabulated in Tables B10 through B18 for Alt 1 and Alt 2A during storms from the west-northwest.

Wave heights calculated during storms from the southwest are tabulated in Tables B19 through B27 for Alt 1, Alt 2A, and Alt 3B. Velocities are tabulated in Tables B28 through B36.

Values from experiments with Alt 2A and the GENESIS 5-year projected shoreline are listed in Tables B37 through B64. Tables B37 through B42 document wave heights measured during storms from west-northwest, and Tables B43 through B48 document velocities measured during storms from west-northwest. Tables B49 through B55 include wave heights measured during storms from the southwest, and Tables B56 through B64 documents velocities measured during storms from southwest. Water levels references in this appendix are: mean lower low water (mllw), mean tide level (mtl), and mean high water (mhw).

Figures for Storms from West-Northwest

Coal tracer studies

Figures B1 through B14 include photographs taken during coal tracer studies with storms from the west-northwest. Figures B1 through B7 were taken during experiments with Alt 1. Figures B8 through B14 were taken during experiments with Alt 2A.
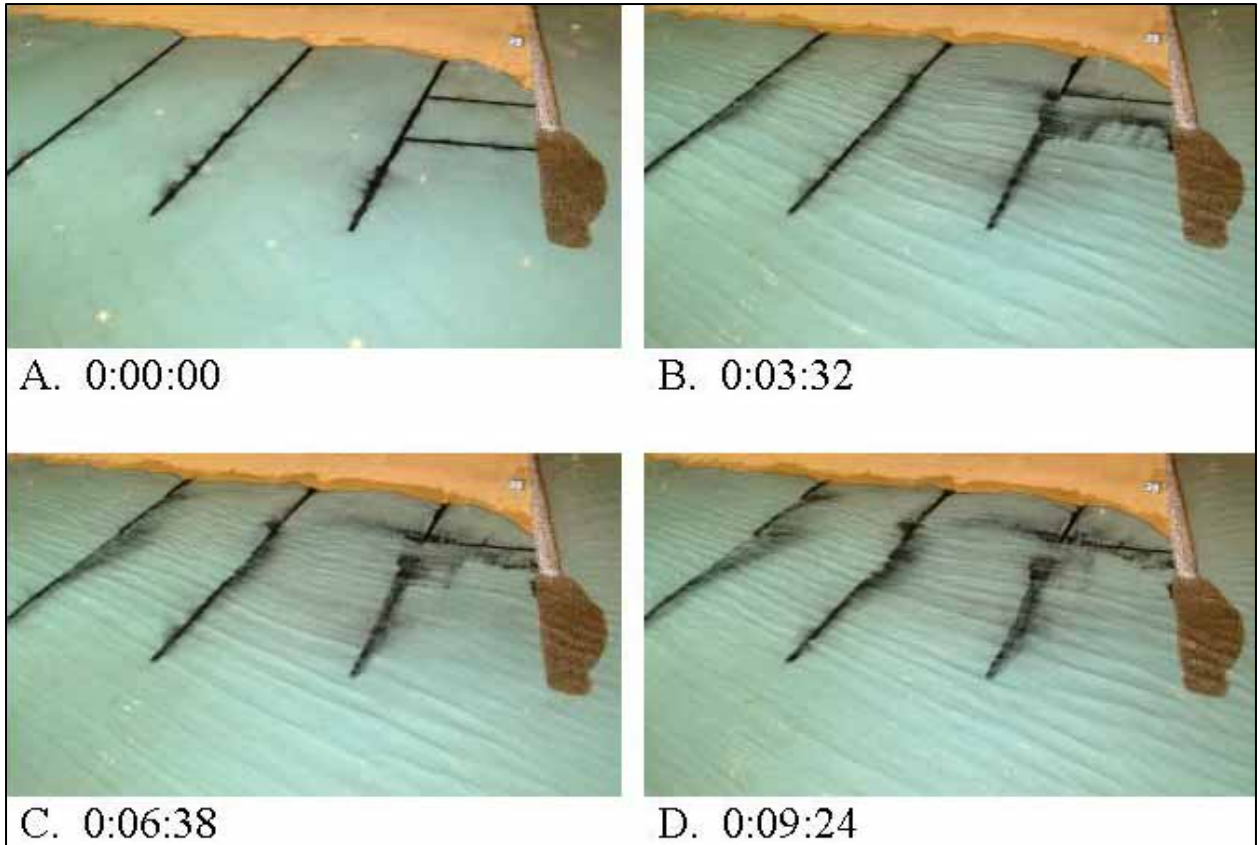
Figure B1.   Coal tracer study for 2-m, 9-sec waves at mllw for Alt 1
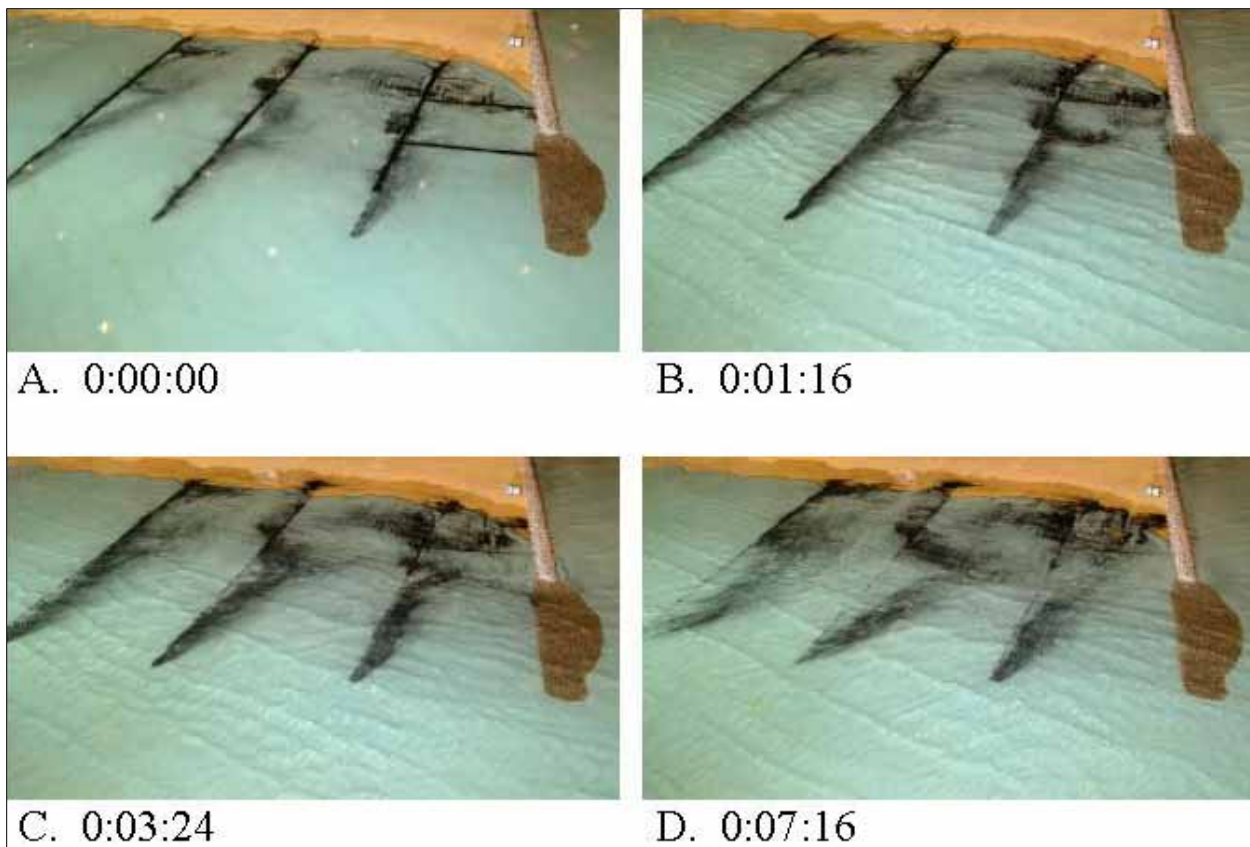
Figure B2.   Coal tracer study for 5-m, 13-sec waves at mllw for Alt 1
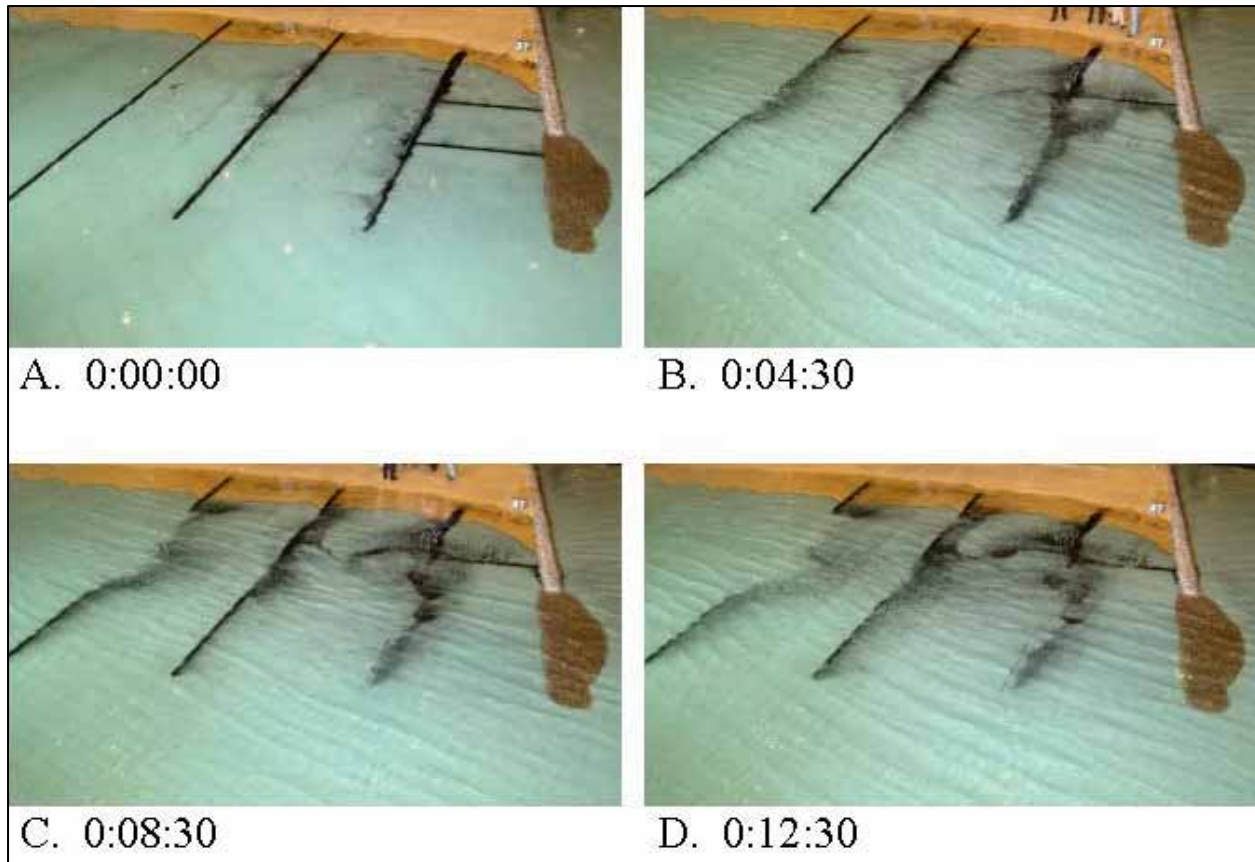
Figure B3.   Coal tracer study for 2-m, 9-sec waves at mtl with flood current for Alt 1
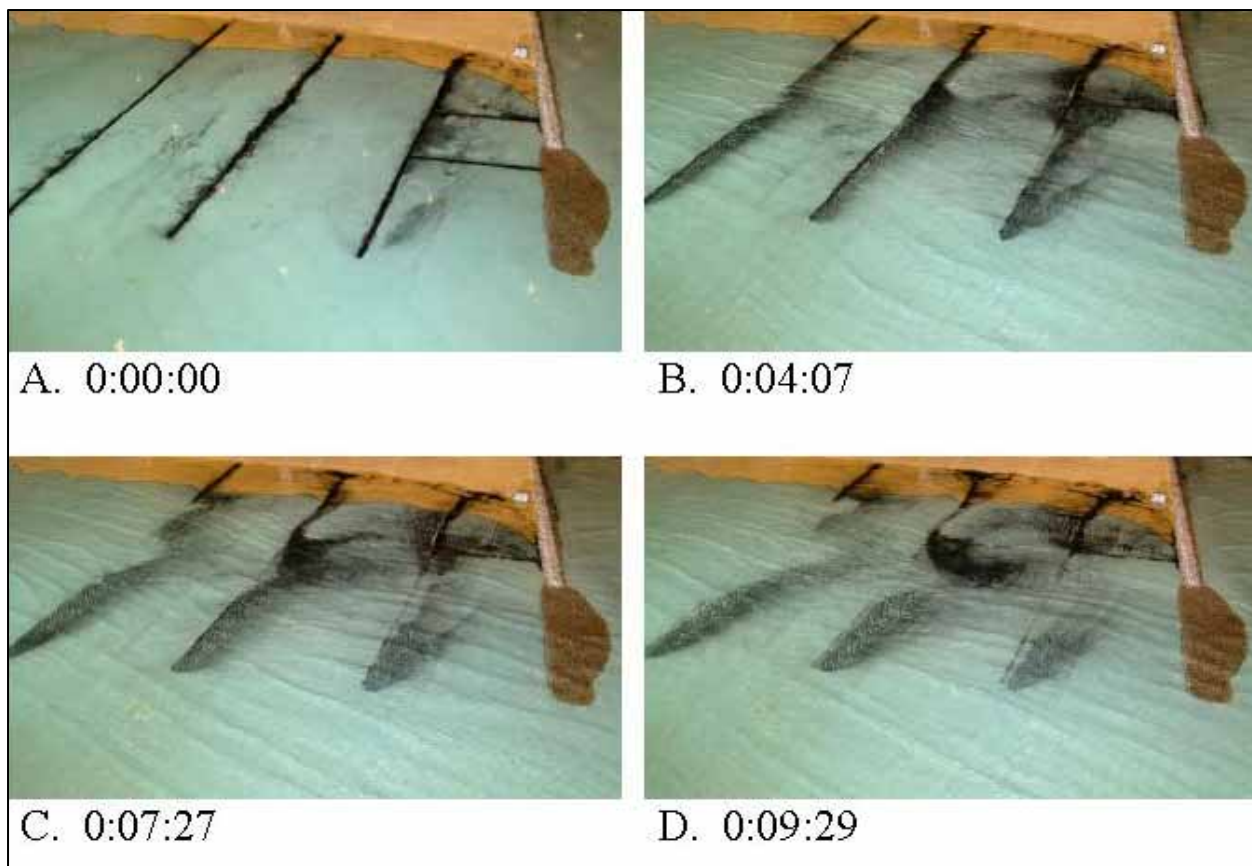
Figure B4.   Coal tracer study for 3-m, 13-sec waves at mtl with flood current for Alt 1
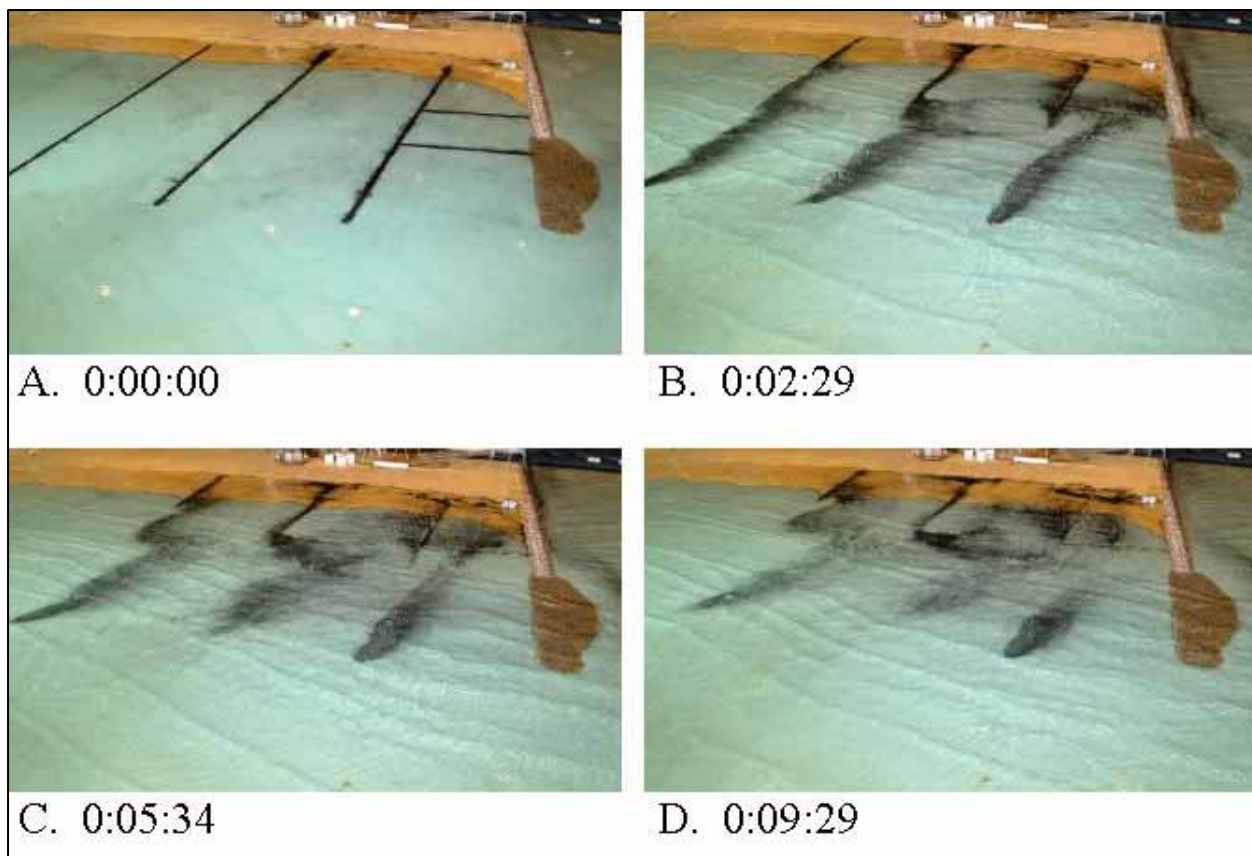
Figure B5.   Coal tracer study for 5-m, 13-sec waves at mtl with flood current for Alt 1
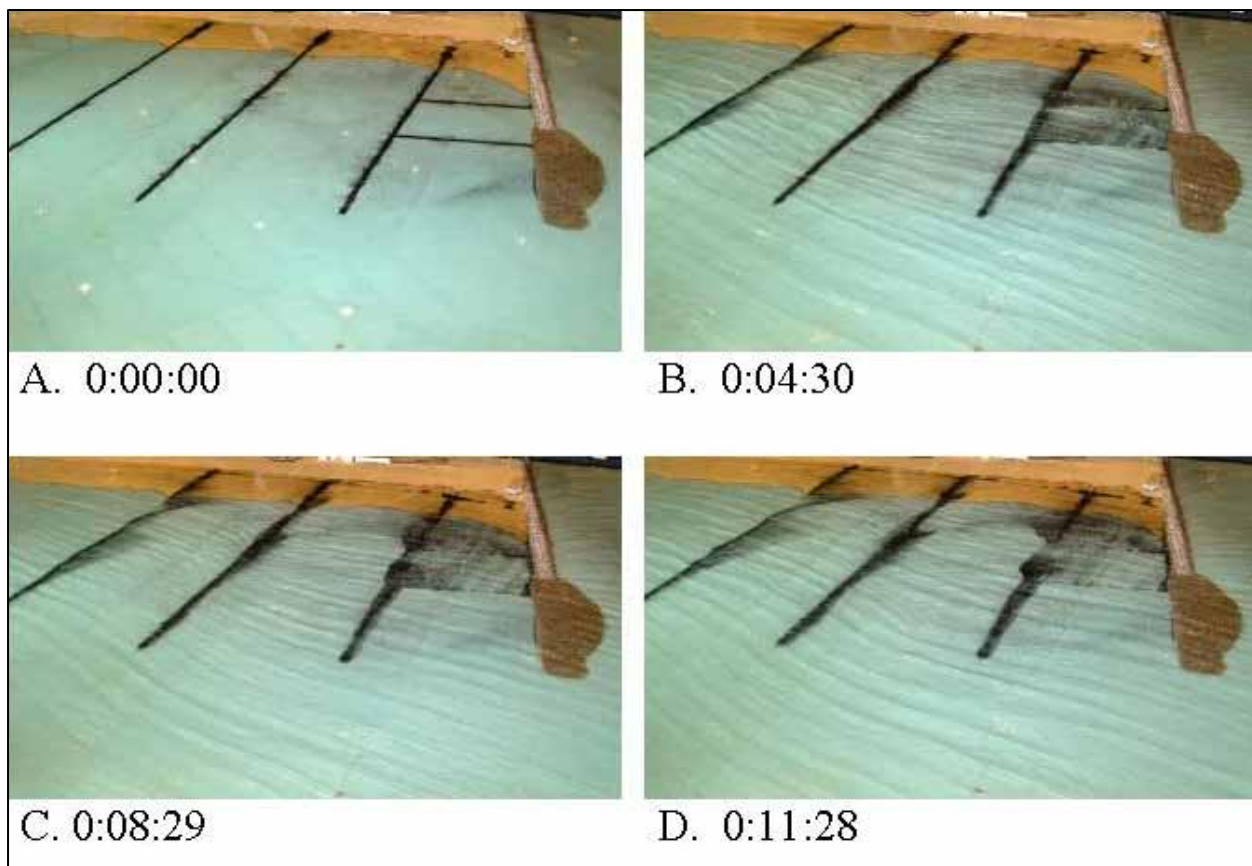
Figure B6.   Coal tracer study for 2-m, 9-sec waves at mhw for Alt 1
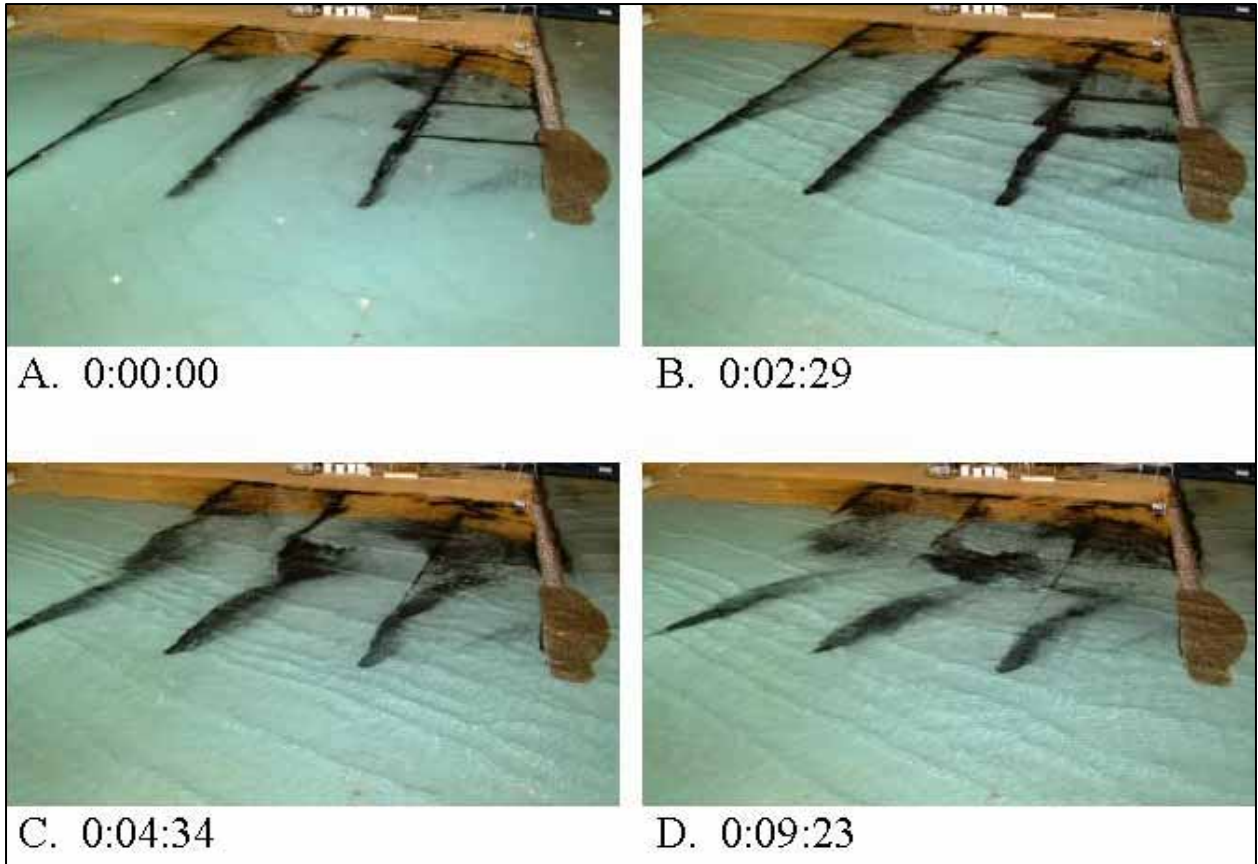
Figure B7.   Coal tracer study for 5-m, 13-sec waves at mhw for Alt 1
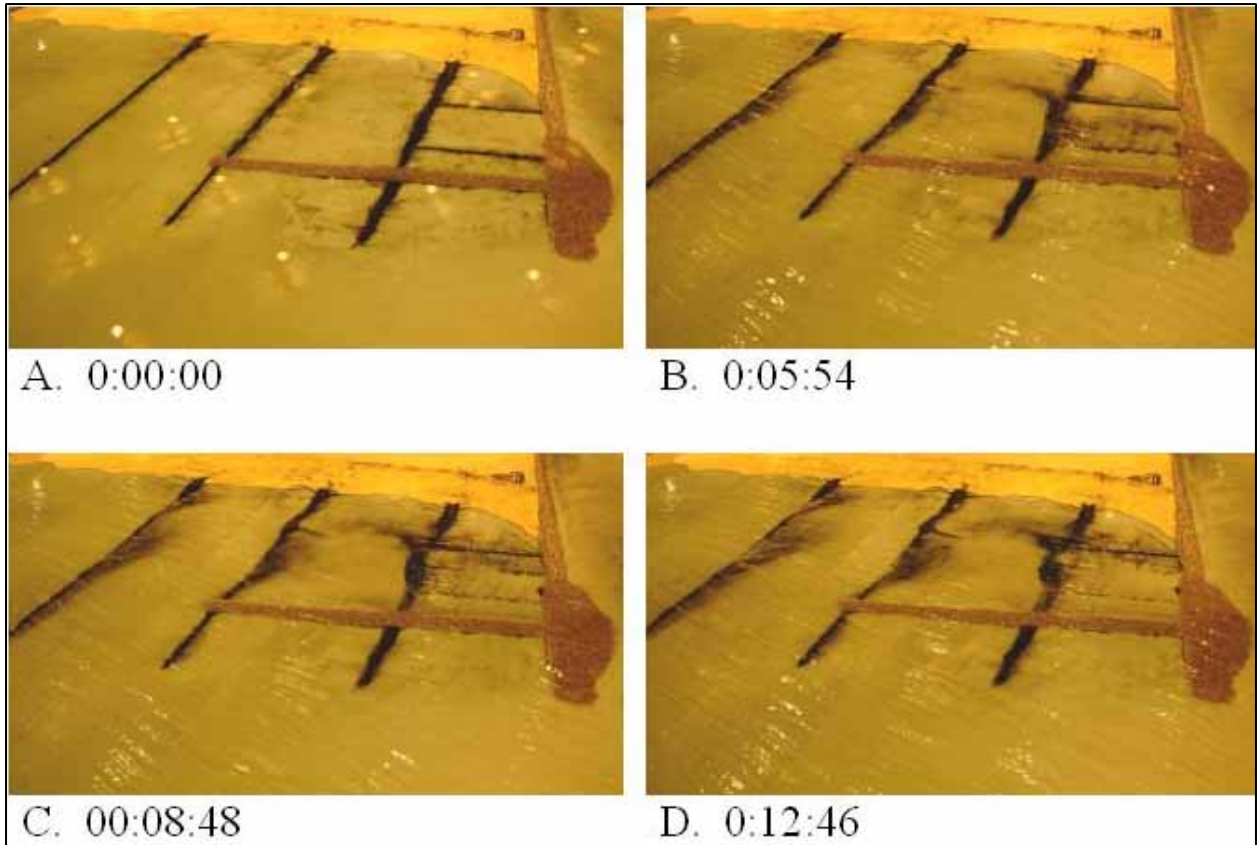
Figure B8.　Coal tracer study for 2-m, 9-sec waves at mllw for Alt 2A
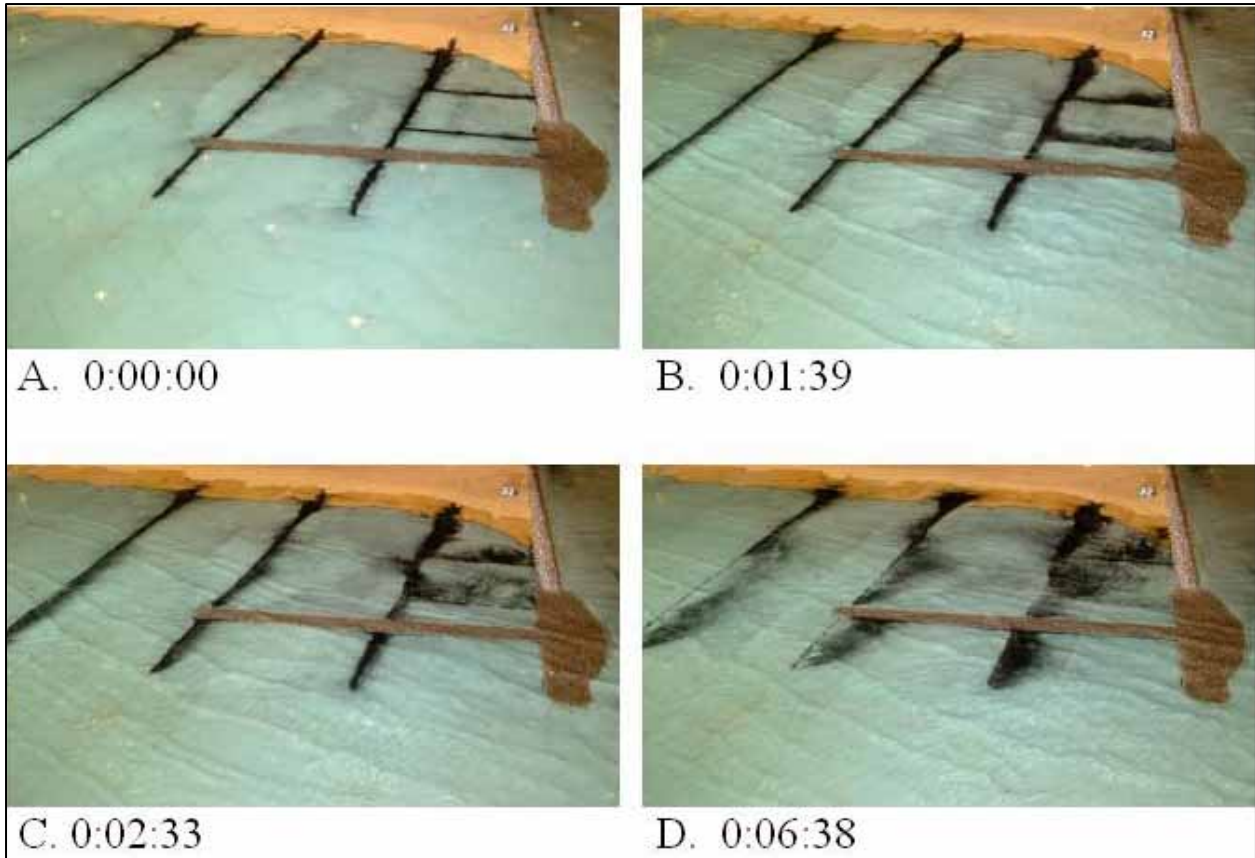
Figure B9.   Coal tracer study for 5-m, 13-sec waves at mllw for Alt 2A
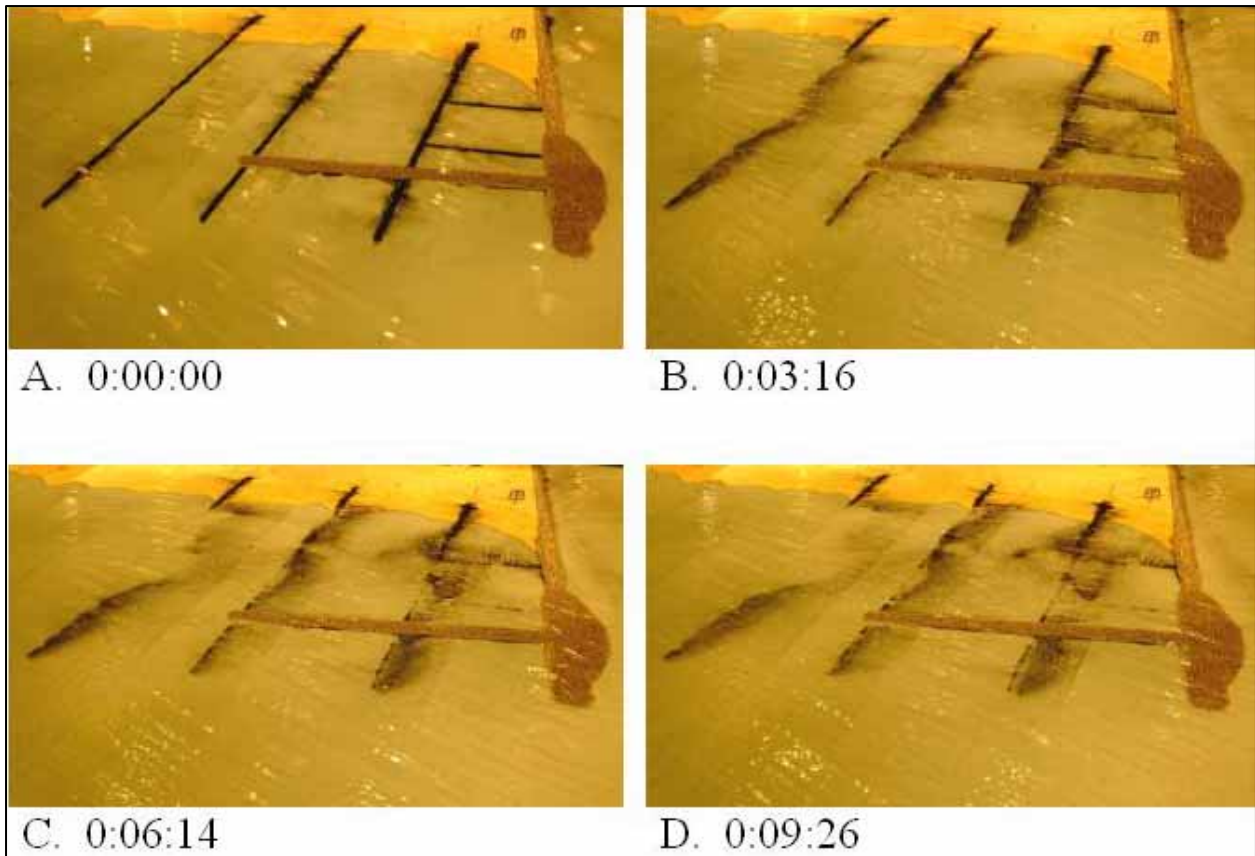
Figure B10. Coal tracer study for 2-m, 9-sec waves at mtl with flood current for Alt 2A
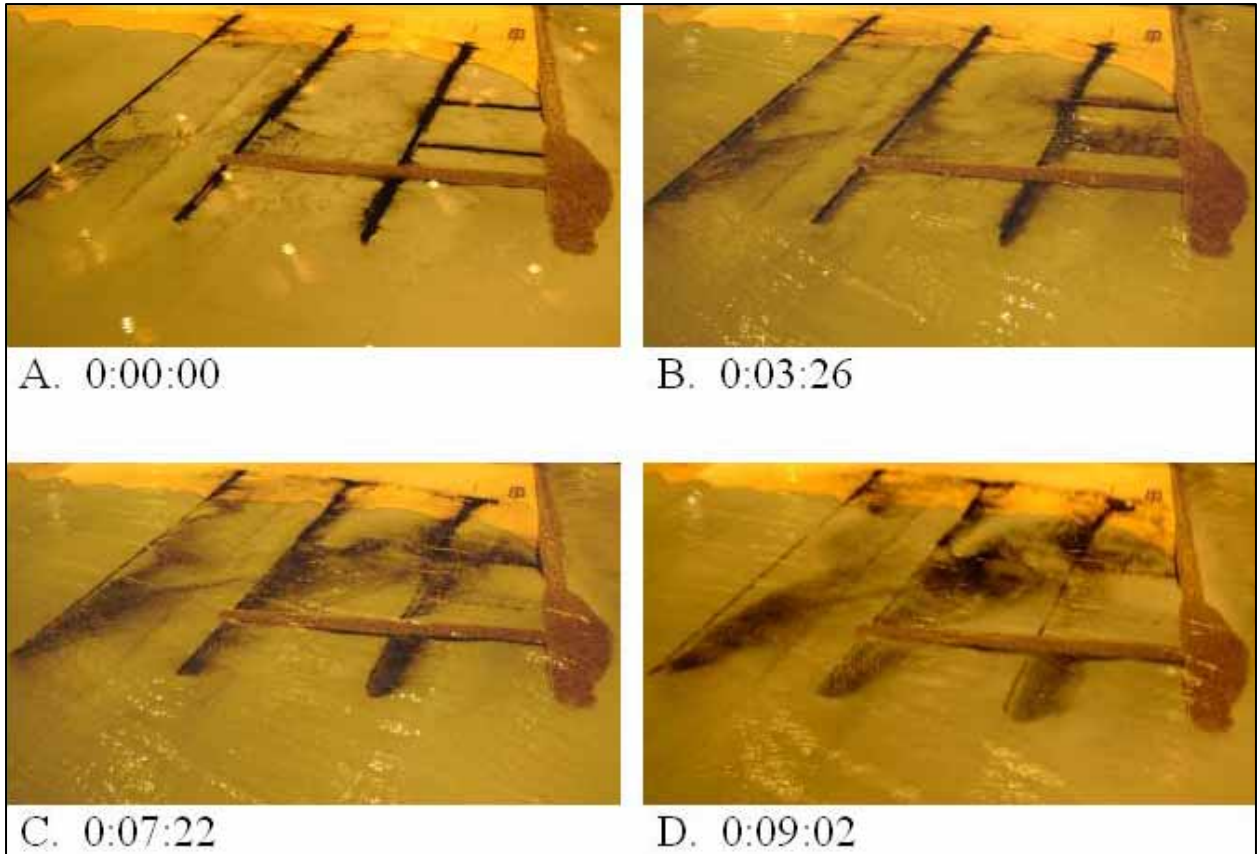
Figure B11. Coal tracer study for 3-m, 13-sec waves at mtl with flood current for Alt 2A
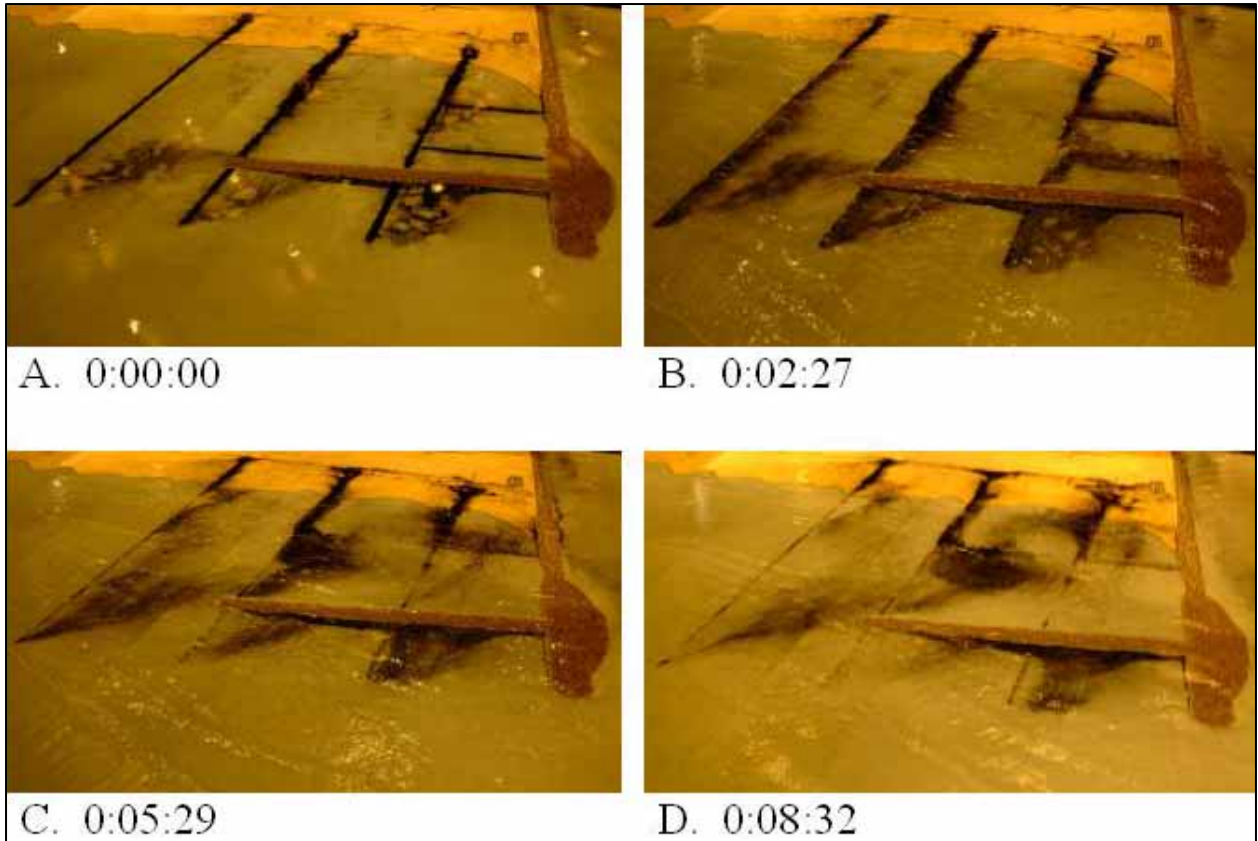
Figure B12. Coal tracer study for 5-m, 13-sec waves at mtl with flood current for Alt 2A
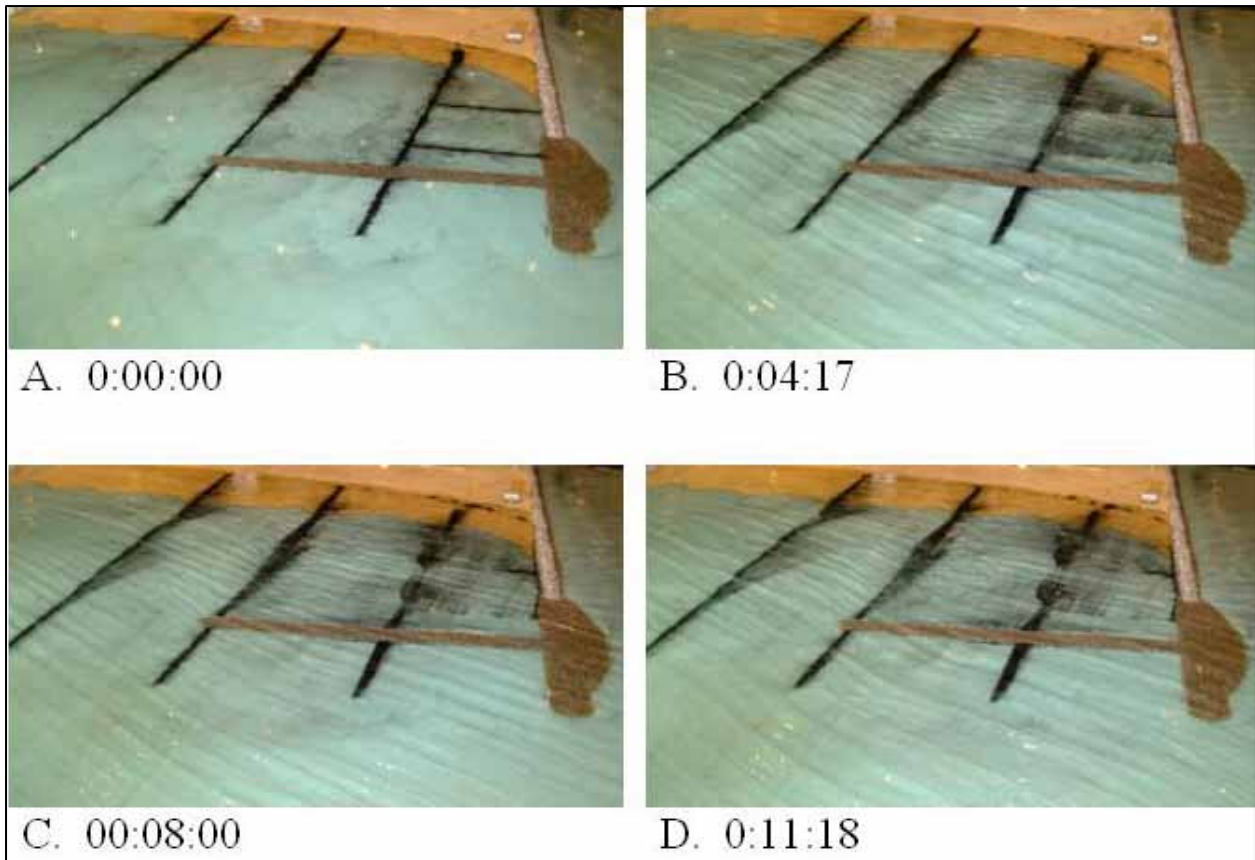
Figure B13. Coal tracer study for 2-m, 9-sec waves at mhw for Alt 2A
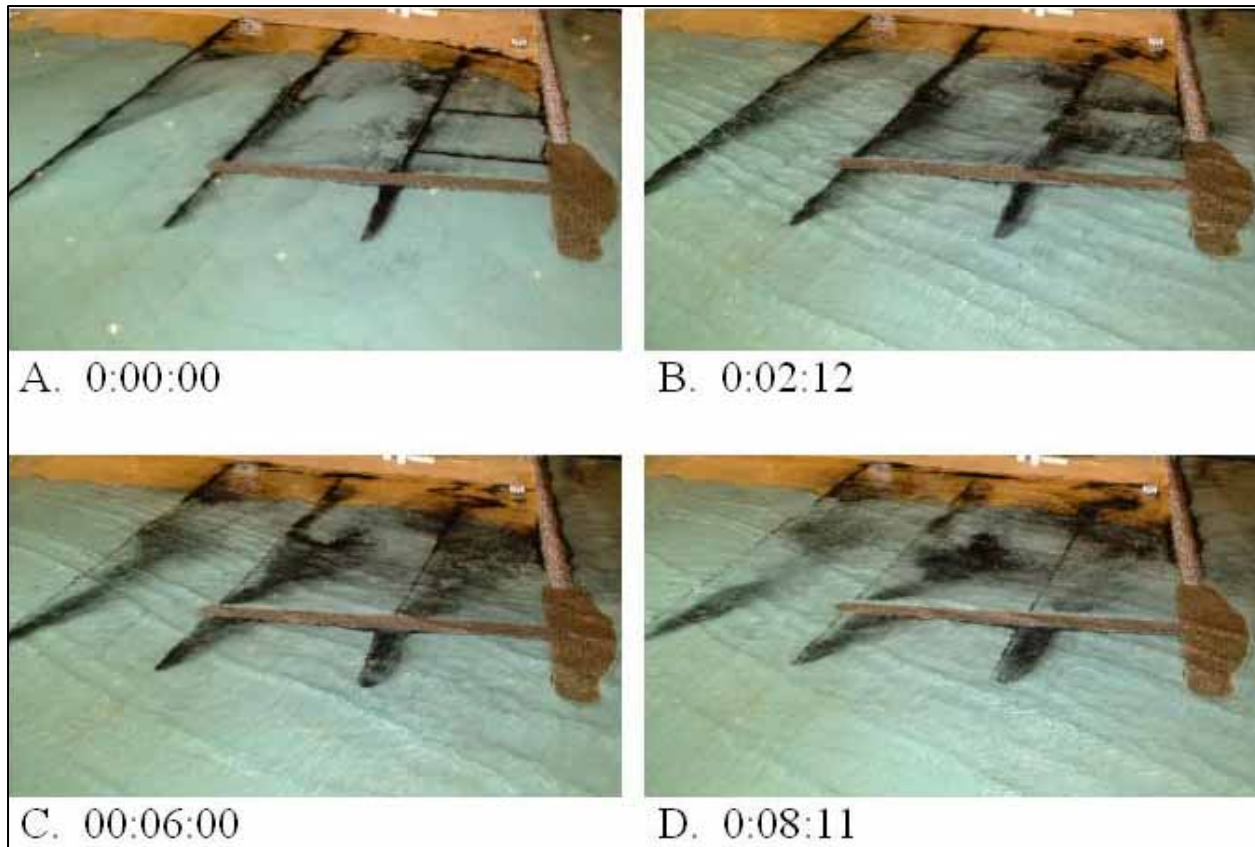
Figure B14. Coal tracer study for 5-m, 13-sec waves at mhw for Alt 2

Dye studies

Figures B15 through B46 include photographs taken during dye studies with wave from the west-northwest. Figures B15 through B23 were taken during experiments with Alt 1, Figures B24 through B32 were taken during experiments with Alt 2A, Figures B33 through B39 were taken during experiments with Alt 2A′, and Figures B40 through B46 were taken during experiments with Alt 3B.
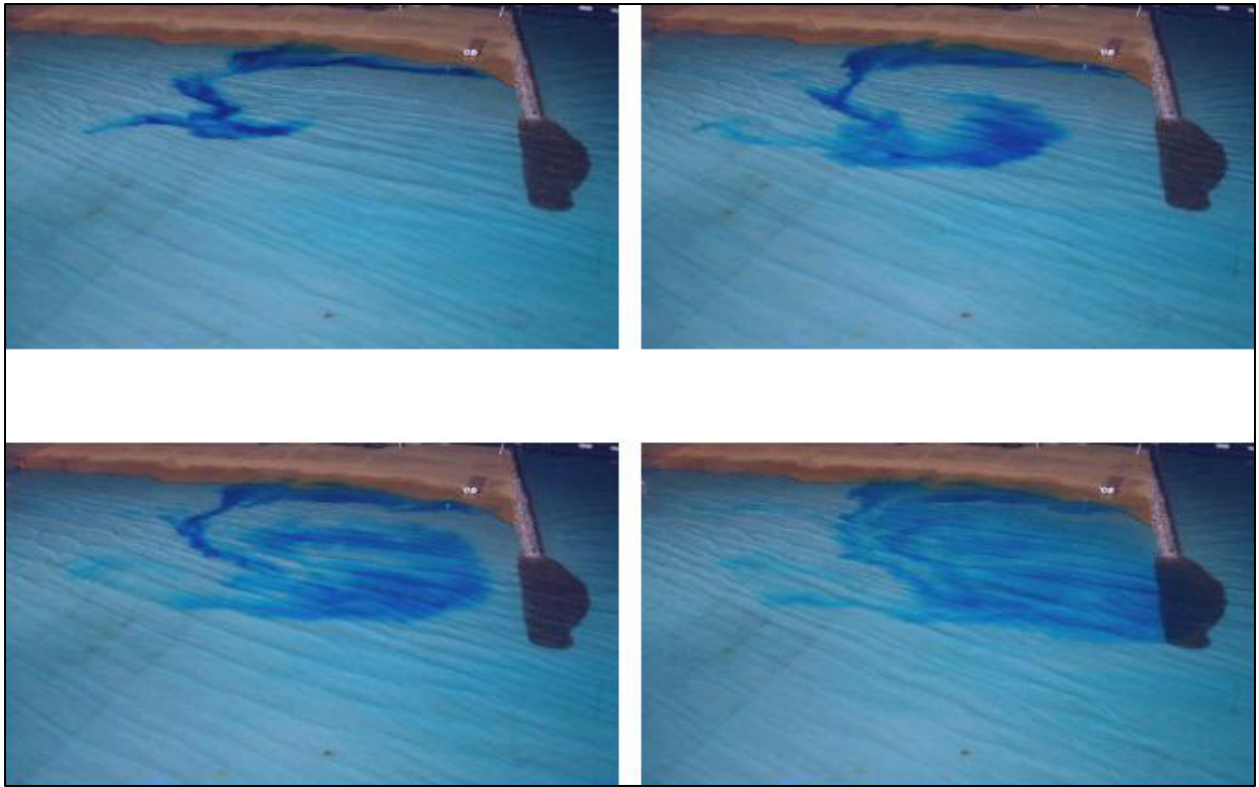
Figure B15. Dye study of 2-m, 9-sec waves from west-northwest at mllw, Alt 1
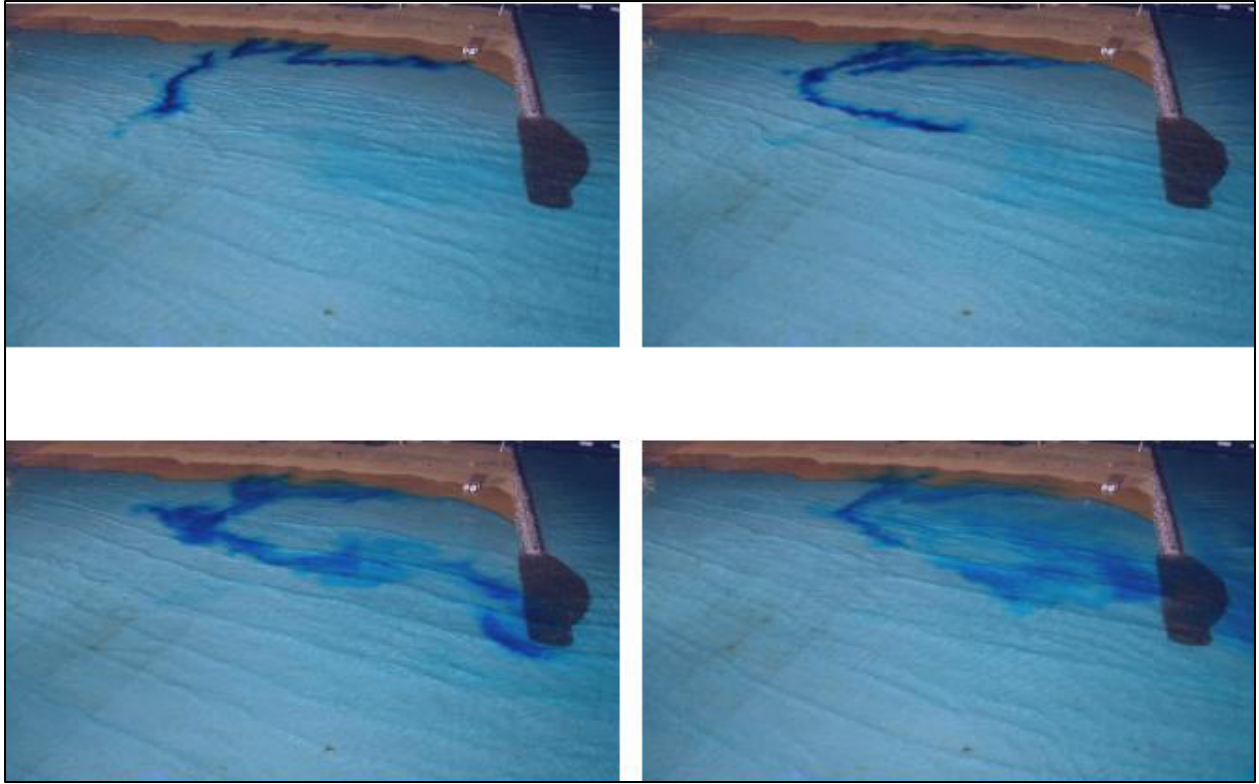
Figure B16. Dye study of 3-m, 13-sec waves from west-northwest at mllw, Alt 1

Figure B17. Dye study of 5-m, 13-sec waves from west-northwest at mllw, Alt 1
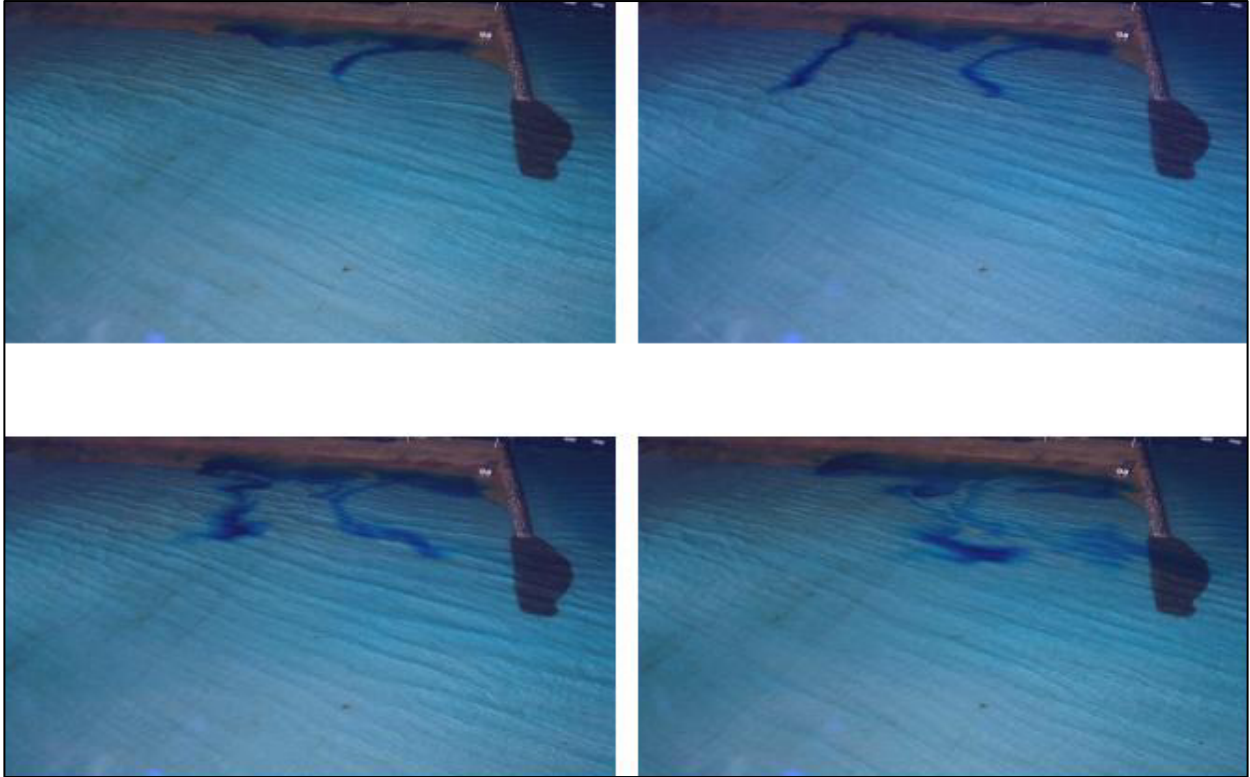
Figure B18. Dye study of 2-m, 9-sec waves from west-northwest at mtl, Alt 1, with full flood current
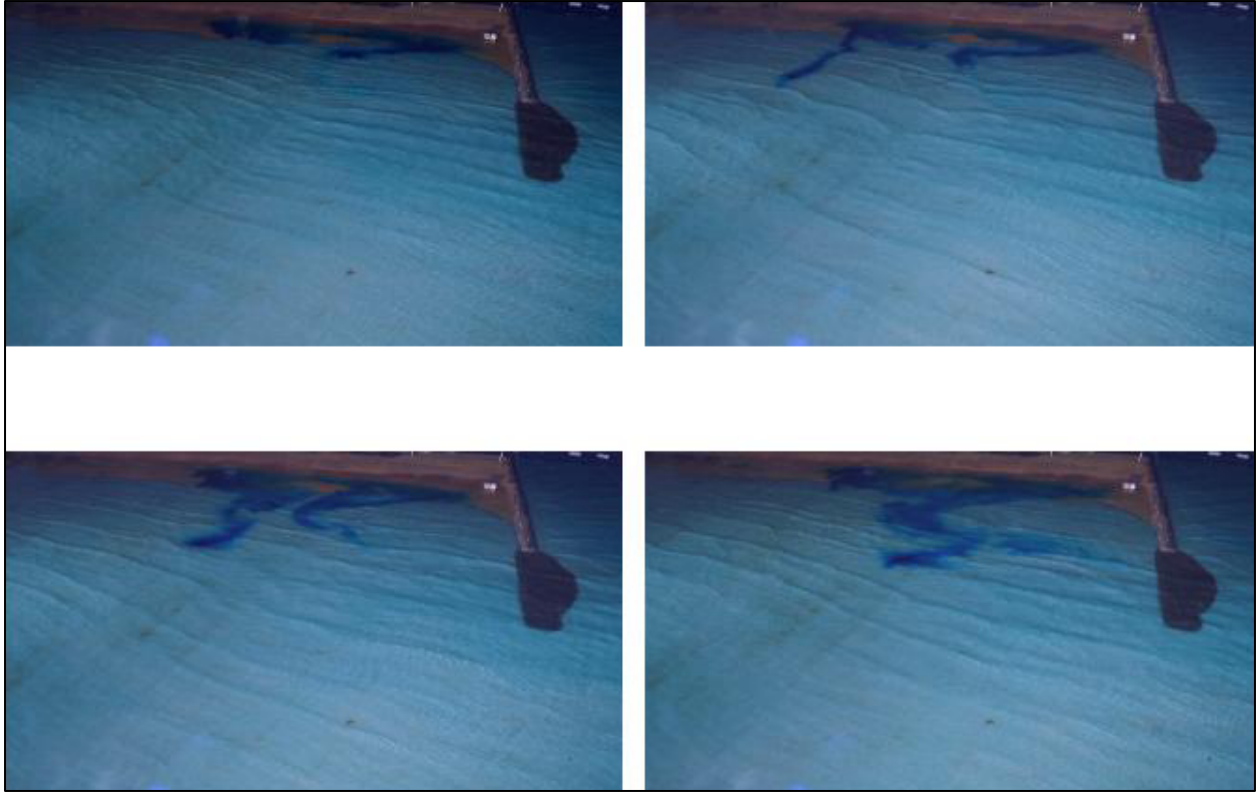
Figure B19. Dye study of 3-m, 13-sec waves from west-northwest at mtl, Alt 1, with full flood current

Figure B20. Dye study of 5-m, 13-sec waves from west-northwest at mtl, Alt 1, with full flood current
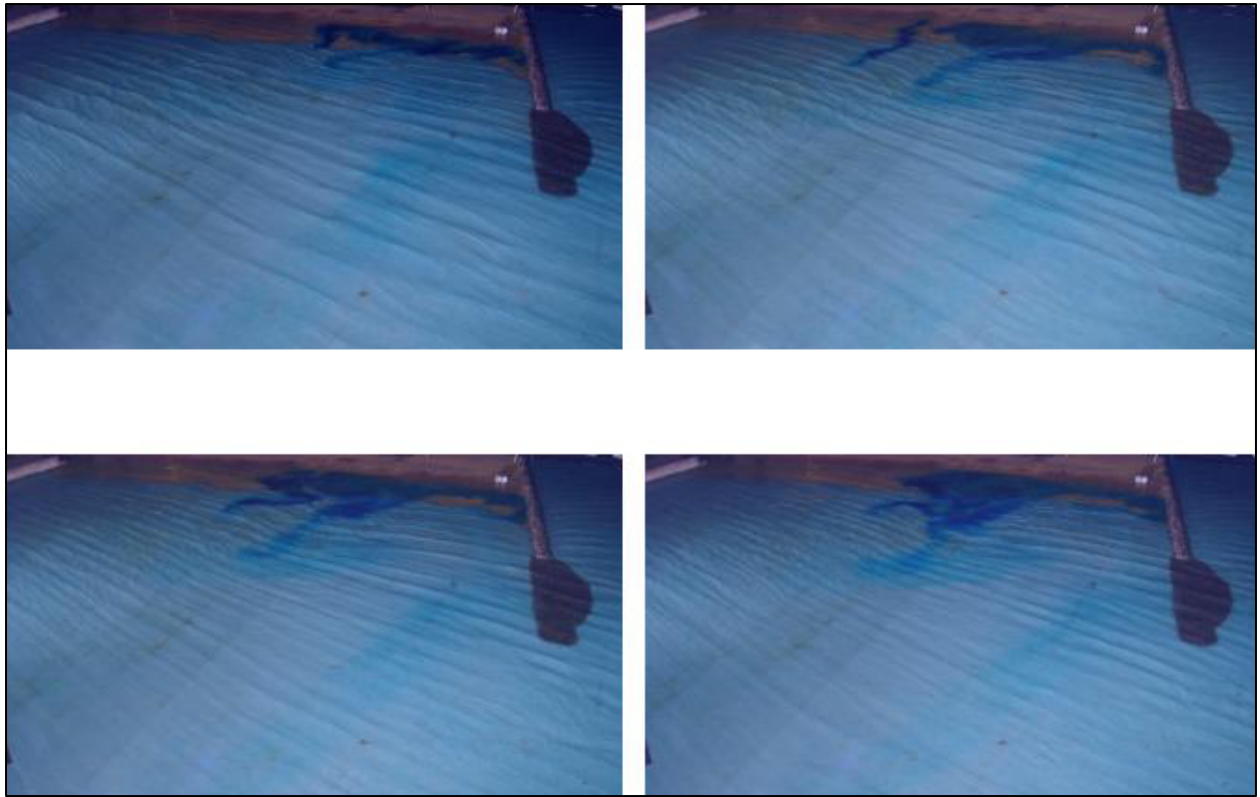
Figure B21. Dye study of 2-m, 9-sec waves from west-northwest at mhw, Alt 1

Figure B22. Dye study of 3-m, 13-sec waves from west-northwest at mhw, Alt 1
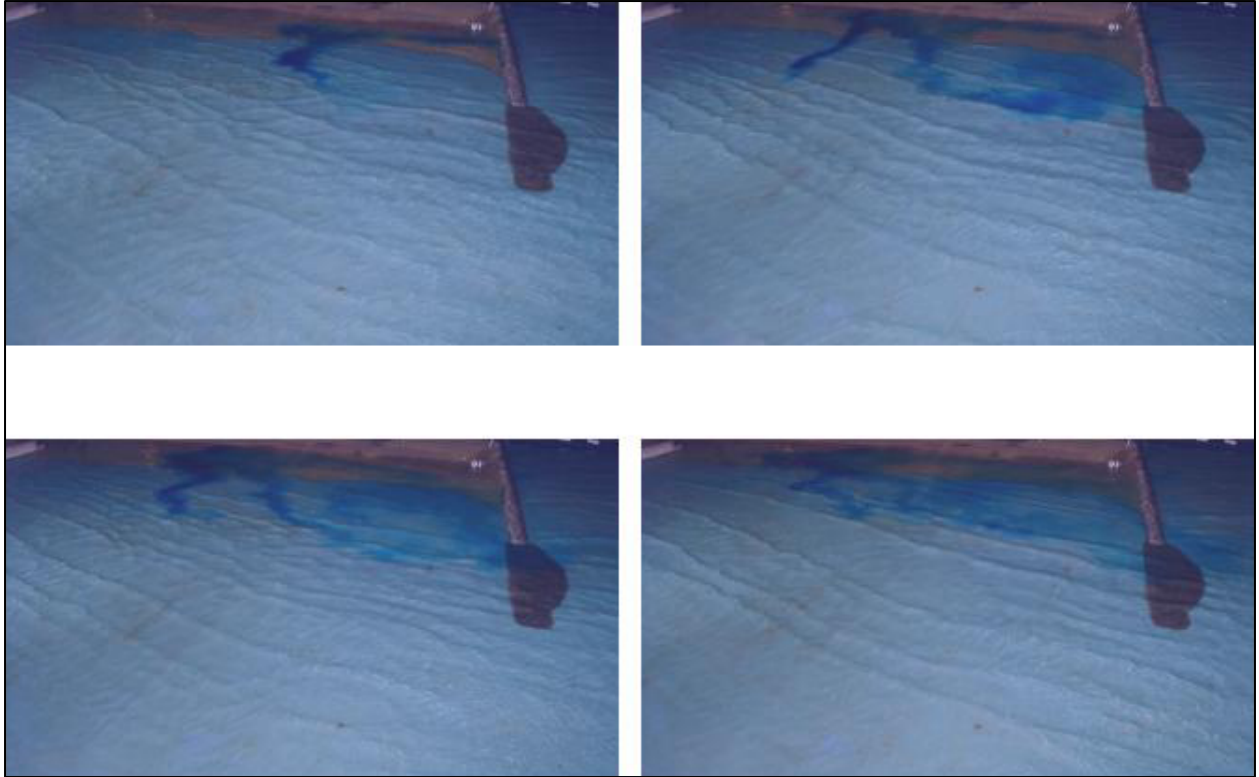
Figure B23. Dye study of 5-m, 13-sec waves from west-northwest at mhw, Alt 1
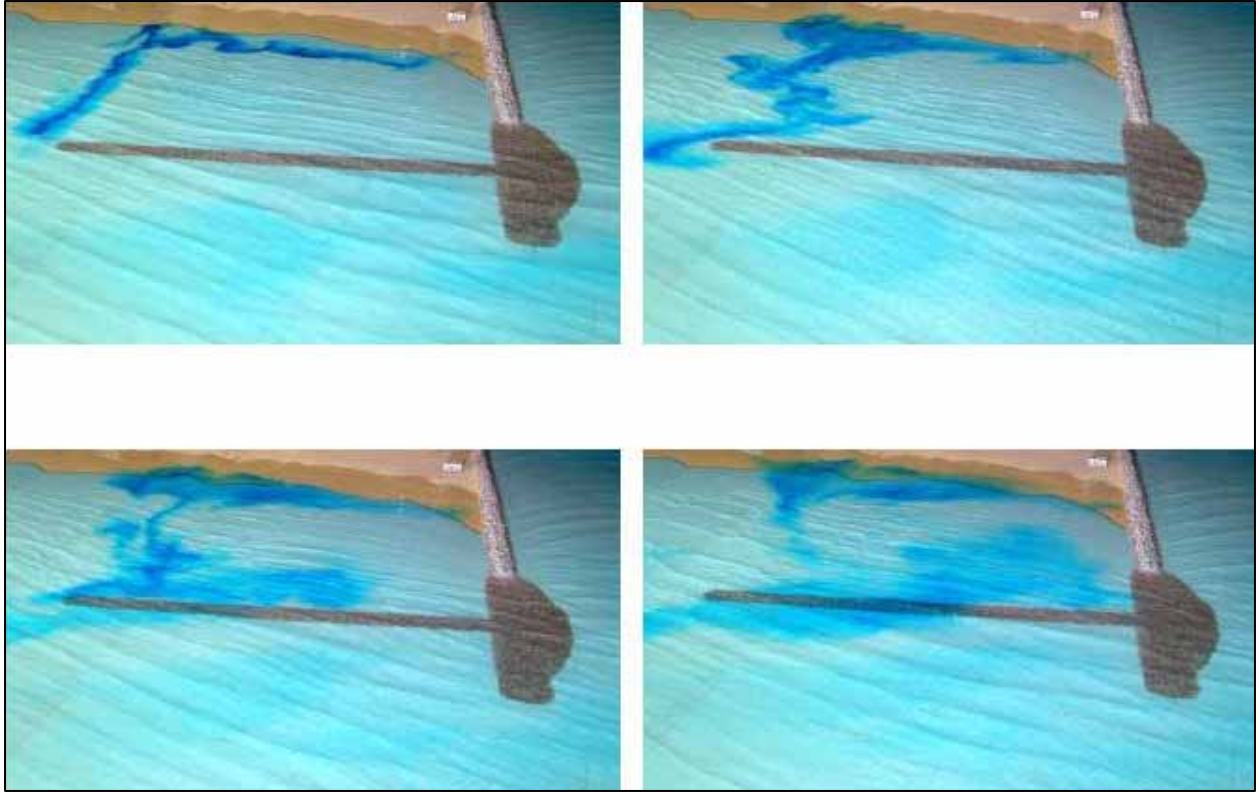
Figure B24. Dye study of 2-m, 9-sec waves from west-northwest at mllw, Alt 2A
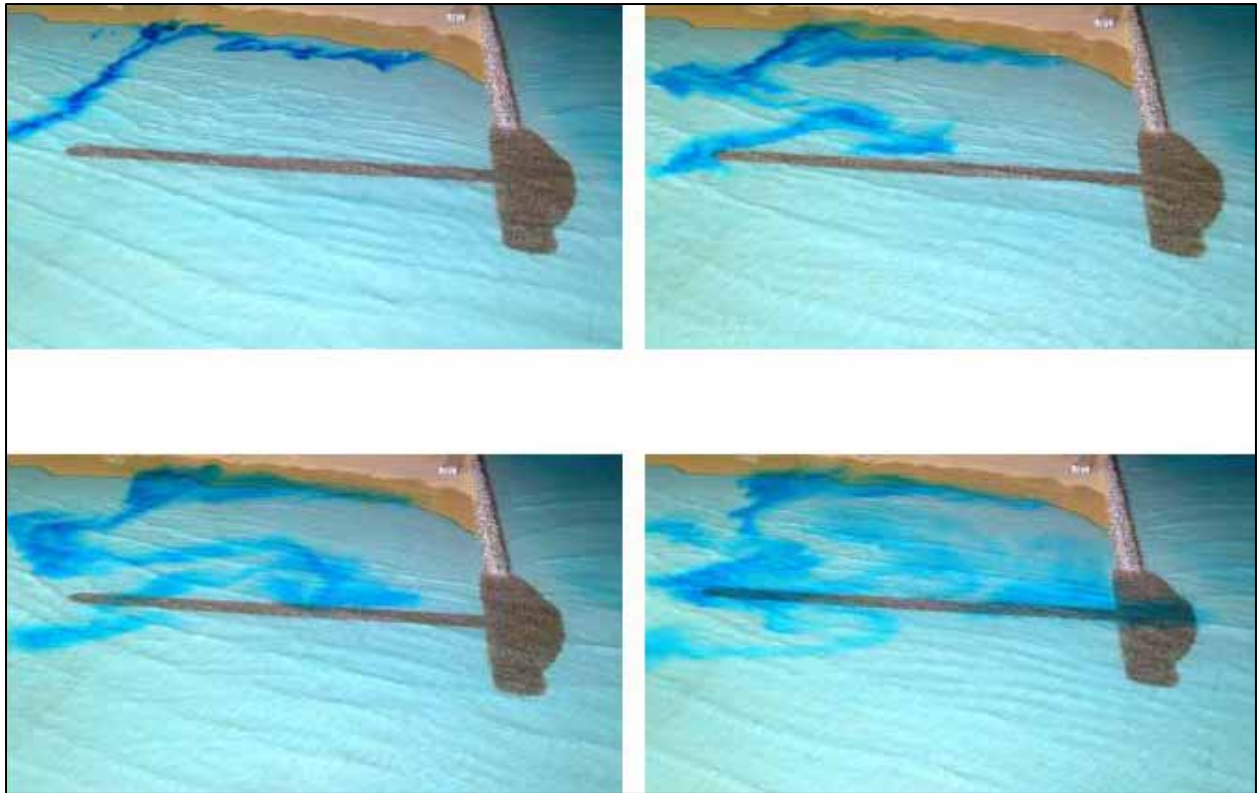
Figure B25. Dye study of 3-m, 13-sec waves from west-northwest at mllw, Alt 1A
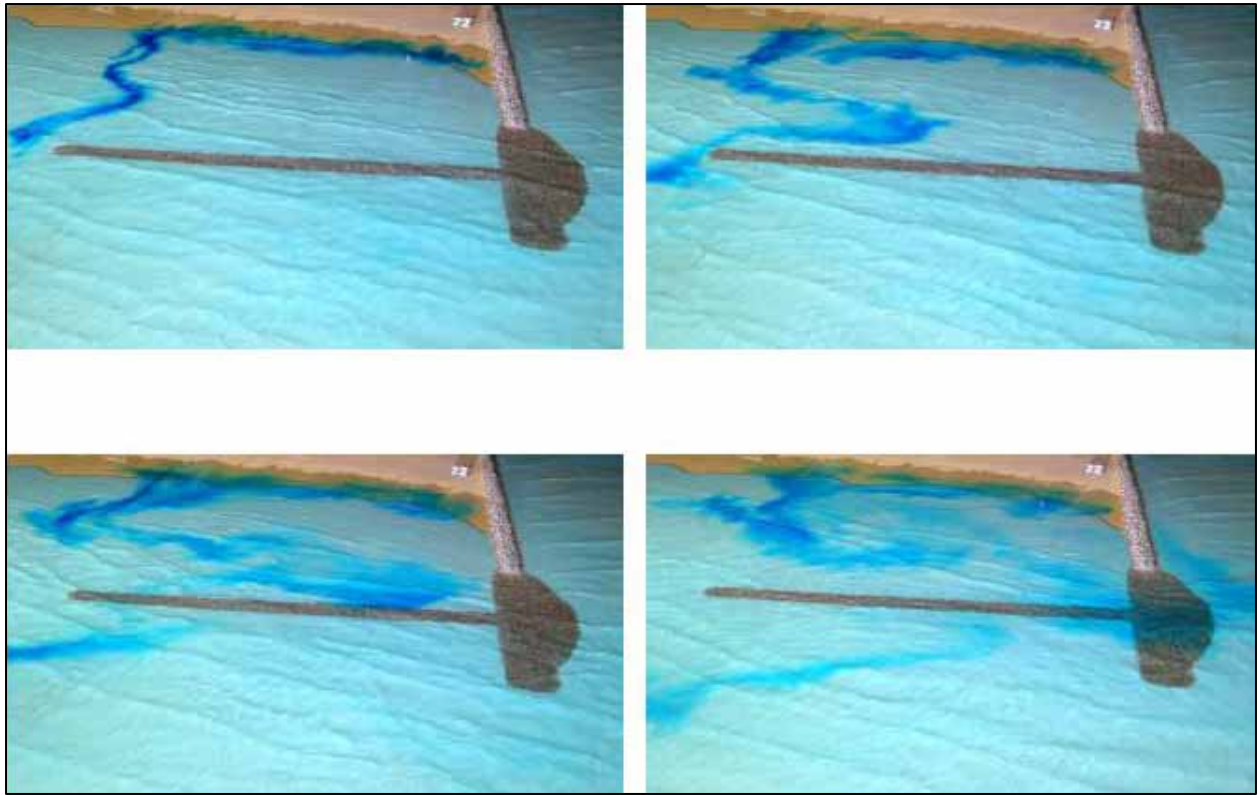
Figure B26. Dye study of 5-m, 13-sec waves from west-northwest at mllw, Alt 2A
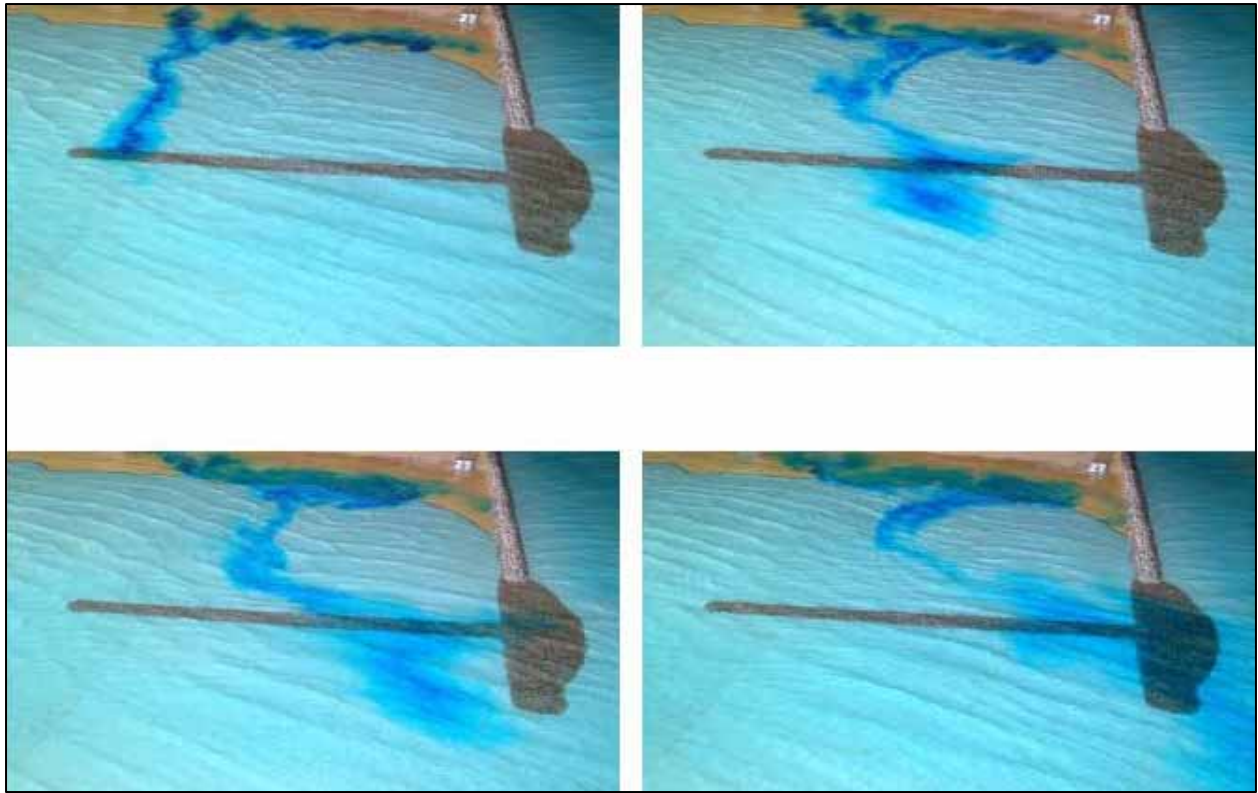
Figure B27. Dye study of 2-m, 9-sec waves from west-northwest at mtl, Alt 2A, with full flood current
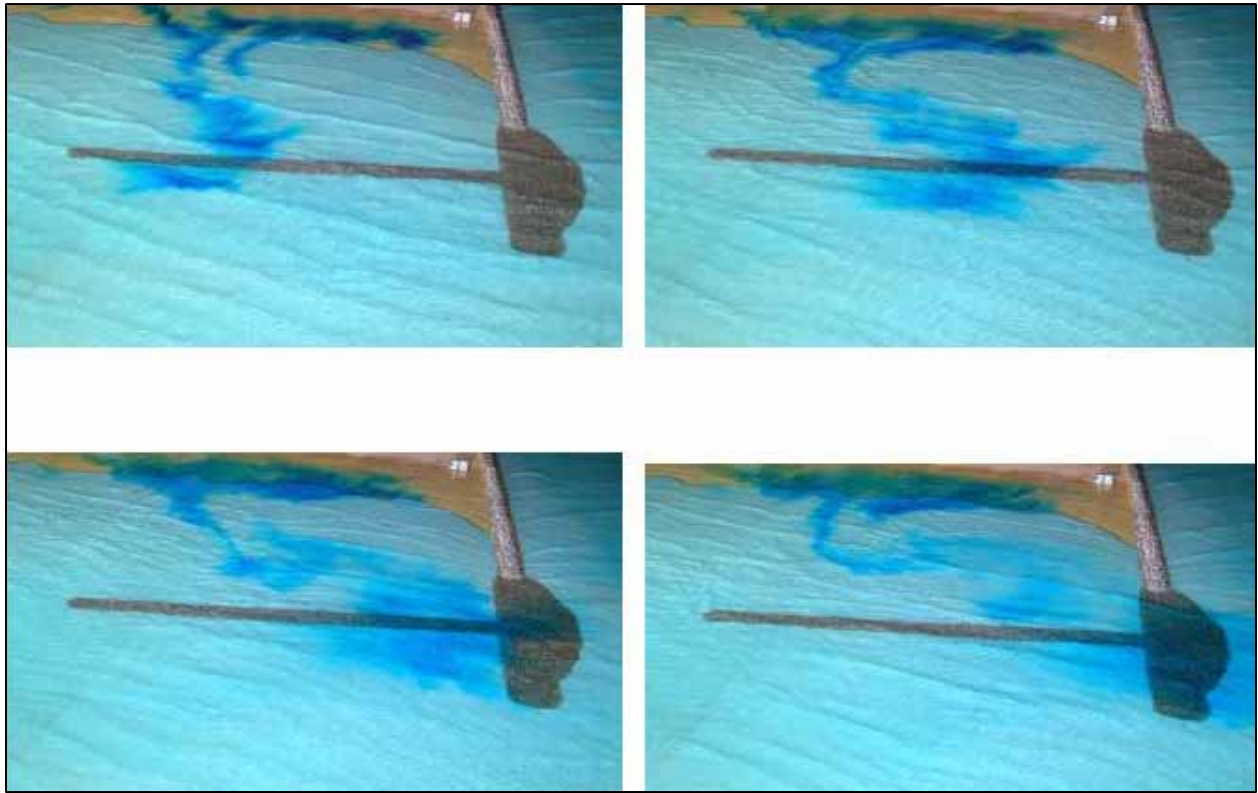
Figure B28. Dye study of 3-m, 13-sec waves from west-northwest at mtl, Alt 2A, with full flood current
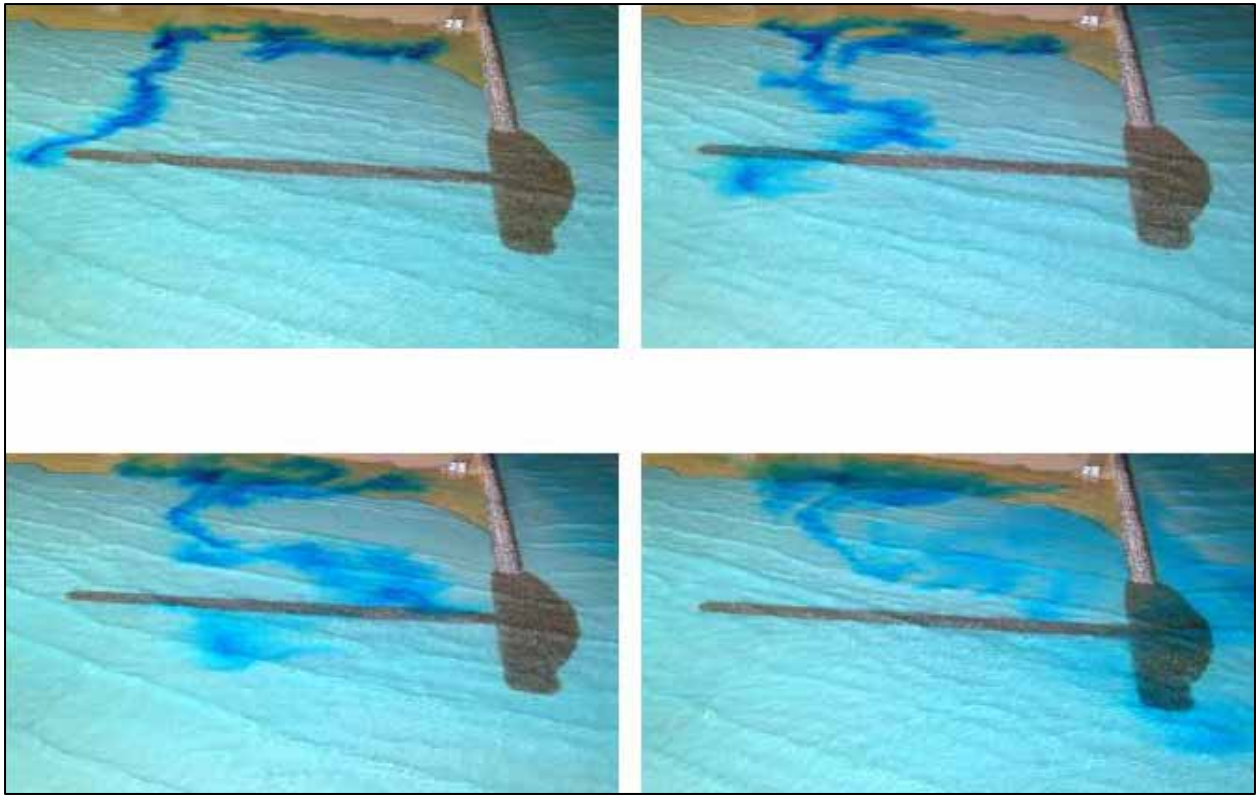
Figure B29. Dye study of 5-m, 13-sec waves from west-northwest at mtl, Alt 2A, with full flood current
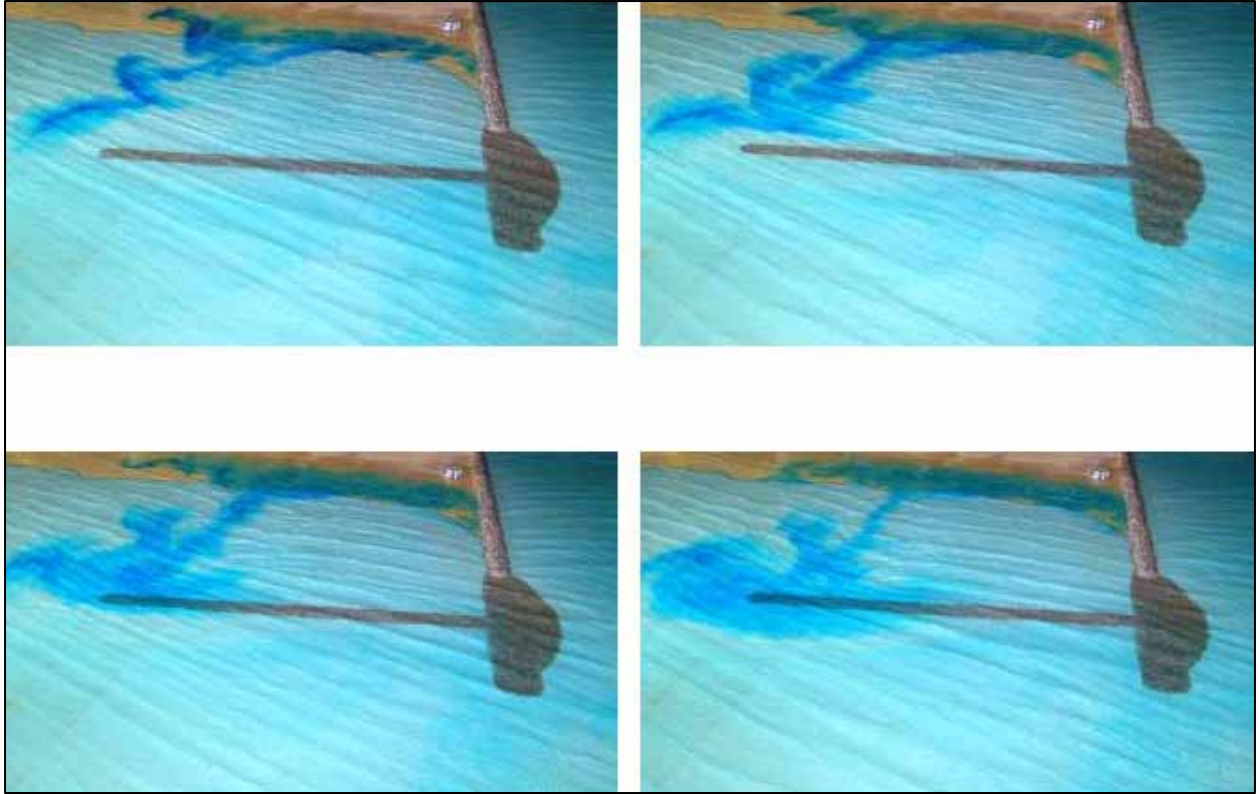
Figure B30. Dye study of 2-m, 9-sec waves from west-northwest at mhw, Alt 2A
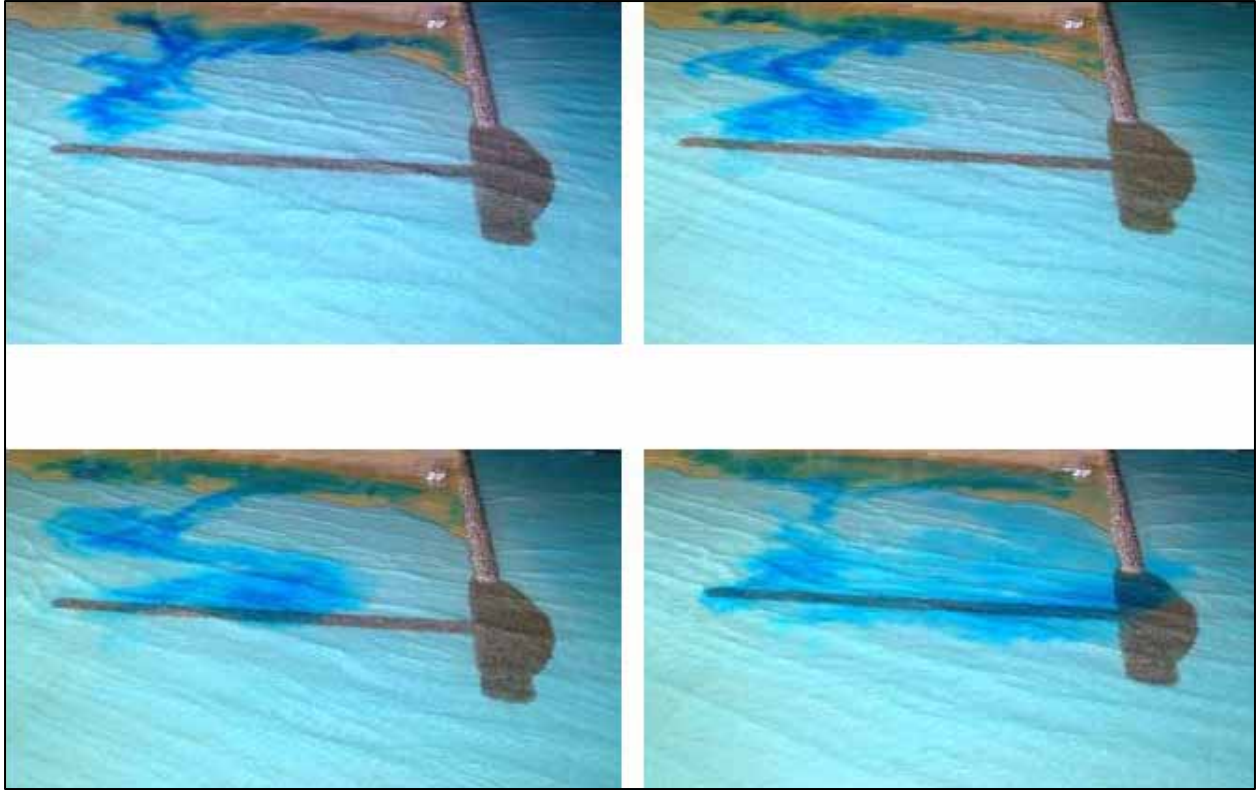
Figure B31. Dye study of 3-m, 13-sec waves from west-northwest at mhw, Alt 2A
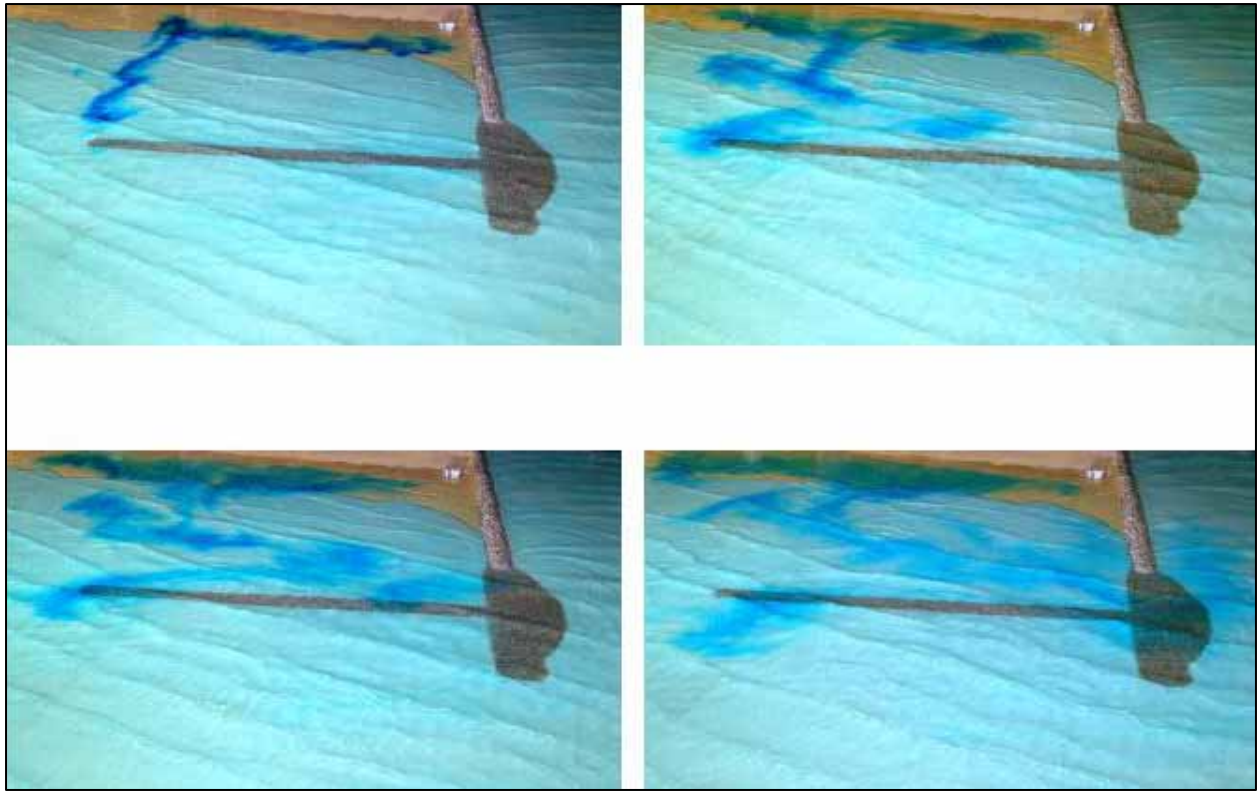
Figure B32. Dye study of 5-m, 13-sec waves from west-northwest at mhw, Alt 2A
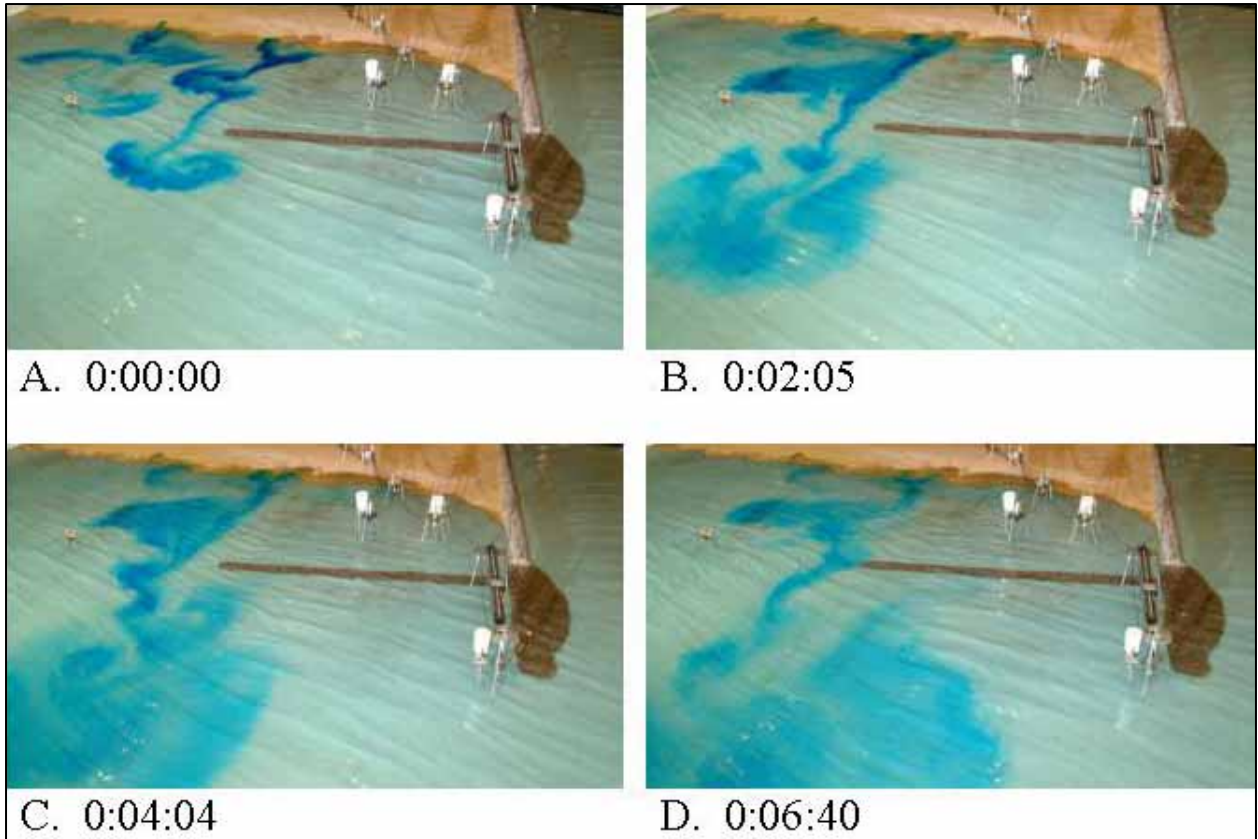
Figure B33. Dye study of 2-m, 9-sec waves from west-northwest at mllw, Alt 2A′
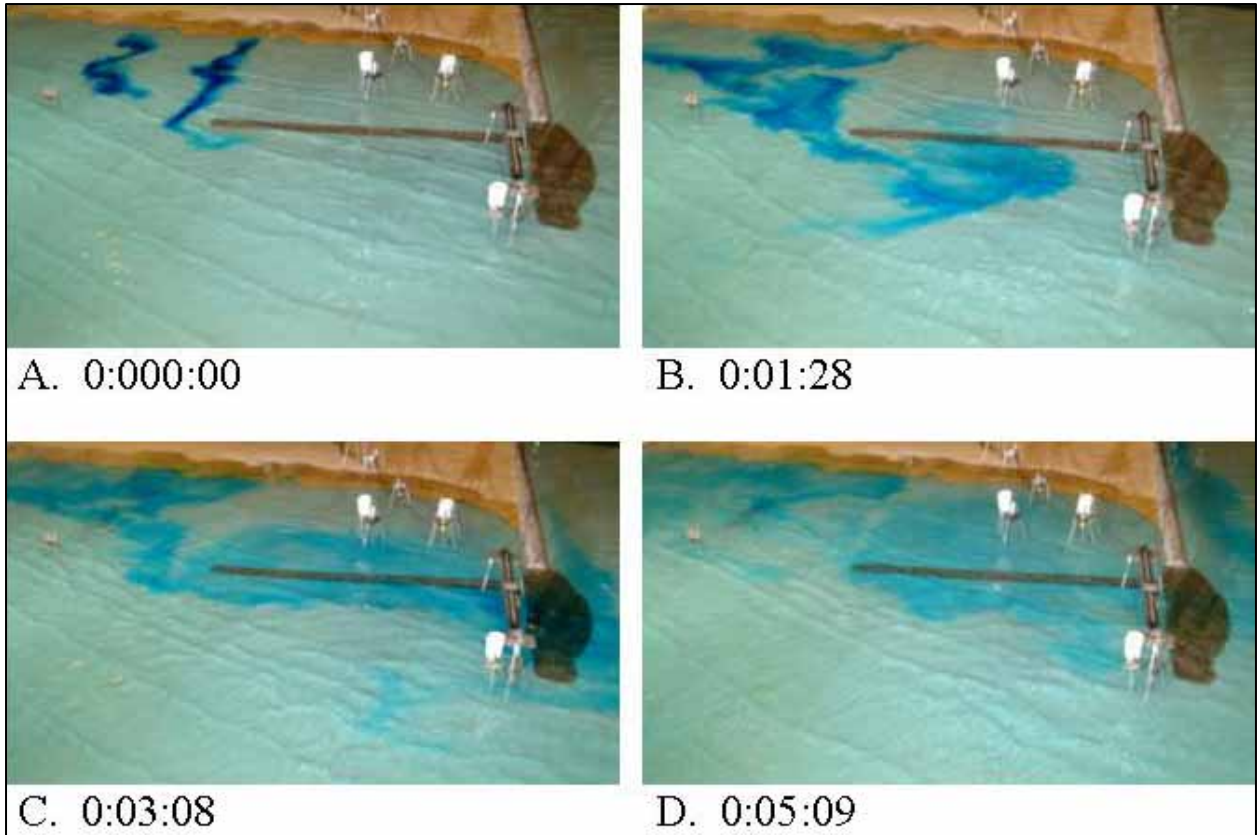
Figure B34. Dye study of 5-m, 13-sec waves from west-northwest at mllw, Alt 2A′
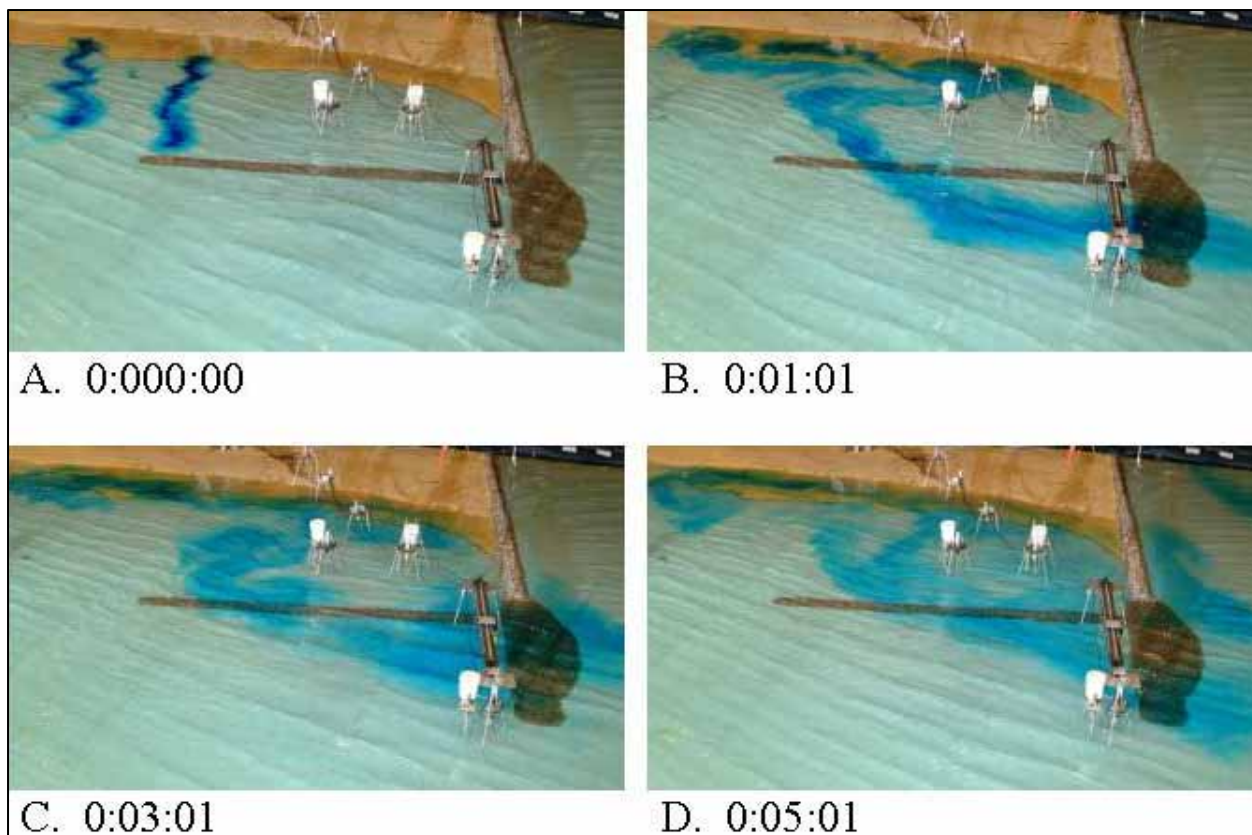
Figure B35. Dye study of 2-m, 9-sec waves from west-northwest at mtl with full flood tidal current, Alt 2A′
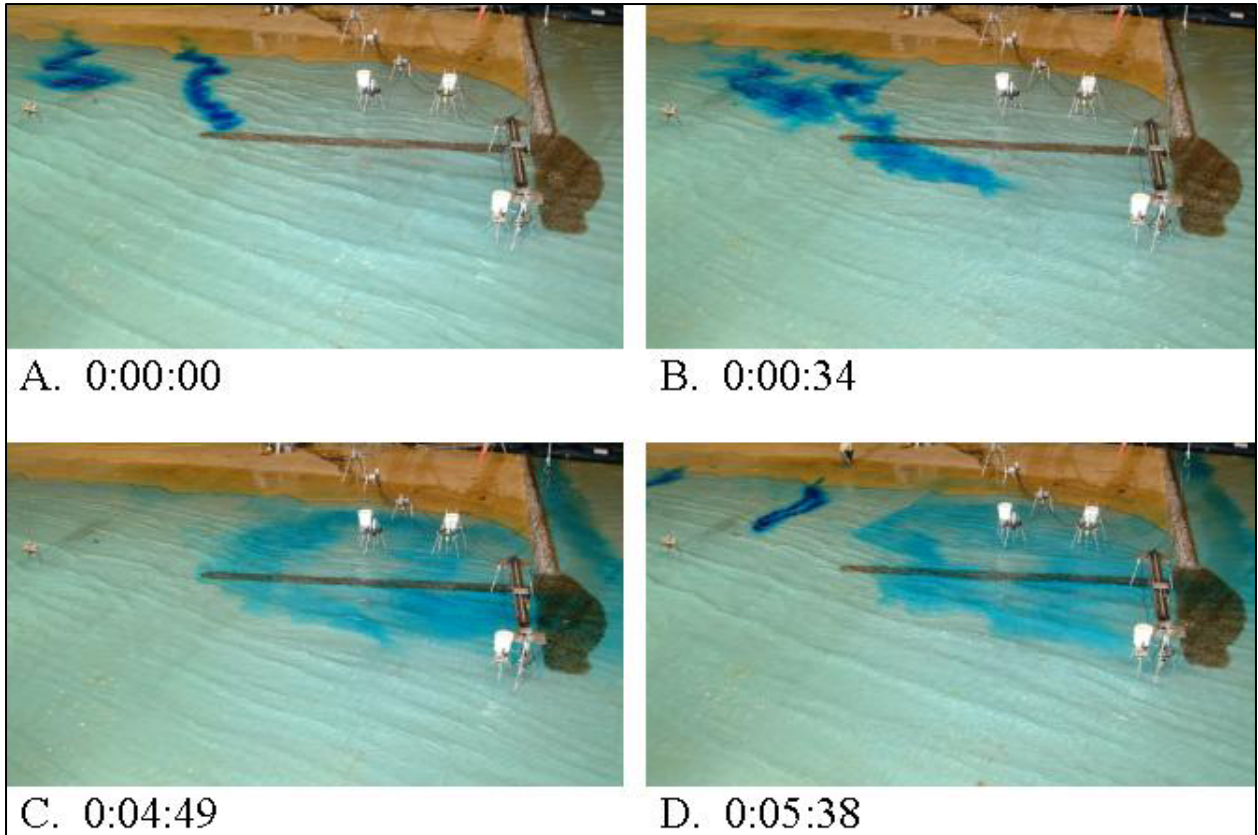
Figure B36. Dye study of 3-m, 13-sec waves from west-northwest at mtl with full flood tidal current, Alt 2A′
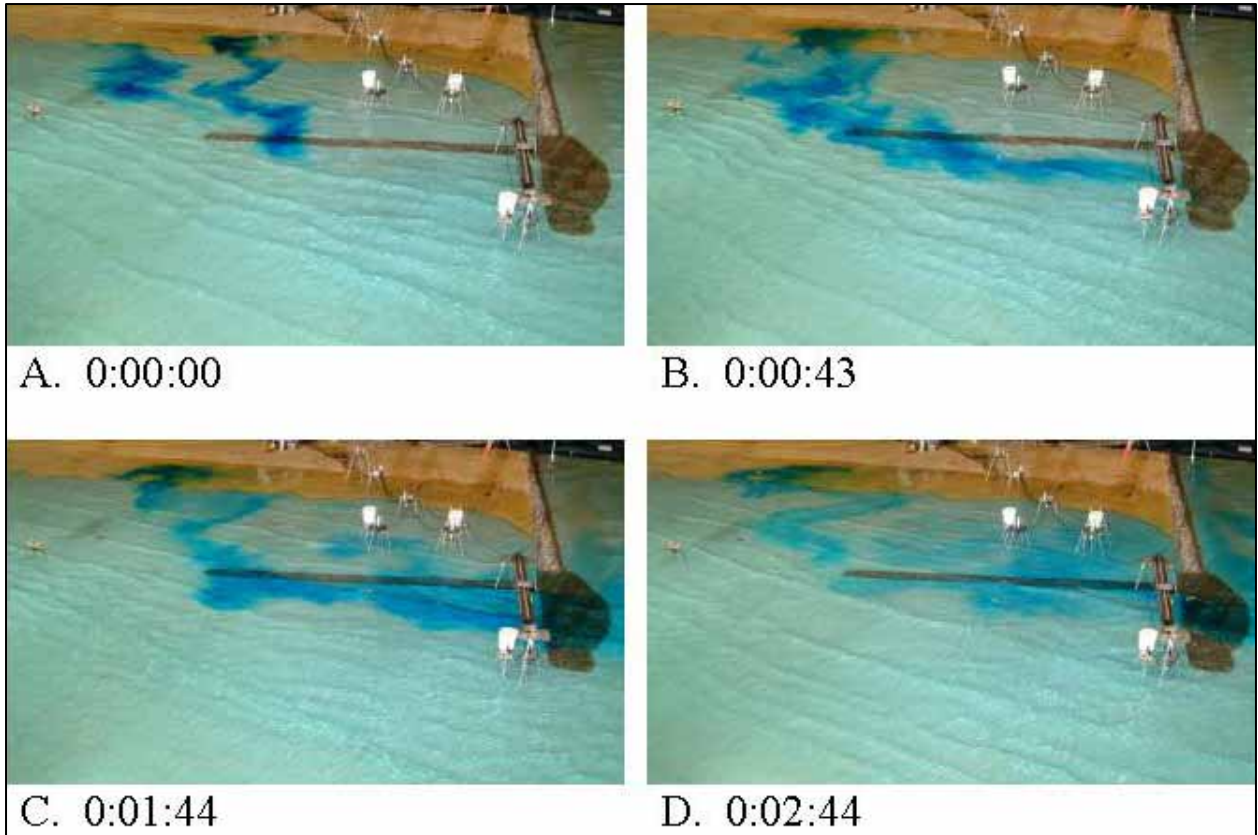
Figure B37. Dye study of 5-m, 13-sec waves from west-northwest at mtl with full flood tidal current, Alt 2A′
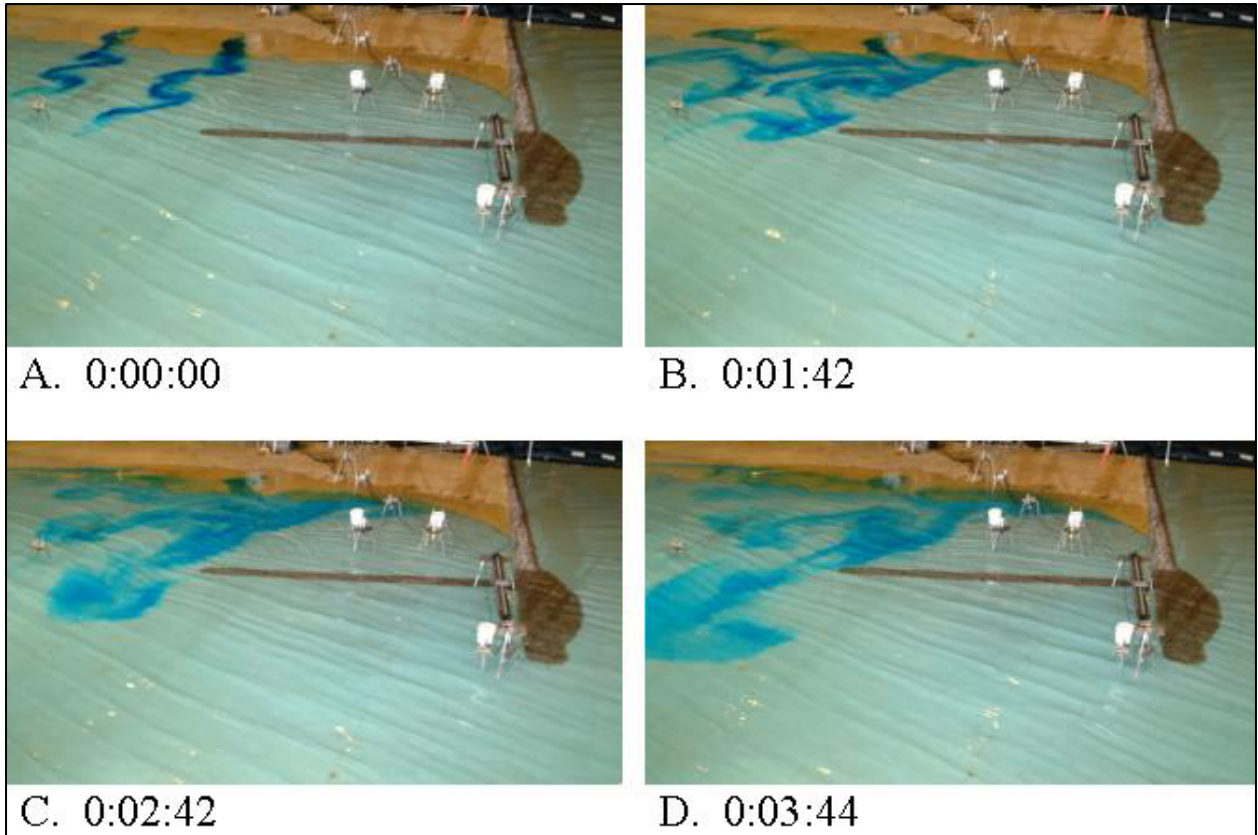
Figure B38. Dye study of 2-m, 9-sec waves from west-northwest at mhw, Alt 2A′
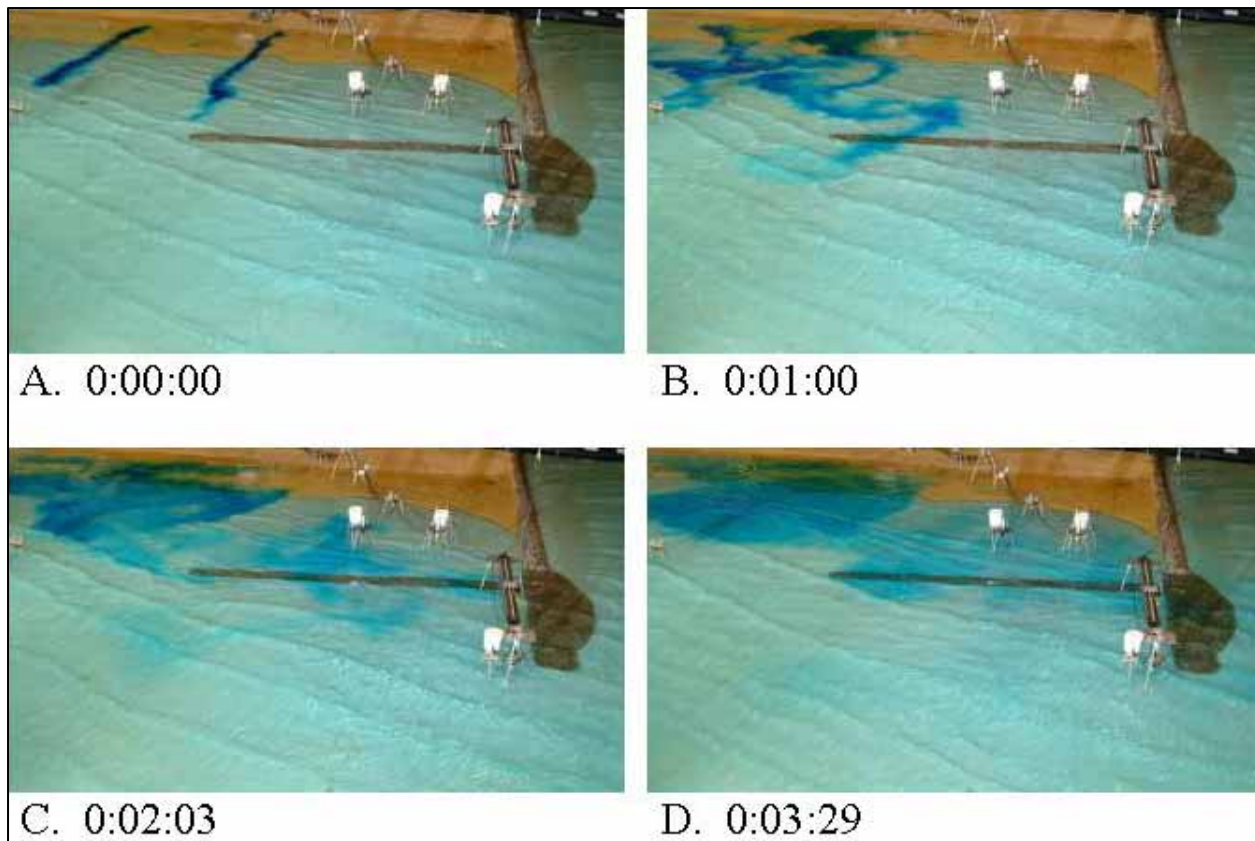
Figure B39. Dye study of 5-m, 13-sec waves from west-northwest at mhw, Alt 2A′
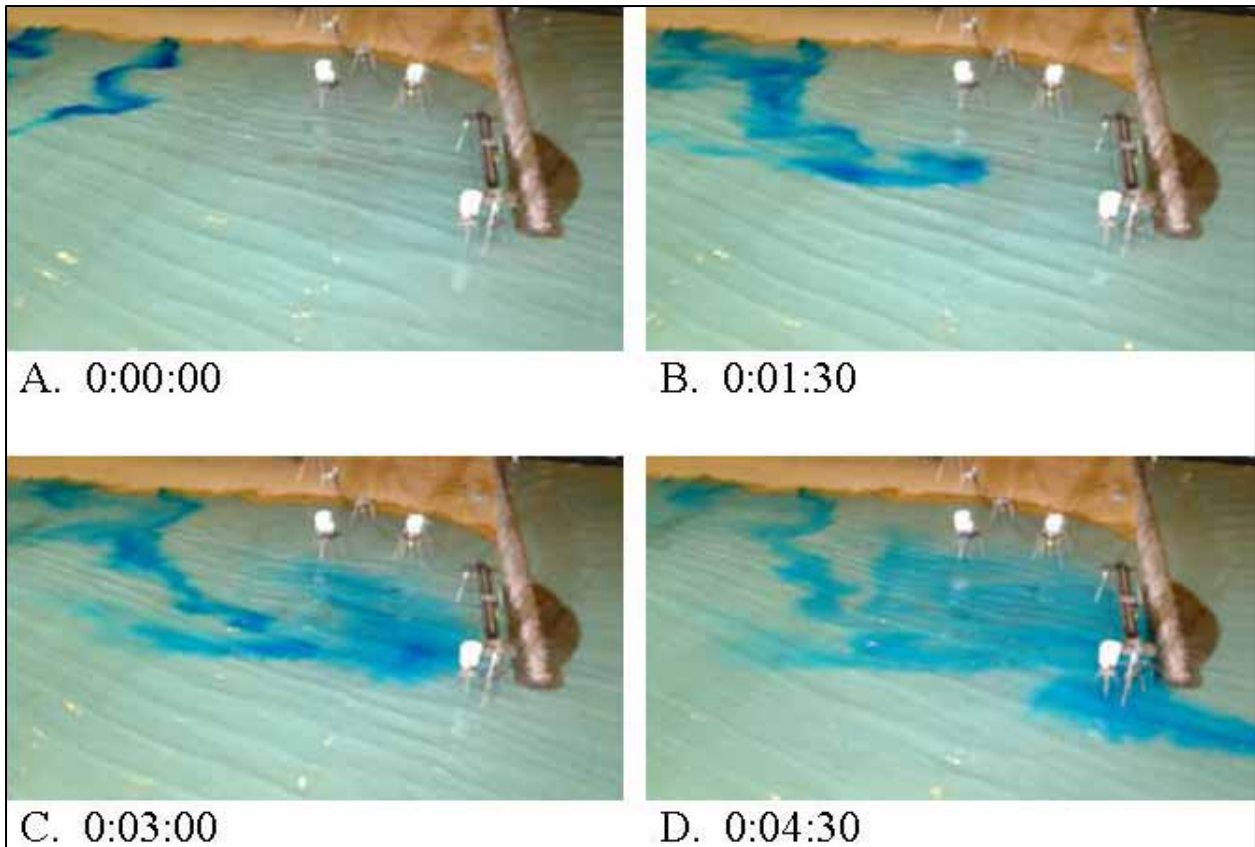
Figure B40. Dye study of Alt 3B for 2-m, 9-sec waves from west-northwest at mllw
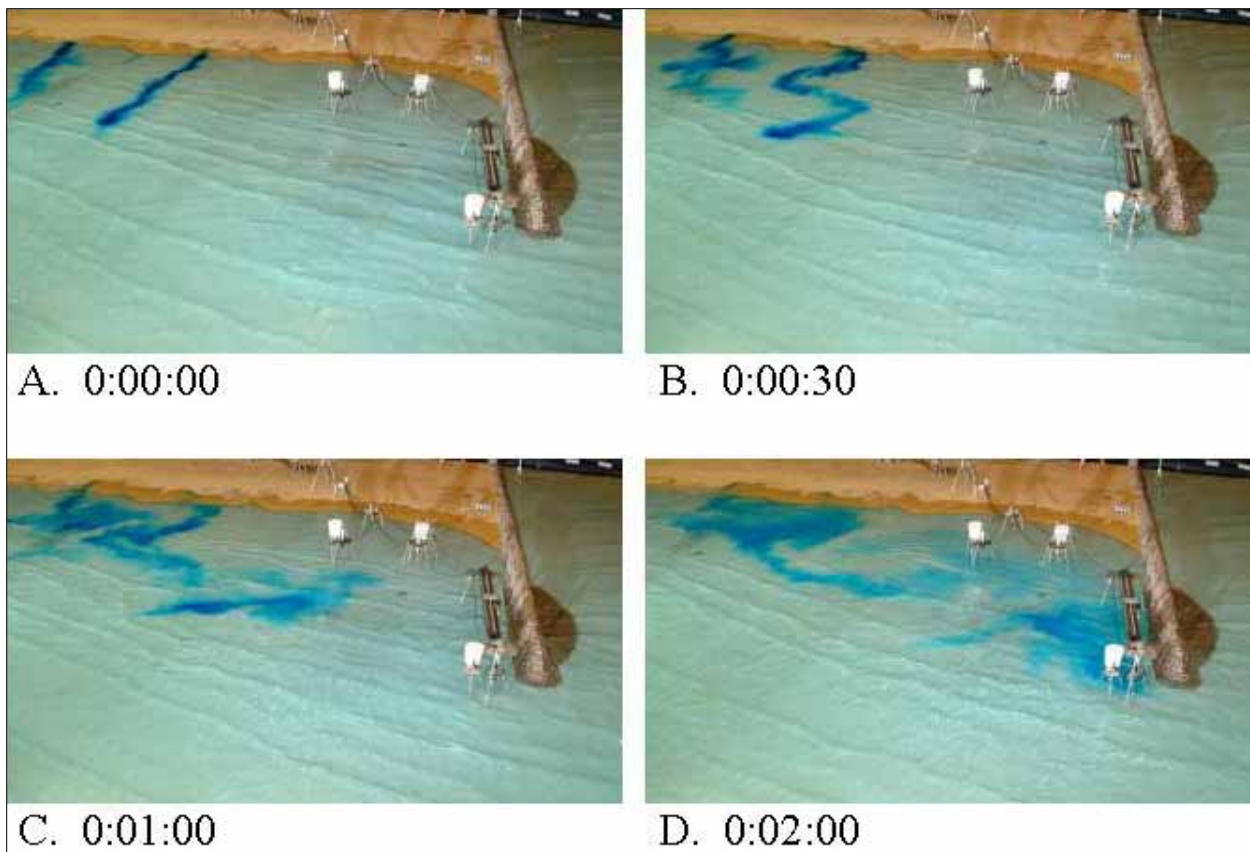
Figure B41. Dye study of Alt 3B for 5-m, 13-sec waves from west-northwest at mllw
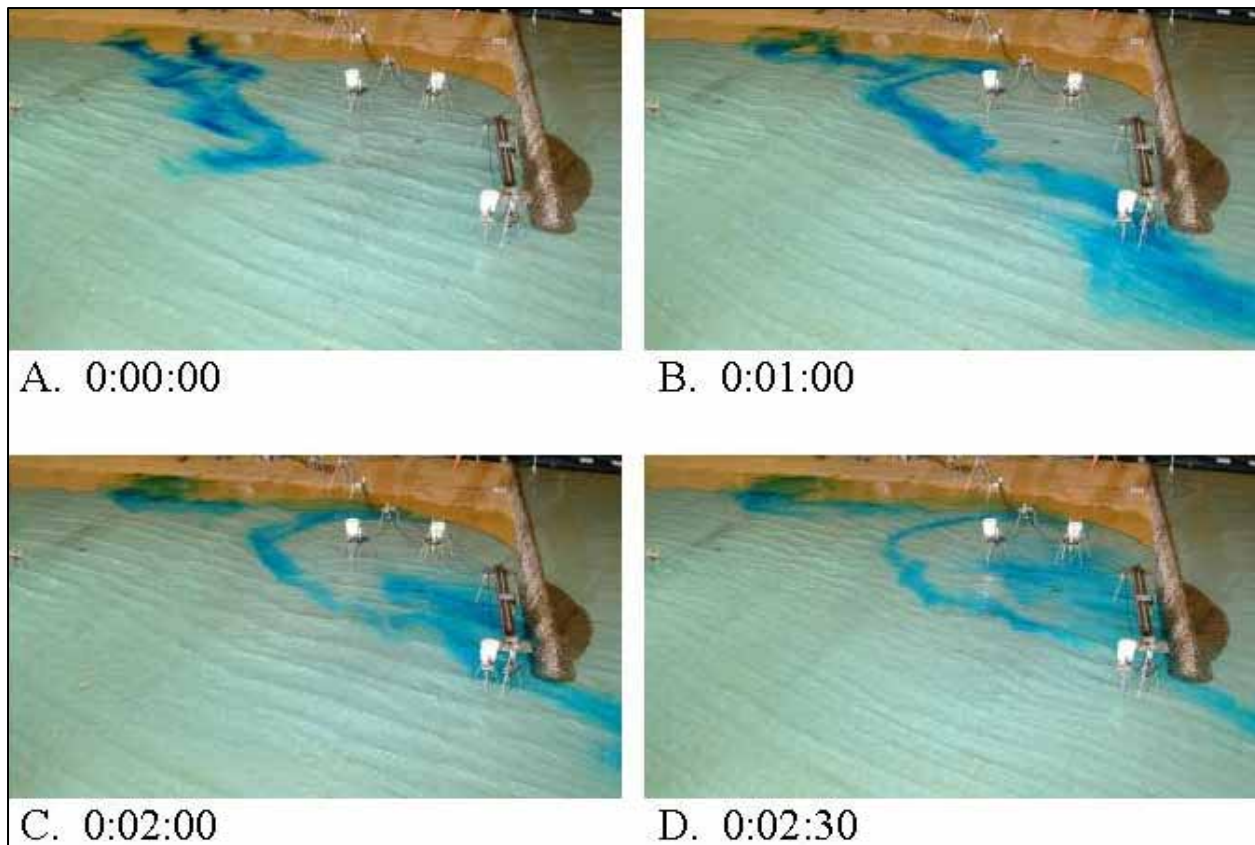
Figure B42. Dye study of Alt 3B for 2-m, 9-sec waves from west-northwest at mtl
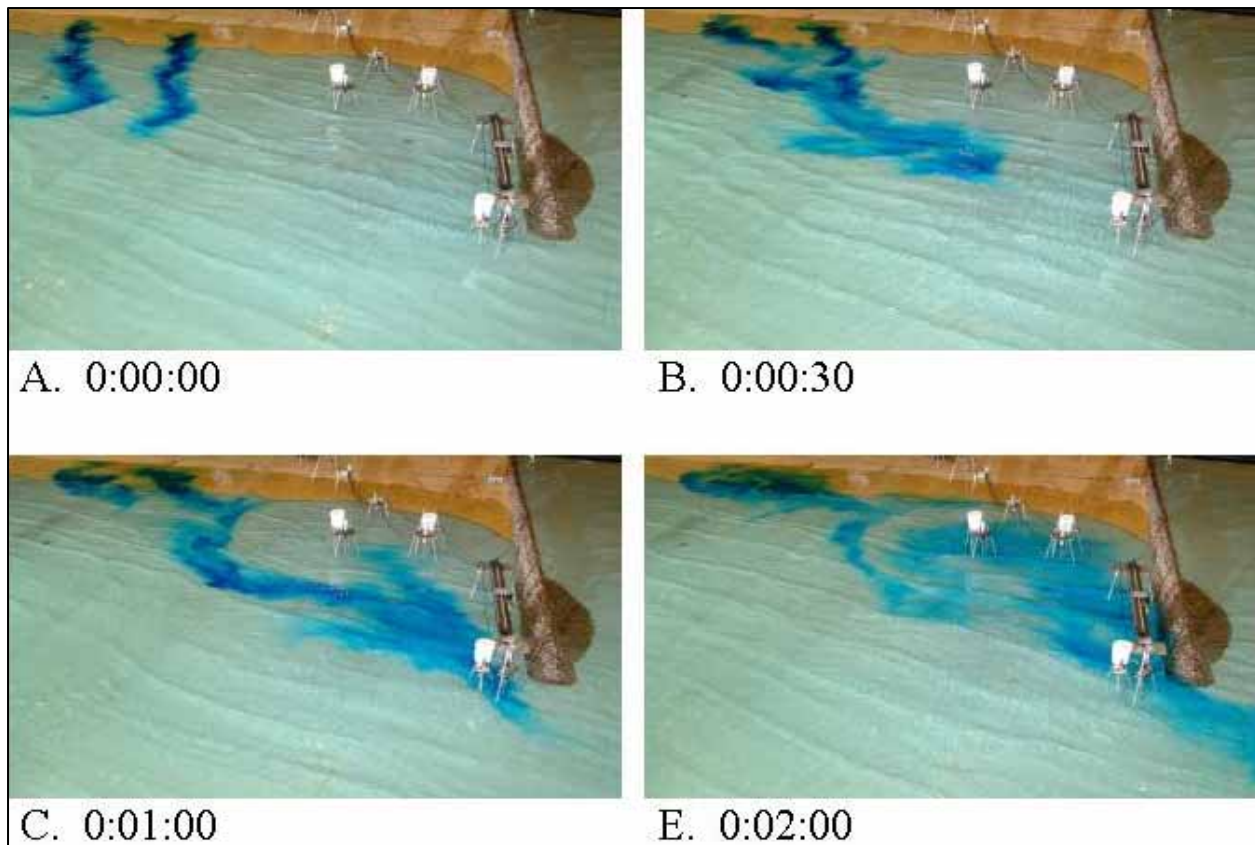
Figure B43. Dye study of Alt 3B for 3-m, 13-sec waves from west-northwest at mtl
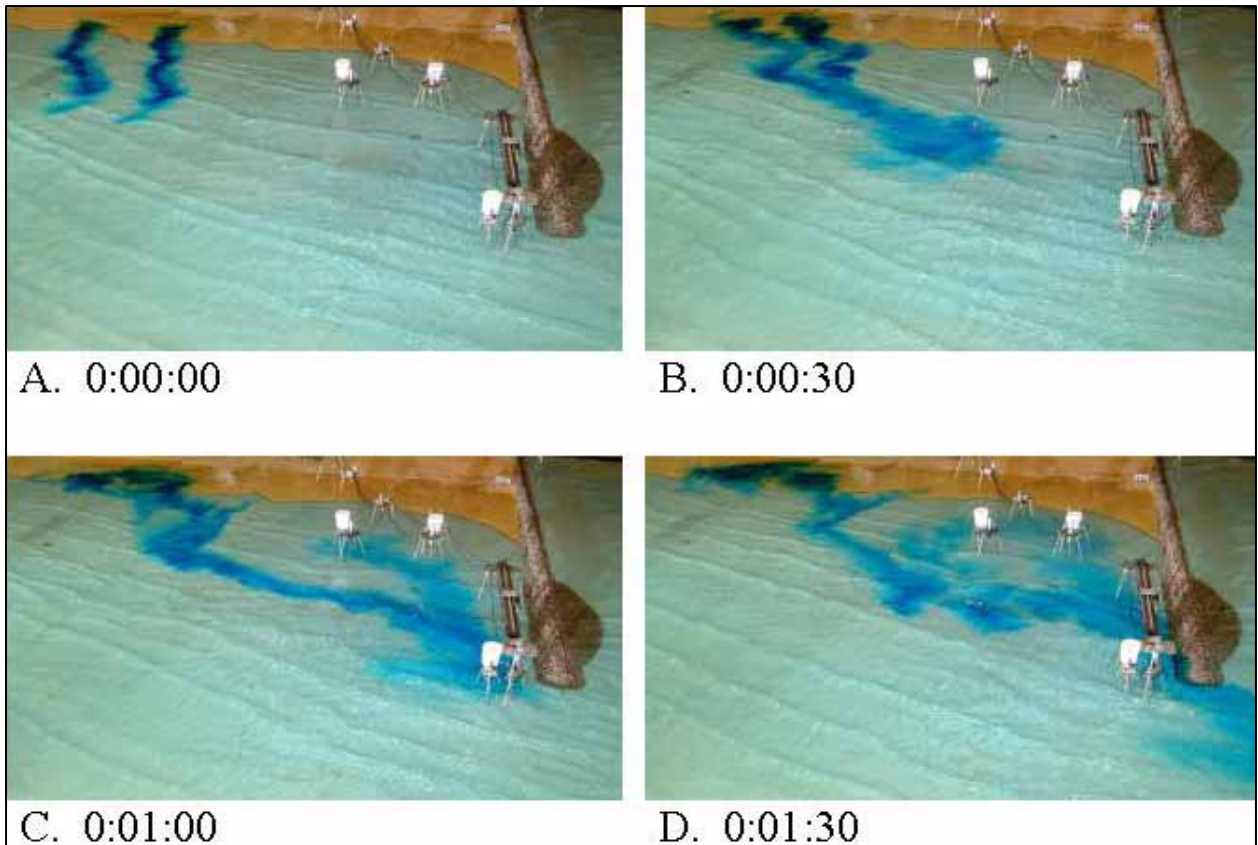
Figure B44. Dye study of Alt 3B for 5-m, 13-sec waves from west-northwest at mtl
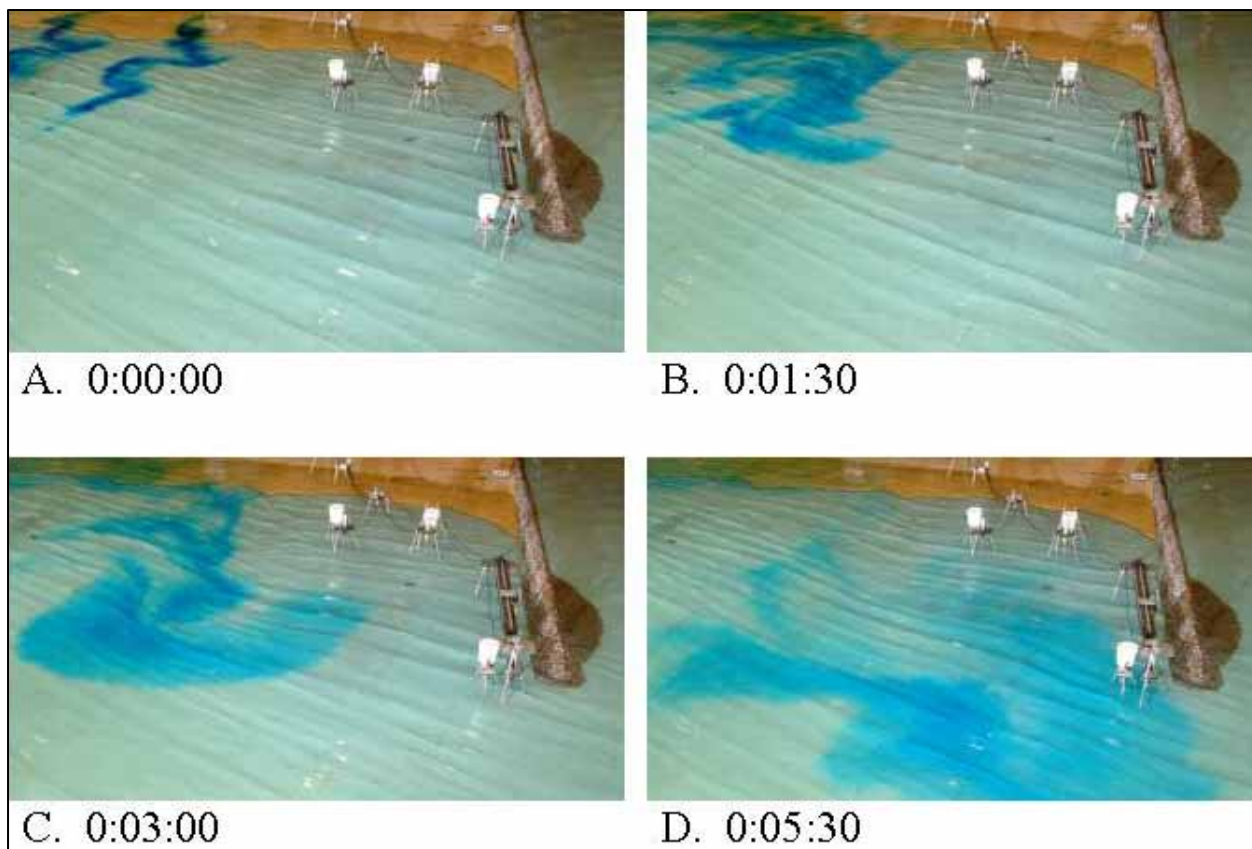
Figure B45. Dye study of Alt 3B for 2-m, 9-sec waves from west-northwest at mhw
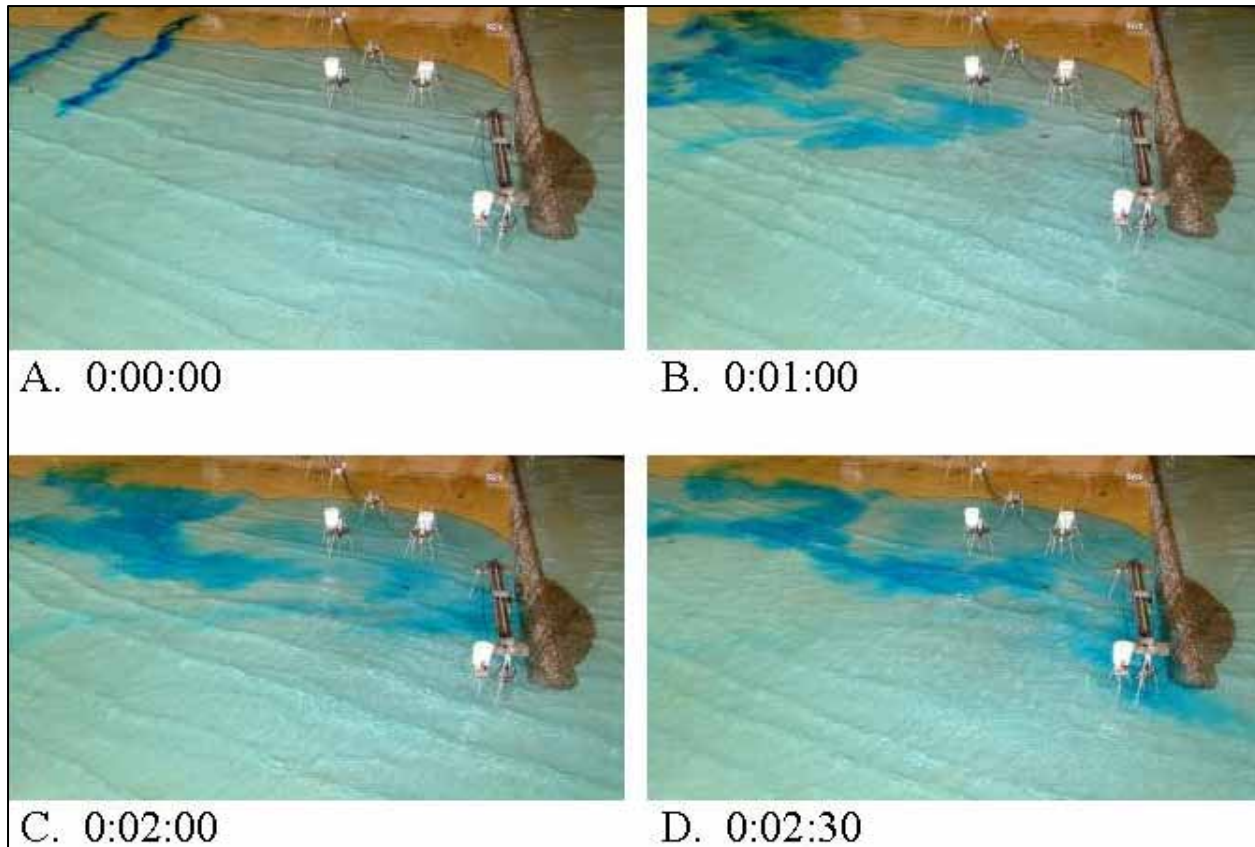
Figure B46. Dye study of Alt 3B for 5-m, 13-sec waves from west-northwest at mhw

Wave heights

Figures B47 through B55 illustrate changes in wave heights with Alt 2A compared to Alt 1. A negative number indicates waves heights with Alt 2A were lower than with Alt 1.

NOTE: CONTOURS AND ELEVATIONS SHOWN IN FEET REFERRED TO MEAN LOWER LOW WATER (MLLW)

LEGEND

-0.1 CHANGE IN WAVE HEIGHT WITH ALT 2A SPUR ADDED

SCALES IN FEET

MODEL   0   5   10   15   20

PROTOTYPE 0   375   750   1125   1500

ALT 1 AND ALT 2A WAVE HEIGHT DIFFERENCE
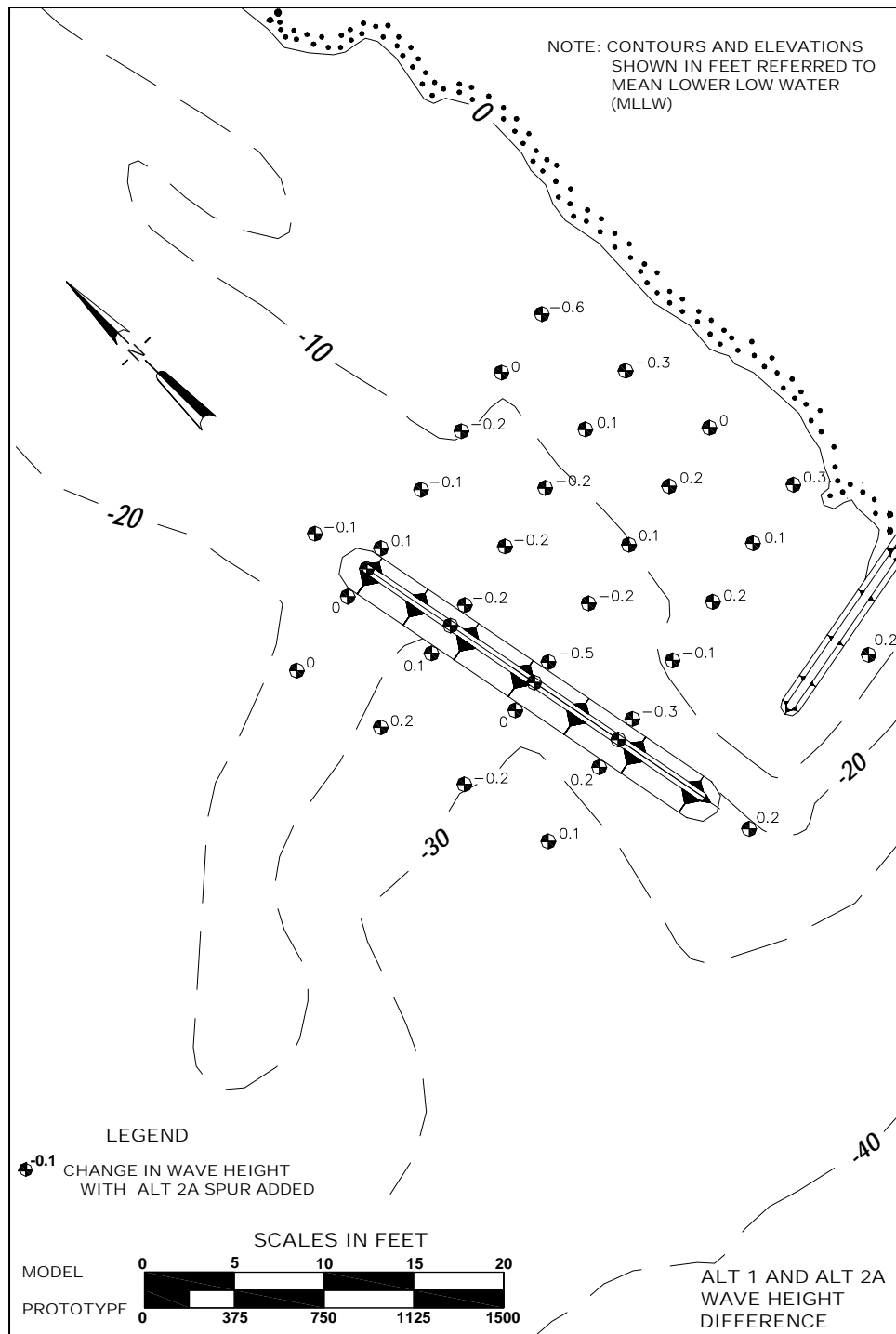
Figure B47. Differences in wave heights from west-northwest between Alt 1 and Alt 2A for 2-m, 9-sec waves at mllw

NOTE: CONTOURS AND ELEVATIONS
SHOWN IN FEET REFERRED TO
MEAN LOWER LOW WATER
(MLLW)

LEGEND

-0.1 CHANGE IN WAVE HEIGHT
WITH ALT 2A SPUR ADDED

SCALES IN FEET

| MODEL | 0 | 5 | 10 | 15 | 20 |
| PROTOTYPE | 0 | 375 | 750 | 1125 | 1500 |

ALT 1 AND ALT 2A
WAVE HEIGHT
DIFFERENCE
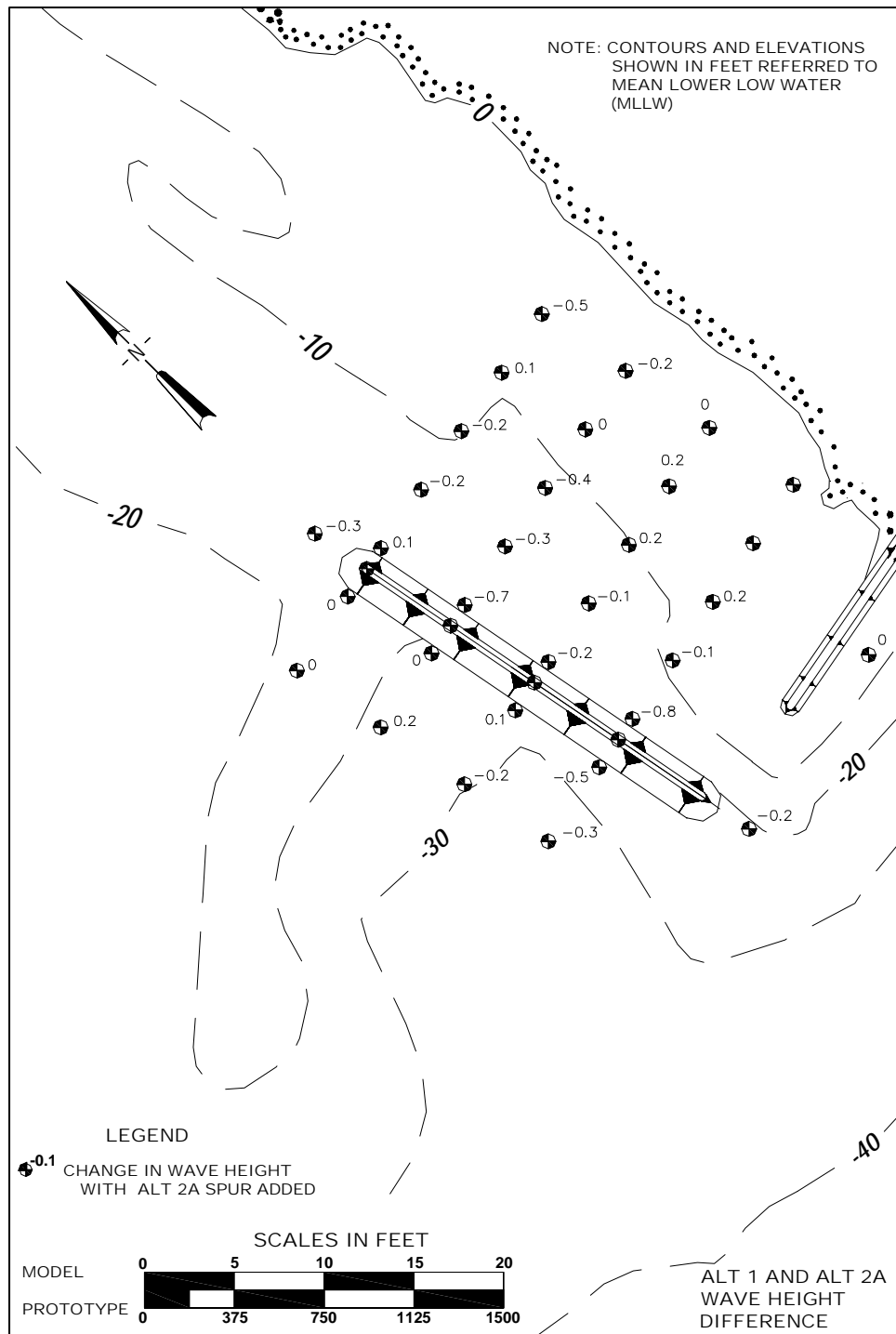
Figure B48. Differences in wave heights from west-northwest between Alt 1 and
Alt 2A for 3-m, 13-sec waves at mllw
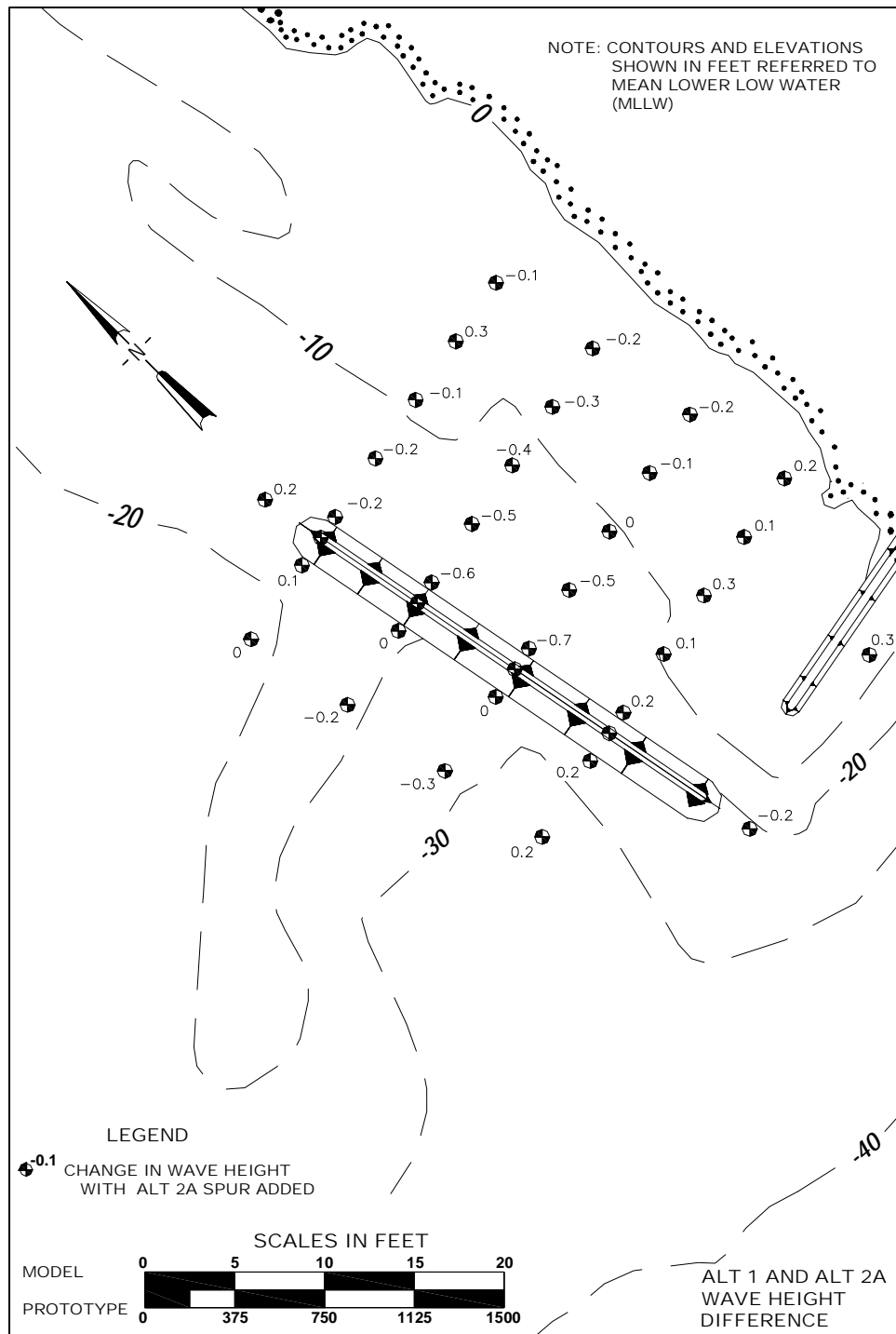
Figure B49. Differences in wave heights from west-northwest between Alt 1 and Alt 2A for 5-m, 13-sec waves at mllw

NOTE: CONTOURS AND ELEVATIONS SHOWN IN FEET REFERRED TO MEAN LOWER LOW WATER (MLLW)

LEGEND

●-0.1 CHANGE IN WAVE HEIGHT WITH ALT 2A SPUR ADDED

SCALES IN FEET

MODEL   0   5   10   15   20
PROTOTYPE 0   375   750   1125   1500

ALT 1 AND ALT 2A WAVE HEIGHT DIFFERENCE
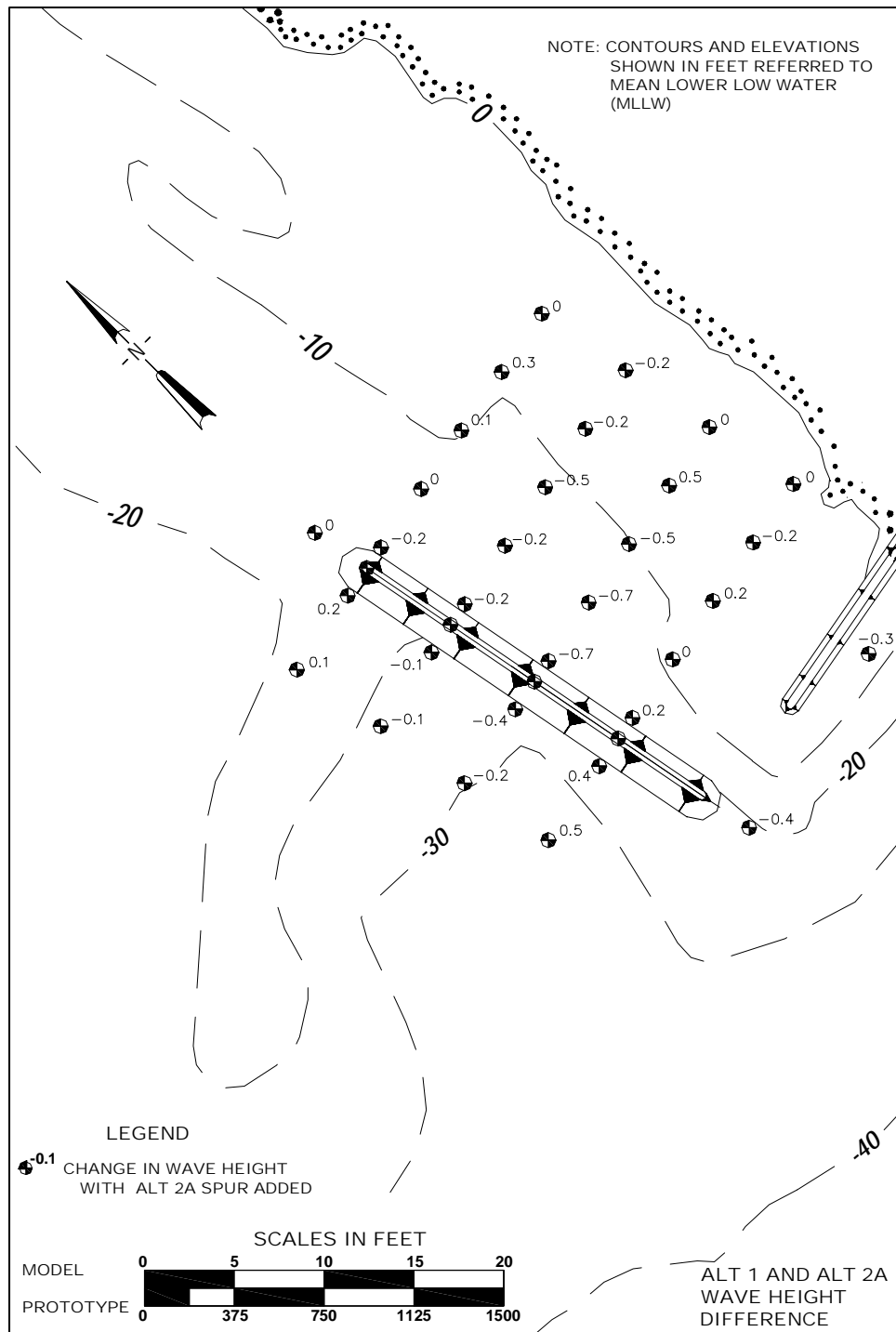
Figure B50. Differences in wave heights from west-northwest between Alt 1 and Alt 2A for 2-m, 9-sec waves at mtl with full flood tidal current
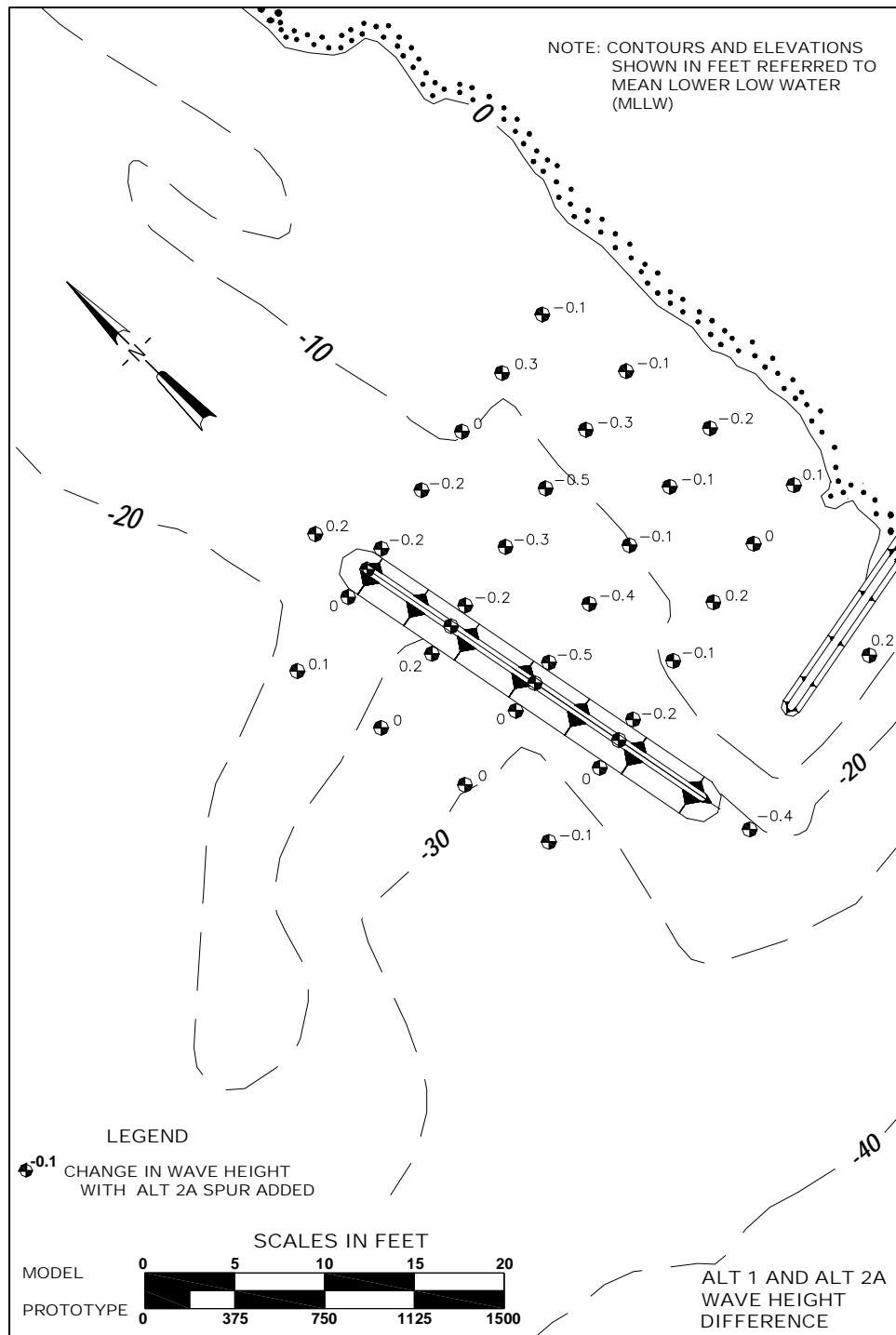
Figure B51. Differences in wave heights from west-northwest between Alt 1 and Alt 2A for 3-m, 13-sec waves at mtl with full flood tidal current
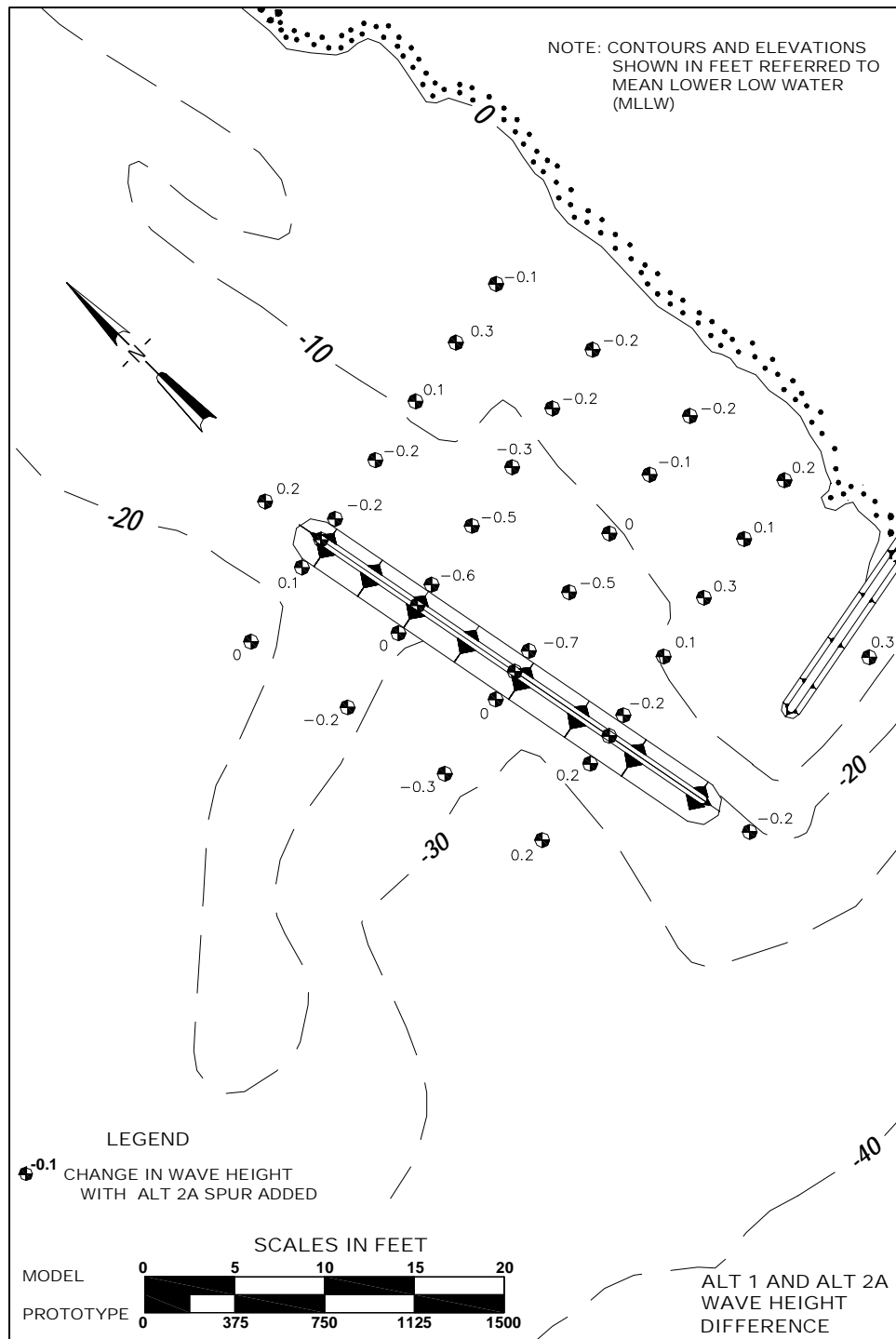
Figure B52. Differences in wave heights from west-northwest between Alt 1 and
Alt 2A for 5-m, 13-sec waves at mtl with full flood tidal current

Figure B53. Differences in wave heights from west-northwest between Alt 1 and
Alt 2A for 2-m, 9-sec waves at mhw
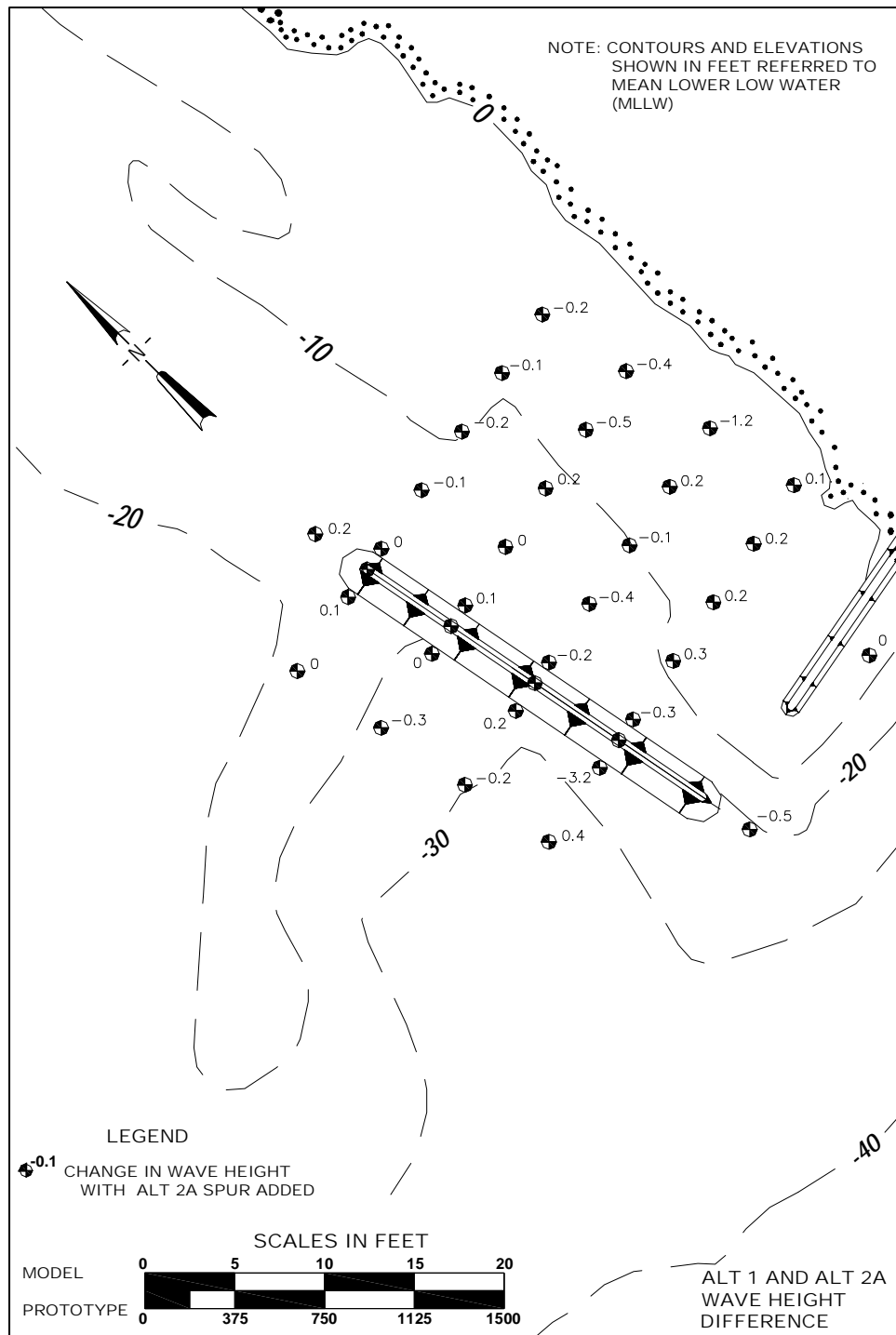
Figure B54. Differences in wave heights from west-northwest between Alt 1 and
Alt 2A for 3-m, 13-sec waves at mhw
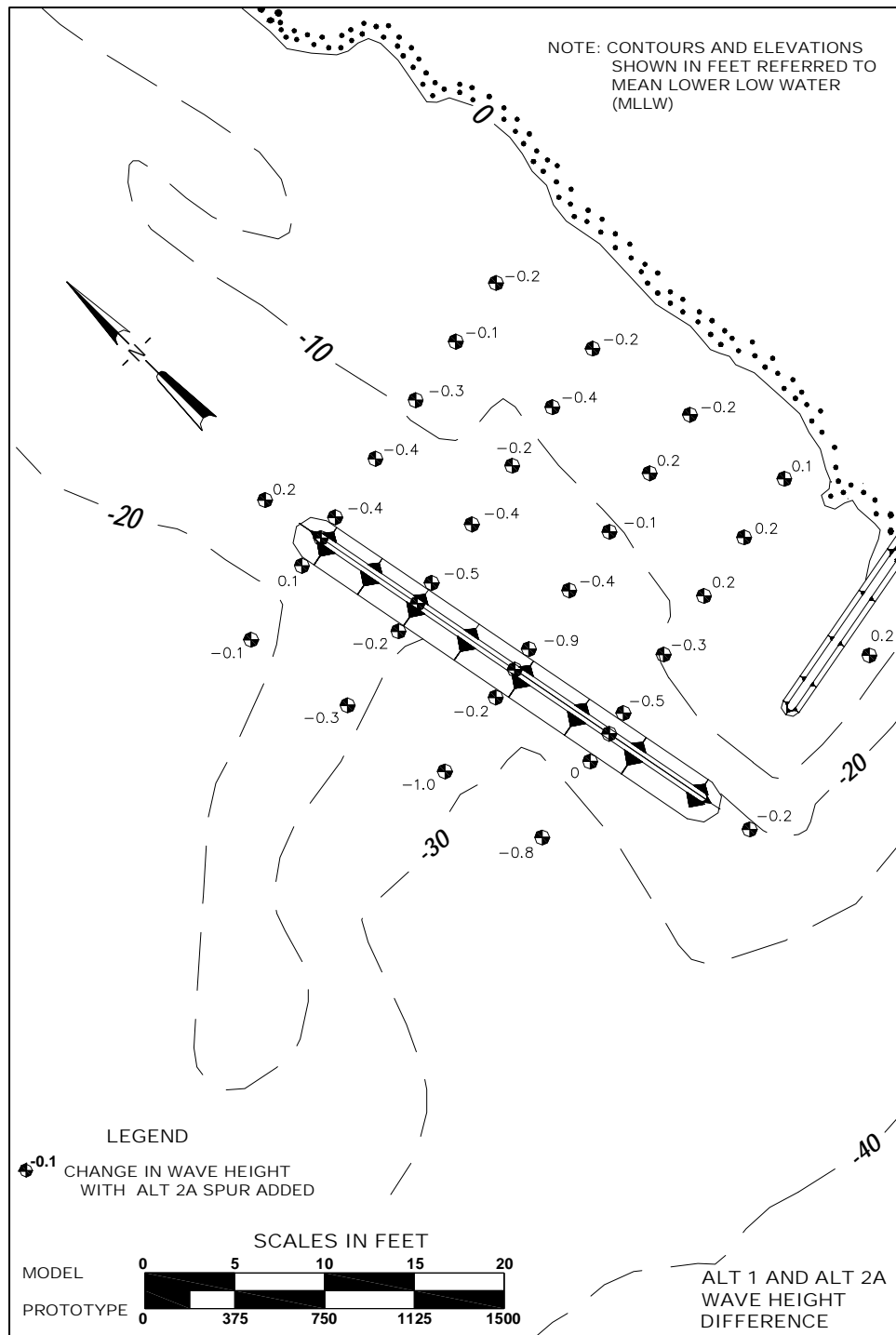
Figure B55. Differences in wave heights from west-northwest between Alt 1 and Alt 2A for 5-m, 13-sec waves at mhw

Figures for Storms from Southwest

Dye studies

Figures B56 through B73 contain photographs taken during dye studies with storms from the southwest. Figures B56 through B64 were taken during experiments with Alt 1. Figures B65 through B75 were taken during experiments with Alt 2A.
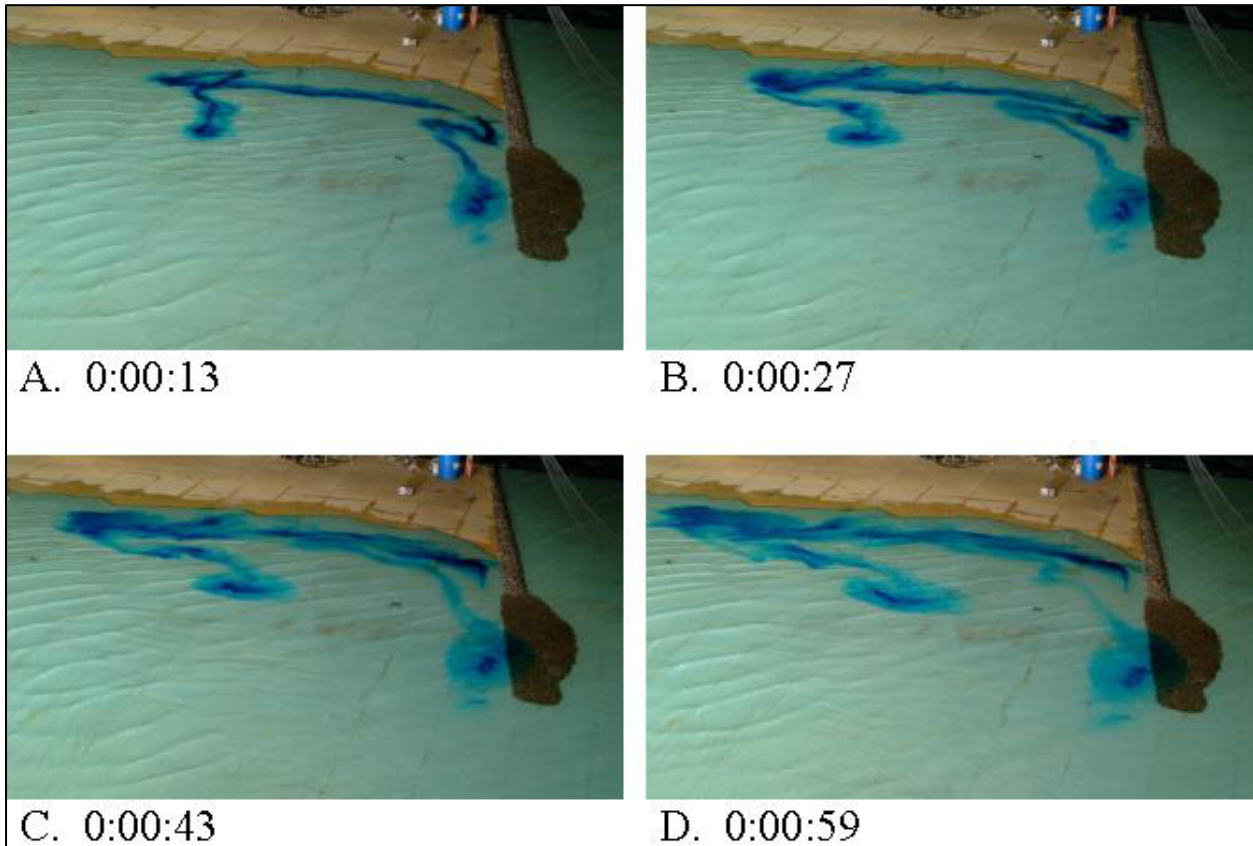
Figure B56. Dye study of 2-m, 9-sec waves from southwest at mllw, Alt 1
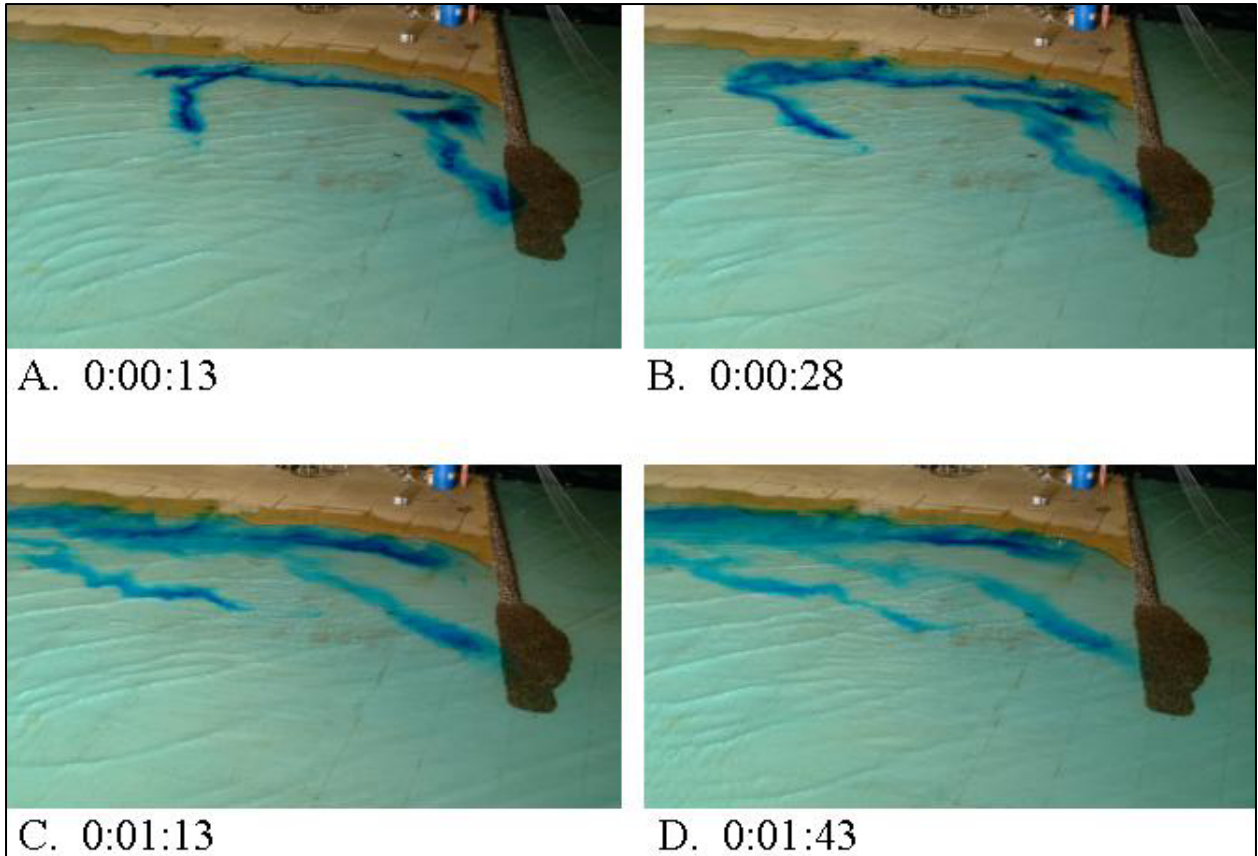
Figure B57. Dye study of 3-m, 12-sec waves from southwest at mllw, Alt 1
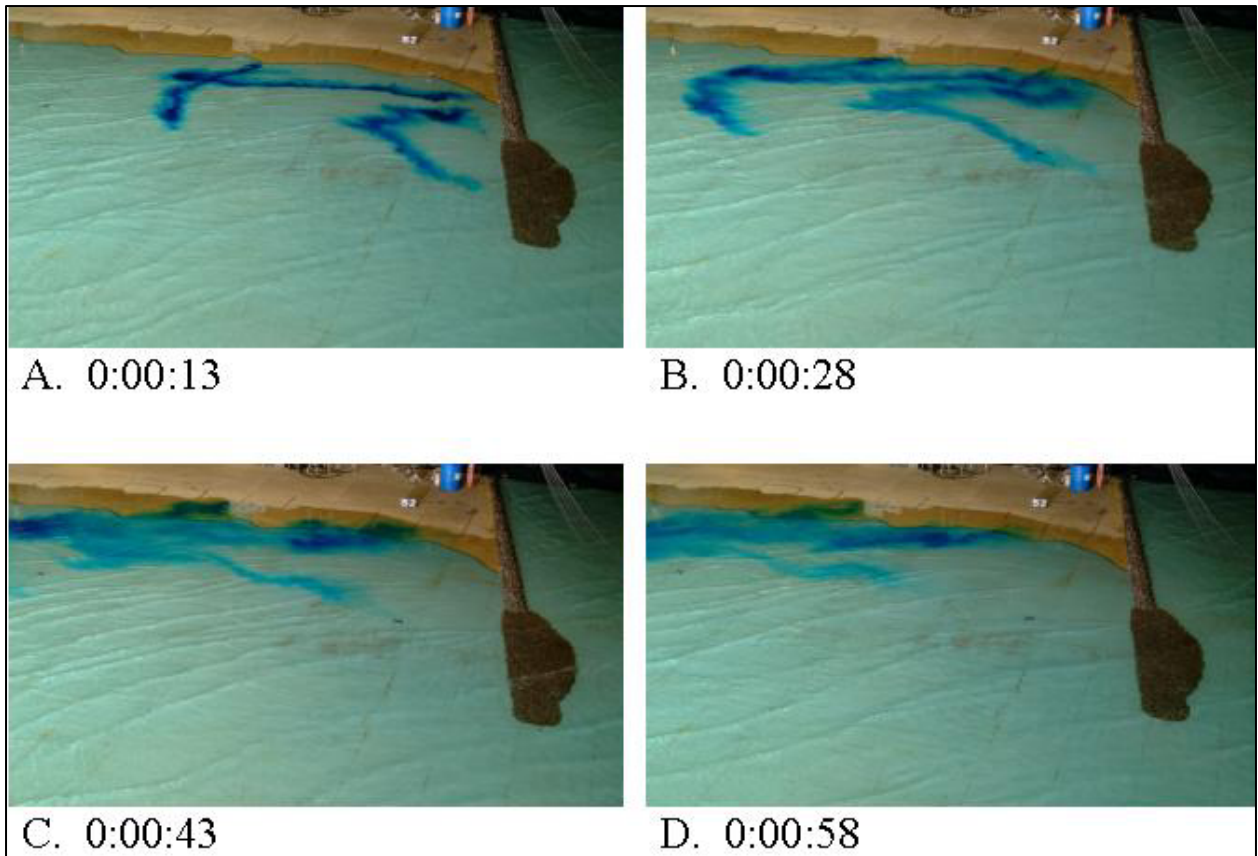
Figure B58. Dye study of 6-m, 16-sec waves from southwest at mllw, Alt 1
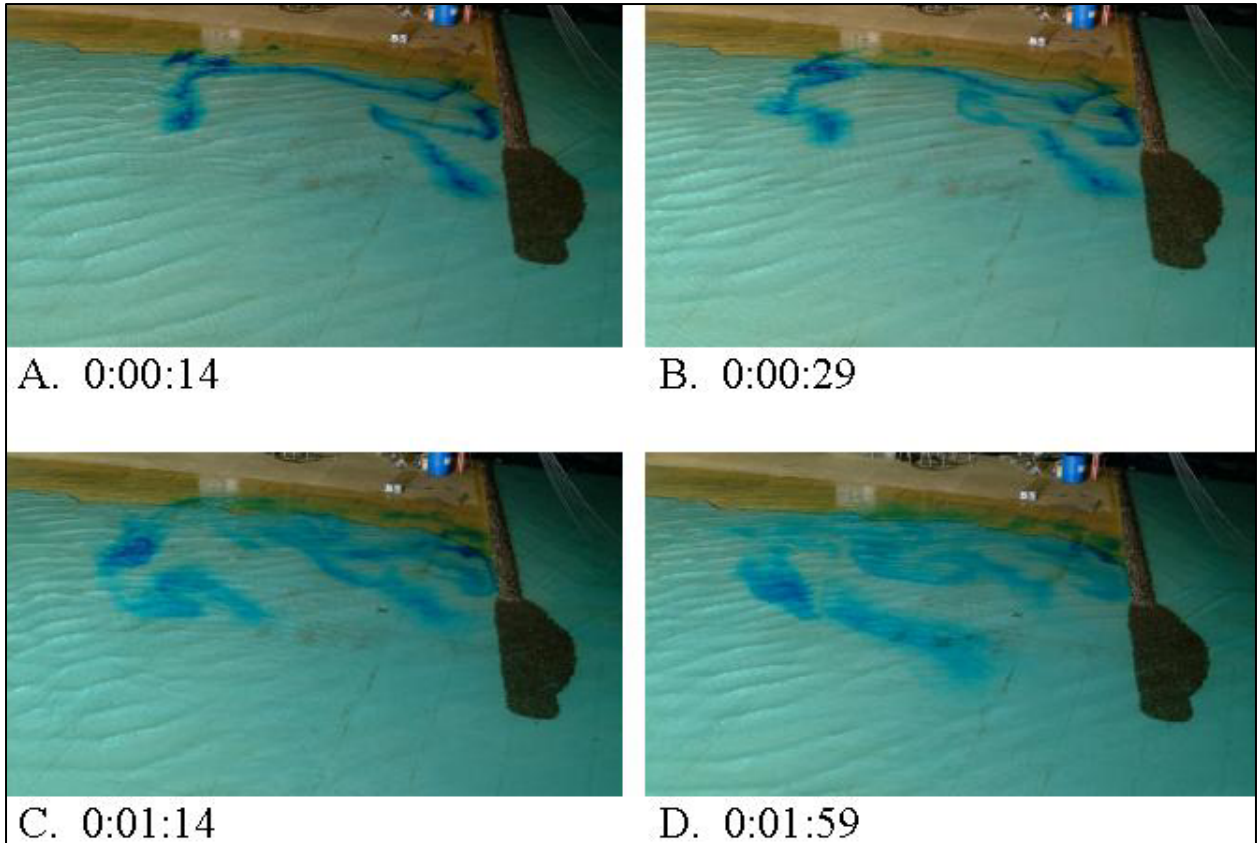
Figure B59. Dye study of 2-m, 9-sec waves from southwest at mtl with full flood tidal current, Alt 1
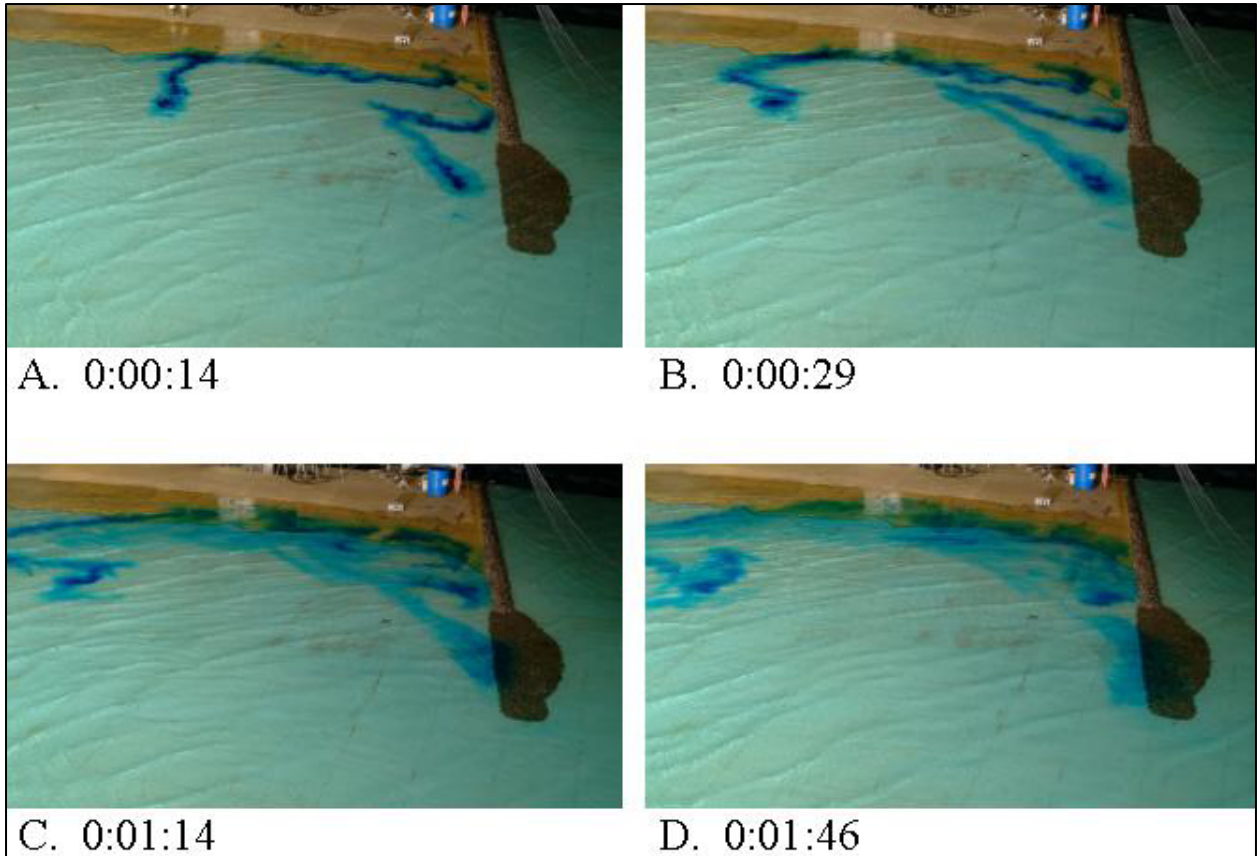
Figure B60. Dye study of 3-m, 12-sec waves from southwest at mtl with full flood tidal current, Alt 1
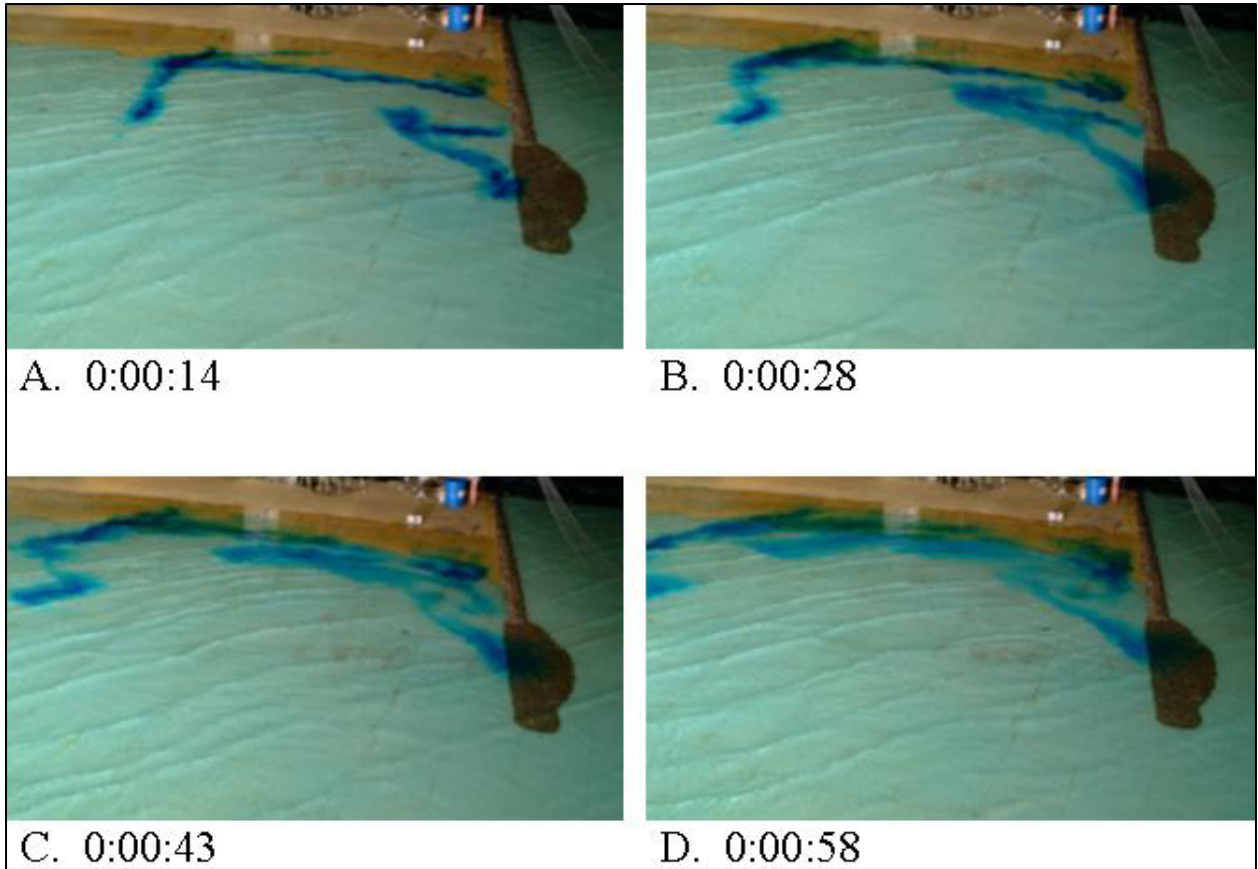
Figure B61. Dye study of 6-m, 16-sec waves from southwest at mtl with full flood tidal current, Alt 1
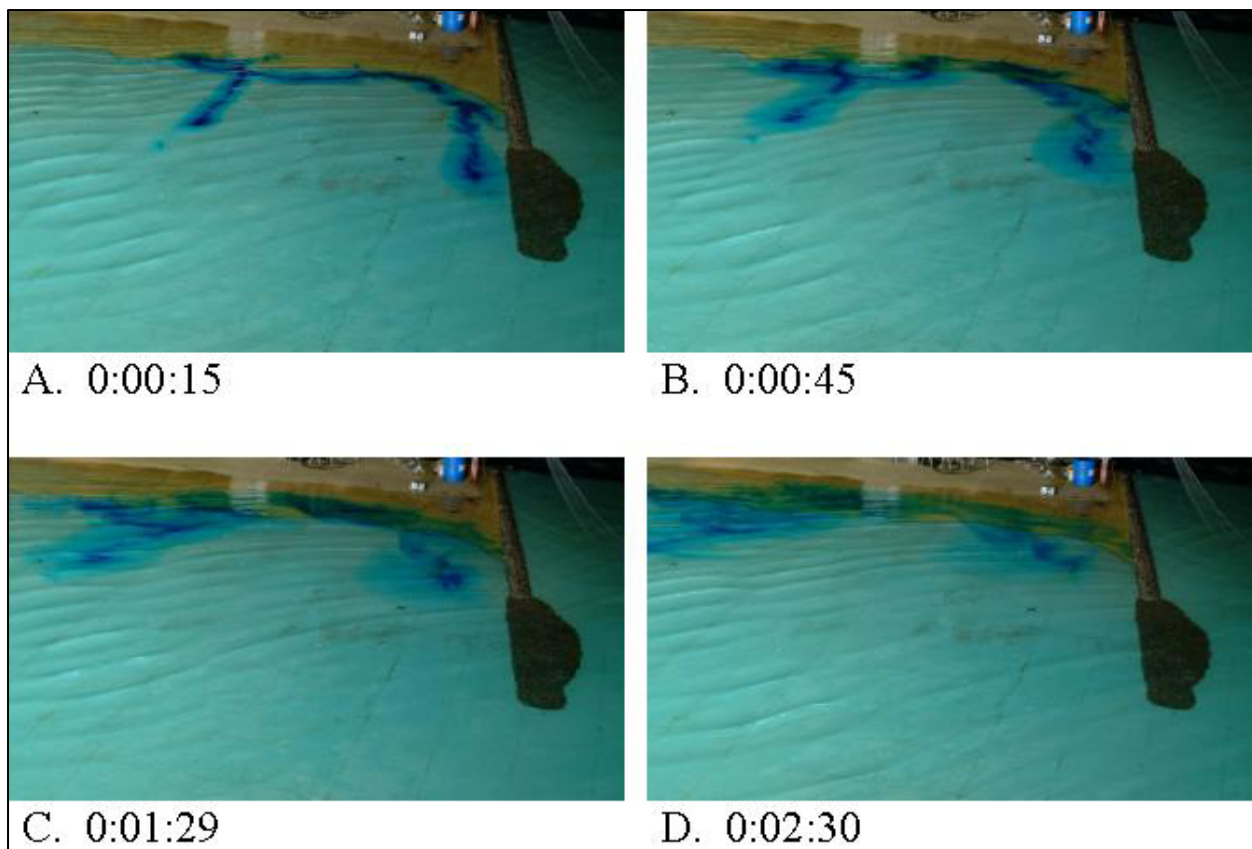
Figure B62. Dye study of 2-m, 9-sec waves from southwest at mhw, Alt 1
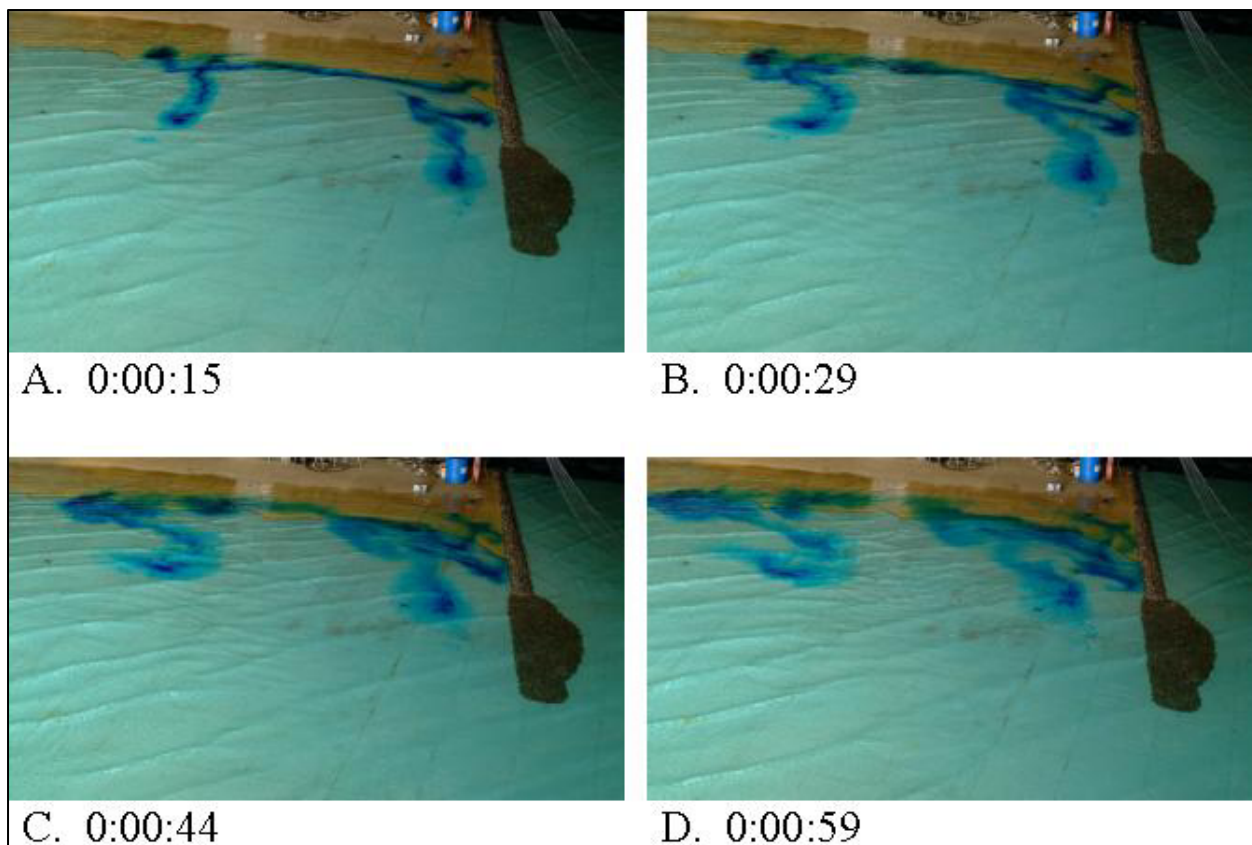
Figure B63. Dye study of 3-m, 12-sec waves from southwest at mhw, Alt 1
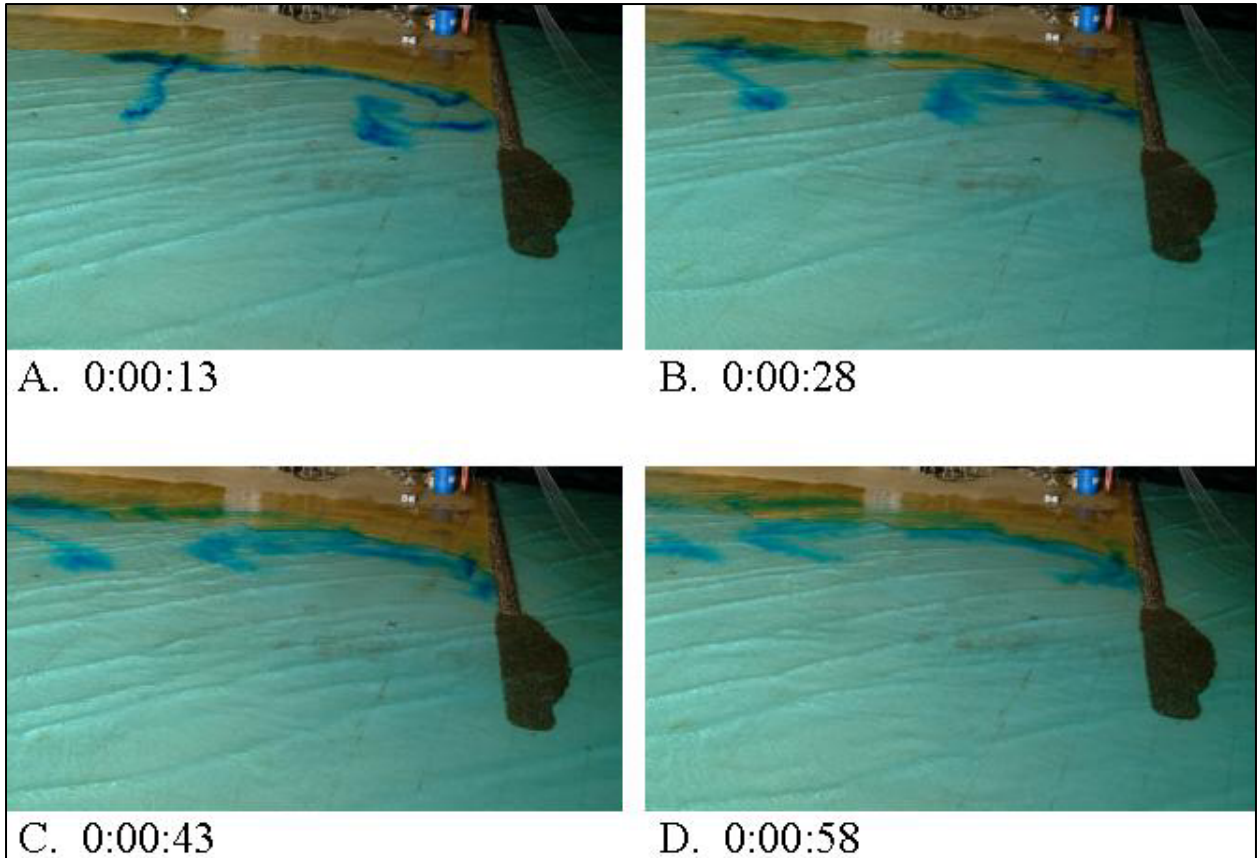
Figure B64. Dye study of 6-m, 16-sec waves from southwest at mhw, Alt 1
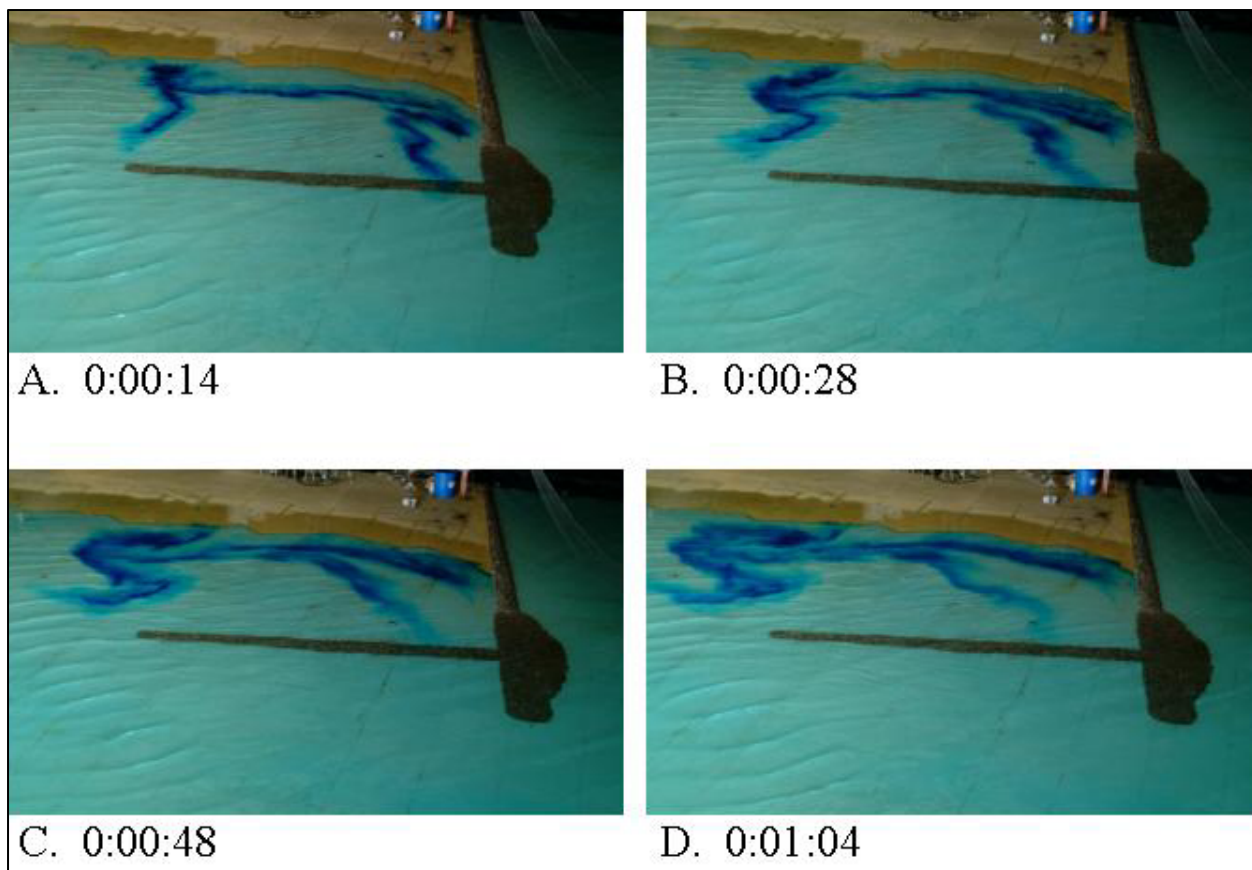
Figure B65. Dye study of 2-m, 9-sec waves from southwest at mllw, Alt 2A
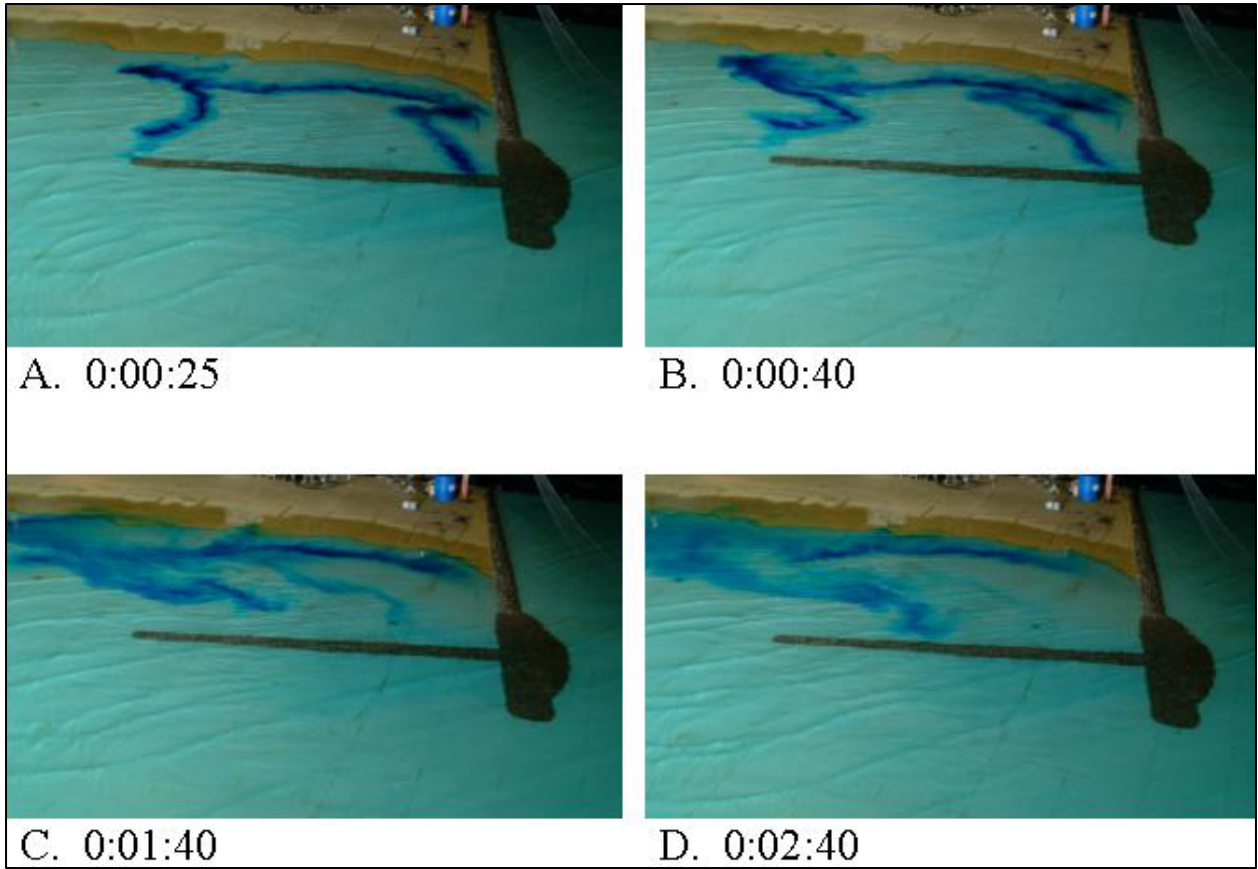
Figure B66. Dye study of 3-m, 12-sec waves from southwest at mllw, Alt 2A
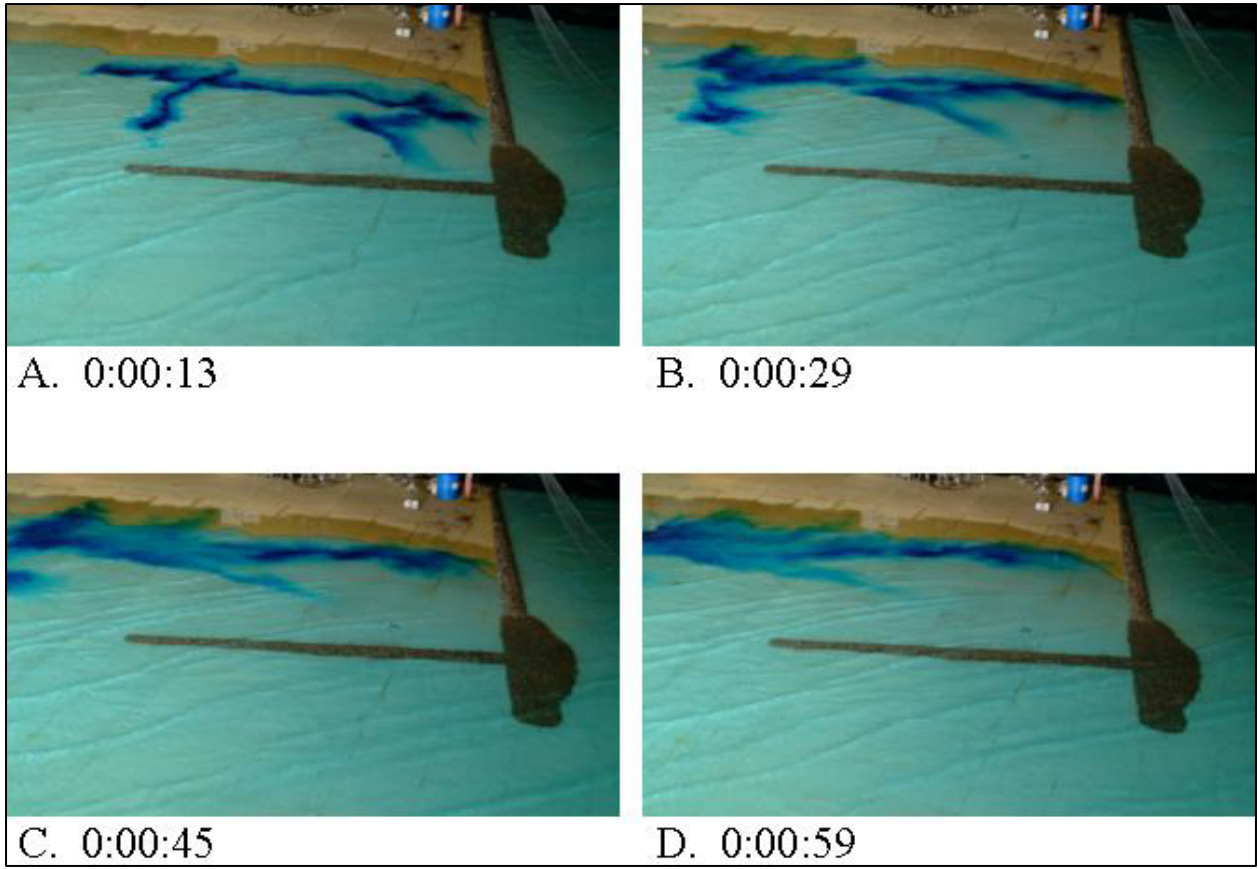
Figure B67. Dye study of 6-m, 16-sec waves from southwest at mllw, Alt 2A
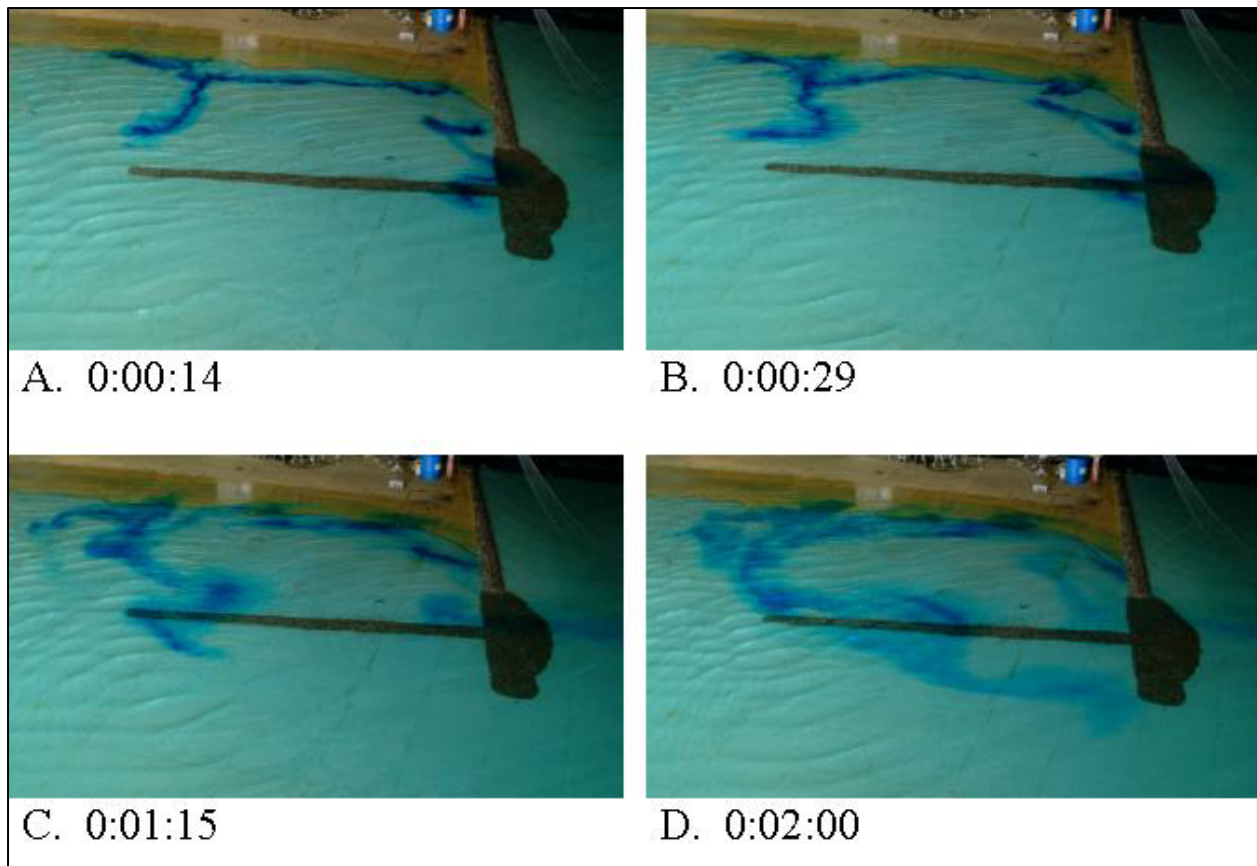
Figure B68. Dye study of 2-m, 9-sec waves from southwest at mtl with full flood tidal current, Alt 2A
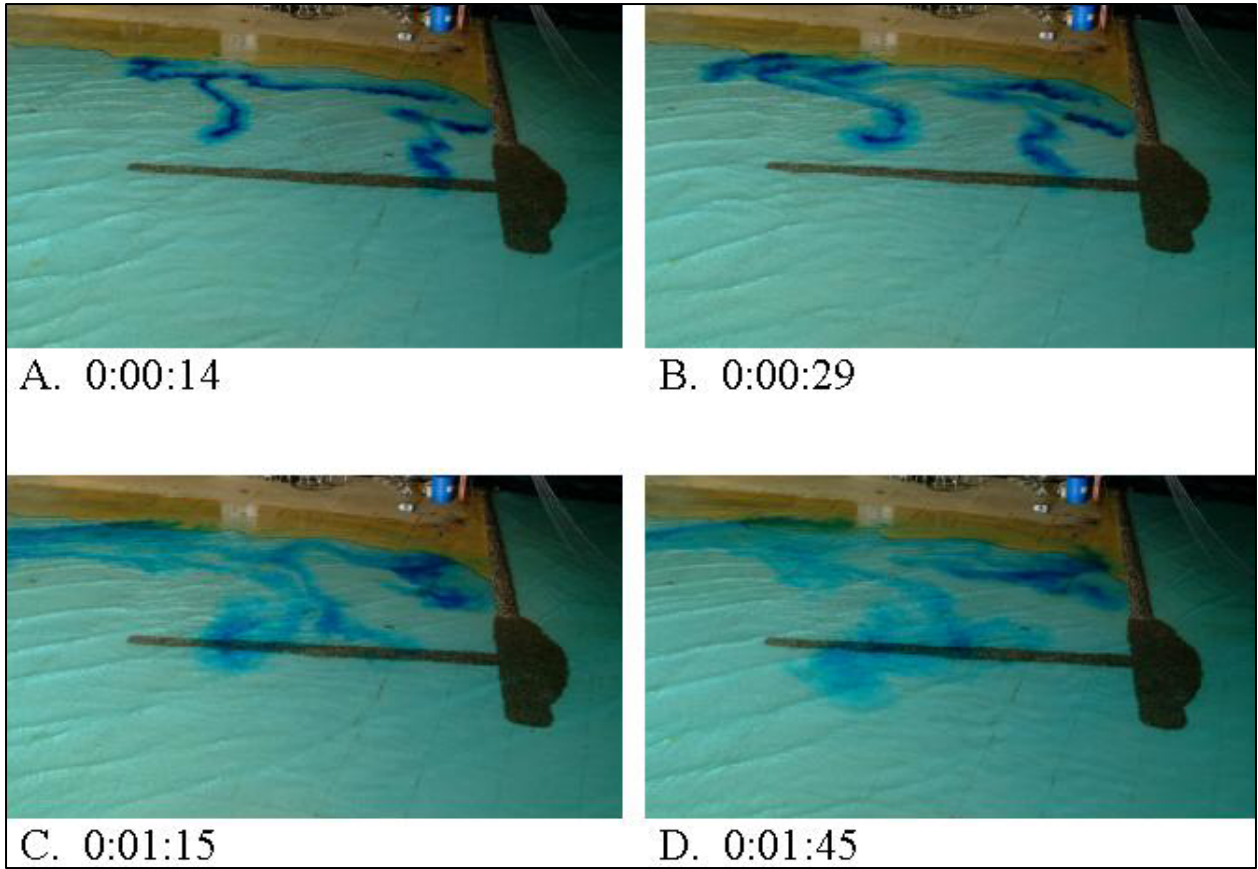
Figure B69. Dye study of 3-m, 12-sec waves from southwest at mtl with full flood tidal current, Alt 2A
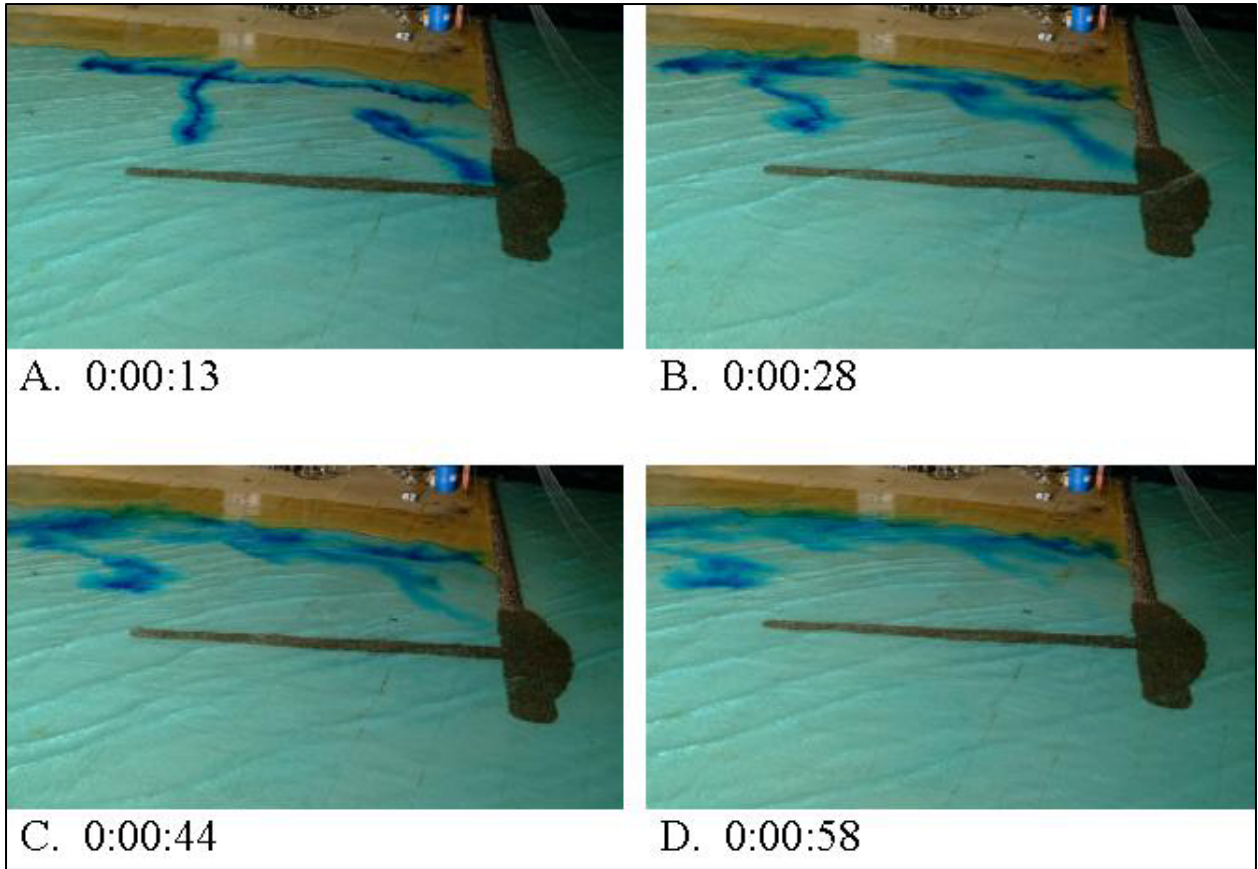
Figure B70. Dye study of 6-m, 16-sec waves from southwest at mtl with full flood tidal current, Alt 2A
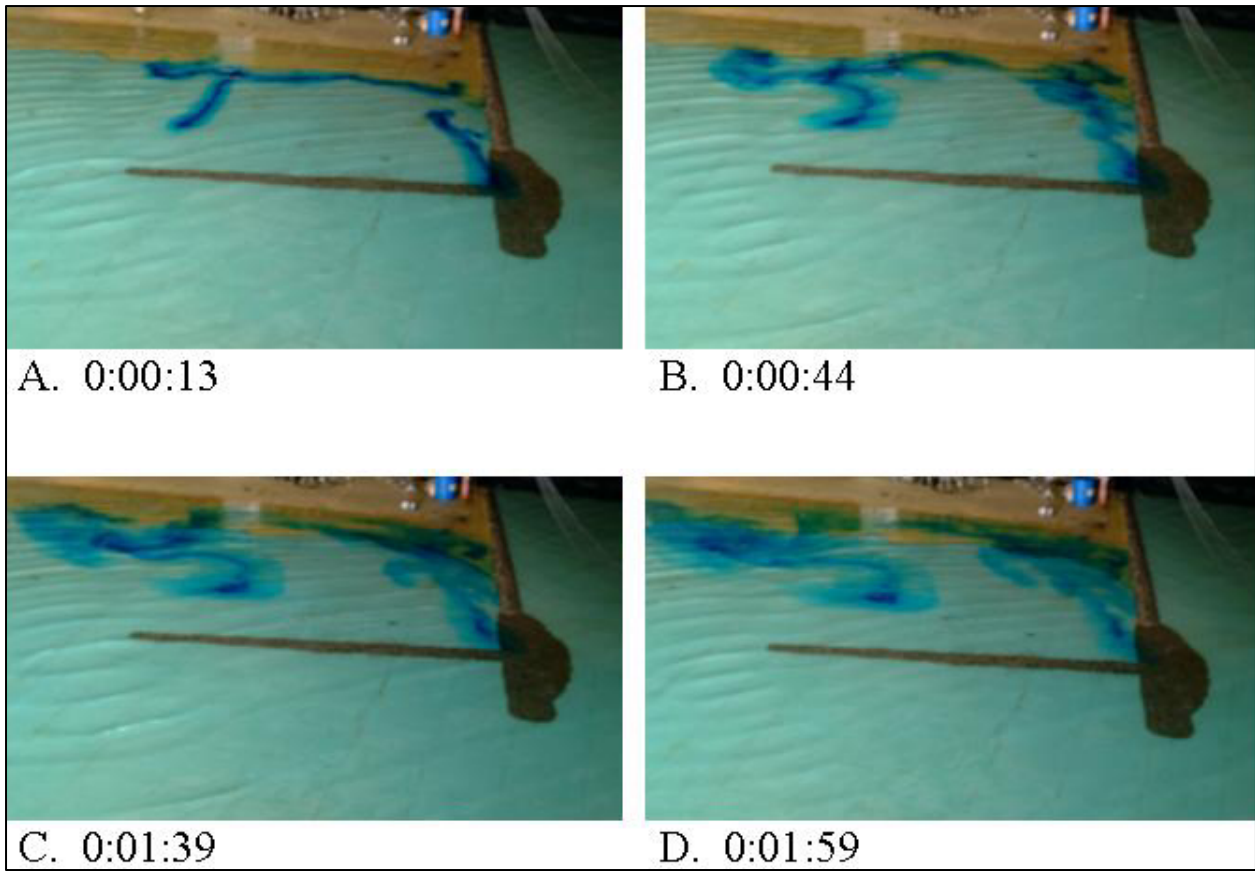
Figure B71. Dye study of 2-m, 9-sec waves from southwest at mhw, Alt 2A
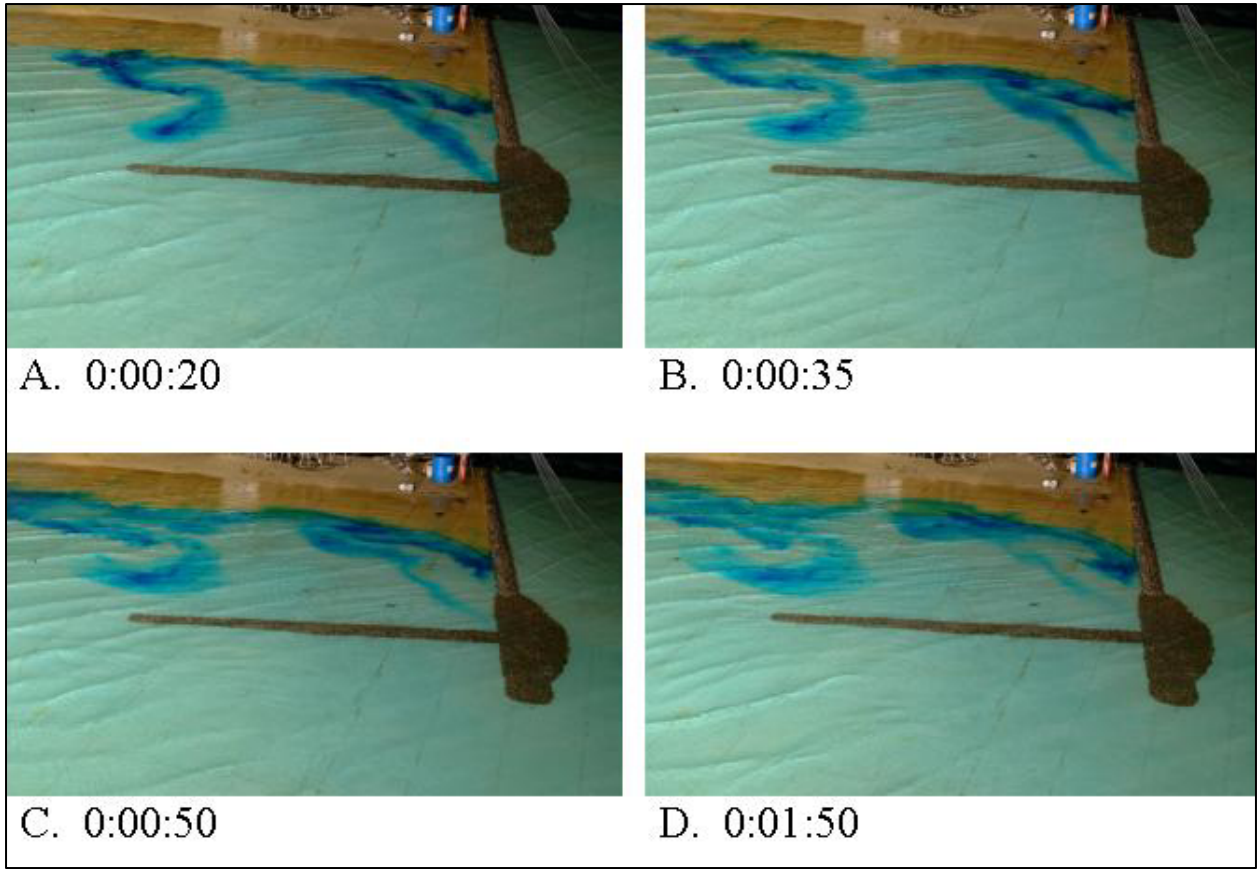
Figure B72. Dye study of 3-m, 12-sec waves from southwest at mhw, Alt 2A
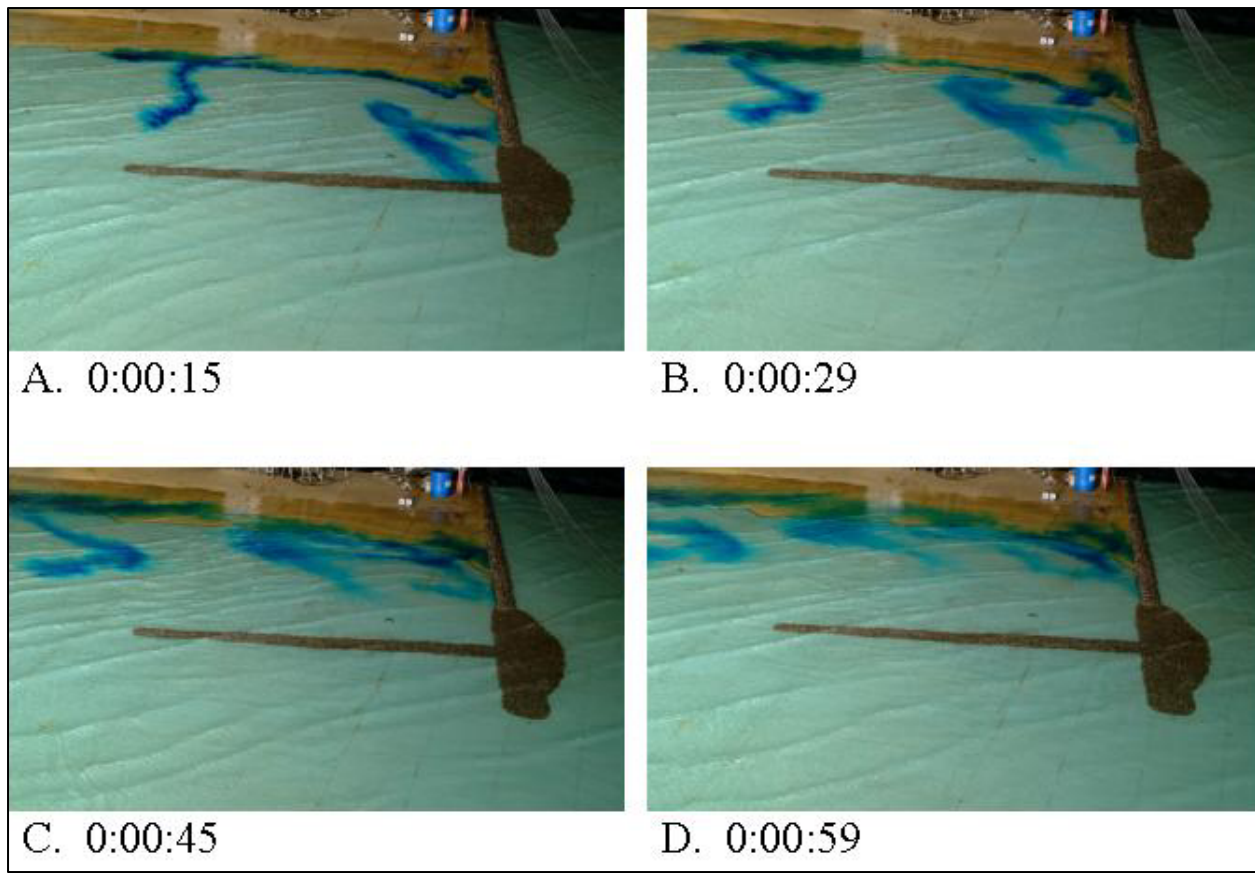
Figure B73. Dye study of 6-m, 16-sec waves from southwest at mhw, Alt 2A

Wave heights

Figures B74 through B82 show differences in wave heights recorded with Alt 2A compared to wave heights with Alt 1. Figures B83 through B91 show differences in wave heights recorded with Alt 3B compared to Alt 1.
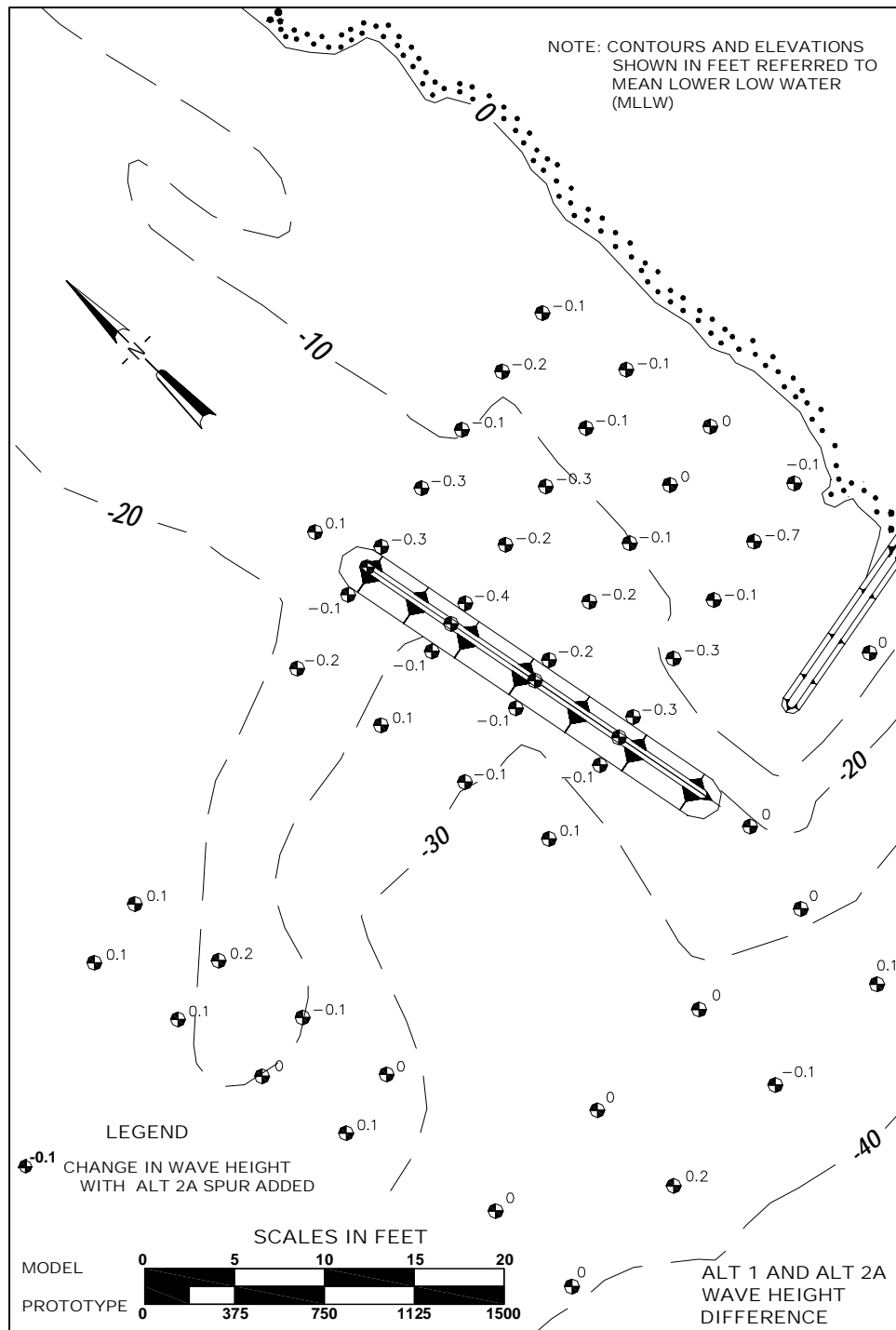
Figure B74. Differences in wave heights between Alt 1 and Alt 2A for 2-m, 9-sec waves from southwest at mllw
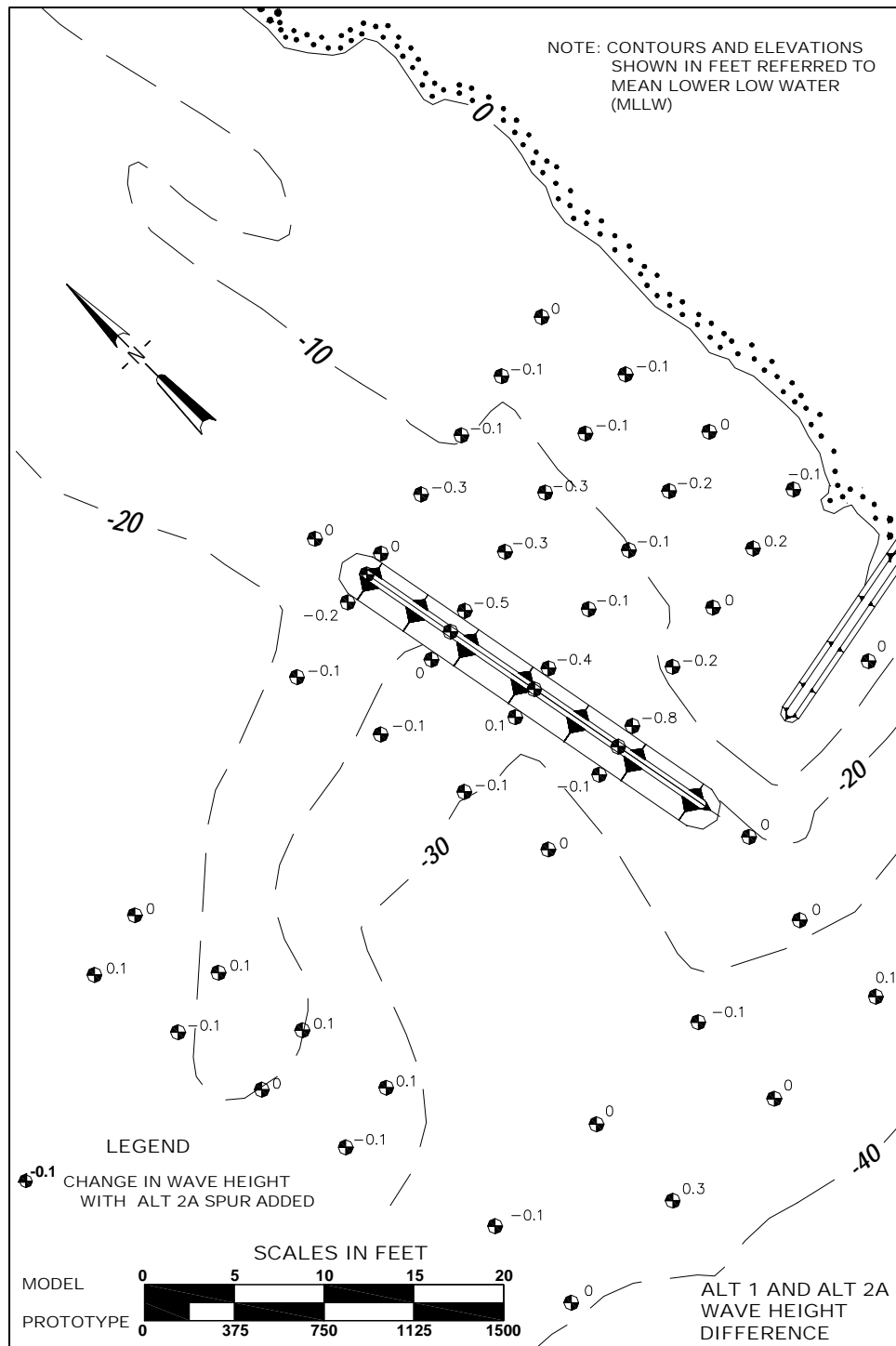
Figure B75.   Differences in wave heights between Alt 1 and Alt 2A for 3-m,
12-sec waves from southwest at mllw
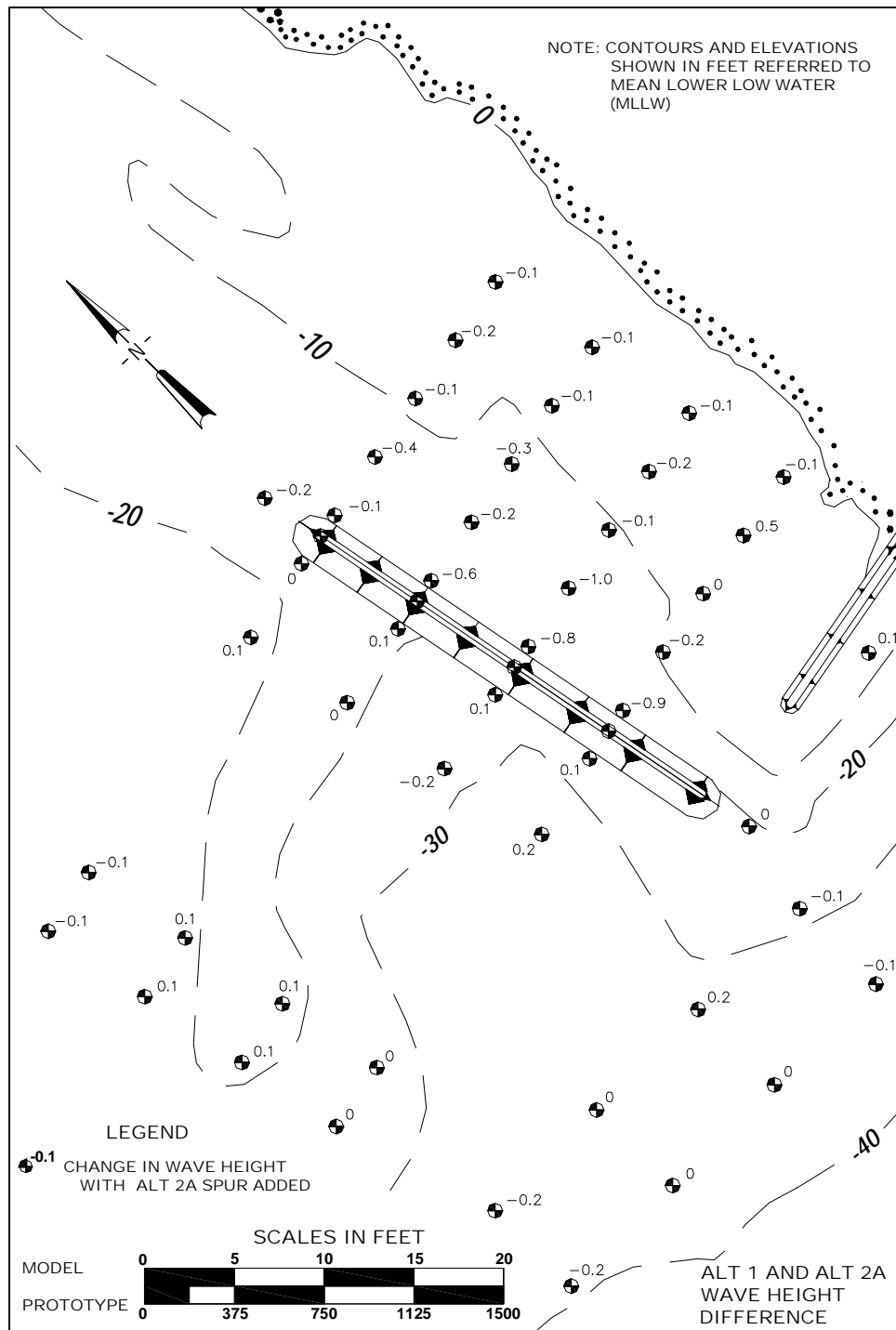
Figure B76. Differences in wave heights between Alt 1 and Alt 2A for 6-m, 16-sec waves from southwest at mllw
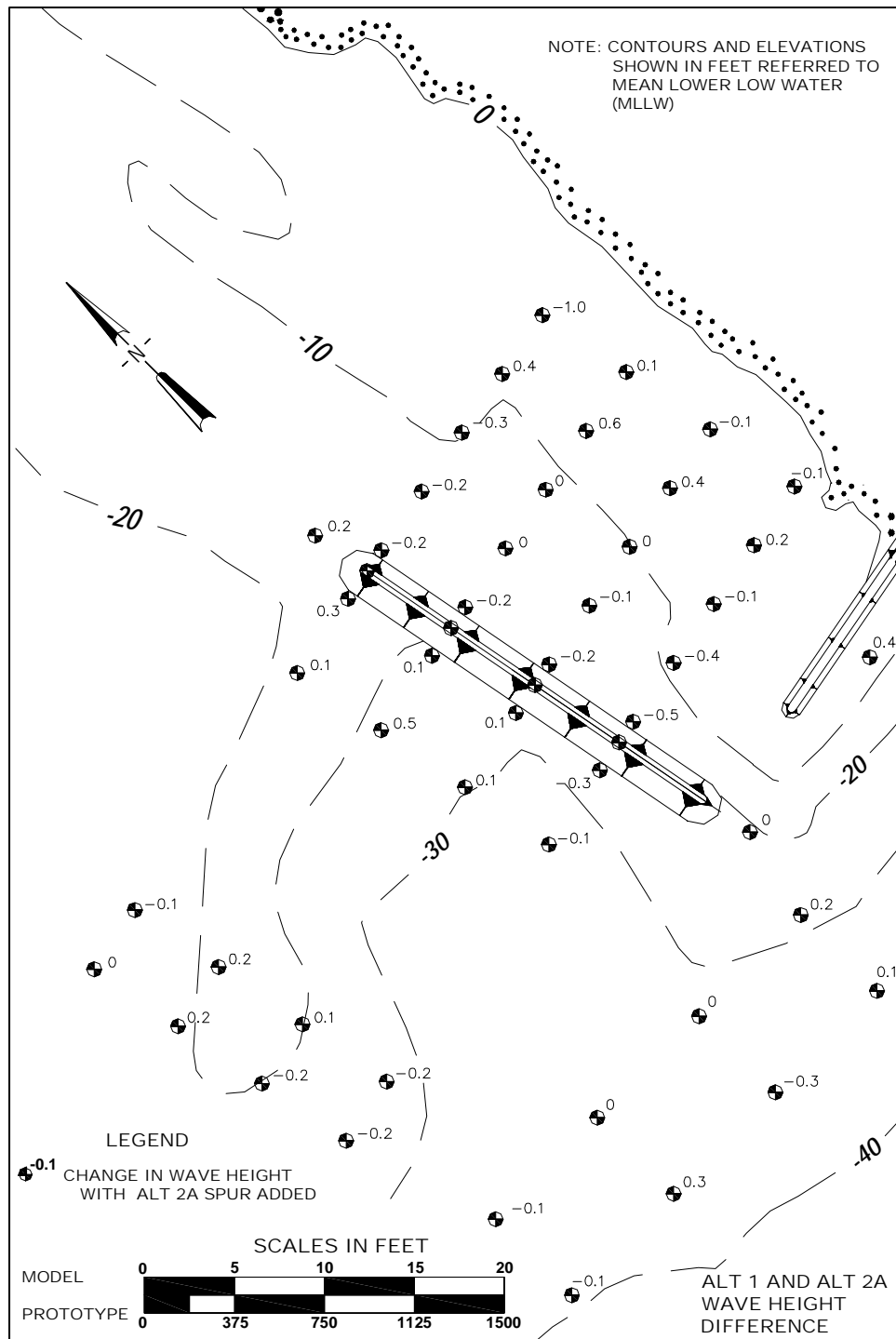
Figure B77. Differences in wave heights between Alt 1 and Alt 2A for 2-m, 9-sec waves from southwest at mtl with full flood tidal current
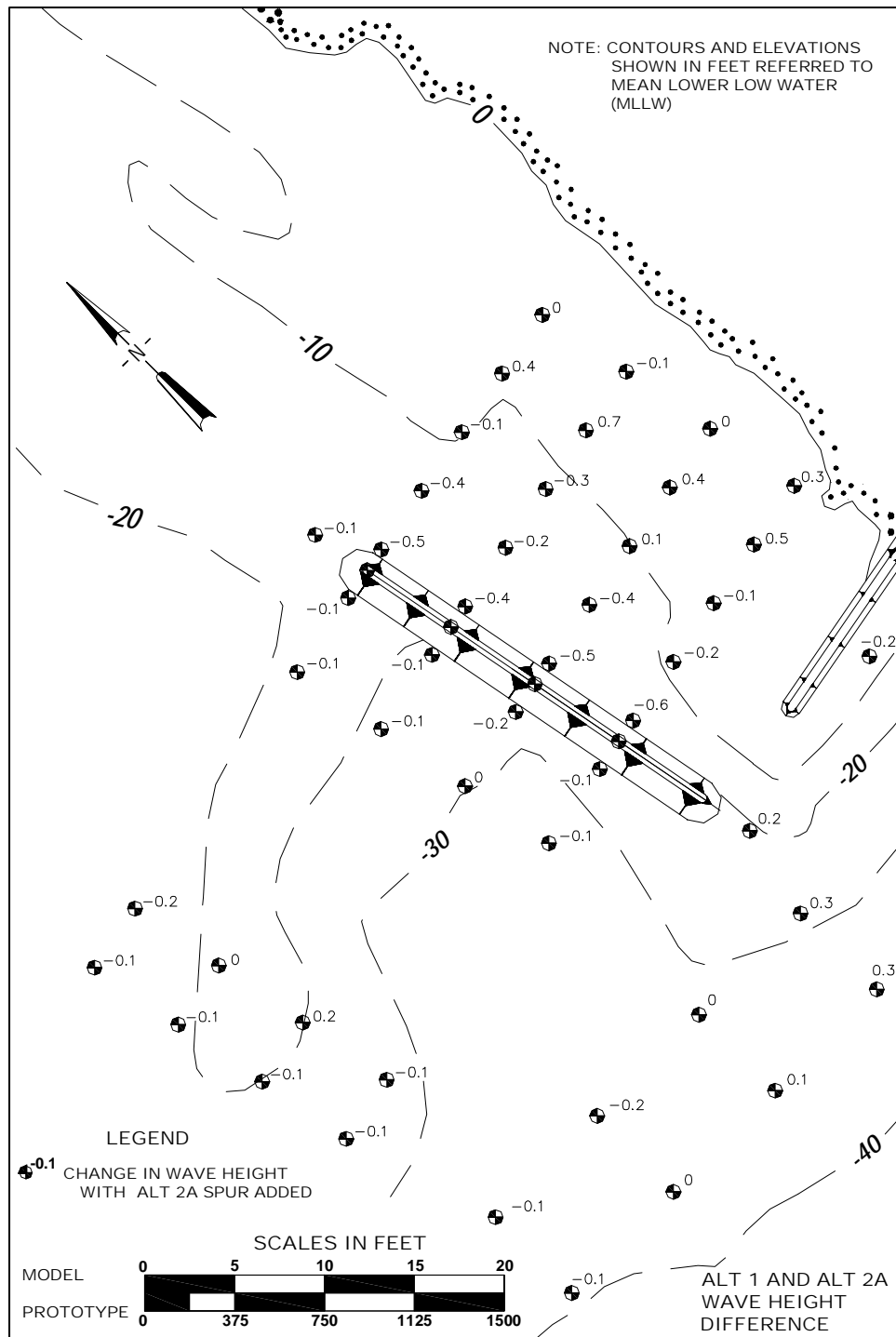
Figure B78. Differences in wave heights between Alt 1 and Alt 2A for 3-m,
12-sec waves from southwest at mtl with full flood tidal current

NOTE: CONTOURS AND ELEVATIONS
SHOWN IN FEET REFERRED TO
MEAN LOWER LOW WATER
(MLLW)

LEGEND

•-0.1 CHANGE IN WAVE HEIGHT
WITH ALT 2A SPUR ADDED

SCALES IN FEET

MODEL

PROTOTYPE

ALT 1 AND ALT 2A
WAVE HEIGHT
DIFFERENCE
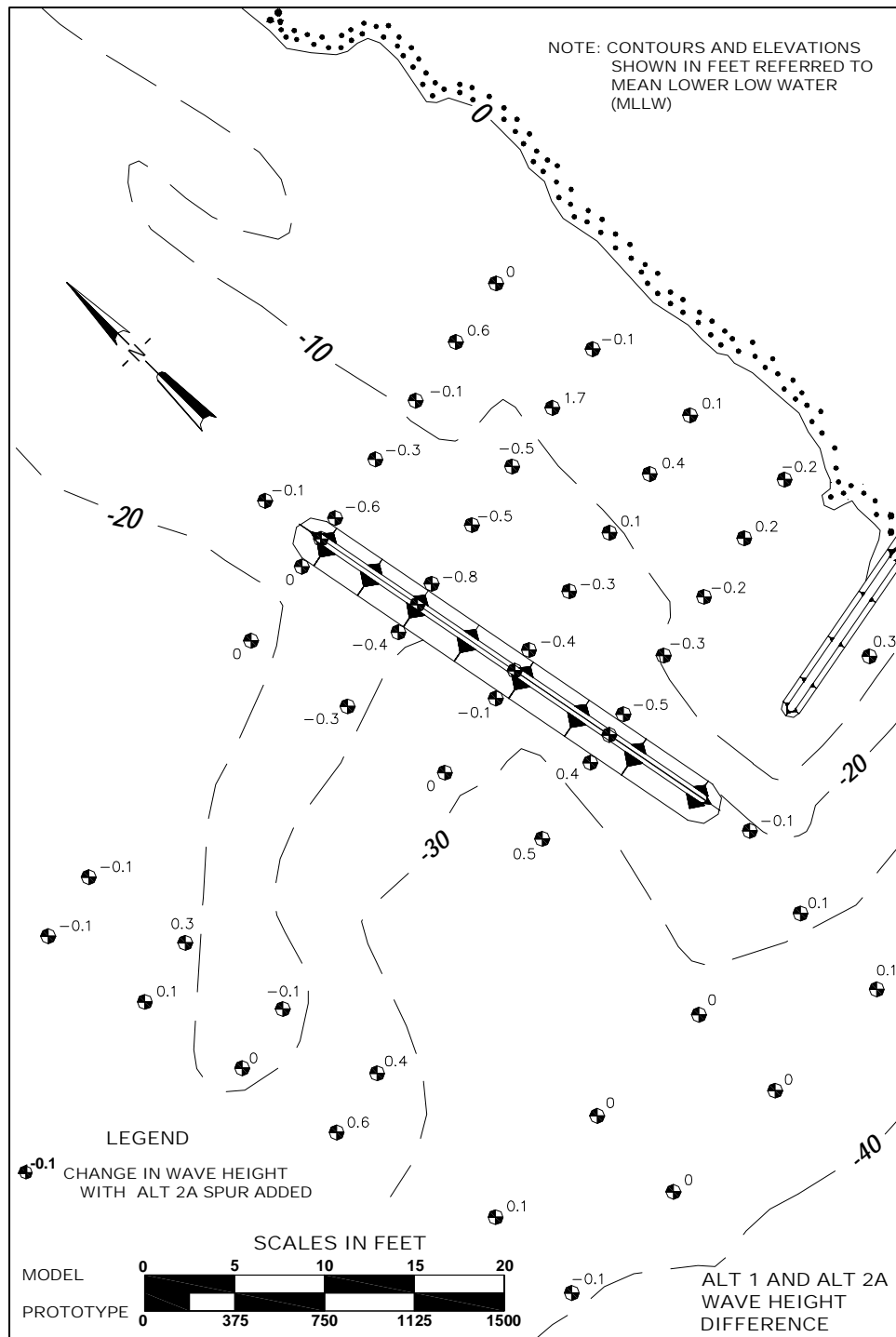
Figure B79. Differences in wave heights between Alt 1 and Alt 2A for 6-m,
16-sec waves from southwest at mtl with full flood tidal current
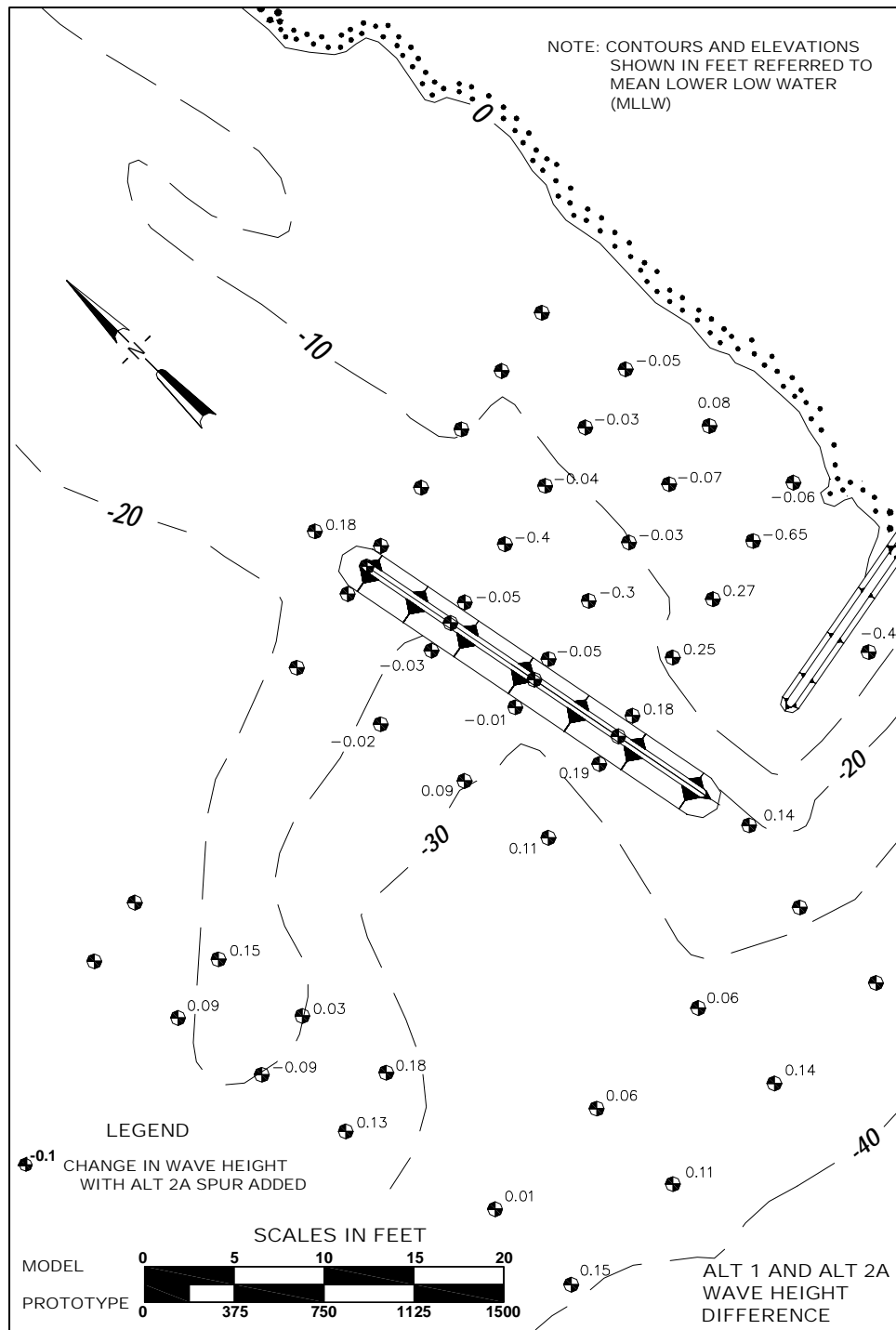
Figure B80. Differences in wave heights between Alt 1 and Alt 2A for 2-m, 9 sec
waves from southwest at mhw
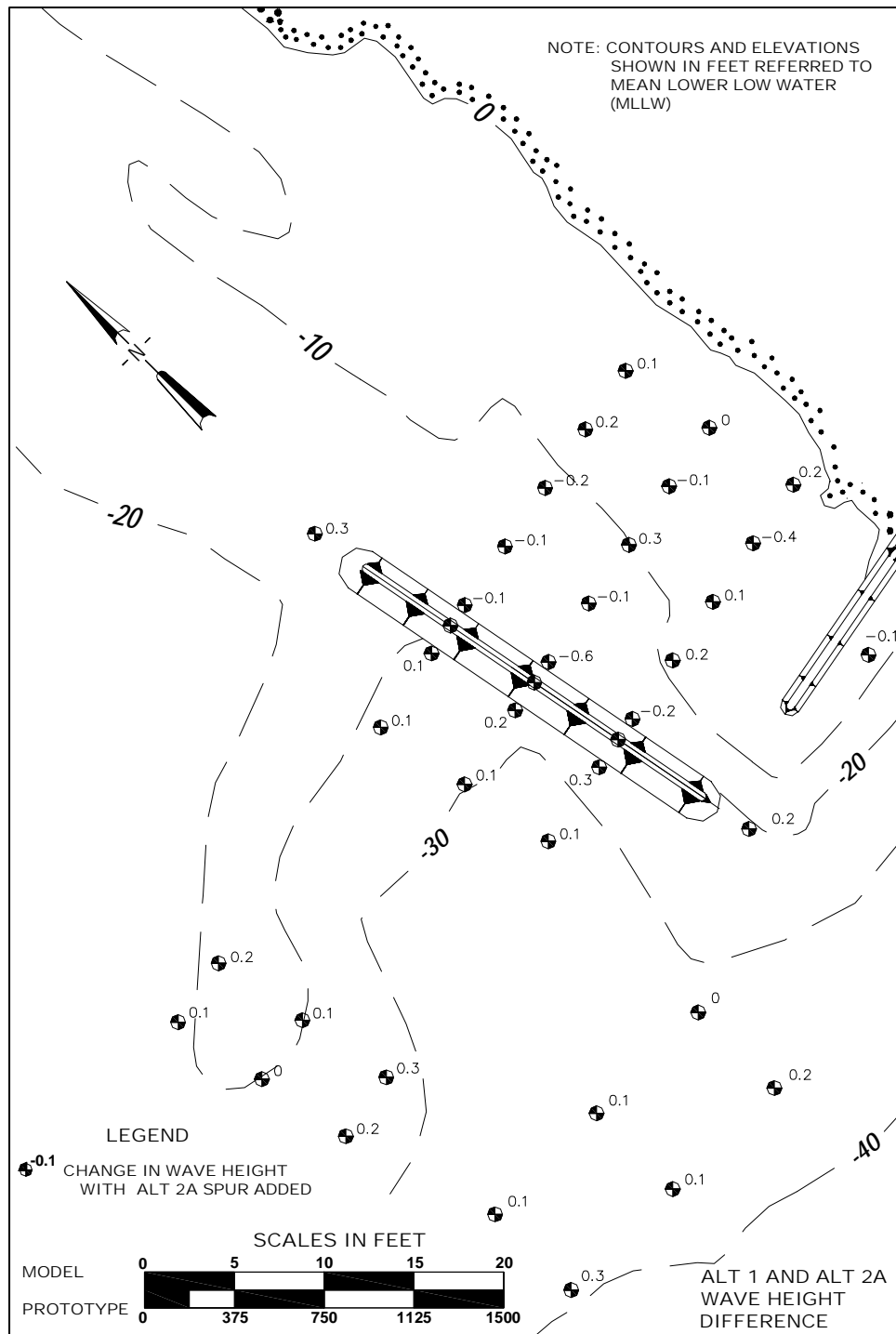
Figure B81. Differences in wave heights between Alt 1 and Alt 2A for 3-m, 12-sec waves from southwest at mhw

NOTE: CONTOURS AND ELEVATIONS
SHOWN IN FEET REFERRED TO
MEAN LOWER LOW WATER
(MLLW)

LEGEND

-0.1 CHANGE IN WAVE HEIGHT
WITH ALT 2A SPUR ADDED

SCALES IN FEET

MODEL

| 0 | 5 | 10 | 15 | 20 |

PROTOTYPE

| 0 | 375 | 750 | 1125 | 1500 |

ALT 1 AND ALT 2A
WAVE HEIGHT
DIFFERENCE
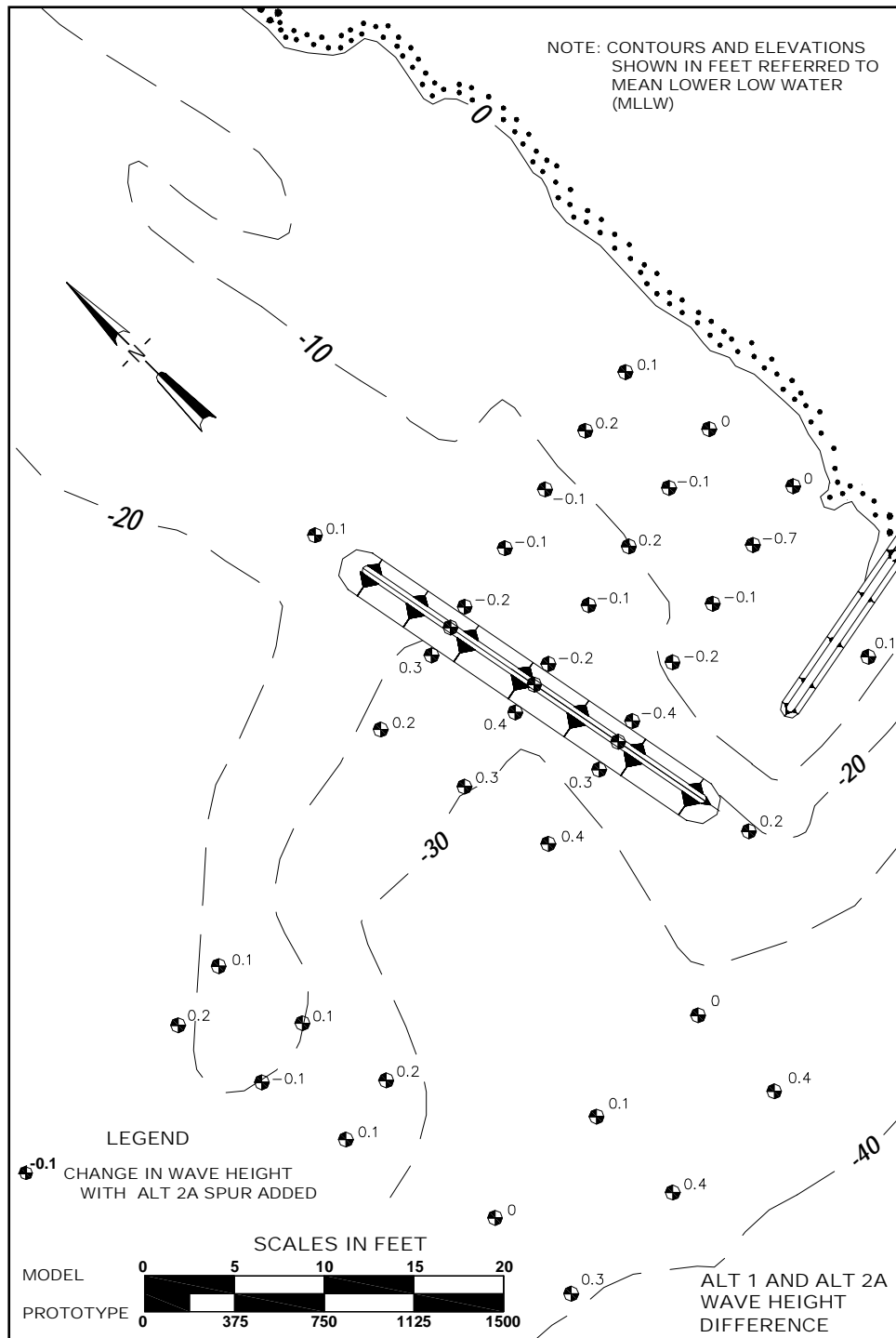
Figure B82. Differences in wave heights between Alt 1 and Alt 2A for 6-m,
16-sec waves from southwest at mhw
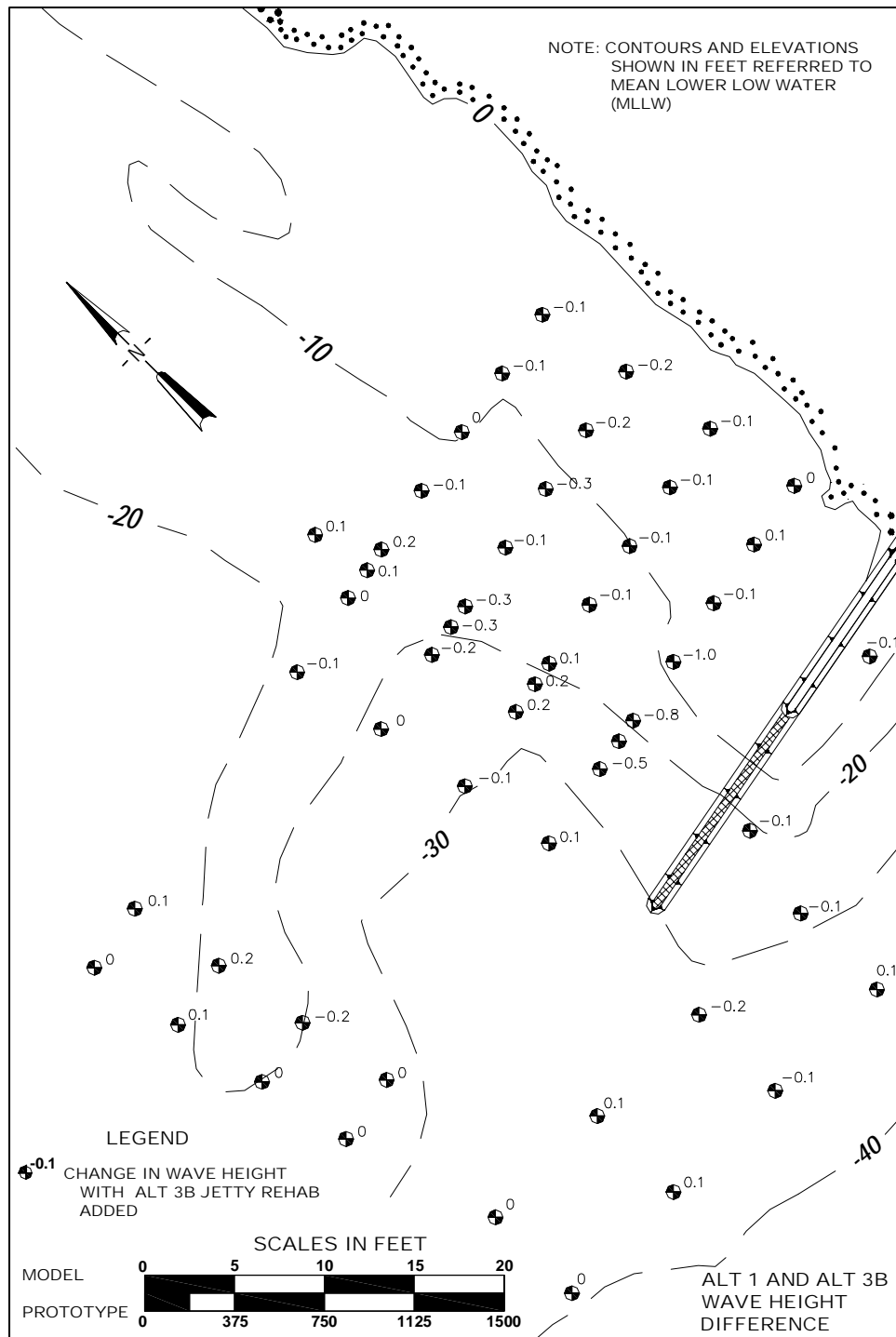
Figure B83. Differences in wave heights between Alt 1 and Alt 3B for 2-m, 9-sec waves from southwest at mllw
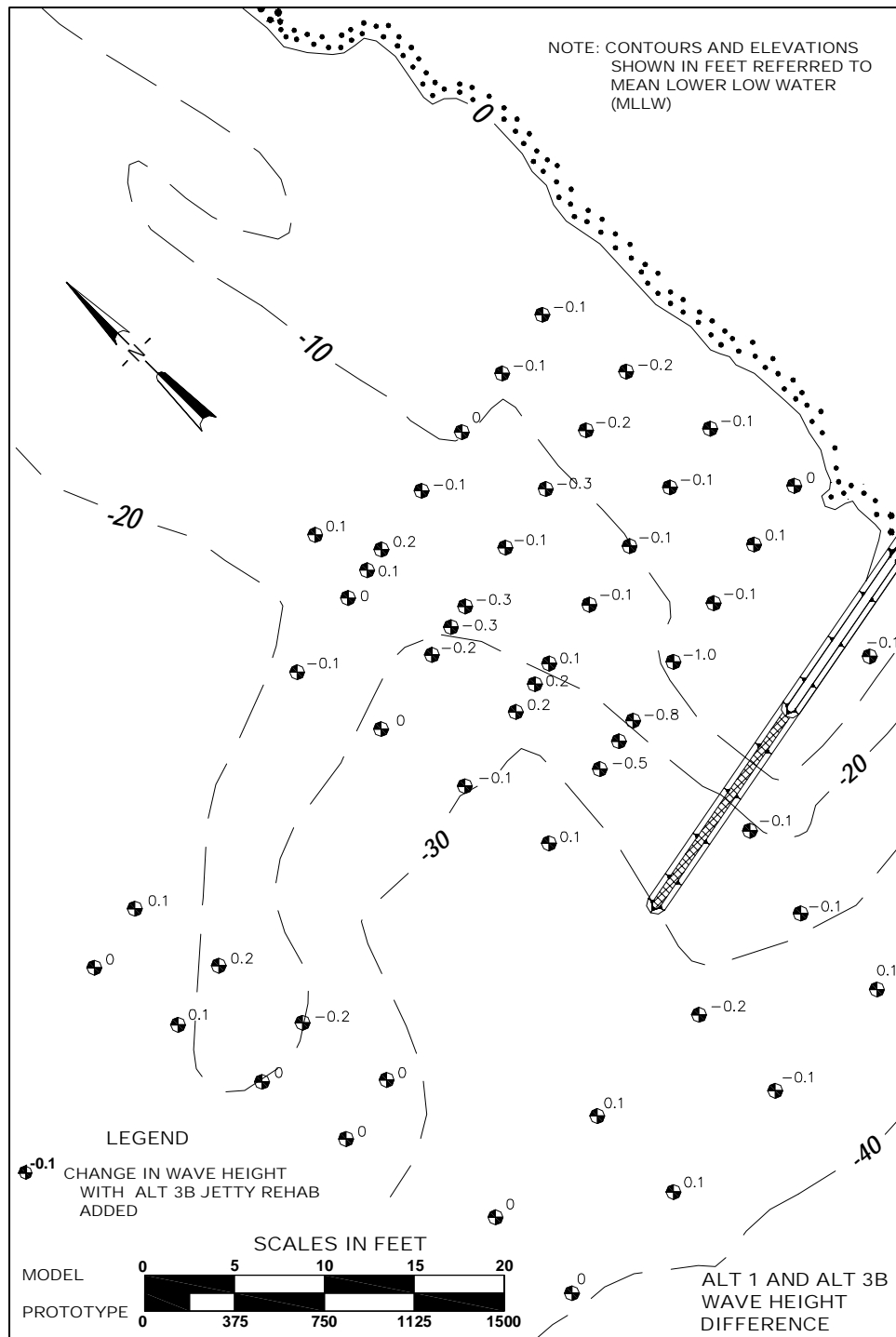
Figure B84. Differences in wave heights between Alt 1 and Alt 3B for 3-m, 12-sec waves from southwest at mllw
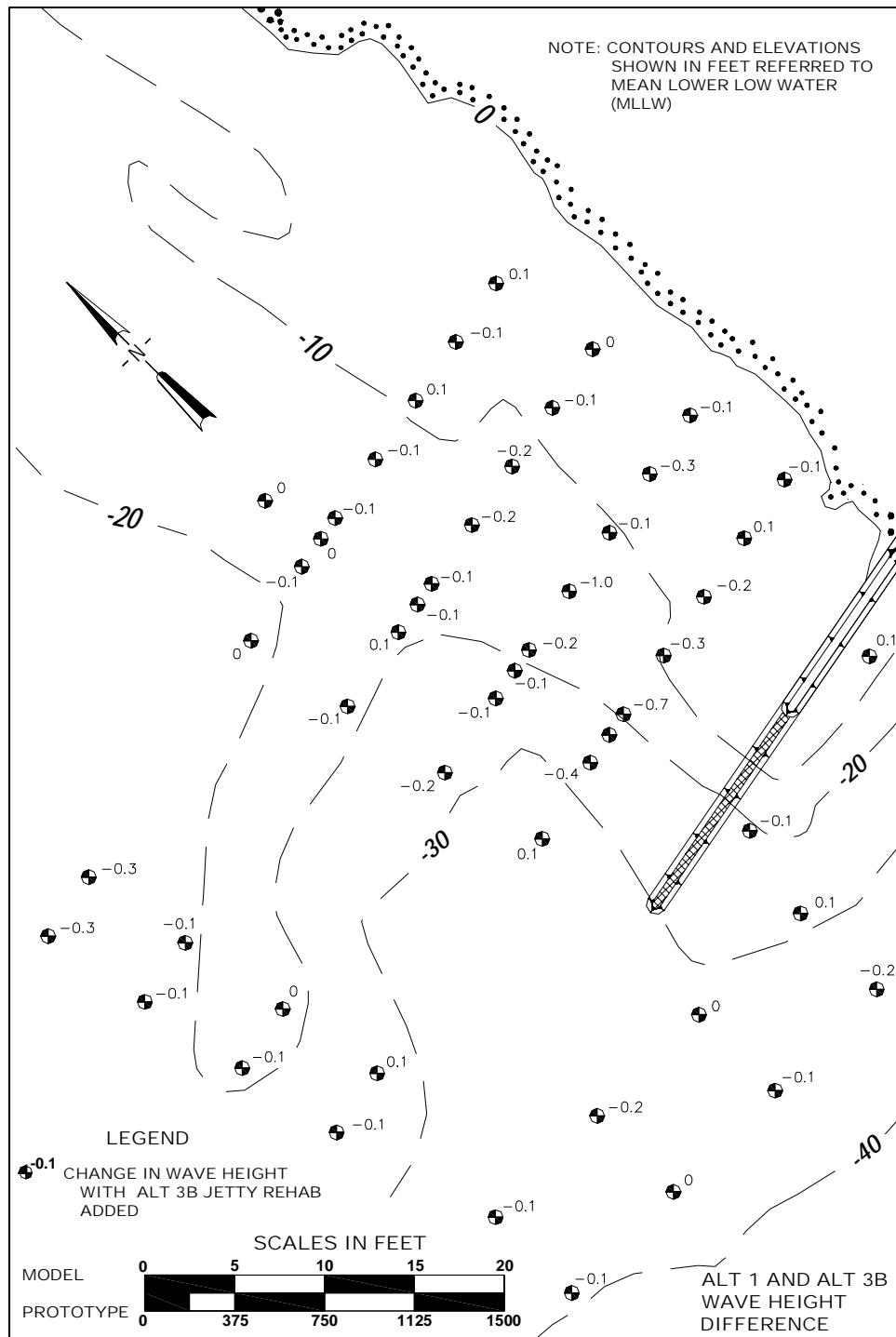
Figure B85. Differences in wave heights between Alt 1 and Alt 3B for 6-m,
16-sec waves from southwest at mllw

NOTE: CONTOURS AND ELEVATIONS SHOWN IN FEET REFERRED TO MEAN LOWER LOW WATER (MLLW)

LEGEND

-0.1 CHANGE IN WAVE HEIGHT WITH ALT 3B JETTY REHAB ADDED

SCALES IN FEET

	0	5	10	15	20
MODEL					
PROTOTYPE	0	375	750	1125	1500

ALT 1 AND ALT 3B WAVE HEIGHT DIFFERENCE
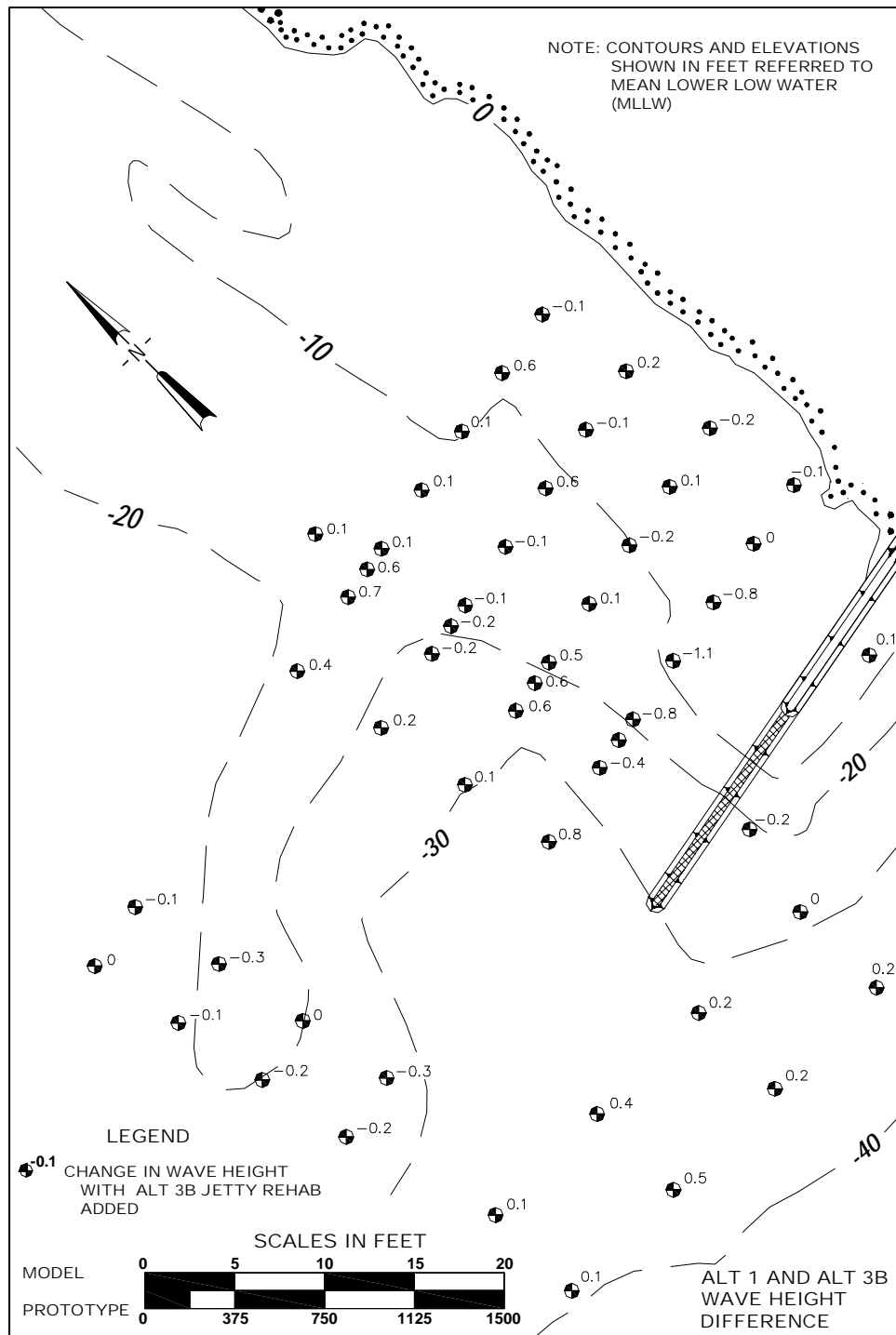
Figure B86. Differences in wave heights between Alt 1 and Alt 3B for 2-m, 9-sec waves from southwest at mtl
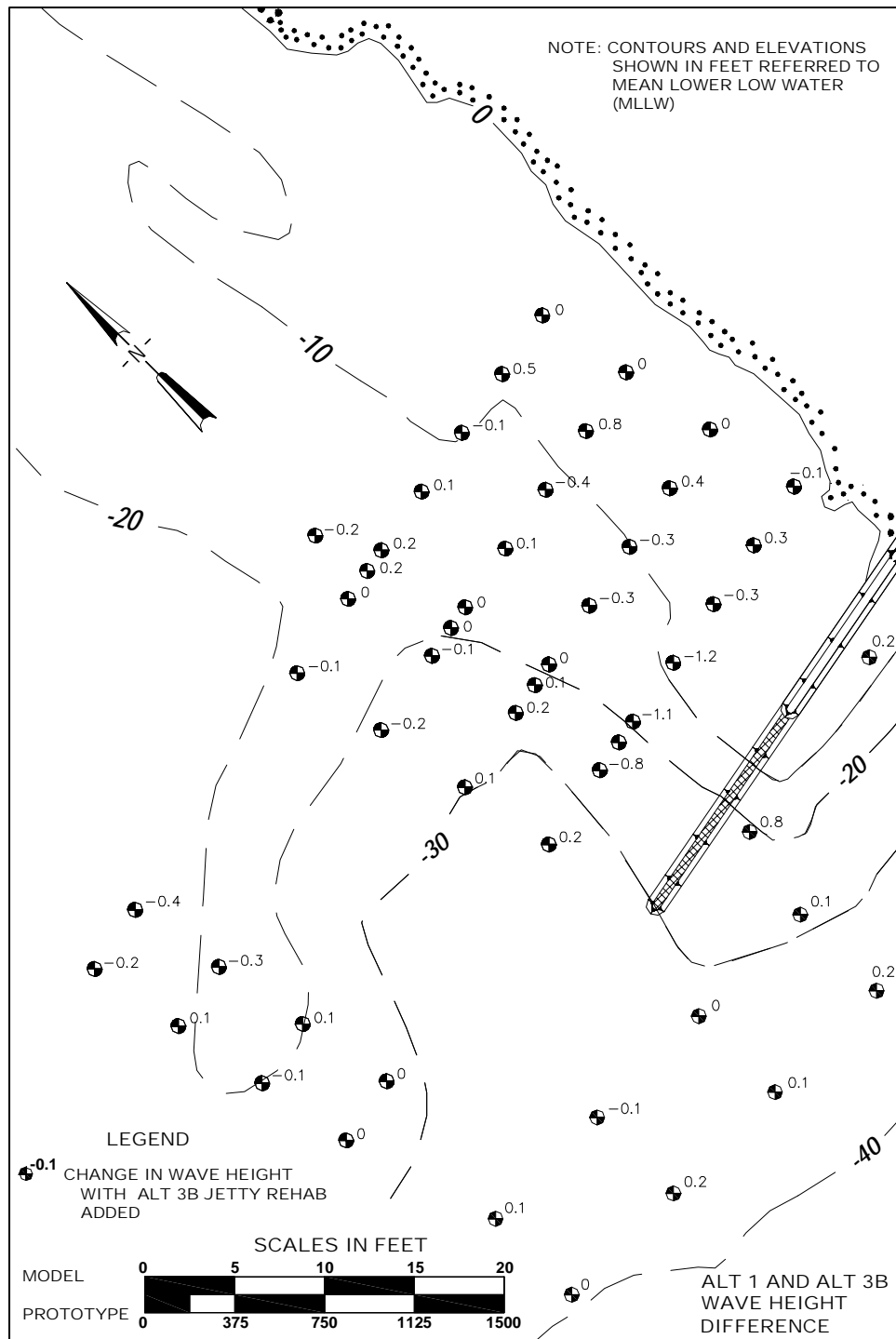
Figure B87. Differences in wave heights between Alt 1 and Alt 3B for 3-m, 12-sec waves from southwest at mtl
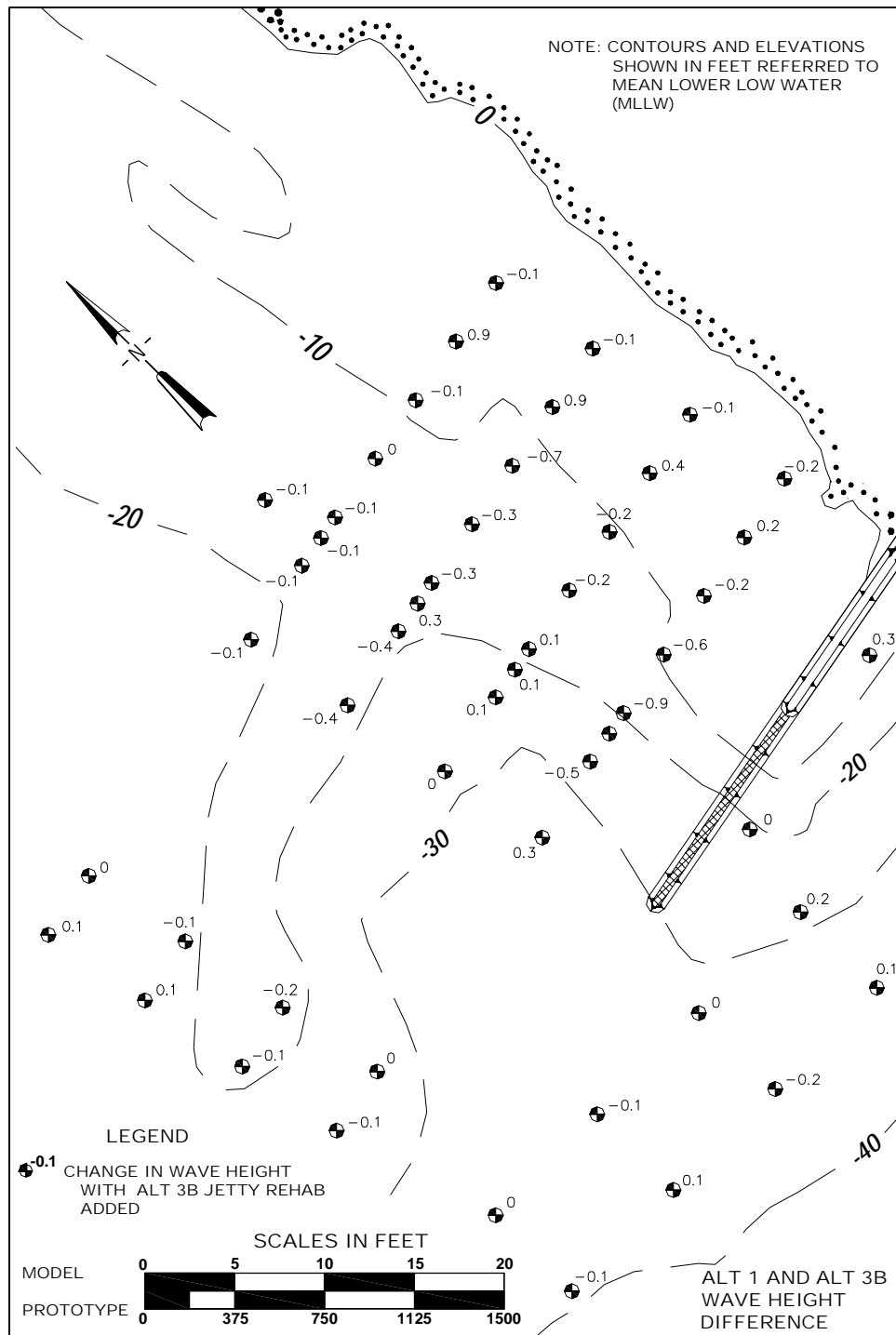
Figure B88. Differences in wave heights between Alt 1 and Alt 3B for 6-m, 16-sec waves from southwest at mtl
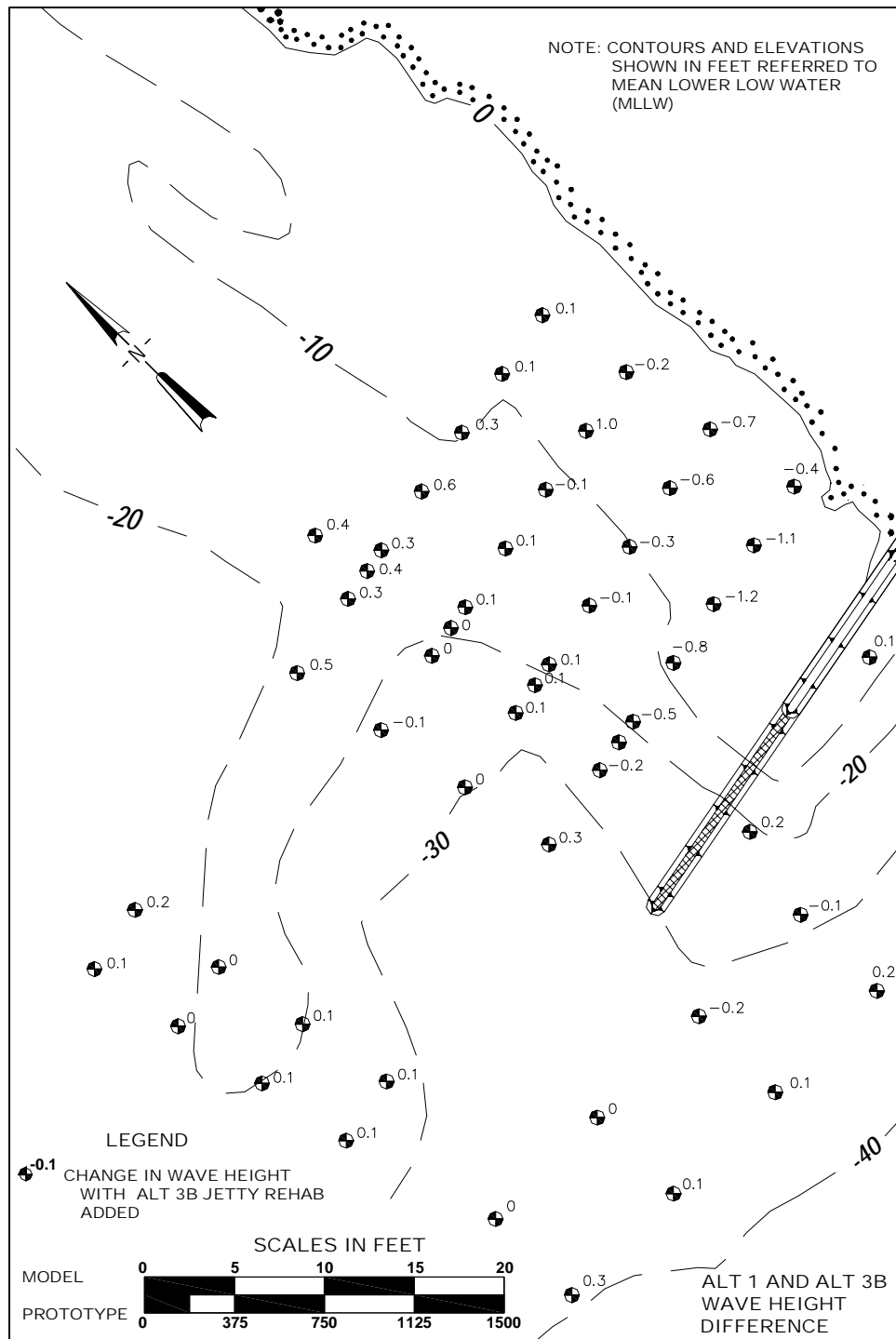
Figure B89. Differences in wave heights between Alt 1 and Alt 3B for 2-m, 9-sec
waves from southwest at mhw
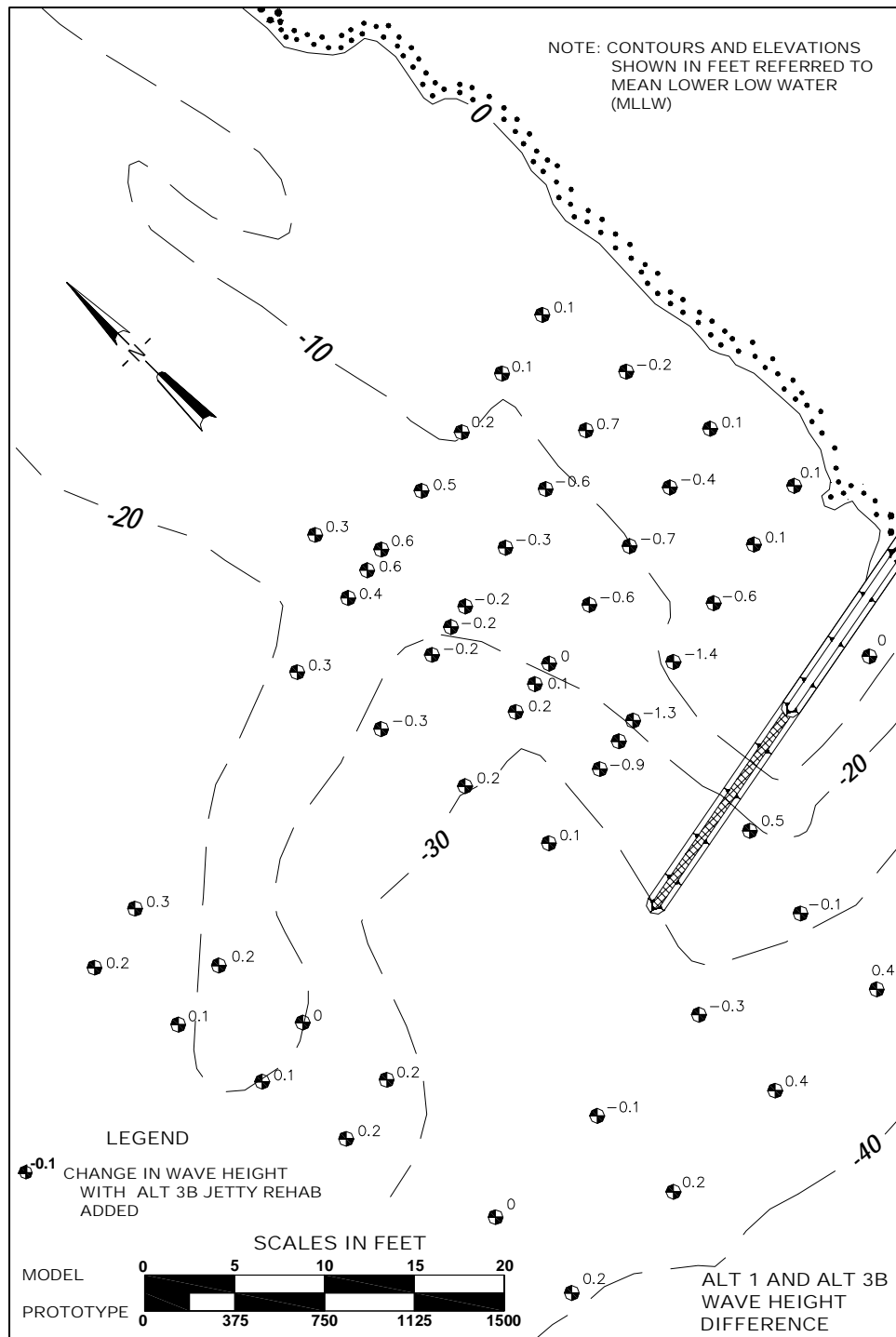
Figure B90. Differences in wave heights between Alt 1 and Alt 3B for 3-m,
12-sec waves from southwest at mhw

Figure B91. Differences in wave heights between Alt 1 and Alt 3B for 6-m, 16-sec waves from southwest at mhw
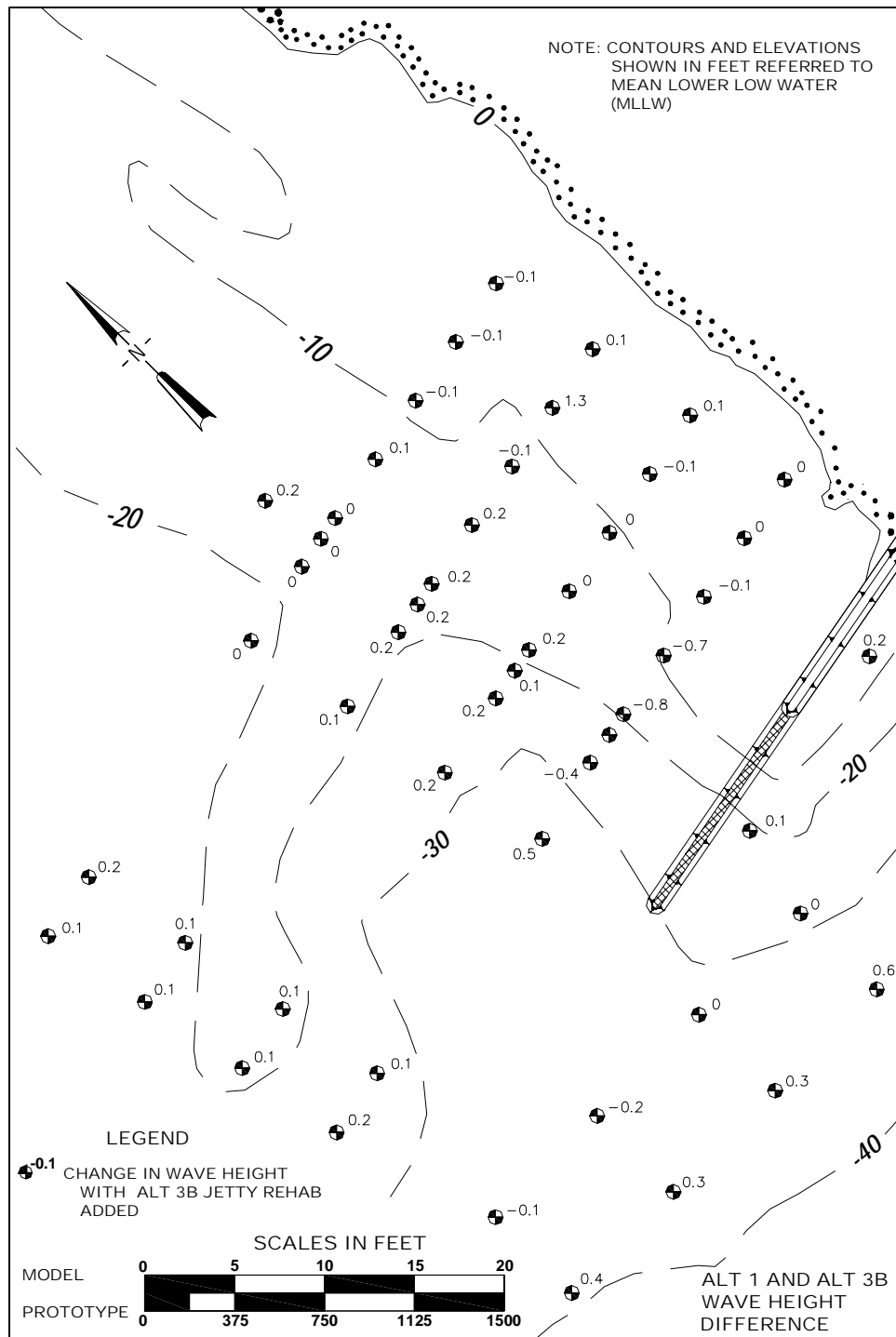
GENESIS 5-Year Projected Shoreline

Storms from west-northwest

Figures B92 through B97 contain photographs taken during dye studies with Alt 2A and the shoreline projected by numerical model GENESIS for 5 years after installation of Alt 2A.
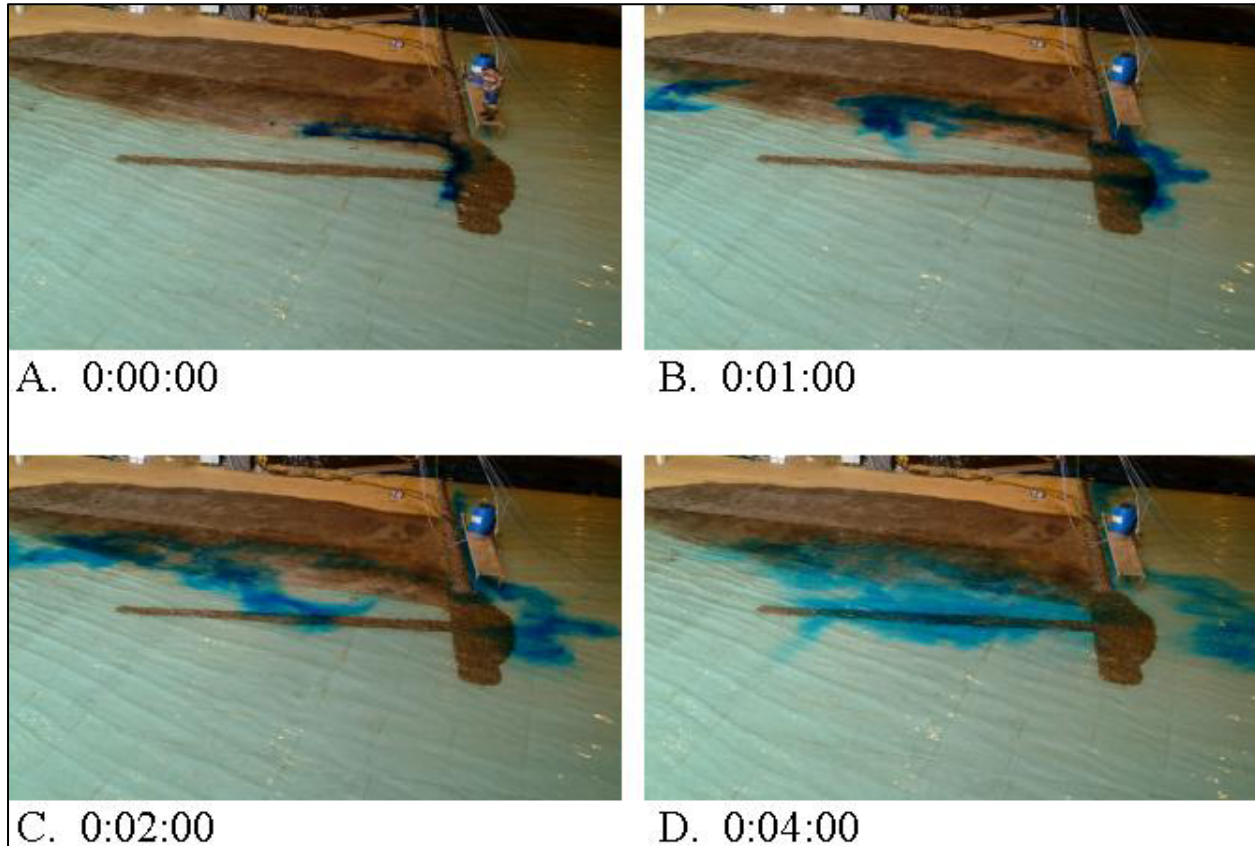
Figure B92. Dye study of 2-m, 9-sec waves from west-northwest at mllw, Alt 2A with 5-year projected shoreline
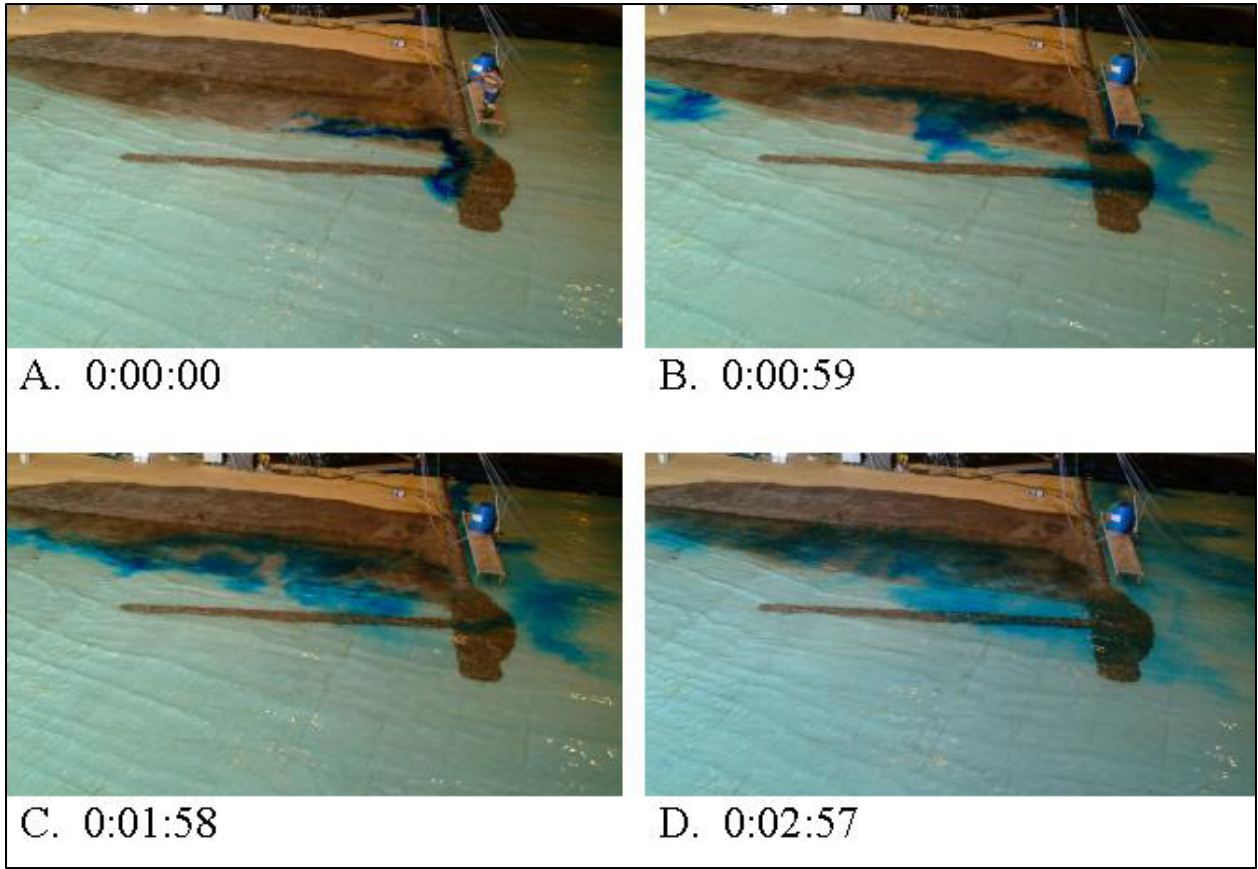
Figure B93. Dye study of 3-m, 13-sec waves from west-northwest at mllw, Alt 2A with 5-year projected shoreline
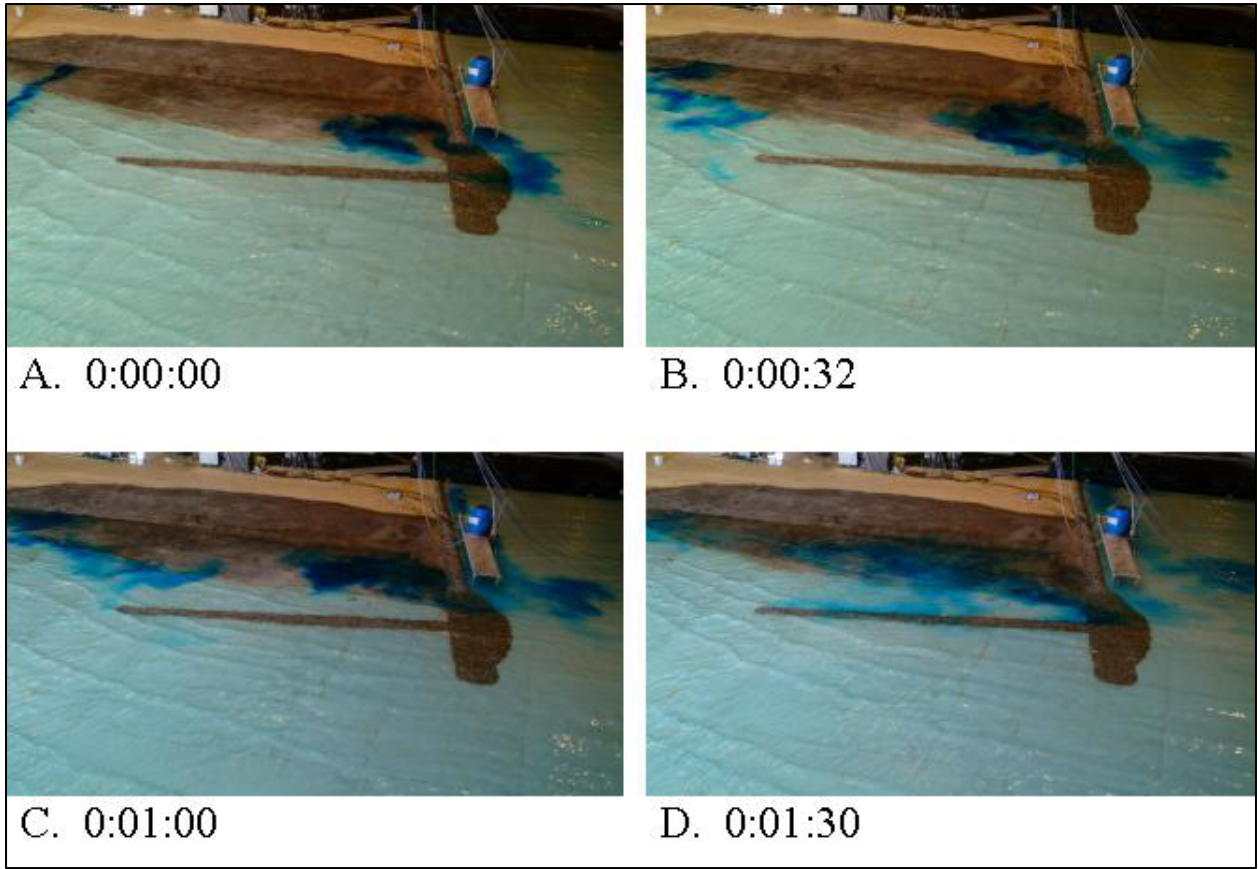
Figure B94. Dye study of 5-m, 13-sec waves from west-northwest at mllw, Alt 2A with 5-year projected shoreline
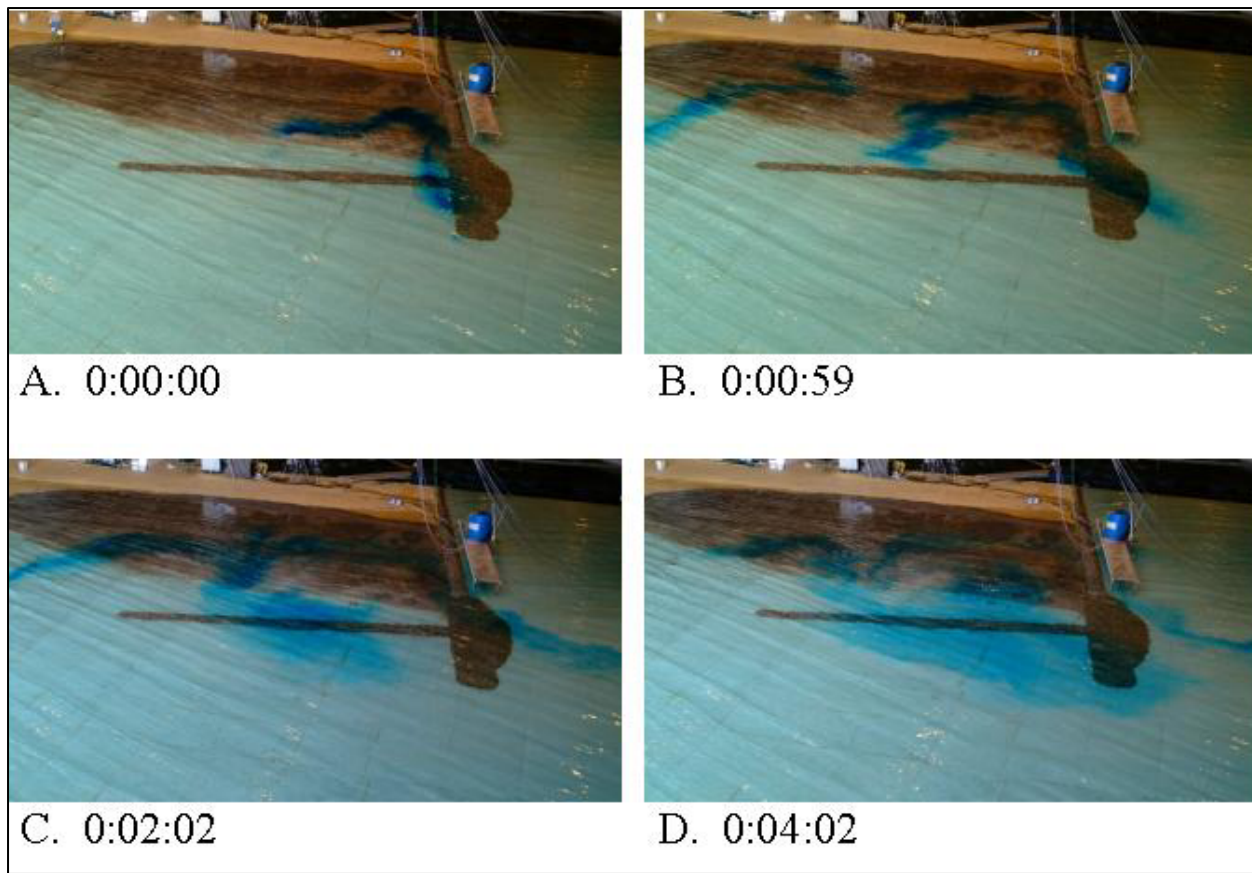
Figure B95. Dye study of 2-m, 9-sec waves from west-northwest at mhw, Alt 2A with 5-year projected shoreline
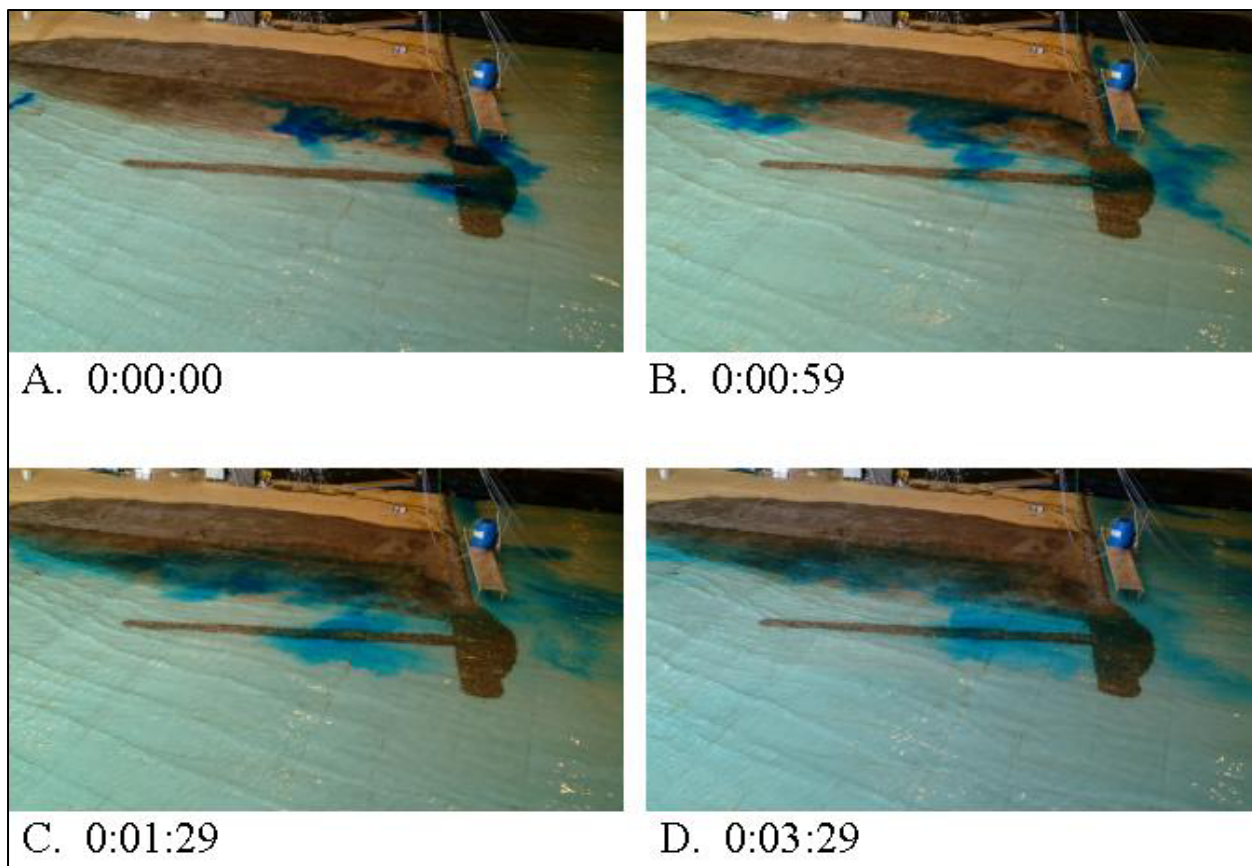
Figure B96. Dye study of 3-m, 13-sec waves from west-northwest at mhw, Alt 2A with 5-year projected shoreline
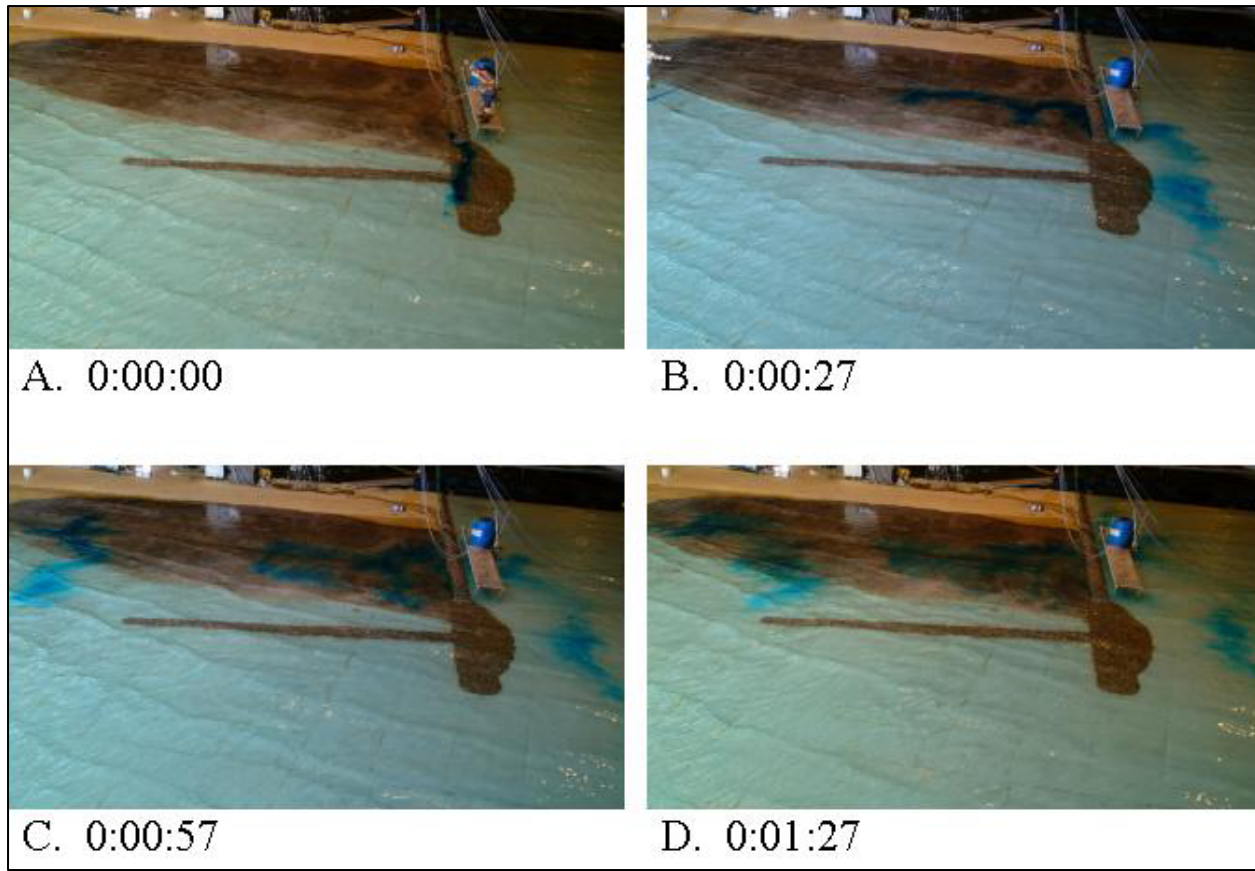
Figure B97. Dye study of 5-m, 13-sec waves from west-northwest at mhw, Alt 2A with 5-year projected shoreline

Storms from southwest

Figures B98 through B106 contain photographs taken during experiments with Alt 2A and the shoreline projected by numerical model GENESIS for 5 years after installation of Alt 2A.
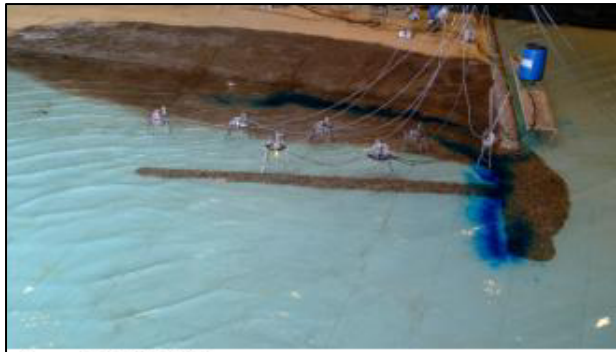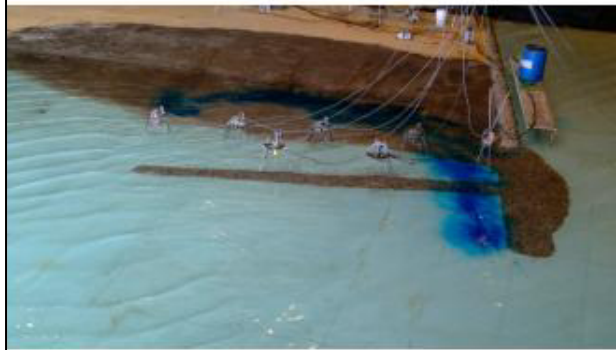
Figure B98. Dye study of 2-m, 9-sec waves from southwest at mllw, Alt 2A with 5-year projected shoreline
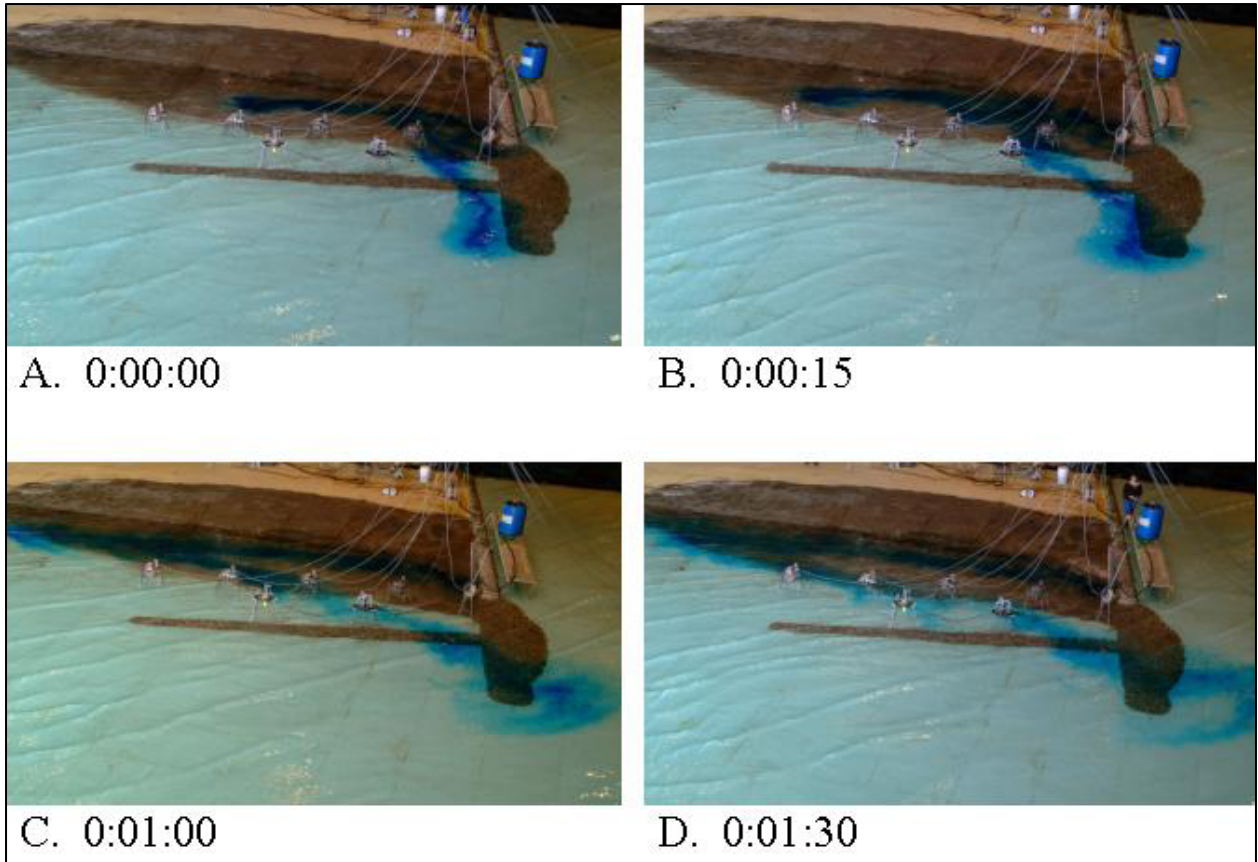
Figure B99. Dye study of 3-m, 12-sec waves from southwest at mllw, Alt 2A with 5-year projected shoreline
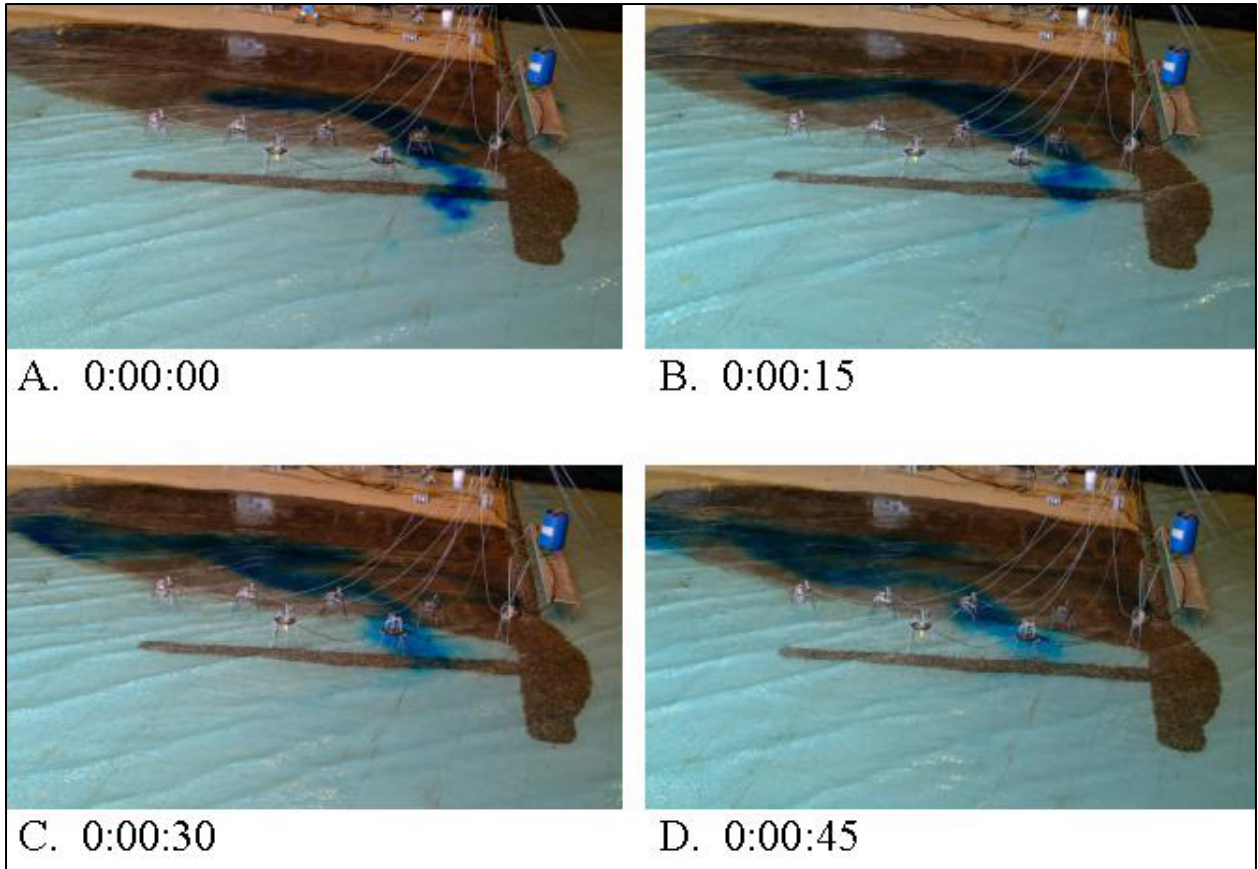
Figure B100. Dye study of 6-m, 16-sec waves from southwest at mllw, Alt 2A with 5-year projected shoreline
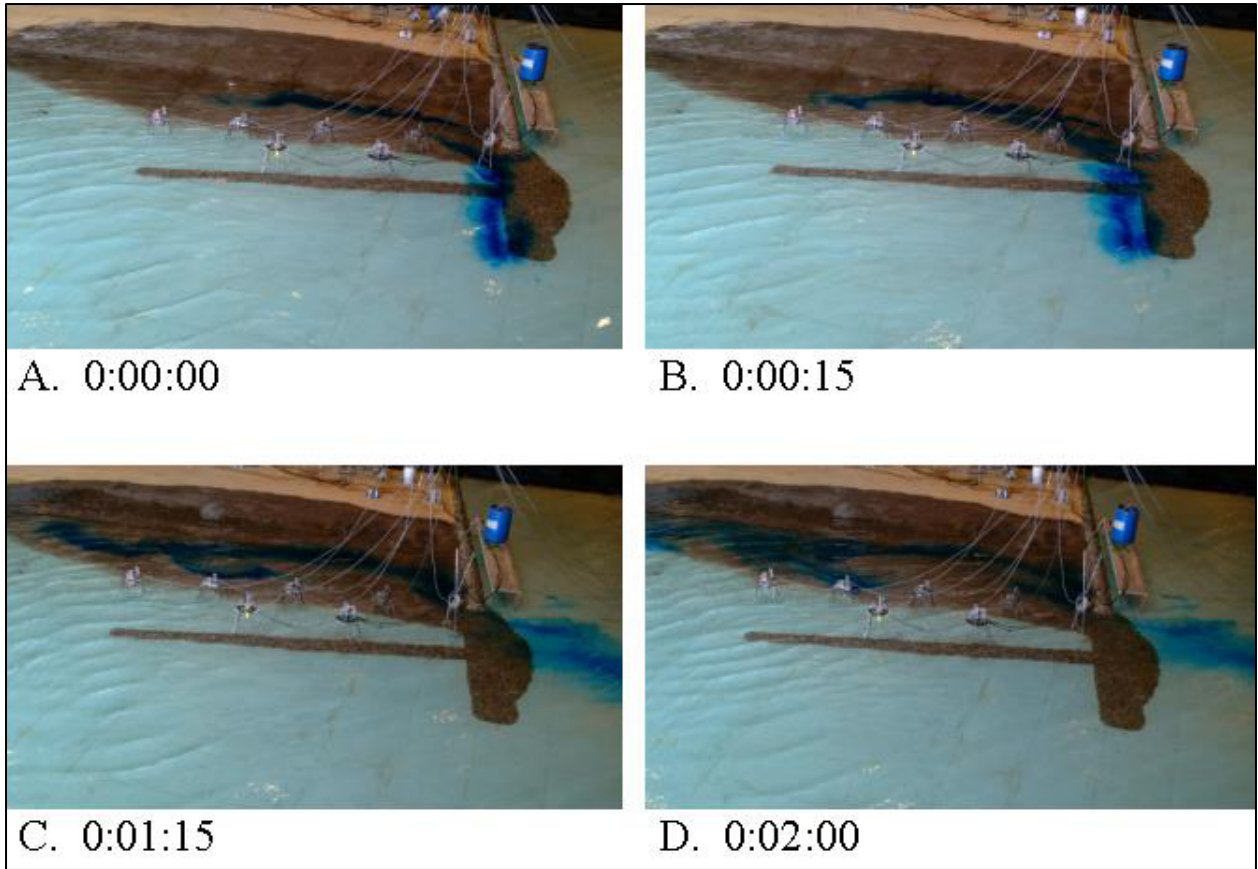
Figure B101. Dye study of 2-m, 9-sec waves from southwest at mtl with full flood tidal current, Alt 2A with 5-year projected shoreline
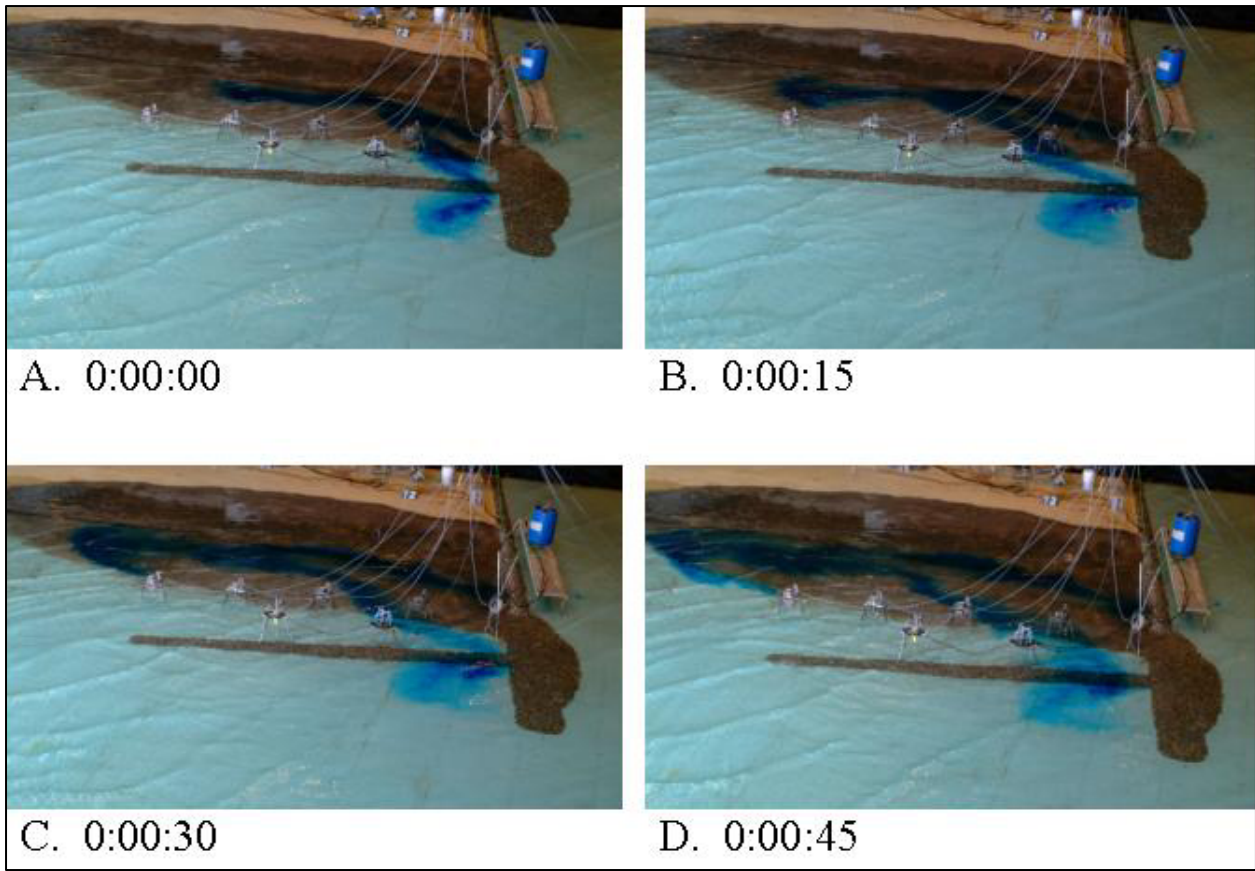
Figure B102. Dye study of 3-m, 12-sec waves from southwest at mtl with full flood tidal current, Alt 2A with 5-year projected shoreline
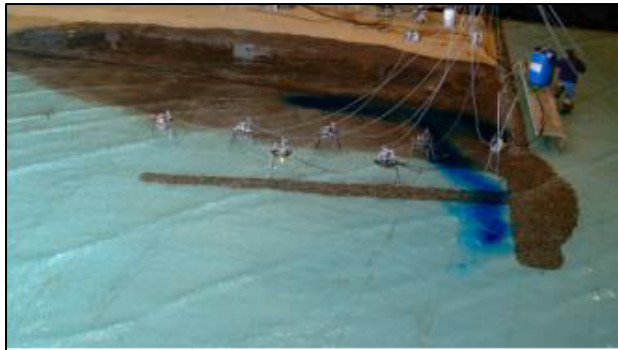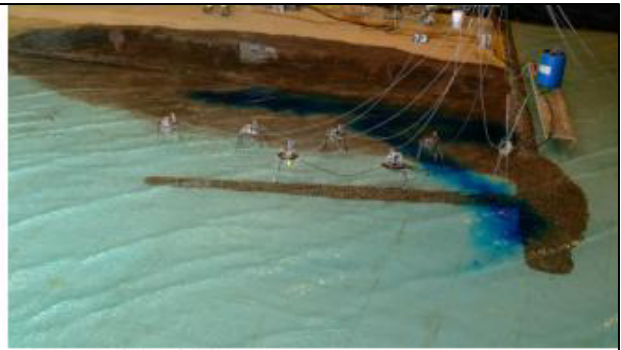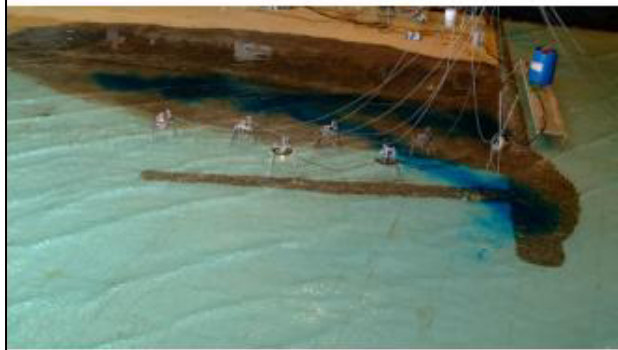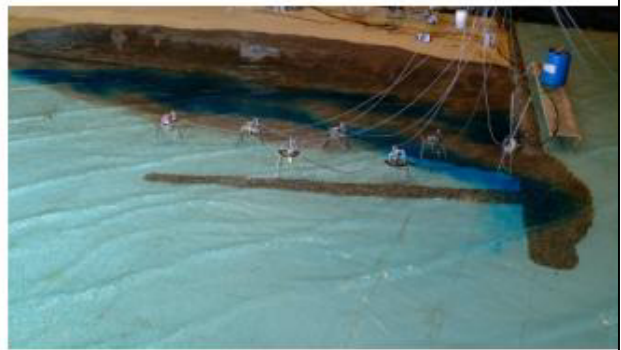
Figure B103. Dye study of 6-m, 16-sec waves from southwest at mtl with full flood tidal current, Alt 2A with 5-year projected shoreline
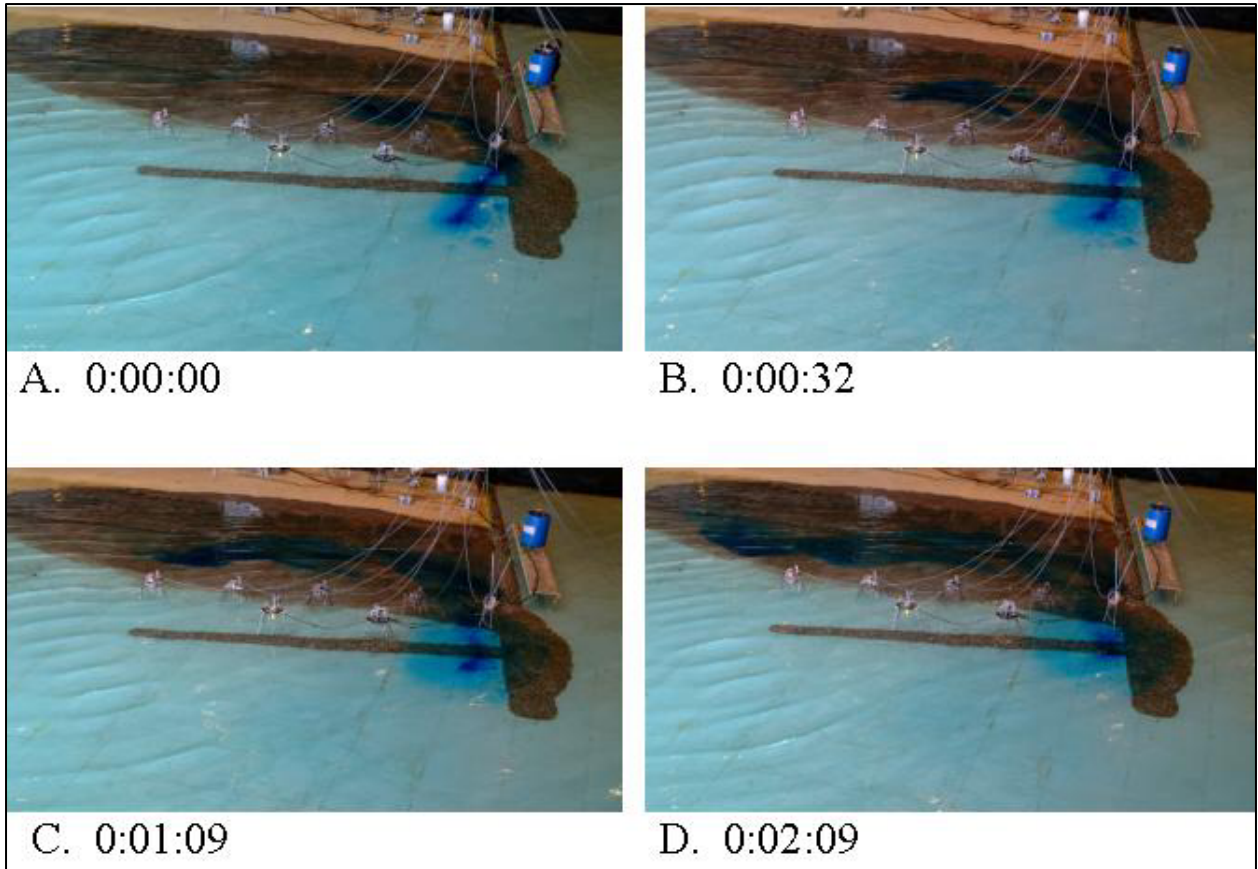
Figure B104. Dye study of 2-m, 9-sec waves from southwest at mhw, Alt 2A with 5-year projected shoreline
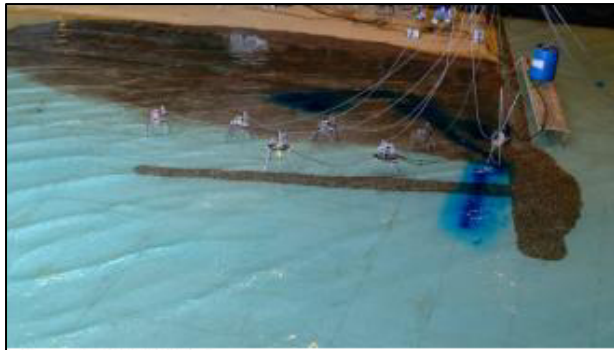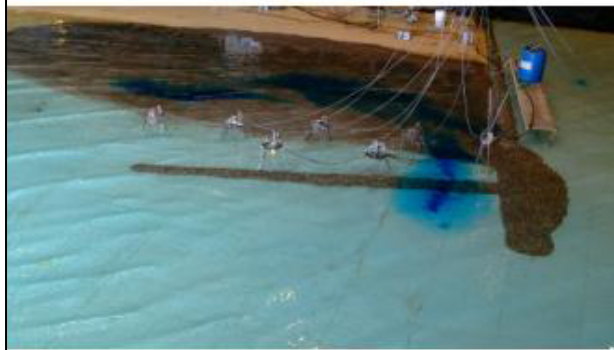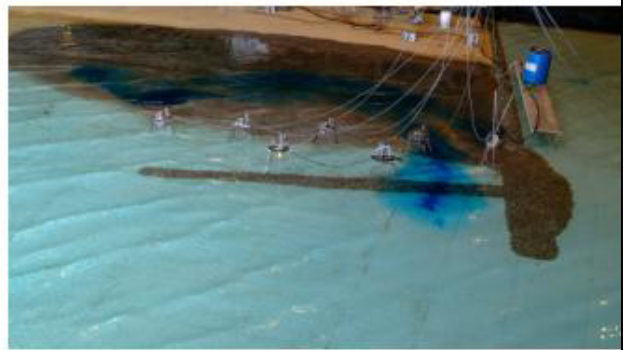
Figure B105. Dye study of 3-m, 12-sec waves from southwest at mhw, Alt 2A with 5-year projected shoreline
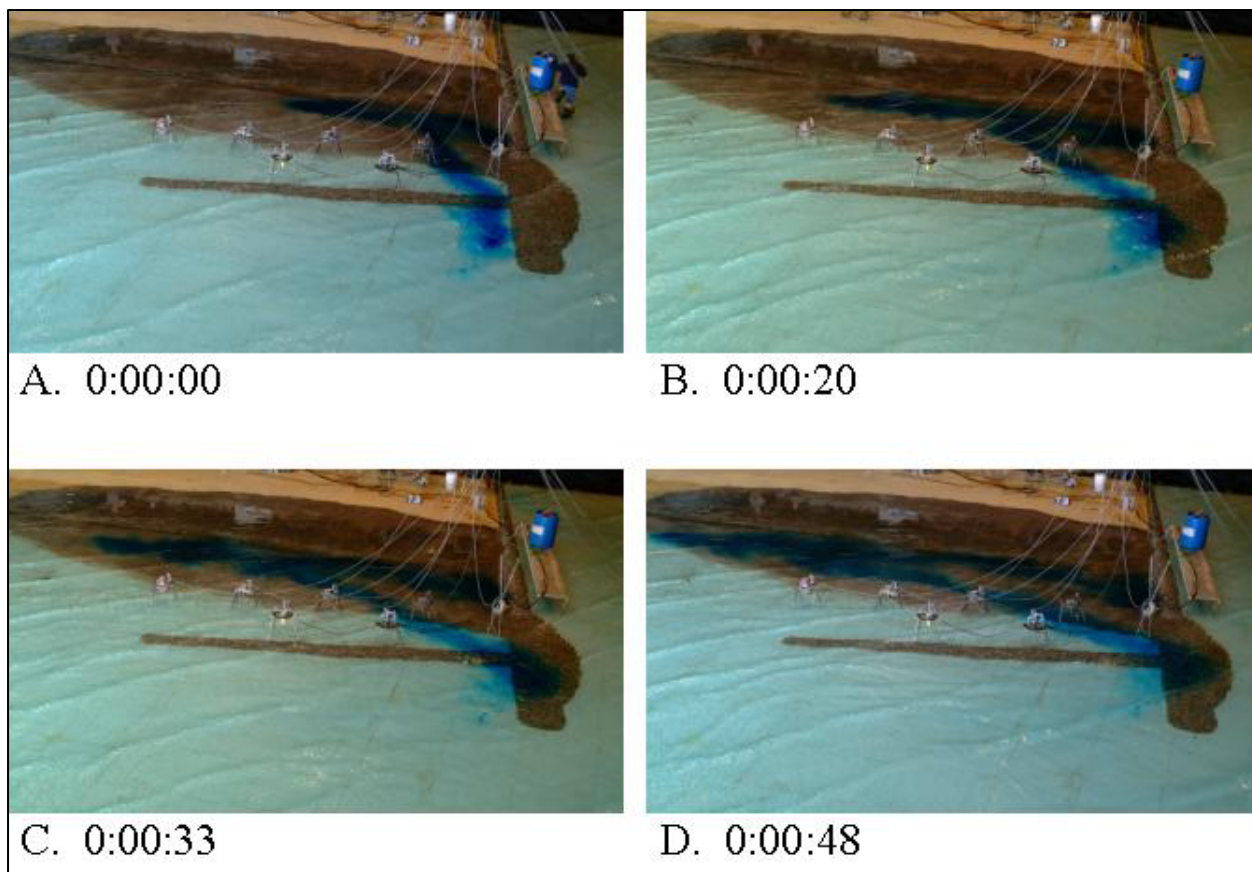
Figure B106. Dye study of 6-m, 16-sec waves from southwest at mhw, Alt 2A with 5-year projected
shoreline

Wave heights

Figures B107 through B113 show changes in wave heights behind the Alt 2A
spur for the 5-year projected shoreline compared to the existing shoreline.

Appendix B   Physical Modeling of North Beach and Jetty
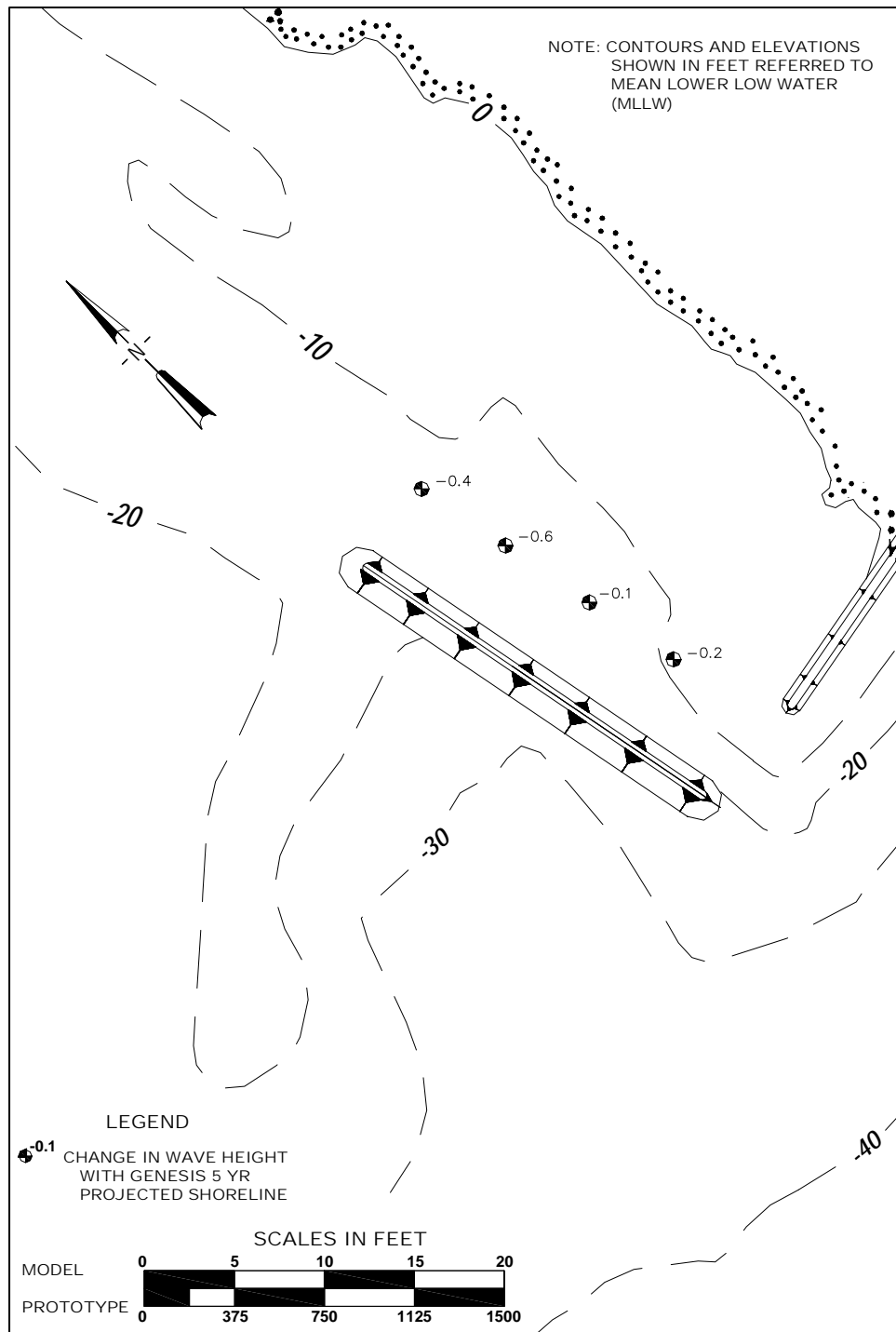
Figure B107. Differences in wave heights between Alt 2A with existing shoreline and Alt 2A with 5-year projected shoreline for 2-m, 9-sec waves from southwest at mllw
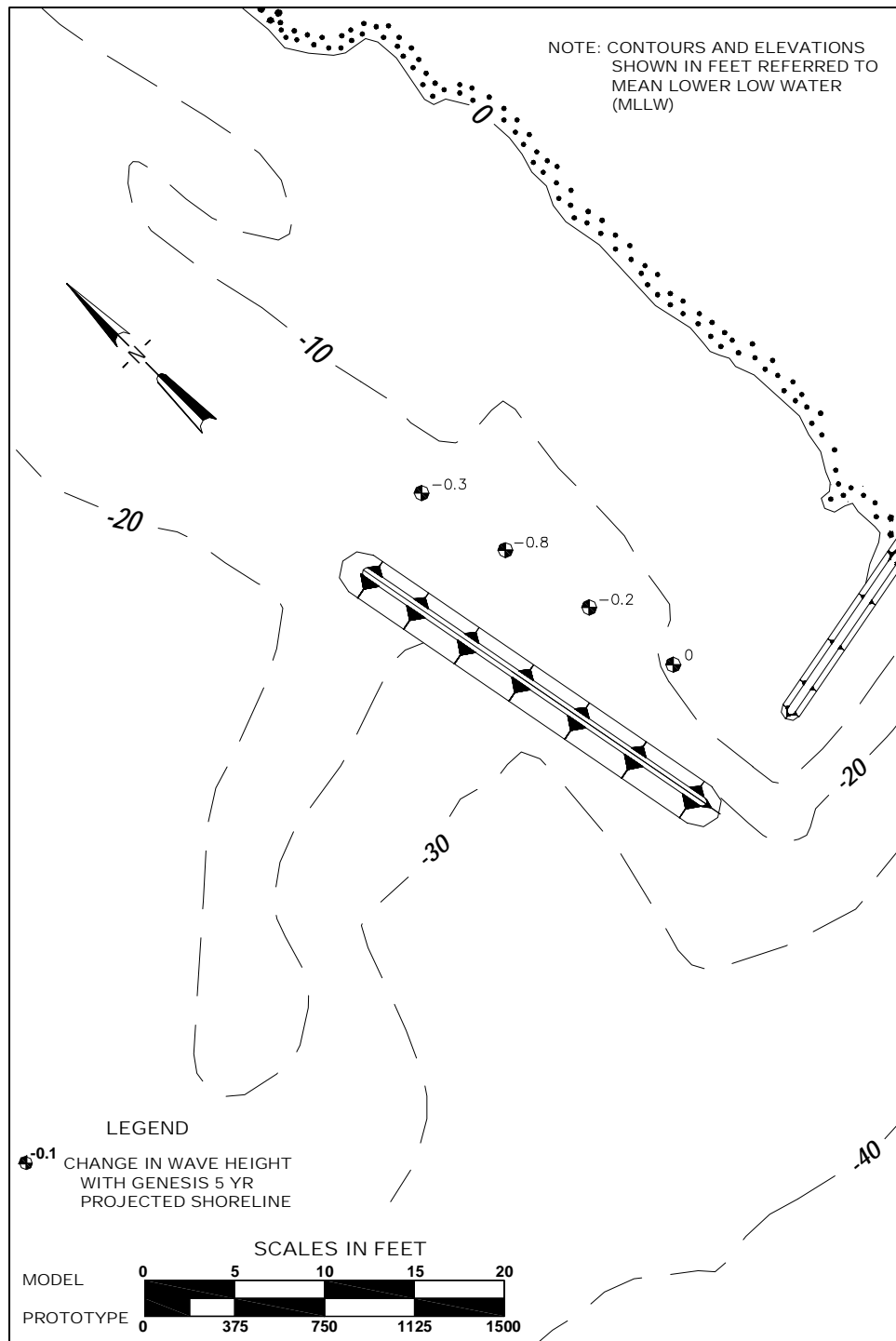
Figure B108. Differences in wave heights between Alt 2A with existing shoreline and Alt 2A with 5-year projected shoreline for 2-m, 9-sec waves from southwest at mtl

NOTE: CONTOURS AND ELEVATIONS
SHOWN IN FEET REFERRED TO
MEAN LOWER LOW WATER
(MLLW)

LEGEND

-0.1 CHANGE IN WAVE HEIGHT
WITH GENESIS 5 YR
PROJECTED SHORELINE

SCALES IN FEET

MODEL

| 0 | 5 | 10 | 15 | 20 |

PROTOTYPE

| 0 | 375 | 750 | 1125 | 1500 |
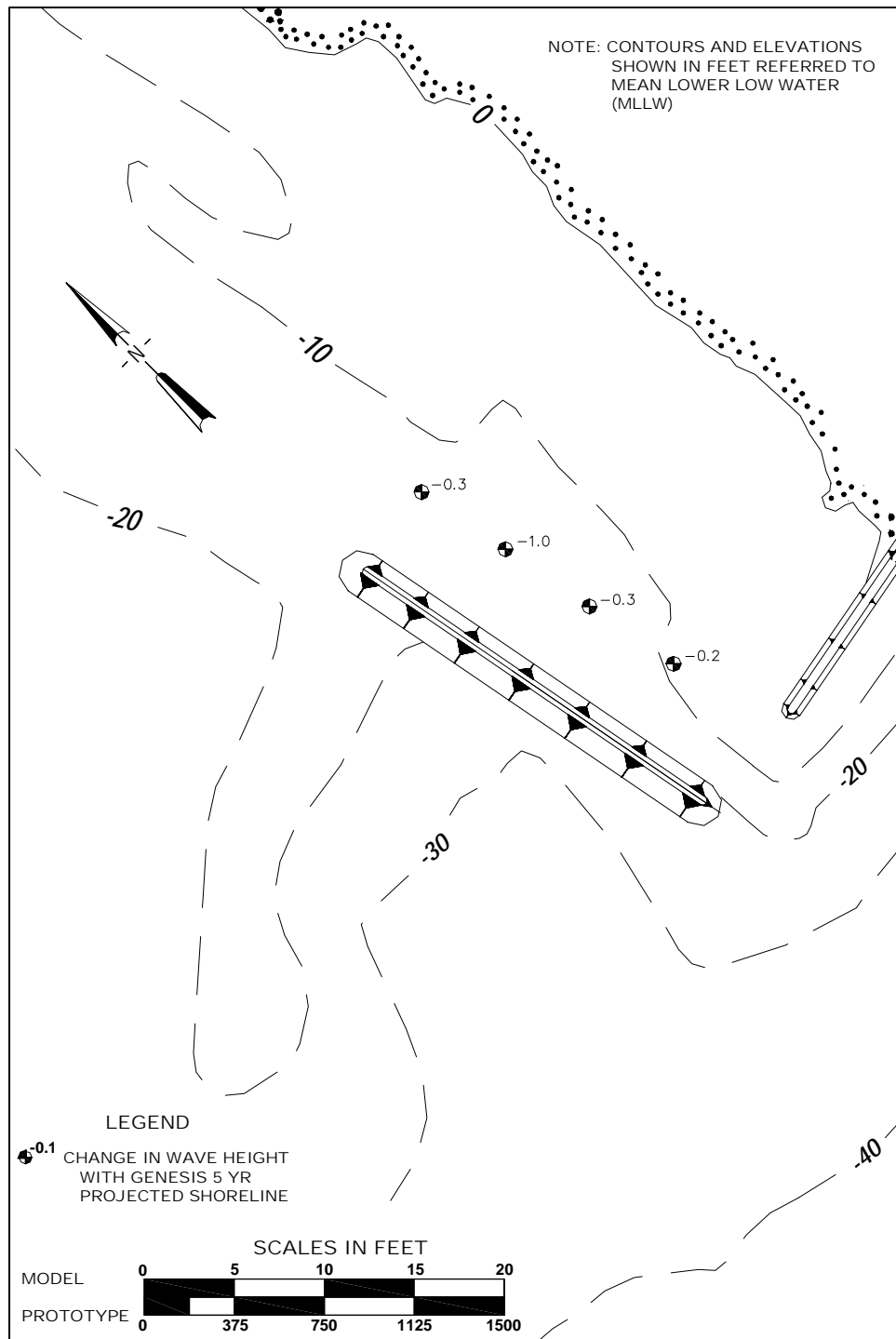
Figure B109. Differences in wave heights between Alt 2A with existing shoreline
and Alt 2A with 5-year projected shoreline for 3-m, 12-sec waves
from southwest at mtl

NOTE: CONTOURS AND ELEVATIONS
SHOWN IN FEET REFERRED TO
MEAN LOWER LOW WATER
(MLLW)

LEGEND

-0.1 CHANGE IN WAVE HEIGHT
WITH GENESIS 5 YR
PROJECTED SHORELINE

SCALES IN FEET

MODEL
0   5   10   15   20

PROTOTYPE
0   375   750   1125   1500
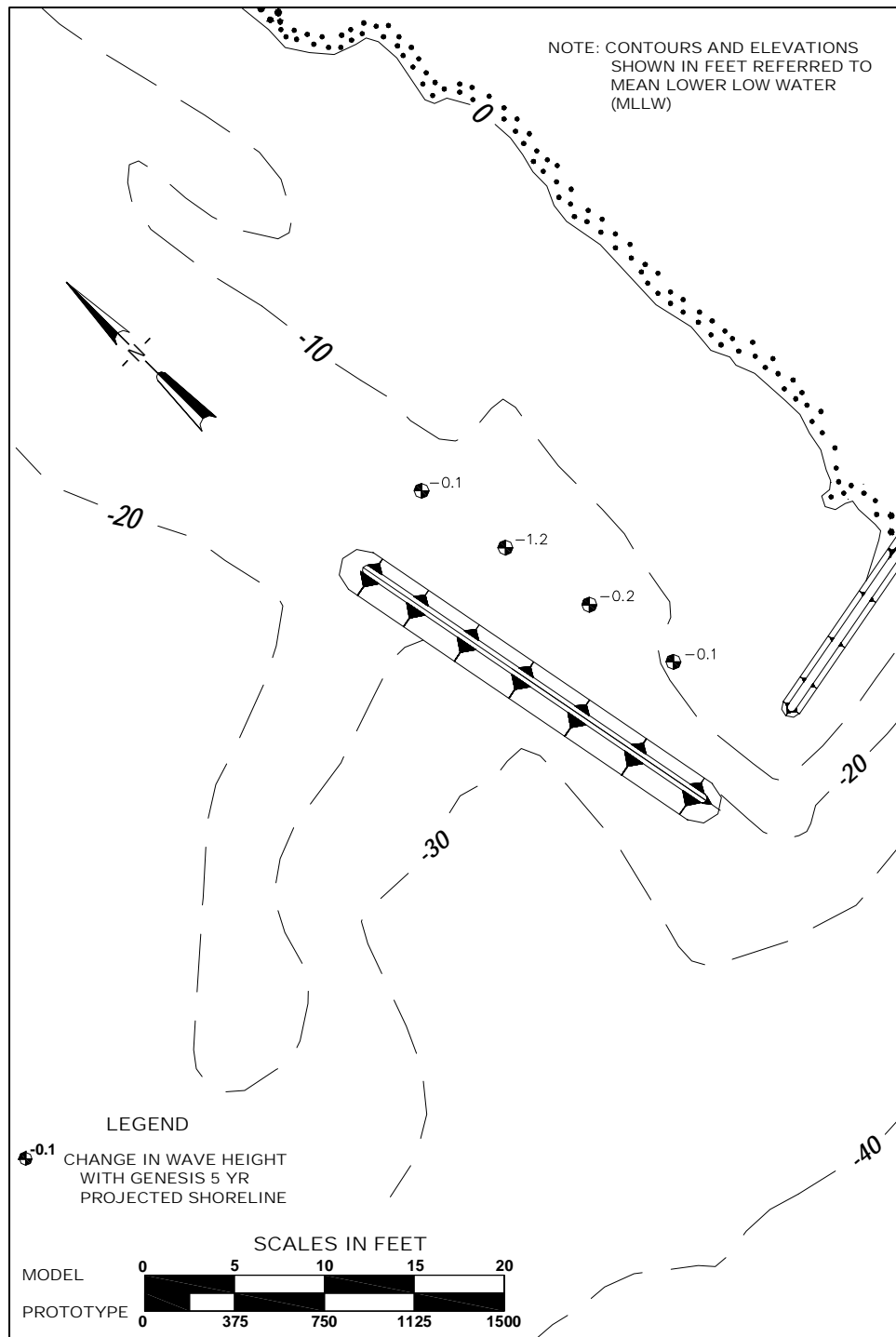
Figure B110. Differences in wave heights between Alt 2A with existing shoreline
and Alt 2A with 5-year projected shoreline for 6-m, 16-sec waves
from southwest at mtl
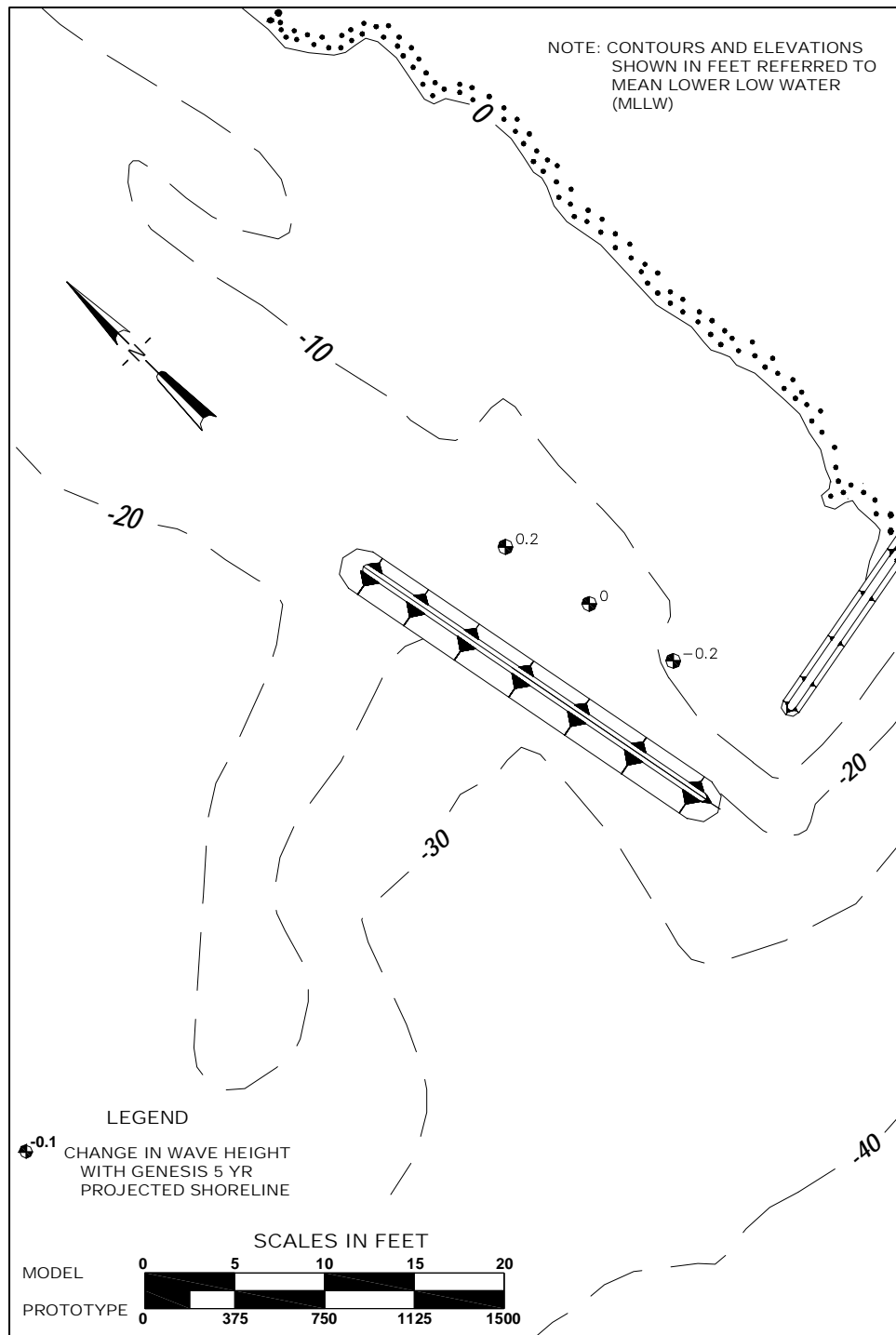
Figure B111. Differences in wave heights between Alt 2A with existing shoreline and Alt 2A with 5-year projected shoreline for 2-m, 9-sec waves from southwest at mhw

NOTE: CONTOURS AND ELEVATIONS
SHOWN IN FEET REFERRED TO
MEAN LOWER LOW WATER
(MLLW)

LEGEND

-0.1 CHANGE IN WAVE HEIGHT
WITH GENESIS 5 YR
PROJECTED SHORELINE

SCALES IN FEET

MODEL

PROTOTYPE

Figure B112. Differences in wave heights between Alt 2A with existing shoreline
and Alt 2A with 5-year projected shoreline for 3-m, 12-sec waves
from southwest at mhw

NOTE: CONTOURS AND ELEVATIONS SHOWN IN FEET REFERRED TO MEAN LOWER LOW WATER (MLLW)

LEGEND

⊕ -0.1 CHANGE IN WAVE HEIGHT WITH GENESIS 5 YR PROJECTED SHORELINE

SCALES IN FEET

MODEL	0	5	10	15	20
PROTOTYPE	0	375	750	1125	1500

Figure B113. Differences in wave heights between Alt 2A with existing shoreline and Alt 2A with 5-year projected shoreline for 6-m, 16-sec waves from southwest at mhw

Tables for Storms from West-Northwest

Wave heights and wave periods

Tables B1 through B9 list wave heights and periods collected during experiments with Alt 1 and Alt 2A.

Table B1
Wave Heights Measured at mllw for 2-m, 9-sec Waves from West-Northwest

Gauge No.	Alternative 1		Alternative 2A	
	Height (m)	Period (sec)	Height (m)	Period (sec)
1	2.18	6.93	2.18	6.75
2	2.03	7.01	2.03	7.01
3	1.35	5.98	1.50	6.58
4	1.35	8.31	1.50	8.40
5	1.95	8.14	2.03	8.05
6	1.95	8.31	2.10	8.23
7	2.03	8.40		
8	2.10	8.31	1.8	7.71
9	1.95	7.88	1.88	7.88
10	1.13	8.49	1.28	7.97
11			0.08	7.79
12			0.30	161.86
13	2.33	8.14	2.10	7.97
14	2.25	8.14	2.25	7.88
15	2.40	8.23		
16	2.48	8.23	1.95	7.53
17	2.18	7.97	1.95	7.71
18	1.80	7.53	1.88	7.62
19	0.53	8.75	0.68	9.01
20	0.53	10.83	0.53	10.65
21	1.88	7.97	2.03	8.23
22	1.88	7.53	1.95	7.36
23	1.80	7.19		
24	1.73	7.10	1.50	7.10
25	1.73	7.01	1.50	6.93
26	1.73	7.19	1.58	7.10
27	0.98	7.62	1.05	7.79
28	0.68	8.57	0.38	7.45
29	1.65	7.27	1.67	7.45
30	1.58	7.27	1.58	7.27
31	1.50	7.19		
32	1.50	7.19	1.58	7.19
33	1.80	7.27	1.73	7.45
34	1.80	7.53	1.65	7.71
35	1.20	7.36	1.20	7.19
36	0.60	9.35	0.08	11.86
37	1.58	7.27	1.50	7.36

Table B2
Wave Heights Measured at mllw for 3-m, 13-sec Waves from West-Northwest

Gauge No.	Alternative 1		Alternative 2A	
	Height (m)	Period (sec)	Height (m)	Period (sec)
1	2.55	10.57	2.48	10.31
2	2.4	11.00	2.4	10.74
3	2.25	10.65	2.03	11.08
4	2.03	11.78	2.04	11.78
5	3.0	11.34	2.7	11.26
6	3.0	11.78	2.55	11.69
7	3.0	11.86		
8	2.93	11.52	2.18	10.74
9	2.33	11.86	2.25	11.17
10	1.28	13.34	1.5	12.90
11			0.38	16.02
12			0.53	127.04
13	2.4	10.31	2.18	10.74
14	2.33	10.39	2.4	11.60
15	2.4	10.57		
16	2.4	10.74	2.18	10.31
17	2.48	11.00	2.4	10.57
18	2.1	10.91	2.25	10.74
19	0.83	16.89	0.975	16.80
20	0.75	25.98	0.75	21.82
21	2.63	10.65	2.78	10.65
22	2.85	11.00	2.85	11.43
23	2.93	10.91		
24	2.93	11.17	2.25	11.26
25	2.55	11.17	2.25	10.74
26	2.25	11.34	1.88	9.79
27	1.2	14.46	1.2	12.47
28	0.83	17.67	0.6	13.59
29	2.63	10.48	2.63	10.48
30	2.48	9.61	2.48	9.79
31	2.4	9.35		
32	2.33	9.61	2.4	9.70
33	2.4	10.83	2.18	10.48
34	1.95	10.91	1.8	10.31
35	1.2	11.69	1.28	11.08
36	0.83	21.90	0.375	15.76
37	2.63	10.91	2.33	10.65

Table B3
Wave Heights Measured at mllw for 5-m, 13-sec Waves from West-Northwest

Gauge No.	Alternative 1		Alternative 2A	
	Height (m)	Period (sec)	Height (m)	Period (sec)
1	4.50	11.00	4.43	10.83
2	4.43	11.26	4.43	11.17
3	2.63	10.83	2.48	11.17
4	2.03	13.42	1.95	12.64
5	2.93	10.22	2.70	10.48
6	2.78	10.65	2.70	10.91
7	2.93	10.57		
8	2.93	10.91	2.25	10.39
9	2.40	11.95	2.40	11.34
10	1.43	16.11	1.58	15.33
11			0.53	22.78
12			0.68	100.89
13	3.08	10.05	2.85	10.31
14	3.23	10.48	3.08	11.17
15	3.38	10.57		
16	3.30	10.74	2.55	11.08
17	2.70	12.38	2.55	11.69
18	2.25	12.99	2.40	12.56
19	0.98	20.18	1.13	19.74
20	0.90	29.79	0.83	25.72
21	3.15	10.65	3.38	10.57
22	3.08	10.83	3.15	11.17
23	3.08	10.57		
24	3.00	10.74	2.33	11.17
25	2.63	11.00	2.48	10.91
26	2.18	10.39	1.95	9.96
27	1.28	14.98	1.28	13.77
28	0.90	20.00	0.75	15.24
29	3.00	9.44	2.93	9.61
30	2.85	10.05	2.93	10.31
31	2.85	10.05		
32	2.85	9.79	2.63	10.39
33	2.55	10.57	2.48	10.83
34	2.10	11.26	1.95	11.17
35	1.35	12.64	1.43	12.30
36	0.90	22.78	0.53	16.89
37	2.85	10.48	2.93	10.22

Table B4
Wave Heights Measured at mtl for 2-m, 9-sec Waves from West-Northwest

Gauge No.	Alternative 1		Alternative 2A	
	Height (m)	Period (sec)	Height (m)	Period (sec)
1	2.4	7.01	2.40	6.93
2	2.25	7.19	2.25	7.10
3	2.03	6.67	1.65	5.72
4	1.43	7.62	1.13	6.84
5	1.88	8.23	2.40	8.05
6	2.18	8.23	2.55	8.14
7	2.25	8.23		
8	2.18	8.05	2.33	7.88
9	2.25	8.05	2.25	7.79
10	1.73	8.05	1.95	7.79
11	1.28	7.88	1.13	7.70
12	0.75	8.31	0.75	8.31
13	2.93	8.14	2.78	8.40
14	2.85	8.14	2.48	8.31
15	2.85	8.14		
16	2.85	8.40	2.18	8.14
17	2.70	8.14	2.03	7.79
18	2.48	8.05	1.95	7.45
19	1.50	7.79	1.95	7.45
20	1.43	7.27	1.43	7.10
21	1.88	7.62	1.80	7.45
22	1.95	7.62	1.88	7.53
23	1.95	7.53		
24	1.88	7.53	1.65	7.36
25	1.88	7.27	1.65	7.36
26	2.10	7.62	1.65	7.36
27	1.95	7.53	1.73	7.45
28	1.43	7.45	1.28	6.93
29	1.73	7.62	1.80	7.45
30	1.73	7.53	1.88	7.45
31	1.73	7.45		
32	1.73	7.40	1.58	7.62
33	1.88	7.62	1.88	7.62
34	1.80	7.36	1.88	7.53
35	1.43	7.53	1.73	7.45
36	1.28	7.19	1.28	7.27
37	1.65	7.45	1.65	7.45

Table B5
Wave Heights Measured at mtl for 3-m, 13-sec Waves from West-Northwest

Gauge No.	Alternative 1		Alternative 2A	
	Height (m)	Period (sec)	Height (m)	Period (sec)
1	2.78	10.57	2.78	10.31
2	2.63	10.57	2.63	10.65
3	2.85	10.83	2.48	11.60
4	2.25	11.52	2.40	11.69
5	2.93	11.95	2.85	11.69
6	3.08	12.30	3.08	12.12
7	3.15	10.04		
8	3.00	11.95	2.78	11.08
9	3.00	12.12	2.93	11.60
10	1.88	11.78	2.10	11.43
11	1.35	12.82	1.35	16.68
12	0.83	17.93	0.90	19.14
13	3.15	10.74	3.15	10.48
14	3.23	11.08	3.23	11.34
15	3.30	11.17		
16	3.38	11.34	2.93	10.57
17	3.45	11.60	3.08	10.74
18	3.00	11.78	2.93	11.17
19	1.88	12.99	1.80	13.77
20	1.58	12.56	1.35	12.90
21	3.08	11.60	3.08	11.78
22	2.70	10.83	2.93	11.26
23	2.70	10.65		
24	2.63	10.83	2.48	10.57
25	2.85	10.74	2.55	11.00
26	2.78	10.13	2.33	9.35
27	2.33	11.43	2.03	11.78
28	1.65	11.95	1.58	12.30
29	2.48	10.39	2.55	10.39
30	2.48	10.13	2.48	10.22
31	2.55	10.22		
32	2.55	10.48	2.33	11.08
33	2.93	11.69	2.78	11.08
34	2.40	10.22	2.40	10.22
35	1.73	10.91	2.03	10.39
36	1.43	11.43	1.35	10.83
37	2.40	11.26	2.55	11.34

Table B6 Wave Heights Measured at mtl for 5-m, 13-sec Waves from West-Northwest				
	Alternative 1		Alternative 2A	
Gauge No.	Height (m)	Period (sec)	Height (m)	Period (sec)
1	4.80	11.26	4.65	11.08
2	4.35	11.17	4.50	11.26
3	3.83	11.95	3.68	11.43
4	2.33	13.60	2.63	12.38
5	3.15	10.31	3.30	11.08
6	3.45	10.83	3.68	11.69
7	3.60	10.74		
8	3.38	10.57	3.15	11.08
9	3.08	11.26	3.15	11.86
10	1.88	13.16	2.18	12.82
11	1.43	15.76	1.50	17.23
12	0.98	24.16	1.13	26.76
13	3.98	10.83	3.68	10.13
14	3.98	10.74	3.98	10.83
15	4.05	10.91		
16	4.05	11.34	3.38	11.00
17	3.75	12.30	3.30	12.30
18	3.15	12.82	3.15	12.64
19	2.03	16.71	1.95	16.11
20	1.65	16.63	1.50	15.85
21	3.83	10.57	3.68	10.74
22	3.68	10.74	3.68	11.43
23	3.75	10.91		
24	3.60	11.26	3.00	11.26
25	3.45	11.00	3.00	11.00
26	3.00	10.74	2.70	10.39
27	2.48	14.12	2.25	13.86
28	1.88	15.93	1.65	14.64
29	3.53	10.65	3.53	10.57
30	3.38	10.74	3.45	10.74
31	3.30	10.39		
32	3.23	10.65	3.08	10.65
33	3.30	10.83	3.08	10.83
34	2.55	11.34	2.63	11.69
35	1.80	11.60	2.10	11.60
36	1.58	13.60	1.50	12.82
37	3.15	10.65	3.38	10.65

Table B7
Wave Heights Measured at mhw for 2-m, 9-sec Waves from West-Northwest

Gauge No.	Alternative 1		Alternative 2A	
	Height (m)	Period (sec)	Height (m)	Period (sec)
1	2.40	7.10	2.48	7.01
2	2.25	7.10	2.33	7.10
3	1.95	6.41	1.95	6.50
4	1.73	7.79	1.80	7.62
5	2.48	8.14	2.40	8.05
6	2.55	8.23	2.55	8.05
7	2.63	8.31		
8	2.55	8.23	2.48	7.97
9	2.63	8.23	2.33	8.05
10	2.40	8.05	2.40	7.88
11	1.80	8.05	1.80	7.88
12	1.20	7.88	1.35	7.97
13	3.08	8.23	2.78	8.05
14	2.85	8.14	2.78	8.14
15	2.93	8.05		
16	2.78	7.97	2.63	7.79
17	2.78	8.14	2.55	8.05
18	2.48	7.88	2.48	7.88
19	1.73	7.45	1.65	7.62
20	1.80	7.45	1.58	7.45
21	2.03	7.36	2.03	7.27
22	2.10	7.27	2.03	6.93
23	2.18	7.36		
24	2.10	7.36	1.88	7.27
25	2.10	7.27	1.95	7.10
26	2.18	7.36	2.10	7.27
27	2.33	7.62	2.03	7.88
28	1.95	7.53	1.73	7.27
29	1.95	7.53	2.03	7.36
30	1.80	7.01	1.88	7.19
31	1.80	7.10		
32	1.88	7.19	1.73	7.01
33	2.03	7.62	1.88	7.36
34	2.03	7.53	2.03	7.45
35	1.80	7.45	1.88	7.36
36	1.95	7.79	1.88	7.97
37	1.80	7.45	1.80	7.27

Table B8
Wave Heights Measured at mhw for 3-m, 13-sec Waves from West-Northwest

Gauge No.	Alternative 1		Alternative 2A	
	Height (m)	Period (sec)	Height (m)	Period (sec)
1	2.85	10.65	2.85	10.39
2	2.70	10.83	2.70	10.57
3	3.38	11.78	2.93	11.60
4	2.48	11.95	2.48	11.78
5	3.08	12.64	2.85	12.58
6	3.08	12.21	3.45	12.58
7	3.15	12.12		
8	3.08	12.30	3.15	11.95
9	3.38	11.34	3.08	11.86
10	2.70	11.78	3.00	11.78
11	1.88	11.86	2.03	11.69
12	1.35	13.16	1.43	13.77
13	3.15	11.52	2.93	11.86
14	3.15	11.60	3.38	11.86
15	3.30	11.69		
16	3.30	11.52	3.15	11.26
17	3.90	11.43	3.53	11.52
18	3.60	11.08	3.53	11.26
19	2.18	11.95	2.40	12.82
20	3.10	11.34	1.95	11.78
21	3.23	12.30	2.93	11.43
22	3.08	12.21	3.08	11.69
23	2.93	11.86		
24	2.78	11.52	2.85	10.91
25	2.78	11.08	2.78	10.39
26	2.78	10.83	2.93	10.39
27	3.00	11.26	2.55	11.43
28	2.40	11.08	2.03	11.00
29	2.70	10.65	2.70	10.74
30	2.55	10.57	2.63	10.48
31	2.55	10.74		
32	2.55	10.39	2.55	10.65
33	3.15	11.60	3.08	11.34
34	3.08	11.17	2.93	10.39
35	2.55	10.74	2.48	10.57
36	2.33	10.91	2.10	10.91
37	2.48	10.83	2.70	10.91

Table B9
Wave Heights Measured at mhw for 5-m, 13-sec Waves from West-Northwest

Gauge No.	Alternative 1		Alternative 2A	
	Height (m)	Period (sec)	Height (m)	Period (sec)
1	5.03	11.17	5.03	11.08
2	4.73	11.29	4.80	11.26
3	4.20	11.95	4.05	11.86
4	2.78	12.47	2.93	12.04
5	3.75	11.00	3.00	12.47
6	3.75	12.04	3.75	12.30
7	3.83	11.95		
8	3.75	11.69	3.30	11.00
9	3.98	12.56	3.68	11.60
10	2.85	12.47	3.08	12.73
11	2.03	15.07	2.18	14.90
12	1.58	19.31	1.65	18.45
13	4.35	11.60	3.30	12.21
14	4.58	11.52	4.43	11.78
15	4.65	11.60		
16	4.58	12.04	3.68	11.86
17	4.43	12.73	4.05	12.38
18	3.98	13.42	3.90	12.90
19	2.25	14.38	2.48	13.94
20	2.33	14.20	2.10	14.12
21	4.65	11.52	4.35	11.60
22	4.43	11.78	4.20	12.21
23	4.35	11.78		
24	4.20	11.69	3.75	11.69
25	4.05	11.26	3.68	11.60
26	3.60	10.91	3.45	10.65
27	3.15	11.95	2.78	12.38
28	2.55	13.34	2.33	13.42
29	4.05	11.08	3.98	10.83
30	4.05	11.08	4.13	11.00
31	4.13	11.08		
32	4.05	11.08	3.68	11.00
33	4.05	10.83	3.68	10.57
34	3.68	11.43	3.38	11.78
35	2.85	11.86	2.78	11.86
36	2.48	12.64	2.25	12.38
37	3.98	11.00	4.13	11.08

Current velocity

Tables B10 through B18 list velocities calculated from velocimeter measurements for Alt 1 and Alt 2A for storms from the west-northwest.

Table B10
Velocity Measurements with 2-m, 9-sec Waves at mllw from West-Northwest

ADV No.	Alternative 1				Alternative 2A			
	Ave. Vel. Offshore (cm/sec)	Ave. Vel. South (cm/sec)	Ave. Vel. Magnitude (cm/sec)	Magnitude of Ave. Vel. (cm/sec)	Ave. Vel. Offshore (cm/sec)	Ave. Vel. South (cm/sec)	Ave. Vel. Magnitude (cm/sec)	Magnitude of Ave. Vel. (cm/sec)
1	-13.17	18.83	45.03	22.98	-23.72		42.32	23.81
2	-20.17	43.78	74.48	48.21	-14.22	50.38	68.64	52.35
3		17.51	57.93	17.65	-2.6	23.25	48.32	23.4

Table B11
Velocity Measurements with 3-m, 13-sec Waves at mllw from West-Northwest

ADV No.	Alternative 1				Alternative 2A			
	Ave. Vel. Offshore (cm/sec)	Ave. Vel. South (cm/sec)	Ave. Vel. Magnitude (cm/sec)	Magnitude of Ave. Vel. (cm/sec)	Ave. Vel. Offshore (cm/sec)	Ave. Vel. South (cm/sec)	Ave. Vel. Magnitude (cm/sec)	Magnitude of Ave. Vel. (cm/sec)
1	-16.82	29.58	66.78	34.03	-35.69	24.44	70.41	43.26
2	-10.24	67.44	93.85	68.21	-12.43	41.87	69.5	43.68
3		75.61	93.84	78.01	-24.92	31.91	65.46	40.48

Table B12
Velocity Measurements with 5-m, 13-sec Waves at mllw from West-Northwest

ADV No.	Alternative 1				Alternative 2A			
	Ave. Vel. Offshore (cm/sec)	Ave. Vel. South (cm/sec)	Ave. Vel. Magnitude (cm/sec)	Magnitude of Ave. Vel. (cm/sec)	Ave. Vel. Offshore (cm/sec)	Ave. Vel. South (cm/sec)	Ave. Vel. Magnitude (cm/sec)	Magnitude of Ave. Vel. (cm/sec)
1	-18.81	66.85	87.64	69.44	-27	50.36	75.13	57.14
2	-18.2	94.21	122.21	95.95	-20.33	46.25	76.32	50.52
3	-22.87	65.21	100.07	69.79	-24.47	38.04	73.94	45.23

Table B13
Velocity Measurements with 2-m, 9-sec Waves at mtl from West-Northwest

ADV No.	Alternative 1				Alternative 2A			
	Ave. Vel. Offshore (cm/sec)	Ave. Vel. South (cm/sec)	Ave. Vel. Magnitude (cm/sec)	Magnitude of Ave. Vel. (cm/sec)	Ave. Vel. Offshore (cm/sec)	Ave. Vel. South (cm/sec)	Ave. Vel. Magnitude (cm/sec)	Magnitude of Ave. Vel. (cm/sec)
1	-15.34	74.20	84.96	75.77	-38.82	80.35	98.92	89.24
2	-37.28	100.16	116.53	106.87	-38.71	81.89	100.33	90.57
3	-26.80	94.20	108.22	97.93	-33.03	84.89	102.33	91.09

Table B14
Velocity Measurements with 3-m, 13-sec Waves at mtl from West-Northwest

ADV No.	Alternative 1				Alternative 2A			
	Ave. Vel. Offshore (cm/sec)	Ave. Vel. South (cm/sec)	Ave. Vel. Magnitude (cm/sec)	Magnitude of Ave. Vel. (cm/sec)	Ave. Vel. Offshore (cm/sec)	Ave. Vel. South (cm/sec)	Ave. Vel. Magnitude (cm/sec)	Magnitude of Ave. Vel. (cm/sec)
1	-27.58	90.20	109.33	94.32	-43.2	82.77	109.63	93.36
2	-38.07	111.13	139.30	117.47	-36.48	83.81	108.89	91.41
3	-23.48	87.83	116.35	90.91	-29.42	81.72	103.49	86.85

Table B15
Velocity Measurements with 5-m, 13-sec Waves at mtl from West-Northwest

ADV No.	Alternative 1				Alternative 2A			
	Ave. Vel. Offshore (cm/sec)	Ave. Vel. South (cm/sec)	Ave. Vel. Magnitude (cm/sec)	Magnitude of Ave. Vel. (cm/sec)	Ave. Vel. Offshore (cm/sec)	Ave. Vel. South (cm/sec)	Ave. Vel. Magnitude (cm/sec)	Magnitude of Ave. Vel. (cm/sec)
1	-29.18	88.47	114.02	93.15	-41.2	79.05	114.06	89.14
2	-28.84	109.87	141.02	113.59	-37.47	81.82	112.2	89.99
3	-50.72	79.09	122.96	93.96	-35.58	79.06	108.53	86.7

Table B16
Velocity Measurements with 2-m, 9-sec Waves at mhw from West-Northwest

ADV No.	Alternative 1				Alternative 2A			
	Ave. Vel. Offshore (cm/sec)	Ave. Vel. South (cm/sec)	Ave. Vel. Magnitude (cm/sec)	Magnitude of Ave. Vel. (cm/sec)	Ave. Vel. Offshore (cm/sec)	Ave. Vel. South (cm/sec)	Ave. Vel. Magnitude (cm/sec)	Magnitude of Ave. Vel. (cm/sec)
1	-1.57	-2.00	35.17	2.53	-1.46		32.12	1.59
2	-25.94	19.30	52.60	32.33	-23.6	28.09	51.23	36.69
3	5.32	0.69	48.82	5.12	-4.53	14.14	46.02	14.84

Table B17
Velocity Measurements with 3-m, 13-sec Waves at mhw from West-Northwest

ADV No.	Alternative 1				Alternative 2A			
	Ave. Vel. Offshore (cm/sec)	Ave. Vel. South (cm/sec)	Ave. Vel. Magnitude (cm/sec)	Magnitude of Ave. Vel. (cm/sec)	Ave. Vel. Offshore (cm/sec)	Ave. Vel. South (cm/sec)	Ave. Vel. Magnitude (cm/sec)	Magnitude of Ave. Vel. (cm/sec)
1	-3.57	8.14	52.63	8.88	-12.39	0.23	52.95	12.4
2	-25.86	48.85	89.08	55.28	-19.32	20.95	66.97	28.5
3	-22.81	60.14	91.81	64.32	-15.95	38.08	65.18	41.28

Appendix B   Physical Modeling of North Beach and Jetty

Table B18
Velocity Measurements with 5-m, 13-sec Waves at mhw from West-Northwest

ADV No.	Alternative 1				Alternative 2A			
	Ave. Vel. Offshore (cm/sec)	Ave. Vel. South (cm/sec)	Ave. Vel. Magnitude (cm/sec)	Magnitude of Ave. Vel. (cm/sec)	Ave. Vel. Offshore (cm/sec)	Ave. Vel. South (cm/sec)	Ave. Vel. Magnitude (cm/sec)	Magnitude of Ave. Vel. (cm/sec)
1	-19.07	41.27	73.03	45.46	-11.41	31.65	56.53	33.65
2	-23.44	68.42	112.65	72.32	-22.81	42.53	88.54	48.26
3	-25.23	59.98	103.32	65.07	-28.89	37.77	84.77	47.55

Tables for Storms from Southwest

Wave heights and wave periods

Tables B19 through B27 list wave heights and wave periods collected during experiments with Alt 1, Alt 2A, and Alt 3B.

Table B19
Wave Heights and Periods with 2-m, 9-sec Waves from Southwest at mllw

Gauge No.	Alternative 1		Alternative 2A		Alternative 3B	
	Height (m)	Period (sec)	Height (m)	Period (sec)	Height (m)	Period (sec)
1	1.95	9.34	1.94	9.09	1.98	9.09
2	2.06	9.09	2.02	9.09	2.03	9.09
3	2.45	9.34	2.49	9.09	2.29	9.34
4	1.81	8.45	2.17	8.87	1.89	9.34
5	1.88	9.09	1.81	8.65	2.63	9.09
6	2.02	8.87	1.69	8.87	1.67	8.87
7	2.12	8.87				
8	2.15	8.87	1.67	9.34	1.40	8.65
9	2.26	8.87	1.85	9.09	1.18	8.87
10	1.90	9.34	1.83	9.34	1.11	9.09
11	0.96	9.34	1.16	9.34	0.97	9.09
12	0.87	10.13	0.75	10.13	0.73	9.09
13	1.86	9.09	1.91	9.09	1.94	9.09
14	1.85	9.09	1.73	9.09	2.48	9.09
15	1.82	9.09			2.37	9.09
16	1.77	9.09	1.56	9.09	2.25	9.09
17	1.77	9.09	1.64	9.09	1.85	9.09
18	1.73	9.34	1.74	9.09	1.54	8.87
19	1.11	9.34	1.46	9.09	1.21	9.09
20	1.20	9.34	1.14	9.34	1.02	9.34
21	1.77	8.87	2.25	9.09	1.98	8.87
22	1.92	8.25	2.00	9.09	1.74	8.45
23	1.92	8.45			1.75	9.09
24	1.86	8.45	1.71	8.45	1.77	9.09
25	1.73	8.87	1.71	8.65	1.80	8.87
26	1.64	9.09	1.68	9.09	1.56	9.09
27	0.93	9.34	1.52	9.34	1.49	9.09
28	1.25	10.13	1.34	9.09	1.16	9.09
29	3.58	9.09	3.64	9.09	3.73	9.09
30	2.95	9.09	3.22	9.09	3.39	9.09
31	2.52	9.09			3.23	9.09
32	2.33	8.87	2.12	9.09	2.89	9.09
33	2.15	9.34	2.00	9.34	2.27	9.34
34	2.16	9.09	1.91	8.87	2.25	9.09
35	1.31	9.09	1.66	8.87	1.90	8.45
36	1.51	9.34	1.44	9.34	1.42	9.34
37	3.08	9.34	3.28	9.09	3.21	9.09
38	2.14	8.87	2.02	8.87	2.27	9.09
39	2.03	9.09	1.96	9.09	2.17	9.09
40	2.12	9.09	2.43	9.09	2.63	9.09
41	1.99	9.09	1.98	9.09	2.40	9.09
42	2.28	8.87	2.02	9.09	2.44	9.09
43	2.32	9.09	2.30	9.09	2.47	9.09
44	1.91	8.87	2.00	8.87	2.11	9.09
45	1.94	9.09	2.17	9.09	1.95	8.87
46	2.68	9.09	2.49	9.34	2.53	9.09
47	2.44	9.09	2.25	8.87	2.16	8.65
48	2.74	9.09	2.57	9.09	2.56	8.87
49	3.49	9.09	3.62	9.09	3.53	9.09
50	2.11	9.09	2.27	9.09	2.03	9.09
51	2.53	9.09	2.74	9.09	2.24	9.09
52	1.83	9.09	1.85	9.09	1.84	9.09
53	1.79	9.09	1.73	9.09	1.73	9.09

Table B20
Wave Heights and Periods with 3-m, 12-sec Waves from Southwest at mllw

Gauge No.	Alternative 1 Height (m)	Alternative 1 Period (sec)	Alternative 2A Height (m)	Alternative 2A Period (sec)	Alternative 3B Height (m)	Alternative 3B Period (sec)
1	2.56	12.23	2.57	12.23	2.56	12.23
2	2.68	12.23	2.68	12.23	2.65	12.23
3	3.24	12.67	3.21	12.67	3.45	14.12
4	2.38	12.67	2.37	12.67	2.36	14.12
5	2.61	12.67	2.62	12.23	2.53	14.12
6	2.80	12.67	2.66	12.67	1.99	14.12
7	2.97	12.67			1.89	14.12
8	2.99	12.67	2.17	12.67	1.75	14.12
9	2.31	12.67	2.12	12.67	1.59	14.12
10	1.17	118.21	1.14	118.21	1.16	118.21
11	0.58	118.21	0.81	118.21	0.62	177.36
12	0.46	177.36	0.38	177.36	0.28	354.71
13	2.36	12.67	2.24	12.23	2.19	14.12
14	2.31	12.67	2.38	12.67	2.20	14.12
15	2.33	12.67			2.22	14.12
16	2.32	12.67	1.97	12.67	2.18	14.12
17	2.20	12.67	2.07	12.67	1.92	14.12
18	1.81	12.67	1.86	12.67	1.70	14.12
19	0.94	118.21	0.88	118.21	0.82	118.21
20	0.74	177.36	0.73	117.36	0.69	177.36
21	2.78	12.67	2.71	12.67	2.87	14.12
22	2.50	12.67	2.54	12.67	2.62	14.12
23	2.51	12.67			2.52	14.12
24	2.41	12.67	1.94	12.67	2.40	14.12
25	2.29	13.14	2.03	13.14	2.17	13.14
26	2.19	12.67	1.93	12.67	2.04	13.14
27	1.40	118.21	1.35	118.21	1.29	118.21
28	0.95	118.21	0.88	118.21	0.95	177.36
29	3.04	12.67	2.99	12.67	2.89	14.12
30	2.88	12.67	2.69	13.14	2.74	14.12
31	2.83	12.67			2.76	14.12
32	2.02	12.67	2.02	13.14	2.70	14.12
33	2.42	12.67	2.11	13.14	2.33	14.12
34	2.02	118.21	1.94	118.21	2.04	118.21
35	1.63	118.21	1.49	118.21	1.46	118.21
36	0.96	118.21	0.93	88.68	0.96	88.68
37	3.05	13.14	3.03	13.14	2.95	13.14
38	2.76	12.67	2.78	12.67	2.78	14.12
39	2.68	12.23	2.60	12.23	2.56	12.23
40	2.94	12.23	3.20	12.23	2.85	11.82
41	2.81	12.23	2.79	12.23	2.55	12.23
42	3.04	12.23	3.04	12.23	2.96	12.23
43	3.16	12.67	3.07	12.67	2.99	12.23
44	2.73	12.23	2.86	12.23	2.61	14.12
45	2.89	12.67	2.90	12.67	2.52	14.12
46	3.25	12.23	3.19	12.23	3.11	12.23
47	2.97	12.23	3.07	12.23	3.18	12.23
48	3.35	12.67	3.39	12.67	3.05	14.12
49	3.58	12.67	3.63	12.67	3.50	14.12
50	2.81	12.67	2.70	12.67	2.76	14.12
51	3.41	12.67	3.46	12.67	3.25	14.12
52	2.36	12.67	2.41	12.67	2.15	14.12
53	2.27	12.67	2.28	12.67	2.06	14.12

Table B21
Wave Heights and Periods with 6-m, 16-sec Waves from Southwest at mllw

Gauge No.	Alternative 1		Alternative 2A		Alternative 3B	
	Height (m)	Period (sec)	Height (m)	Period (sec)	Height (m)	Period (sec)
1	5.93	14.57	6.33	16.12	5.57	16.12
2	5.77	15.42	6.20	16.12	5.56	15.12
3	4.68	16.89	4.72	16.89	4.56	88.68
4	3.52	88.69	3.62	88.68	3.60	88.68
5	4.25	16.89	4.42	17.74	4.35	16.89
6	4.22	16.89	4.28	16.89	3.78	16.89
7	4.19	16.89				
8	4.01	16.89	3.10	16.89	3.36	16.89
9	2.78	16.89	2.57	88.68	2.52	16.89
10	1.81	88.68	1.78	88.68	1.65	118.21
11	1.03	118.21	1.53	118.21	1.17	118.21
12	0.89	354.71	0.79	354.71	0.80	354.71
13	3.58	15.42	3.38	17.74	3.38	14.78
14	3.64	17.74	3.51	16.89	3.52	14.78
15	3.68	16.89			3.54	14.78
16	3.63	16.89	2.88	16.89	3.44	16.89
17	3.63	16.89	2.59	16.89	2.65	16.89
18	2.21	88.68	2.09	118.21	2.13	118.21
19	1.54	88.68	1.38	88.68	1.29	354.71
20	1.24	354.71	1.18	354.71	1.16	354.71
21	3.41	14.19	3.40	16.89	3.36	14.78
22	3.20	14.19	3.28	14.19	3.26	14.19
23	3.25	14.19			3.18	14.19
24	3.12	14.19	2.51	14.19	3.07	14.19
25	2.79	16.89	2.57	20.86	2.64	25.34
26	2.44	118.21	2.19	118.21	2.25	118.21
27	1.66	118.21	1.59	88.68	1.52	354.71
28	1.32	354.71	1.21	354.71	1.28	354.71
29	3.09	16.89	3.18	16.89	3.07	16.89
30	2.99	16.89	2.98	16.89	2.93	14.19
31	2.98	16.89			2.94	14.19
32	2.92	16.89	2.22	16.89	2.87	14.19
33	2.74	118.21	2.39	118.21	2.69	23.65
34	2.23	118.21	2.14	118.21	2.28	25.34
35	1.80	118.21	1.64	118.21	1.68	354.71
36	1.29	354.21	1.24	354.71	1.36	354.71
37	2.98	11.44	2.79	14.78	2.96	16.89
38	5.55	16.12	5.34	16.12	5.46	16.12
39	4.99	16.12	4.83	16.12	4.89	16.12
40	5.80	16.12	5.79	16.12	5.76	16.12
41	5.41	16.12	5.42	16.89	5.24	16.12
42	5.72	16.12	5.69	16.12	5.62	16.12
43	5.15	16.12	5.30	16.12	5.18	16.12
44	5.90	16.12	5.83	16.12	5.67	16.12
45	5.00	16.89	4.93	16.89	5.05	17.74
46	4.08	16.12	4.09	16.12	3.95	16.12
47	3.96	16.89	3.94	14.78	4.04	16.89
48	3.66	16.89	3.75	16.89	3.53	16.89
49	3.74	16.12	3.82	14.78	3.72	16.89
50	3.53	16.12	3.58	16.12	3.40	16.89
51	3.38	16.89	3.47	16.89	3.29	16.12
52	3.48	15.42	3.43	16.89	3.22	16.89
53	3.45	16.12	3.36	16.12	3.20	16.12

Appendix B   Physical Modeling of North Beach and Jetty

Table B22
Wave Heights and Periods with 2-m, 9-sec Waves from Southwest at mtl with Full Flood Tidal Current

Gauge No.	Alternative 1		Alternative 2A		Alternative 3B	
	Height (m)	Period (sec)	Height (m)	Period (sec)	Height (m)	Period (sec)
1	1.95	9.34	1.94	9.09	1.98	9.09
2	2.06	9.09	2.02	9.09	2.03	9.09
3	2.45	9.34	2.49	9.09	2.29	9.34
4	1.81	8.45	2.17	8.87	1.89	9.34
5	1.88	9.09	1.81	8.65	2.63	9.09
6	2.02	8.87	1.69	8.87	1.67	8.87
7	2.12	8.87				
8	2.15	8.87	1.67	9.34	1.40	8.65
9	2.26	8.87	1.85	9.09	1.18	8.87
10	1.90	9.34	1.83	9.34	1.11	9.09
11	0.96	9.34	1.16	9.34	0.97	9.09
12	0.87	10.13	0.75	10.13	0.73	9.09
13	1.86	9.09	1.91	9.09	1.94	9.09
14	1.85	9.09	1.73	9.09	2.48	9.09
15	1.82	9.09			2.37	9.09
16	1.77	9.09	1.56	9.09	2.25	9.09
17	1.77	9.09	1.64	9.09	1.85	9.09
18	1.73	9.34	1.74	9.09	1.54	8.87
19	1.11	9.34	1.46	9.09	1.21	9.09
20	1.20	9.34	1.14	9.34	1.02	9.34
21	1.77	8.87	2.25	9.09	1.98	8.87
22	1.92	8.25	2.00	9.09	1.74	8.45
23	1.92	8.45			1.75	9.09
24	1.86	8.45	1.71	8.45	1.77	9.09
25	1.73	8.87	1.71	8.65	1.80	8.87
26	1.64	9.09	1.68	9.09	1.56	9.09
27	0.93	9.34	1.52	9.34	1.49	9.09
28	1.25	10.13	1.34	9.09	1.16	9.09
29	3.58	9.09	3.64	9.09	3.73	9.09
30	2.95	9.09	3.22	9.09	3.39	9.09
31	2.52	9.09			3.23	9.09
32	2.33	8.87	2.12	9.09	2.89	9.09
33	2.15	9.34	2.00	9.34	2.27	9.34
34	2.16	9.09	1.91	8.87	2.25	9.09
35	1.31	9.09	1.66	8.87	1.90	8.45
36	1.51	9.34	1.44	9.34	1.42	9.34
37	3.08	9.34	3.28	9.09	3.21	9.09
38	2.14	8.87	2.02	8.87	2.27	9.09
39	2.03	9.09	1.96	9.09	2.17	9.09
40	2.12	9.09	2.43	9.09	2.63	9.09
41	1.99	9.09	1.98	9.09	2.40	9.09
42	2.28	8.87	2.02	9.09	2.44	9.09
43	2.32	9.09	2.30	9.09	2.47	9.09
44	1.91	8.87	2.00	8.87	2.11	9.09
45	1.94	9.09	2.17	9.09	1.95	8.87
46	2.68	9.09	2.49	9.34	2.53	9.09
47	2.44	9.09	2.25	8.87	2.16	8.65
48	2.74	9.09	2.57	9.09	2.56	8.87
49	3.49	9.09	3.62	9.09	3.53	9.09
50	2.11	9.09	2.27	9.09	2.03	9.09
51	2.53	9.09	2.74	9.09	2.24	9.09
52	1.83	9.09	1.85	9.09	1.84	9.09
53	1.79	9.09	1.73	9.09	1.73	9.09

Table B23
Wave Heights and Periods with 3-m, 12-sec Waves from Southwest at mtl with Full Flood Tidal Current

Gauge No.	Alternative 1		Alternative 2A		Alternative 3B	
	Height (m)	Period (sec)	Height (m)	Period (sec)	Height (m)	Period (sec)
1	3.09	11.82	3.11	12.23	3.15	12.23
2	3.30	12.23	3.24	12.23	3.27	12.23
3	3.63	12.67	3.84	12.23	4.40	12.23
4	3.27	12.67	3.09	12.67	3.44	12.67
5	3.16	12.67	3.06	12.67	3.39	12.67
6	3.26	12.67	3.13	12.67	2.47	12.67
7	3.33	12.67				
8	3.29	12.67	2.74	12.67	2.17	12.67
9	3.18	12.67	2.94	12.27	2.02	12.67
10	2.03	12.67	1.90	12.67	1.73	12.67
11	1.11	118.21	1.64	12.67	1.40	118.21
12	1.01	354.71	1.29	118.21	0.92	354.71
13	2.78	12.67	2.76	12.73	2.89	12.23
14	2.92	12.67	2.75	12.73	3.12	12.67
15	2.98	12.67			3.08	12.67
16	2.97	12.67	2.45	12.67	3.01	12.67
17	2.91	12.67	2.55	13.14	2.64	12.67
18	2.54	12.67	2.63	12.67	2.27	12.67
19	1.28	118.21	1.64	12.67	1.64	118.21
20	1.30	88.68	1.26	118.21	1.34	118.21
21	2.95	12.67	5.69	12.67	2.76	12.23
22	2.93	12.67	2.81	12.67	2.79	12.23
23	2.84	12.67			2.83	12.23
24	2.75	12.67	2.36	12.67	2.78	12.23
25	2.65	13.14	2.45	12.67	2.73	12.67
26	2.61	13.14	2.31	13.14	2.25	12.67
27	1.33	13.14	2.07	13.14	2.13	12.67
28	1.60	118.21	1.52	118.21	1.61	118.21
29	3.55	12.67	3.45	12.67	3.46	12.67
30	3.14	13.14	3.02	12.67	3.18	12.67
31	3.07	13.14			3.24	12.67
32	2.96	13.14	2.46	12.67	3.16	12.67
33	2.81	13.14	2.42	12.67	2.88	13.14
34	2.61	12.67	2.52	12.67	2.48	12.67
35	1.79	118.21	2.20	118.21	2.28	12.67
36	1.67	118.21	1.65	118.21	1.71	118.21
37	3.42	12.67	3.29	13.14	3.26	12.67
38	3.46	12.23	3.38	12.67	3.45	12.23
39	3.24	12.23	3.18	12.23	3.29	12.23
40	3.65	12.23	3.68	12.23	3.83	12.23
41	3.41	12.23	3.20	12.23	3.29	12.23
42	3.68	12.23	3.80	12.23	3.75	12.23
43	3.60	12.67	3.62	12.23	3.63	12.23
44	3.12	12.67	3.38	12.67	3.34	12.23
45	3.29	12.67	3.56	12.23	3.35	12.23
46	4.06	12.67	4.01	12.23	4.08	12.23
47	3.59	12.23	3.66	12.23	3.57	12.23
48	4.34	12.67	4.27	12.67	4.24	12.67
49	4.30	12.23	4.48	12.67	4.44	12.23
50	3.78	12.67	3.68	12.23	3.87	12.67
51	4.28	12.67	4.31	12.67	3.99	12.67
52	3.16	12.67	3.10	12.67	2.99	12.67
53	3.39	12.67	3.17	12.67	3.03	12.67

Table B24
Wave Heights and Periods with 6-m, 16-sec Waves from Southwest at mtl with Full Flood Tidal Current

Gauge No.	Alternative 1		Alternative 2A		Alternative 3B	
	Height (m)	Period (sec)	Height (m)	Period (sec)	Height (m)	Period (sec)
1	5.14	16.12	5.17	16.12	5.17	16.12
2	5.03	16.12	5.07	16.12	5.04	16.12
3	5.37	16.12	5.31	16.12	5.33	16.12
4	4.04	88.68	4.33	16.12	4.34	88.68
5	4.43	16.12	4.97	16.12	4.72	16.12
6	4.52	16.12	4.92	16.89	2.39	16.89
7	4.59	16.12				
8	4.42	16.89	3.93	16.89	3.56	16.89
9	3.71	16.89	3.37	17.74	3.14	16.89
10	2.48	118.21	2.26	118.21	2.25	16.89
11	1.40	118.21	1.64	118.21	1.61	118.21
12	1.38	88.68	1.19	88.68	1.20	354.71
13	3.85	16.89	3.86	16.89	3.85	16.89
14	3.92	16.89	3.99	16.89	4.01	16.89
15	3.97	16.89			4.09	16.89
16	3.88	16.89	3.44	16.89	3.96	16.89
17	3.63	17.74	3.33	16.89	3.41	16.89
18	2.87	16.89	2.95	118.21	2.70	16.89
19	1.49	118.21	1.90	118.21	1.89	118.21
20	1.63	88.68	1.76	118.21	1.55	88.24
21	4.02	16.89	3.68	16.89	3.60	16.89
22	4.03	16.89	3.64	16.89	3.68	16.89
23	3.98	16.89			3.70	16.89
24	3.85	16.89	3.04	16.89	3.56	16.89
25	3.65	16.89	3.11	16.89	3.32	17.74
26	3.35	16.89	2.84	118.21	2.70	16.89
27	1.49	118.21	3.23	118.21	2.43	16.89
28	1.87	118.21	1.76	118.21	1.75	118.21
29	3.87	16.89	3.84	16.89	3.75	16.89
30	3.55	16.89	3.54	16.89	3.43	16.89
31	3.58	16.89			3.44	16.89
32	3.47	16.89	2.91	16.89	3.33	16.89
33	3.23	16.89	2.94	17.74	3.26	16.89
34	2.86	17.74	2.97	118.21	2.77	16.89
35	1.90	118.21	2.49	118.21	2.41	118.21
36	1.88	118.24	1.87	118.21	1.83	118.21
37	3.70	16.89	3.64	16.89	3.63	16.89
38	5.33	16.12	5.23	16.12	5.28	16.12
39	4.72	16.12	4.81	16.12	4.73	16.12
40	5.68	16.12	5.69	16.12	5.75	16.12
41	5.09	16.12	5.08	16.12	4.95	16.12
42	5.83	16.12	5.80	16.12	5.62	16.12
43	5.41	16.12	5.42	16.12	5.44	16.12
44	5.67	16.12	5.73	16.12	5.74	16.12
45	5.44	16.12	5.38	16.12	5.61	16.12
46	4.67	16.12	5.23	16.12	4.53	16.12
47	4.45	16.12	4.81	16.12	4.45	16.12
48	4.48	16.12	4.52	16.12	4.38	16.89
49	4.73	16.12	4.66	16.12	4.52	16.12
50	4.04	15.42	4.17	16.12	4.10	16.12
51	4.22	16.12	4.48	16.12	4.15	16.12
52	3.93	16.12	3.88	16.12	4.05	16.12
53	3.99	16.12	3.92	16.12	3.99	16.12

Table B25
Wave Heights and Periods with 2-m, 9-sec Waves from Southwest at mhw

Gauge No.	Alternative 1		Alternative 2A		Alternative 3B	
	Height (m)	Period (sec)	Height (m)	Period (sec)	Height (m)	Period (sec)
1	1.86	9.09	1.92	9.09	1.91	9.09
2	1.98	9.09	2.06	9.09	2.05	9.09
3	2.18	9.09	2.32	9.09	2.39	9.09
4	1.98	8.45	1.94	8.87	2.06	8.45
5	1.63	8.65	1.74	9.09	1.94	8.45
6	1.57	9.09	1.76	9.09	1.41	9.09
7	1.64	9.09				
8	1.67	9.09	1.85	9.09	1.17	9.09
9	1.72	9.09	1.97	9.09	0.92	9.09
10	2.01	9.09	2.28	9.09	0.84	9.09
11	1.84	10.06	1.19	9.34	0.74	8.87
12	1.17	10.06	1.11	9.34	0.73	8.87
13	1.48	9.09	1.57	9.09	1.44	9.09
14	1.48	9.09	1.47	9.59	1.62	9.09
15	1.50	9.09	1.57	9.34	1.63	9.09
16	1.47	9.09	1.42	9.09	1.59	9.09
17	1.53	9.09			1.40	8.45
18	1.60	8.87	1.57	9.09	1.26	9.09
19	1.76	8.45	1.69	8.45	1.16	9.09
20	1.65	9.34	1.73	9.34	1.00	9.09
21	1.39	8.25	1.37	8.25	1.32	8.25
22	1.68	8.87	1.65	8.87	1.68	8.87
23	1.69	8.87	1.75	8.87	1.71	8.87
24	1.61	9.09	1.56	8.87	1.69	9.09
25	1.48	9.34			1.54	9.09
26	1.45	9.34	1.41	9.34	1.40	9.86
27	0.77	10.13	0.74	10.13	1.76	8.45
28	1.26	8.65	1.21	8.65	1.02	8.45
29	3.12	9.34			3.62	9.34
30	1.48	9.09			1.79	9.34
31	1.28	9.86			1.63	9.34
32	1.34	9.59			1.68	8.45
33	1.58	9.09			2.14	9.34
34	1.41	8.87			1.75	10.13
35	1.37	9.09			1.49	8.87
36	1.29	9.34			1.40	9.34
37	3.27	10.06	3.45	9.09	3.66	9.09
38	1.83	1.83	1.98	8.65	2.08	9.09
39	1.87	9.55	1.88	9.09	1.91	9.09
40	2.13	9.09	2.24	9.09	2.23	9.09
41	1.96	9.09	2.02	9.09	1.92	9.09
42	1.89	8.87	2.03	9.34	1.99	9.09
43	2.17	8.87	2.23	9.09	1.99	9.09
44	1.81	9.09			1.97	8.87
45	2.03	9.09			1.96	9.09
46	2.12	9.34	2.25	9.34	2.19	9.34
47	2.00	9.09	2.18	9.09	2.13	9.09
48	2.59	9.09	2.50	9.09	2.65	9.09
49	3.02	9.09	3.15	9.09	3.13	9.09
50	1.91	9.09	2.00	9.09	1.87	9.09
51	2.25	9.09	2.40	9.34	2.21	9.09
52	1.70	9.09			1.84	9.09
53	1.51	9.09			1.68	8.87

Table B26
Wave Heights and Periods with 3-m, 12-sec Waves from Southwest at mhw

Gauge No.	Alternative 1		Alternative 2A		Alternative 3B	
	Height (m)	Period (sec)	Height (m)	Period (sec)	Height (m)	Period (sec)
1	3.08	12.23	3.17	12.23	3.17	12.23
2	3.20	12.23	3.29	12.23	3.28	12.23
3	3.89	12.23	4.06	12.23	4.34	12.23
4	3.68	12.67	3.63	12.23	3.72	12.23
5	3.09	12.23	3.16	12.67	3.23	12.67
6	3.21	12.67	3.47	12.67	2.35	12.67
7	3.34	12.23				
8	3.38	12.23	3.16	12.23	2.06	12.23
9	3.30	12.67	3.45	12.67	1.86	12.23
10	2.47	12.67	2.61	12.67	1.89	12.23
11	1.62	118.21	1.18	118.21	1.68	12.67
12	1.25	88.68	1.40	88.68	1.37	88.68
13	2.72	12.67	2.80	12.67	2.94	12.67
14	2.83	12.67	2.98	12.67	3.06	12.67
15	2.91	12.67			2.99	12.67
16	2.89	12.67	2.26	12.67	2.90	12.67
17	3.03	12.67	2.90	12.67	2.45	12.67
18	2.94	12.67	3.22	12.67	2.26	12.67
19	2.31	12.67	2.19	12.67	1.95	12.67
20	1.62	88.68	1.64	88.68	1.70	12.67
21	3.04	12.67	3.14	12.67	2.76	12.23
22	2.87	12.23	2.99	12.23	2.64	12.67
23	2.82	12.23			2.60	12.23
24	2.72	12.23	2.60	12.23	2.53	12.67
25	2.75	12.67	2.66	12.67	2.50	12.67
26	2.96	12.67	2.79	12.67	2.38	12.67
27	1.52	13.14	1.75	13.14	2.17	13.14
28	2.01	118.21	2.08	13.14	1.89	118.21
29	3.99	12.67			4.29	12.67
30	3.56	12.67			3.96	12.67
31	3.44	12.67			4.00	12.67
32	3.24	12.67			3.87	12.67
33	2.74	12.67			3.23	12.67
34	2.68	13.64			2.90	12.23
35	2.53	16.67			2.59	12.23
36	2.14	118.21			2.21	118.21
37	3.95	12.67	4.25	12.67	4.20	12.23
38	3.24	12.23	3.51	12.23	3.48	12.23
39	3.15	12.23	3.23	12.23	3.14	12.23
40	3.59	12.23	3.71	12.23	3.76	12.23
41	3.42	12.23	3.53	12.67	3.31	12.23
42	3.51	12.23	3.70	12.23	3.92	12.23
43	3.80	12.23	3.83	12.23	3.55	12.23
44	3.34	12.23			3.69	12.23
45	3.57	12.23			3.46	12.23
46	3.85	12.23	4.02	12.23	4.09	12.23
47	3.34	12.23	3.60	12.23	3.52	12.23
48	4.16	12.23	4.18	12.23	4.03	12.23
49	4.50	12.67	4.55	12.67	4.53	12.67
50	3.52	12.23	3.65	12.67	3.61	12.23
51	4.11	12.67	4.27	12.67	4.35	12.67
52	2.61	12.67			2.80	12.67
53	2.67	12.67			2.98	12.67

Table B27
Wave Heights and Periods with 6-m, 16-sec Waves from Southwest at mhw

Gauge No.	Alternative 1		Alternative 2A		Alternative 3B	
	Height (m)	Period (sec)	Height (m)	Period (sec)	Height (m)	Period (sec)
1	5.57	16.12	5.75	16.12	5.76	16.12
2	5.45	16.12	5.56	16.12	5.61	16.12
3	5.47	16.89	5.69	16.89	5.56	16.89
4	4.78	88.68	4.84	88.68	5.02	88.68
5	4.72	16.12	5.08	16.12	5.26	16.12
6	4.82	16.12	5.13	16.12	4.45	16.12
7	4.97	16.12				
8	4.77	16.12	4.37	16.12	3.99	16.12
9	4.13	16.12	3.98	16.89	3.47	16.12
10	2.98	118.21	2.93	118.21	2.90	118.21
11	2.16	118.21	1.44	118.21	2.20	118.21
12	1.69	88.68	1.68	88.68	1.68	88.68
13	4.21	16.89	4.52	16.89	4.37	16.89
14	4.24	16.89	4.61	16.89	4.48	16.89
15	4.37	16.89			4.48	16.89
16	4.23	16.89	4.06	16.89	4.40	16.89
17	4.03	16.89	3.96	16.89	4.05	16.89
18	3.49	17.74	3.68	17.74	3.52	17.74
19	2.64	118.21	1.61	118.21	2.51	118.21
20	2.03	88.68	2.06	88.68	2.09	88.68
21	4.19	16.12	4.41	16.12	4.25	16.12
22	4.06	16.89	4.35	16.89	4.28	16.89
23	4.07	16.89			4.27	16.89
24	3.88	16.12	3.72	16.89	4.12	16.89
25	3.82	16.89	3.76	16.89	4.05	17.74
26	3.60	16.89	3.51	17.74	3.55	17.74
27	1.65	118.21	1.89	118.21	2.97	118.21
28	2.24	88.68	2.35	88.68	2.36	118.21
29	4.25	16.12			4.28	16.12
30	4.06	16.12			4.03	16.12
31	4.05	16.89			4.05	16.89
32	3.93	16.89			3.95	16.89
33	3.68	16.89			3.81	16.89
34	3.63	17.74			3.58	17.74
35	3.16	118.21			3.05	118.21
36	2.43	118.21			2.38	118.21
37	4.08	16.89	4.15	16.89	4.25	16.89
38	5.61	16.12	5.93	16.12	5.96	16.12
39	5.54	16.12	5.56	16.12	5.45	16.12
40	5.77	16.12	6.13	16.89	6.11	16.12
41	6.03	16.12	6.10	16.89	5.85	16.12
42	5.86	16.12	6.25	16.12	6.18	16.12
43	5.99	16.12	5.95	16.12	6.01	16.12
44	5.91	16.12			6.48	16.12
45	5.99	16.12			5.99	16.12
46	5.18	16.12	5.31	88.68	5.38	16.12
47	4.88	16.12	5.08	16.12	4.95	16.12
48	4.76	16.12	4.70	16.89	4.81	16.12
49	4.98	16.12	5.03	16.89	5.05	16.12
50	4.43	15.42	4.58	15.42	4.54	15.42
51	4.58	16.12	4.71	16.12	4.65	16.12
52	4.17	16.12			4.25	16.12
53	4.25	15.42			4.42	15.42

Appendix B   Physical Modeling of North Beach and Jetty

Current velocity

Tables B28 through B36 list velocities calculated from velocimeter measurements during experiments with Alt 1, Alt 2A, and Alt 3B with storms from the southwest.

Table B28
Velocity Measurements with 2-m, 9-sec Waves at mllw from Southwest

ADV No.	Alternative 1				Alternative 2A				Alternative 3B			
	Ave. Vel. Offshore (cm/sec)	Ave. Vel. South (cm/sec)	Ave. Vel. Magnitude (cm/sec)	Magnitude of Ave. Vel. (cm/sec)	Ave. Vel. Offshore (cm/sec)	Ave. Vel. South (cm/sec)	Ave. Vel. Magnitude (cm/sec)	Magnitude of Ave. Vel. (cm/sec)	Ave. Vel. Offshore (cm/sec)	Ave. Vel. South (cm/sec)	Ave. Vel. Magnitude (cm/sec)	Magnitude of Ave. Vel. (cm/sec)
1	13.30	-10.13	43.94	16.72	13.15	-13.5	42.38	18.85	-1.46	-9.04	47.26	9.16
2	-1.85	21.05	39.79	21.13	-2.19	4.7	30.50	5.19	-5.66	5.69	37.66	8.03
3	-13.26	4.45	41.65	13.99	-60.86	7.46	71.73	61.32	-11.00	-2.45	37.73	11.30
4	14.29	-11.61	58.81	18.41	8.12	-10.39	45.85	13.19	1.87	-1.92	15.25	2.68
5	-0.66	-2.41	44.41	2.50	1.59	5.37	54.95	5.60	0.78	5.79	21.56	5.84
6	-6.41	-14.07	40.13	15.46	-9.54	-12.64	42.36	15.83	8.62	-5.65	42.13	10.31

Table B29
Velocity Measurements with 3-m, 12-sec Waves at mllw from Southwest

ADV No..	Alternative 1				Alternative 2A				Alternative 3B			
	Ave. Vel. Offshore (cm/sec)	Ave. Vel. South (cm/sec)	Ave. Vel. Magnitude (cm/sec)	Magnitude of Ave. Vel. (cm/sec)	Ave. Vel. Offshore (cm/sec)	Ave. Vel. South (cm/sec)	Ave. Vel. Magnitude (cm/sec)	Magnitude of Ave. Vel. (cm/sec)	Ave. Vel. Offshore (cm/sec)	Ave. Vel. South (cm/sec)	Ave. Vel. Magnitude (cm/sec)	Magnitude of Ave. Vel. (cm/sec)
1	21.02	-25.69	56.43	33.20	25.25	-30.07	57.37	39.27	25.41	-30.78	60.23	39.91
2	-7.01	28.94	60.32	29.77	-5.47	-3.63	45.03	6.56	-4.66	4.39	54.24	6.40
3	-12.69	7.50	52.72	14.74	-70.30	11.82	86.72	71.29	1.90	0.16	49.55	1.90
4	31.08	-29.20	67.84	42.64	28.02	-22.90	55.59	36.18	6.74	-1.81	27.83	6.97
5	2.30	8.13	56.53	8.45	13.53	9.82	59.65	16.72	0.94	8.21	28.03	8.27
6	-11.75	-14.82	52.74	18.92	-13.12	-14.88	53.97	19.84	-3.45	-10.29	53.42	10.86

Table B30
Velocity Measurements with 6-m, 16-sec Waves at mllw from Southwest

ADV No.	Alternative 1				Alternative 2A				Alternative 3B			
	Ave. Vel. Offshore (cm/sec)	Ave. Vel. South (cm/sec)	Ave. Vel. Magnitude (cm/sec)	Magnitude of Ave. Vel. (cm/sec)	Ave. Vel. Offshore (cm/sec)	Ave. Vel. South (cm/sec)	Ave. Vel. Magnitude (cm/sec)	Magnitude of Ave. Vel. (cm/sec)	Ave. Vel. Offshore (cm/sec)	Ave. Vel. South (cm/sec)	Ave. Vel. Magnitude (cm/sec)	Magnitude of Ave. Vel. (cm/sec)
1	10.30	-54.64	71.14	55.60	16.80	-41.92	68.46	45.16	18.49	-57.88	75.87	60.76
2	15.66	-15.21	78.50	21.83	13.29	-16.70	63.16	21.34	14.91	-16.59	78.26	22.31
3	-20.15	-4.69	86.49	20.69	-37.48	-8.90	77.49	38.52	12.98	-9.55	78.69	16.12
4	52.58	-63.54	106.71	82.47	55.03	-51.13	95.31	75.12	4.51	-7.34	57.29	8.62
5	3.33	41.05	82.48	41.18	15.66	24.61	88.13	29.17	2.03	20.37	63.42	20.47
6	-34.30	30.94	106.73	46.19	-35.43	21.27	101.89	41.33	-15.87	13.45	98.39	20.80

Table B31
Velocity Measurements with 2-m, 9-sec Waves at mtl from Southwest with Full Flood Current

ADV No.	Alternative 1				Alternative 2A				Alternative 3B			
	Ave. Vel. Offshore (cm/sec)	Ave. Vel. South (cm/sec)	Ave. Vel. Magnitude (cm/sec)	Magnitude of Ave. Vel. (cm/sec)	Ave. Vel. Offshore (cm/sec)	Ave. Vel. South (cm/sec)	Ave. Vel. Magnitude (cm/sec)	Magnitude of Ave. Vel. (cm/sec)	Ave. Vel. Offshore (cm/sec)	Ave. Vel. South (cm/sec)	Ave. Vel. Magnitude (cm/sec)	Magnitude of Ave. Vel. (cm/sec)
1	-16.63	56.79	80.68	59.18	-23.12	45.48	71.39	51.02	-26.30	42.30	74.82	49.81
2	-22.82	51.83	64.62	56.63	-22.08	55.26	65.09	59.51	-14.92	28.21	52.08	31.91
3	-0.06	23.28	41.63	23.28	2.03	29.77	44.34	29.84	-20.93	9.16	39.97	22.84
4	-12.93	-7.41	53.98	14.91	-26.12	8.46	52.55	27.46	1.66	6.99	15.46	7.19
5	-37.66	28.33	69.19	47.13	-22.97	8.25	50.31	24.41	-3.86	-19.71	33.52	20.08
6	-55.74	-22.93	68.88	60.27	-53.44	-21.82	65.34	57.73	-12.37	-44.60	54.94	46.29

Table B32
Velocity Measurements with 3-m, 12-sec Waves at mtl from Southwest with Full Flood Current

ADV. No.	Alternative 1				Alternative 2A				Alternative 3B			
	Ave. Vel. Offshore (cm/sec)	Ave. Vel. South (cm/sec)	Ave. Vel. Magnitude (cm/sec)	Magnitude of Ave. Vel. (cm/sec)	Ave. Vel. Offshore (cm/sec)	Ave. Vel. South (cm/sec)	Ave. Vel. Magnitude (cm/sec)	Magnitude of Ave. Vel. (cm/sec)	Ave. Vel. Offshore (cm/sec)	Ave. Vel. South (cm/sec)	Ave. Vel. Magnitude (cm/sec)	Magnitude of Ave. Vel. (cm/sec)
1	0.13	-0.41	58.98	0.43	0.56	6.60	55.24	6.62	-8.72	4.17	64.72	9.66
2	-8.08	13.77	58.41	15.97	-10.45	7.01	51.58	12.58	-4.92	11.40	56.42	12.42
3	-49.70	9.15	82.63	50.53	-41.91	6.48	69.84	42.40	-12.10	3.83	50.16	12.69
4	18.43	-30.05	70.96	35.25	13.56	-17.65	60.38	22.26	6.52	14.85	31.32	16.21
5	1.66	25.48	67.68	25.53	2.40	15.01	67.25	15.20	-0.86	-2.73	38.42	2.86
6	-6.19	7.83	60.53	9.99	-20.70	-7.53	61.58	22.03	-12.81	-31.00	65.19	33.54

Table B33
Velocity Measurements with 6-m, 16-sec Waves at mtl from Southwest with Full Flood Current

ADV No.	Alternative 1				Alternative 2A				Alternative 3B			
	Ave. Vel. Offshore (cm/sec)	Ave. Vel. South (cm/sec)	Ave. Vel. Magnitude (cm/sec)	Magnitude of Ave. Vel. (cm/sec)	Ave. Vel. Offshore (cm/sec)	Ave. Vel. South (cm/sec)	Ave. Vel. Magnitude (cm/sec)	Magnitude of Ave. Vel. (cm/sec)	Ave. Vel. Offshore (cm/sec)	Ave. Vel. South (cm/sec)	Ave. Vel. Magnitude (cm/sec)	Magnitude of Ave. Vel. (cm/sec)
1	-3.81	-7.86	49.70	8.73	-4.84	-10.57	71.09	11.63	-10.51	-17.11	73.13	20.08
2	23.51	-2.28	73.52	23.62	9.49	0.41	61.09	9.49	10.90	4.09	70.44	11.64
3	-19.03	6.37	81.66	20.06	-37.54	5.81	75.05	37.99	0.51	2.37	67.46	2.43
4	7.35	-26.89	82.30	27.88	12.10	-28.70	76.81	31.15	3.99	5.93	47.32	7.15
5	-27.66	28.19	91.64	39.49	-29.68	36.79	96.34	47.27	-1.38	-3.28	52.01	3.56
6	-43.36	7.43	100.34	43.99	-48.67	9.34	99.49	49.56	-33.24	-39.93	97.29	51.29

Appendix B   Physical Modeling of North Beach and Jetty

Table B34
Velocity Measurements with 2-m, 9-sec Waves at mhw from Southwest

ADV No.	Alternative 1				Alternative 2A				Alternative 3B			
	Ave. Vel. Offshore (cm/sec)	Ave. Vel. South (cm/sec)	Ave. Vel. Magnitude (cm/sec)	Magnitude of Ave. Vel. (cm/sec)	Ave. Vel. Offshore (cm/sec)	Ave. Vel. South (cm/sec)	Ave. Vel. Magnitude (cm/sec)	Magnitude of Ave. Vel. (cm/sec)	Ave. Vel. Offshore (cm/sec)	Ave. Vel. South (cm/sec)	Ave. Vel. Magnitude (cm/sec)	Magnitude of Ave. Vel. (cm/sec)
1	8.85	-11.02	33.82	14.14	7.79	-1.29	39.56	7.9	-0.81	1.33	44.92	1.55
2	6.17	-4.03	24.58	7.37	-1.58	0.02	24.08	1.58	2.22	-14.00	31.22	14.16
3	-28.56	12.78	52.24	31.29	-22.68	2.90	36.63	22.87	-2.15	-6.91	28.64	7.23
4	2.18	-10.99	42.38	11.20	1.99	-12.03	41.23	12.19	9.01	1.96	17.88	9.22
5	2.07	6.11	36.29	6.46	-1.15	9.61	41.78	9.68	-3.44	-2.09	22.45	4.03
6	-0.52	-5.47	31.38	5.49	-7.19	-9.22	33.37	11.69	-9.41	-9.97	30.34	13.70

Table B35
Velocity Measurements with 3-m, 12-sec Waves at mhw from Southwest

ADV No.	Alternative 1				Alternative 2A				Alternative 3B			
	Ave. Vel. Offshore (cm/sec)	Ave. Vel. South (cm/sec)	Ave. Vel. Magnitude (cm/sec)	Magnitude of Ave. Vel. (cm/sec)	Ave. Vel. Offshore (cm/sec)	Ave. Vel. South (cm/sec)	Ave. Vel. Magnitude (cm/sec)	Magnitude of Ave. Vel. (cm/sec)	Ave. Vel. Offshore (cm/sec)	Ave. Vel. South (cm/sec)	Ave. Vel. Magnitude (cm/sec)	Magnitude of Ave. Vel. (cm/sec)
1	22.18	-22.92	65.67	31.89	24.62	-25.30	66.21	35.3	17.20	-20.73	68.09	26.94
2	-1.00	7.15	49.29	7.22	-0.24	2.64	44.39	2.65	-0.69	-17.42	55.51	17.44
3	-36.28	14.13	70.94	38.93	-34.49	7.50	64.29	35.29	-9.29	-12.54	47.66	15.61
4	11.42	-21.28	62.65	24.15	9.34	-17.89	61.51	20.18	8.65	3.20	30.23	9.22
5	0.77	19.63	65.09	19.65	0.50	10.85	60.79	10.86	2.52	6.19	28.67	6.68
6	-3.26	-5.12	55.42	6.07	-12.65	-9.23	56.67	15.66	-7.60	4.84	51.71	9.01

Table B36
Velocity Measurements with 6-m, 16-sec Waves at mhw from Southwest

ADV No.	Alternative 1				Alternative 2A				Alternative 3B			
	Ave. Vel. Offshore (cm/sec)	Ave. Vel. South (cm/sec)	Ave. Vel. Magnitude (cm/sec)	Magnitude of Ave. Vel. (cm/sec)	Ave. Vel. Offshore (cm/sec)	Ave. Vel. South (cm/sec)	Ave. Vel. Magnitude (cm/sec)	Magnitude of Ave. Vel. (cm/sec)	Ave. Vel. Offshore (cm/sec)	Ave. Vel. South (cm/sec)	Ave. Vel. Magnitude (cm/sec)	Magnitude of Ave. Vel. (cm/sec)
1	22.62	-58.21	85.60	62.45	22.01	-43.35	73.89	48.62	-10.75	-3.60	62.53	11.34
2	28.67	-17.08	82.52	33.37	19.76	-9.85	71.34	22.07	25.91	-24.56	84.63	35.70
3	-17.07	-11.35	88.44	20.50	-30.43	-4.79	80.38	30.80	19.09	-28.18	78.84	34.04
4	24.47	-62.55	101.55	67.16	28.49	-50.32	91.96	57.83	2.08	-14.42	56.36	14.57
5	-0.81	49.63	93.57	49.63	-11.85	48.27	103.44	49.71	5.66	32.08	64.31	32.57
6	-5.68	33.92	94.70	34.39	-16.18	25.22	96.98	29.97	-15.63	17.72	93.74	23.63

Tables for GENESIS 5-Year Projected Shoreline

Storms from west-northwest

Wave heights and wave periods. Tables B37 through B42 list wave heights and periods collected during experiments with Alt 2A and the shoreline projected by numerical model GENESIS for 5 years after installation of Alt 2A.

Table B37
Wave Heights and Periods for 2-m, 9-sec Waves from West-Northwest at mllw, Alt 2A with 5-year Projected Shoreline

Gauge No.	Wave Height (m)	Wave Period (sec)
1	2.08	8.87
2	2.20	9.09
9	1.70	9.09
17	2.17	9.34
25	1.54	9.09
33	1.67	9.34

Table B38
Wave Heights and Periods for 3-m, 12-sec Waves from West-Northwest at mllw, Alt 2A with 5-year Projected Shoreline

Gauge No.	Wave Height (m)	Wave Period (sec)
1	2.82	12.67
2	3.01	13.14
9	2.10	118.21
17	2.65	14.19
25	2.66	14.19
33	2.31	14.19

Table B39
Wave Heights and Periods for 5-m, 13-sec Waves from West-Northwest at mllw, Alt 2A with 5-year Projected Shoreline

Gauge No.	Wave Height (m)	Wave Period (sec)
1	4.63	12.67
2	5.03	13.14
9	2.27	118.21
17	2.76	14.19
25	2.71	35.47
33	2.44	14.78

Table B40
Wave Heights and Periods for 2-m, 9-sec Waves from West-Northwest at mhw, Alt 2A with 5-year Projected Shoreline

Gauge No.	Wave Height (m)	Wave Period (sec)
1	2.37	8.87
2	2.48	8.87
9	2.62	9.34
17	2.53	9.09
25	2.08	9.34
33	1.87	9.09

Table B41
Wave Heights and Periods for 3-m, 12-sec Waves from West-Northwest at mhw, Alt 2A with 5-year Projected Shoreline

Gauge No.	Wave Height (m)	Wave Period (sec)
1	3.19	12.23
2	3.31	12.67
9	3.49	12.67
17	3.82	12.67
25	3.57	15.42
33	3.32	12.67

Table B42
Wave Heights and Periods for 5-m, 13-sec Waves from West-Northwest at mhw, Alt 2A with 5-year Projected Shoreline

Gauge No.	Wave Height (m)	Wave Period (sec)
1	5.21	12.23
2	5.50	12.67
9	3.96	14.19
17	4.34	13.64
25	4.22	10.13
33	3.87	14.19

Current velocity. Tables B43 through B48 list velocities calculated from velocimeter measurements collected during experiments with Alt 2A and the shoreline projected by numerical model GENESIS for 5 years after installation of Alt 2A.

Table B43
Velocity Measurements with 2-m, 9-sec Waves at mllw from West-Northwest with Alt 2A and 5-year Projected Shoreline

ADV No.	Ave. Vel. Offshore (cm/sec)	Ave. Vel. South (cm/sec)	Ave. Vel. Magnitude (cm/sec)	Magnitude of Ave. Vel. (cm/sec)
2	-14.3	19.24	41.74	23.97
3	4.2	18.92	36.44	19.38
4	-3.64	16.38	55.67	16.78

Table B44
Velocity Measurements with 3-m, 13-sec Waves at mllw from West-Northwest with Alt 2A and 5-year Projected Shoreline

ADV No.	Ave. Vel. Offshore (cm/sec)	Ave. Vel. South (cm/sec)	Ave. Vel. Magnitude (cm/sec)	Magnitude of Ave. Vel. (cm/sec)
2	-16.82	29.58	66.78	34.03
3	-10.24	67.44	93.85	68.21
4		75.61	93.84	78.01

Table B45
Velocity Measurements with 5-m, 13-sec Waves at mllw from West-Northwest with Alt 2A and 5-year Projected Shoreline

ADV No.	Ave. Vel. Offshore (cm/sec)	Ave. Vel. South (cm/sec)	Ave. Vel. Magnitude (cm/sec)	Magnitude of Ave. Vel. (cm/sec)
2	-19.27	16.14	59.93	25.14
3	-8.06	18.03	50.03	19.75
4	-10.88	31.86	90.30	33.67

Table B46
Velocity Measurements with 2-m, 9-sec Waves at mhw from West-Northwest with Alt 2A and 5-year Projected Shoreline

ADV No.	Ave. Vel. Offshore (cm/sec)	Ave. Vel. South (cm/sec)	Ave. Vel. Magnitude (cm/sec)	Magnitude of Ave. Vel. (cm/sec)
2	-16.64	13.29	36.93	21.30
3	7.91	4.65	36.35	9.18
4	-0.73	-8.75	51.71	8.78

Table B47
Velocity Measurements with 3-m, 13-sec Waves at mhw from West-Northwest with Alt 2A and 5-year Projected Shoreline

ADV No.	Ave. Vel. Offshore (cm/sec)	Ave. Vel. South (cm/sec)	Ave. Vel. Magnitude (cm/sec)	Magnitude of Ave. Vel. (cm/sec)
2	-15.31	15.28	61.24	21.63
3	-2.19	28.01	61.57	28.1
4	-35.83	-4.77	83.59	36.15

Table B48
Velocity Measurements with 5-m, 13-sec Waves at mhw from West-Northwest with Alt 2A and 5-year Projected Shoreline

ADV No.	Ave. Vel. Offshore (cm/sec)	Ave. Vel. South (cm/sec)	Ave. Vel. Magnitude (cm/sec)	Magnitude of Ave. Vel. (cm/sec)
2	-12.20	29.26	74.66	31.70
3	-13.07	32.73	72.82	35.24
4	-71.41	25.07	123.33	

Storms from southwest

Wave heights and wave periods. Tables B49 through B55 list wave heights and periods collected during experiments with Alt 2A and the shoreline projected by numerical model GENESIS for 5 years after installation of Alt 2A.

Table B49
Wave Heights and Periods for 2-m, 9-sec Waves from Southwest at mllw, Alt 2A with 5-year Projected Shoreline

Gauge No.	Height (m)	Period (sec)
1	2.08	9.09
2	2.22	9.09
9	1.69	8.65
17	1.54	9.09
25	1.12	9.09
33	1.64	9.34

Table B50
Wave Heights and Periods for 2-m, 9-sec Waves from Southwest at mtl, Alt 2A with 5-year Projected Shoreline

Gauge No.	Height (m)	Period (sec)
1	2.00	9.09
2	2.13	9.09
9	1.84	9.09
17	1.49	8.87
25	0.89	9.09
33	1.73	9.34

Table B51
Wave Heights and Periods for 3-m, 12-sec Waves from Southwest at mtl, Alt 2A with 5-year Projected Shoreline

Gauge No.	Height (m)	Period (sec)
1	3.21	11.82
2	3.41	12.23
9	2.70	12.67
17	2.28	12.67
25	1.44	12.67
33	2.15	13.14

Table B52
Wave Heights and Periods for 6-m, 16-sec Waves from Southwest at mtl, Alt 2A with 5-year Projected Shoreline

Gauge No.	Height (m)	Period (sec)
1	5.36	16.12
2	5.27	16.12
9	3.25	16.89
17	3.14	16.89
25	1.95	16.89
33	2.80	16.89

Table B53
Wave Heights and Periods for 2-m, 9-sec Waves from Southwest at mhw, Alt 2A with 5-year Projected Shoreline

Gauge No.	Height (m)	Period (sec)
1	1.97	9.09
2	2.11	9.09
9	1.75	9.09
17	1.46	9.09
25	0.72	9.09
33	1.67	9.09

Table B54
Wave Heights and Periods for 3-m, 12-sec Waves from Southwest at mhw, Alt 2A with 5-year Projected Shoreline

Gauge No.	Height (m)	Period (sec)
1	3.22	12.23
2	3.39	12.23
9	3.08	12.67
17	2.59	12.67
25	1.29	12.67
33	2.59	13.14

Table B55
Wave Heights and Periods for 6-m, 16-sec Waves from Southwest at mhw, Alt 2A with 5-year Projected Shoreline

Gauge No.	Height (m)	Period (sec)
1	5.59	16.12
2	5.79	16.12
9	3.95	16.89
17	4.05	16.89
25	2.00	16.89
33	3.48	16.89

Velocity studies. Tables B56 through B64 list velocities calculated from velocimeter measurements collected during experiments with Alt 2A and the shoreline projected by numerical model GENESIS for 5 years after installation of Alt 2A.

Table B56
Velocity Measurements with 2-m, 9-sec Waves at mllw from Southwest with Alt 2A and 5-year Projected Shoreline

ADV No.	Ave. Vel. Offshore (cm/sec)	Ave. Vel. South (cm/sec)	Ave. Vel. Magnitude (cm/sec)	Magnitude of Ave. Vel. (cm/sec)
2	-12.98	3.54	31.42	13.46
3	-20.50	-16.27	41.54	26.17
4	41.84	-8.54	70.75	42.71

Table B57
Velocity Measurements with 3-m, 12-sec Waves at mllw from Southwest with Alt 2A and 5-year Projected Shoreline

ADV No.	Ave. Vel. Offshore (cm/sec)	Ave. Vel. South (cm/sec)	Ave. Vel. Magnitude (cm/sec)	Magnitude of Ave. Vel. (cm/sec)
2	-9.27	-2.16	42.72	9.52
3	1.98	-37.36	53.84	37.42
4	73.74	-18.62	101.22	76.06

Table B58
Velocity Measurements with 6-m, 16-sec Waves at mllw from Southwest with Alt 2A and 5-year Projected Shoreline

ADV No.	Ave. Vel. Offshore (cm/sec)	Ave. Vel. South (cm/sec)	Ave. Vel. Magnitude (cm/sec)	Magnitude of Ave. Vel. (cm/sec)
2	3.61	-23.31	53.86	23.59
3	6.72	-44.90	71.47	45.40
4	93.51	-26.75	137.84	97.26

Table B59
Velocity Measurements with 2-m, 9-sec Waves at mtl from Southwest with Alt 2A and 5-year Projected Shoreline

ADV No.	Ave. Vel. Offshore (cm/sec)	Ave. Vel. South (cm/sec)	Ave. Vel. Magnitude (cm/sec)	Magnitude of Ave. Vel. (cm/sec)
2	-5.33	27.32	35.88	27.84
3	5.22	20.58	35.53	21.23
4	-5.77	-4.77	49.40	7.49

Table B60
Velocity Measurements with 3-m, 12-sec Waves at mtl from Southwest
with Alt 2A and 5-year Projected Shoreline

ADV No.	Ave. Vel. Offshore (cm/sec)	Ave. Vel. South (cm/sec)	Ave. Vel. Magnitude (cm/sec)	Magnitude of Ave. Vel. (cm/sec)
2	-5.03	5.79	34.45	7.66
3	5.72	-6.69	41.97	8.80
4	37.62	-24.44	77.58	44.86

Table B61
Velocity Measurements with 6-m, 16-sec Waves at mtl from Southwest
with Alt 2A and 5-year Projected Shoreline

ADV No.	Ave. Vel. Offshore (cm/sec)	Ave. Vel. South (cm/sec)	Ave. Vel. Magnitude (cm/sec)	Magnitude of Ave. Vel. (cm/sec)
2	2.46	-7.35	51.70	7.75
3	6.21	-10.64	60.90	12.31
4	65.88	-38.53	107.77	76.32

Table B62
Velocity Measurements with 2-m, 9-sec Waves at mhw from Southwest with Alt 2A and 5-year Projected Shoreline

ADV No.	Ave. Vel. Offshore (cm/sec)	Ave. Vel. South (cm/sec)	Ave. Vel. Magnitude (cm/sec)	Magnitude of Ave. Vel. (cm/sec)
2	8.89	-8.53	52.57	12.32
3	14.34	-12.33	65.93	18.91
4	52.16	-58.53	110.52	78.39

Table B63
Velocity Measurements with 3-m, 12-sec Waves at mhw from Southwest with Alt 2A and 5-year Projected Shoreline

ADV No.	Ave. Vel. Offshore (cm/sec)	Ave. Vel. South (cm/sec)	Ave. Vel. Magnitude (cm/sec)	Magnitude of Ave. Vel. (cm/sec)
2	4.98	-4.70	31.50	6.85
3	5.48	-13.29	39.02	14.37
4	26.95	-20.07	76.20	33.60

Table B64
Velocity Measurements with 6-m, 16-sec Waves at mhw from Southwest with Alt 2A and 5-year Projected Shoreline

ADV No.	Ave. Vel. Offshore (cm/sec)	Ave. Vel. South (cm/sec)	Ave. Vel. Magnitude (cm/sec)	Magnitude of Ave. Vel. (cm/sec)
2	1.02	11.36	21.48	11.41
3	3.34	-7.34	25.50	8.06
4	10.12	-9.12	34.26	13.63

Appendix C
Literature Review of Cross-Shore Sediment Transport by Rip Currents[1]

Sediment transport by rip currents was represented in the shoreline change modeling described in Chapter 6 of Volume I of this report. Sediment transport by rip currents is a relatively unstudied coastal process. This appendix reviews background material on rip currents.

Introduction

Rip currents are strong narrow currents that flow seaward through the surf zone. These currents normally increase the longshore current velocity in the dominant direction on the updrift side of the rip zone and decrease or reverse the longshore current direction on the downdrift side (Shepard and Inman 1950). The current strength and the distance that rip currents extend seaward are related to the height of the incoming waves (Shepard, Emery, and LaFond 1941). Each incident wave system forms a characteristic pattern of longshore and rip currents (McKenzie 1958; Harris 1961, 1964). The result is a circulation cell in the nearshore.

Rips are a major component of the surf zone circulation, and they are often the dominant mechanism for offshore transport of water and sediment. Several mechanisms have been proposed for the generation and spacing of rip current cells. Quantification of the sediment transport enters the formulation of sediment budgets and predictions of shoreline evolution. In the context of sediment budgets and shoreline change modeling, several quantities are required to estimate, in time and space, the volume of sand transported by rips. Rip currents are not permanent features; they flow intermittently with fluctuations in velocity. Most rip currents shift position along the beach, unless they are located adjacent to jetties or headlands. A comprehensive description of a rip current system and

---

[1] Written by Ty V. Wamsley, U.S. Army Engineer Research and Development Center, Coastal and Hydraulics Laboratory, Vicksburg, MS.

prediction of the response of the adjacent shoreline requires the ability to identify the location, spacing, size, strength, and persistence of rip currents.

Mechanisms for Rip Current Generation and Spacing

The current pattern that dominates the nearshore circulation partially depends on the angle of wave approach. If waves break parallel to the shoreline trend, generated currents will form a circulation cell. If waves break at large angles to shore, the longshore current flows parallel to shore, confined between the breakers and the shoreline. Circulation cells may also form if waves break at small angles to the shoreline or if beach topography controls the pattern of nearshore currents (Harris 1964; Komar 1998).

Shepard and Inman (1950) demonstrated that rip currents can be created by longshore variations in wave height, are usually periodic in time and space, and increase in velocity with increasing wave height. Several causes for the variation in wave height have been proposed. Shepard and Inman (1950) identified wave convergence or divergence over irregular offshore bathymetry as one explanation. Also, in places where relatively straight beaches are terminated on the downdrift side by an obstruction, a pronounced rip often extends seaward. Generation mechanisms that require a longshore variability in the boundary (i.e., bottom topography or structures) have been termed structural interaction mechanisms (Dalrymple 1978). Bowen (1969) applied the concept of radiation stress, the excess momentum due to the presence of waves, to investigate how circulation patterns are produced by the interaction of the wave field with longshore variation in the nearshore region. The longshore variation can be induced by changes in bathymetry. The theory showed that rip currents occur in the surf zone where breakers are lowest, which is in agreement with field observations. Noda (1974) developed an analytical model of wave-induced circulation cells and rip currents that incorporated the interaction of incoming waves with bottom topography as the driving mechanism, abstracting in part work presented in Noda et al. (1974). More recently, Haas, Svendsen, and Haller (1998) and Sorensen, Schaffer, and Madsen (1998) have also applied numerical circulation models that produce rip currents driven by the wave-bottom topography interaction.

Engineered and natural structures also influence the nearshore circulation. Liu and Mei (1976) investigated rip current generation at groins. Numerical results showed rip current cells with a spacing corresponding to $L_0/(2 \sin\theta_0)$ where L_0 = deepwater wavelength and θ_0 = deepwater wave angle of incident wave trains. Mei and Angelides (1977) examined the circulation around a circular island and the formation of a single rip in the lee of the island.

Regular systems of rips are also found on natural beaches where there are no regular variations in the bathymetry. Generation mechanisms that can occur on uniformly planar beaches are termed wave interaction mechanisms (Dalrymple 1978). Bowen and Inman (1969) performed experiments in which the interaction between edge waves and incident waves of the same frequency created

circulation cells that included rips. The rip currents were well correlated with edge waves, the rips occurring at alternate antinodes of displacement of the edge waves. The spacing of the rip currents was therefore equal to the longshore wavelength of the edge waves. Field observations made in the Gulf of California suggest that this mechanism acts on natural beaches.

Hino (1974) developed a second wave interaction model. The formation of a nearshore circulation system with rips was shown to be the result of hydrodynamic instability caused by radiation stresses. The instability model is based on a feedback between the deforming bottom and the flow field. The Hino (1974) theory predicts rip current spacing to be about four times the surf zone width. McKenzie (1958) was the first to observe the correlation of rip current spacing with the width of the surf zone.

Sasaki (1974) investigated the applicability of the Bowen and Inman (1969) and Hino (1974) theories by describing them with the surf-similarity parameter, ξ. Sasaki (1974) found that the edge wave theory of Bowen and Inman (1969) can be applied if ξ is greater than unity. The instability theory of Hino (1974) gave a good circulation pattern estimate for values of ξ between about 0.23 and 1.0. Sasaki (1975) then developed a theory on rip current spacing based on the concept of infra-gravity waves when ξ is less than 0.23 and found rip current spacing (Y_r) to be:

$$Y_r = 157\xi_0{}^2 \qquad (0.23 > \xi_o > 0.08) \tag{C1}$$

with

$$\xi_0 = \frac{\tan\beta}{\left(H_0/L_0\right)^{0.5}} \tag{C2}$$

where $\tan\beta$ = beach slope, and H_0 = deepwater wave height.

A wave interaction model introduced by Dalrymple (1975) proposed that the spatial variation in the setup and setdown, caused by intersecting wave trains of the same period, creates longshore variations in wave height and the mean water level on the open coast. Currents flow from regions of high setup, or high waves, to regions of low waves where they flow offshore in a rip current. The predicted spacing of the rip currents caused by intersecting wave trains is:

$$Y_r = \frac{L_0}{\left(\sin\theta_0 - \sin\zeta_0\right)} \tag{C3}$$

where θ_0 and ζ_0 = the deepwater wave ray angles of the intersecting wave trains, measured clockwise from a shore-normal axis. An analysis by Dalrymple and Lozano (1978) showed that wave-current interaction can support steady state rip current circulation, but could not treat the initiation mechanism.

Fowler and Dalrymple (1990) examined the forcing of nearshore circulation by incident wave groups. As incident wave trains propagate towards the shore they alternatively reinforce and cancel each other out, creating periodic longshore variations in wave height. Lines of cancellation, or nodal lines, can be seen in the wave field. If incident wave trains are of the same frequency, rip currents develop at the intersection of nodal lines. The spacing is predicted similar to Dalrymple (1975).

$$Y_r = \frac{2\pi}{\left(k_2 \sin \theta_2 - k_1 \sin \theta_1 \right)} \qquad \text{(C4)}$$

where

k = wave number ($2\pi/L$)
L = local wavelength
θ = wave angle of the incident wave trains

If the incident wave trains have slightly different frequencies, it was found that rip currents could still be generated and that they migrate slowly along the beach with the slowly moving nodal lines. The rip spacing was somewhat overpredicted, and this was thought to be due to the use of linear theory and a shallow-water assumption invoked to develop the theory.

Murray and Reydellet (2001) introduced a model in which rip currents are self-organized, rather than being forced by bathymetric features or incident wave patterns. Their model predicts that rip currents can arise from a wave-current interaction that dissipates wave energy, onshore mass transport by waves, offshore flow responding to imbalances between radiation-stress gradients and setup in the surf zone, alongshore flow responding to alongshore surface slopes, and alongshore dispersion of cross-shore momentum.

Cook (1970) made field observations of the occurrence of rip currents in southern California. He concluded that the generation of the rips was influenced by wave conditions, beach morphology, tidal level, and wind. The existence of rip currents was highly dependent upon the height and period of waves reaching the shoreline. The beach morphology was also found to affect rip currents in several ways, including the steepness of the foreshore and the presence of cusps and rip channels. Rip currents were poorly developed along steep beaches. The existence of rip channels, formed during high-energy conditions, facilitates the development of rips at lower energy conditions. Cook (1970) also found that strong on- or offshore winds might influence rip current generation. An onshore wind may hinder the development of rip currents by transporting surface water toward the shore and may even eliminate rips entirely. Offshore winds reduce wave drift and likewise may diminish the potential for rip current development.

Short and Brander (1999) investigated the relationship between rip current spacing and the regional wave climate. They found a strong correlation between rip spacing and levels of wave energy. They conclude, however, that there is still no adequate explanation for the variation in rip spacing between different beaches.

Ranasinghe et al. (2000) analyzed daily time exposure video images to examine the effect of incident waves on the spacing and persistence of rip channels at Palm Beach, Australia. Results indicated that rip channels do not have a preferred location along the beach and that rip spacing did not increase with increase in wave height. These results suggest that bathymetric features are the dominant controlling mechanism once rip currents are formed.

Morphological Feedback and Rip Current Persistence

McKenzie (1958) was the first to suggest that nearshore circulation may be dominated by storm-induced bathymetry for long periods after a storm. Cook (1970) found that rip channels are cut during prolonged periods of high waves and then gradually fill under calmer conditions. But, once the high-energy bathymetry is established, the rip currents are able to persist over periods of time with varying wave conditions. Sonu (1972) found a correlation between circulation patterns and surf zone bathymetry. Longshore currents moved across the undulatory bathymetry from shallow to deeper regions, with rips at the depressions.

Aagaard, Greenwood, and Nielsen (1997) found that rip persistence depends on the extent of wave energy dissipation in the rip neck. At low tide, when wave energy dissipation was intense and occurred across a wide zone, the rip was active. At high tide, the reduced wave dissipation and a restricted zone of wave breaking usually resulted in the rip being inactive. Aagaard, Greenwood, and Nielsen (1997) determined that the tidally dependent rip behavior is suggested by the ratio γ_s of significant wave height to water depth in the rip neck. Based on field data from the North Sea coast at Jutland, Denmark, rip activity developed when γ_s reached a critical value of approximately 0.35 in the rip neck.

Brander (1999a) concludes that morphologic control, modulated by hydrodynamic forcing, plays an important role in the temporal behavior of rip flow. Rip circulation is driven by longshore and cross-shore pressure gradients within the surf zone and is maintained by the bathymetric feedback. Therefore, rip current behavior and form is dictated by the nature and degree of the coadjustments between morphology, hydrodynamics, and sediment transport. Brander (1999a) introduced a function to provide an initial quantitative assessment of the morphodynamic coadjustment between morphology and flow velocity in an evolving low-energy rip:

$$\mu_r = -18.6\alpha_r + 17.8 \tag{C5}$$

where

$$\mu_r = \frac{u_r T}{H_{rms}} \tag{C6}$$

$$\alpha_r = \frac{A_r}{A_{rHT}} \tag{C7}$$

with

$u_{r=}$ mean, depth-averaged flow velocity in the rip channel
$T =$ peak wave period
$H_{rms} = =$ root-mean-square wave height
$A_r =$ average cross-sectional area available for rip flow
$A_{rHT} =$ cross-sectional area available for rip flow at high tide

Observations and analysis made by Ranasinghe et al. (2000) suggest that rip flows are bathymetrically controlled once the rip channels are formed. They found that rips are fairly persistent in time and migrate in the longshore direction under obliquely incident waves. Sufficiently strong longshore currents cause rip channel migration in the direction of the longshore current. Ranasinghe et al. (2000) also found that rip channels disappear when storms rework the nearshore morphology and then reappear in a different location when the storms subside.

Rip Current Strength and Rip Channel Size

Shepard, Emery, and LaFond (1941) correlated rip current strength with increasing wave height. McKenzie (1958) and Harris (1961, 1964) observed in field studies that heavy seas produced strong rips and smaller waves produced weaker, more numerous rips. Cook (1970) also observed that the largest rips are formed during periods of intense wave activity and found the influence of the tidal cycle on rip size and strength to be ambiguous. Sonu (1972), however, observed that the intensity of wave breaking, controlled by the tide, corresponded with a proportionally stronger circulation. Thus, rip currents velocities were generally stronger at low tide and weaker at high tide. Using a two-dimensional (2-D) depth-averaged hydrodynamic model, Ranasinghe et al. (2000) found that rip velocity increased with increasing wave height. The model results also predicted increased rip velocity with falling tide levels.

Aagaard, Greenwood, and Nielsen (1997) suggest that the amount of water returned seaward by any rip should depend on the onshore discharge of water by waves breaking across the bar and on the spacing between rip channels. Therefore,

$$u_r = \left(Q_{drift} + Q_{roller} \right) \frac{Y_r}{A_r} \tag{C8}$$

$Q_{drift} =$ onshore discharge of water between rips due to mass transport in waves (Stokes drift) and $Q_{roller} =$ the mass transport in wave rollers.

$$Q_{drift} = \frac{CBH^2}{h_b}$$ (C9)

$$Q_{roller} = \frac{A_s}{T}$$ (C10)

where

C = wave celerity
B = wave profile coefficient (1/12 for saw-tooth bores)
H = local wave height
h_b = water depth over the bar crest away from rips
A_s = cross-sectional area of a surface roller ($\sim 0.9H^2$)

Aagaard, Greenwood, and Nielsen (1997) found that, for normally incident waves, rip current velocities were well correlated with velocities predicted from the simple model.

Brander (1999a) found that rip current velocity was modulated by the tide, experiencing maximums at low tide and minimums at high tide. He also found that rip velocity decreases with cross-sectional area and is predicted by a linear function (Equation C5), which provides an initial quantitative assessment of the morphodynamic coadjustment between morphology and flow velocity. The underlying hypothesis of Brander's (1999a) work is that rip current velocity is maximized when morphological expression of the rip channel is amplified.

Rip current strength may also be altered by wave-current interaction (LeBlond and Tang 1974; Noda et al. 1974). Noda et al. (1974) developed a numerical model of wave transformation, nearshore circulation, and wave-current interaction, and they found that the wave-current interaction altered incoming wave characteristics in the nearshore and thus reduced the magnitude of circulation velocities and horizontal circulation pattern. Similarly, the model of Haas, Svendsen, and Haller (1998) predicts that the offshore extent of rip currents is reduced when wave-current interaction is included. Yu and Slinn (2003) also report that wave-current interaction reduces rip current strength and restricts their offshore extent.

Zyserman, Fredsoe, and Deigaard (1990) presented a method to determine the dimensions of rip current systems (including the width and depth of rip channels). The method is based on an overall sediment balance in the nearshore region and assumes equilibrium conditions exist and that no erosion or accretion occurs.

Sediment Transport in Rip Currents

Rip currents have long been recognized as a mechanism for offshore sediment transport (Shepard, Emery, and LaFond 1941). The first sediment

transport study relating to rip currents was made by Ingle (1966), who found that dyed sand grains being moved by longshore currents were intercepted and transported offshore by rips. Cook (1970) noted that rips can transport large volumes of sand to the inner shelf and can cause beach erosion.

Based on field data from the North Sea, Aagaard, Greenwood, and Nielsen (1997) found that sediment flux in the rip neck channel depends on the tidal stage. Large offshore transport due to a rip current occurred at low tide. Smaller onshore transport due to oscillatory incident waves and weak mean currents occurred at high tide. Sediment concentrations were moderately dependent on tidal stage, with higher concentrations occurring at low tide.

Few attempts have been made to quantify the sediment transport of rip currents. The number of direct measurements of sediment transport in rips is limited and little is known about these processes. Dolan et al. (1987) estimated the sediment lost from a littoral cell by rip currents using data from the Littoral Environmental Observation (LEO) program and plausible assumptions. The transport rate in each rip (Q_r) is computed as:

$$Q_r = \frac{A_r u_r c_r}{\rho_s}$$

(C11)

where c_r = suspended load concentration, and ρ_s = density of sand. The volume of sand being transported for a particular stretch of beach was then calculated by multiplying the transport rate times the number of rips and the percent chance of rip occurrence.

Brander (1999b) conducted the most comprehensive study on sediment transport processes in rip currents. He found that the vertical distribution of sediment flux in the rip neck exhibited an exponential decrease in flux away from the bed. The magnitude of the flux was strongly influenced by the velocity of the flow. Therefore, the bulk of transported sediment moves close to the bed with approximately 50 percent of total sediment flux in the rip channel occurring in the bottom 10 percent of flow, whereas 15 percent occurs in the upper half of the water column.

Another finding by Brander (1999b) is the strong functional relationship between the transport rate and the velocity cubed. Through linear least squares regression, Brander (1999b) developed the following expression for rip current transport, q_r, in units of kg/min.

$$q_r = 27.6u_r^3 + 0.92$$

(C12)

This relationship indicates that sediment transport in rips increases as rip current velocity cubed. Sediment transport, however, is complicated by sediment entrainment, tidal modulation, and the need to consider the combined effects of waves and currents. Equation C12 was developed for a low-energy rip current system. However, Brander and Short (2000) presented evidence to suggest that a

distinct morphodynamic scaling relationship exists between high- and low-energy environments. Results from sediment transport studies in low-energy systems may therefore be applicable to large-scale systems. The existence of such a scaling factor also implies that the physical connection between waves, currents, and morphology, both within and between beach systems, are related to variations in wave energy.

Brander (1999b) applied the Shields parameter *S* as a criterion for predicting sediment entrainment.

$$S = \frac{\tau}{\rho (s-1) gD}$$
(C13)

where

τ = bed shear stress
$s = (\rho_s - \rho)/\rho$
ρ = density of seawater
g = acceleration due to gravity
D = median sediment grain size

Under combined waves and currents the bed shear stress is:

$$\tau = \rho \left(u_c^2 + u_w^2 \right)$$
(C14)

where u_c and u_w = the time-averaged shear velocity computed following a method outlined by Nielsen (1992) for currents and waves, respectively.

Brander (1999b) observed that sediment entrainment in the feeder current and rip channels of a circulation cell is different. Sediment entrainment in the feeder channel is minimized at low tide because increased wave breaking and dissipation across nearshore bars inhibits wave motion and reduces the value of *S*. Therefore, despite higher flow velocities in the feeder current at low tide, the potential for transport is inhibited by the reduction in sediment entrained.

Sediment entrainment in the rip channel, however, is maximized at low tide and minimized at high tide. Because flow velocities are also maximized at low tide (as discussed in the previous section), the offshore transport is greatest then. At high tide, both sediment entrainment and flow velocities are minimized, but still significant. Thus, although much smaller at high tide, transport in the rip channel occurs throughout the tidal cycle (Brander 1999b).

Wave and current contributions should not be considered separately, but superimposed (Grant and Madsen 1979). Nonlinear interactions exist between waves and currents, and the sediment transport under their combined action is likely to differ from the sum of the individual contributions (Beach and Sternberg 1992).

The proportionality of the transport rate to the velocity cubed provides evidence that perhaps a Bagnold-type approach may be suitable for modeling sediment transport in rip currents. Conceptually, the Bagnold model is based on the concept that the waves act to entrain sediments while a current transports the sediment. The data in the Brander (1999b) study support this concept.

Estimating Sand Transport by Rip Currents

Rip currents are an integral component of the nearshore circulation system along most of the world's beaches and a major mechanism for the offshore transport of water and sediments. Estimating the transport by rip currents and the resulting shoreline change requires prediction of transport in time and space. The volume of the sediment actually removed from the active littoral zone must also be determined. The complexities of prediction and possible mechanisms to make first-order estimates are discussed in the following paragraphs.

Spacing, persistence, size, and strength of rip currents

Predicting the response of the shoreline and sediment budget to rip currents requires specifying the location, spacing, persistence, size, and strength, of the rip currents. Numerous studies have been conducted to explain the generation and spacing of rips along the beach. To date, no single theory adequately accounts for the spacing of rip currents on different beaches. The observed rip current patterns on natural beaches are probably the product of a combination of driving mechanisms and physical boundary conditions (Short and Brander 1999). Bathymetric features are likely the dominant controlling mechanism once rip currents are formed. Therefore, observation and bathymetric data may be valuable sources for specifying locations. Numerical circulation models may also provide guidance on where rips may form.

The generation and persistence of rip currents depends on several factors. First, in the case of shore-perpendicular structures, rip formation is governed by the direction of the longshore current. The structure redirects the feeding longshore current offshore. In the absence of structures, the generation of rip currents is influenced in large part to the angle of wave approach. For waves approaching the shoreline at a large angle, rip currents will typically not develop or be weak. Waves approaching perpendicular to or at small angles promote the generation of rips. Rip persistence is also strongly influenced by bathymetry. Aagaard, Greenwood, and Nielsen (1997) found that the development of rip flows depends on wave dissipation in the rip neck, which is suggested by the ratio of significant wave height to water depth, γ_s. This concept is consistent with the underlying indication of research that rip flows are sensitive to the degree of morphological expression at the rip channel. The determination of critical values of wave angle approach and/or γ_s for rip current development may provide a mechanism for defining rip persistence.

Rip channel size is primarily determined by wave energy conditions. Brander (1999a) developed a model of rip channel evolution under decreasing energy

conditions. The model is analogous to the Wright and Short (1984) model of beach states. Under decreasing energy conditions, the rip system evolution was characterized by a narrowing and deepening of the channel, a gradual reduction of A_r. The reduced energy levels allow onshore transport of sediments that contribute to the constriction of the rip channel. Brander (1999a) also developed a function relating A_r to average rip current velocities. The function is a quantitative assessment of the morphodynamic coadjustment between morphology and flow velocity. An average size of a rip may be identifiable from bathymetric data or aerial photography.

Rip current velocities appear to be determined by incident wave heights and modulated by tidal level. Several investigators have correlated rip current velocity with increasing wave height (Shepard, Emery, and LaFond 1941; McKenzie 1958; Harris 1961; Cook 1970; Sonu 1972; Ranasinghe et al. 2000). Some of these researchers (Sonu 1972; Ranasinghe et al. 2000) and others (Brander 1999a; Aagaard, Greenwood, and Nielsen 1997) have also recognized the influence of the tidal cycle. Brander (1999a) relates velocity to the cross-sectional area of the rip channel. Aagaard Greenwood, and Nielsen (1997) were able to predict velocities for normally incident waves by means of a simple model based on onshore discharge of water by breaking waves. Using this method and assuming depth-limited breaking, it may be possible to estimate changes in rip flow velocity with changes in tide level. The estimation of rip velocities may also be obtained from field measurements or physical and numerical circulation model results.

Potential offshore transport of rip currents

Sediment transport in rip currents is determined by a combination of several processes that change in time and space. Despite the complexities and given the current state of knowledge, a simple approach similar to Equation C10 may be appropriate for estimating transport in cases where sufficient data are available. Equation C10 requires a cross-sectional area of flow, a rip current velocity, and sediment concentration in the rip channel and gives and estimate of potential transport for a single rip current. The formulation is complicated by the fact that the velocity and sediment concentration of rip flow are tidally modulated. Estimates of the number of rips and persistence (also tidally modulated) are required to obtain an offshore transport estimate for an entire system.

Sediment removed from littoral system

The portion of rip transport actually removed from the littoral zone determines the response of the shoreline. Sand removal from the active nearshore zone can occur as an "overshooting" of sediment by strong rips, as described by Dolan et al. (1987). Sediment can also be removed by rip transport that carries sediment out past a jetty that is then carried by the longshore current into an inlet. Dolan et al. (1987) estimated an "overshooting" rate of 15 percent at Oceanside, CA. Such an estimate would need to be made based on all available data for a specific site. For the case of transport around a jetty, one possible method would

be to determine the percent removed based on the direction of longshore transport when a rip current is present.

References

Aagaard, T., Greenwood, B., and Nielsen, J. (1997). "Mean currents and sediment transport in a rip channel," *Marine Geology* 140, 25-45.

Beach, R., and Sternberg, R. (1992). "Suspended sediment transport in the surf zone: Response to incident wave and longshore current interaction," *Marine Geology* 108, 275-294.

Brander, R. W. (1999a). "Field observations on morphodynamic evolution of a low-energy rip current system," *Marine Geology* 157, 199-217.

Brander, R. W. (1999b). "Sediment transport in low-energy rip current systems," *Journal of Coastal Research* 15(3), 839-849.

Brander, R. W., and Short, A. D. (2000). "Morphodynamics of a large-scale rip current system at Muriwai Beach, New Zealand," *Marine Geology* 165, 27-39.

Bowen, A. J. (1969). "Rip currents I," *Journal of Geophysical Research* 74, 5,467-5,478.

Bowen, A. J., and Inman, D. L. (1969). "Rip currents II," *Journal of Geophysical Research* 74, 5,479-5,490.

Cook, D. O. (1970). "The occurrence and geologic work of rip currents off Southern California," *Marine Geology* 9, 173-186.

Dalrymple, R. A. (1975). "A mechanism for rip current generation on an open coast," *Journal of Geophysical Research* 80, 3,485-3,487.

Dalrymple, R. A. (1978). "Rip currents and their causes," *Proceedings 16th Coastal Engineering Conference*, American Society of Civil Engineers (ASCE), 1,414-1,427.

Dalrymple, R. A., and Lozano, C. J. (1978). "Wave-current interaction models for rip currents," *Journal of Geophysical Research* 83, 6,063-6,071.

Dolan, T. J., Castens, P. G., Sonu, C. J., and Egense, A. K. (1987). "Review of sediment budget methodology: Oceanside littoral cell, California," *Proceedings Coastal Sediments '87*, ASCE, 1,289-1,304.

Fowler, R. E., and Dalrymple, R. A. (1990). "Wave group forced nearshore circulation," *Proceedings 22nd Coastal Engineering Conference*, ASCE, 729-742.

Grant, W. D., and Madsen, O. S. (1979). "Combined wave and current interaction with a rough bottom," *Journal of Geophysical Research* 84, 1,797-1,808.

Haas, K. A., Svendsen, I. A., and Haller, M. C. (1998). "Numerical modeling of nearshore circulation on a barred beach with rip channels." *Proceedings 26th Coastal Engineering Conference*, ASCE, 729-742.

Harris, T. F. W. (1961). "The nearshore circulation of water," *CSIR Symposium S2*, South Africa, 18-30.

Harris, T. F. W. (1964). "A qualitative study of the nearshore circulation off a natal beach with a submerged longshore sand bar," M.S. thesis, University of Natal, Durban, South Africa.

Hino, M. (1974). "Theory on formation of rip-current and cuspidal coast," *Proceedings 14th Coastal Engineering Conference*, ASCE, 901-919.

Ingle, J. (1966). *The movement of beach sand*. Elsevier, Amsterdam, 221 p.

Komar, P. (1998). *Beach processes and sedimentation*. Prentice-Hall, New Jersey, 544 p.

LeBlond. P. H., and Tang, C. L. (1974). "On energy coupling between waves and rip currents." *Journal of Geophysical Research* 79, 811-816.

Liu, P. L., and Mei, C. C. (1976). "Water motion on a beach in the presence of a breakwater, I and II," *Journal of Geophysical Research* 81, 3,079-3,094.

McKenzie, R. (1958). "Rip current systems," *Journal of Geology* 66(2), 103-113.

Mei, C. C., and Angelides, D. (1977). "Longshore circulation around a conical island," *Coastal Engineering* 1, 31-42.

Murray, A. B., and Reydellet, G. (2001). "A rip current model based on hypothesized wave/current interaction," *Journal of Coastal Research* 17(3), 517-530.

Nielsen, P. (1992). *Coastal bottom boundary layers and sediment transport*. World Scientific, London, 324 p.

Noda, E. K. (1974). "Wave-induced nearshore circulation," *Journal of Geophysical Research* 79, 4,097-4,106.

Noda, E. K., Sonu, C. J., Rupert, V. C., and Collins, J. I. (1974). "Nearshore circulations under sea breeze conditions and wave-current interactions in the surf zone," *Report TETRA-P-72-149-4*, Tetra Tech, Inc., Pasadena, CA.

Ranasinghe, R., Symonds, G., Black, K., and Holman, R. (2000). "Processes governing rip spacing, persistence, and strength in a swell dominated

microtidal environment," *Proceedings 27th Coastal Engineering Conference*, ASCE, 454-467.

Sasaki, T. (1974). "Field investigations on nearshore currents on a gently sloping bottom," Ph.D. diss., University of Tokyo, Tokyo, Japan.

Sasaki, T. (1975). "Simulation of shoreline and nearshore current," *Proceedings Civil Engineering in the Oceans III*, ASCE, 179-196.

Shepard, F. P., Emery, K. O., and LaFond, E. C. (1941). "Rip currents, a process of geological importance," *Journal of Geology* 49, 337-369.

Shepard, F. P., and Inman, D. L. (1950). "Nearshore circulation," *Proceedings First Conference on Coastal Engineering*, Council on Wave Research, Berkeley, 50-59.

Short, A. D., and Brander, R. W. (1999). "Regional variations in rip density," *Journal of Coastal Research* 15(3), 813-822.

Sonu, C. (1972). "Field observations of nearshore circulation and meandering currents," *Journal of Geophysical Research* 77, 3,232-3,247.

Sorensen, O. R., Schaffer, H. A., and Madsen, P. A. (1998). "Surf zone dynamics simulated by a Boussinesq type model: III. Wave-induced horizontal nearshore circulations," *Coastal Engineering* 33, 155-176.

Wright, L. D., and Short, A. D. (1984). "Morphodynamic variability of surf zones and beaches: A synthesis," *Marine Geology* 56, 93-118.

Yu, J., and Slinn, D. N. (2003). "Effects of wave-current interaction on rip currents," *Journal of Geophysical Research* 108(C3), 1-19.

Zyserman, J., Fredsoe, J., and Deigaard, R. (1990). "Prediction of the dimensions of a rip current system on a coast with bars," *Proceedings 22nd Coastal Engineering Conference*, ASCE, 959-972.

Appendix D
Field Data Collection[1]

This appendix provides background information to supplement material presented in Chapter 4 of Volume I of this report.

Introduction

This appendix provides background information on the field data collection in and around the entrance to Grays Harbor between 2001 and 2002 as part of the Study of North Jetty Performance and Entrance Navigation Channel Maintenance, Grays Harbor, Washington. Pacific International (PI) Engineering, PLLC conducted field measurements, data processing, and analysis for the U.S. Army Engineer Research and Development Center, Coastal Hydraulics Laboratory (CHL) under its Broad Agency Announcement contract DACW42-01-C-0002. An overview of the data collection program is followed by descriptions of the data collection methods and equipment, deployment methods, data recovery, data processing and quality checks, and time-series plots of the measured parameters. Further information on the platform design, instrument configuration and deployment methods can be found in Osborne, Hericks, and Kraus (2002a).

High-quality field measurements are an integral part of the design process for new and existing coastal engineering projects. A key to success in modeling is a field measurement program to obtain as much information as possible about forcing (input) parameters and, especially, model output parameters. Calibration and verification data assist in reducing uncertainty of model output so that final results become useful, quantitative approximations (Kamphuis 2000). Carefully collected, high-resolution field measurements yield valuable insights to aid in the interpretation of processes active in a project area.

One of the major challenges in the northeastern Pacific Ocean is to obtain field measurements when large breaking waves and strong currents are present most of the time, particularly in the surf zone and in close proximity to coastal structures such as jetties and breakwaters. Conventional methods such as SCUBA diver assistance or over-the-side vessel deployments are not feasible in such environments in terms of safety, economics, and logistics. Alternative

---

[1] Written by Philip D. Osborne and David B. Hericks, Pacific International Engineering, PLLC, Edmonds, Washington.

approaches including the use of helicopters (e.g., McGehee and Mayers 2000) and innovative intertidal deployment techniques have been adopted.

The measurement program had two objectives, the first being to investigate coastal processes associated with waves, currents, and sediment transport in the proposed project area. The approach was to obtain detailed field measurements from the proposed project area suitable for estimating sand transport rates in the surf zone and near a submerged jetty. The analysis of these measurements provides information needed to test hypotheses concerning mechanisms for southward sediment bypassing of the north jetty and on the relative importance of cross-shore and longshore sediment transport on Ocean Shores Beach. The second objective of the measurements was to provide information to verify wave, current, and transport numerical models, thereby advancing their value as design tools to aid in the optimization of project performance.

Overview

Data collection included deployment of (a) SonTek Hydra arrays to measure waves, currents, and suspended sediment concentrations (SSC) in the intertidal surf zone on north beach, and (b) tripod-mounted SonTek Acoustic Doppler Profiler (ADP) and Hydra systems to measure waves, currents, and SSC in deeper water. Description of the methods of deployment may also be found in Osborne et al. (2002b).

Seven tripods equipped with ADP/Hydra systems were deployed near the inlet entrance from September to November 1999 at approximately the same time as five tripods deployed by the U.S. Geological Survey (USGS) on the ebb shoal to the north and south of the inlet as part of its nearshore processes study in 1999. These data have been described previously by Hericks and Simpson (2000) and analyzed by Osborne, Hericks, and Kraus (2002a). Further analysis of the USGS data set has been presented by Sherwood et al. (2001).

In winter and spring 2001, four Hydra systems were deployed and recovered multiple times near the mean lower low water (mllw) shoreline along north beach north of the north jetty. The systems are referred to hereafter as Surf and Inter-tidal Dynamics Sensor Platforms (SIDSEP). At the same time, two ADP/Hydra systems referred to hereafter as High-Energy Sub-Tidal Tripods (HESTT) were deployed and recovered by an HH-60J helicopter in deeper water. In spring 2002, three additional HESTT (sta OS 7, OS 8, OS 9 as described in Chapter 4 of Volume I) were deployed by helicopter along North Beach and two Hydra platforms were deployed by research vessel inside the entrance to Grays Harbor at Damon Point (sta DP 1, DP 2). Figure D1 indicates the approximate deployment locations for the SIDSEP (sta OS 1, OS 2, OS 3, OS 4), HESTT (sta OS 5, OS 6, OS 7, OS 8, OS 9) and Damon Point platforms (sta DP 1, DP 2). Table D1 indicates deployment/retrieval dates and time, location, and elevations.

The SIDSEP were located at elevations from +0.3 to -0.3 m (+1 to -1 ft) mllw and from 80 to 140 m (262 to 460 ft) offshore of the mhhw contour (+9.4 ft mllw). The position of sta OS 3 was shifted north in the spring deployment to bring it in line with the USGS' Middle instrument transect). Station OS 5 was located north of the submerged portion of the jetty approximately 610 m (2,000 ft) offshore of the mhhw line at a bottom elevation of -5.5 m (-18 ft) mllw.

Station OS 6 was located approximately 1,040 m (3,412 ft) offshore of the mhhw line at a bottom elevation of -9.1 m (-30 ft) mllw. In 2002, sta OS 7, OS 8 and OS 9 were deployed parallel to shore, north of sta OS 5 and approximately 305 m (1,000 ft) offshore of the mhhw line and at approximately -3.6 m (-11 ft) mllw. Stations DP 1 and DP 2 were deployed inside the entrance to Grays Harbor along the western shore of Damon Point, at approximately -2.1 m (-7 ft) mllw.
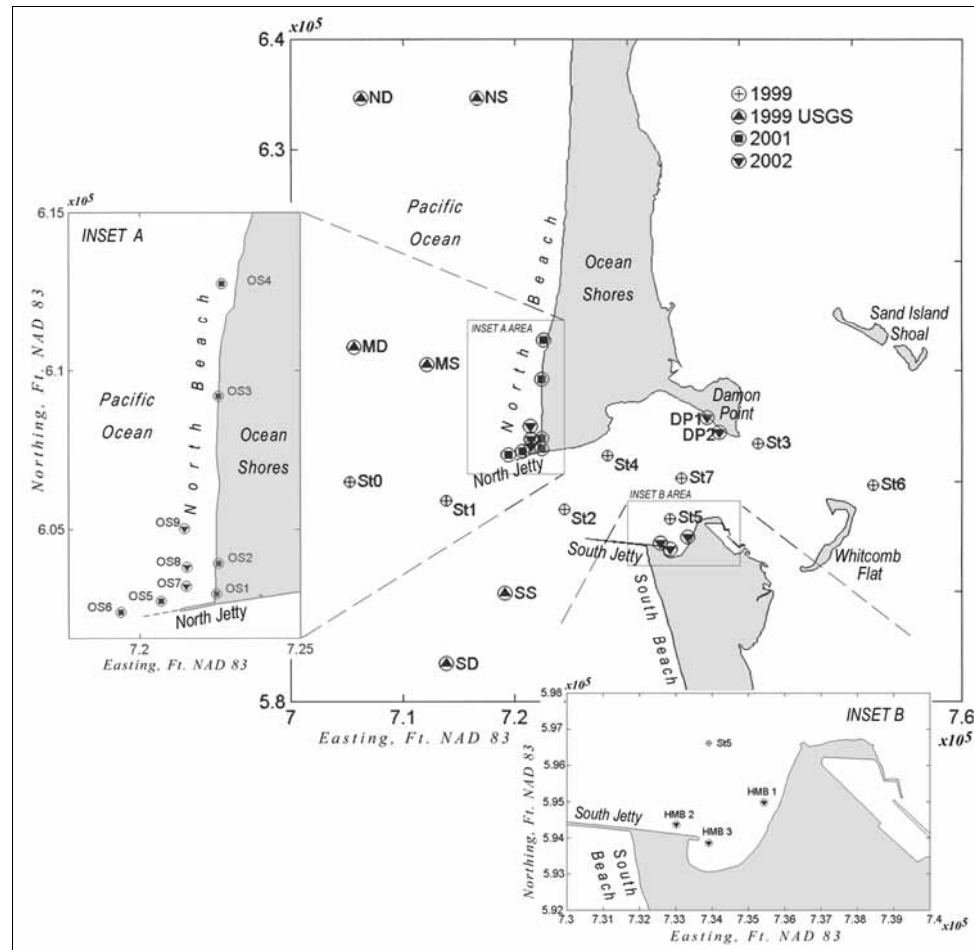
Figure D1. Instrument deployment locations

In 2001, several ADP transects together with grab samples of SSC and bottom sediment were obtained near the north jetty; ADP transects were also obtained from the outer and inner inlet in September 2001. Concurrent with the spring 2001 deployment, the USGS deployed six tripod systems on the Grays Harbor ebb shoal to the north and south of the inlet (sta ND, NS, MD, MS, SD, SS; Figure D1).

PI Engineering processed the data with SonTek and in-house software. Initial quality checks of the data from the first deployment of SIDSEP (6-9 February 2001) indicated that a portion of the velocity data from the Hydra's ADV Ocean current meters was compromised by velocity ambiguities. The most likely cause of these errors appeared to be a low velocity range setting of

200 cm/sec, but, more importantly, movement of the sensor head during impact by breaking waves. Therefore, two SIDSEP were redeployed at approximately the same locations as sta OS1 and OS2 on 13 March and recovered on 14 March to test these hypotheses. The velocity range was set to 500 cm/sec, and a tension strap was added to stabilize the sensor head. Data quality checks indicate that most of the data from the redeployment were of satisfactory quality for verification information for modeling. Further analysis determined that a large number of the velocity ambiguities in the first data set could be replaced with results of linear interpolation between accepted data points without introducing significant bias to the data set. Generally, a high percentage of good-quality HESTT data were recovered for each deployment.

Table D1
Tripod Deployment and Retrieval Locations

Station ID	Deployment Date	Position				Time UTC	Elevation[3]	Retrieval Date
		Latitude[1]	Longitude[1]	Easting[2]	Northing[2]			
OS 1	2/6/01	N 46 55.6849	W 124 10.5397	E 722403.99184	N 602949.19666	000	+0.99	2/9/01
	3/13/01	N 46 55.6849	W 124 10.5397	E 722403.99184	N 602949.19666		+4.92	3/14/01
	5/6/01	N 46 55.6849	W 124 10.5397	E 722403.99148	N 602949.19666		+0.33	5/11/01
OS 2	2/6/01	N 46 55.8448	W 124 10.5378	E 722457.17047	N 603919.70895	000	+0.27	2/9/01
	3/13/01	N 46 55.8448	W 124 10.5378	E 722457.17047	N 603919.70895		+3.94	3/14/01
	5/6/01	N 46 55.8448	W 124 10.5378	E 722457.17047	N 603919.7089		-0.98	5/11/01
OS 3	2/6/01	N 46 56.1246	W 124 10.5789	E 722365.46084	N 605626.57237	000	+0.82	2/9/01
	5/6/01	N 46 56.7117	W 124 10.5967	E 722457.71219	N 609194.78814		+0.66	5/11/01
OS 4	2/6/01	N 46 57.2974	W 124 10.6108	E 722564.97698	N 612753.79472	000	-0.96	2/9/01
	5/6/01	N 46 57.2974	W 124 10.6108	E 722654.97698	N 612753.79472		+0.33	5/11/01
OS 5	5/4/01	N 46 55.6333	W 124 10.9500	E 720682.69016	N 602715.55556	1800	-19.04	5/30/01
OS 6	5/4/01	N 46 55.5667	W 124 11.2500	E 719415.89071	N 602369.51831	1800	-30.94	5/30/01
OS 7	4/4/02	N 46 55.7167	W 124 10.7667	E 605806.71654	N 737173.92930	1900		
OS 8	4/4/02	N 46 55.8167	W 124 10.7667	E 604400.25224	N 738281.01147	1900	-11	5/28/02
OS 9	4/4/02	N 46 56.0167	W 124 10.8000	E 603186.33412	N 721468.78628	1900	-11	5/28/02
DP 1	3/29/02	N 46 56.2668	W 124 7.0279	E 603793.51327	N 721497.13051	1900	-7	5/2/02
DP 2	3/29/02	N 46 56.0440	W 124 06.7468	E 605014.33728	N 721415.32018	1900	-7	5/2/02

[1] Format is D dd mm.mmmm, where D = N, S, E, or W; ddd = 1 to 3 digits, degrees; mm.mmmm = two digits and four decimal places, minutes.
[2] Referred to North American Datum of 1983 – Washington South 4,602 (in feet).
[3] In feet referred to mean lower low water (mllw).

Data collection methods and equipment

Surf and Intertidal Dynamics Sensor Platform (SIDSEP). SIDSEP were designed to allow for deployment of the instruments on the intertidal zone of a high-energy beach and to position the instruments above the beach surface to minimize sediment disturbance by the frame and sensors. Each pod contains a SonTek Hydra configured with a high-resolution pressure sensor, Acoustic Doppler Velocimeter Ocean (ADVO) and two optical back-scatterance sensors (sta OBS 3) (Figure D2). The combined velocity measured near the beach

surface by the ADVO and suspended sediment measurements by the sta OBS 3 enable the calculation of suspended sediment flux. The combined measurements of the ADVO and pressure sensor enable the calculation of directional wave information. The sampling method for all instruments is shown in Table D2.

Each SIDSEP frame is constructed of marine grade aluminum and has six 25-pound lead weights attached to the inside of the frame. The total frame weight, with instruments, is approximately 200 pounds when submerged. The SIDSEP are approximately 7 ft long, 2 ft wide, and 1 ft high (Figure D3).
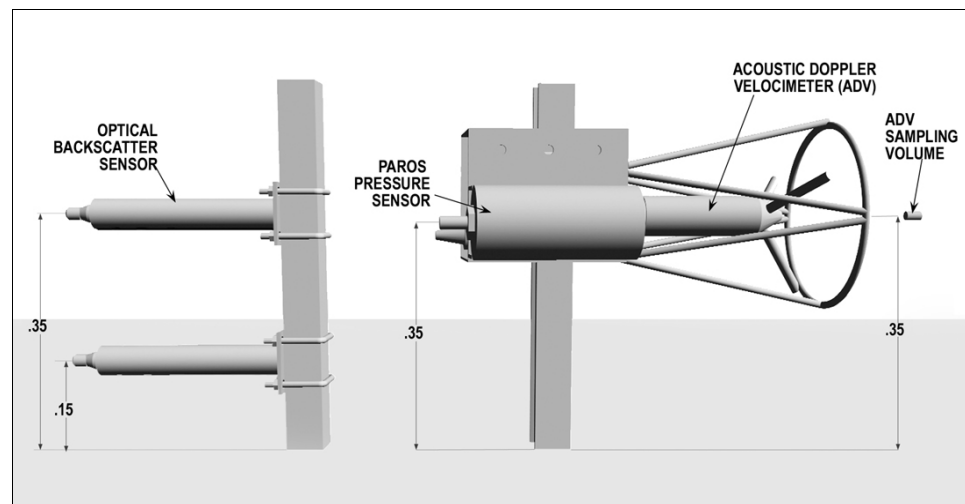
Figure D2. SIDSEP instrument configuration and nominal dimensions

All equipment were tested, assembled, and transported from Seattle; only minor assembly was required on the beach at Ocean Shores. Figure D2 illustrates the position of instruments comprising the SIDSEP. After all instruments are attached to the SIDSEP, a function check of all equipment was conducted. The ADVO sensor, which houses the Hydra compass, was aligned horizontally. The compass and tilt sensors were positioned within the sensor head to provide correct heading, pitch, and roll data.

High-Energy Sub-Tidal Tripods (HESTT). The HESTT were designed to be deployed and retrieved by helicopter from the high-energy wave environment at the seaward end of the north jetty. Each of the tripods is constructed of marine grade aluminum and has eighteen 50-pound lead weights attached to the frame. The total frame weight, with instruments, is approximately 1,200 pounds when submerged. Wooden pallets were placed on the base of the tripod legs and attached with lag bolts (Figure D4); the pallets prevent the tripods from sinking in to the sea bed and were designed to break free from the legs during tripod recovery.

Instrument packages on the HESTT consisted of an ADP configured to operate at 1,500 kHz for recording nondirectional wave data, water level, and

current speed and direction through the water column in 0.5-m bins. The tripods also contained a SonTek Hydra configured with a high-resolution pressure sensor, ADVO, and two OBS-3 sensors. Each tripod also supported two sediment traps for capturing suspended sediment.

Table D2
Data Sampling Method

	Equip.	Data Type	Recorded Data	Start Recording	Record Interval (min)	Record Duration (min)	Sample Frequency (Hz)	Samples Recorded/ Burst
Winter Deployment	Hydra (OS 1-4)	Directional wave burst	Orbital velocity & pressure burst	Every 40 min	40	34.14	4	8,192
	Hydra (OS 1-4)	OBS suspended sediment concentra-tion	Counts	Every 40 min	40	34.14	4	8,192
Spring Deployment	Hydra (OS 1-4)	Directional wave burst	Velocity & pressure	Every 20 min	20	17.067	4	4,096
	Hydra (OS 1-4)	OBS suspended sediment concentration	Counts	Every 20 min	20	17.067	4	4,096
Spring Deployment	Hydra (OS 5-6)	Directional wave burst	Velocity & pressure	Every 30 min	30	17.067	4	4,096
	Hydra (OS 5-6)	OBS suspended sediment concentration	Counts	Every 30 min	30	17.067	4	4,096
	ADP (OS 5-6)	Current velocity profiles	Velocity	Every 6 min	6	3	1,500 kHz	
	ADP (OS 5-6)	Depth, waves	Pressure	Every 60 min	60	17.067	4	4,096
Spring Deployment 2002	Hydra (OS 8-9 DP 1-2)	Directional wave burst	Orbital velocity & pressure burst	Every 60 min	60	17.067	4	4,096
	Hydra (OS 8-9 DP 1-2)	OBS suspended sediment concentration	Counts	Every 60 min	60	17.067	4	4,096
	ADP (OS 8-9)	Current velocity profiles	Velocity	Every 6 min	6	3	1,500 kHz	
	ADP (OS 8-9)	Depth, waves	Pressure	Every 60 min	60	17.067	4	4,096
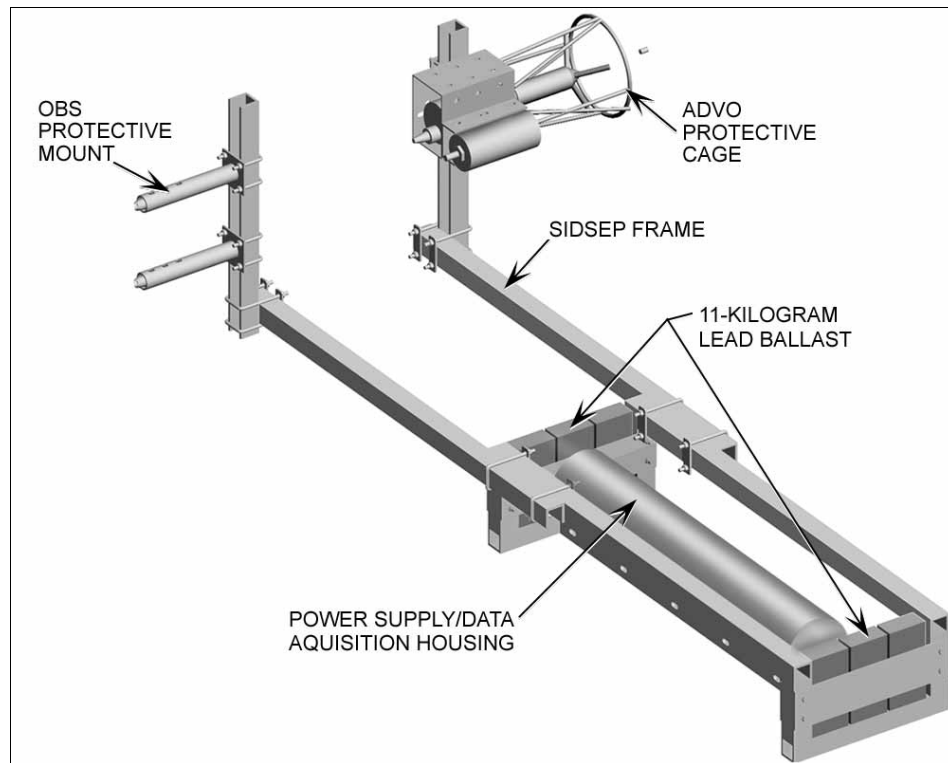
Figure D3.   SIDSEP 3-D configuration showing instrument position relative to data logger power supply housing and lead ballast
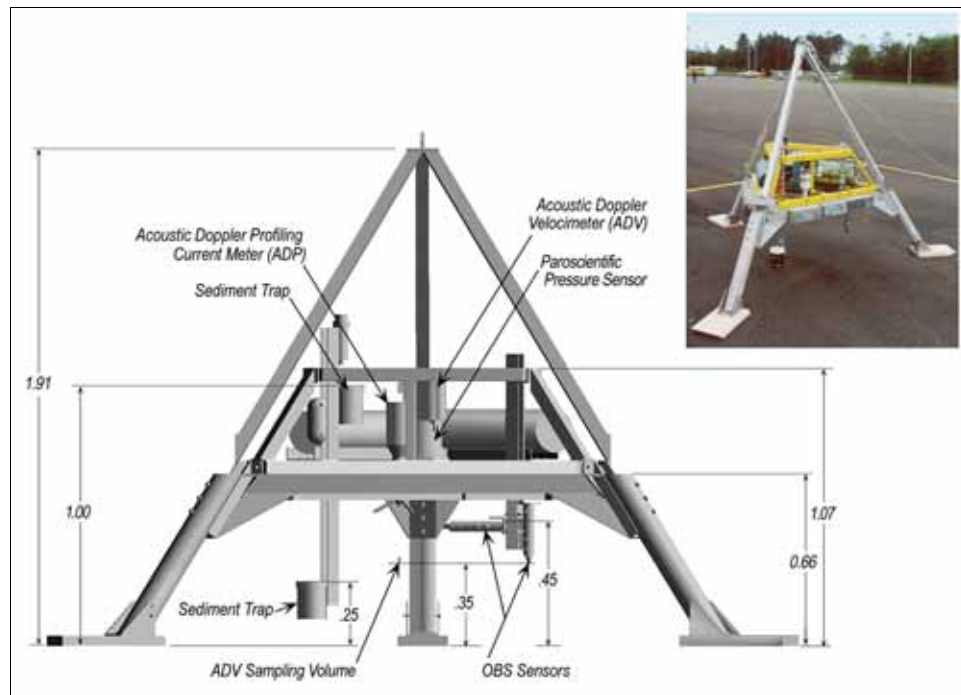

Figure D4. HESTT instrument configuration and nominal dimensions

Deployment Method

SIDSEP. The SIDSEP were transported to the beach by pickup truck and placed near the mllw shoreline with a hand-pushed, four-wheeled cart. A 4-ft by 2-ft by 1-ft hole was dug at the station by hand. The SIDSEP was placed in the hole, and then the hole was back-filled with sand removed in digging the hole to restore beach contours (Figure D5). Two 1.5-in.-diam aluminum pipes were driven 3 to 4 ft vertically into the beach and attached to the upright instrument supports for added stability.

The SIDSEP were deployed during low tide, and recovered at low tide 3 days later. Personnel remained in the vicinity of the study site to periodically observe the equipment; the instruments were checked at each low tide to ensure that they were positioned correctly and were not in danger of being lost or buried. A bright orange flag with a 5-ft fiberglass shaft was mounted on the aluminum pipe to increase visibility of the pods and to inform surfers and swimmers of their presence while submerged.

A differential GPS receiver mounted on the top of the hand-pushed cart was used to accurately position the SIDSEP at predetermined locations. When on station, the SIDSEP was lowered into the excavated hole using the winch system installed on the cart.

HESTT. The HESTT were partially assembled and transported to Ocean Shores airport by box truck for final assembly and deployment by helicopter. The method and hardware for deploying and recovering the tripods essentially follows that outlined by McGehee and Mayers (2000) with a few minor modifications and improvements for use of a Sikorsky HH-60J "Jayhawk" helicopter (Figures D6 and D7).

Assistance was requested from the U.S. Coast Guard (USCG) Air Station Astoria because personnel there had familiarity with the deployment site and prior experience with instrument deployments on the Oregon Coast (e.g., Pollock 1995). Advantages of the HH-60J are its capability to remain airborne for durations up to 7 hr, a 6,000-lb lift capacity, a cargo hook and rescue hoist, and a Rockwell-Collins HFCS-8000 automated flight management system that integrates all of the helicopter's communications and navigation equipment. The pilot can program the autopilot to fly to a predetermined location automatically, freeing the pilot and co-pilot to assist in visual observation of the deployment operation. In addition, this system can automatically bring the HH-60J to a hover at an altitude of 50 ft above a specified location. This feature is especially useful in rough weather for locating and relocating deployed instruments.

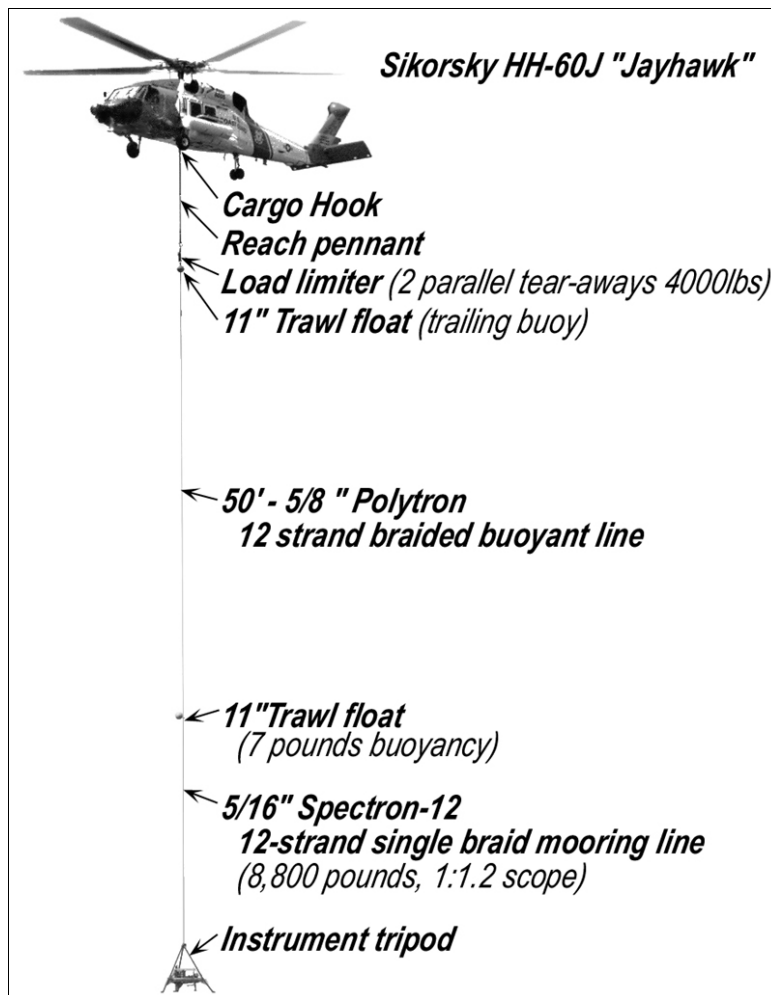Figure D5.   SIDSEP installation on Ocean Shores Beach

Figure D6.　Principal components of helicopter tripod
deployment/recovery system

The principal components of the deployment/recovery system consist of the instrument tripod, a mooring line, an 11-in.-diam trawl float with 7 pounds buoyancy, a 50-ft -buoyant recovery line with an 11-in.-diam trailing trawl float, a grapnel, the helicopter winch and line, a reach pennant and a load limiter system (Figure D7). During deployment the buoyant recovery line was attached directly to the cargo hook on the HH-60J and flown to the deployment site. The assembly was then lowered until slack appeared in the buoyant line, indicating the tripod was in position on the sea bottom. The pilot then released the buoyant line from the cargo hook. During recovery, the floating line was approached perpendicularly with the grappling hook just below the water surface. Continuing forward and upward the floating line was picked up by the grappling hook, the trailing buoy providing a stop if required. The buoyant line was then lifted to the helicopter using the helicopter's winch system (Figure D6), load limiters and a reach pennant were attached to the end of the buoyant line

Figure D7.   HH-60J helicopter (USCG Air Station Astoria) retrieving buoyant
              line and trailing float from surface with a grapnel at sta OS 5
              (30 May 2001)

and the free end placed manually on the cargo hook by means of the reach
pennant. At that point the load was lifted and returned to base at Ocean Shores
airport. The load limiter system was designed as a safety measure to prevent
dynamic or static loads from exceeding the design strength (4,000 pounds) of the
mooring assembly. This was the case for jetty tripod sta OS 7, which had been
deeply buried by sediment. Upon recovery attempt, the load limiters parted. A
diver reconnaissance confirmed that sta OS 7 was buried in more than 4 ft of
sediment. The instrument pods were deployed and recovered at high tide near
slack to avoid any unnecessary drag on the moorings during deployment and
recovery.

    ADP current transects. Currents were measured along transects from a
moving vessel to characterize the spatial variation in circulation around the north
jetty and inside the harbor entrance during a flood tide in May and September
2001. Approximately 1,500-m-long transects were run parallel to the jetty on the
north and south sides, and perpendicular to the jetty, covering the north portion
of the inlet and area of the submerged portion of the jetty in May 2001
(Figure D8). Currents were measured along three sets of transect loops (A, B, C)
in the inlet during 2 days of measurements in September 2001. Loop A ran
perpendicular to the north and south jetties, out to midchannel near Damon Point
and back to its origin to complete a large triangle transect. Loop B shared the
same origin of Loop A near the south jetty and traversed a smaller triangle, inset
of Loop A. Loop C continued further into Grays Harbor, near the Westport
Marina and inside of Damon Point (Figure D9).
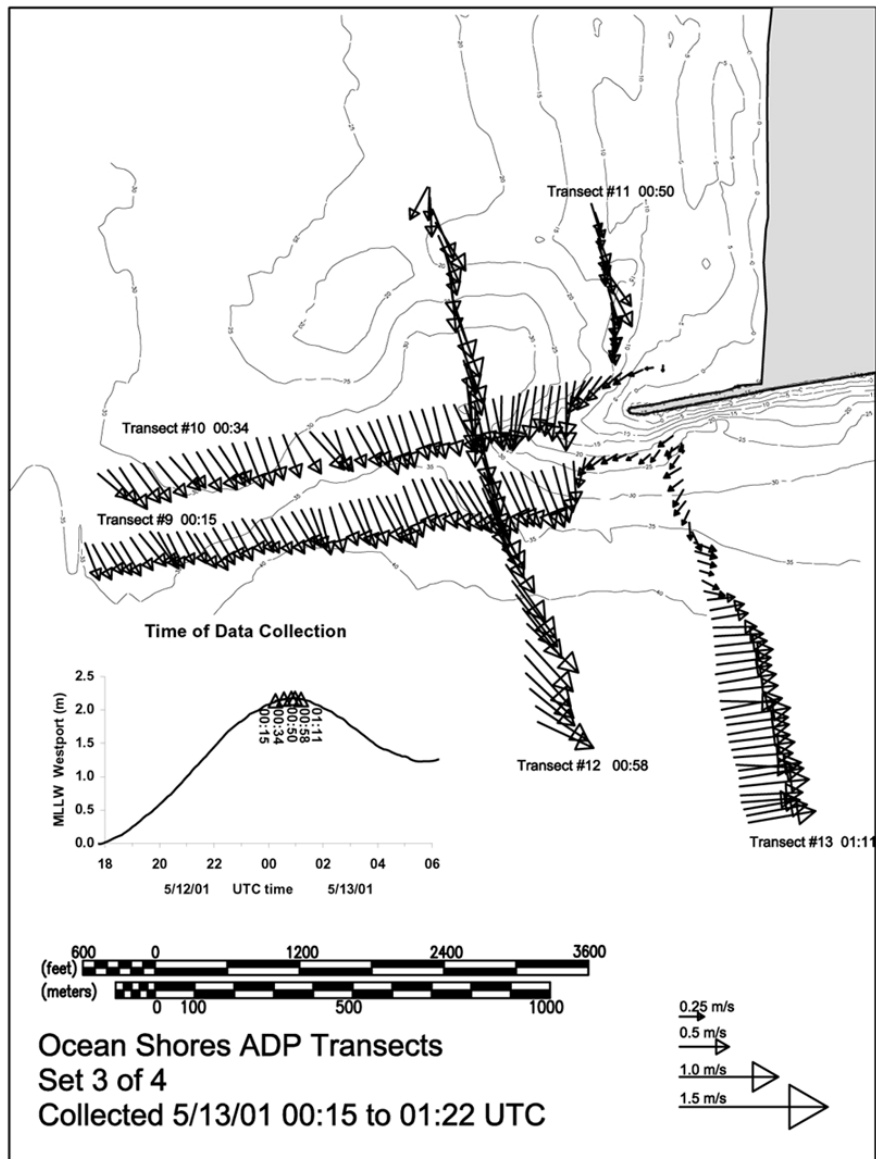
Figure D8. ADP transects May 2001

Current and depth data were collected on two separate data acquisition systems, each with simultaneous position and time input from a single DGPS receiver. At the north jetty, one series of four transects, consisting of two perpendicular and two parallel transects, was typically collected in an hour. Four series of transects were collected over a 5-hr period from approximately half way through the flood until the beginning of the ebb. In the inlet, transect loops A and B together and loop C required approximately 2 hr for each circumnavigation. Transects were collected over a 14-hr period from low tide to low tide on 2 consecutive days. Each current profile is divided into 0.5-m cells, beginning 1 m below the surface to 0.5 m above the bottom. Current profiles were collected once every 5 sec, corresponding to approximately 8- to 10-m horizontal distance.
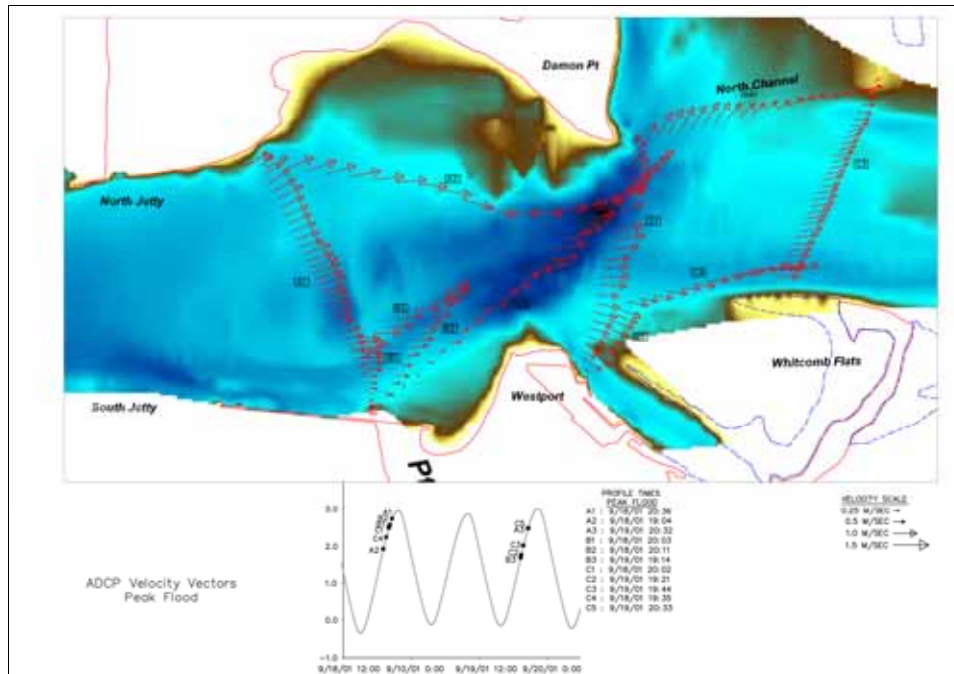
Figure D9. ADP transects September 2001

Water samples

Two near-bottom water samples were collected in the vicinity of the two tripod stations on 12 May at 0.5-m elevation above bottom. The samples were analyzed for Total Suspended Solids (TSS) to document sediment concentration in the water column during a flood tide.

Calibration of optical backscatter sensors

All OBS-3 sensors deployed with Hydra systems were calibrated for suspended sediment concentration. OBS signals are recorded by the Hydra system in "counts" ranging from 100 to 65,000, which must be converted to the desired units during post-processing. Calibrations were performed in a turbidity chamber following the specifications recommended by the manufacturer. Instrument gains were set prior to deployment using tap water (minimum) and 800 nephelometric turbidity units (ntu) Formazin standard solution (maximum). OBS deployed on the SIDSEP were calibrated over a range of 0 to 32 g/L at four concentrations (2 g/L, 8 g/L, 16 g/L and 32 g/L) with sand collected from north beach near mllw. OBS deployed on the jetty tripods were calibrated over a range of 0 to 24 g/L range at five concentrations (2 g/L, 4 g/L, 8 g/L, 16 g/L and 24 g/L) with sediment from the grab sample obtained near sta OS 6.

OBS calibration data (number of points = 1028 at 4 Hz) were extracted from the Hydra files and average, standard deviation, minimum, maximum and coefficient of variation were computed and the series plotted for a visual quality check. Coefficient of variation was typically 10 percent and not more than 15 percent for acceptable calibration results. Second-order polynomial curves fit to the calibration data yielded high correlations (average $R^2 = 0.9991$). Calibration

coefficients are summarized in Table D3. In processing the measured time series, the calibration formula was applied to each "instantaneous" sample of sensor "counts" to convert OBS data to suspended sediment concentration in grams per liter.

Data Recovery

Data recovered from all instrumentation deployed on the SIDSEP and HESTT are summarized in Table D4. Table D4 shows the deployments and recovery times for the deployments as well as the total amount of recorded and processed data. Pressure data loss occurred as a result of instrument emergence at low tide. Velocity data loss occurred as a result of sensor motion and instrument emergence at low tide. HESTT sta OS 7 was not recovered.

Table D3
OBS Calibration Results (2001/2002)

| Deployment | Station No. | Serial No. | Elevation Above Bed (m) | Calibration Coefficients for 0-24 g/L Range | | | R^2 |
				A	B	C	
3	OS 5	1408	0.25	2.426949E-09	3.077946E-04	-4.565425E-01	9.939048E-01
1, 2, 3	OS 1	1407	0.15	3.551526E-09	5.334601E-04	-3.856765E-01	9.997643E-01
3	OS 6	1405	0.25	2.697483E-09	2.031709E-04	-5.407930E-02	9.998382E-01
1, 2, 3	OS 1	1404	0.35	4.036252E-09	5.126042E-04	-3.682450E-01	9.992964E-01
1, 3	OS 2	1403	0.35	3.988815E-09	5.295308E-04	-2.384312E-01	9.999436E-01
1, 3	OS 2	1402	0.15	1.529892E-09	6.022695E-04	-4.643728E-01	9.997717E-01
1, 3	OS 3	1401	0.15	1.999875E-09	5.789079E-04	-5.981259E-01	9.990675E-01
1, 3	OS 3	1400	0.35	3.300025E-09	5.162753E-04	-3.977704E-01	9.994902E-01
1, 3	OS 4	1399	0.15	3.760698E-09	5.007529E-04	-4.960281E-01	9.996216E-01
1, 3	OS 4	1398	0.35	3.159039E-09	5.422607E-04	-6.163681E-01	9.995151E-01
2	OS 2	1399	0.15	3.760698E-09	5.007529E-04	-4.960281E-01	9.996216E-01
2	OS 2	1398	0.35	3.159039E-09	5.422607E-04	-6.163681E-01	9.995151E-01
3	OS 6	1397	0.45	2.873761E-09	2.006019E-04	-6.002029E-02	9.998503E-01
3	OS 5	1396	0.45	5.281074E-09	2.373572E-04	-3.549462E-03	9.989898E-01
1 (2002)	OS 8	1396	0.45	3.0378E-09	1.3080E-04	7.2474E-02	9.9696E-01
1 (2002)	OS 8	1409	0.30	2.0852E-09	1.4803E-04	3.5401E-02	9.9831E-01
1 (2002)	OS 9	1398	0.45	3.1242E-09	1.2599E-04	7.7119E-02	9.9914E-01
1 (2002)	OS 9	1399	0.30	3.2116E-09	1.2123E-04	6.4162E-02	9.9842E-01
1 (2002)	DP 1	1403	0.35	-3.0908E-10	4.1389E-04	-7.6709E-01	9.8815E-01
1 (2002)	DP 1	1406	0.50	-1.4420E-10	3.9452E-04	-7.1883E-01	9.8955E-01
1 (2002)	DP 1	1402	0.35	4.2812E-10	3.5737E-04	-5.5125E-01	9.9422E-01
1 (2002)	DP 2	1404	0.50	1.9600E-10	3.7711E-04	-5.4821E-01	9.9404E-01

Calibration Formula: $y = Ax^2 + Bx + C$.
Where y is suspended sediment concentration in g/L, x is OBS sensor "counts", and A, B, and C are calibration coefficients.

Table D4
Data Recovery

Deployment 1 (2/6/01 to 2/9/01)				
Hydra Data Recovery	**sta OS 1**	**sta OS 2**	**sta OS 3**	**sta OS 4**
Station/File Name	OS1D1001.ADR	OS2D1001.ADR	OS3D1001.ADR	OS4D1001.ADR
Original File Size (bytes)	26977863	26977863	26977863	26977863
Number of Recorded bursts (8192 samples/burst)	113	113	113	113
Time of first Recorded burst	2/6/01 - 0000	2/6/01 - 0000	2/6/01 0000	2/6/01 0000
Time of last Recorded burst	2/9/01 - 0000	2/9/01 - 0000	2/9/01 0000	2/9/01 0000
Number of Processed Bursts	113	113	113	113
Number of Usable Bursts (Pressure)	62	80	69	80
Number of Usable Bursts (Velocity)	24	20	29	51
Percent Data Recovery (Pressure/Velocity)	55.9% 21.2%	70.8% 17.7%	61.1% 25.7%	70.8% 45.1%
Deployment 2 (3/13/01 to 3/14/01)				
Hydra Data Recovery	**sta OS 1**	**sta OS 2**		
Station/File name	OS1D2001.ADR	OS2D2001.ADR		
Original file size (bytes)	8775717	8942913		
Number of recorded bursts (8192 samples/burst)	36	37		
Time of first recorded burst	3/13/01 - 1800	3/13/01 - 1800		
Time of last recorded burst	3/14/01 - 1720	3/14/01 - 1800		
Number of processed bursts	36	37		
Number of usable bursts (Pressure)	11	11		
Number of usable bursts (Velocity)	11	11		
Percent data recovery (Pressure/Velocity)	30%	30%		
Deployment 3 (5/6/01 to 5/11/01)				
Hydra Data Recovery	**sta OS 1**	**sta OS 2**	**sta OS 3**	**sta OS 4**
Station/File name	OS1D3001.ADR	OS2D3001.ADR	OS3D3001.ADR	OS4D3001.ADR
Original file size (bytes)	44937837	44982267	45026115	45056719
Number of recorded bursts (8192 samples/burst)	378	378	378	379
Time of first recorded burst	5/6/01 - 1300	5/6/01 - 1300	5/6/01 1300	5/6/01 1300
Time of last recorded burst	5/11/01 - 1840	5/11/01 - 1840	5/11/01 1840	5/11/01 1900
Number of processed bursts	378	378	378	379
Number of usable bursts (pressure)	246	239	244	268
				(Continued)

Table D4 (Concluded)

Deployment 1 (2/6/01 to 2/9/01)				
Hydra Data Recovery	**sta OS 1**	**sta OS 2**	**sta OS 3**	**sta OS 4**
Percent data recovery (pressure/velocity)	65%	63%	65%	71%
Station/File name	S5VD1001.ADR	S6VD2001.ADR	S5PD1001.ADP	S6PD1001.ADP
Original file size (bytes)	149677637	149736101	10274928	10804438
Number of recorded bursts (8192 samples/burst)	1259	1259	6298	6299
Time of first recorded burst	5/4/01 - 1800	5/4/01 - 1800	5/4/01 1800	5/4/01 1800
Time of last recorded burst	5/30/01 - 2300	5/30/01 - 2300	5/30/01 2342	5/30/01 2348
Number of processed bursts	1259	1259	6298	6299
Number of usable bursts (pressure)	1250	1246	6251	6228
Number of usable bursts (velocity)	1238	704	6251	6238
Percent data recovery (pressure/velocity)	(99%/98%)	(99%/56%)	99%	99%
Spring Deployment 2002				
Hydra Data Recovery	**sta OS 8**	**sta OS 9**	**sta DP 1**	**sta DP 2**
Station/File name	OS8V1001.ADR	OS9V1001.ADR	DP1V1001.ADR	DP2V1001.ADR
Original file size (bytes)	173017659	173017659	97483681	97483681
Number of recorded bursts	1455	1455	820	820
Time of first recorded burst	3/28/02 - 1900	3/28/02 - 19l00	3/29/02 1900	3/29/02 1900
Time of last recorded burst	5/28/02/ - 0900	5/28/02 - 0900	5/2/02 2200	5/2/02 2200
Number of processed bursts	1455	1455	820	820
Number of usable bursts (pressure)	1454	1454	770	769
Number of usable burst (velocity)	695	1294	665	770
Percent data recovery (pressure)	99%	99%	94%	94%
Percent data recovery (velocity)	48%	81%	94%	94%
ADP Data Recovery	**sta OS 8**	**sta OS 9**		
Station/File name	OS8P1001.ADP	OS9P1001ADP		
Original file size (bytes)	22065487	19562366		
Number of recorded bursts	14719	13050		
Time of first recorded burst	3/28/02 - 1900	3/28/02 - 1900		
Time of last recorded burst	5/28/02 - 0224	5/28/02 - 0354		
Number of processed bursts	14719	11829		
Number of usable bursts (pressure)	14713	11829		
Number of usable burst (velocity)	14713	11829		
Percent data recovery (pressure)	99%	91%		
Percent data recovery (velocity)	99%	91%		

Data Processing and Quality Checks

A preliminary visual data quality check was performed on raw Hydra data from both the beach pods and jetty tripods using Sontek ViewHydra software. Data were extracted from raw data files (*.adr) using SonTek Hydra extraction software and written to ASCII time series (*.ts), header (*.hdr) and control (*.ctl) files. All remaining processing and post-processing was accomplished using in-house PI Engineering software.

Processing and quality checking of extracted time series files consisted of the following steps:

a. Plotting header file parameters (*.HDR): Heading, pitch, and roll angles, mean temperature, and mean pressure, and bed position (if relevant) were plotted as time series as a step in the data quality check process to identify periods when instruments may have shifted position or been subject to burial or fouling.

b. Calibration and conversion of time series: A Matlab routine (preprocadvhts_v5.m) and associated subroutines processed the extracted time series files and produced corrected and calibrated ASCII time series files (*.tsc). The routine accomplished the following:

(1) Horizontal components (E, N) of ADVO velocities were corrected from magnetic north to true north direction using the magnetic declination for the location and time of deployment.

(2) Pressure measurements were converted to static water depth above the ADV using mean barometric pressure and water density (calculated from temperature and estimated salinity) during the deployment period (p2h.m). Measured water temperature and estimated salinity were converted to water density using the International Equation of State of Seawater 1980 (IES80) (Folonoff and Millard 1983). Bursts were eliminated from post-processing analyses that were above the water surface through comparing the height of the bin with the water depth mean.

(3) Static water depths were converted to water-surface elevation series suitable for wave height and period calculation by correcting for pressure attenuation as a function of depth and wave frequency (p2eta.m). Corrections were carried out in the frequency domain and converted to the time domain for output. The attenuation correction factor is based on the linear wave theory dispersion relation and the maximum frequency cutoff is based on that reported by Earle, McGehee, and Tubman (1995) and is dependent on the water depth.

(4) Optical backscatterance sensor (OBS) counts were converted to suspended sediment concentration using laboratory calibration coefficients (obscal-os.txt). OBS on the SIDSEP were calibrated in a turbidity tank with bed sediment from the deployment site prior to the deployment. OBS on the HESTT were post-calibrated using sediment from a grab sample collected near sta OS 6. Data were inspected for evidence of bio-fouling and sensor burial. Bio-fouling

and the approach to burial are indicated in the SSC signal by rising background or change in the sensor offset. Complete burial is indicated by a significant change in sensor offset. Subjective estimates of when bio-fouling or burial became significant and affected data were discarded from analysis.

(5) Processed time series data were output to *.tsc files identical in format to the extracted *.ts format.

(6) Burst-averaged summary statistics files (*.sts) were generated by taking the mean and variance of the processed data for each 2048-point burst.

c. Matlab routine plotbursts_*.m was used to plot time series to conduct final QC on data, remove spikes and velocity ambiguities, calculate and plot autospectra, cross-spectra, and to calculate a correlation score on velocity data. The correlation score expresses the percentage of the record in which velocity correlations are above a threshold. In this case, a threshold of 70 percent was the a basis for selecting useful velocity data.

Data post-processing was performed on the velocity (E, N, U) data to remove poor quality or erroneous data. Poor quality data is typically a result of environmental conditions, which cause poor acoustic signal return and low signal correlation. Instrument motion problems can also cause velocity ambiguities that are out of range. Time series plots of the measured burst-averaged parameters subjected to post-processing are provided in Figures D10 to D108.

Current transect data were initially processed with ADP manufacturer's software to correct for vessel movement using ADP bottom track or DGPS-derived vessel velocity. Data quality filtering was performed to remove velocity measurements with low signal-to-noise ratios. The resultant speed and direction data were horizontally smoothed using a 5- or 7-point Gaussian filter (profile averaging) and vertically smoothed using a 3-point Gaussian filter (cell averaging). This filtering helps to minimize some of the uncorrected high-frequency velocity error resulting from vessel heave, pitch, roll and rapid turning. Depths measured simultaneously with current data were corrected using a water-surface elevation time series to produce bottom elevations referenced to datum. Spikes in depth data and noise in the digital depth data were cross-referenced to paper echosounder records and erroneous data were either smoothed or deleted.

Current profile speed and direction were merged with bottom elevation data to produce cross-sectional plots of speed and direction relative to distance along the planned transect line. Plots of cross-sectional ADP transect data are shown in Figures D39 to D100.

Vertical speed profiles were depth-averaged from 1 m below the water surface to 0.5 m above bottom. Current direction was first multiplied by the current speed and then averaged to obtain a speed-weighted depth-averaged current direction. Depth-averaged speed and direction vectors were then scaled and plotted as plan-view vectors overlaid on a chart of the study area (Examples are shown in Figures D8 and D9).

Data Quality

The quality of the data obtained at the four stations was verified by plotting pressure and velocity data of the individual bursts using the SonTek ViewHydra software. Header files (*.HDR) produced by the SonTek ADV software during initial raw data processing contain burst statistics for evaluating: mean heading, pitch and roll angles, mean temperature, and mean pressure. Recorded heading and pitch and roll angles were inspected to determine if there were significant changes in pod orientation and tilt.

ADV data were screened using SonTek ViewHYDRA software. All stations encountered periods when the signal quality was below acceptable levels or when velocities exceeded the velocity range settings. That conclusion was made from observing the ADV receiver correlations while employing filter options. Sensor movement, or intermittent or continuous emergence of the sensor near low tide is inferred to cause poor data quality. In post-processing usable velocity data, velocity ambiguities including spikes greater than ±2 m/sec were removed by iterative linear interpolation between adjacent good data points.

Following recovery it was noted that the Druck pressure sensor for sta OS 3 was drained of silicone fluid and partially filled with sand. This probably caused an air bubble in the outer pressure sensor area that biased the readings at this location.

ADP transect data were viewed, pre-processed, and filtered using SonTek ViewADP software. The quality of the ADP data is good, with some obvious inconsistencies in current speed over short periods. These inconsistencies in current velocity are indicative of the dynamic environment and the motion of the ADP instrument during data collection. The instances of visually incongruent data correlate with high standard deviations in the velocity data, which are likely the result of vessel motion that are not compensated for by the instrument, external sensors, and software. The use of the smoothing tools in the post-processing software is helpful in overcoming the occasional poor quality recorded data. A signal-to-noise ratio filter (>15-20 dB) was also used to remove data with poor acoustic quality. The few instances where this filter did remove data were in slightly deeper water (10-15m), farther from the shoreline where there may be less particulate matter to reflect the acoustic signal back to the instrument. Very little of the ADP transect data was discarded because of poor quality.

References

Earle, M. D., McGehee, D., Tubman, M. (1995). "Field wave gaging program, wave data analysis standard," Instruction Report CERC-91-1, U.S. Army Engineer Waterways Experiment Station.

Folonoff, N. P., and Millard, R. C., Jr. (1983). "Algorithms for computation of fundamental properties of seawater," UNESCO Technical Papers in *Marine Science* 44, Division of Marine Sciences, UNESCO, Paris, France.

Hericks, D., and Simpson, D. (2000). "Grays Harbor estuary physical dynamic study," Final Data Report: September 11, 1999 - November 17, 1999.

Kamphuis, J. W. (2000). "Designing with models," *Proceedings 27th Coastal Engineering Conference*, ASCE, Reston, VA, 19-32.

McGehee, D. D., and Mayers, C. J. (2000). "Deploying and recovering marine instruments with a helicopter," Coastal Engineering Technical Note ERDC/CHL CETN-V1-34, U.S. Army Engineer Research and Development Center, Coastal and Hydraulics Laboratory, Vicksburg, MS.

Osborne, P. D., Hericks, D. B., and Kraus, N. C. (2002a). "Deployment of oceanographic instruments in high energy environments and near structures," Coastal and Hydraulics Engineering Technical Note CHETN ERDC/CHL-IV-46, U.S. Army Engineer Research and Development Center, Vicksburg, MS. http://chl.wes.army.mil/library/publications/chetn/pdf/chetn-iv46.pdf <http://cirp.wes.army.mil/cirp/cetns/HeliPod.pdf>

Osborne, P. D., Hericks, D. B., Kraus, N. C., and Parry, R. M. (2002b) "Wide area measurements of sediment transport at a large inlet, Grays Harbor, Washington," *Proceedings 28th International Conference on Coastal Engineering*, World Scientific Press, 3,053-3,064.

Pollock, C. E. (1995). "Effectiveness of spur jetties at Siuslaw River, Oregon; Report 2; Localized current flow patterns induced by spur jetties: Airborne current measurement system and prototype/physical model correlation," Technical Report CERC-95-14, Coastal Engineering Research Center, U.S. Army Engineer Waterways Experiment Station, Vicksburg, MS.

Sherwood, C. R., Gelfenbaum, G., Howd, P. A. and Palmsten, M. L. (2001). "Sediment transport on a high-energy ebb-tidal delta," *Proceedings Coastal Dynamics '01*, Reston, VA, American Society of Civil Engineers (ASCE), 473-482.

Figures D10 to D13

This section contains plots of time series of significant wave height, peak period and direction measured at Grays Harbor CDIP buoy (3601) during instrument deployments (February, March, and May 2001 and March, April, and May 2002).
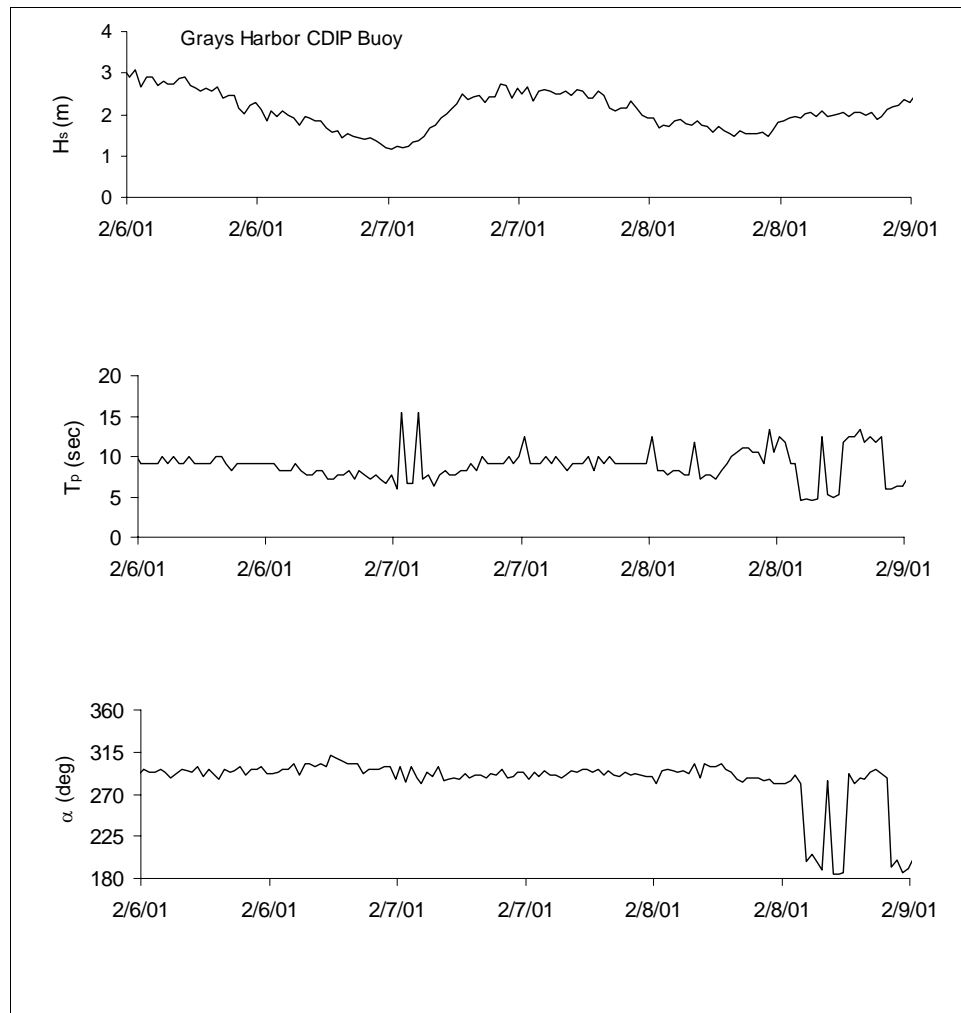
Figure D10. SIDSEP Deployment 1, 6-9 February 2001
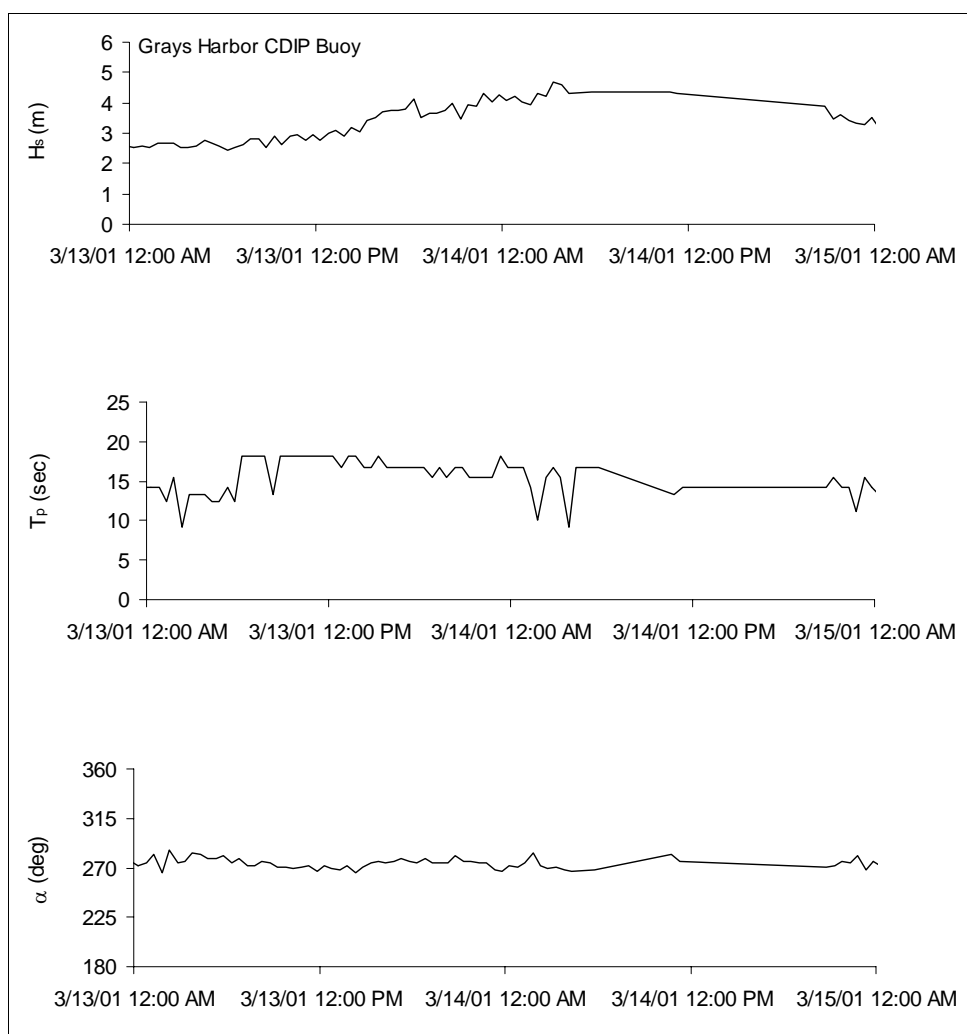
Figure D11. SIDSEP Deployment 2, 13-15 March 2001
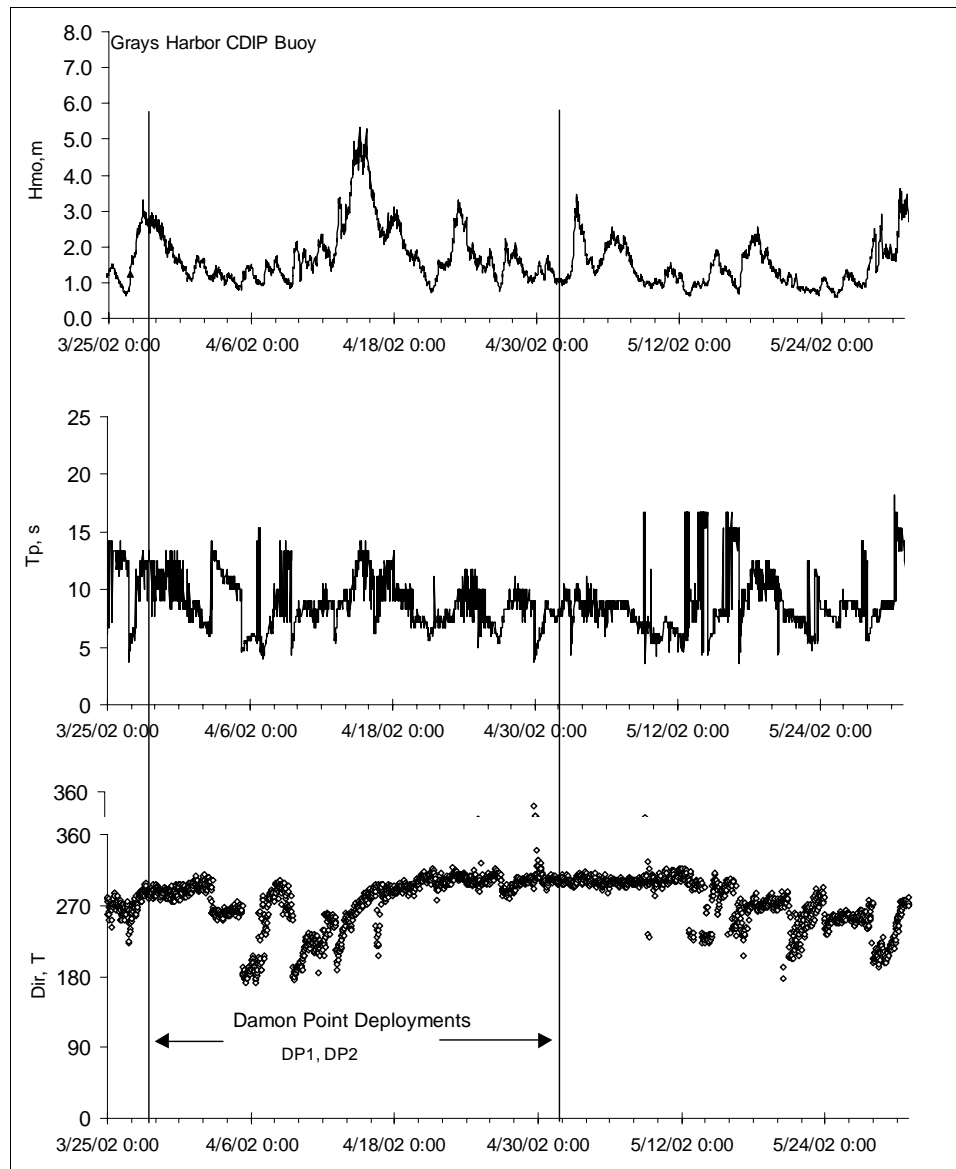
Figure D12. HESTT deployment, 25 March - 30 May 2002
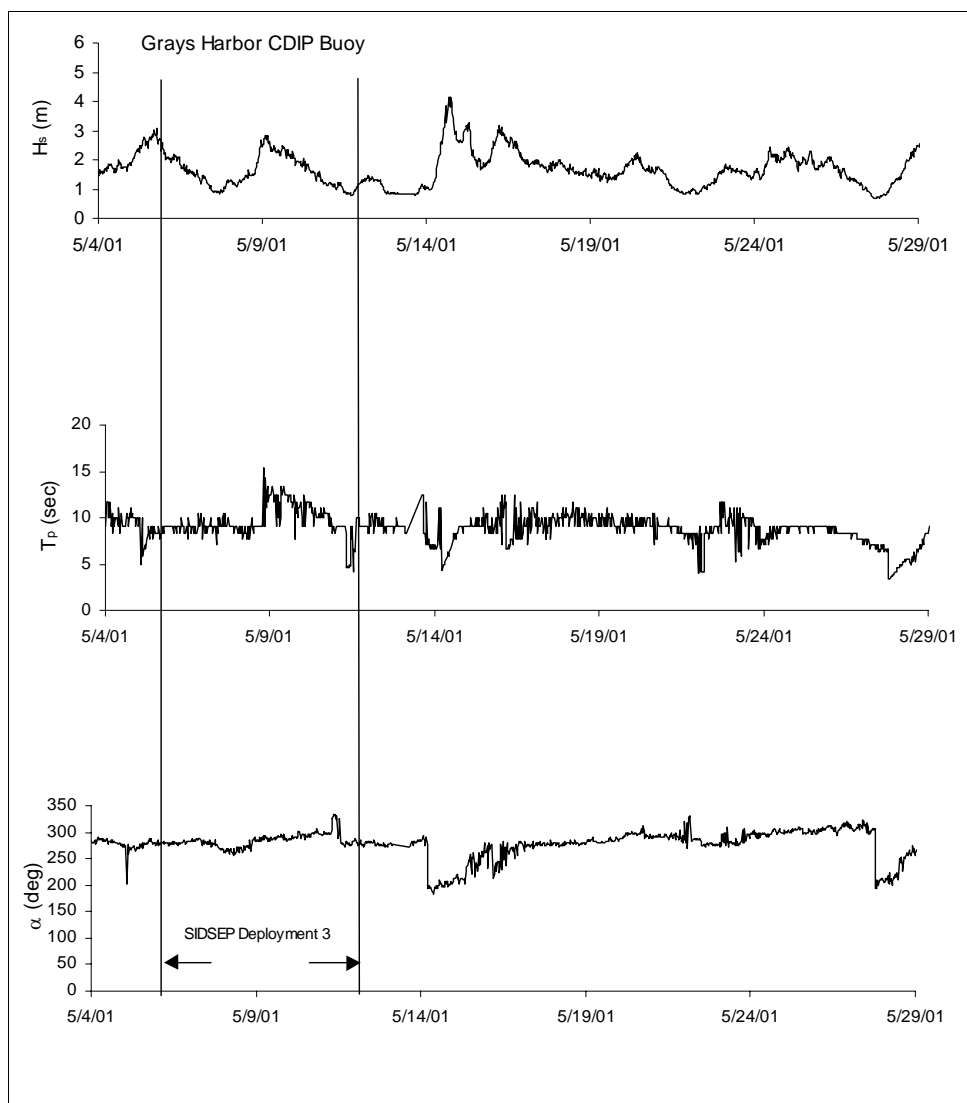
Figure D13. HESTT deployment, 4-30 May 2001

Figures D14 to D38

This section contains plots of time series of significant wave height, peak period, wave direction, easting and northing velocity, and suspended sediment concentration from sta OS 1-6, 2001 and OS 8-9, DP 1-2, 2002.

Deployment 1
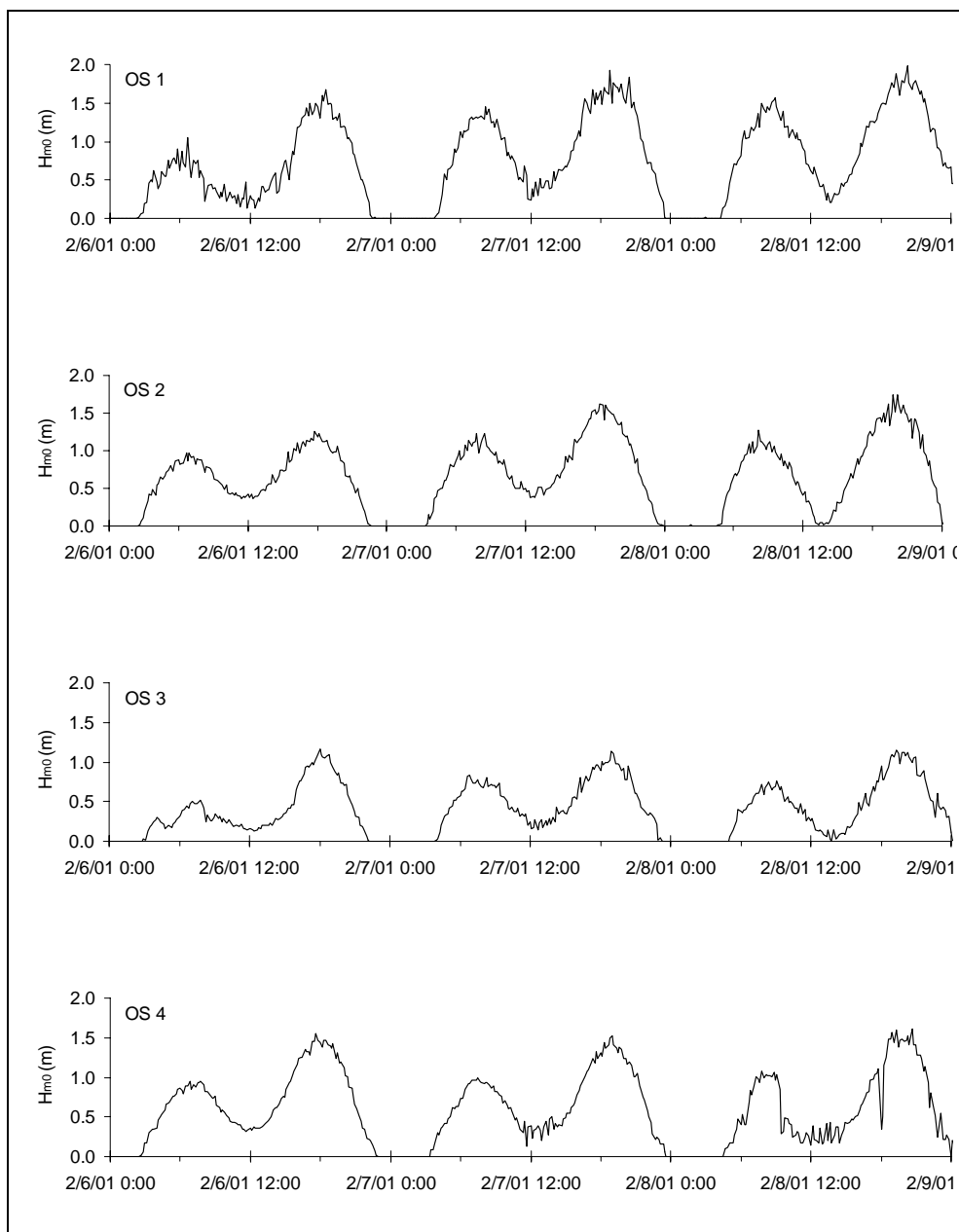
Figure D14.   SIDSEP wave height measurements, Deployment 1, 6-9 February 2001
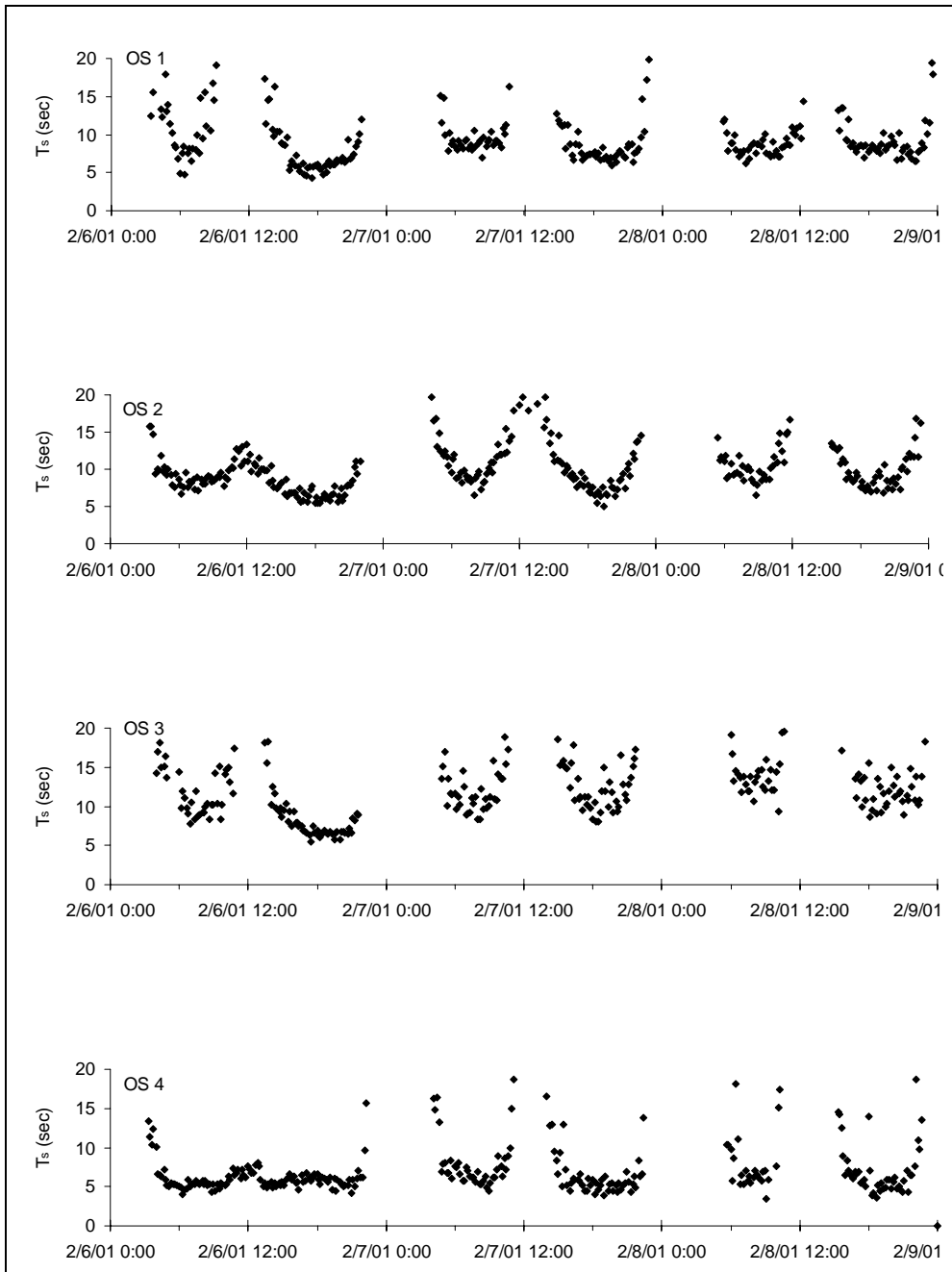
Figure D15. SIDSEP significant period measurements, Deployment 1,
6-9 February 2001
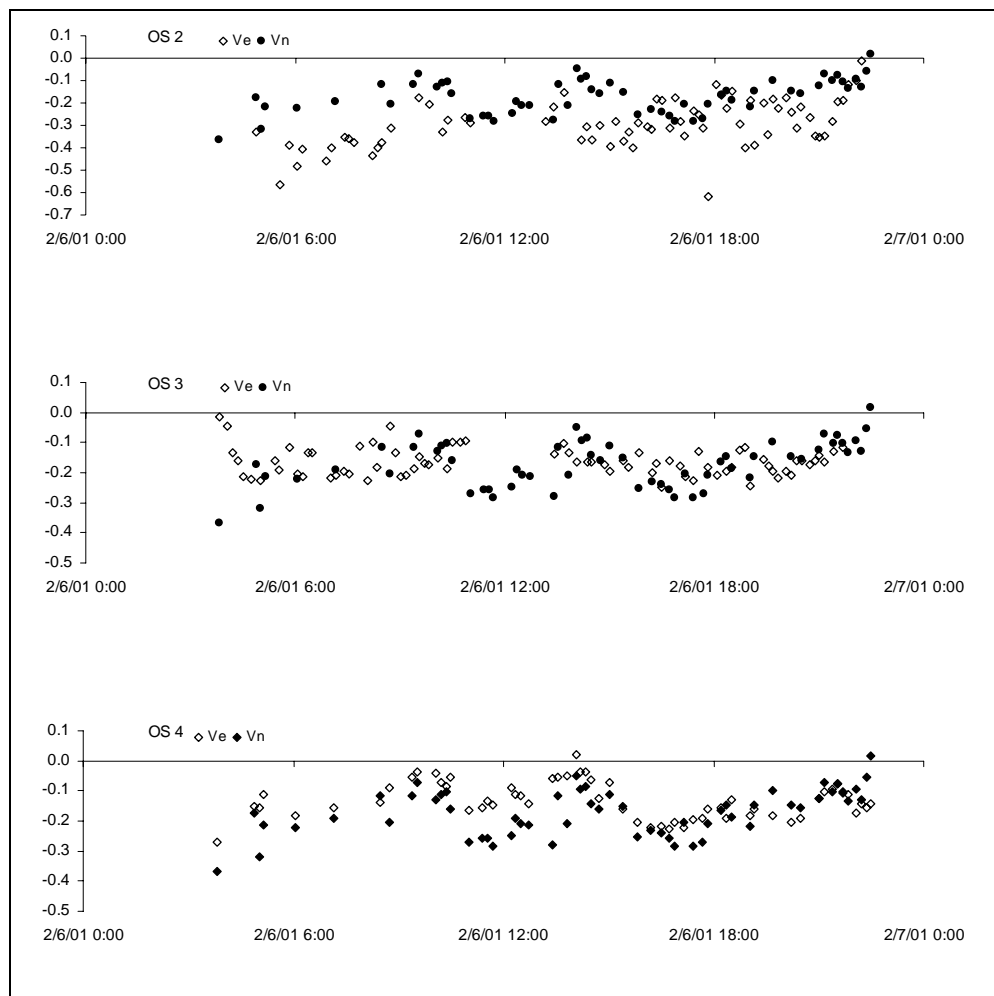
Figure D16. SIDSEP velocity measurements, Deployment 1, 6-9 February 2001
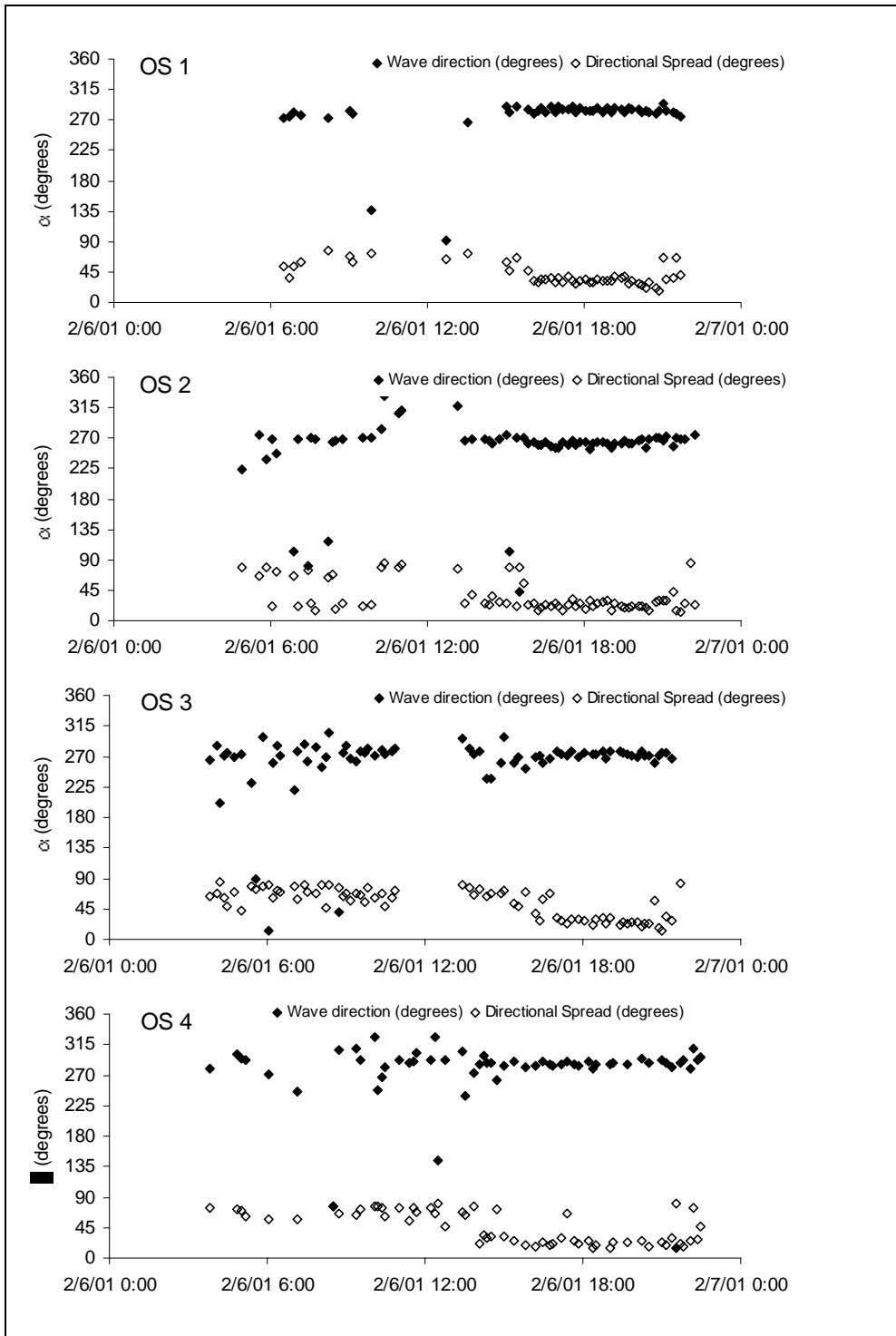
Figure D17. SIDSEP wave direction measurements, Deployment 1,
6-9 February 2001
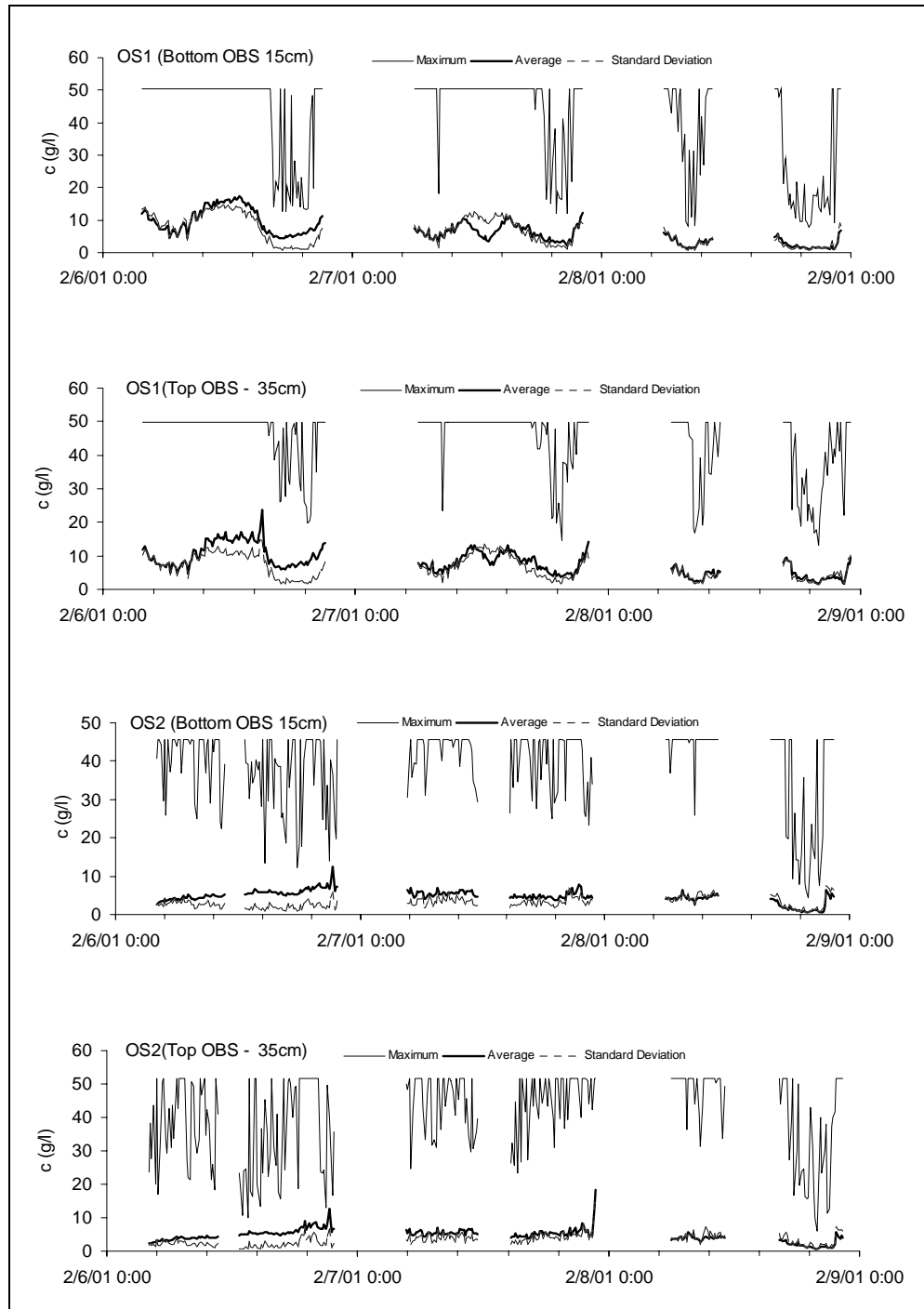
Figure D18. SIDSEP SSC measurements, Deployment 1, 6-9 February 2001
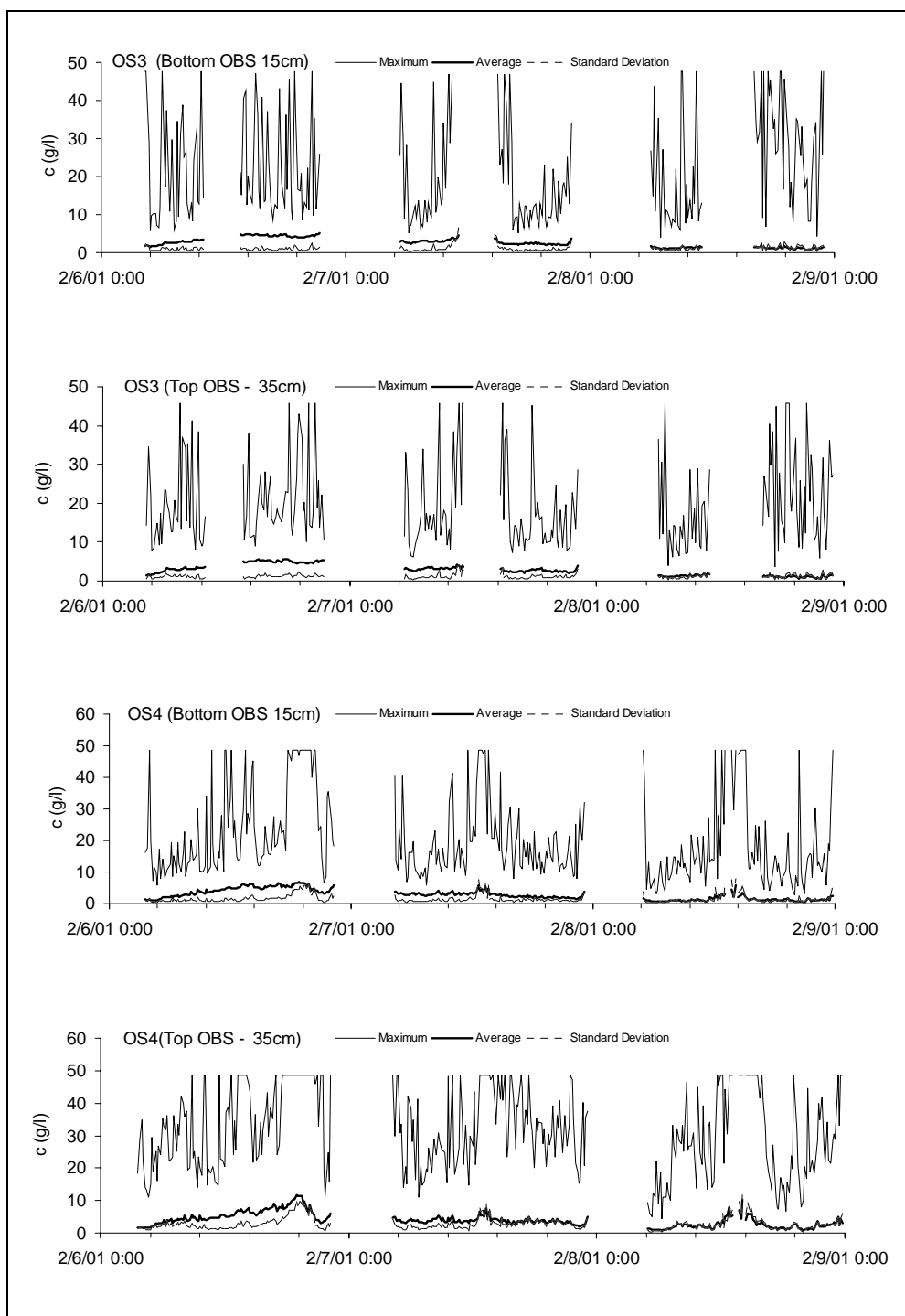
Figure D19. SIDSEP SSC measurements, Deployment 1, 6-9 February 2001

Deployment 2
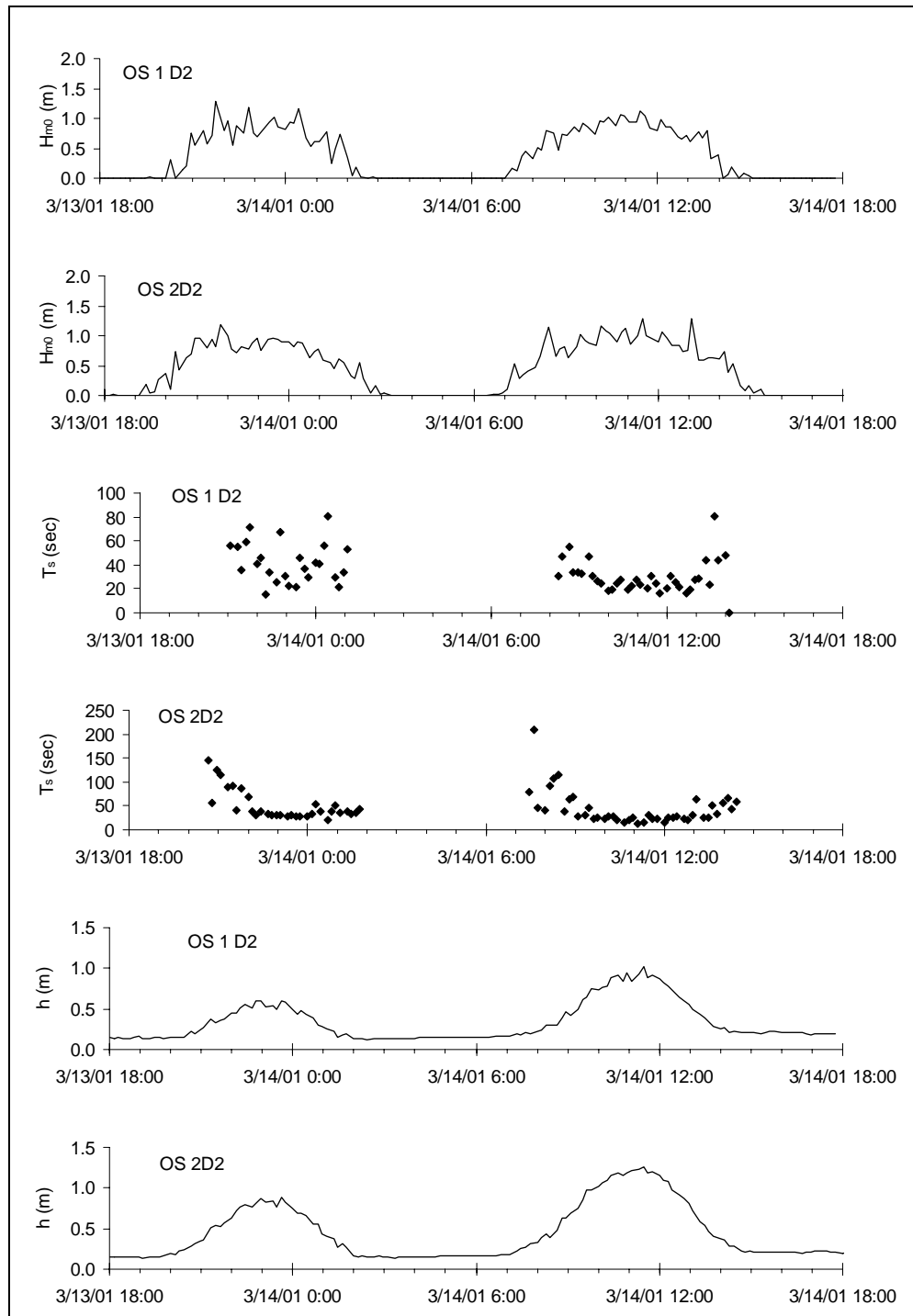
Figure D20.   SIDSEP (sta OS 1, OS 2) wave height, period, and sensor height measurements, Deployment 2, 13-14 March 2001
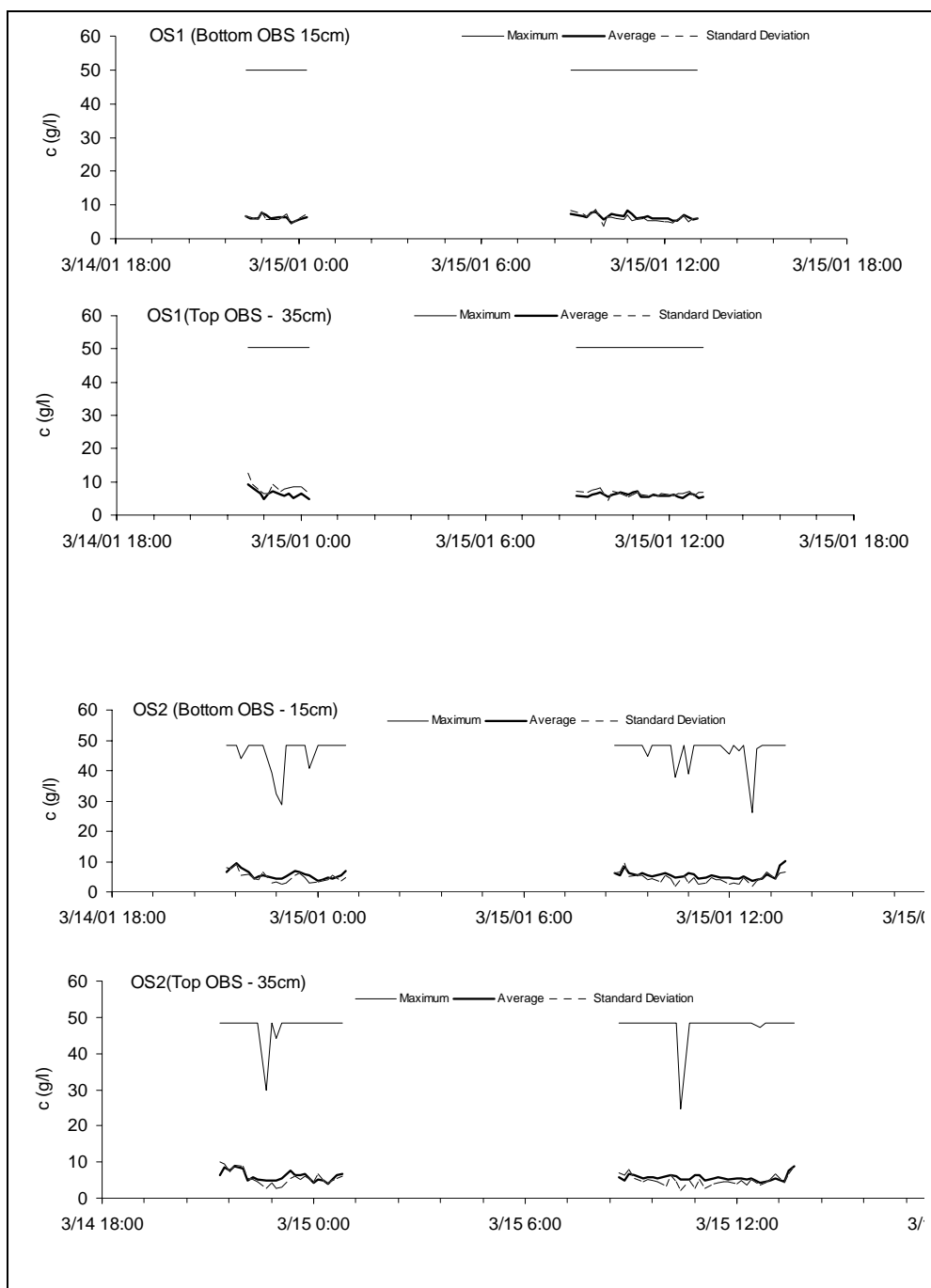
Figure D21.   SIDSEP (sta OS 1, OS 2) SSC measurements, Deployment 2, 14-15 March 2001

Deployment 3
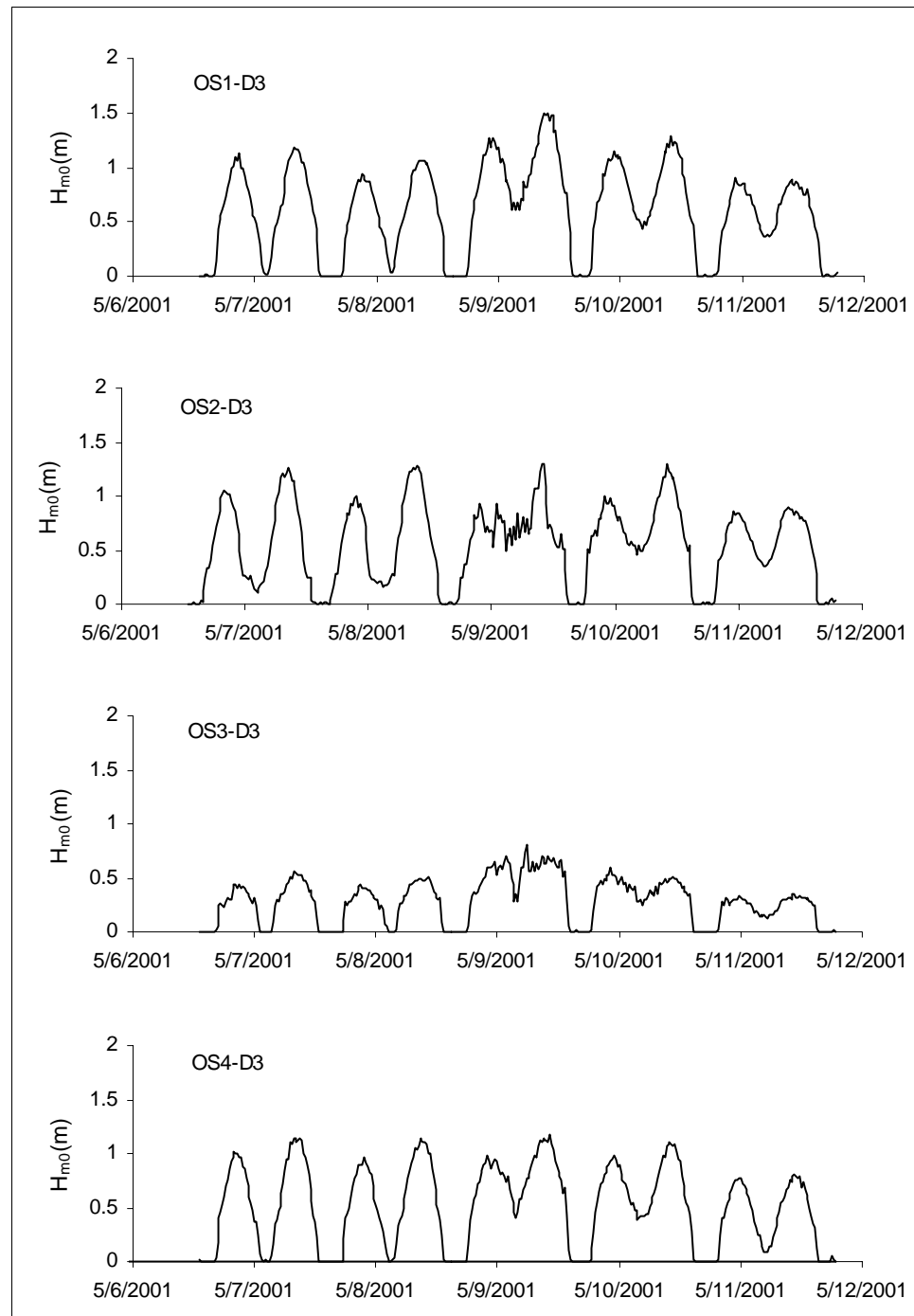
Figure D22.   SIDSEP wave height measurements, Deployment 3, 6-12 May 2001
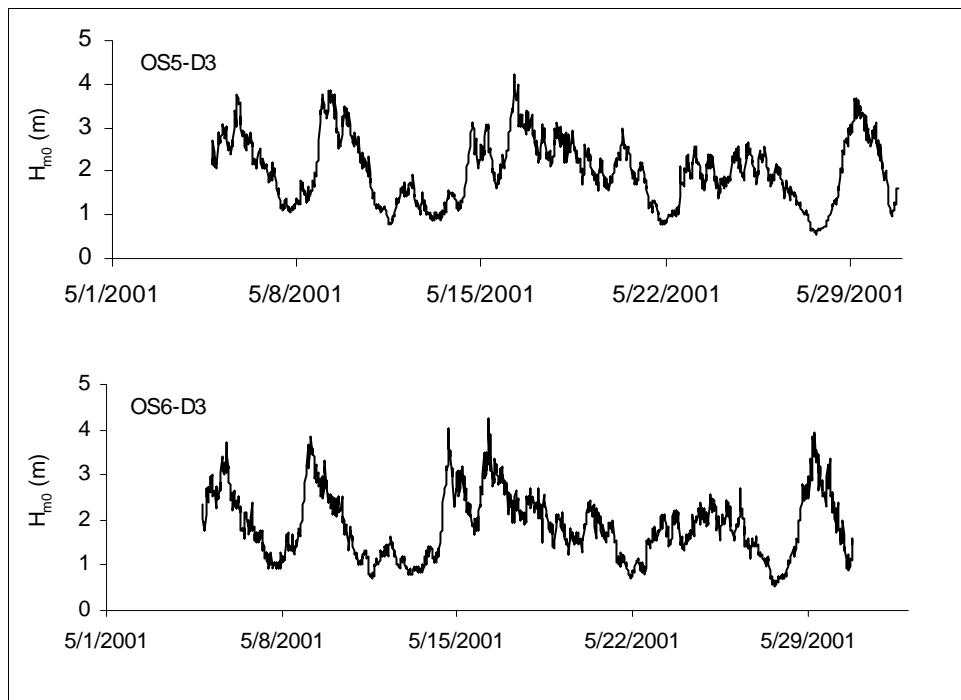
Figure D23.   HESTT wave height measurements, Deployment 3,
                       1-30 May 2001
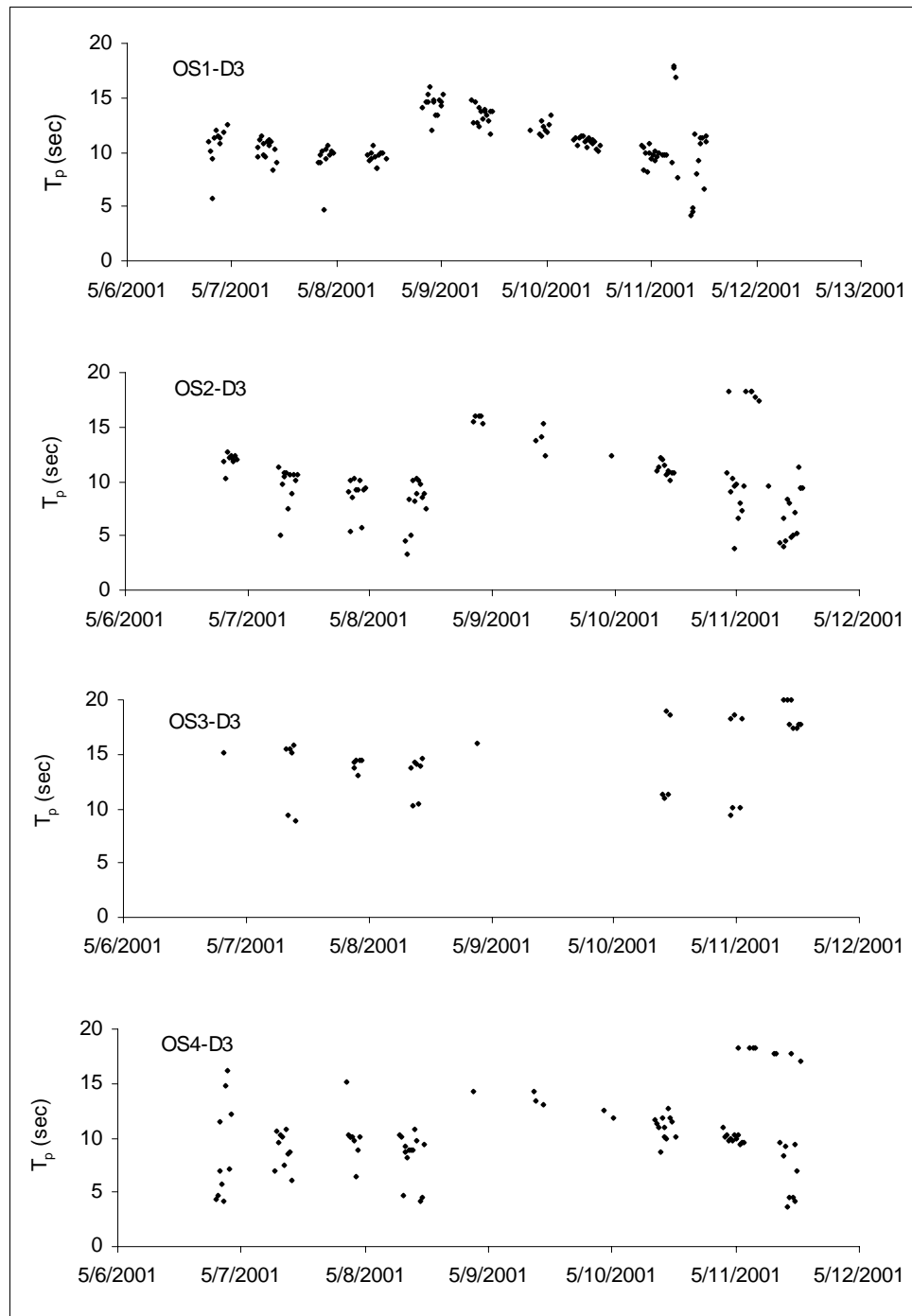
Figure D24. SIDSEP peak period measurements, Deployment 3, 6-12 May 2001
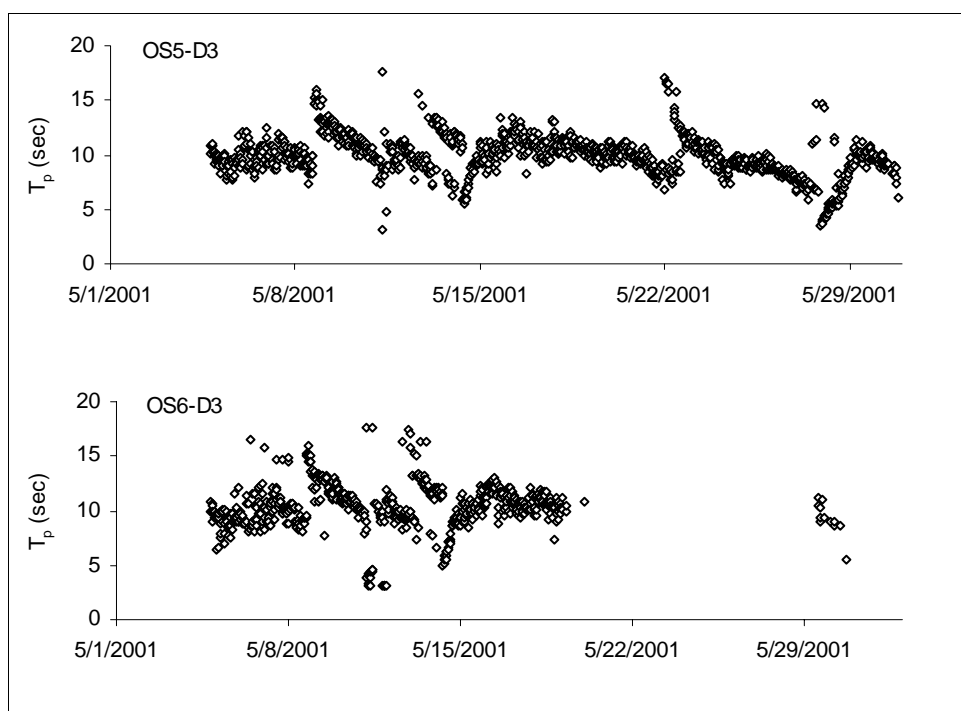
Figure D25. HESTT peak period measurements, Deployment 3, 1-30 May 2001
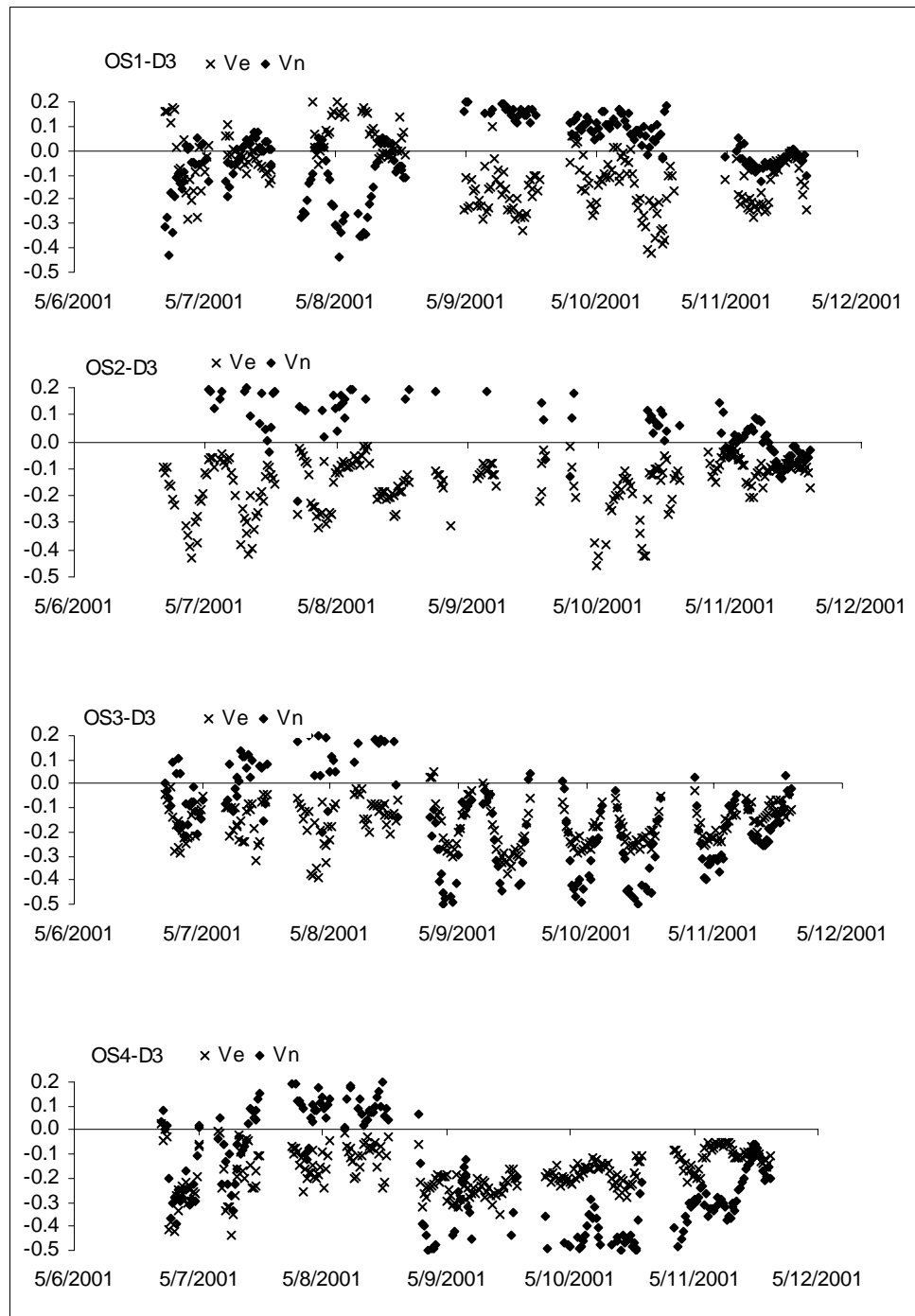
Figure D26. SIDSEP velocity measurements, Deployment 3, 6-12 May 2001
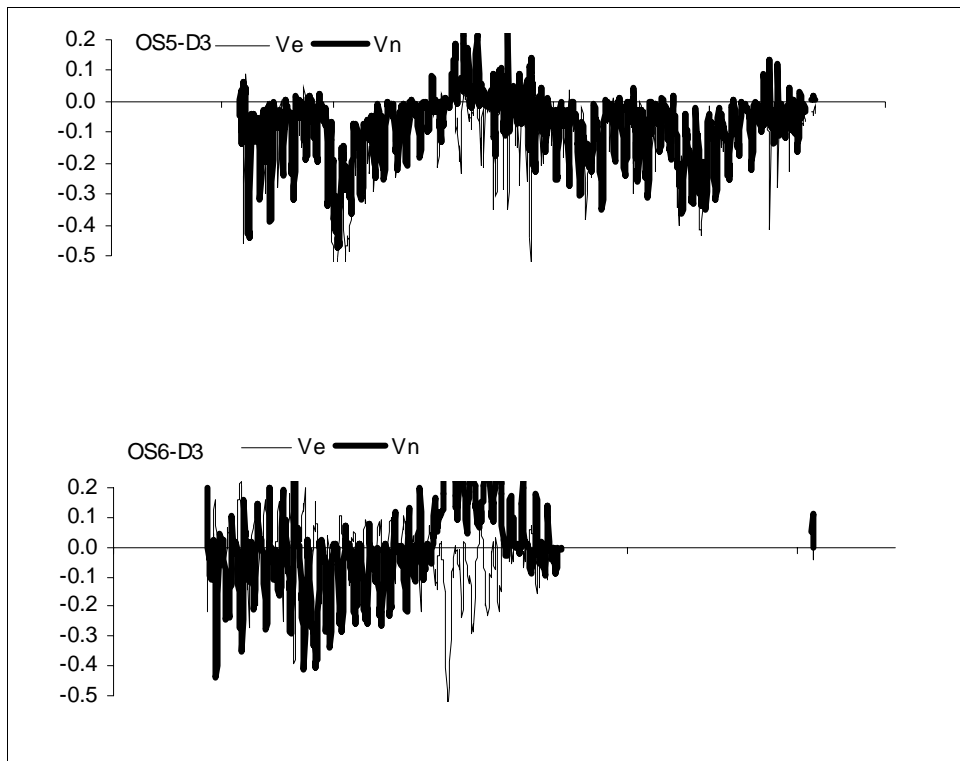
Figure D27. HESTT velocity measurements, Deployment 3, 1-30 May 2001
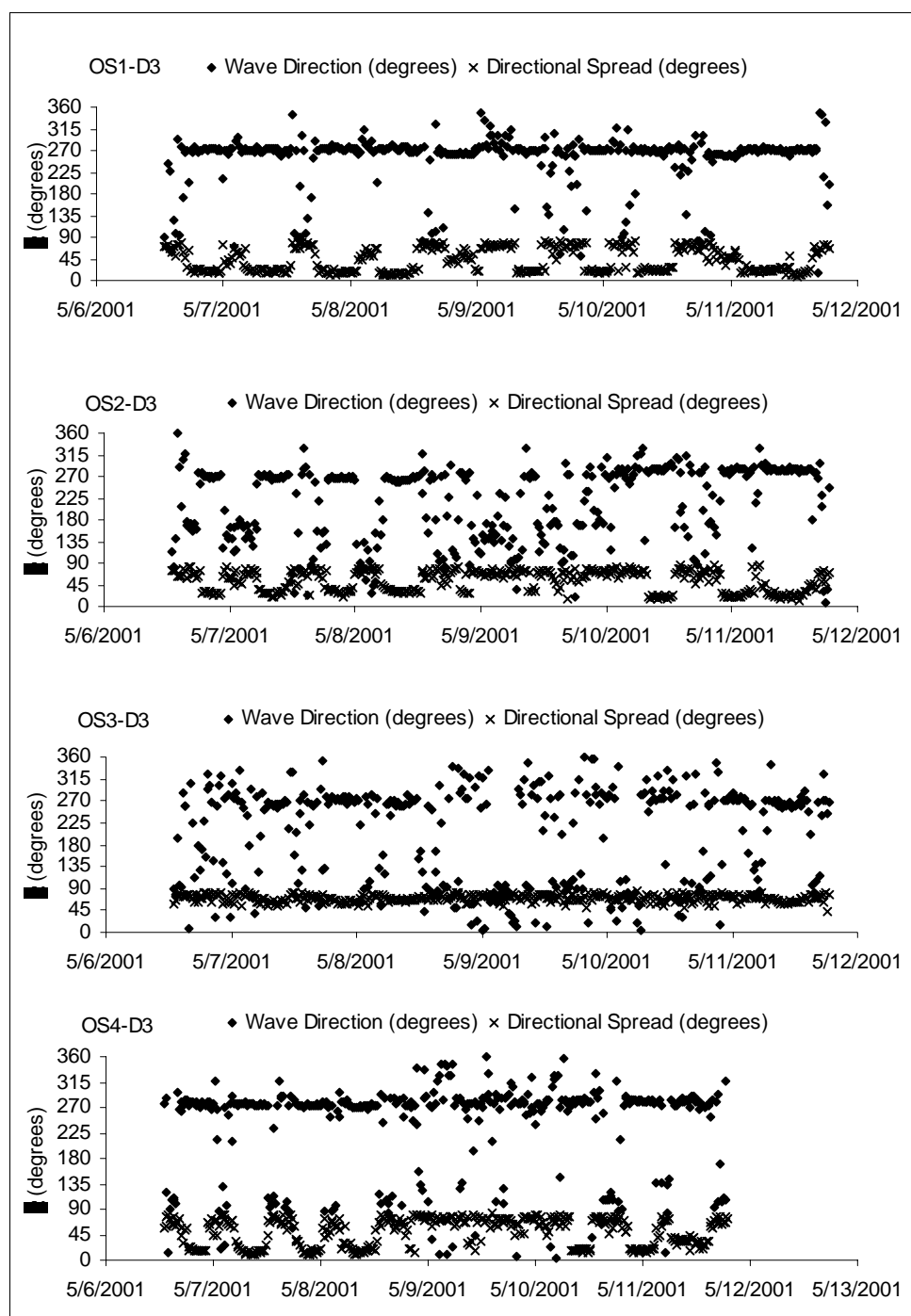
Figure D28. SIDSEP wave direction measurements, Deployment 3, 6-12 May 2001
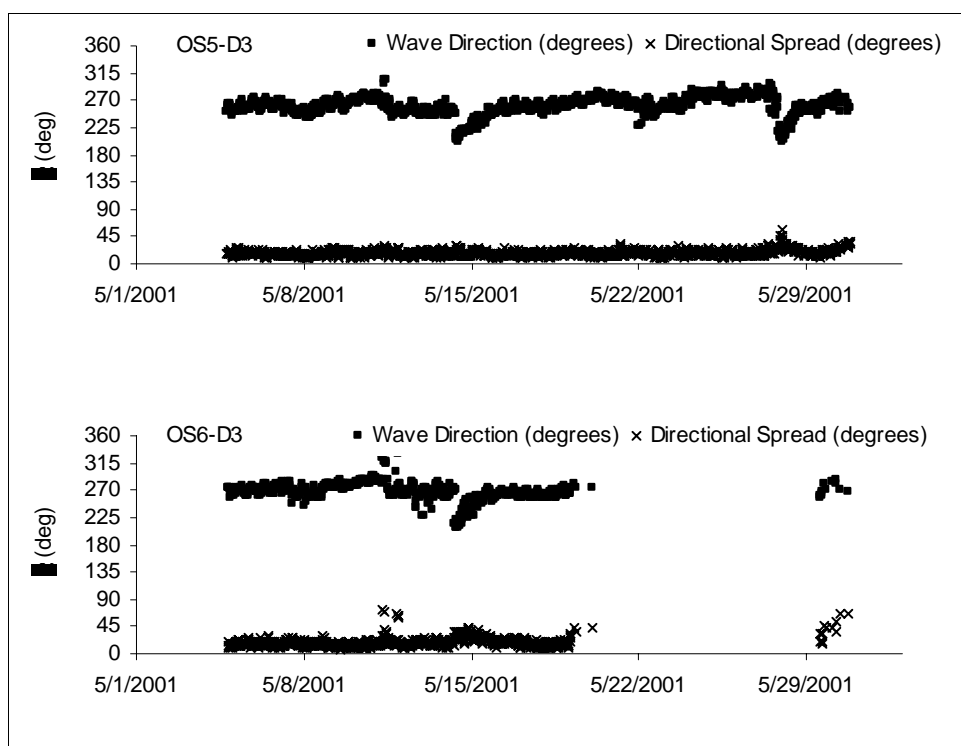
Figure D29.   HESTT wave direction measurements, Deployment 3, 1-30 May
2001
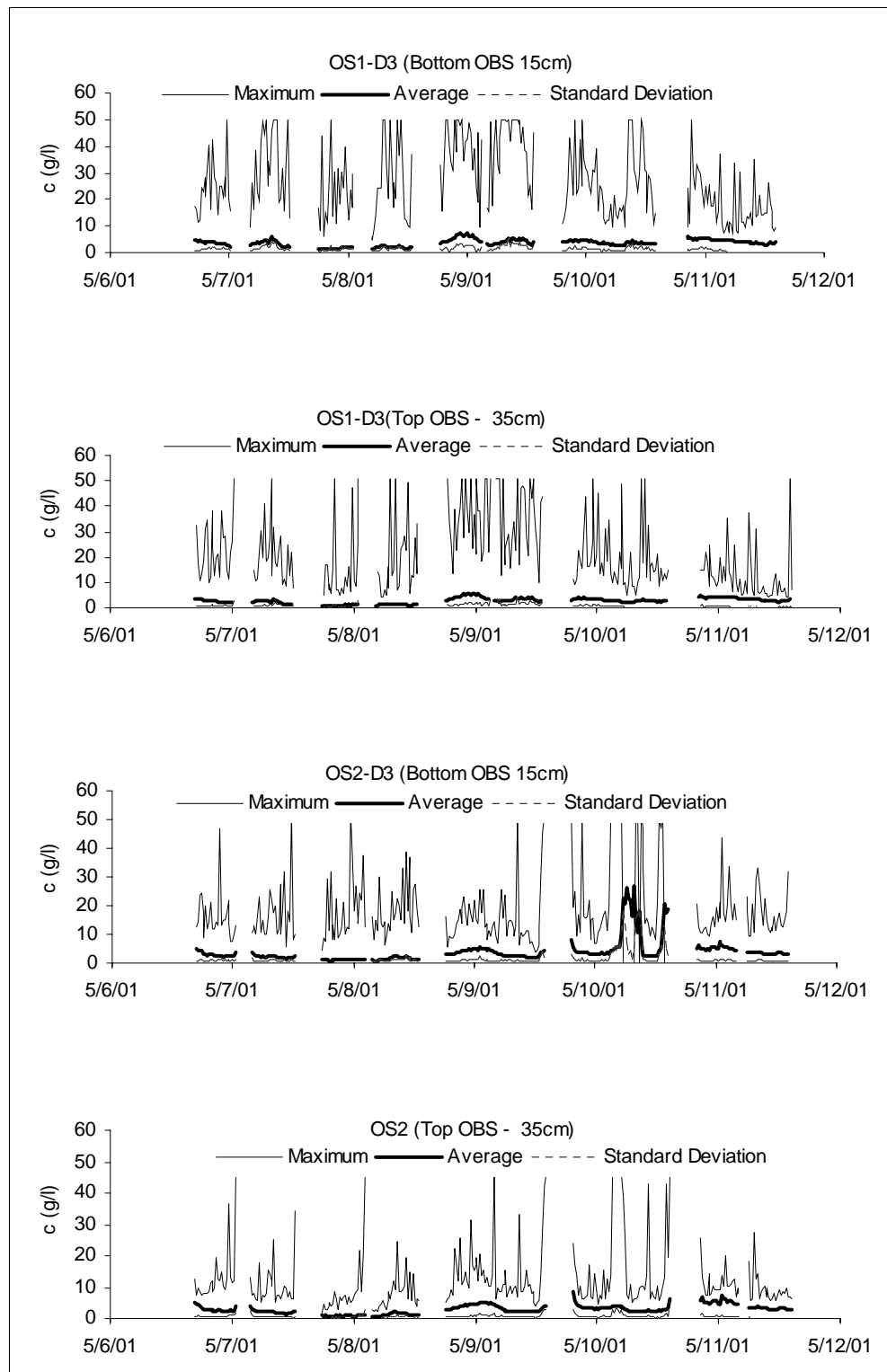
Figure D30. SIDSEP SSC measurements, Deployment 3, 6-12 May 2001
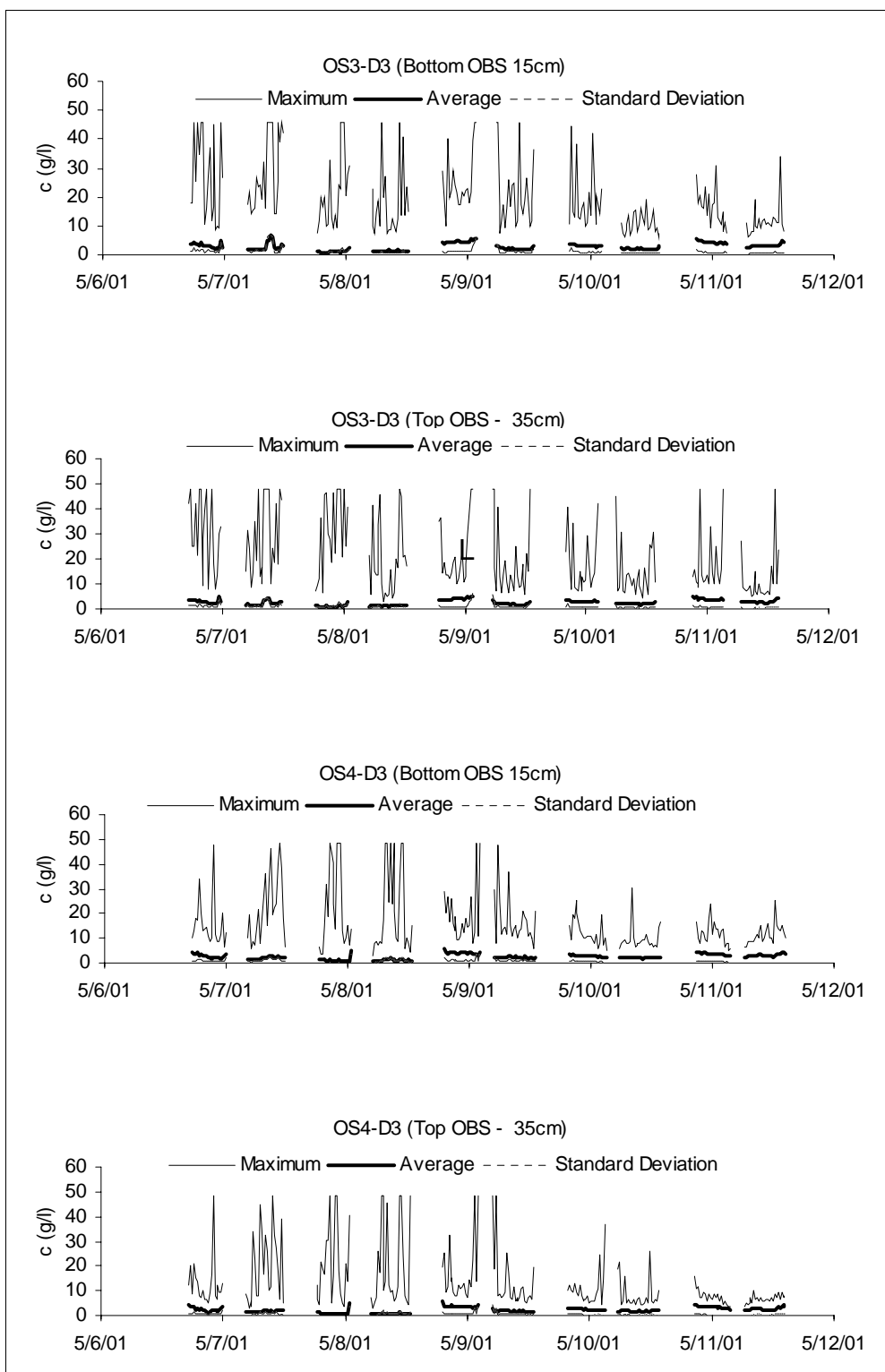
Figure D31. SIDSEP SSC measurements, Deployment 3, 6-12 May 2001
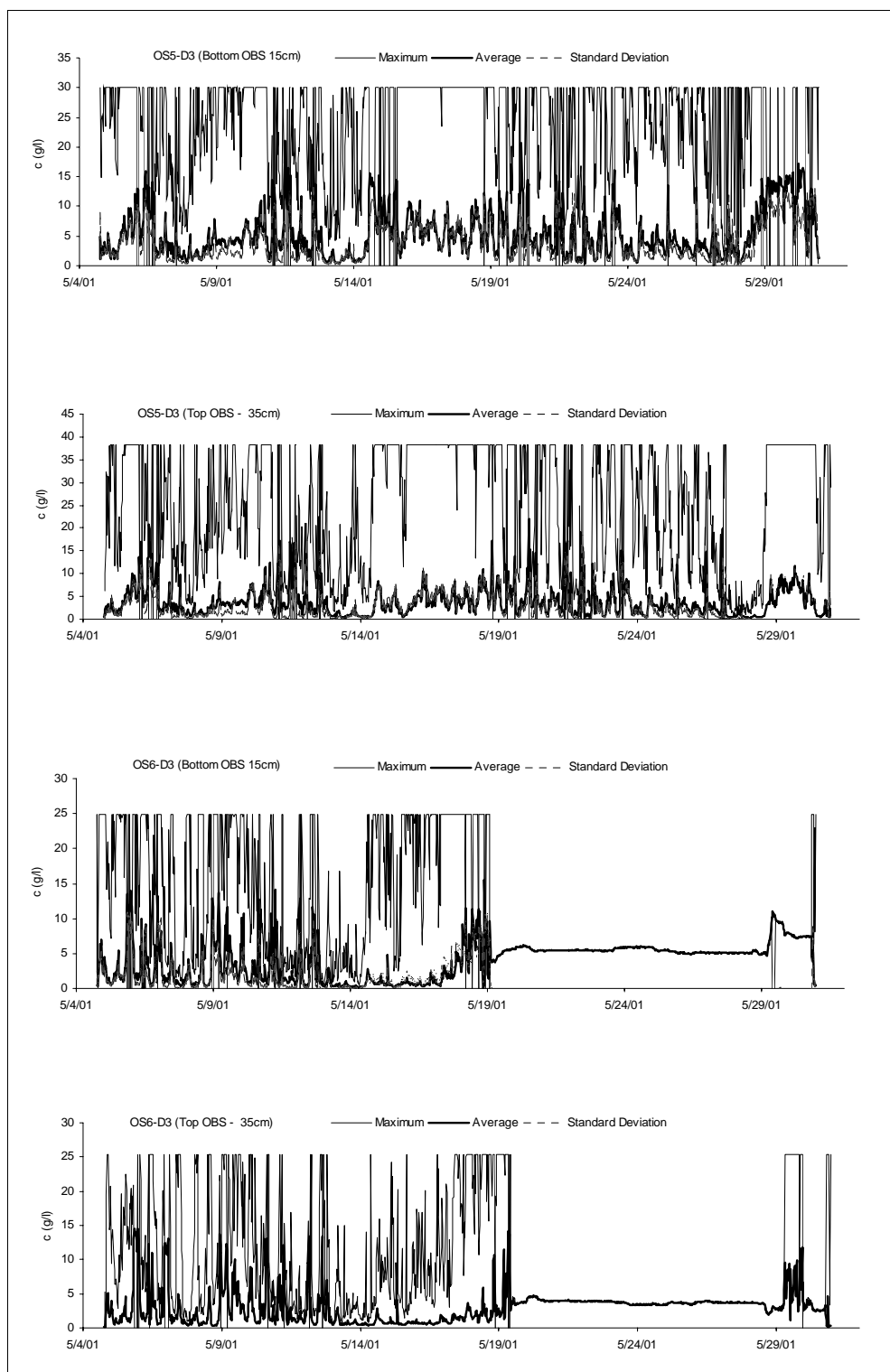
Figure D32. HESTT SSC measurements, Deployment 3, 1-30 May 2001

2002 Deployment
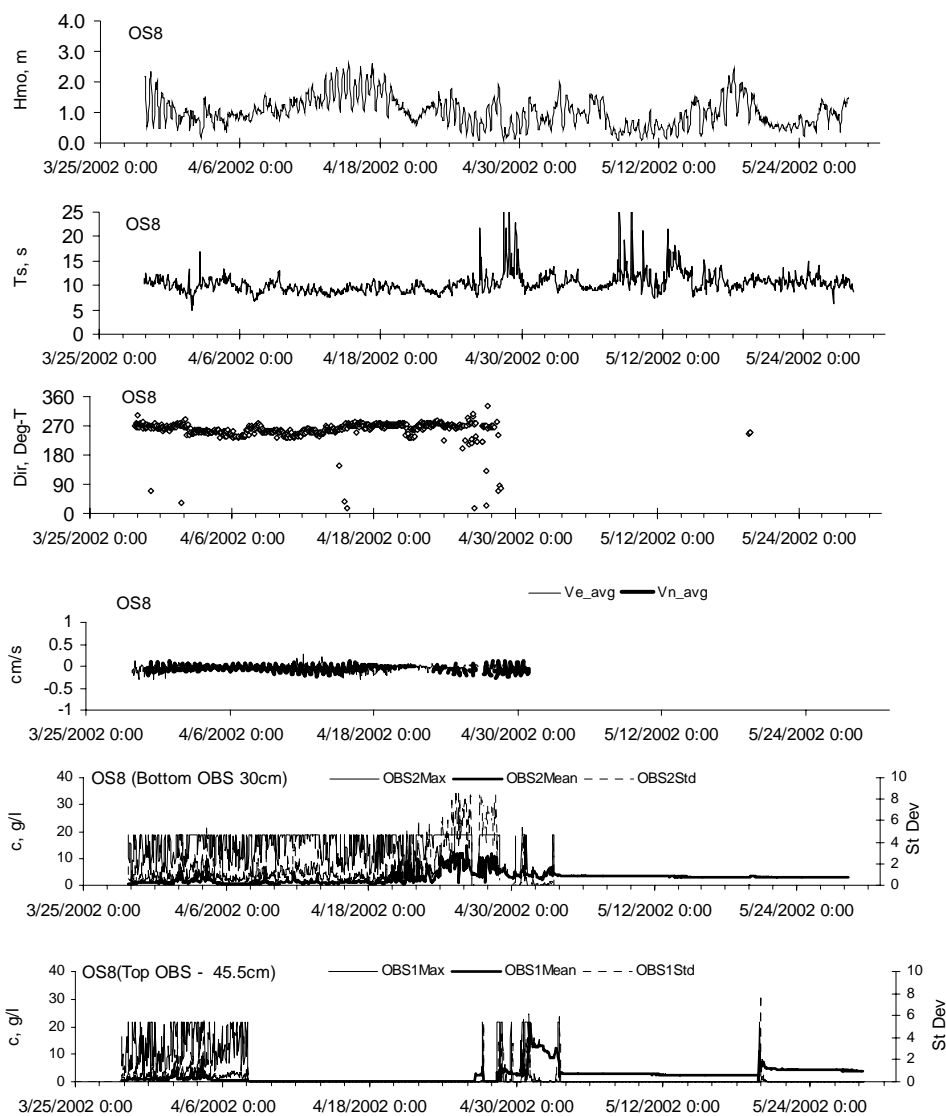
Figure D33.   HESTT (sta OS 8) deployment measurements, 29 March to
30 May 2002
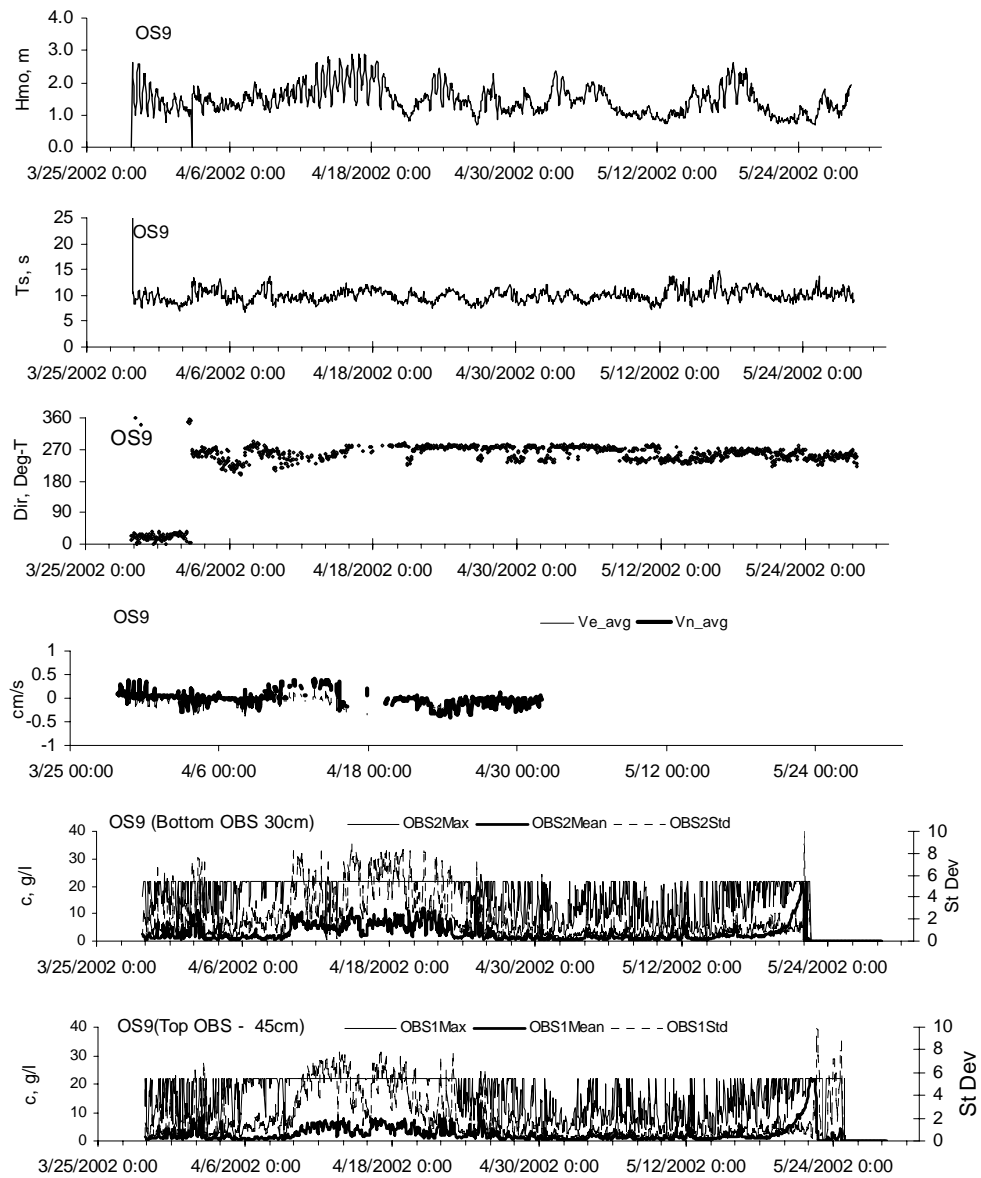
Figure D34.   HESTT (sta OS 9) deployment measurements, 29 March to
30 May 2002
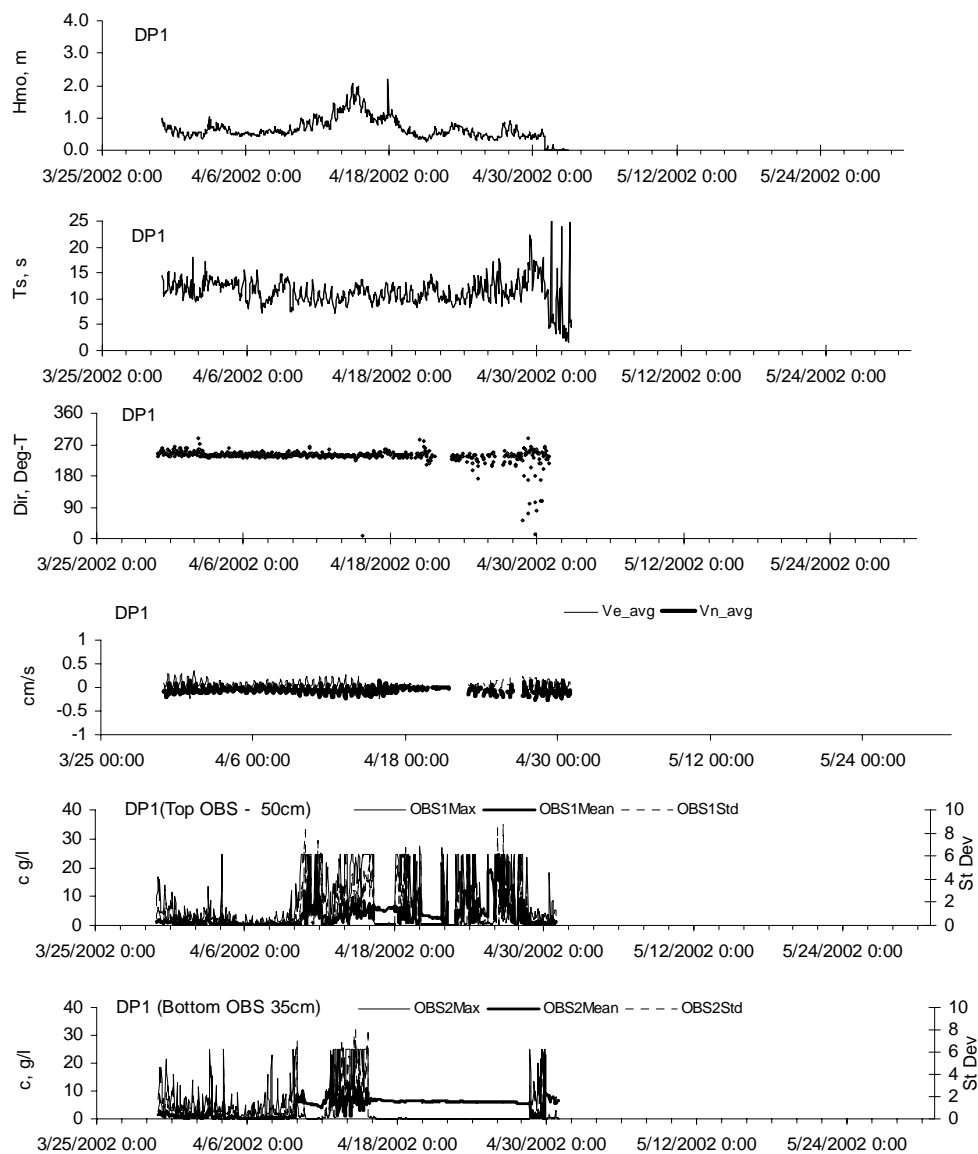
Figure D35.   Hydra platform (sta DP 1) deployment measurements, 29 March to
2 May 2002
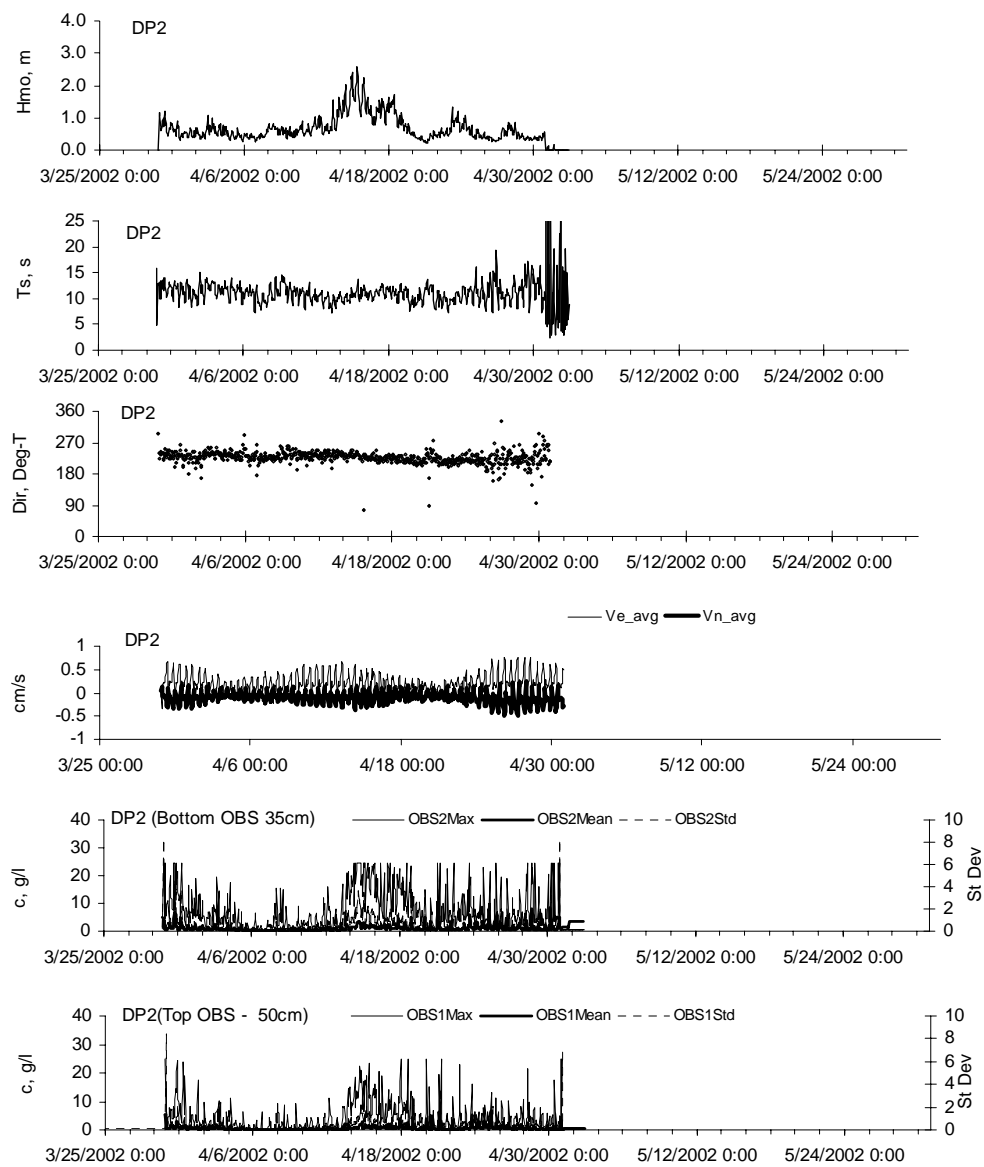
Figure D36.   Hydra platform (sta DP 2) deployment measurements, 29 March to 2 May 2002
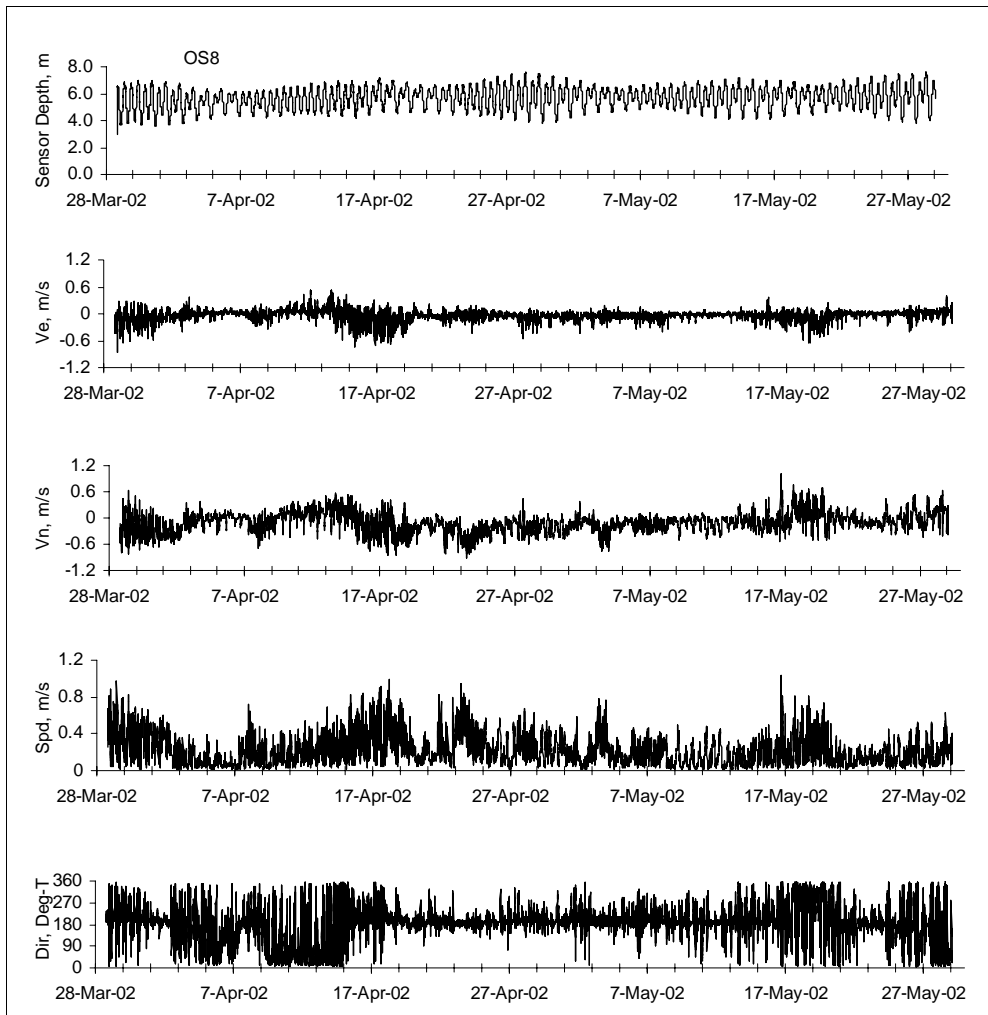
Figure D37.   HESTT (sta OS 8) ADP deployment measurements, 29 March to 30 May 2002
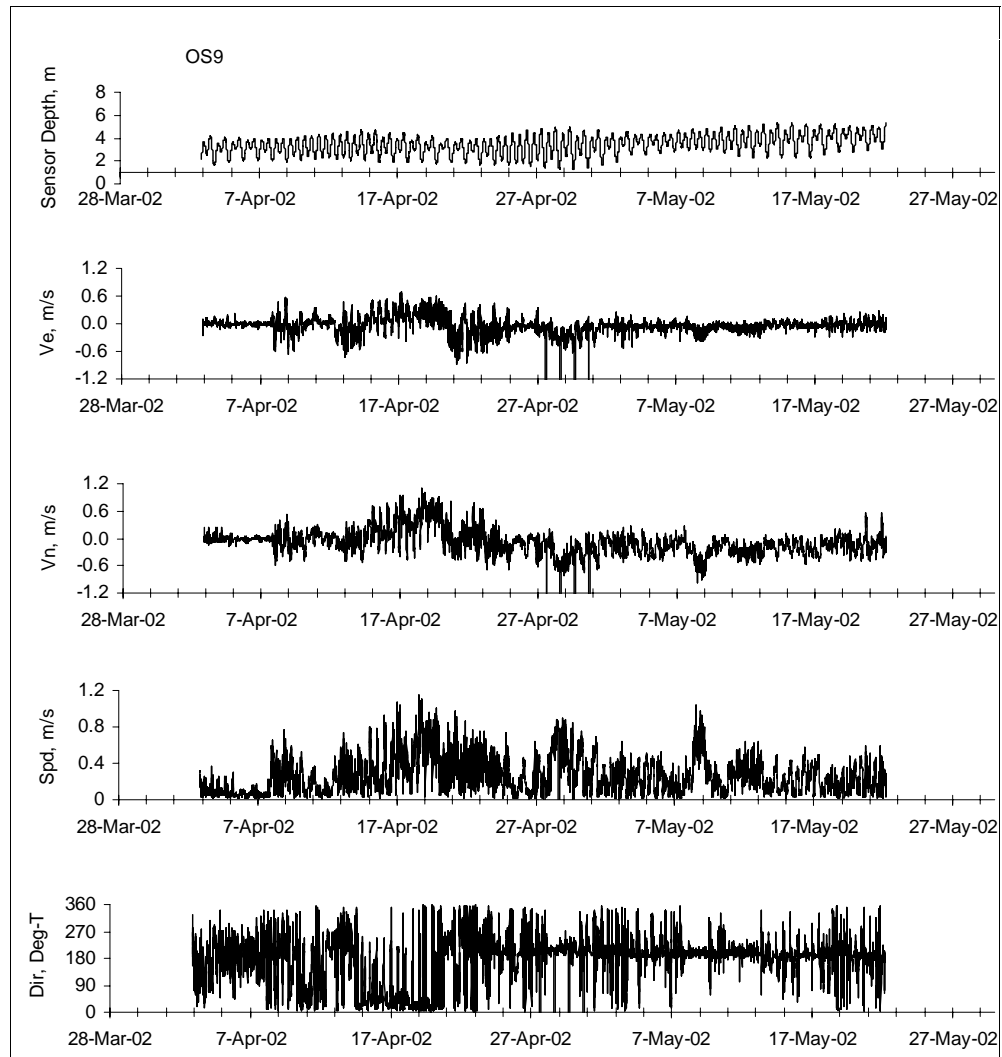
Figure D38.   HESTT (sta OS 9) ADP deployment measurements, 29 March to 30 May 2002

Figures D39 to D100

ADP Current Transect Data
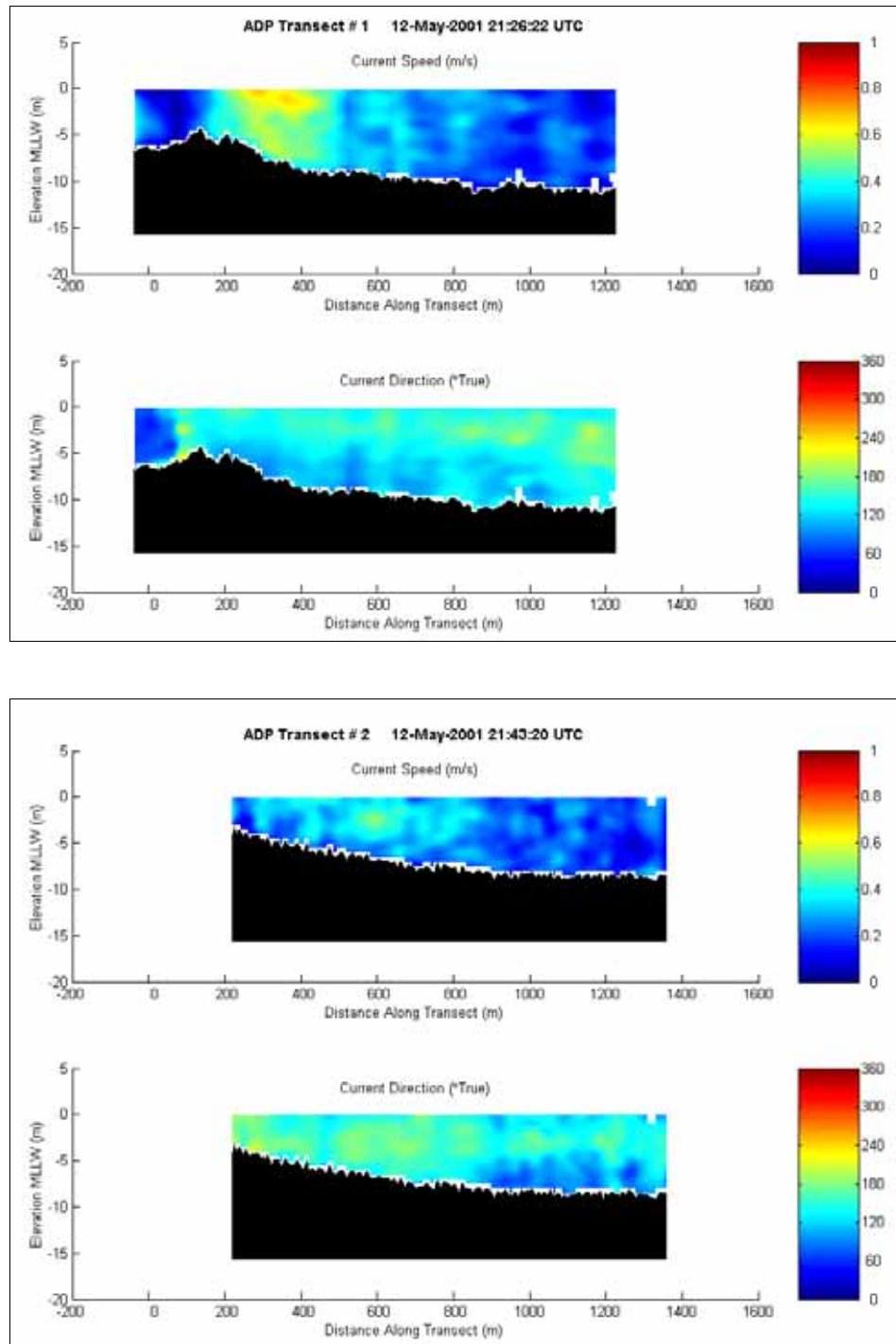
Figure D39.   Current speed and direction at ADP Transect 1 at 2126 (upper)
and Transect 2 at 2143 (lower) on 12 May 2001
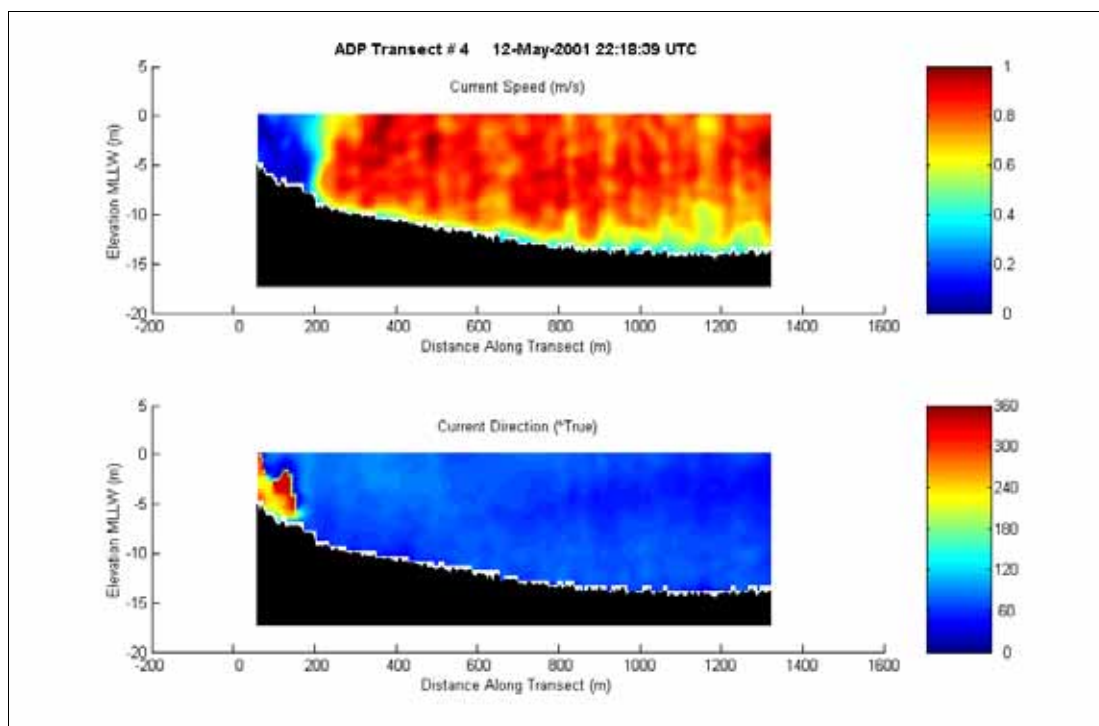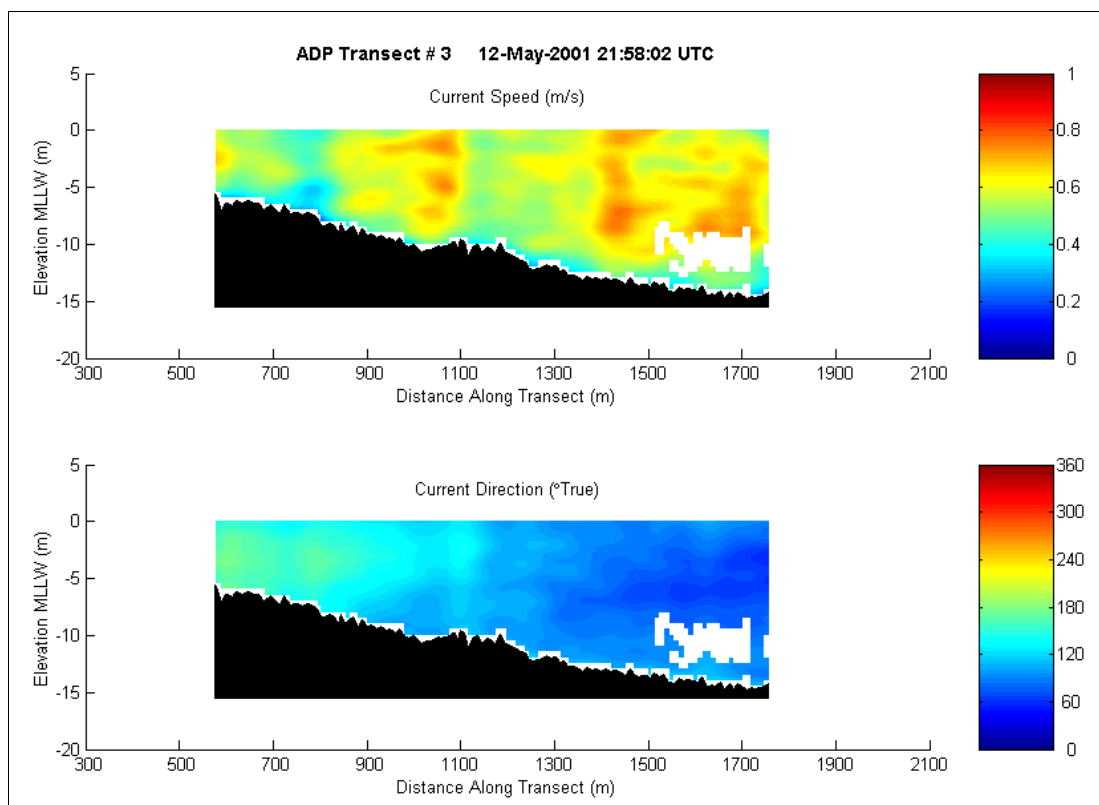
Figure D40.   Current speed and direction at ADP Transect 3 at 2158 (upper)
             and Transect 4 at 2118 (lower) on 12 May 2001
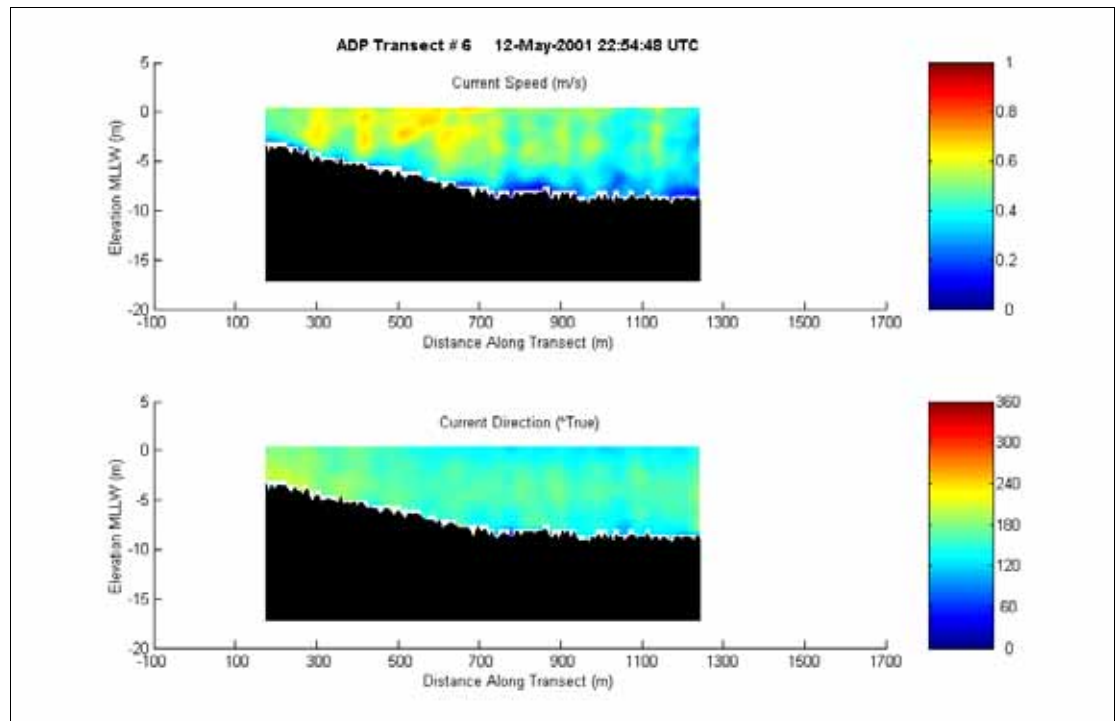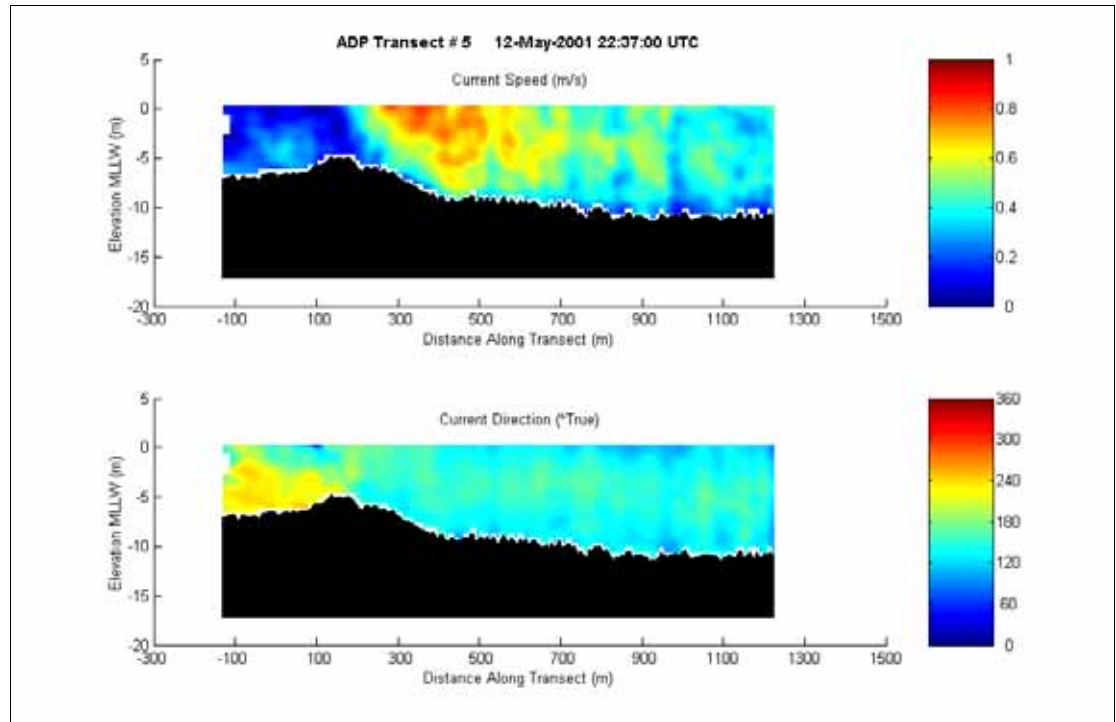
Figure D41.   Current speed and direction at ADP Transect 5 at 2237 (upper)
and Transect 6 at 2254 (lower) on 12 May 2001
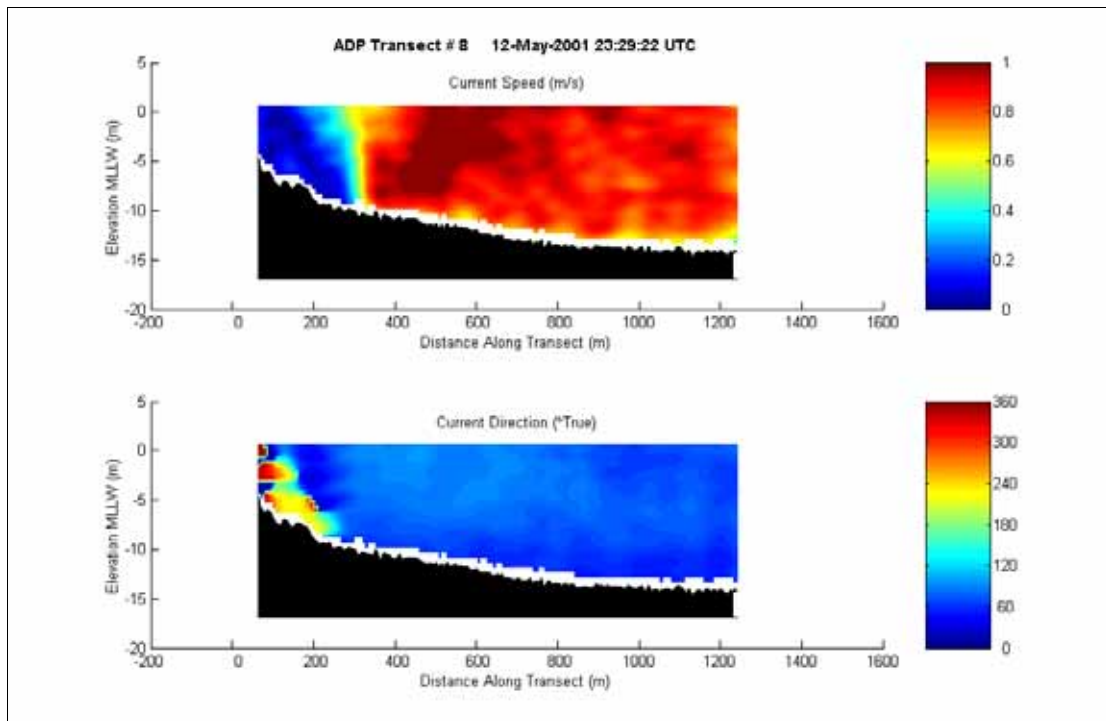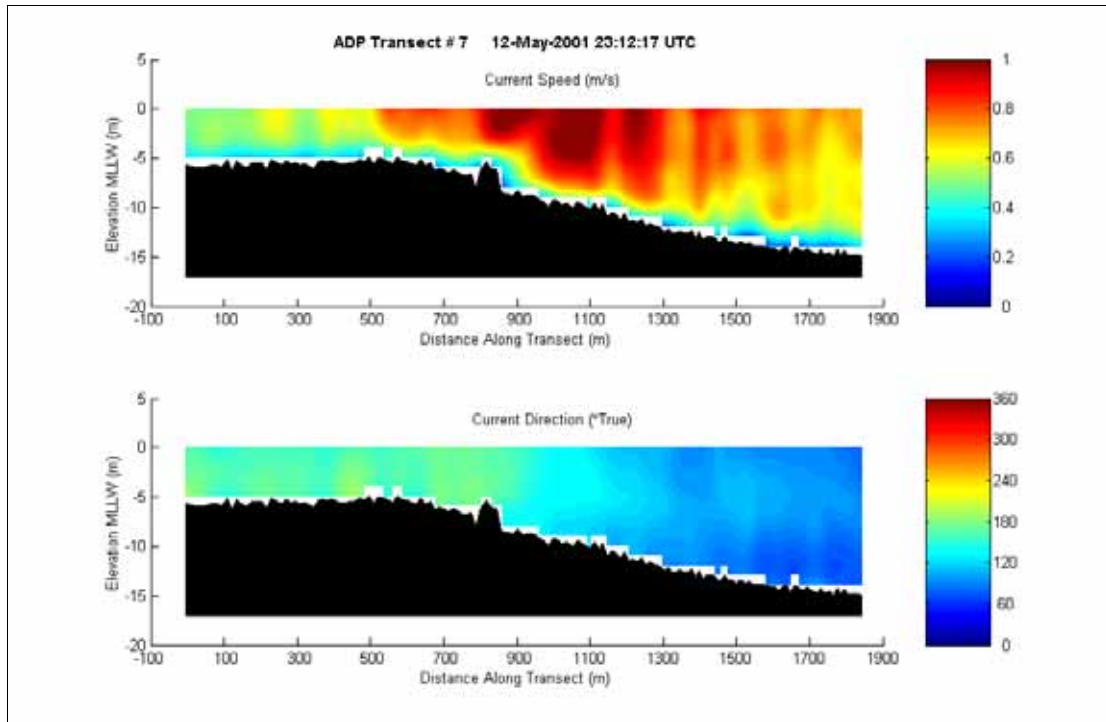
Figure D42.   Current speed and direction at ADP Transect 7 at 2312 (upper)
and Transect 8 at 2329 (lower) on 12 May 2001
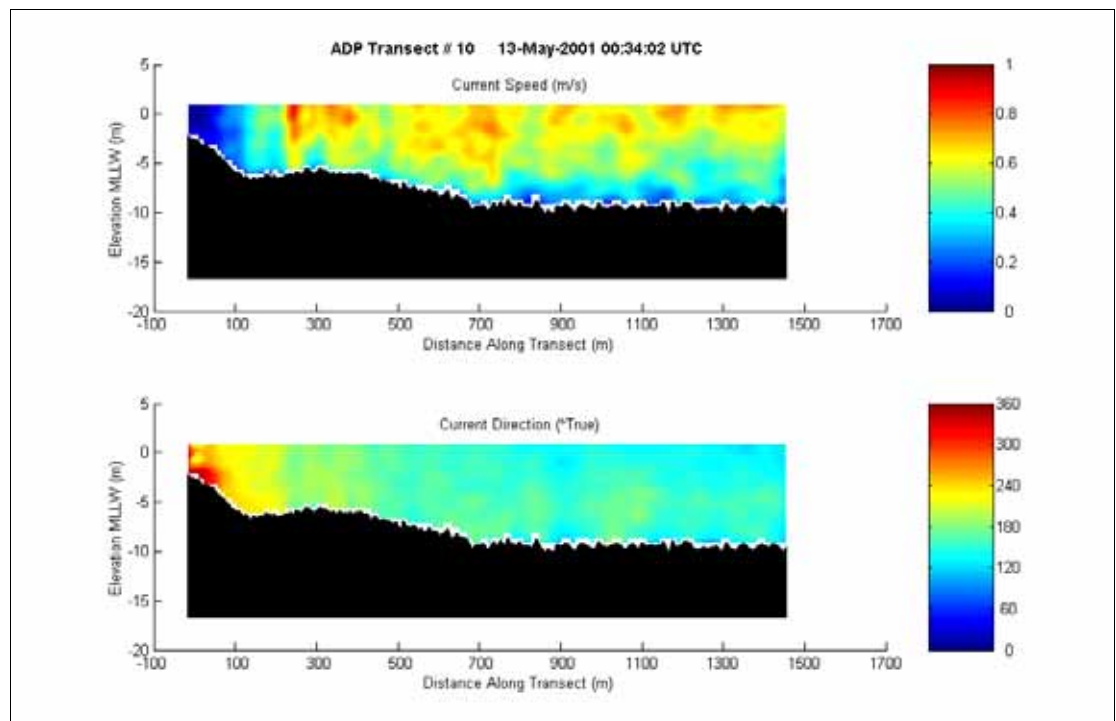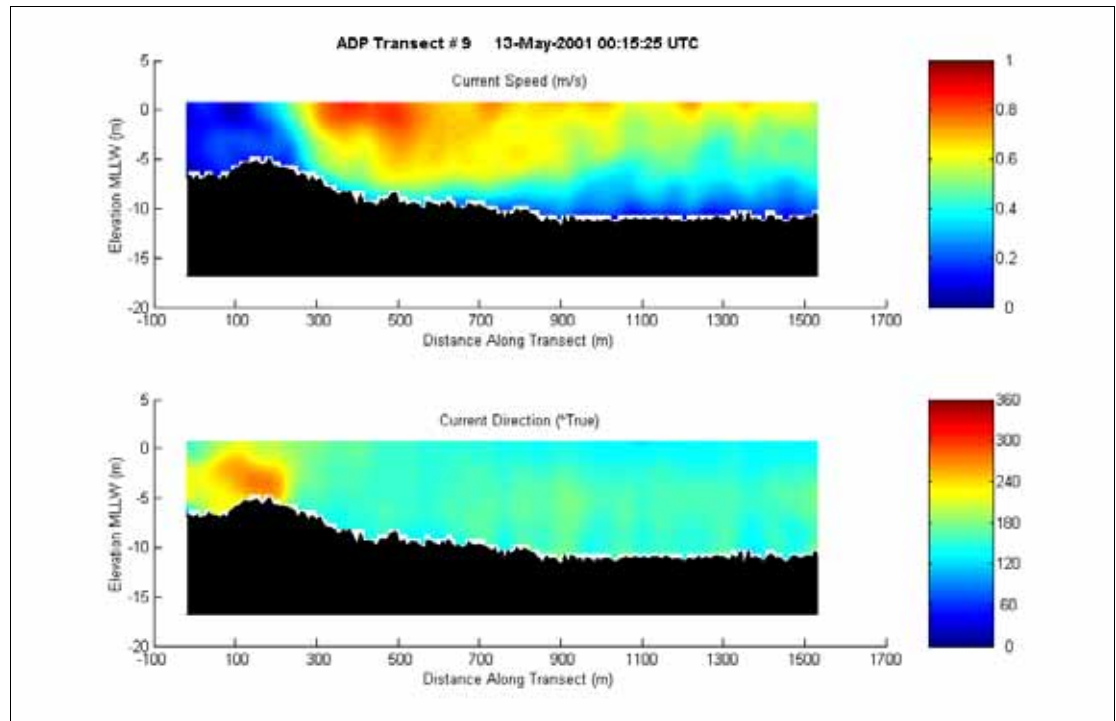
Figure D43.   Current speed and direction at ADP Transect 9 at 0015 (upper) and Transect 10 at 0034 (lower) on 13 May 2001
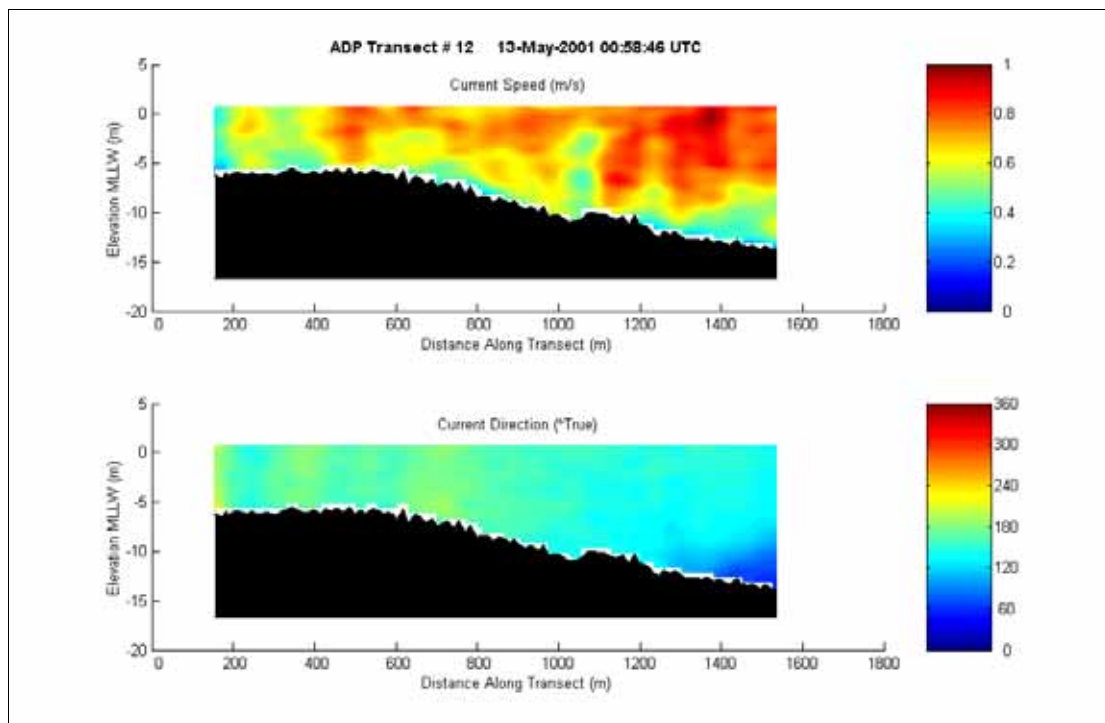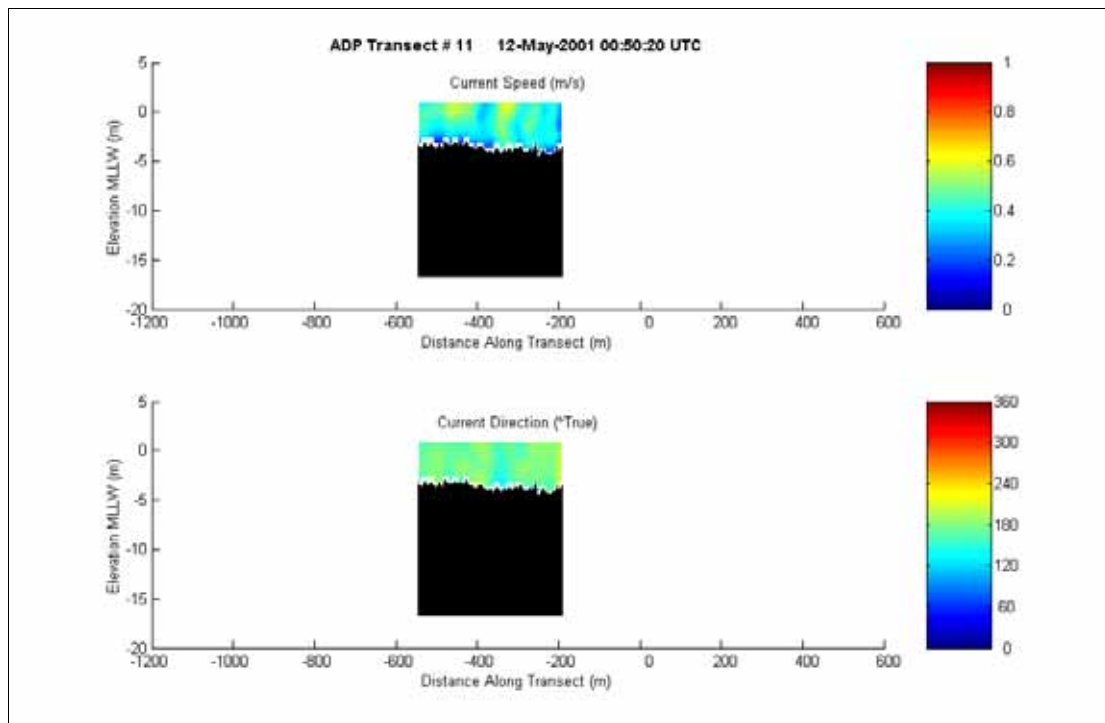
Figure D44.   Current speed and direction at ADP Transect 11 at 0050 (upper)
                       on 12 May 2001 and Transect 12 at 0058 (lower) on 13 May 2001
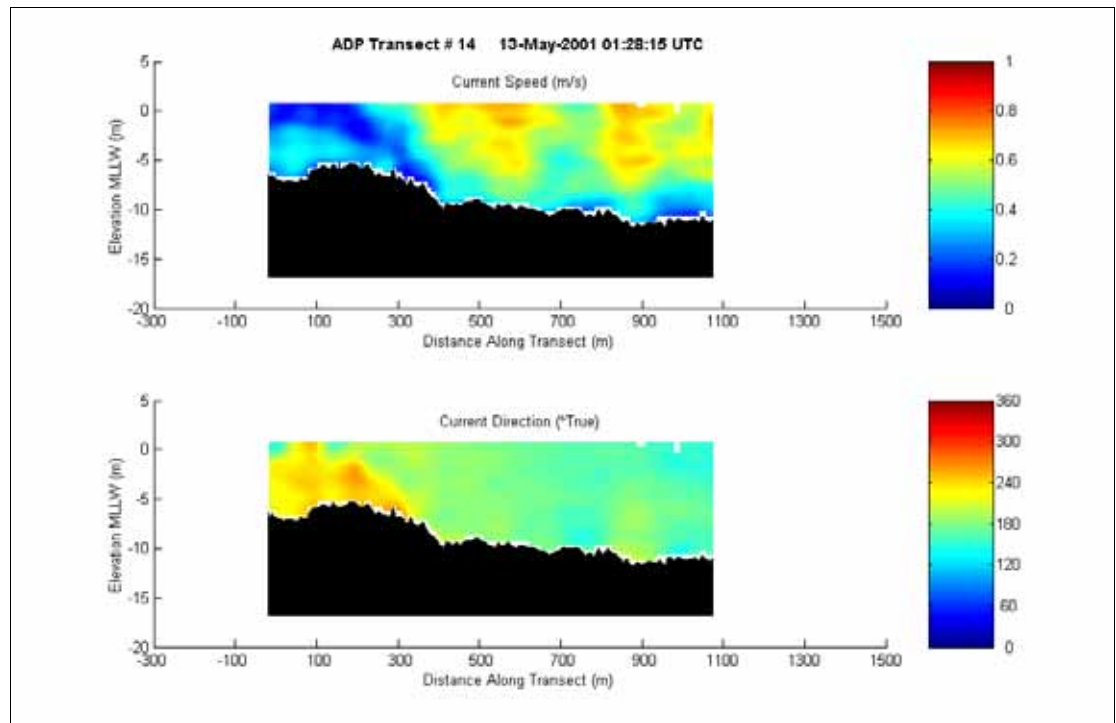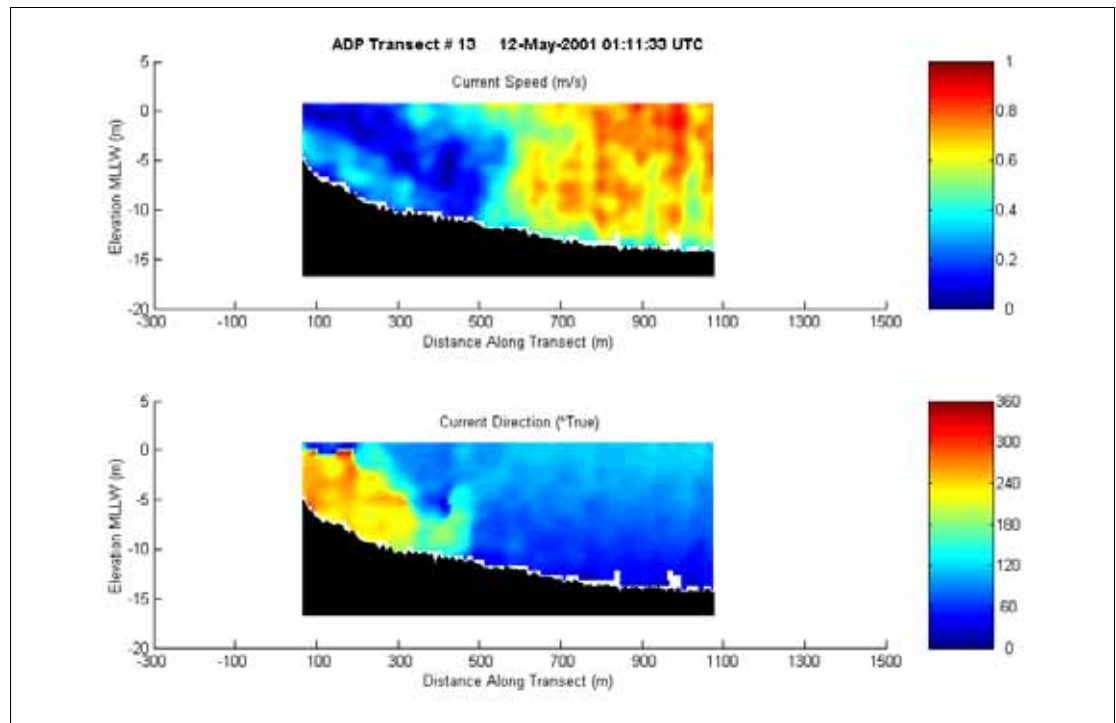
Figure D45.   Current speed and direction at ADP Transect 13 at 0111 (upper)
and Transect 14 at 0128 (lower) on 13 May 2001
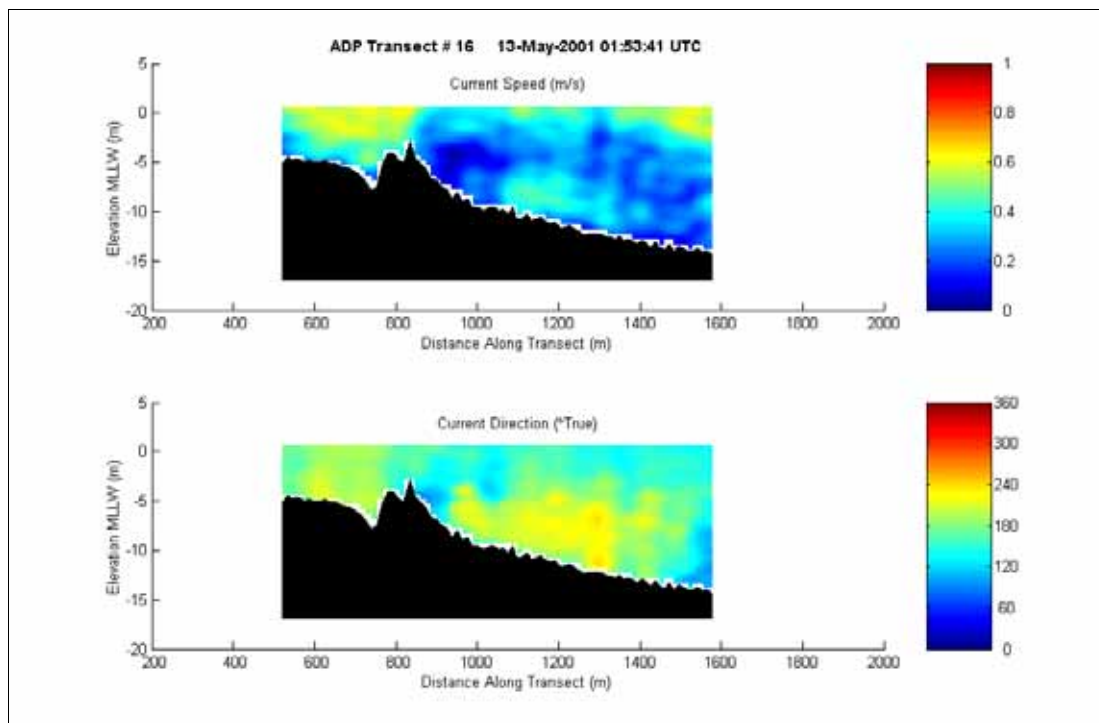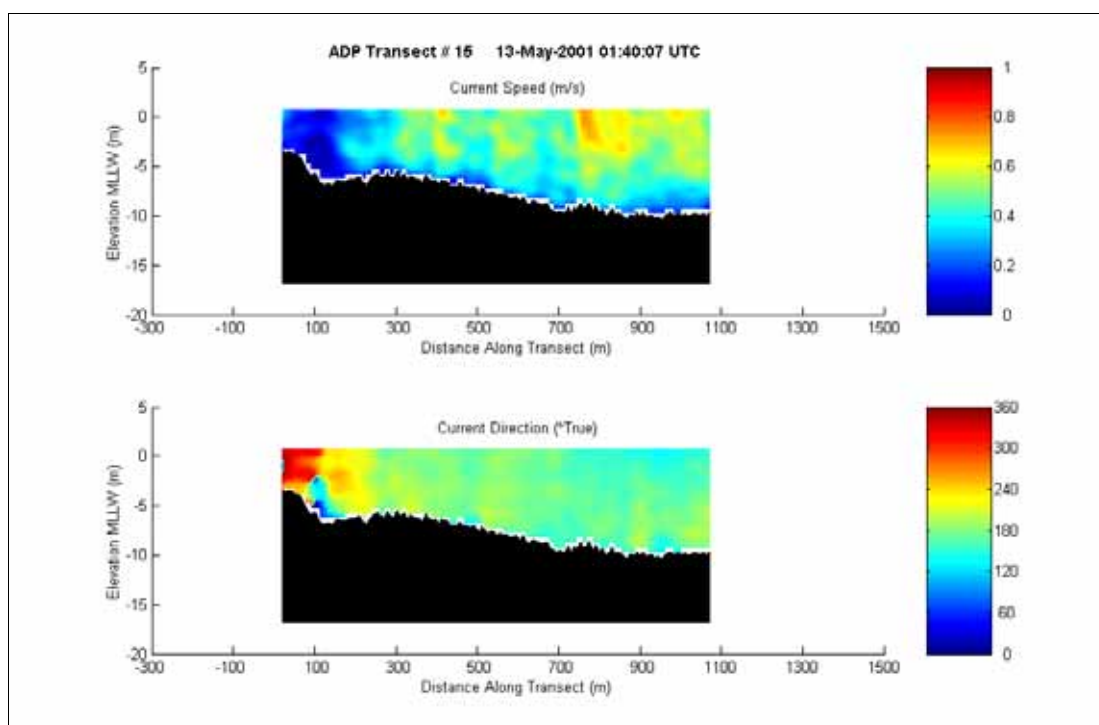
Figure D46. Current speed and direction at ADP Transect 15 at 0140 (upper) and Transect 16 at 0153 (lower) on 13 May 2001
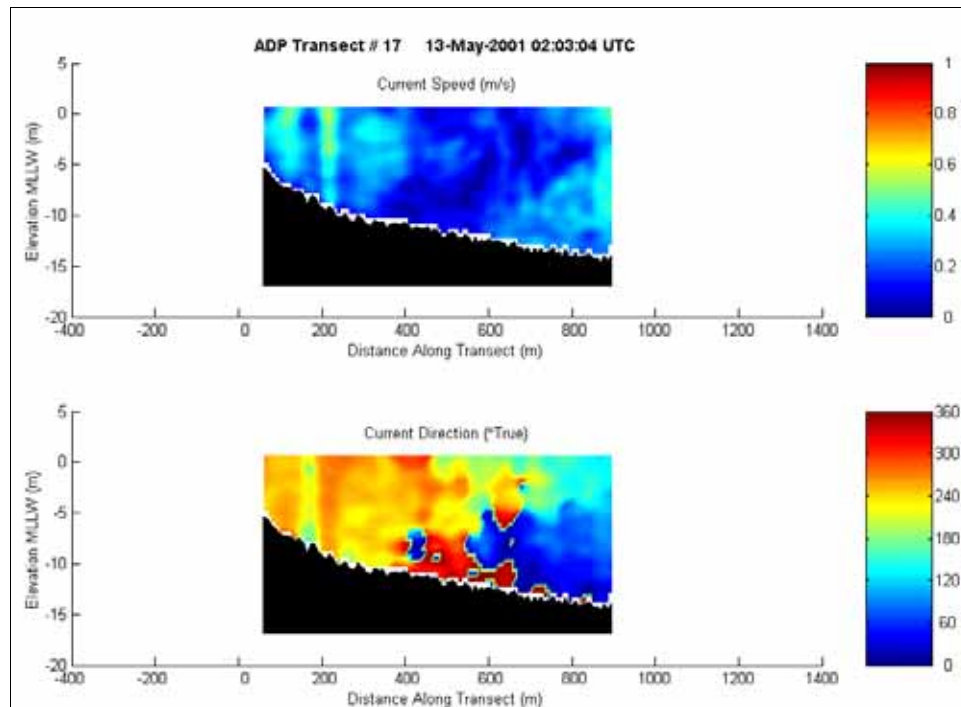
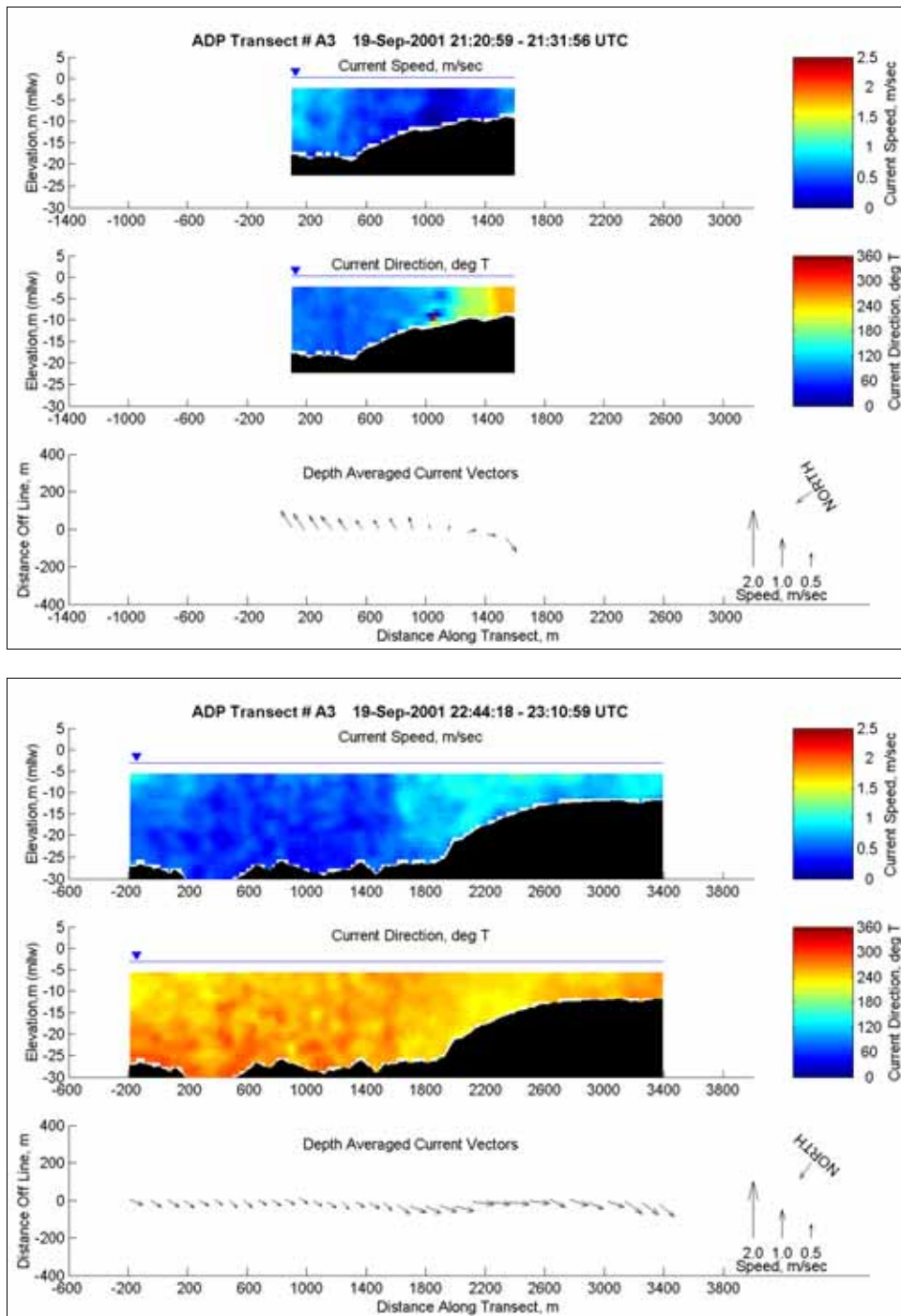Figure D47.   Current speed and direction at ADP Transect 17 at 0203 on
13 May 2001
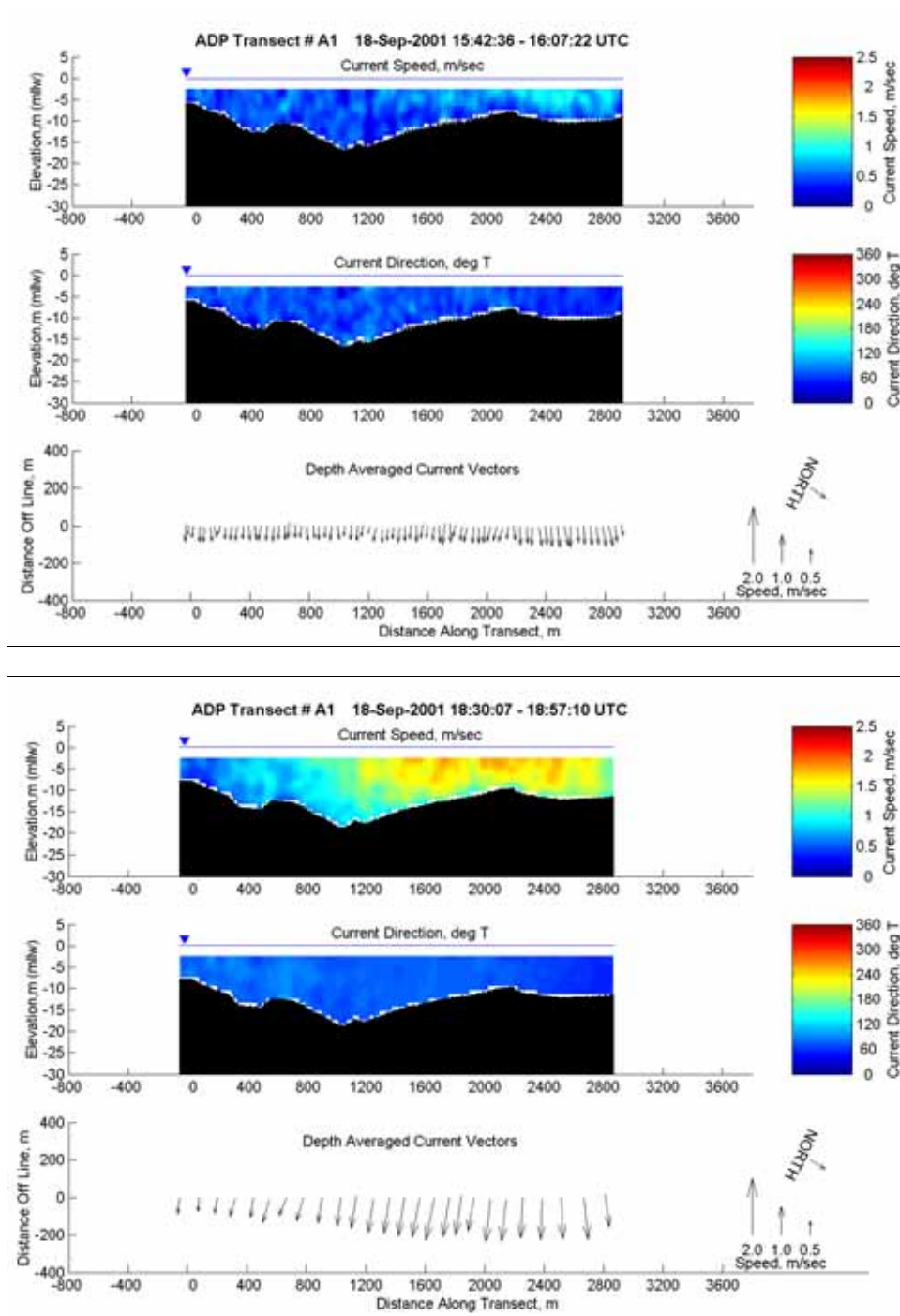
Figure D48.   Current speed, direction, and depth-averaged current vectors at
            ADP Transect A1 from 1542 to 1607 (upper) and 1830 to 1857
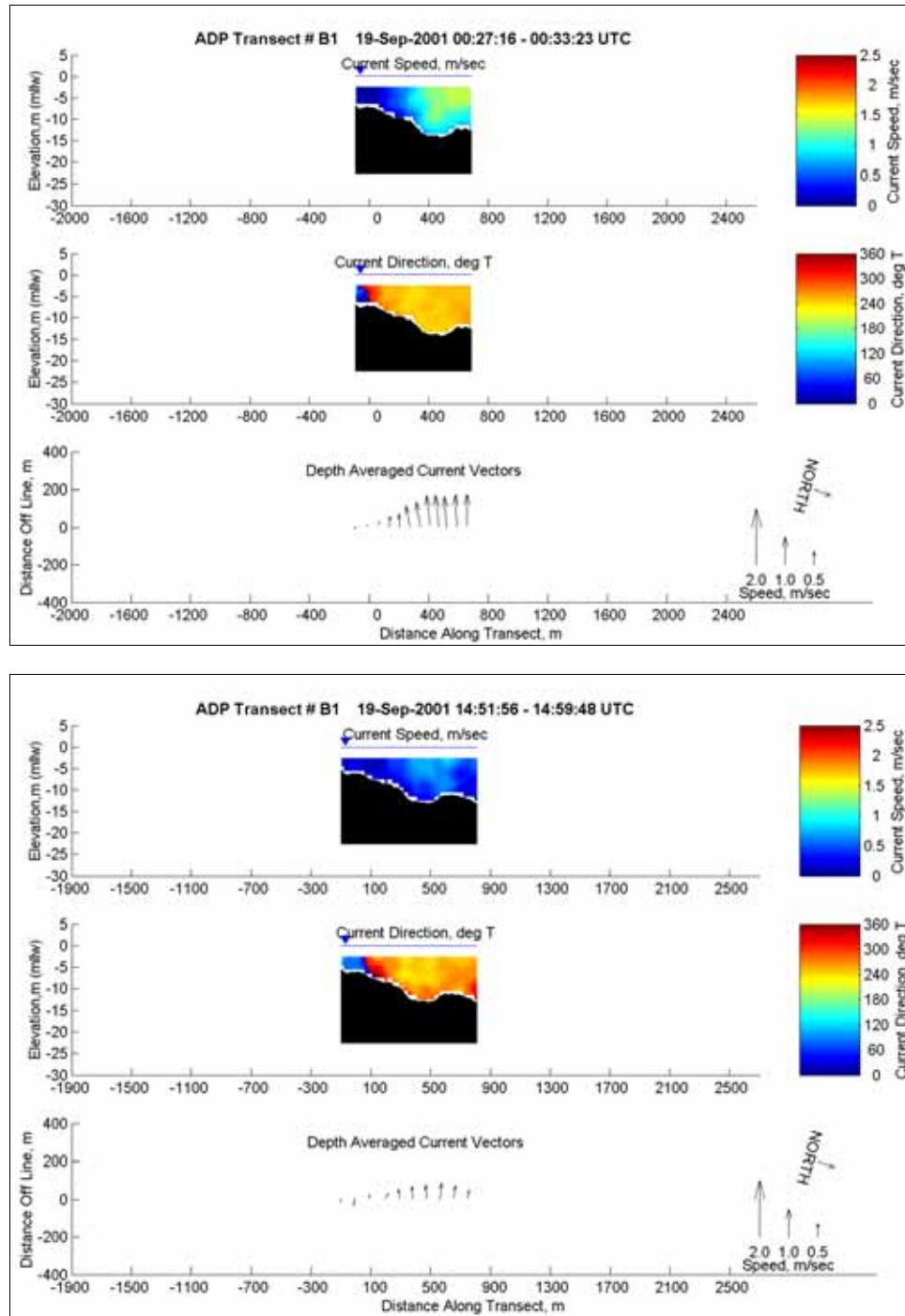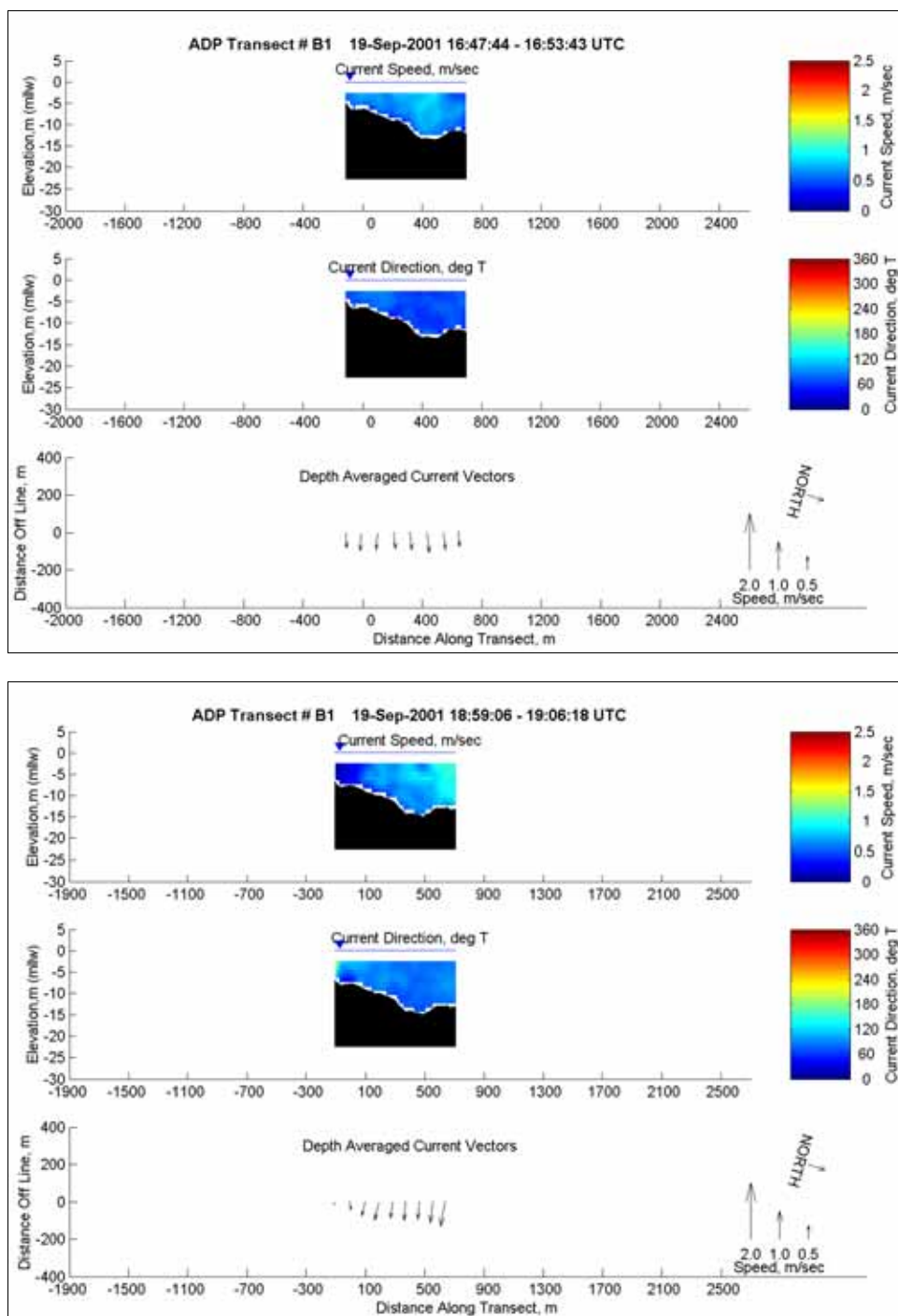   (lower) on 18 September 2001
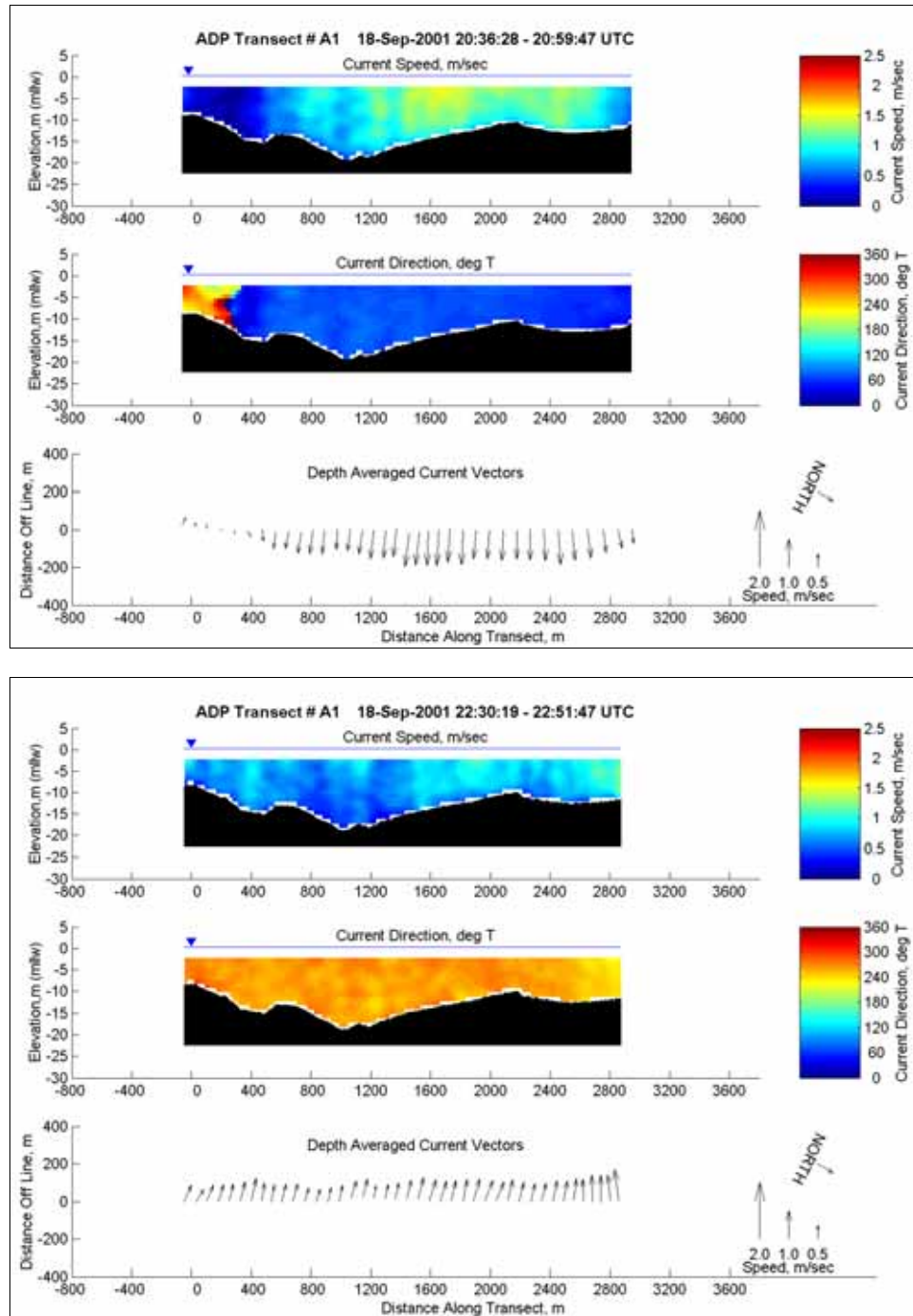
Figure D49.   Current speed, direction, and depth-averaged current vectors at ADP Transect A1 from 2036 to 2059 (upper) and 2230 to 2251 (lower) on 18 September 2001
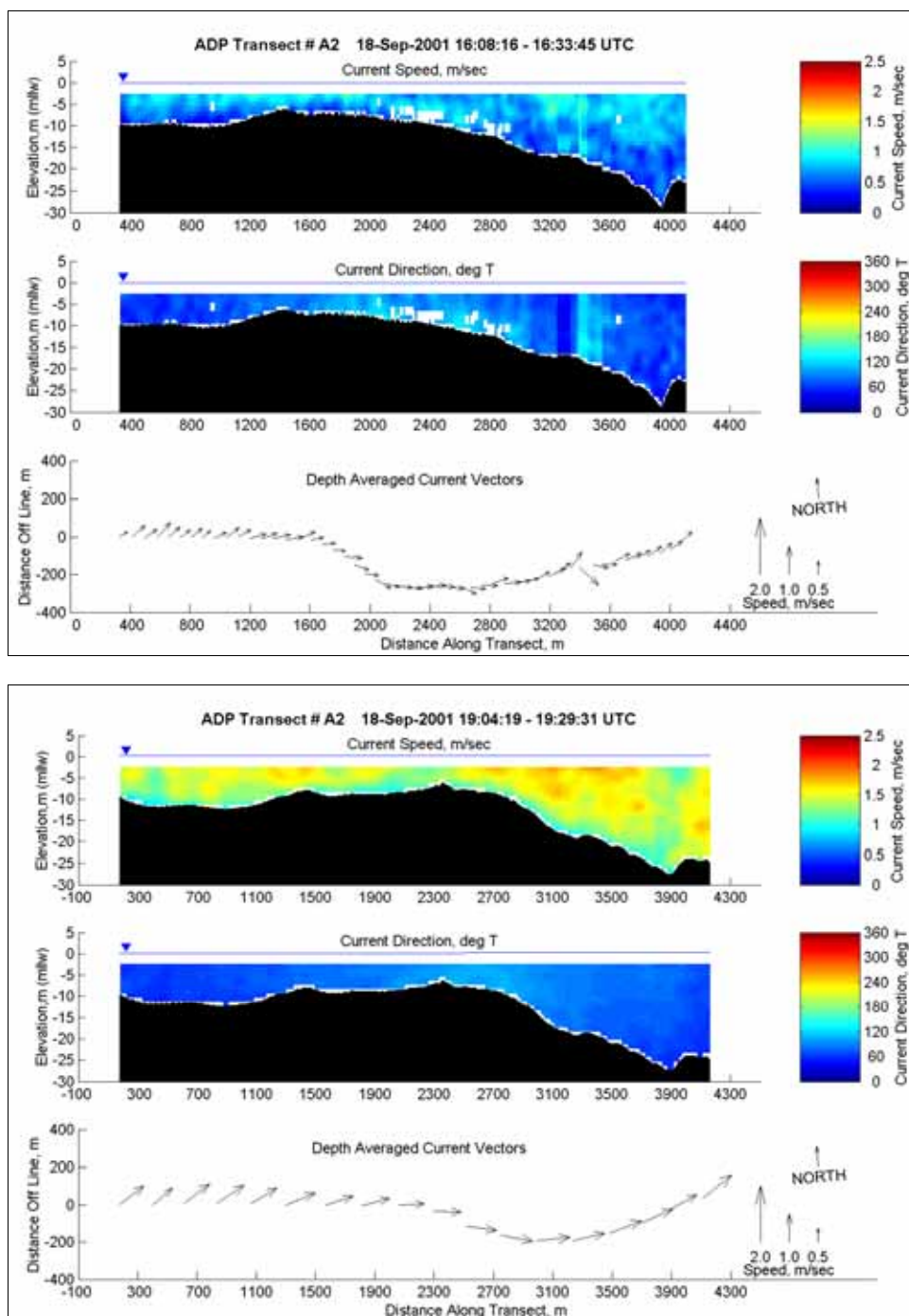
Figure D50.   Current speed, direction, and depth-averaged current vectors at
ADP Transect A2 from 1608 to 1633 (upper) and 1904 to 1929
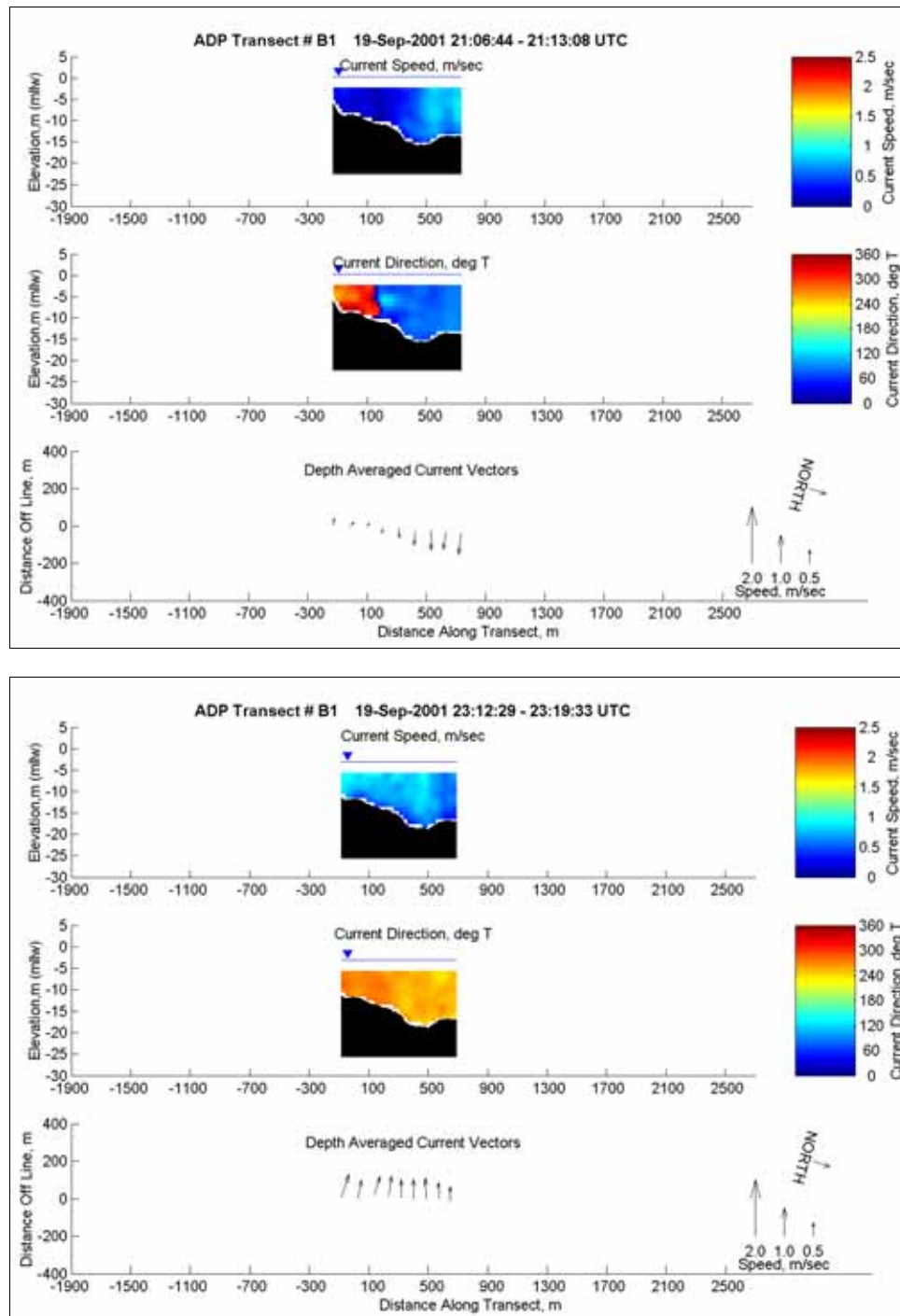(lower) on 18 September 2001
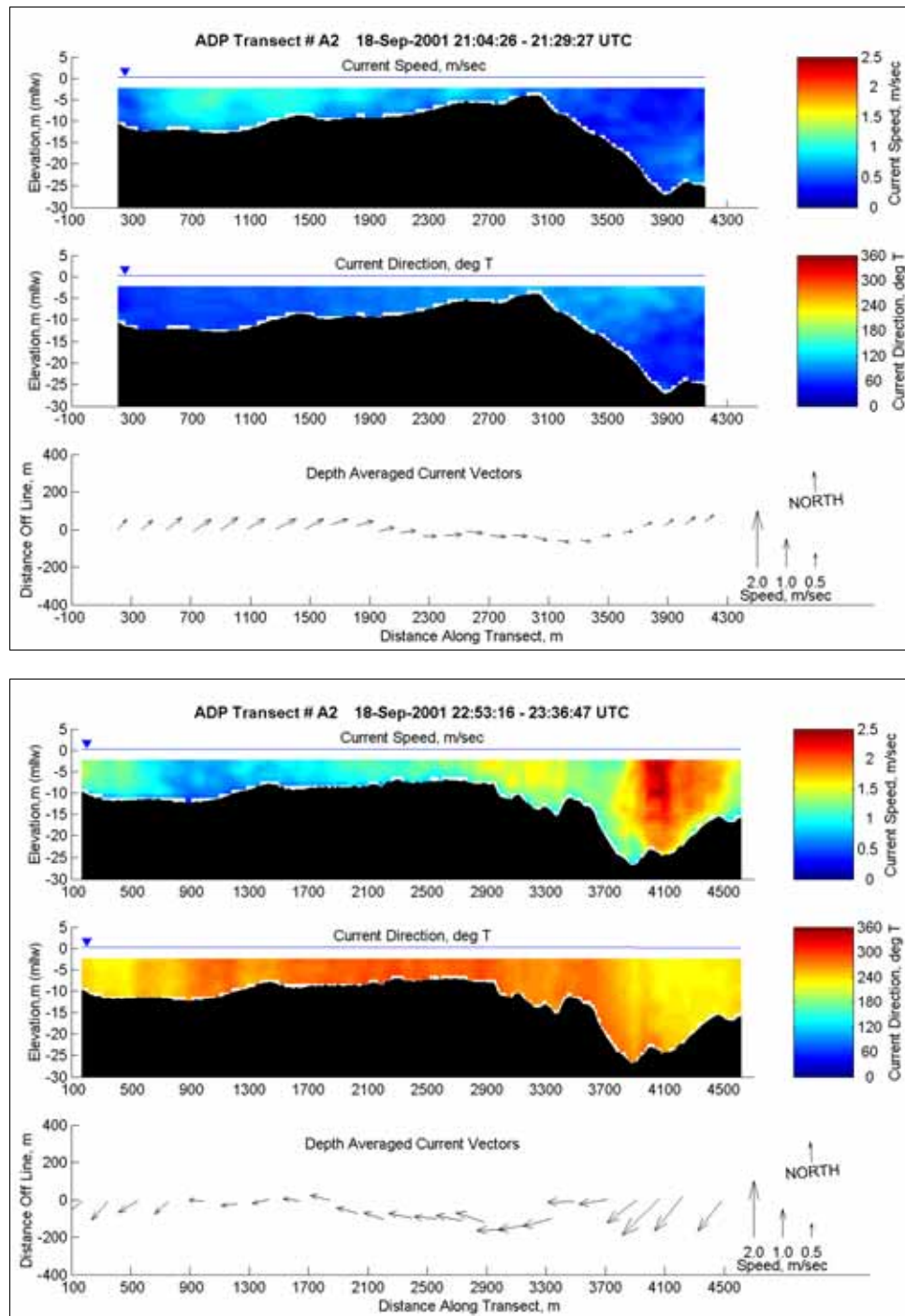
Figure D51. Current speed, direction, and depth-averaged current vectors at ADP Transect A2 from 2104 to 2129 (upper) and 2253 to 2336 (lower) on 18 September 2001
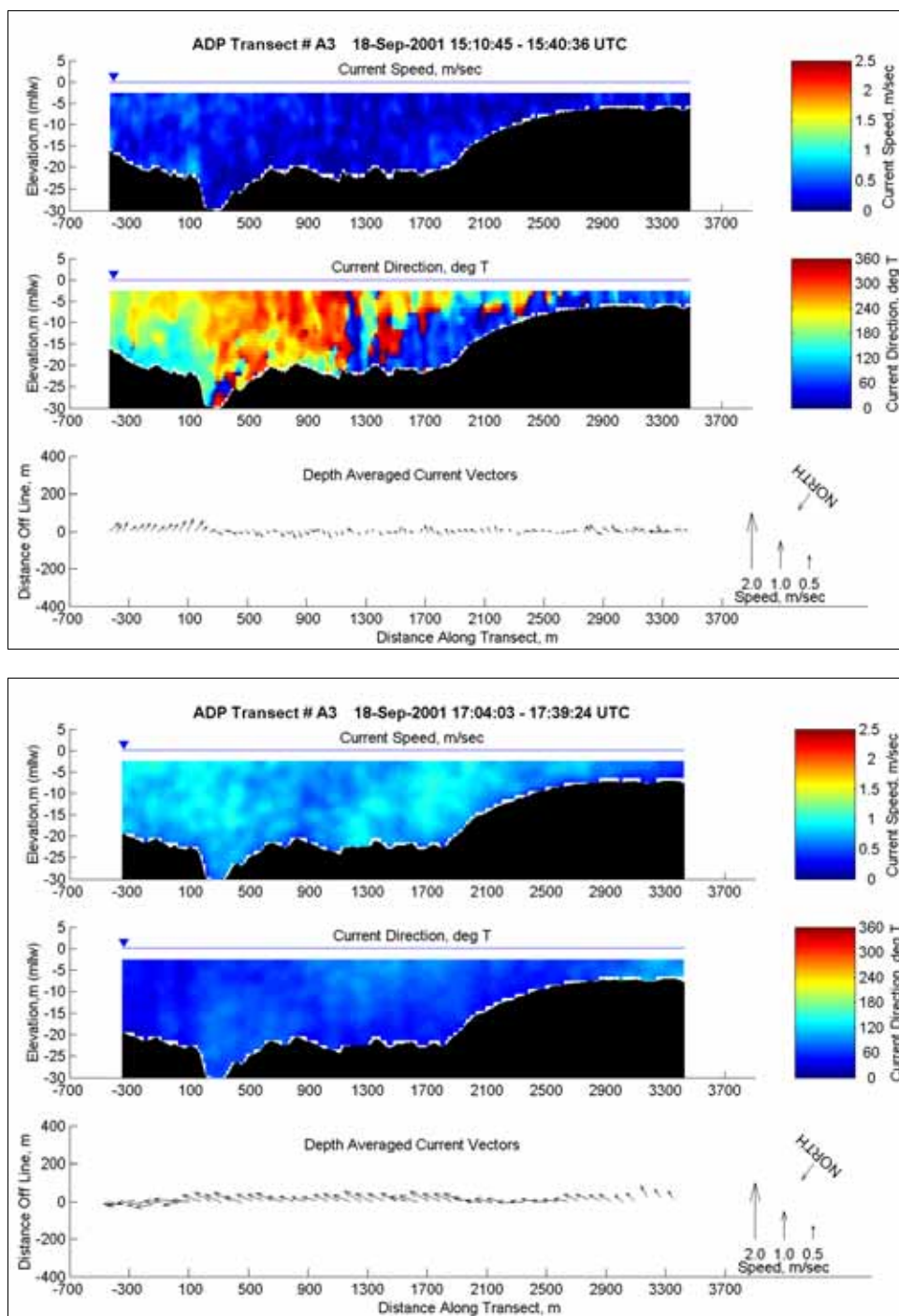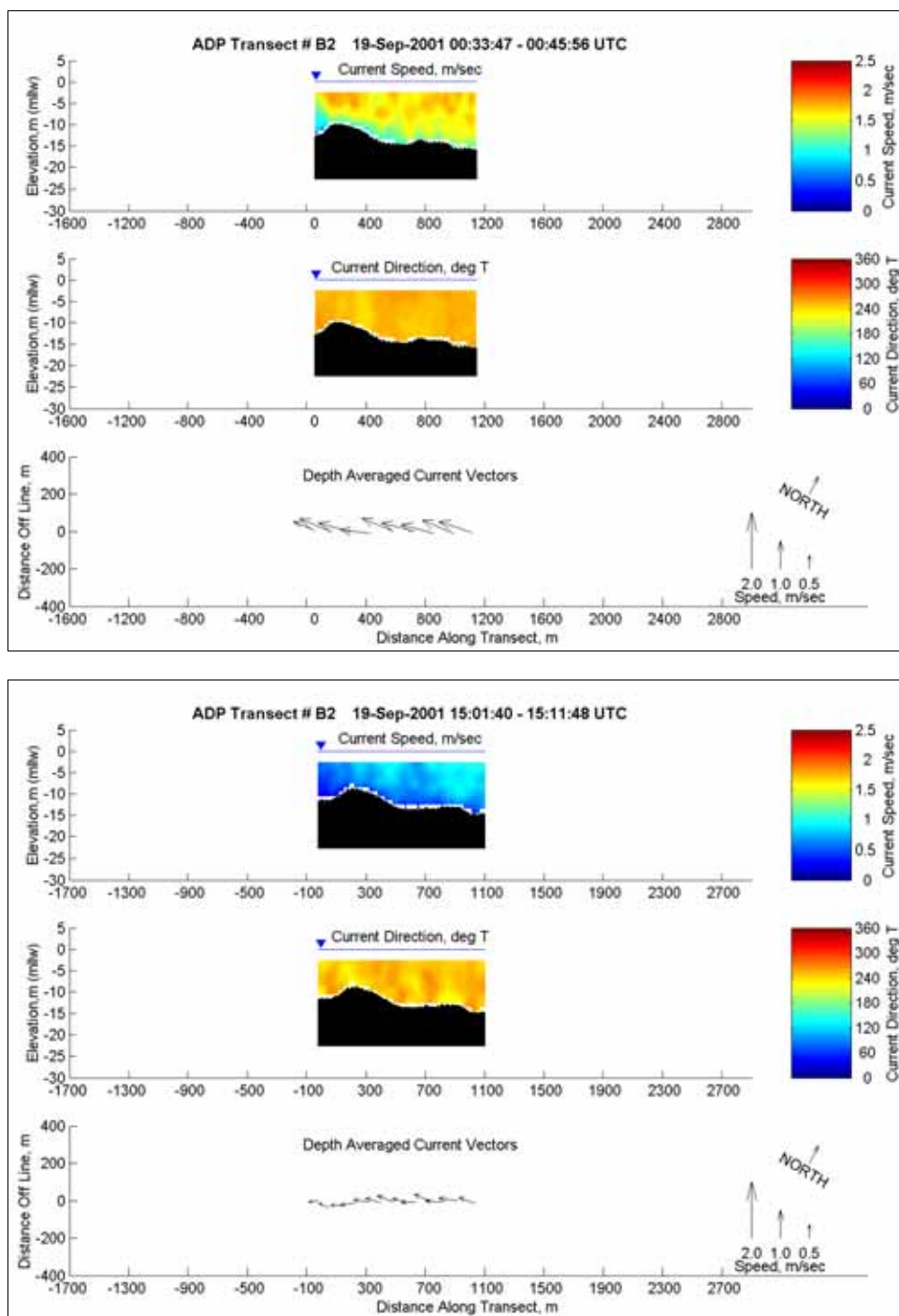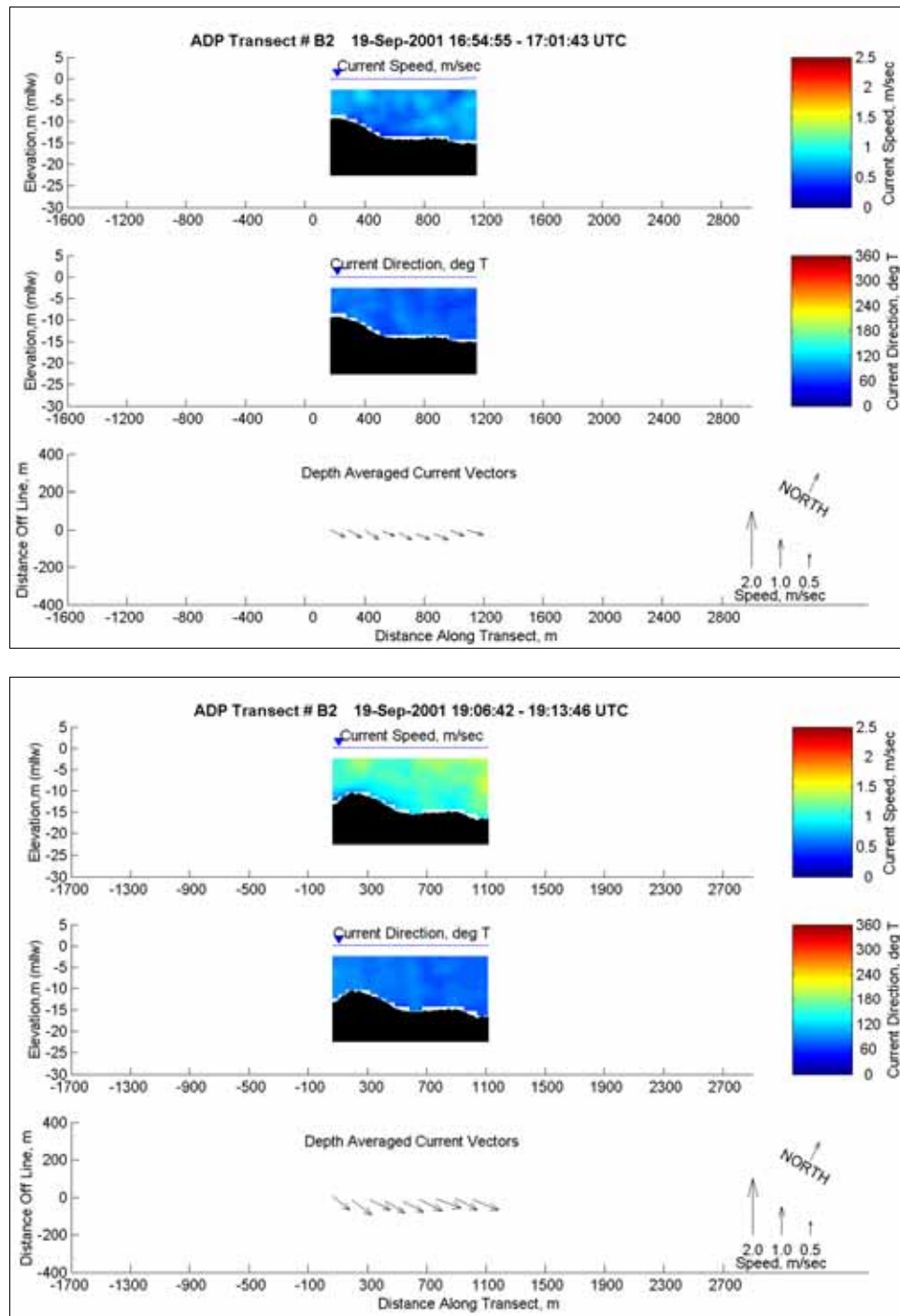
Figure D52.   Current speed, direction, and depth-averaged current vectors at ADP Transect A3 from 1510 to 1540 (upper) and 1704 to 1739 (lower) on 18 September 2001
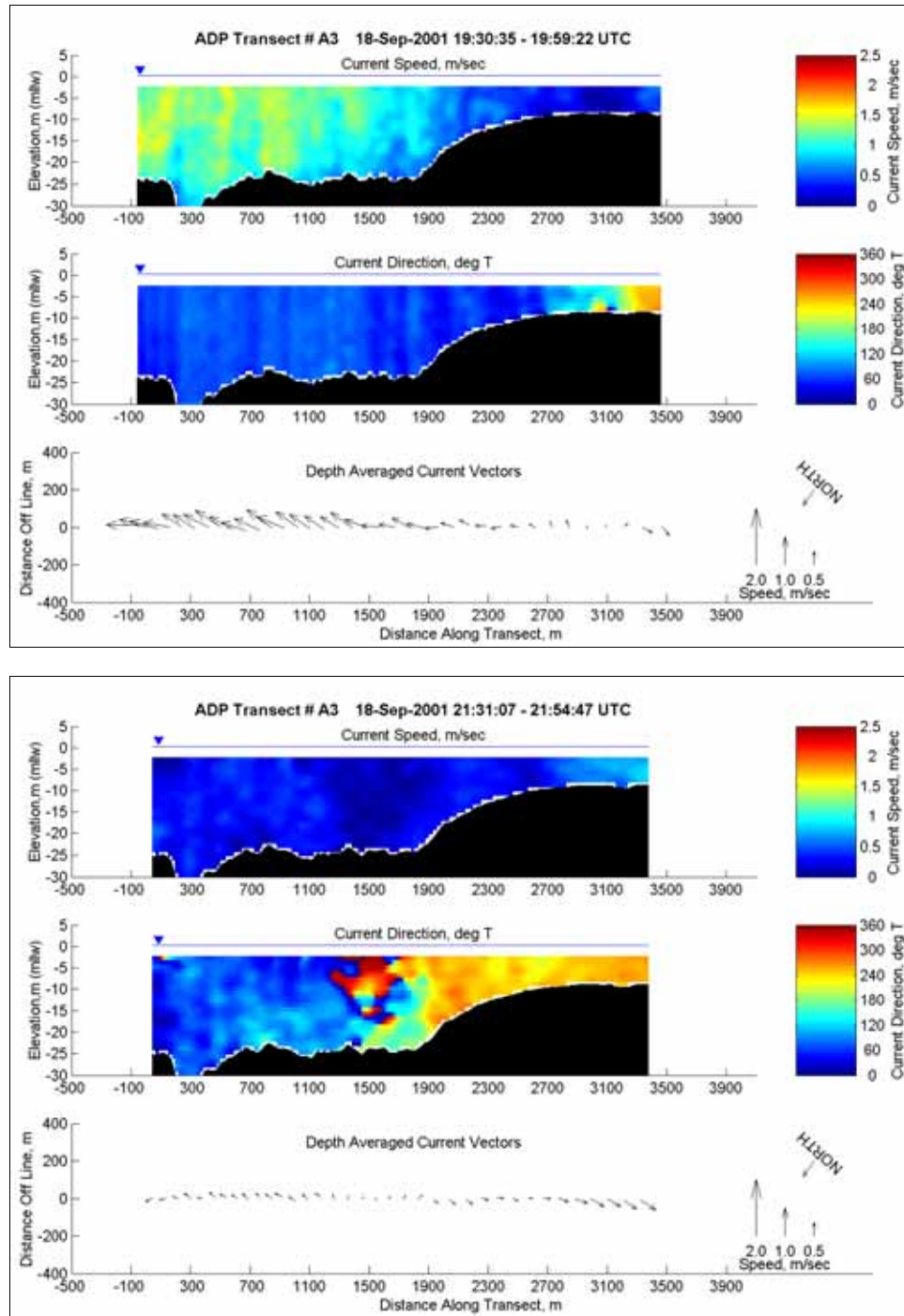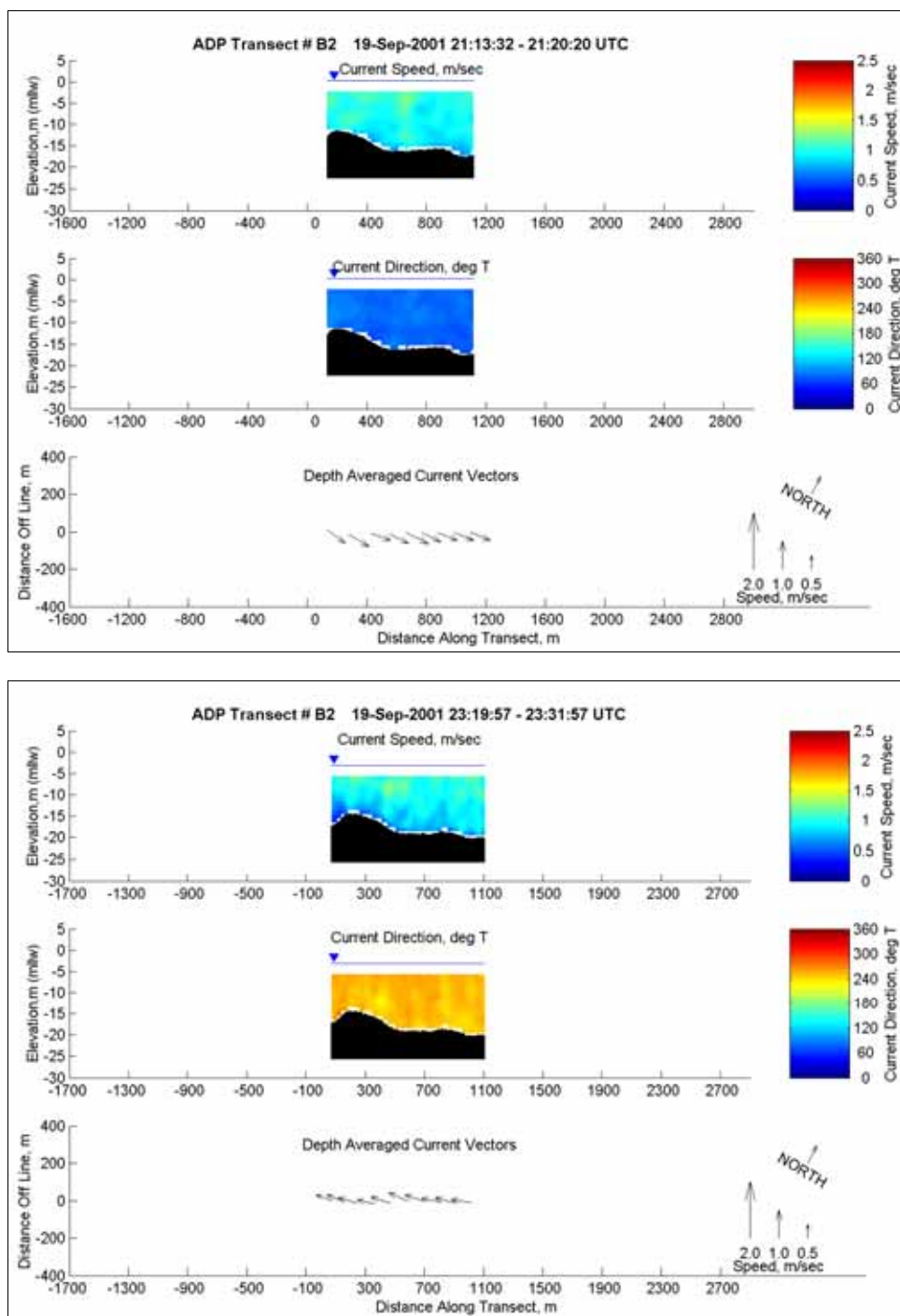
Figure D53. Current speed, direction, and depth-averaged current vectors at
ADP Transect A3 from 1930 to 1959 (upper) and 2131 to 2154
(lower) on 18 September 2001
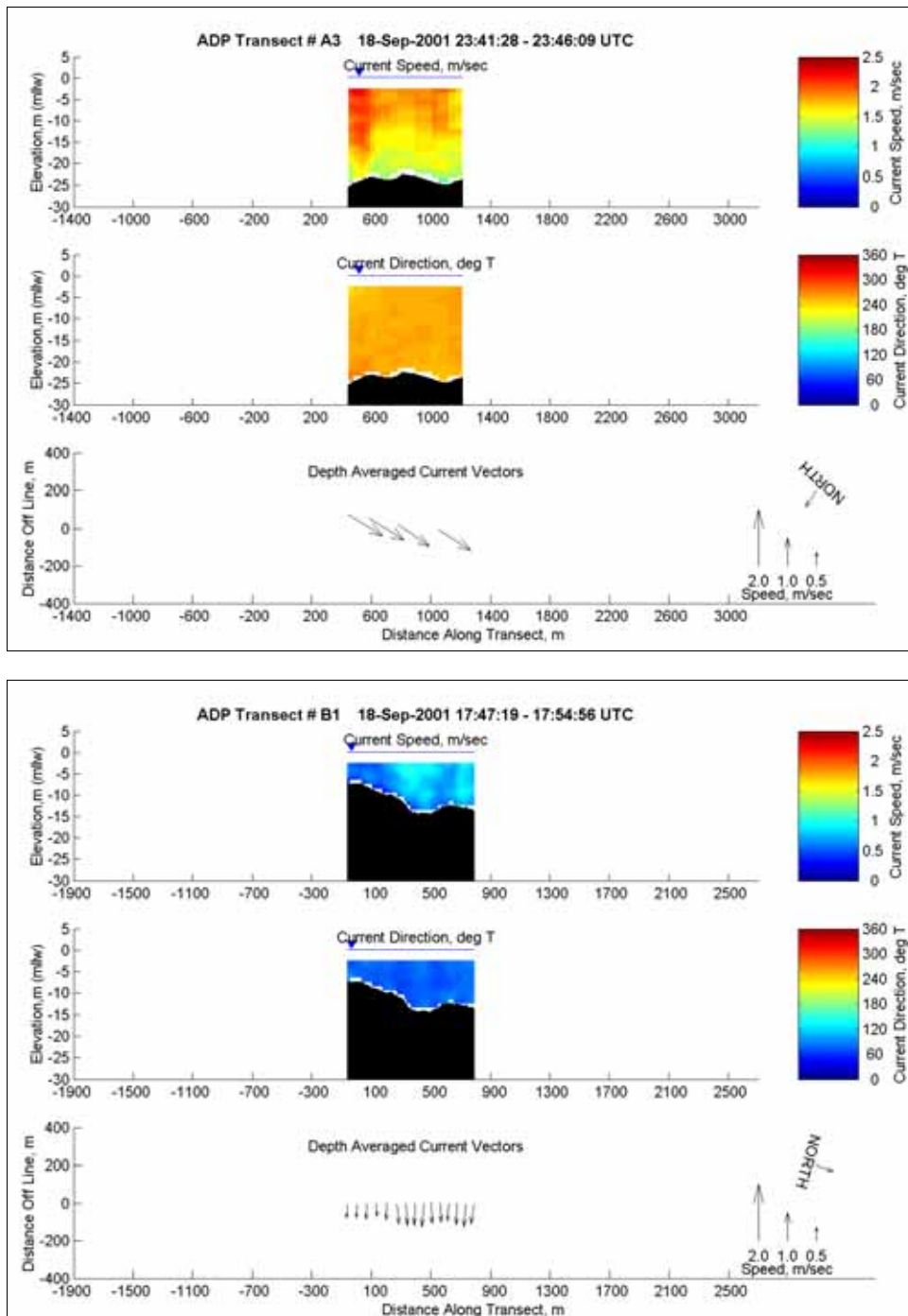
Figure D54.   Current speed, direction, and depth-averaged current vectors at ADP Transect A3 from 2341 to 2346 (upper) and Transect B1 from 1747 to 1754 (lower) on 18 September 2001
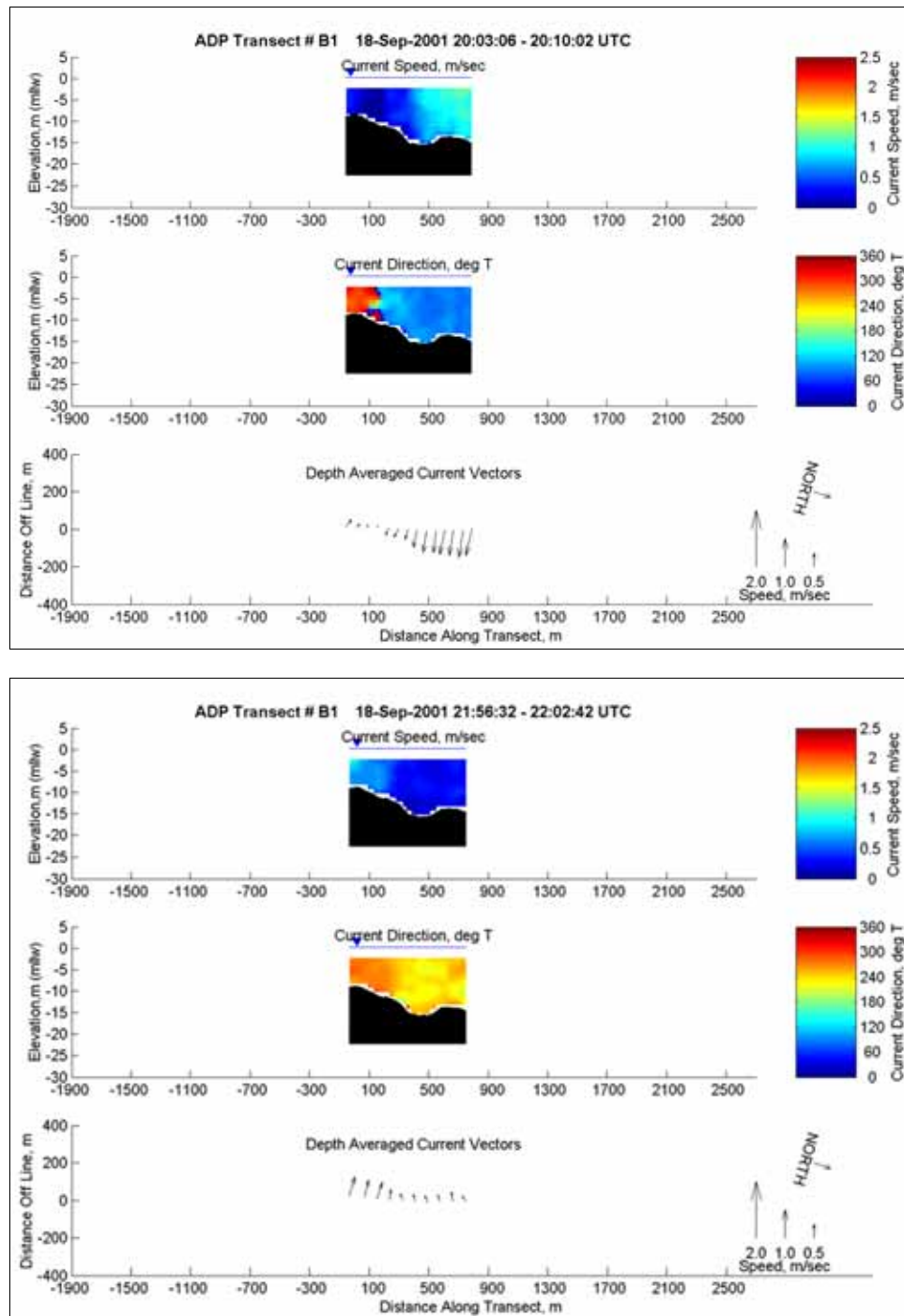
Figure D55.   Current speed, direction, and depth-averaged current vectors at
             ADP Transect B1 from 2003 to 2010 (upper) and 2156 to 2202
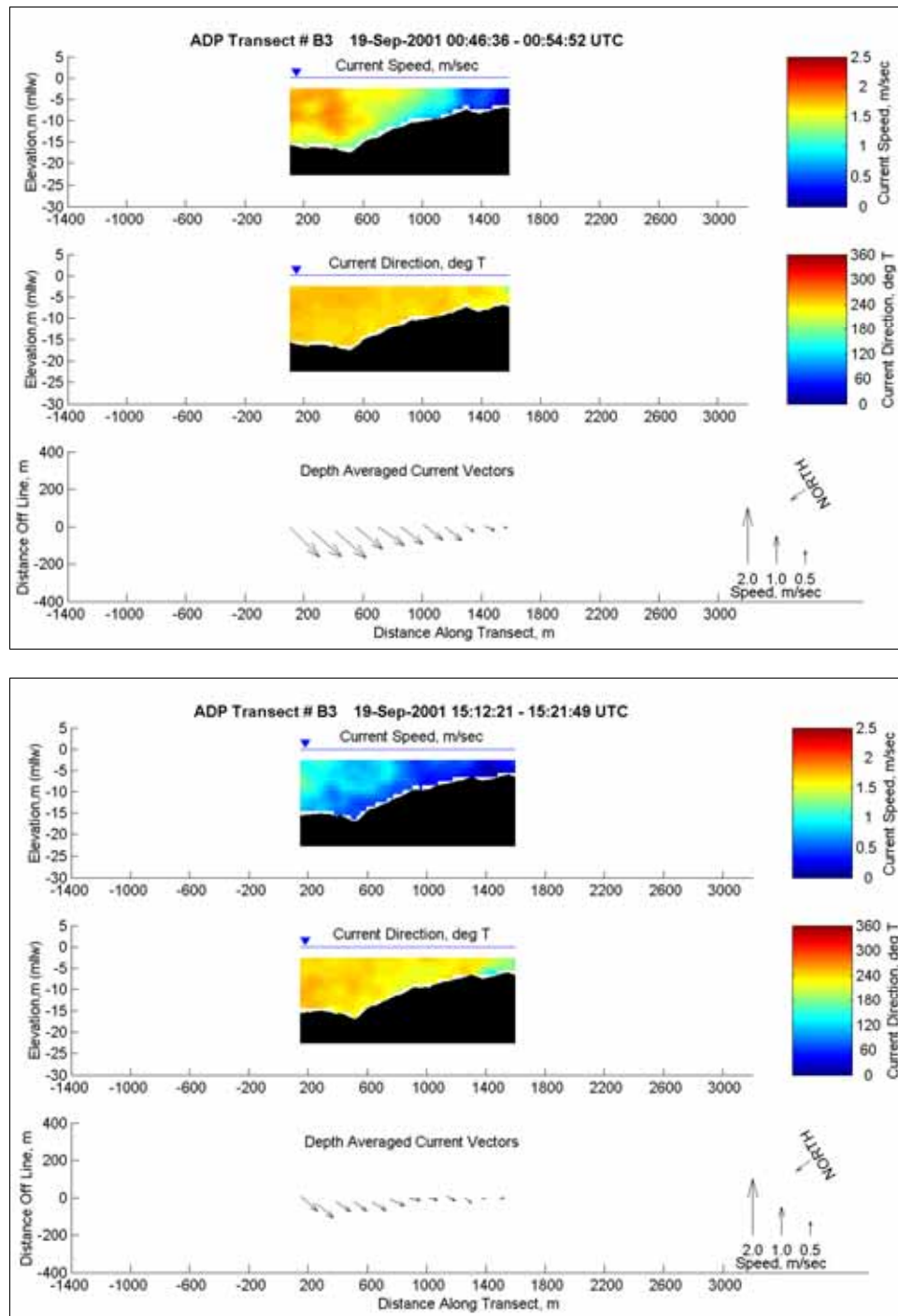   (lower) on 18 September 2001
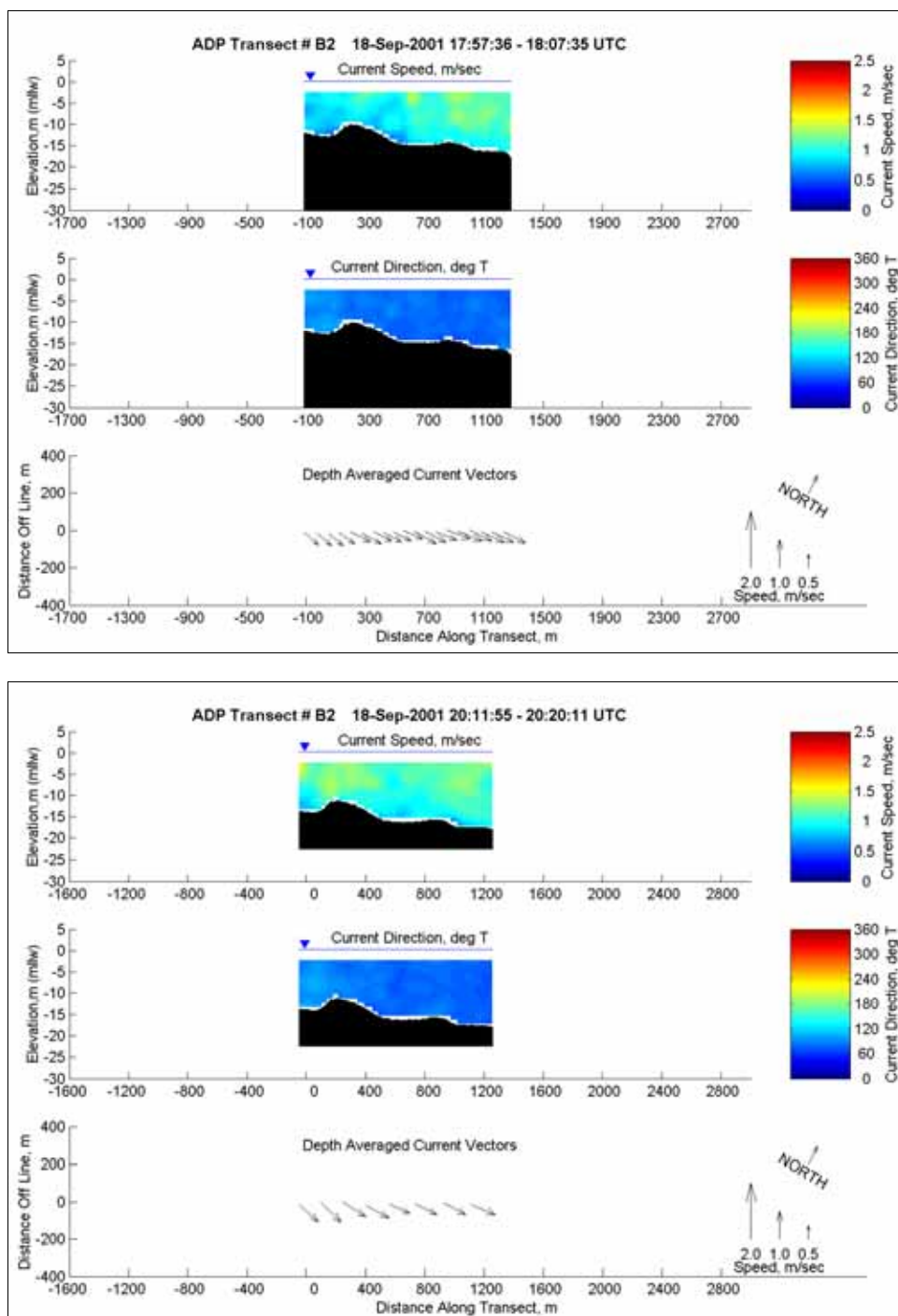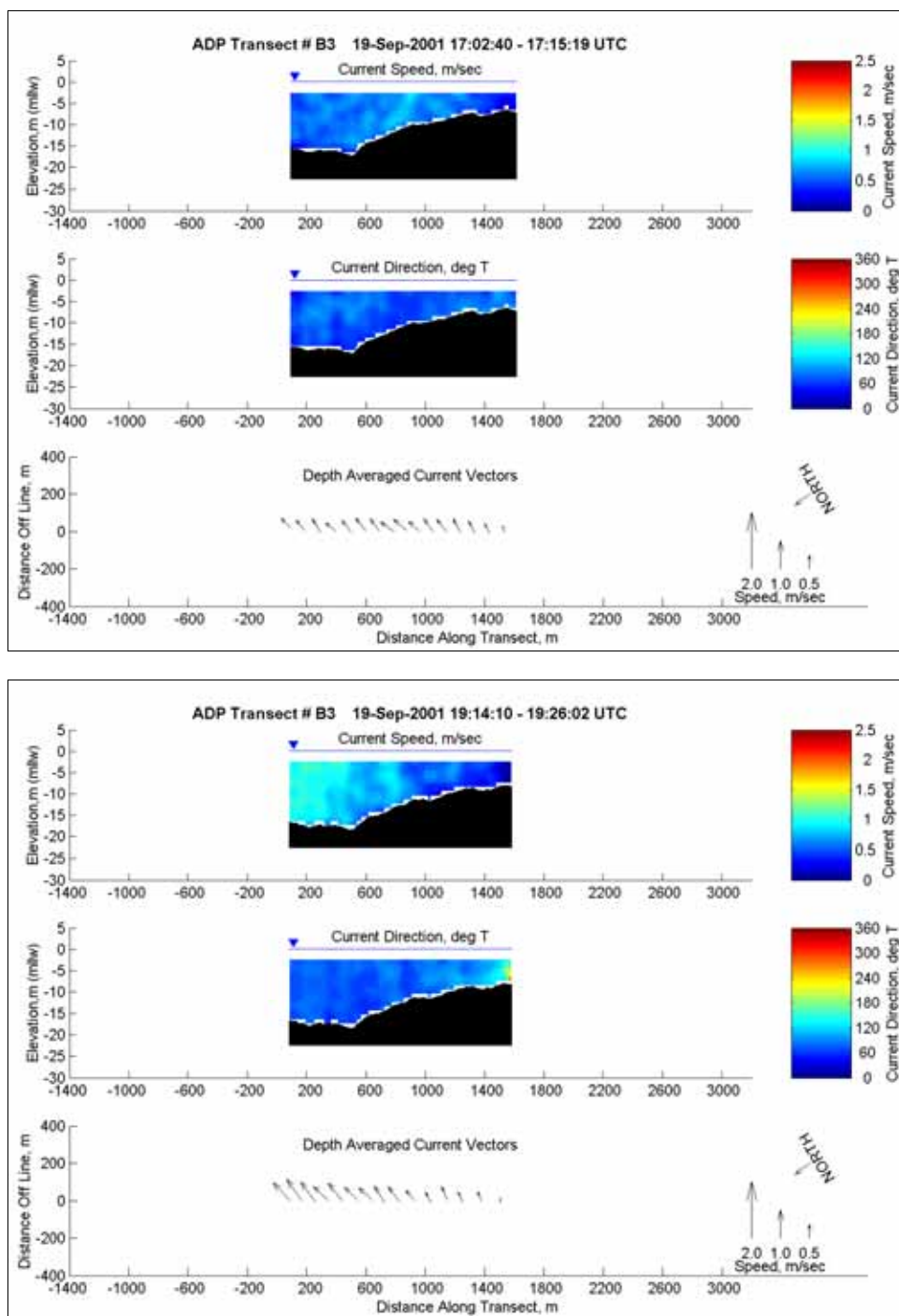
Figure D56.   Current speed, direction, and depth-averaged current vectors at
              ADP Transect B2 from 1757 to 1807 (upper) and 2011 to 2020
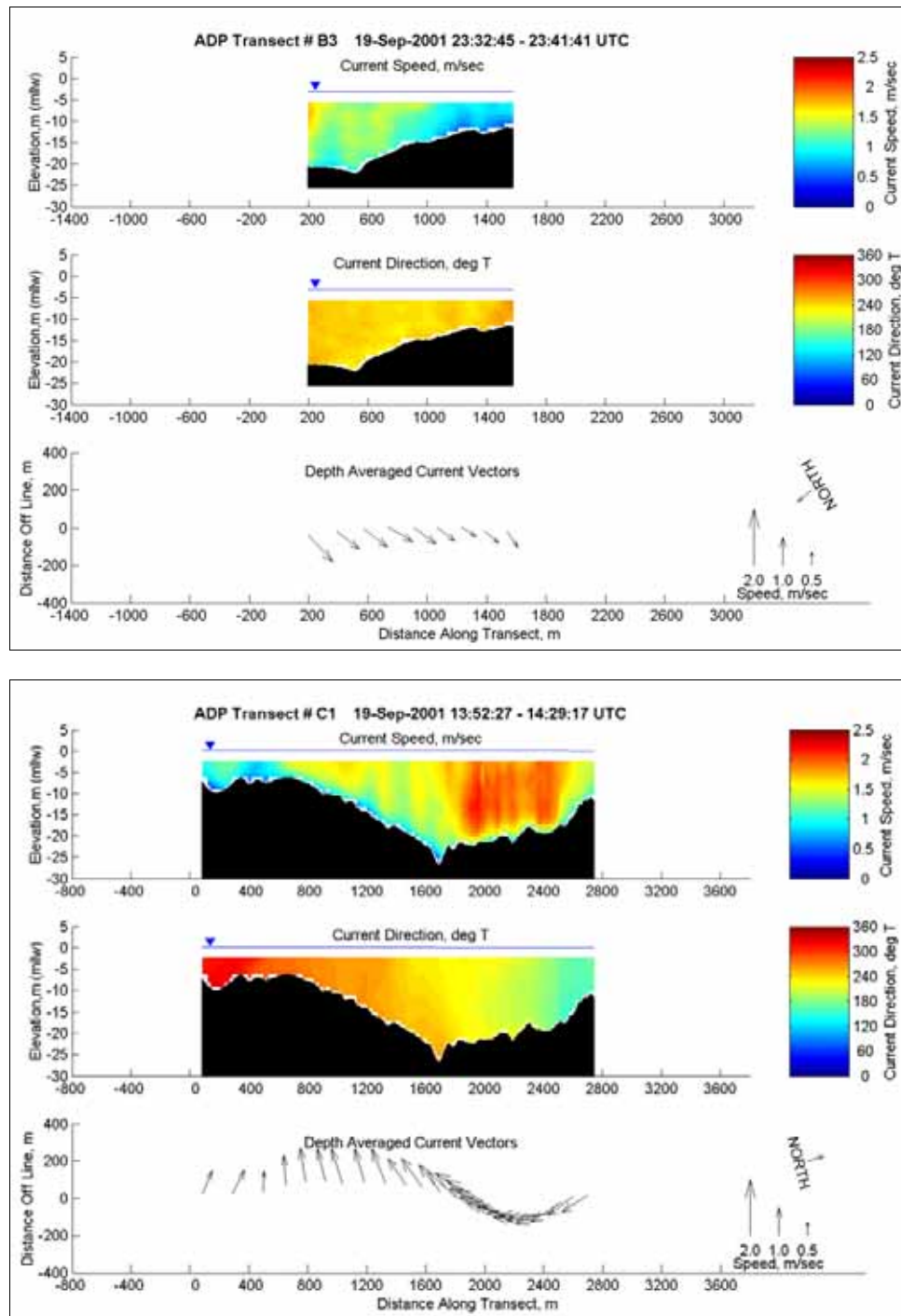   (lower) on 18 September 2001
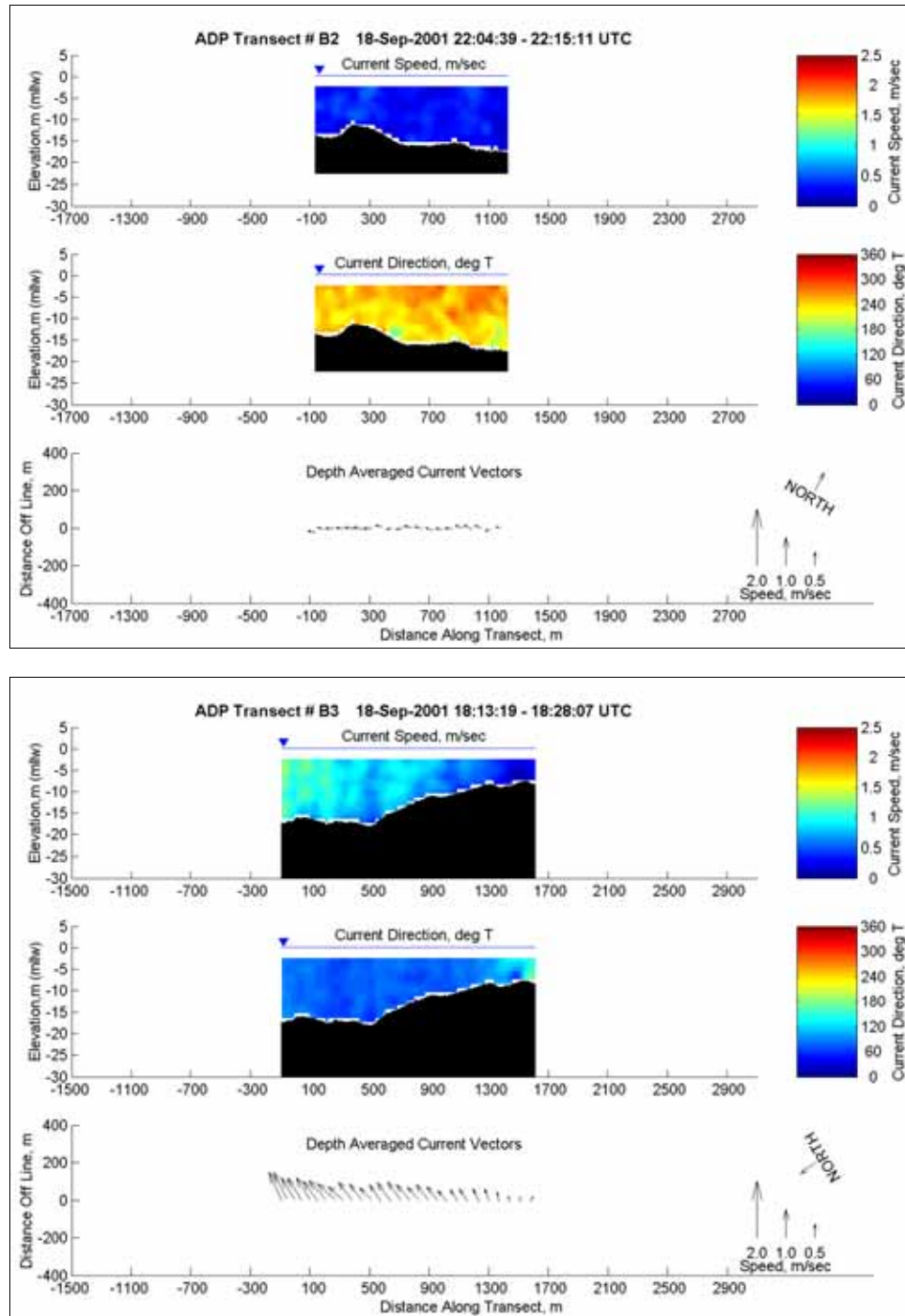
Figure D57. Current speed, direction, and depth-averaged current vectors at ADP Transect B2 from 2204 to 2215 (upper) and Transect B3 from 1813 to 1828 (lower) on 18 September 2001
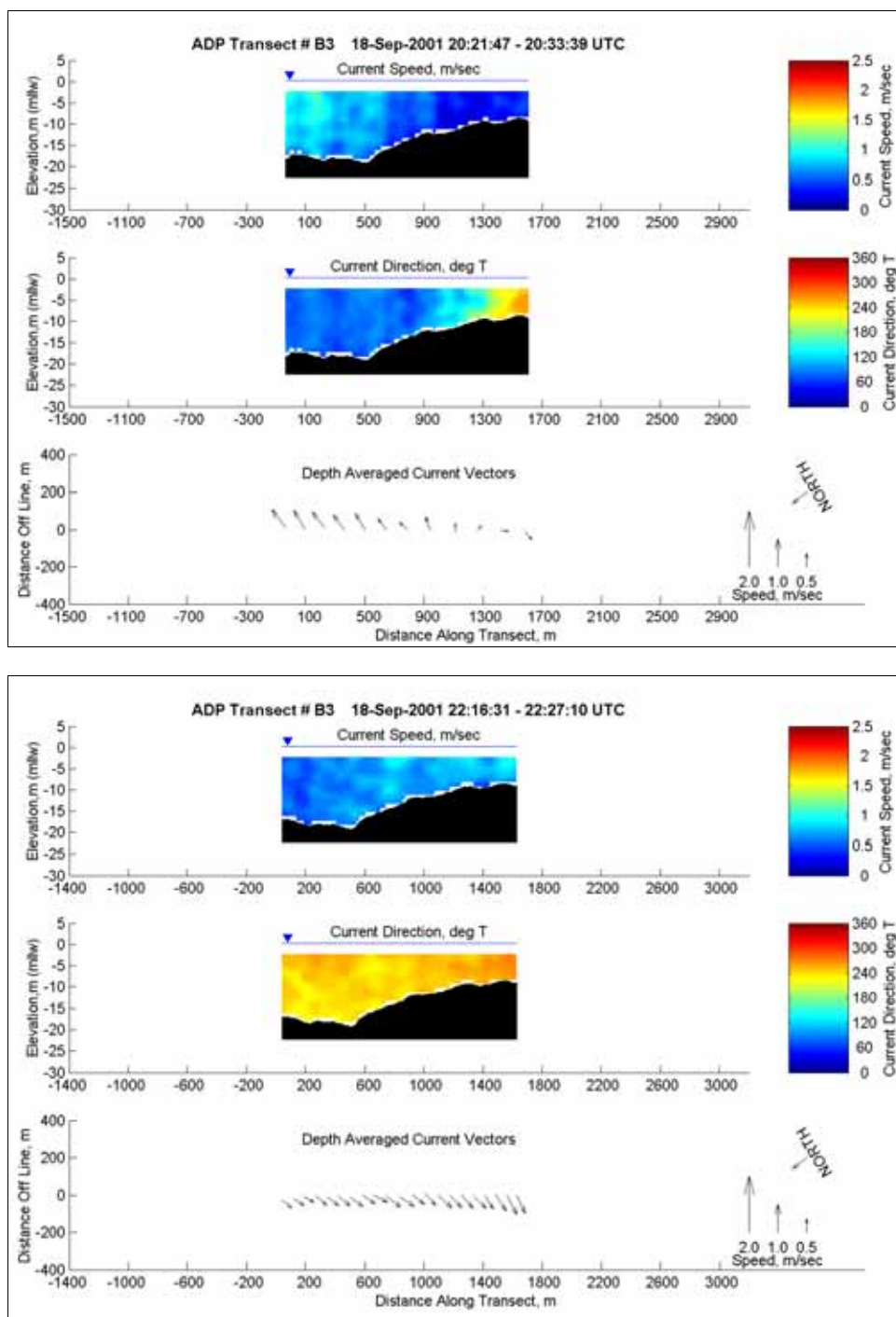
Figure D58. Current speed, direction, and depth-averaged current vectors at ADP Transect B3 from 2021 to 2033 (upper) and 2216 to 2227 (lower) on 18 September 2001
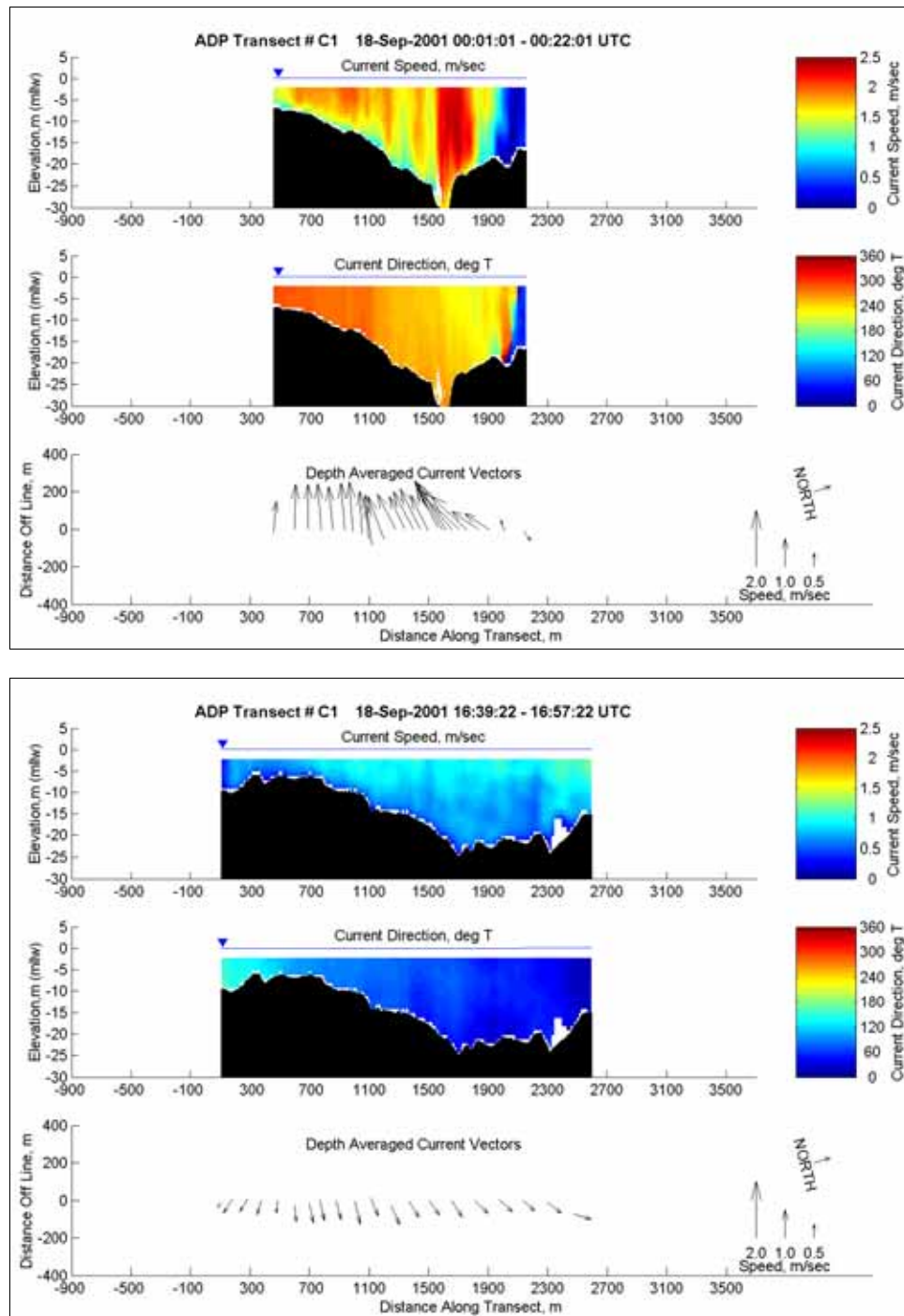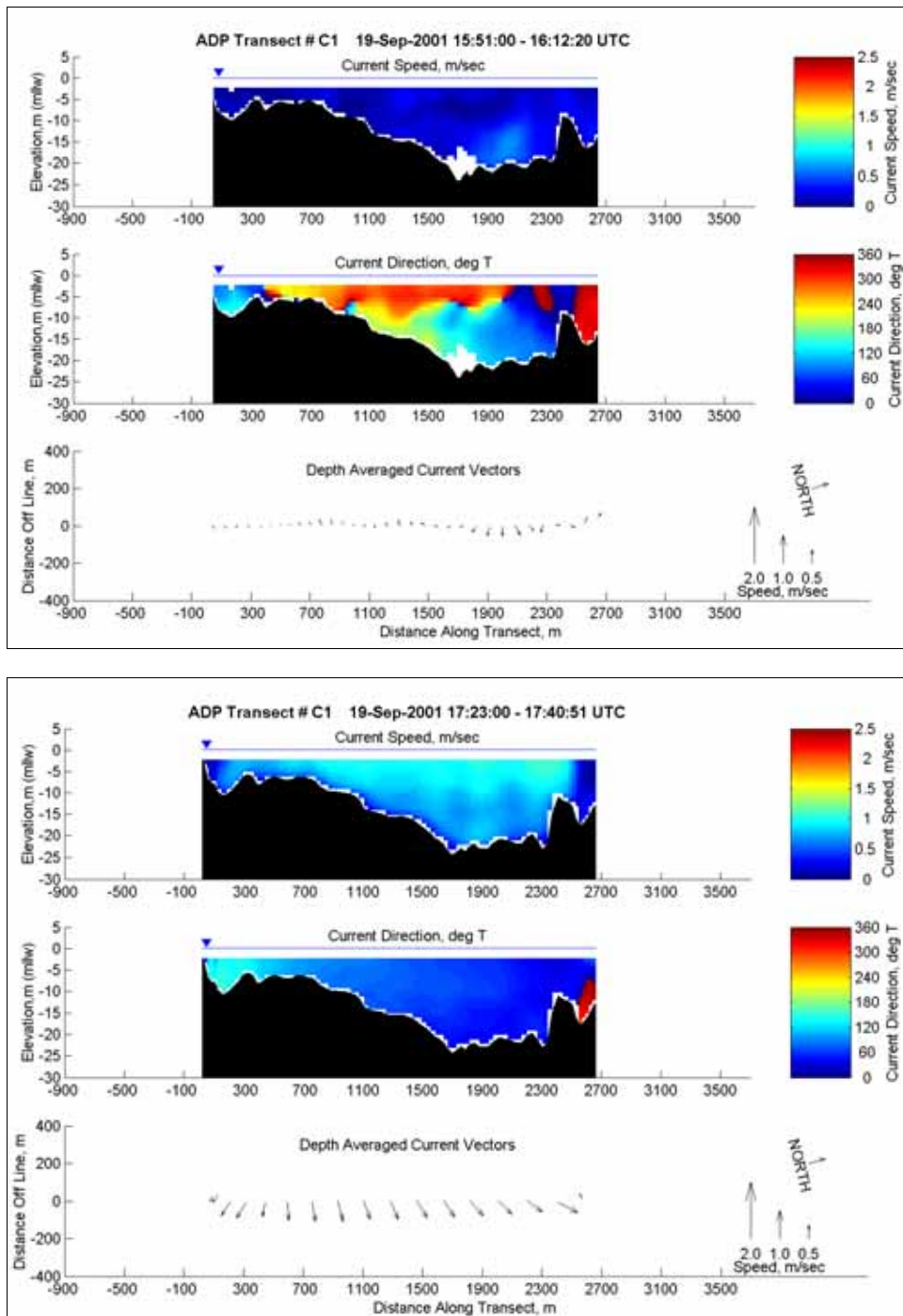
Figure D59.   Current speed, direction, and depth-averaged current vectors at
ADP Transect C1 from 0001 to 0022 (upper) and 1639 to 1657
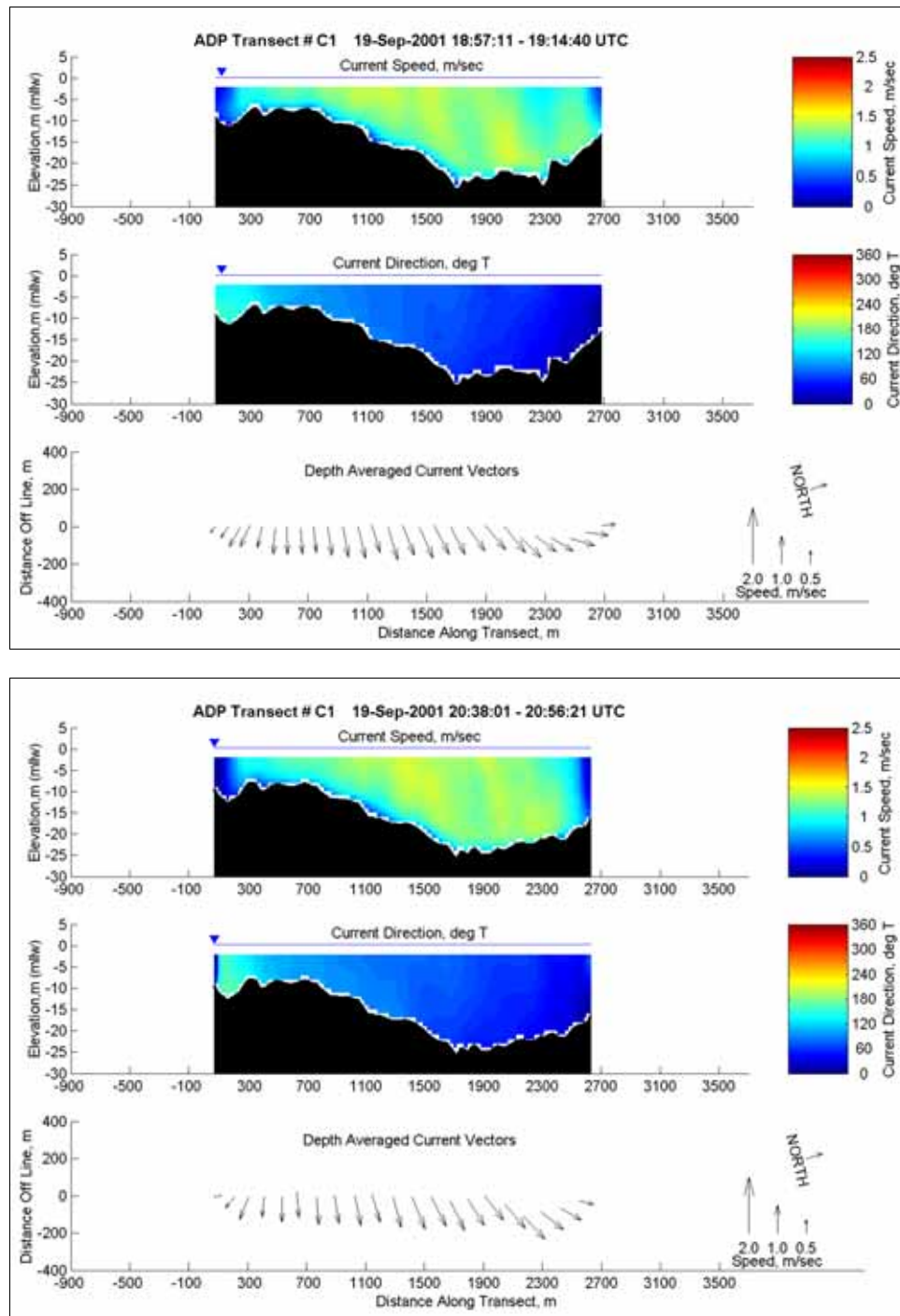(lower) on 18 September 2001
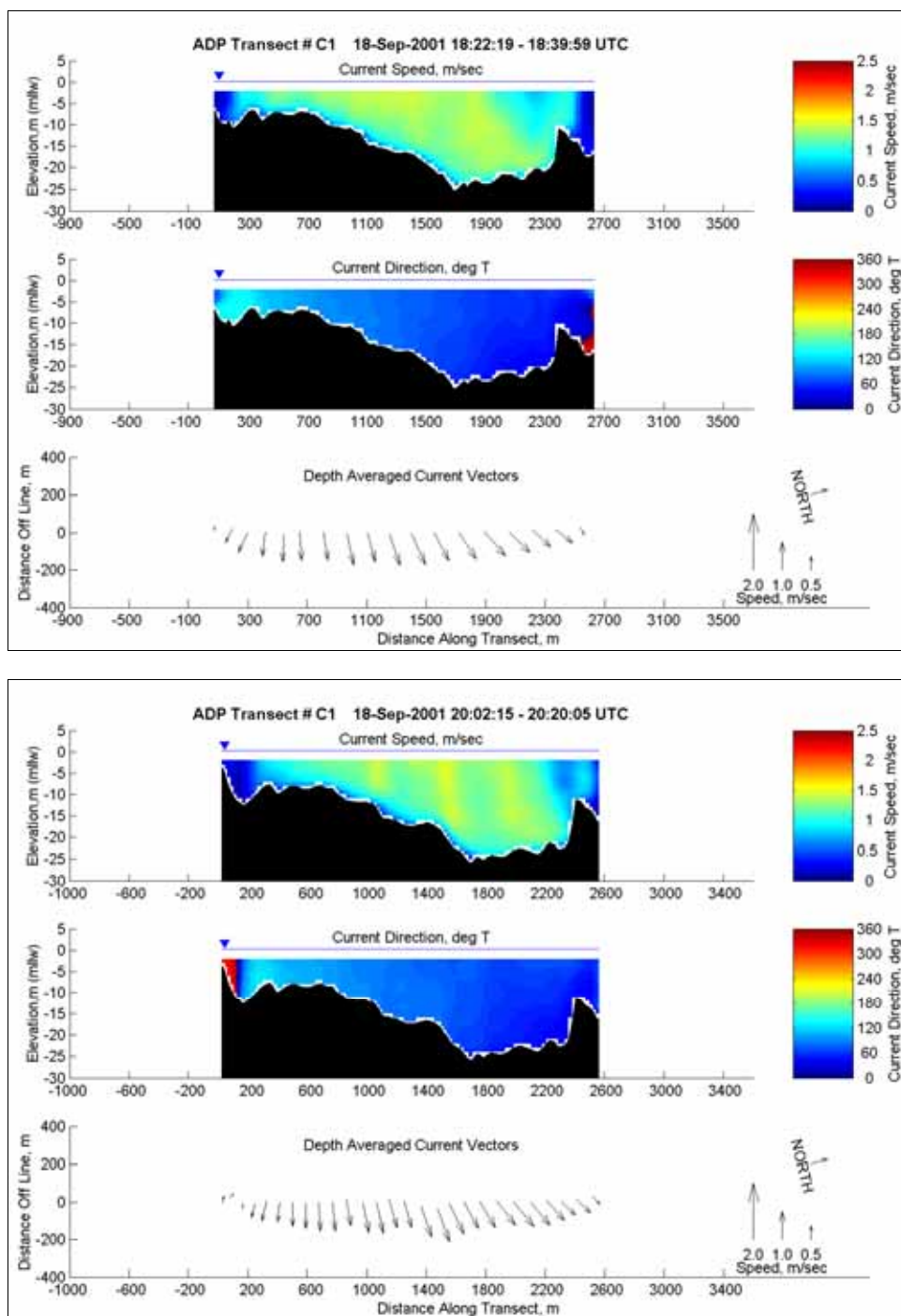
Figure D60. Current speed, direction, and depth-averaged current vectors at ADP Transect C1 from 1822 to 1839 (upper) and 2002 to 2020 (lower) on 18 September 2001
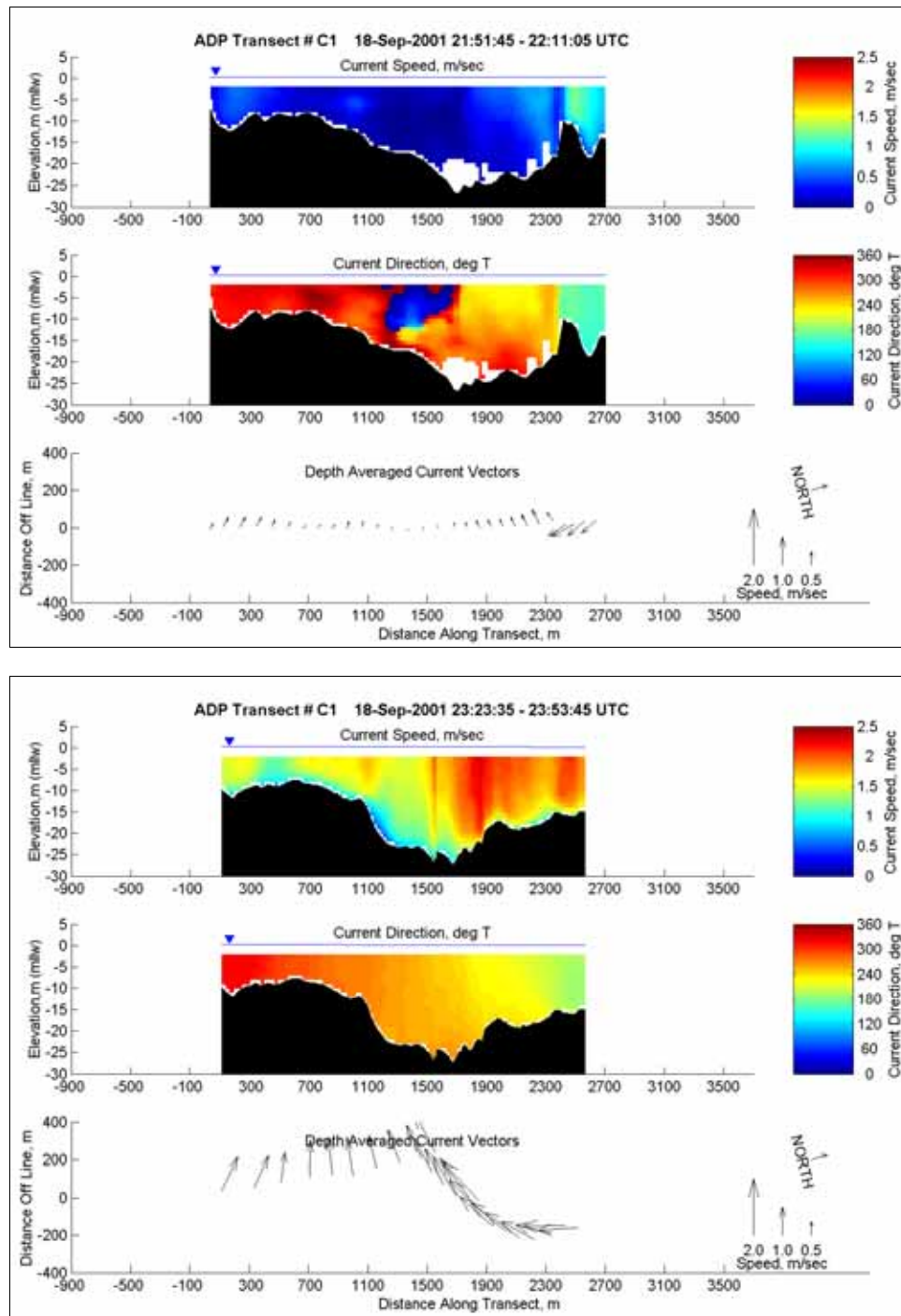
Figure D61. Current speed, direction, and depth-averaged current vectors at ADP Transect C1 from 2151 to 2211 (upper) and 2323 to 2353 (lower) on 18 September 2001
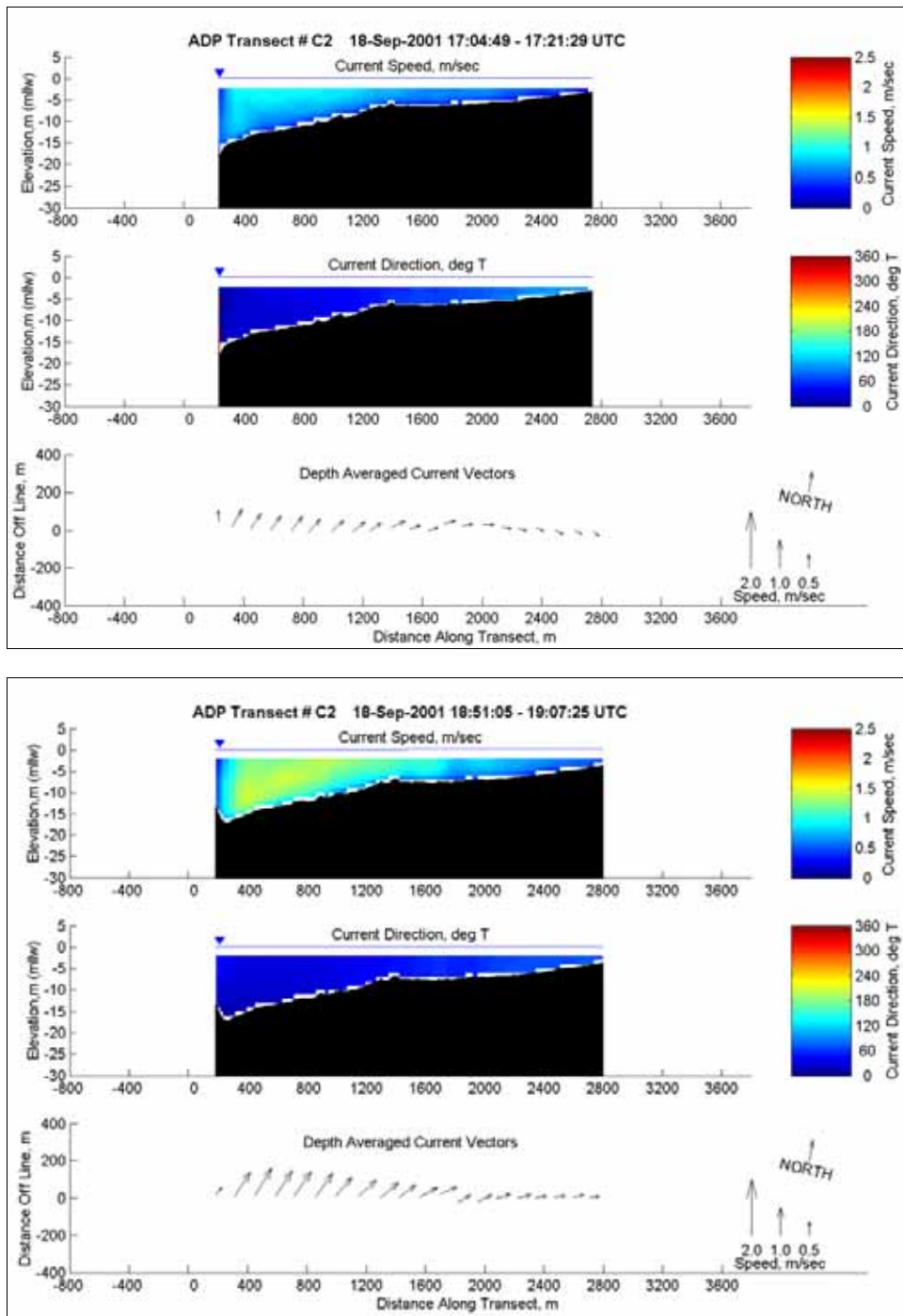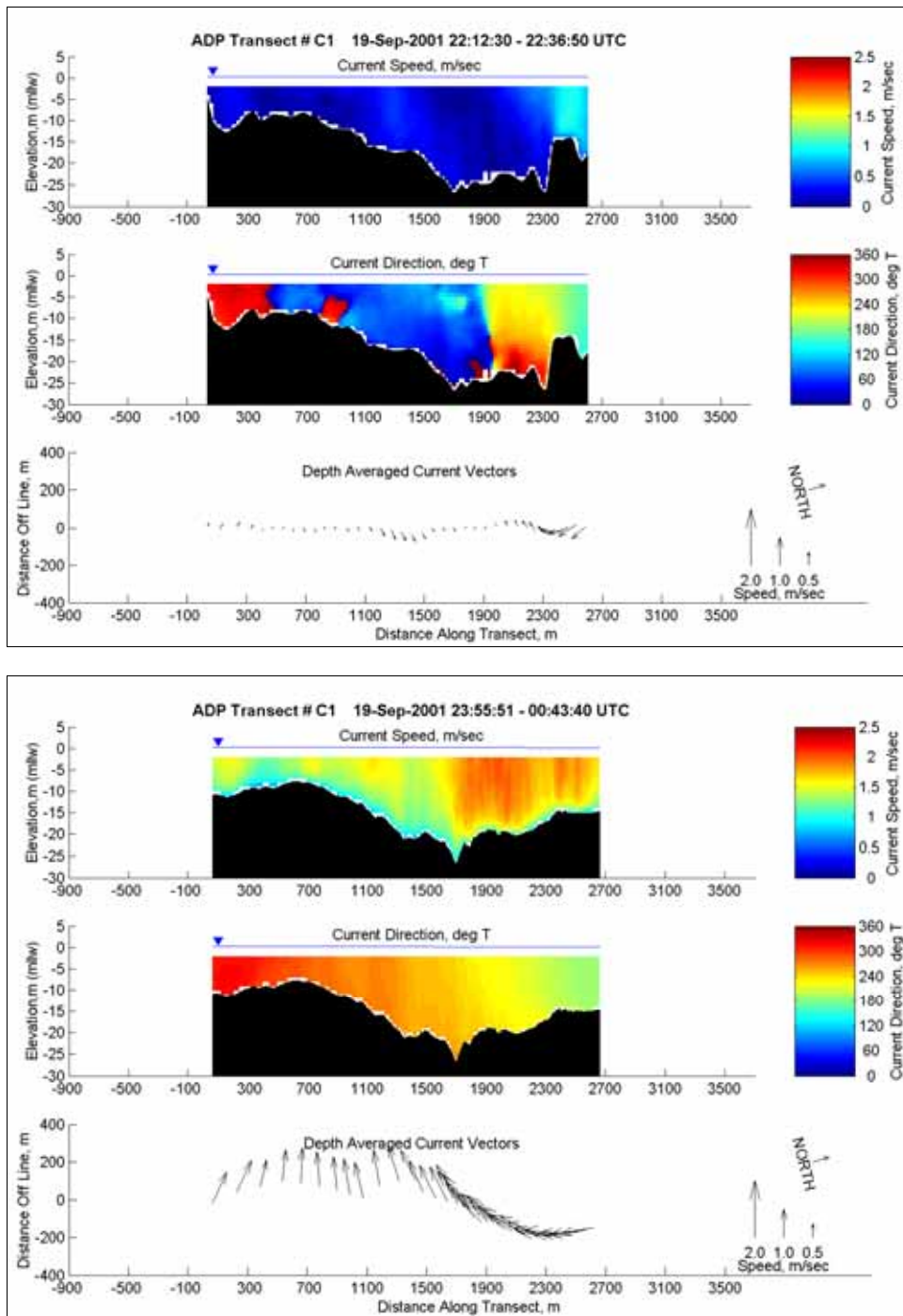
Figure D62. Current speed, direction, and depth-averaged current vectors at ADP Transect C2 from 1704 to 1721 (upper) and 1851 to 1907 (lower) on 18 September 2001
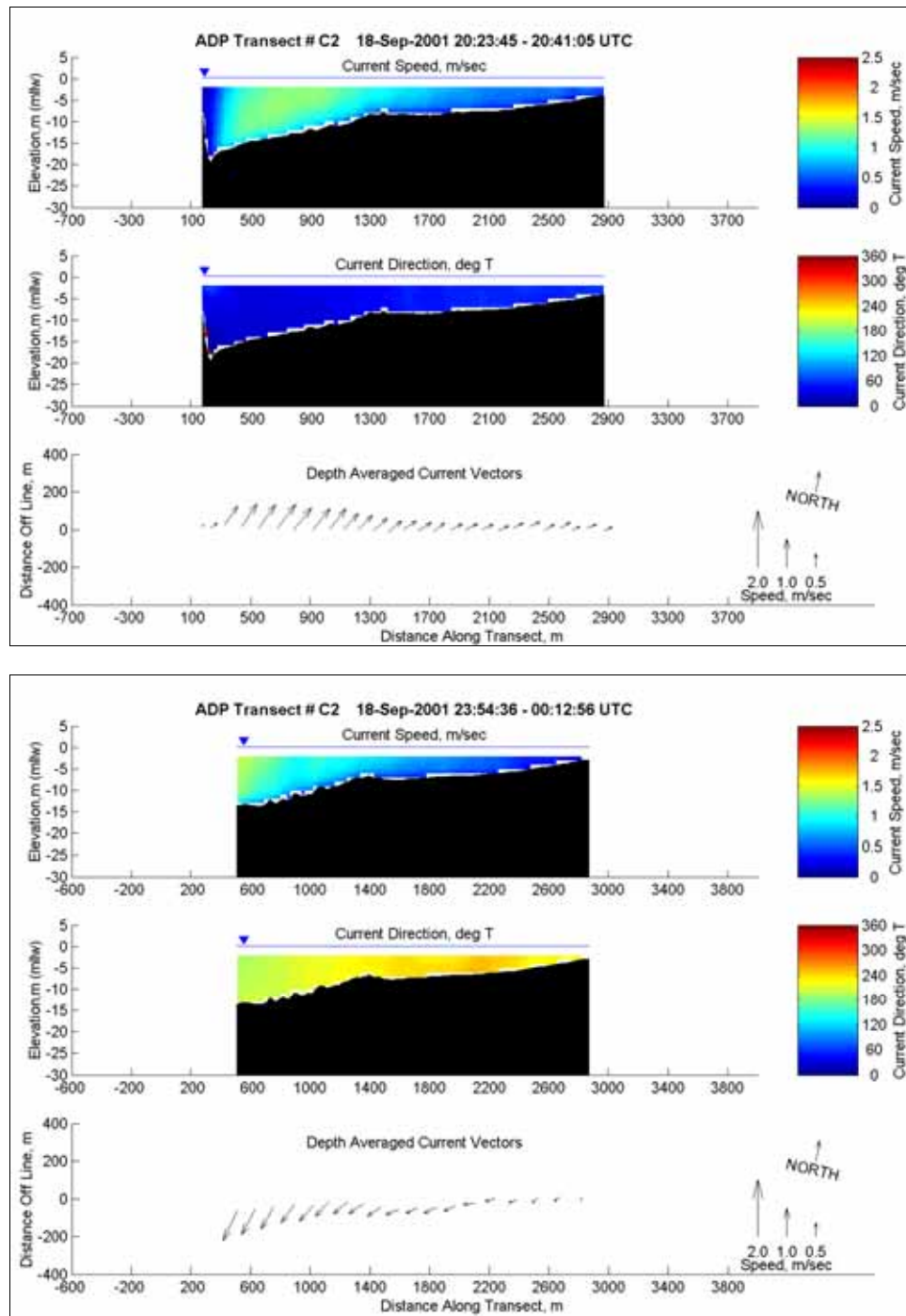
Figure D63. Current speed, direction, and depth-averaged current vectors at ADP Transect C2 from 2023 to 2041 (upper) and 2354 to 0012 (lower) on 18 September 2001
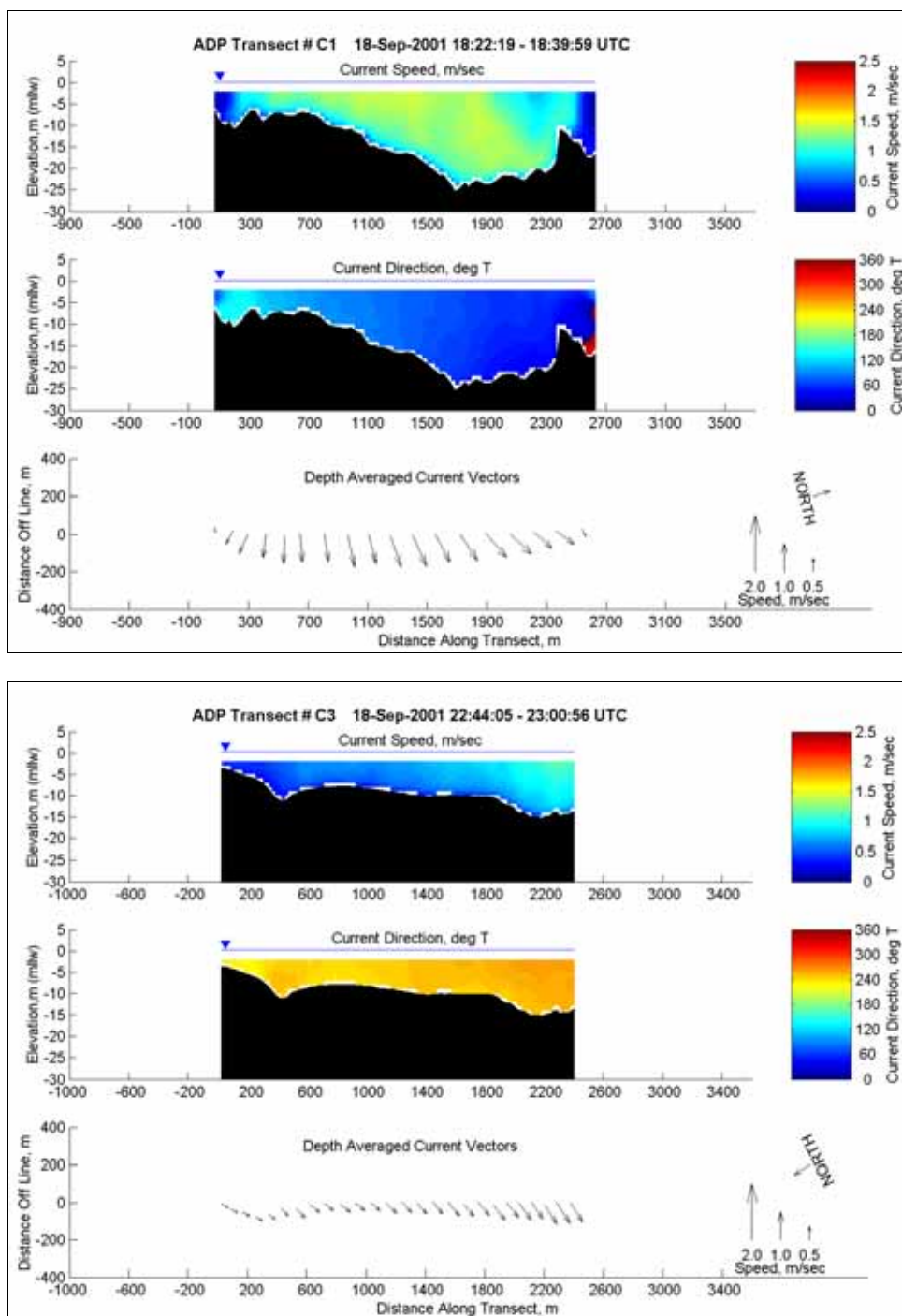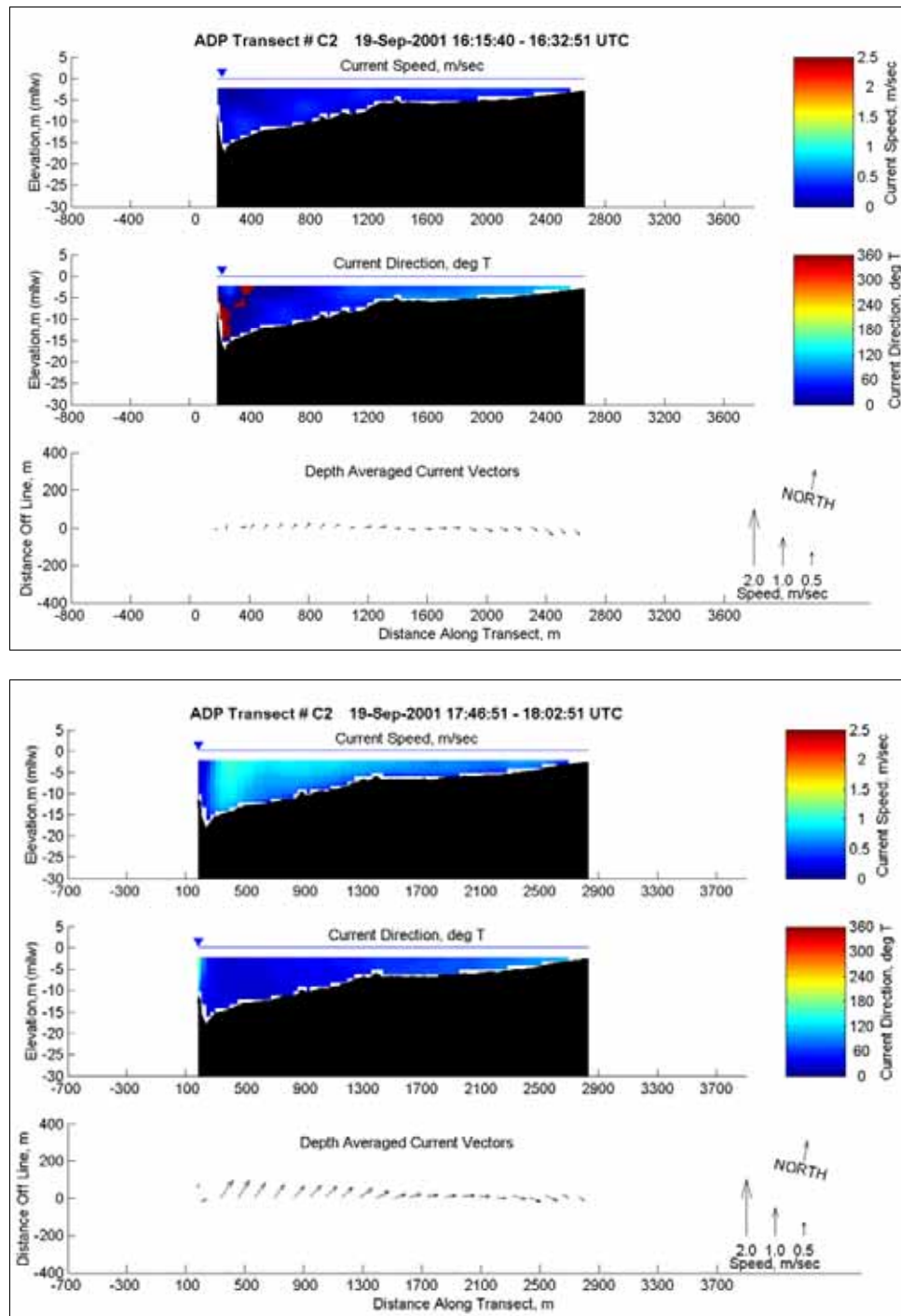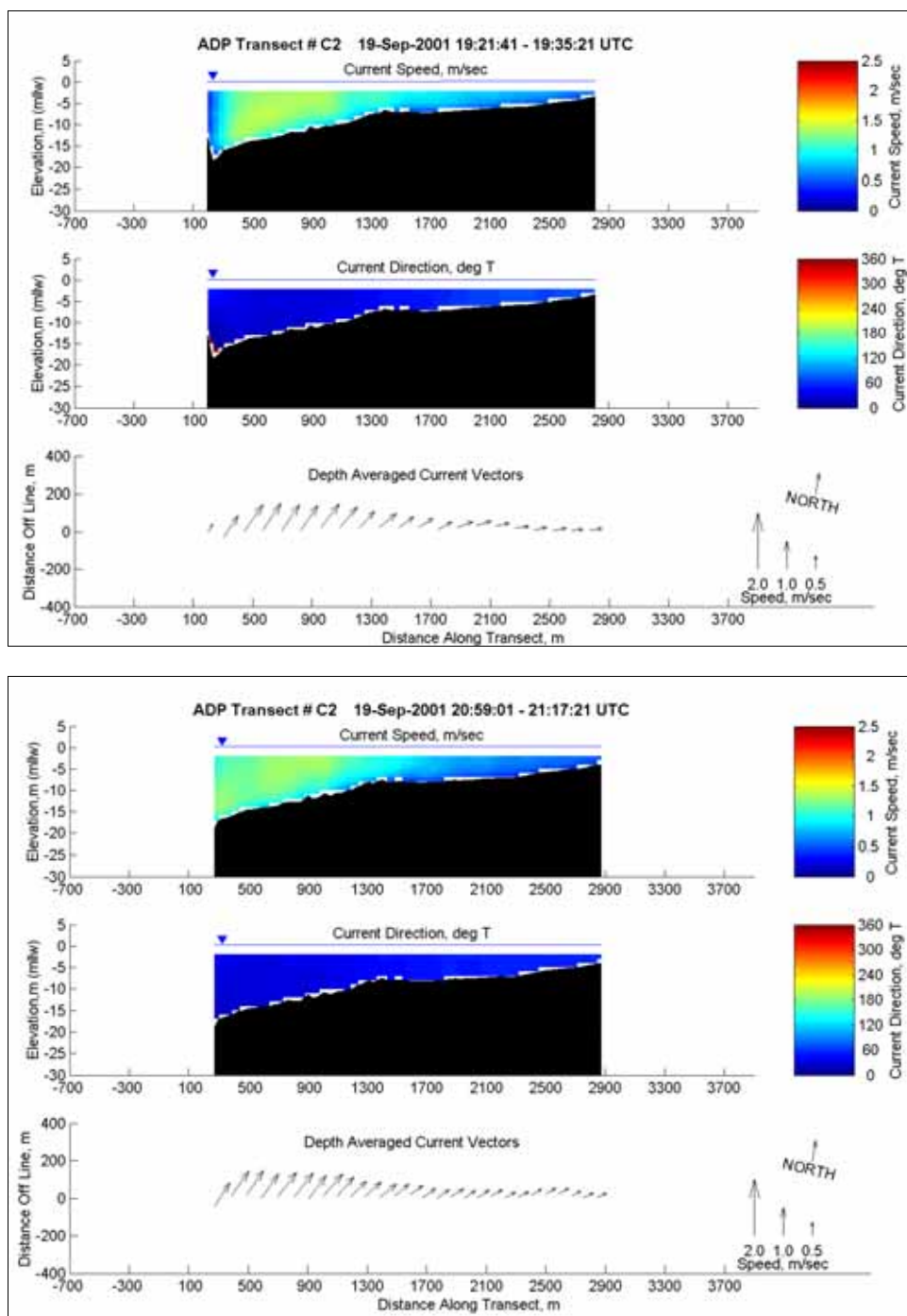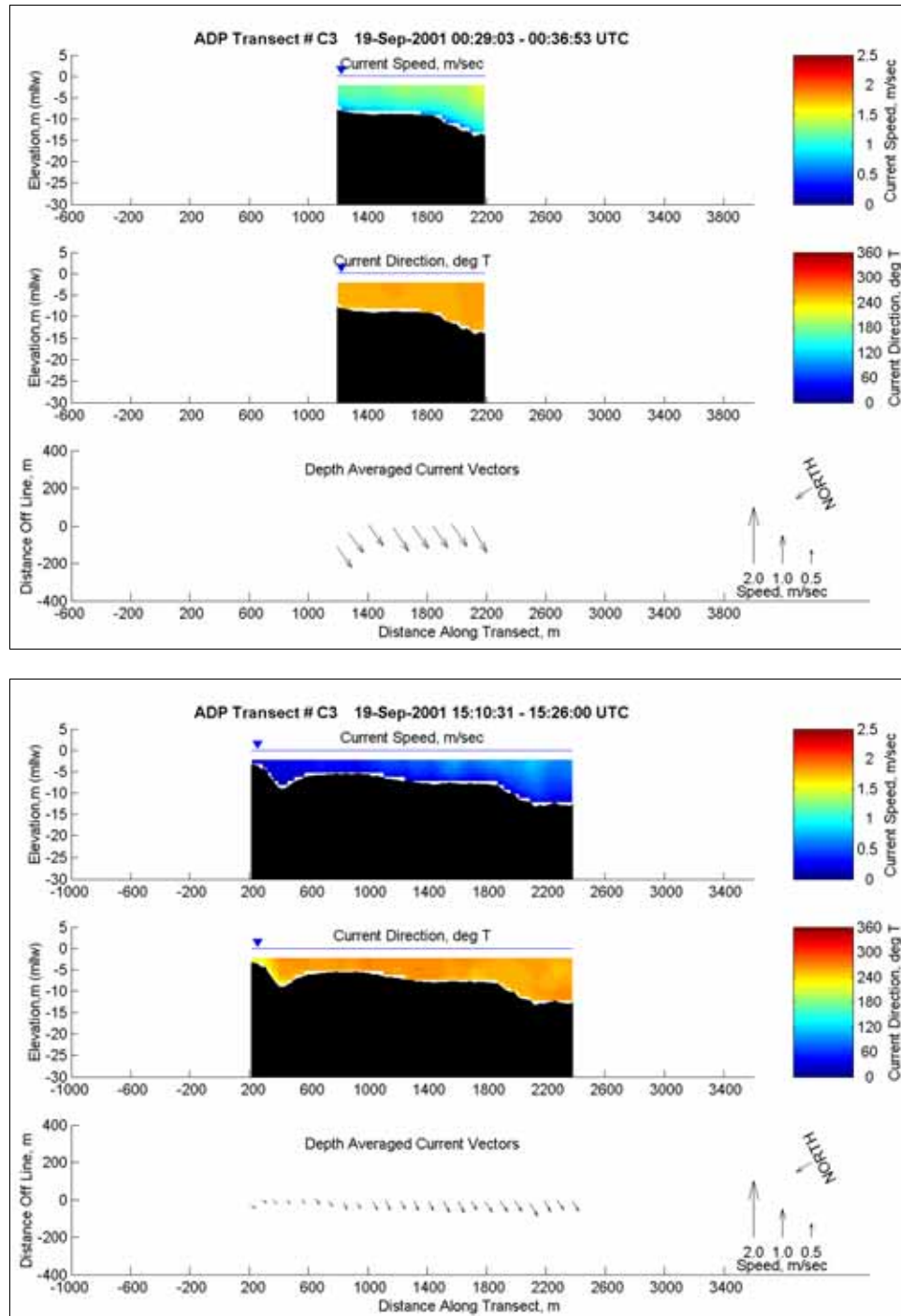
Figure D64.   Current speed, direction, and depth-averaged current vectors at
ADP Transect C1 from 1822 to 1839 (upper) and Transect C3 from
2244 to 2300 (lower) on 18 September 2001
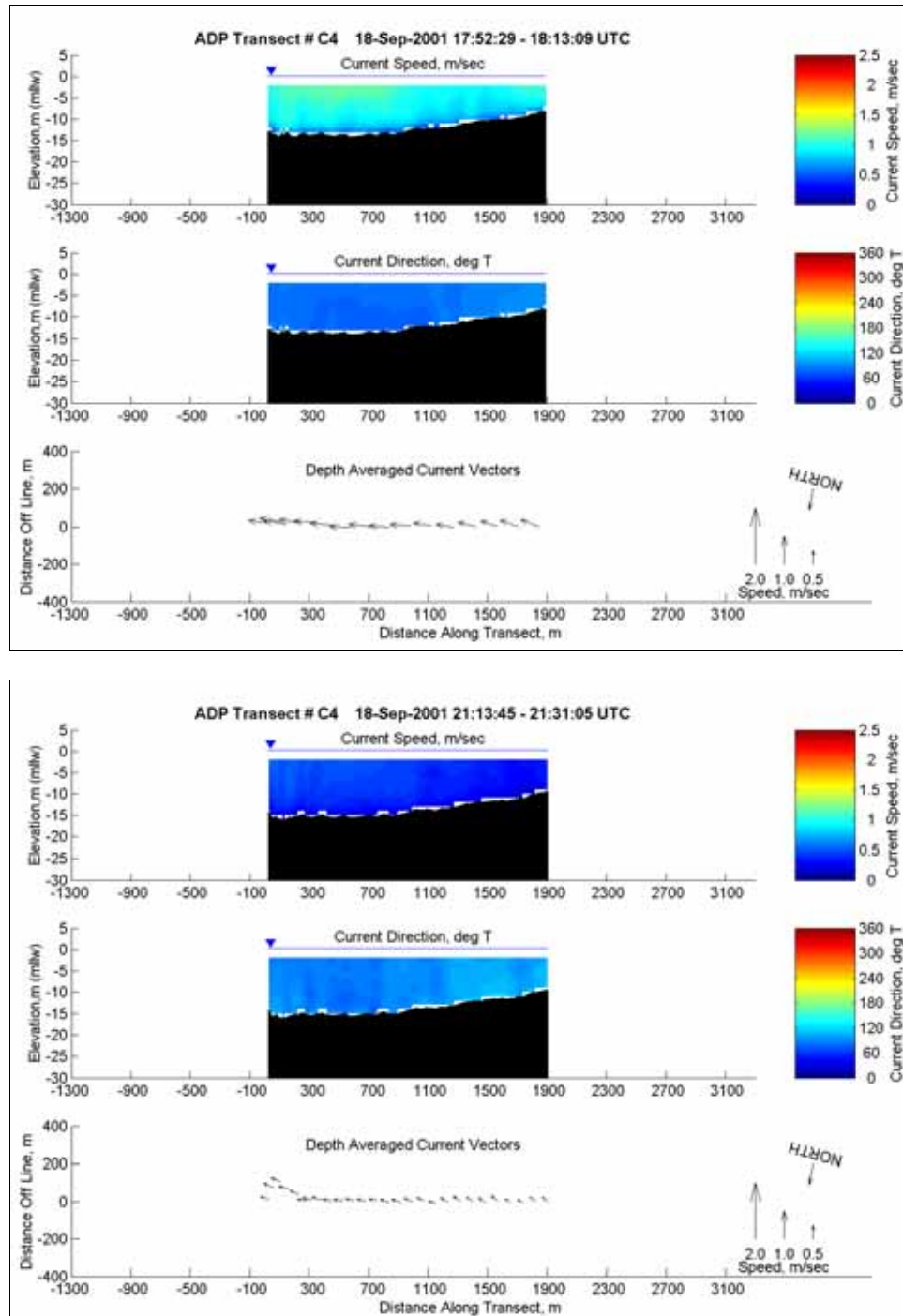
Figure D65. Current speed, direction, and depth-averaged current vectors at ADP Transect C4 from 1752 to 1813 (upper) and Transect C4 from 2113 to 2131 (lower) on 18 September 2001
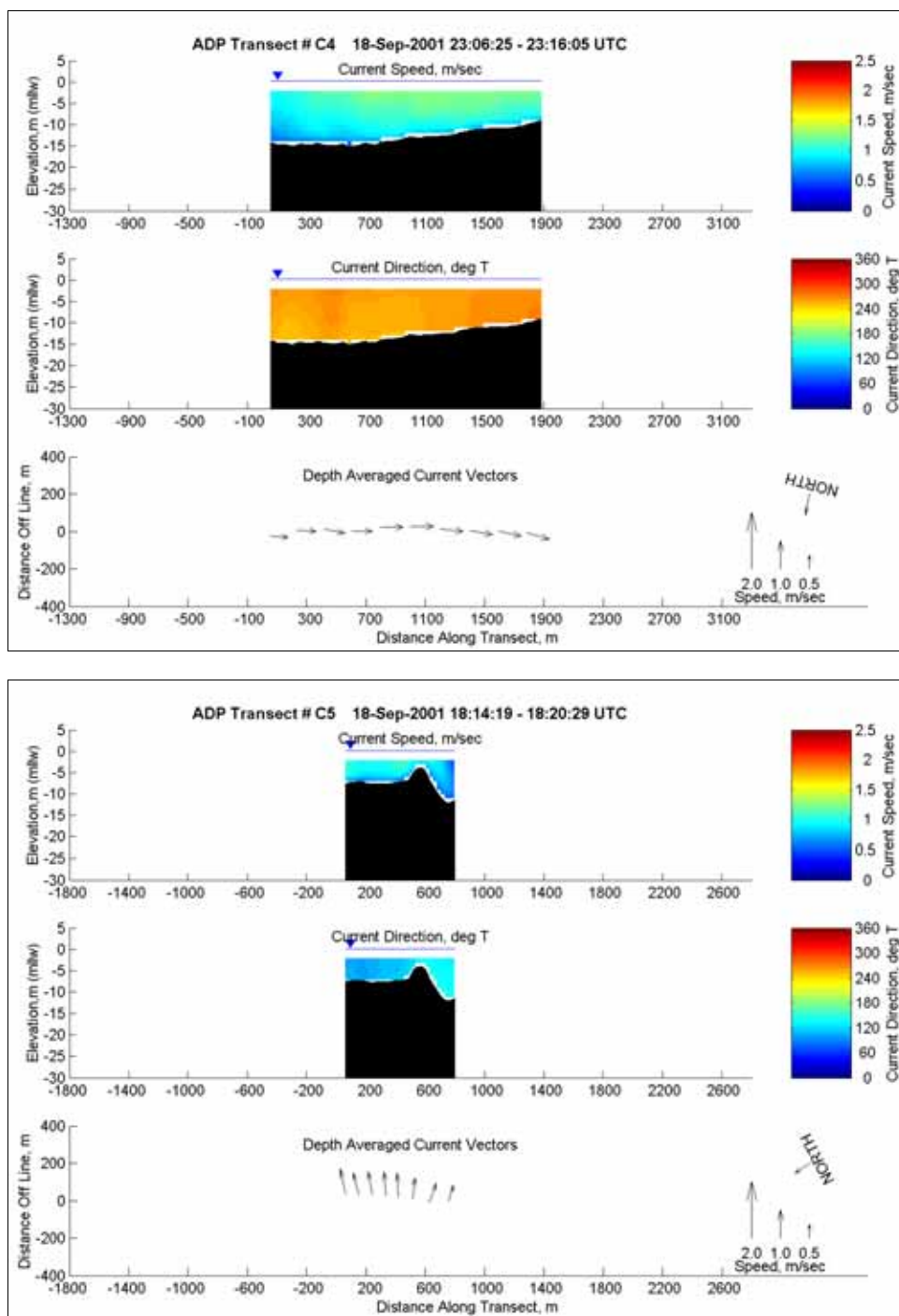
Figure D66.   Current speed, direction, and depth-averaged current vectors at
ADP Transect C4 from 2306 to 2316 (upper) and Transect C5 from
1814 to 1820 (lower) on 18 September 2001
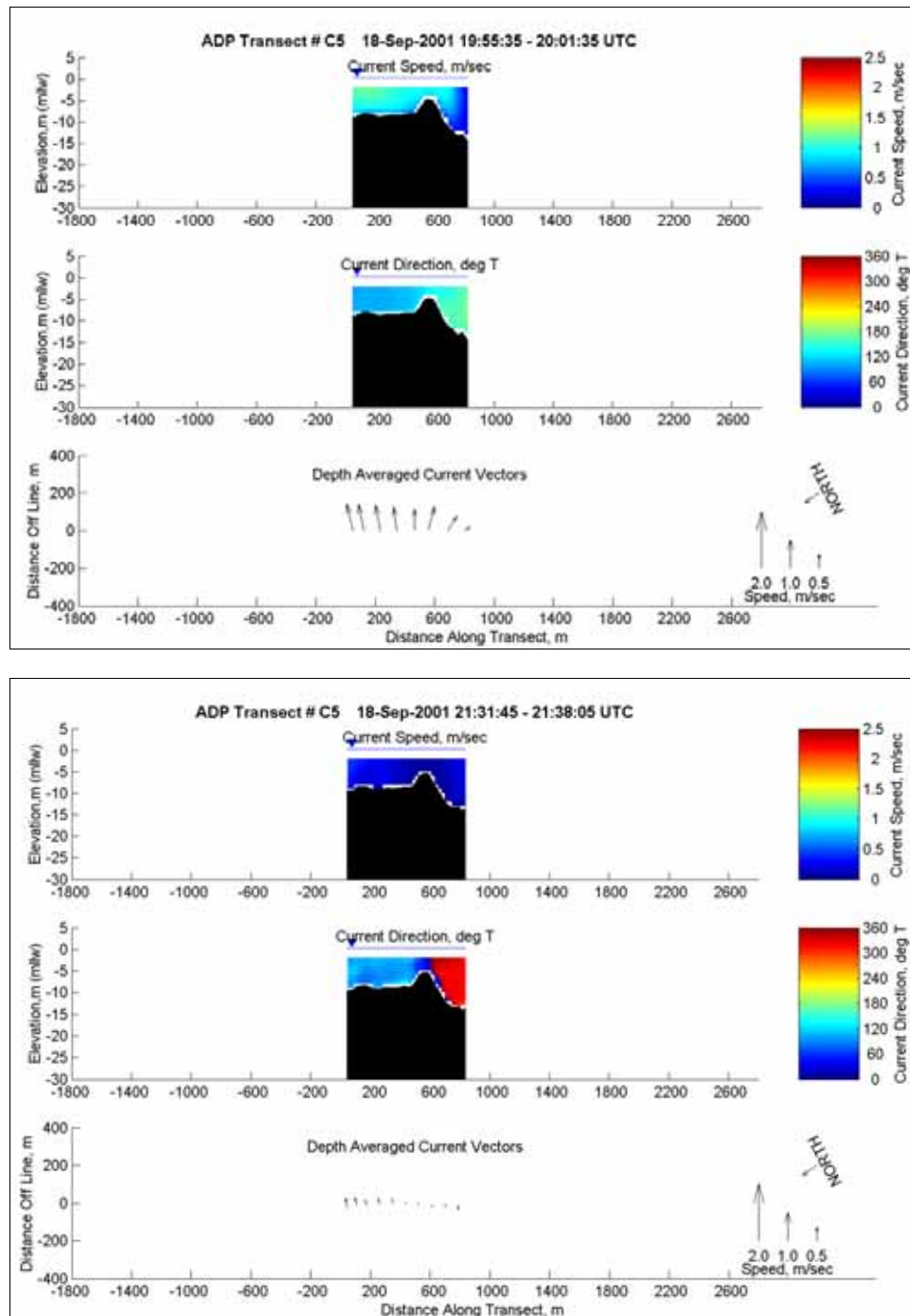
Figure D67.   Current speed, direction, and depth-averaged current vectors at ADP Transect C5 from 1955 to 2001 (upper) and 2131 to 2138 (lower) on 18 September 2001
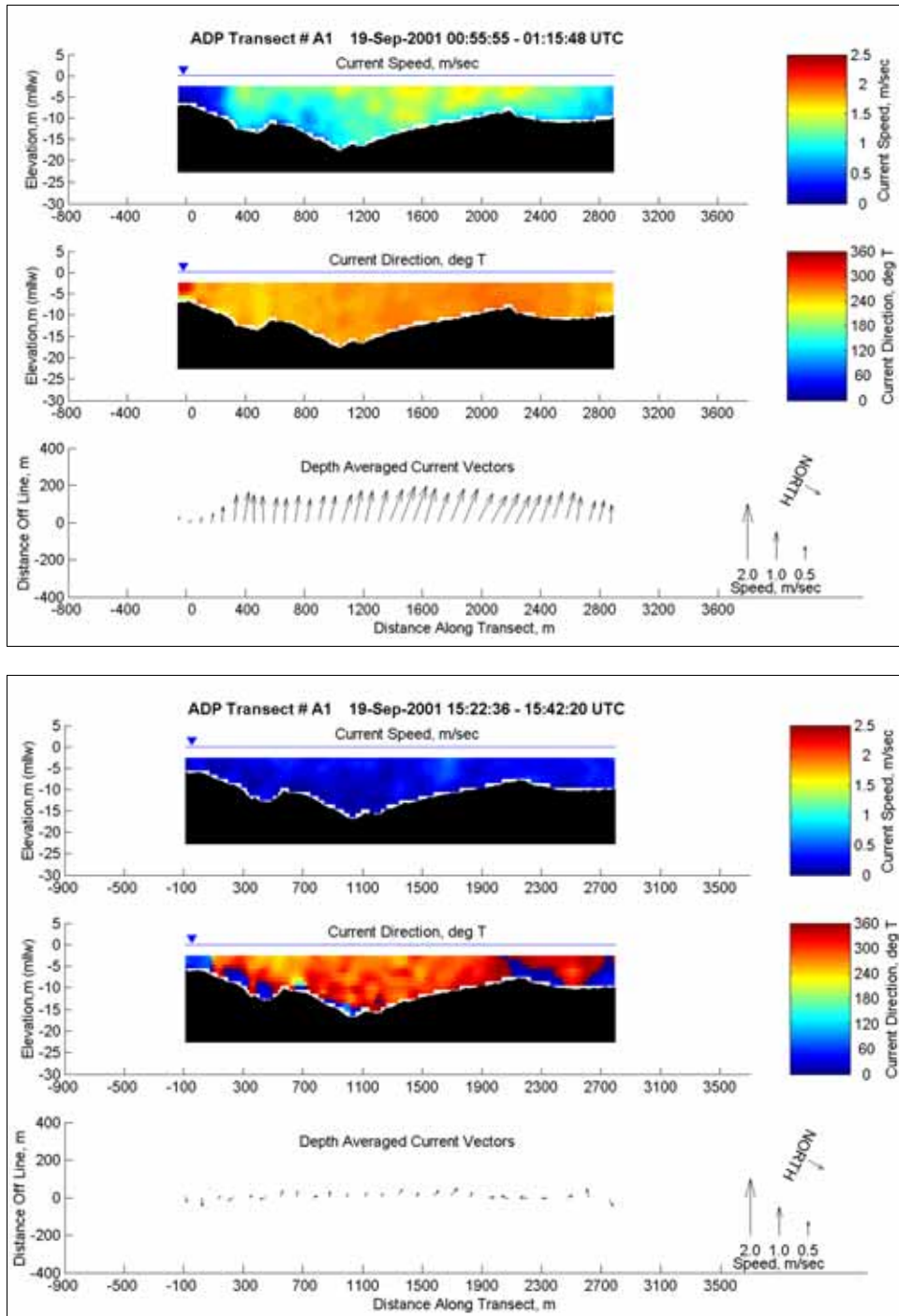
Figure D68.   Current speed, direction, and depth-averaged current vectors at
ADP Transect A1 from 0055 to 0115 (upper) and 1522 to 1542
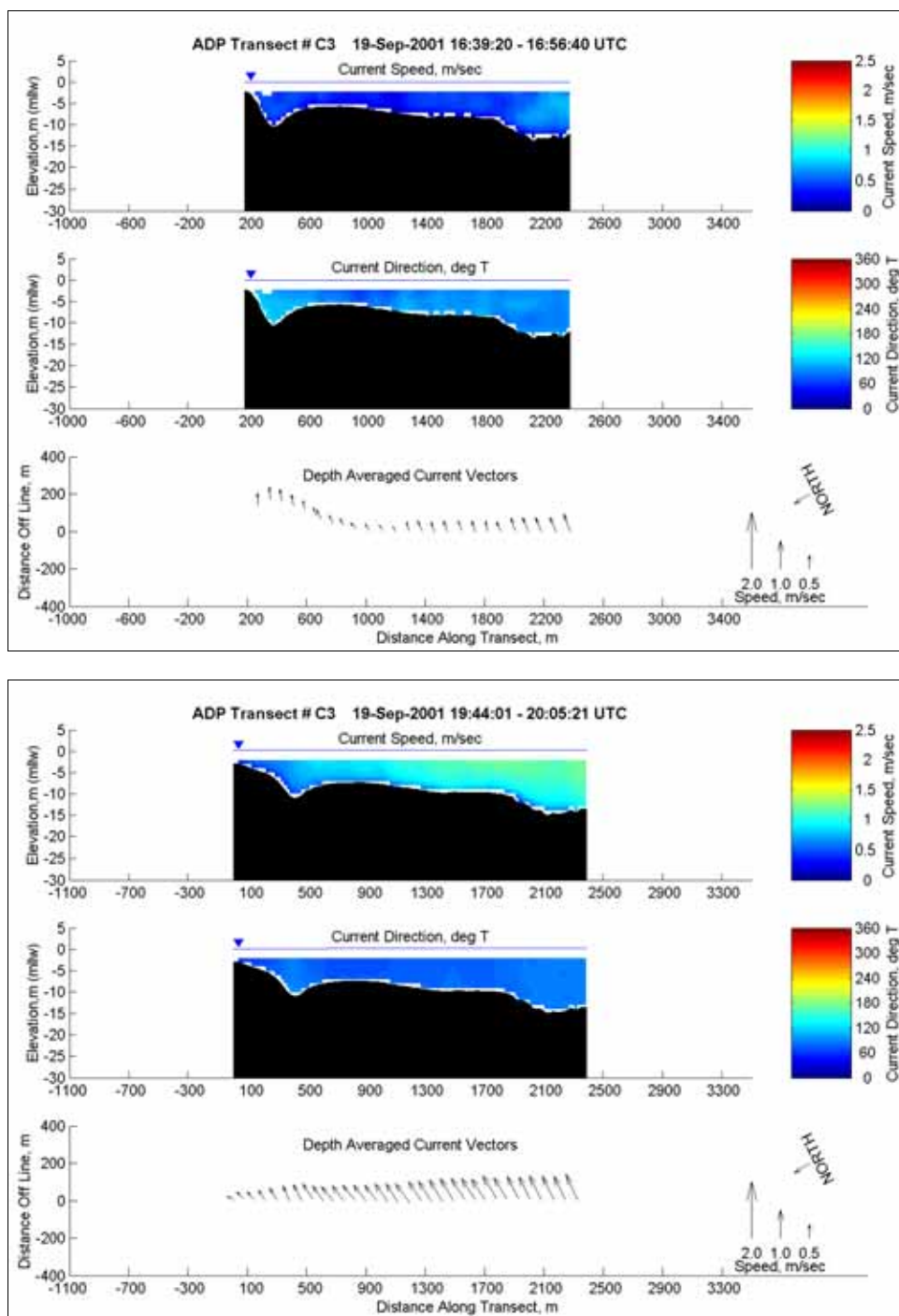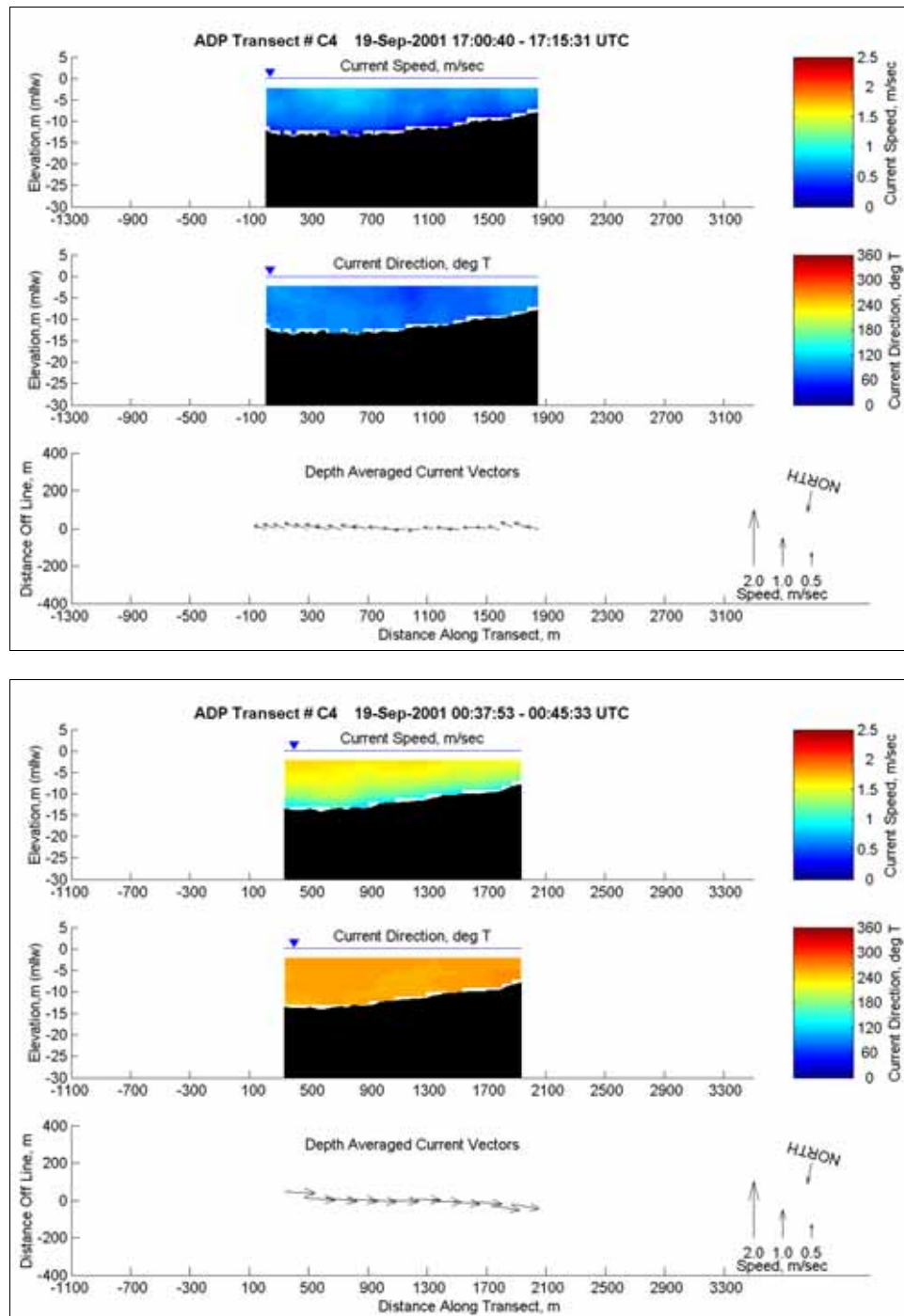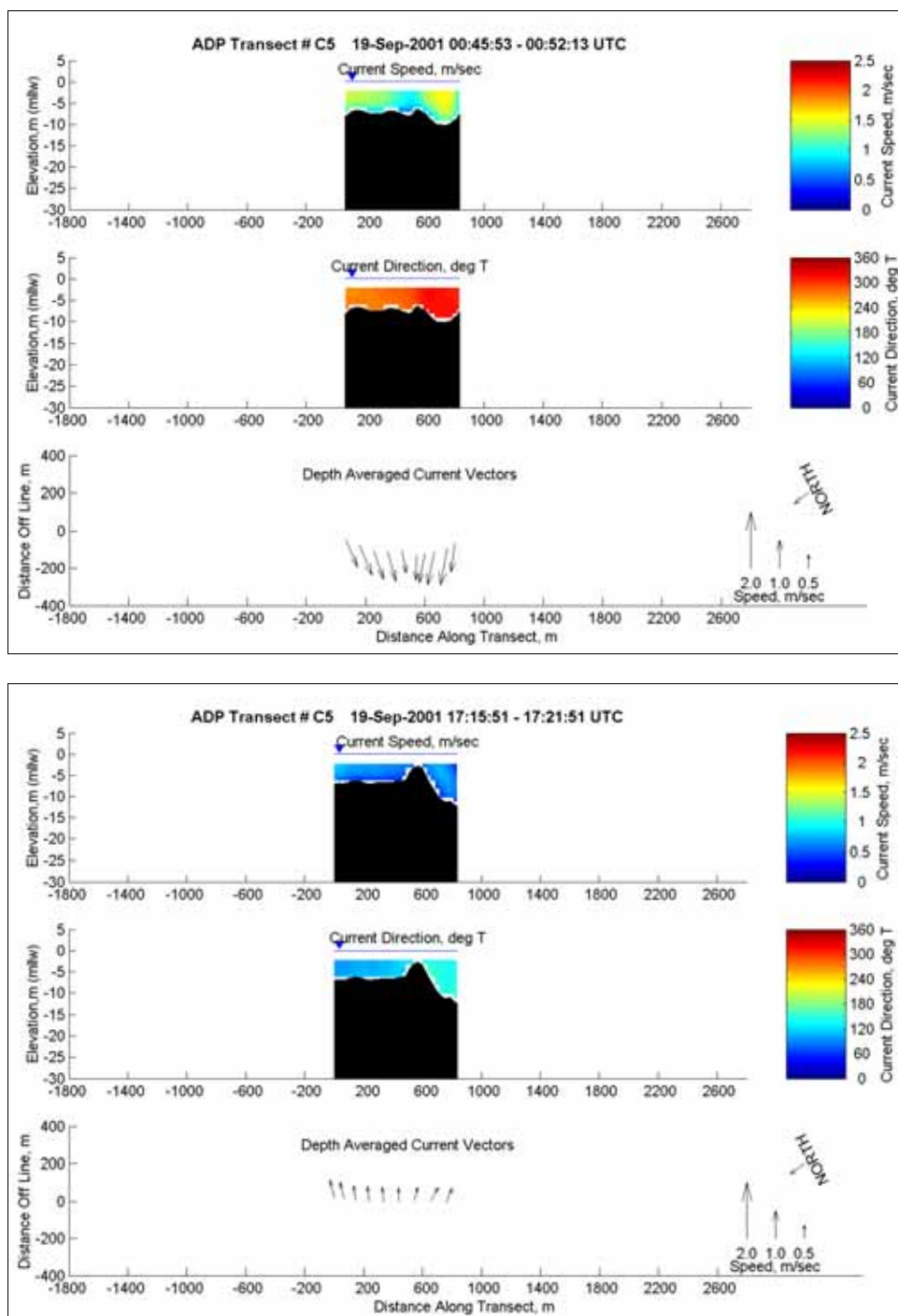(lower) on 19 September 2001
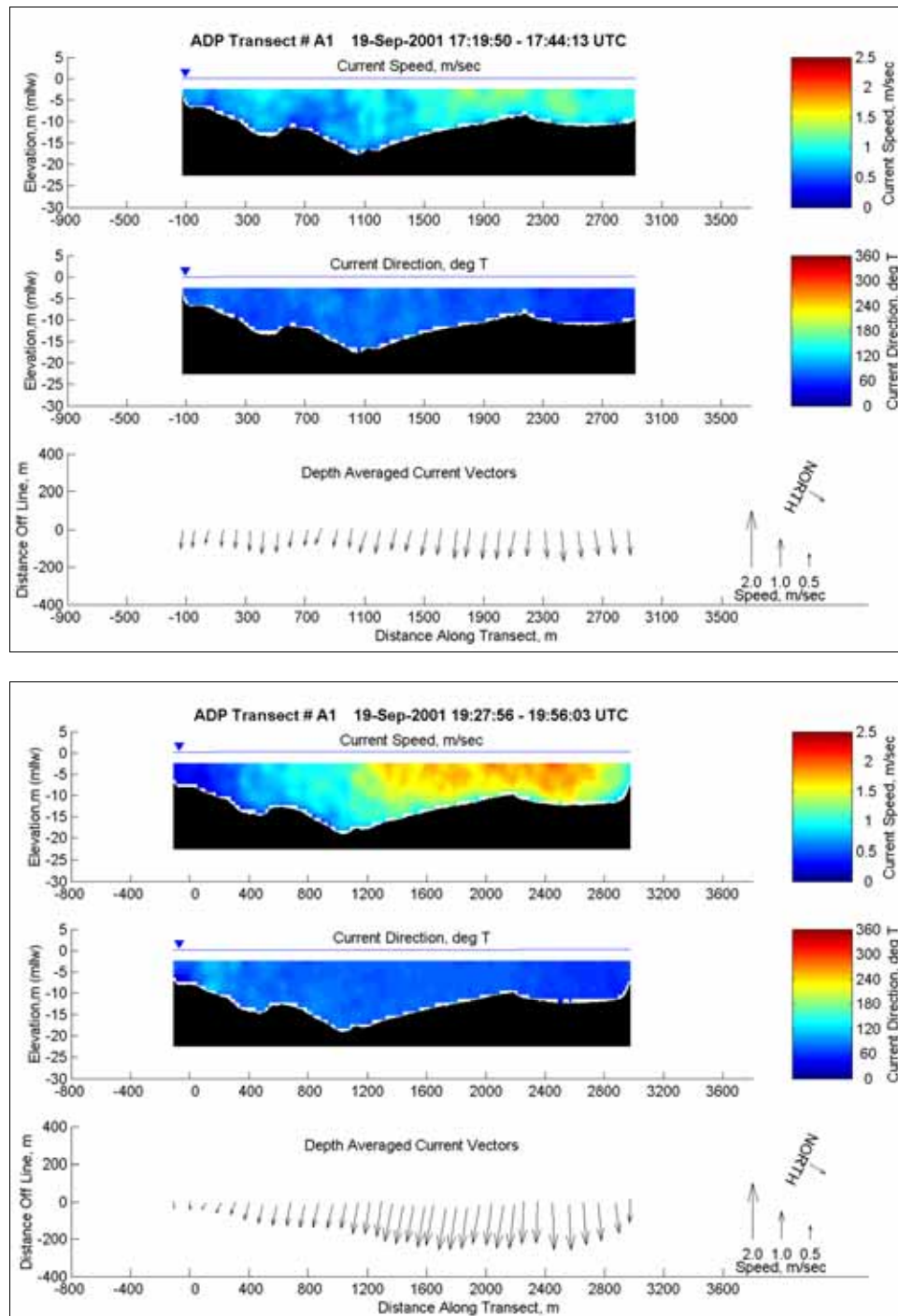
Figure D69.   Current speed, direction, and depth-averaged current vectors at
ADP Transect A1 from 1719 to 1744 (upper) and 1927 to 1956
(lower) on 19 September 2001
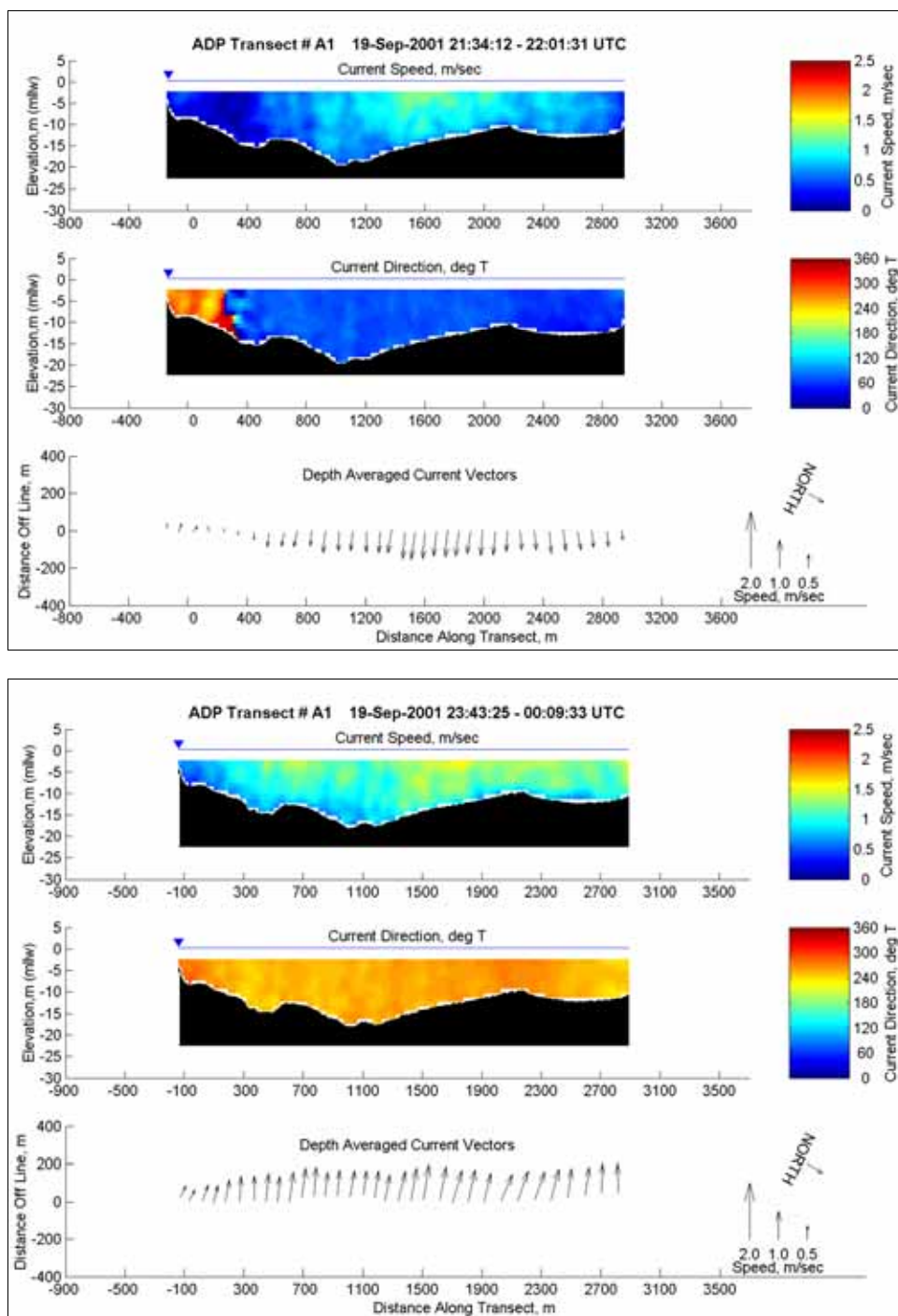
Figure D70. Current speed, direction, and depth-averaged current vectors at
ADP Transect A1 from 2134 to 2201 (upper) and 2343 to 0009
(lower) on 19 September 2001
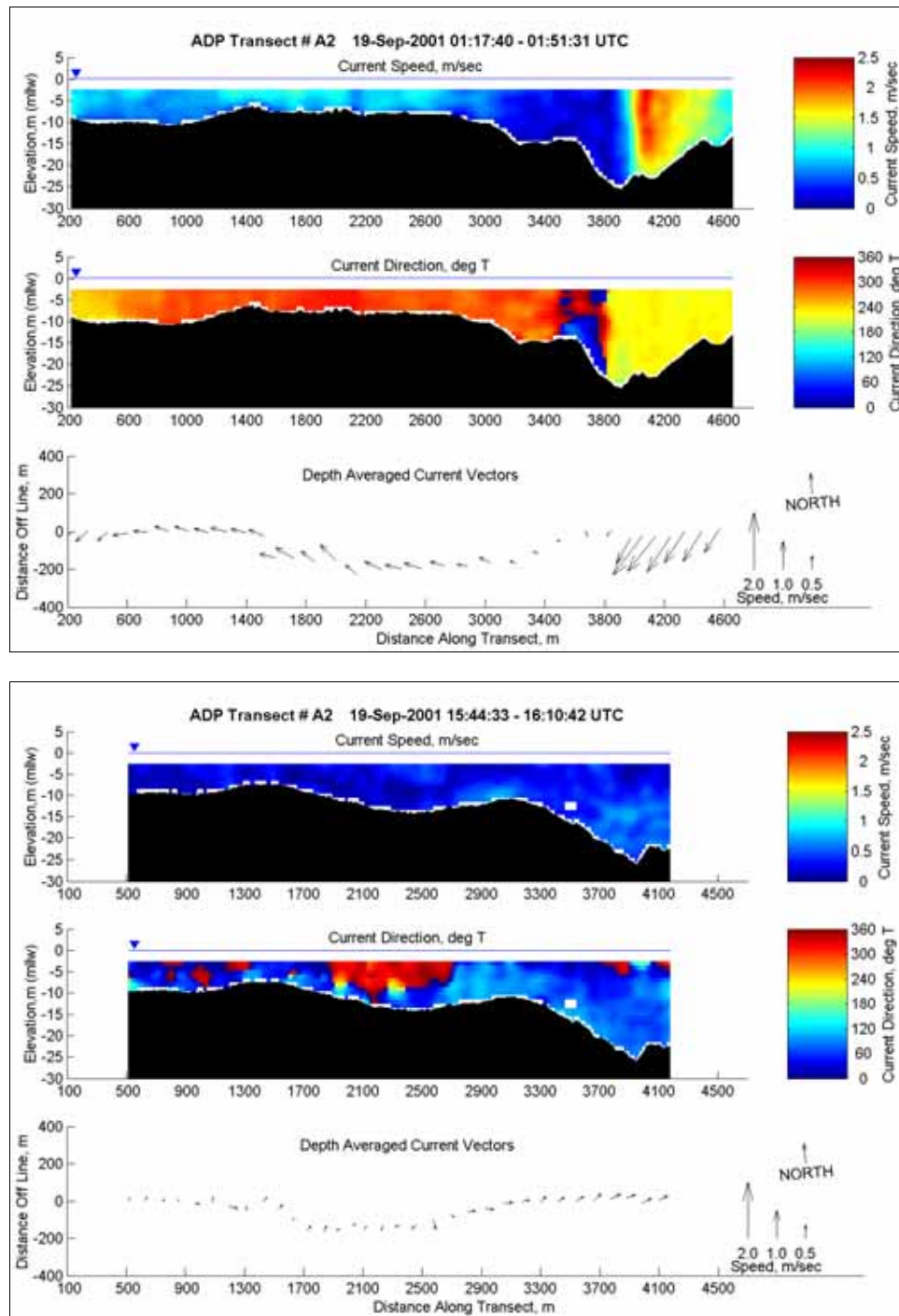
Figure D71.   Current speed, direction, and depth-averaged current vectors at ADP Transect A2 from 1740 to 151 (upper) and 1544 to 1610 (lower) on 19 September 2001
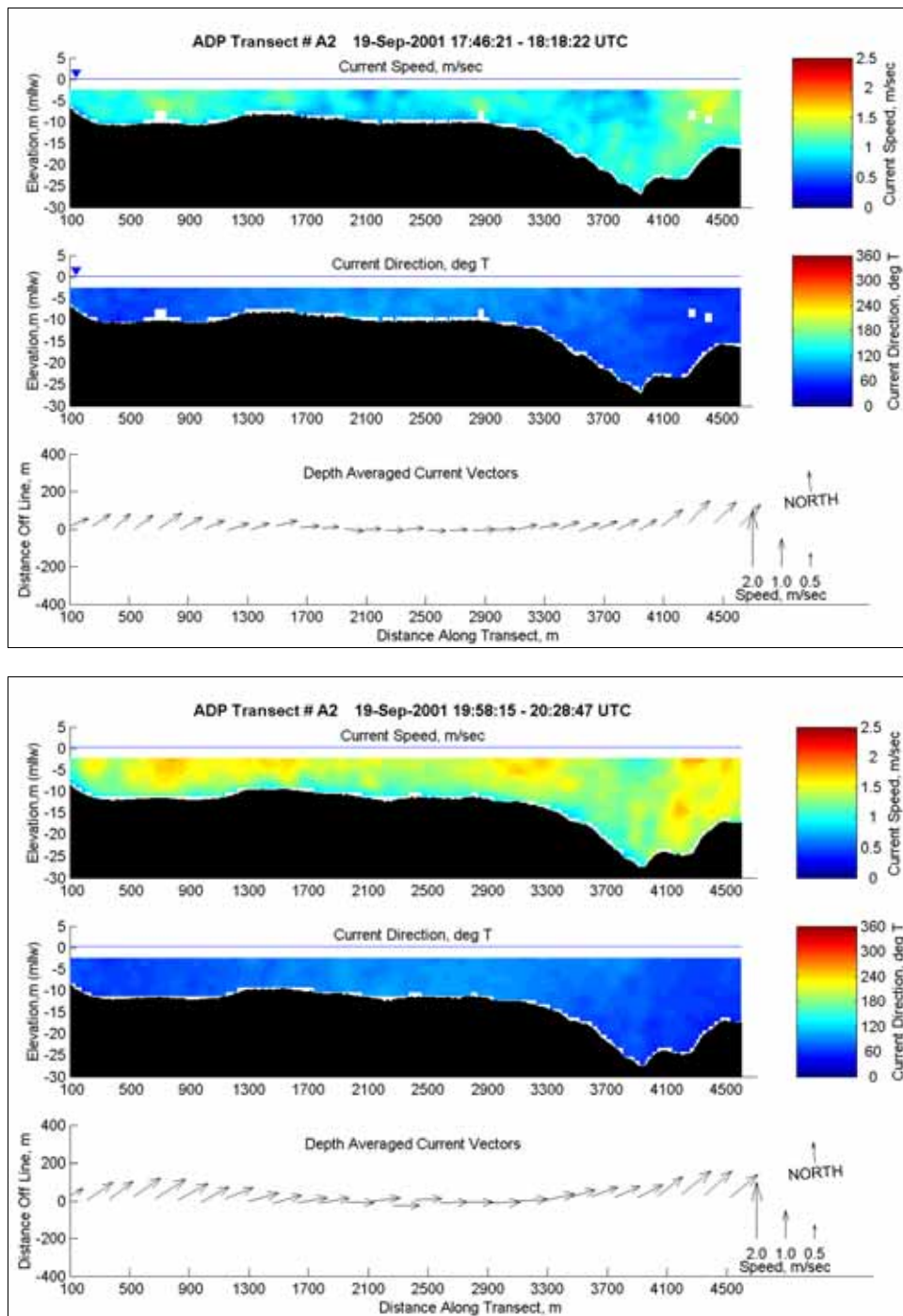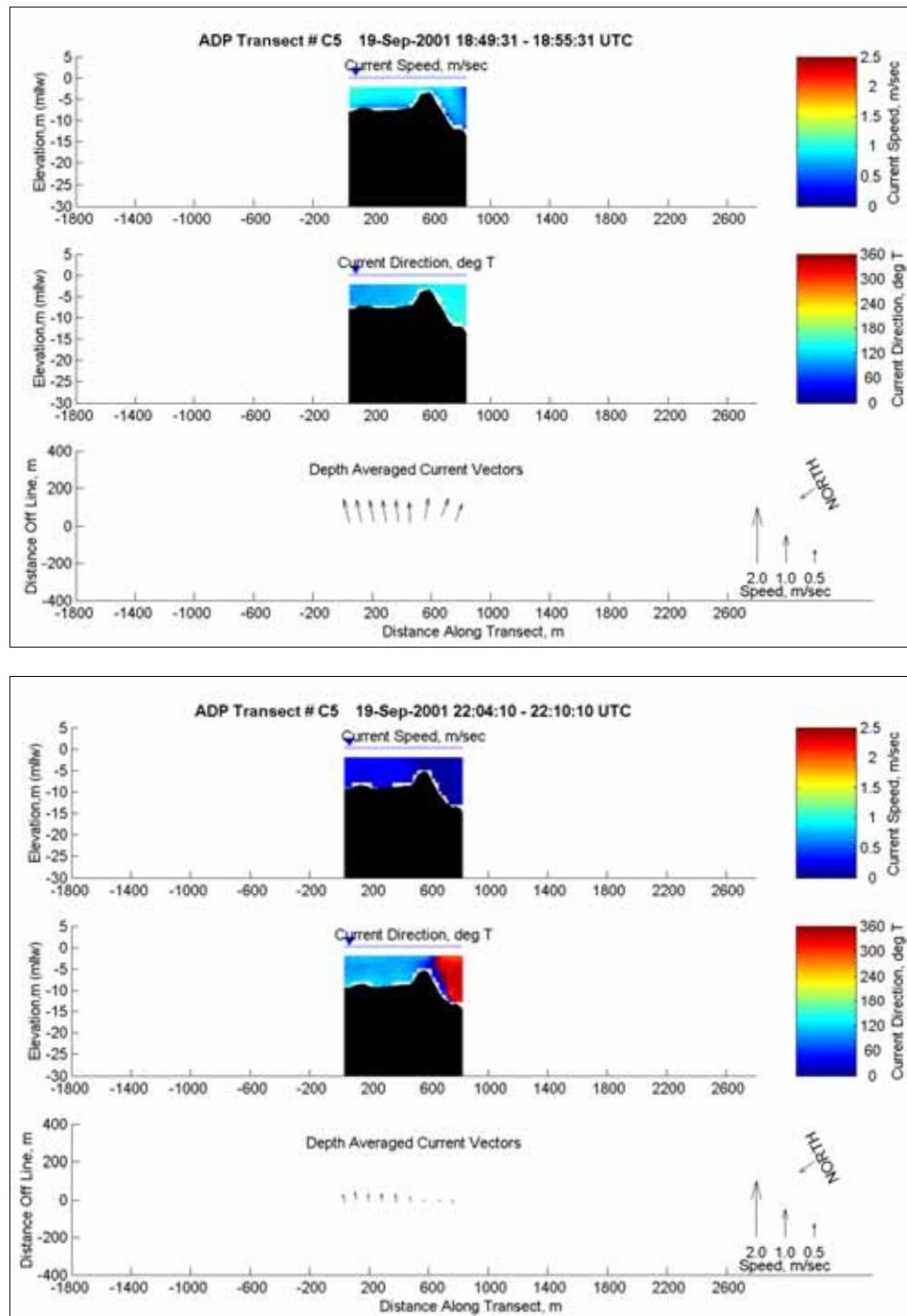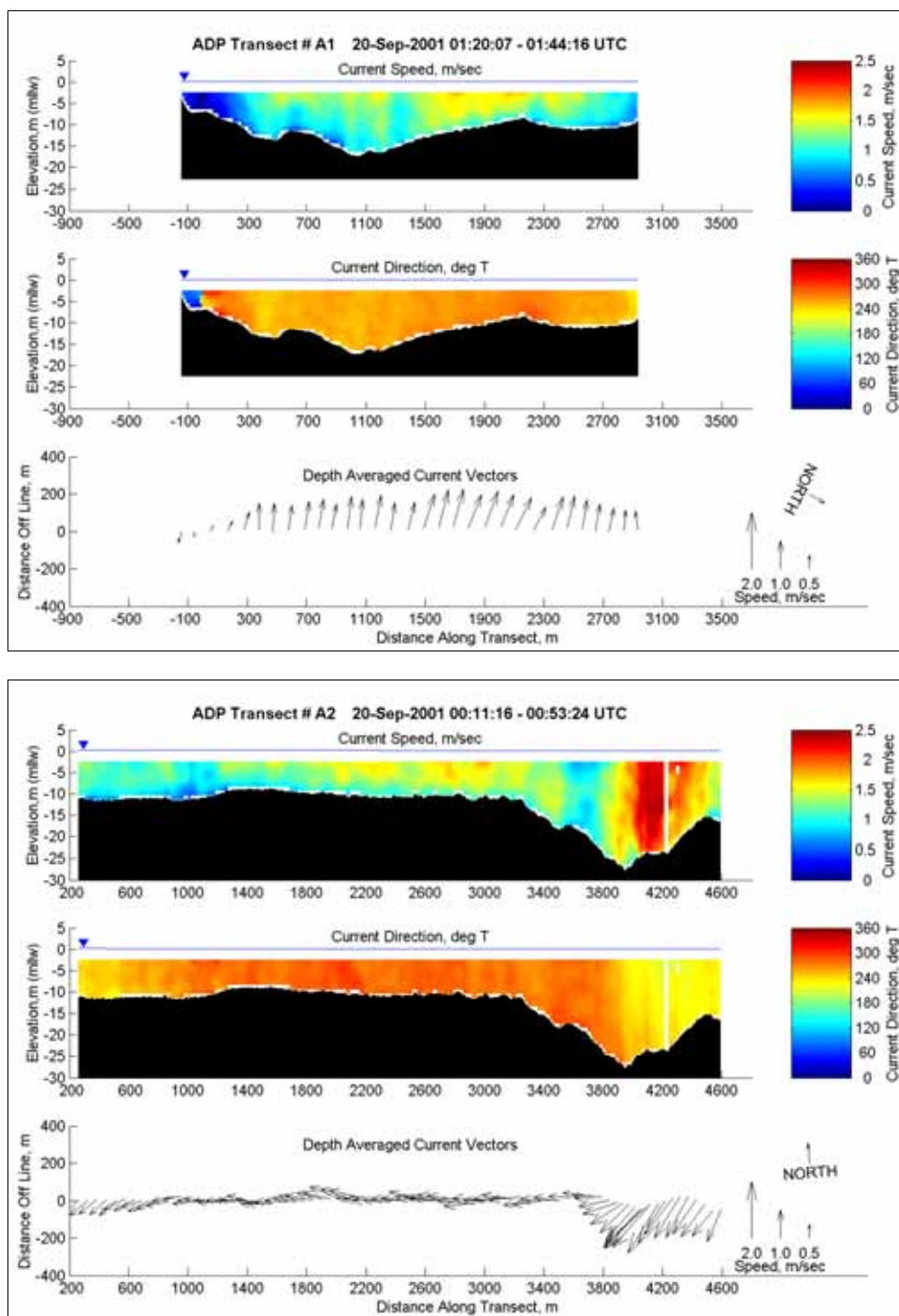
Figure D72. Current speed, direction, and depth-averaged current vectors at
ADP Transect A2 from 1746 to 1818 (upper) and Transect A3 from
1958 to 2028 (lower) on 19 September 2001
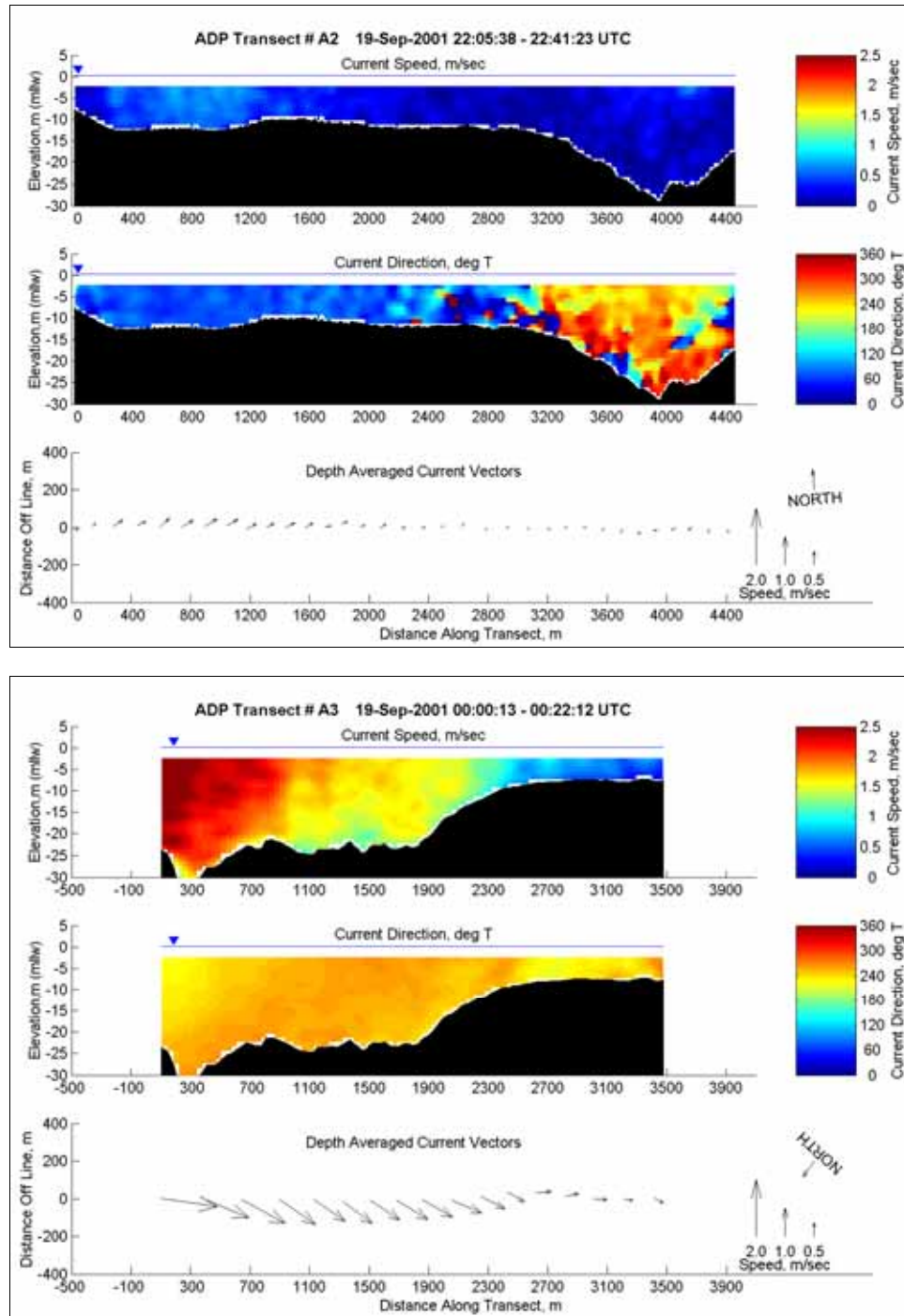
Figure D73. Current speed, direction, and depth-averaged current vectors at ADP Transect A2 from 2205 to 2241 (upper) and Transect A3 0000 to 0022 (lower) on 19 September 2001
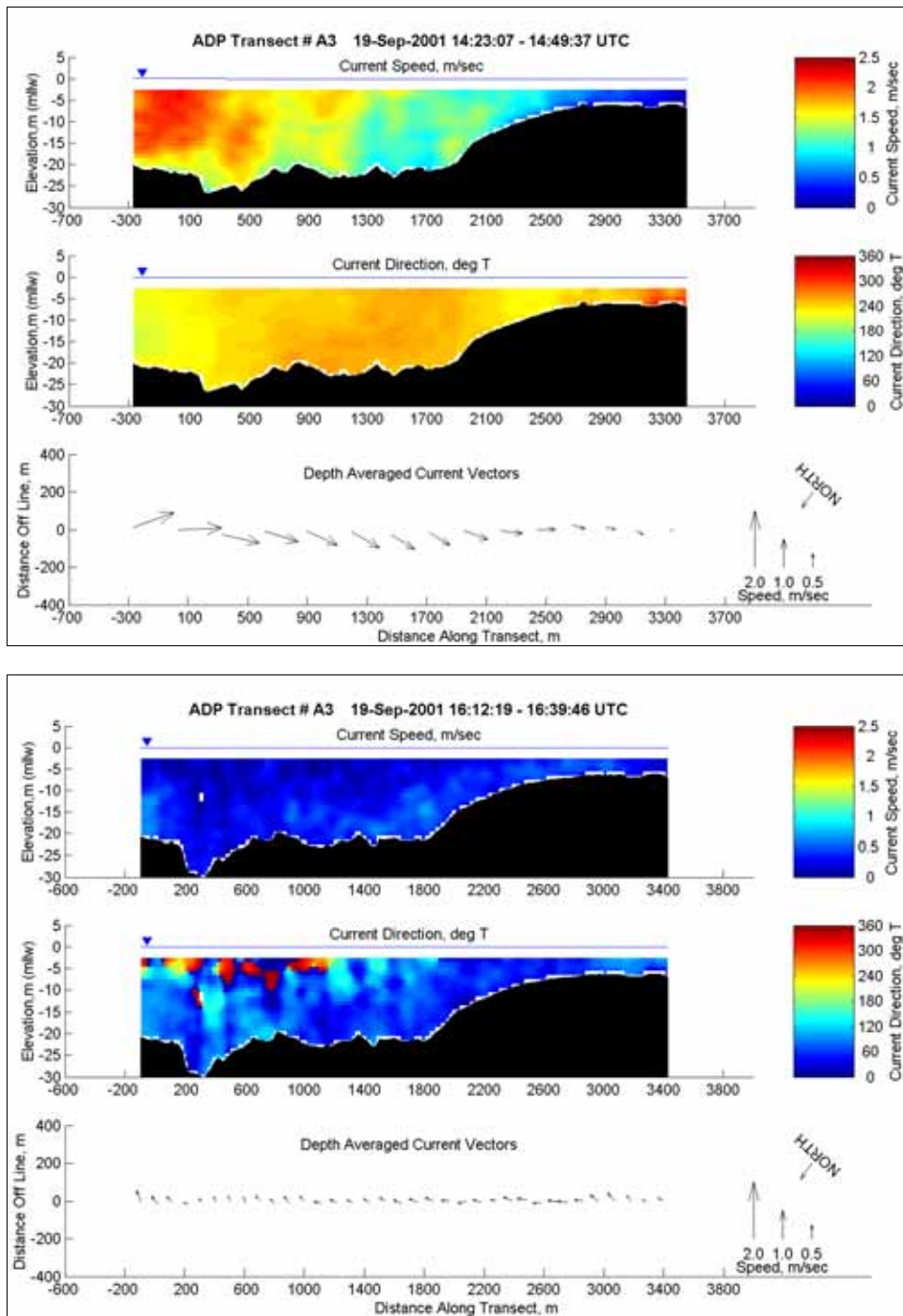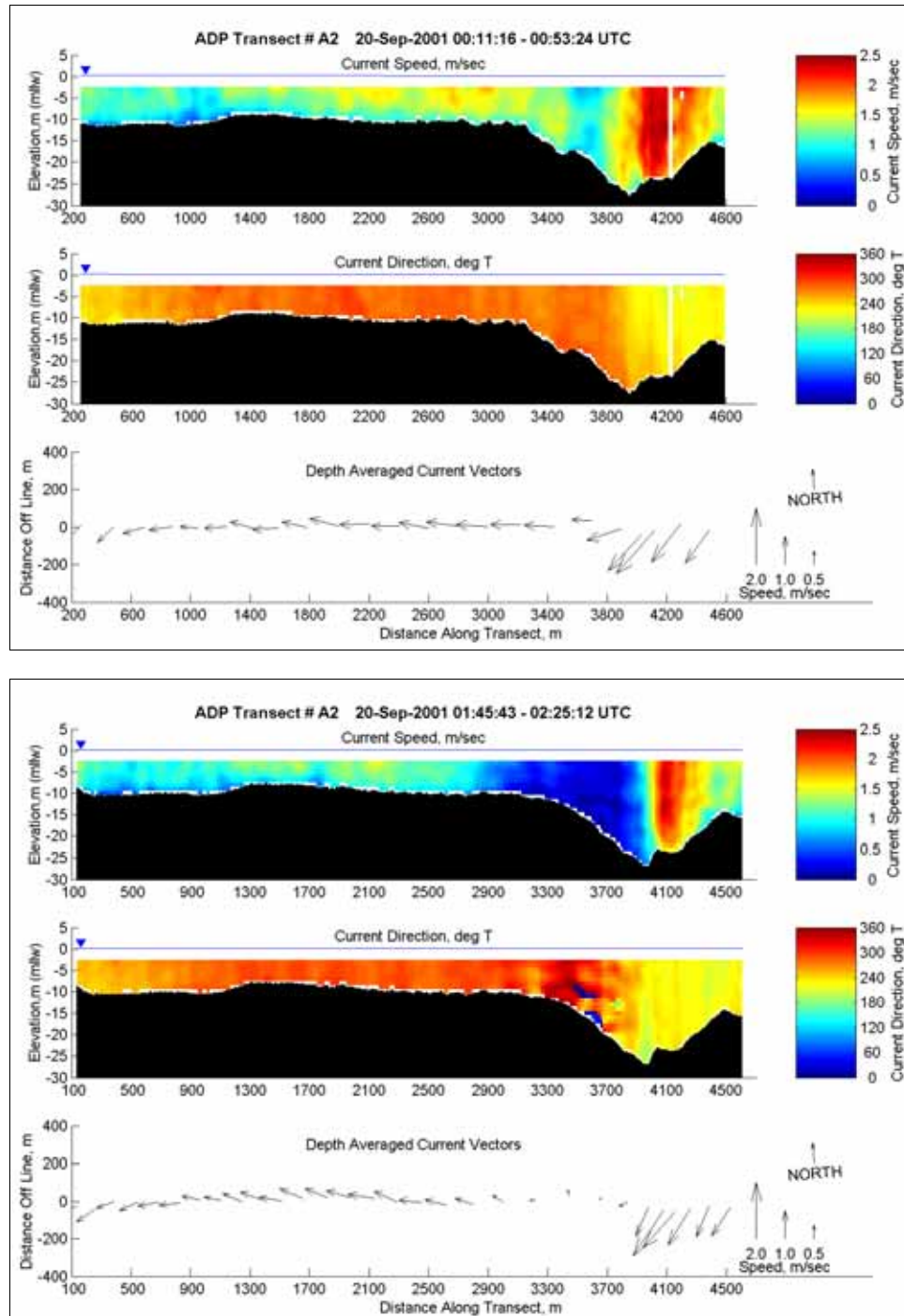
Figure D74.   Current speed, direction, and depth-averaged current vectors at
ADP Transect A3 from 1423 to 1449 (upper) and 1612 to 1639
(lower) on 19 September 2001
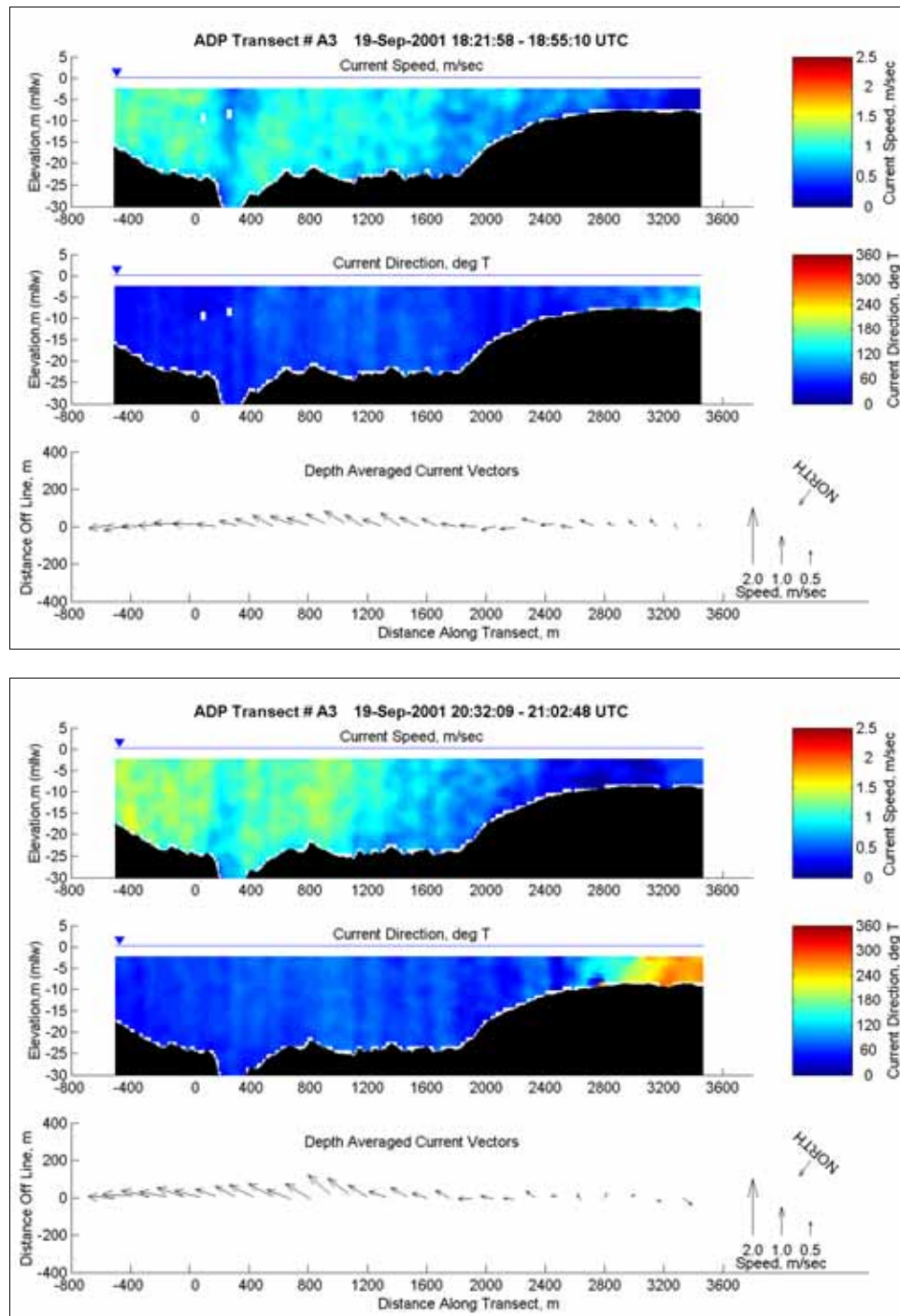
Figure D75.   Current speed, direction, and depth-averaged current vectors at
                ADP Transect A3 from 1821 to 1855 (upper) and 2032 to 2102
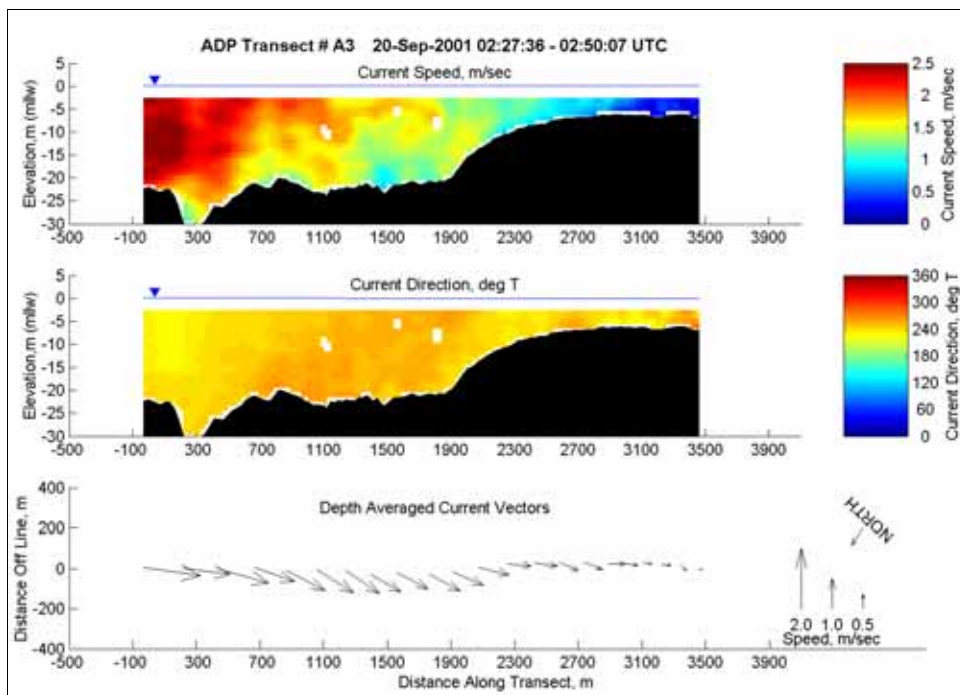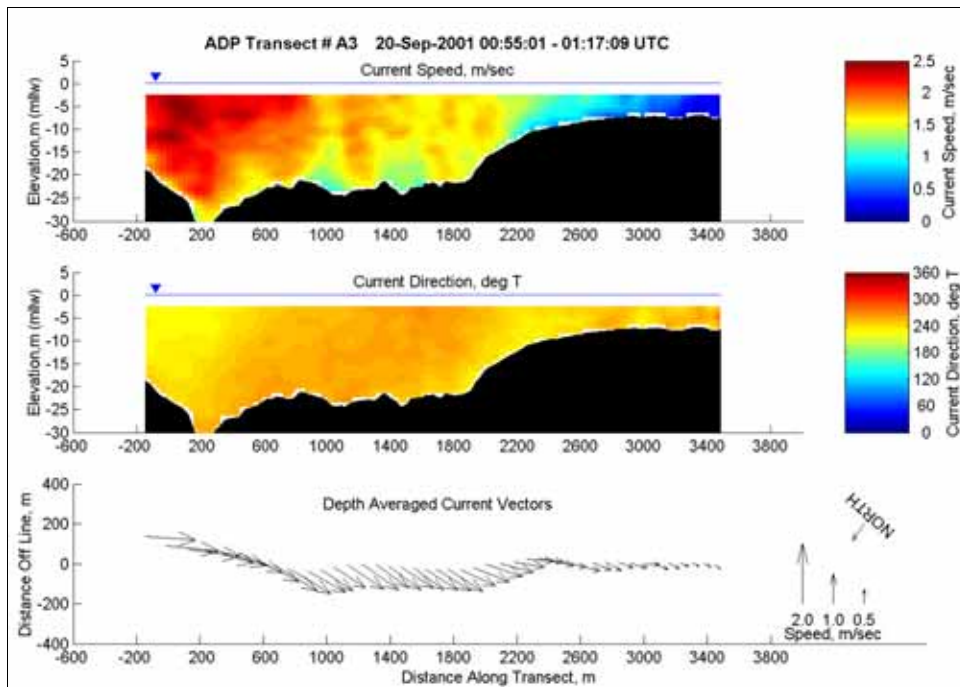   (lower) on 19 September 2001

Figure D76. Current speed, direction, and depth-averaged current vectors at
ADP Transect A3 from 2120 to 2131 (upper) and 2244 to 2310
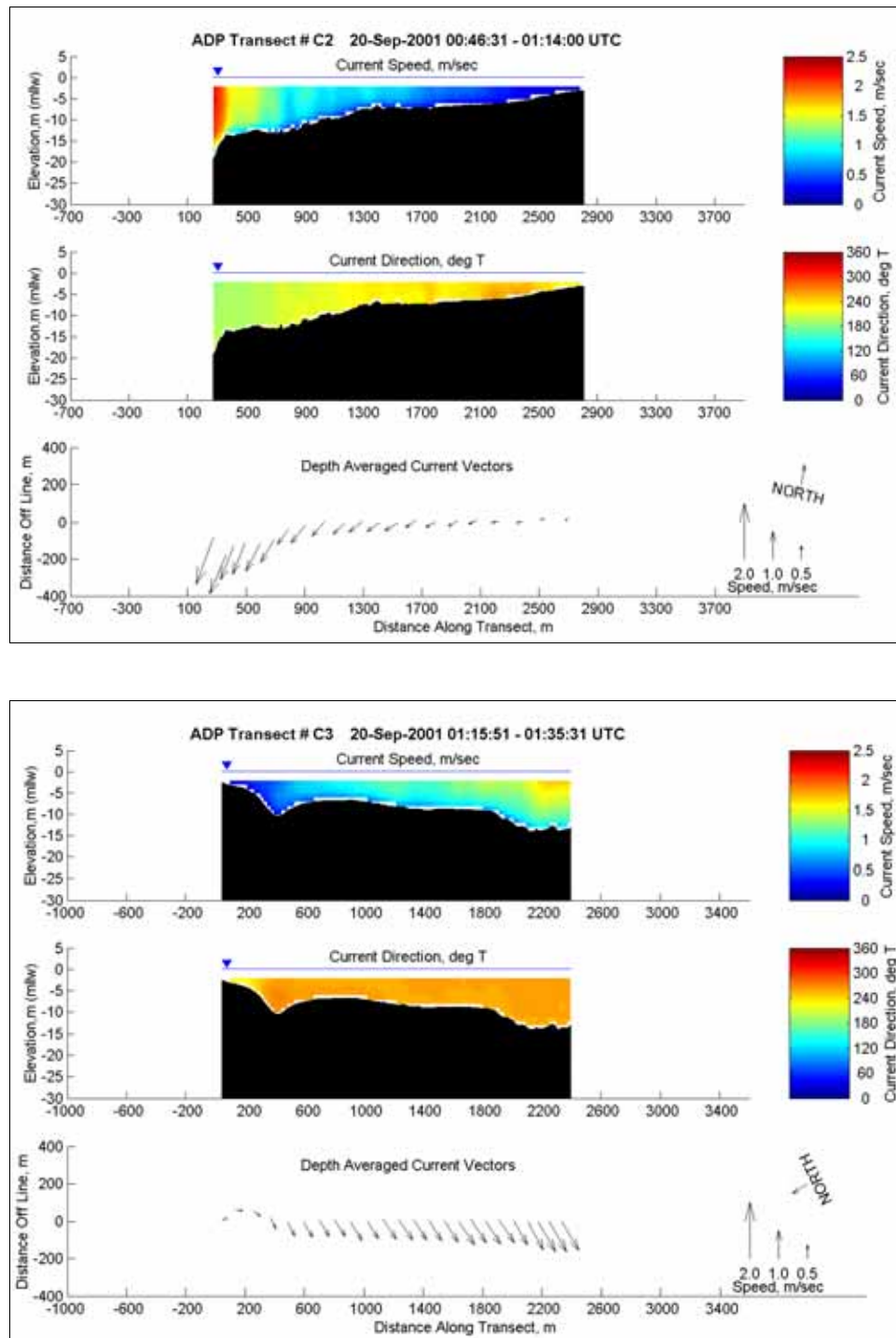(lower) on 19 September 2001

Figure D77.   Current speed, direction, and depth-averaged current vectors at ADP Transect B1 from 0027 to 0033 (upper) and 1451 to 1459 (lower) on 19 September 2001

Figure D78.   Current speed, direction, and depth-averaged current vectors at
ADP Transect B1 from 1647 to 1653 (upper) and 1859 to 1906
(lower) on 19 September 2001

Figure D79. Current speed, direction, and depth-averaged current vectors at ADP Transect B1 from 2106 to 2113 (upper) and 2312 to 2319 (lower) on 19 September 2001

Figure D80.   Current speed, direction, and depth-averaged current vectors at
ADP Transect B2 from 0033 to 0045 (upper) and 1501 to 1511
(lower) on 19 September 2001

Figure D81.   Current speed, direction, and depth-averaged current vectors at ADP Transect B2 from 1654 to 1701 (upper) and 1906 to 1913 (lower) on 19 September 2001

Figure D82. Current speed, direction, and depth-averaged current vectors at ADP Transect B2 from 2113 to 2120 (upper) and 2319 to 2331 (lower) on 19 September 2001

Figure D83. Current speed, direction, and depth-averaged current vectors at ADP Transect B3 from 0046 to 0054 (upper) and 1512 to 1521 (lower) on 19 September 2001

Figure D84. Current speed, direction, and depth-averaged current vectors at ADP Transect B3 from 1702 to 1715 (upper) and 1914 to 1926 (lower) on 19 September 2001

Figure D85.   Current speed, direction, and depth-averaged current vectors at ADP Transect C3 from 2332 to 2341 (upper) and Transect C1 from 1352 to 1429 (lower) on 19 September 2001

Figure D86. Current speed, direction, and depth-averaged current vectors at ADP Transect C1 from 1551 to 1612 (upper) and 1723 to 1740 (lower) on 19 September 2001

Figure D87.   Current speed, direction, and depth-averaged current vectors at
               ADP Transect C1 from 1857 to 1914 (upper) and 2038 to 2056
               (lower) on 19 September 2001

Figure D88.   Current speed, direction, and depth-averaged current vectors at
ADP Transect C1 from 2212 to 2236 (upper) and 2355 to 0043
(lower) on 19 September 2001

Figure D89. Current speed, direction, and depth-averaged current vectors at ADP Transect C2 from 1615 to 1632 (upper) and 1746 to 1802 (lower) on 19 September 2001

Figure D90. Current speed, direction, and depth-averaged current vectors at ADP Transect C2 from 1921 to 1935 (upper) and 2059 to 2117 (lower) on 19 September 2001

Figure D91.　Current speed, direction, and depth-averaged current vectors at ADP Transect C3 from 0029 to 0036 (upper) and 1510 to 1526 (lower) on 19 September 2001

Figure D92.   Current speed, direction, and depth averaged current vectors at
ADP Transect C3 from 1639 to 1656 (upper) and 1944 to 2005
(lower) on 19 September 2001

Figure D93.   Current speed, direction, and depth-averaged current vectors at ADP Transect C4 from 1700 to 1715 (upper) and 0037 to 0045 (lower) on 19 September 2001

Figure D94.   Current speed, direction, and depth-averaged current vectors at
                ADP Transect C5 from 0045 to 0052 (upper) and 1715 to 1721
                (lower) on 19 September 2001

Figure D95.   Current speed, direction, and depth-averaged current vectors at ADP Transect C5 from 1849 to 1855 (upper) and 2204 to 2210 (lower) on 19 September 2001

Figure D96.   Current speed, direction, and depth-averaged current vectors at
ADP Transect A1 from 0120 to 0144 (upper) and Transect A2
0011 to 0053 (lower) on 20 September 2001

Figure D97.   Current speed, direction, and depth-averaged current vectors at
ADP Transect A2 from 0011 to 0053 (upper) and 0145 to 0225
(lower) on 20 September 2001

Figure D98. Current speed, direction, and depth-averaged current vectors at ADP Transect A3 from 0055 to 0117 (upper) and 0227 to 0250 (lower) on 20 September 2001

Figure D99.   Current speed, direction, and depth-averaged current vectors at
ADP Transect C2 from 0046 to 0114 (upper) and Transect C3 from
0115 to 0135 on 20 September 2001
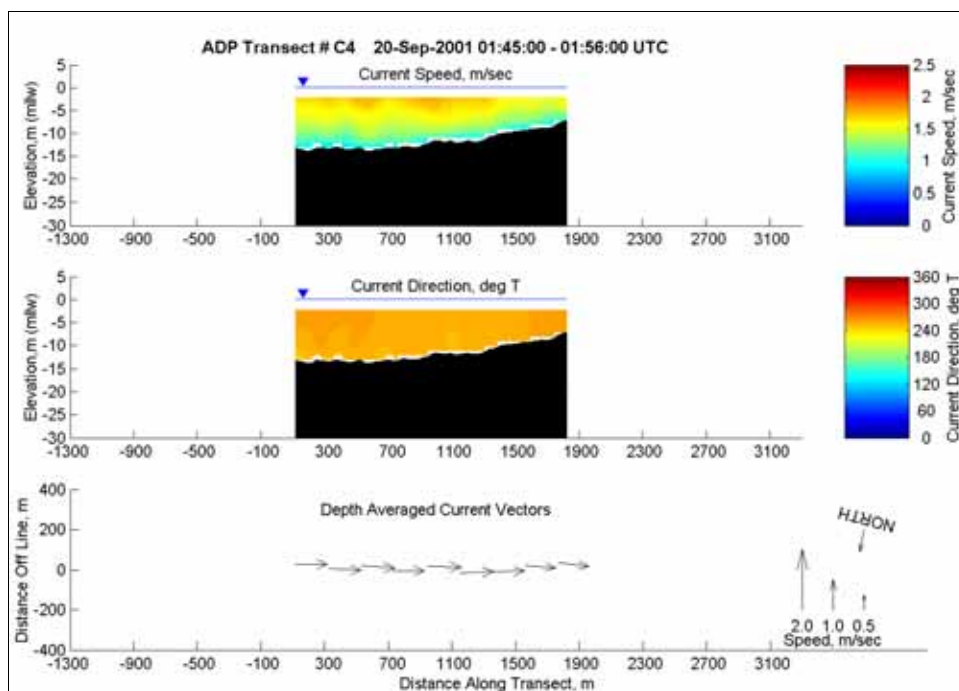
Figure D100. Current speed, direction, and depth-averaged current vectors at ADP Transect C4 from 0145 to 0156 on 20 September 2001

Figures D101 to D108

ADV ocean data quality parameters- heading, pitch and roll, and average signal correlation.
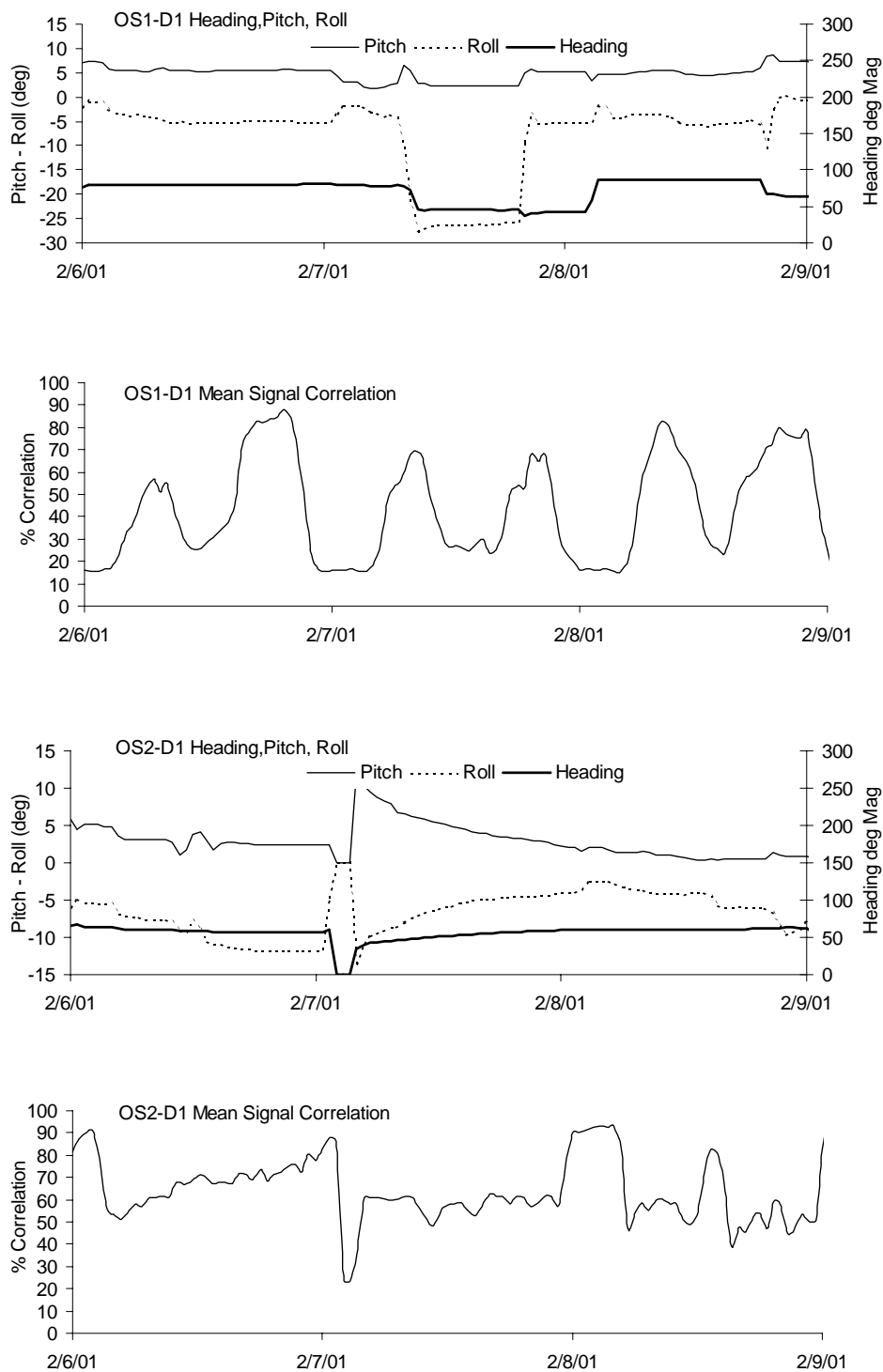
Figure D101.   SIDSEP data quality parameters, Deployment 1, 2-9 February 2001
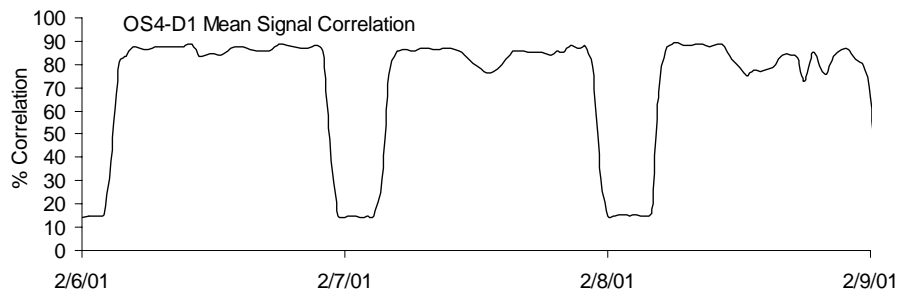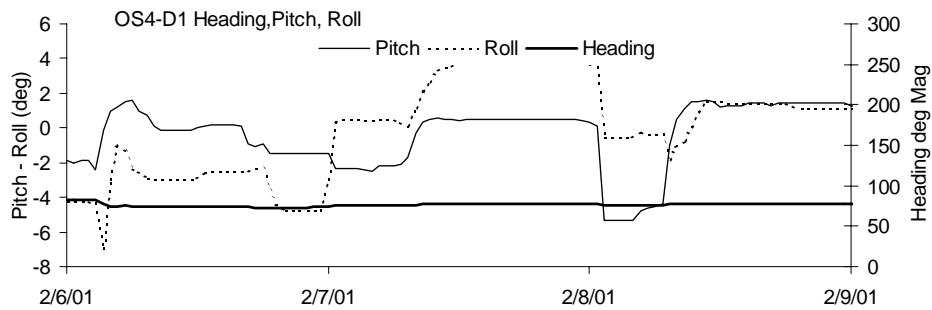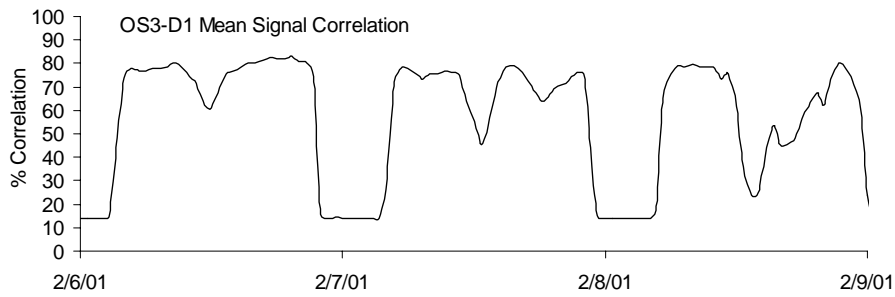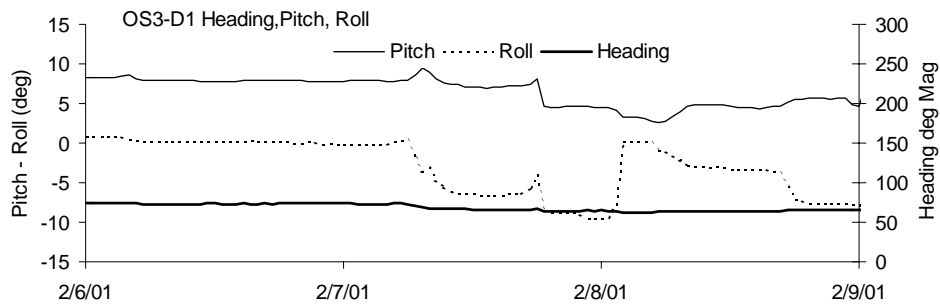
Figure D102.   SIDSEP data quality parameters, Deployment 1, 2-9 February 2001
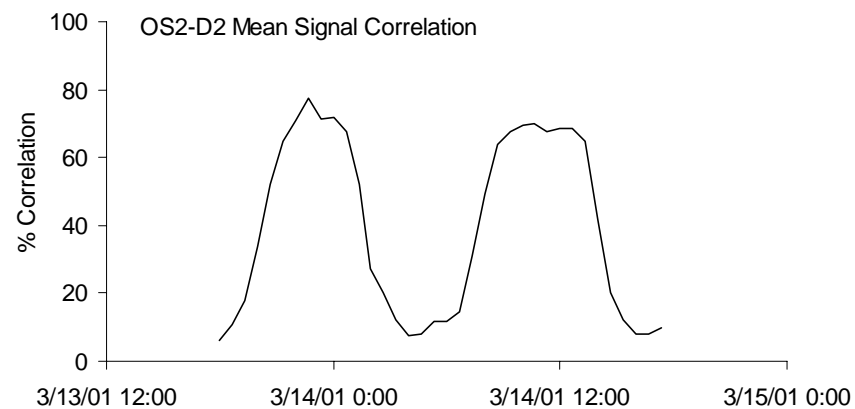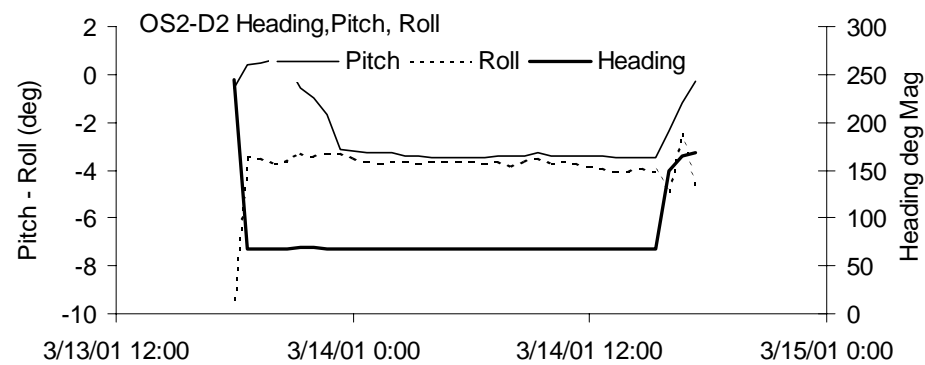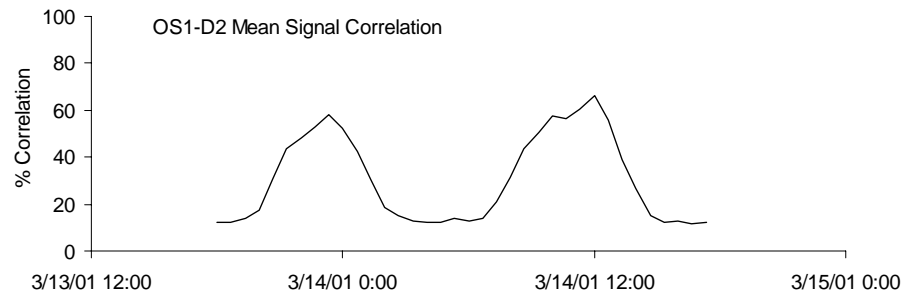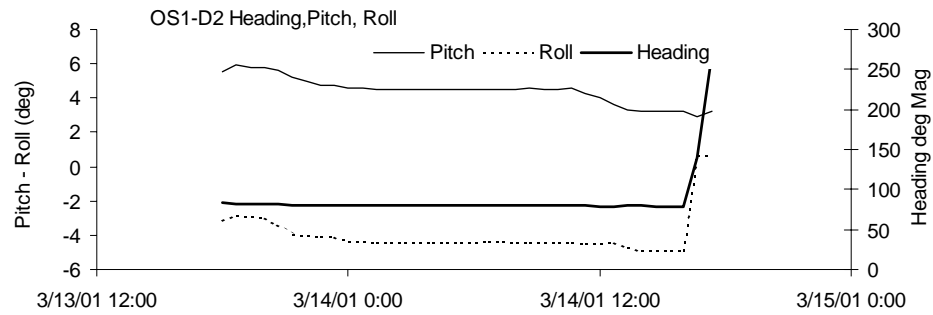
Figure D103.   SIDSEP data quality parameters, Deployment 2, 14-15 March 2001
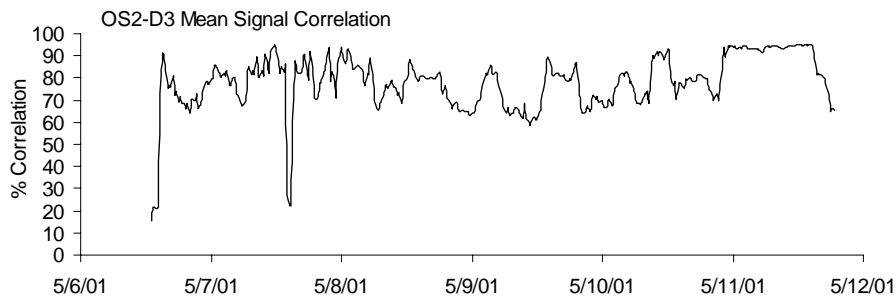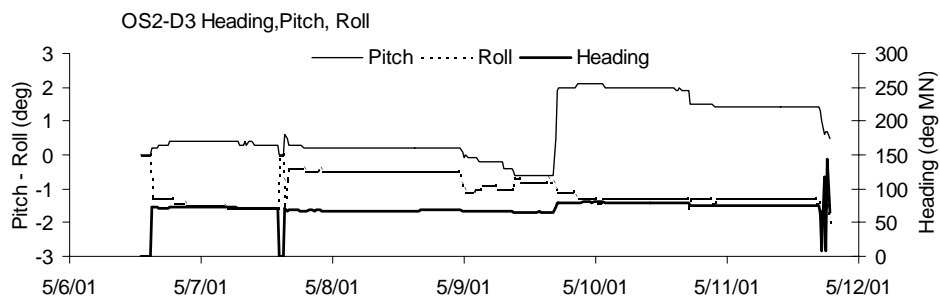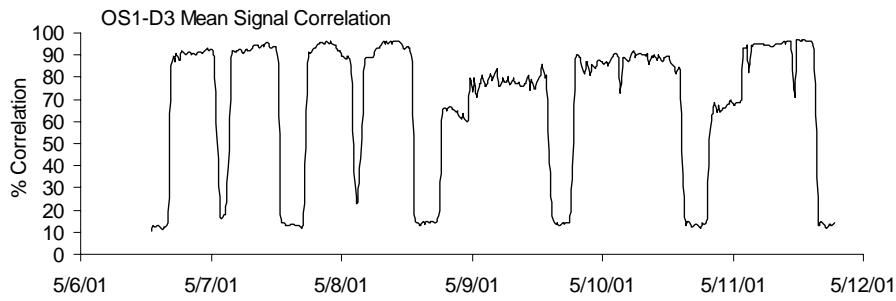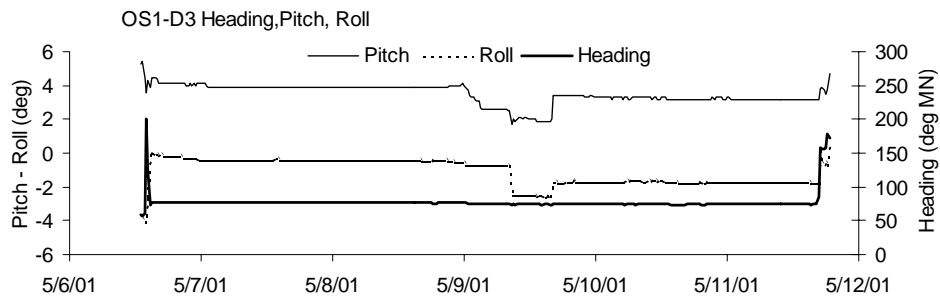
Figure D104. SIDSEP data quality parameters, Deployment 3, 6-12 May 2001

OS3-D3 Heading,Pitch, Roll

OS3-D3 Mean Signal Correlation

OS4-D3 Heading, Pitch, Roll

OS4-D3 Mean Signal Correlation
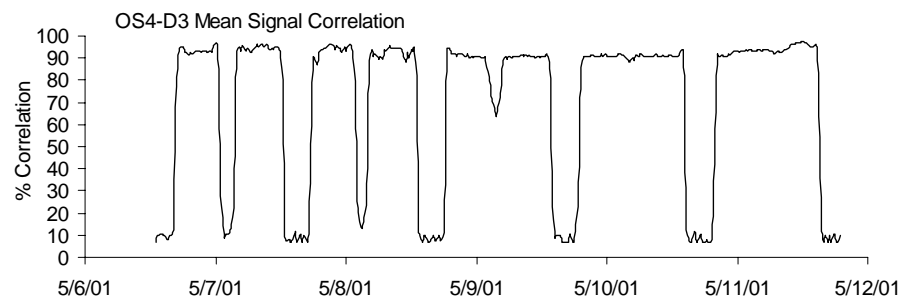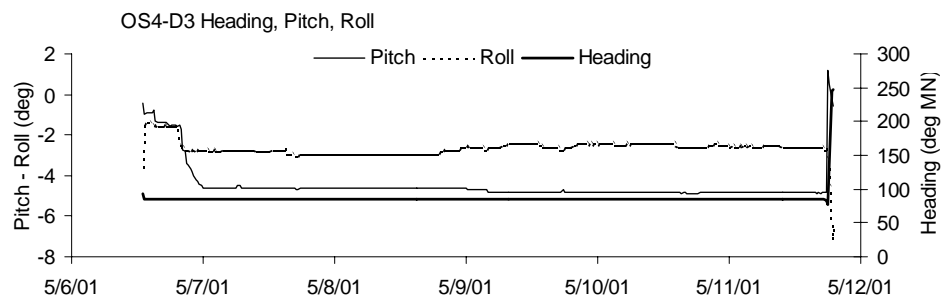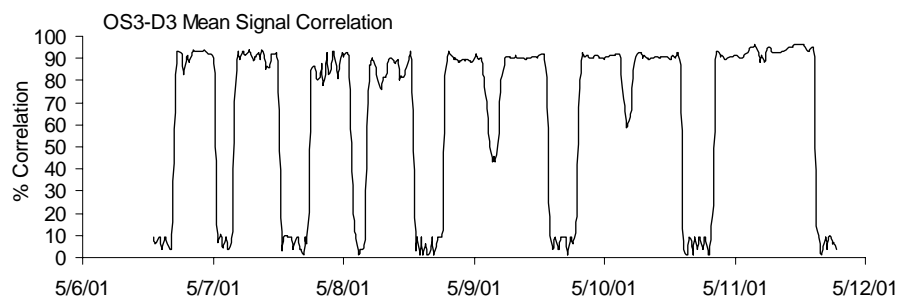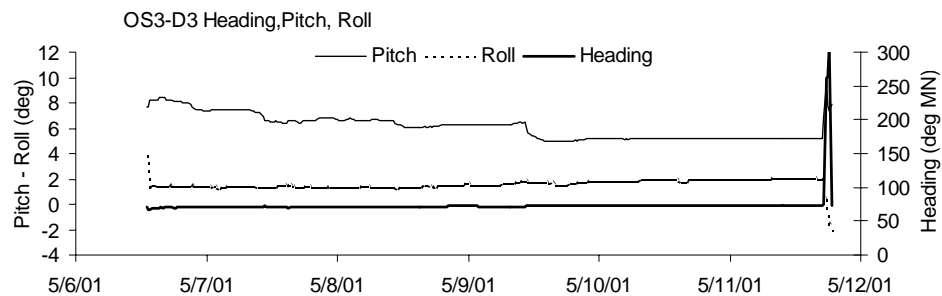
Figure D105. SIDSEP data quality parameters, Deployment 3, 6-12 May 2001
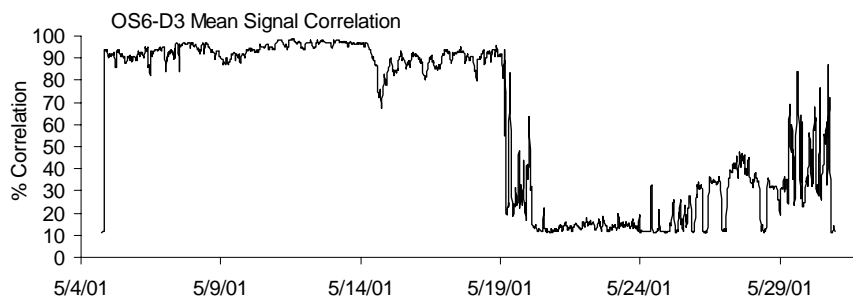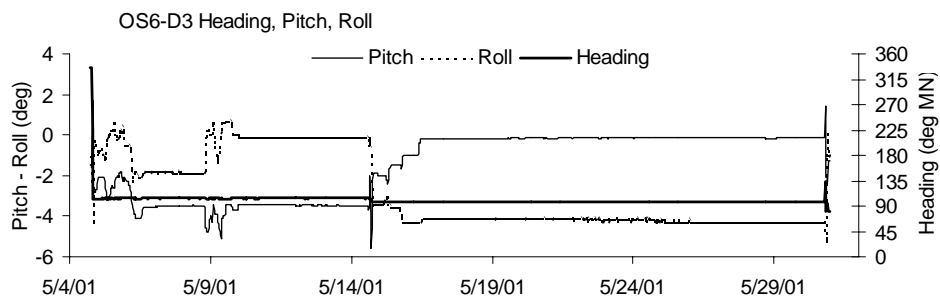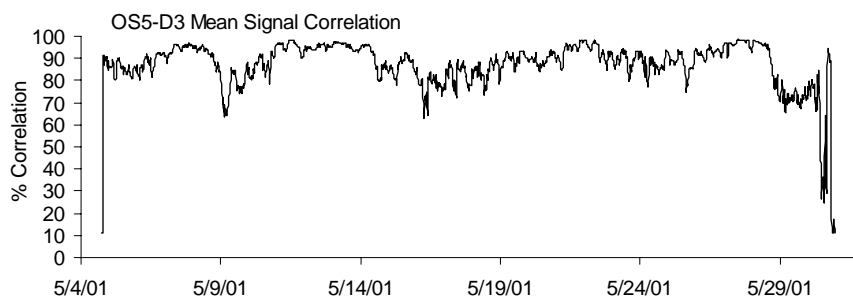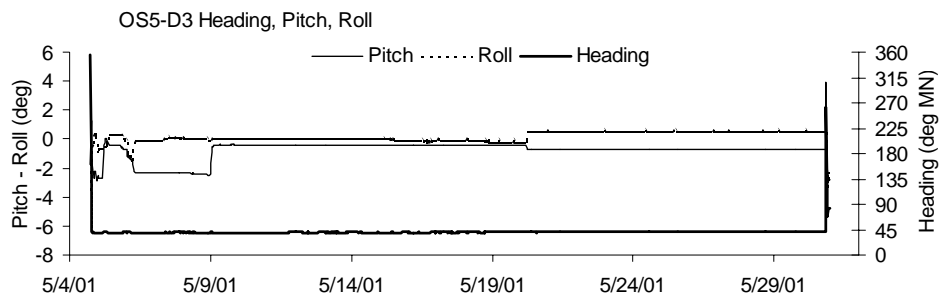
Figure D106. HESTT data quality parameters, Deployment 3, 4-30 May 2001
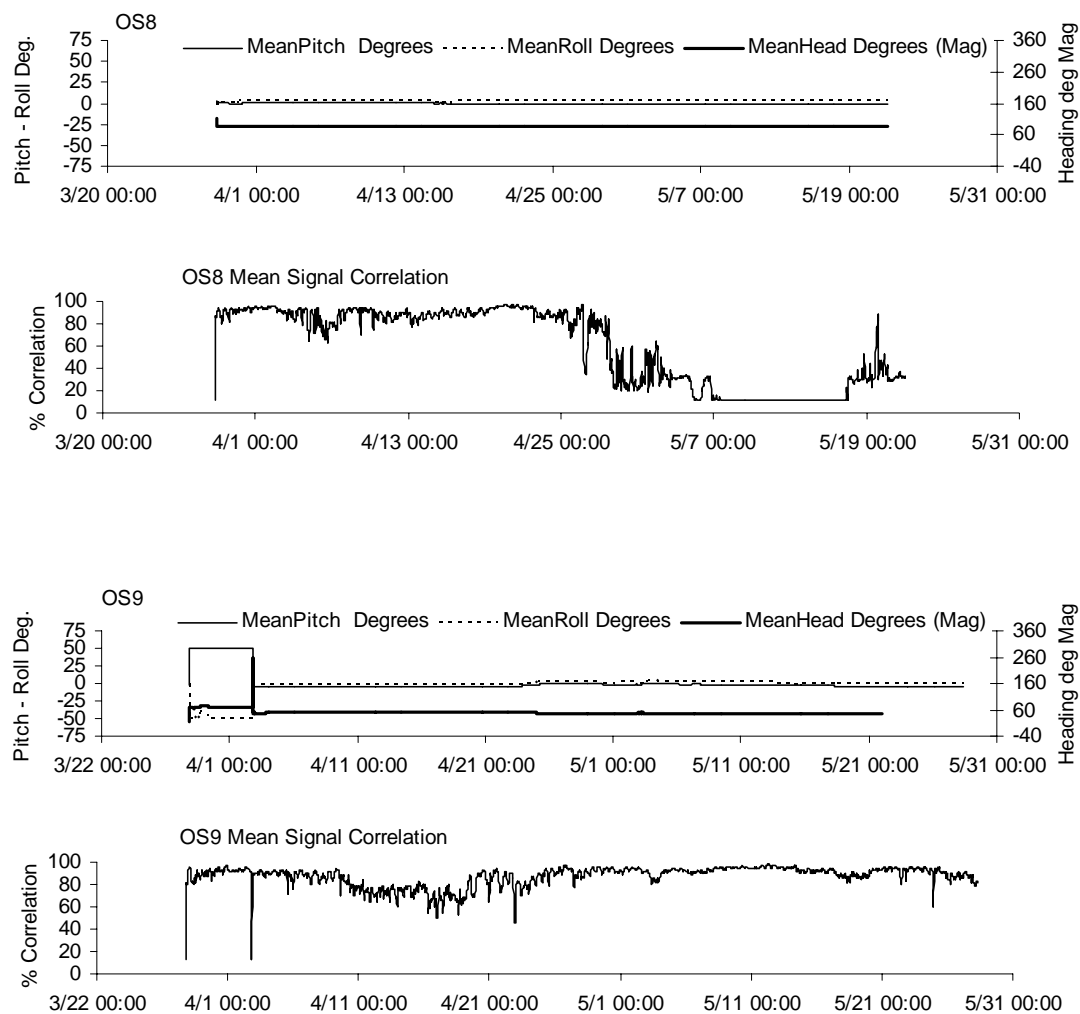
Figure D107.   HESTT (sta OS 8 and OS 9) data quality parameters, 29 March –
              30 May 2002
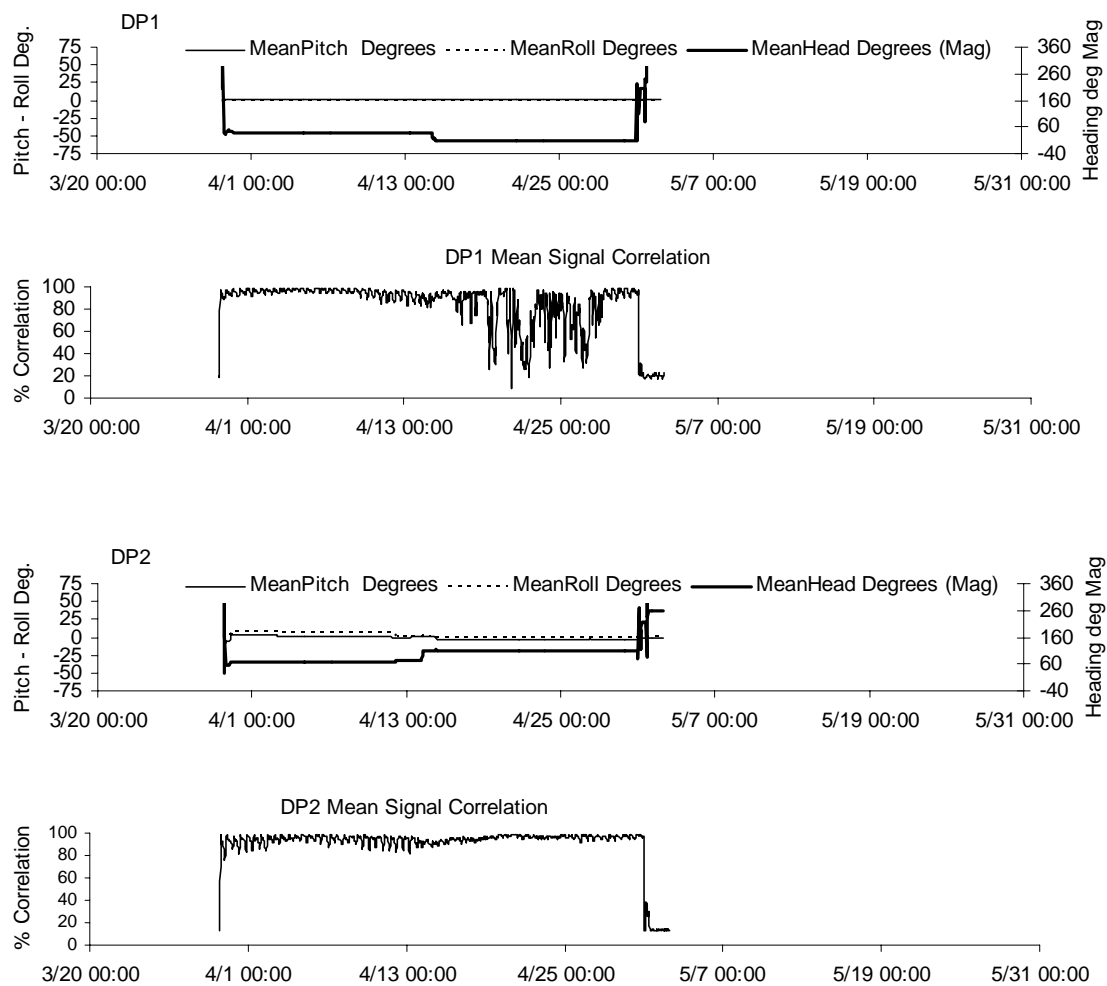
Figure D108.   Hydra platforms (DP-1, DP-2) data quality parameters,
29 March - 5 May 2002

Appendix E
Tidal Circulation Simulation Results

This appendix contains plan view plots of each of the 66 ADCIRC-STWAVE simulations at peak flood and peak ebb current developed as part of the work described in Chapter 7 of Volume I. The first two figures (Figures E1 and E2) are the ADCIRC grid for the plan-view plot areas depicted in Figures E3 through E376. The grids were included to show the fine resolution in the north jetty project area and the coarser resolution in the far field. Coarser grid resolution at the south jetty and at Westport may not represent all wave-induced currents and eddies in these areas. The coarse resolution enabled efficient calculation of the overall circulation pattern through the inlet while computing detailed hydrodynamics in the project area. Evaluation of project alternatives in the Ocean Shores/north jetty region was accomplished with this approach. Circulation patterns at the south jetty and Westport in these figures should not be consulted for design. Color contours for the plan view maps indicate current magnitude. Current vectors are scaled to magnitude and indicate current directions for a given tide and wave condition.

Difference maps were created for each alternative compared to the corresponding existing condition. For example, Runs 108, 112, 116, 120, and 124 are compared to Run 104 because each is for west-northwest, spring tide conditions. Runs are defined in Table E1. Difference maps at peak flood and peak ebb for each alternative are given in Figures E267 through E376. Red and yellow color contours indicate a large or moderate increase in current magnitude, respectively. Blue and light blue color contours indicate a large or moderate decrease in current magnitude, respectively. The vectors do not indicate differences, but represent current vectors for the project alternative.

Time series plots of velocity components at the 16 node locations were completed for the 30 Steering Module simulations (Runs 104-133). Each plot compares the current component for existing conditions to all corresponding project alternatives. For example, Runs 108 (Alt 2A), 112 (Alt 2B), 116 (Alt 3A), 120 (Alt 3B), and 124 (Alt 4A) are compared to Run 104 (Existing) because each is for west-northwest, spring tide conditions. The locations of nodes are given in Figure 377, and the time series plots are presented in Figures E378 through E537.
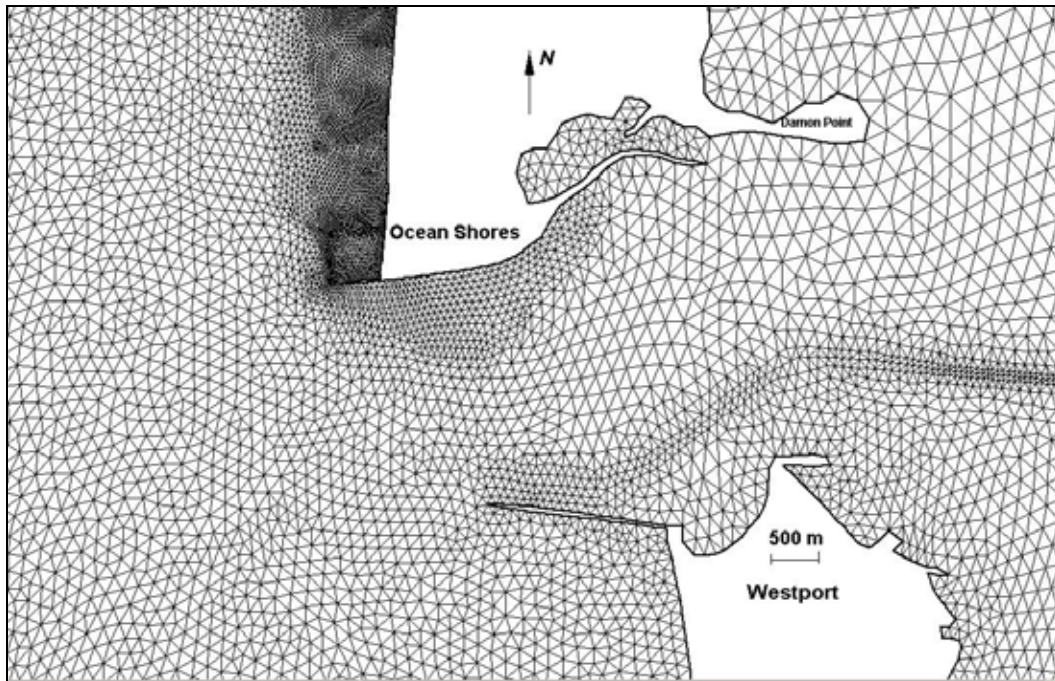
Plan View Plots of Current

Figure E1. Portion of ADCIRC grid associated with all "inlet view" figures
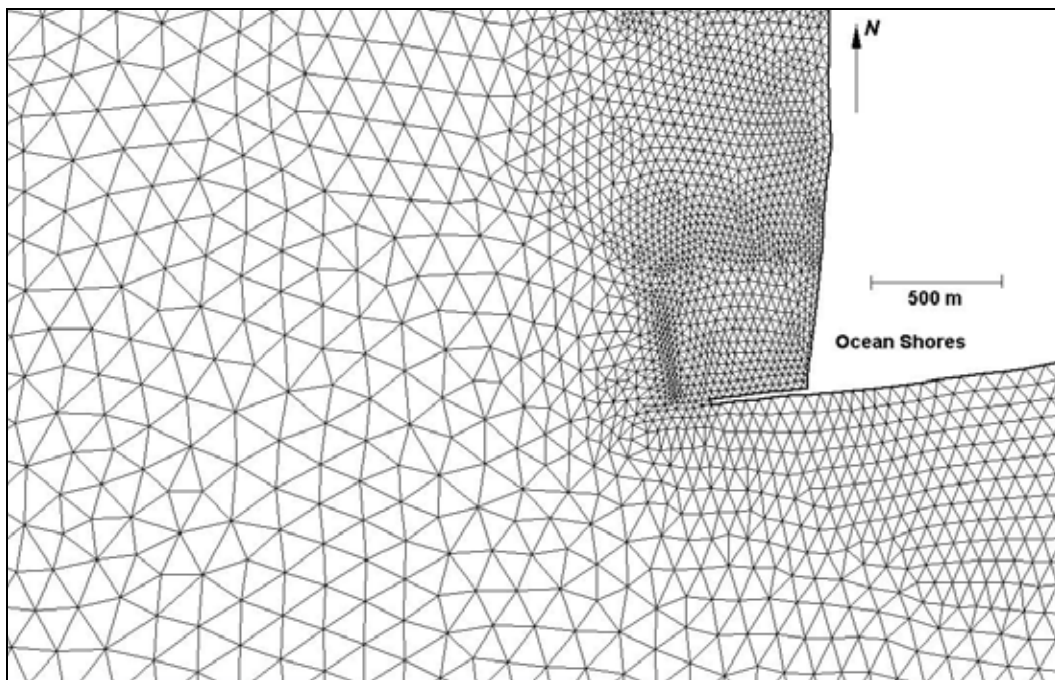

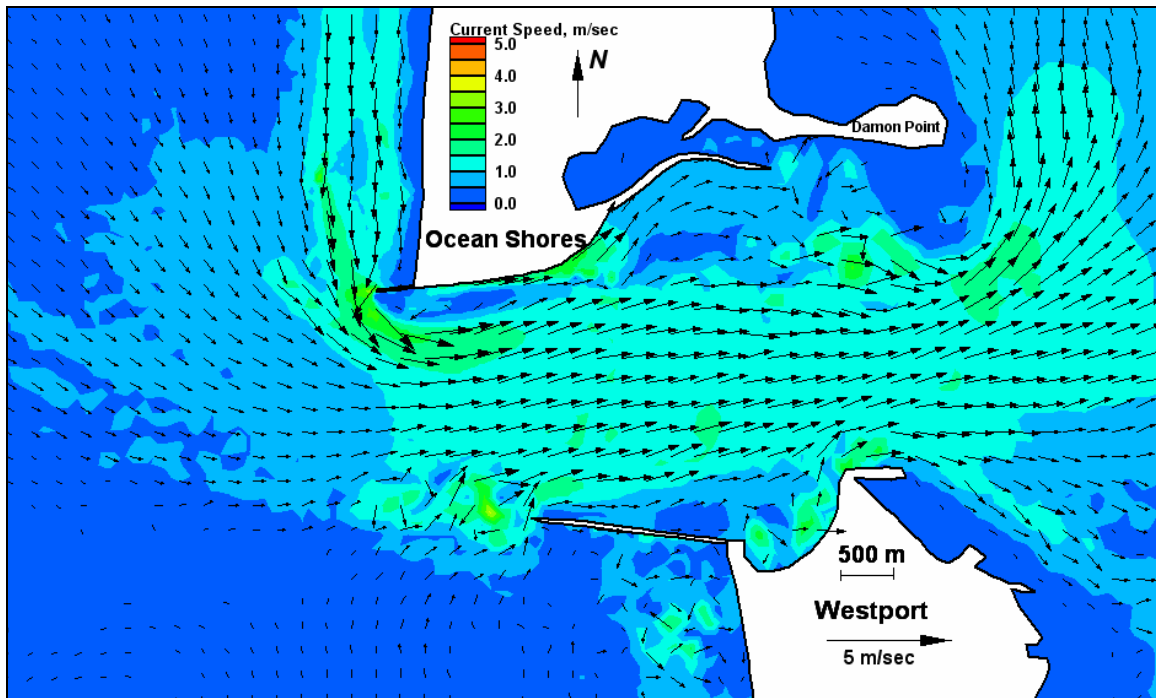Figure E2. Portion of ADCIRC grid associated with all "north jetty view" figures

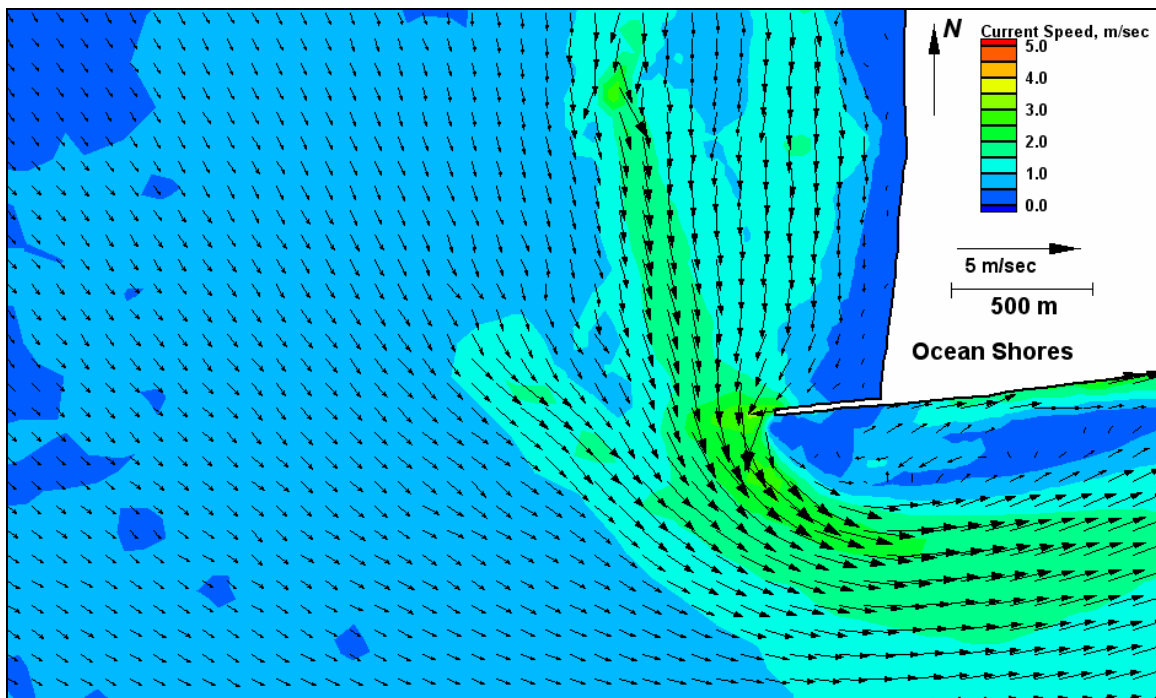Figure E3. Run 104 (existing, west-northwest, spring tide), inlet view of flood tide

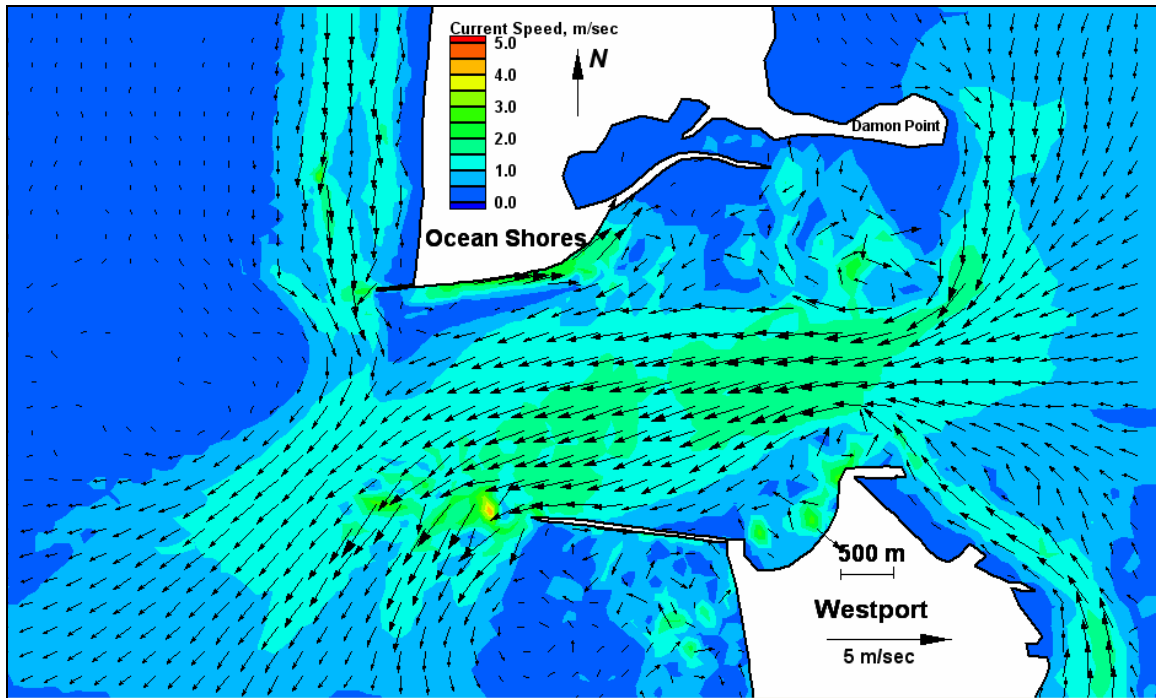Figure E4. Run 104 (existing, west-northwest, spring tide), north jetty view of flood tide

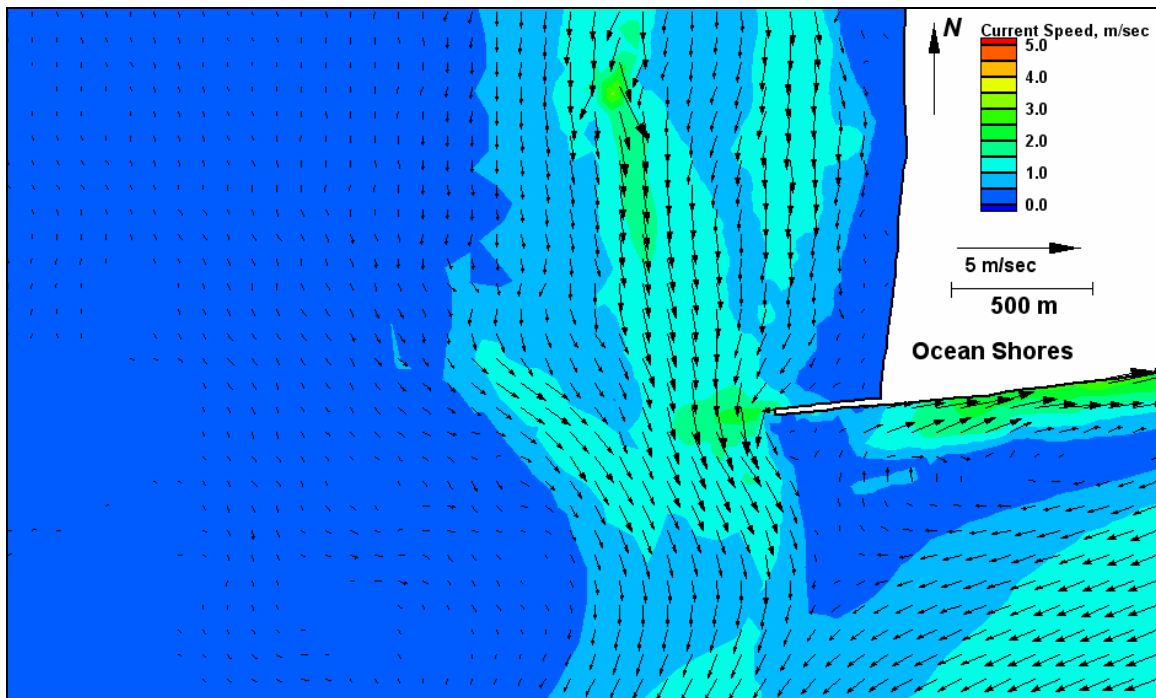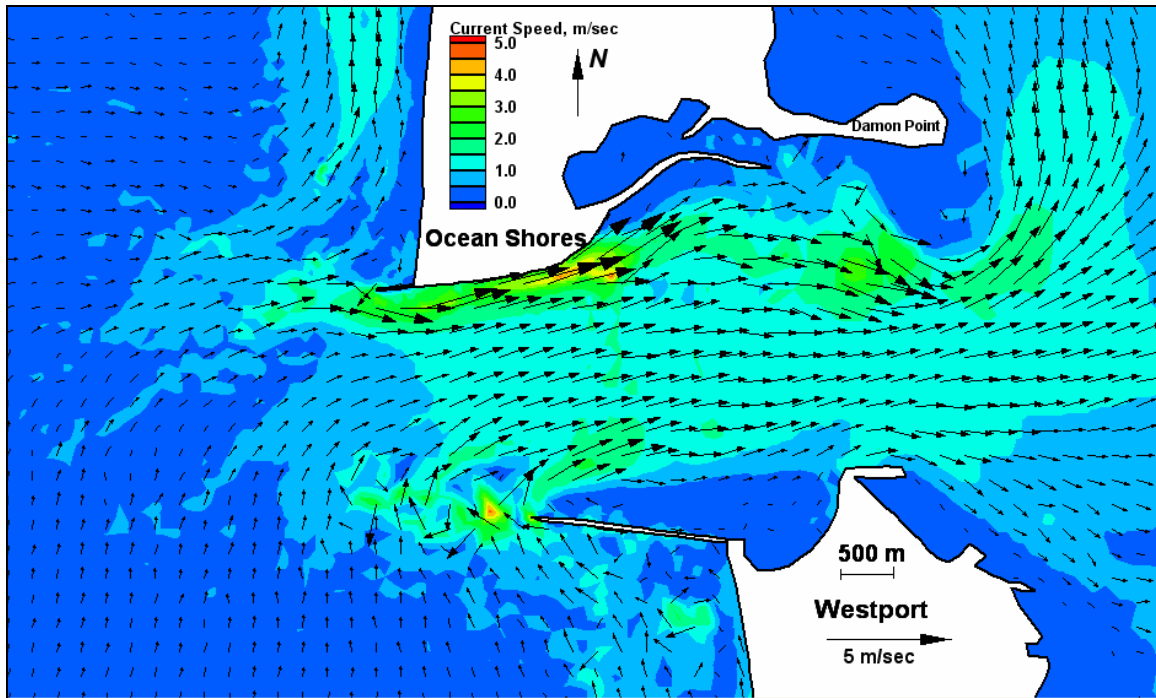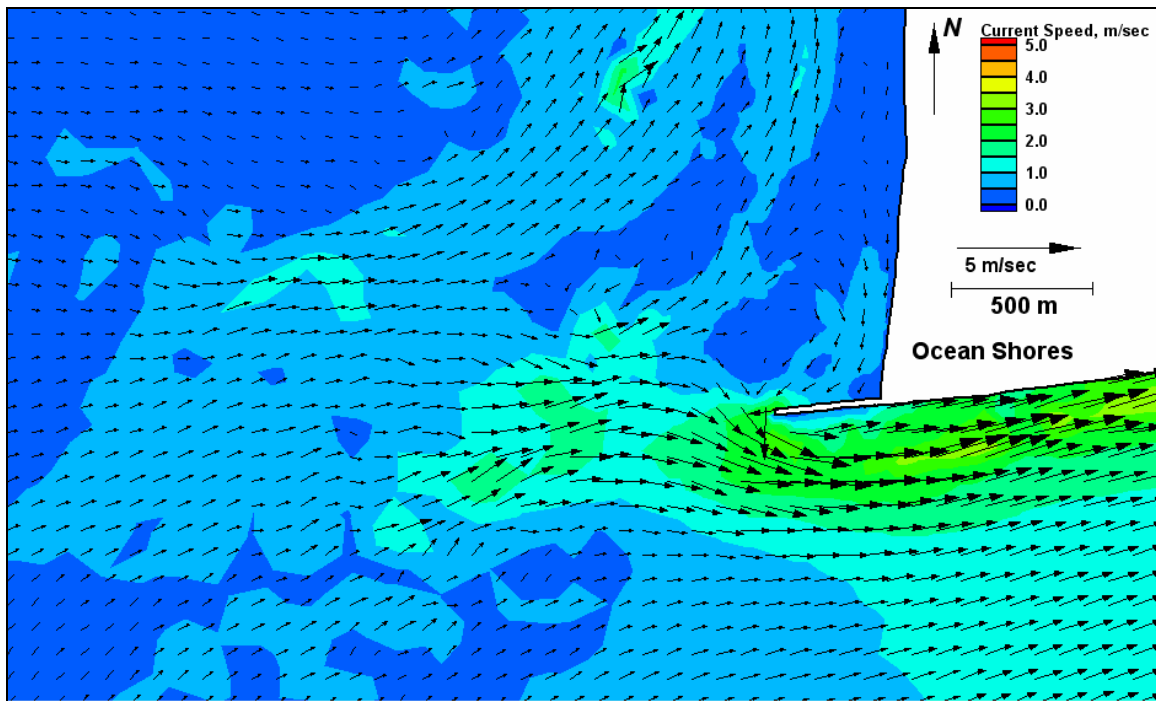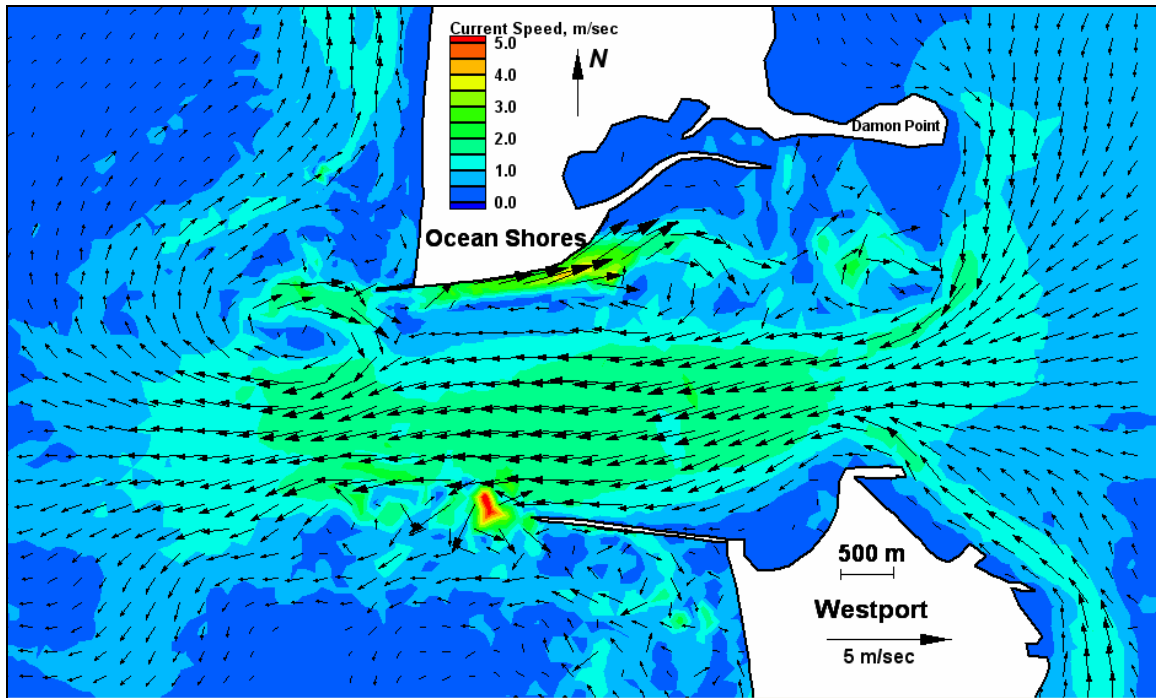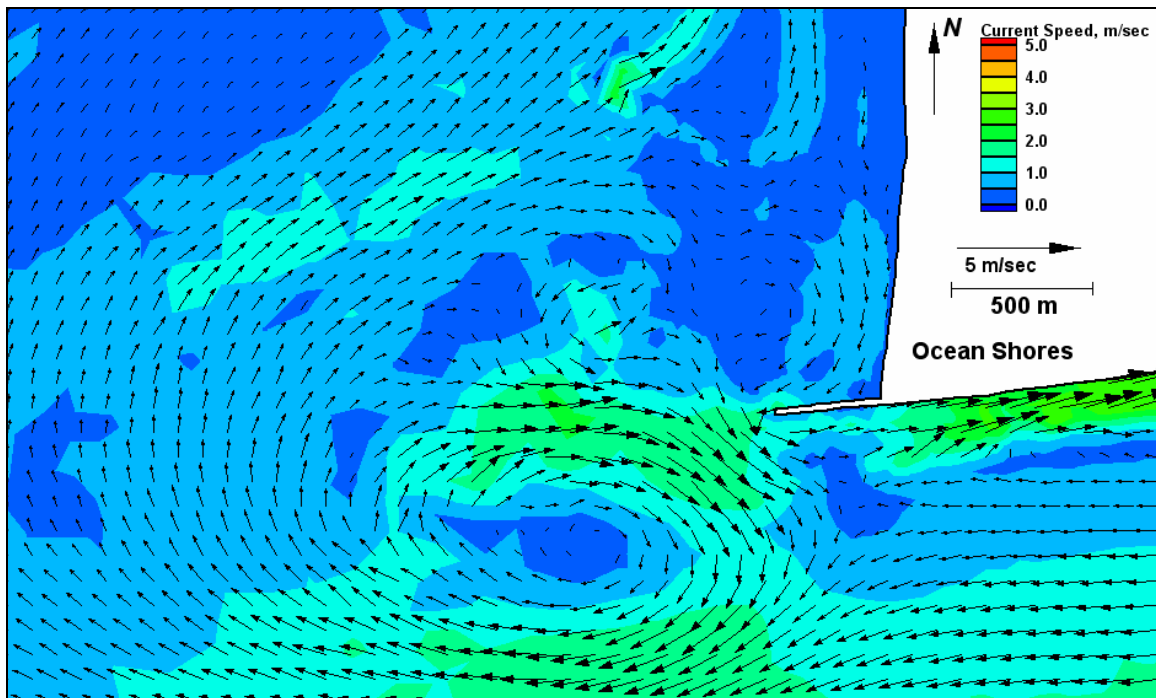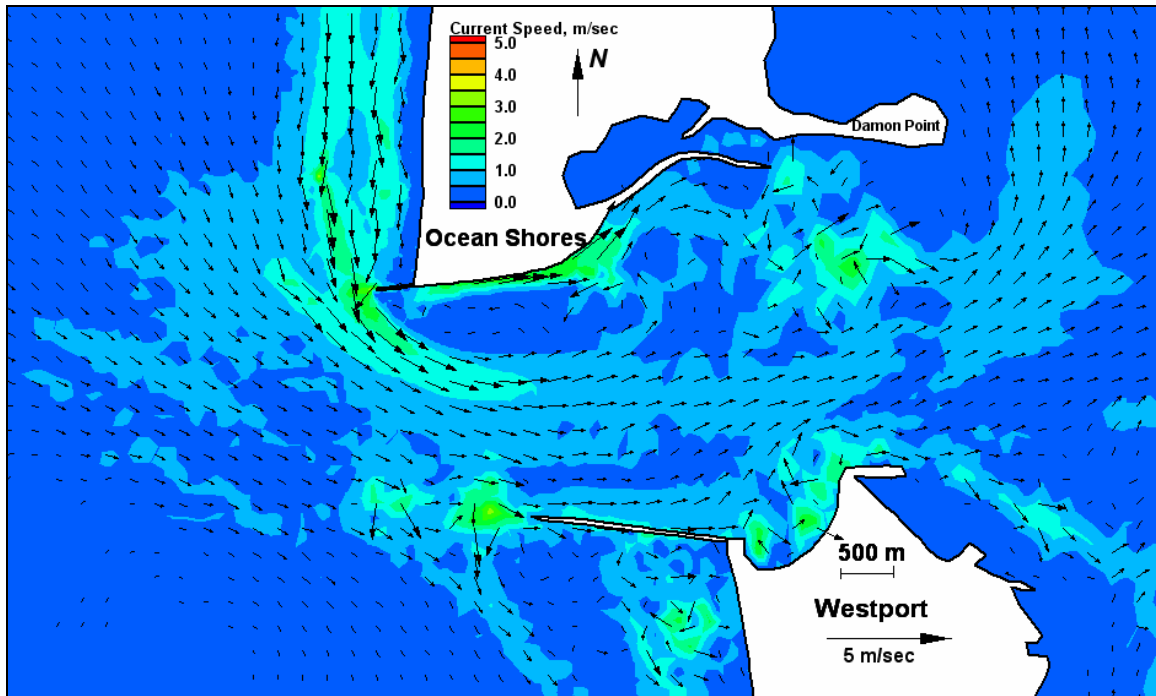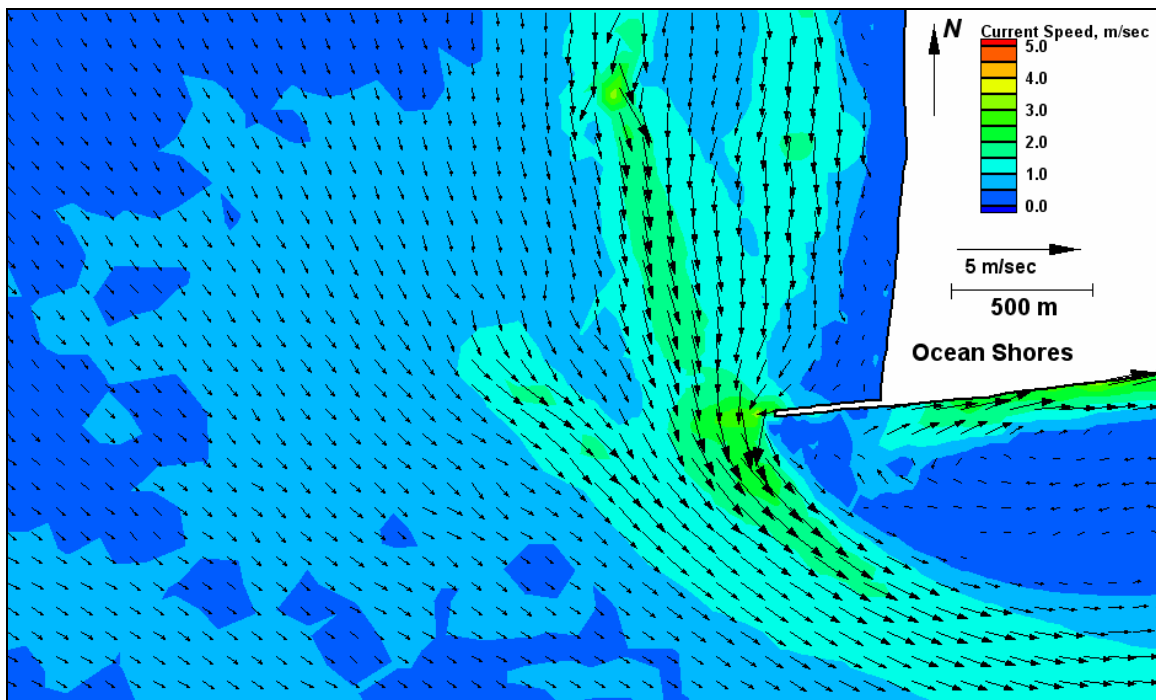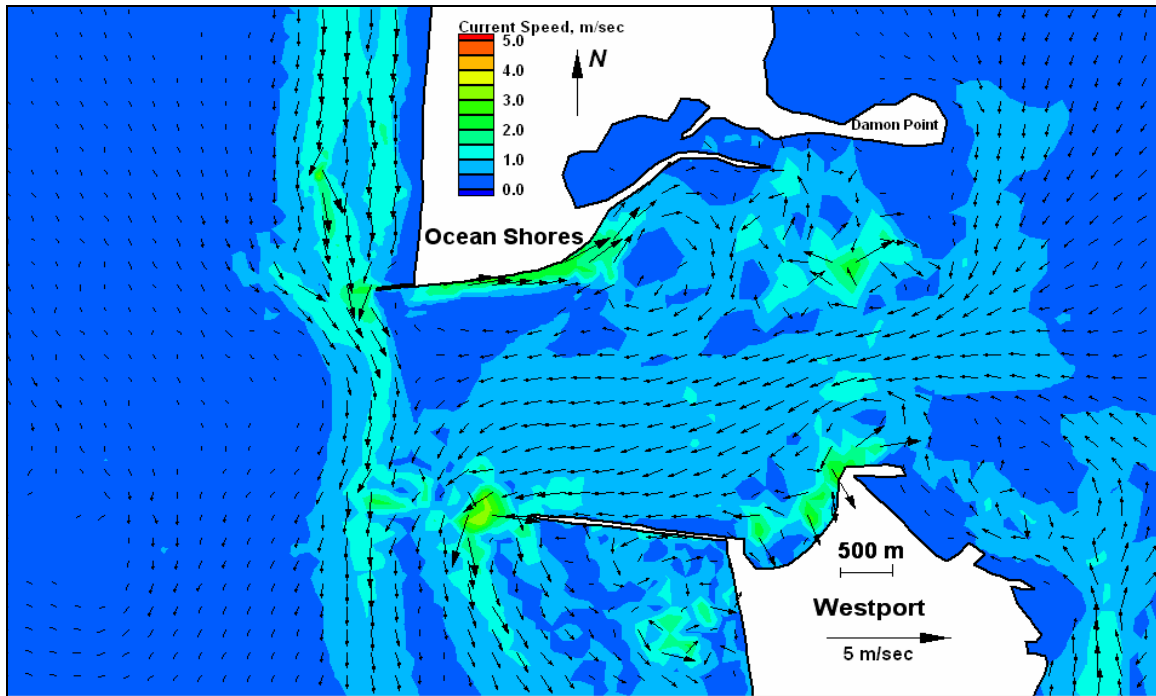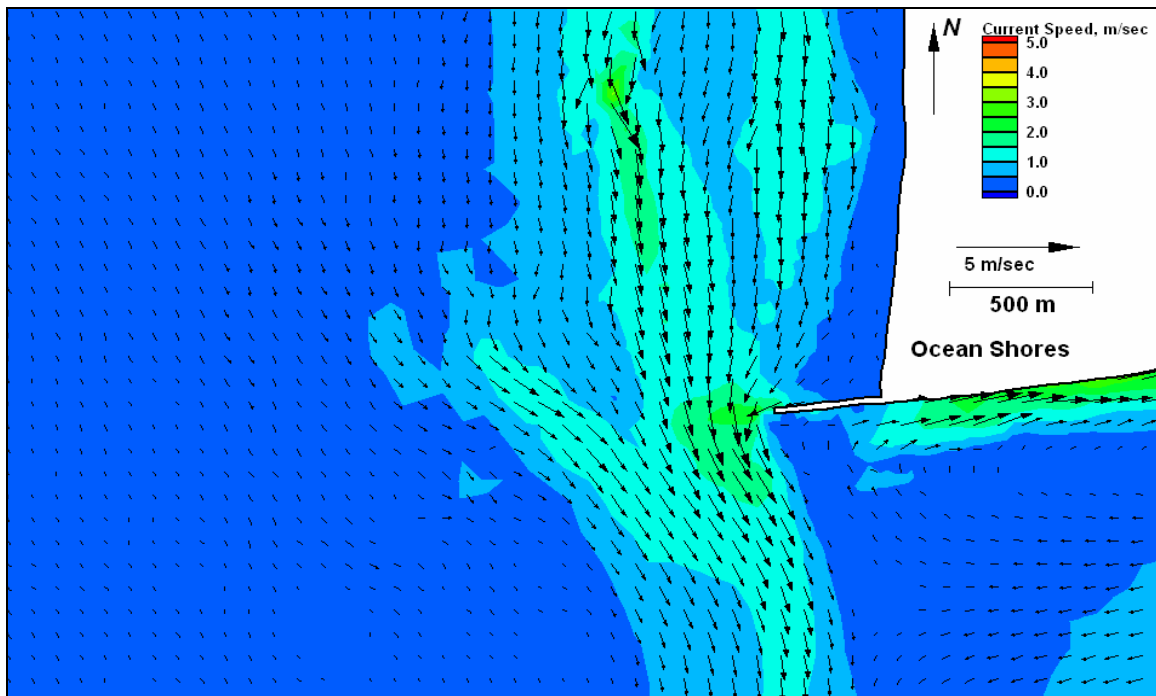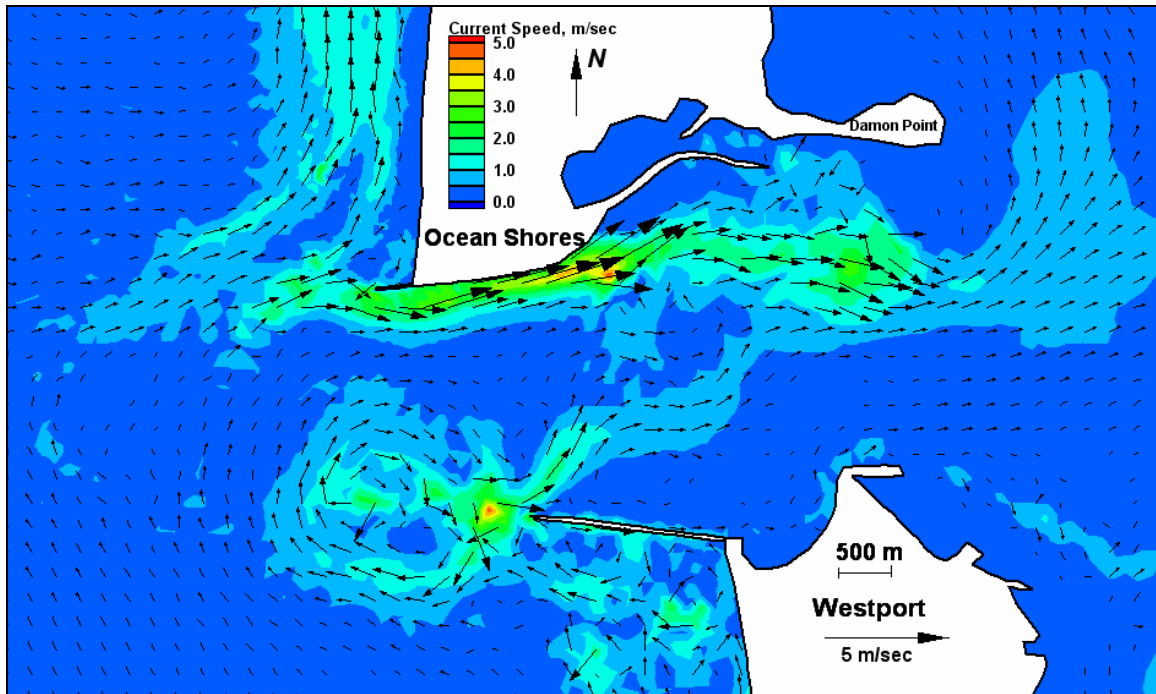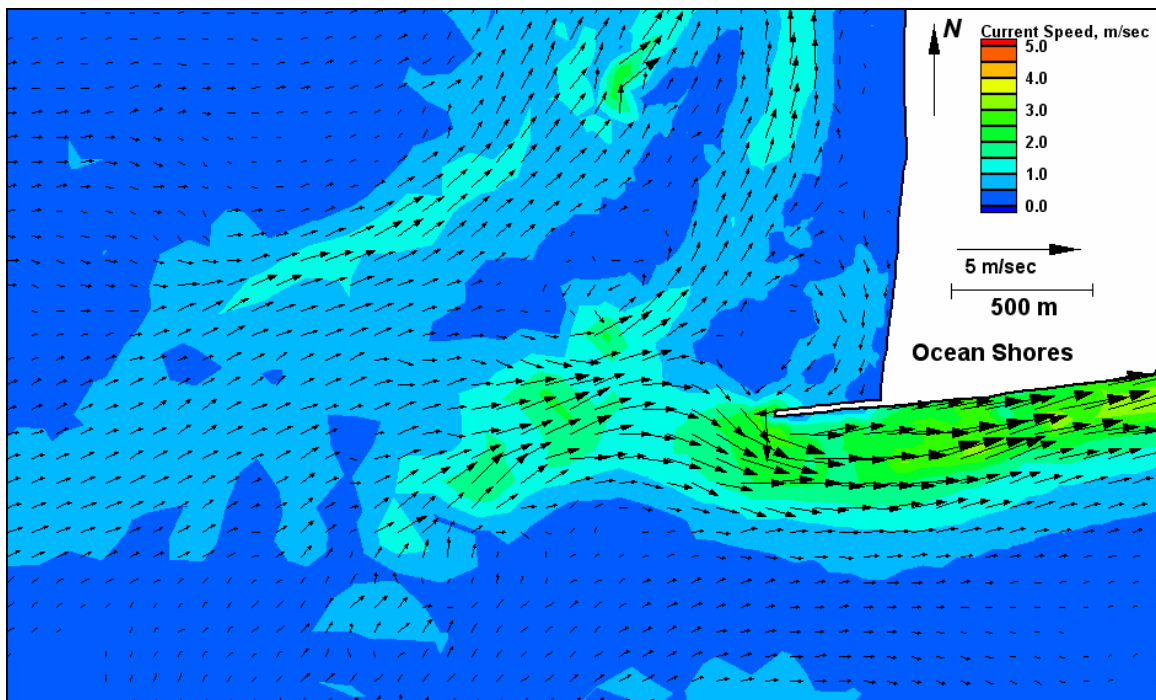Figure E5. Run 104 (existing, west-northwest, spring tide), inlet view of ebb tide

Figure E6. Run 104 (existing, west-northwest, spring tide), north jetty view of ebb tide

Appendix E   Tidal Circulation Simulation Results

Figure E7. Run 105 (existing, west-southwest, spring tide), inlet view of flood tide

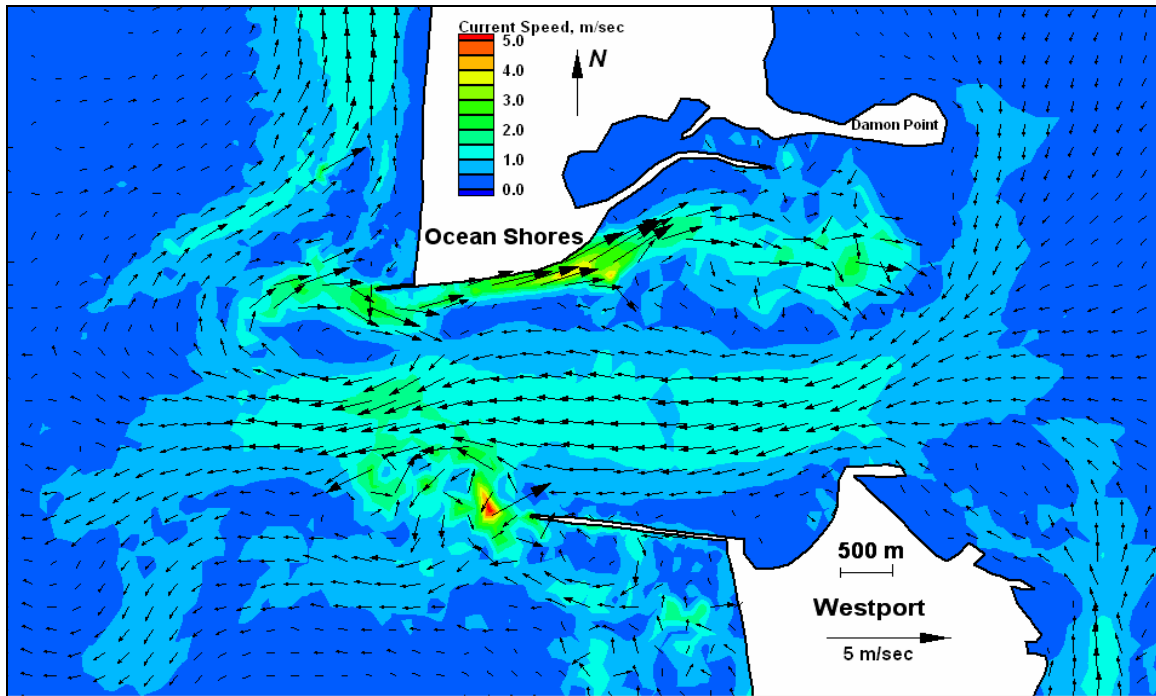Figure E8. Run 105 (existing, west-southwest, spring tide), north jetty view of flood tide

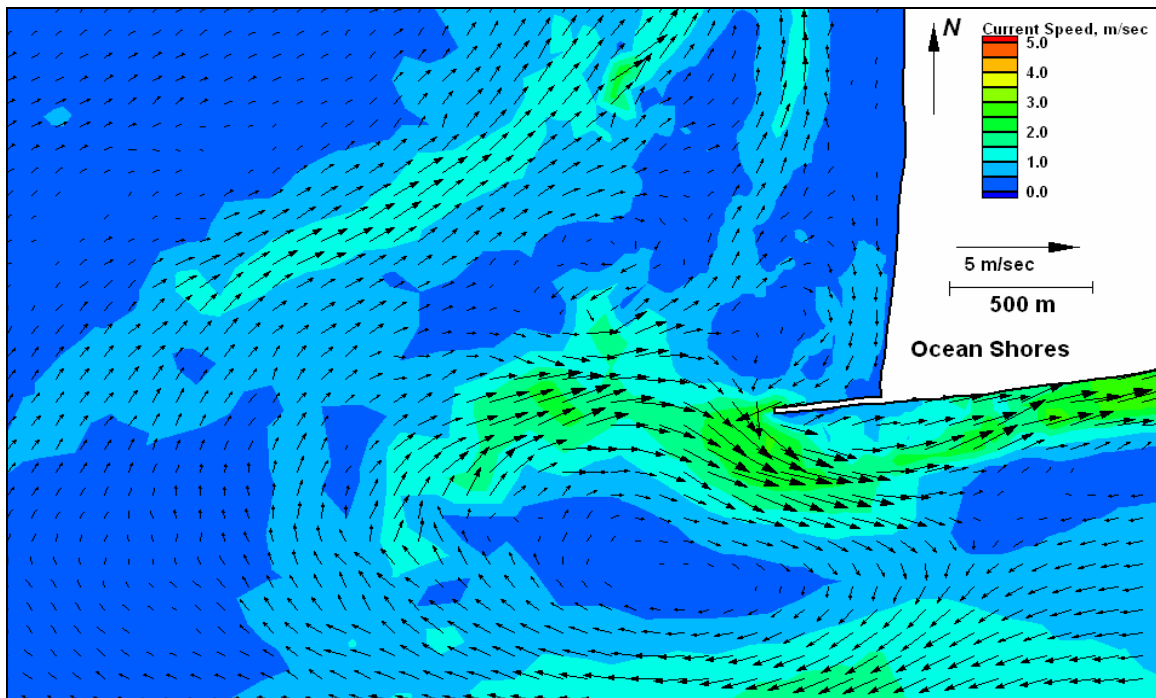Figure E9. Run 105 (existing, west-southwest, spring tide), inlet view of ebb tide

Figure E10. Run 105 (existing, west-southwest, spring tide), north jetty view of ebb tide

Figure E11. Run 106 (existing, west-northwest, neap tide), inlet view of flood tide
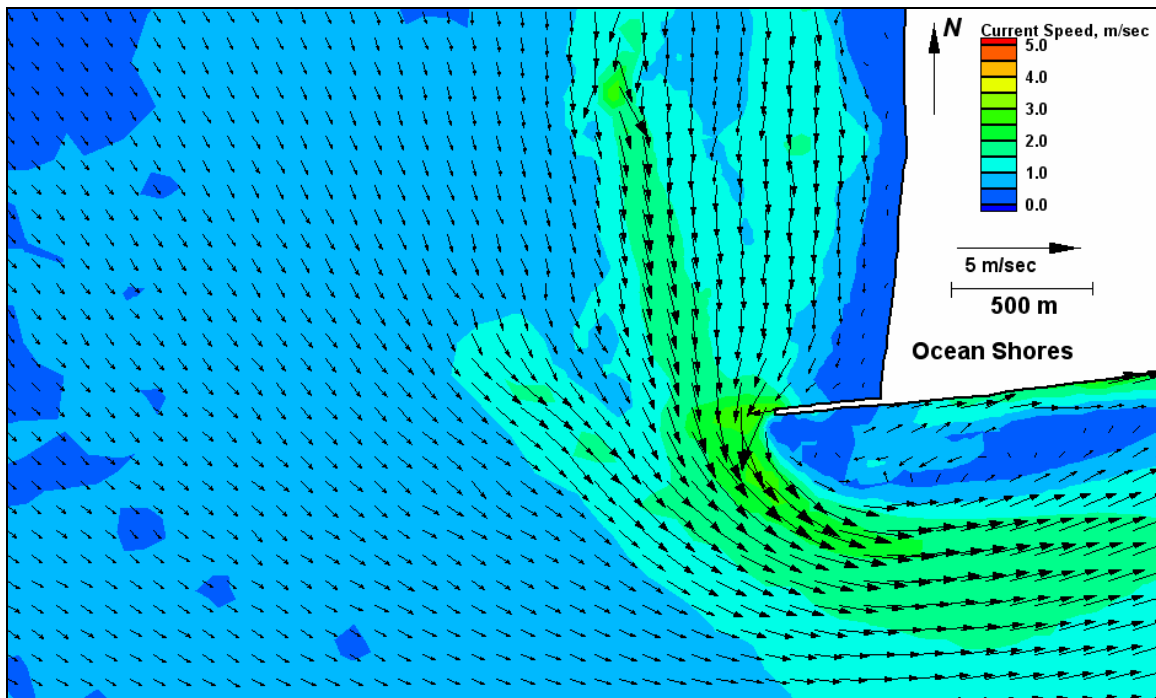

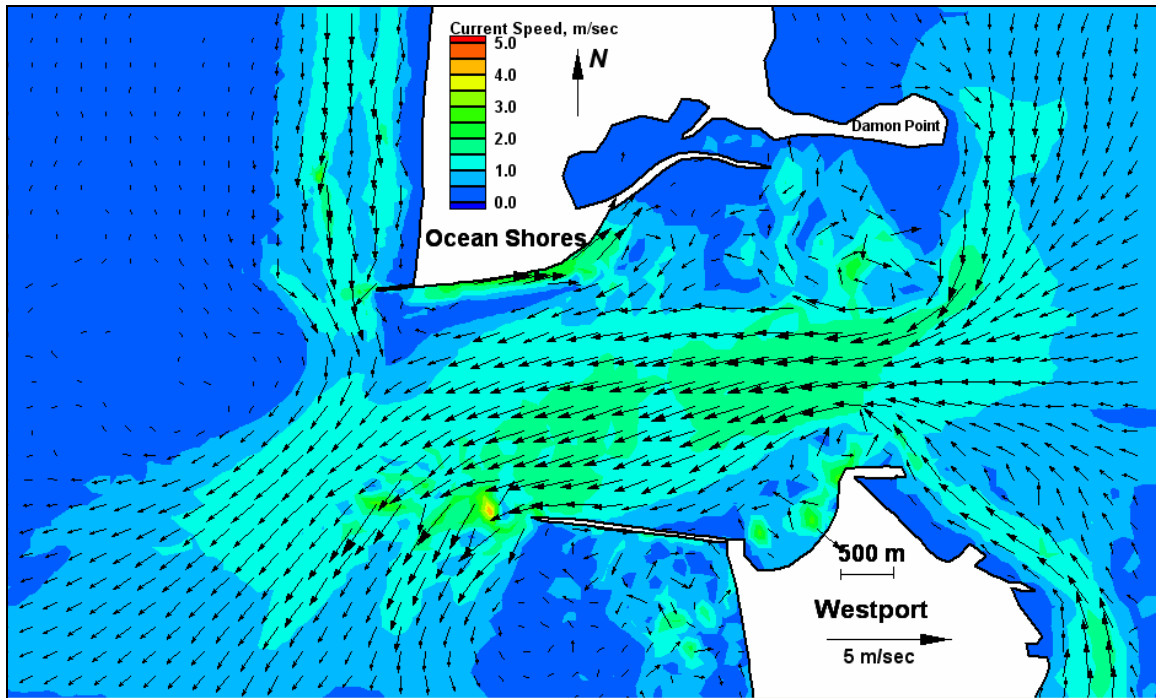Figure E12. Run 106 (existing, west-northwest, neap tide), north jetty view of flood tide

Figure E13. Run 106 (existing, west-northwest, neap tide), inlet view of ebb tide

Figure E14. Run 106 (existing, west-northwest, neap tide), north view of ebb tide

Figure E15. Run 107 (existing, west-northwest, neap tide), inlet view of flood tide

Figure E16. Run 107 (existing, west-northwest, neap tide), north jetty view of flood tide

Figure E17. Run 107 (existing, west-southwest, neap tide), inlet view of ebb tide tide

Figure E18. Run 107 (existing, west-southwest, neap tide), north jetty view of ebb tide
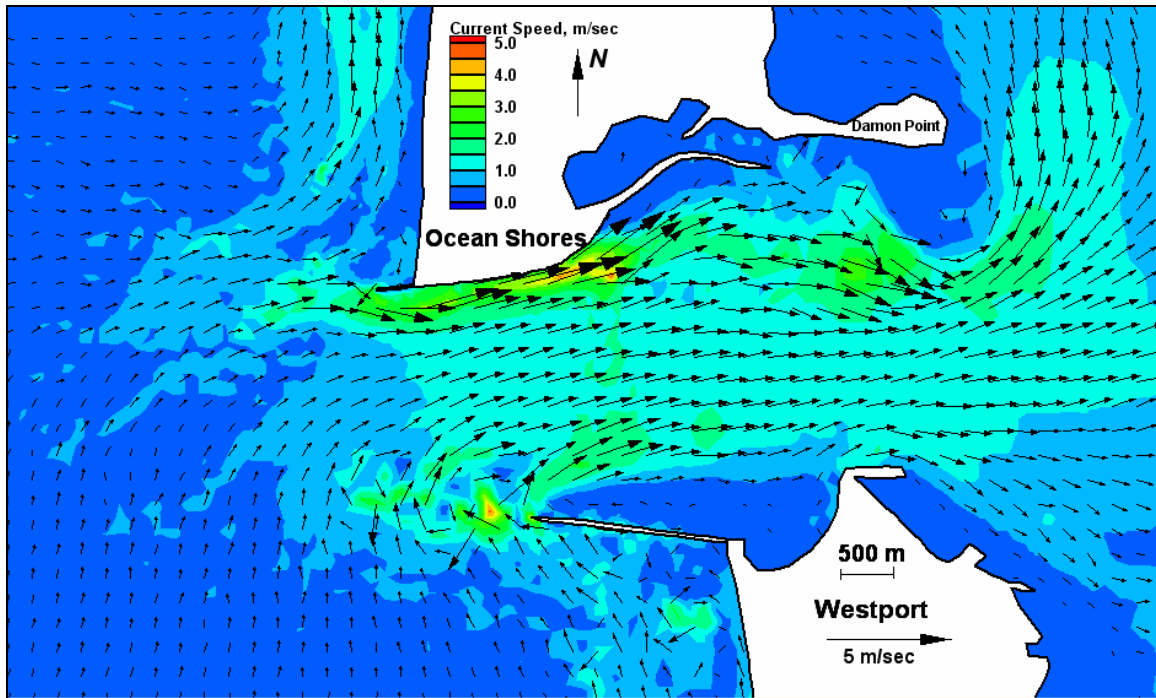
E10
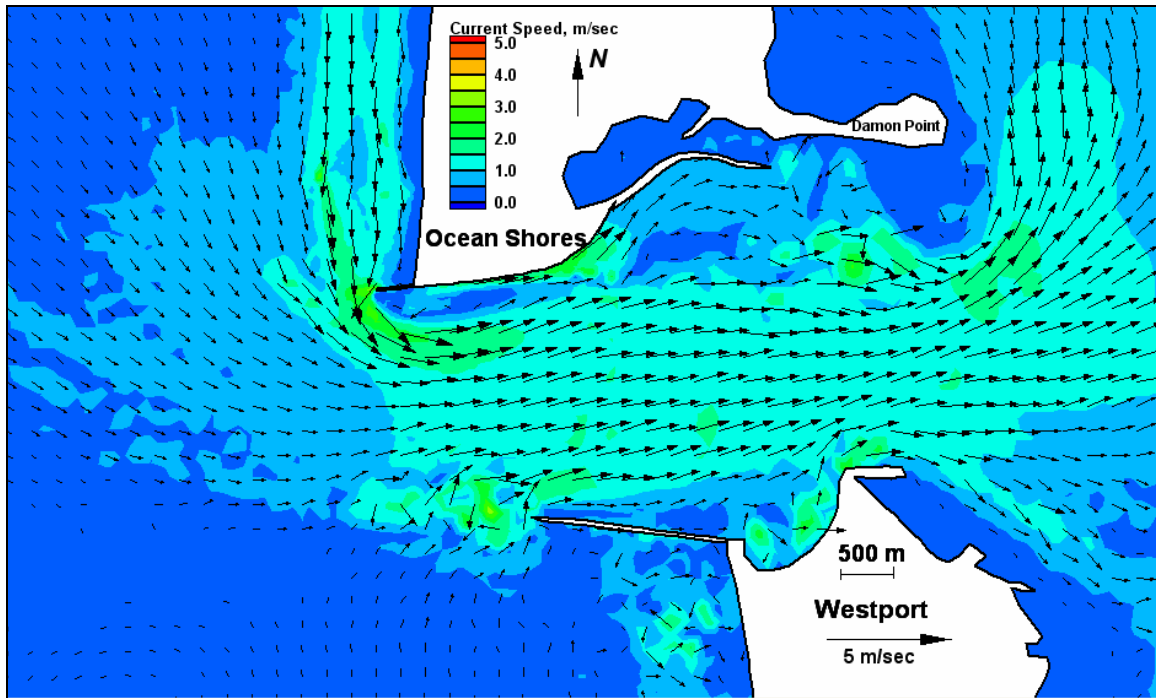
Figure E19. Run 108 (Alt 2A, west-northwest, spring tide), inlet view of flood tide

Figure E20. Run 108 (Alt 2A, west-northwest, spring tide), north jetty view of flood tide

Figure E21. Run 108 (Alt 2A, west-northwest, spring tide), inlet view of ebb tide
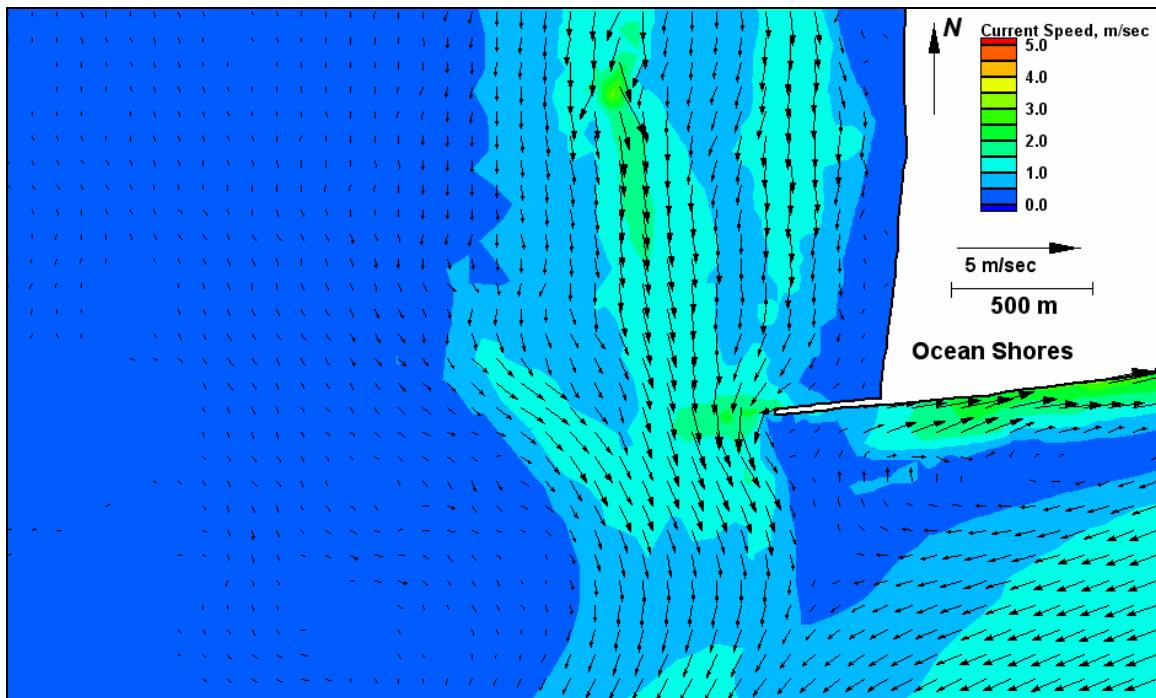
Figure E22. Run 108 (Alt 2A, west-northwest, spring tide), north jetty view of ebb tide

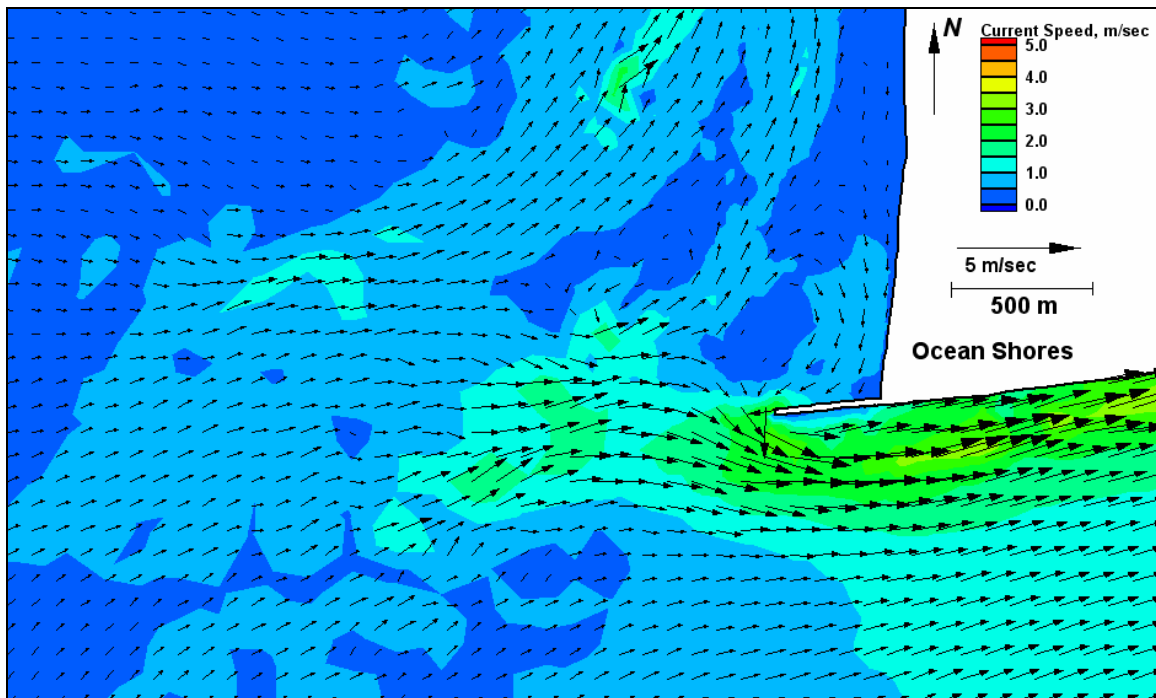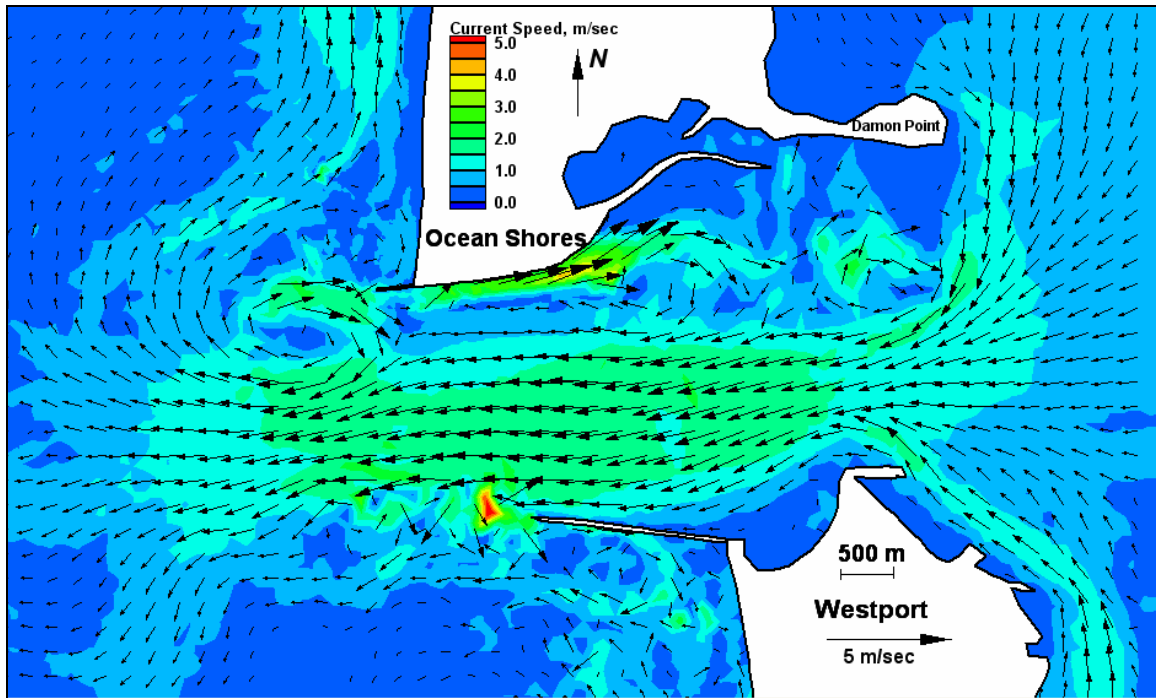Figure E23. Run 109 (Alt 2A, west-northwest, spring tide), inlet view of flood tide

Figure E24. Run 109 (Alt 2A, west-southwest, spring tide), north jetty view of flood tide

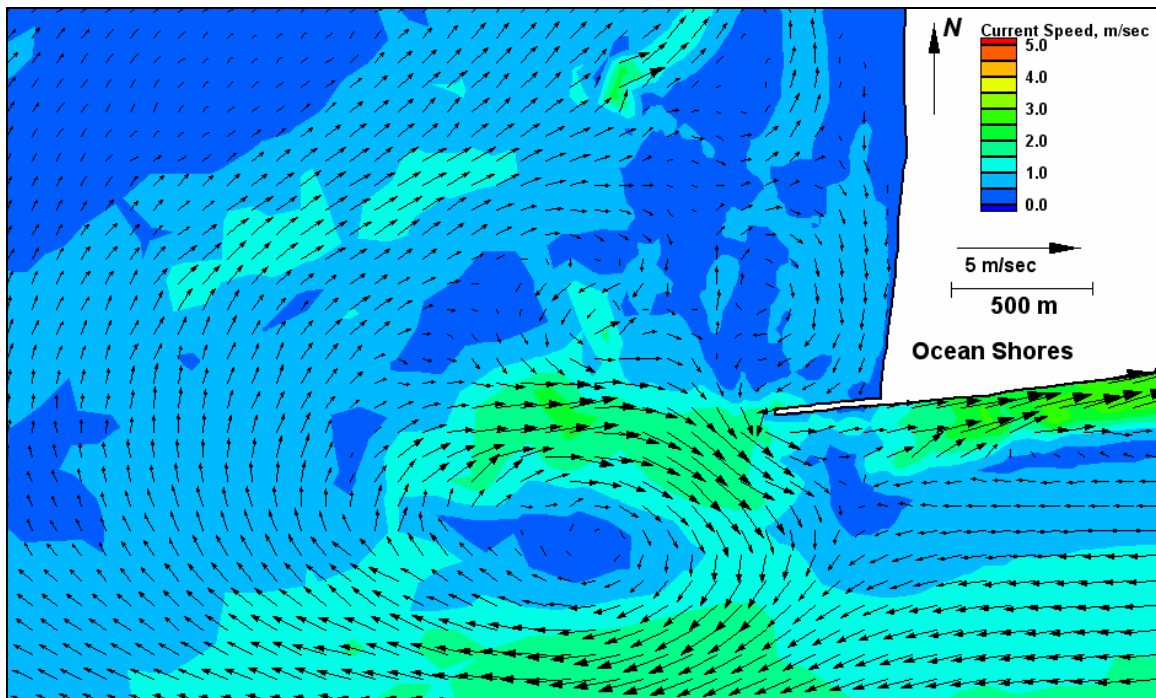Figure E25. Run 109 (Alt 2A, west-southwest, spring tide), inlet view of ebb tide

Figure E26. Run 109 (Alt 2A, west-southwest, spring tide), north jetty view of ebb tide
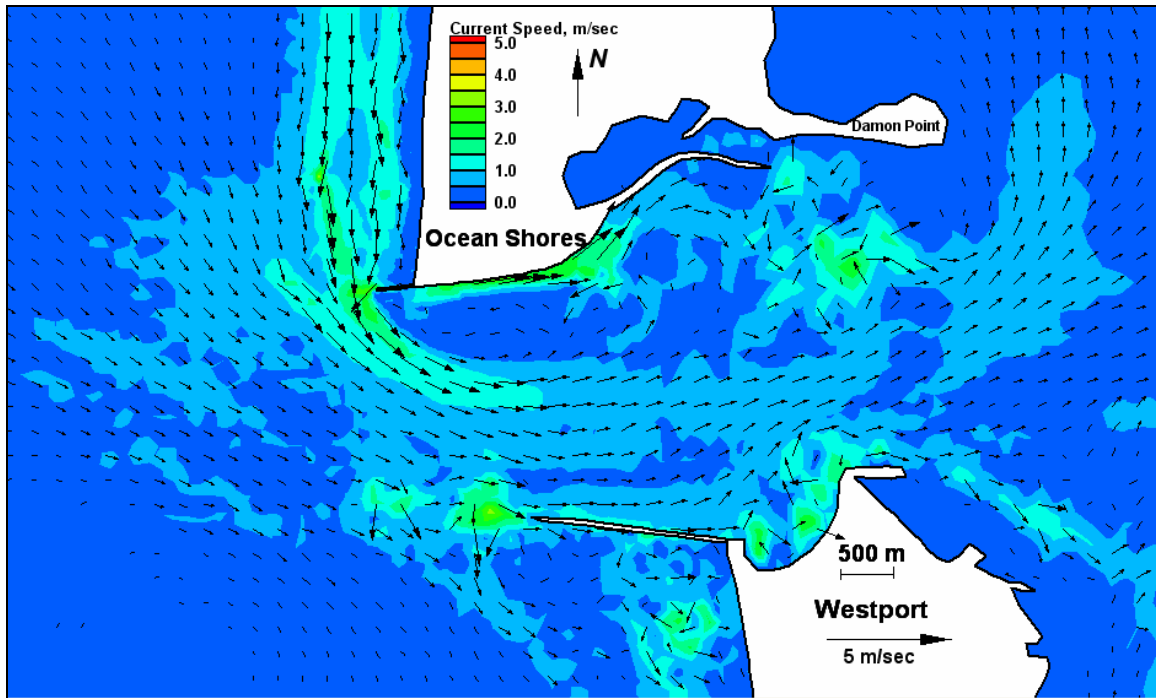
E14

Figure E27. Run 110 (Alt 2A, west-northwest, neap tide), inlet view of flood tide
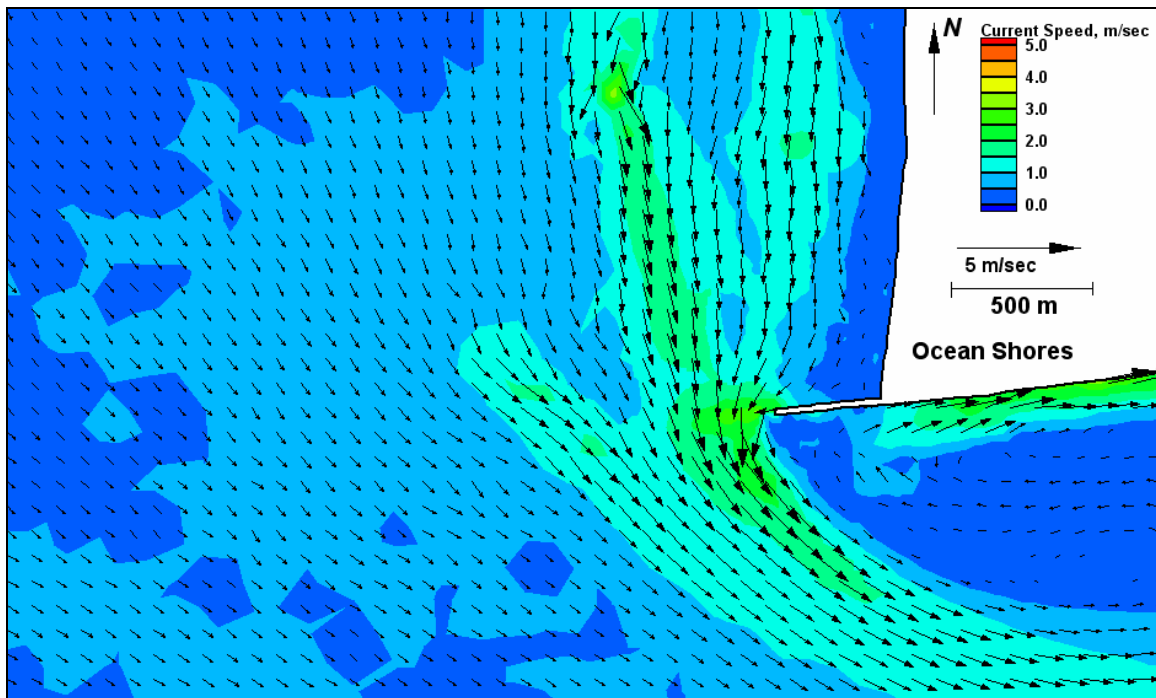

Figure E28. Run 110 (Alt 2A, west-northwest, neap tide), north jetty view of flood tide
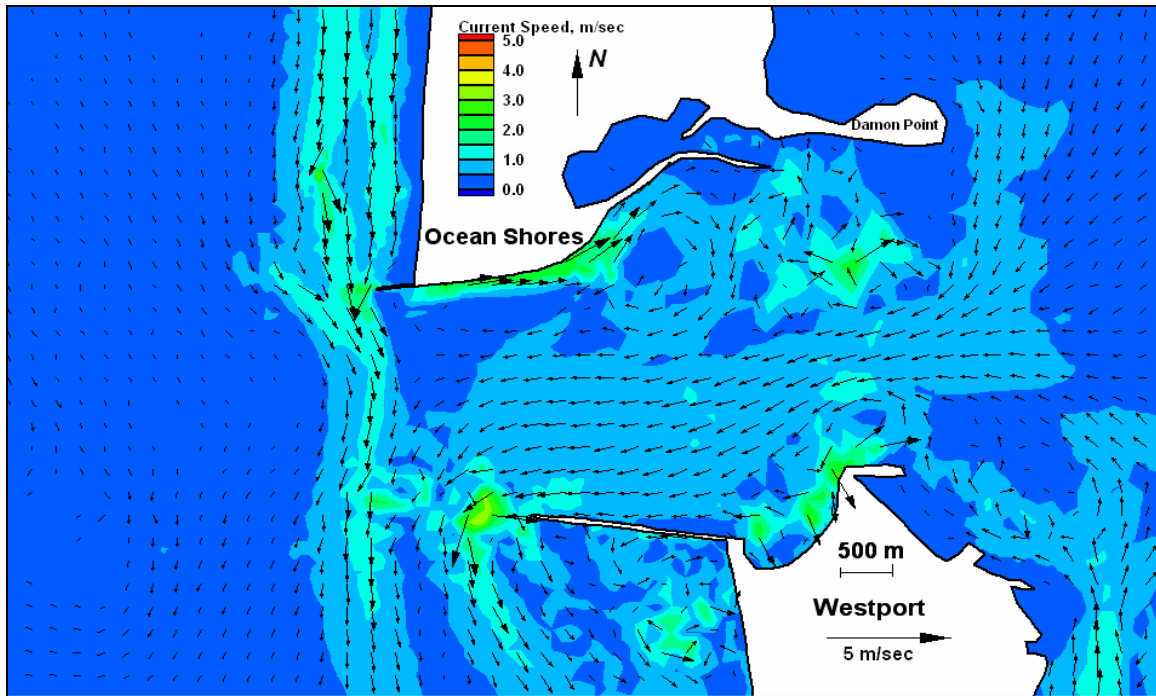
Figure E29. Run 110 (Alt 2A, west-northwest, neap tide), inlet view of ebb tide

Figure E30. Run 110 (Alt 2A, west-northwest, neap tide), north jetty view of ebb tide

E16

Figure E31. Run 111 (Alt 2A, west-southwest, neap tide), inlet view of flood tide

Figure E32. Run 111 (Alt 2A, west-northwest, neap tide), north jetty view of flood tide

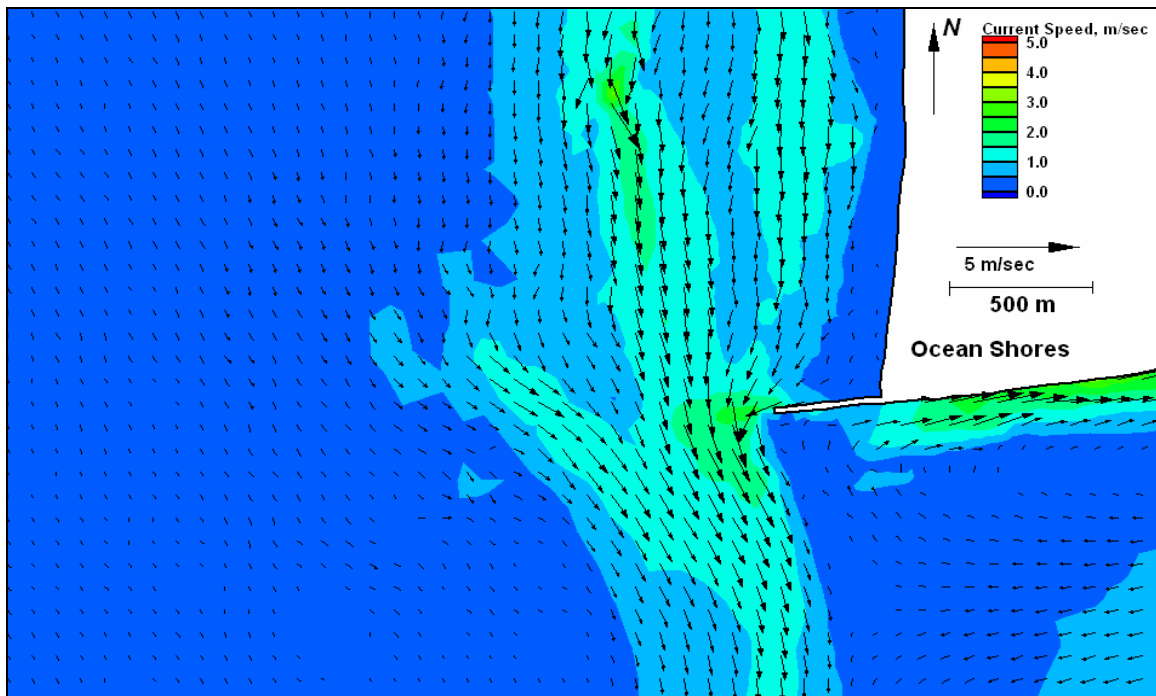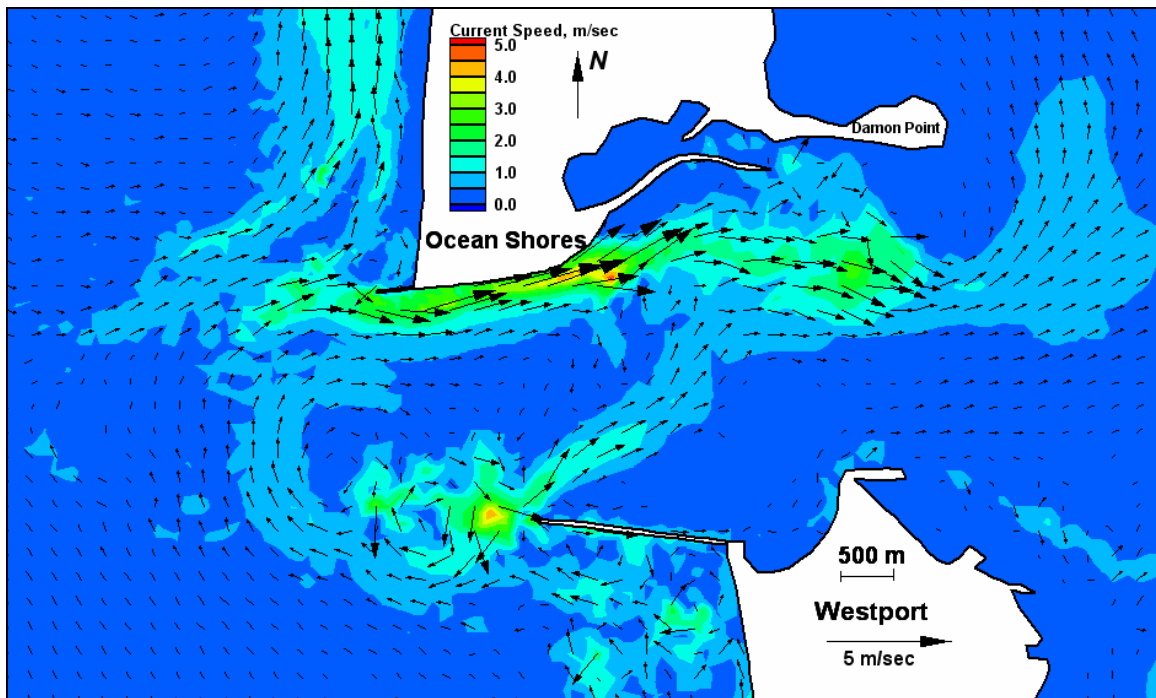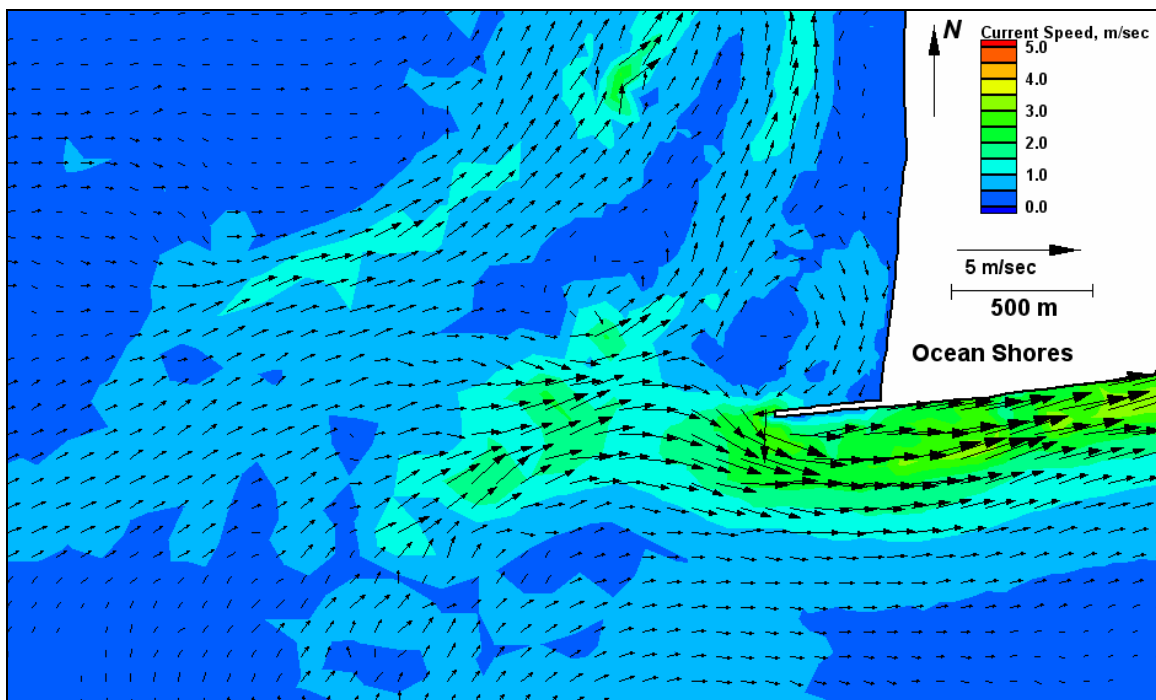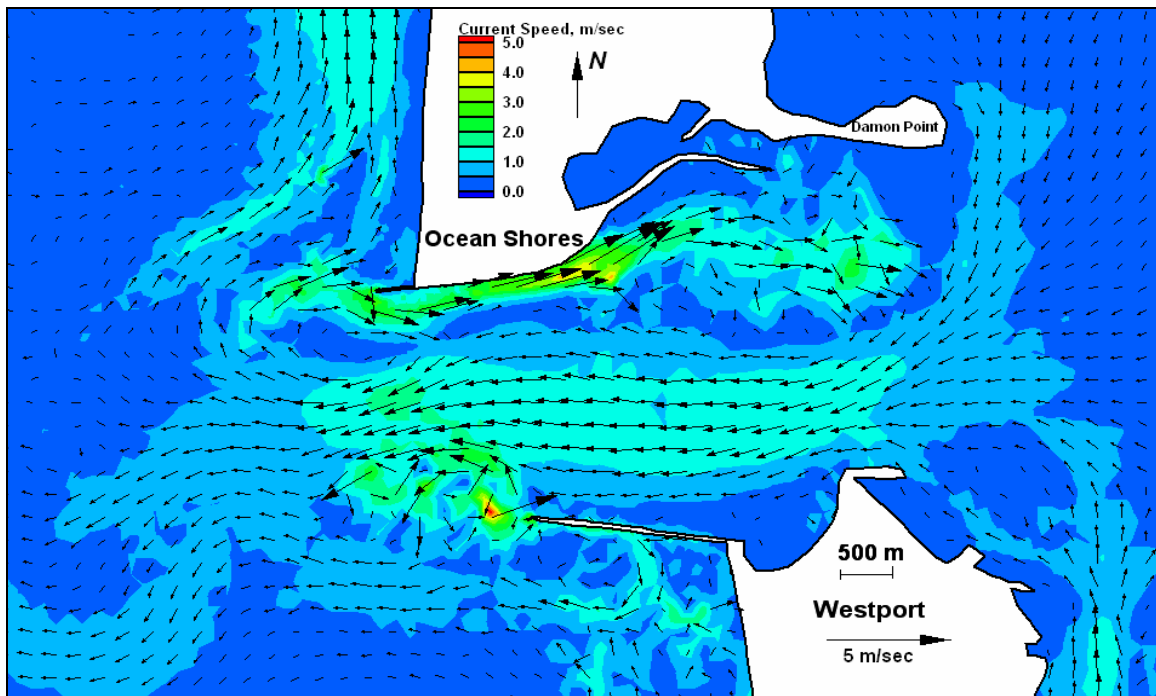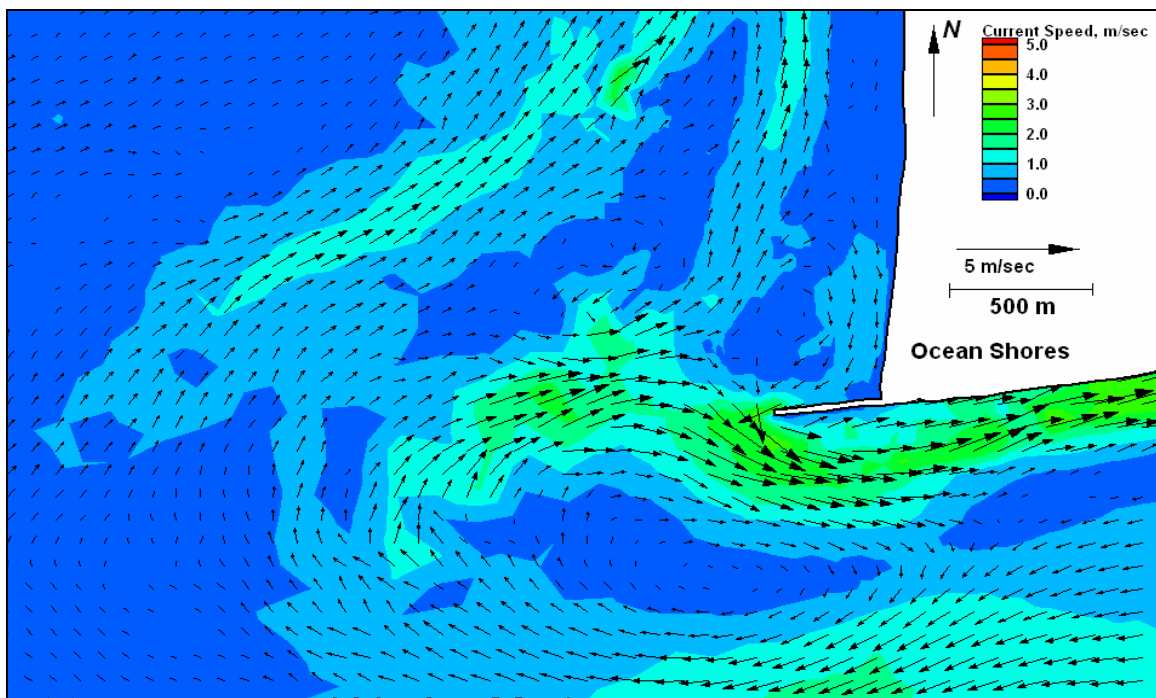Figure E33. Run 111 (Alt 2A, west-northwest, neap tide), inlet view of ebb tide

Figure E34. Run 111 (Alt 2A, west-northwest, neap tide), north jetty view of ebb tide

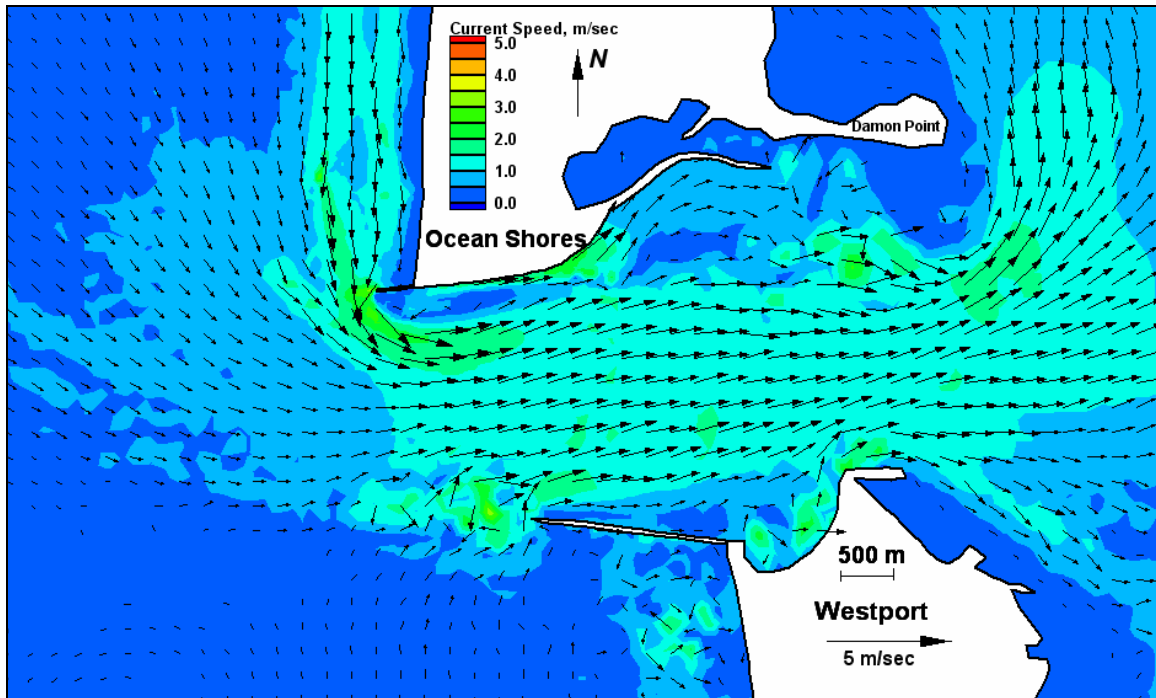Appendix E   Tidal Circulation Simulation Results

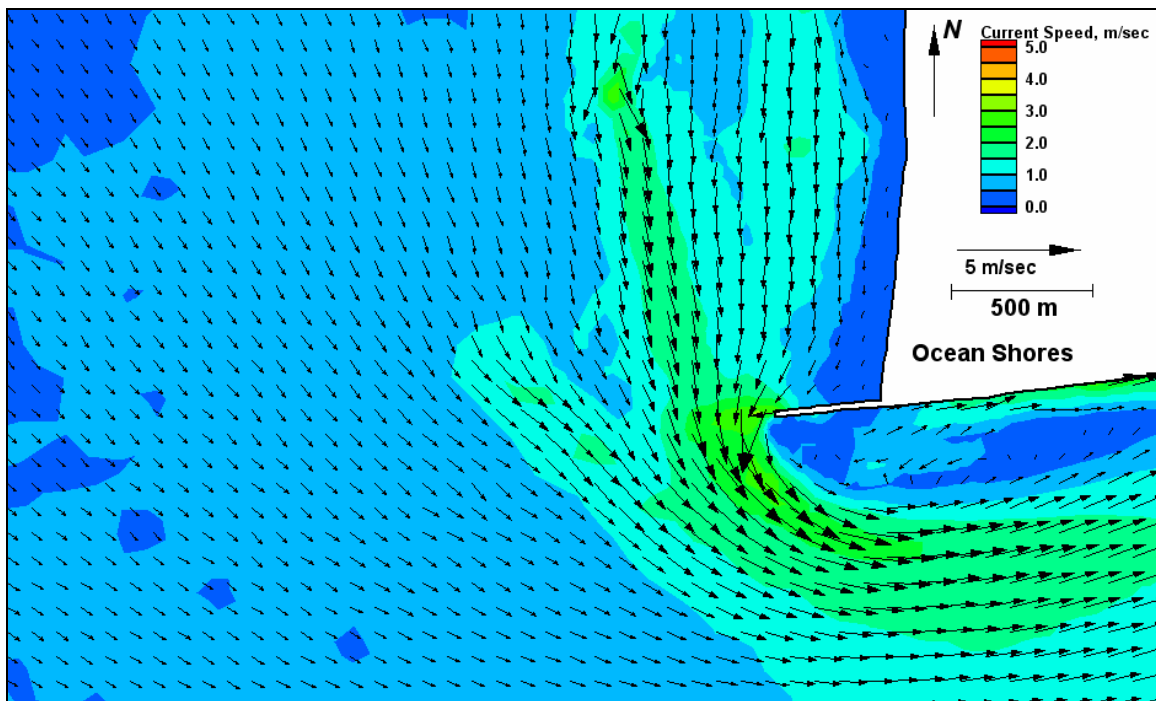Figure E35. Run 112 (Alt 2B, west-northwest, spring tide), inlet view of flood tide

Figure E36. Run 112 (Alt 2B, west-northwest, spring tide), north jetty view of flood tide

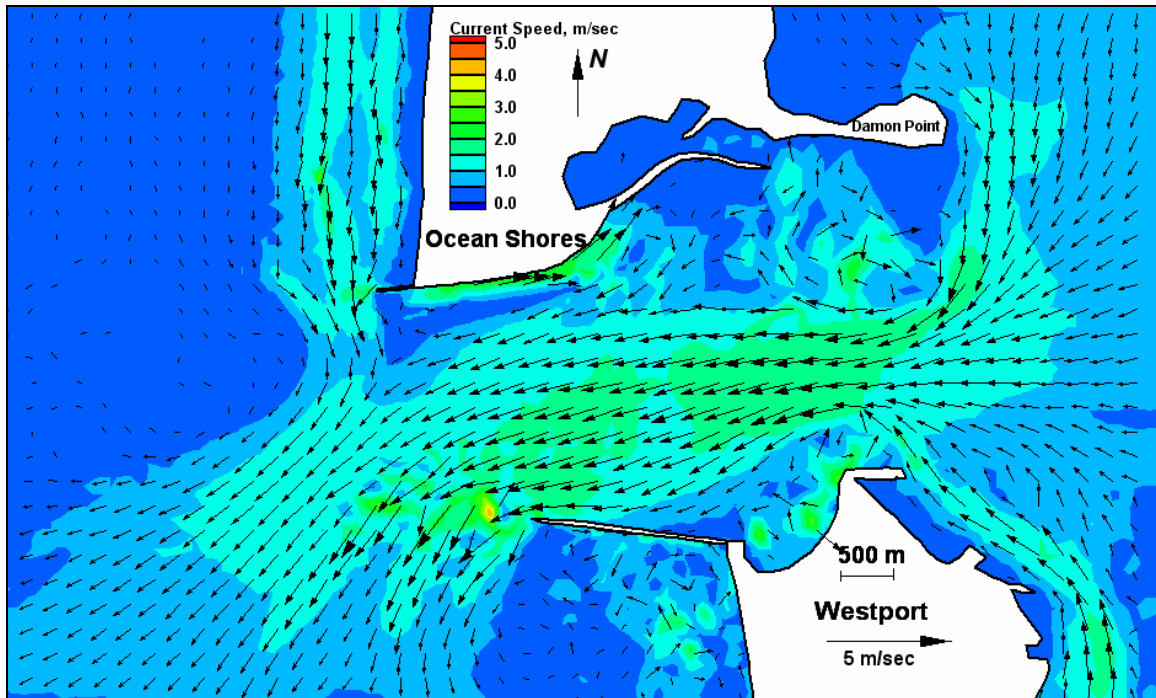Figure E37. Run 112 (Alt 2B, west-northwest, spring tide), inlet view of ebb tide

Figure E38. Run 112 (Alt 2B, west-northwest, spring tide), north jetty view of ebb tide

Appendix E   Tidal Circulation Simulation Results

Figure E39. Run 113 (Alt 2B, west-soutwest, spring tide), inlet view of flood tide

Figure E40. Run 113 (Alt 2B, west-southwest, spring tide), north jetty view of flood tide

Figure E41. Run 113 (Alt 2B, west-southwest, spring tide), inlet view of ebb tide

Figure E42. Run 113 (Alt 2B, west-southwest, spring tide), north jetty view of ebb tide

E22
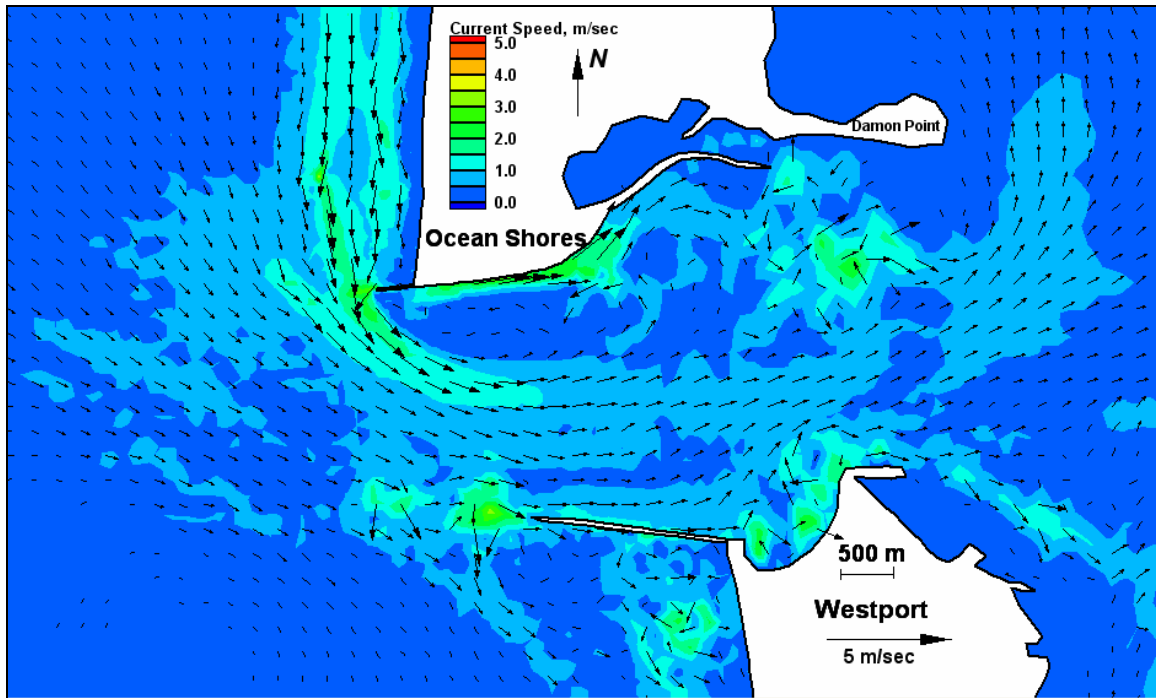
Figure E43. Run 114 (Alt 2B, west-northwest, neap tide), inlet view of flood tide

Figure E44. Run 114 (Alt 2B, west-southwest, spring tide), north jetty view of flood tide

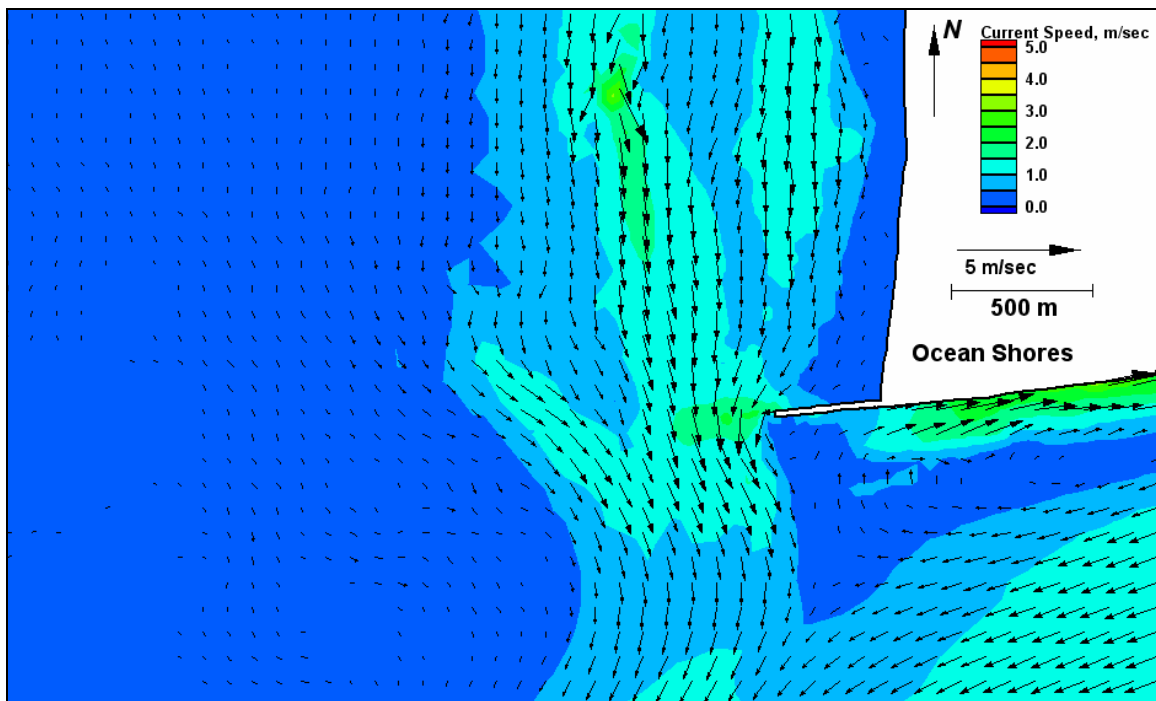Figure E45. Run 114 (Alt 2B, west-southwest, spring tide), inlet view of ebb tide

Figure E46. Run 114 (Alt 2B, west-southwest, spring tide), north jetty view of ebb tide
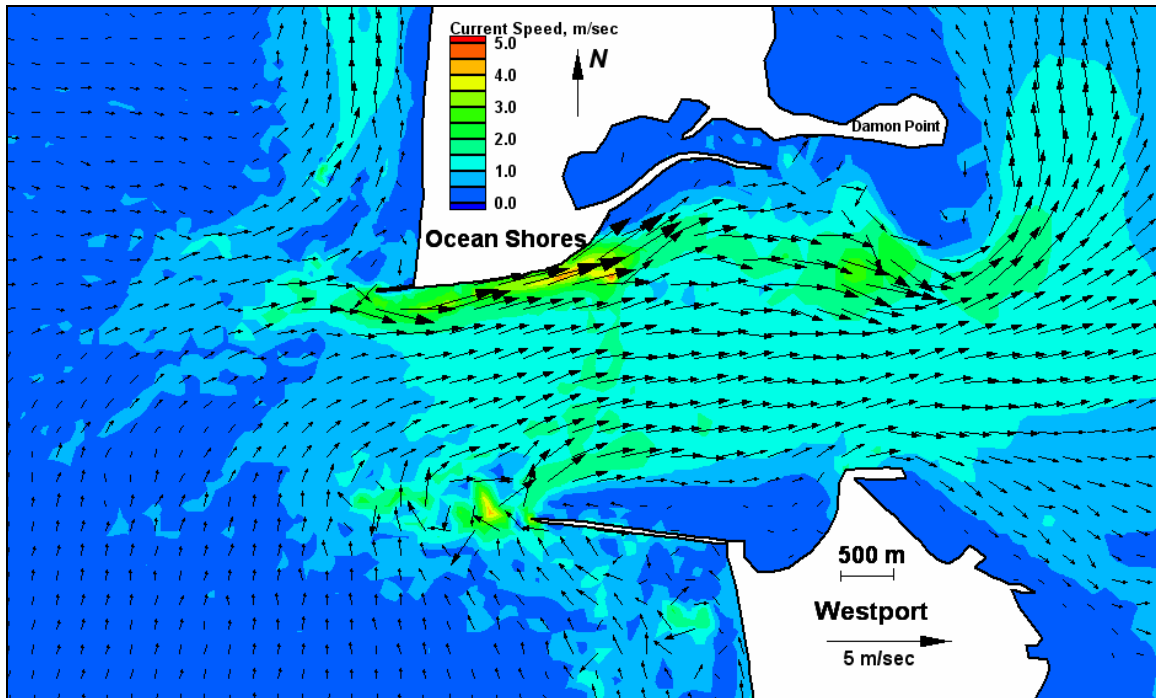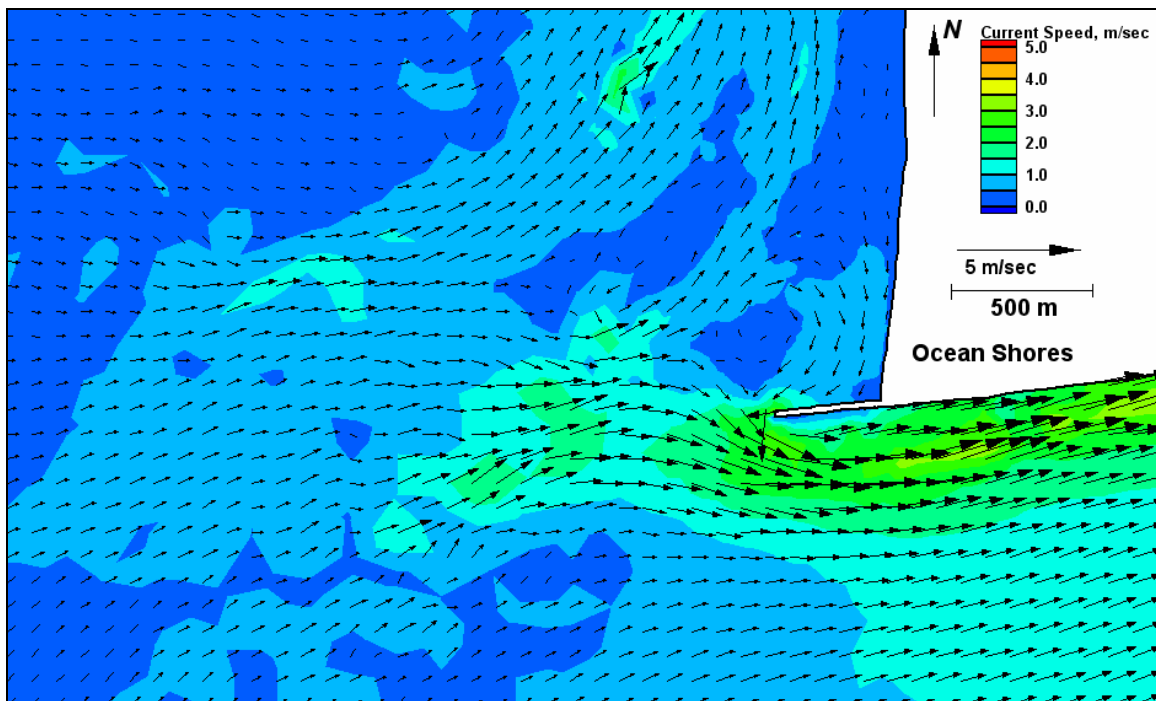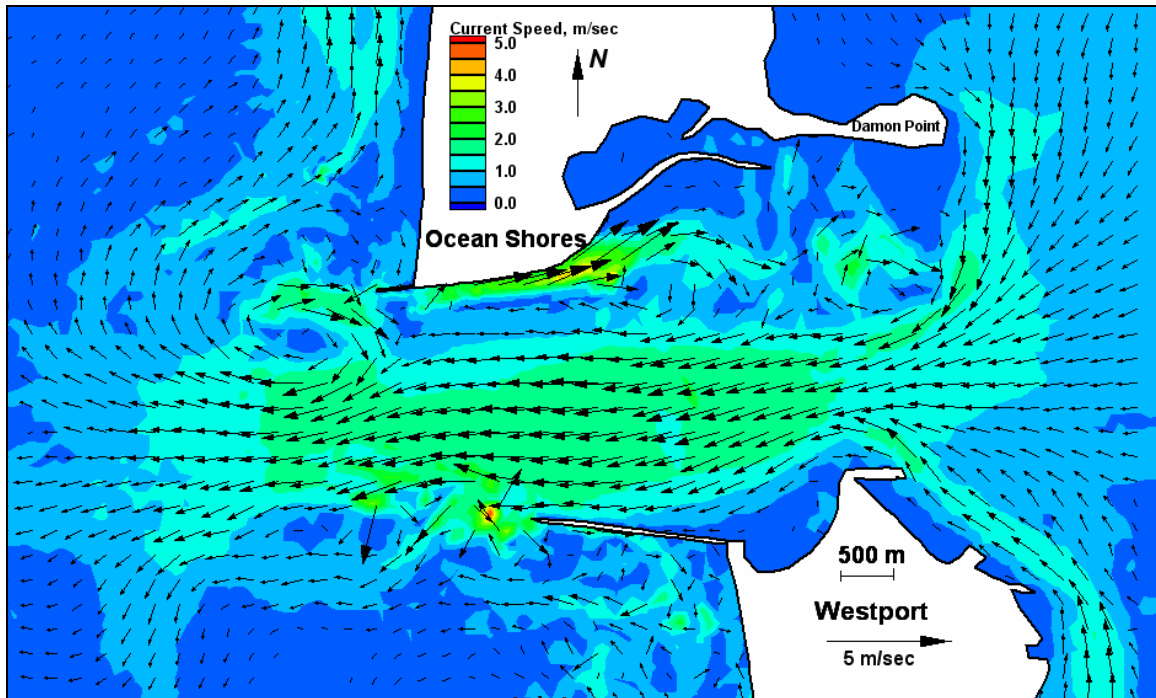
Figure E47. Run 115 (Alt 2B, west-southwest, neap tide), inlet view of flood tide

Figure E48. Run 115 (Alt 2B, west-southwest, neap tide), north jetty view of flood tide

Figure E49. Run 115 (Alt 2B, west-southwest, neap tide), inlet view of ebb tide

Figure E50. Run 115 (Alt 2B, west-southwest, neap tide), north jetty view of ebb tide

Appendix E   Tidal Circulation Simulation Results

Figure E51. Run 116 (Alt 3A, west-northwest, spring tide), inlet view of flood tide

Figure E52. Run 116 (Alt 3A, west-northwest, spring tide), north jetty view of flood tide

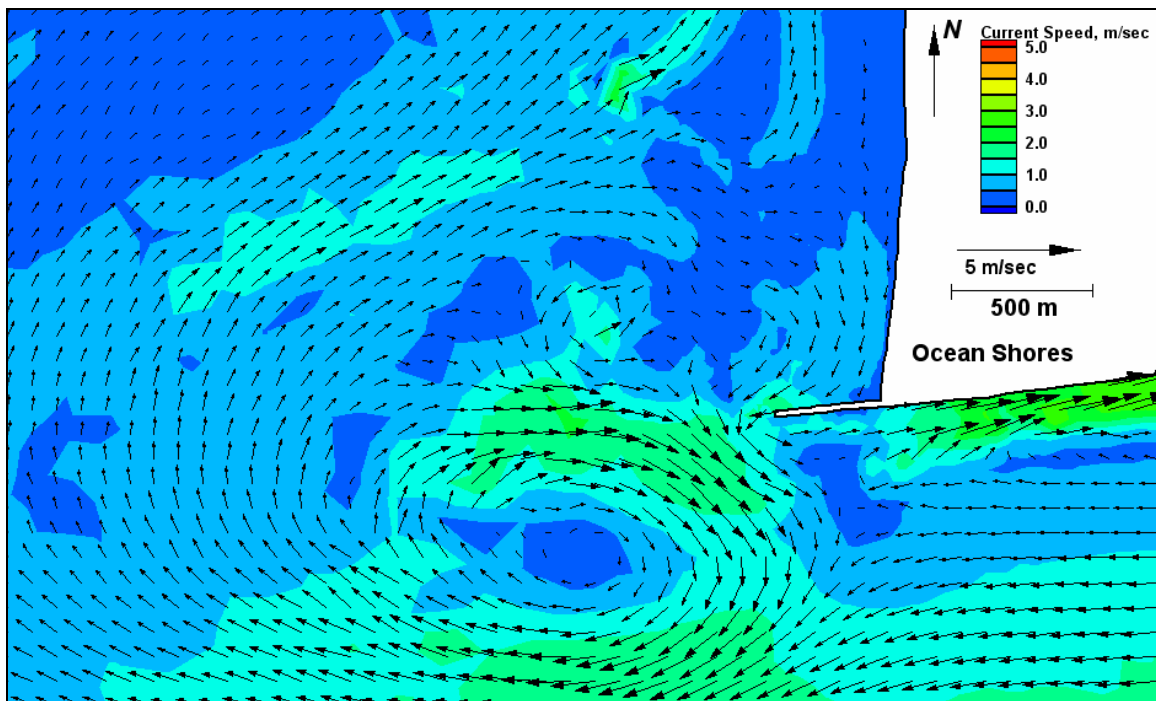Figure E53. Run 116 (Alt 3A, west-northwest, spring tide), inlet view of ebb tide

Figure E54. Run 116 (Alt 3A, west-northwest, spring tide), north jetty view of ebb tide

Appendix E   Tidal Circulation Simulation Results

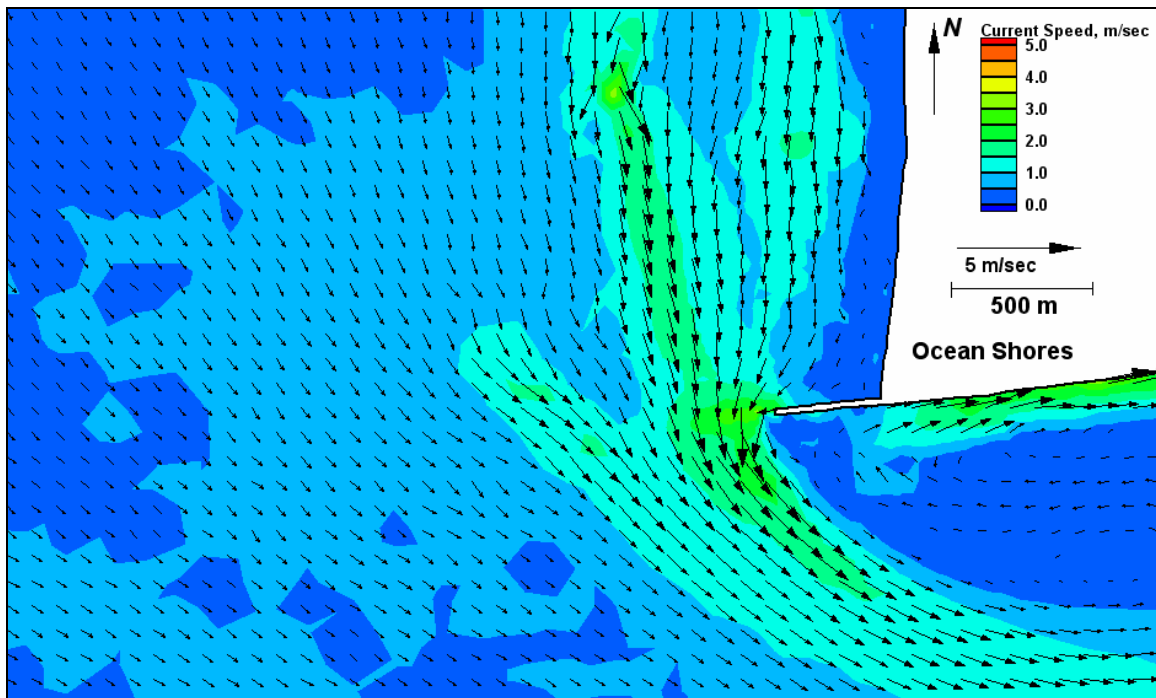Figure E55. Run 117 (Alt 3A, west-southwest, spring tide), inlet view of flood tide

Figure E56. Run 117 (Alt 3A, west-southwest, spring tide), north jetty view of flood tide
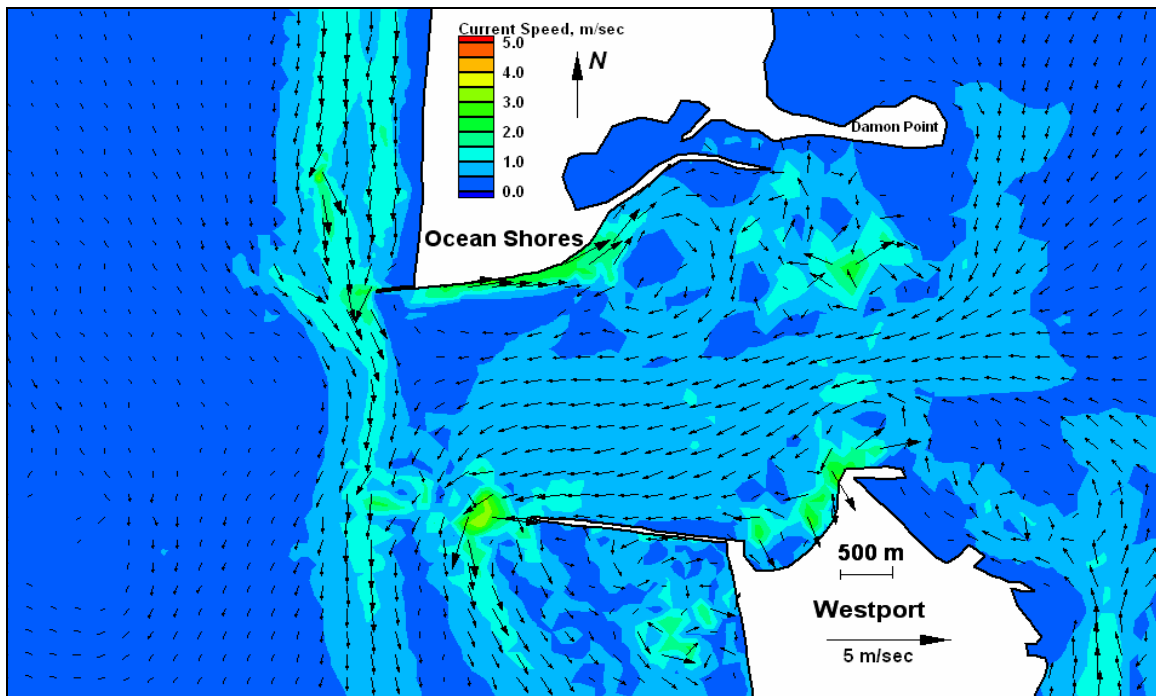
Figure E57. Run 117 (Alt 3A, west-southwest, spring tide), inlet view of ebb tide
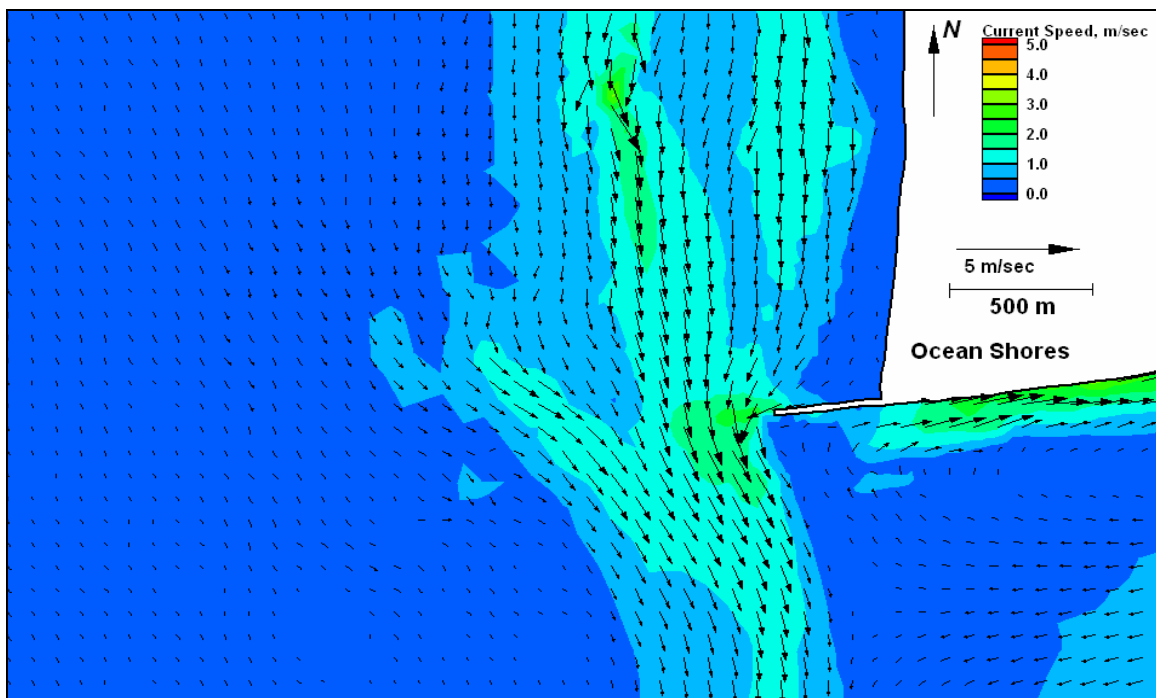

Figure E58. Run 117 (Alt 3A, west-southwest, spring tide), north jetty view of ebb tide
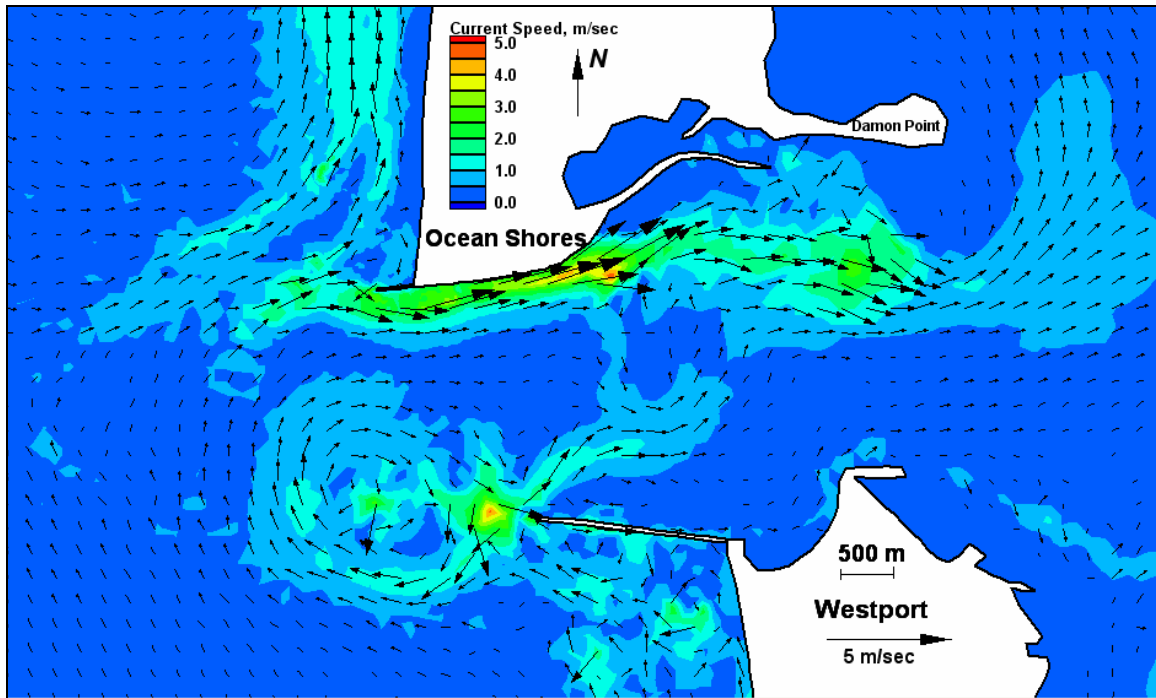
E30
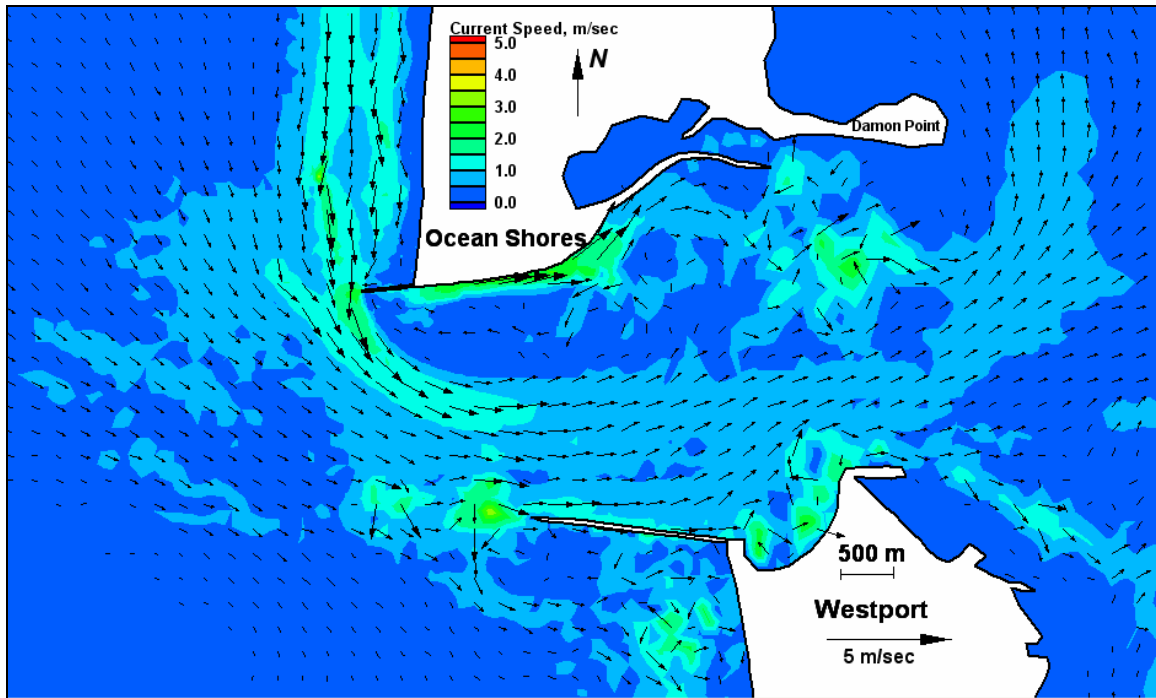
Figure E59. Run 118 (Alt 3A, west-northwest, neap tide), inlet view of flood tide

Figure E60. Run 118 (Alt 3A, west-northwest, neap tide), north jetty view of flood tide

Figure E61. Run 118 (Alt 3A, west-northwest, neap tide), inlet view of ebb tide

Figure E62. Run 118 (Alt 3A, west-northwest, neap tide), north jetty view of ebb tide

E32

Figure E63. Run 119 (Alt 3A, west-southwest, neap tide), inlet view of flood tide
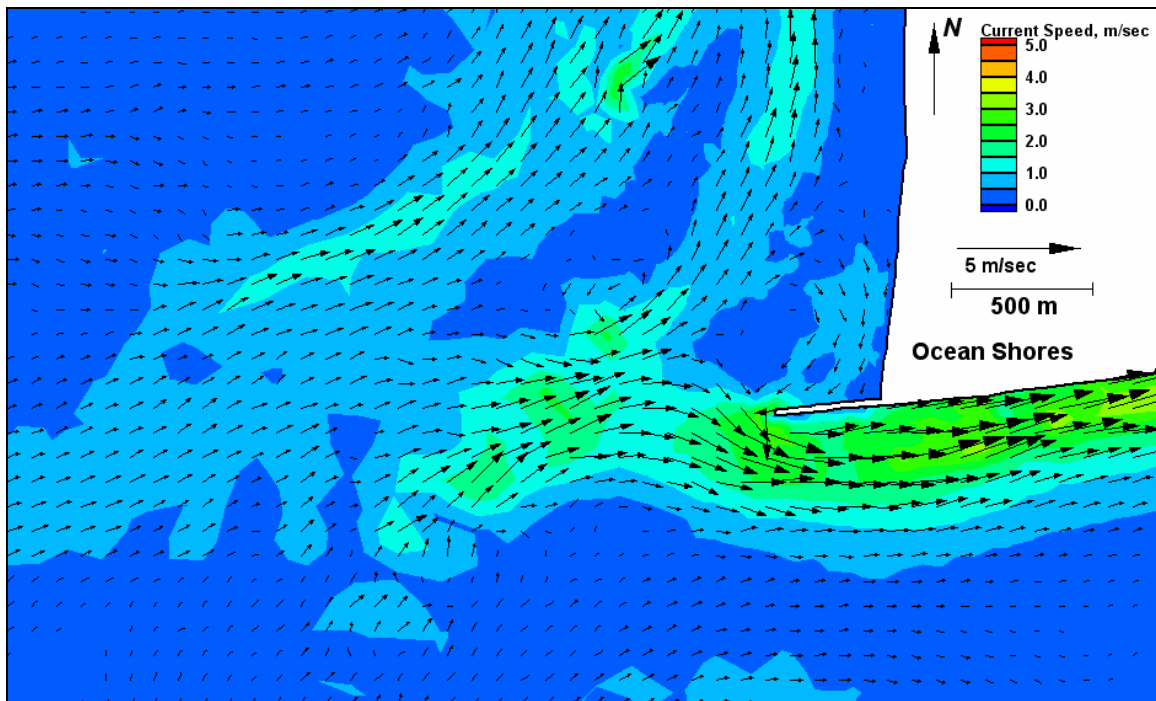

Figure E64. Run 119 (Alt 3A, west-southwest, neap tide), north jetty view of flood tide
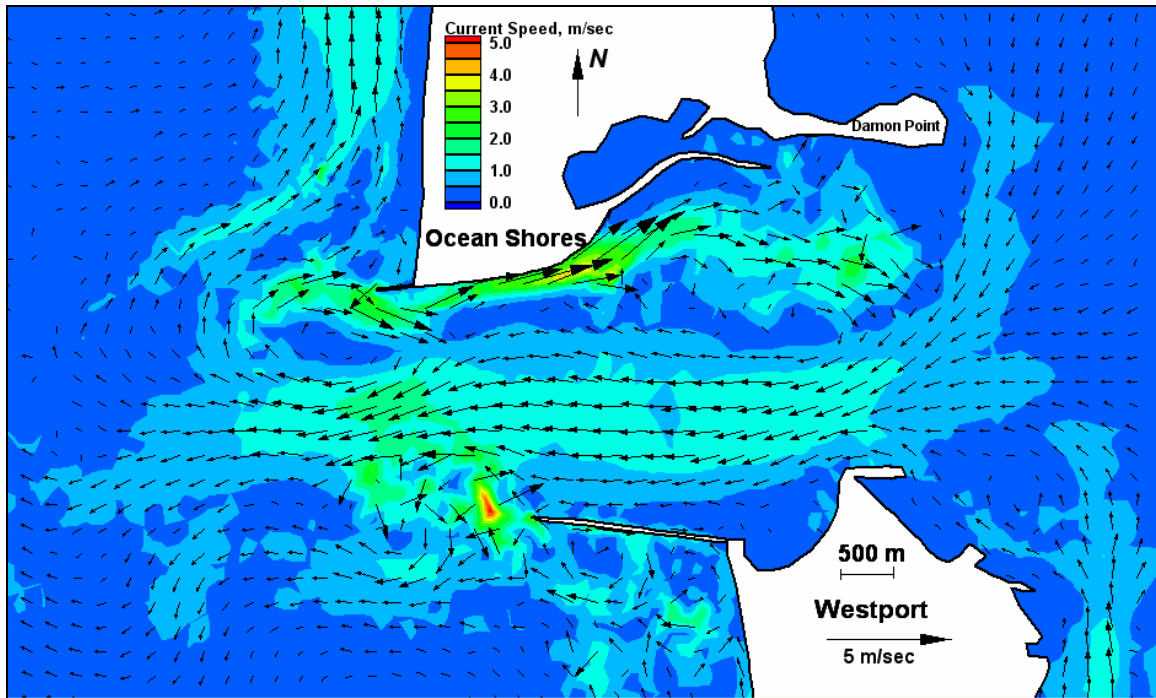
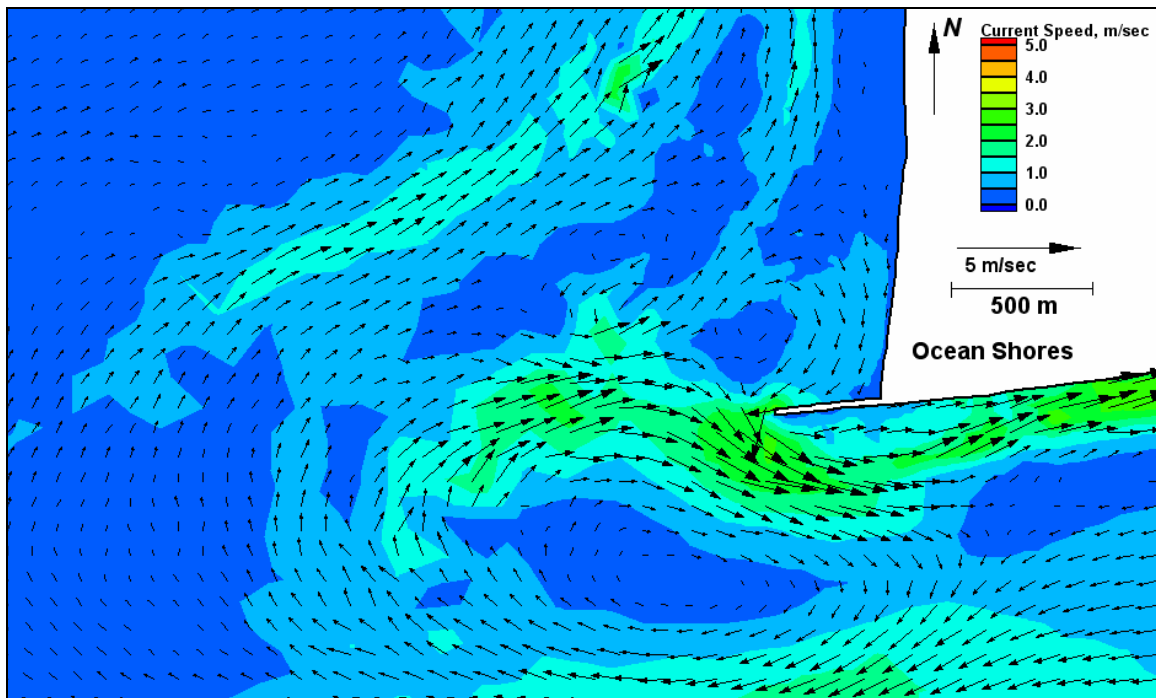Figure E65. Run 119 (Alt 3A, west-southwest, neap tide), inlet view of ebb tide

Figure E66. Run 119 (Alt 3A, west-southwest, neap tide), north jetty view of ebb tide
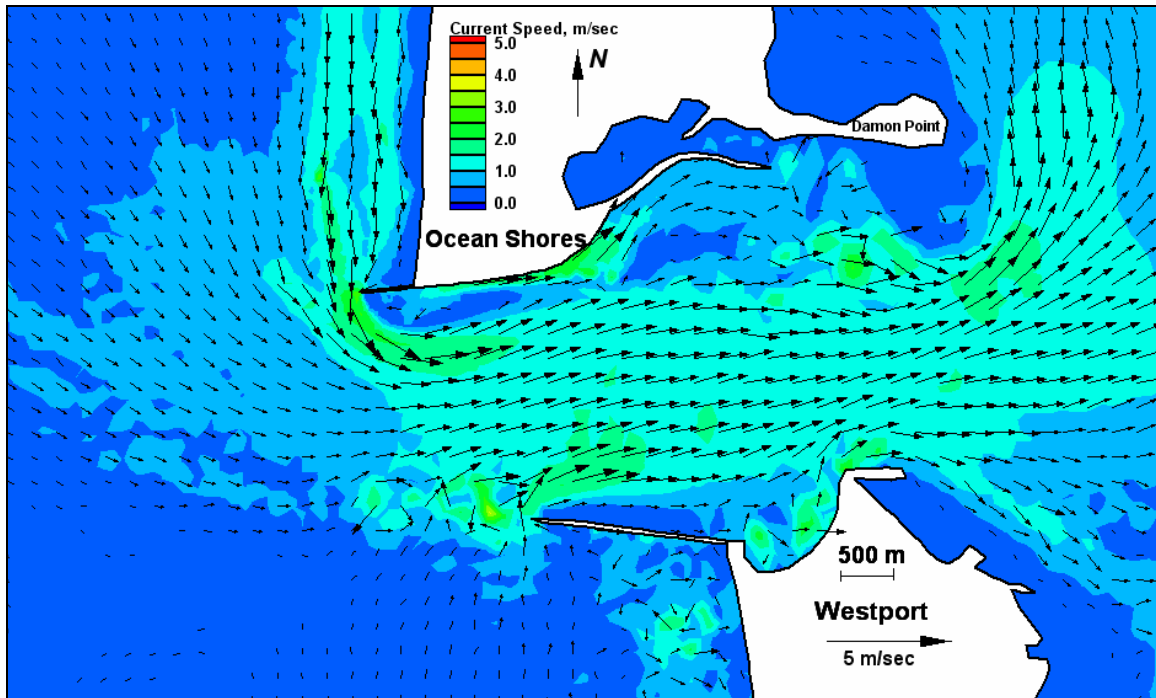
E34
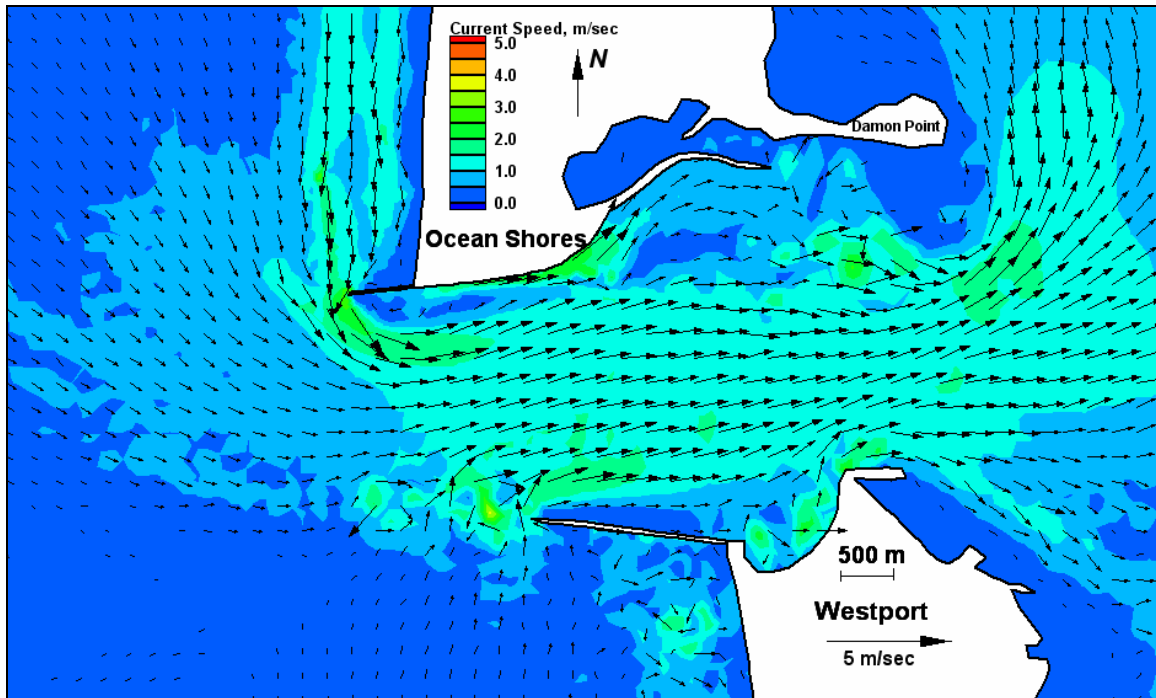
Figure E67. Run 120 (Alt 3B, west-northwest, spring tide), inlet view of flood tide

Figure E68. Run 120 (Alt 3B, west-northwest, spring tide), north jetty view of flood tide

Figure E69. Run 120 (Alt 3B, west-northwest, spring tide), inlet view of ebb tide

Figure E70. Run 120 (Alt 3B, west-northwest, spring tide), north jetty view of ebb tide
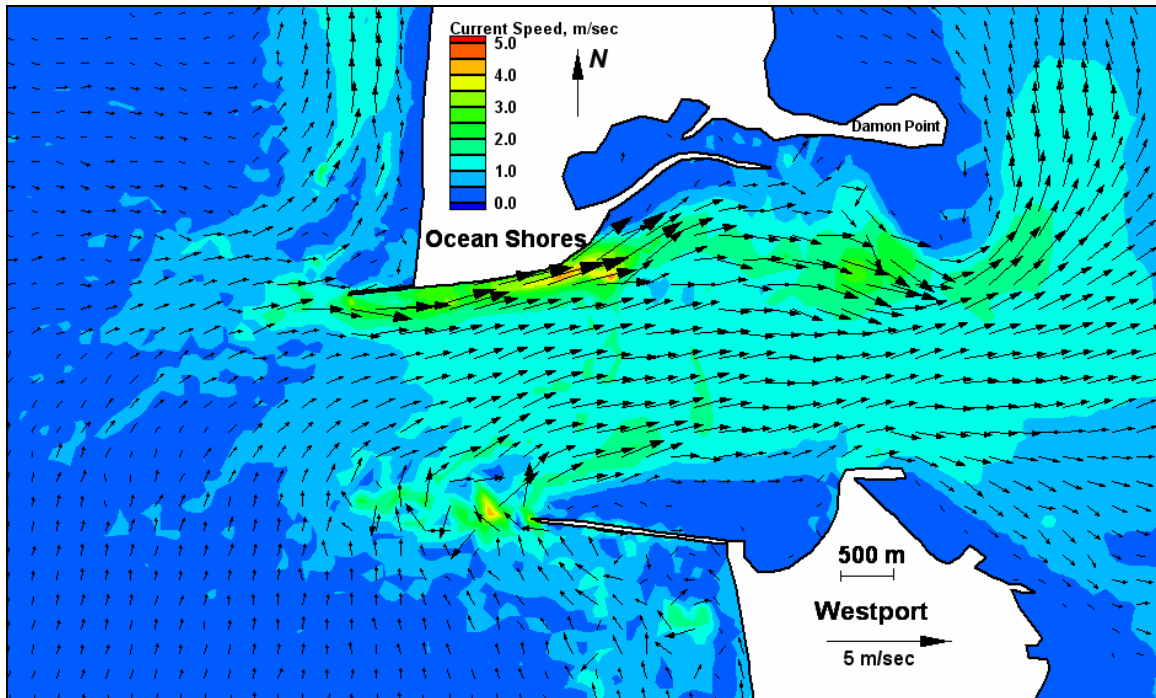
Figure E71. Run 121 (Alt 3B, west-southwest, spring tide), inlet view of flood tide
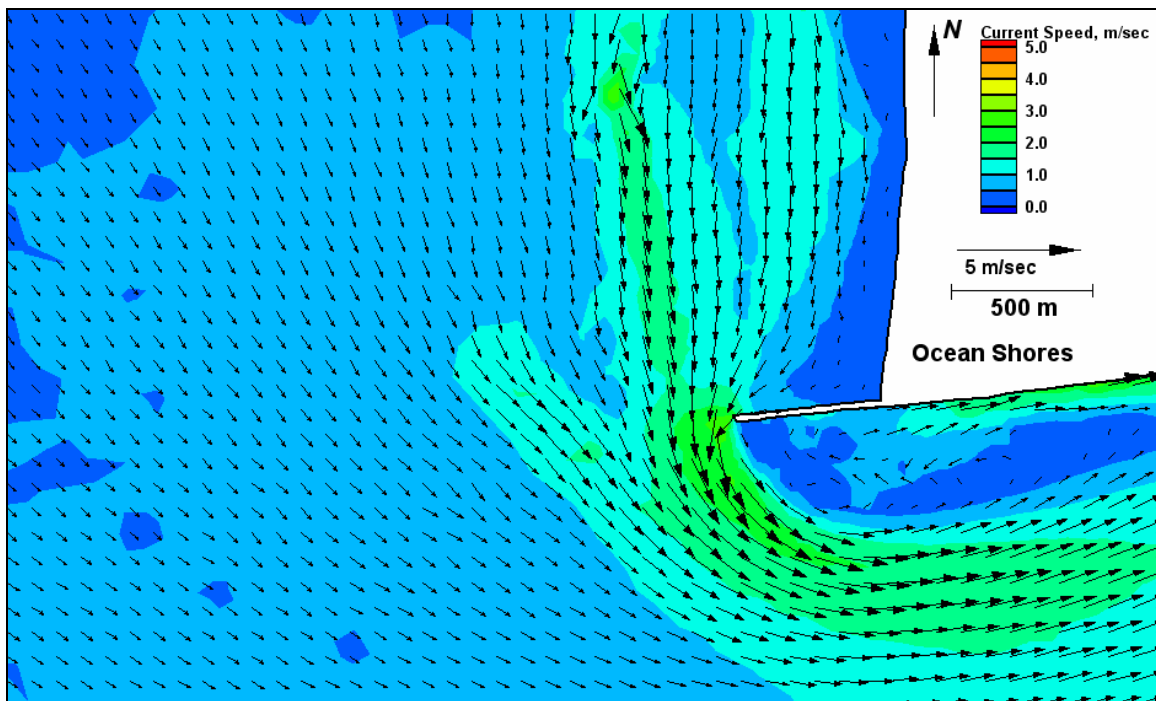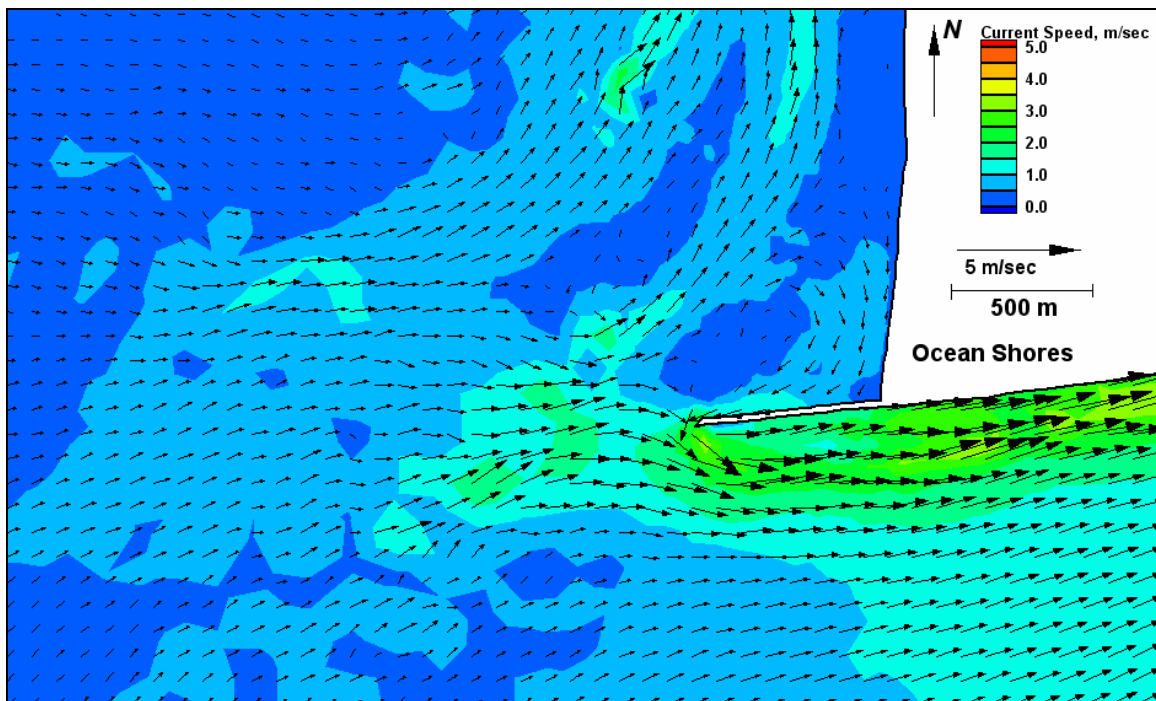

Figure E72. Run 121 (Alt 3B, west-southwest, spring tide), north jetty view of flood tide
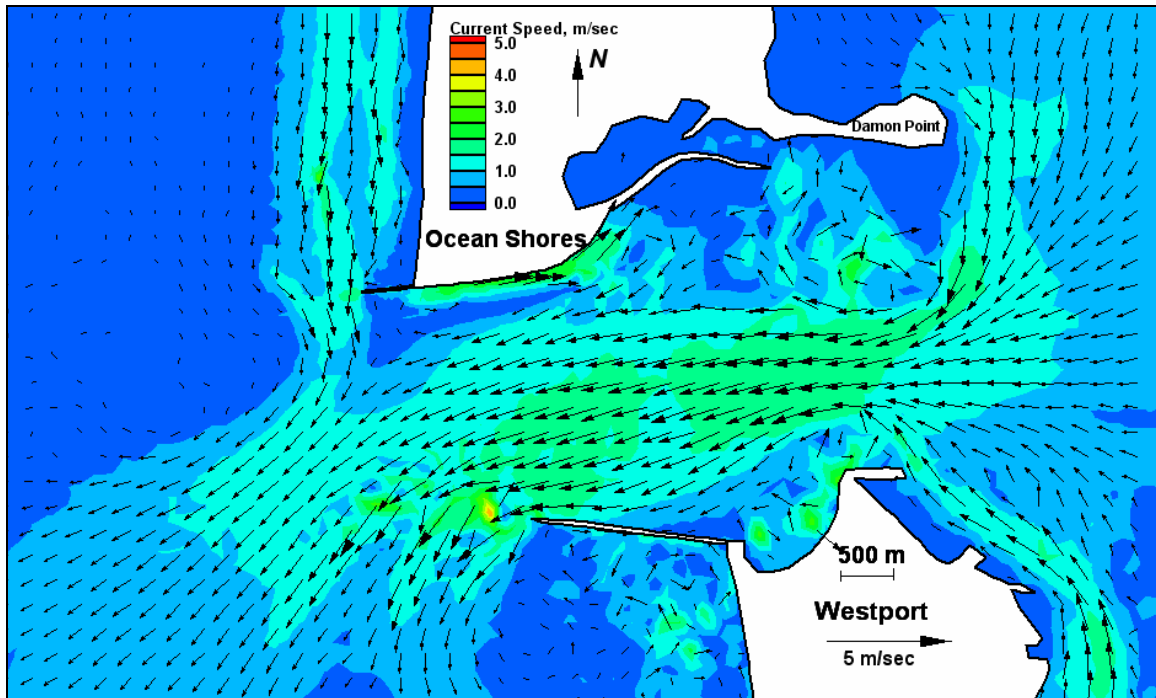
Figure E73. Run 121 (Alt 3B, west-southwest, spring tide), inlet view of ebb tide
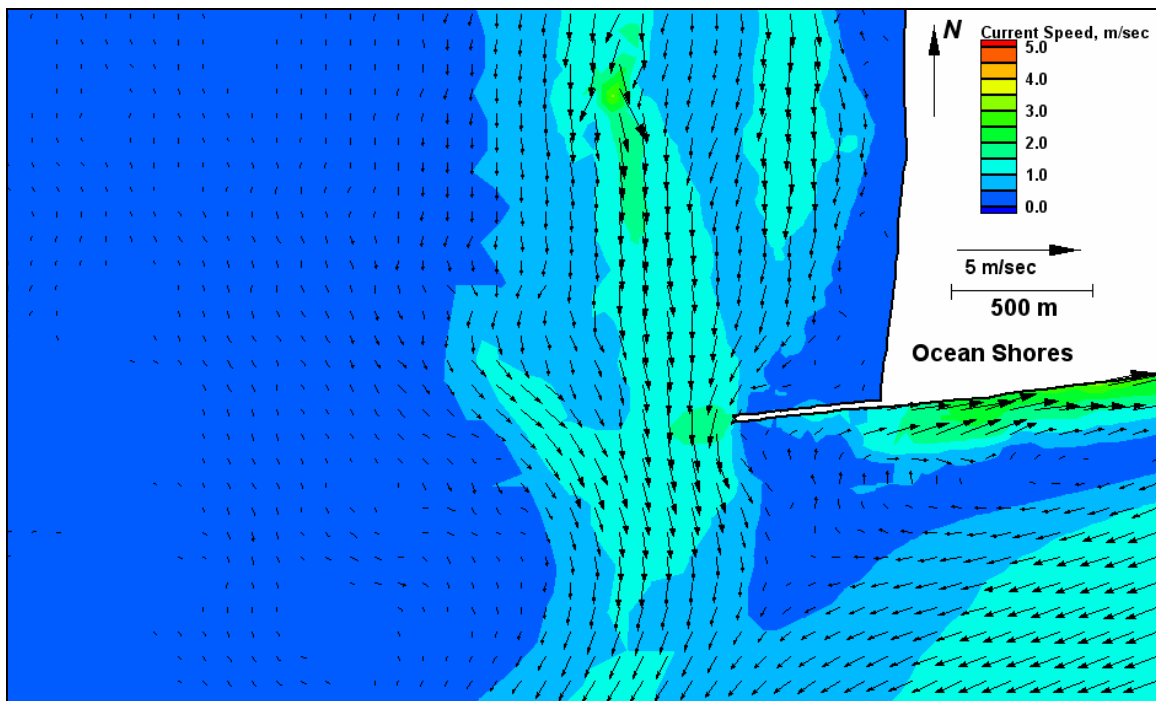

Figure E74. Run 121 (Alt 3B, west-southwest, spring tide), north jetty view of ebb tide
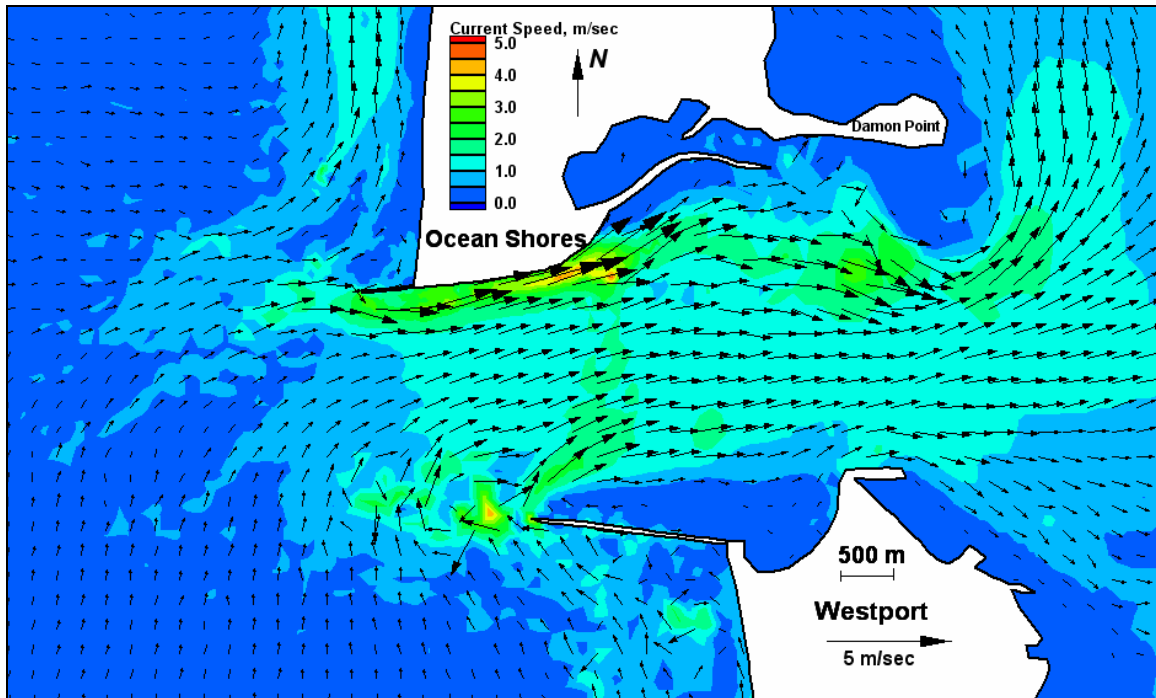
E38
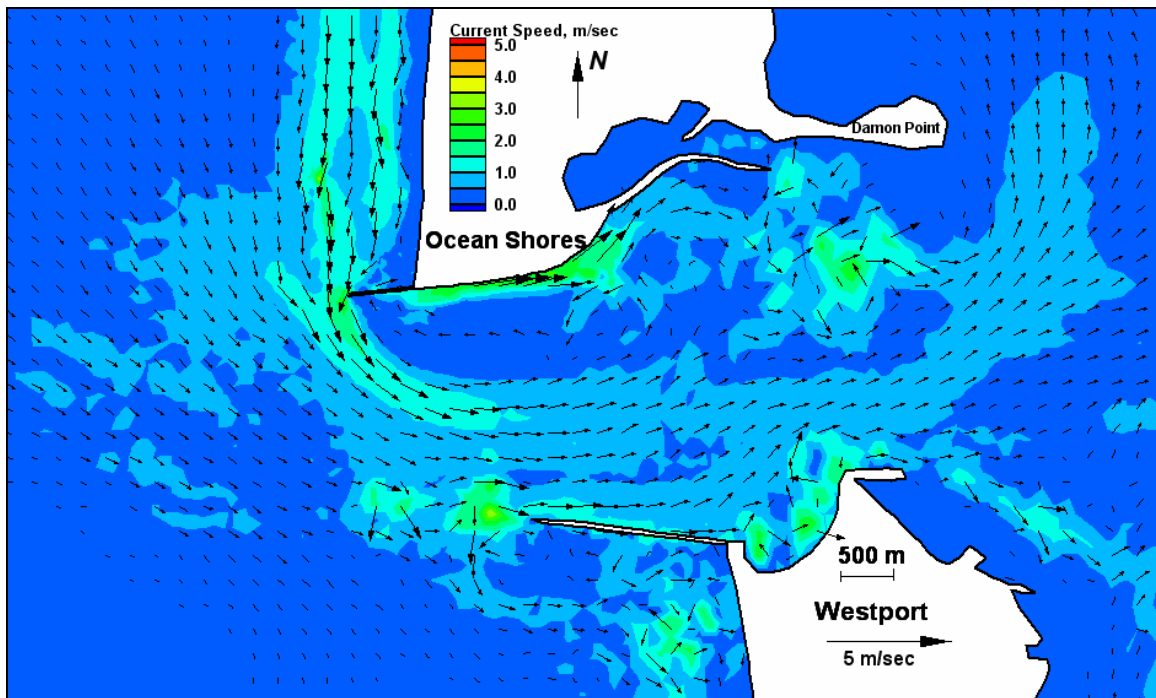
Figure E75. Run 122 (Alt 3B, west-northwest, neap tide), inlet view of flood tide

Figure E76. Run 122 (Alt 3B, west-northwest, neap tide), north jetty view of flood tide

Figure E77. Run 122 (Alt 3B, west-northwest, neap tide), inlet view of ebb tide
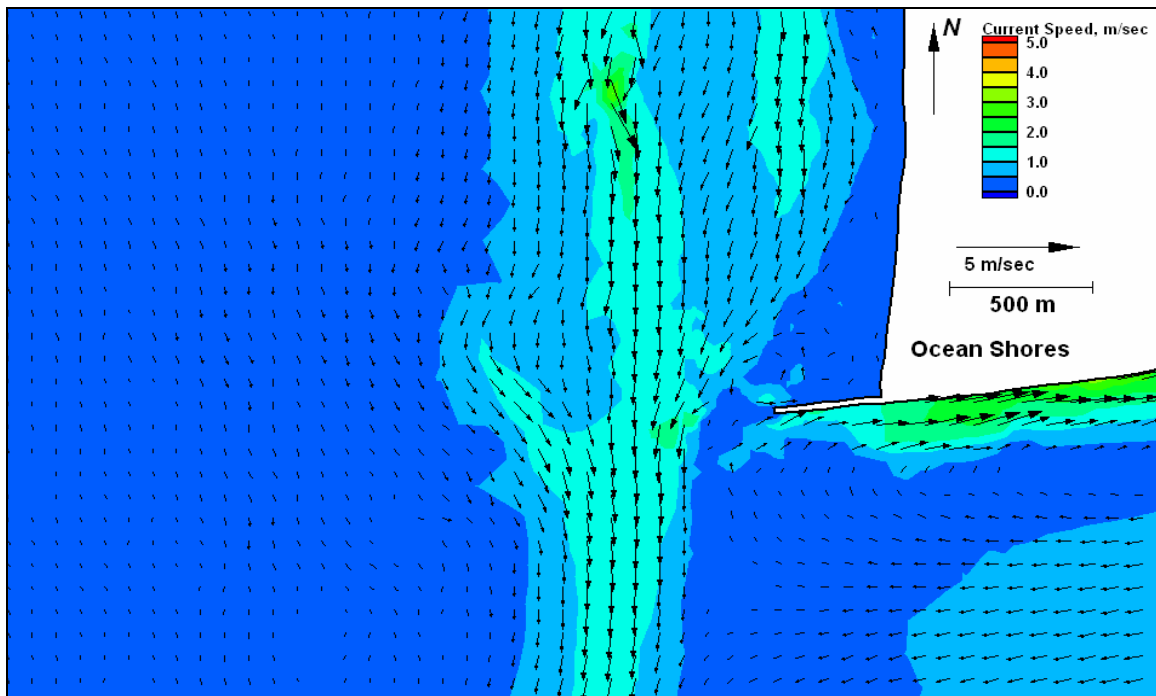
Figure E78. Run 122 (Alt 3B, west-northwest, neap tide), north jetty view of ebb tide

E40
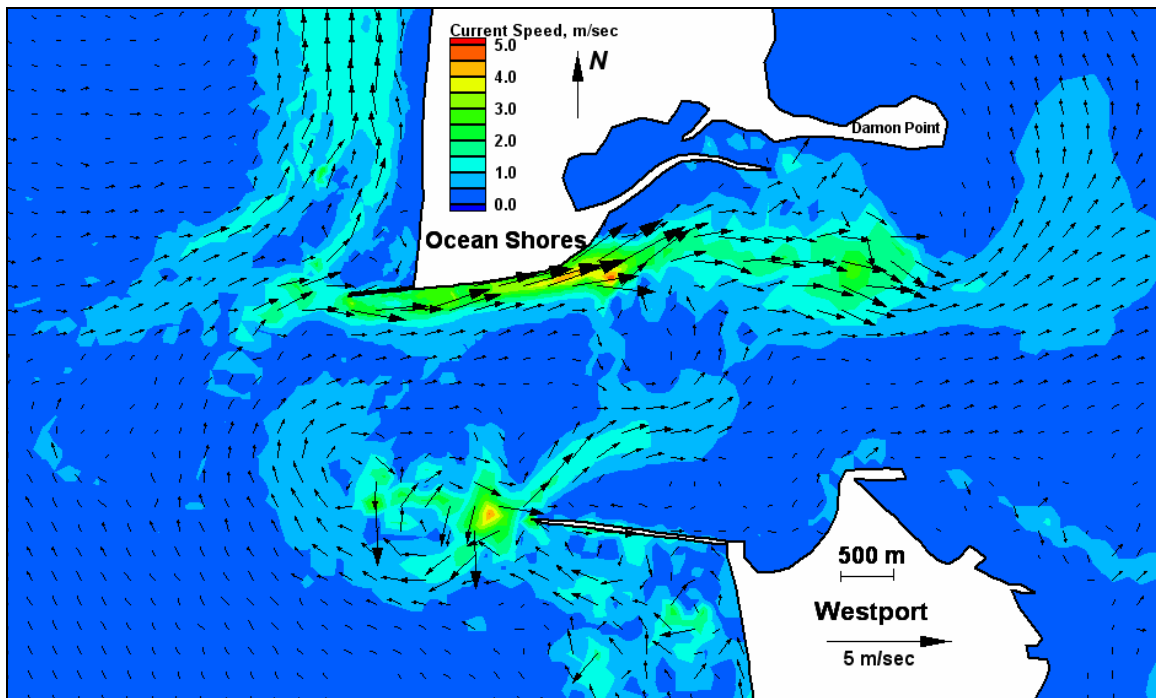
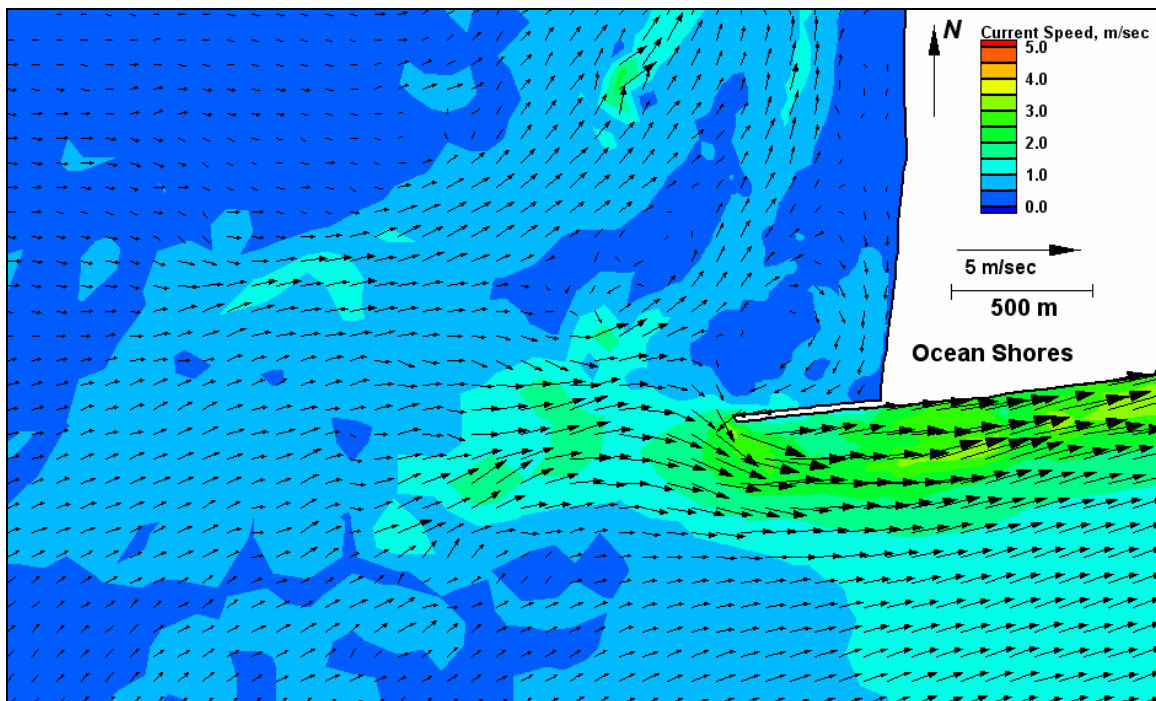Figure E79. Run 123 (Alt 3B, west-southwest, neap tide), inlet view of flood tide

Figure E80. Run 123 (Alt 3B, west-southwest, neap tide), north jetty view of flood tide
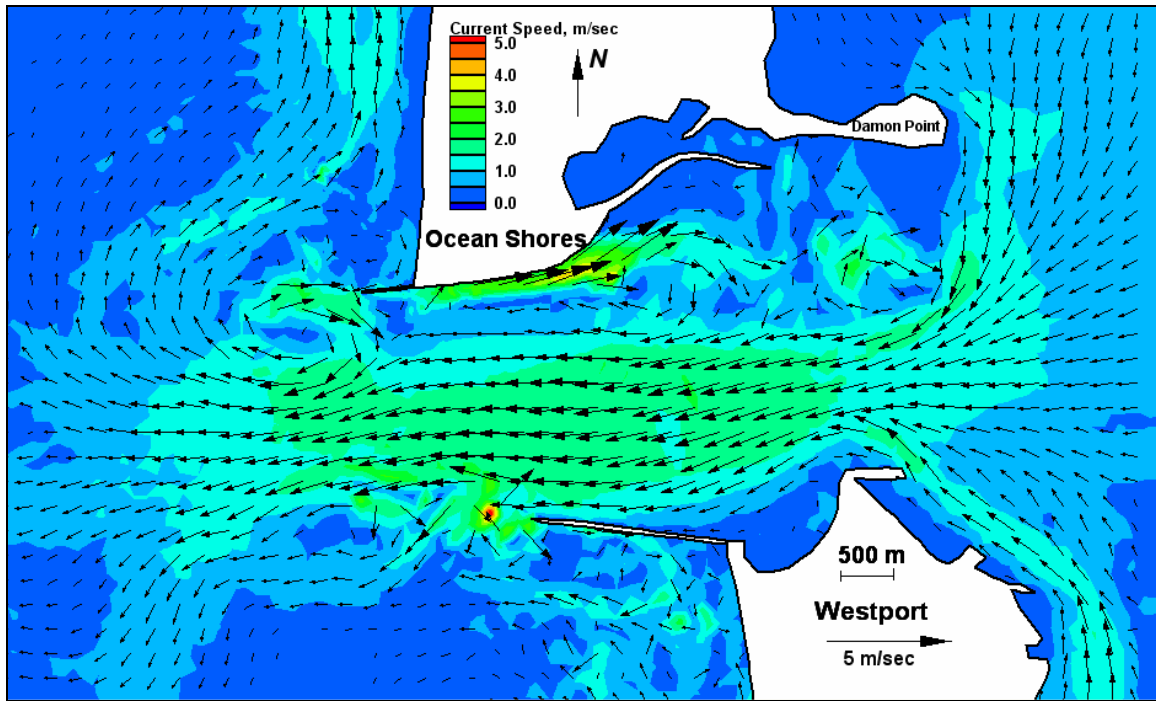
Figure E81. Run 123 (Alt 3B, west-southwest, neap tide), inlet view of ebb tide

Figure E82. Run 123 (Alt 3B, west-southwest, neap tide), north jetty view of ebb tide

E42
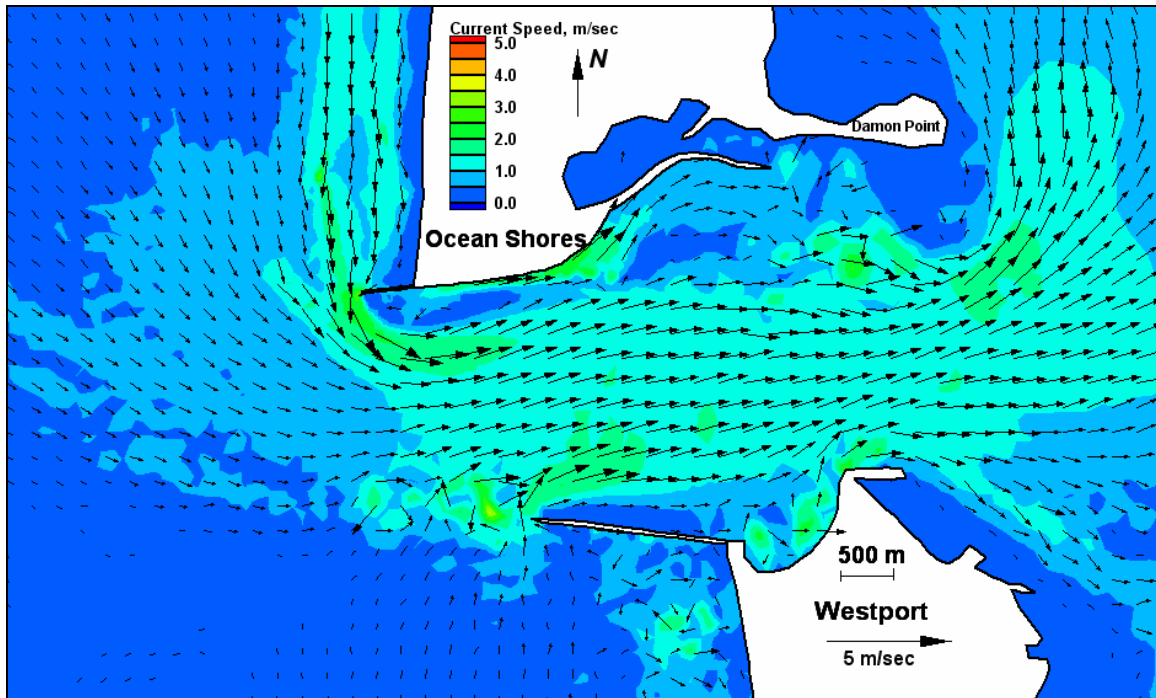
Figure E83. Run 124 (Alt 4A, west-northwest, spring tide), inlet view of flood tide

Figure E84. Run 124 (Alt 4A, west-northwest, spring tide), north jetty view of flood tide

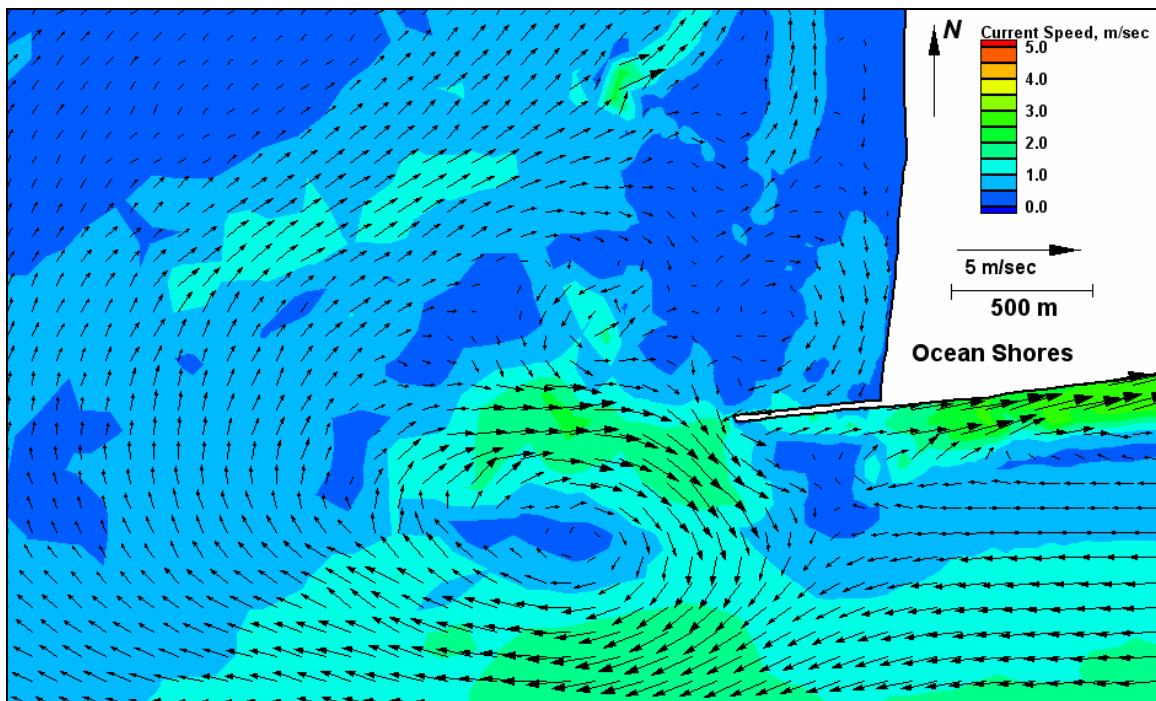Figure E85. Run 124 (Alt 4A, west-northwest, spring tide), inlet view of ebb tide

Figure E86. Run 124 (Alt 4A, west-northwest, spring tide), north jetty view of ebb tide

E44

Figure E87. Run 125 (Alt 4A, west-southwest, spring tide), inlet view of flood tide

Figure E88. Run 125 (Alt 4A, west-southwest, spring tide), north jetty view of flood tide

Figure E89. Run 125 (Alt 4A, west-southwest, spring tide), inlet view of ebb tide

Figure E90. Run 125 (Alt 4A, west-southwest, spring tide), north jetty view of ebb tide

E46
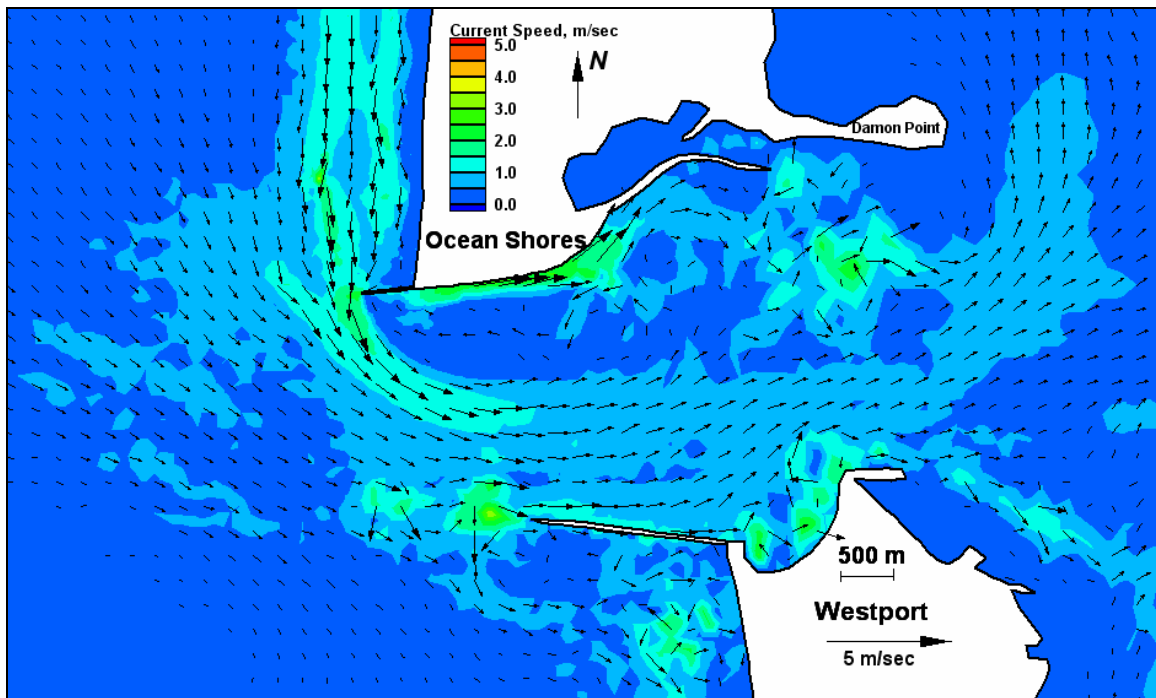
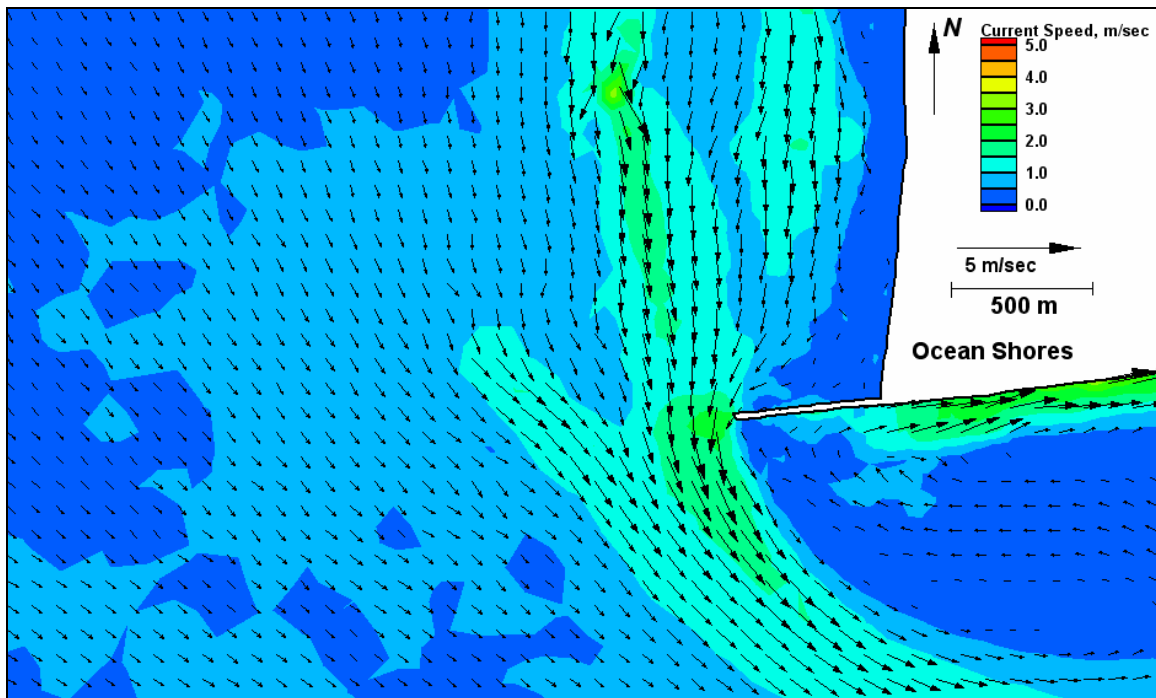Figure E91. Run 126 (Alt 4A, west-northwest, neap tide), inlet view of flood tide

Figure E92. Run 126 (Alt 4A, west-northwest, neap tide), north jetty view of flood tide
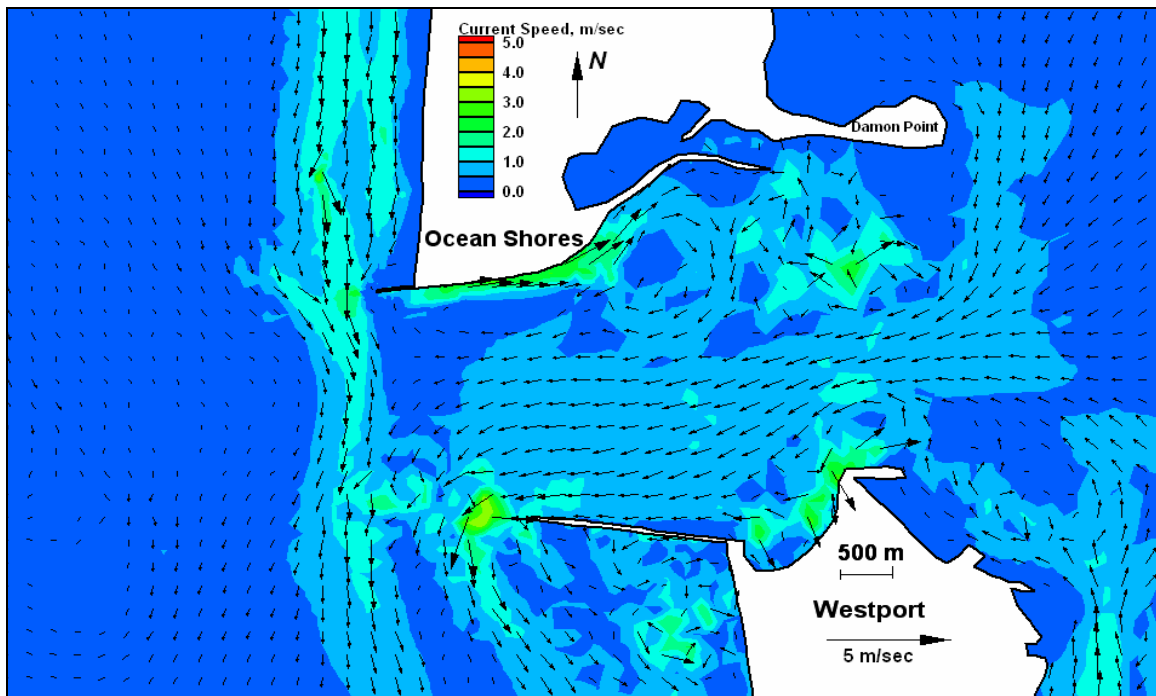
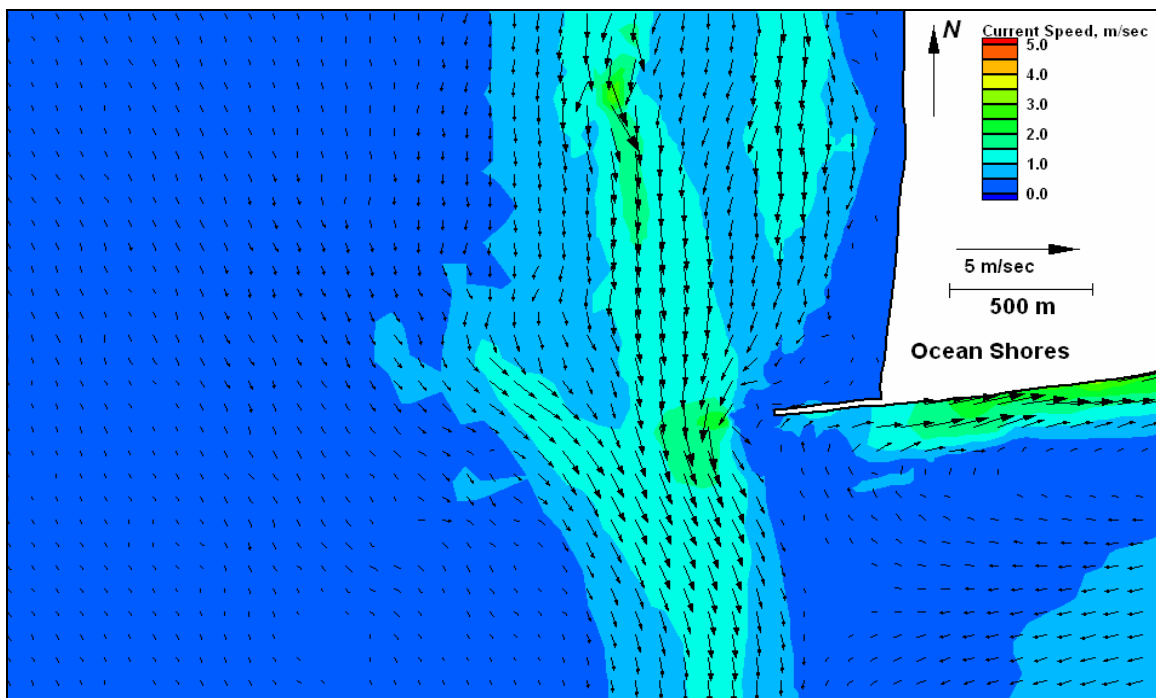Figure E93. Run 126 (Alt 4A, west-northwest, neap tide), inlet view of ebb tide
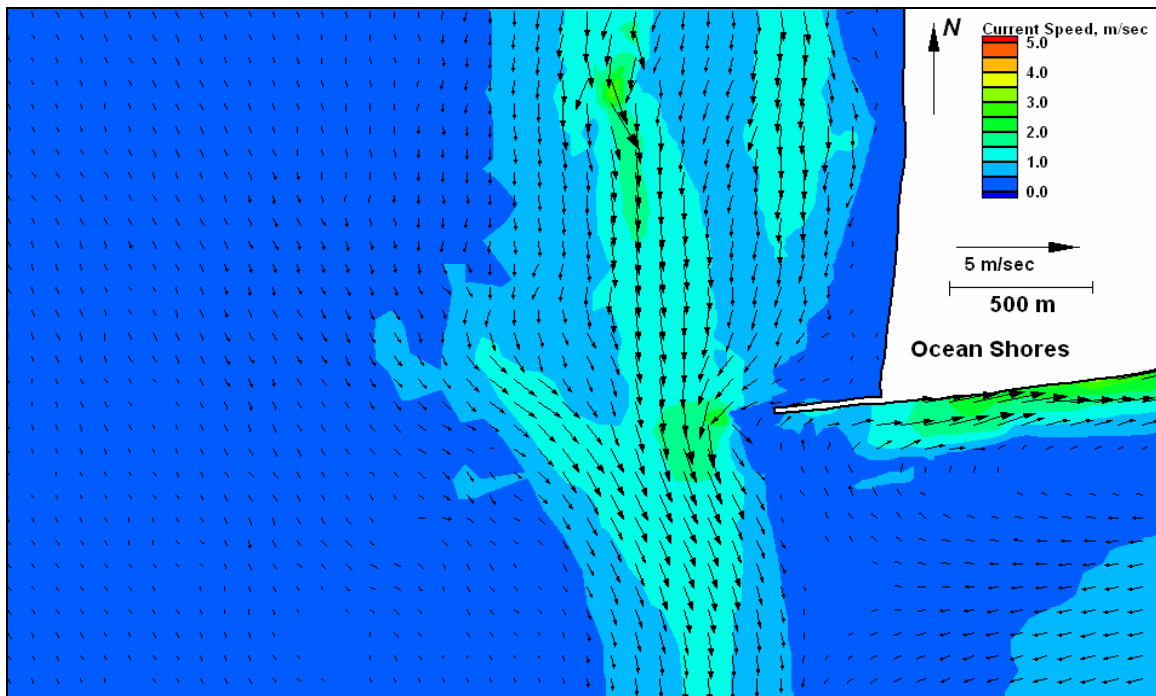
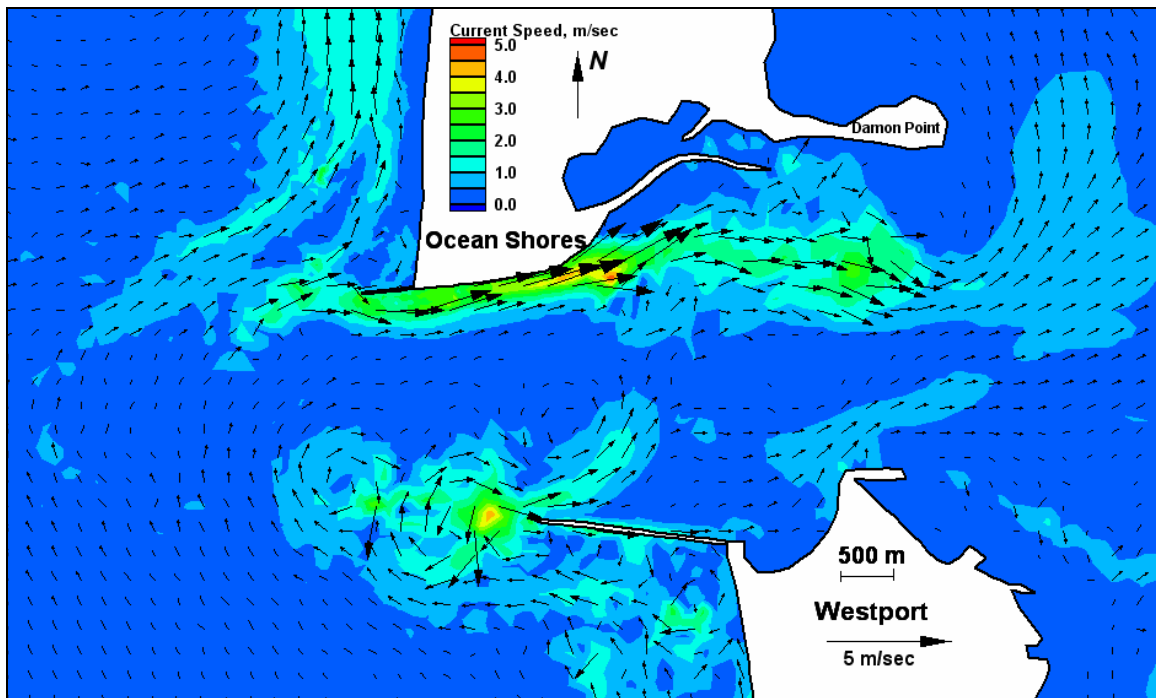Figure E94. Run 126 (Alt 4A, west-northwest, neap tide), north jetty view of ebb tide
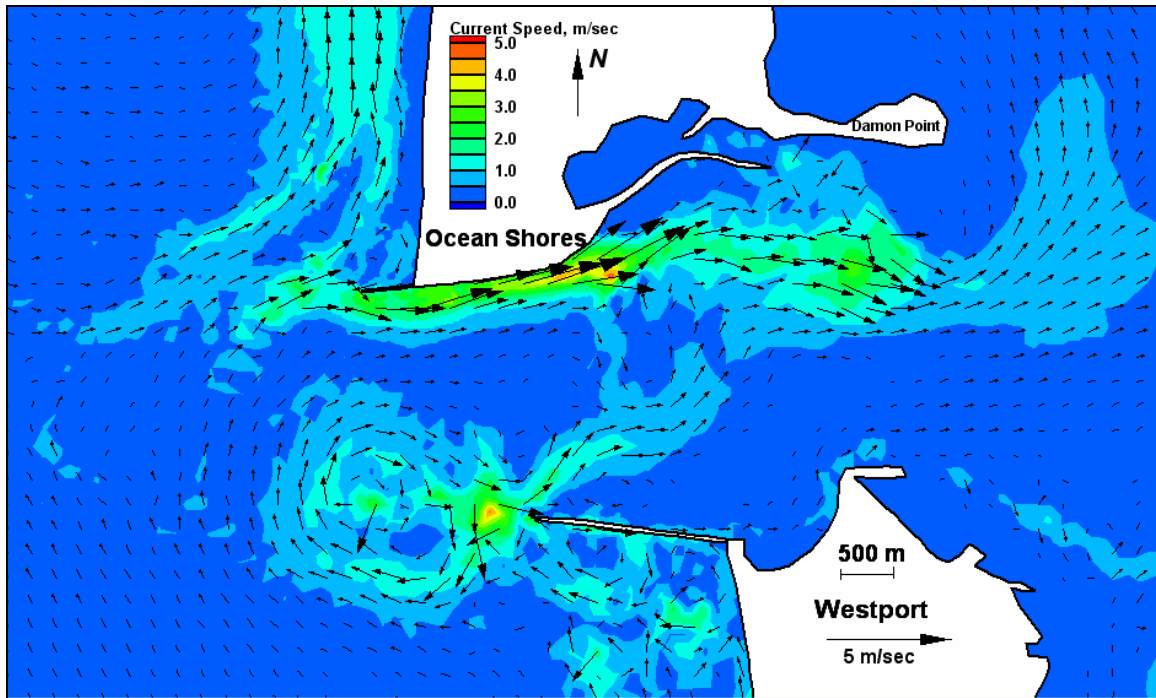
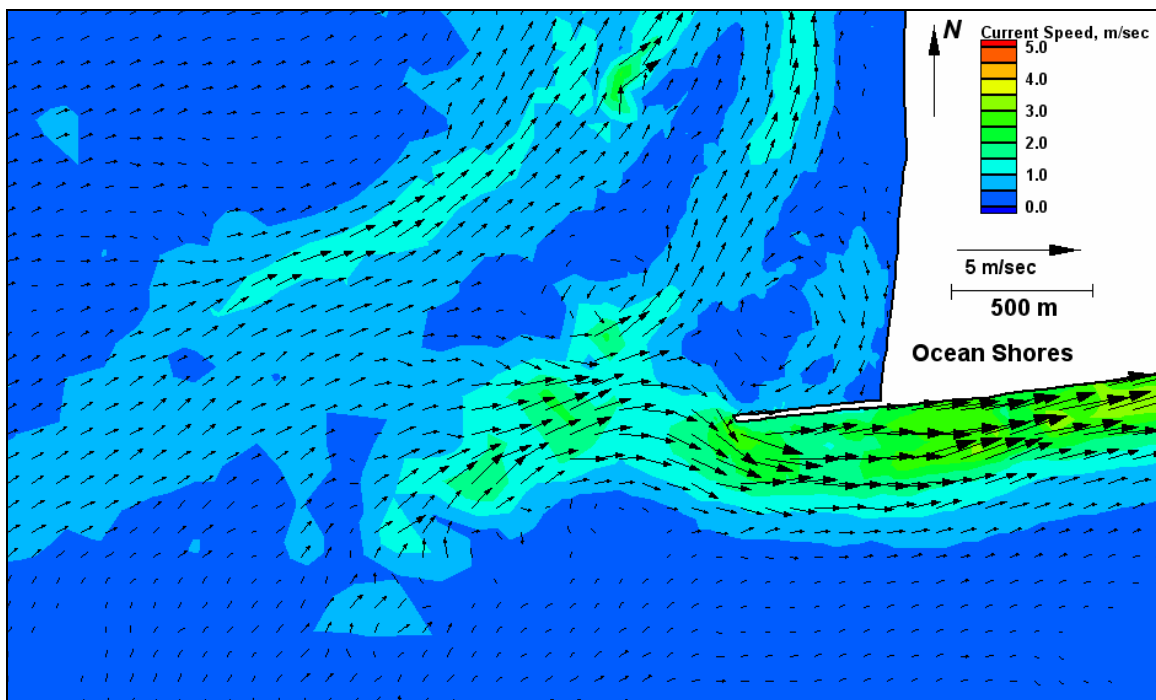Figure E95. Run 127 (Alt 4A, west-southwest, neap tide), inlet view of flood tide
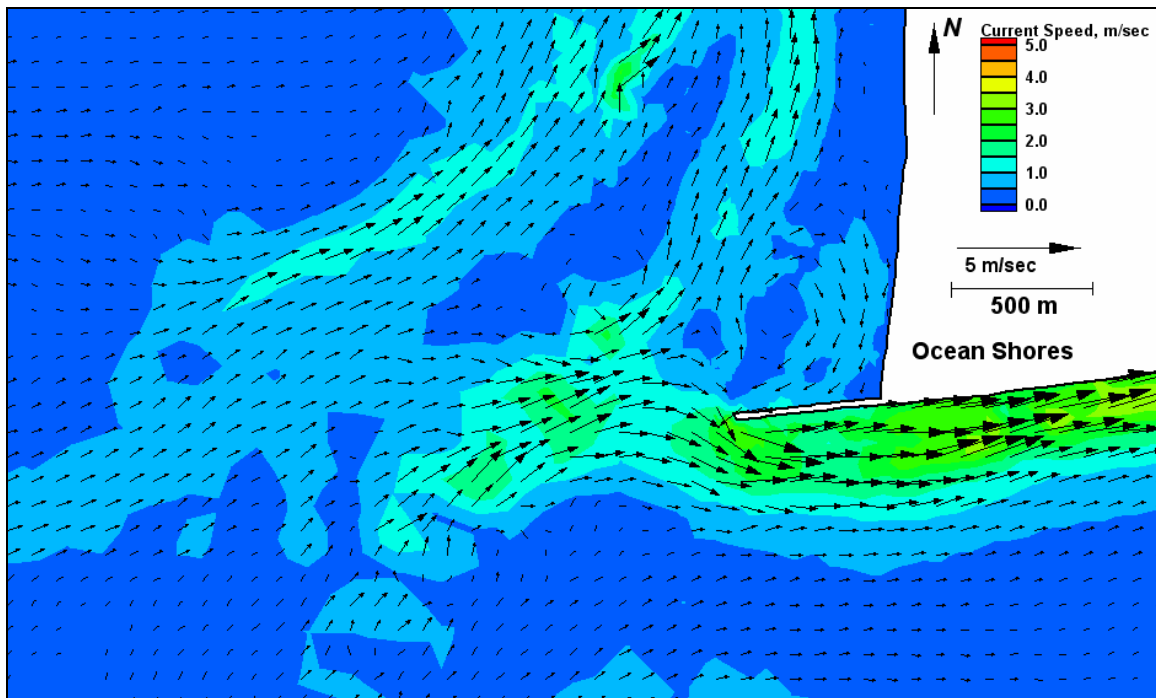
Figure E96. Run 127 (Alt 4A, west-southwest, neap tide), north jetty view of flood tide
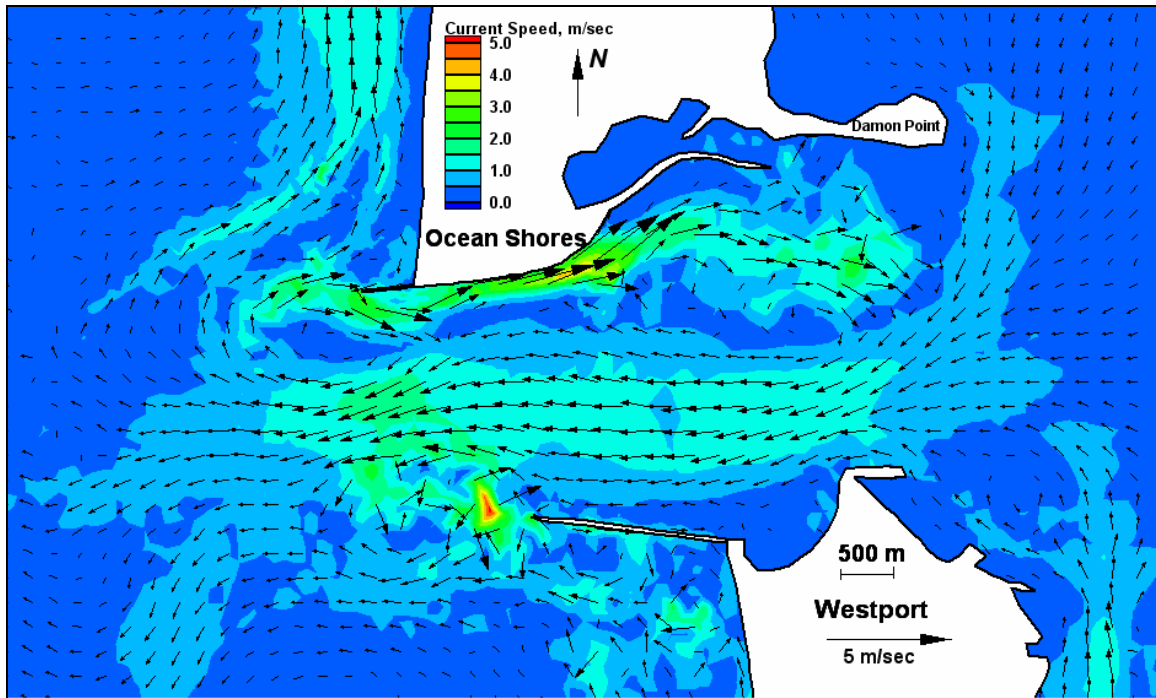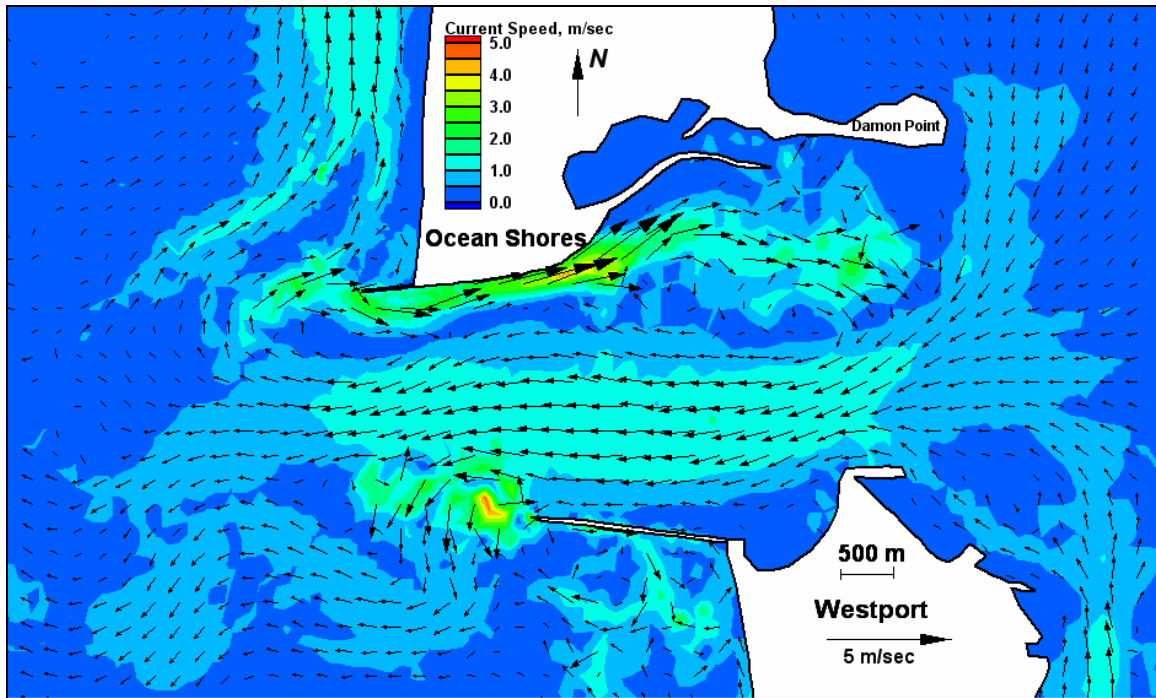
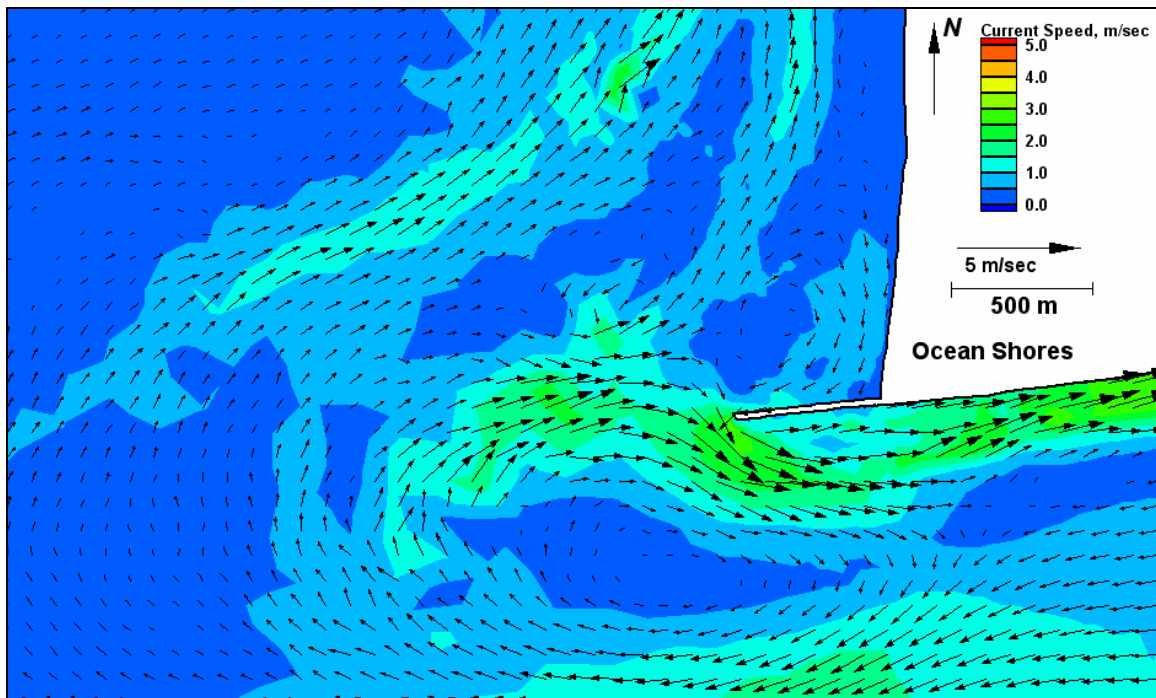Figure E97. Run 127 (Alt 4A, west-southwest, neap tide), inlet view of ebb tide
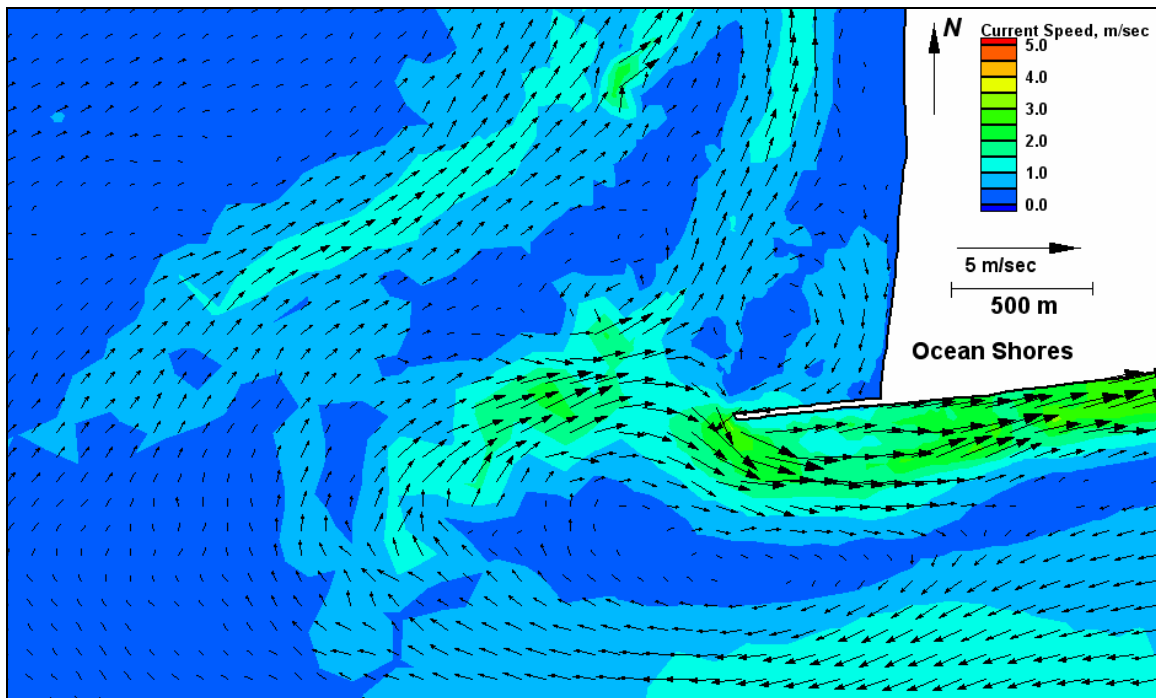
Figure E98. Run 127 (Alt 4A, west-southwest, neap tide), north jetty view of ebb tide

Figure E99. Run 128 (existing, west, spring tide), inlet view of flood tide

Figure E100. Run 128 (existing, west, spring tide), north jetty view of flood tide

Figure E101. Run 128 (existing, west, spring tide), inlet view of ebb tide

Figure E102. Run 128 (existing, west, spring tide), north jetty view of ebb tide

Figure E103. Run 129 (Alt 2A, west, spring tide), inlet view of flood tide

Figure E104. Run 129 (Alt 2A, west, spring tide), north jetty view of flood tide

Figure E105. Run 129 (Alt 2A, west, spring tide), inlet view of ebb tide
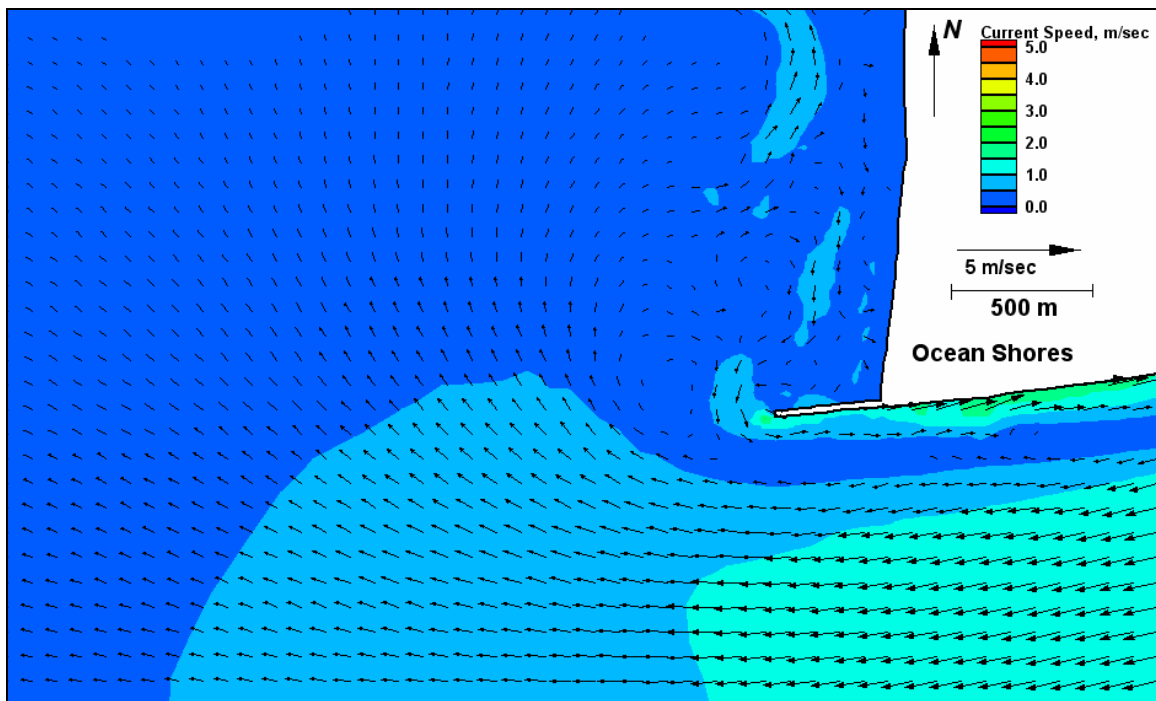
Figure E106. Run 129 (Alt 2A, west, spring tide), north jetty view of ebb tide
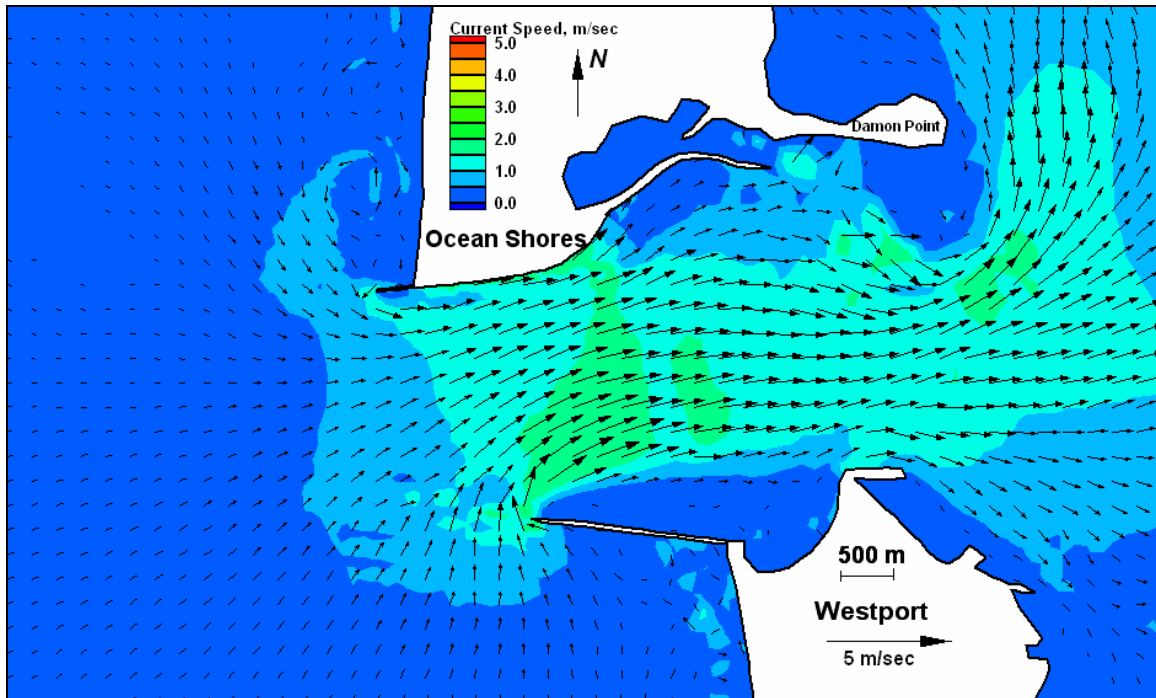
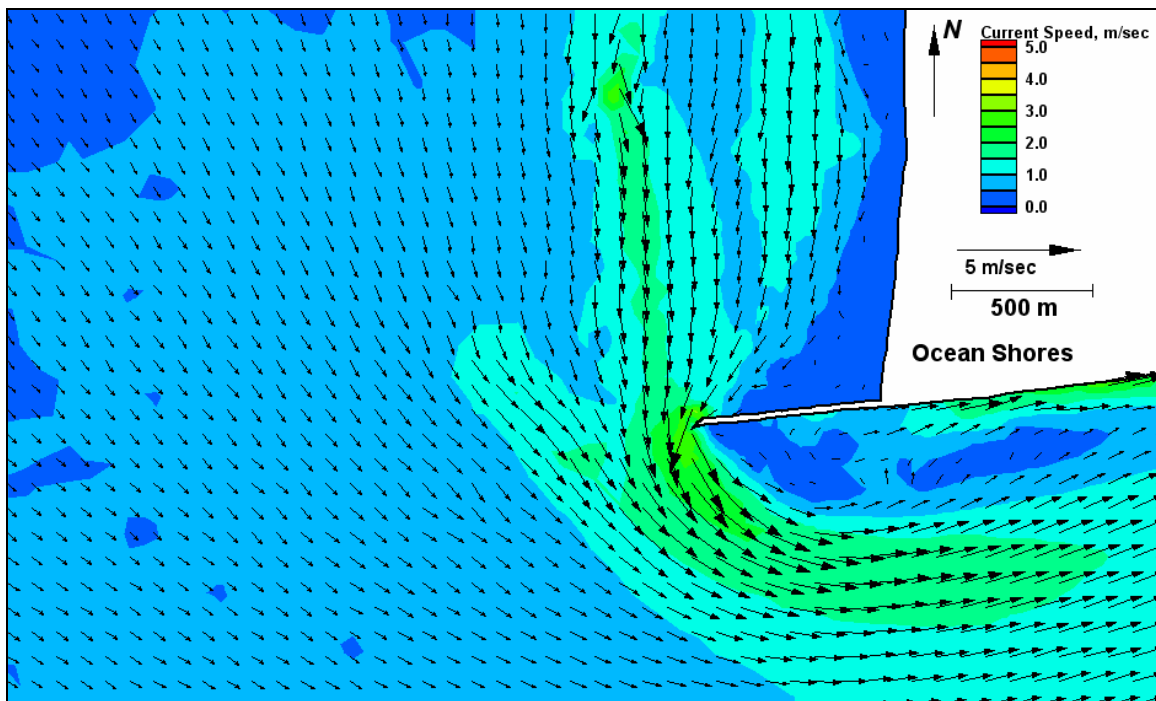Figure E107. Run 130 (Alt 2B, west, spring tide), inlet view of flood tide

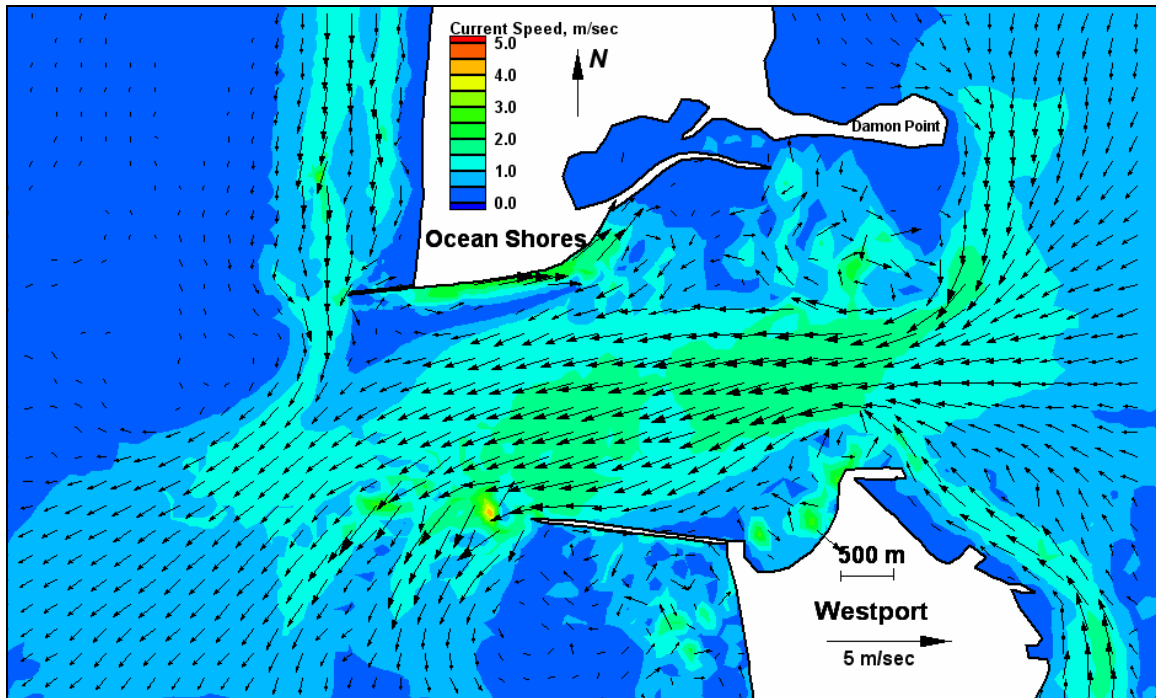Figure E108. Run 130 (Alt 2B, west, spring tide), north jetty view of flood tide
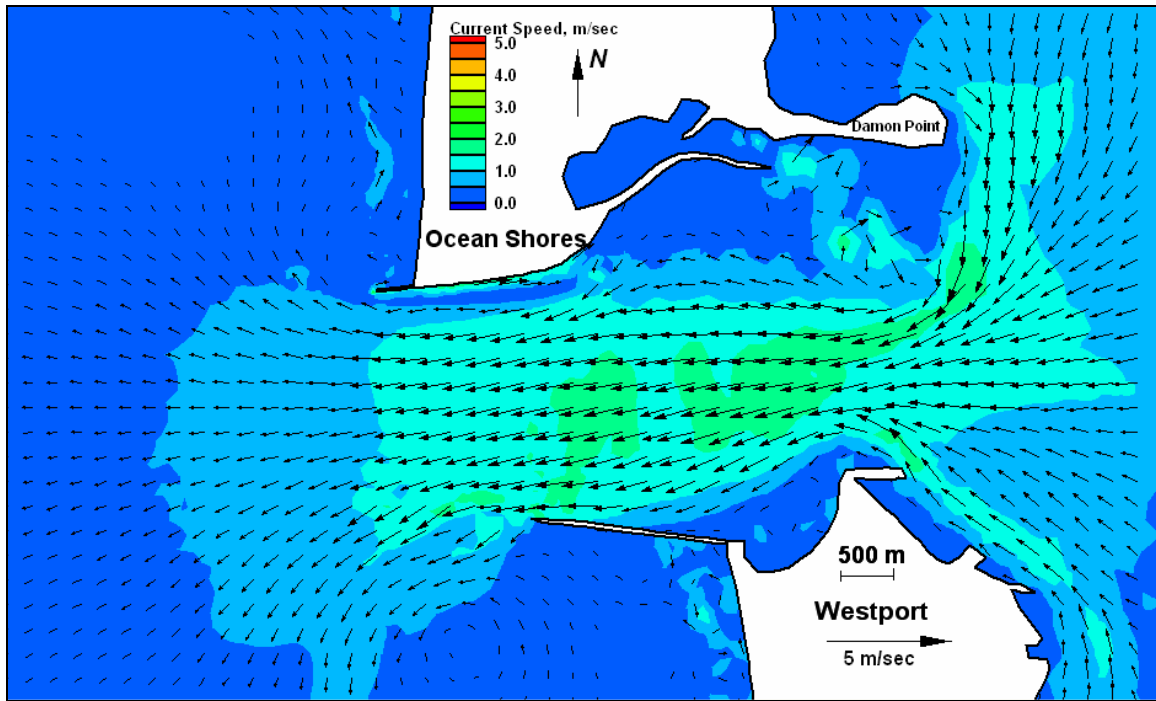
Figure E109. Run 130 (Alt 2B, west, spring tide), inlet view of ebb tide
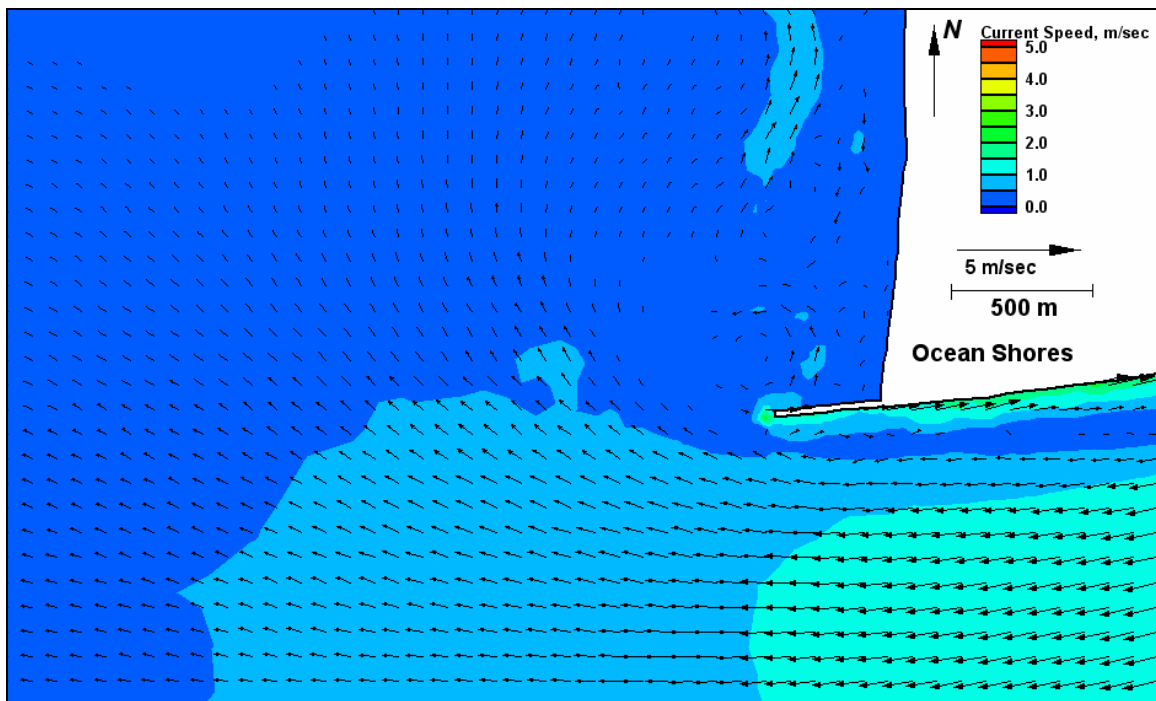
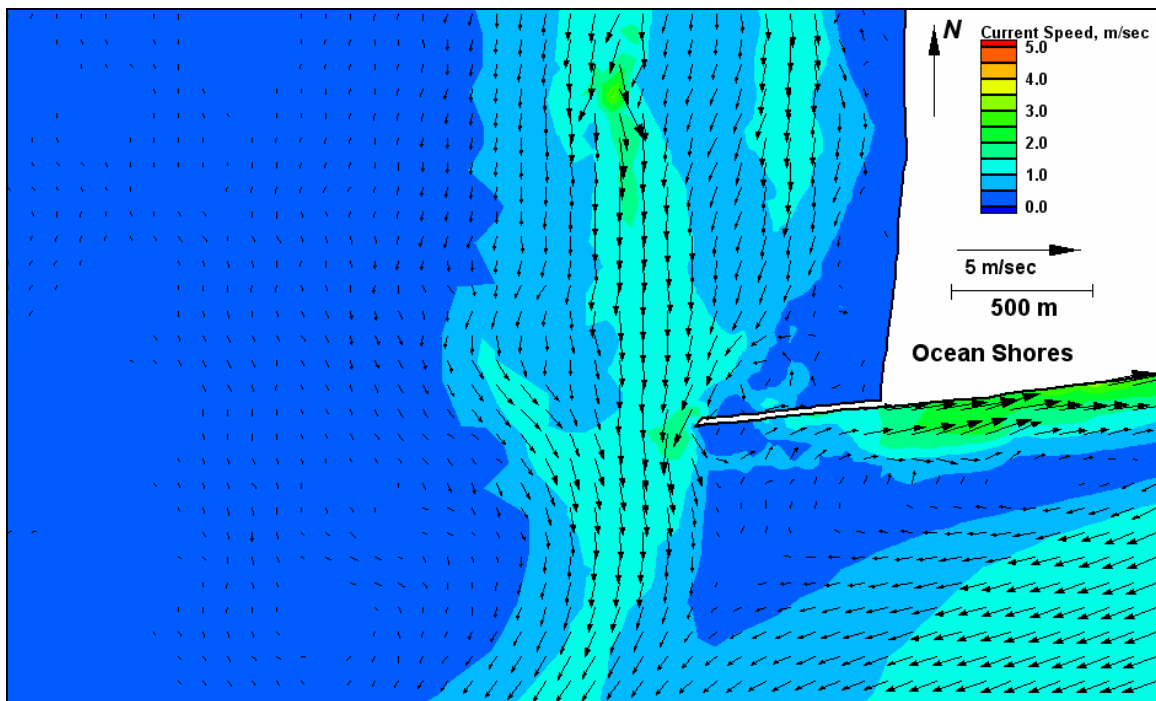Figure E110. Run 130 (Alt 2B, west, spring tide), north jetty view of ebb tide

Appendix E   Tidal Circulation Simulation Results
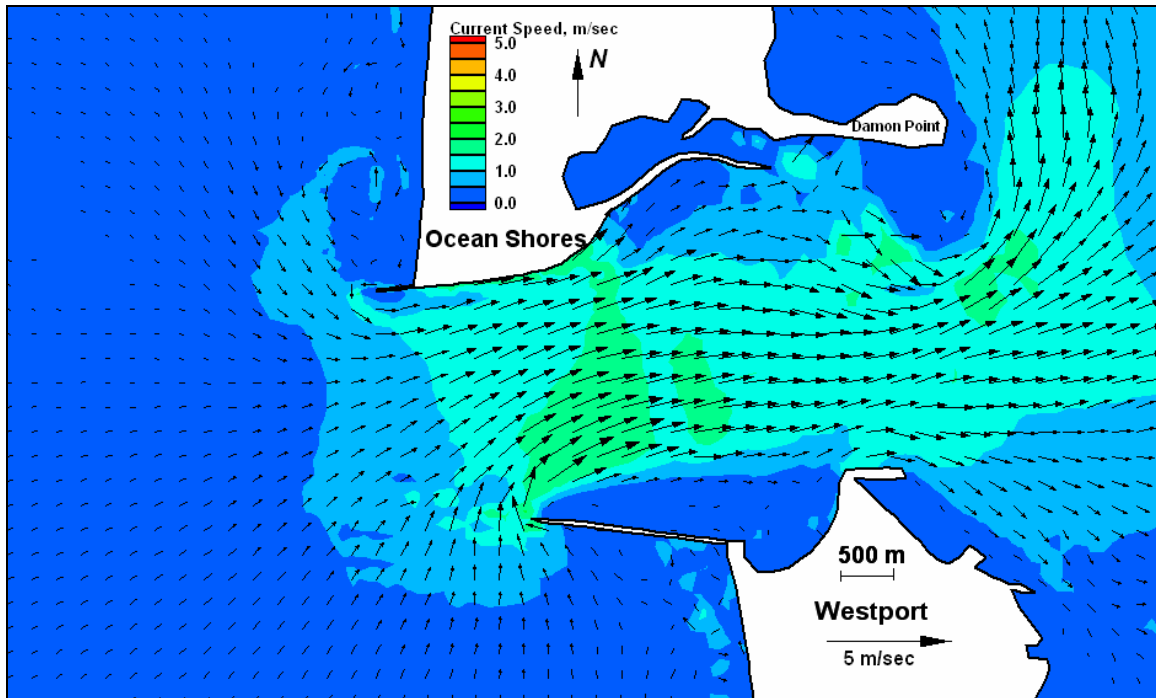
Figure E111. Run 131 (Alt 3A, west, spring tide), inlet view of flood tide
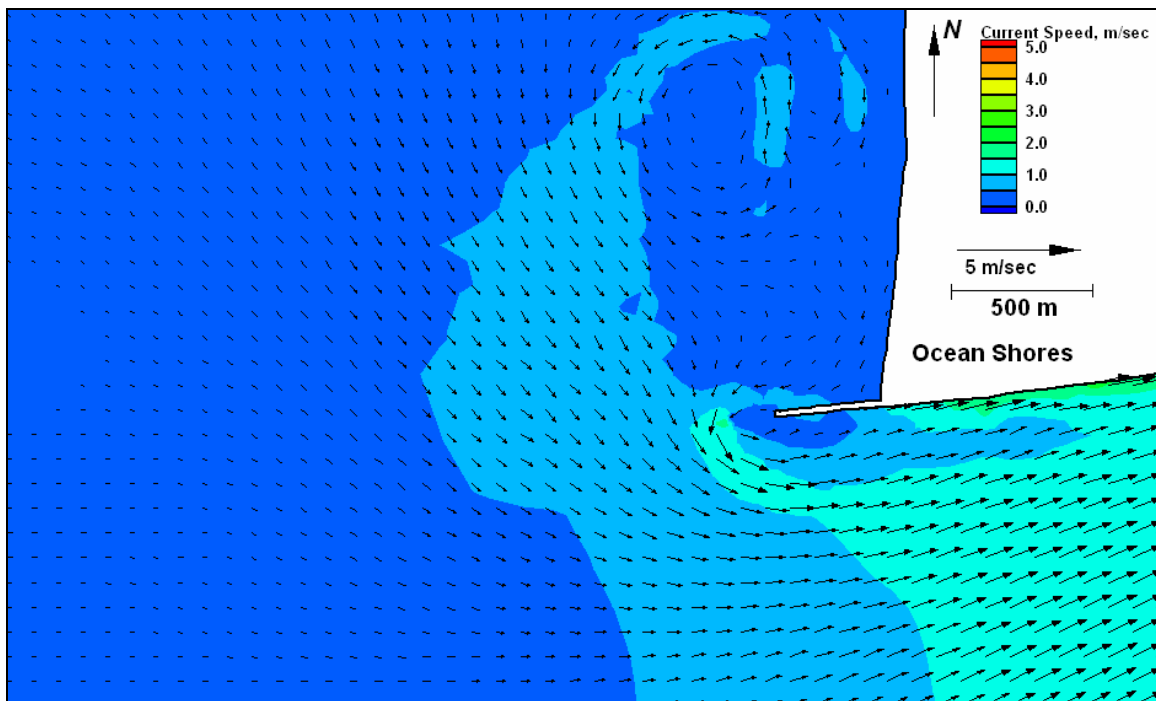
Figure E112. Run 131 (Alt 3A, west, spring tide), north jetty view of flood tide

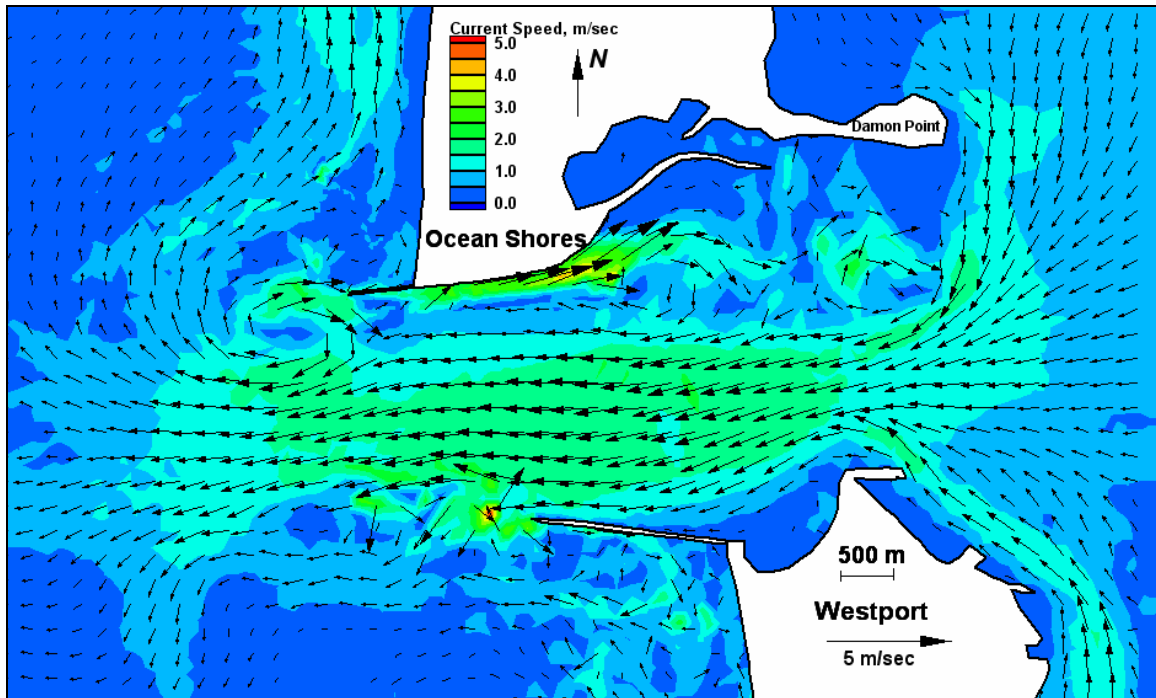Figure E113. Run 131 (Alt 3A, west, spring tide), inlet view of ebb tide

Figure E114. Run 131 (Alt 3A, west, spring tide), north jetty view of ebb tide

Appendix E   Tidal Circulation Simulation Results
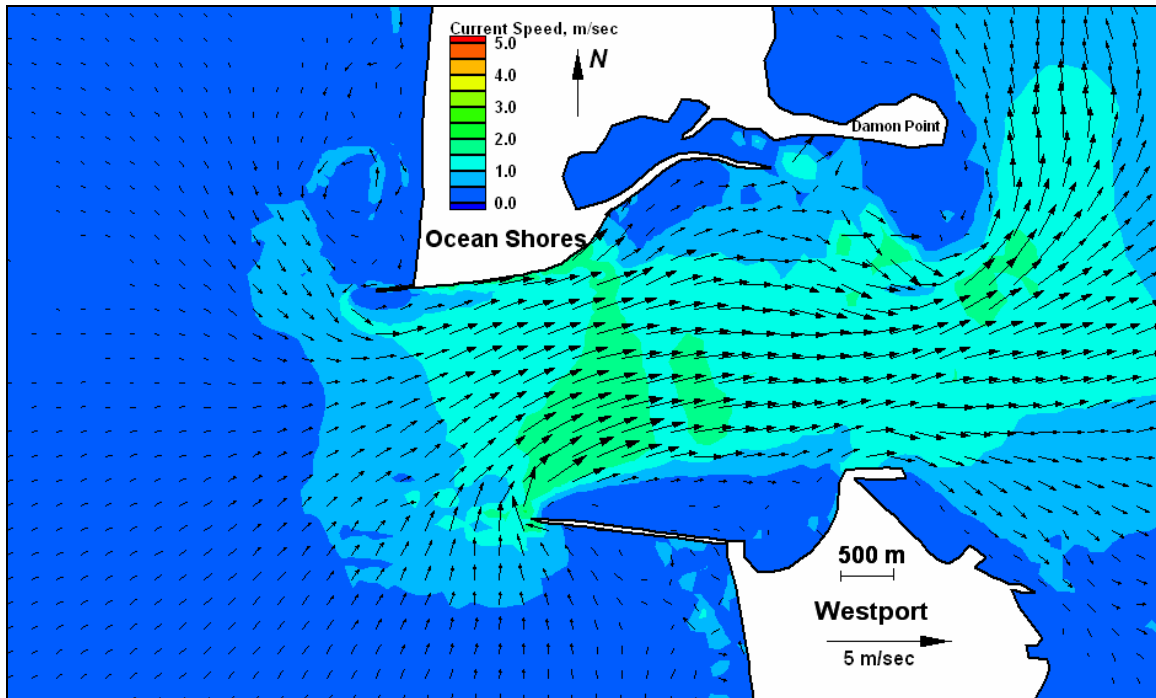
Figure E115. Run 132 (Alt 3B, west, spring tide), inlet view of flood tide
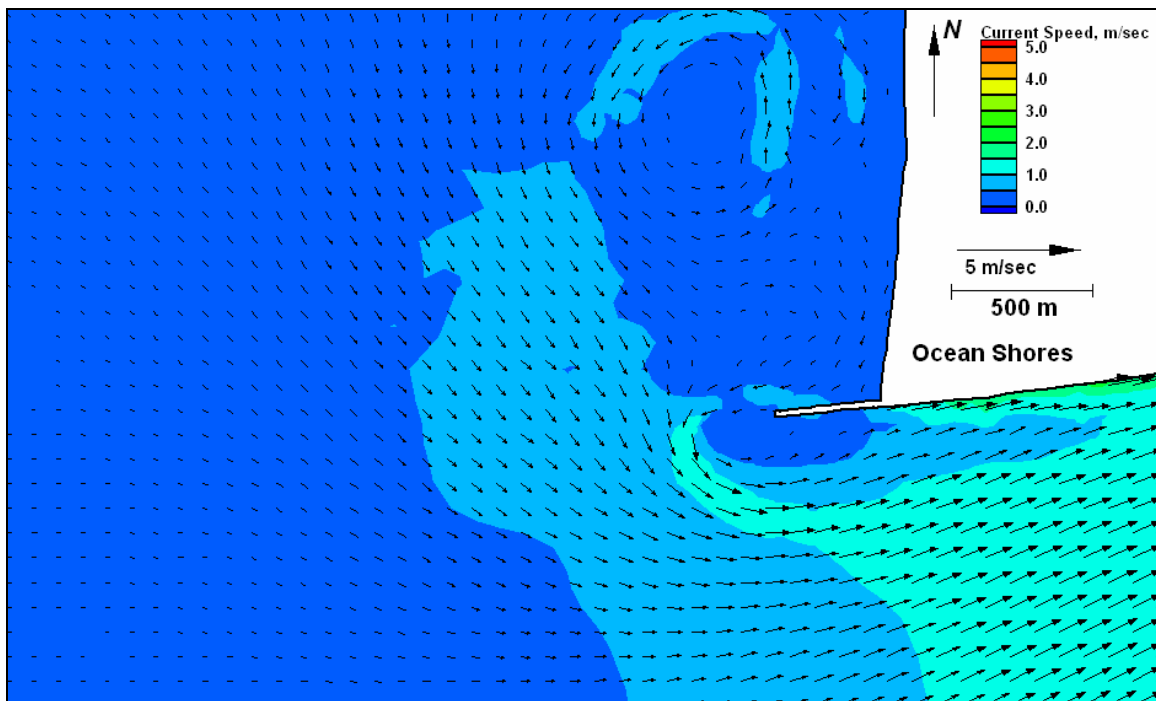
Figure E116. Run 132 (Alt 3B, west, spring tide), north jetty view of flood tide
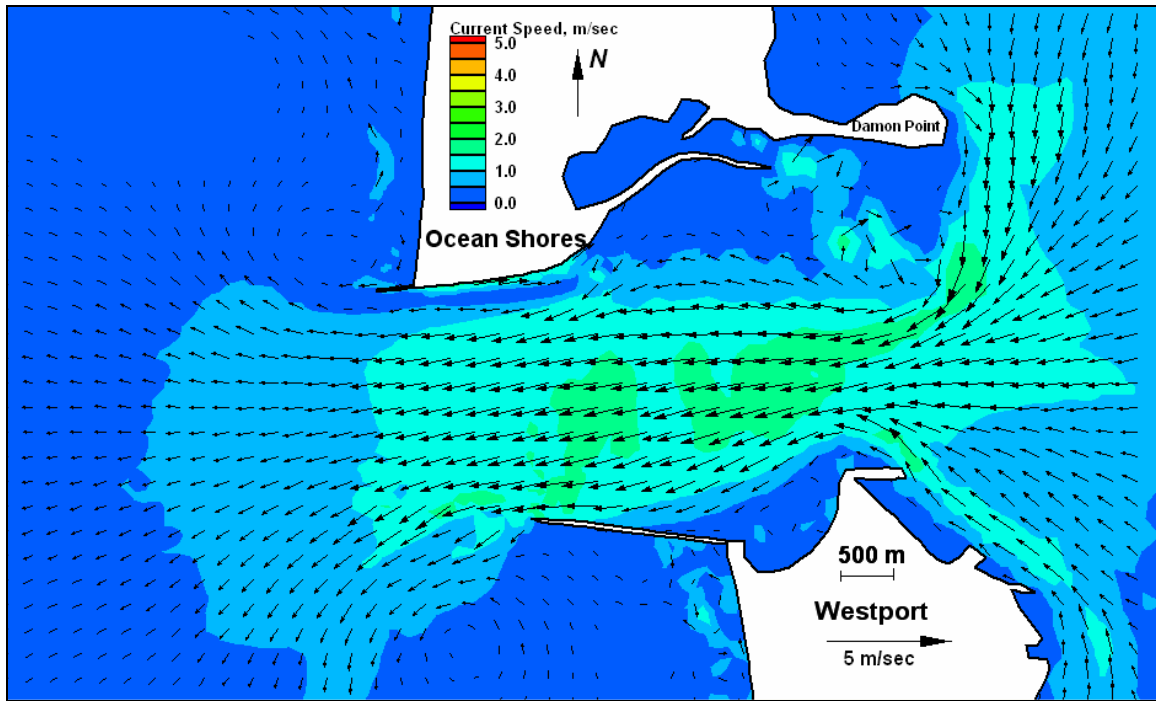
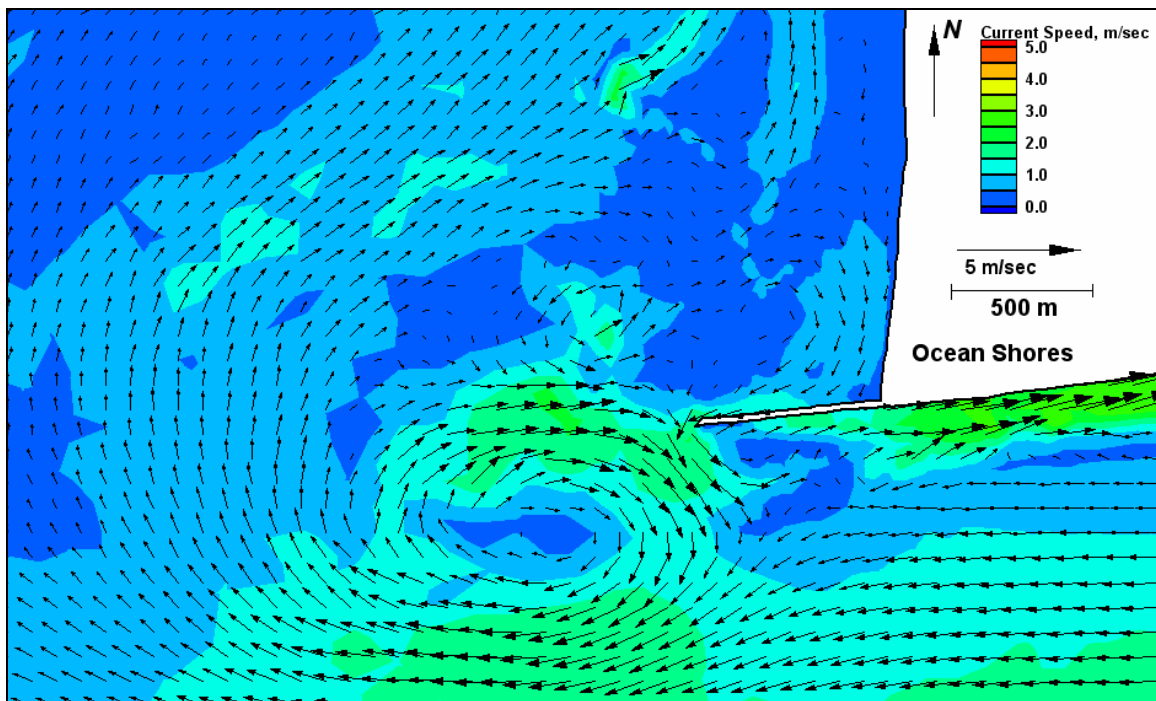Figure E117. Run 132 (Alt 3B, west, spring tide), inlet view of ebb tide
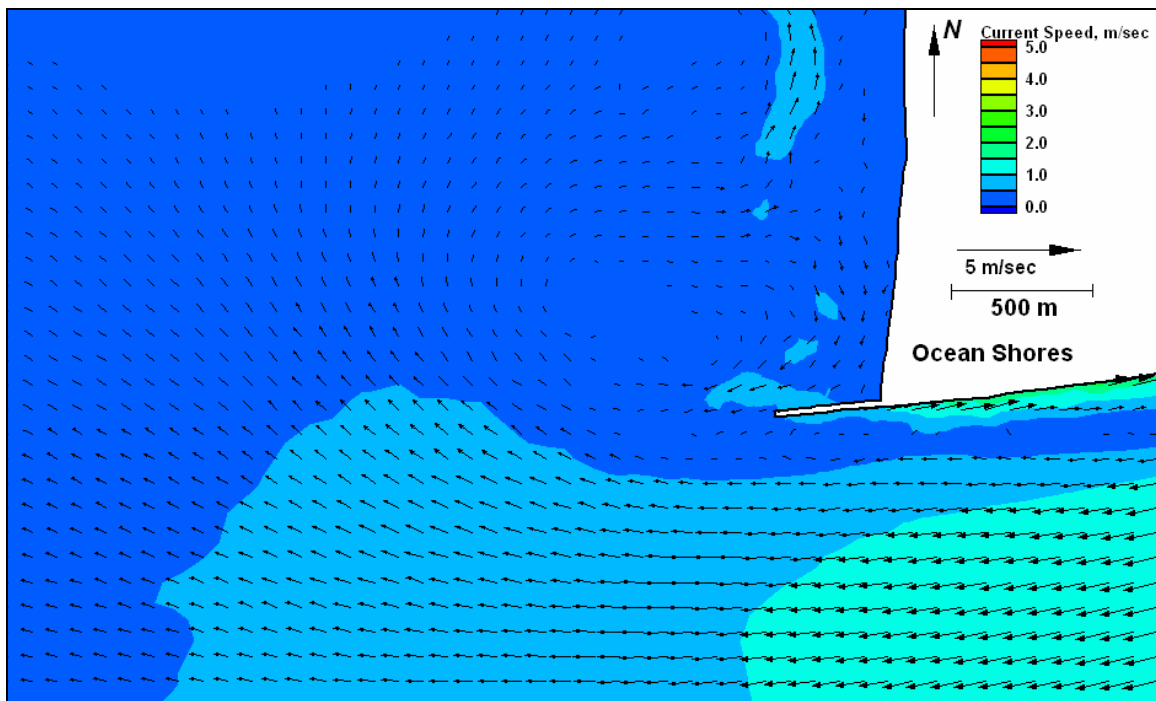
Figure E118. Run 132 (Alt 3B, west, spring tide), north jetty view of ebb tide
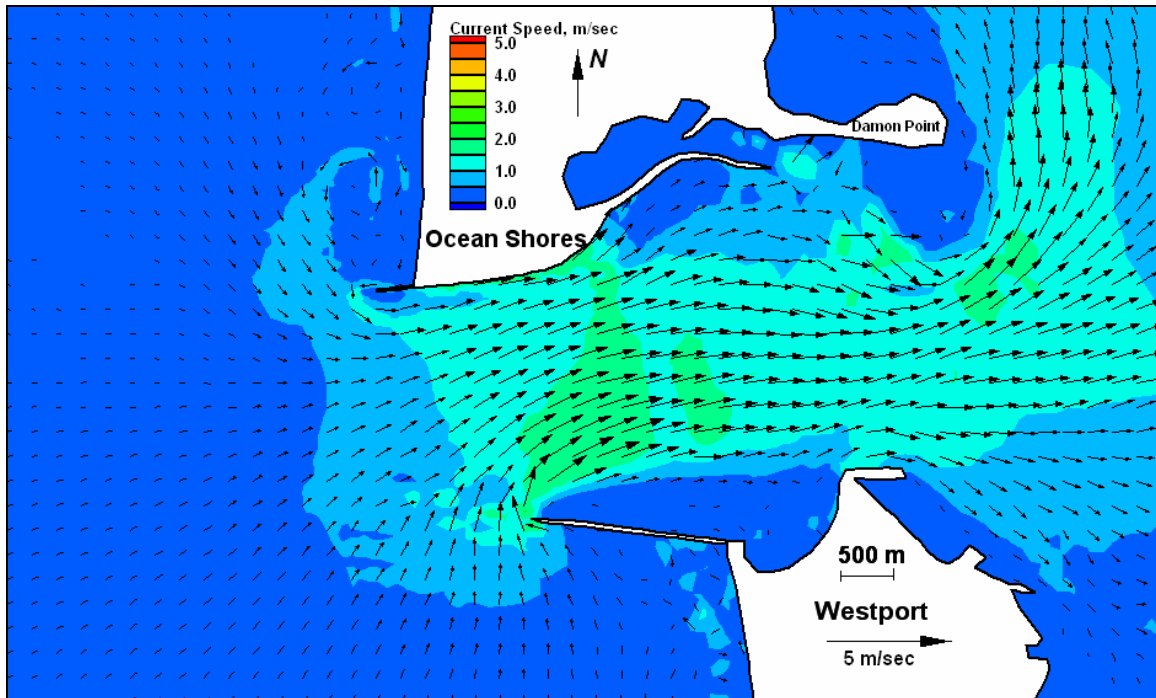
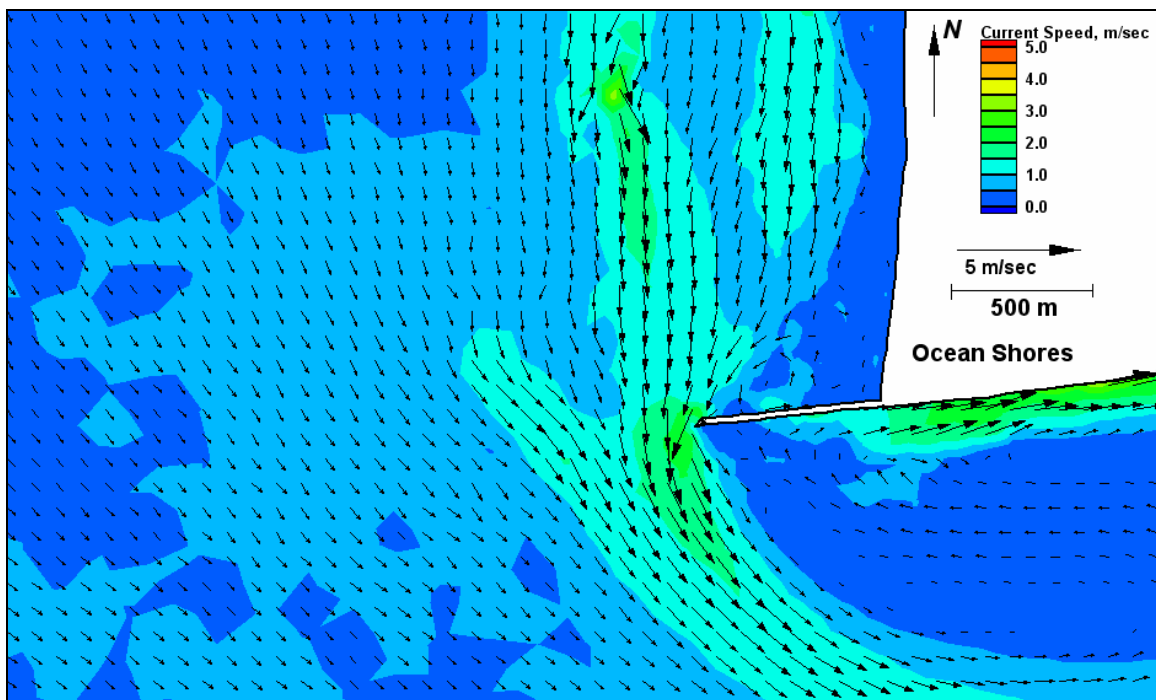Figure E119. Run 133 (Alt 4A, west, spring tide), inlet view of flood tide

Figure E120. Run 133 (Alt 4A, west, spring tide), north jetty view of flood tide
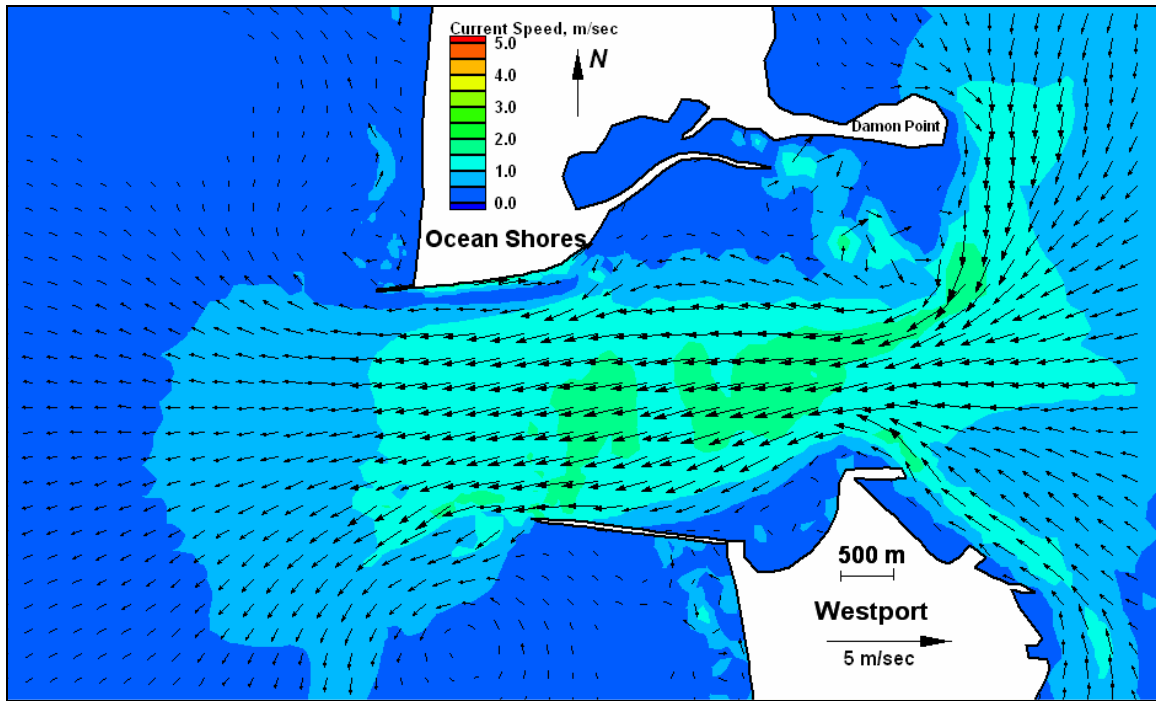
Figure E121. Run 133 (Alt 4A, west, spring tide), inlet view of ebb tide
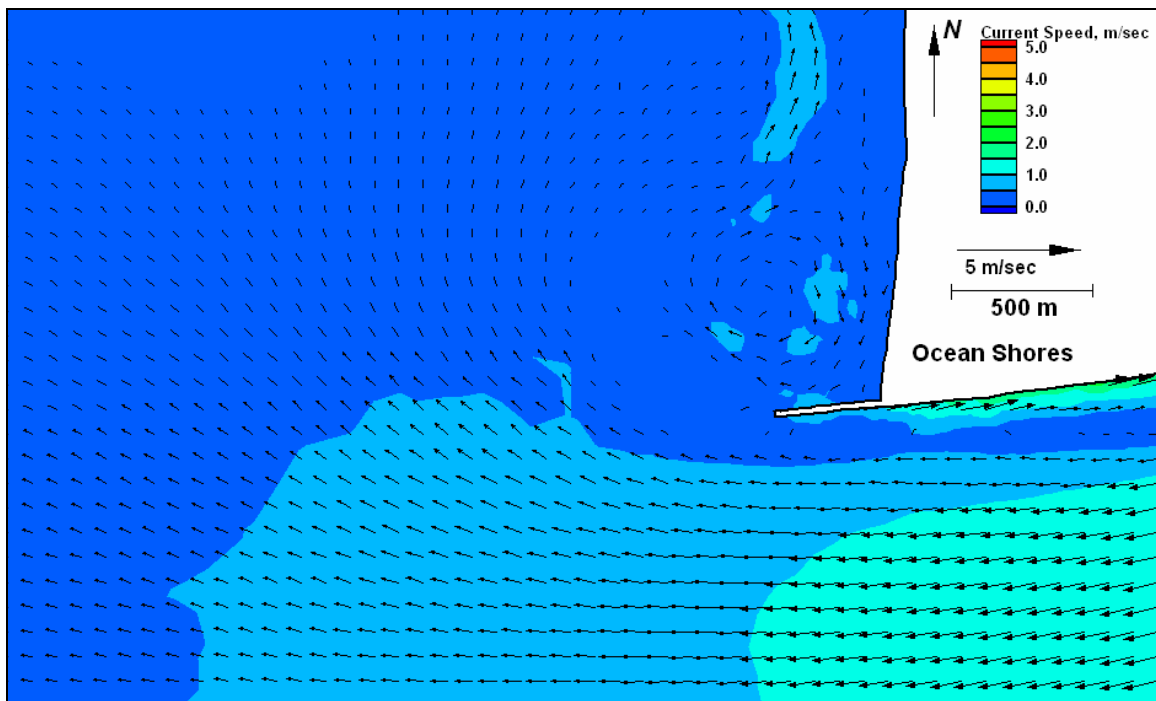
Figure E122. Run 133 (Alt 4A, west, spring tide), north jetty view of ebb tide

Appendix E   Tidal Circulation Simulation Results
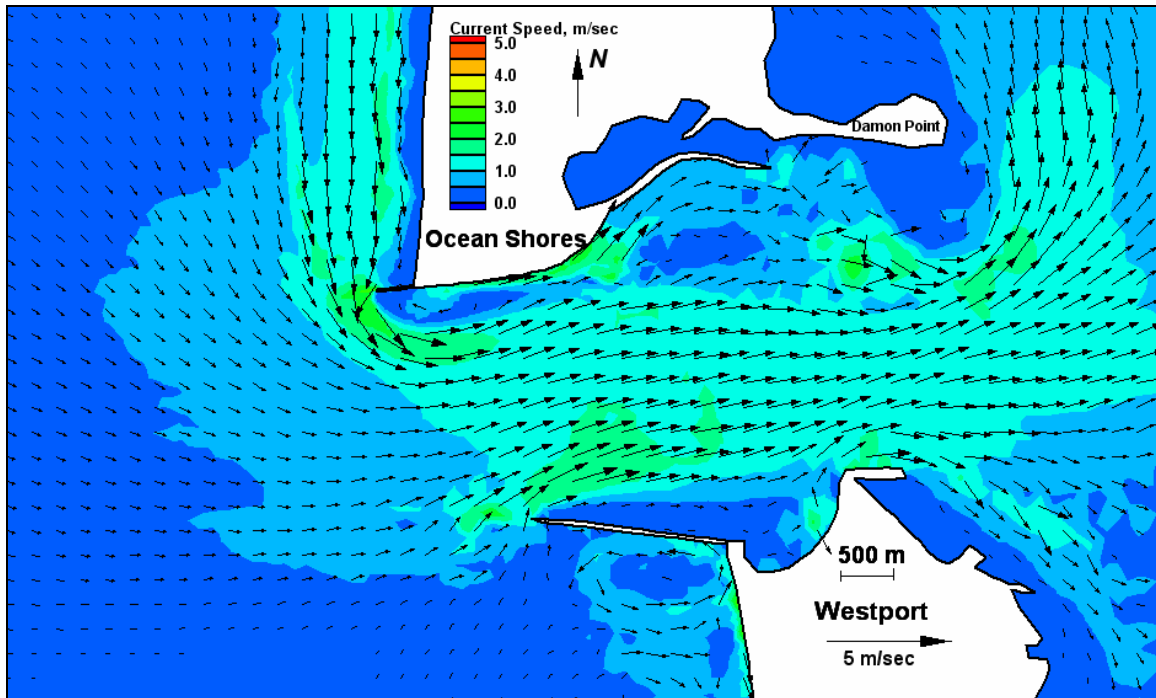
Figure E123. Run 134 (existing, west-northwest, spring tide), inlet view of flood tide

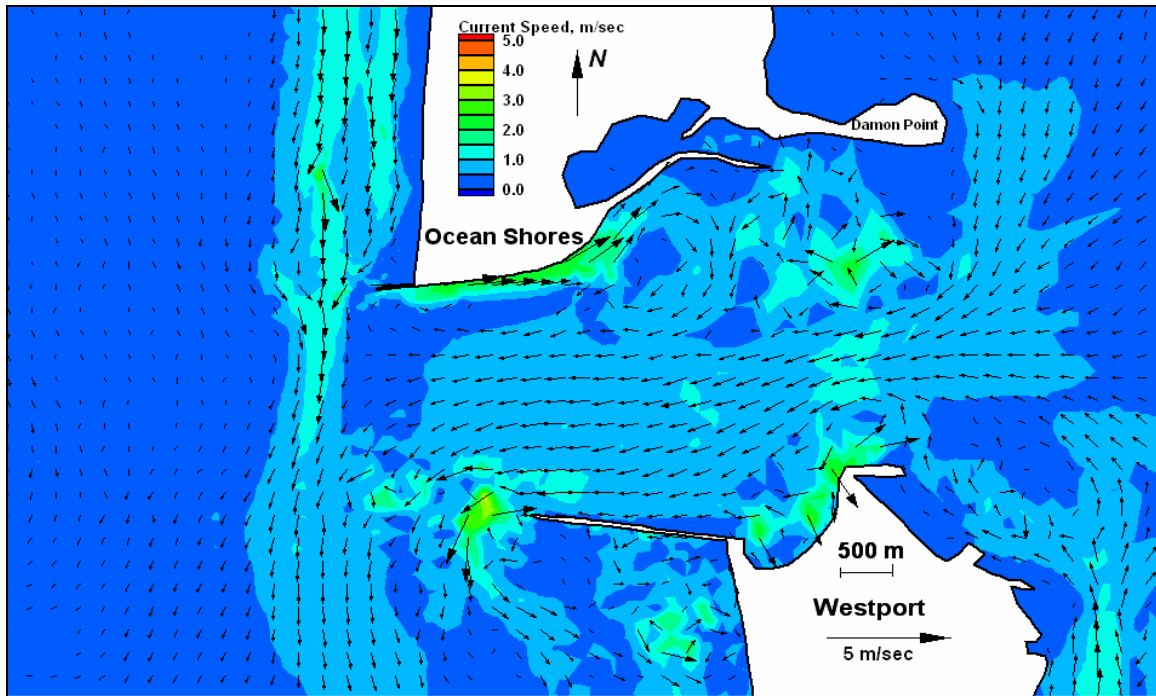Figure E124. Run 134 (existing, west-northwest, spring tide), north jetty view of flood tide

Figure E125. Run 134 (existing, west-northwest, spring tide), inlet view of ebb tide

Figure E126. Run 134 (existing, west-northwest, spring tide), north jetty view of ebb tide

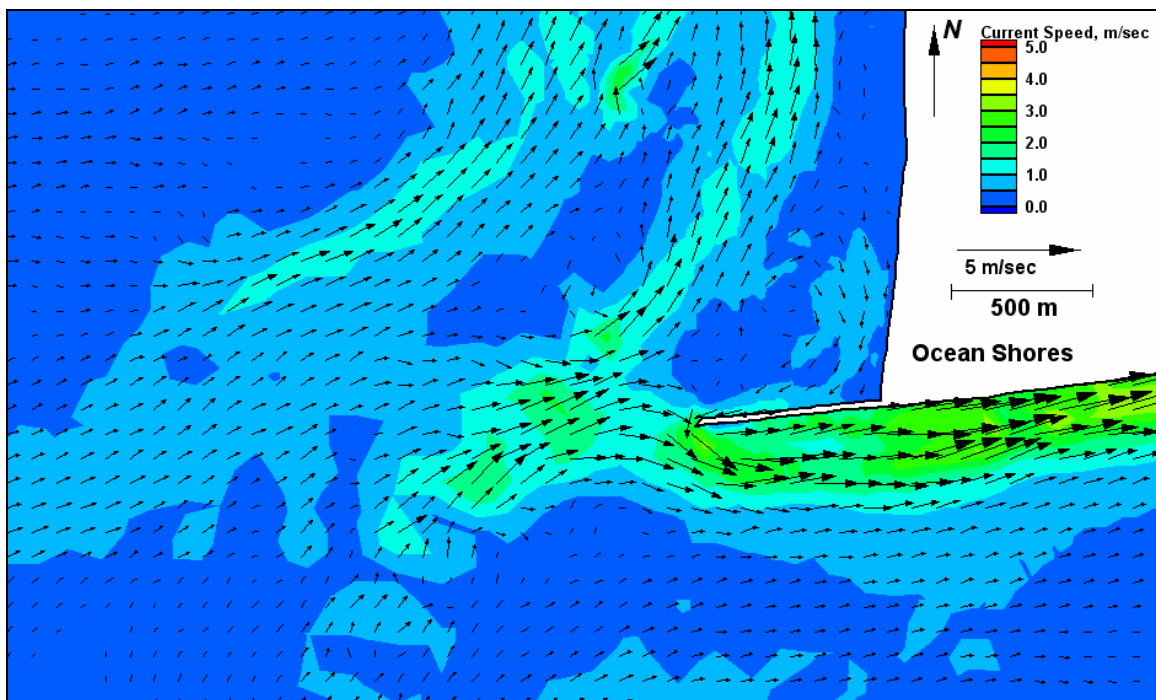Figure E127. Run 135 (Alt 2A, west-northwest, spring tide), inlet view of flood tide

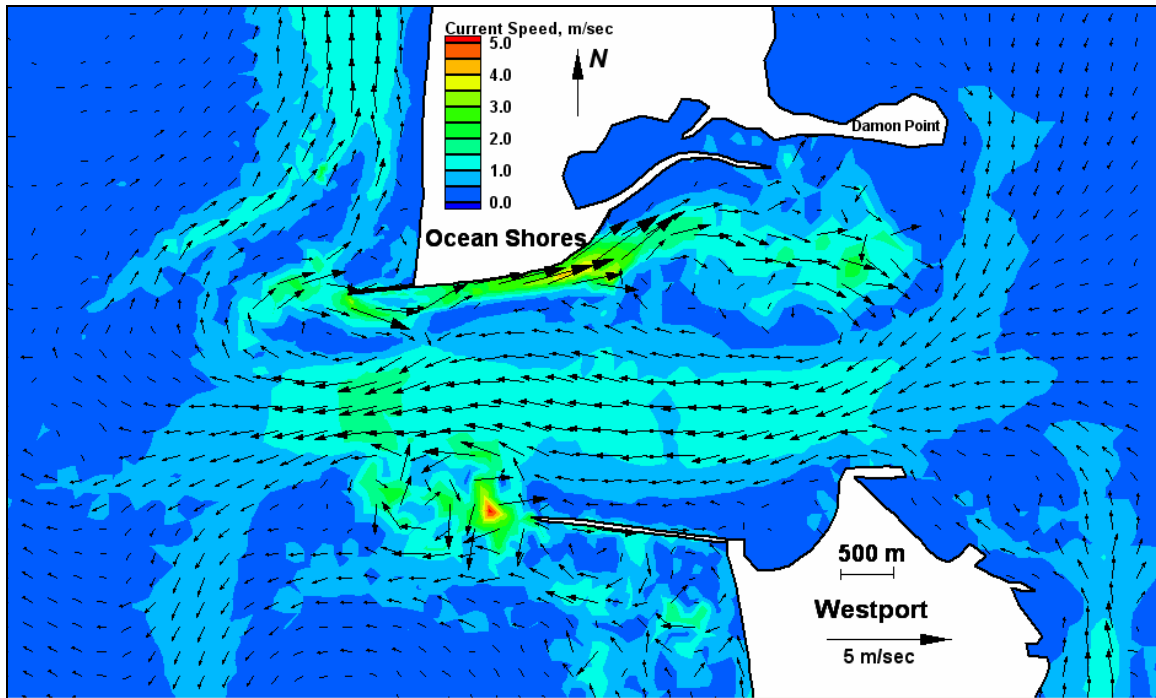Figure E128. Run 135 (Alt 2A, west-northwest, spring tide), north jetty view of flood tide

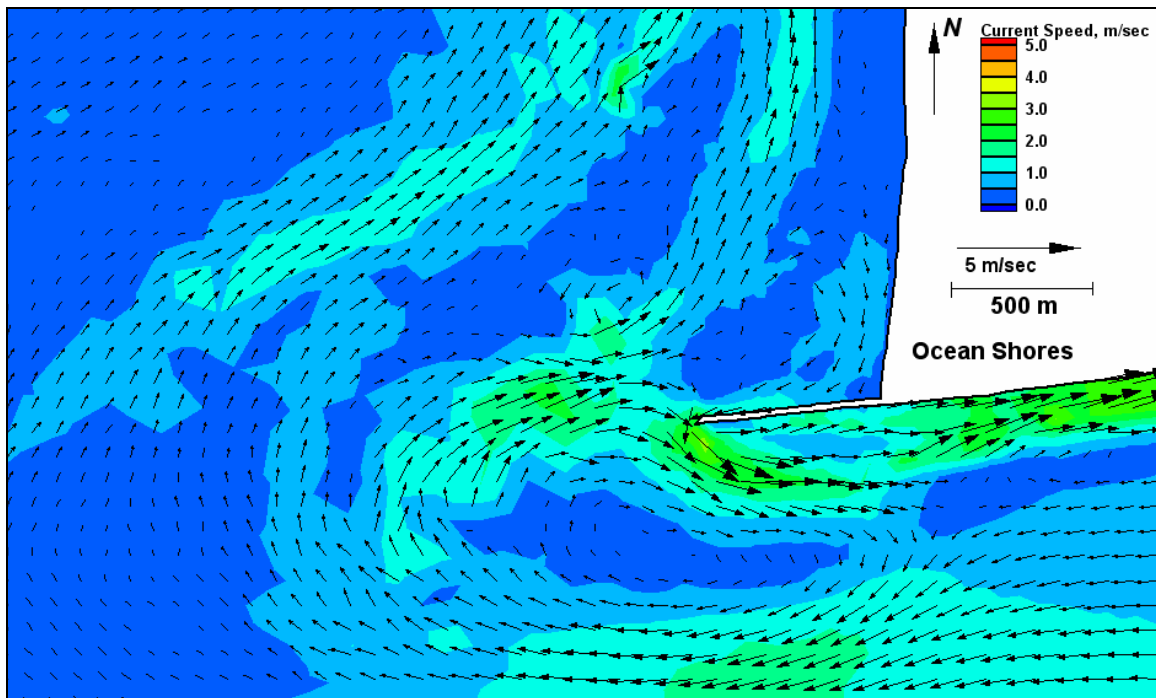Figure E129. Run 135 (Alt 2A, west-northwest, spring tide), inlet view of ebb tide

Figure E130. Run 135 (Alt 2A, west-northwest, spring tide), north jetty view of ebb tide

Appendix E   Tidal Circulation Simulation Results

Figure E131. Run 136 (Alt 2B, west-northwest, spring tide), inlet view of flood tide
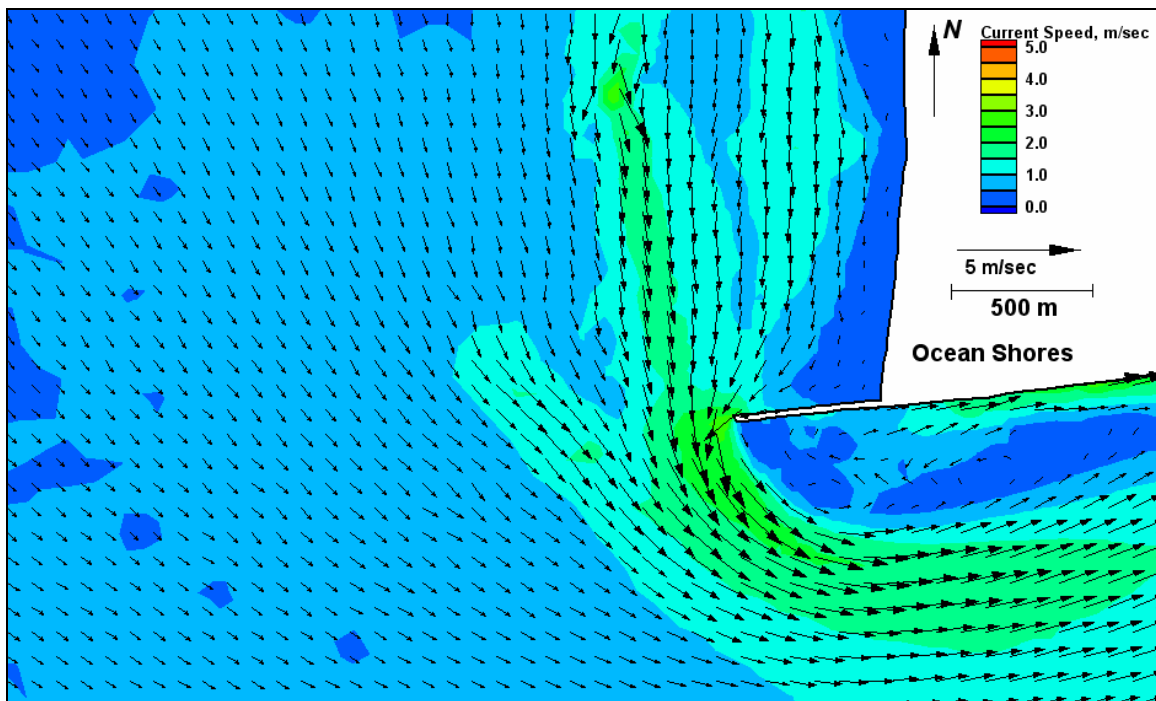

Figure E132. Run 136 (Alt 2B, west-northwest, spring tide), north jetty view of flood tide

Figure E133. Run 136 (Alt 2B, west-northwest, spring tide), inlet view of ebb tide

Figure E134. Run 136 (Alt 2B, west-northwest, spring tide), north jetty view of ebb tide

E68

Figure E135. Run 137 (Alt 3A, west-northwest, spring tide), inlet view of flood tide

Figure E136. Run 137 (Alt 3A, west-northwest, spring tide), north jetty view of flood tide
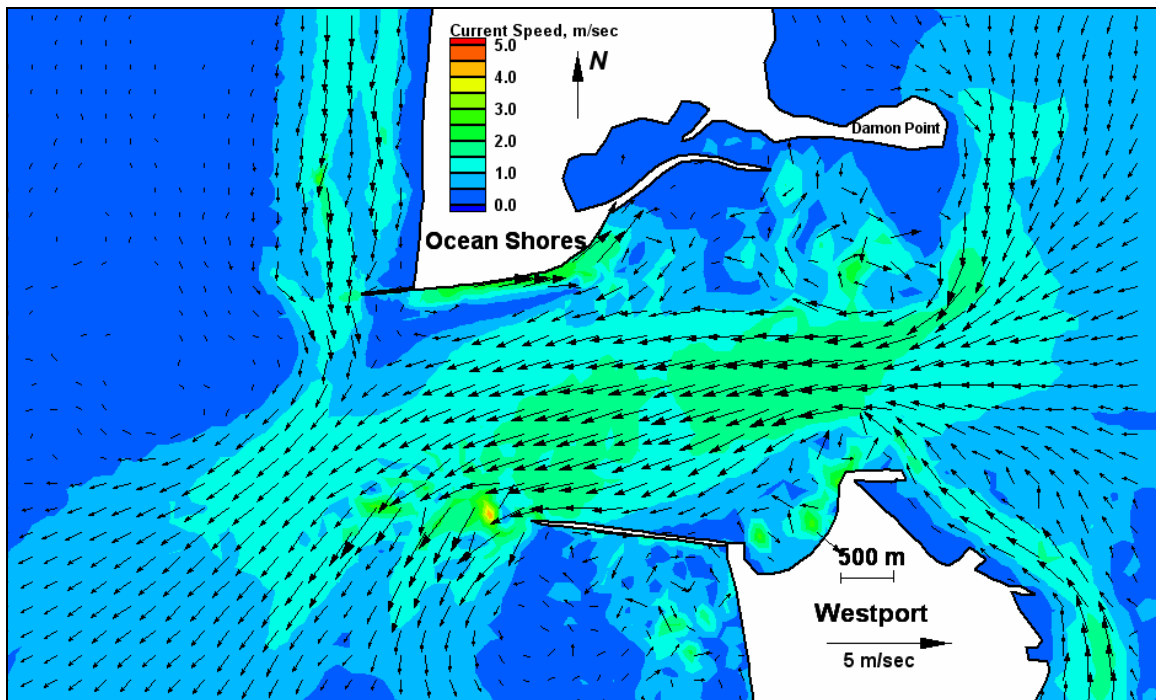
Figure E137. Run 137 (Alt 3A, west-northwest, spring tide), inlet view of ebb tide
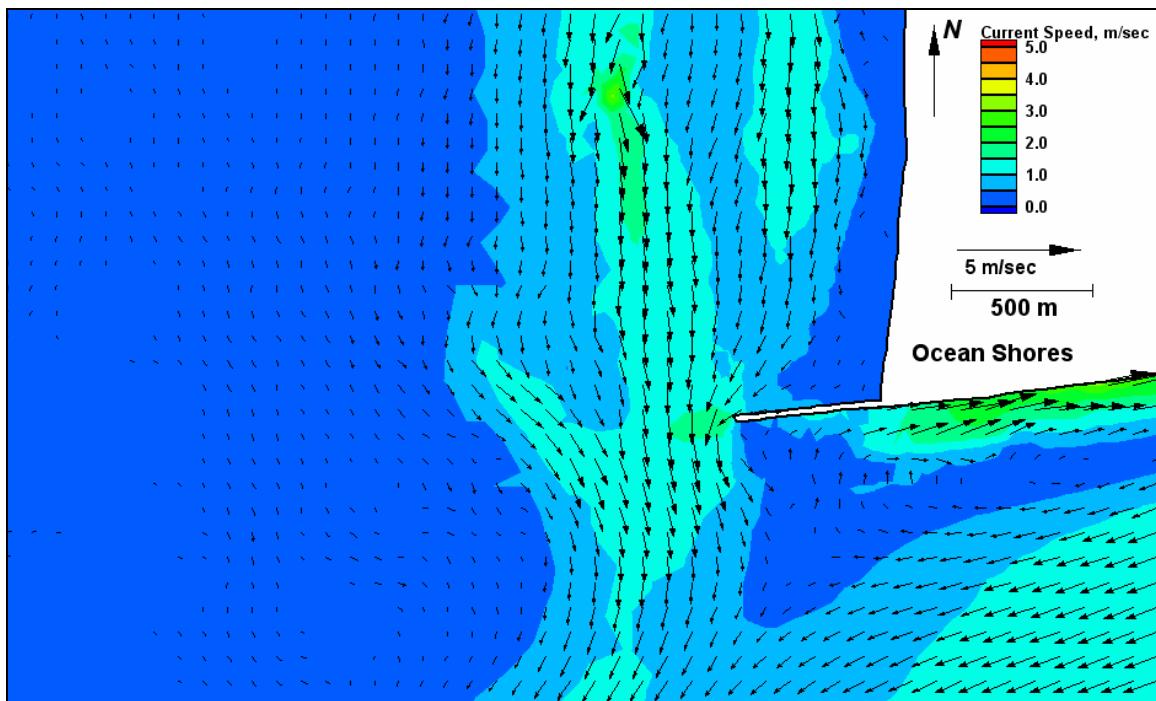

Figure E138. Run 137 (Alt 3A, west-northwest, spring tide), north jetty view of ebb tide
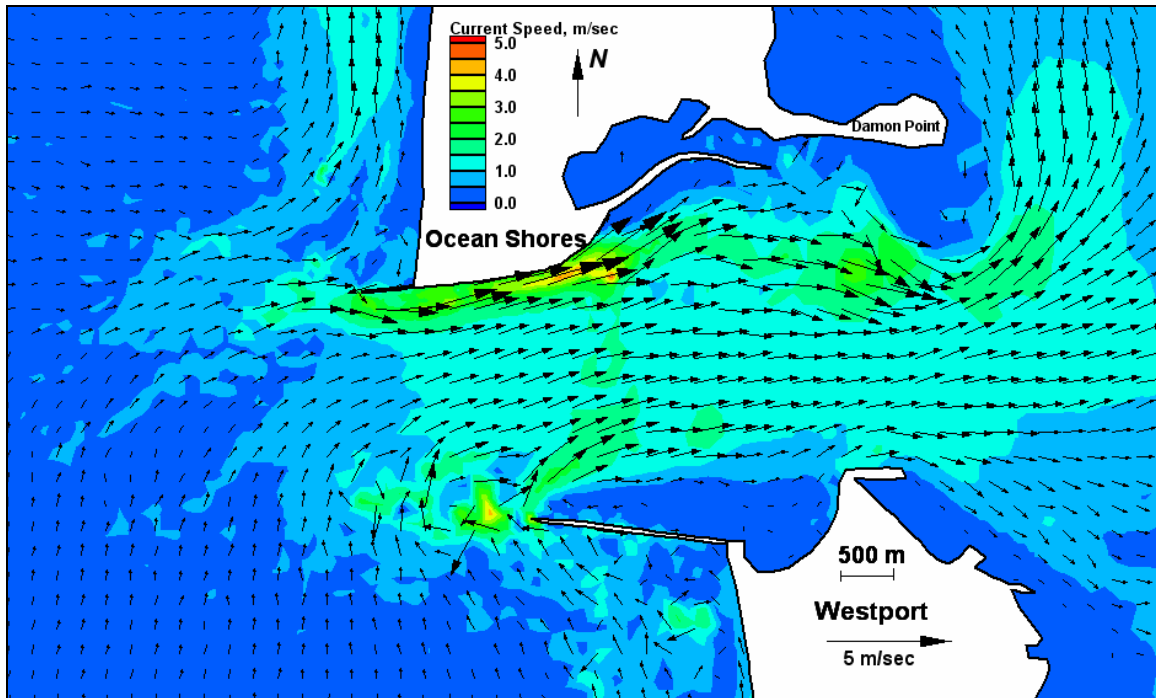
Figure E139. Run 138 (Alt 3B, west-northwest, spring tide), inlet view of flood tide

Figure E140. Run 138 (Alt 3B, west-northwest, spring tide), north jetty view of flood tide

Figure E141. Run 138 (Alt 3B, west-northwest, spring tide), inlet view of ebb tide
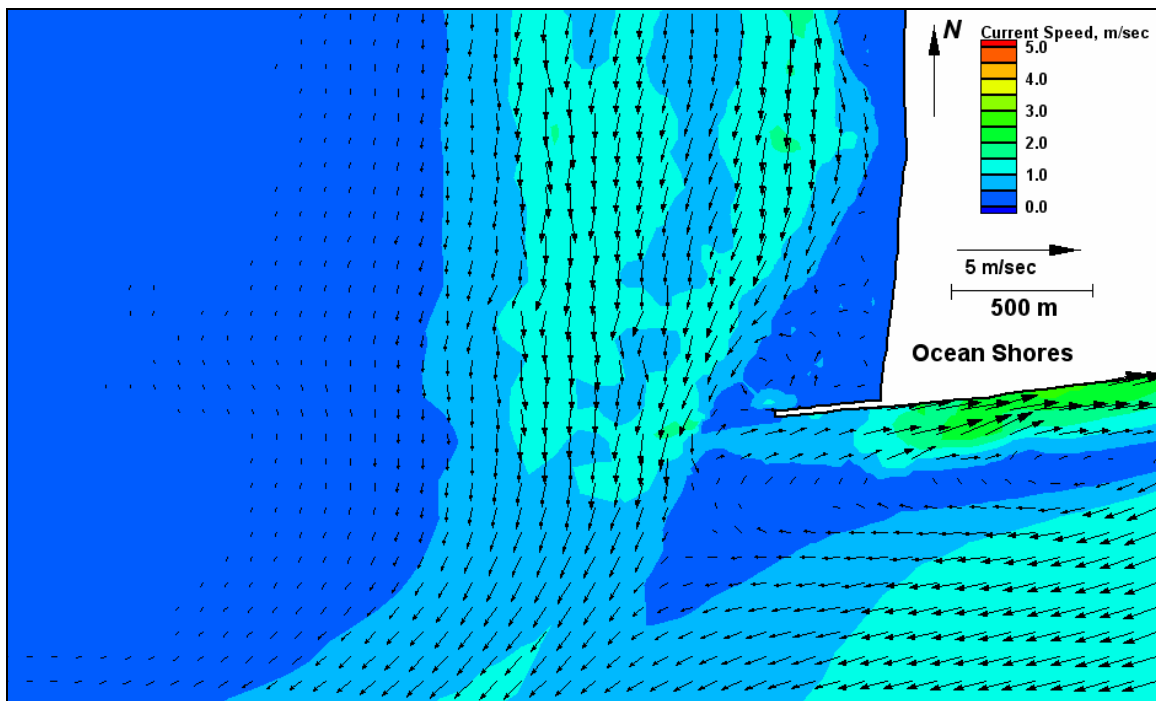
Figure E142. Run 138 (Alt 3B, west-northwest, spring tide), north jetty view of ebb tide

E72

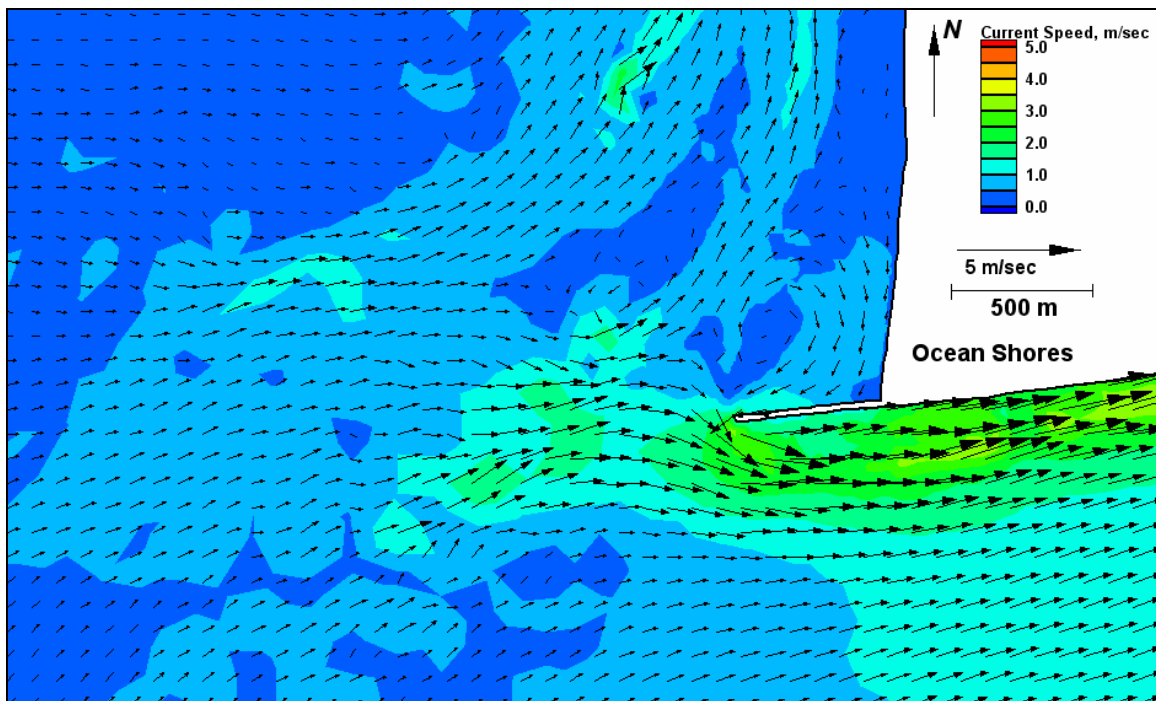Figure E143. Run 139 (Alt 4A, west-northwest, spring tide), inlet view of flood tide

Figure E144. Run 139 (Alt 4A, west-northwest, spring tide), north jetty view of flood tide
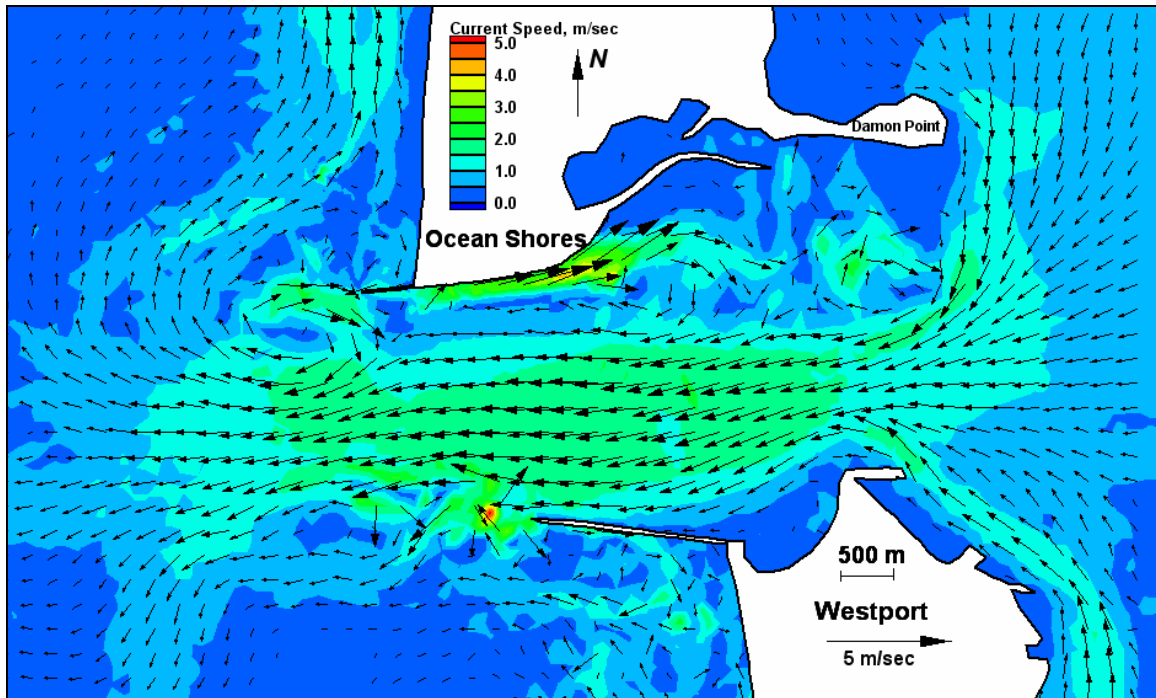
Figure E145. Run 139 (Alt 4A, west-northwest, spring tide), inlet view of ebb tide
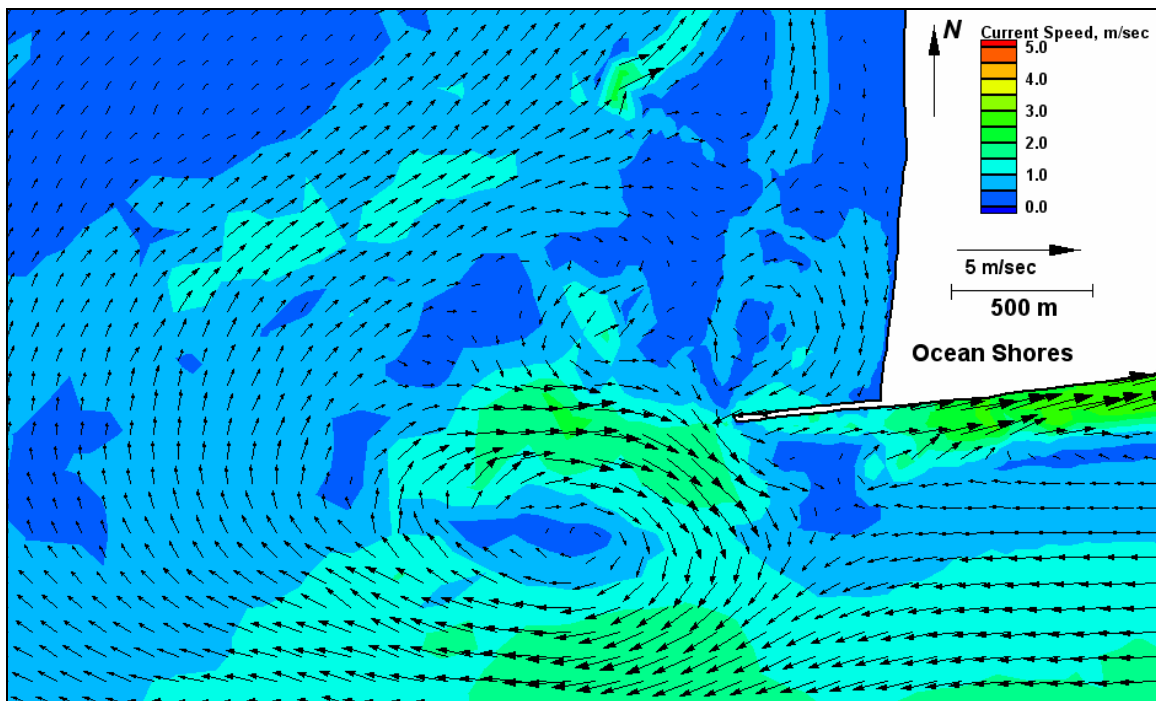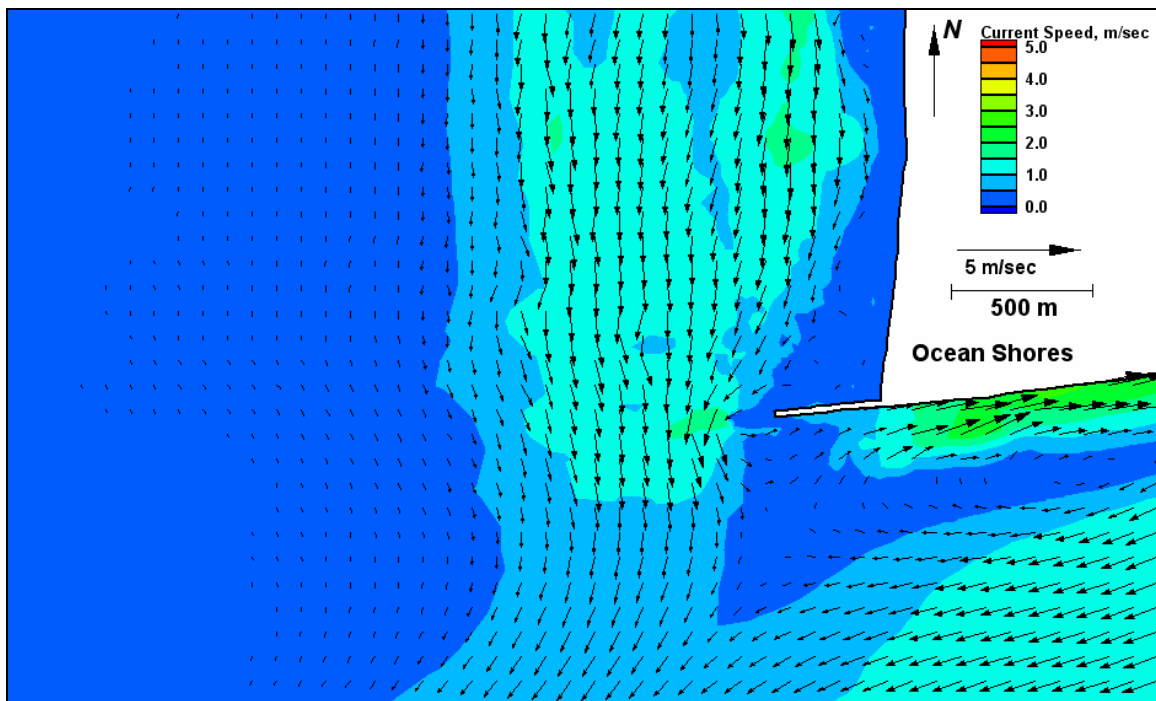

Figure E146. Run 139 (Alt 4A, west-northwest, spring tide), north jetty view of ebb tide
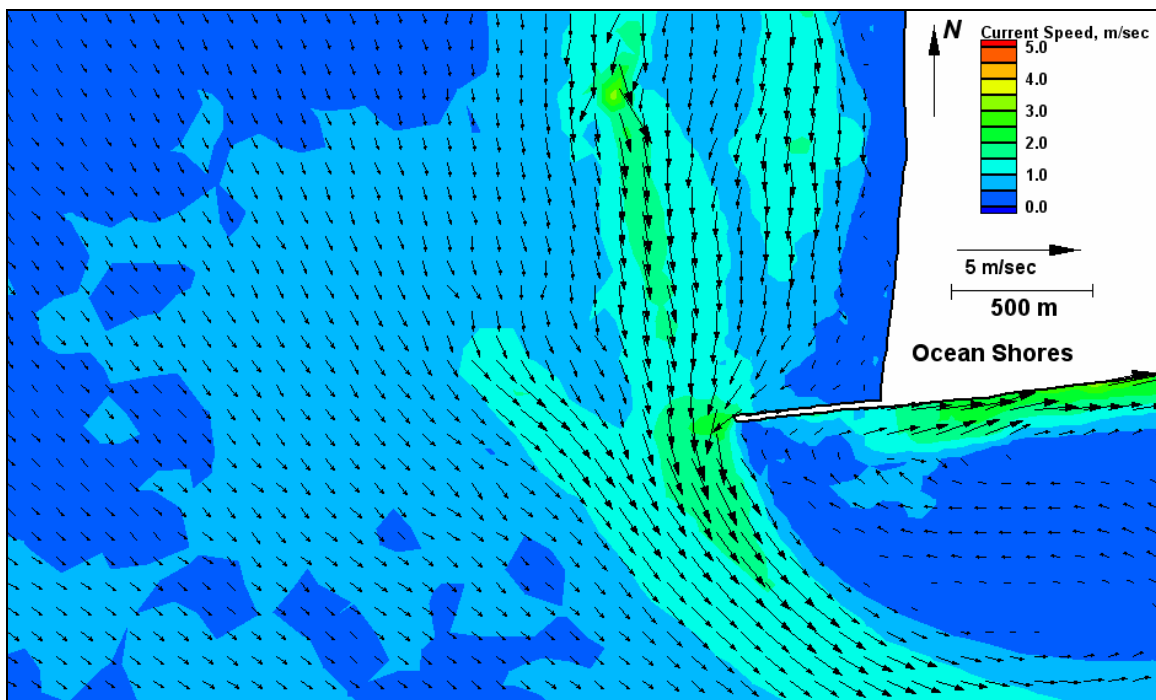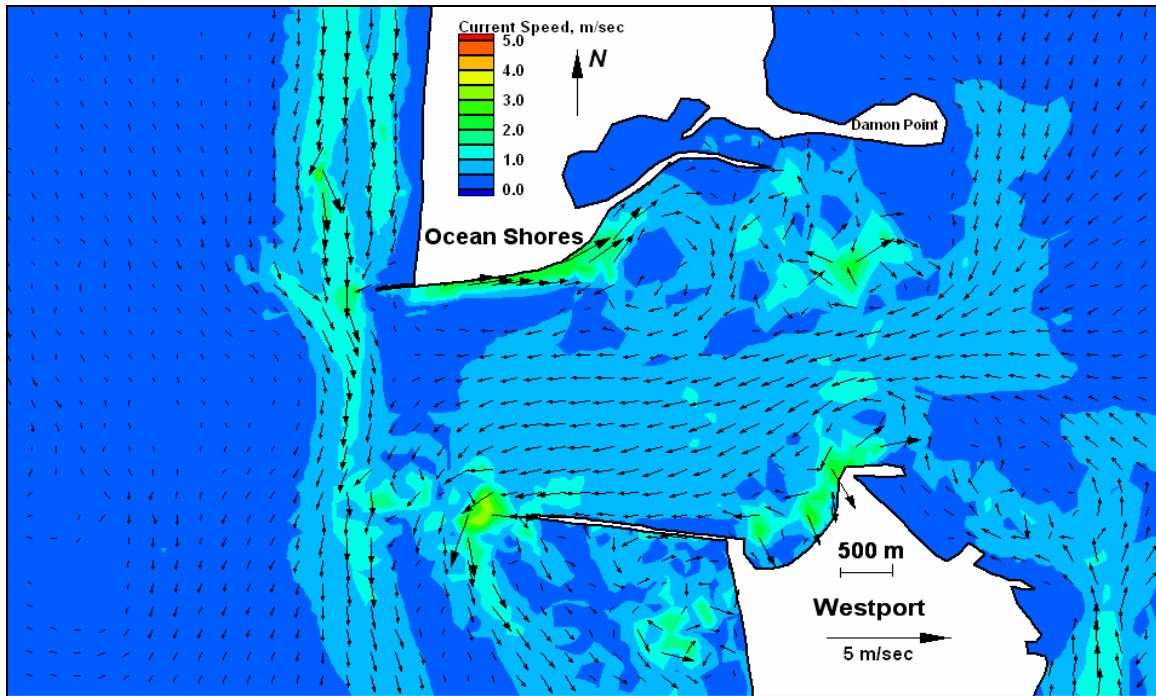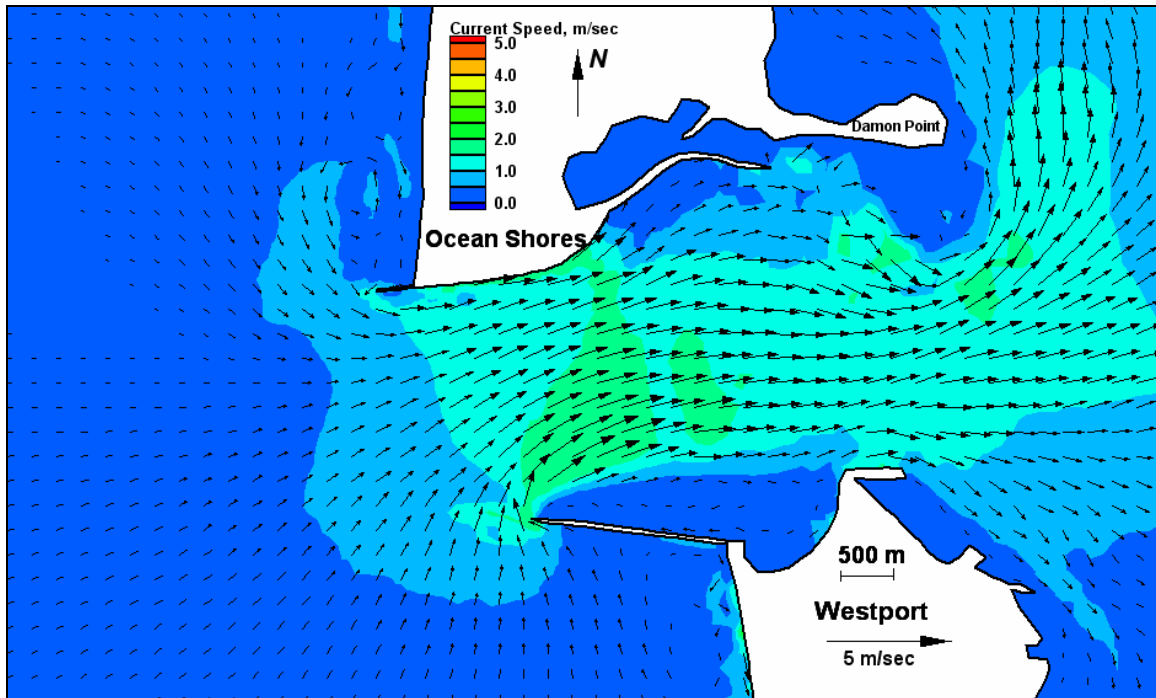
Figure E147. Run 140 (existing, west, spring tide), inlet view of flood tide
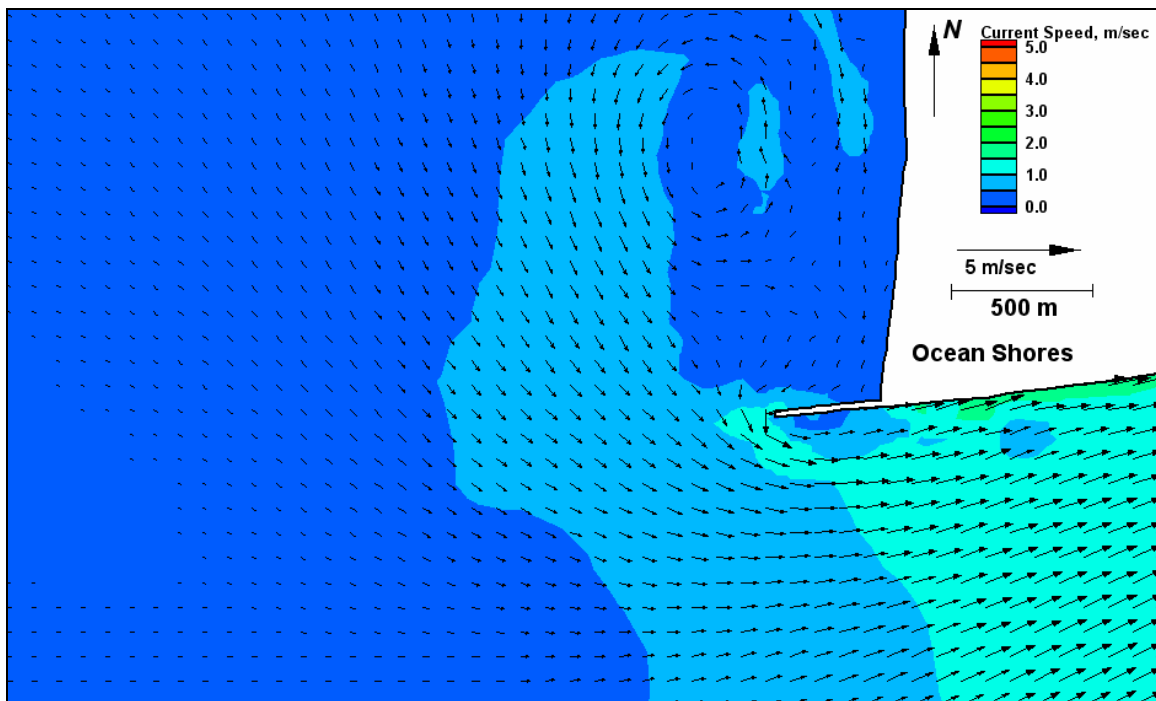
Figure E148. Run 140 (existing, west, spring tide), north jetty view of flood tide
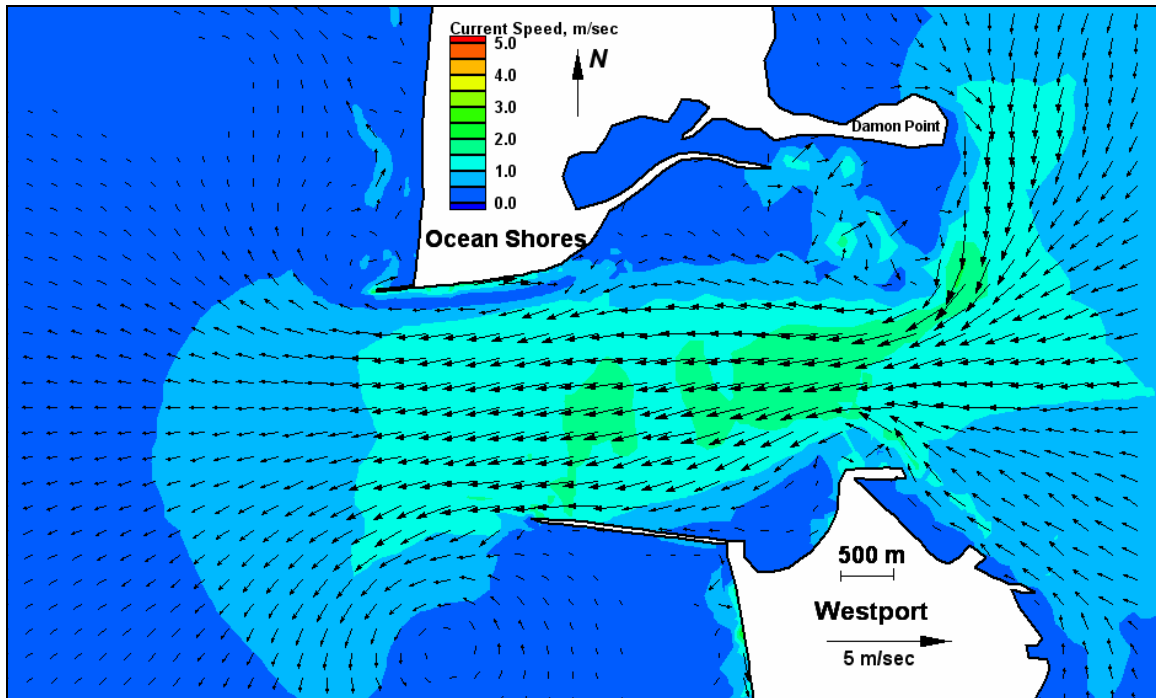
Figure E149. Run 140 (existing, west, spring tide), inlet view of ebb tide
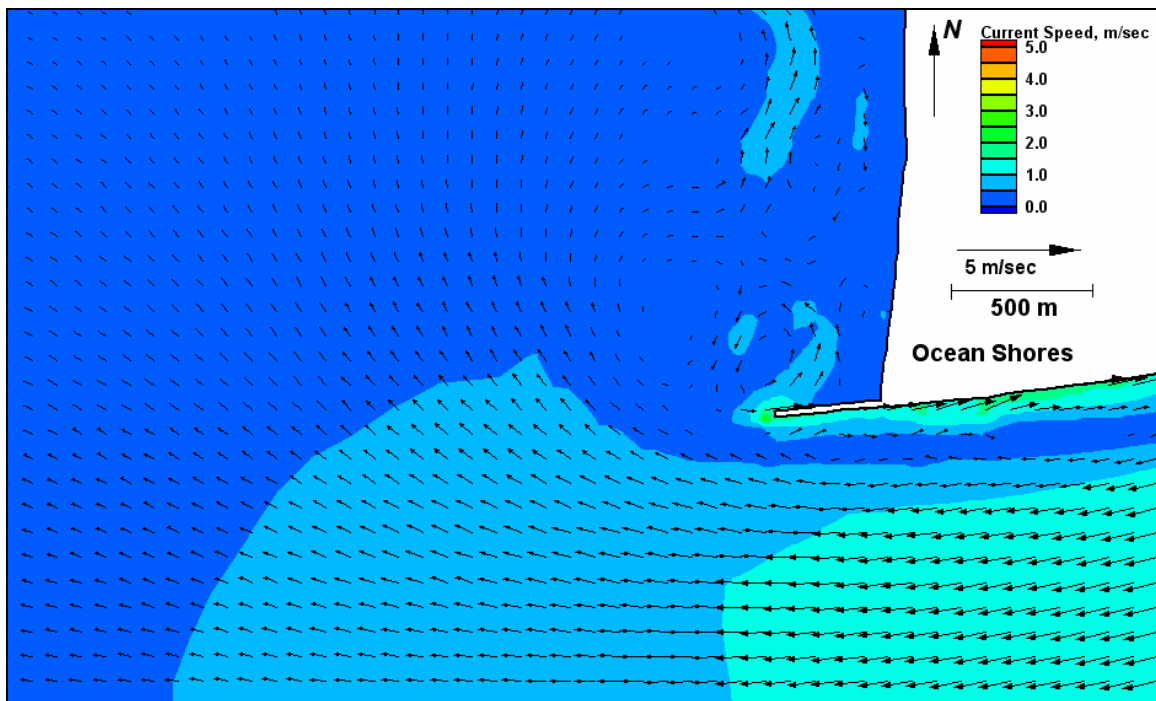
Figure E150. Run 140 (existing, west, spring tide), north jetty view of ebb tide
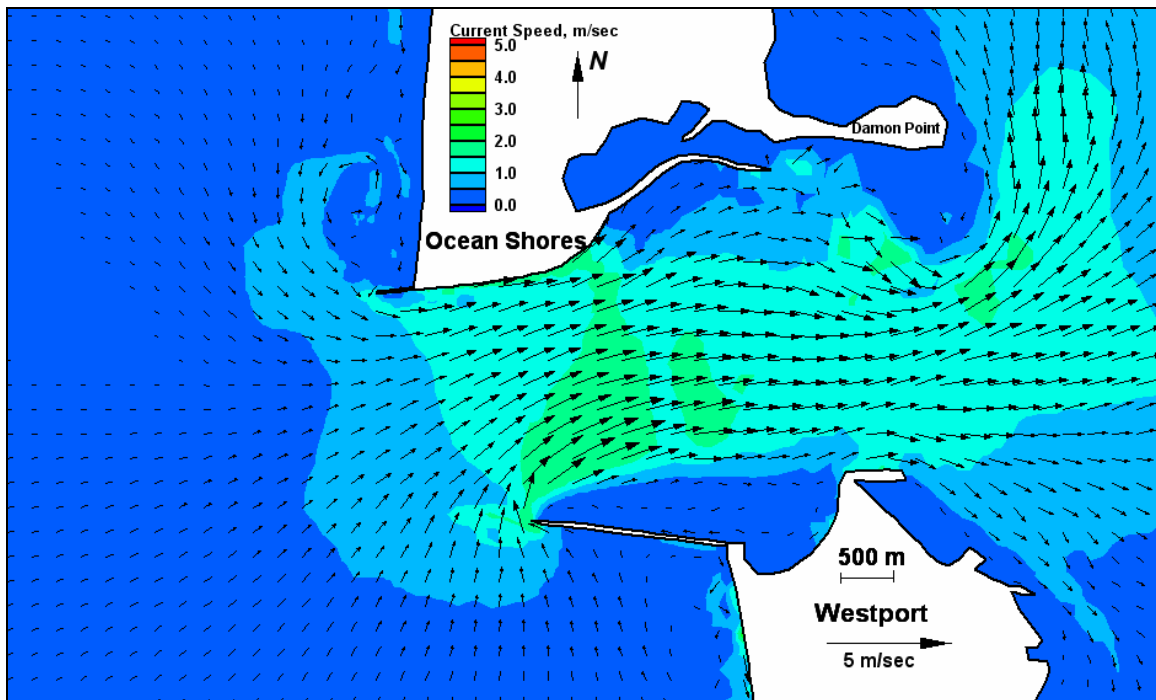
Figure E151. Run 141 (Alt 2A, west, spring tide), inlet view of flood tide
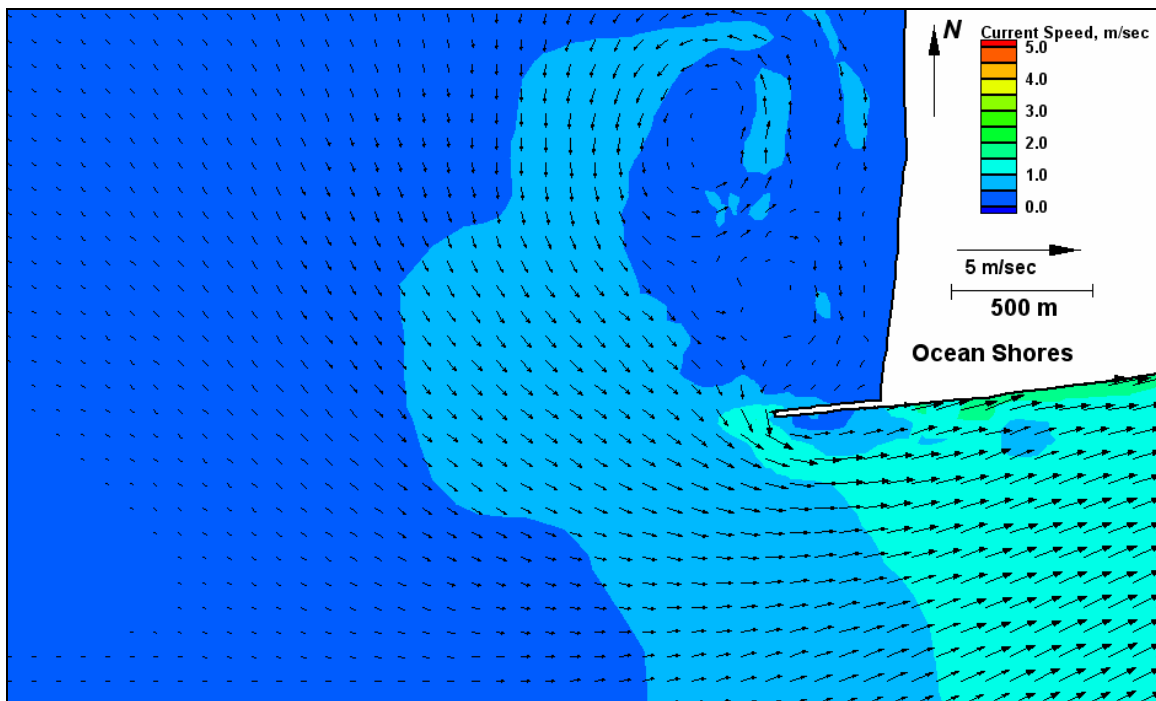
Figure E152. Run 141 (Alt 2A, west, spring tide), north jetty view of flood tide

Figure E153. Run 141 (Alt 2A, west, spring tide), inlet view of ebb tide

Figure E154. Run 141 (Alt 2A, west, spring tide), north jetty view of ebb tide
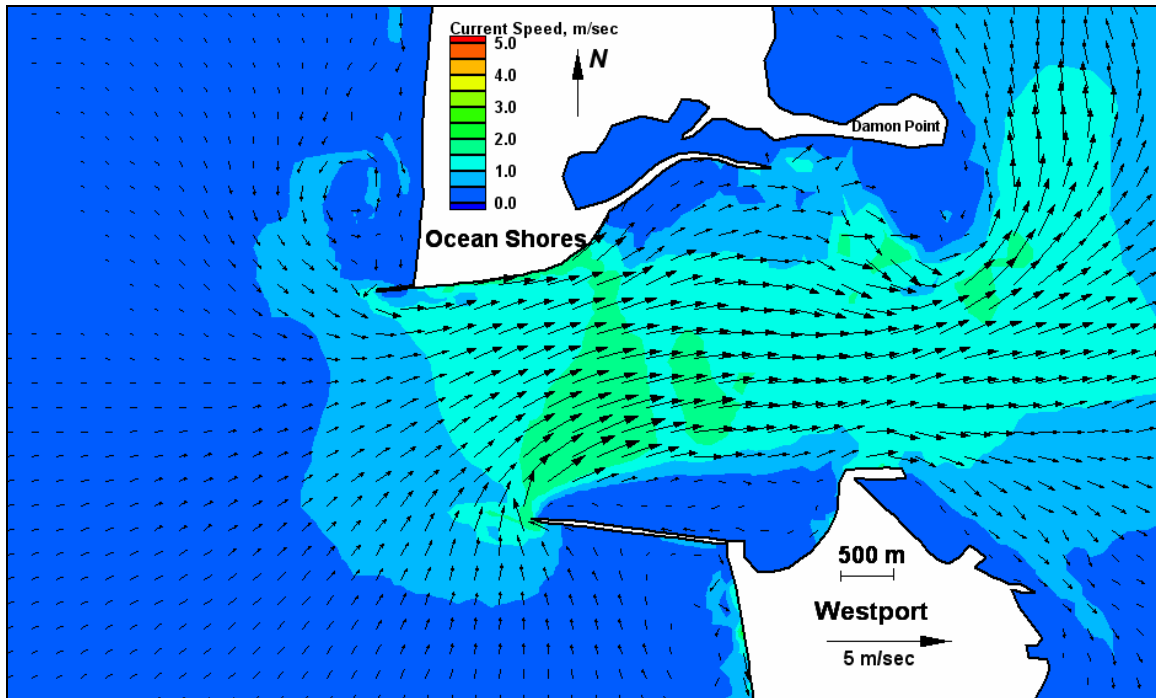
Figure E155. Run 142 (Alt 2B, west, spring tide), inlet view of flood tide
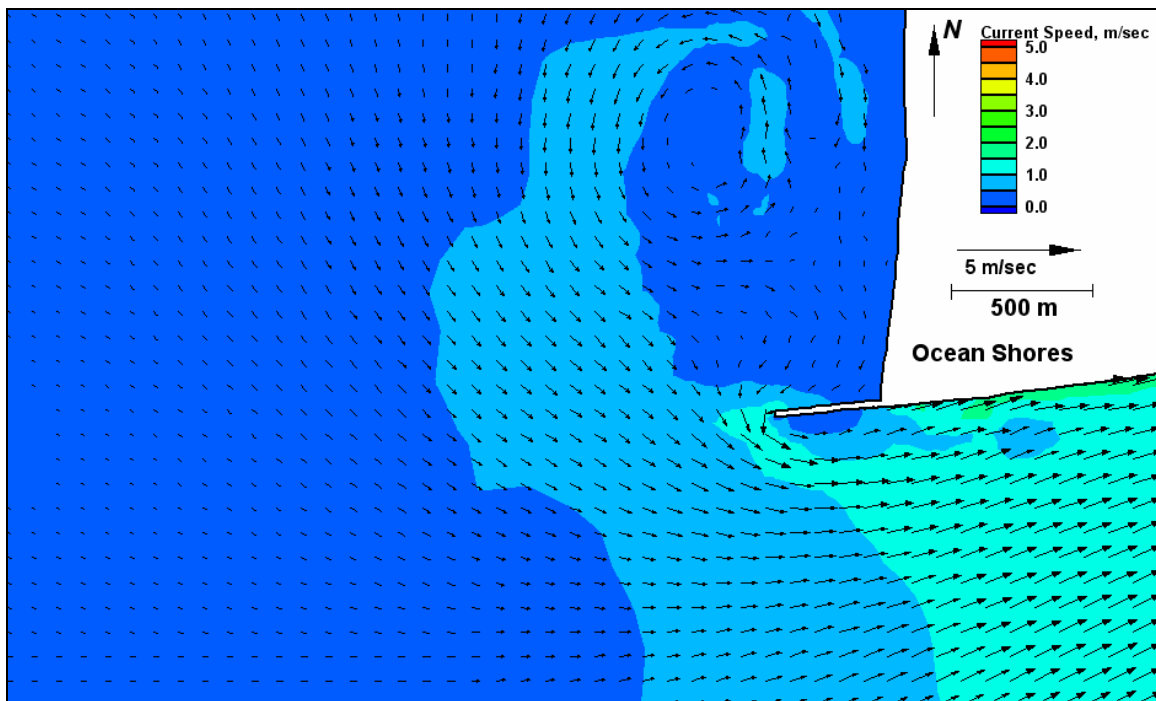
Figure E156. Run 142 (Alt 2B, west, spring tide), north jetty view of flood tide
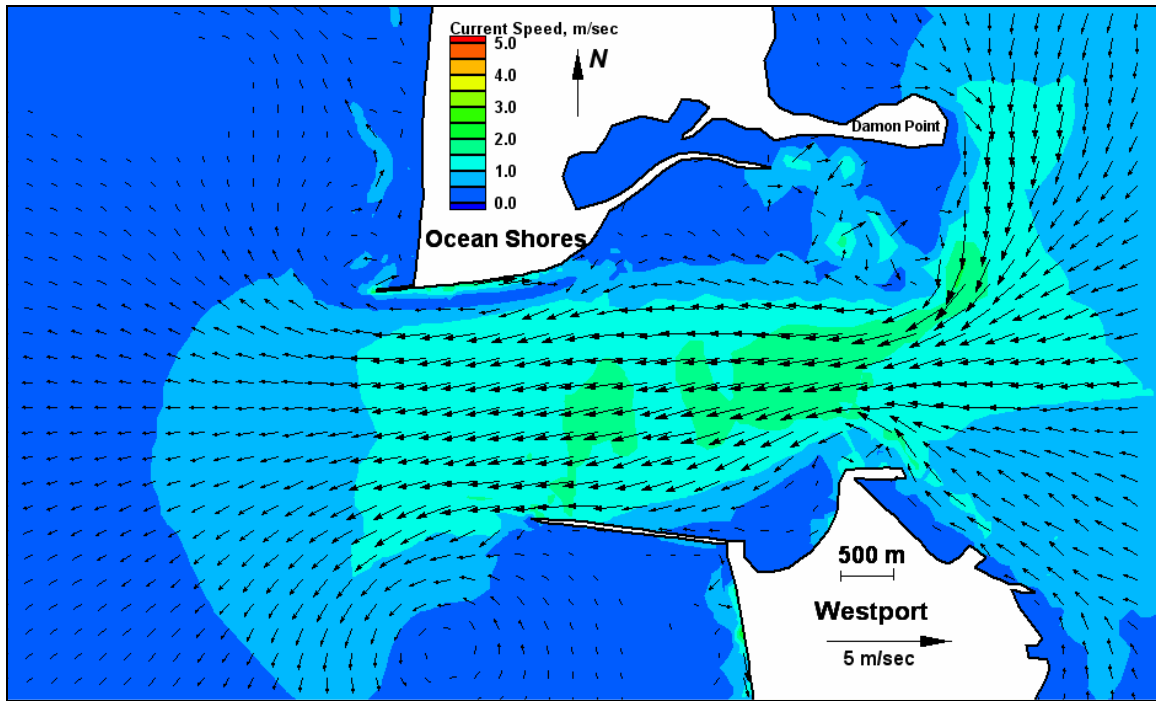
Figure E157. Run 142 (Alt 2B, west, spring tide), inlet view of ebb tide
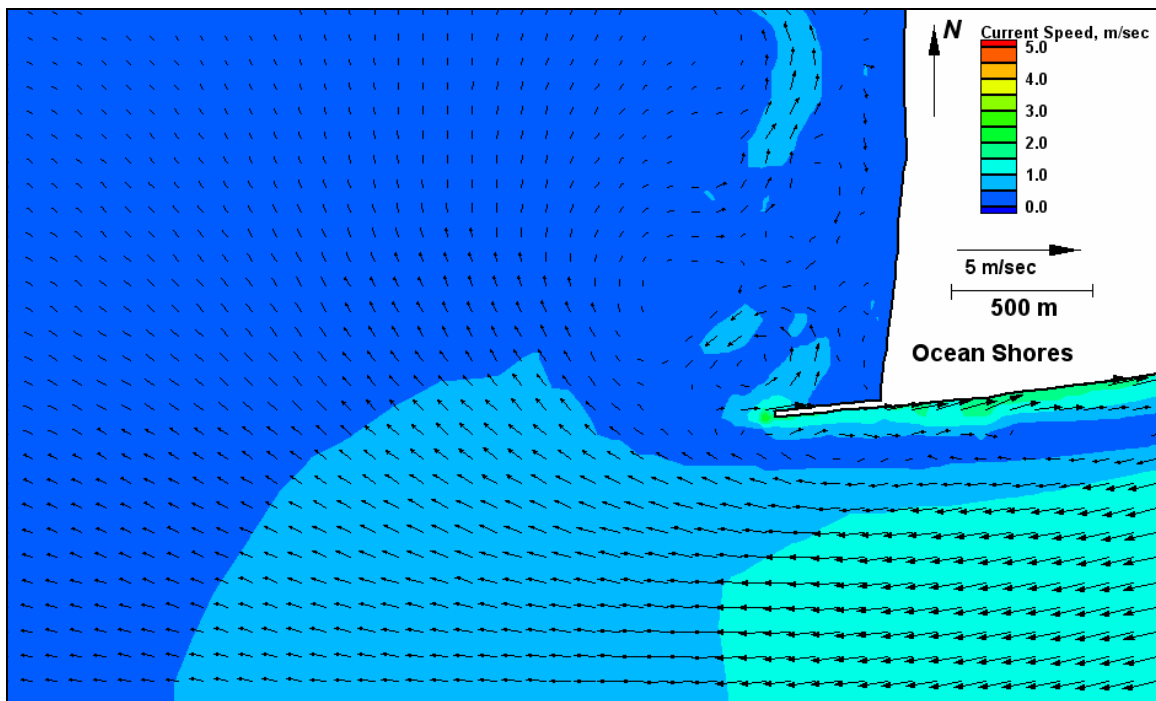
Figure E158. Run 142 (Alt 2B, west, spring tide), north jetty view of ebb tide
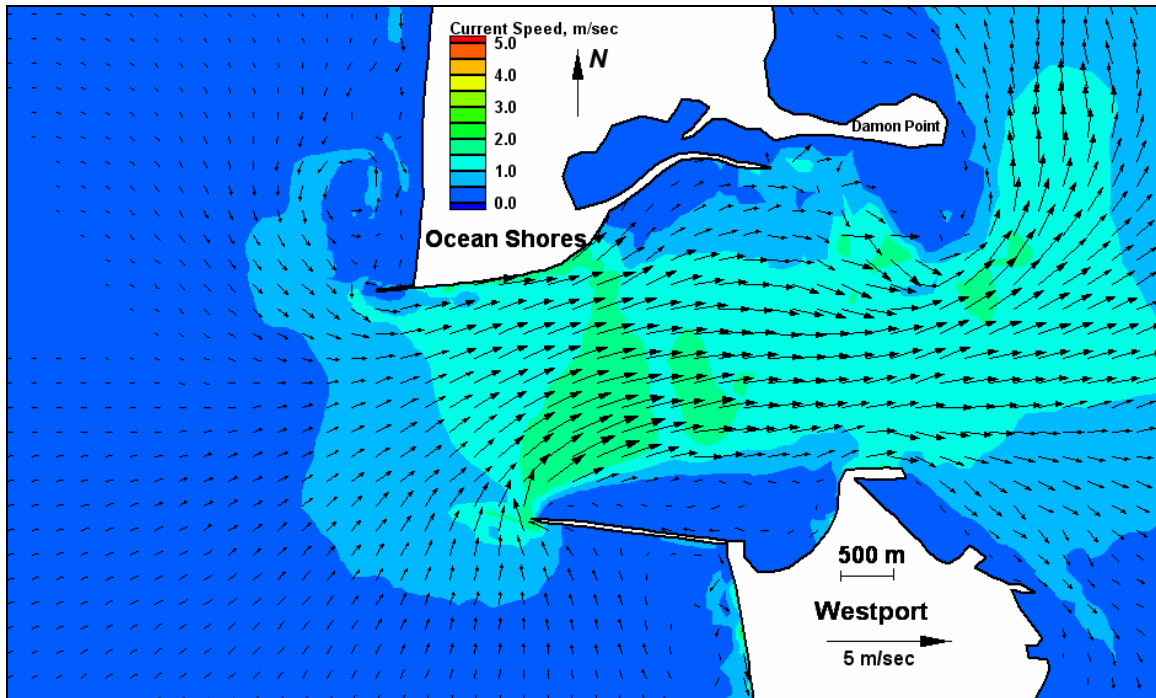
Figure E159. Run 143 (Alt 3A, west, spring tide), inlet view of flood tide
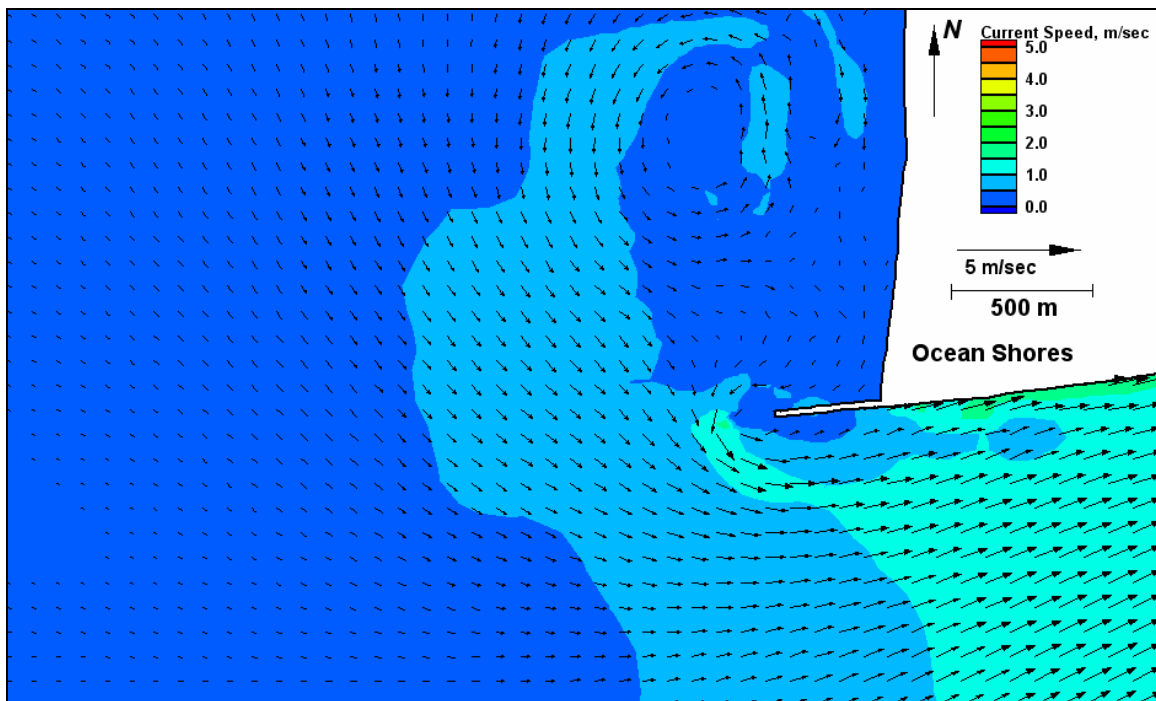
Figure E160. Run 143 (Alt 3A, west, spring tide), north jetty view of flood tide
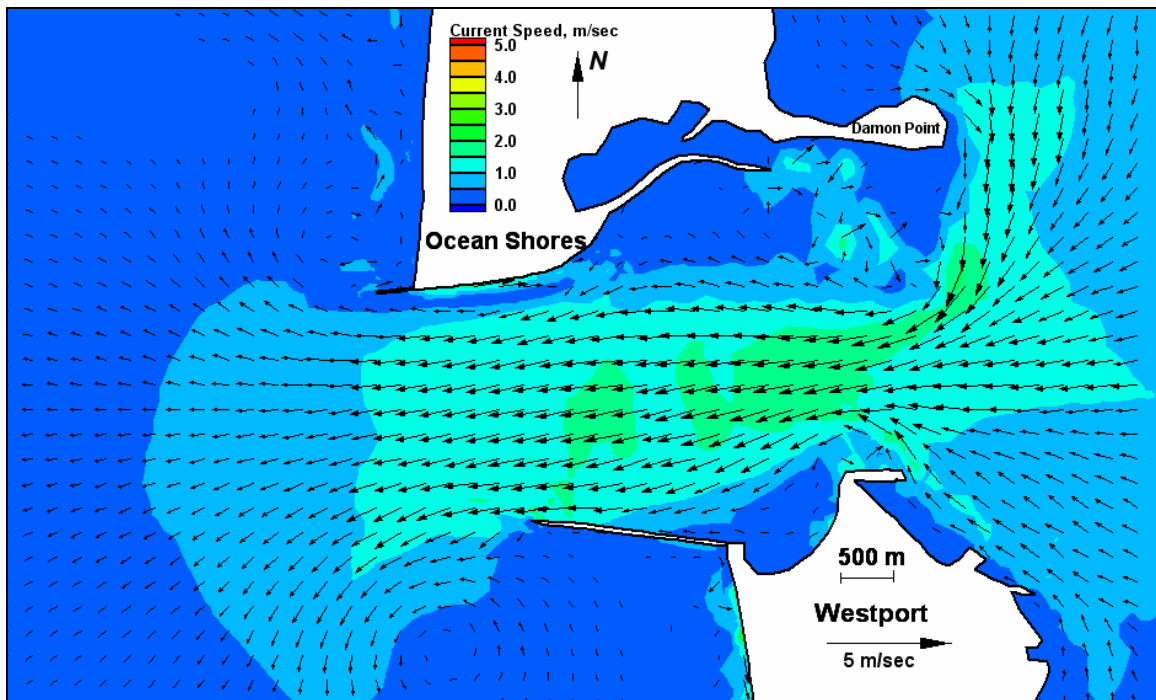
Figure E161. Run 143 (Alt 3A, west, spring tide), inlet view of ebb tide
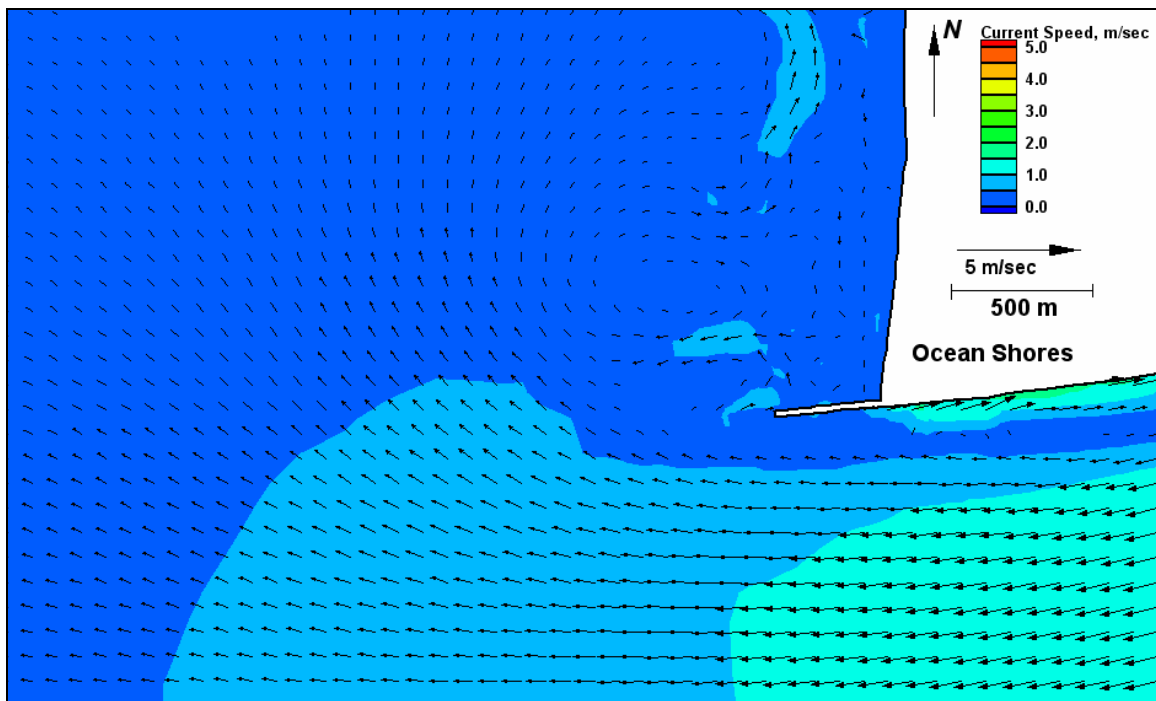
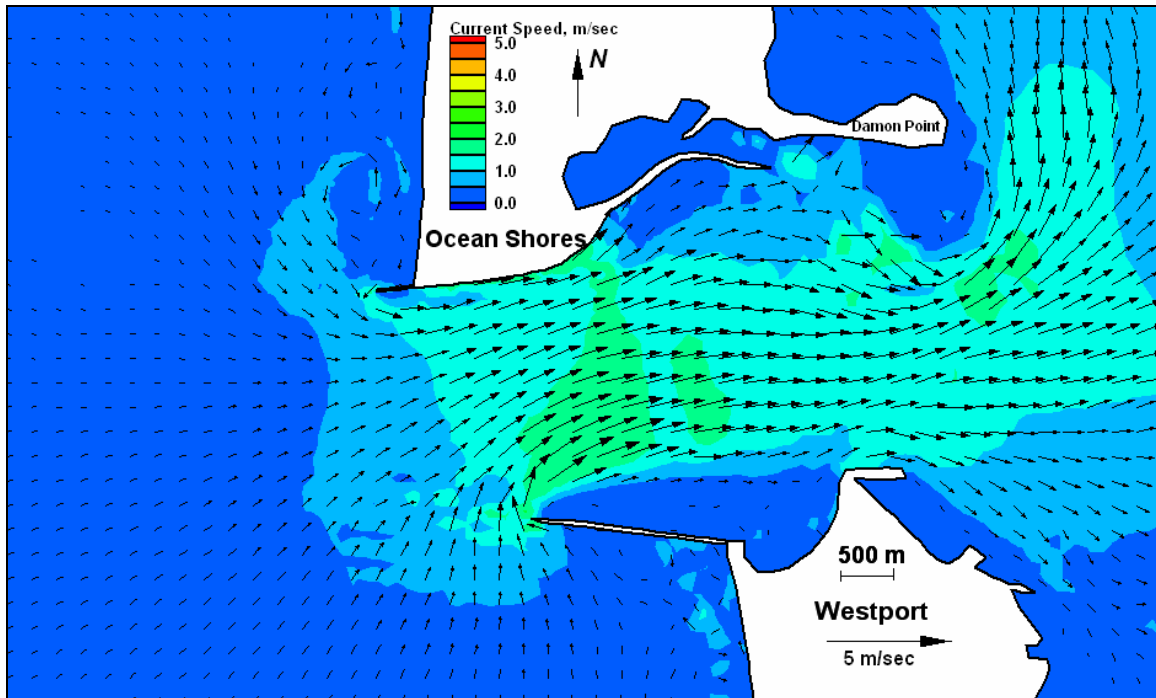Figure E162. Run 143 (Alt 3A, west, spring tide), north jetty view of ebb tide
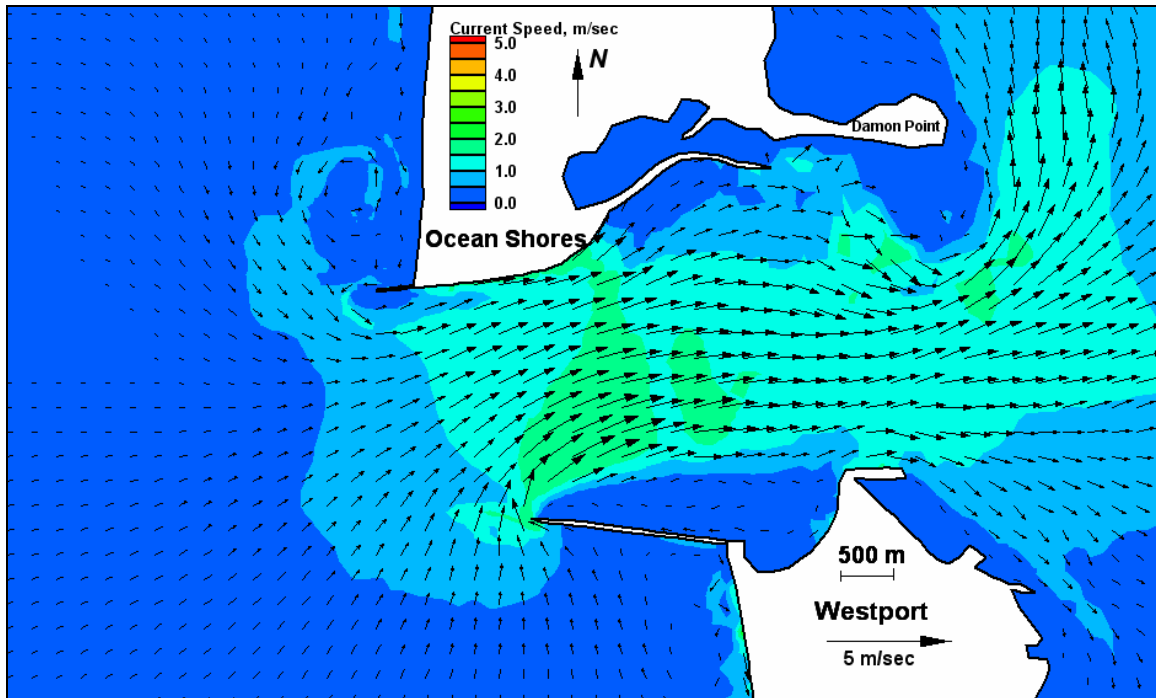
Figure E163. Run 144 (Alt 3B, west, spring tide), inlet view of flood tide
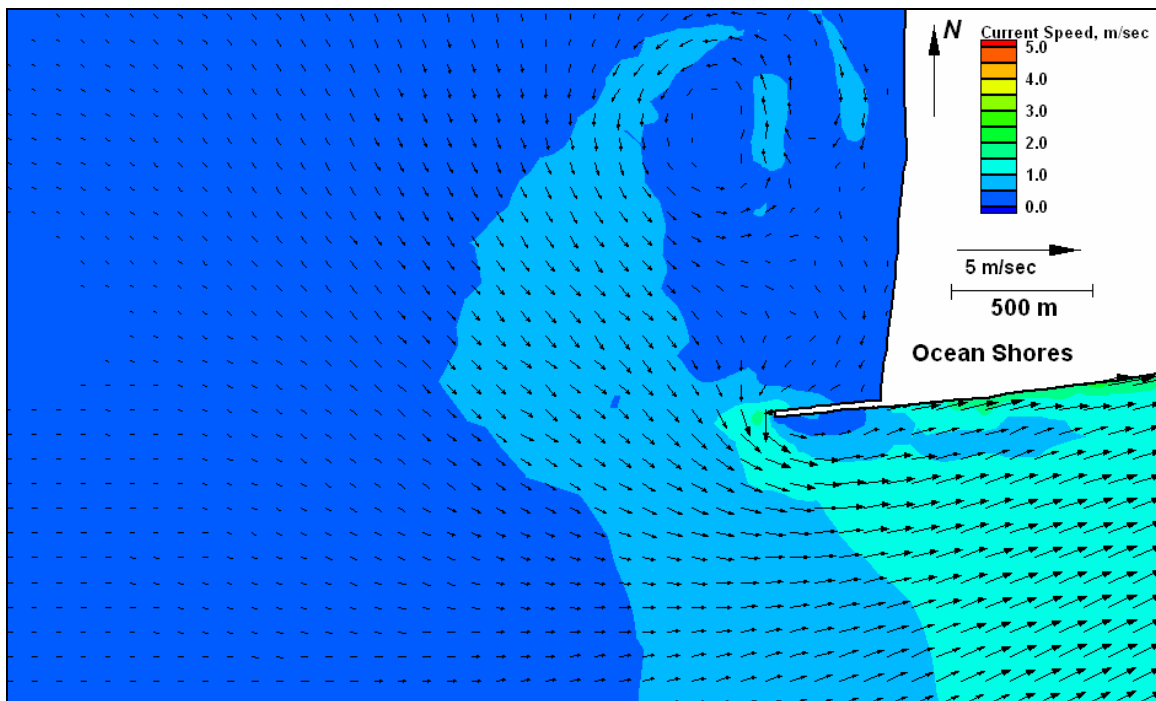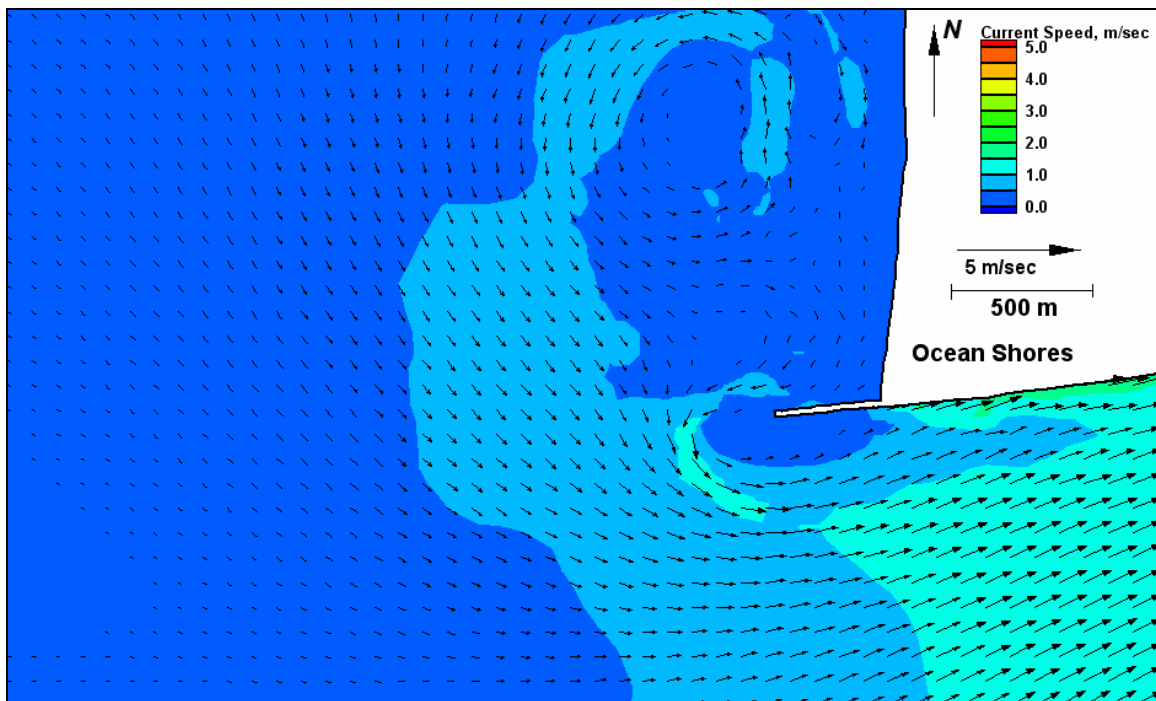

Figure E164. Run 144 (Alt 3B, west, spring tide), north jetty view of flood tide
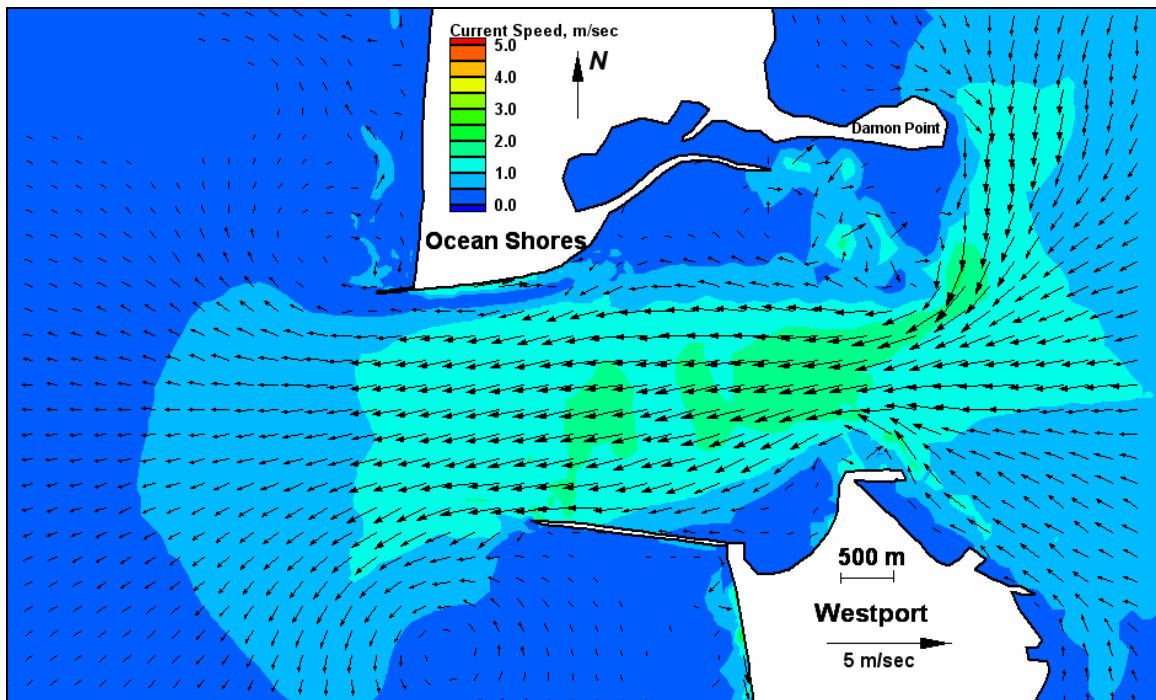
Figure E165. Run 144 (Alt 3B, west, spring tide), inlet view of ebb tide
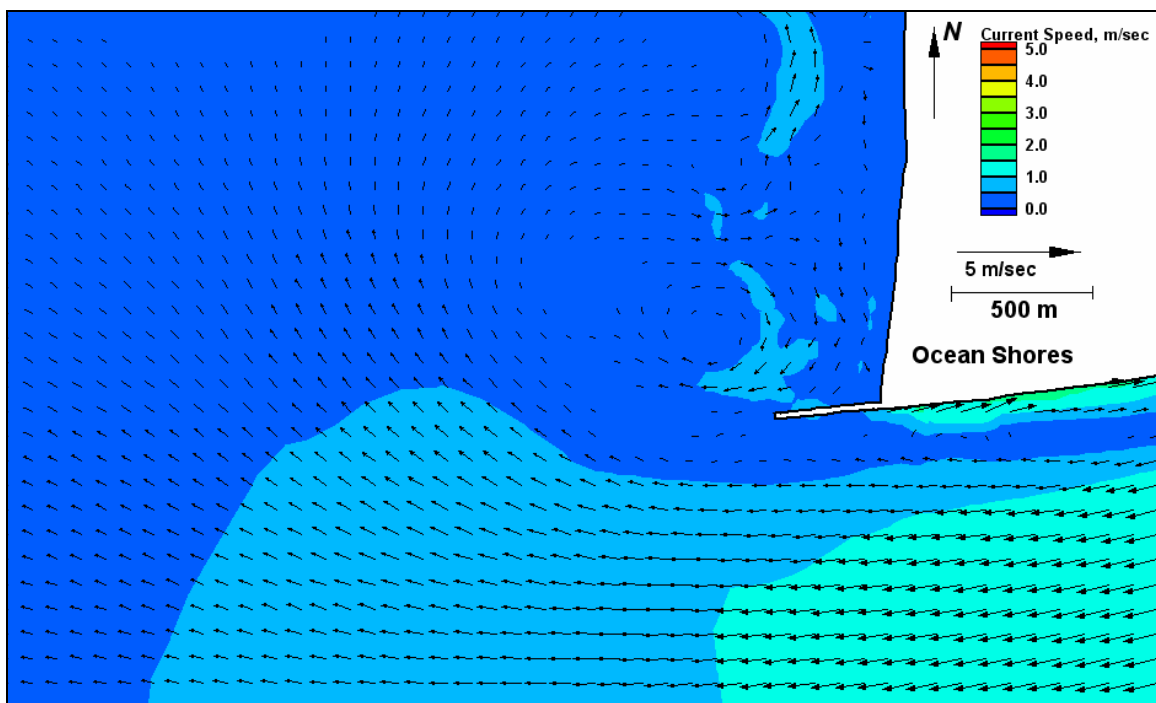
Figure E166. Run 144 (Alt 3B, west, spring tide), north jetty view of ebb tide
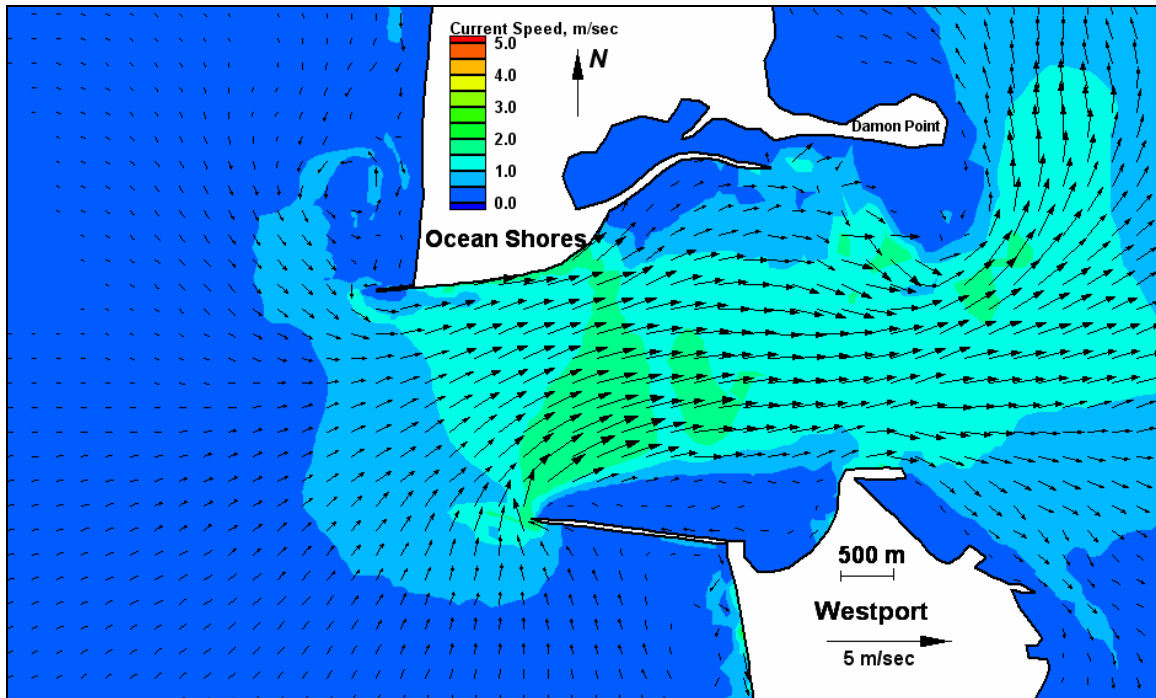
Figure E167. Run 145 (Alt 4A, west, spring tide), inlet view of flood tide
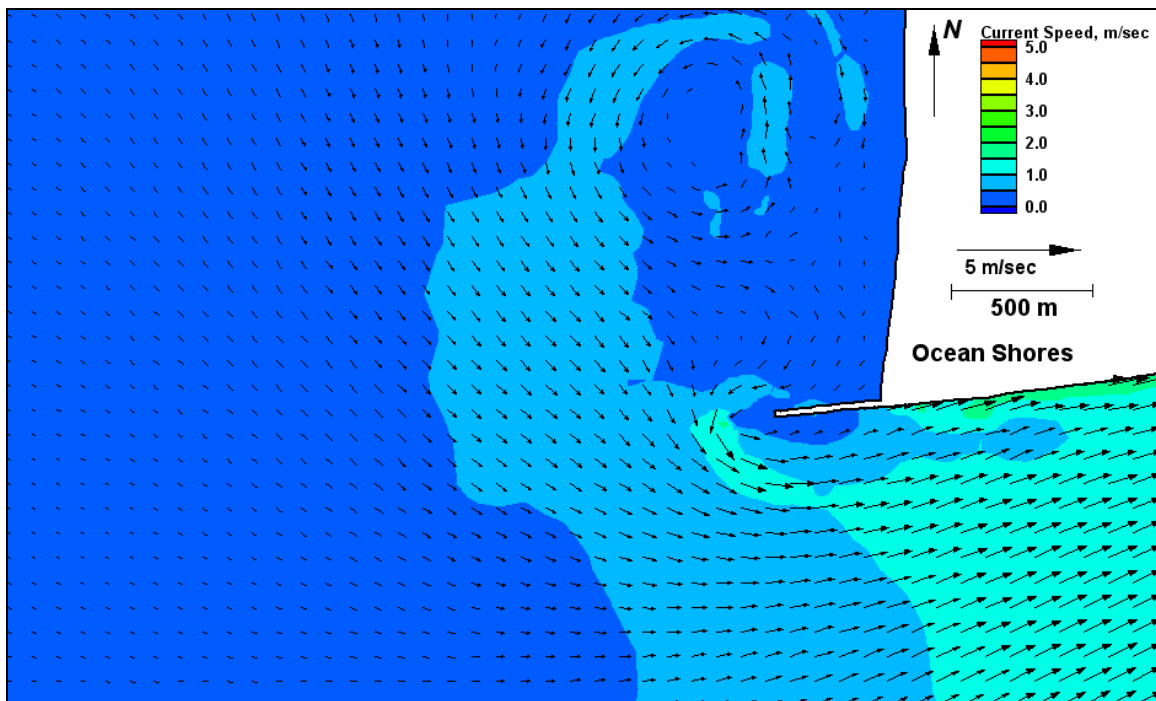
Figure E168. Run 145 (Alt 4A, west, spring tide), north jetty view of flood tide

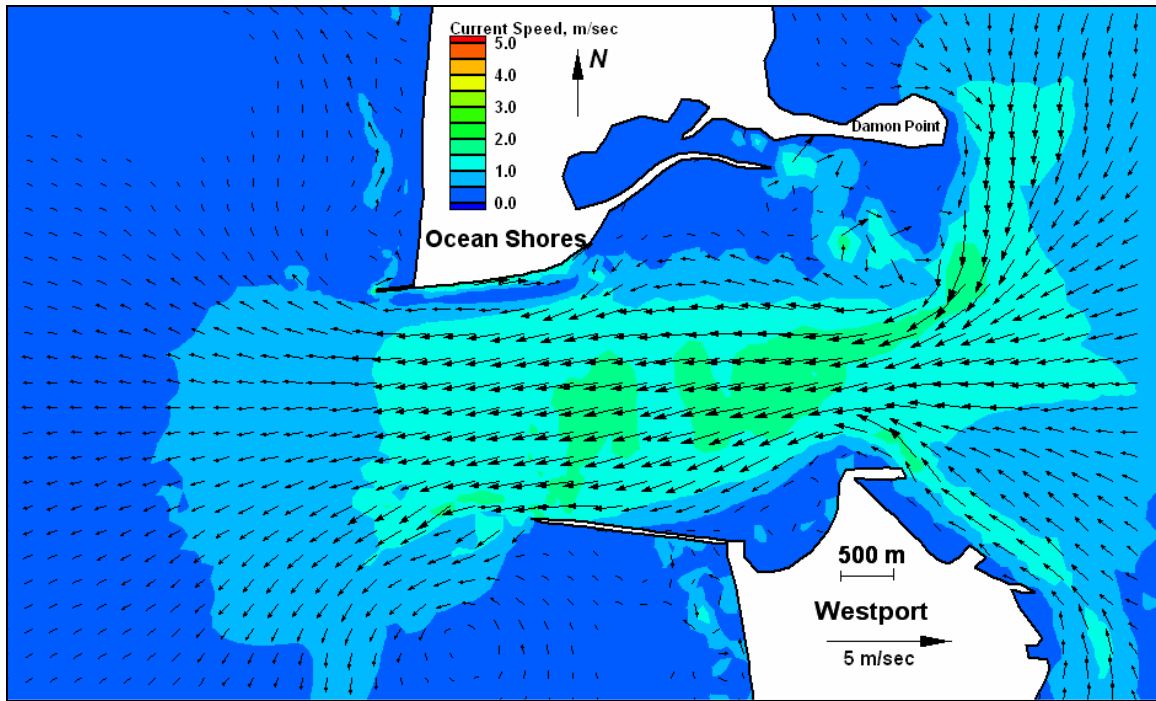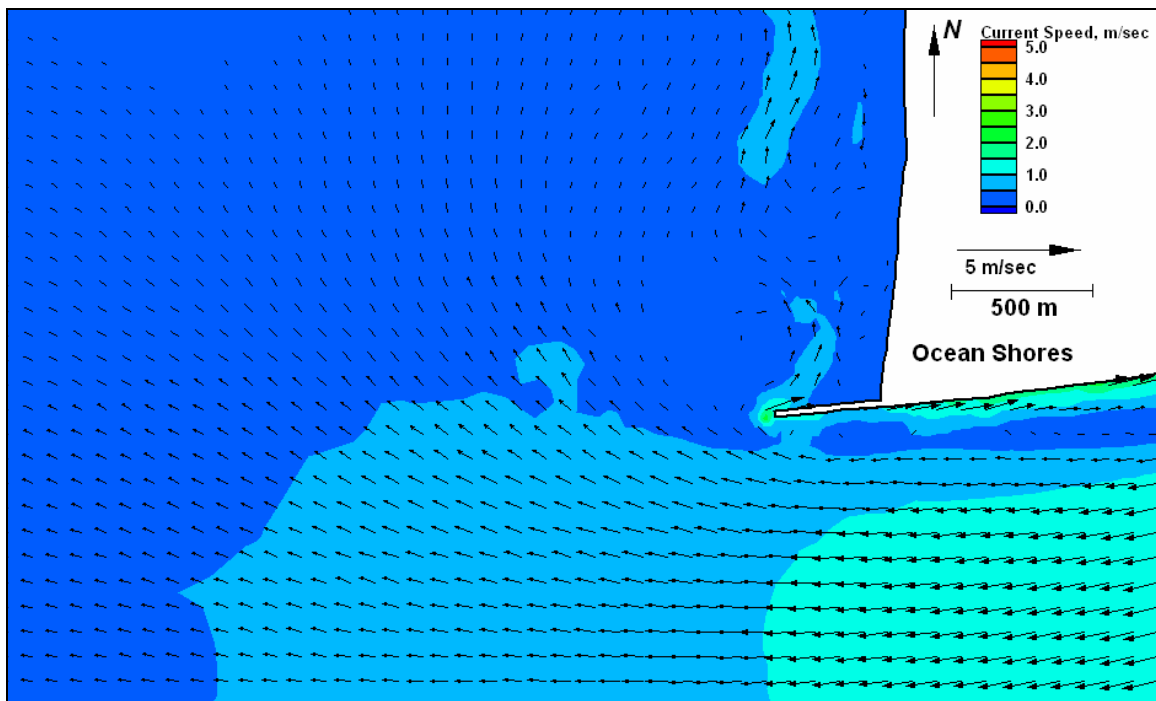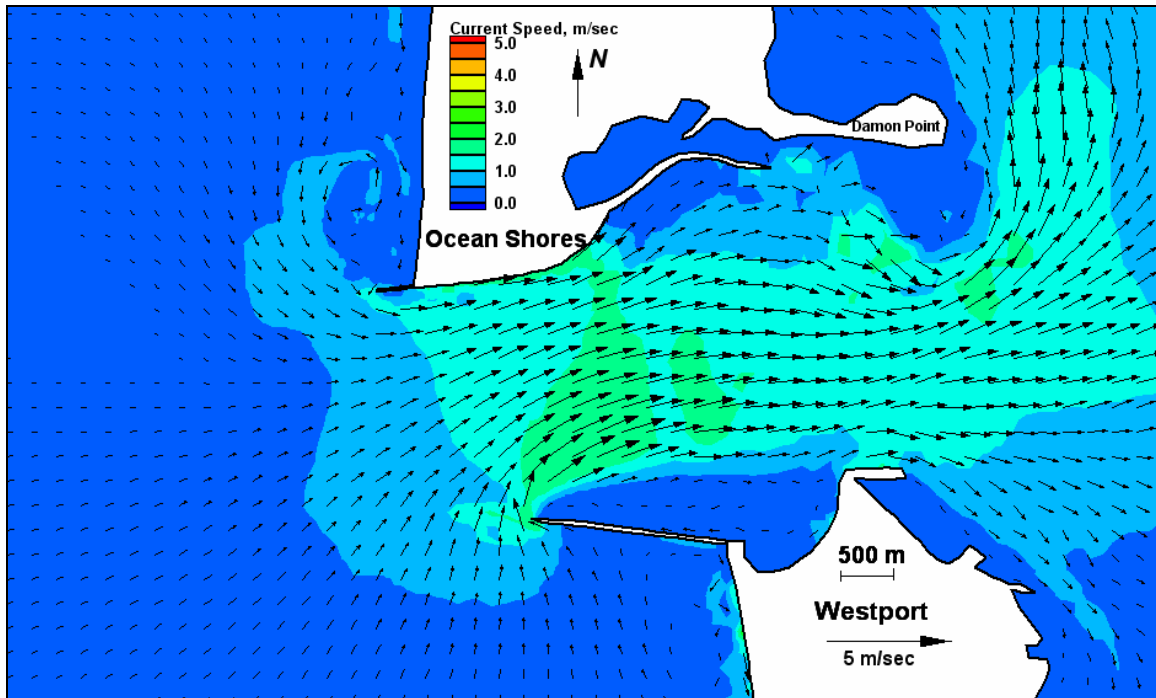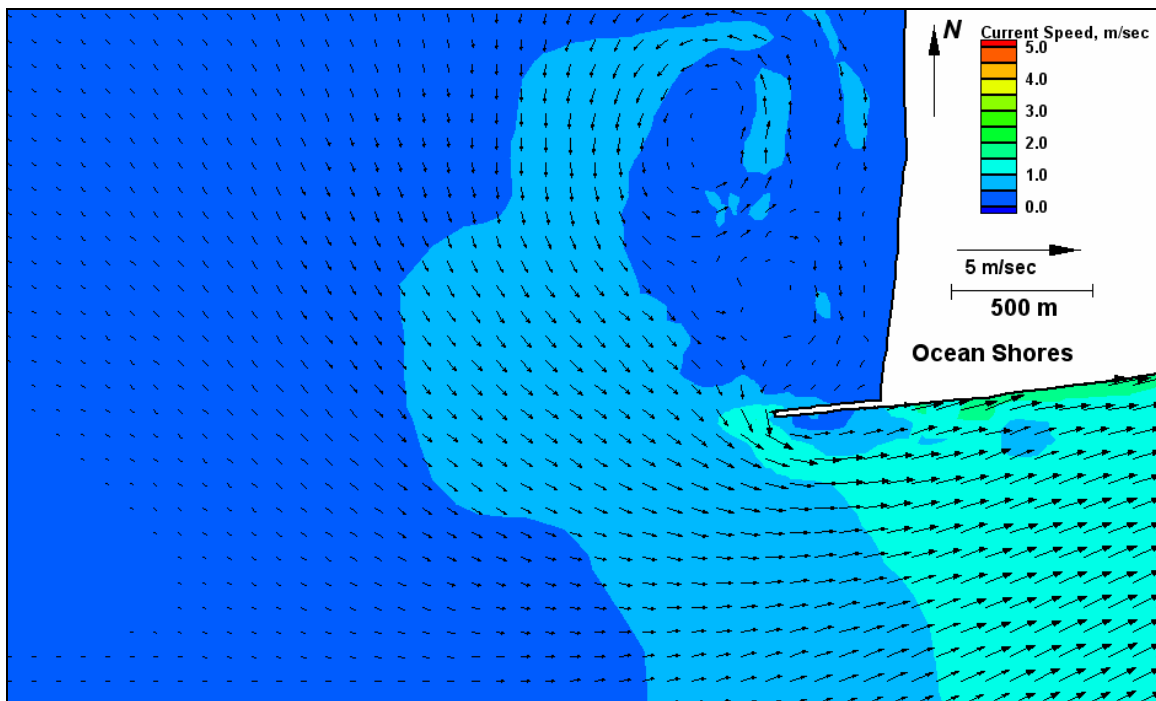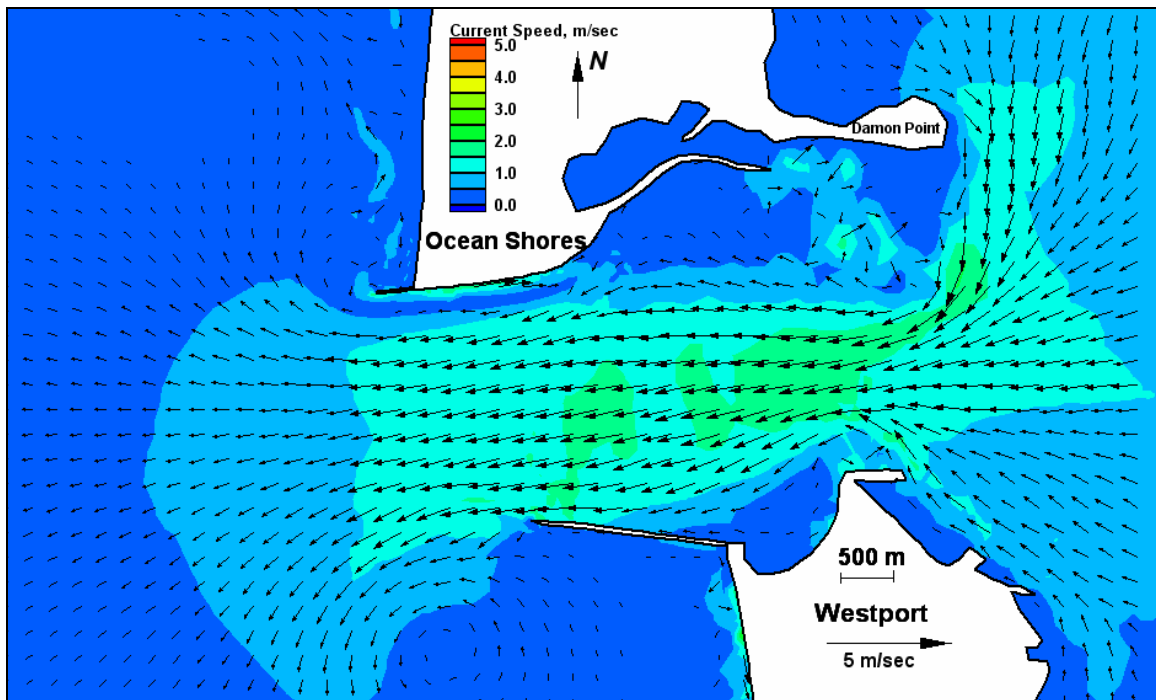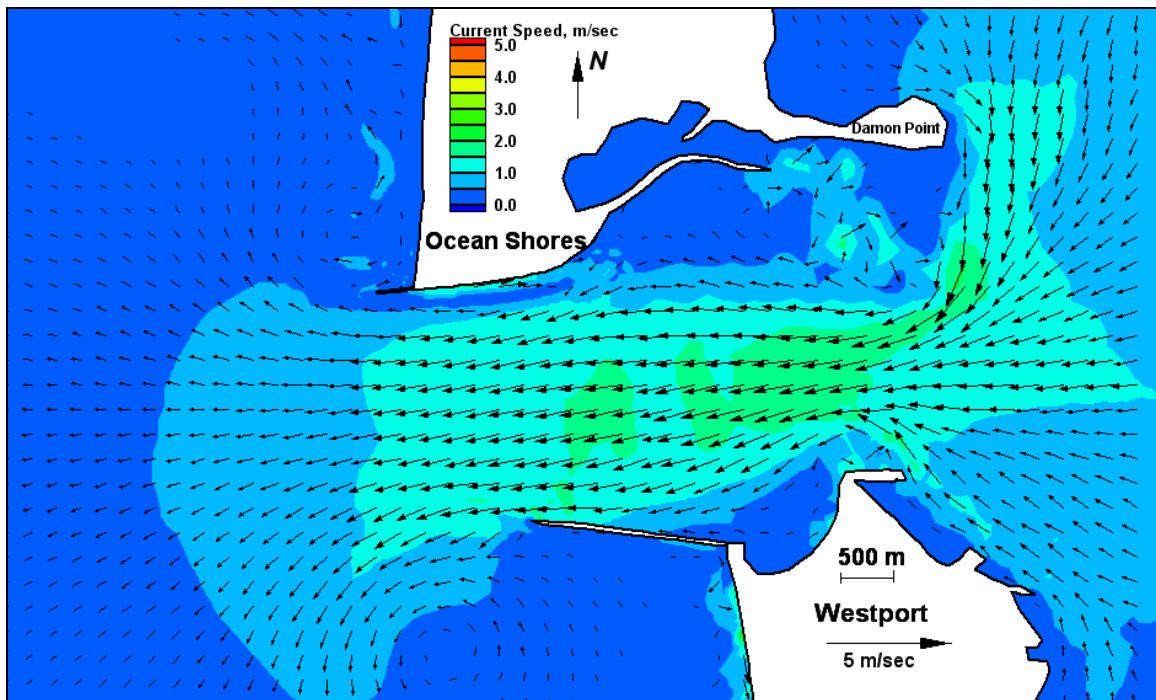Figure E169. Run 145 (Alt 4A, west, spring tide), inlet view of ebb tide
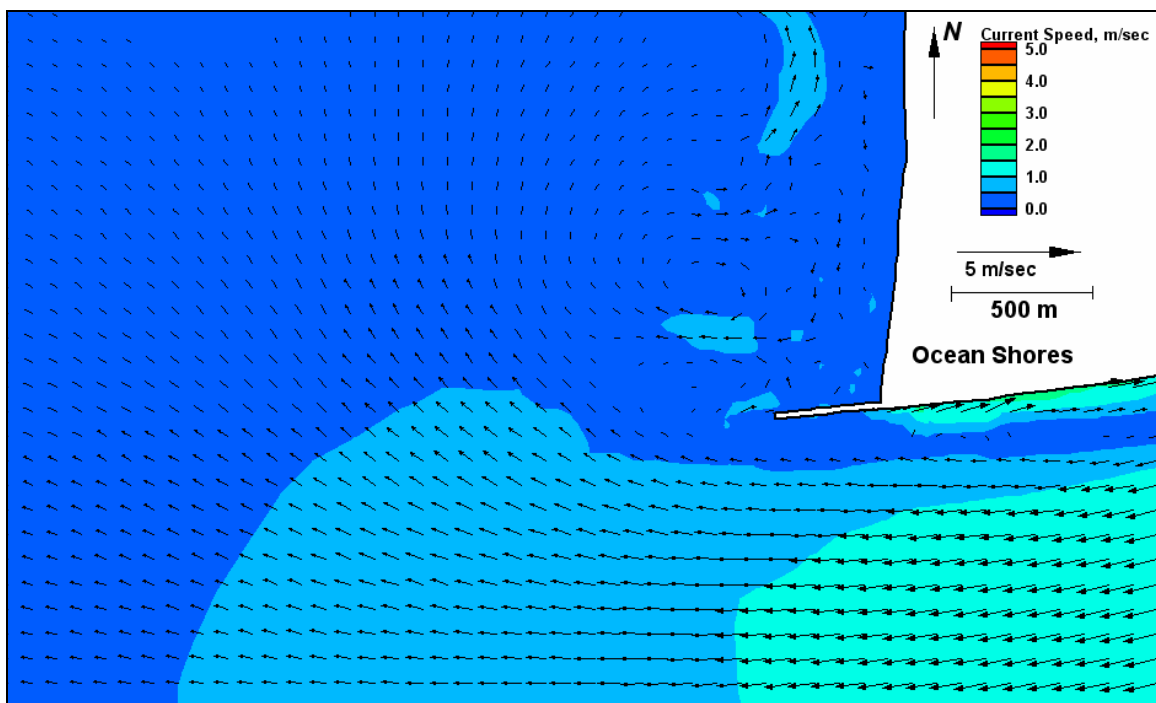
Figure E170. Run 145 (Alt 4A, west, spring tide), north jetty view of ebb tide
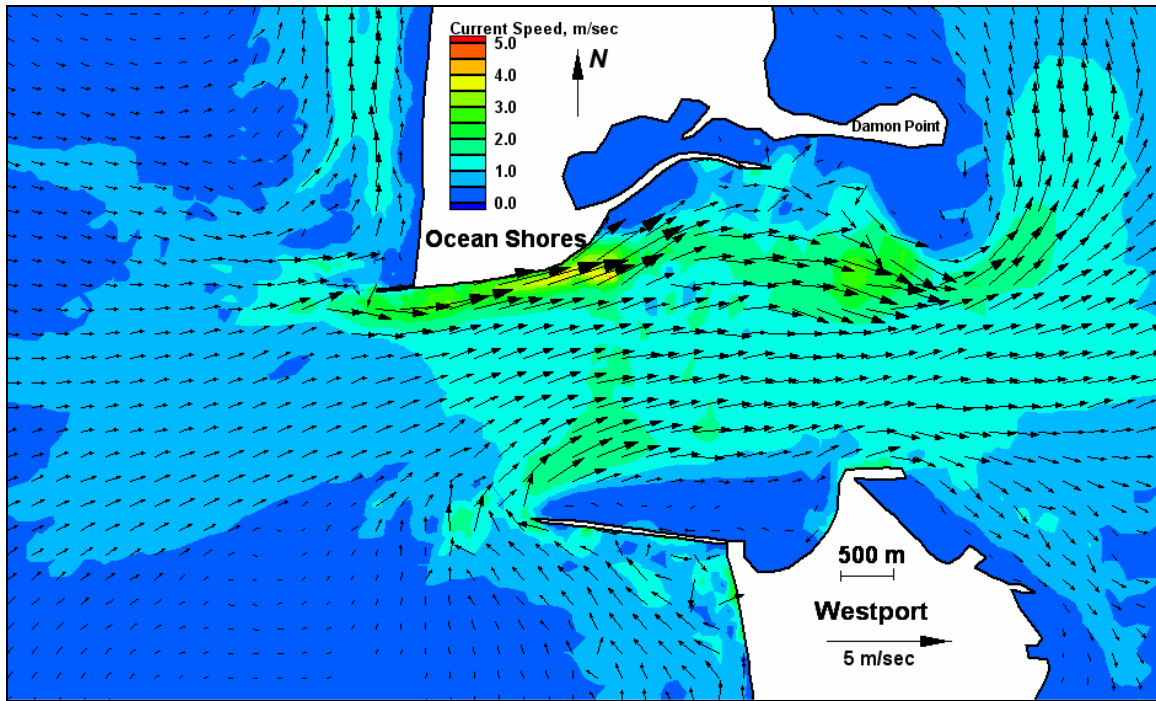
Figure E171. Run 146 (existing, west-southwest, spring tide), inlet view of flood tide
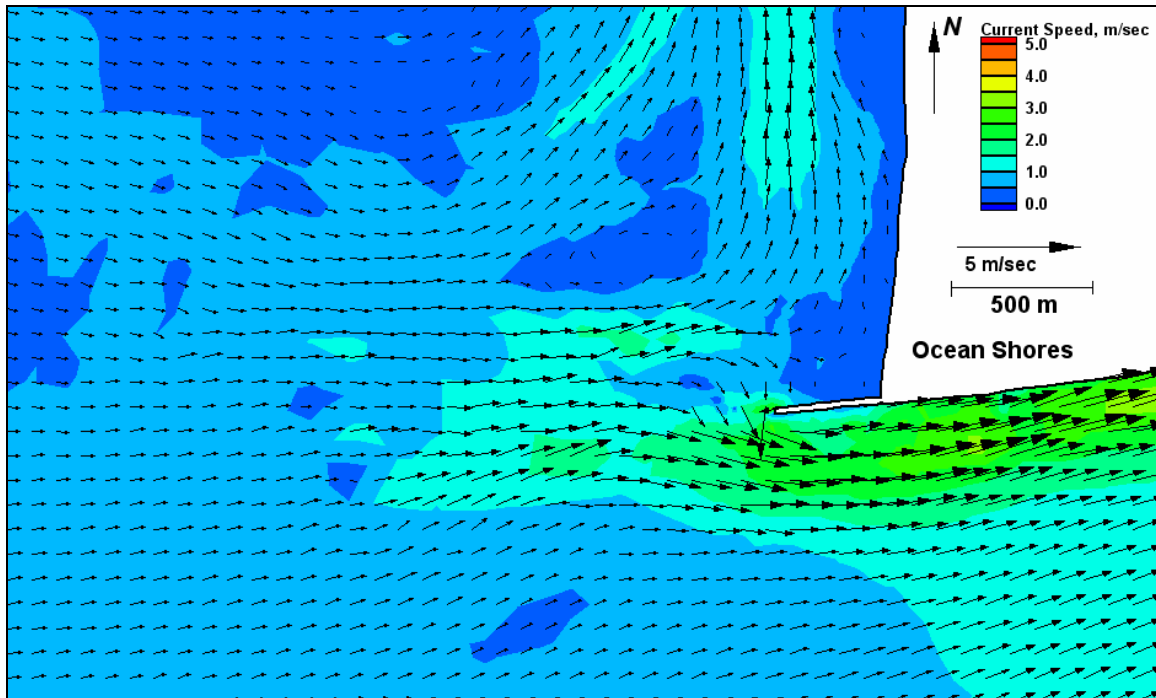
Figure E172. Run 146 (existing, west-southwest, spring tide), north jetty view of flood tide
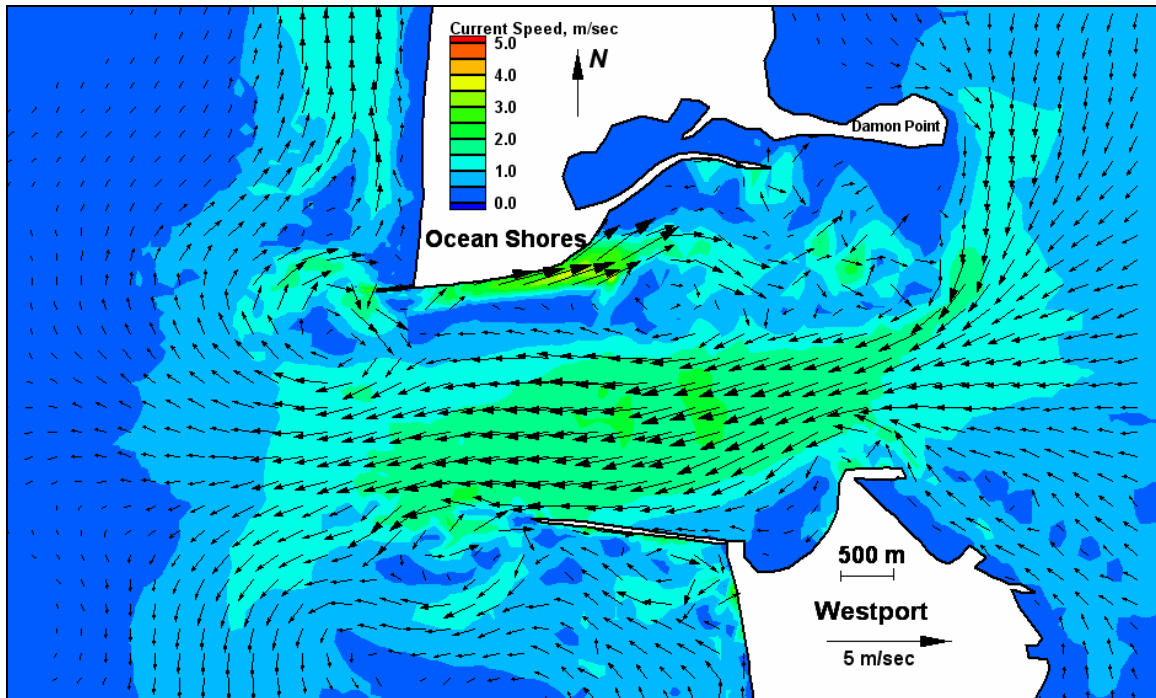
Figure E173. Run 146 (existing, west-southwest, spring tide), inlet view of ebb tide
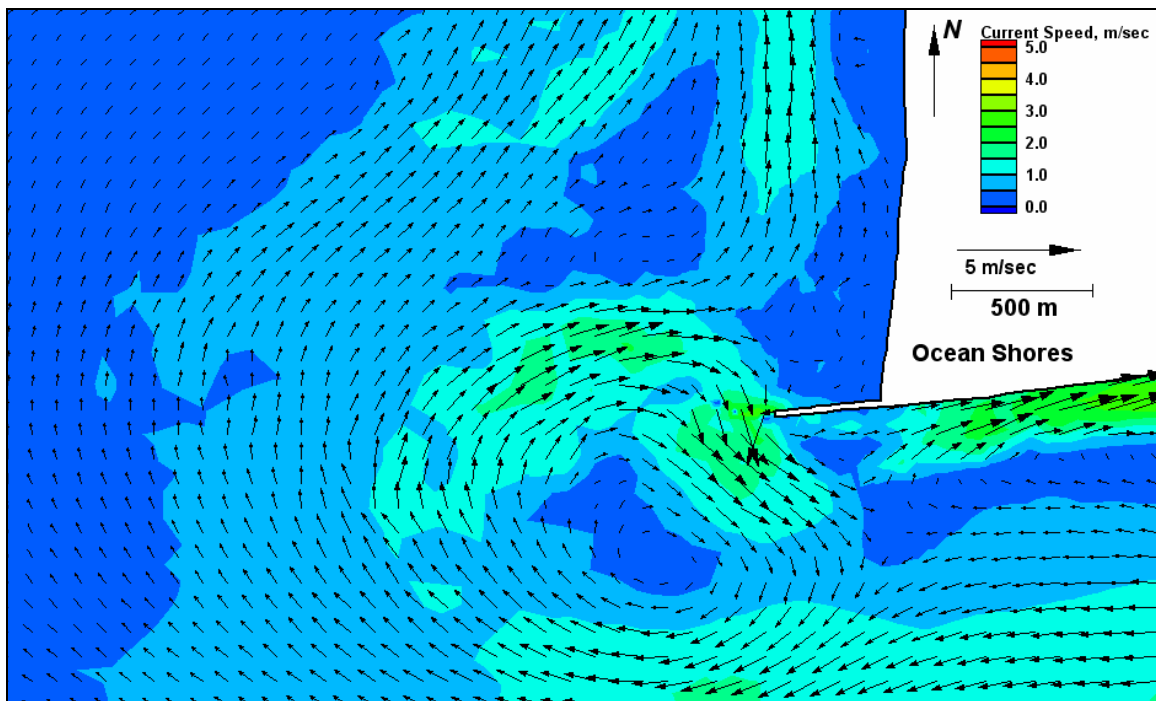
Figure E174. Run 146 (existing, west-southwest, spring tide), north jetty view of ebb tide
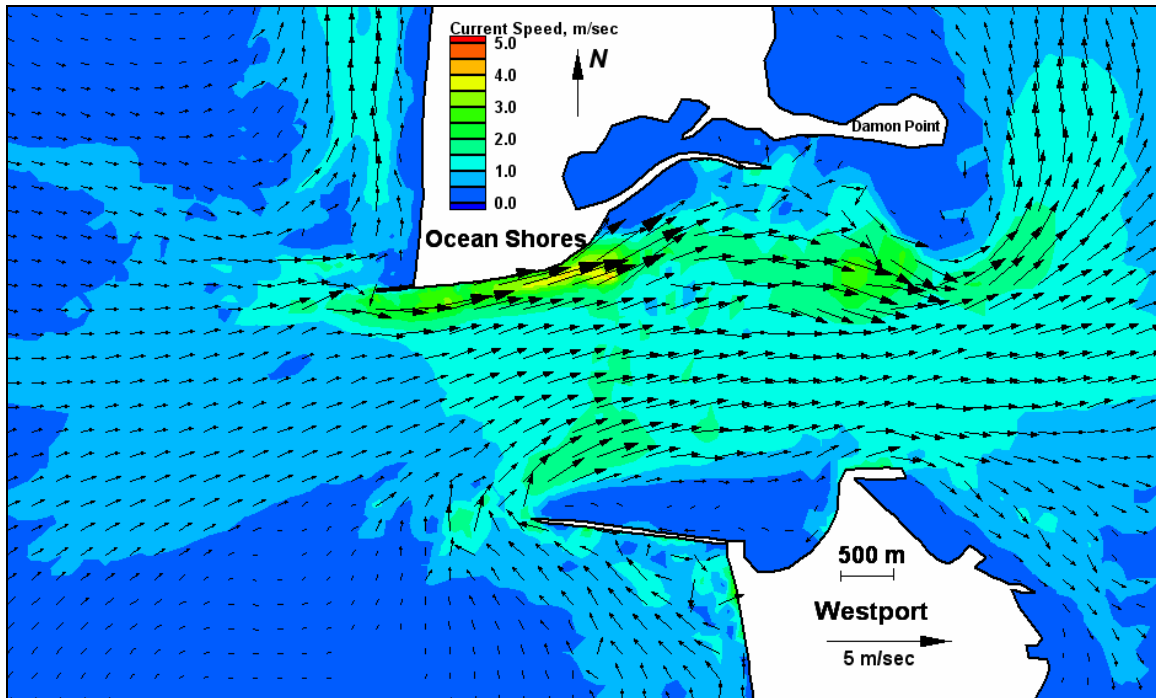
Figure E175. Run 147 (Alt 2A, west-southwest, spring tide), inlet view of flood tide
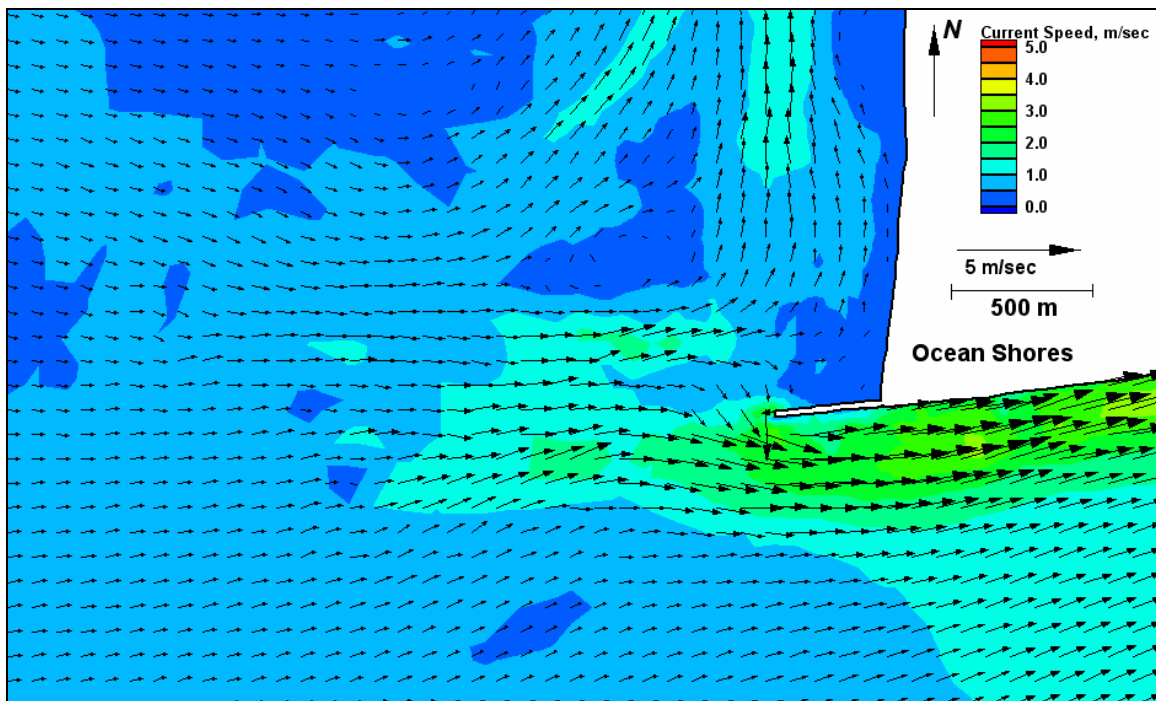
Figure E176. Run 147 (Alt 2A, west-southwest, spring tide), north jetty view of flood tide
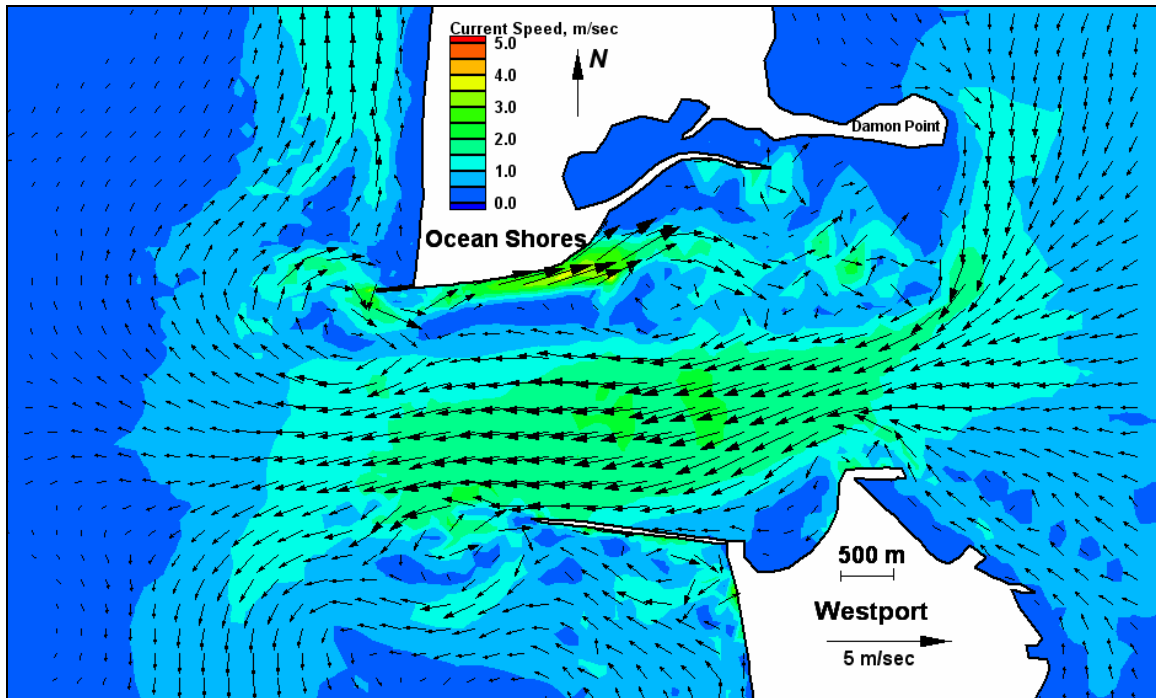
Figure E177. Run 147 (Alt 2A, west-southwest, spring tide), inlet view of ebb tide
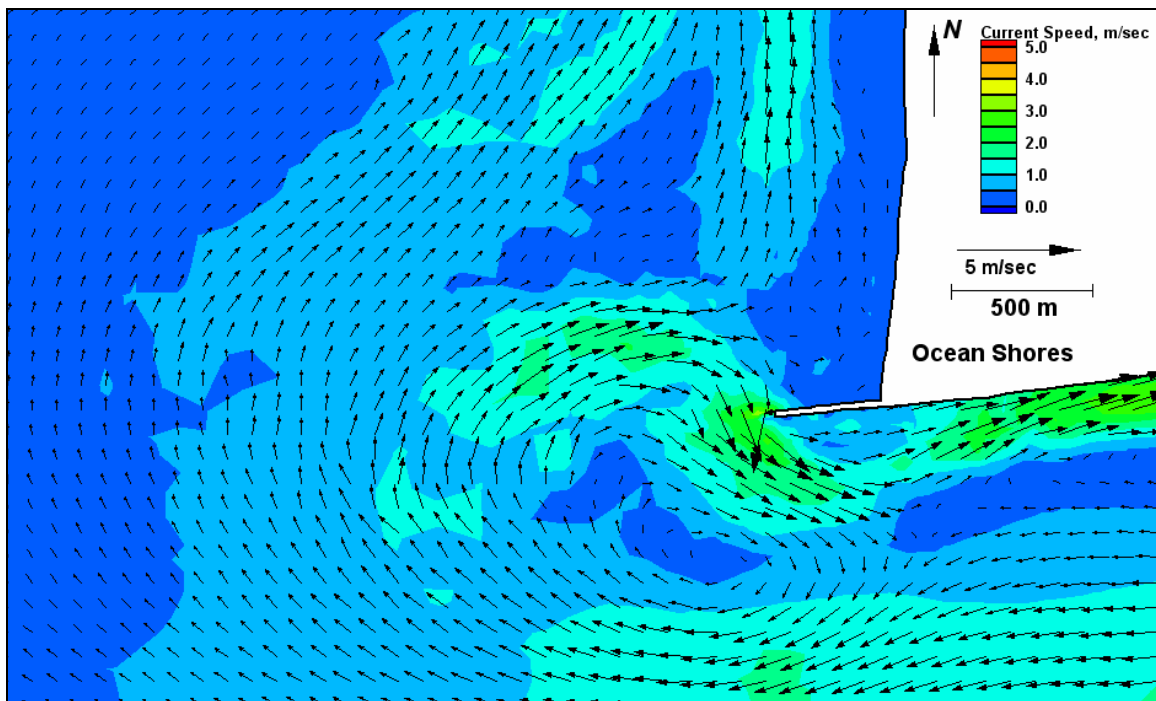
Figure E178. Run 147 (Alt 2A, west-southwest, spring tide), north jetty view of ebb tide
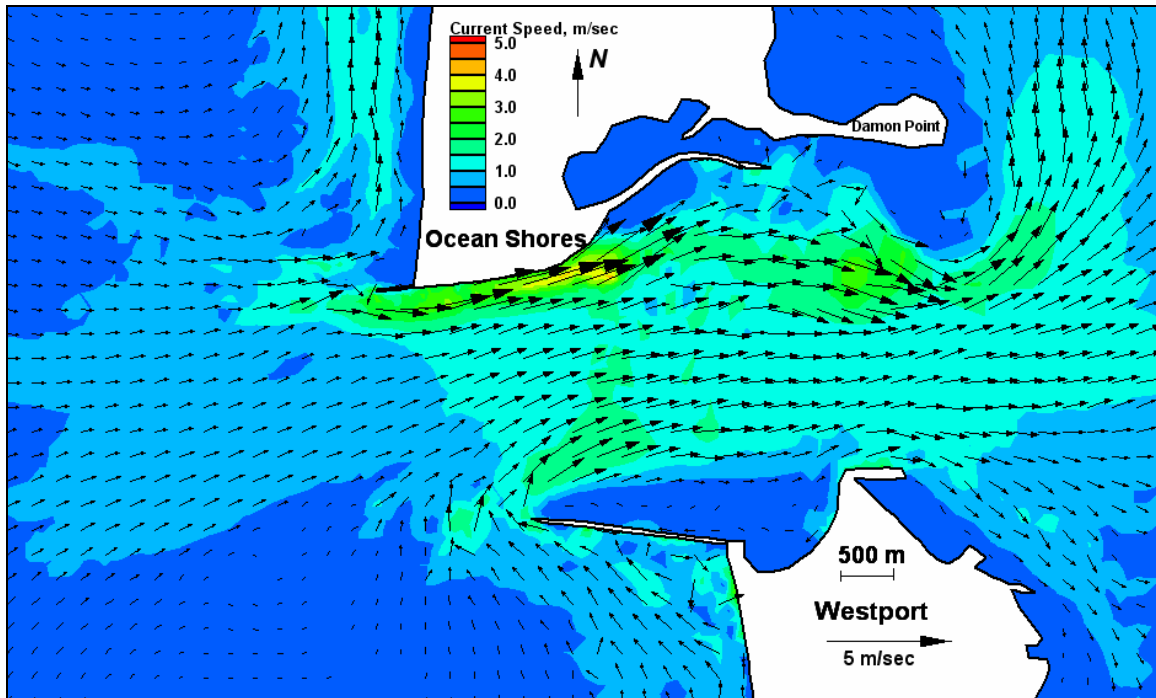
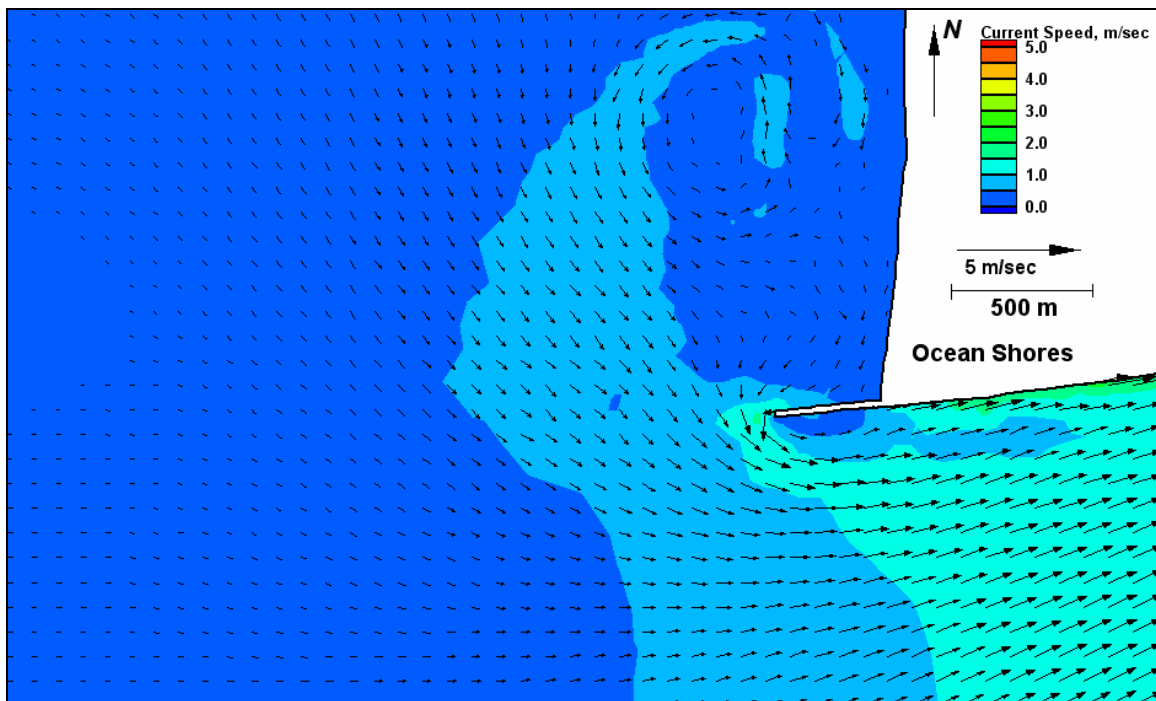Figure E179. Run 148 (Alt 2B, west-southwest, spring tide), inlet view of flood tide
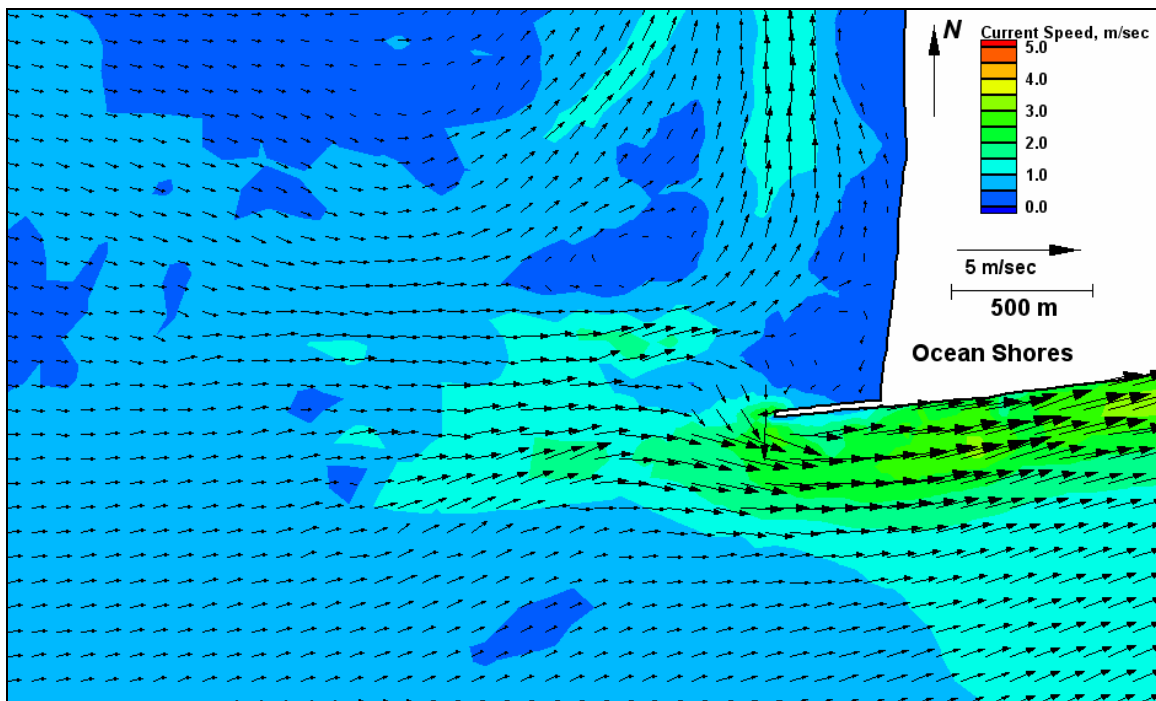
Figure E180. Run 148 (Alt 2B, west-southwest, spring tide), north jetty view of flood tide
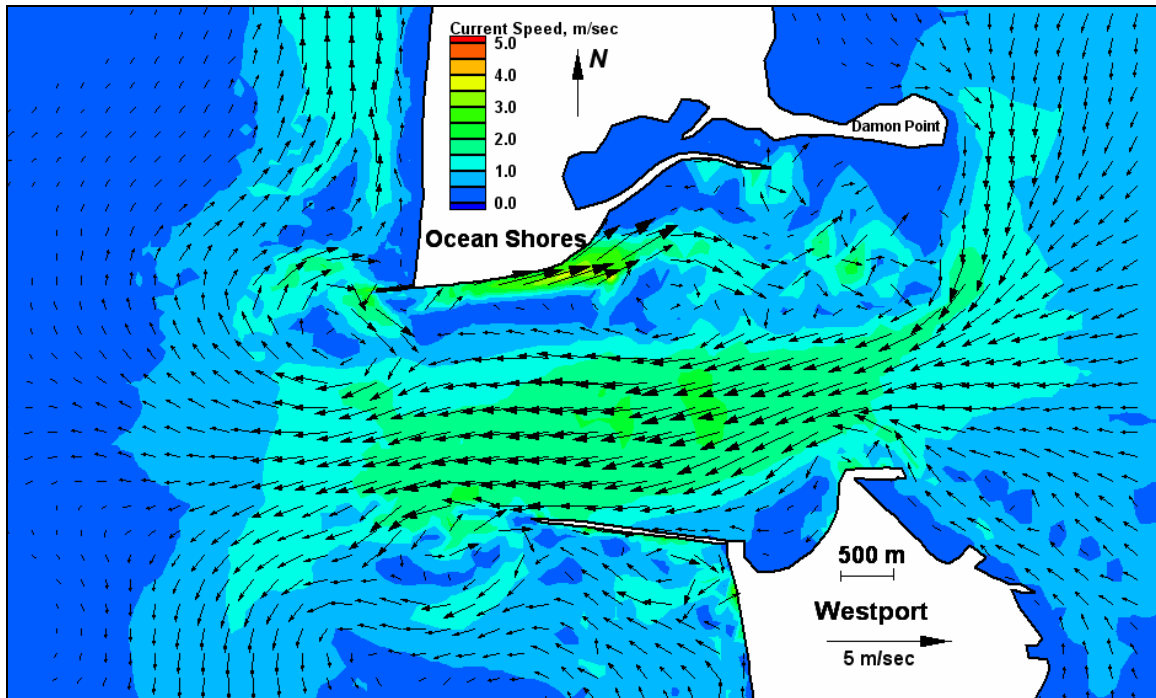
Figure E181. Run 148 (Alt 2B, west-southwest, spring tide), inlet view of ebb tide
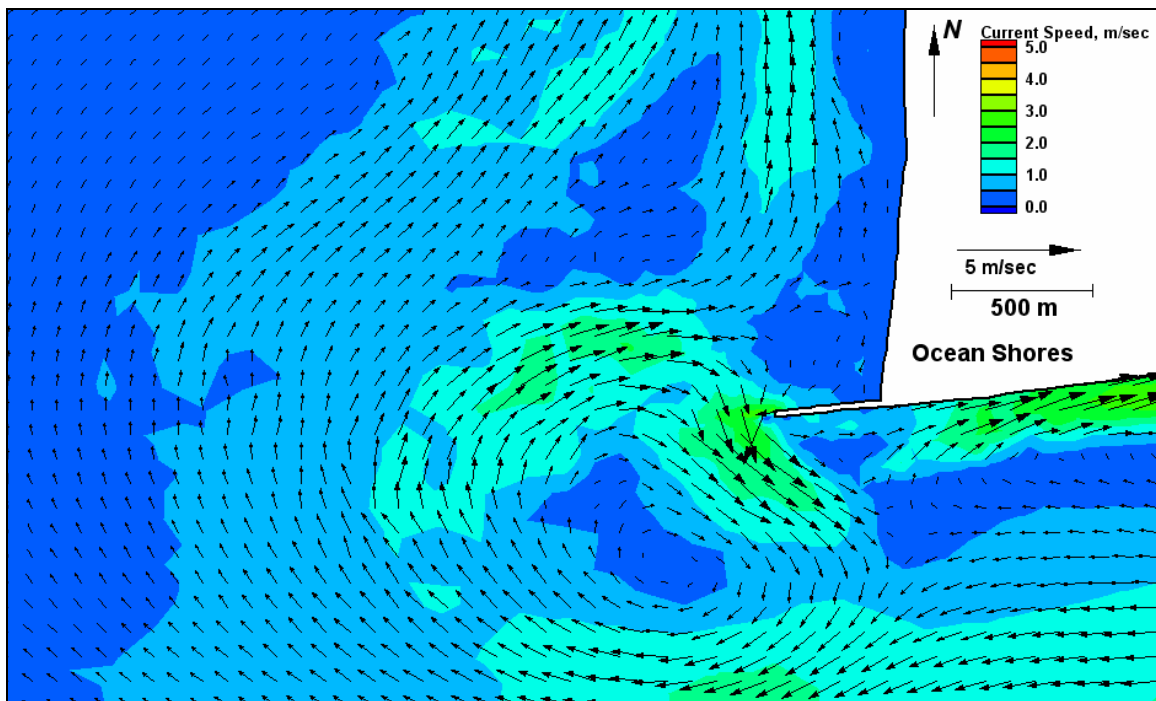
Figure E182. Run 148 (Alt 2B, west-southwest, spring tide), north jetty view of ebb tide

E92
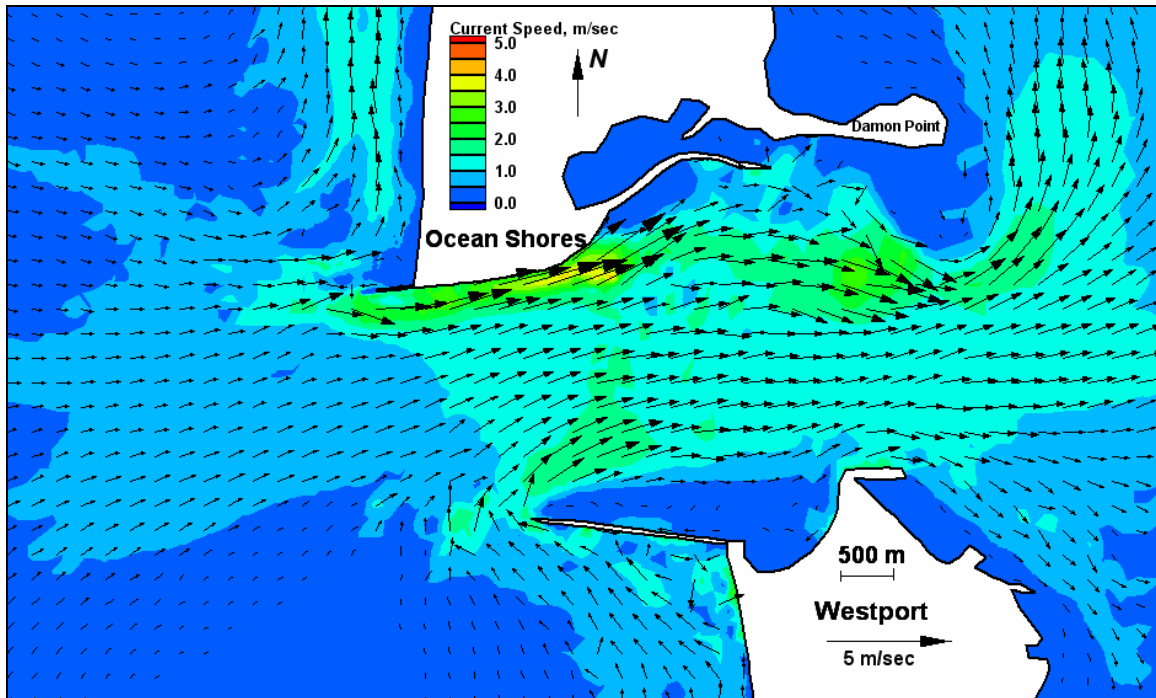
Figure E183. Run 149 (Alt 3A, west-southwest, spring tide), inlet view of flood tide
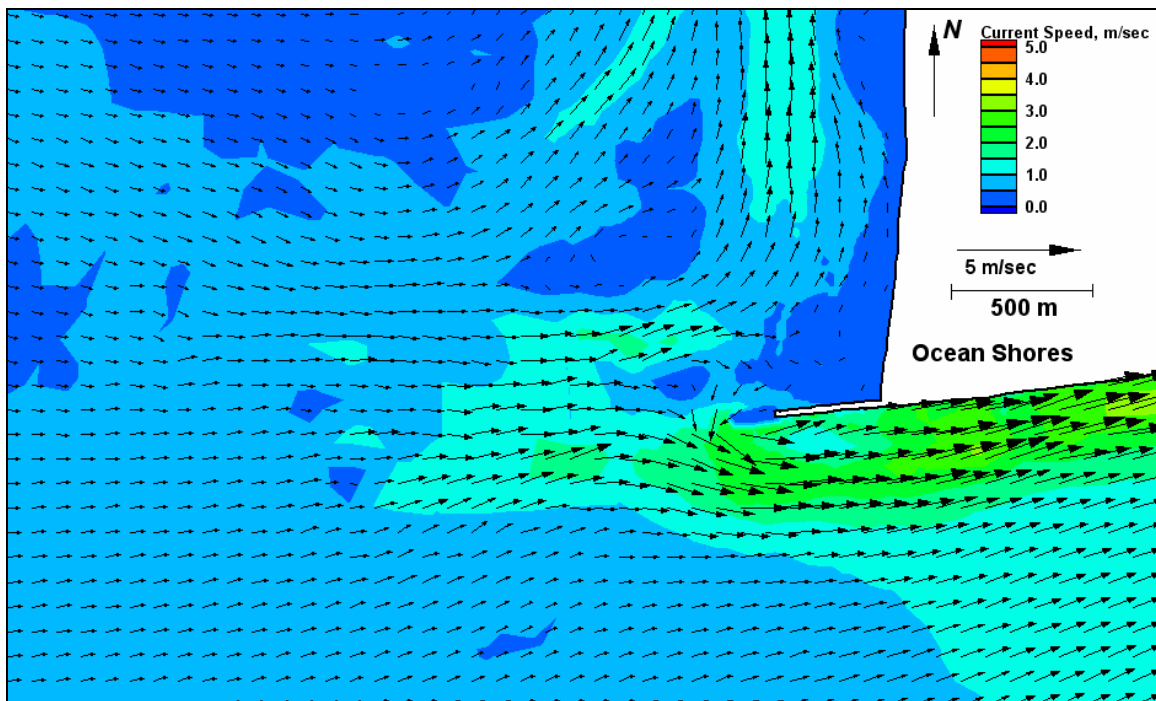
Figure E184. Run 149 (Alt 3A, west-southwest, spring tide), north jetty view of flood tide
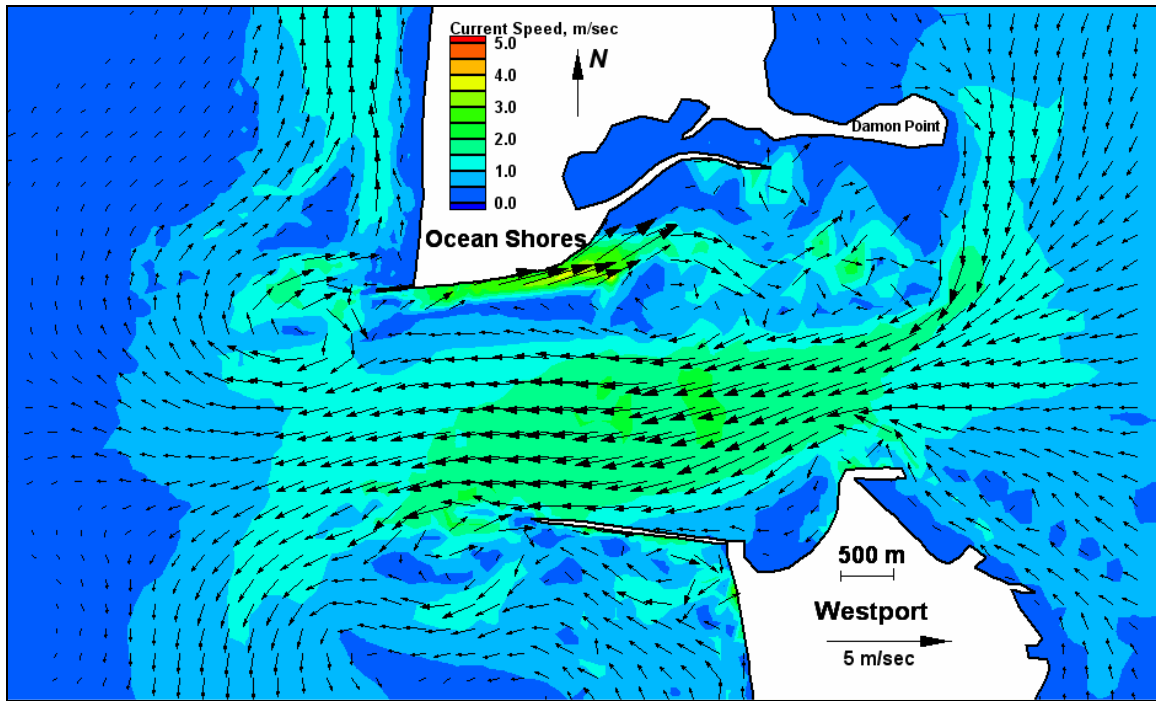
Figure E185. Run 149 (Alt 3A, west-southwest, spring tide), inlet view of ebb tide
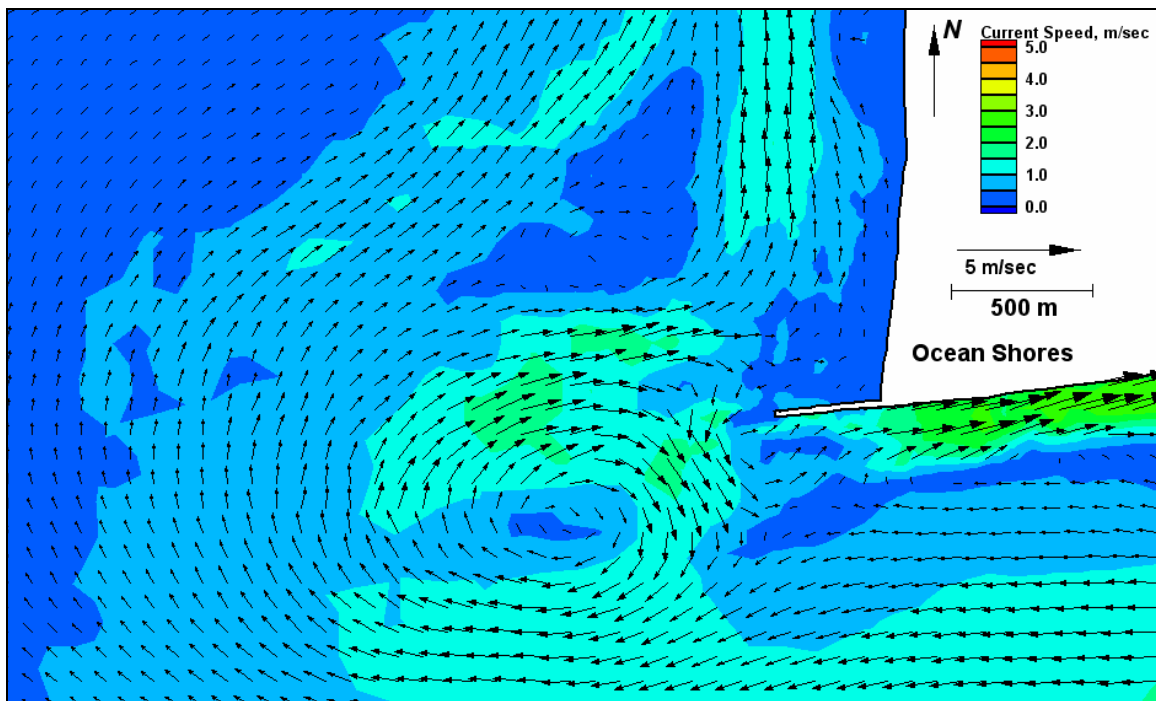
Figure E186. Run 149 (Alt 3A, west-southwest, spring tide), north jetty view of ebb tide
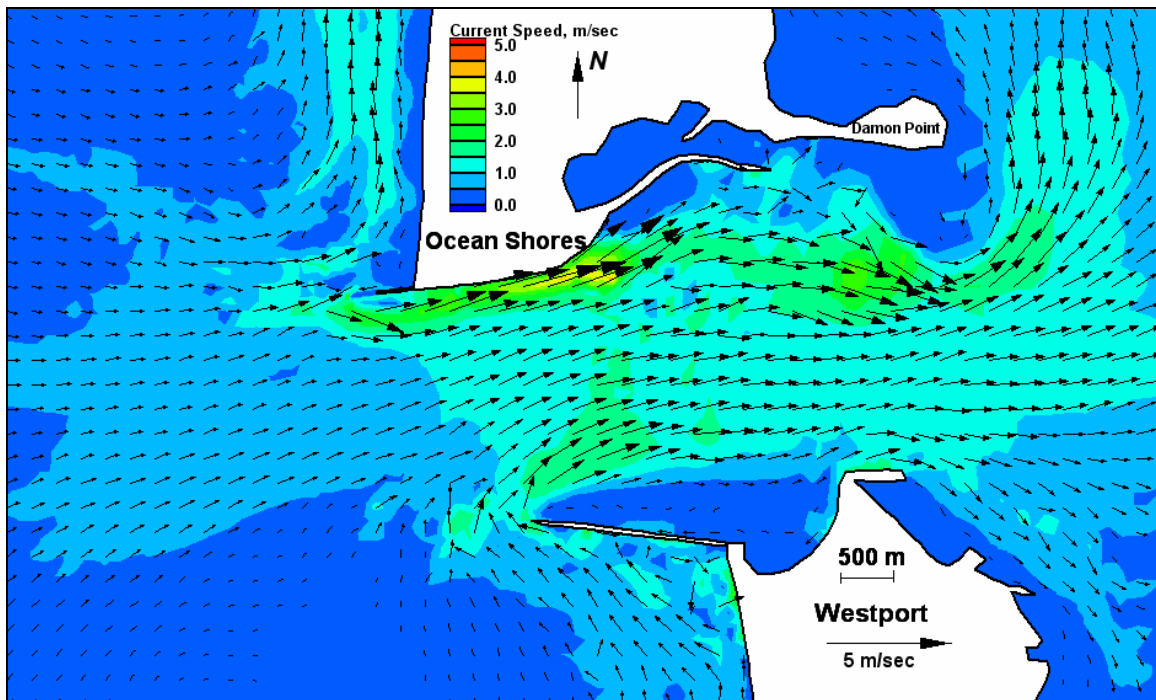
Figure E187. Run 150 (Alt 3B, west-southwest, spring tide), inlet view of flood tide
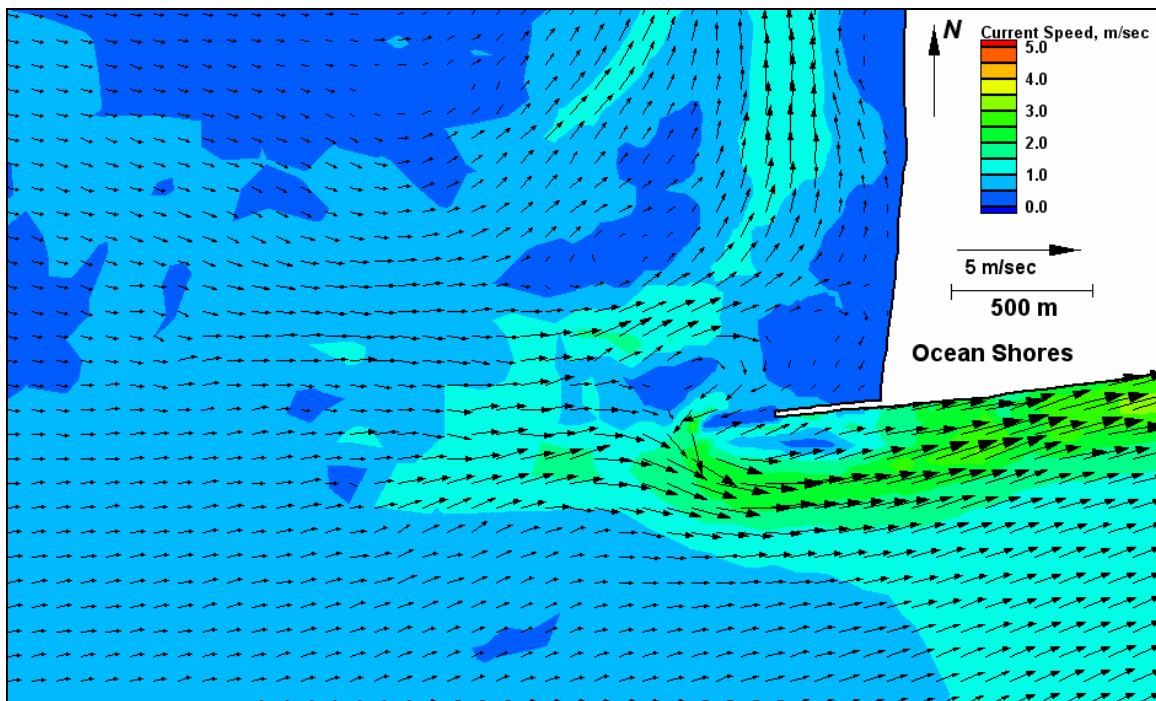
Figure E188. Run 150 (Alt 3B, west-southwest, spring tide), north jetty view of flood tide
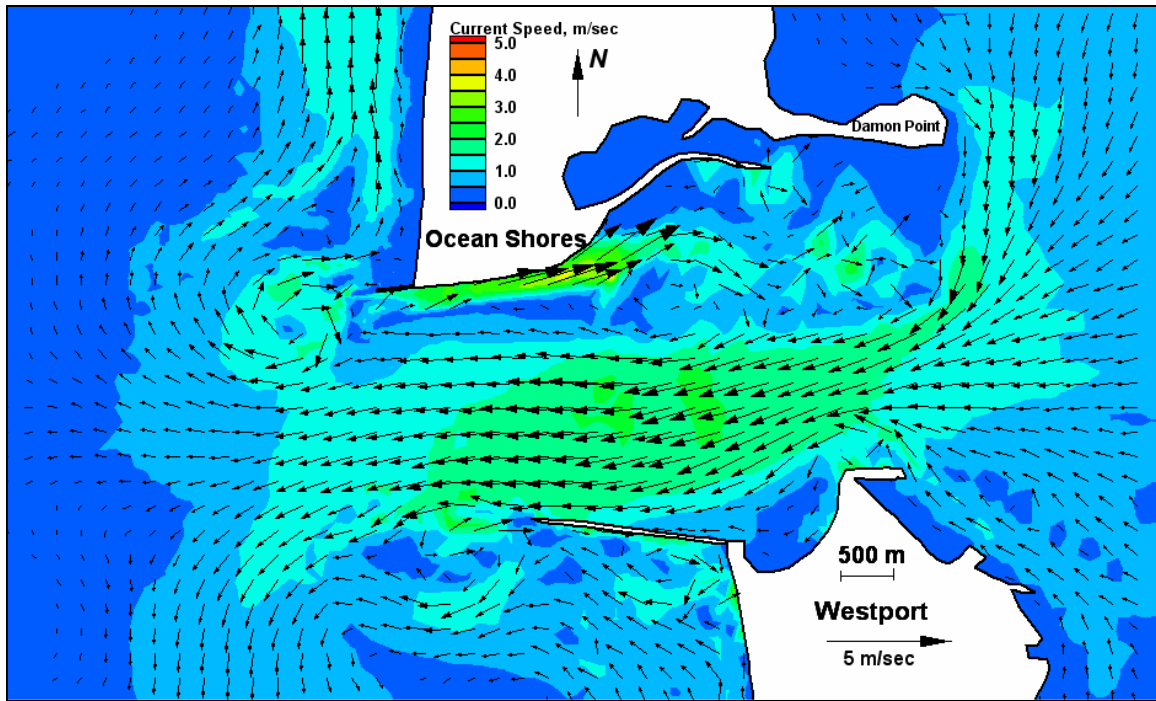
Figure E189. Run 150 (Alt 3B, west-southwest, spring tide), inlet view of ebb tide
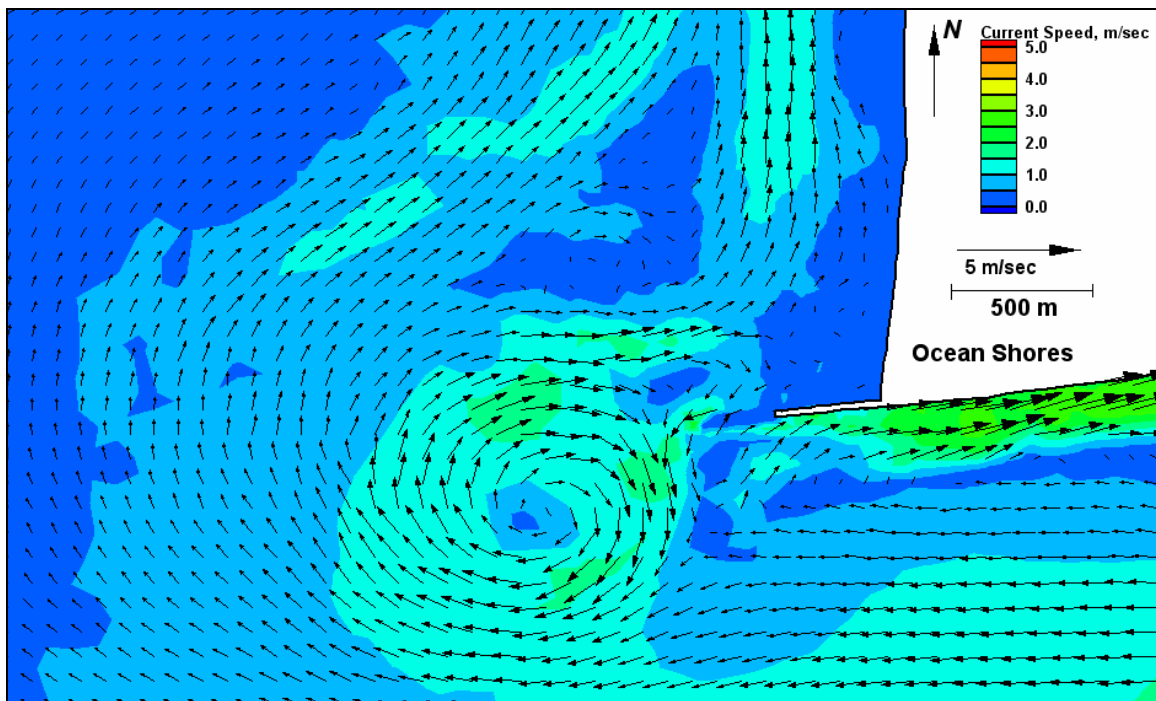
Figure E190. Run 150 (Alt 3B, west-southwest, spring tide), north jetty view of ebb tide
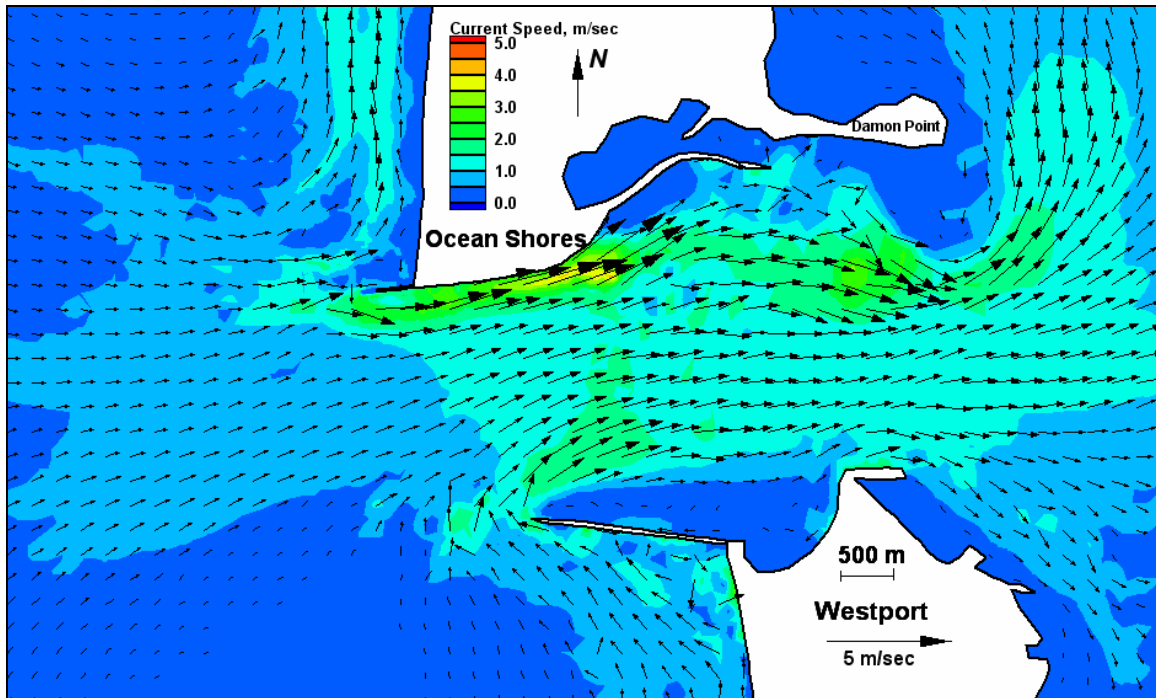
Figure E191. Run 151 (Alt 4A, west-southwest, spring tide), inlet view of flood tide
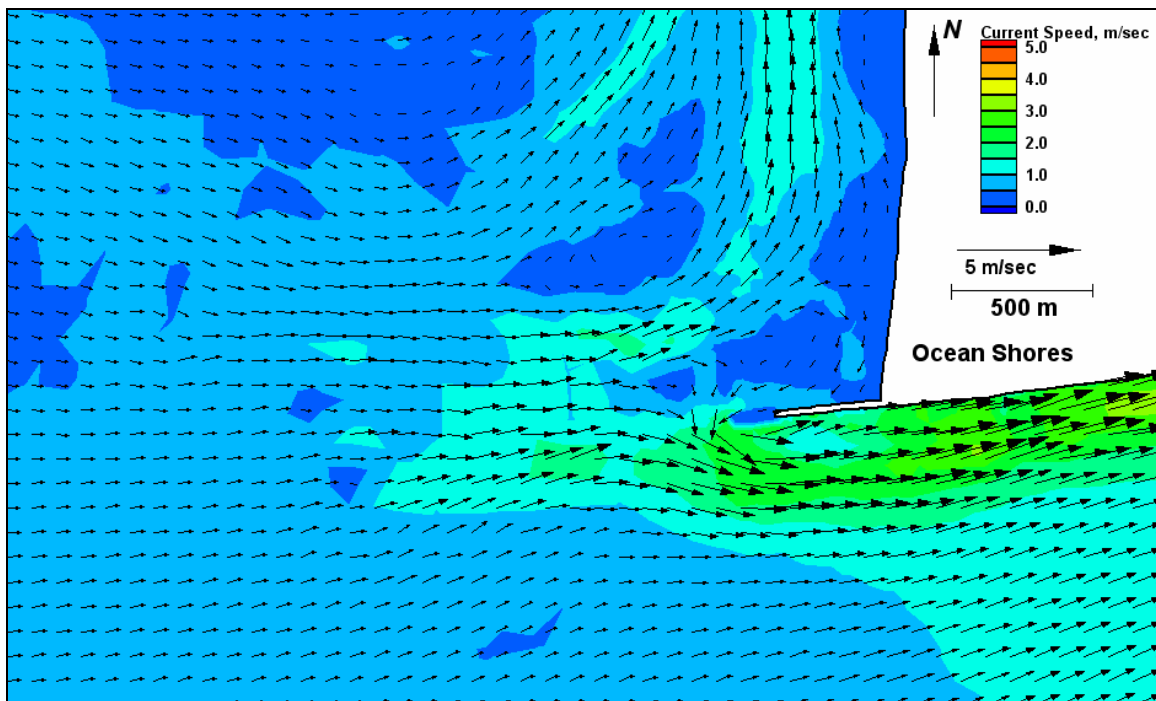
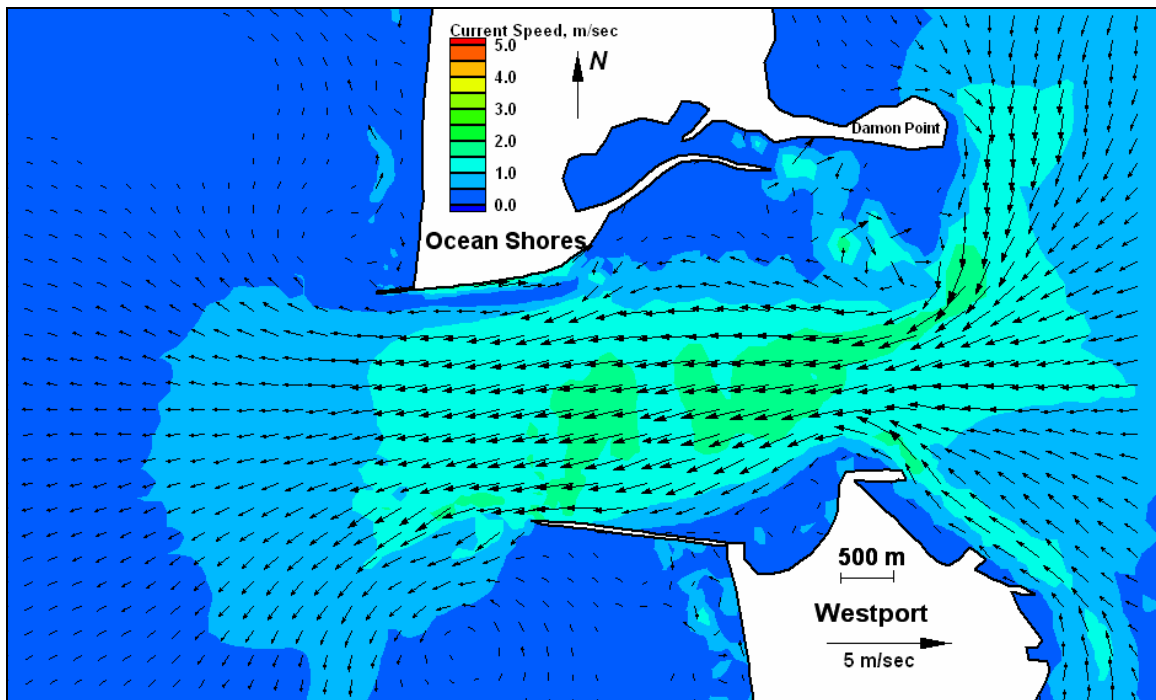Figure E192. Run 151 (Alt 4A, west-southwest, spring tide), north jetty view of flood tide
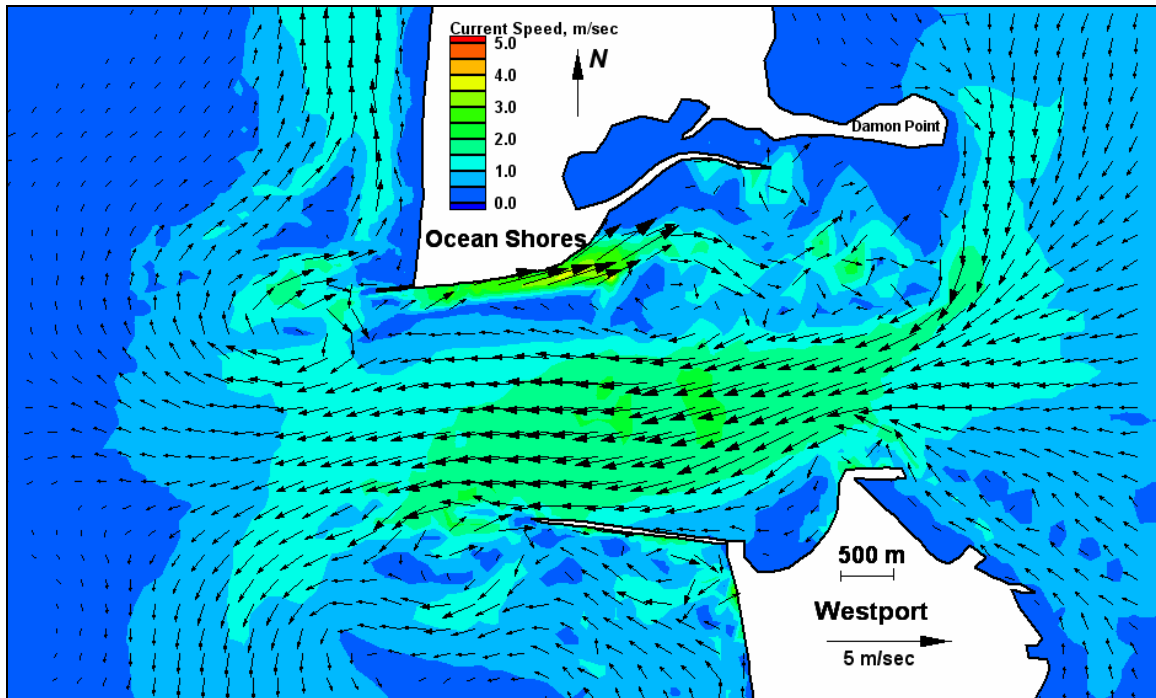
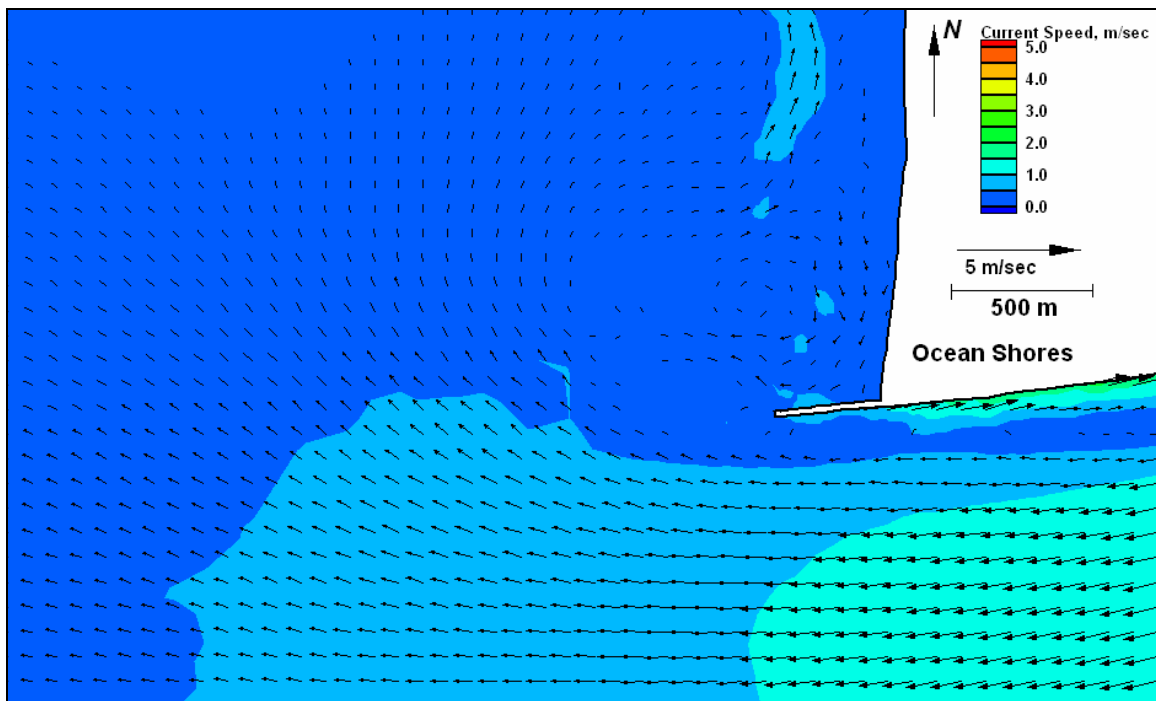Figure E193. Run 151 (Alt 4A, west-southwest, spring tide), inlet view of ebb tide
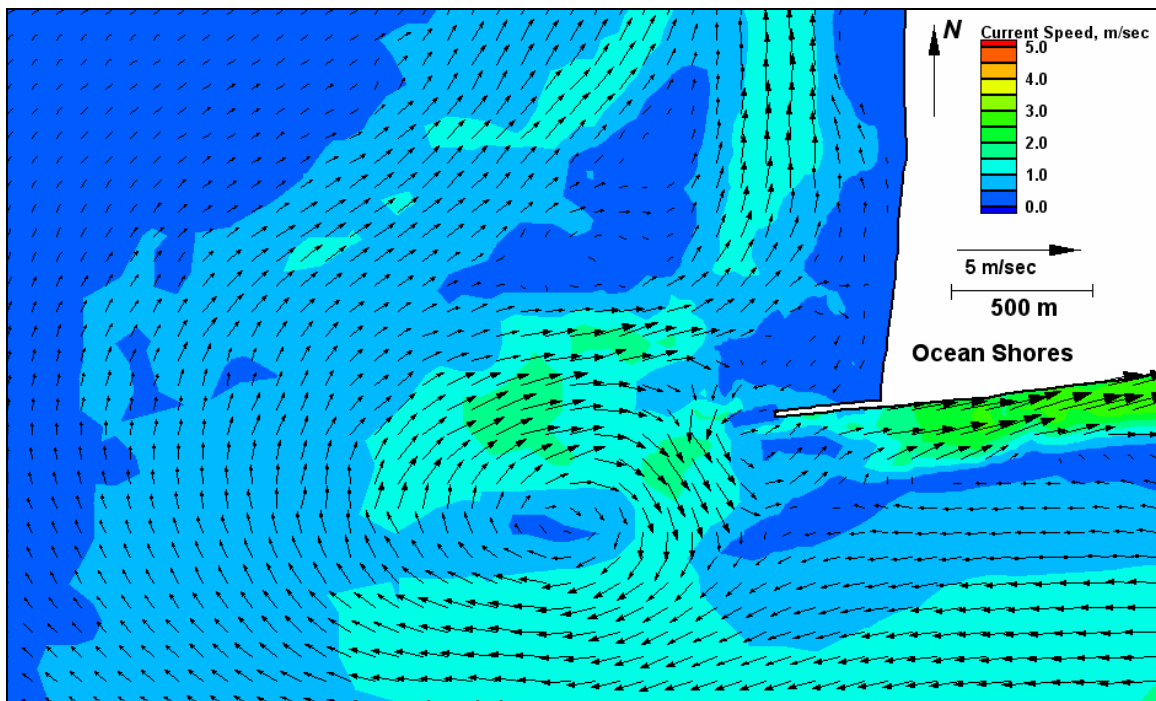
Figure E194. Run 151 (Alt 4A, west-southwest, spring tide), north jetty view of ebb tide

E98
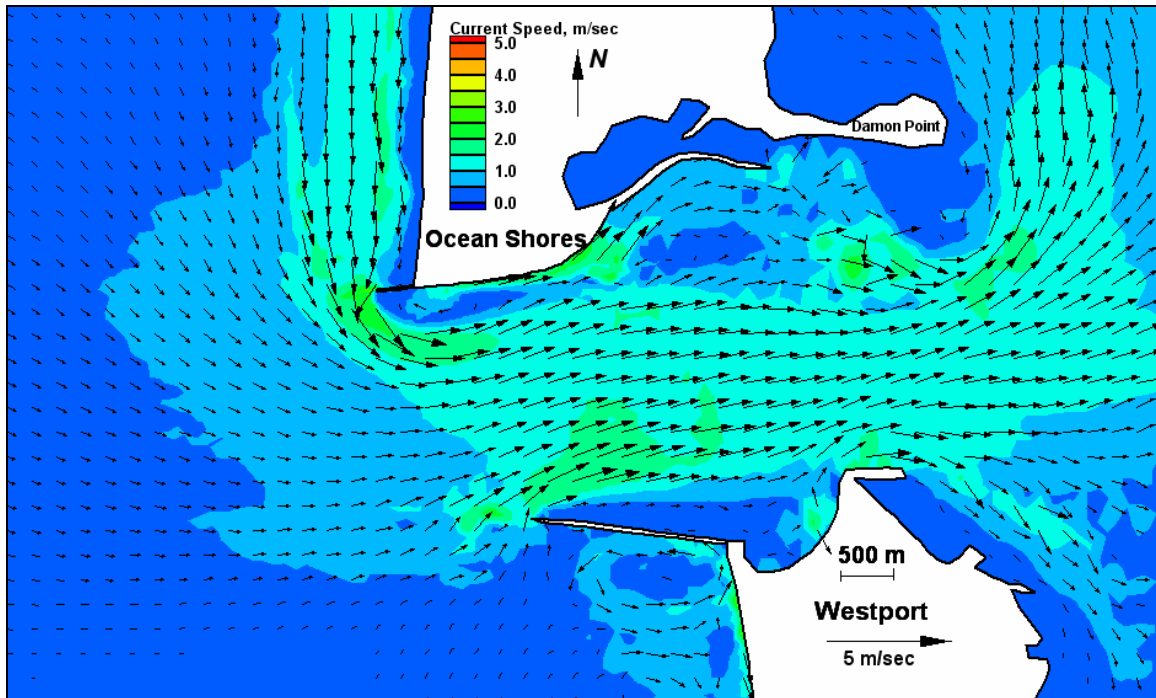
Figure E195. Run 152 (existing, west-northwest, spring tide), inlet view of flood tide
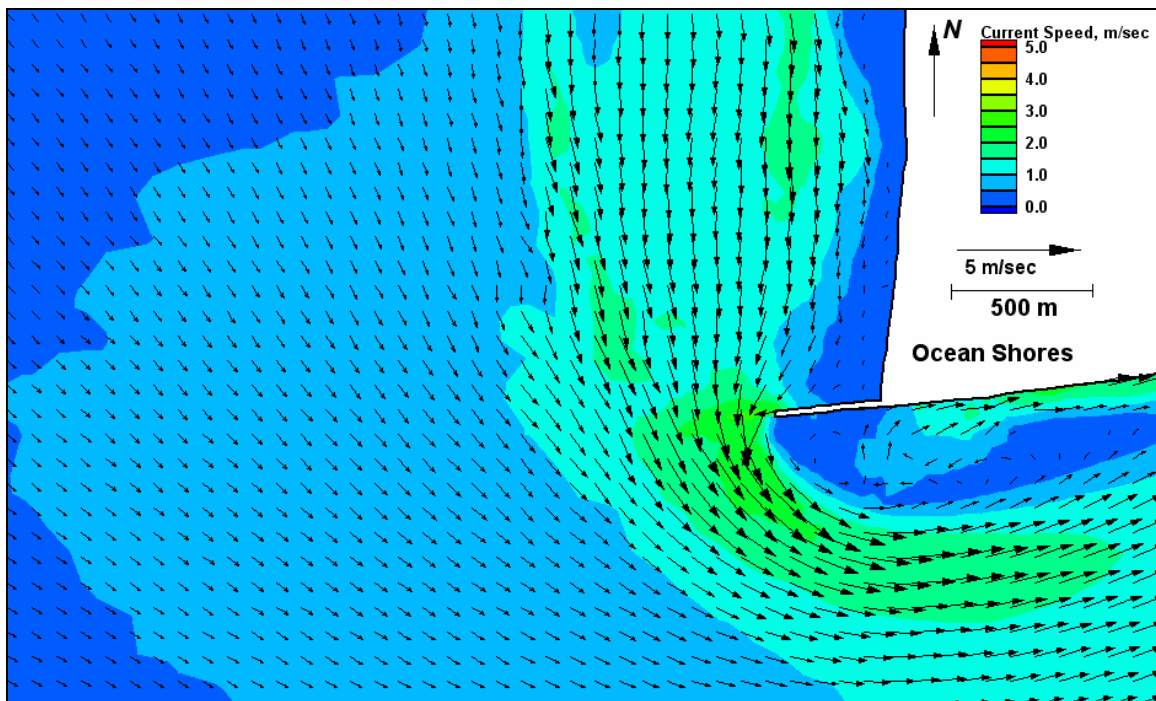
Figure E196. Run 152 (existing, west-northwest, spring tide), north jetty view of flood tide
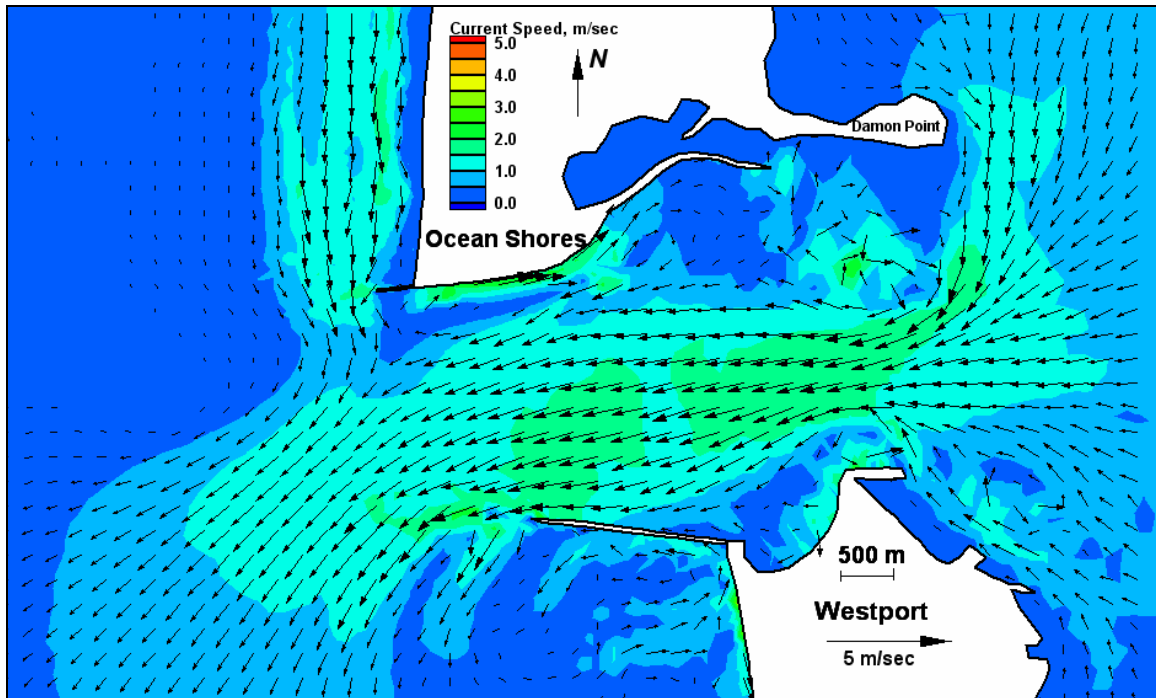
Figure E197. Run 152 (existing, west-northwest, spring tide), inlet view of ebb tide
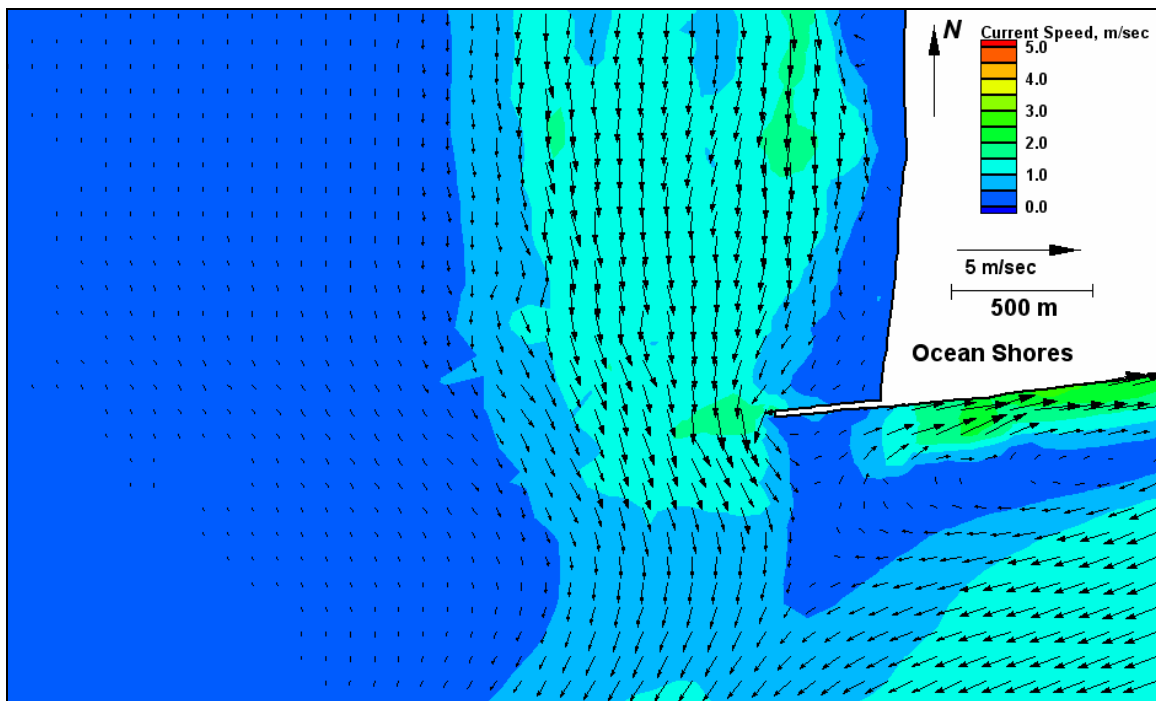
Figure E198. Run 152 (existing, west-northwest, spring tide), north jetty view of ebb tide
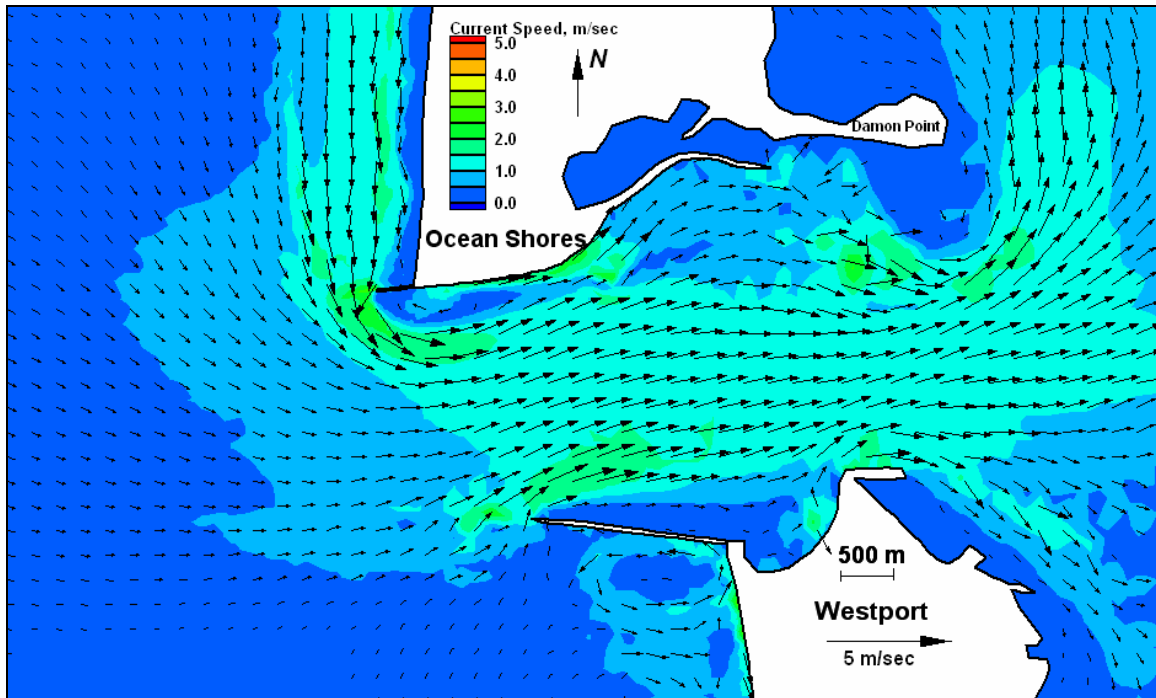
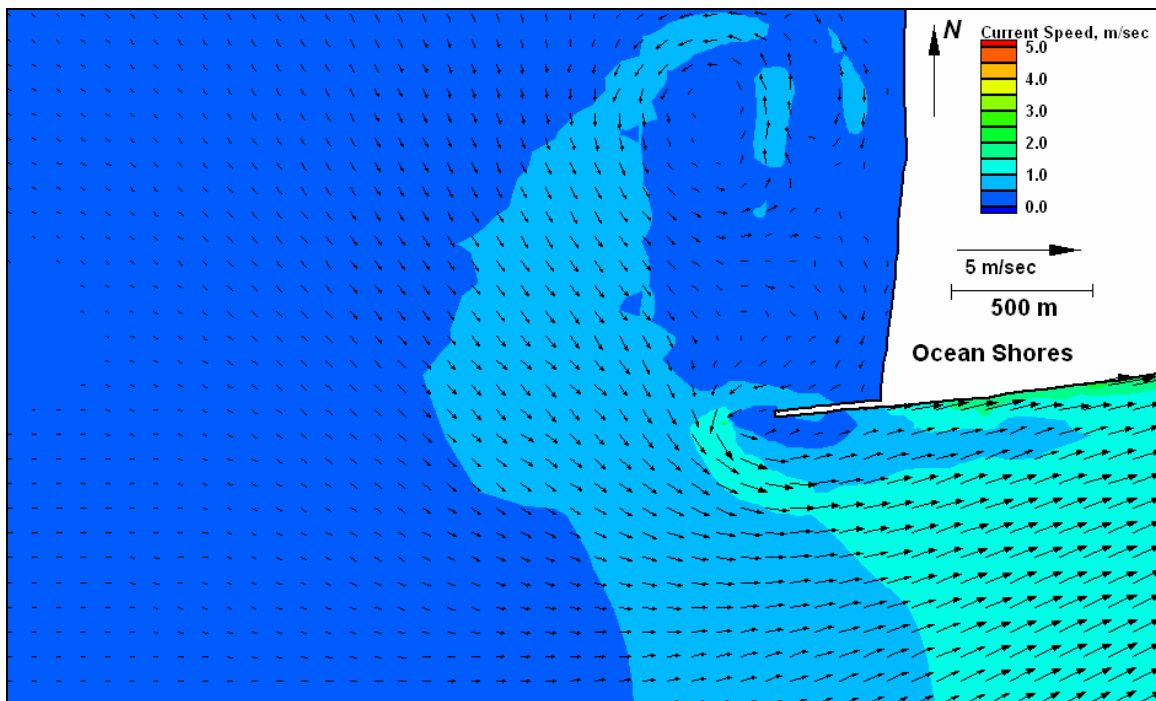Figure E199. Run 153 (Alt 2A, west-northwest, spring tide), inlet view of flood tide
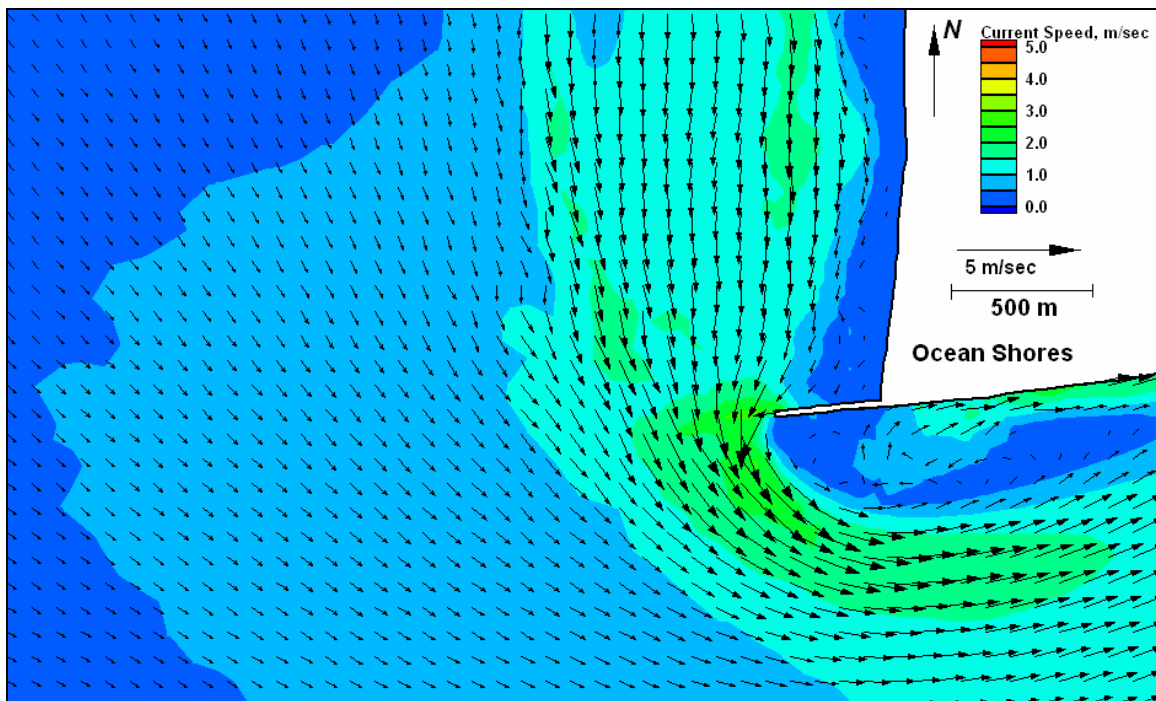
Figure E200. Run 153 (existing, west-northwest, spring tide), north jetty view of flood tide
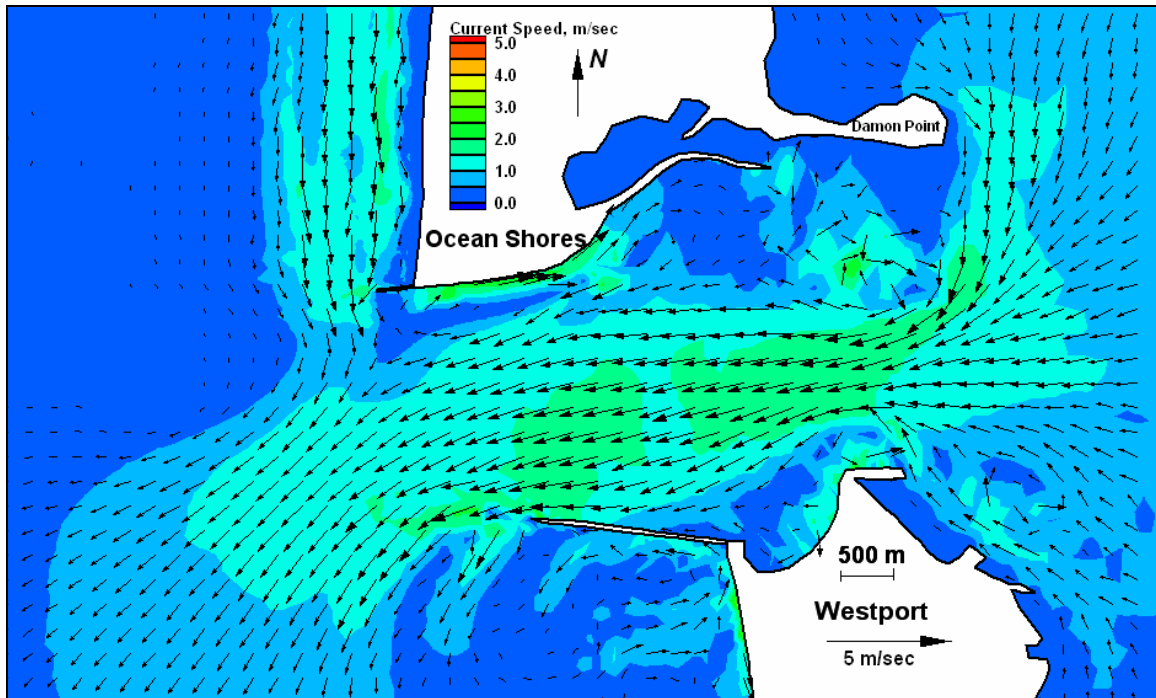
Figure E201. Run 153 (existing, west-northwest, spring tide), inlet view of ebb tide
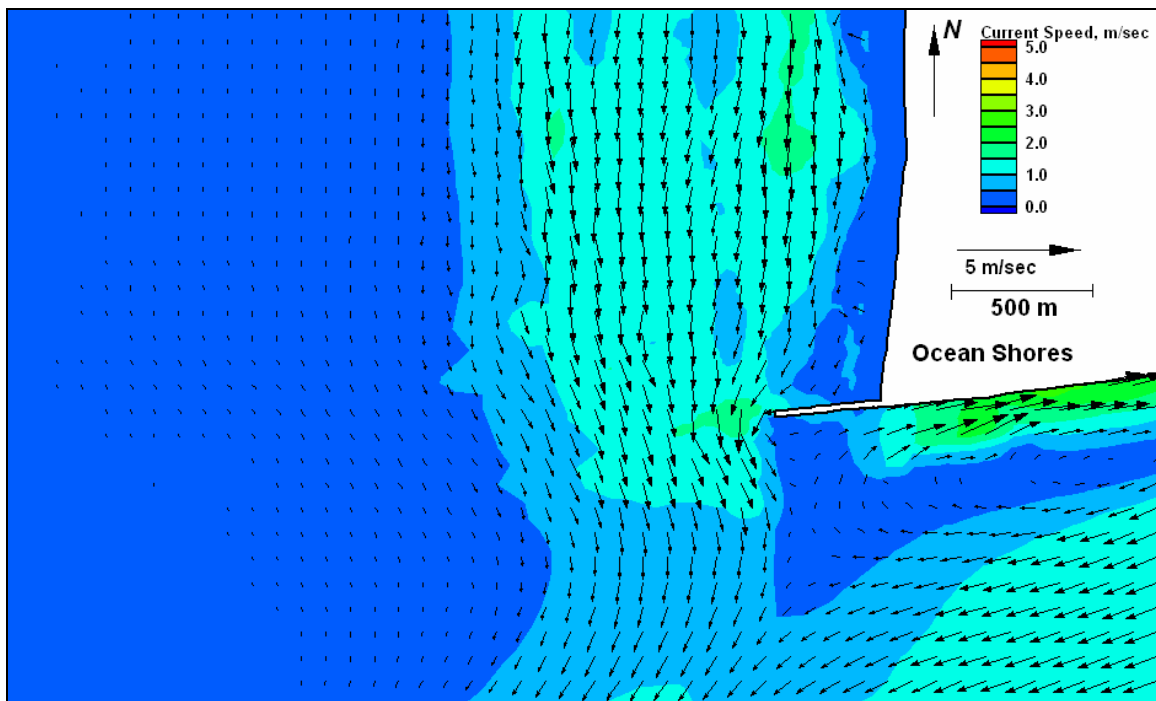
Figure E202. Run 153 (existing, west-northwest, spring tide), north jetty view of ebb tide
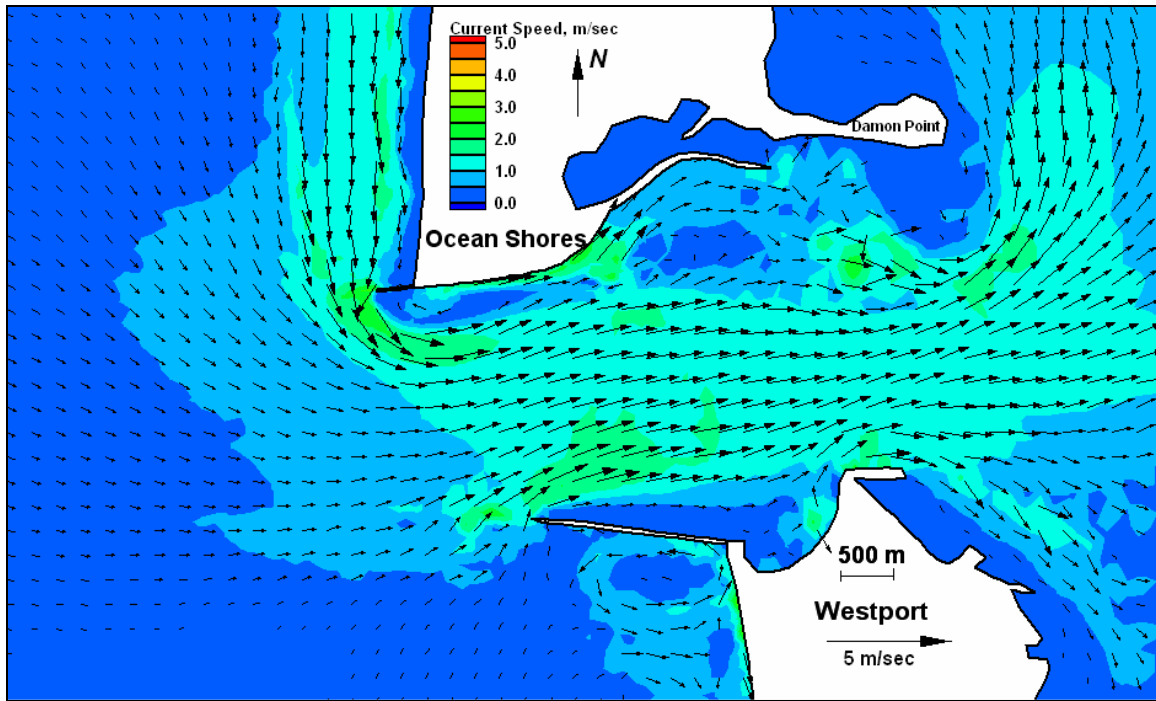
Figure E203. Run 154 (Alt 2B, west-northwest, spring tide), inlet view of flood tide
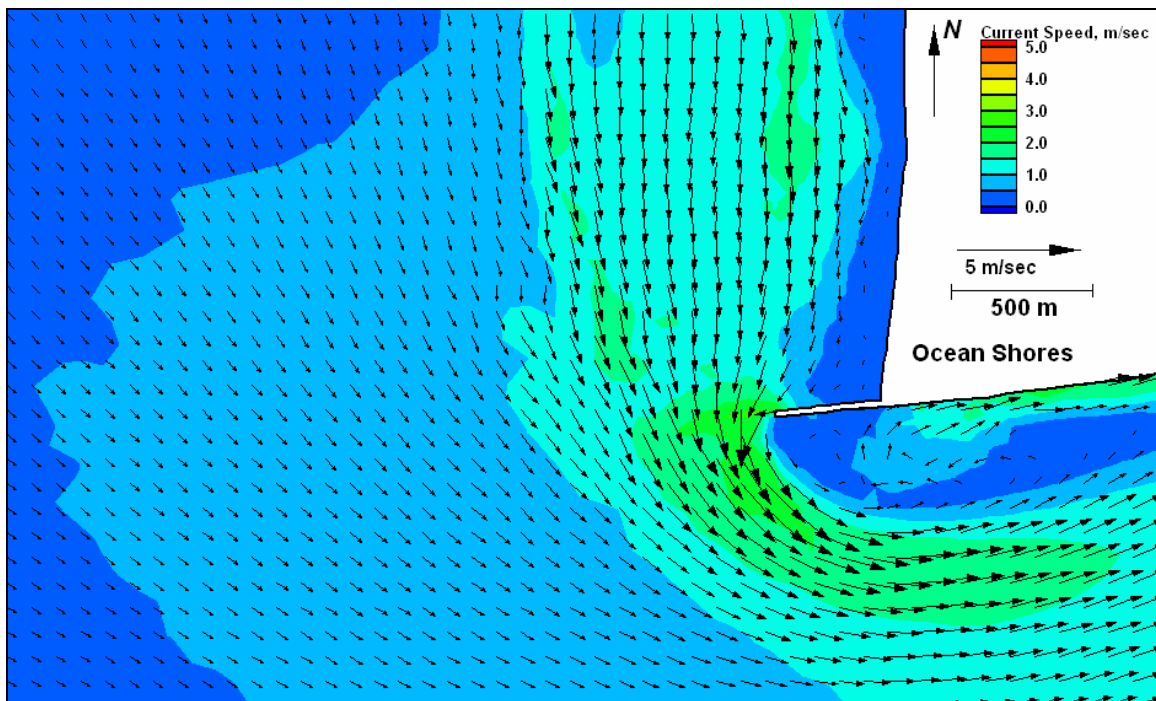
Figure E204. Run 154 (Alt 2B, west-northwest, spring tide), north jetty view of flood tide
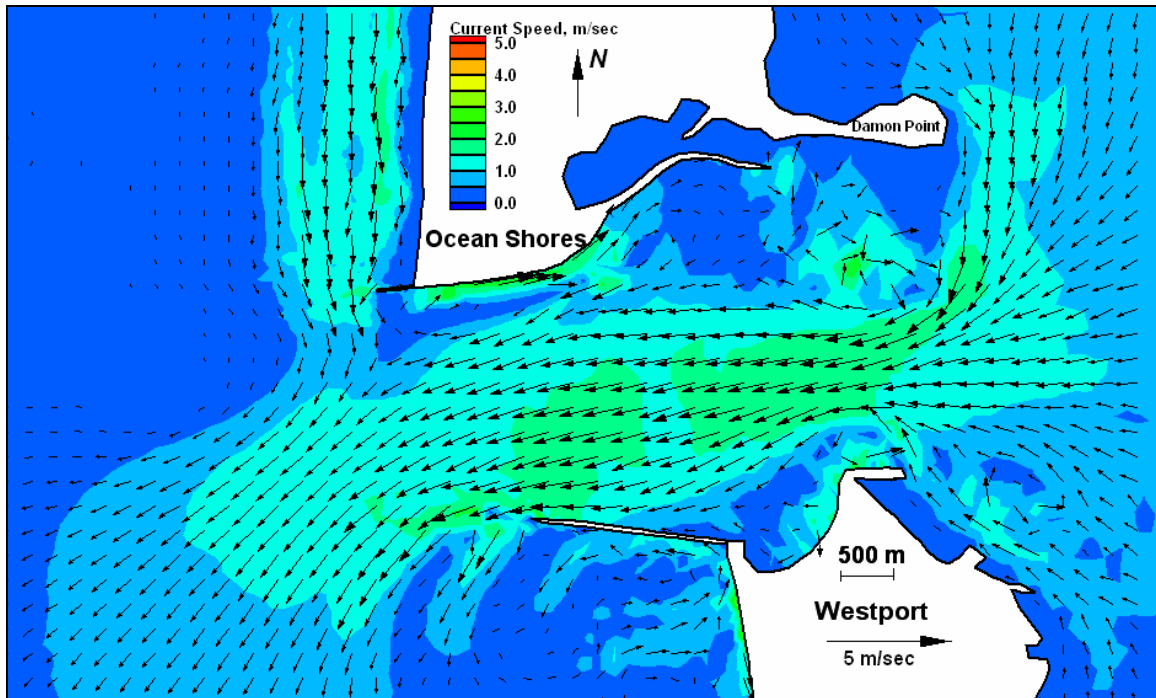
Figure E205. Run 154 (Alt 2B, west-northwest, spring tide), inlet view of ebb tide
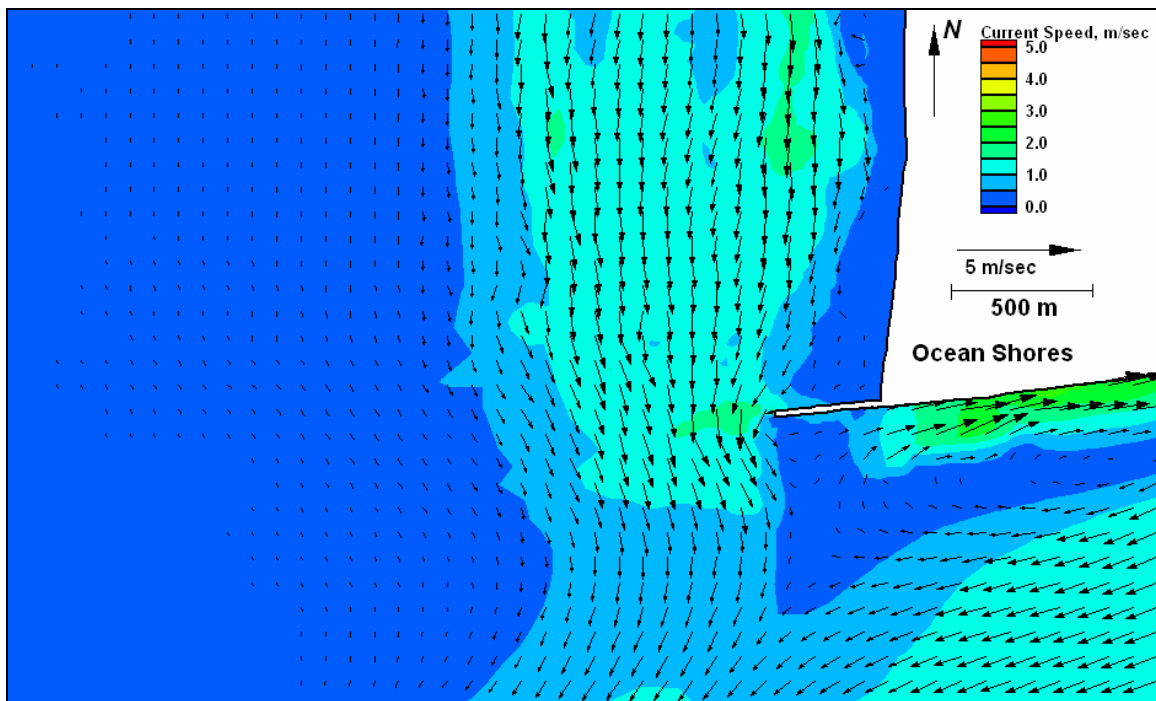
Figure E206. Run 154 (Alt 2B, west-northwest, spring tide), north jetty view of ebb tide

Appendix E   Tidal Circulation Simulation Results
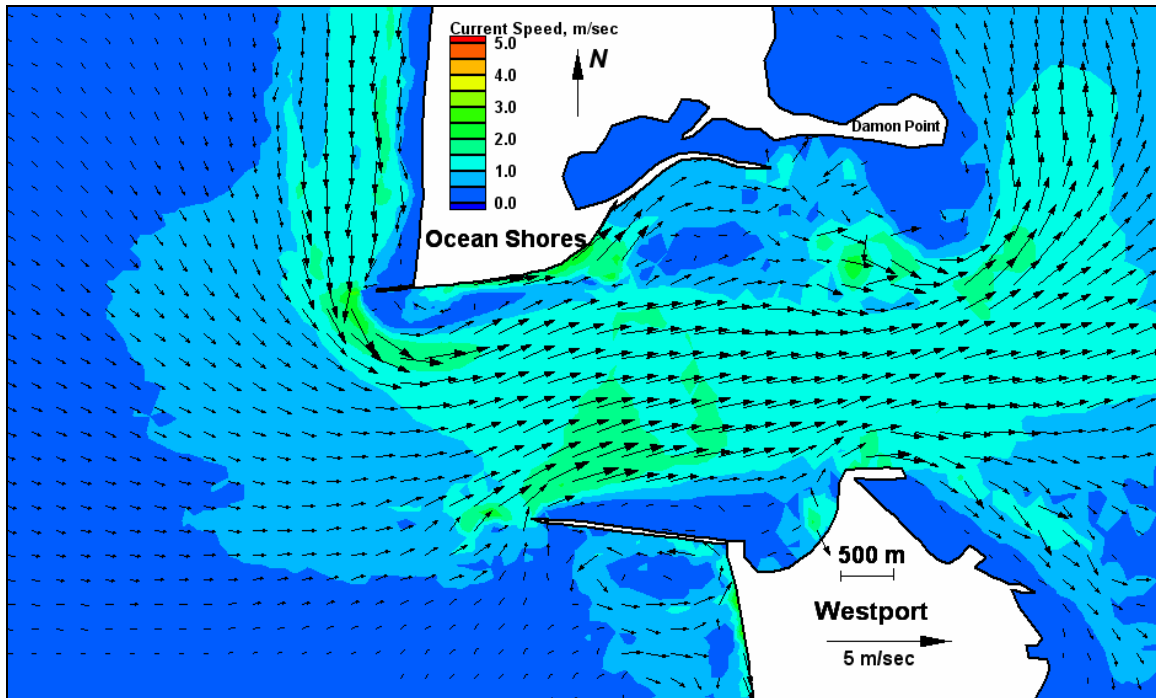
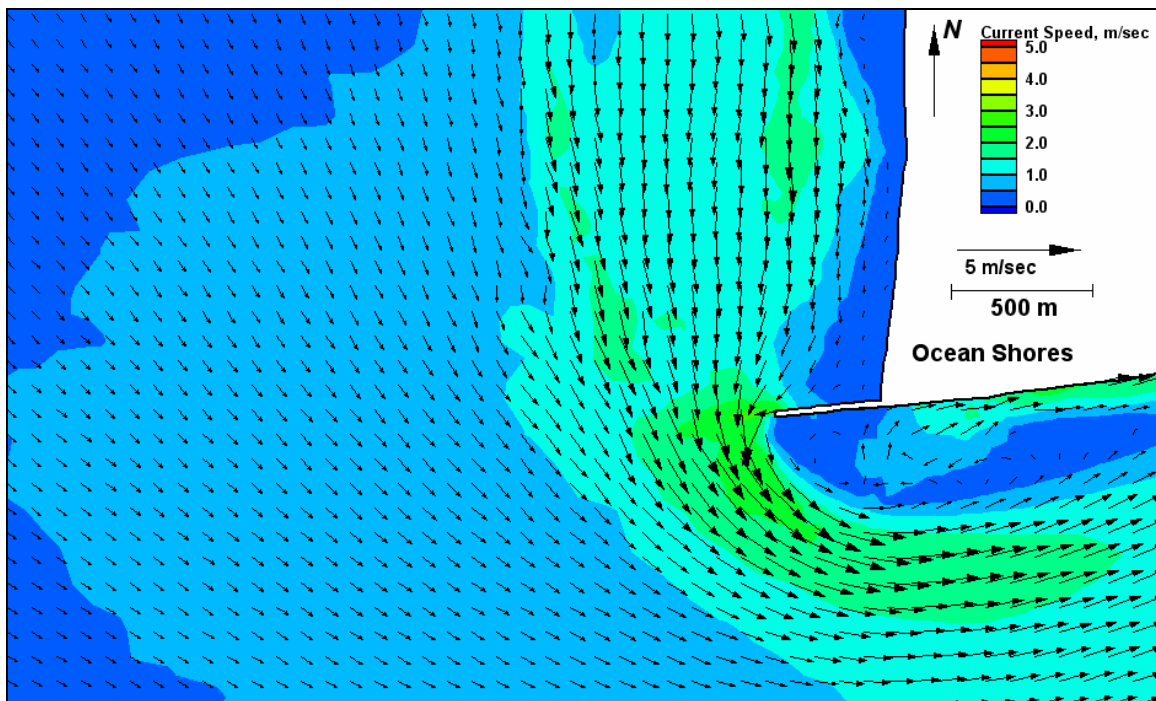Figure E207. Run 155 (Alt 3A, west-northwest, spring tide), inlet view of flood tide
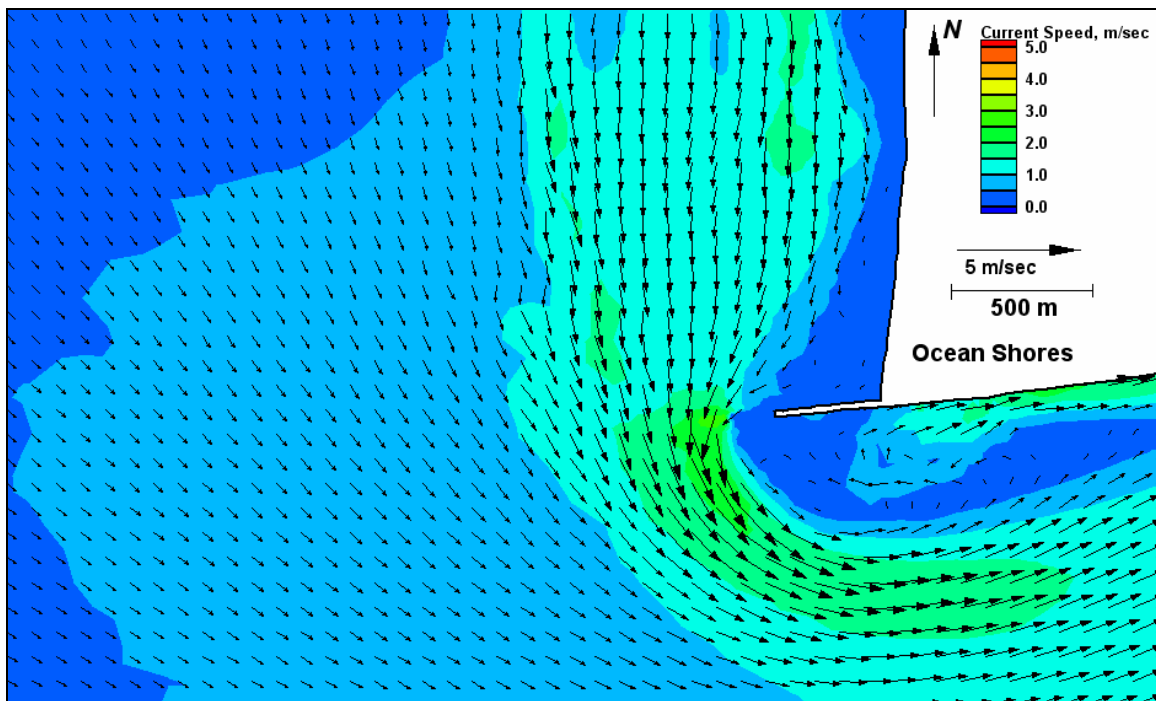
Figure E208. Run 155 (Alt 2B, west-northwest, spring tide), north jetty view of flood tide
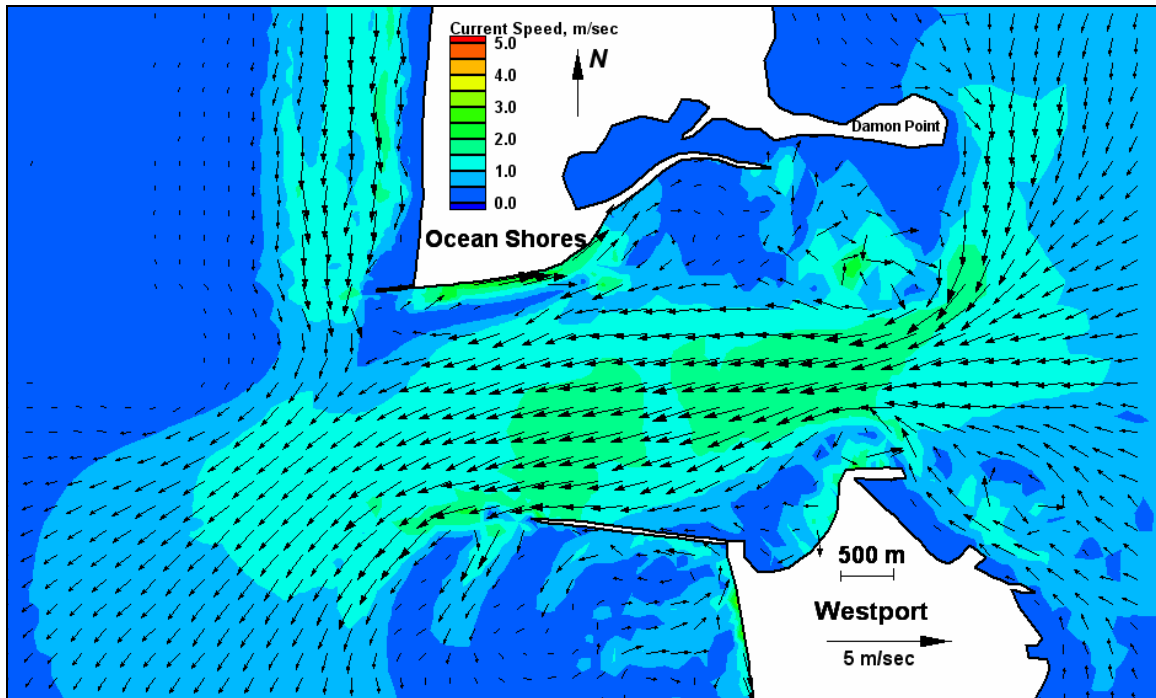
Figure E209. Run 155 (Alt 2B, west-northwest, spring tide), inlet view of ebb tide
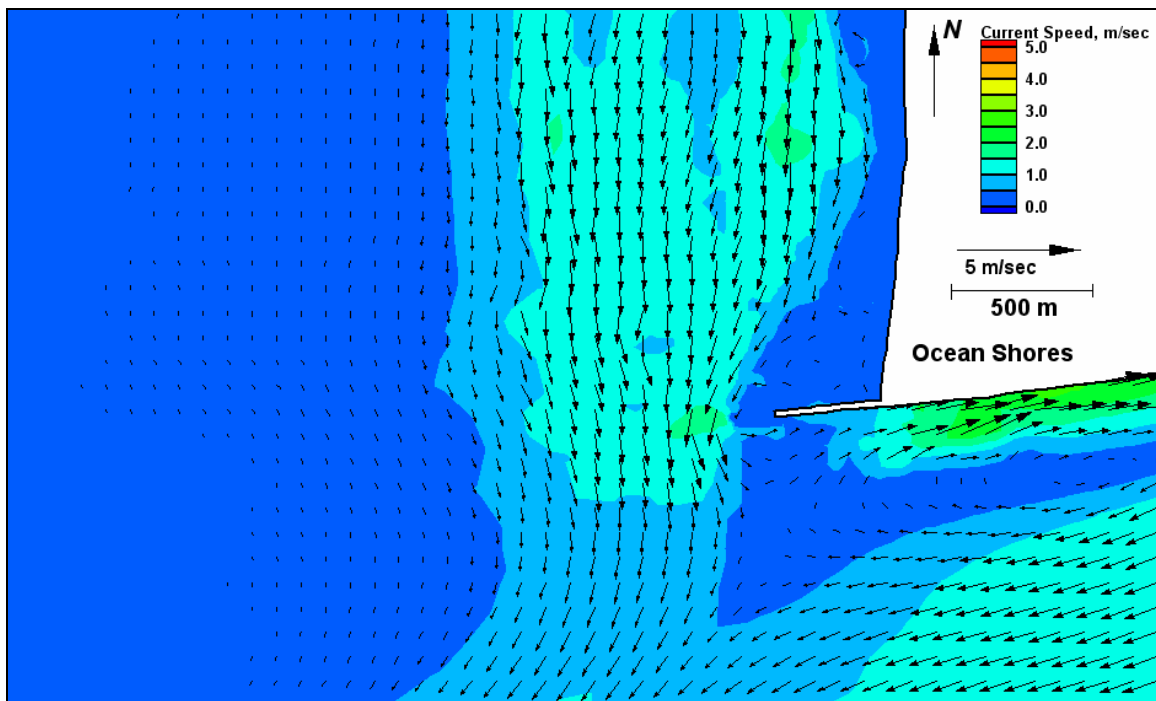
Figure E210. Run 155 (Alt 2B, west-northwest, spring tide), north jetty view of ebb tide

E106
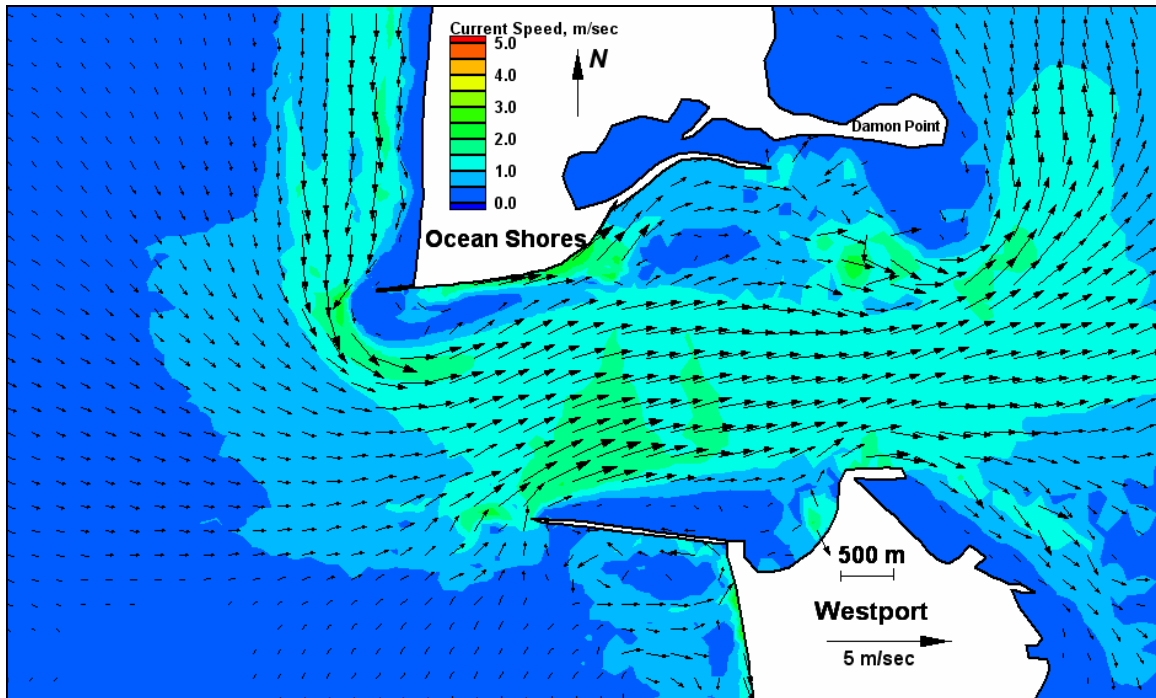
Figure E211. Run 156 (Alt 3B, west-northwest, spring tide), inlet view of flood tide
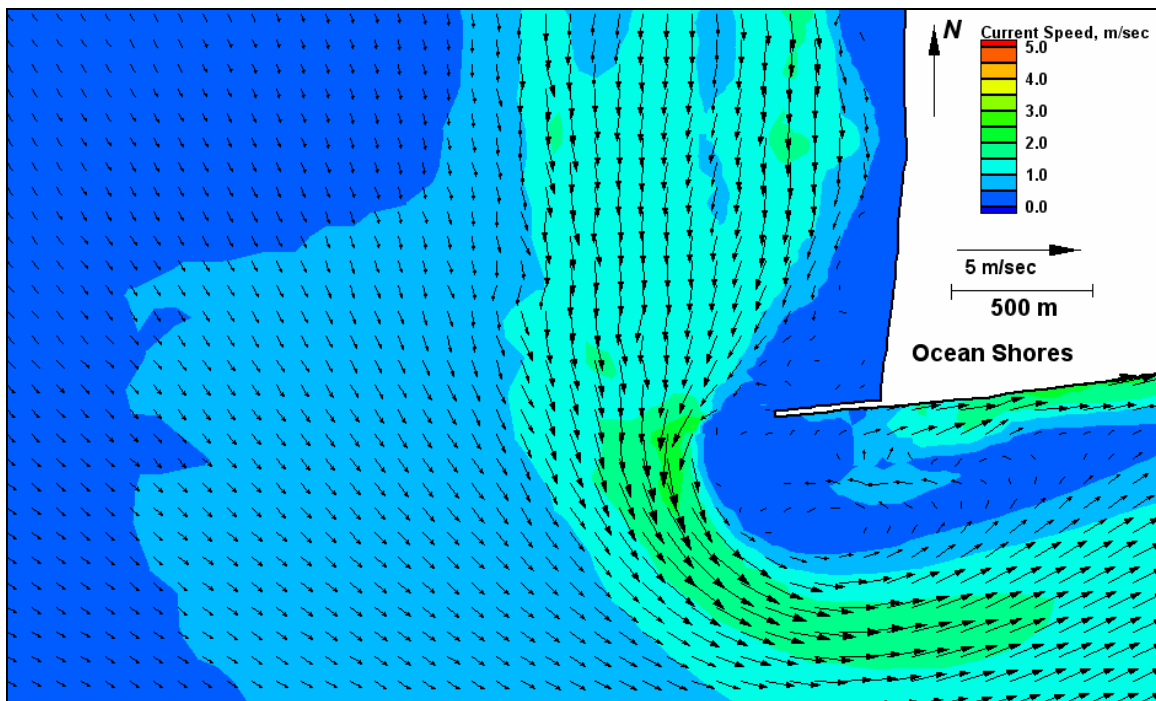
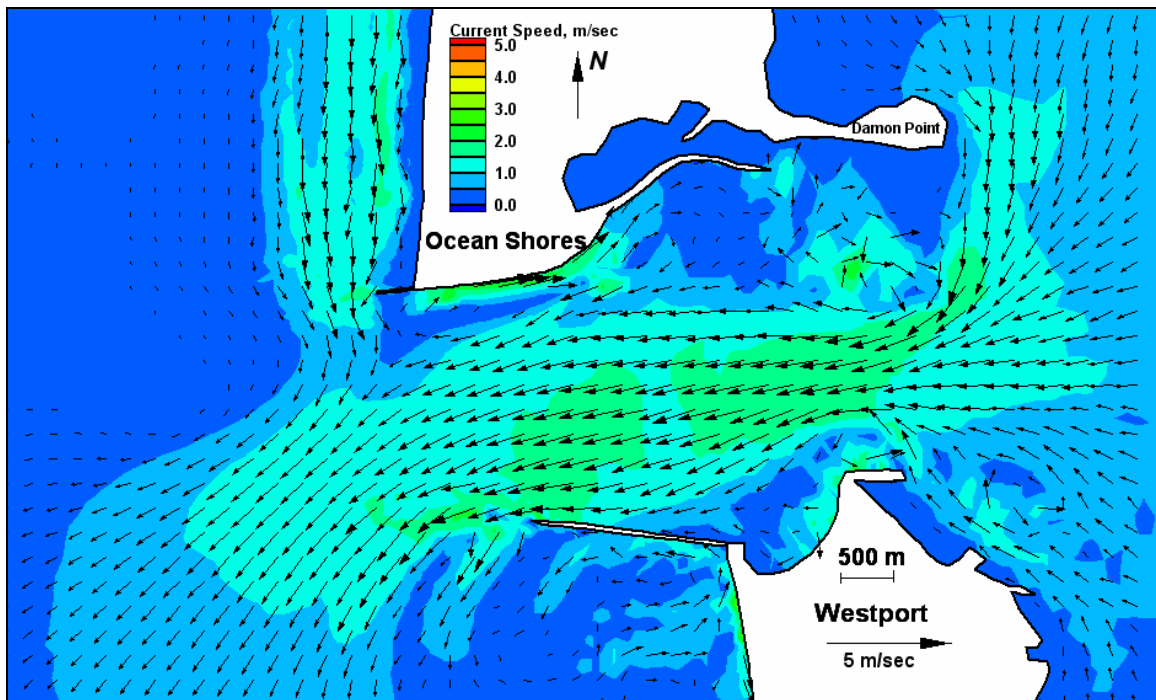Figure E212. Run 156 (Alt 2B, west-northwest, spring tide), north jetty view of flood tide
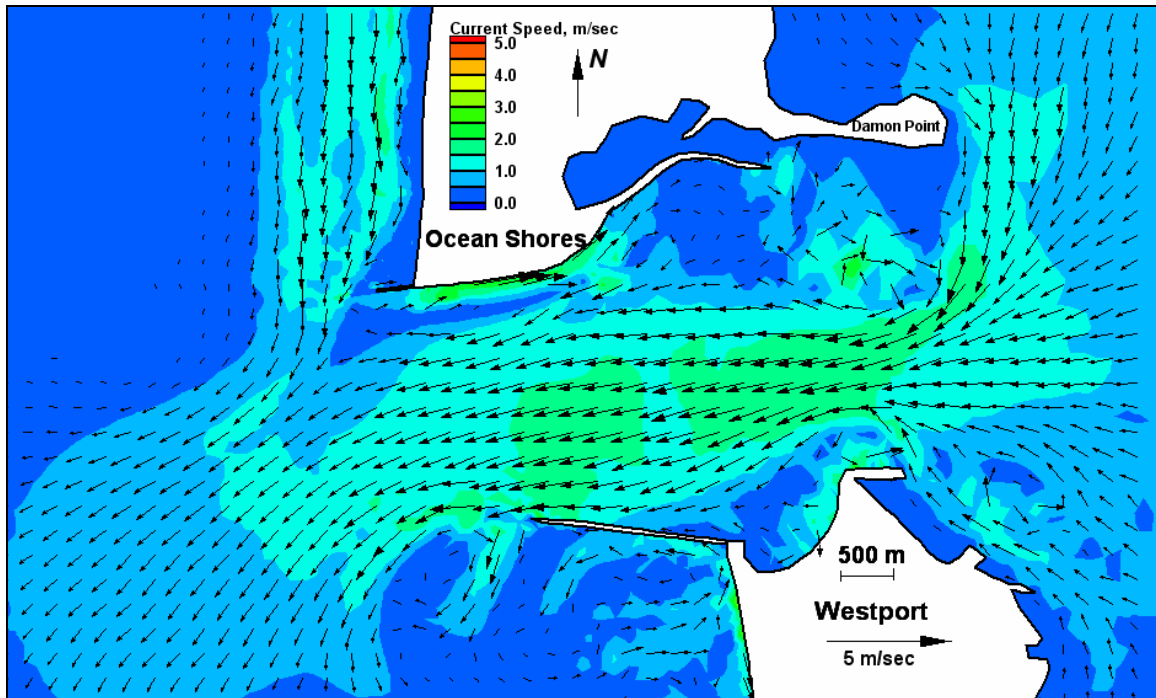
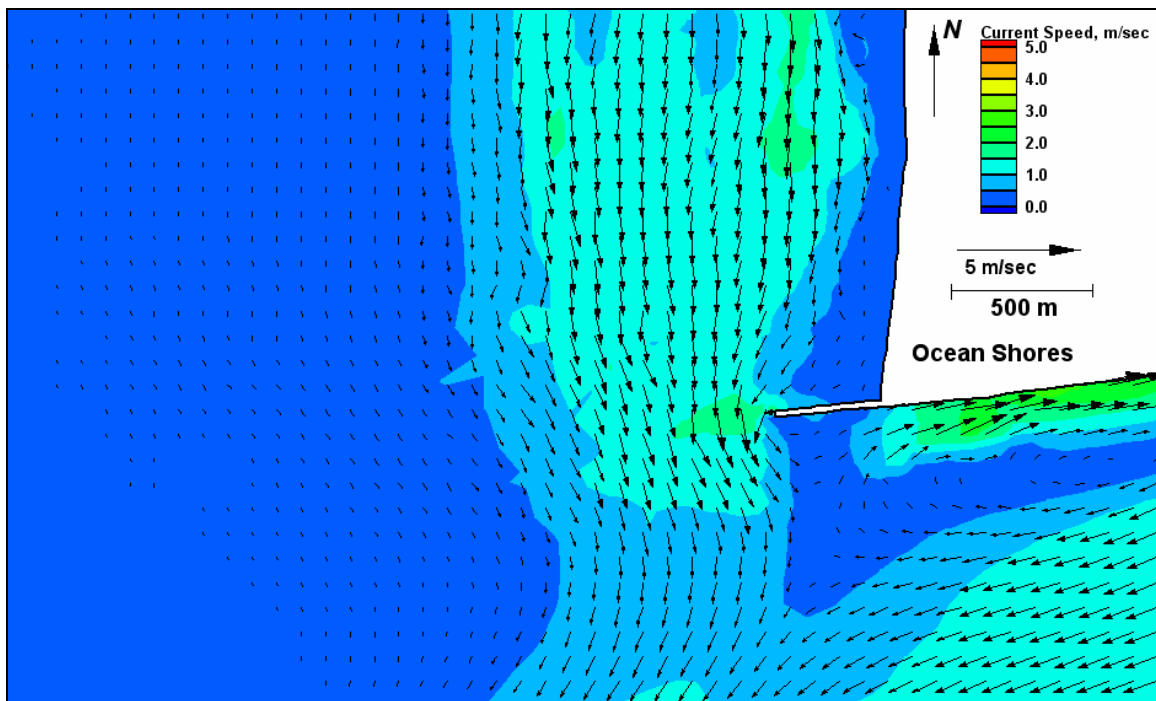Figure E213. Run 156 (Alt 2B, west-northwest, spring tide), inlet view of ebb tide
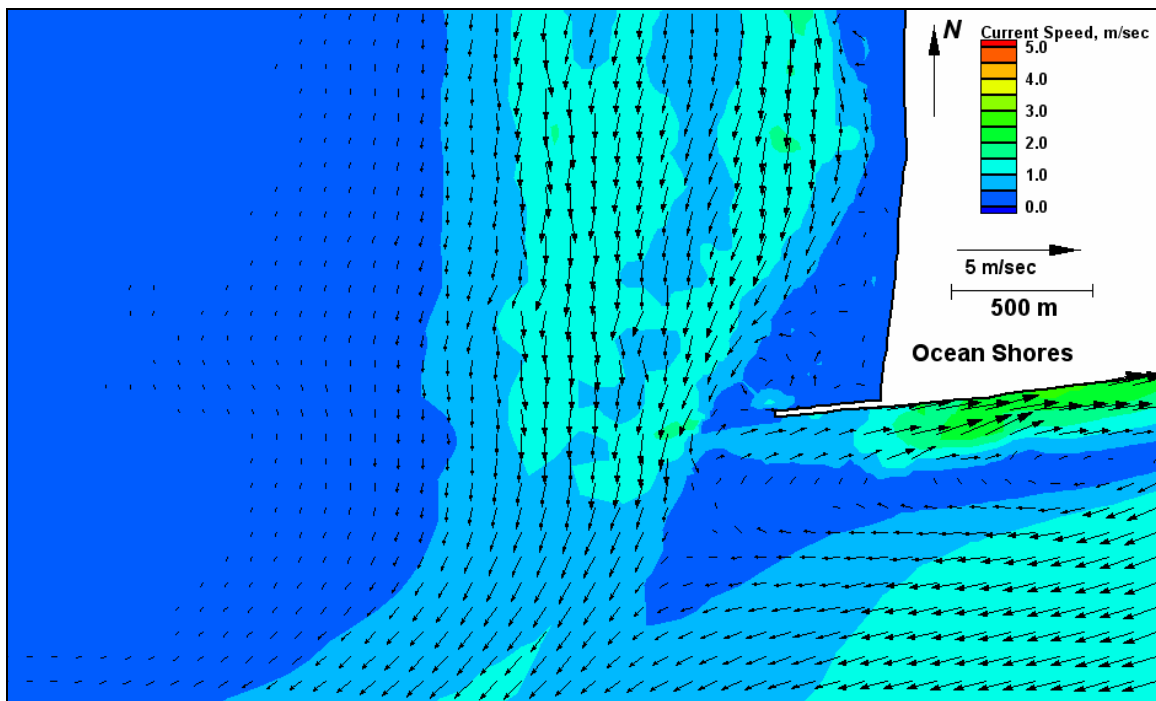
Figure E214. Run 156 (Alt 2B, west-northwest, spring tide), north jetty view of ebb tide
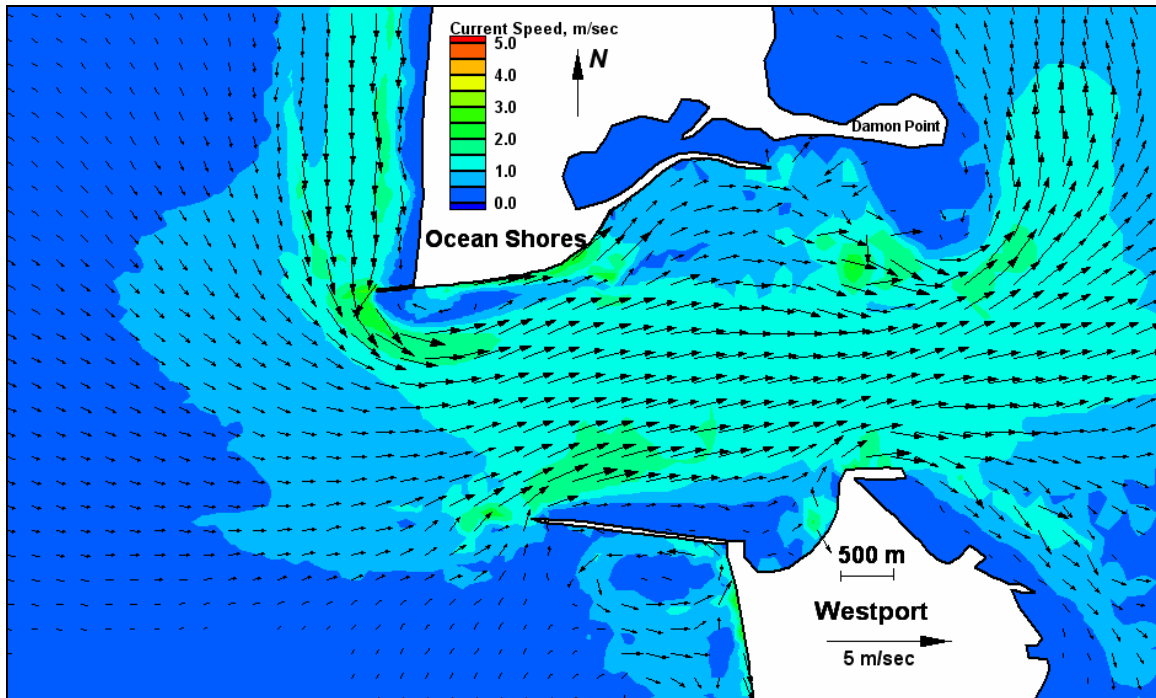
E108
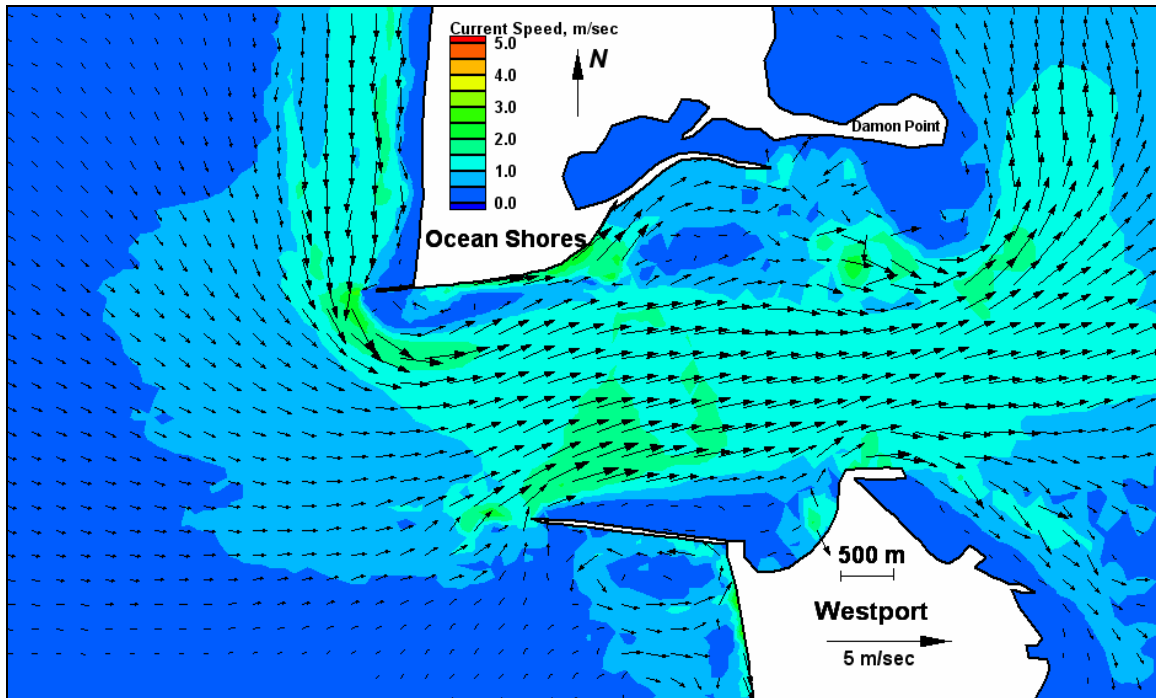
Figure E215. Run 157 (Alt 4A, west-northwest, spring tide), inlet view of flood tide
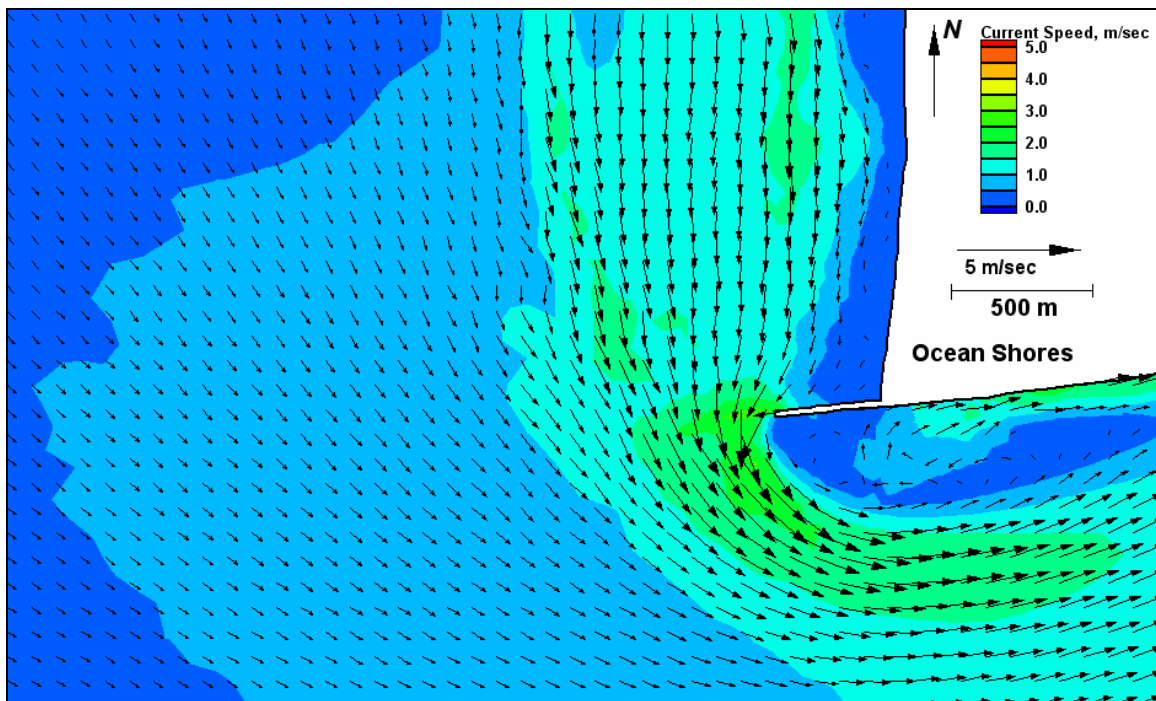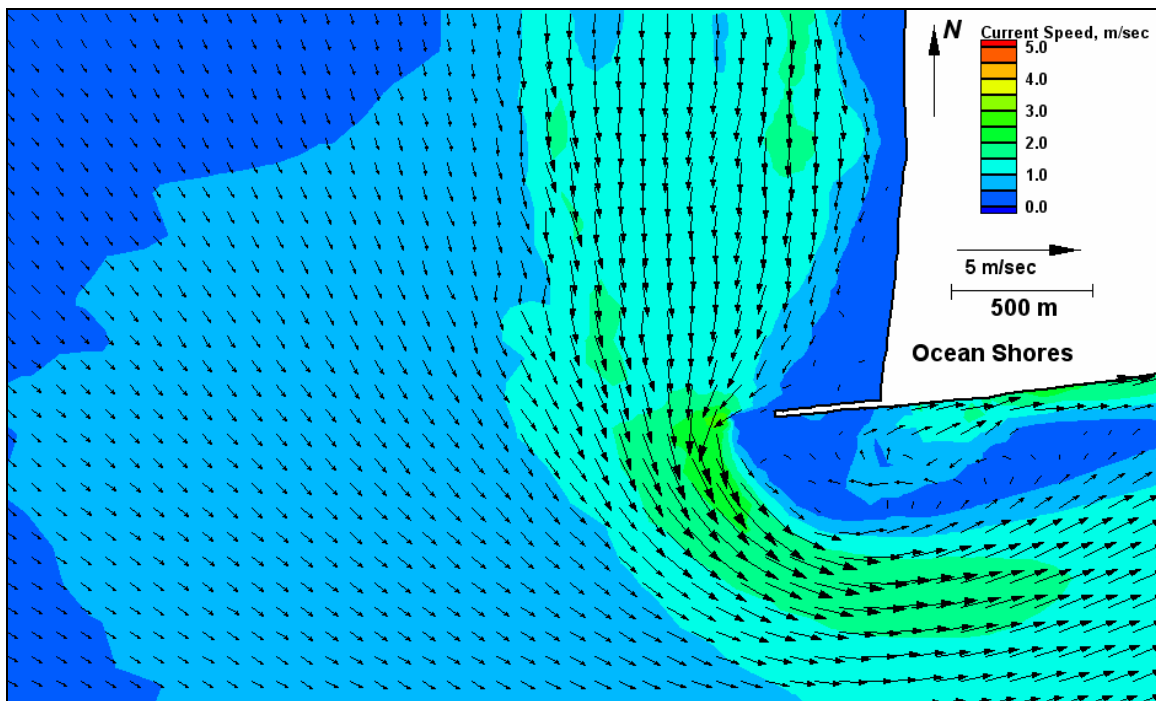

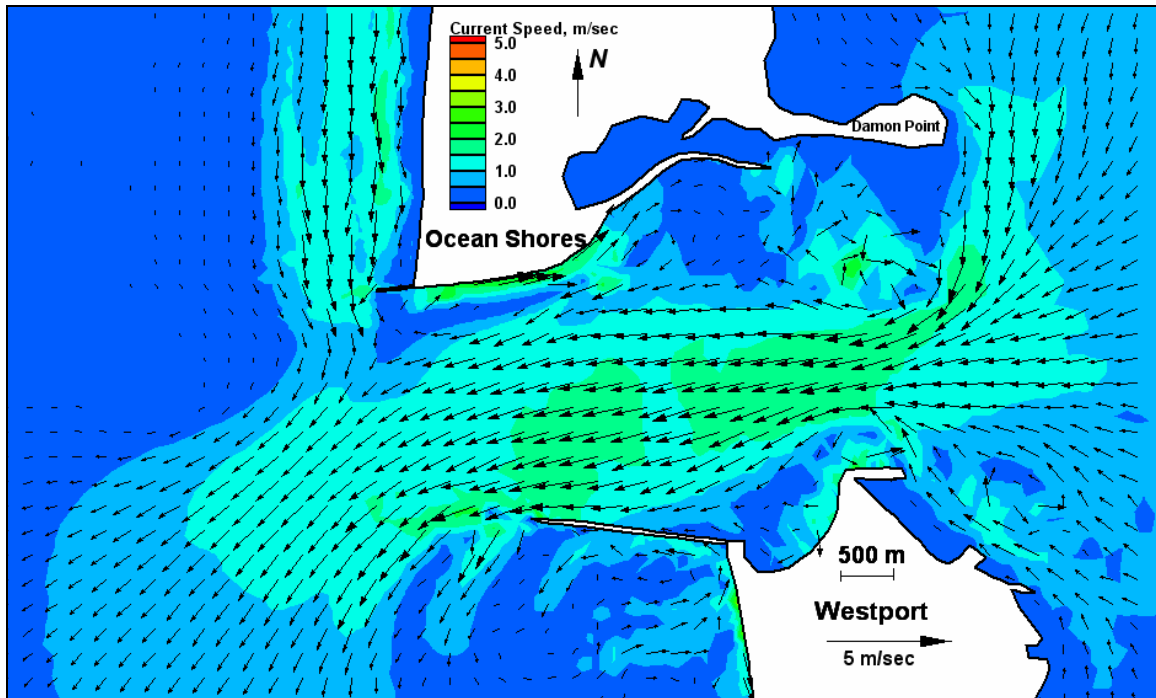Figure E216. Run 157 (Alt 4A, west-northwest, spring tide), north jetty view of flood tide
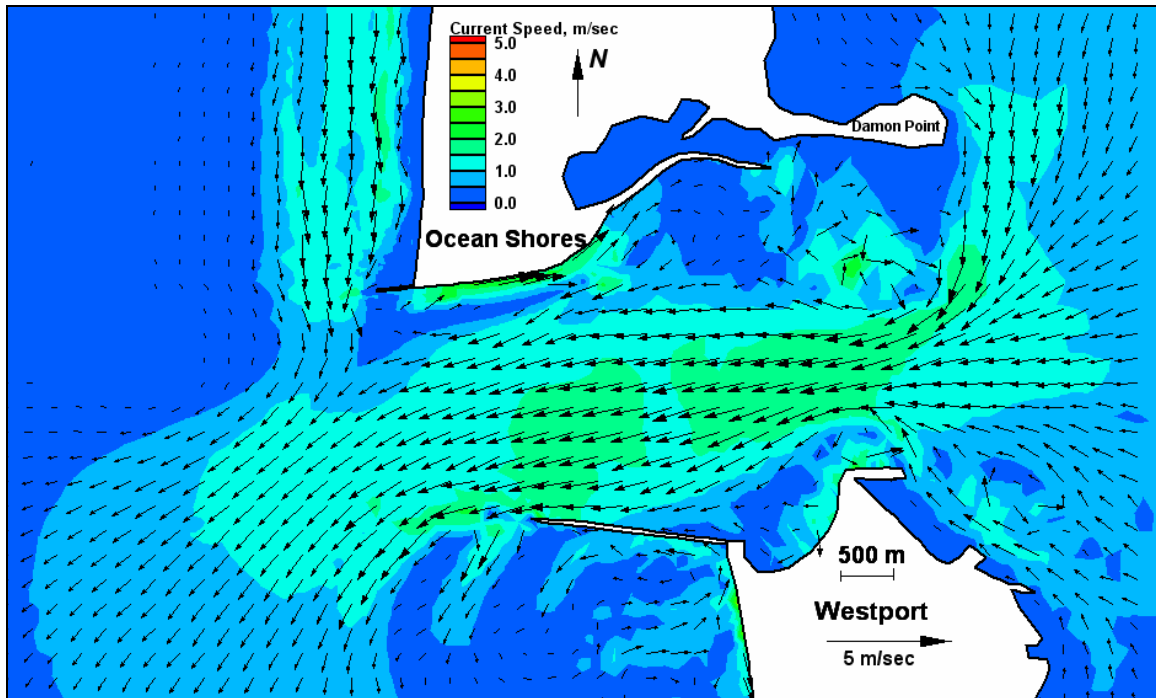
Figure E217. Run 157 (Alt 4A, west-northwest, spring tide), inlet view of ebb tide
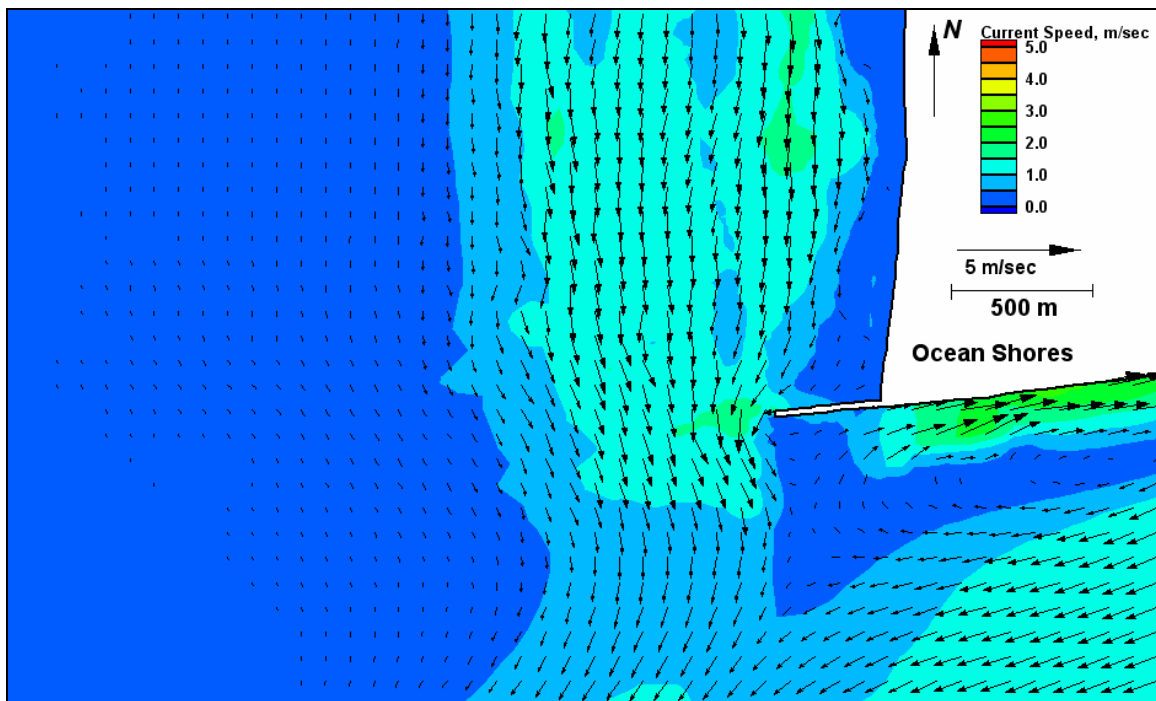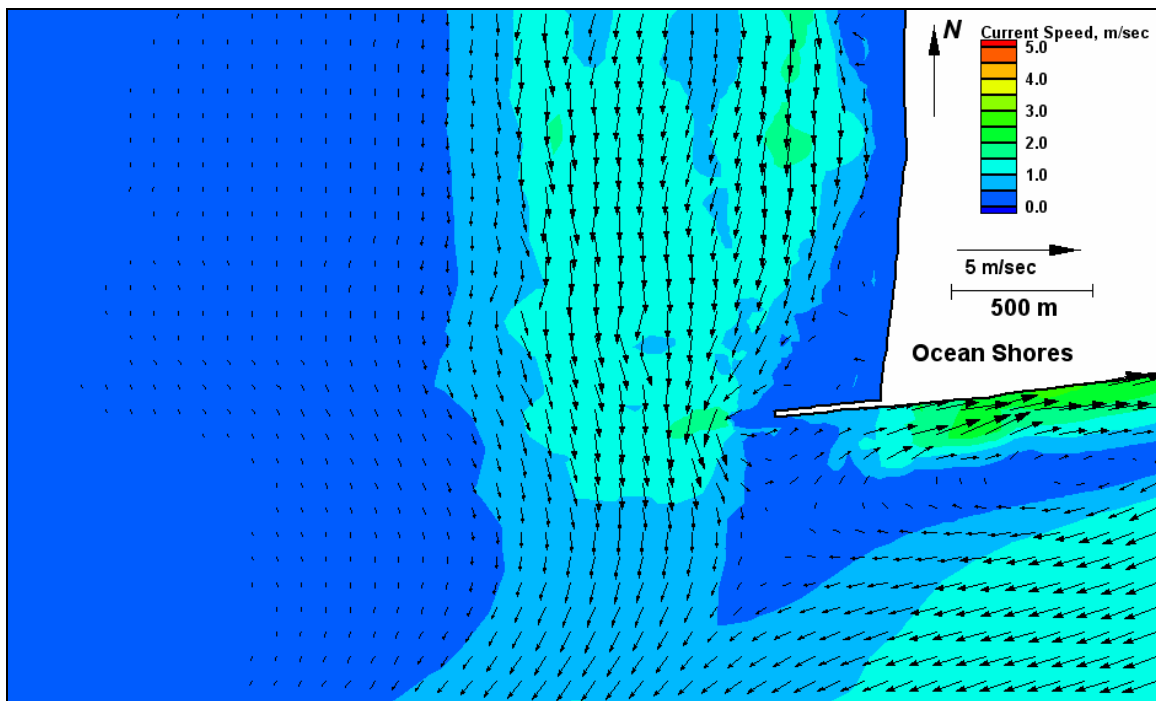

Figure E218. Run 157 (Alt 4A, west-northwest, spring tide), north jetty view of ebb tide
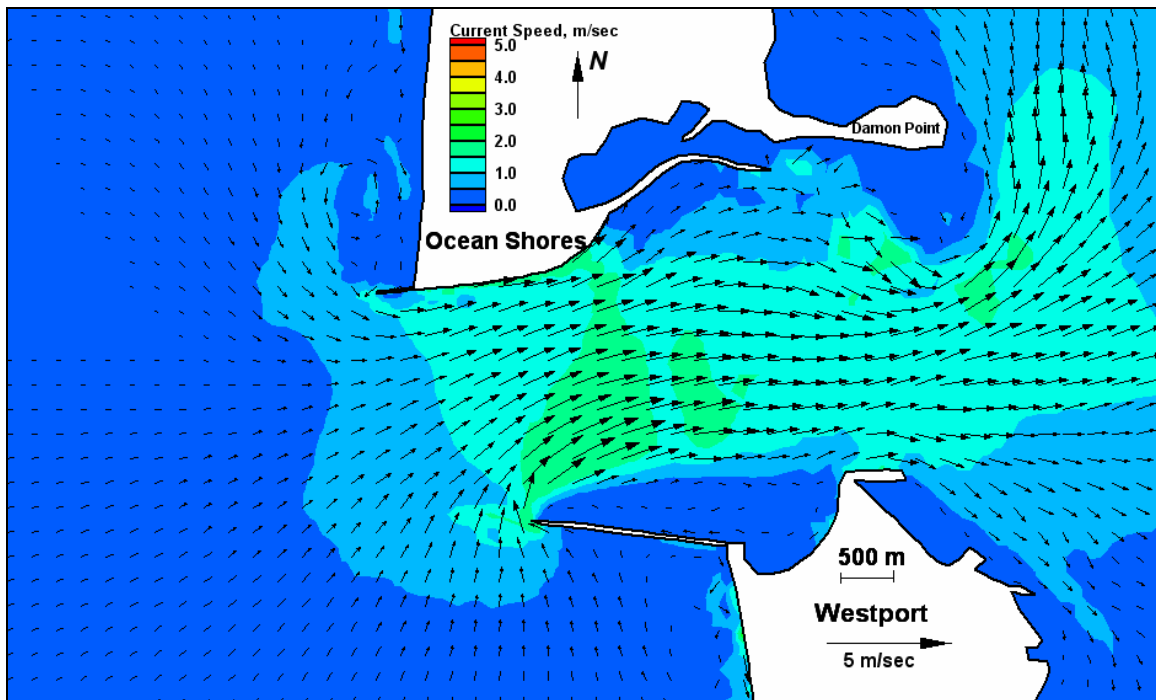
Figure E219. Run 158 (existing, west, spring tide), inlet view of flood tide
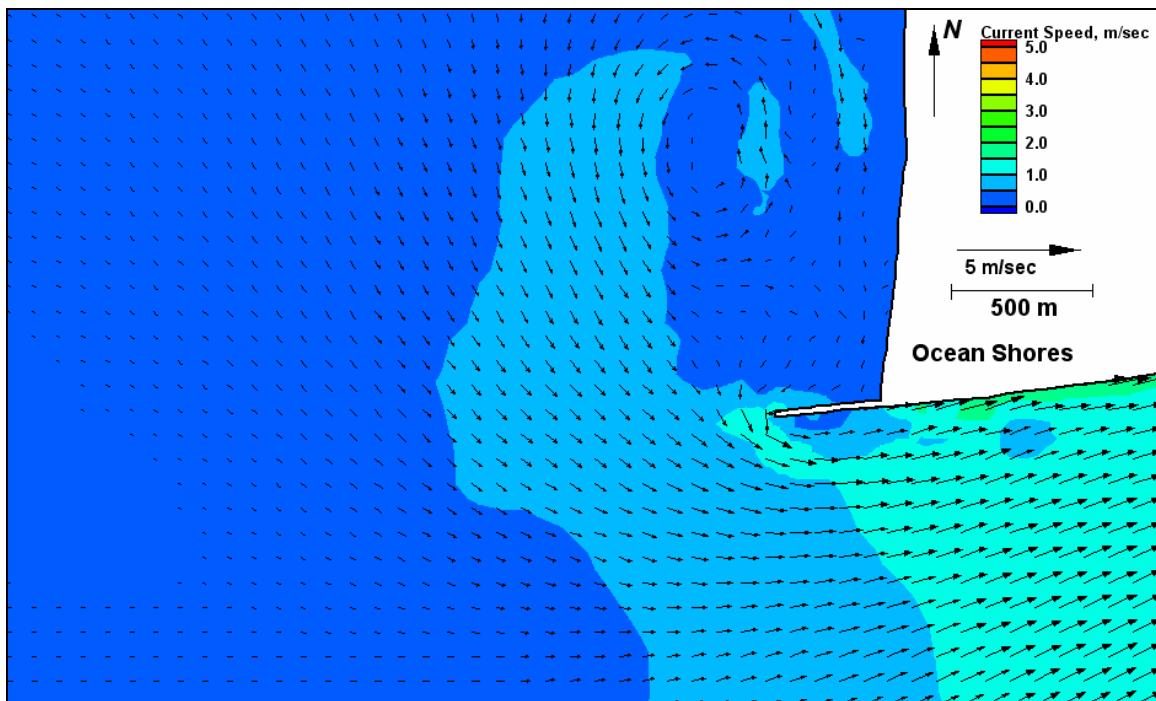
Figure E220. Run 158 (existing, west, spring tide), north jetty view of flood tide
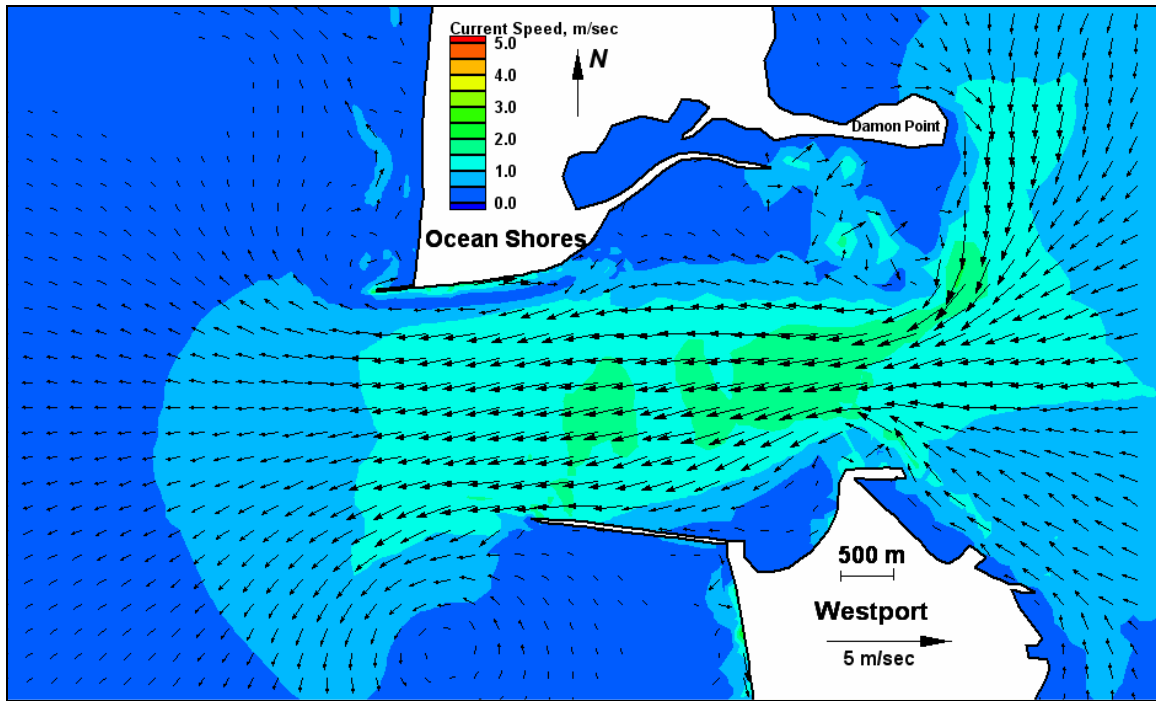
Figure E221. Run 158 (existing, west, spring tide), inlet view of ebb tide
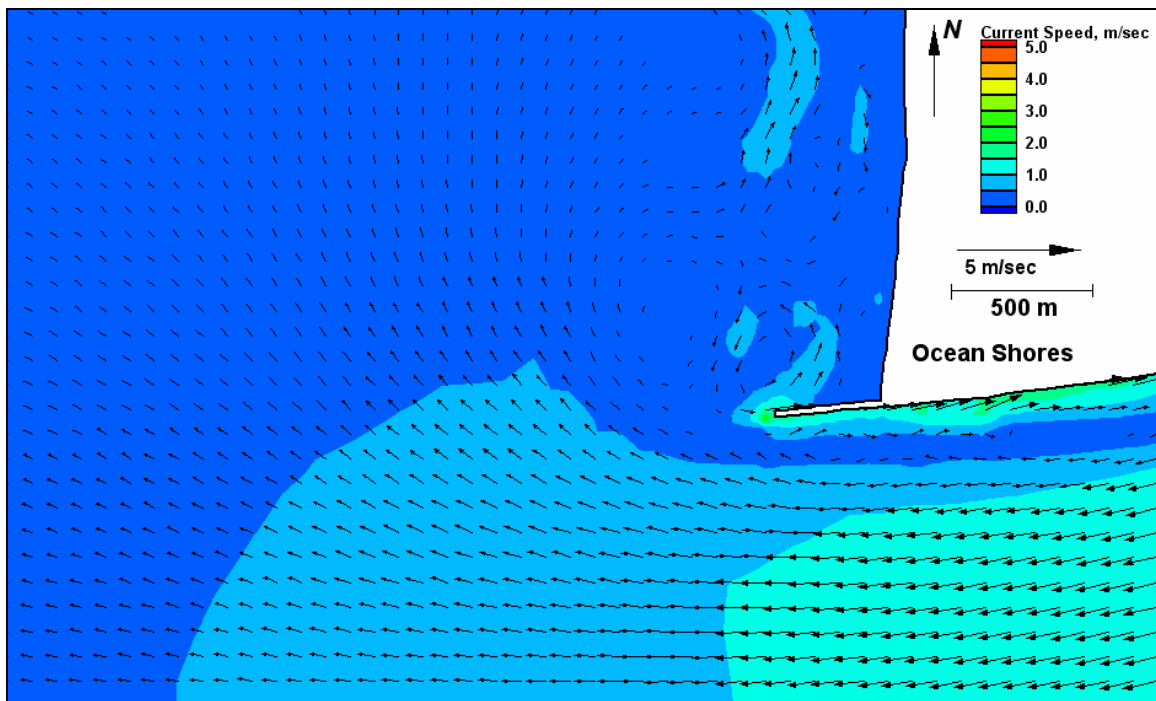
Figure E222. Run 158 (existing, west, spring tide), north jetty view of ebb tide

E112
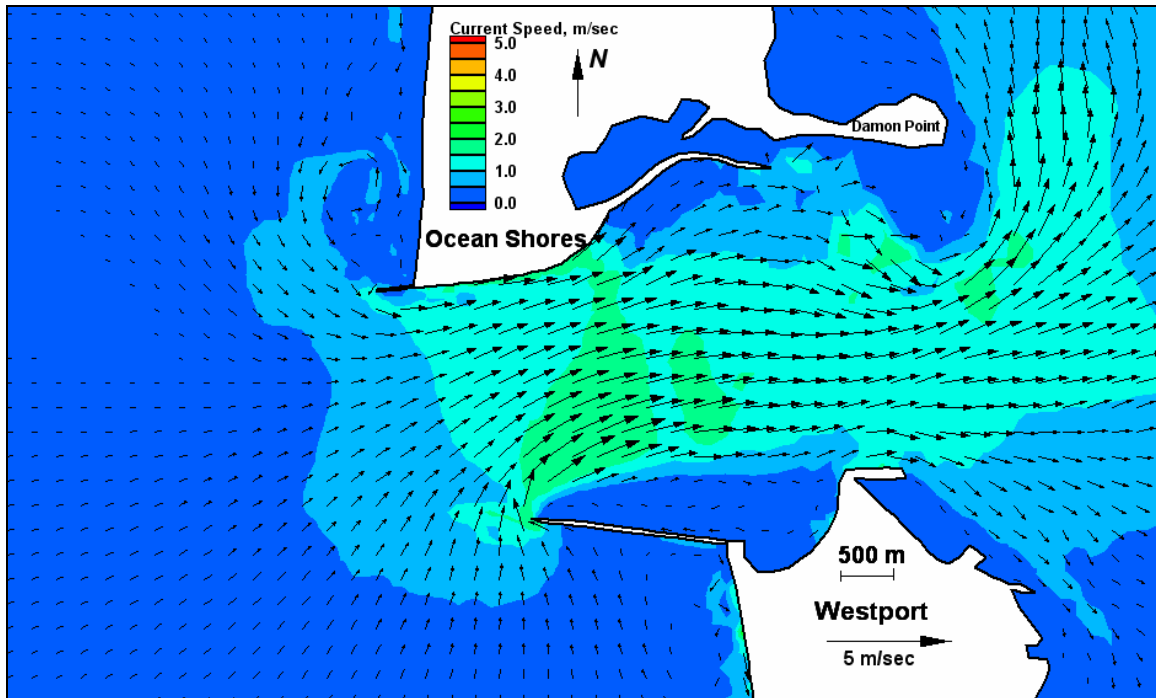
Figure E223. Run 159 (Alt 2A, west, spring tide), inlet view of flood tide
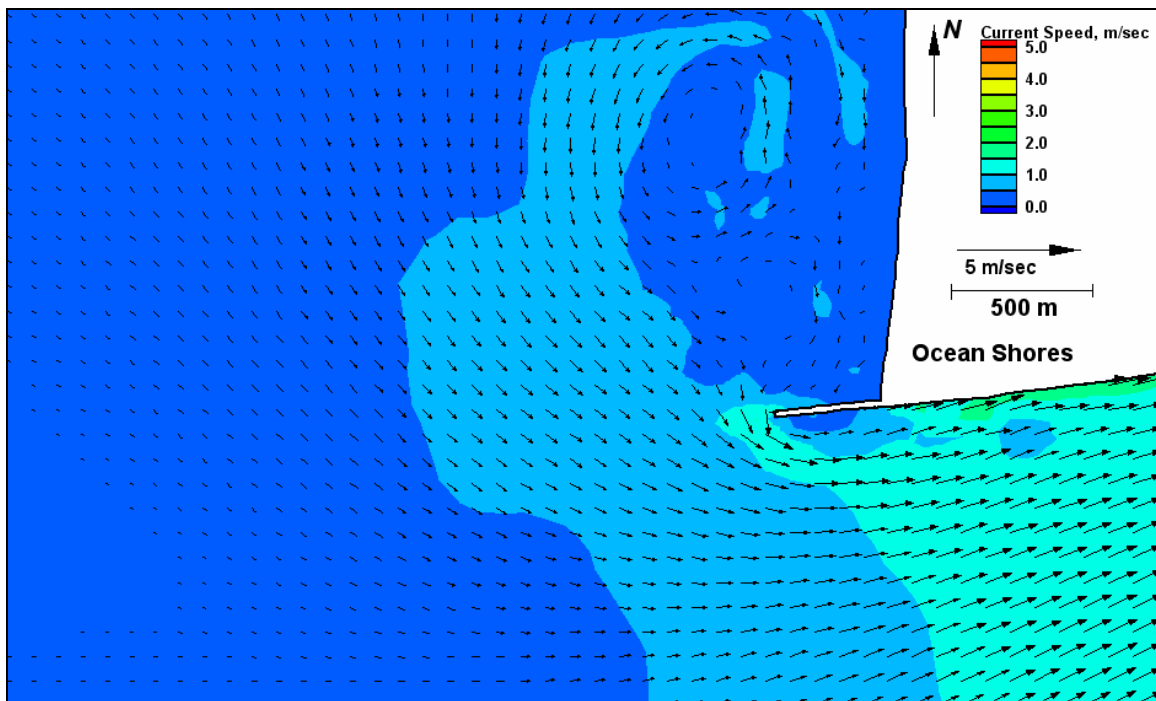
Figure E224. Run 159 (Alt 2A, west, spring tide), north jetty view of flood tide
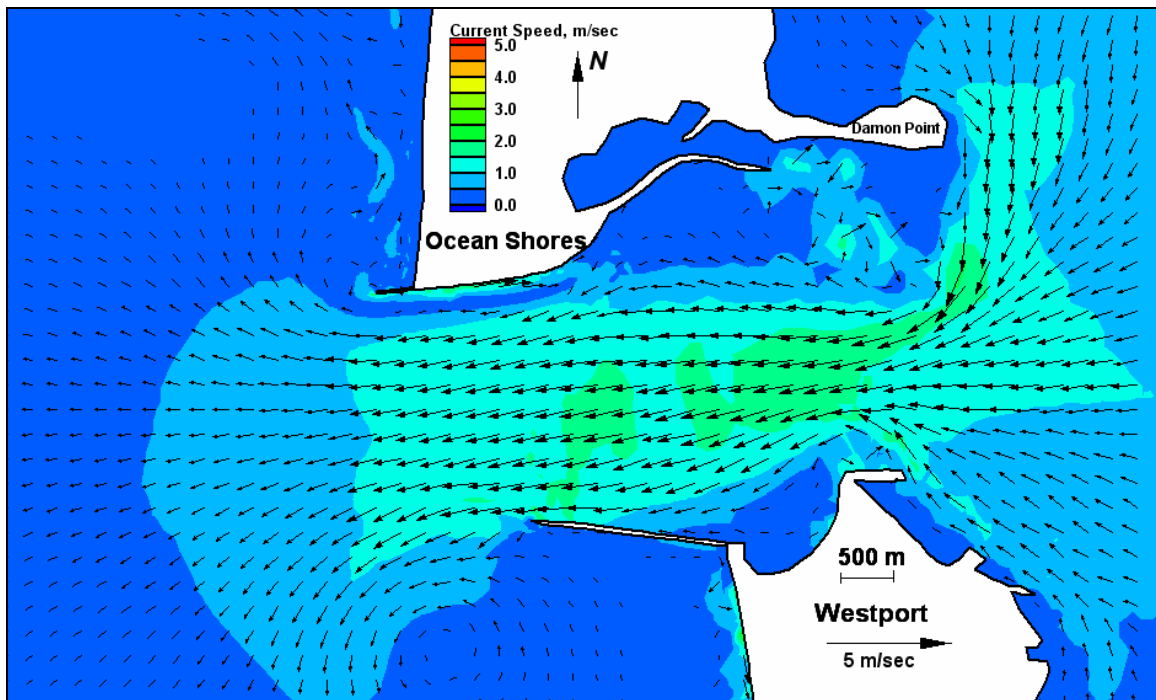
Figure E225. Run 159 (Alt 2A, west, spring tide), inlet view of ebb tide
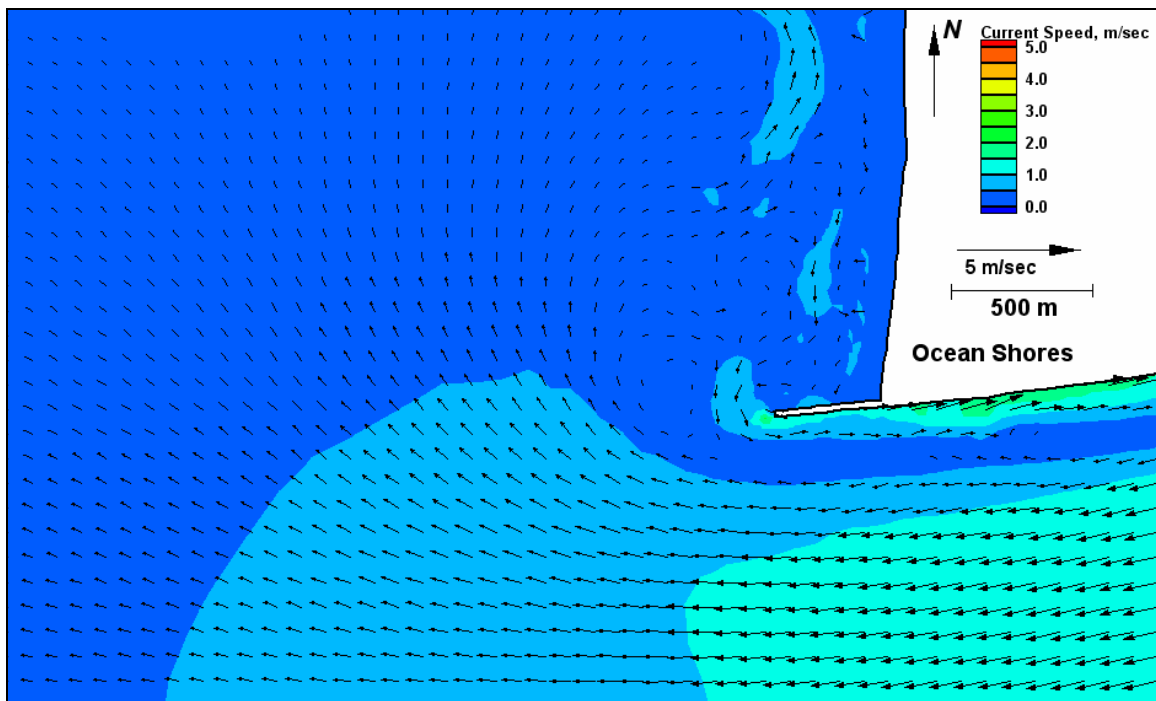
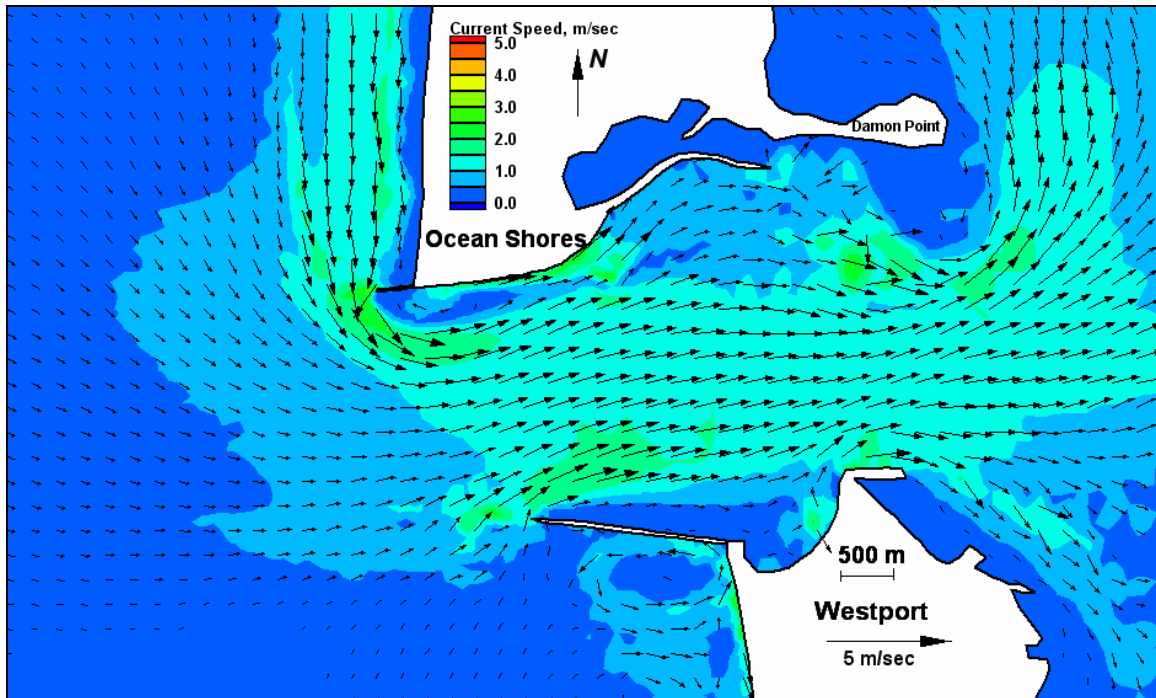Figure E226. Run 159 (Alt 2A, west, spring tide), north jetty view of ebb tide
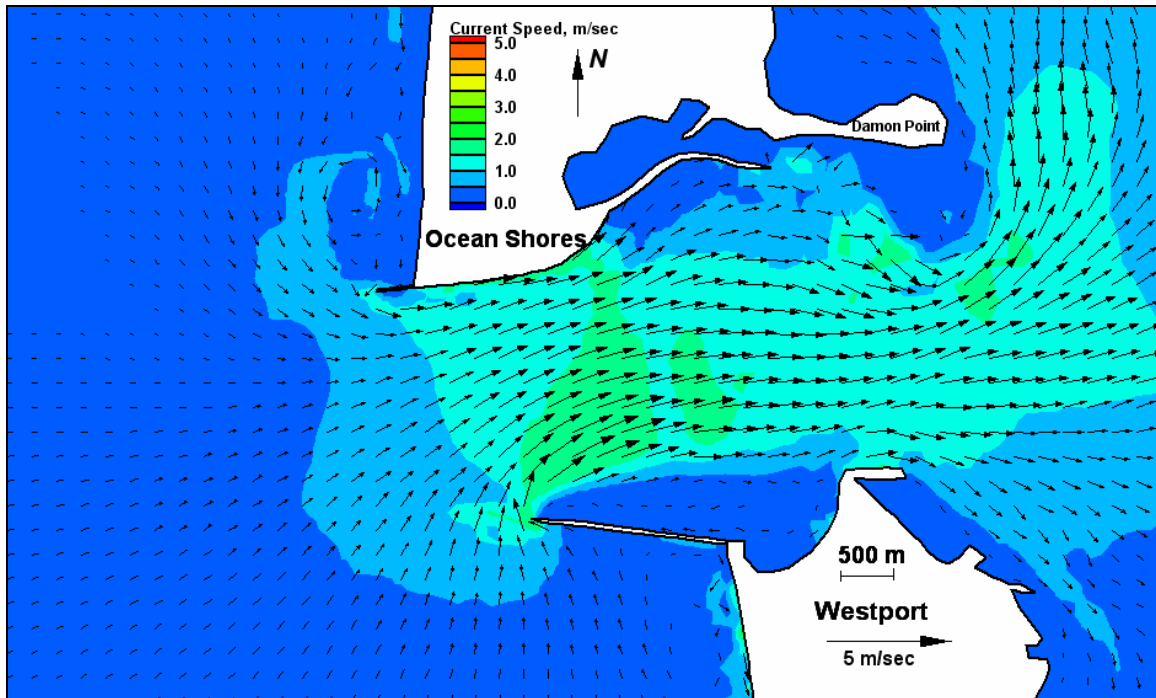
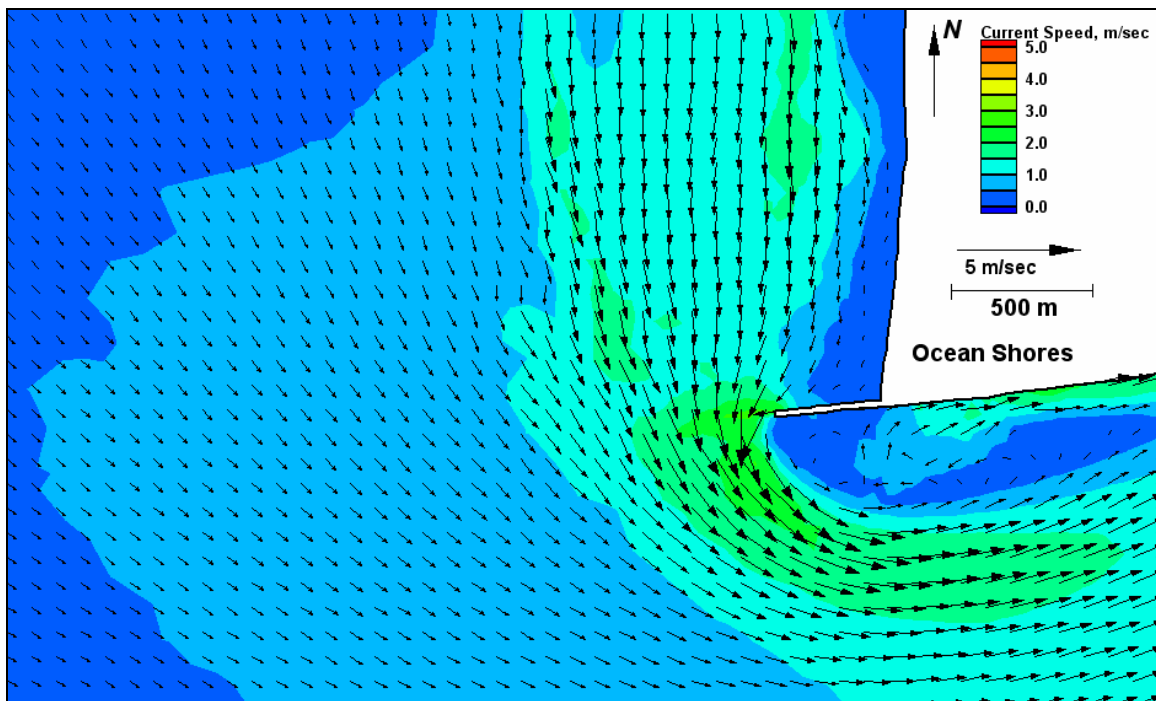Figure E227. Run 160 (Alt 2B, west, spring tide), inlet view of flood tide
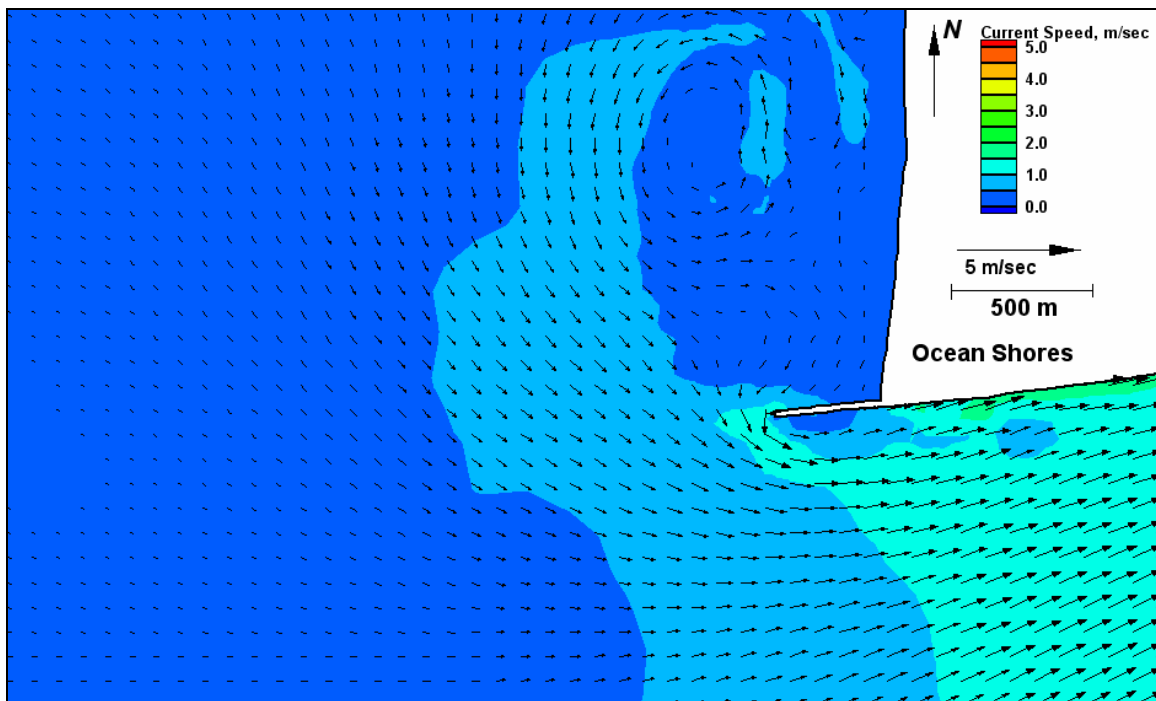
Figure E228. Run 160 (Alt 2B, west, spring tide), north jetty view of flood tide
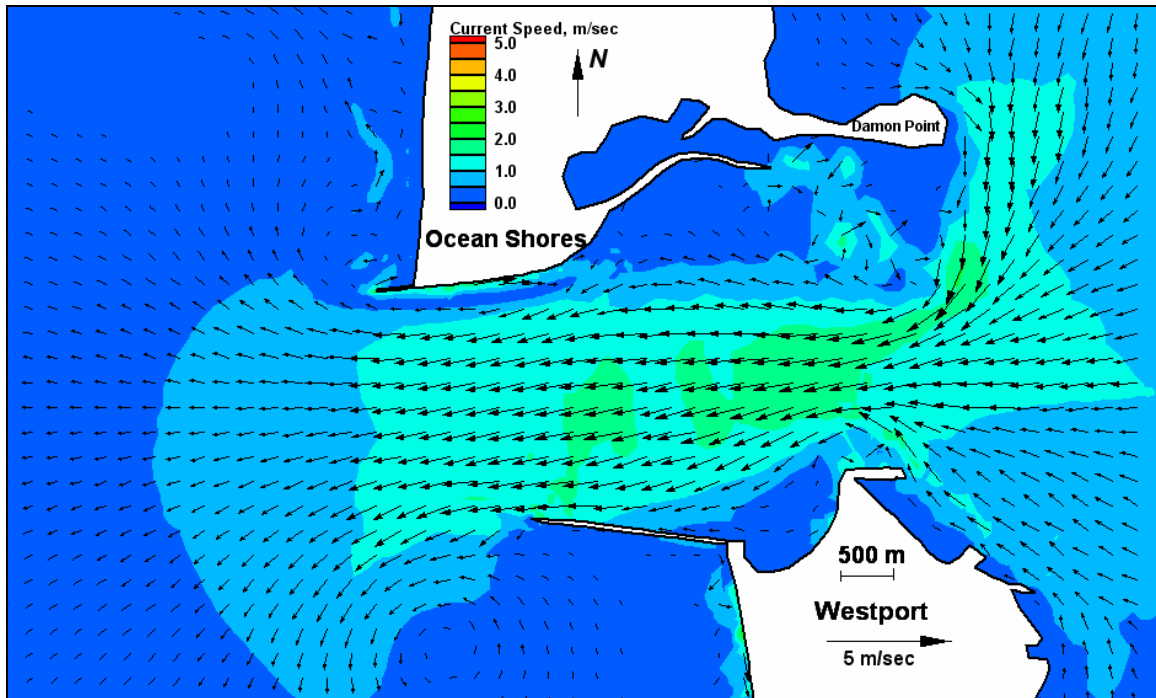
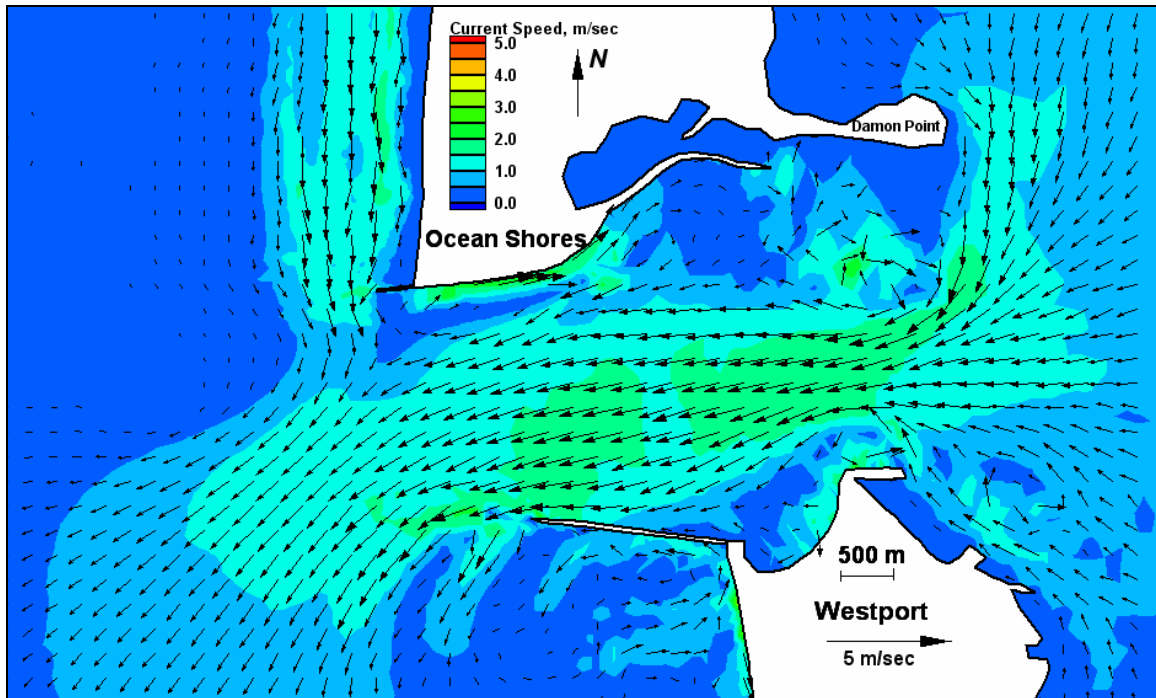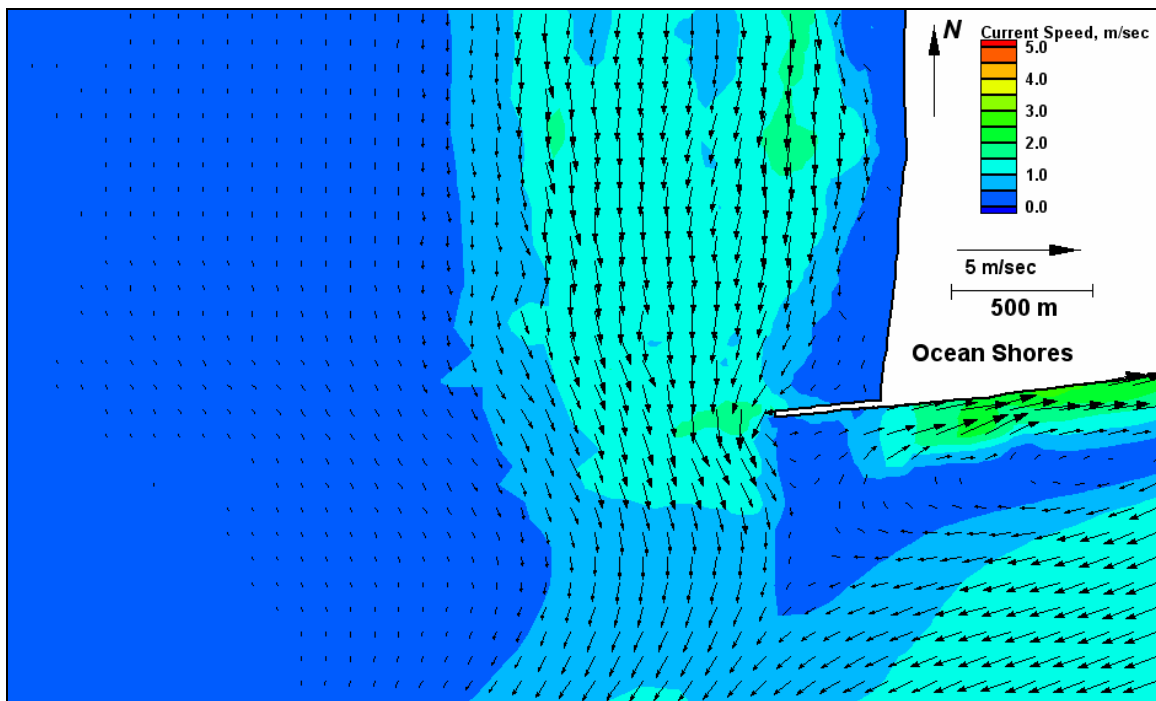Figure E229. Run 160 (Alt 2B, west, spring tide), inlet view of ebb tide
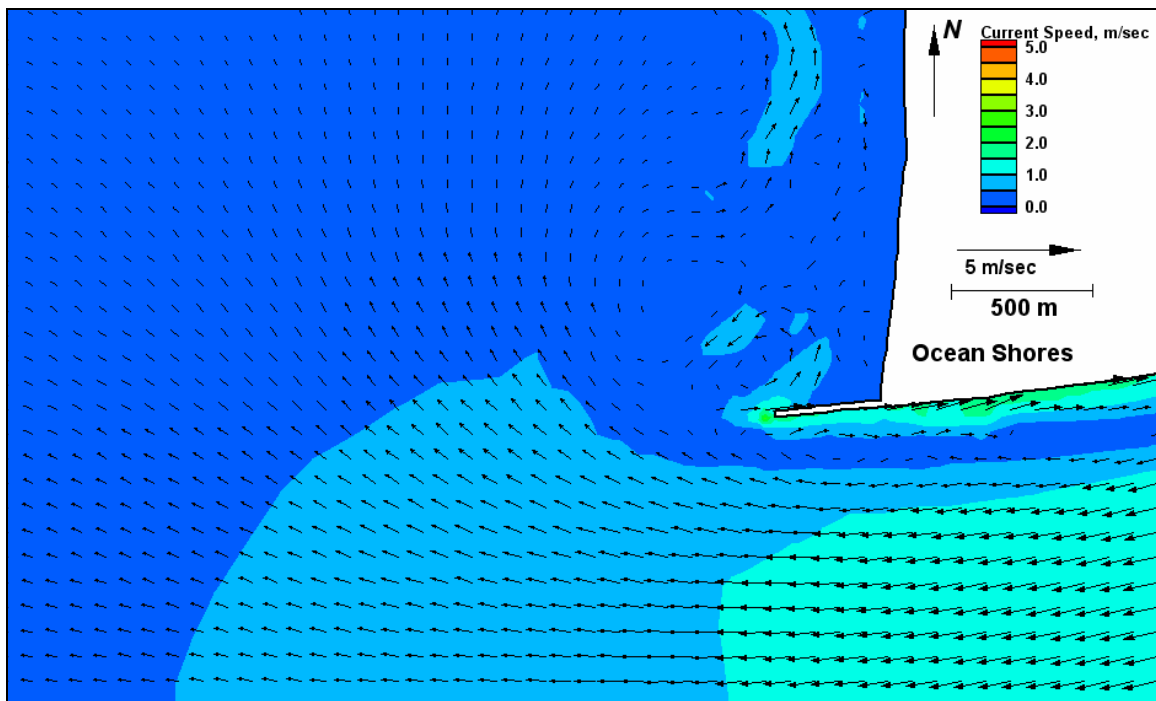
Figure E230. Run 160 (Alt 2B, west, spring tide), north jetty view of ebb tide
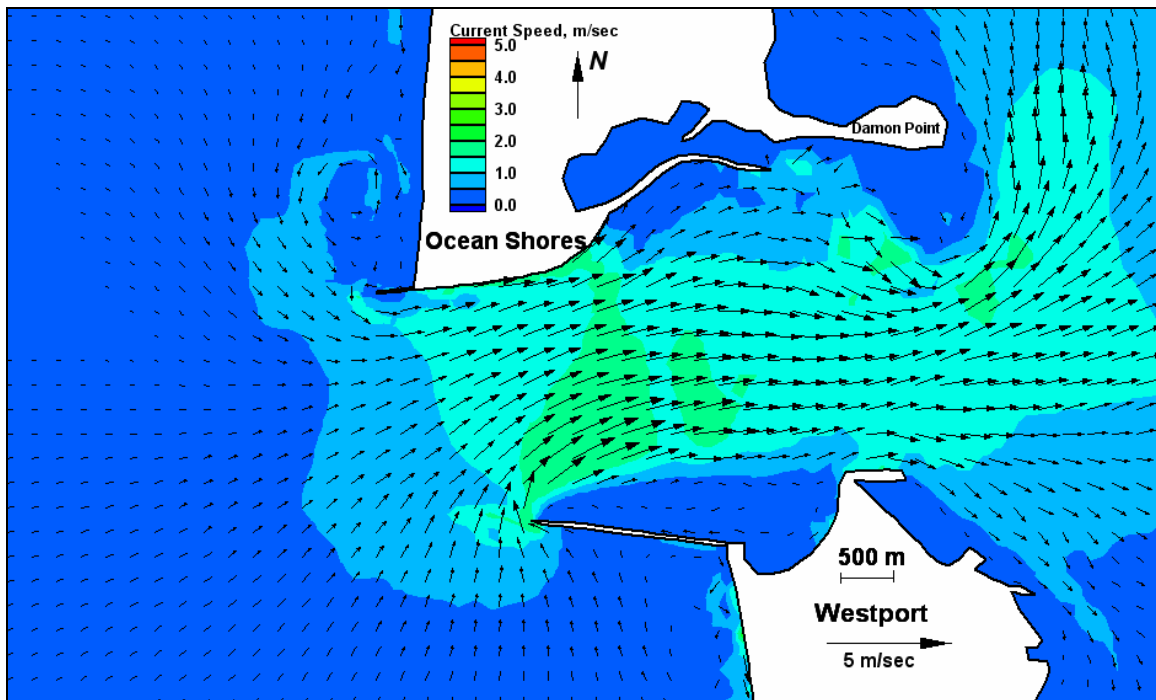
Figure E231. Run 161 (Alt 3A, west, spring tide), inlet view of flood tide
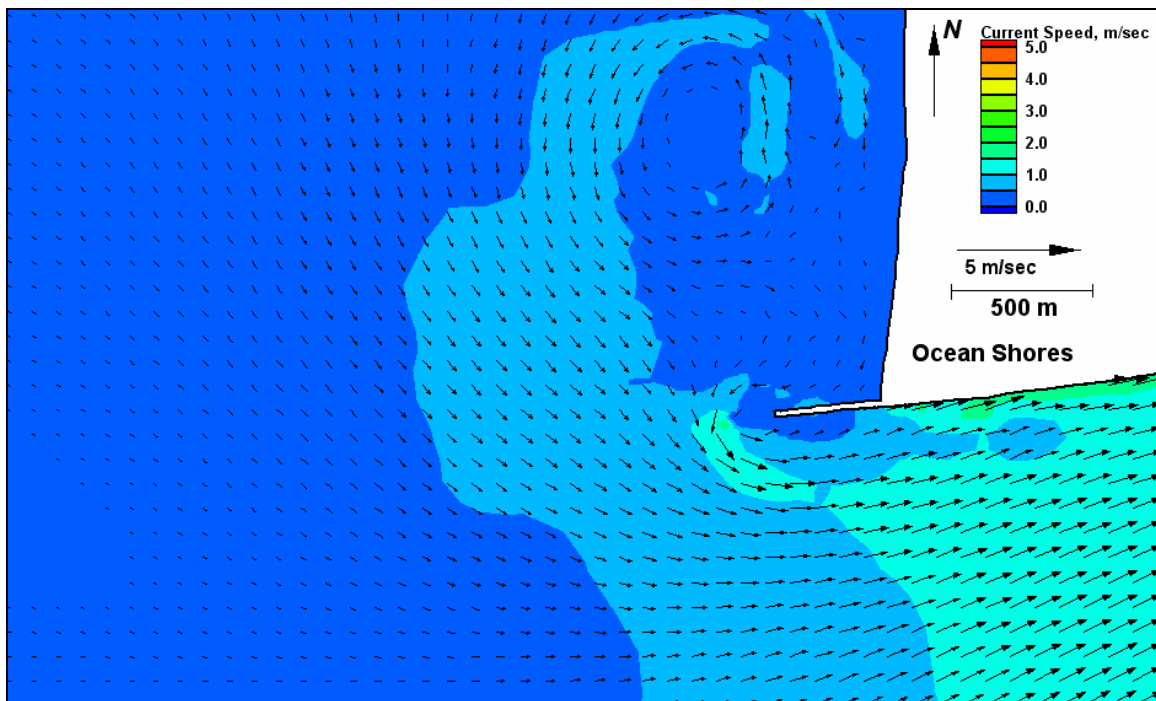
Figure E232. Run 161 (Alt 3A, west, spring tide), north jetty view of flood tide
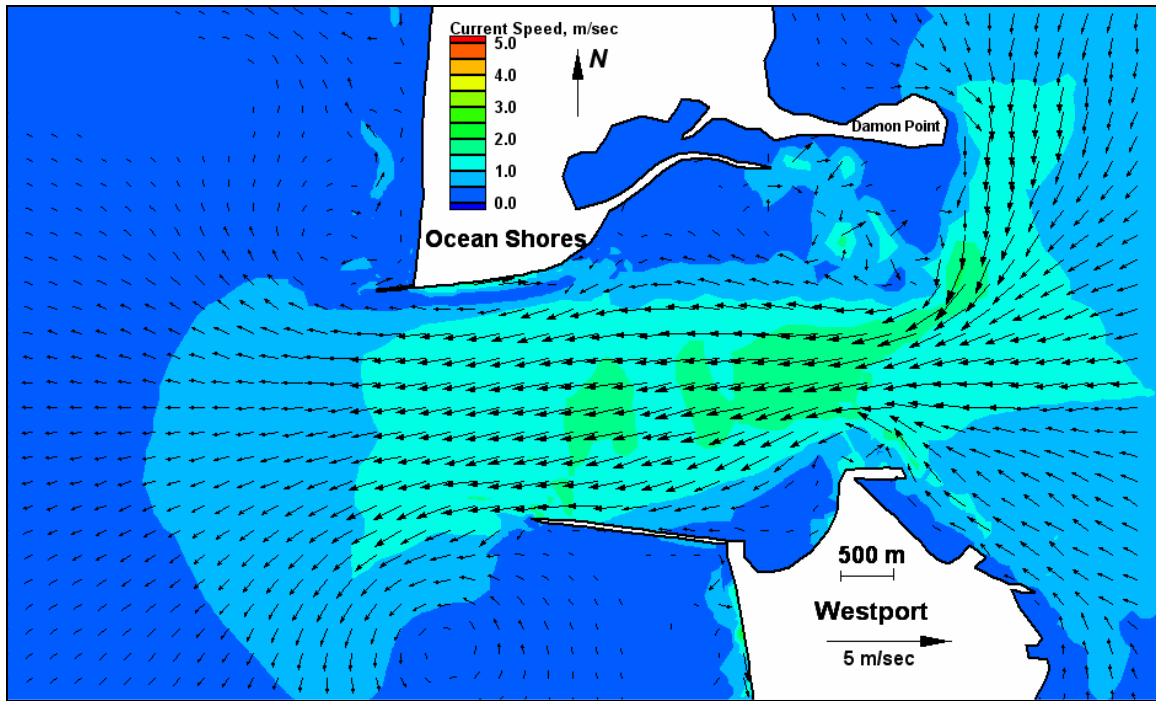
Figure E233. Run 161 (Alt 3A, west, spring tide), inlet view of ebb tide
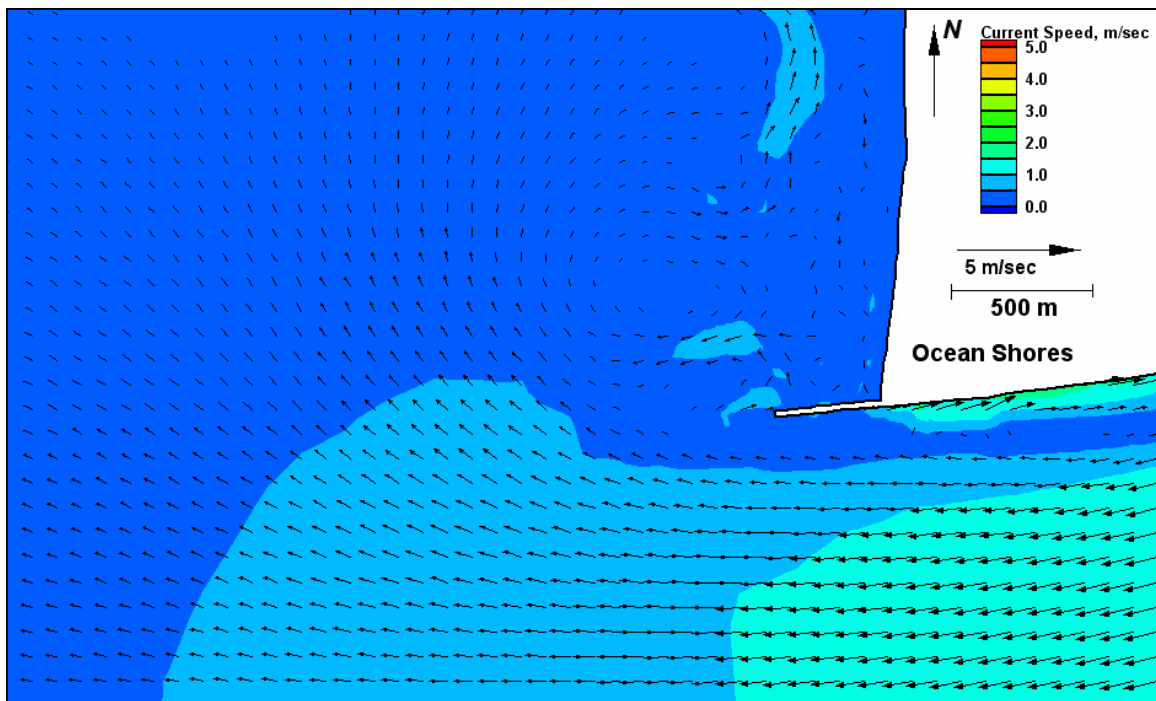
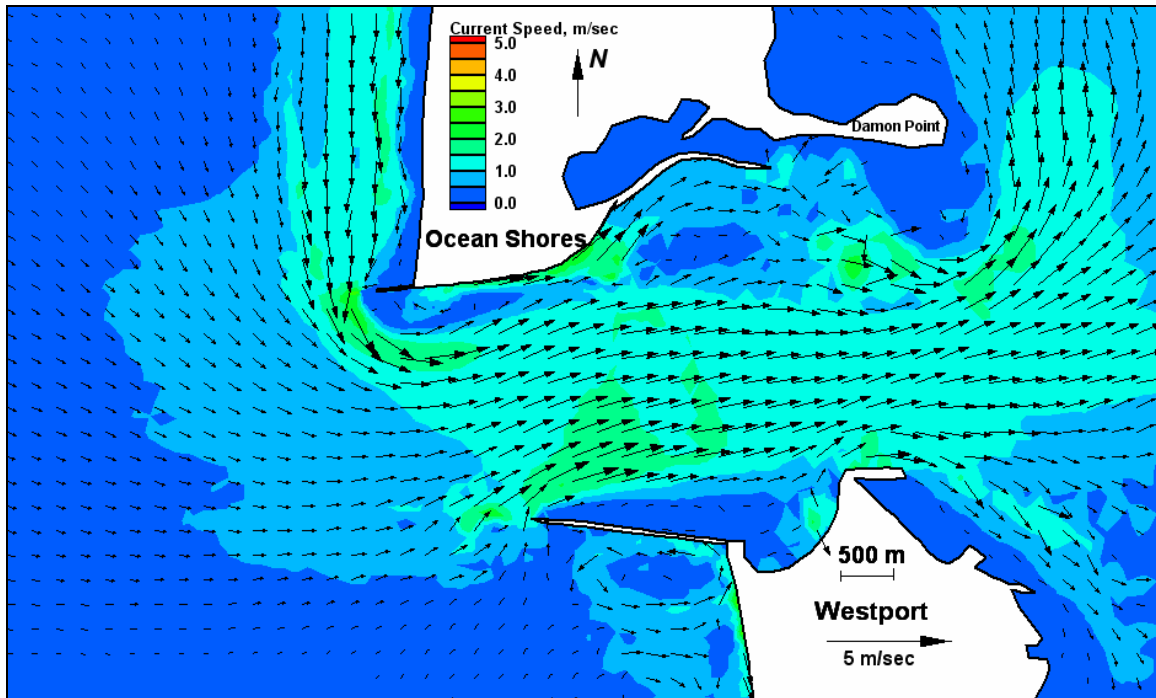Figure E234. Run 161 (Alt 3A, west, spring tide), north jetty view of ebb tide
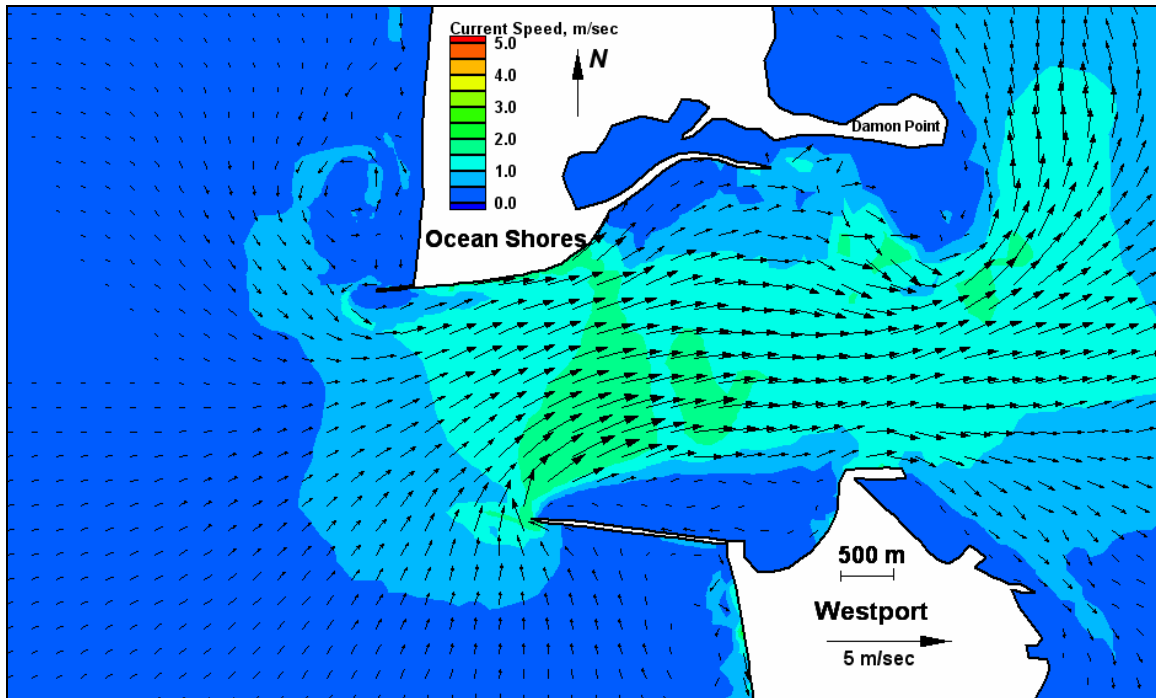
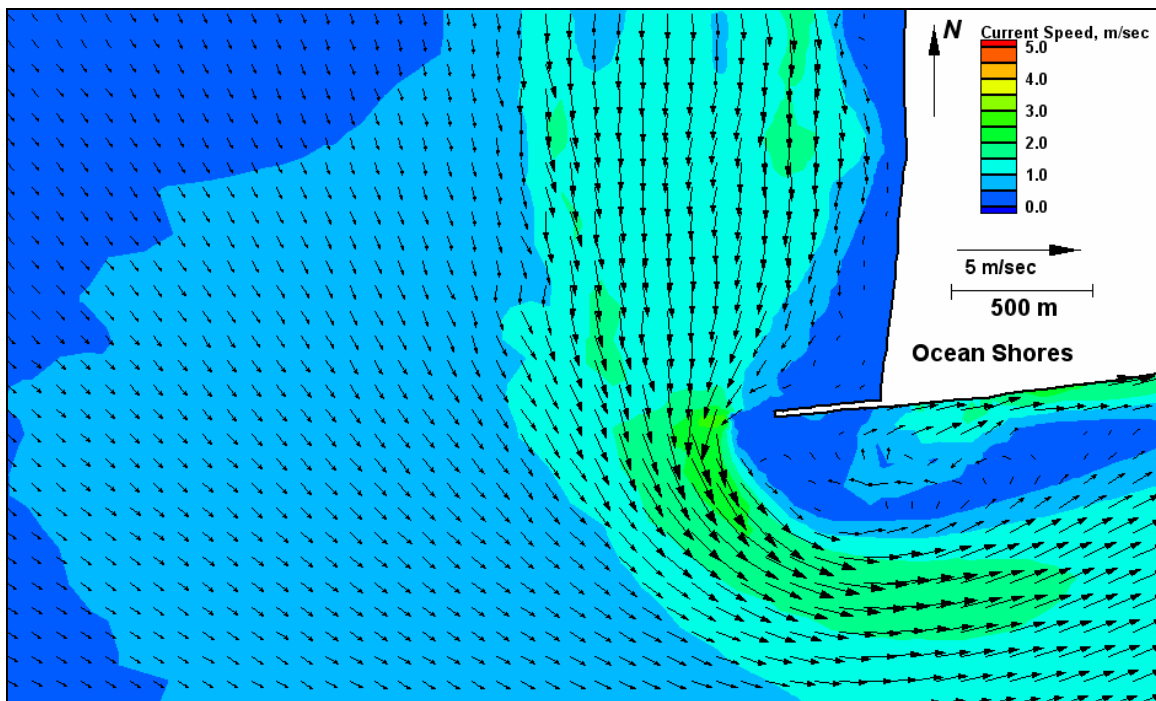Figure E235. Run 162 (Alt 3B, west, spring tide), inlet view of flood tide
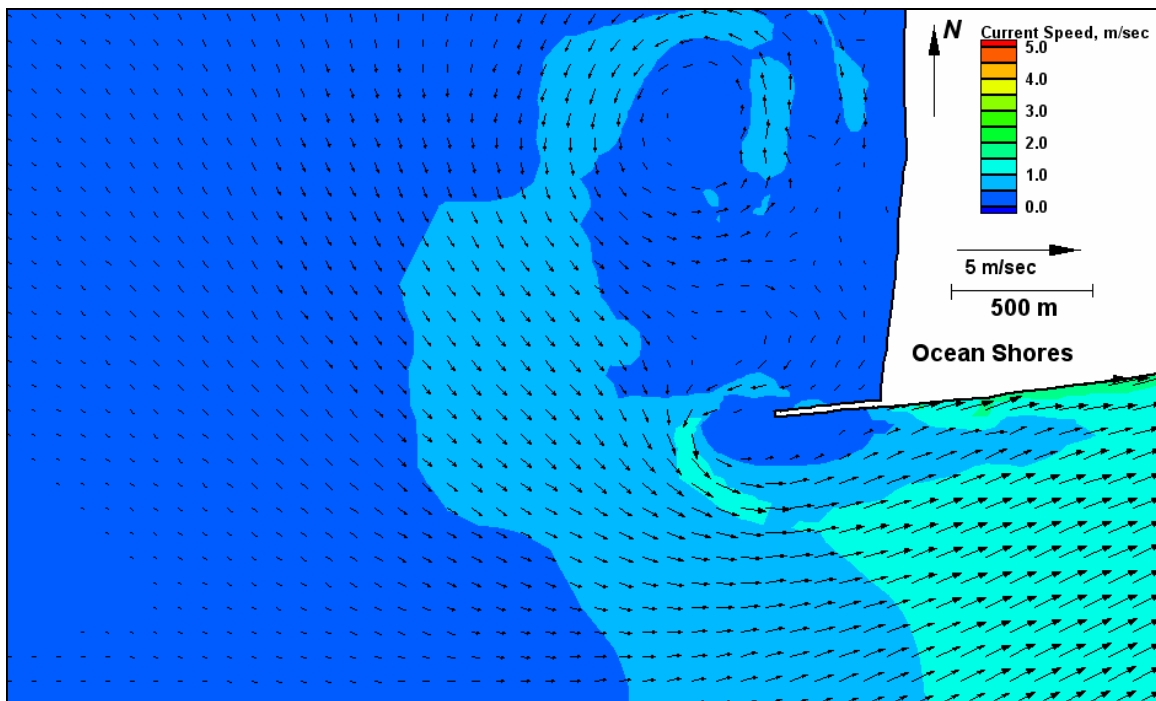
Figure E236. Run 162 (Alt 3B, west, spring tide), north jetty view of flood tide
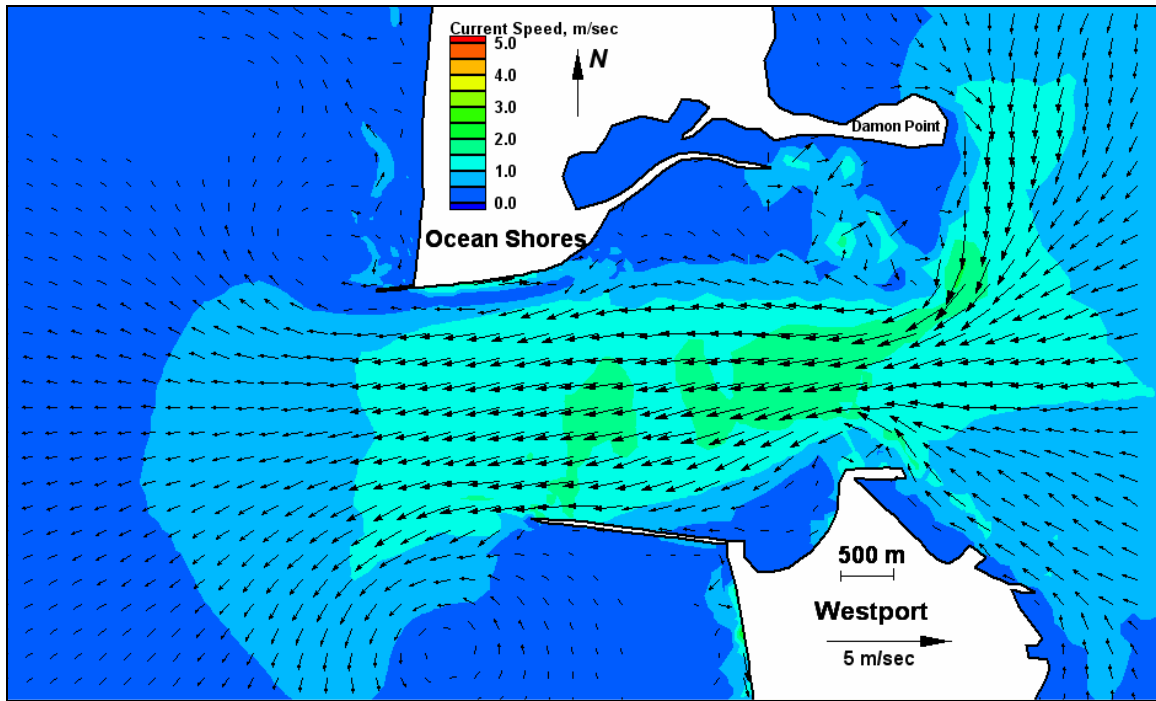
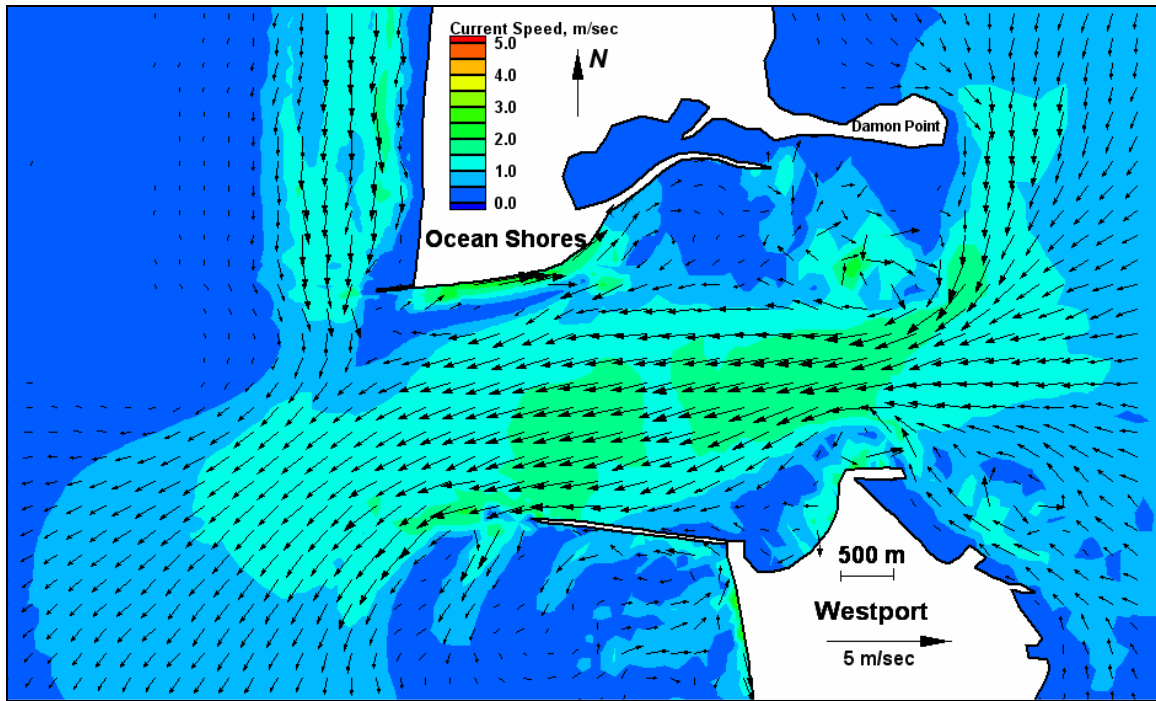Figure E237. Run 162 (Alt 3B, west, spring tide), inlet view of ebb tide
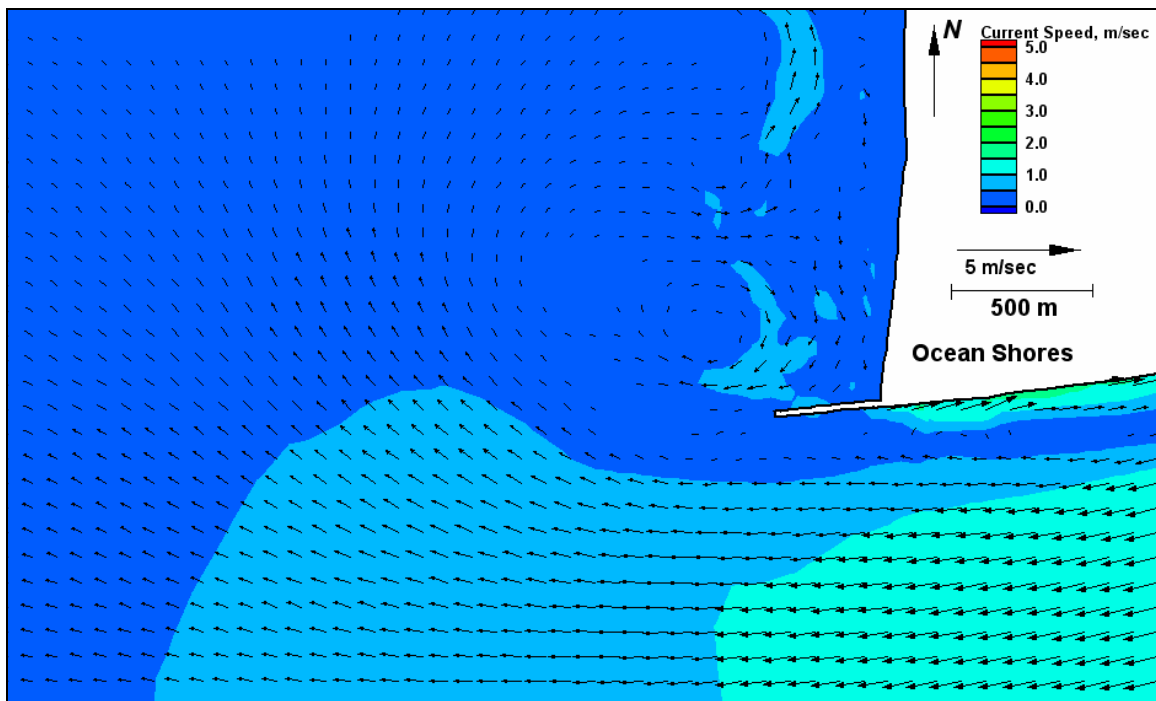
Figure E238. Run 162 (Alt 3B, west, spring tide), north jetty view of ebb tide
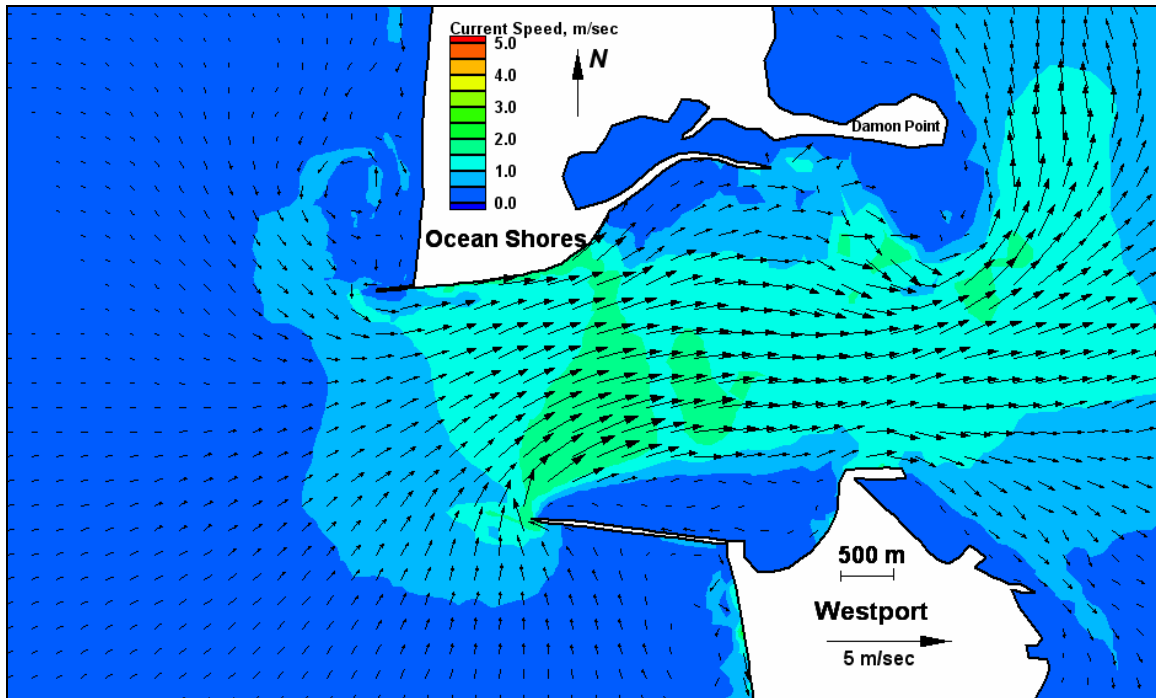
Figure E239. Run 163 (Alt 4A, west, spring tide), inlet view of flood tide
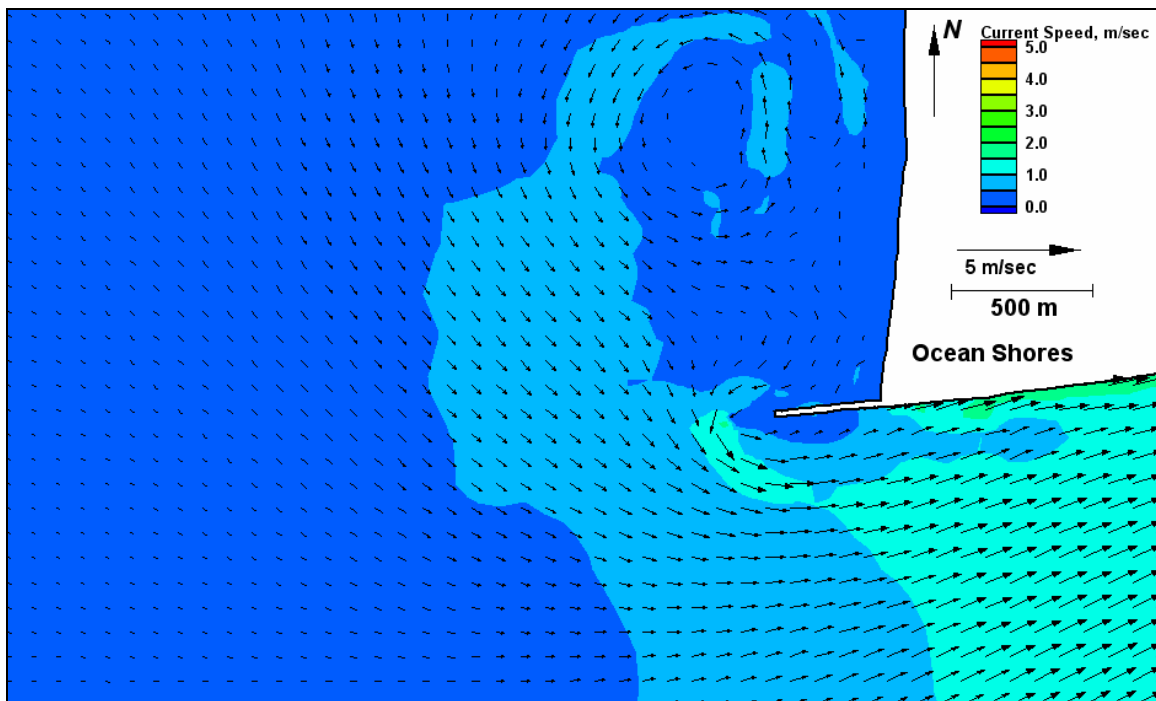
Figure E240. Run 163 (Alt 4A, west, spring tide), north jetty view of flood tide
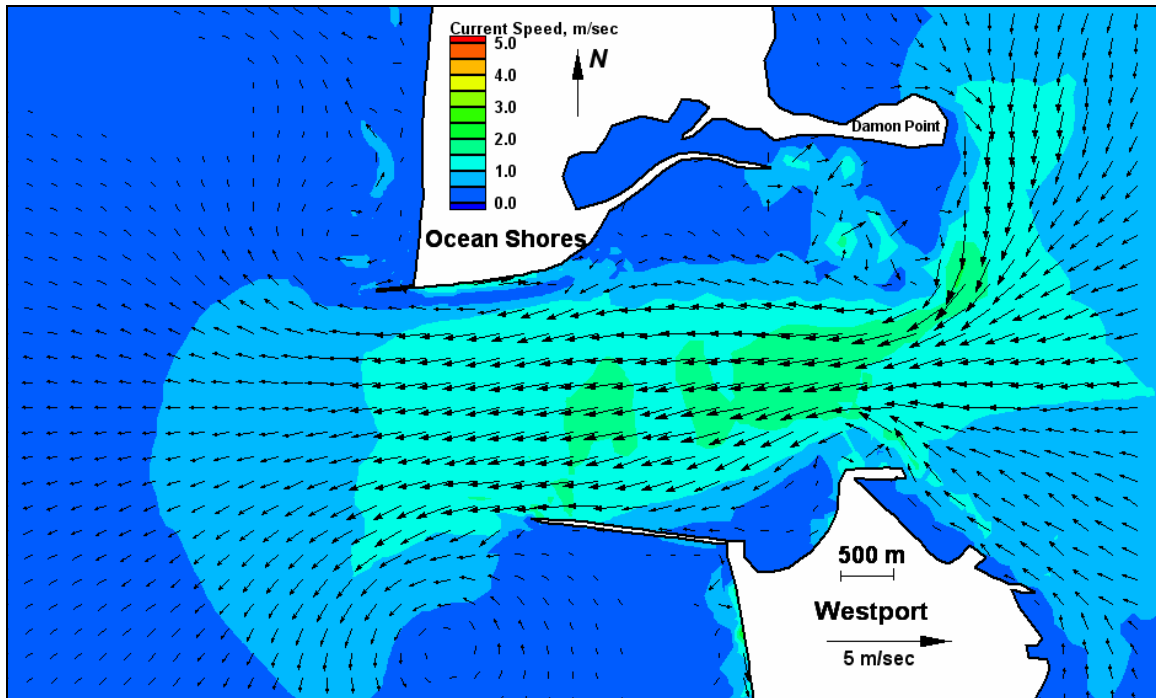
Figure E241. Run 163 (Alt 4A, west, spring tide), inlet view of ebb tide
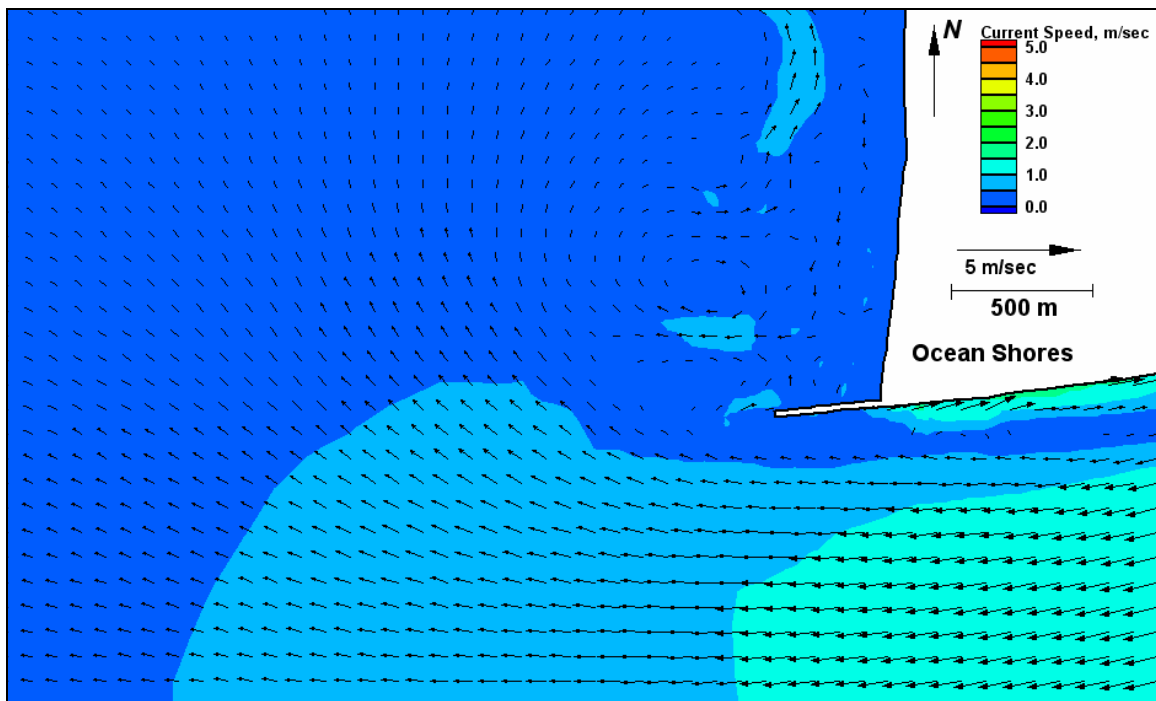
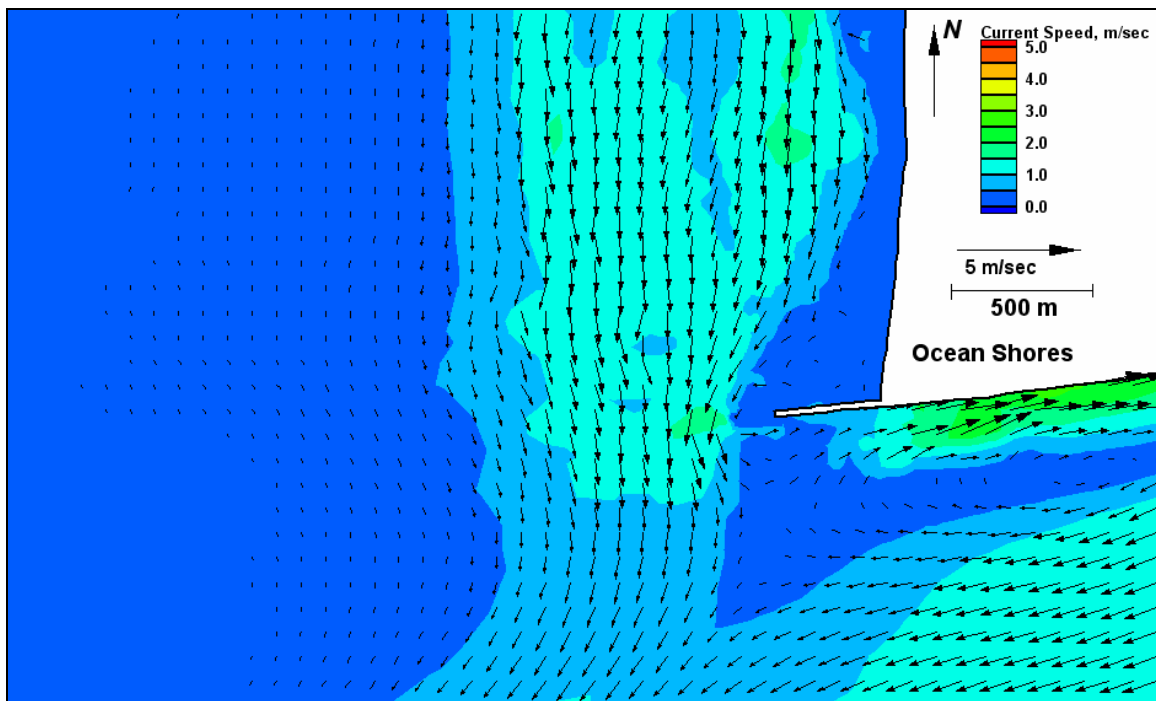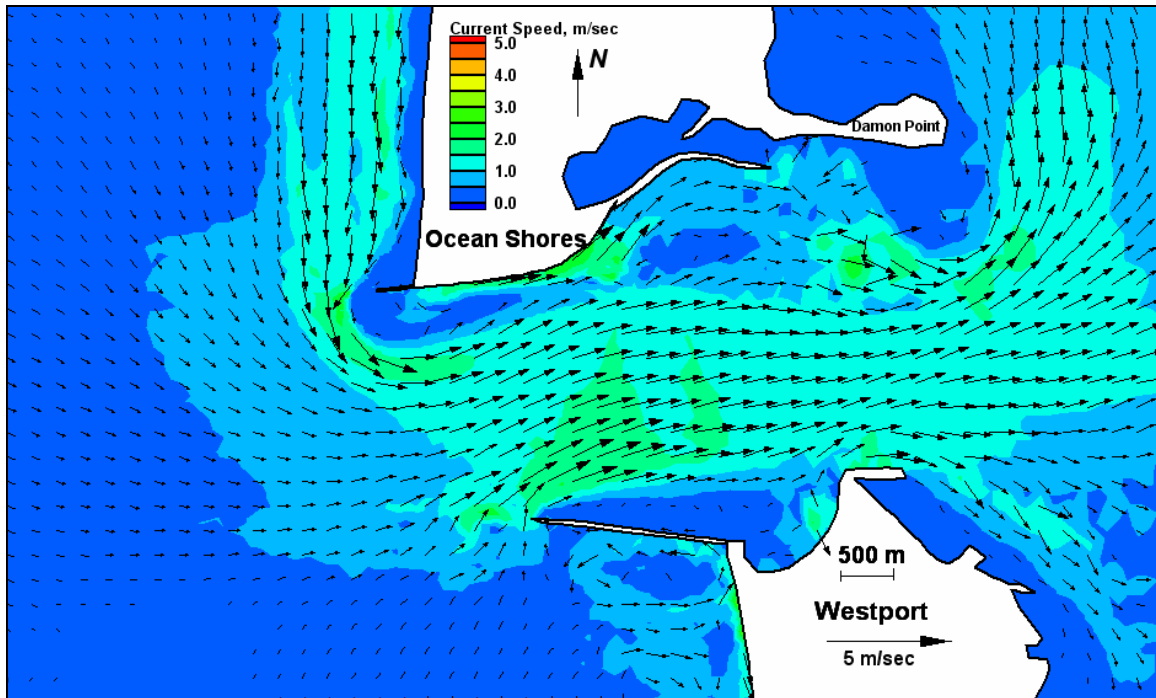Figure E242. Run 163 (Alt 4A, west, spring tide), north jetty view of ebb tide
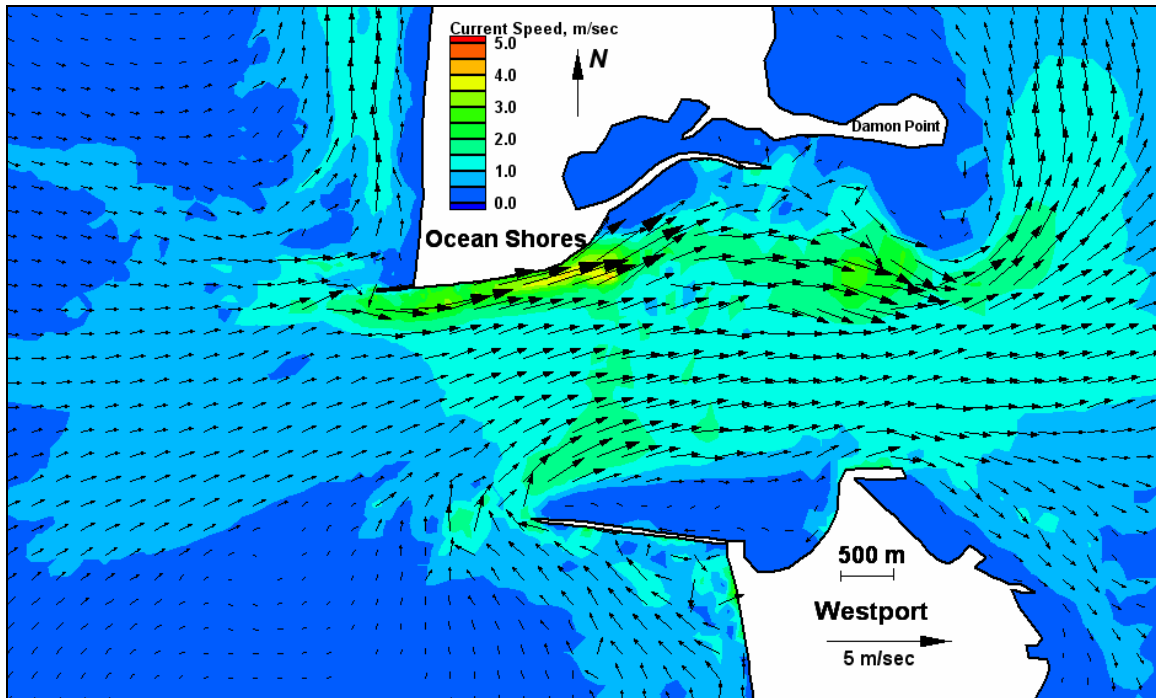
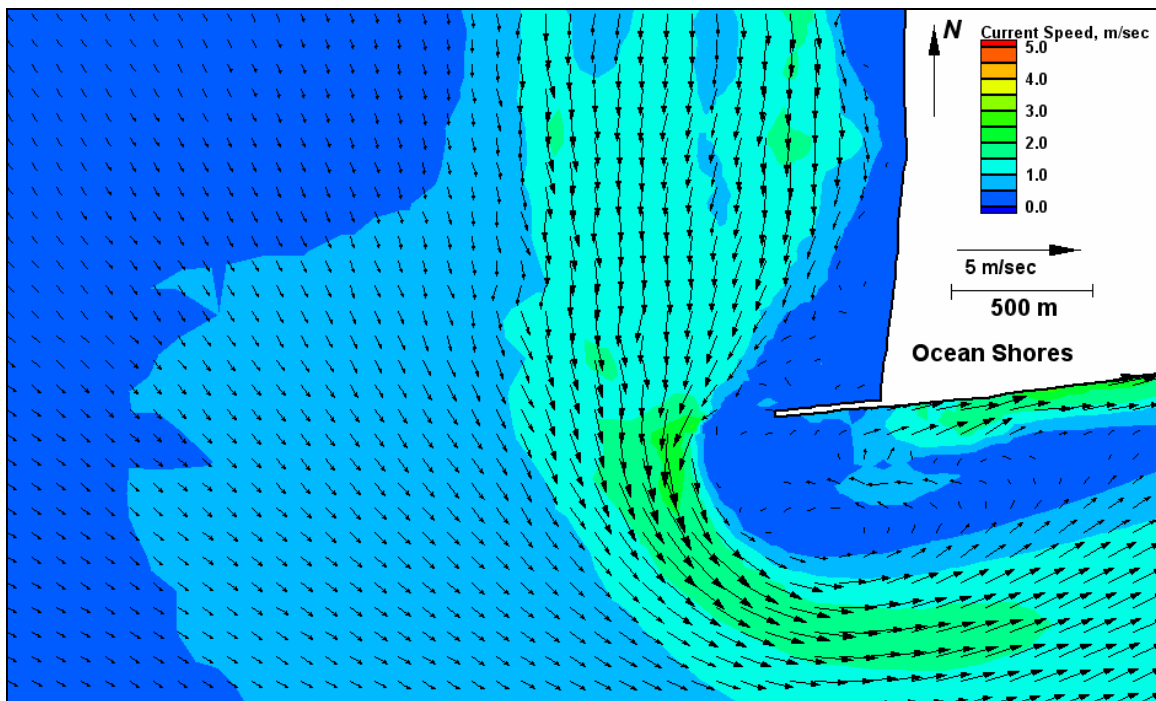Figure E243. Run 164 (existing, west-southwest, spring tide), inlet view of flood tide
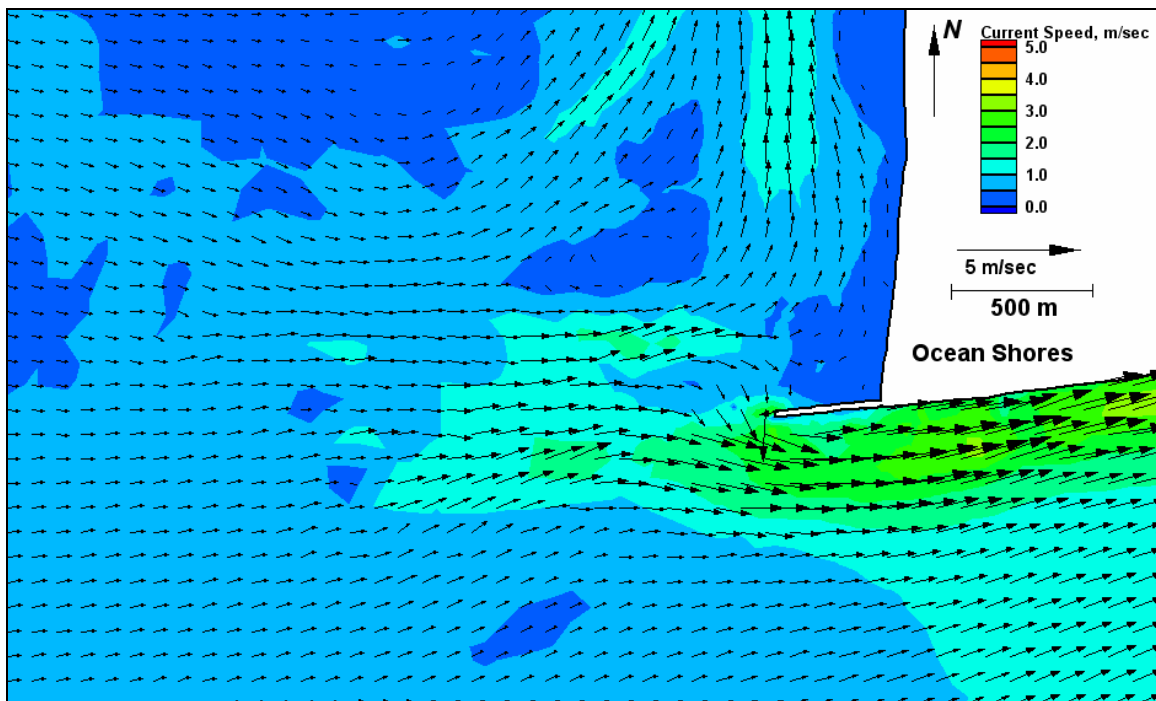
Figure E244. Run 164 (existing, west-southwest, spring tide), north jetty view of flood tide
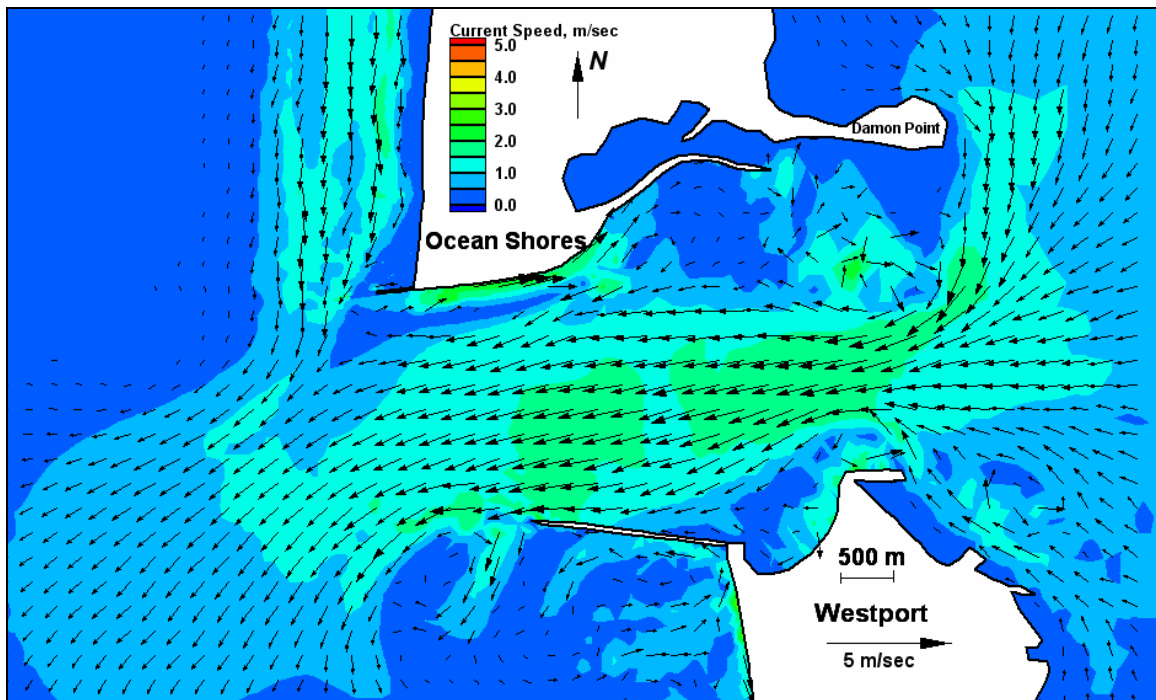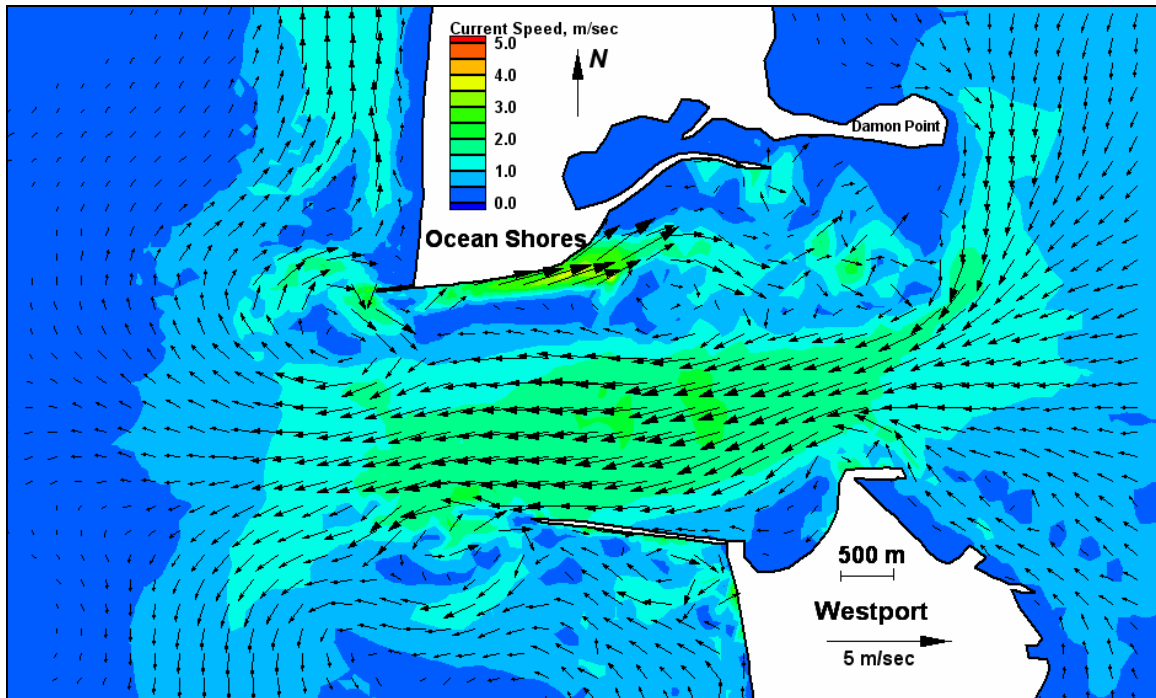
Figure E245. Run 164 (existing, west-southwest, spring tide), inlet view of ebb tide
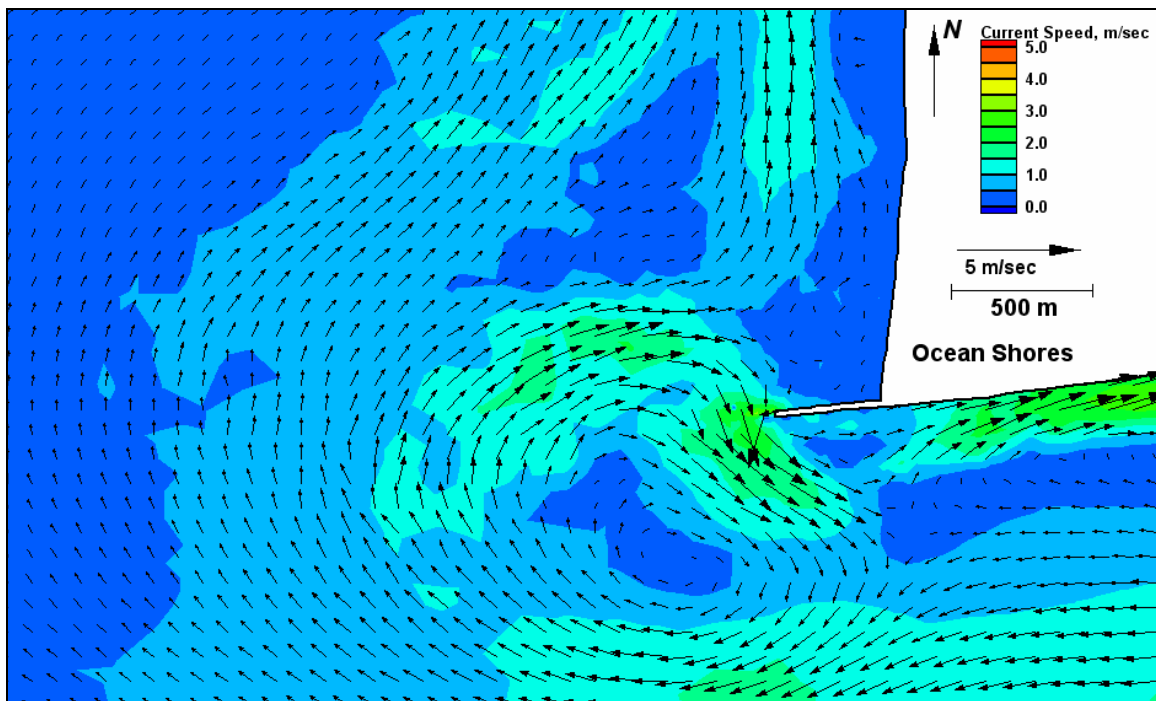
Figure E246. Run 164 (existing, west-southwest, spring tide), north jetty view of ebb tide
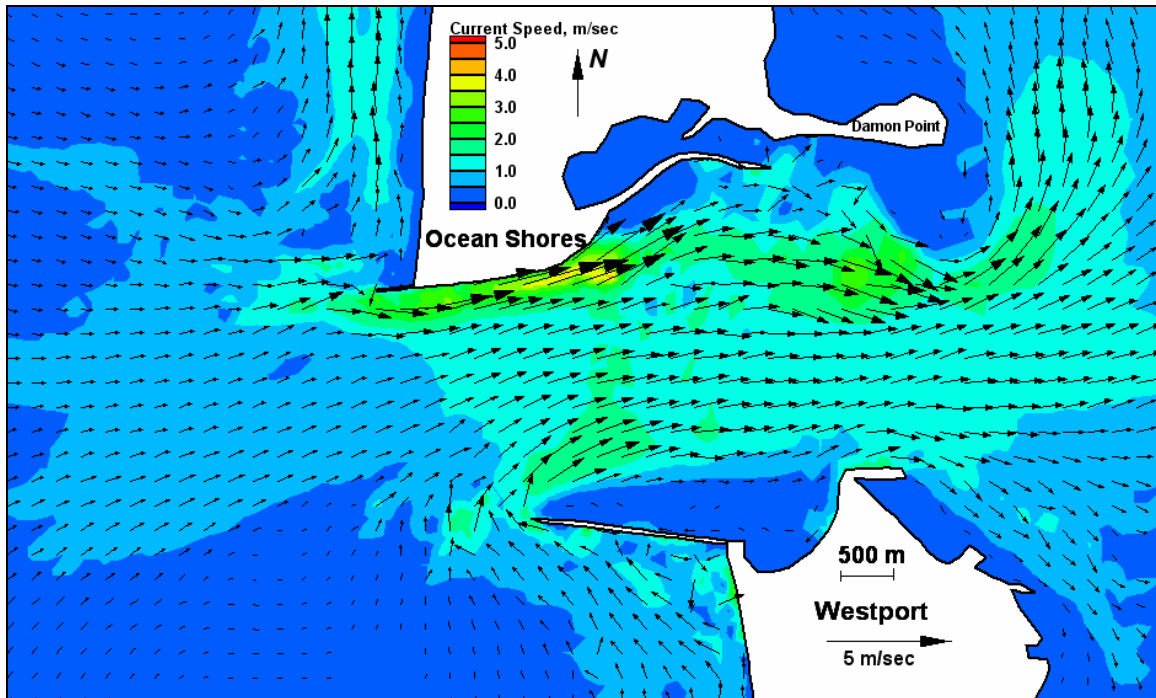
Figure E247. Run 165 (Alt 2A, west-southwest, spring tide), inlet view of flood tide
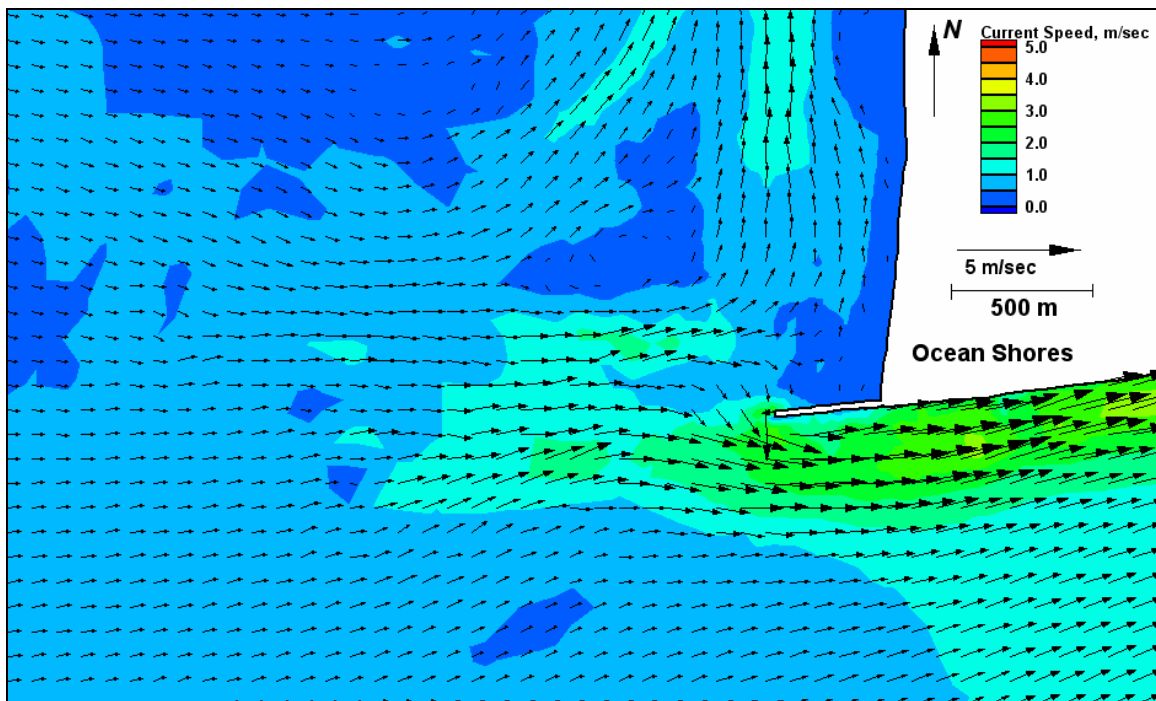
Figure E248. Run 165 (Alt 2A, west-southwest, spring tide), north jetty view of flood tide
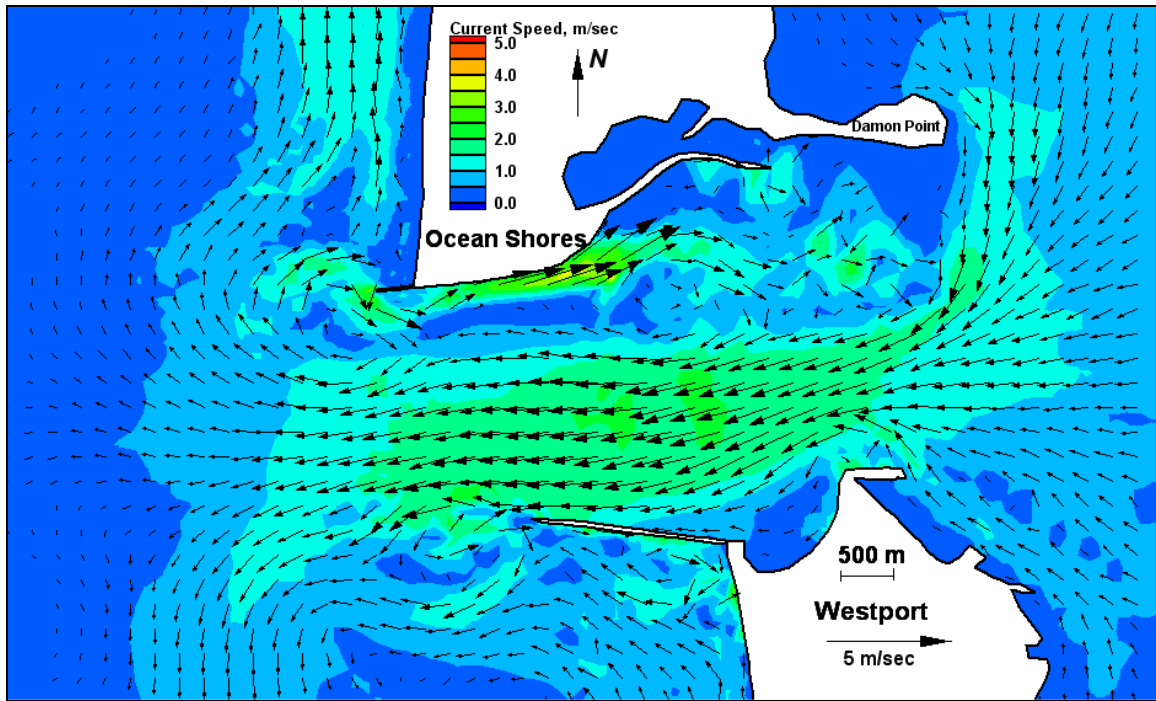
Figure E249. Run 165 (Alt 2A, west-southwest, spring tide), inlet view of ebb tide
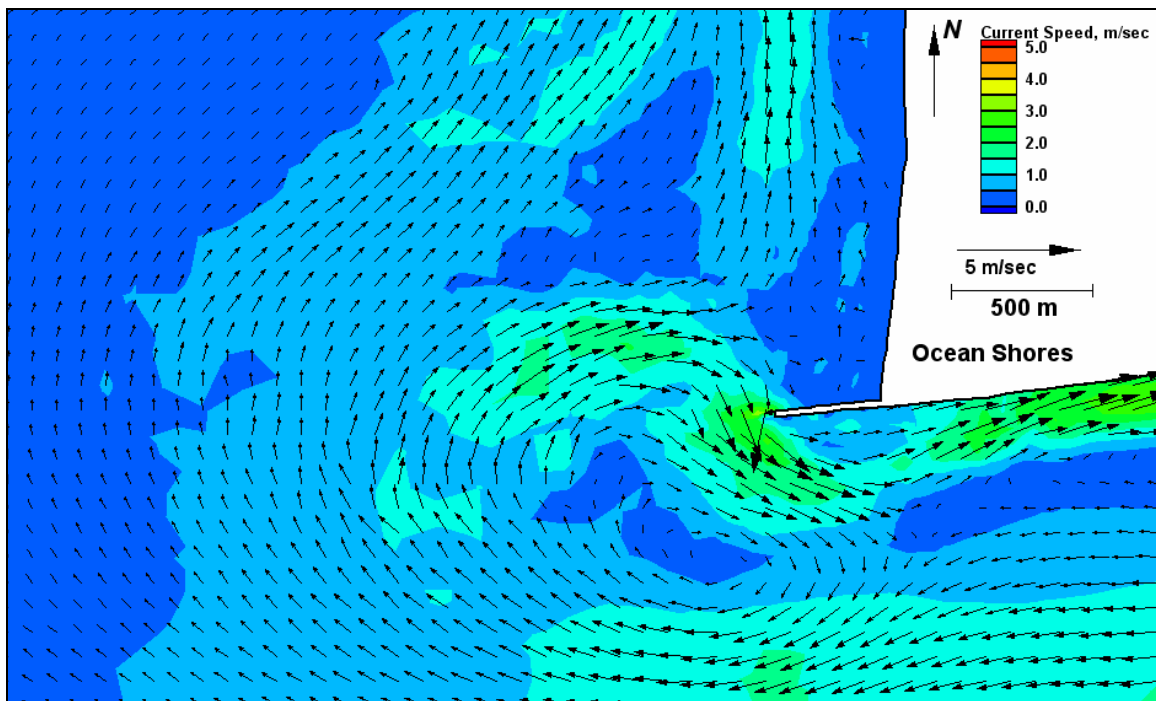

Figure E250. Run 165 (Alt 2A, west-southwest, spring tide), north jetty view of ebb tide
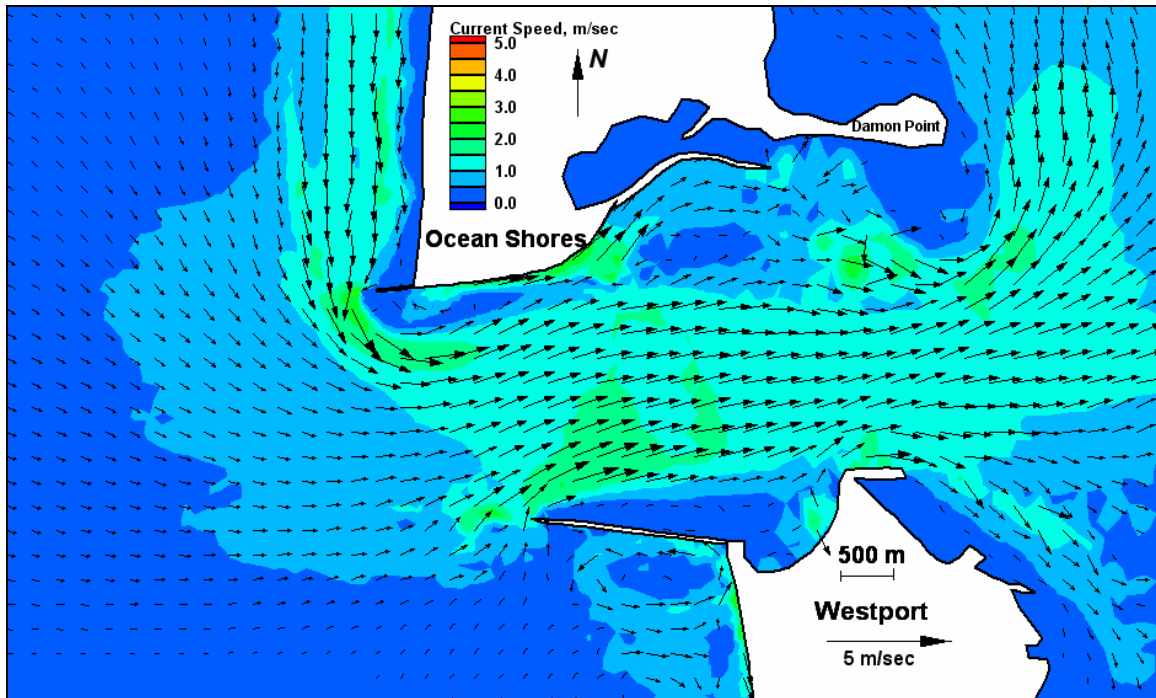
E126
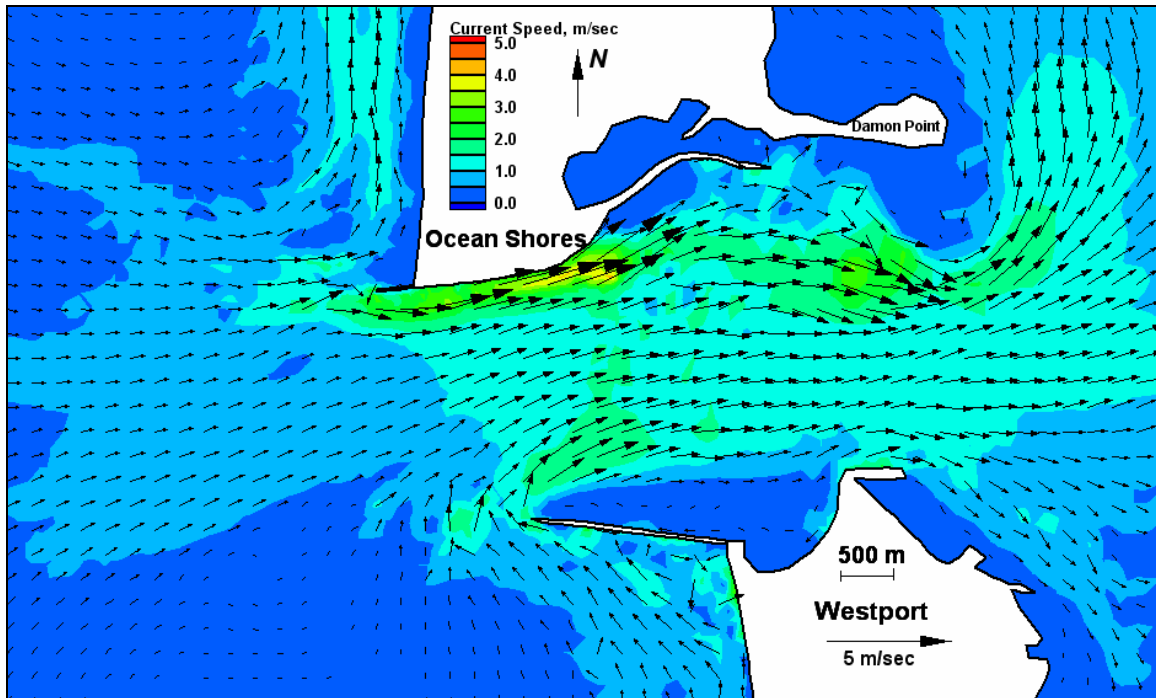
Figure E251. Run 166 (Alt 2B, west-southwest, spring tide), inlet view of flood tide
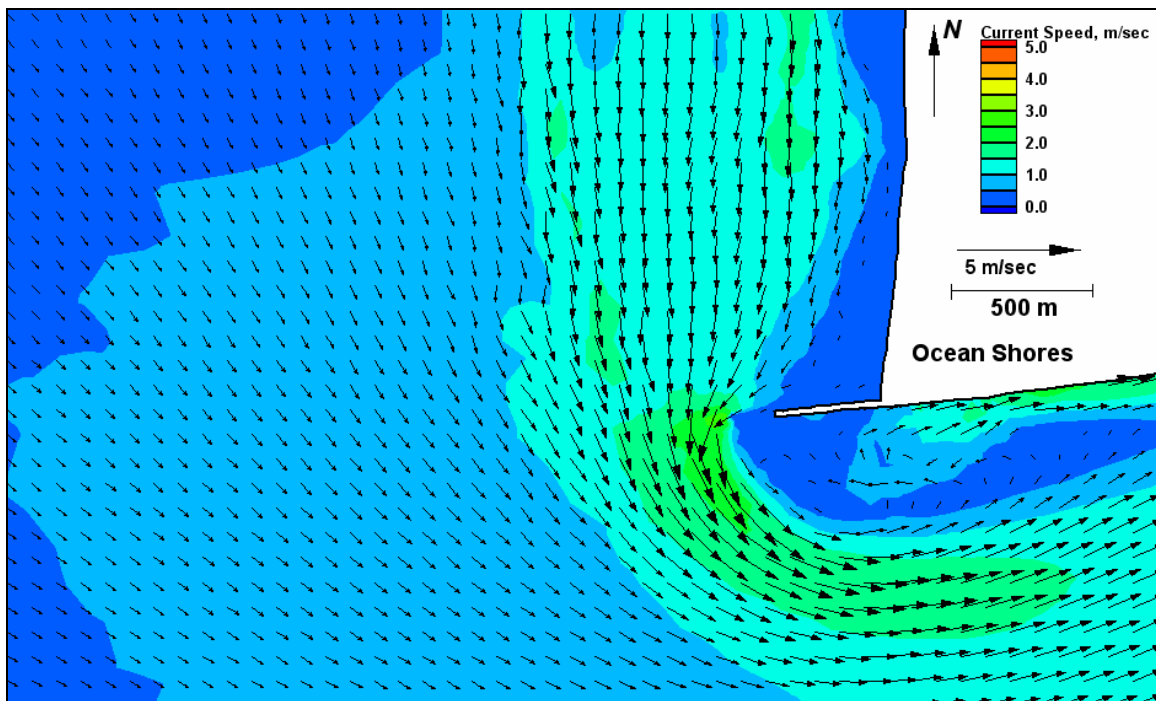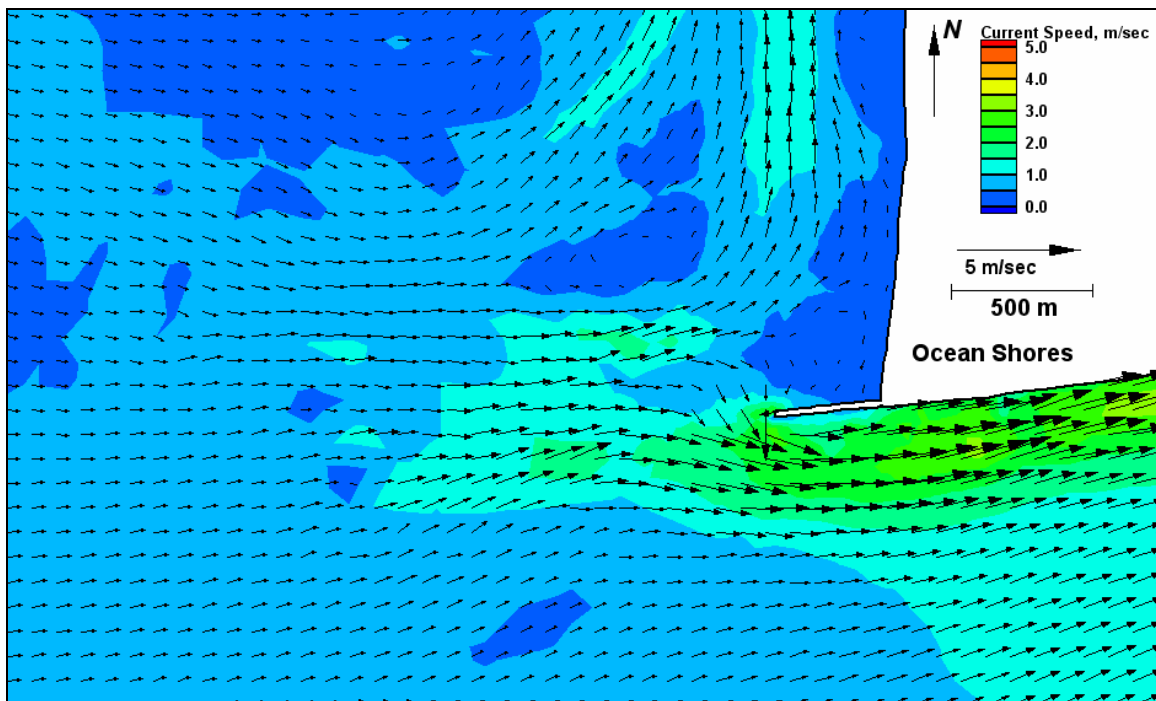

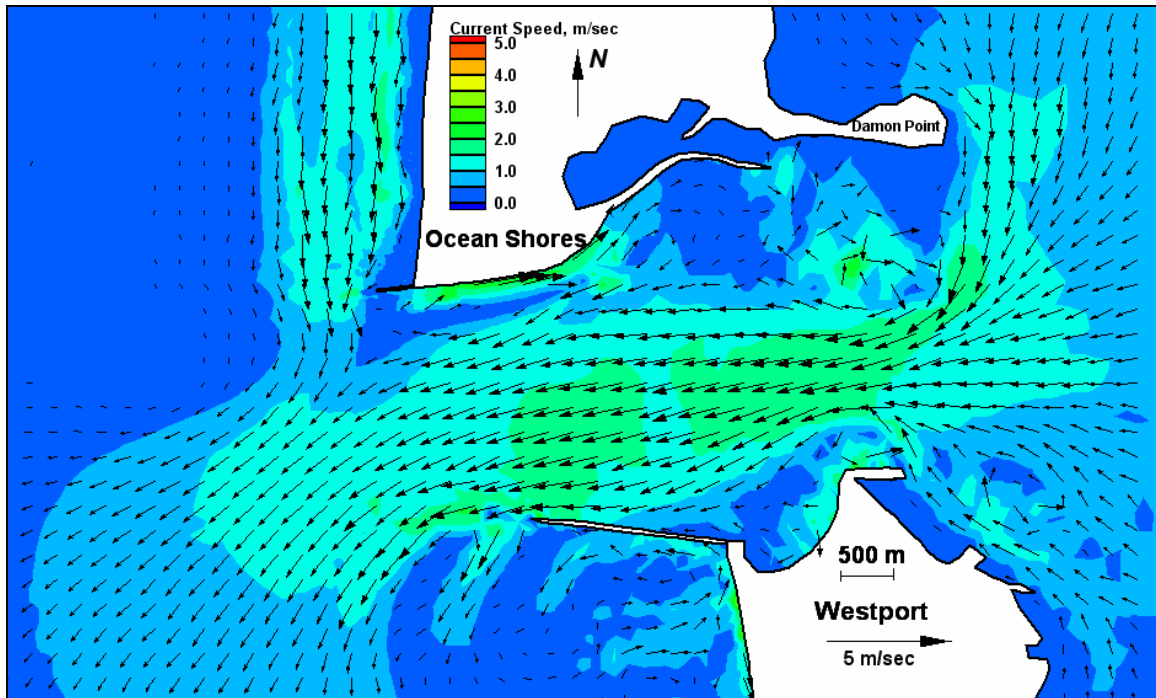Figure E252. Run 166 (Alt 2B, west-southwest, spring tide), north jetty view of flood tide
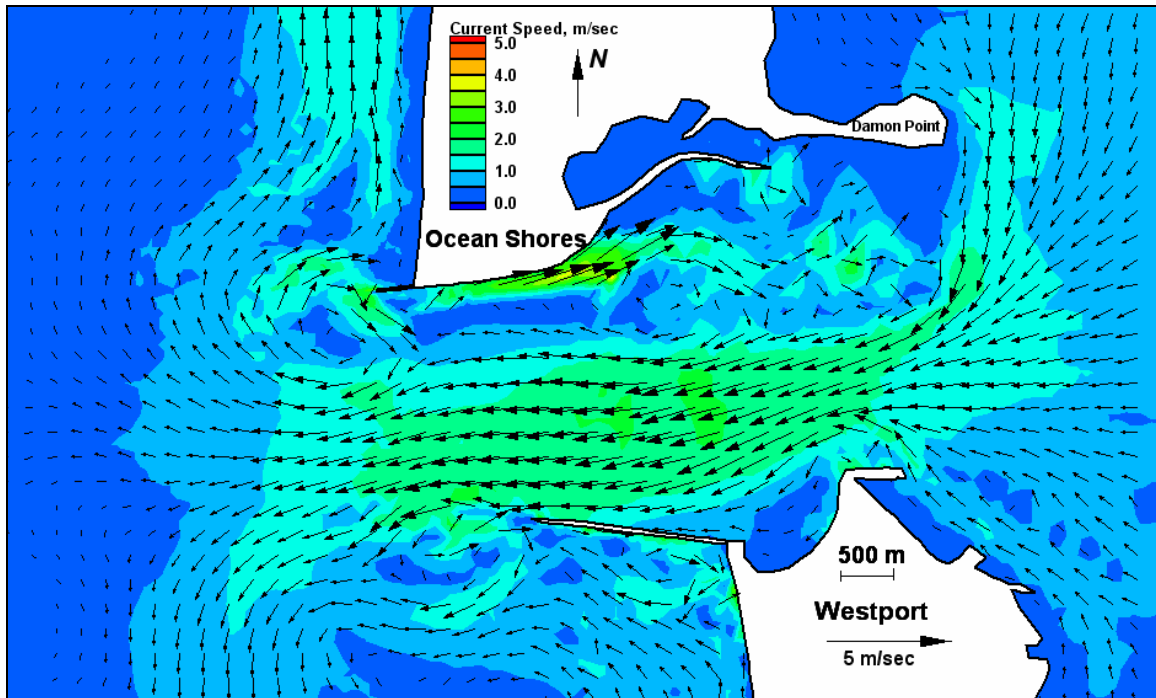
Figure E253. Run 166 (Alt 2B, west-southwest, spring tide), inlet view of ebb tide
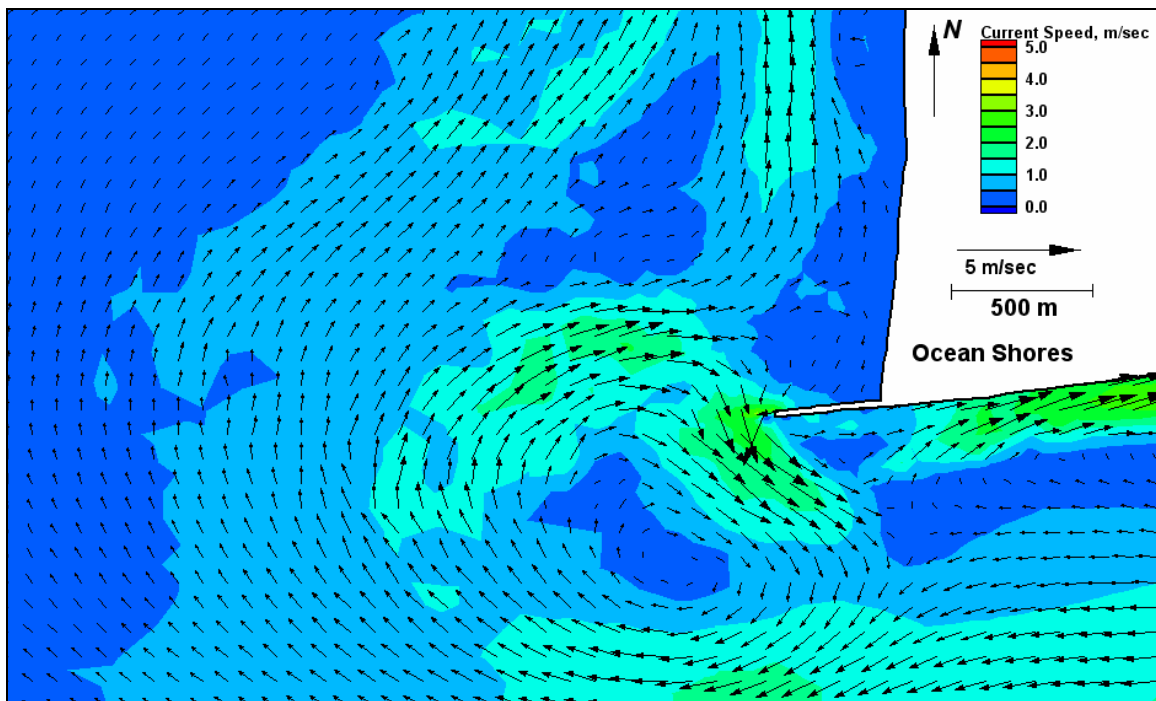
Figure E254. Run 166 (Alt 2B, west-southwest, spring tide), north jetty view of ebb tide
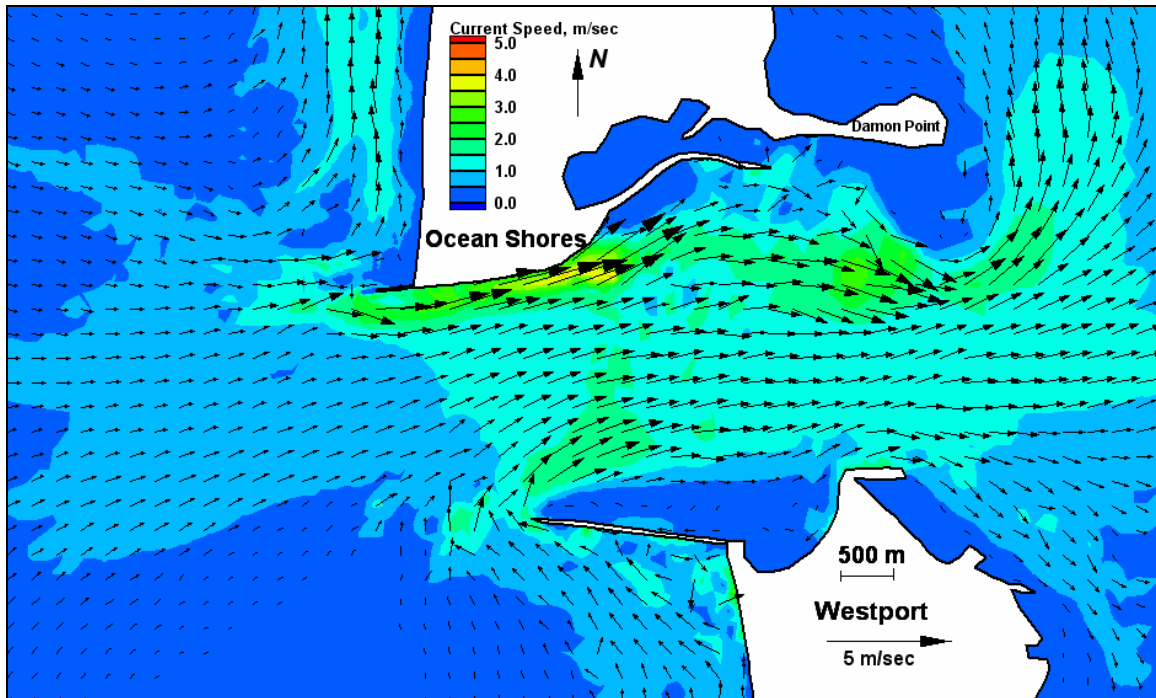
Figure E255. Run 167 (Alt 3A, west-southwest, spring tide), inlet view of flood tide
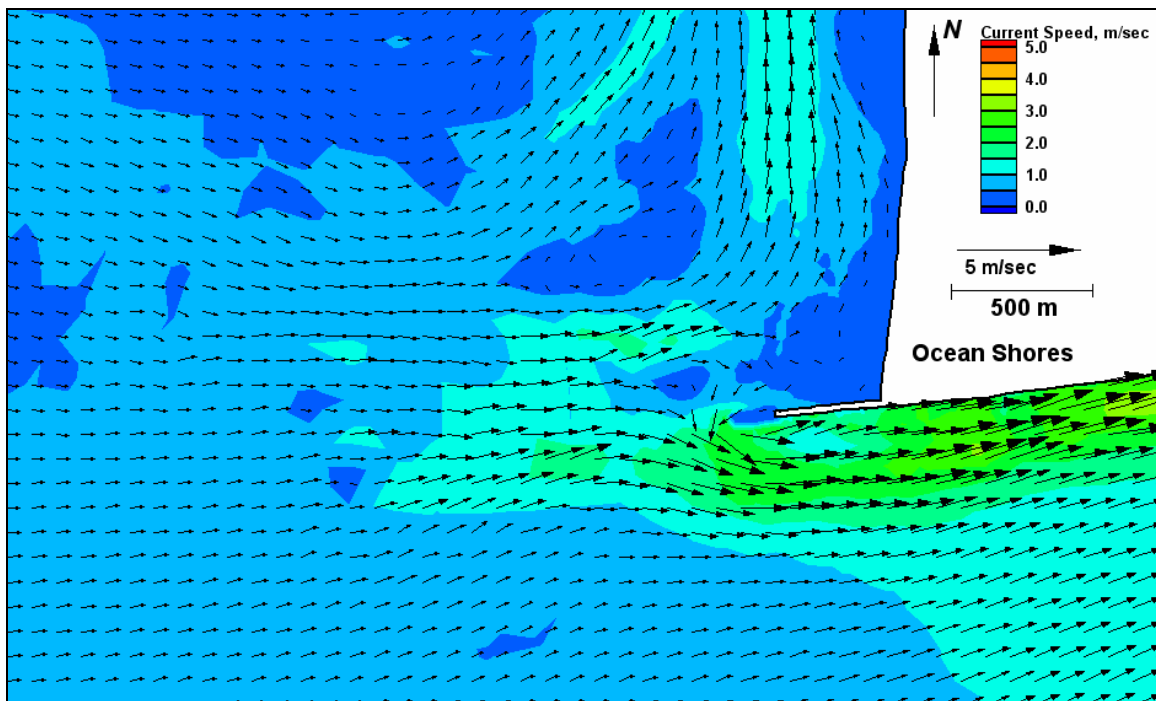
Figure E256. Run 167 (Alt 3A, west-southwest, spring tide), north jetty view of flood tide
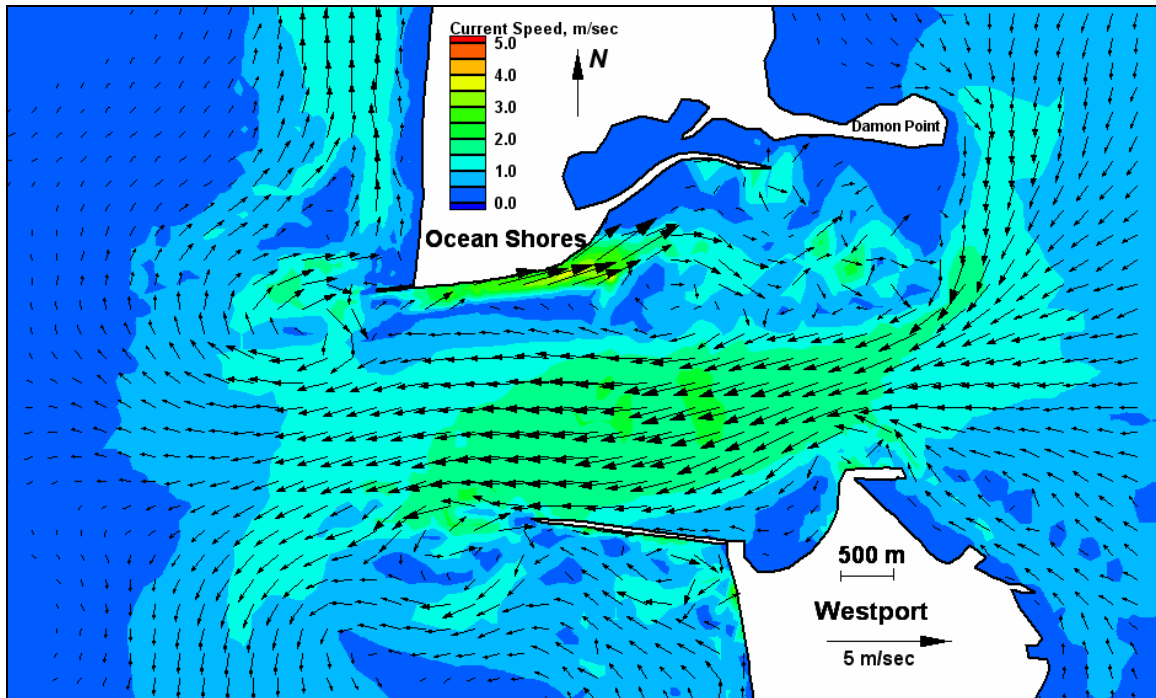
Figure E257. Run 167 (Alt 3A, west-southwest, spring tide), inlet view of ebb tide
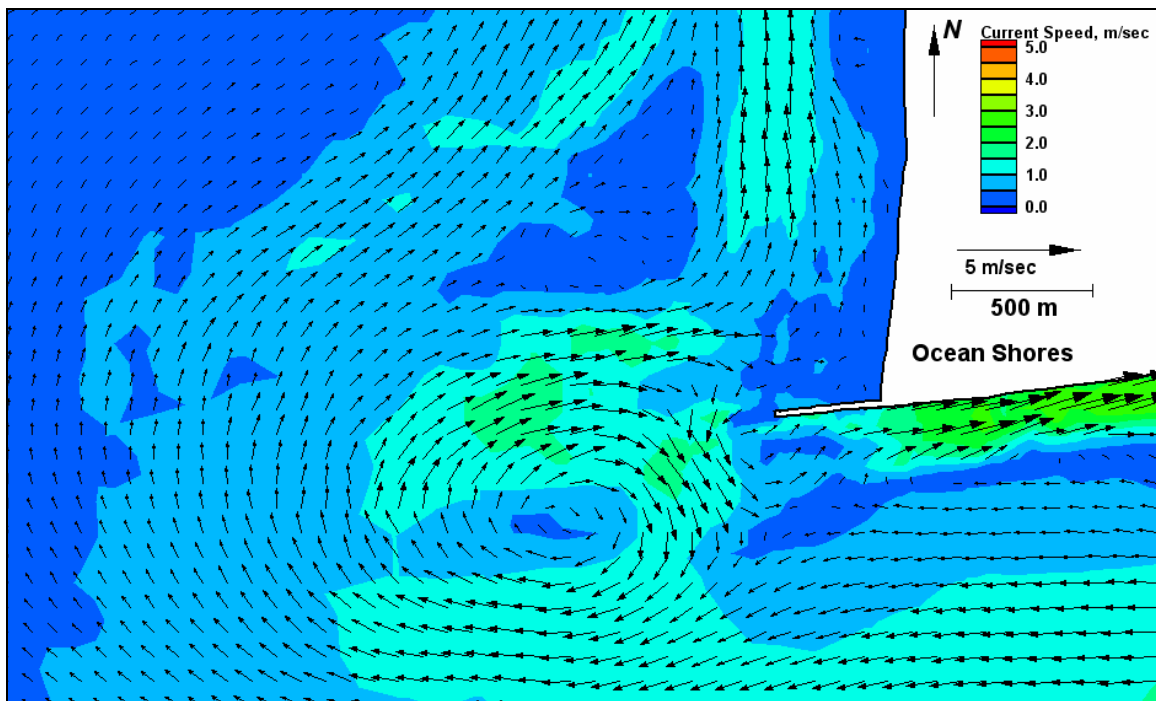

Figure E258. Run 167 (Alt 3A, west-southwest, spring tide), north jetty view of ebb tide

Appendix E   Tidal Circulation Simulation Results
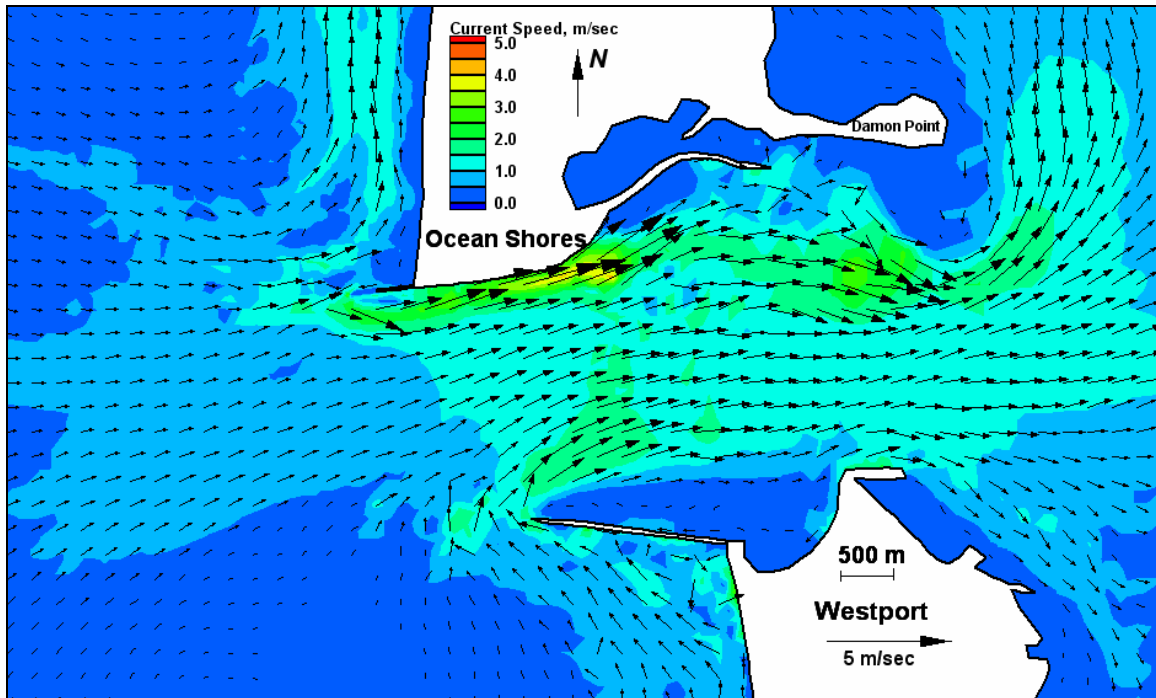
Figure E259. Run 168 (Alt 3B, west-southwest, spring tide), inlet view of flood tide
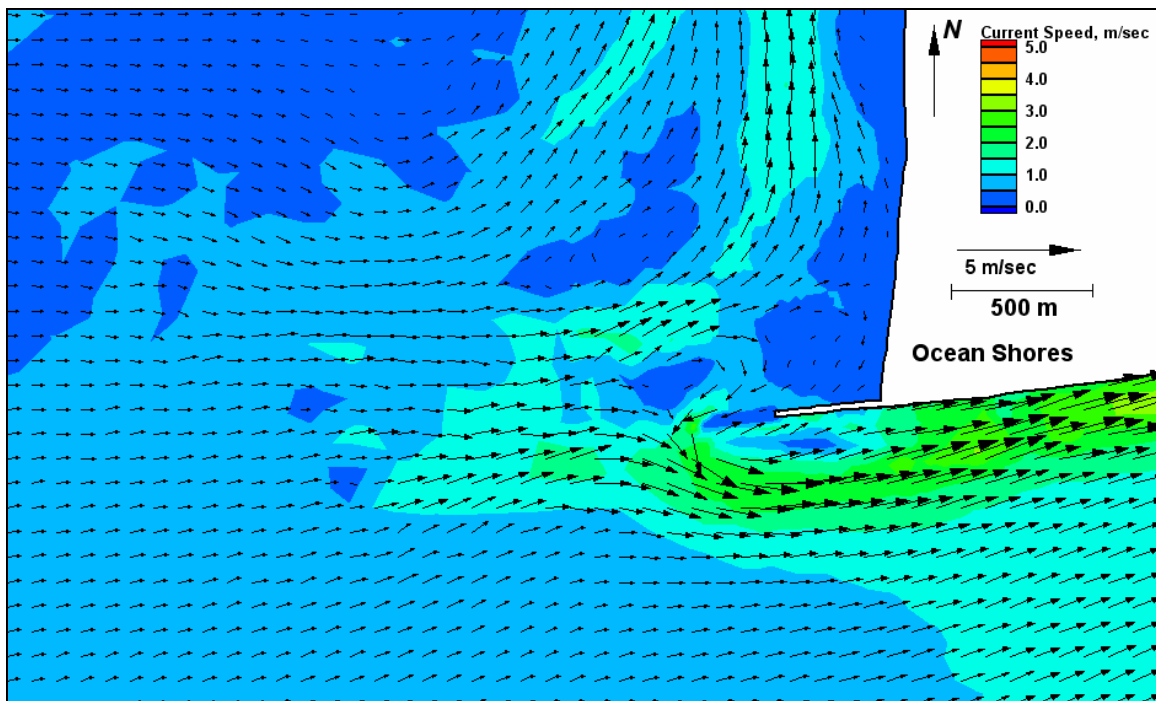
Figure E260. Run 168 (Alt 3B, west-southwest, spring tide), north jetty view of flood tide
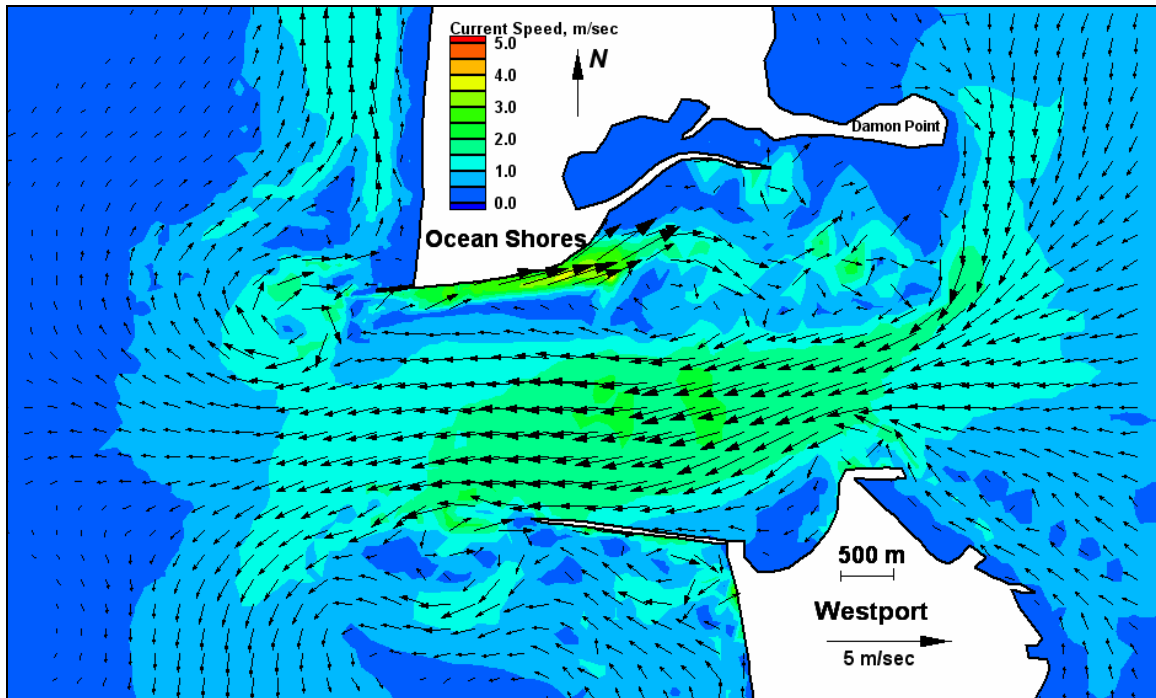
Figure E261. Run 168 (Alt 3B, west-southwest, spring tide), inlet view of ebb tide
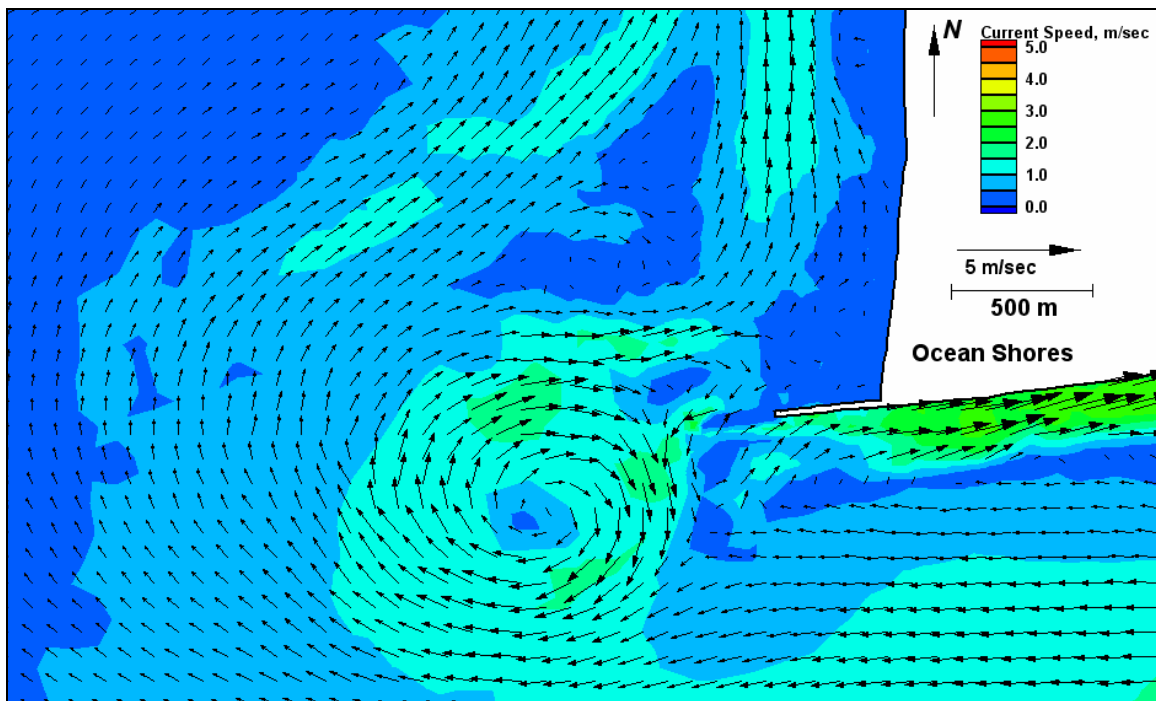
Figure E262. Run 168 (Alt 3B, west-southwest, spring tide), north jetty view of ebb tide

Appendix E   Tidal Circulation Simulation Results
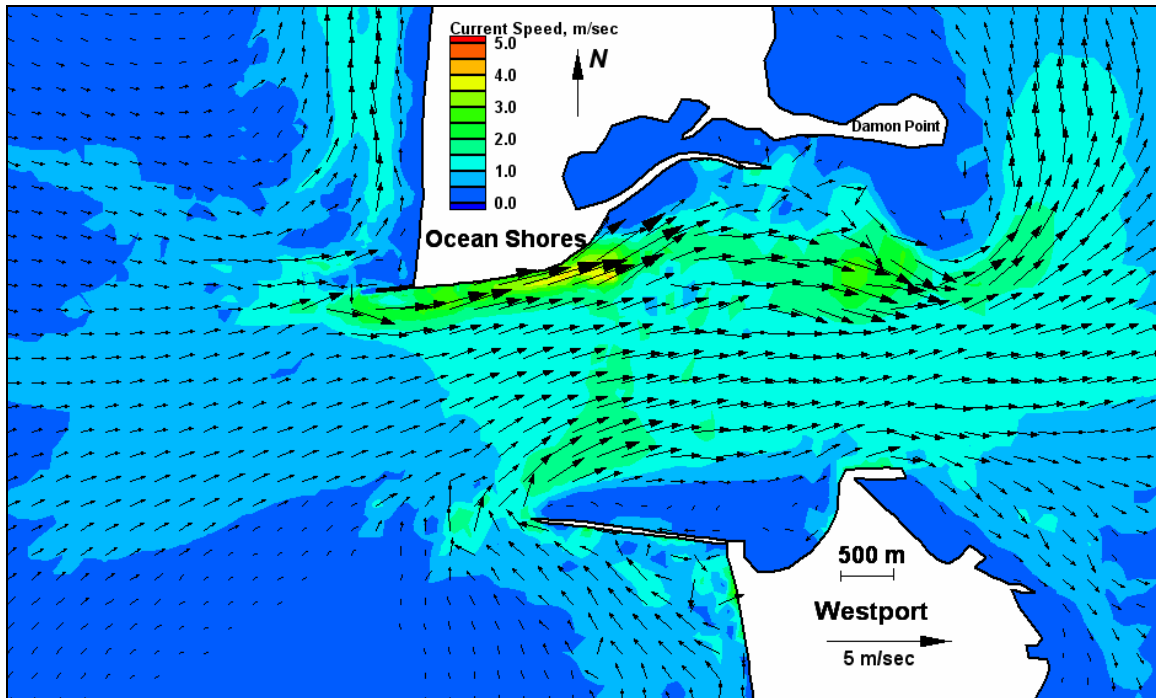
Figure E263. Run 169 (Alt 4A, west-southwest, spring tide), inlet view of flood tide
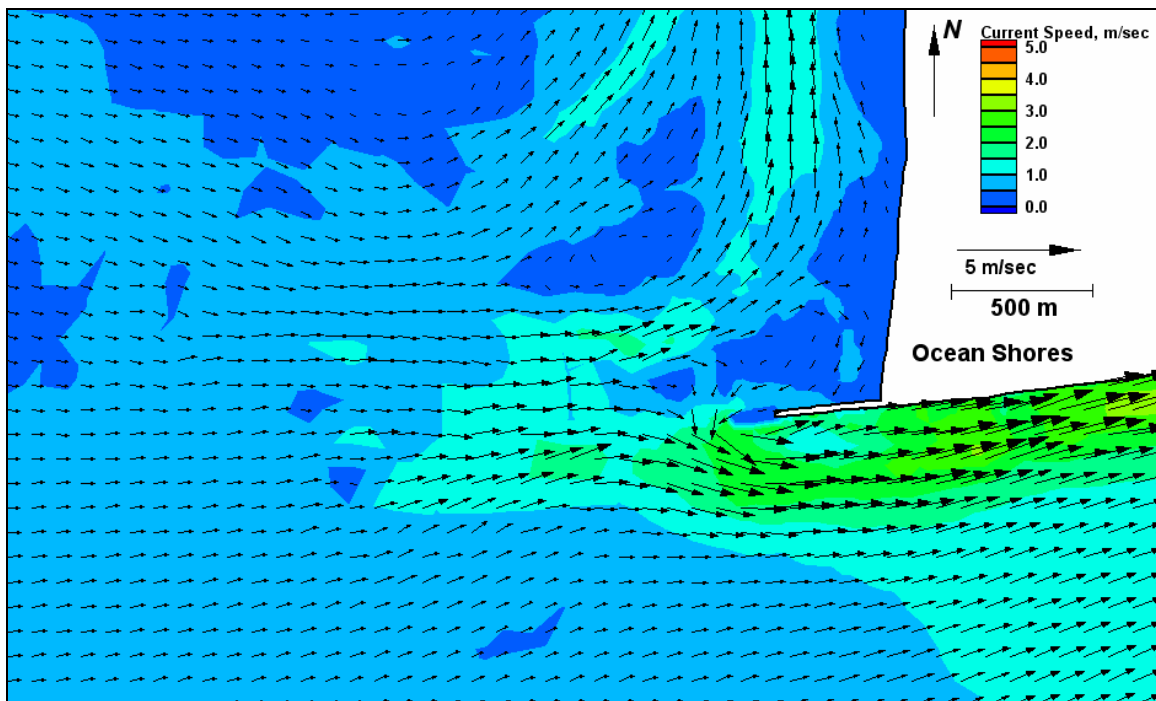
Figure E264. Run 169 (Alt 4A, west-southwest, spring tide), north jetty view of flood tide
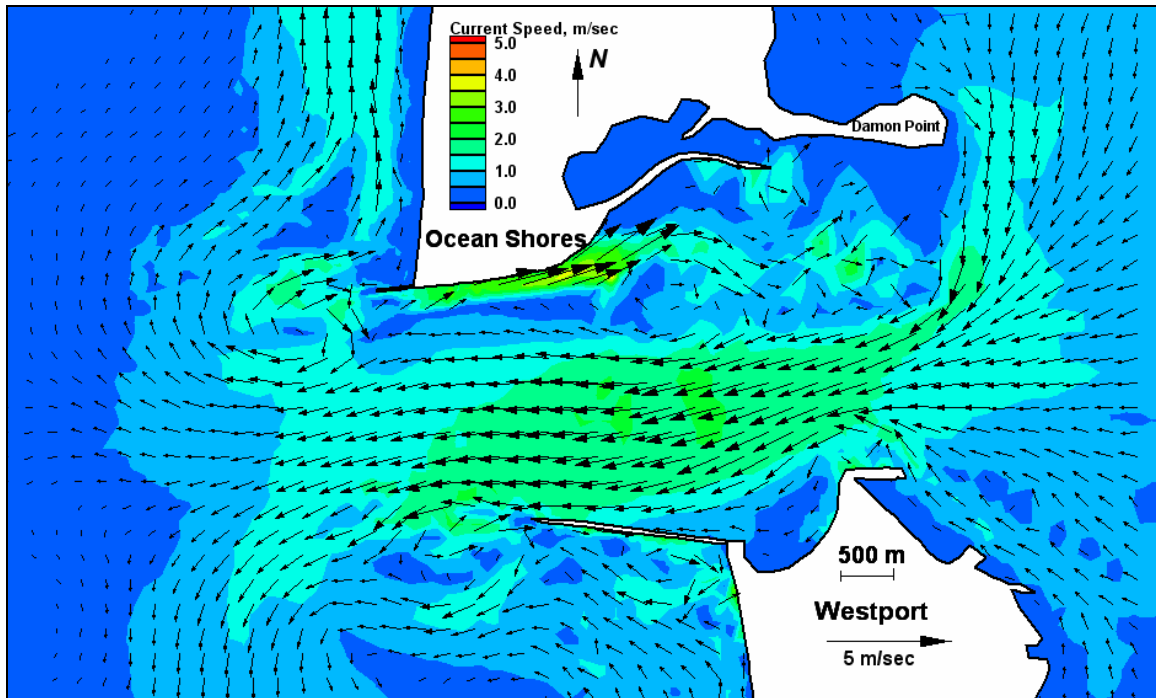
Figure E265. Run 169 (Alt 4A, west-southwest, spring tide), inlet view of ebb tide
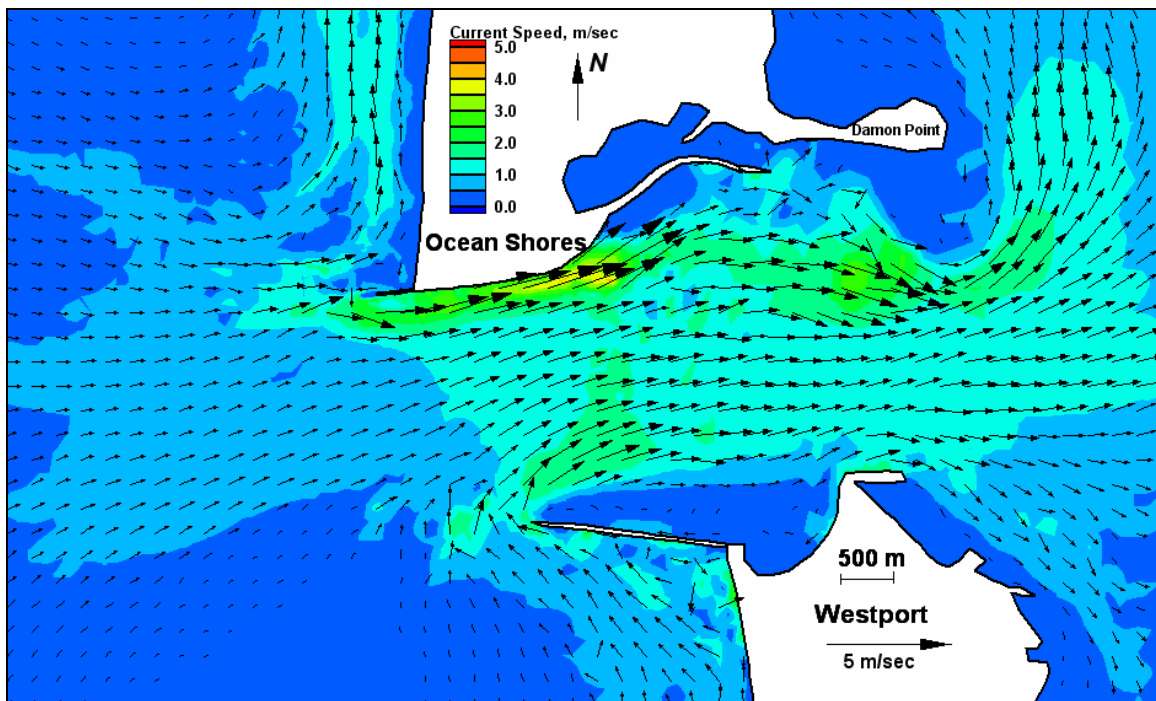
Figure E266. Run 169 (Alt 4A, west-southwest, spring tide), north jetty view of ebb tide

E134

Difference Maps of Current
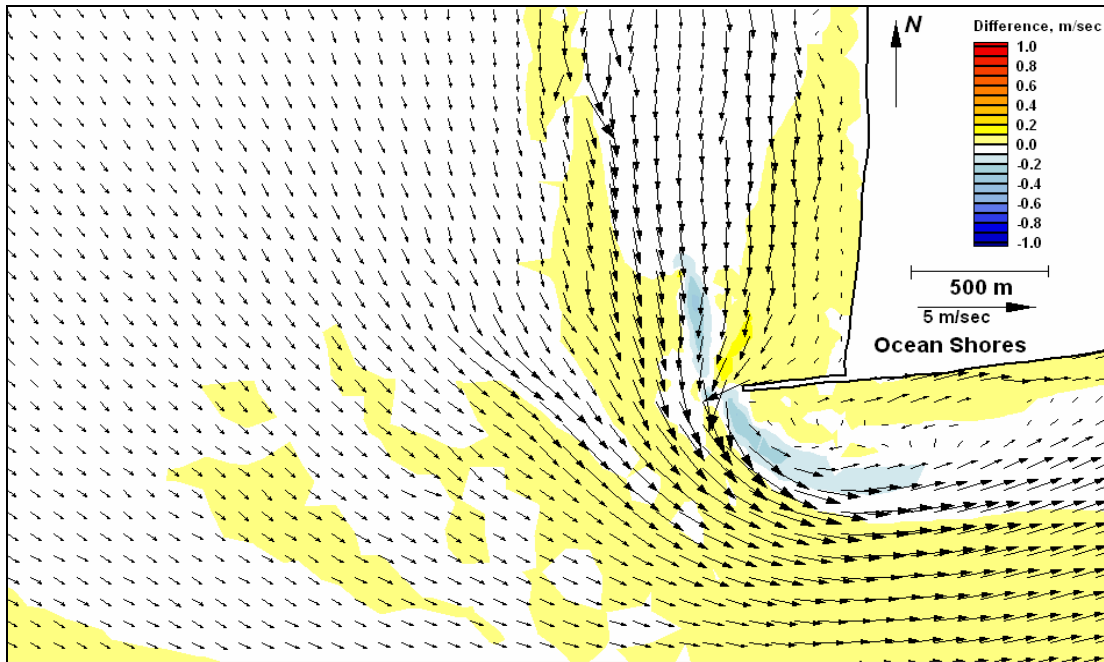
Figure E267. Difference map 108-104 for peak flood
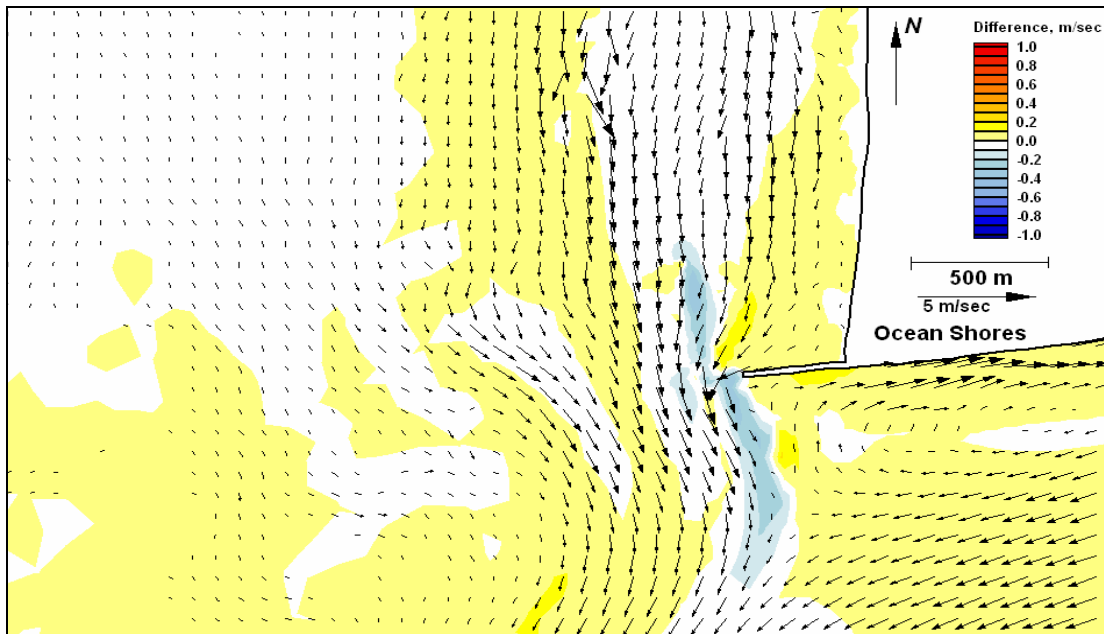
Figure E268. Difference map 108-104 for peak ebb
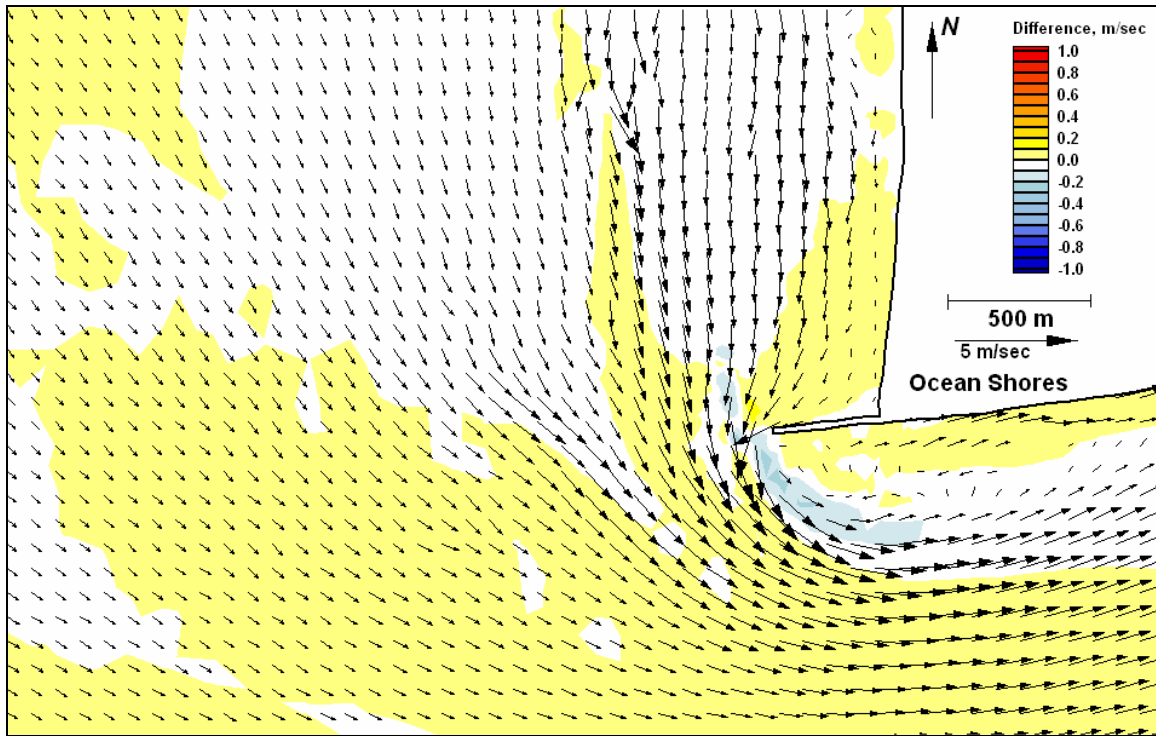
Figure E269. Difference map 112-104 for peak flood
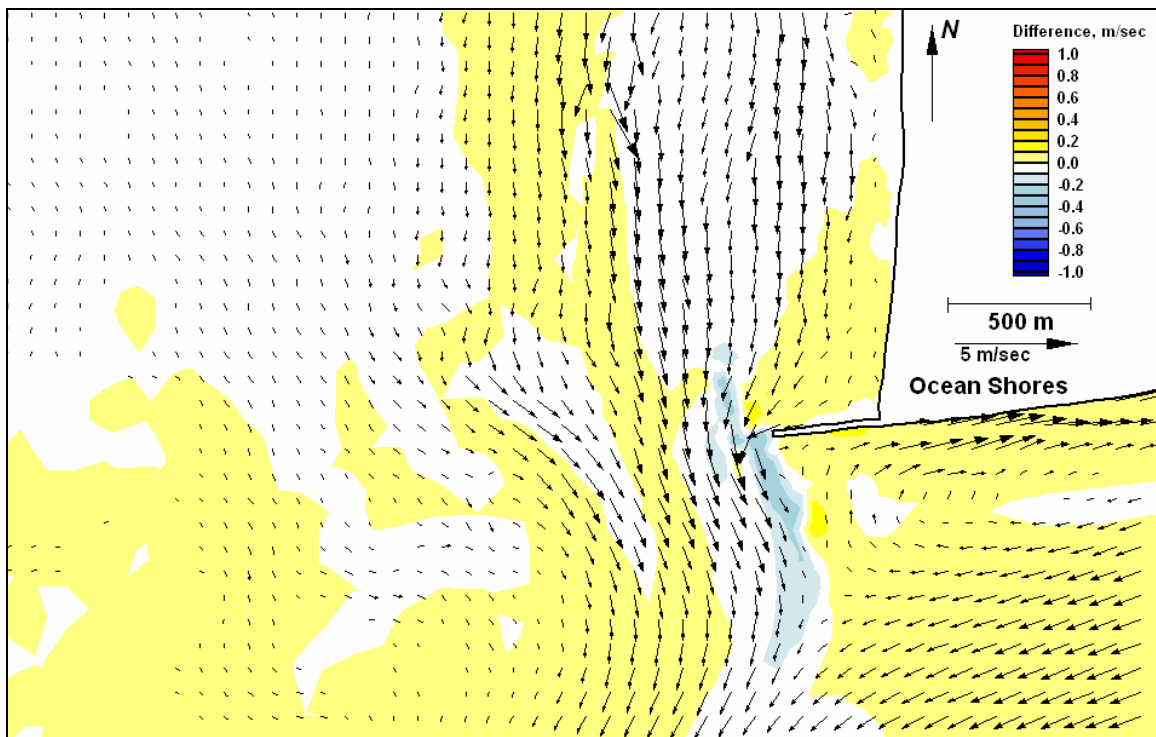
Figure E270. Difference map 112-104 for peak ebb
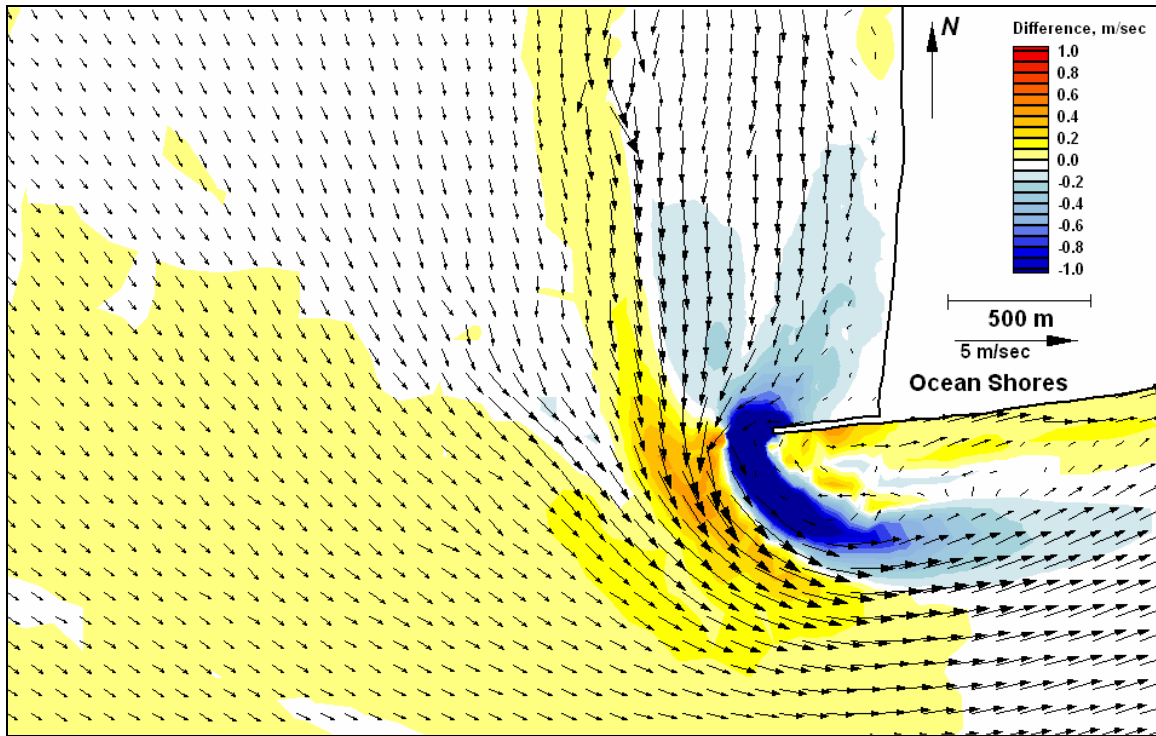
Figure E271. Difference map 116-104 for peak flood
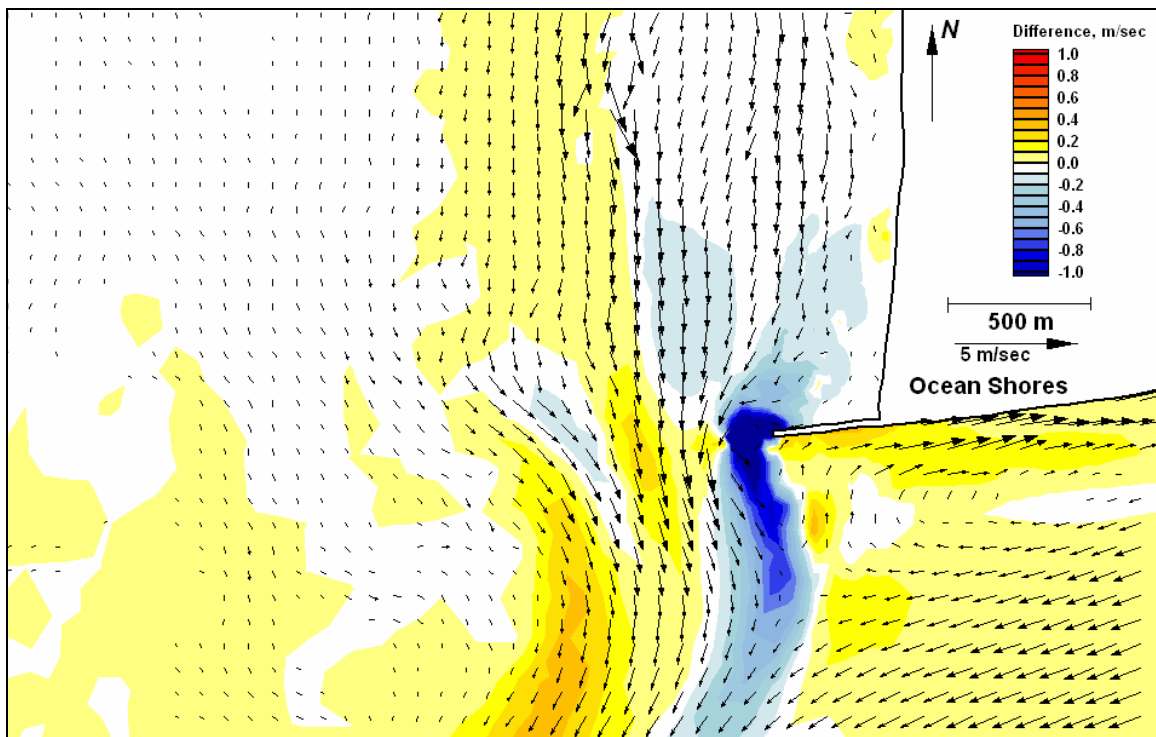
Figure E272. Difference map 116-104 for peak ebb
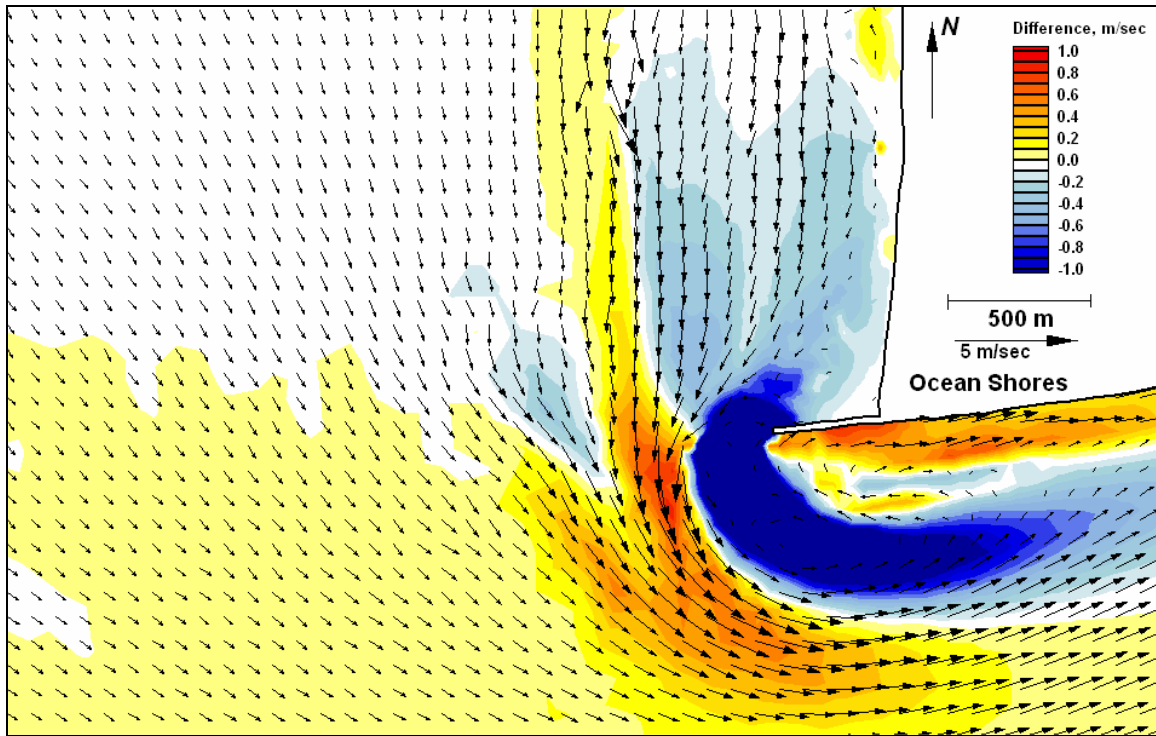
Figure E273. Difference map 120-104 for peak flood
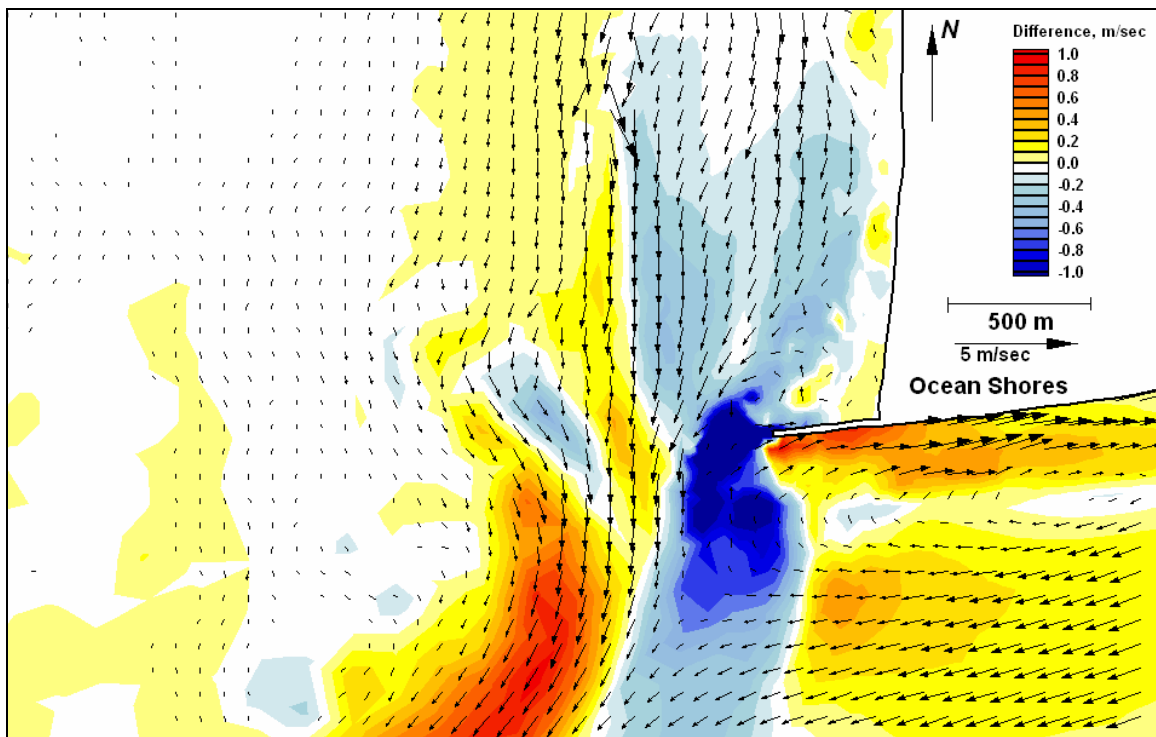
Figure E274. Difference map 120-104 for peak ebb

Appendix E   Tidal Circulation Simulation Results
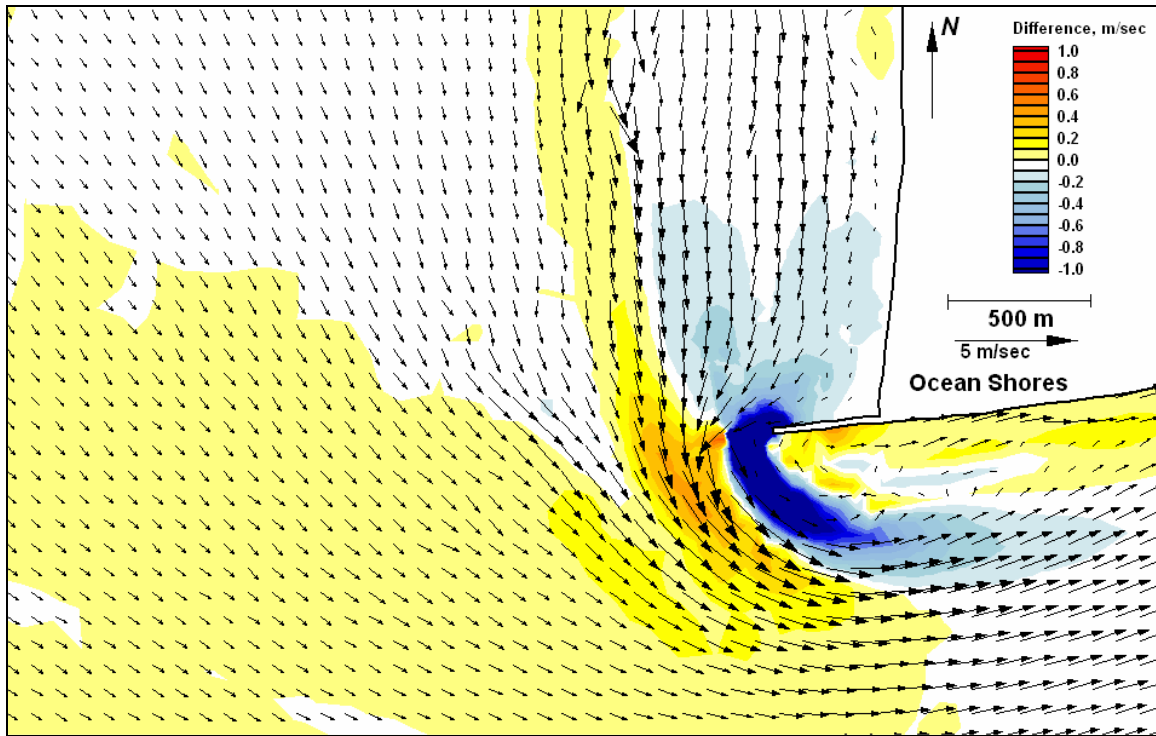
Figure E275. Difference map 124-104 for peak flood
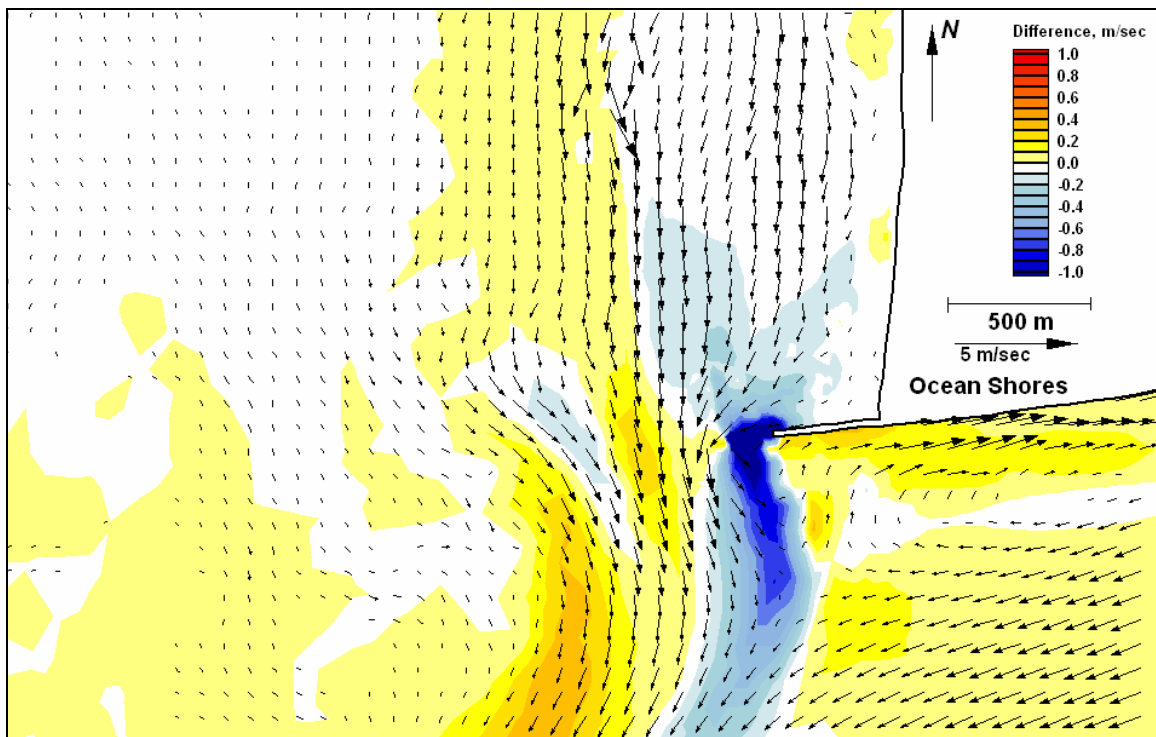
Figure E276. Difference map 124-104 for peak ebb
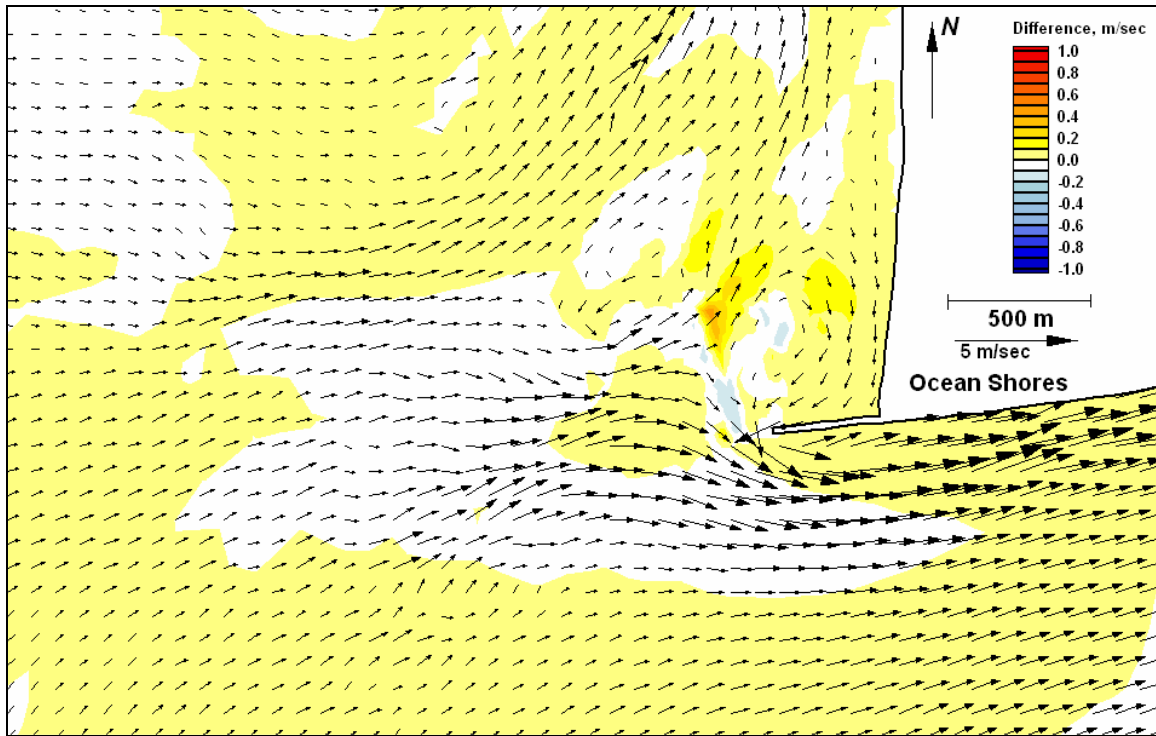
Figure E277. Difference map 109-105 for peak flood
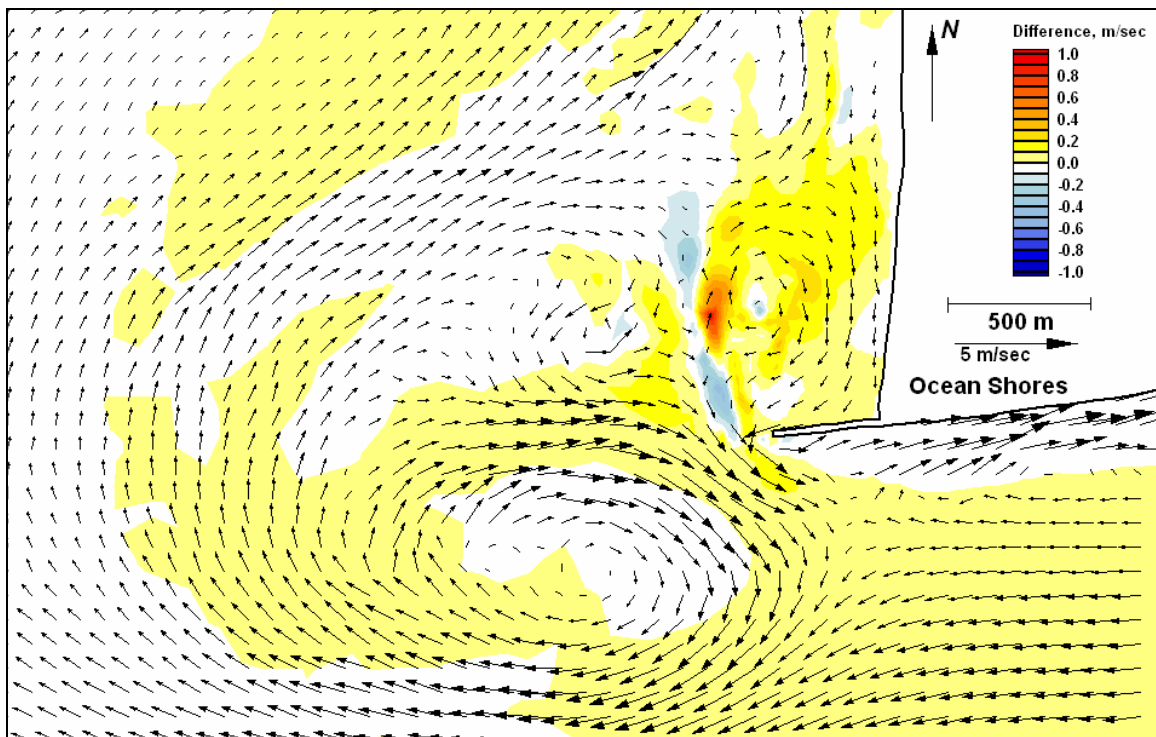
Figure E278. Difference map 109-105 for peak ebb

Appendix E   Tidal Circulation Simulation Results
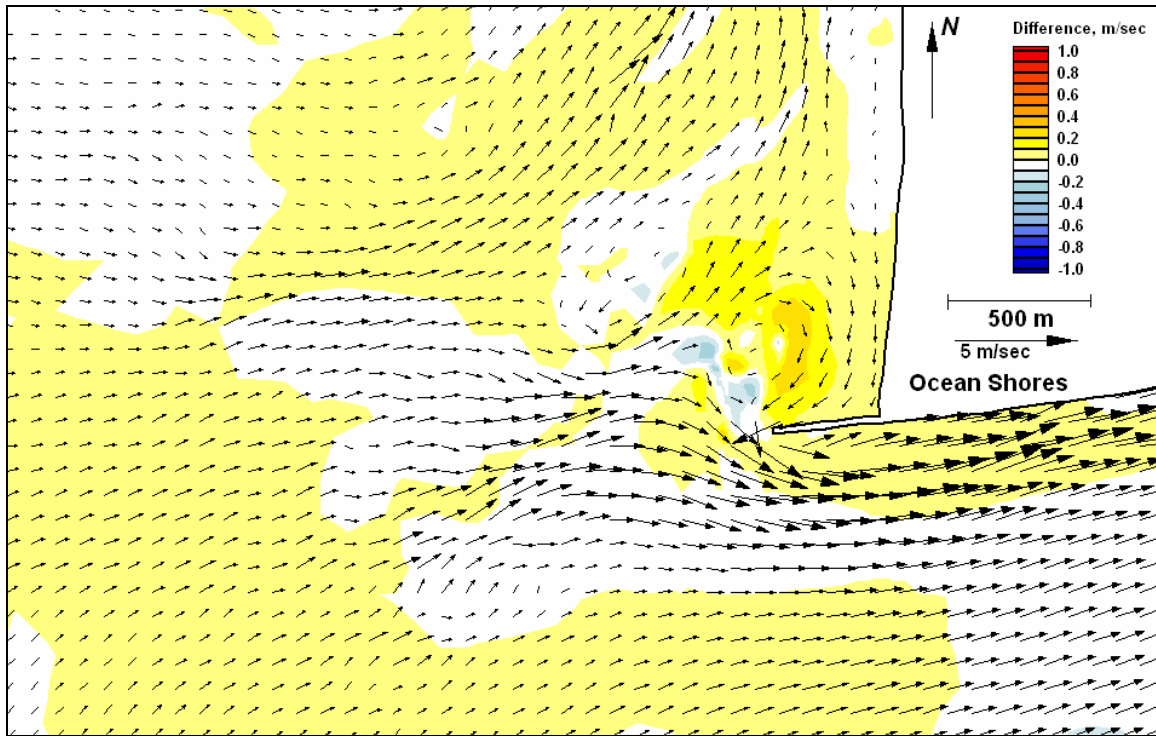
Figure E279. Difference map 113-105 for peak flood
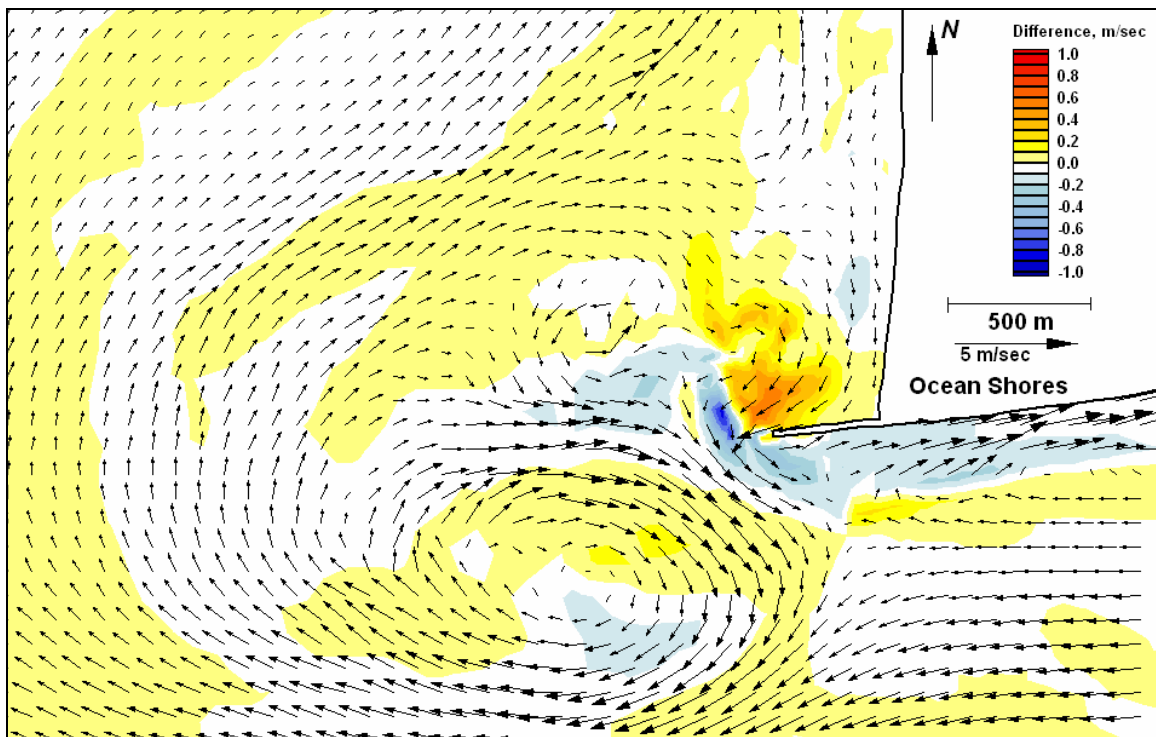
Figure E280. Difference map 113-105 for peak ebb
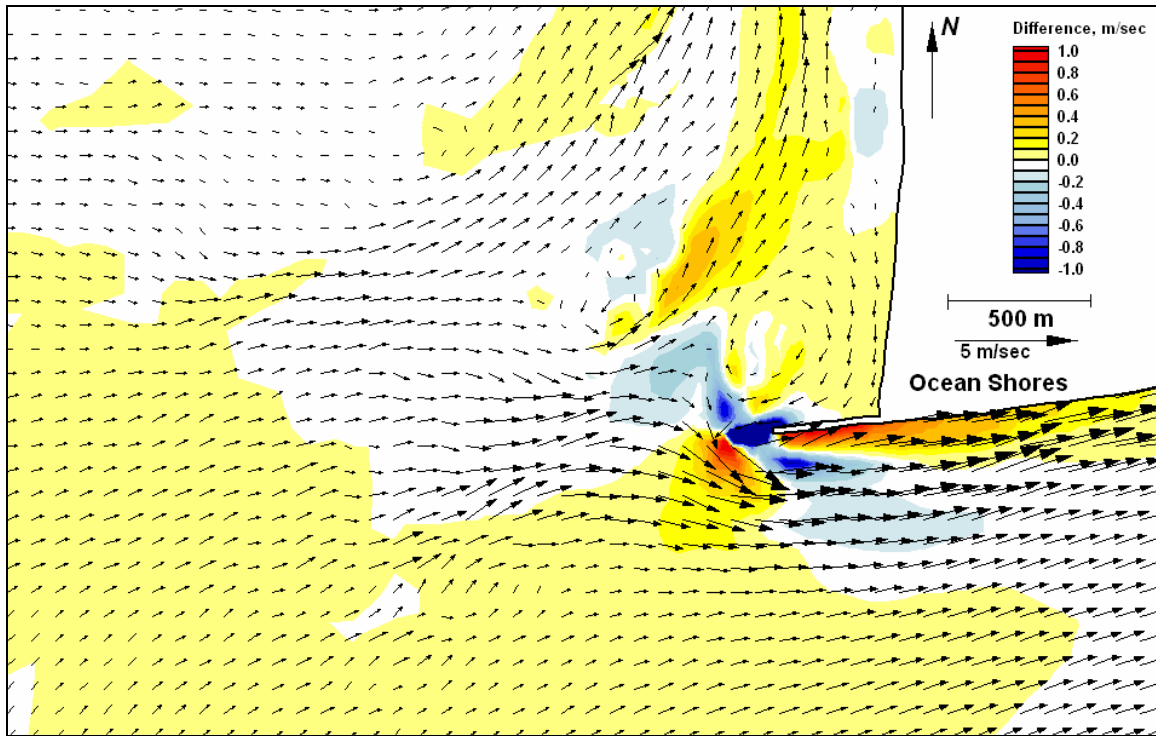
Figure E281. Difference map 117-105 for peak flood
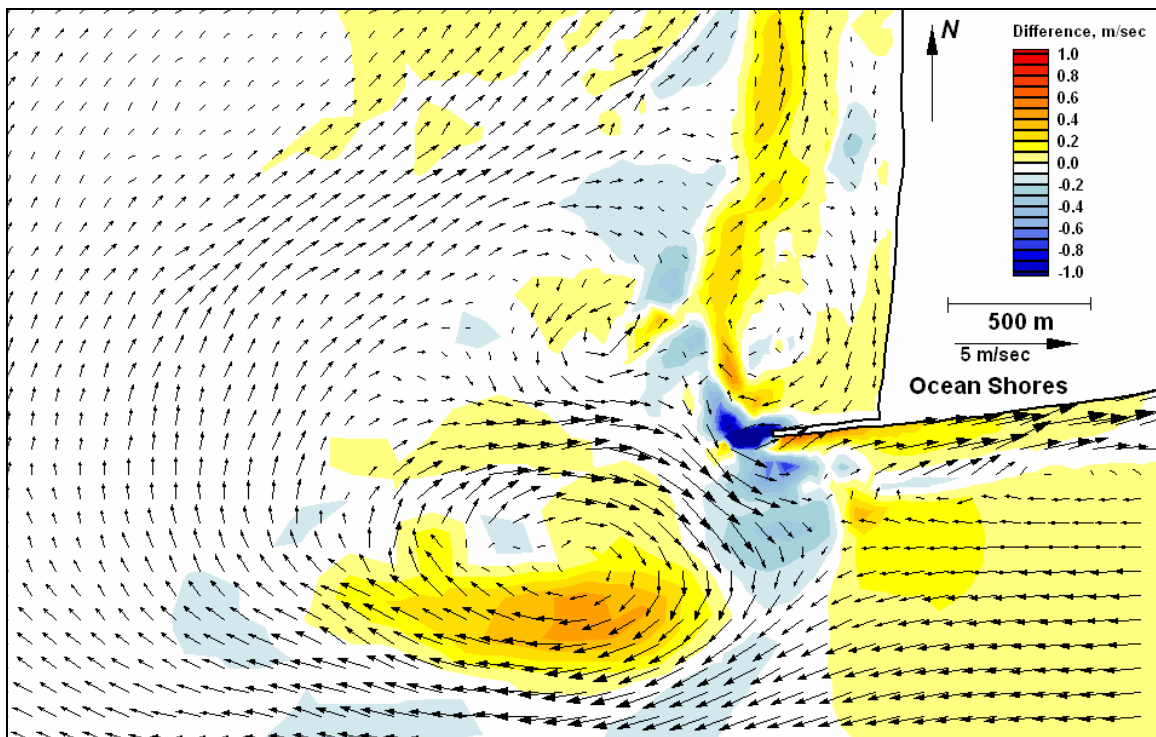
Figure E282. Difference map 117-105 for peak ebb
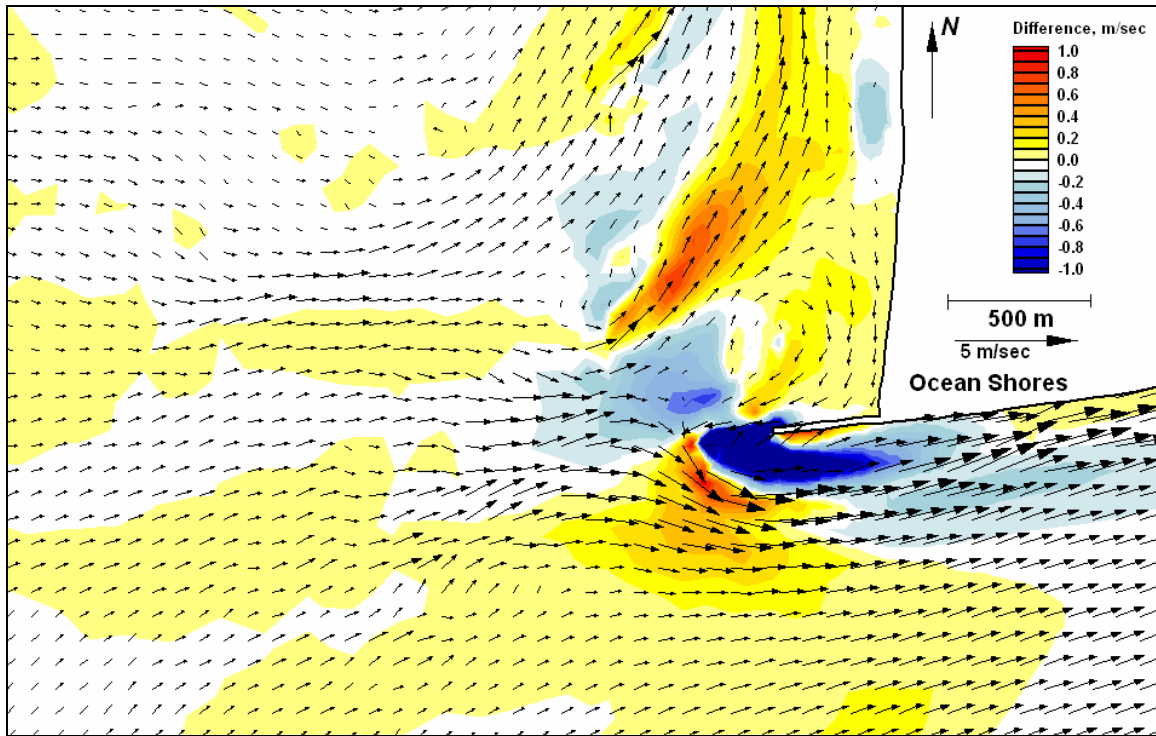
Figure E283. Difference map 121-105 for peak flood
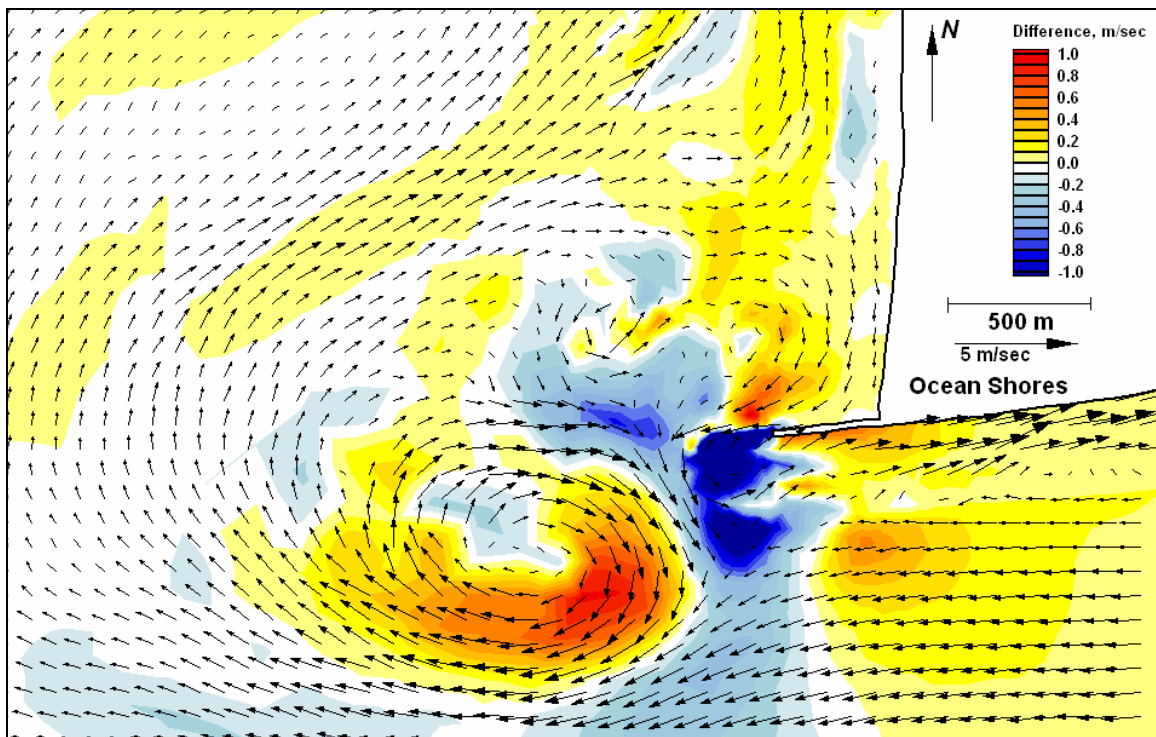
Figure E284. Difference map 121-105 for peak ebb
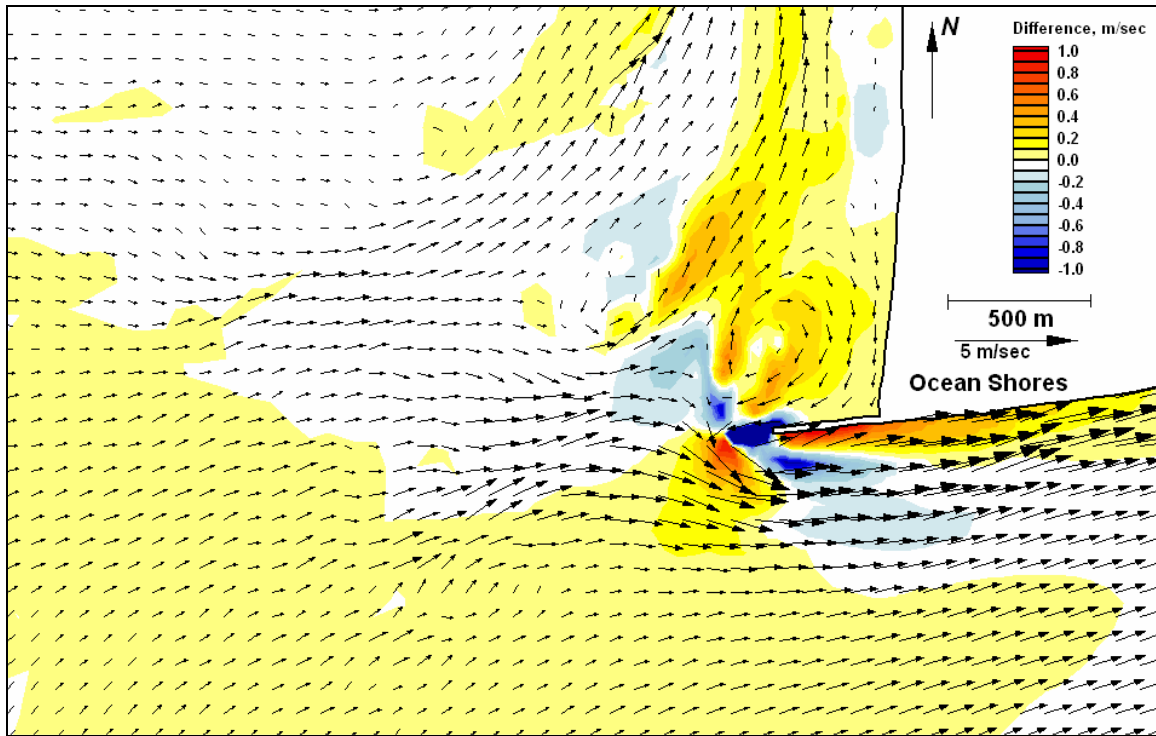
Figure E285. Difference map 125-105 for peak flood
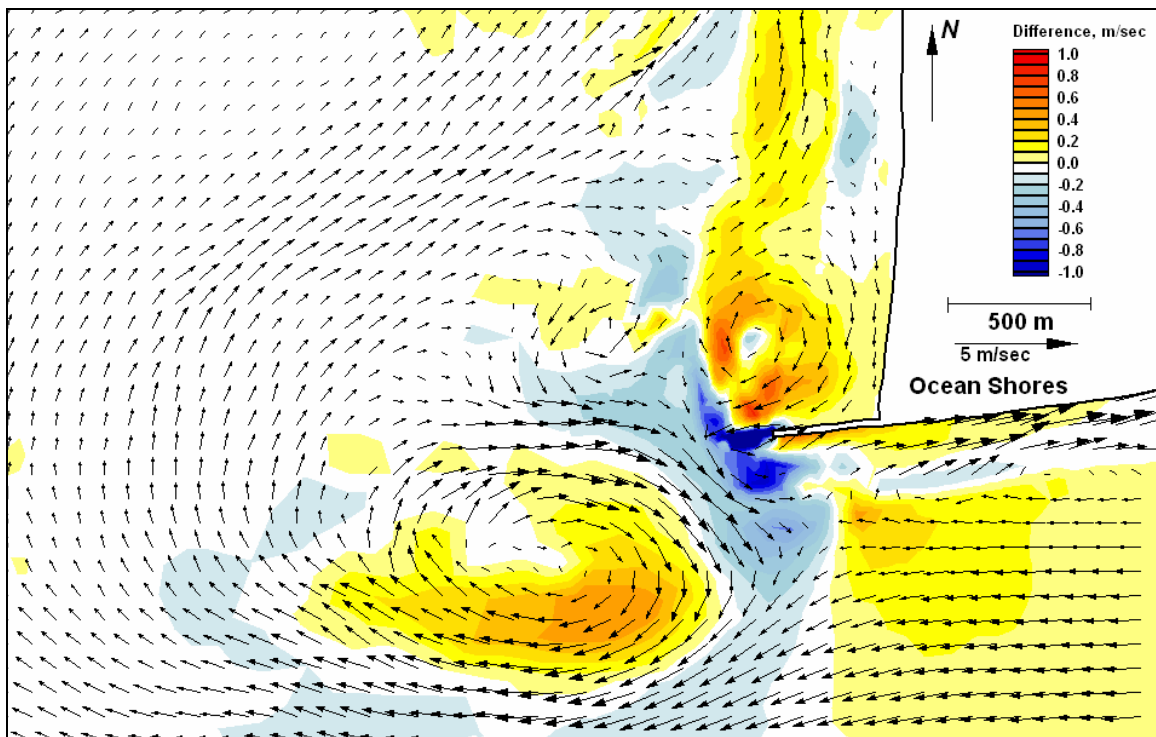
Figure E286. Difference map 125-105 for peak ebb

Appendix E   Tidal Circulation Simulation Results
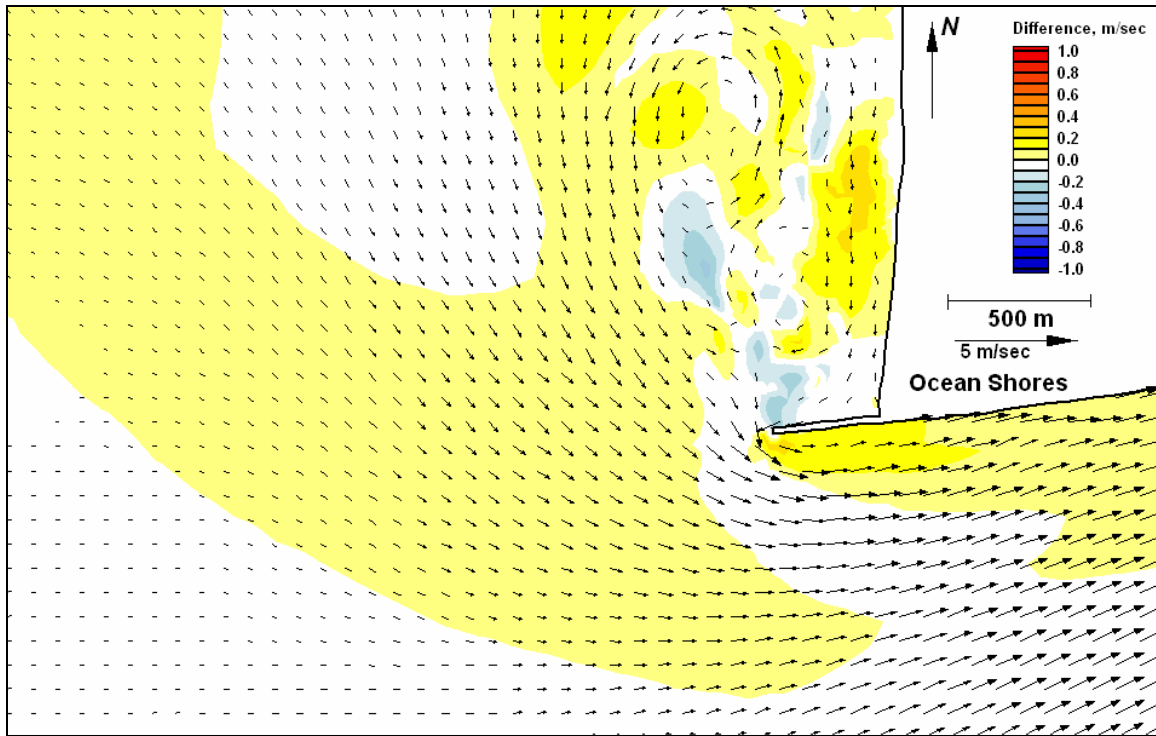
Figure E287. Difference map 129-128 for peak flood
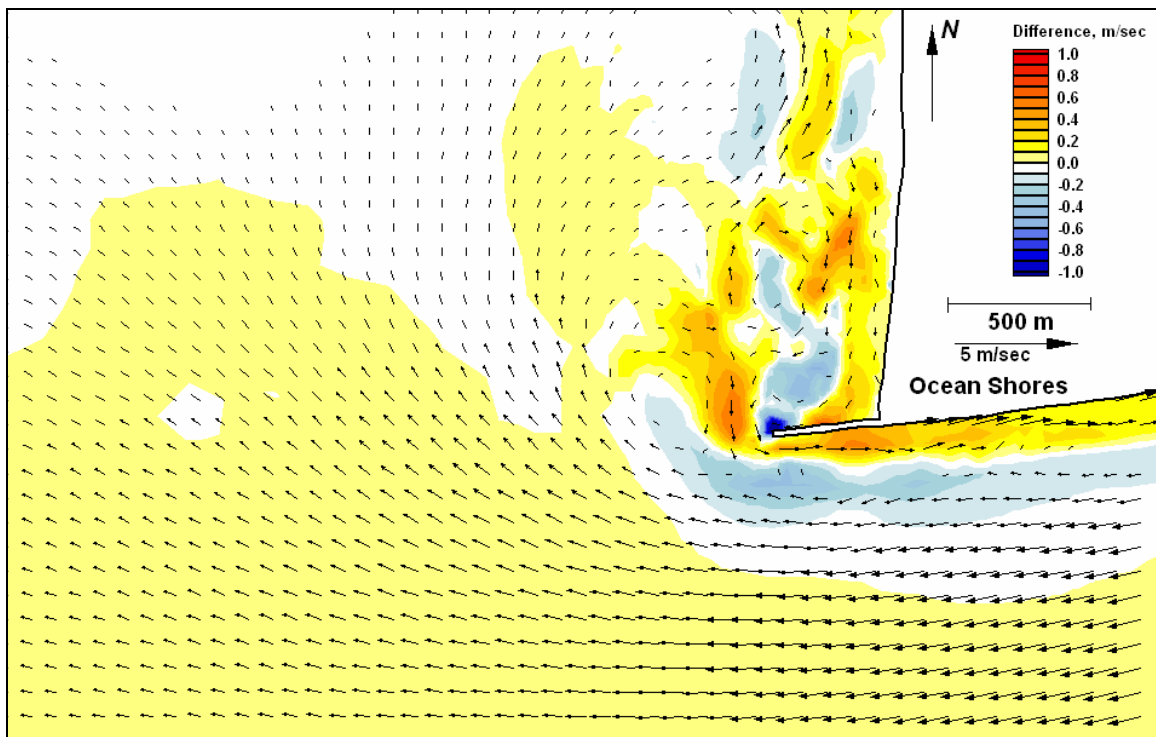
Figure E288. Difference map 129-128 for peak ebb
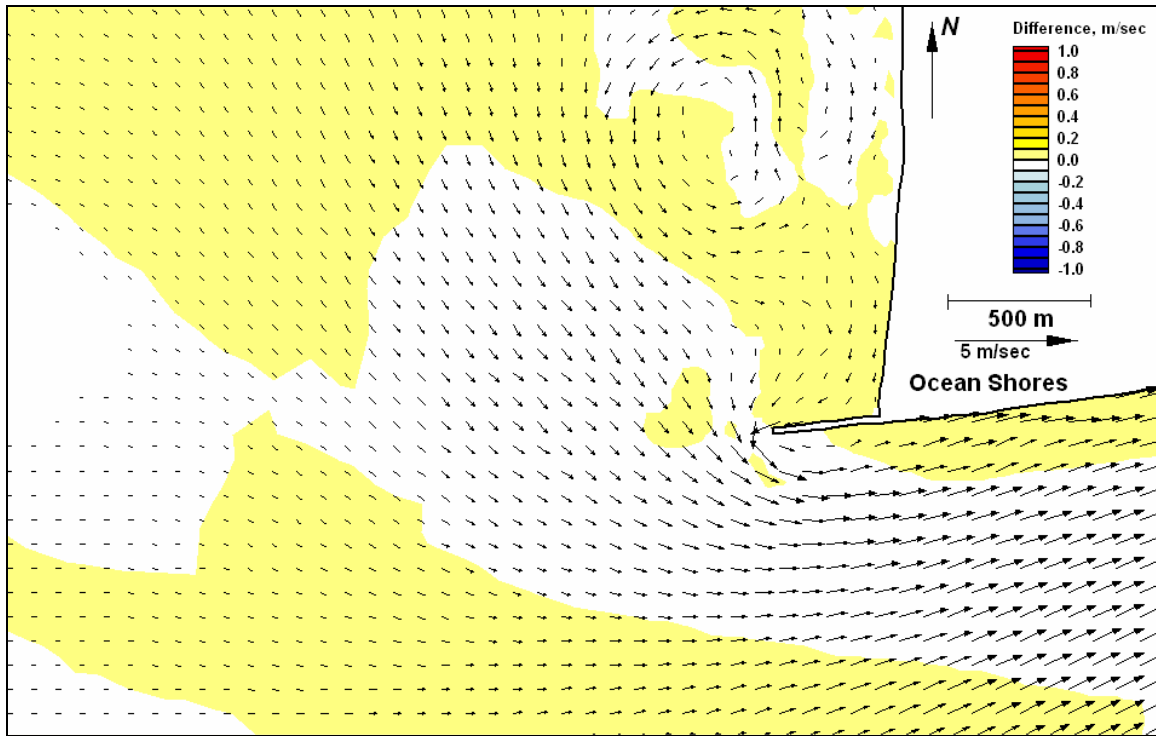
Figure E289. Difference map 130-128 for peak flood
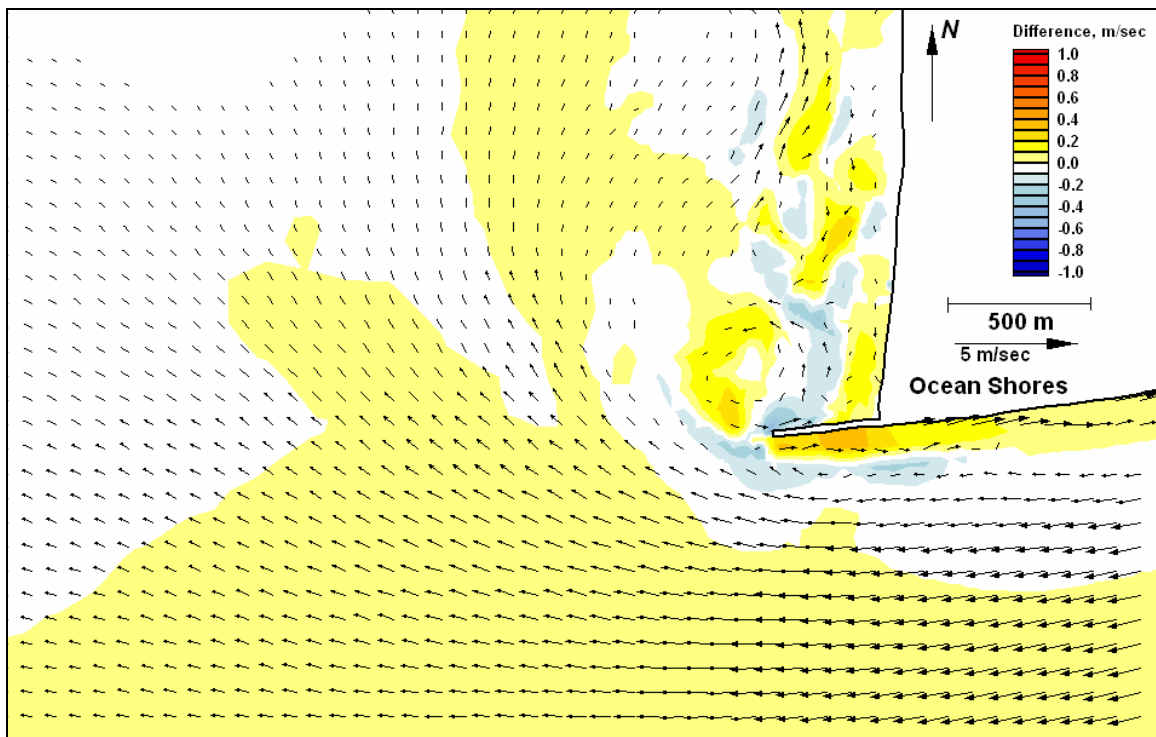
Figure E290. Difference map 130-128 for peak ebb

Appendix E   Tidal Circulation Simulation Results
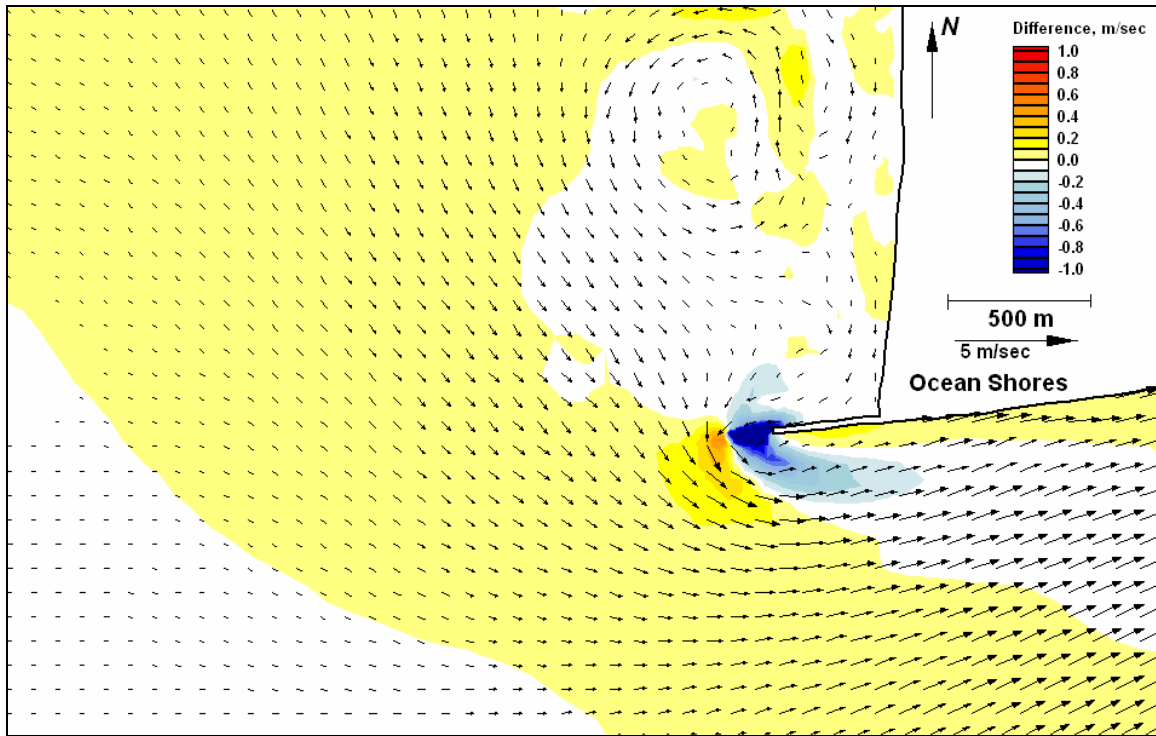
Figure E291. Difference map 131-128 for peak flood
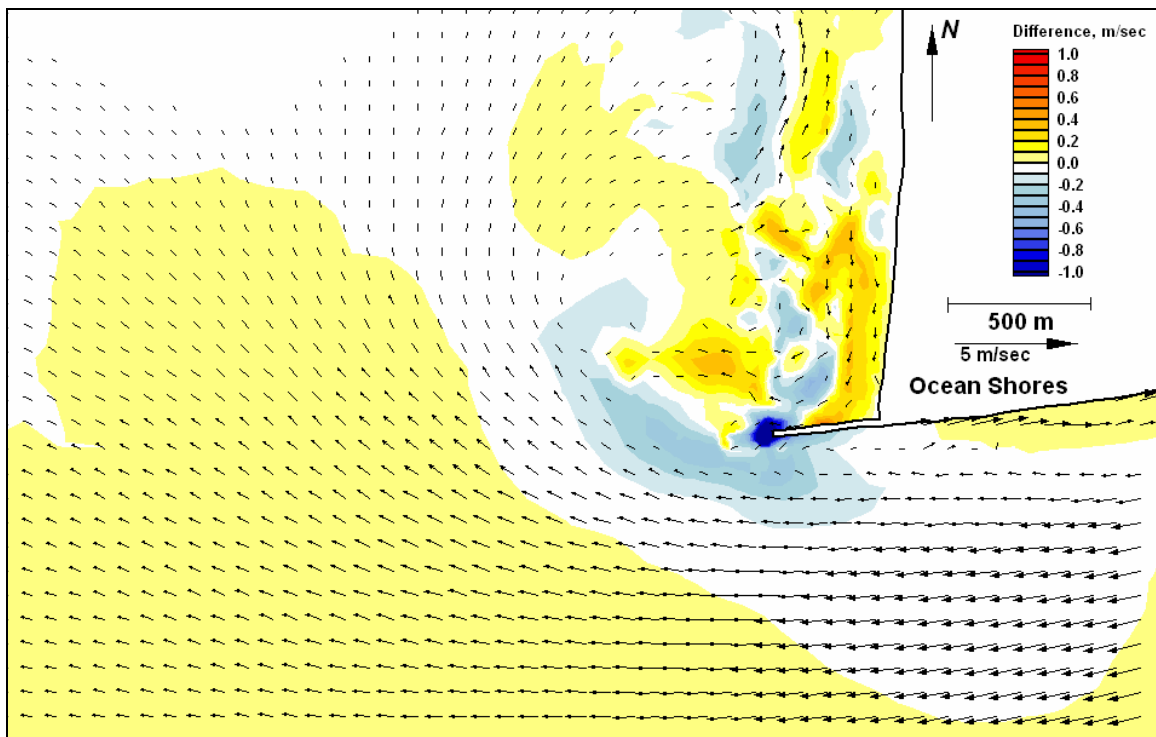
Figure E292. Difference map 131-128 for peak ebb
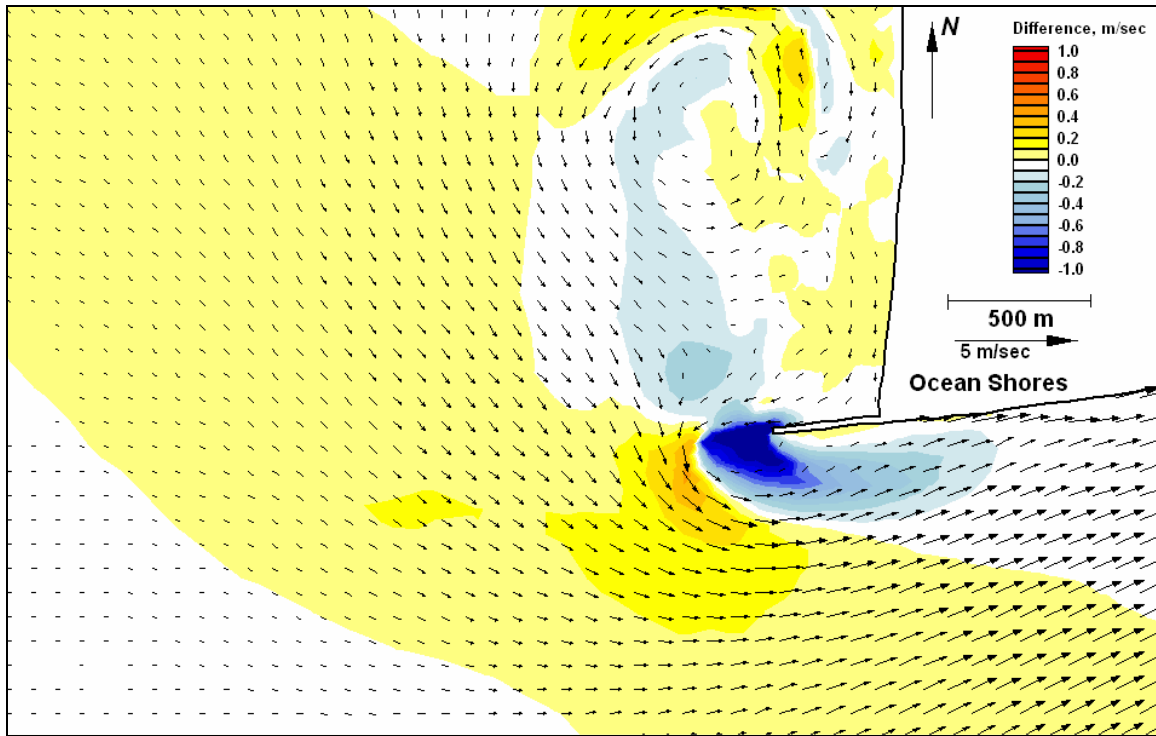
Figure E293. Difference map 132-128 for peak flood
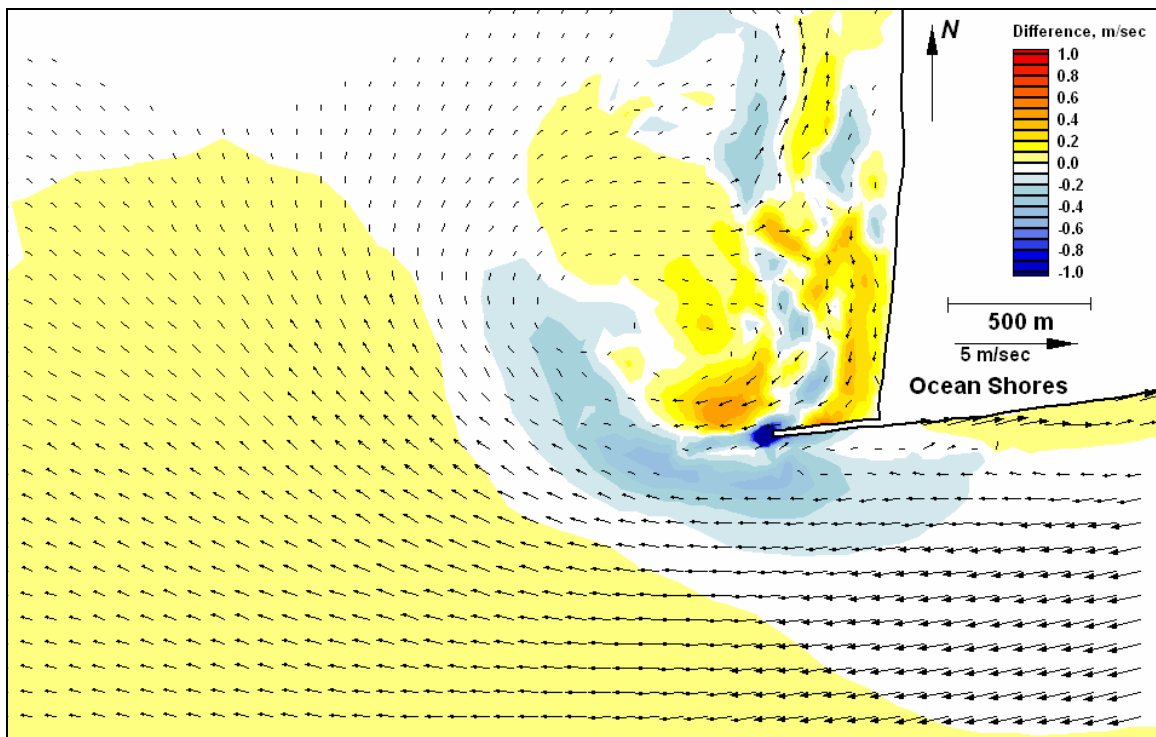
Figure E294. Difference map 132-128 for peak ebb
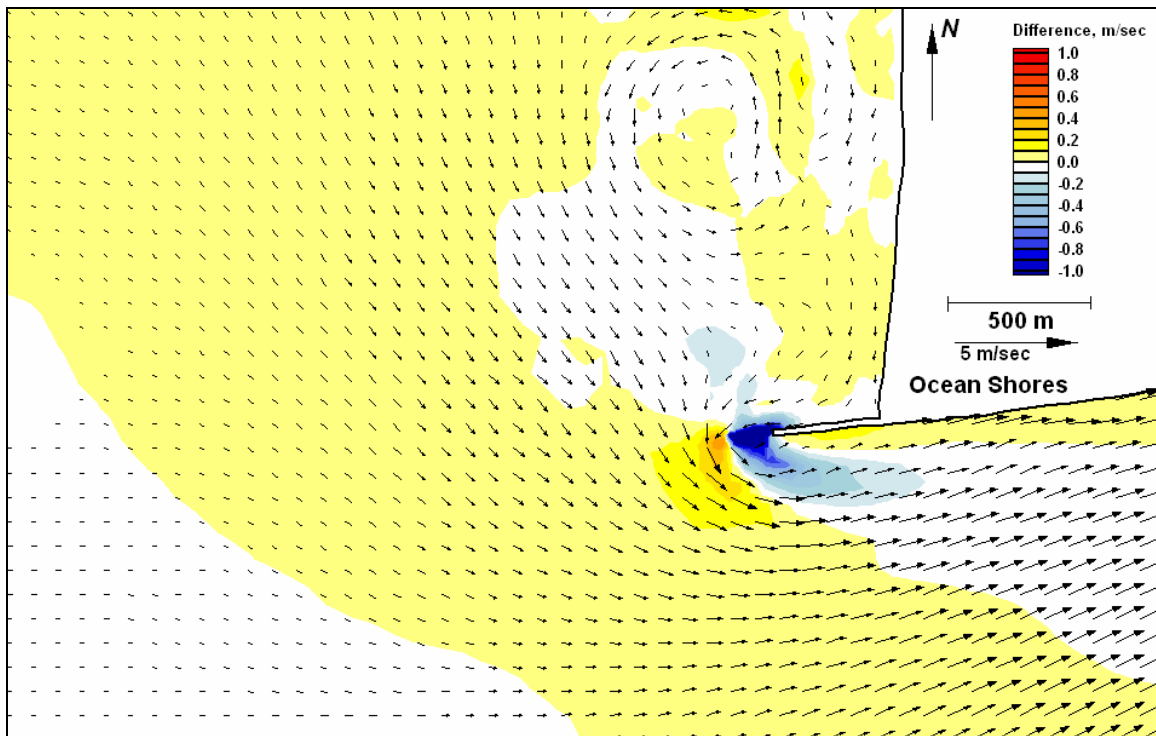
Figure E295. Difference map 133-128 for peak flood
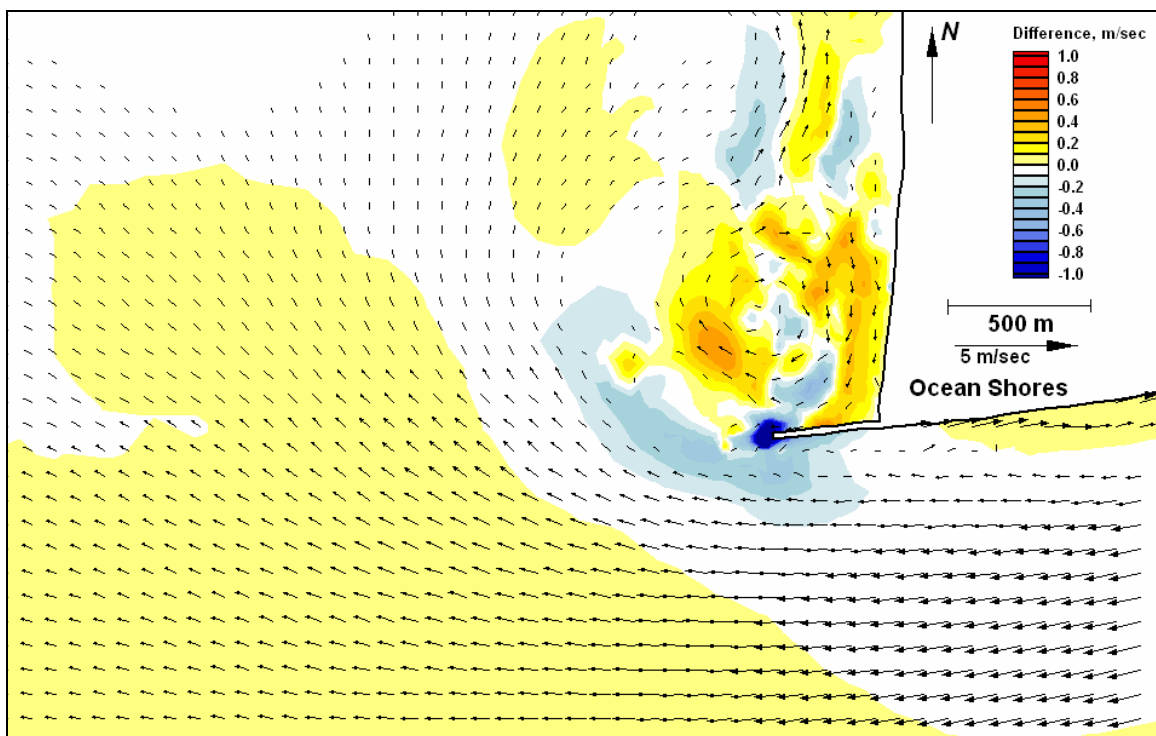
Figure E296. Difference map 133-128 for peak ebb
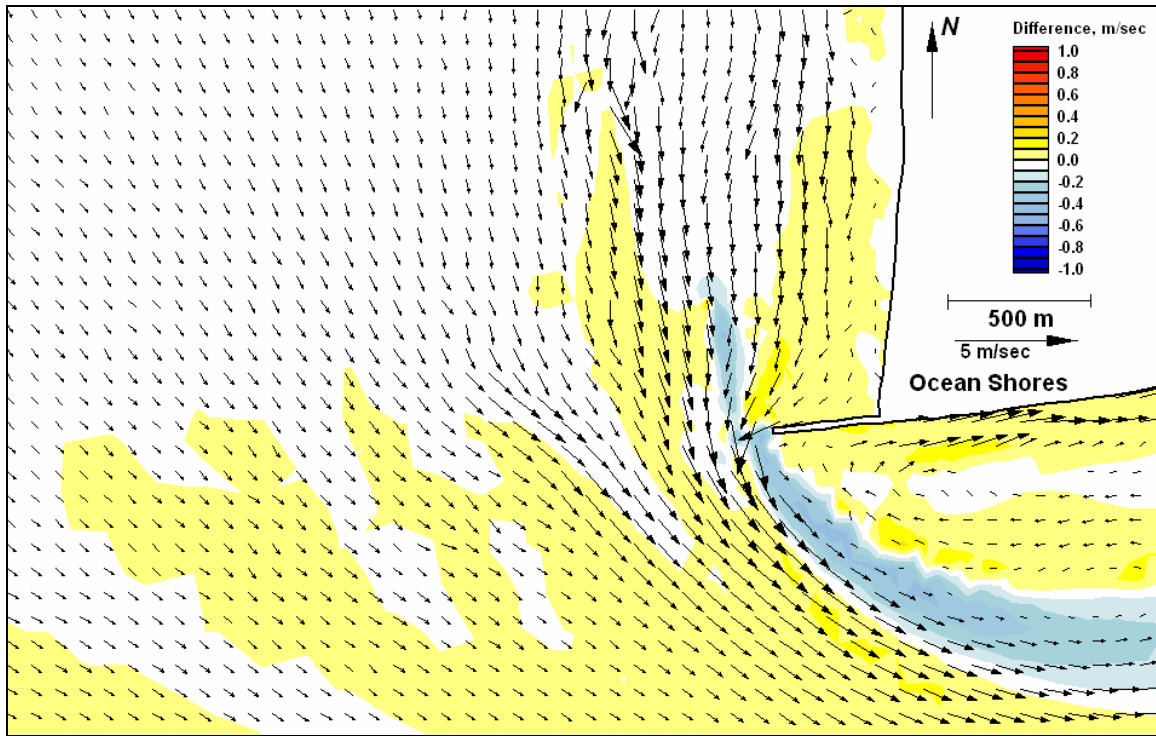
Figure E297. Difference map 110-106 for peak flood
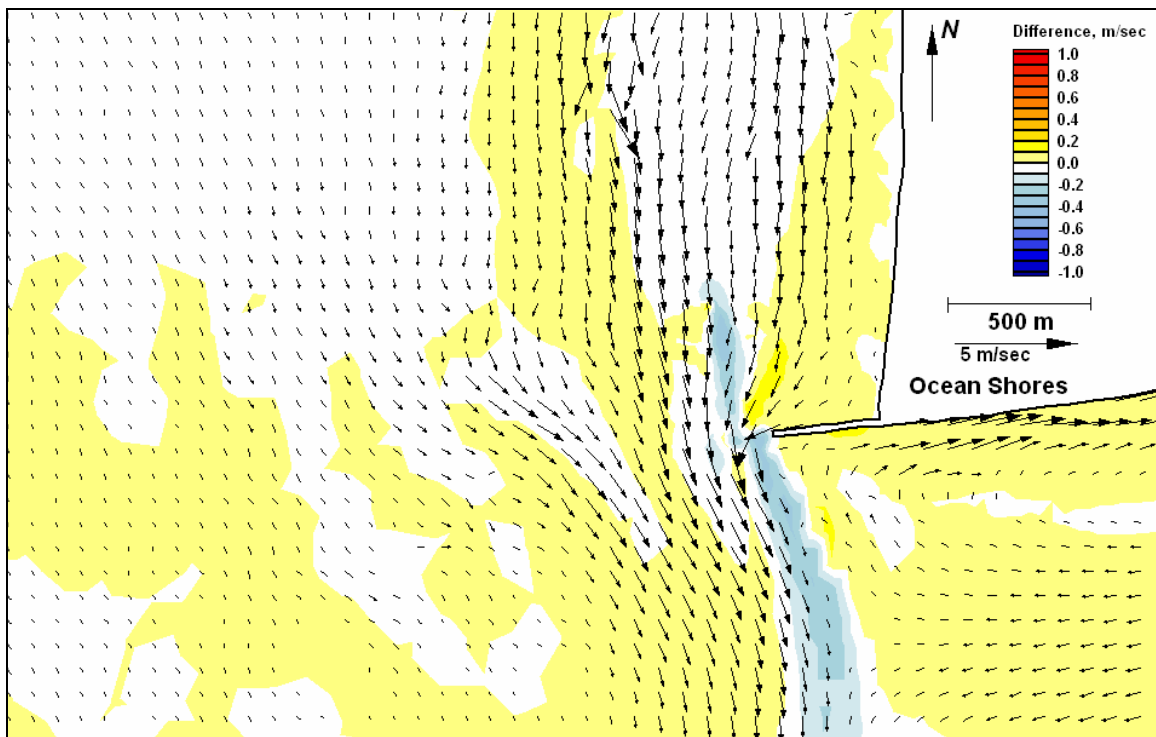
Figure E298. Difference map 110-106 for peak ebb
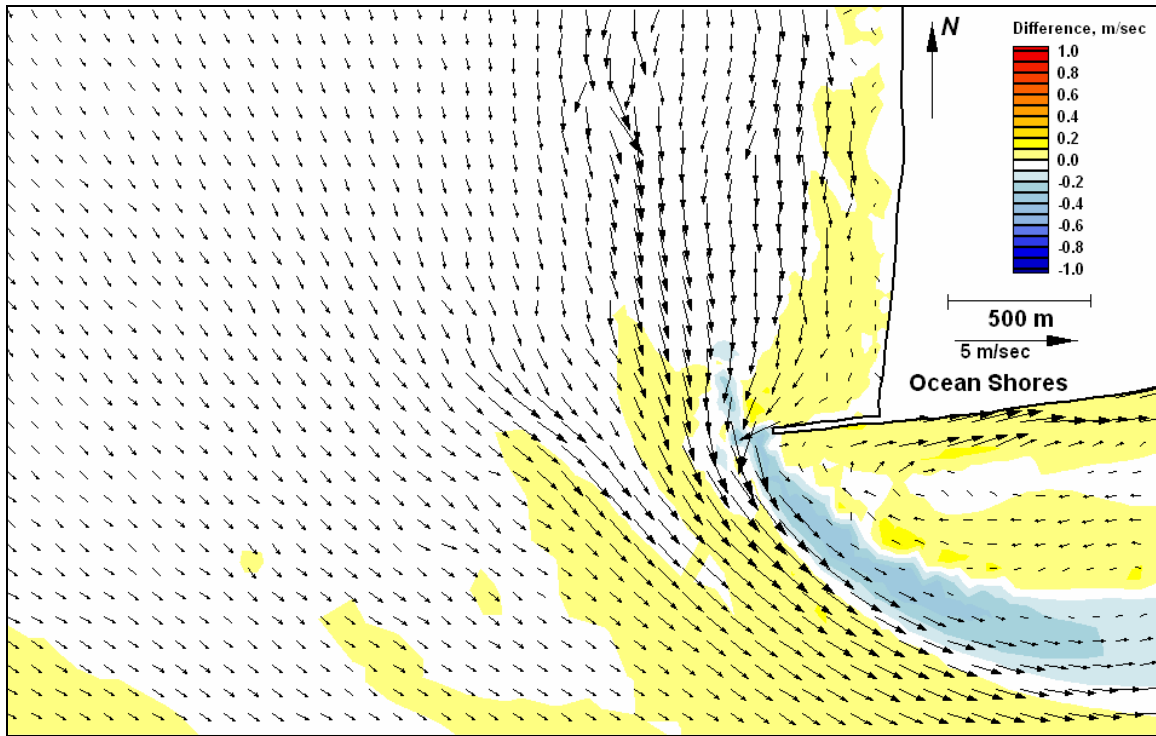
Figure E299. Difference map 114-106 for peak flood
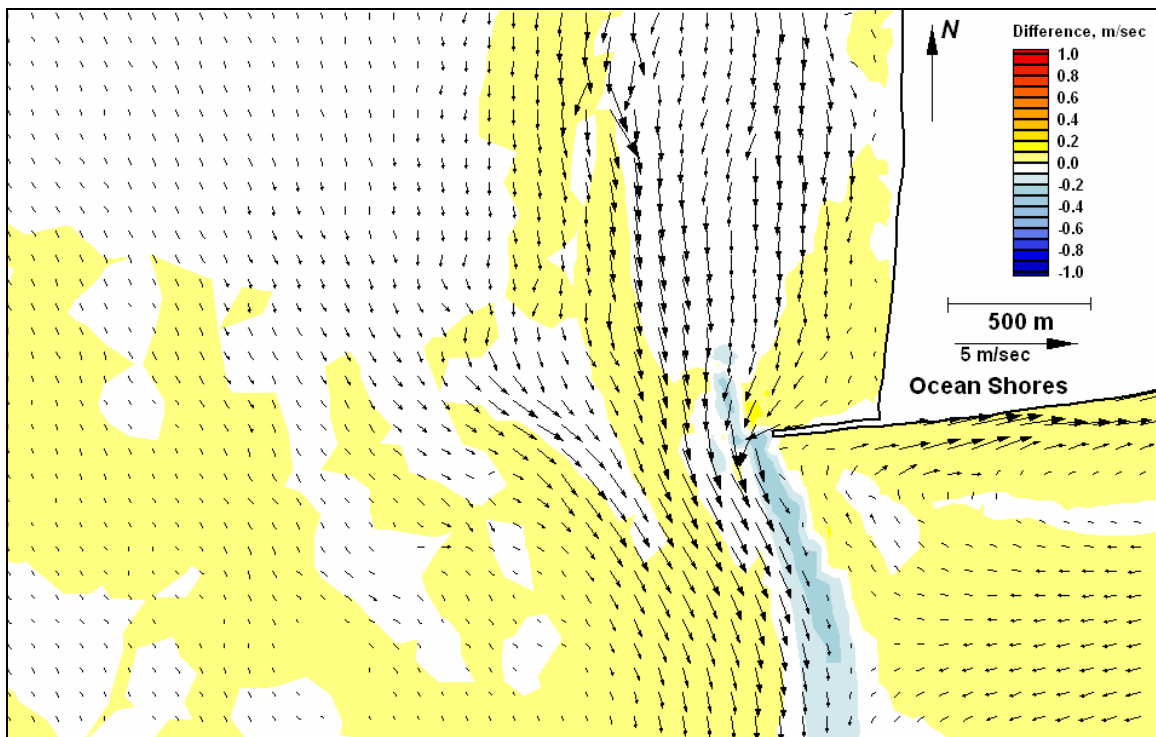
Figure E300. Difference map 114-106 for peak ebb
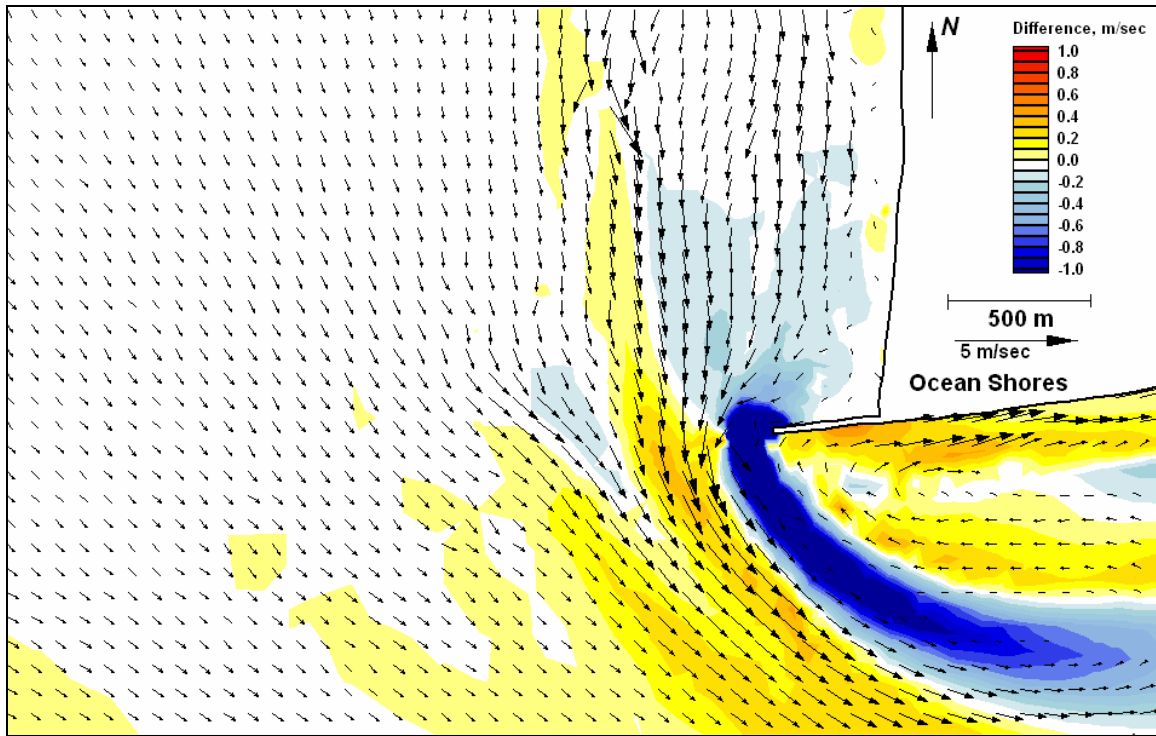
Figure E301. Difference map 118-106 for peak flood
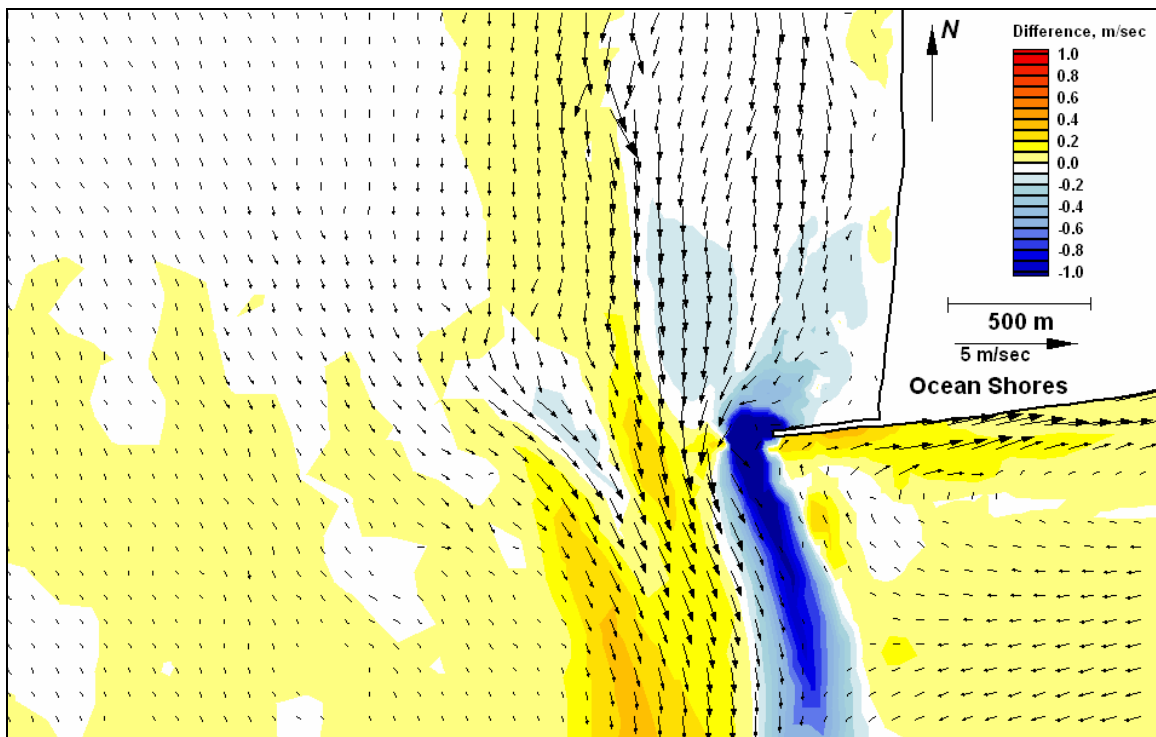
Figure E302. Difference map 118-106 for peak ebb
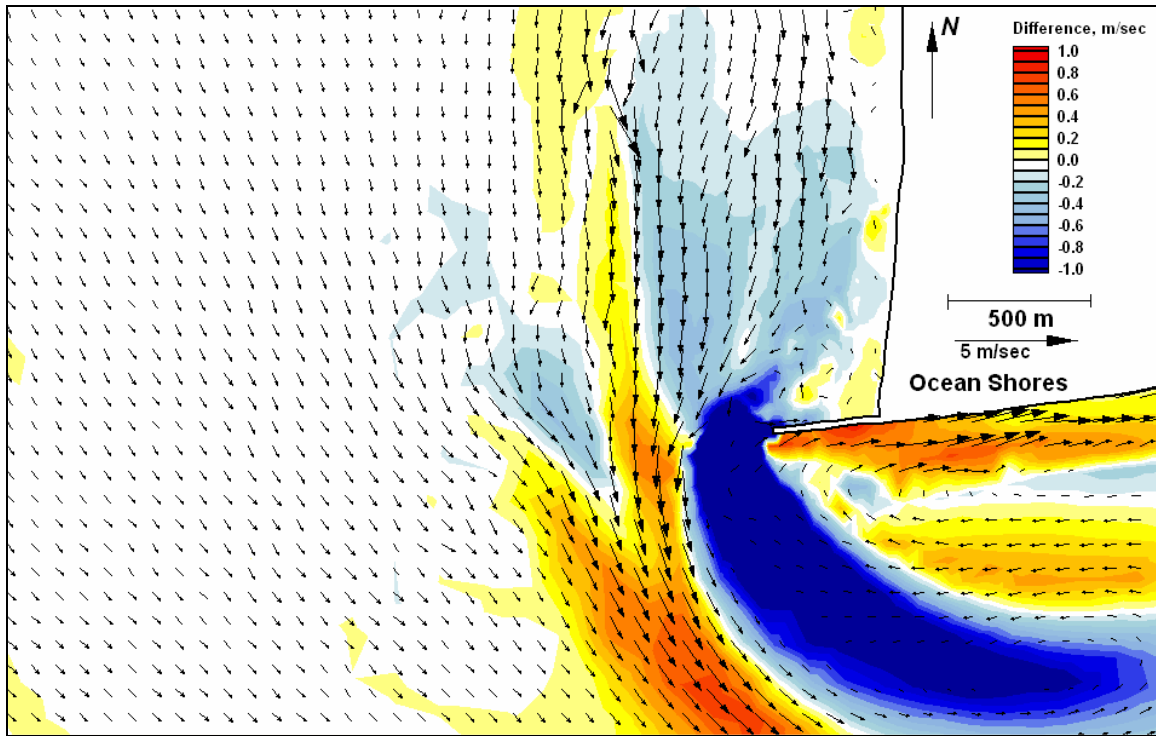
Figure E303. Difference map 122-106 for peak flood
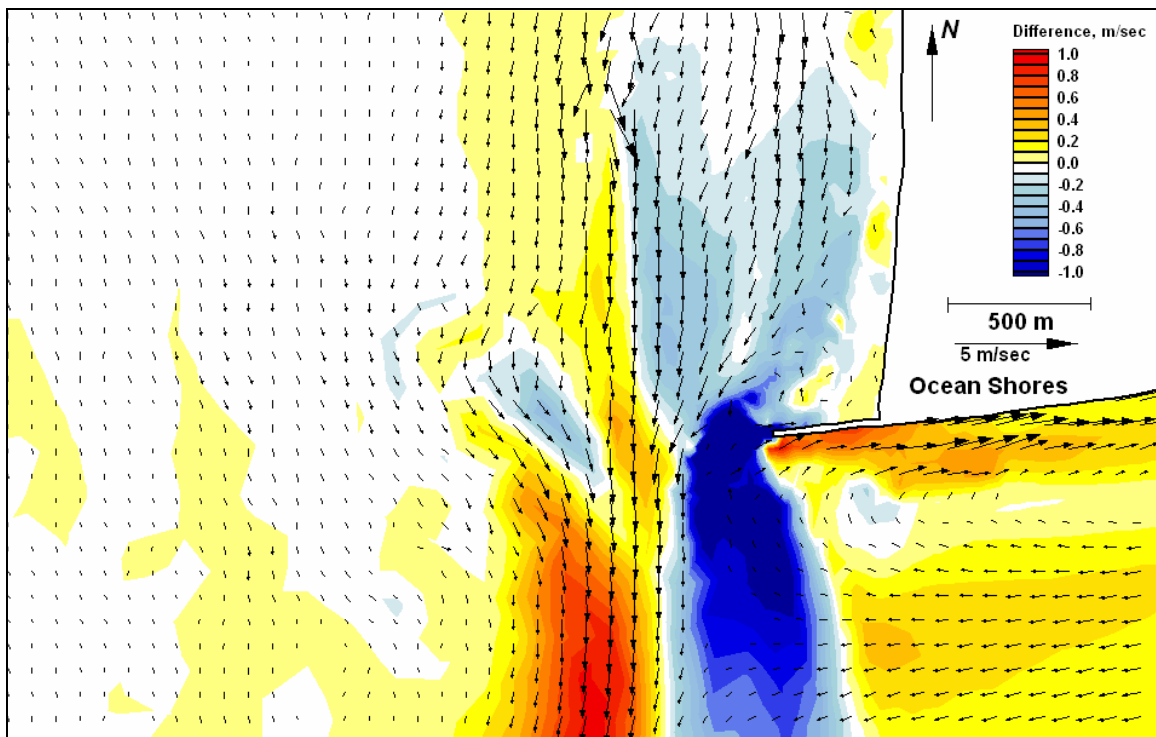
Figure E304. Difference map 122-106 for peak ebb
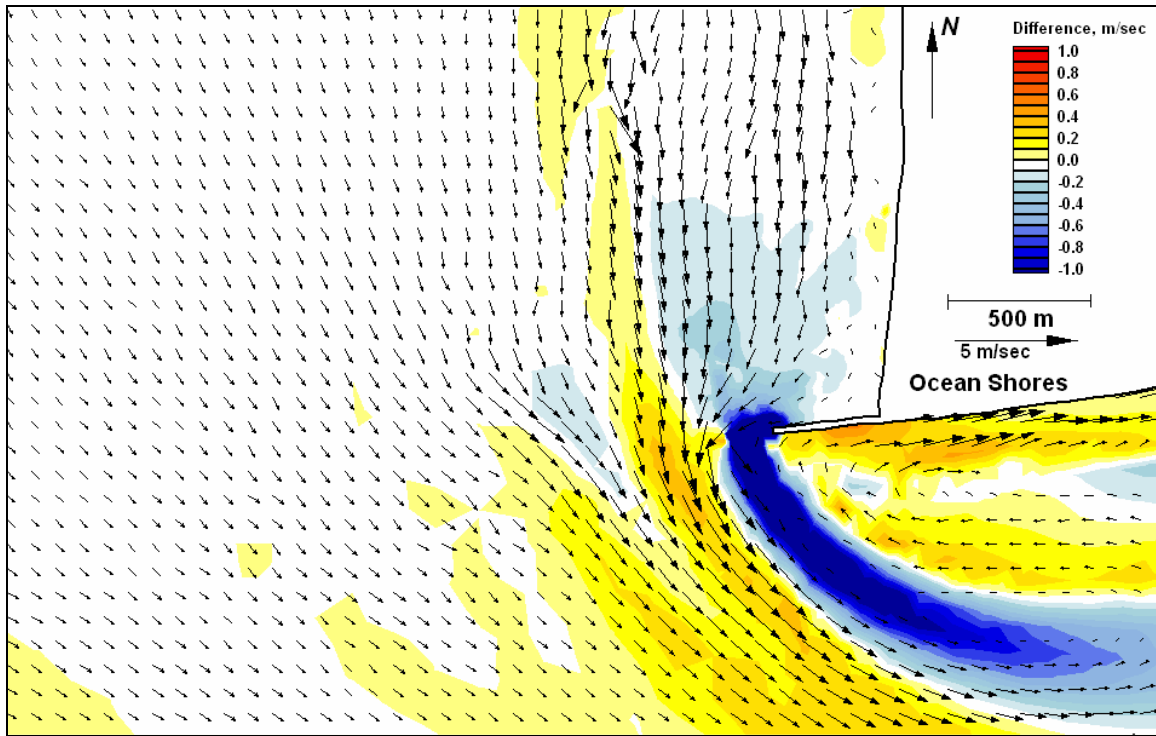
Figure E305. Difference map 126-106 for peak flood
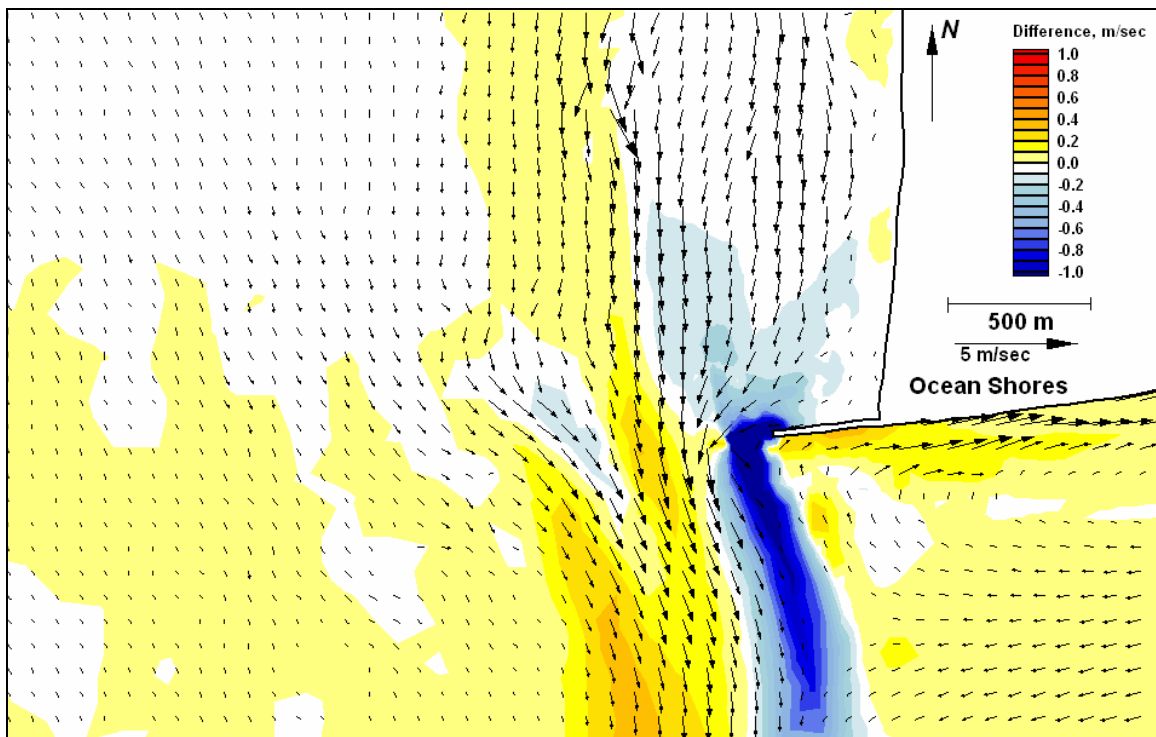
Figure E306. Difference map 126-106 for peak ebb

Appendix E   Tidal Circulation Simulation Results
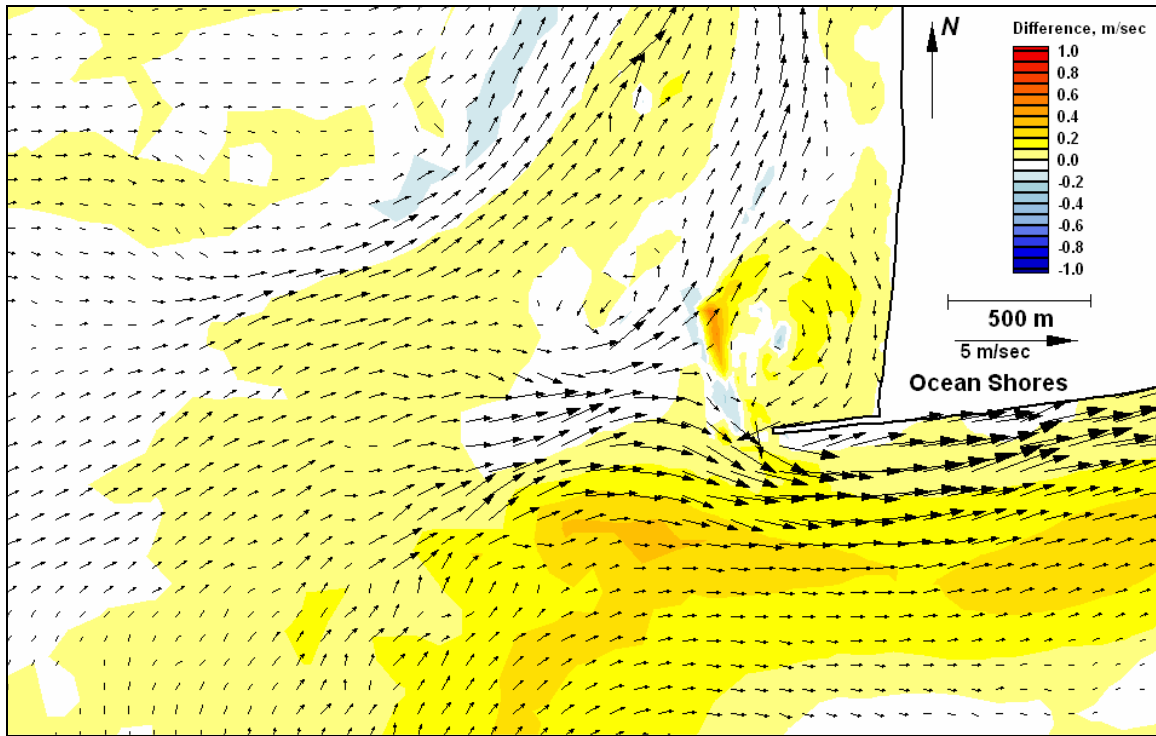
Figure E307. Difference map 111-107 for peak flood
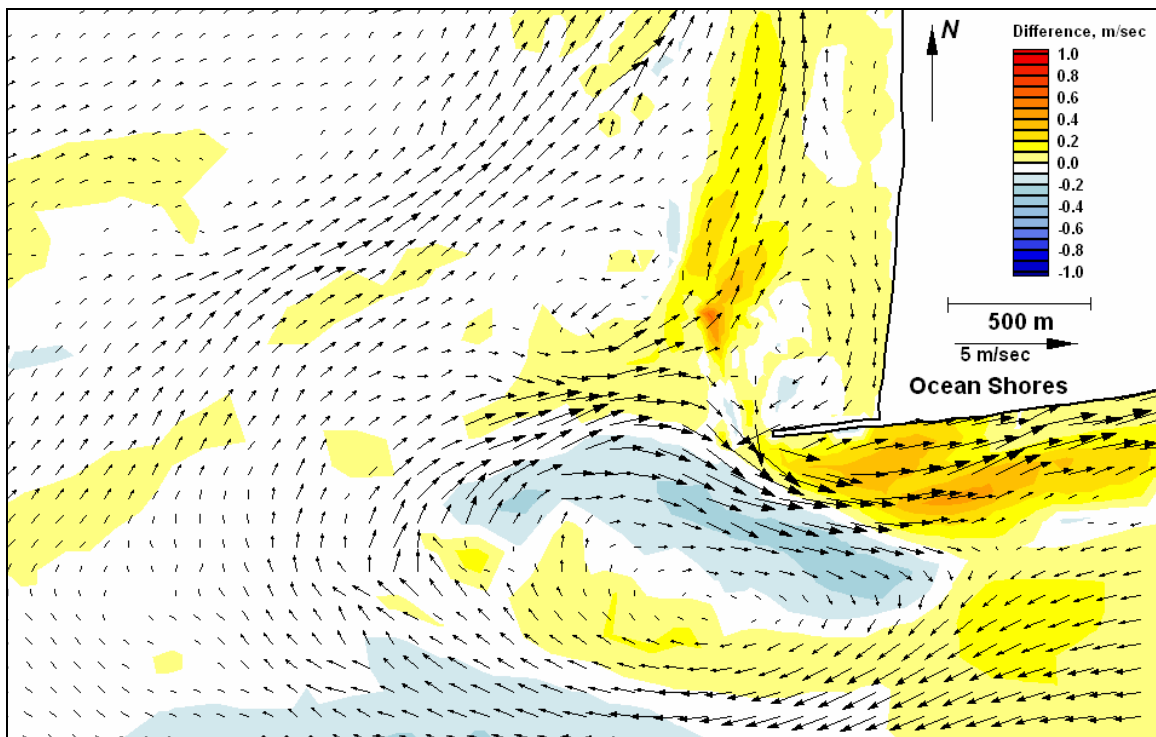
Figure E308. Difference map 111-107 for peak ebb
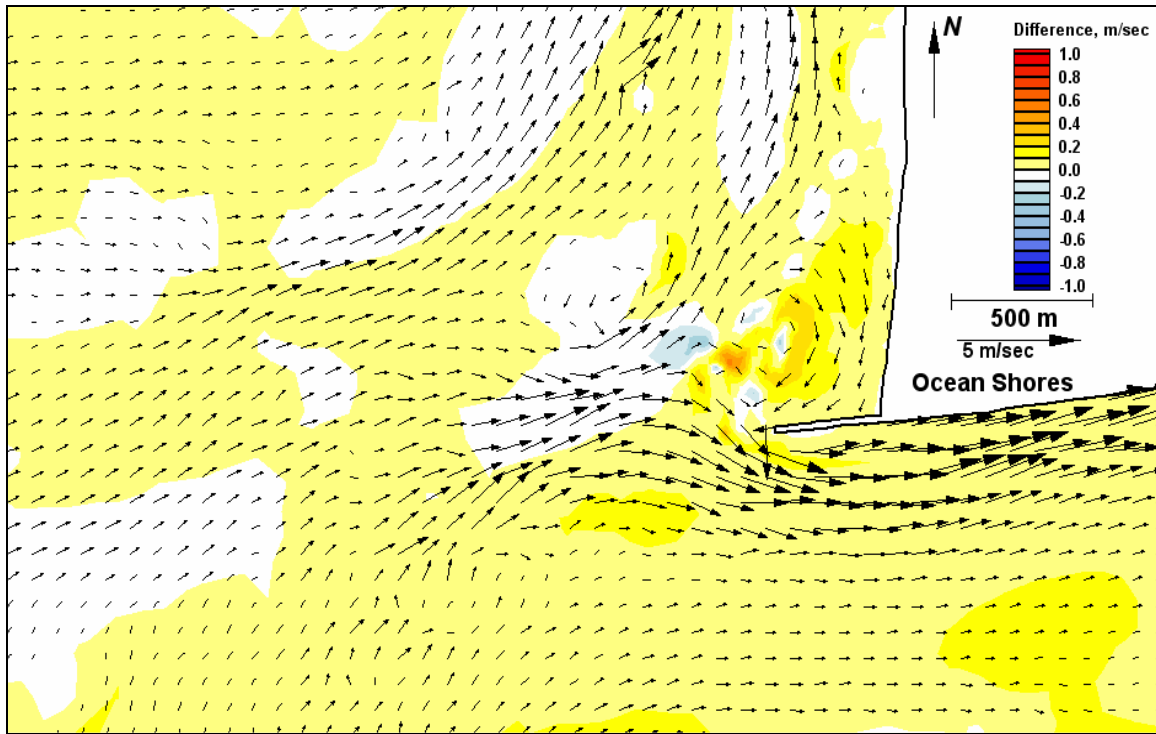
Figure E309. Difference map 115-107 for peak flood
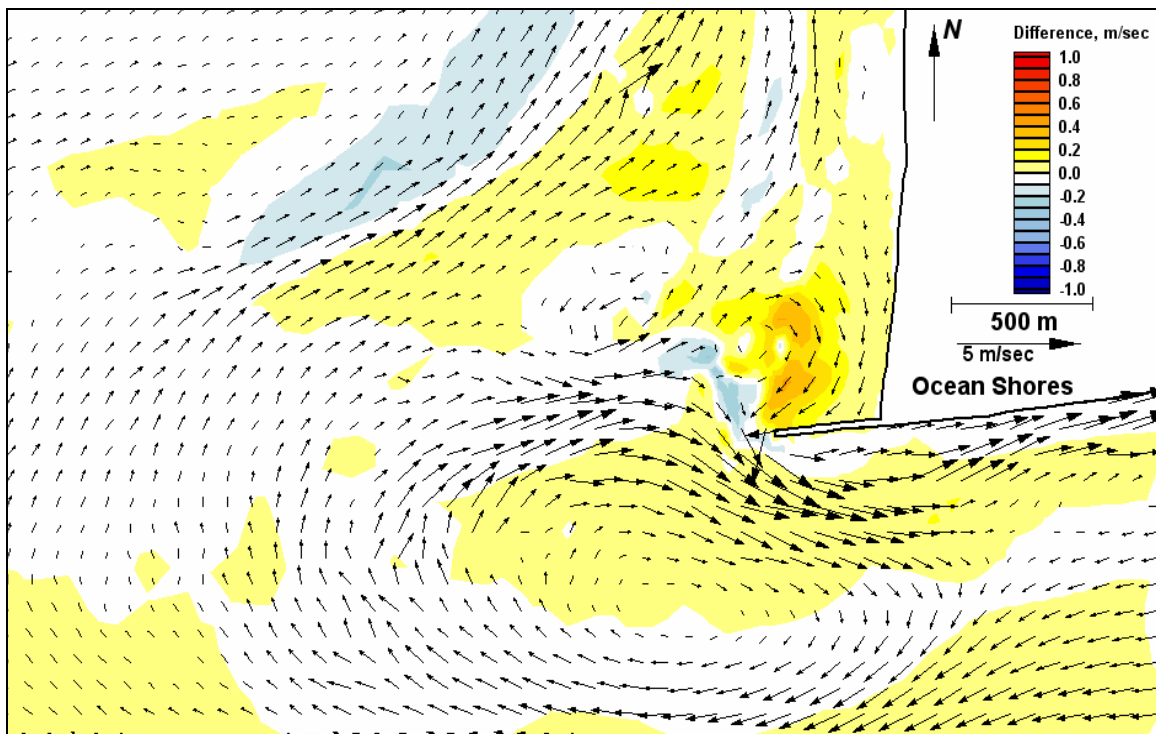
Figure E310. Difference map 115-107 for peak ebb

Appendix E   Tidal Circulation Simulation Results
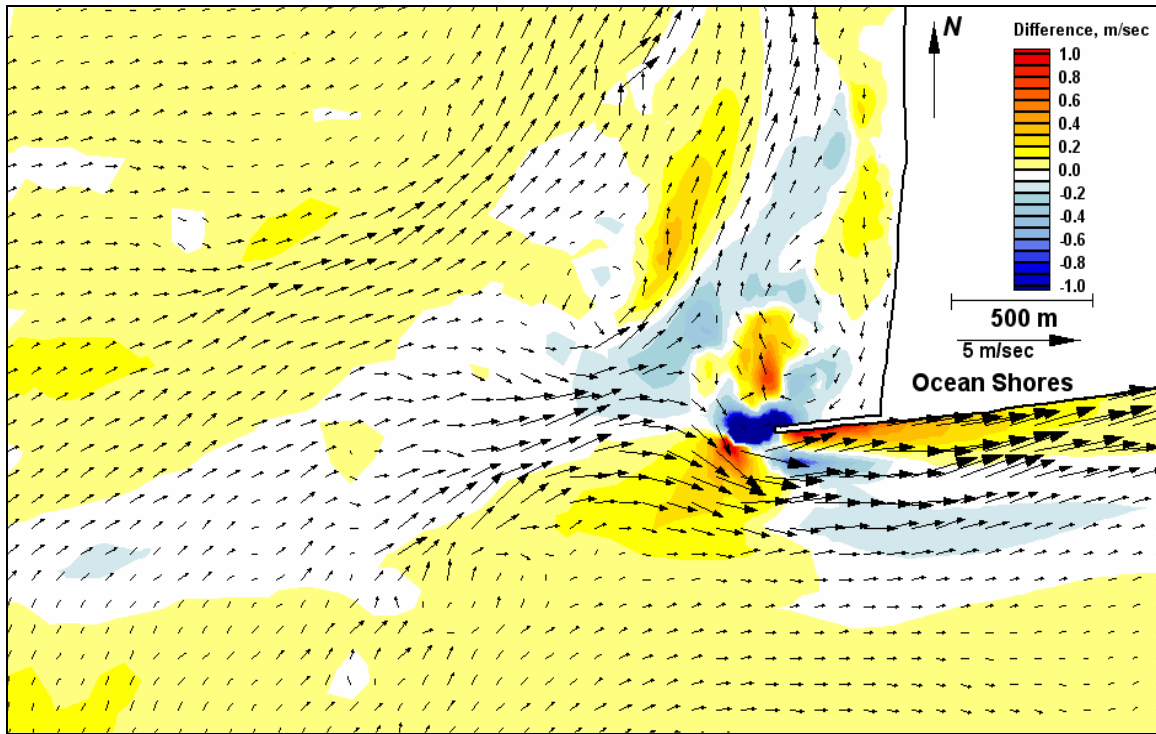
Figure E311. Difference map 119-107 for peak flood
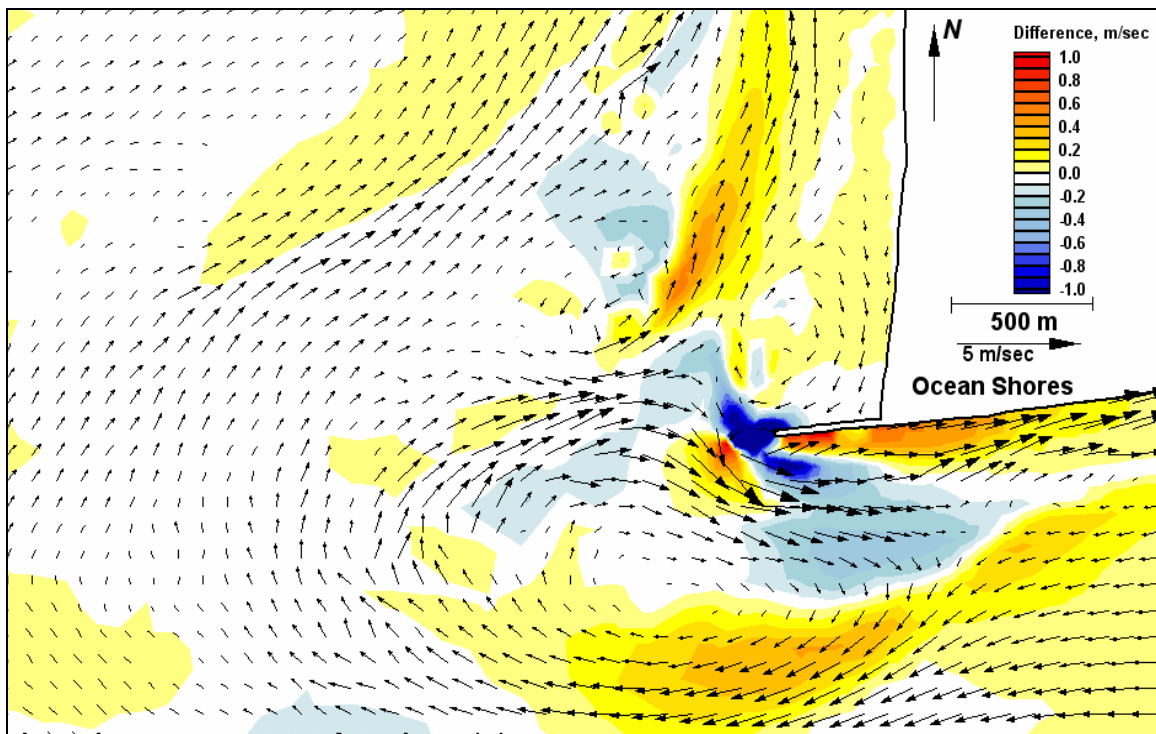
Figure E312. Difference map 119-107 for peak ebb
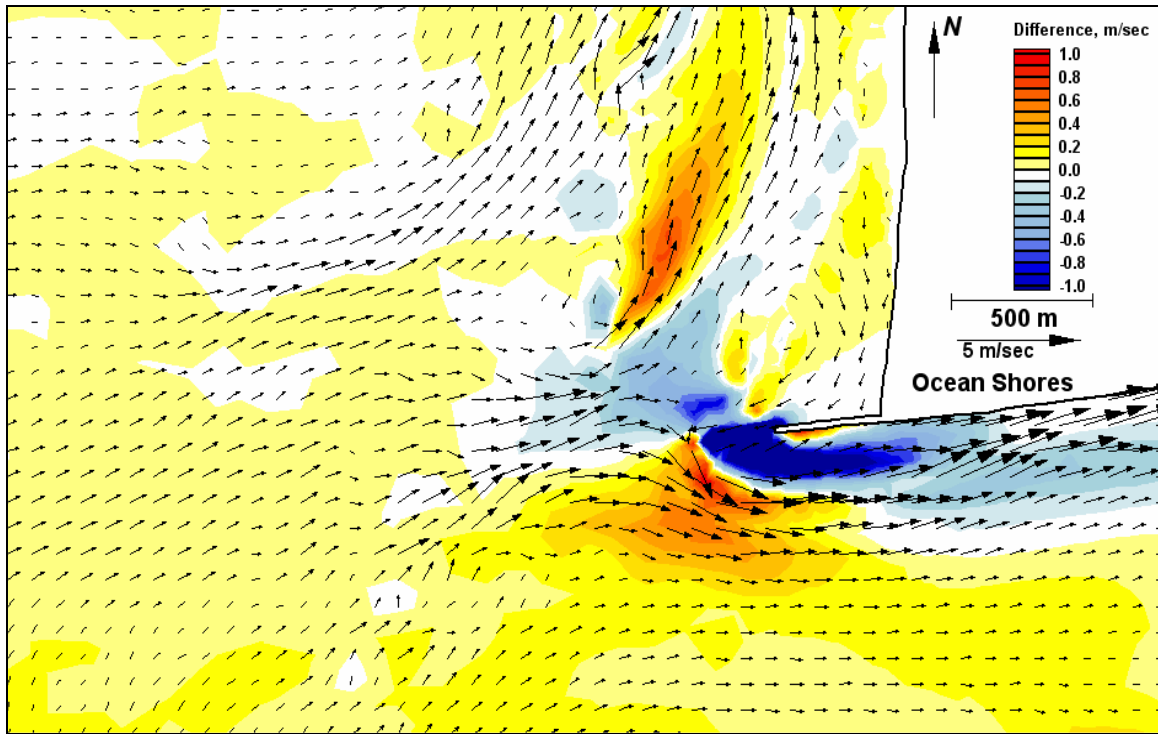
Figure E313. Difference map 123-107 for peak flood
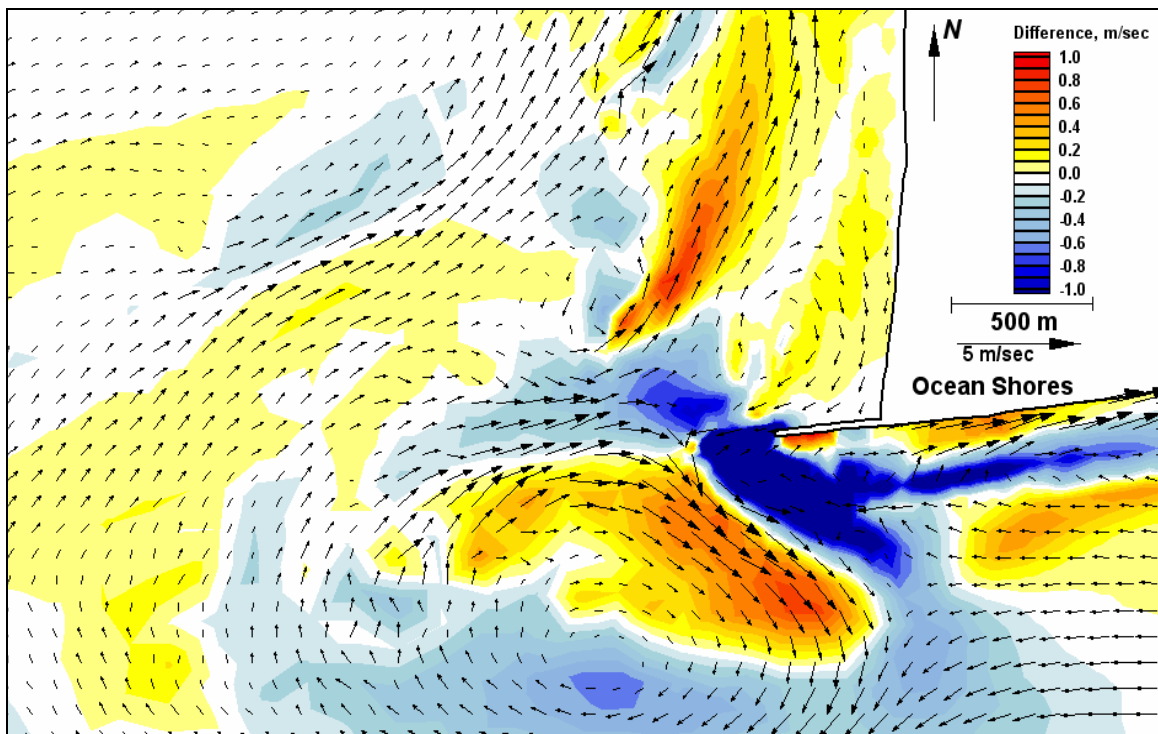
Figure E314. Difference map 123-107 for peak ebb

Appendix E   Tidal Circulation Simulation Results
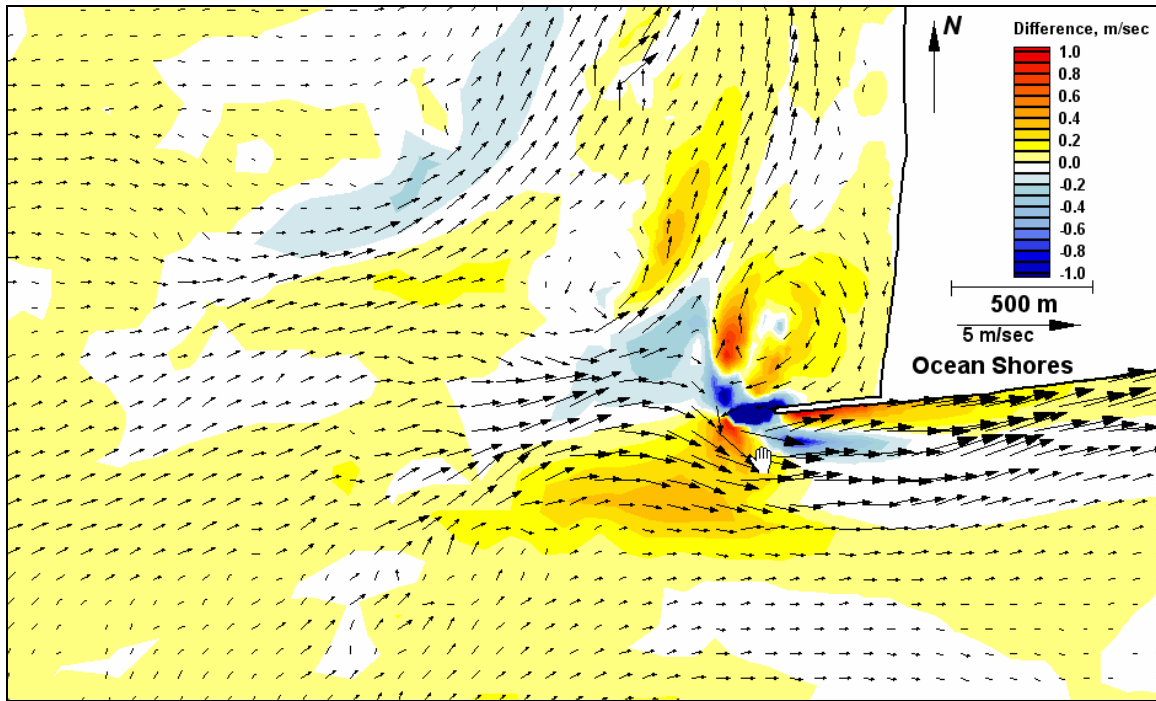
Figure E315. Difference map 127-107 for peak flood
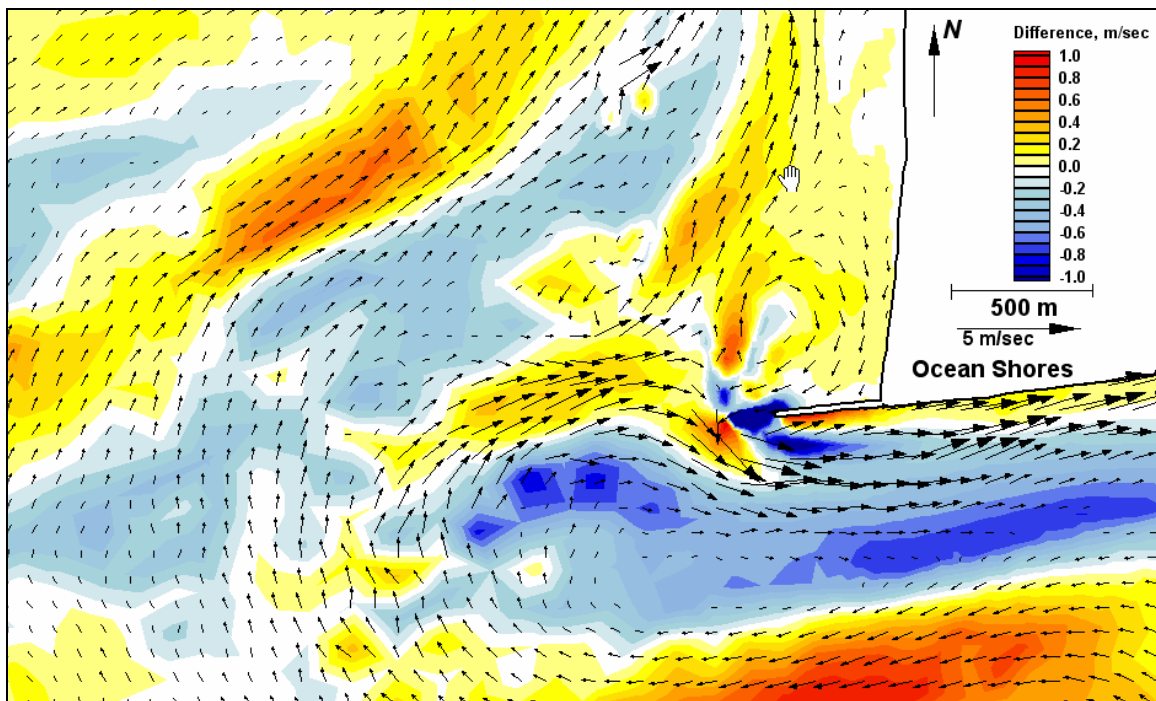
Figure E316. Difference map 127-107 for peak ebb
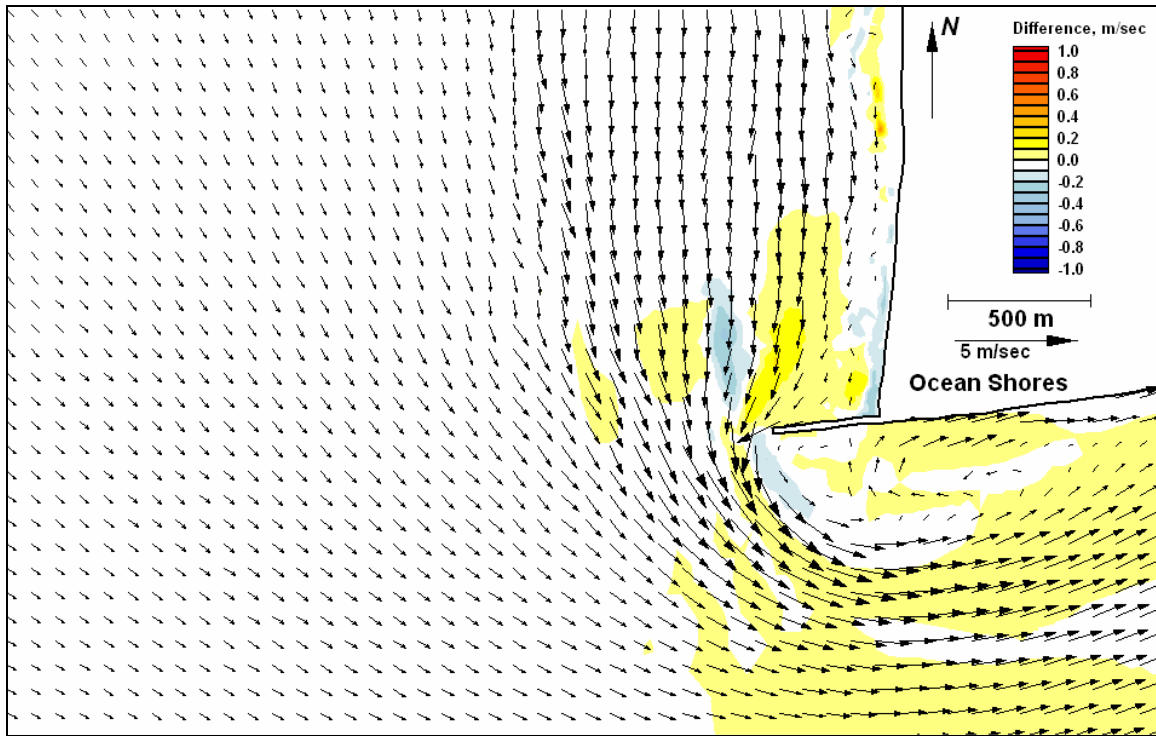
Figure E317. Difference map 135-134 for peak flood
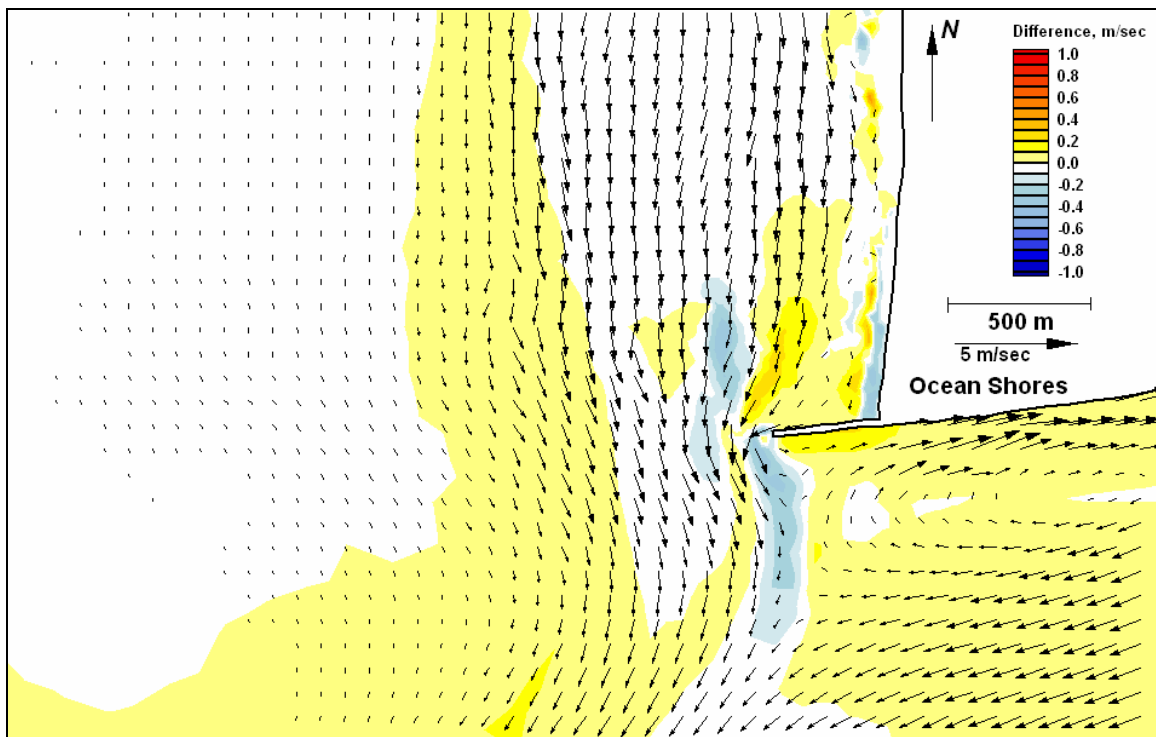
Figure E318. Difference map 135-134 for peak ebb

Appendix E   Tidal Circulation Simulation Results
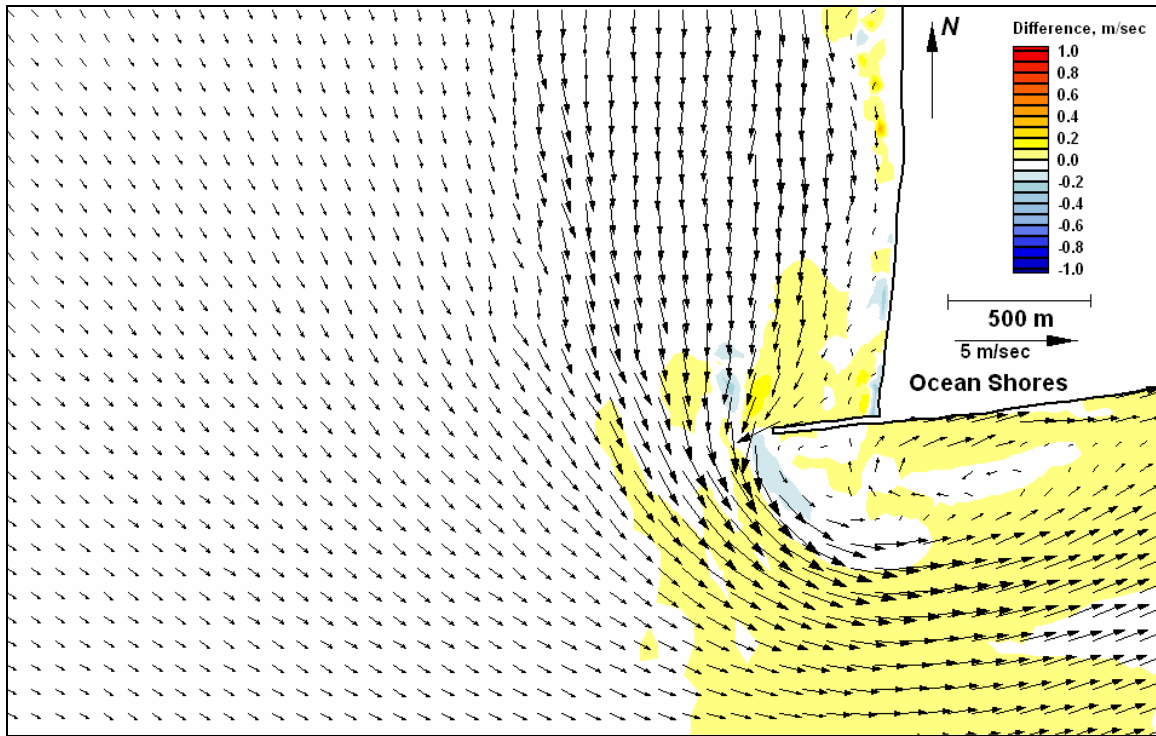
Figure E319. Difference map 136-134 for peak flood
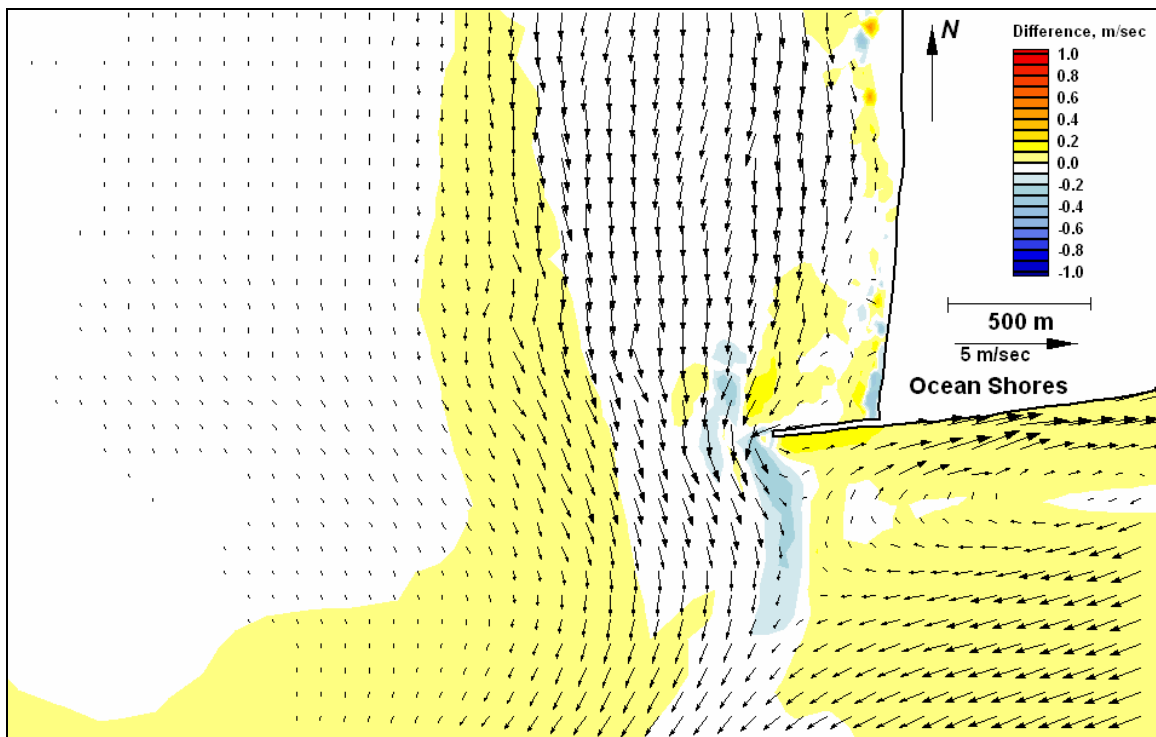
Figure E320. Difference map 136-134 for peak ebb
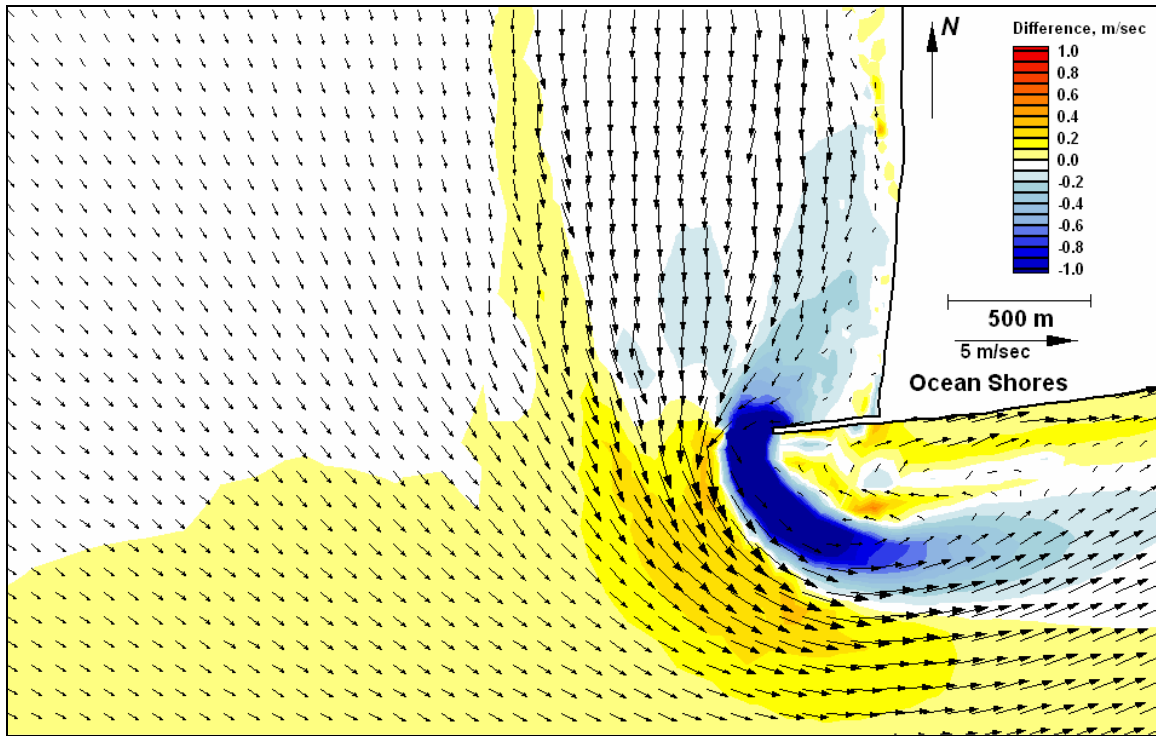
Figure E321. Difference map 137-134 for peak flood
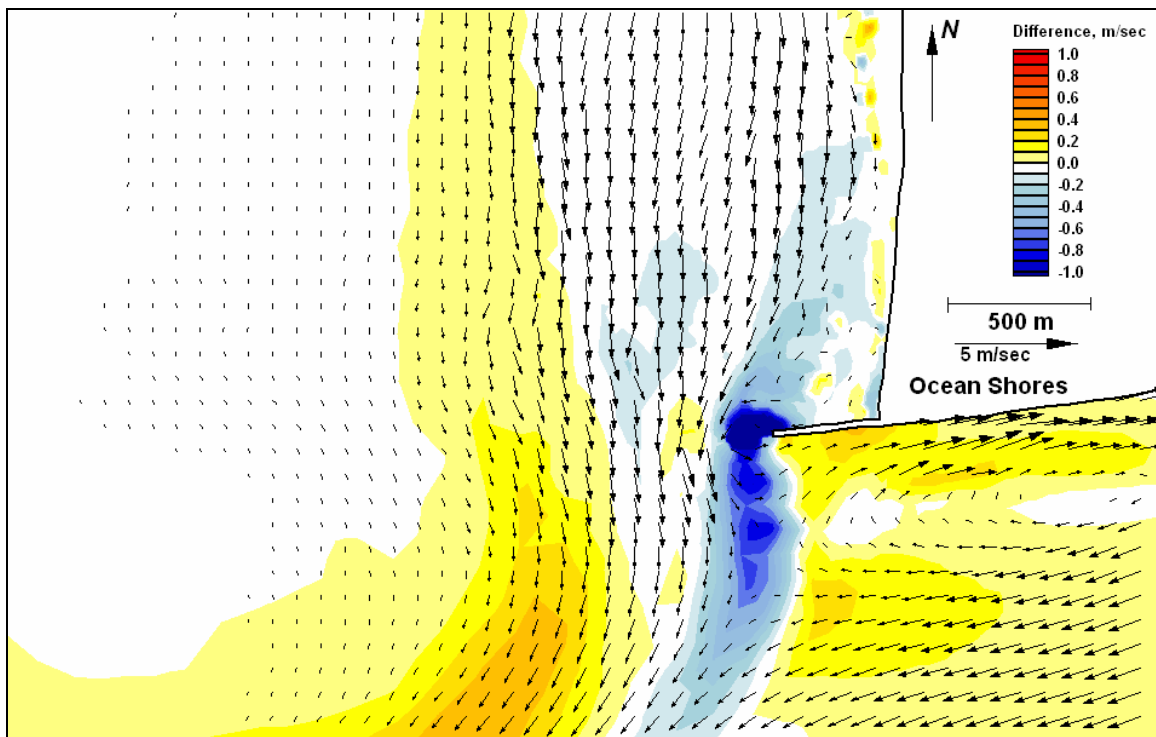
Figure E322. Difference map 137-134 for peak ebb

Appendix E   Tidal Circulation Simulation Results
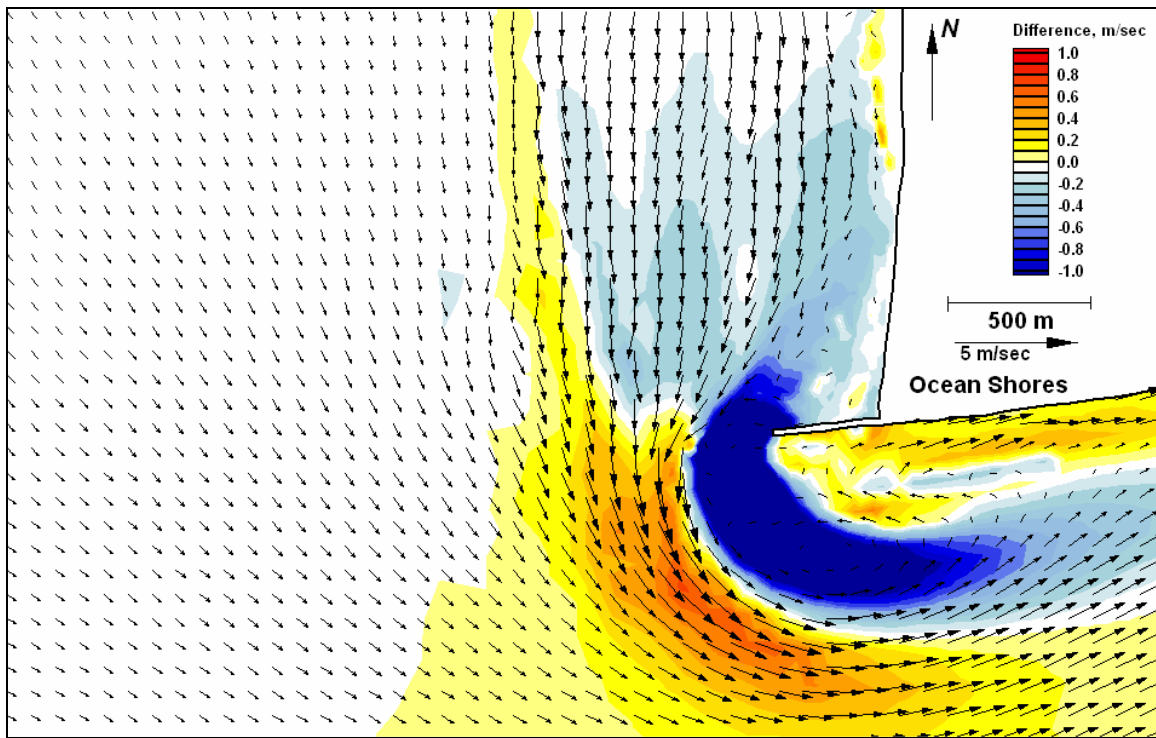
Figure E323. Difference map 138-134 for peak flood
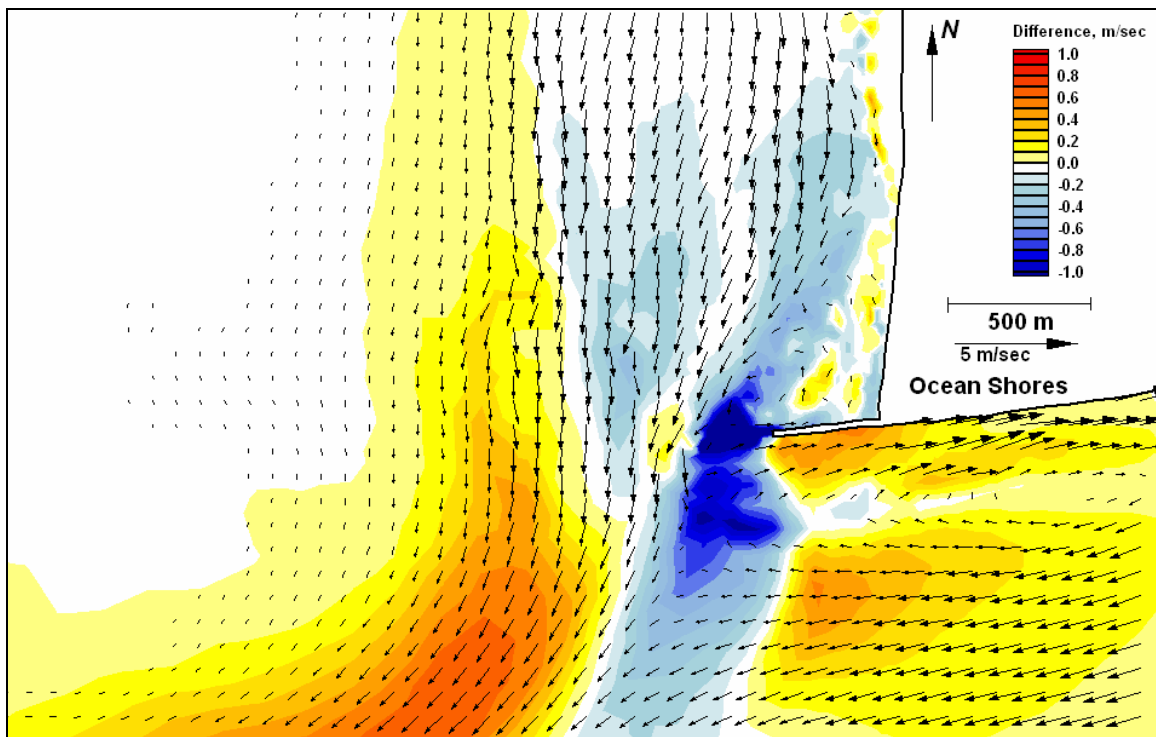
Figure E324. Difference map 138-134 for peak ebb
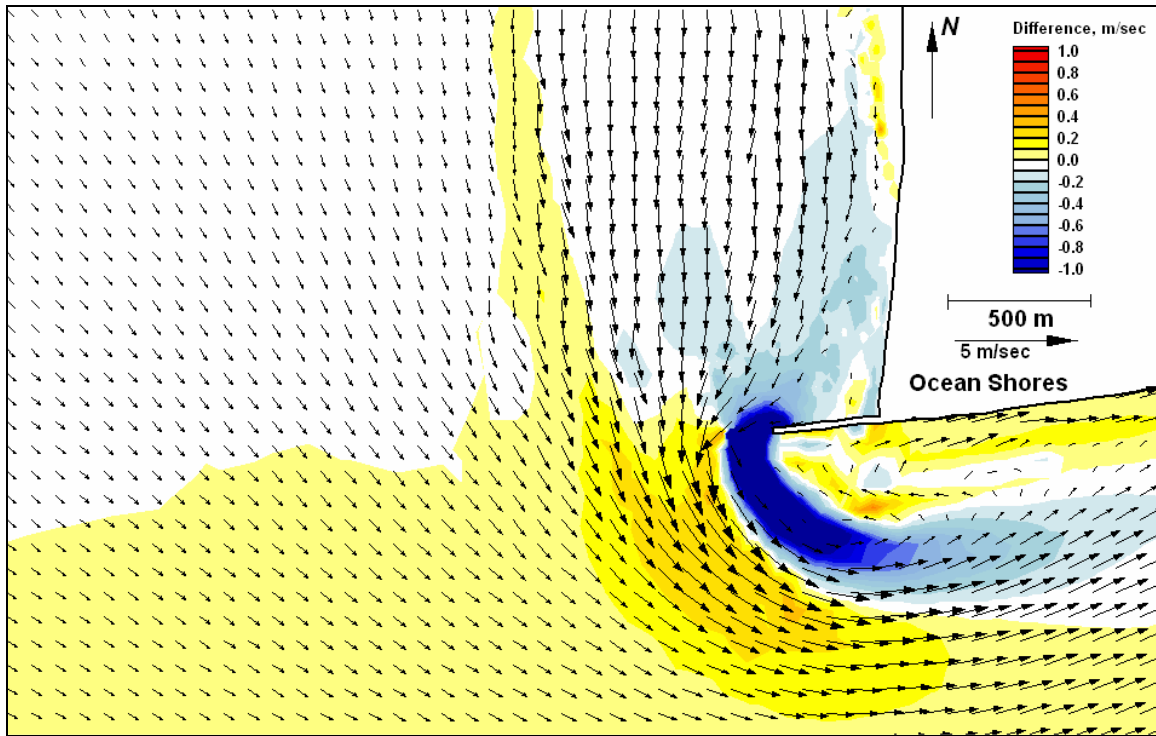
Figure E325. Difference map 139-134 for peak flood
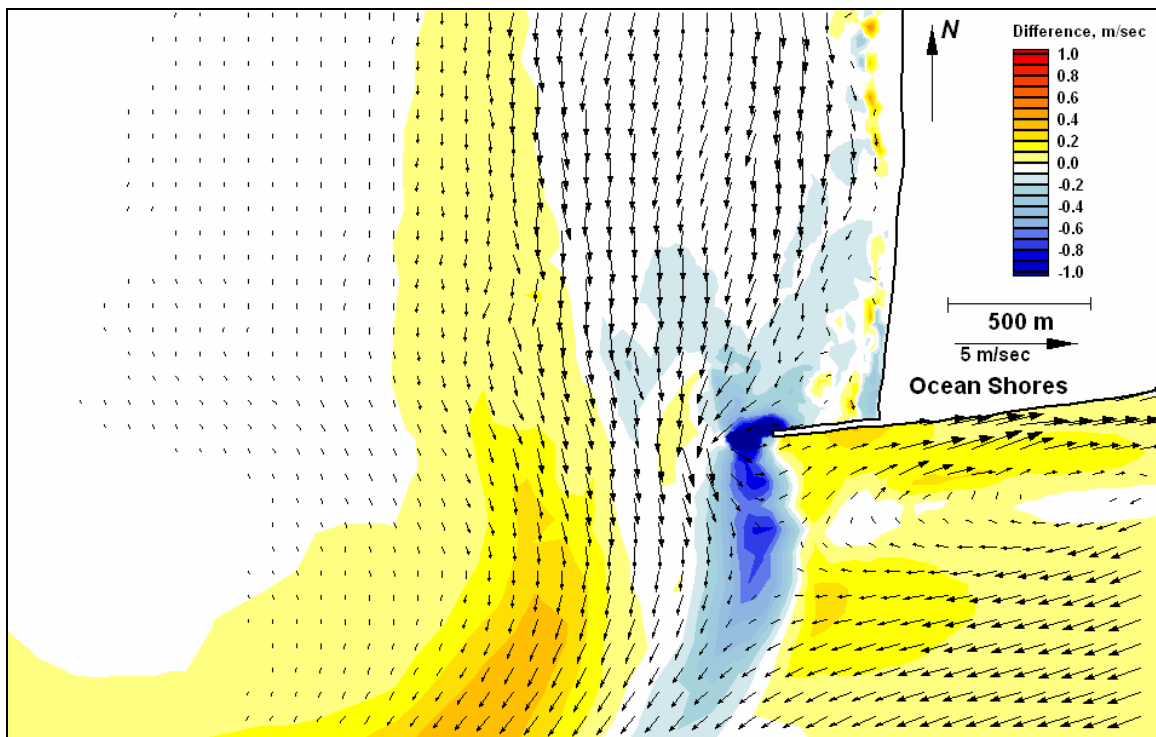
Figure E326. Difference map 139-134 for peak ebb

Appendix E   Tidal Circulation Simulation Results
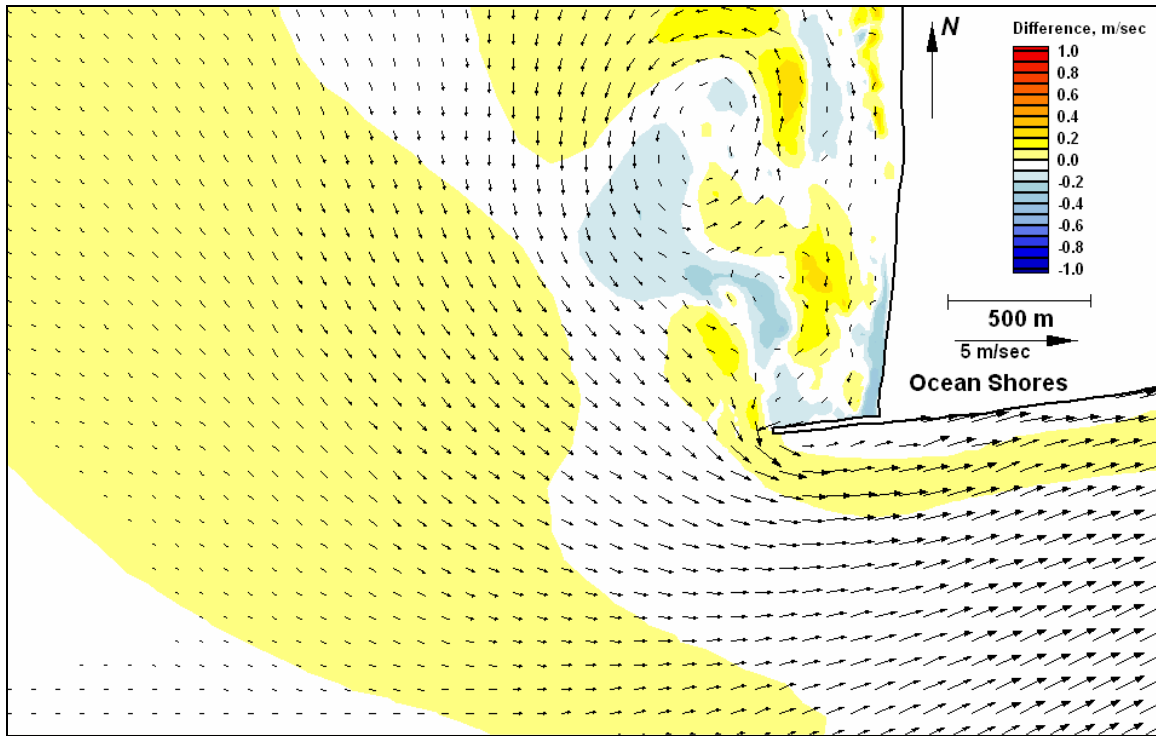
Figure E327. Difference map 141-140 for peak flood
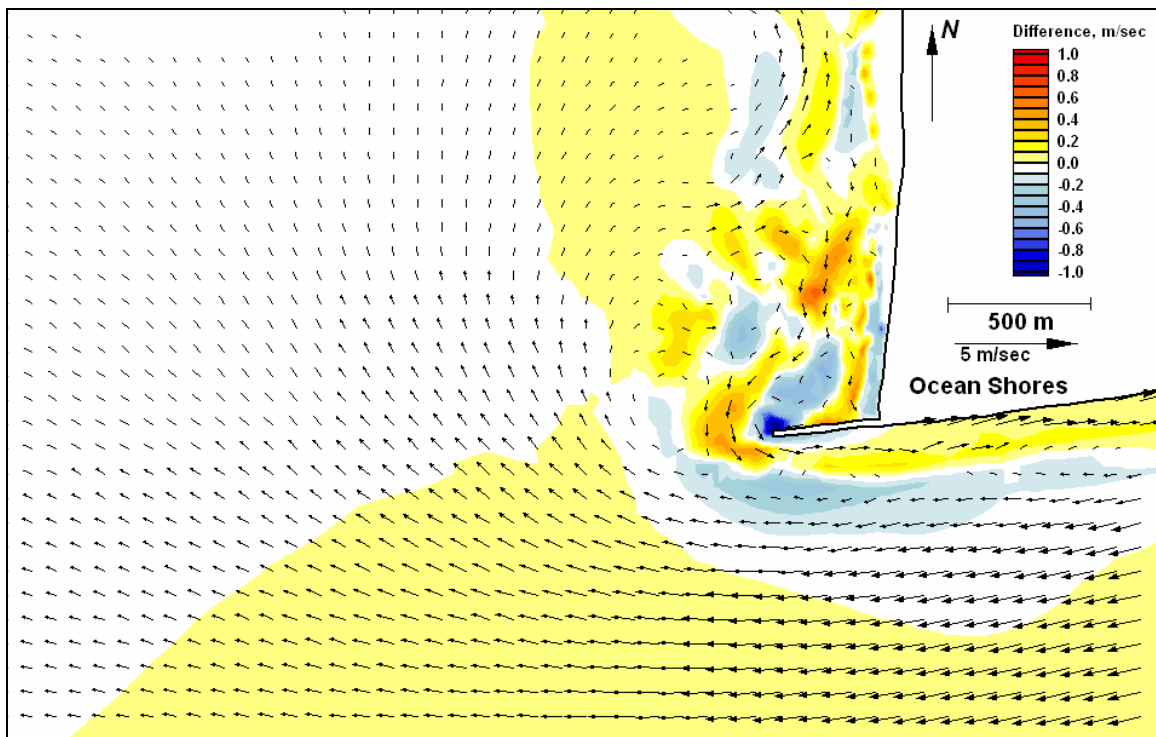
Figure E328. Difference map 141-140 for peak ebb
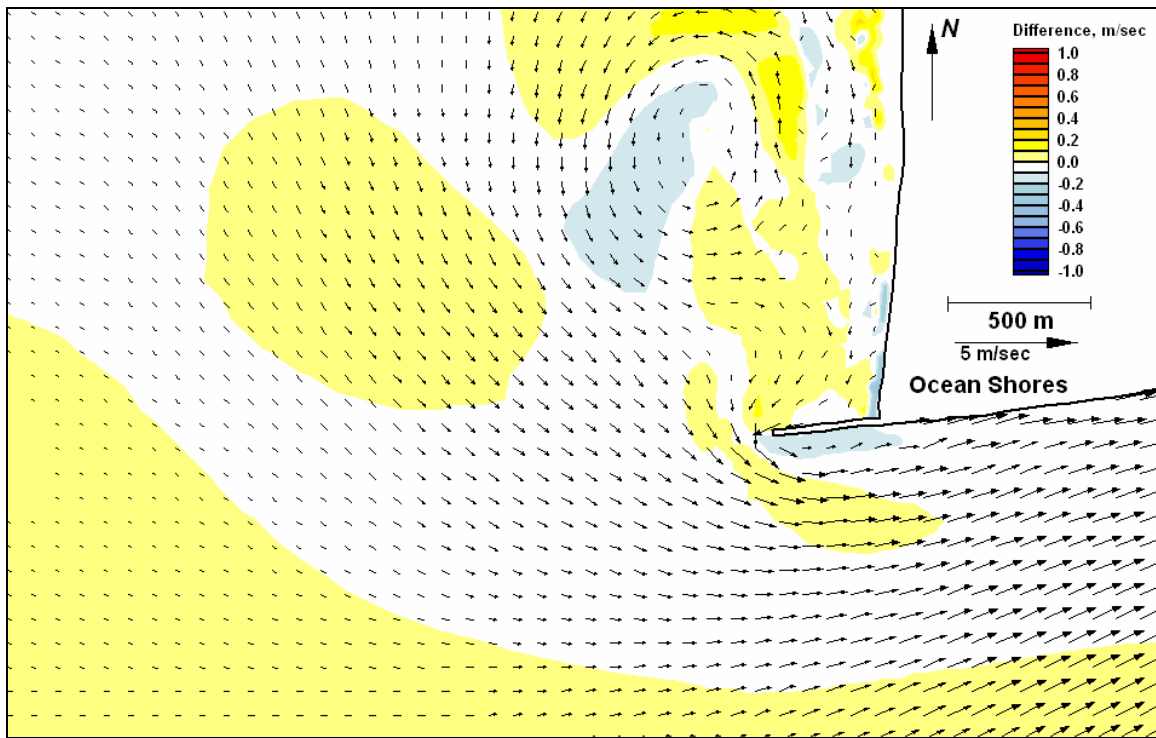
Figure E329. Difference map 142-140 for peak flood
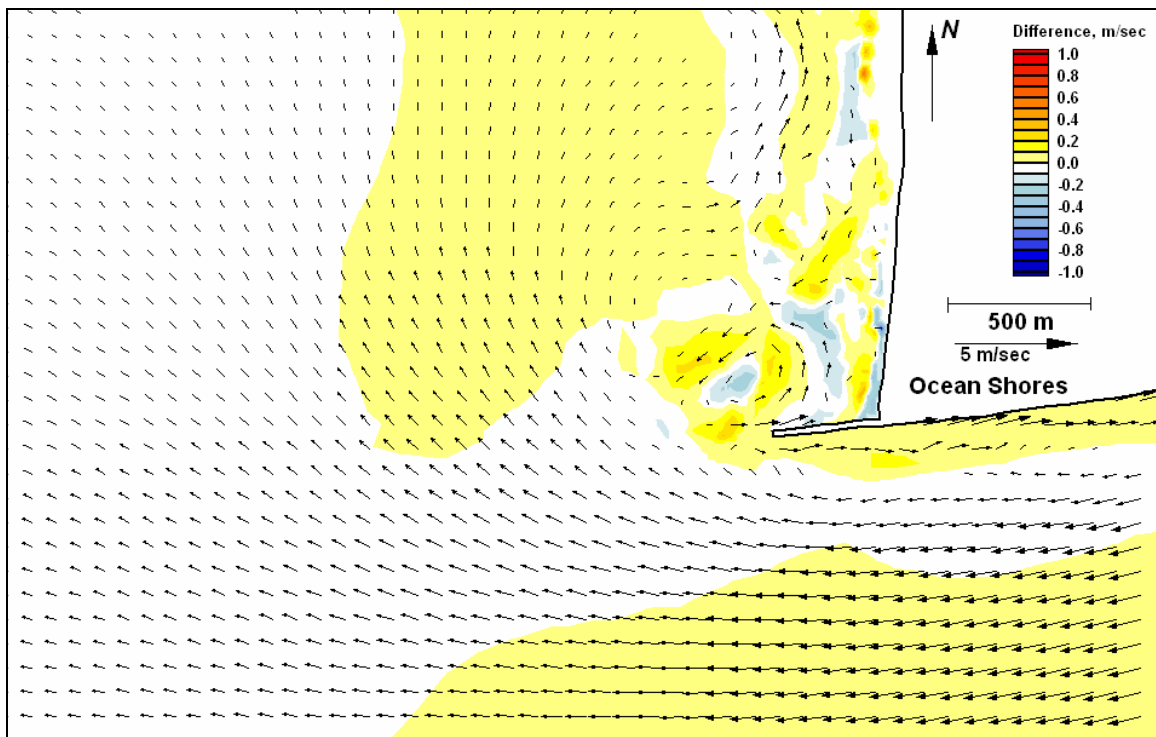
Figure E330. Difference map 142-140 for peak ebb
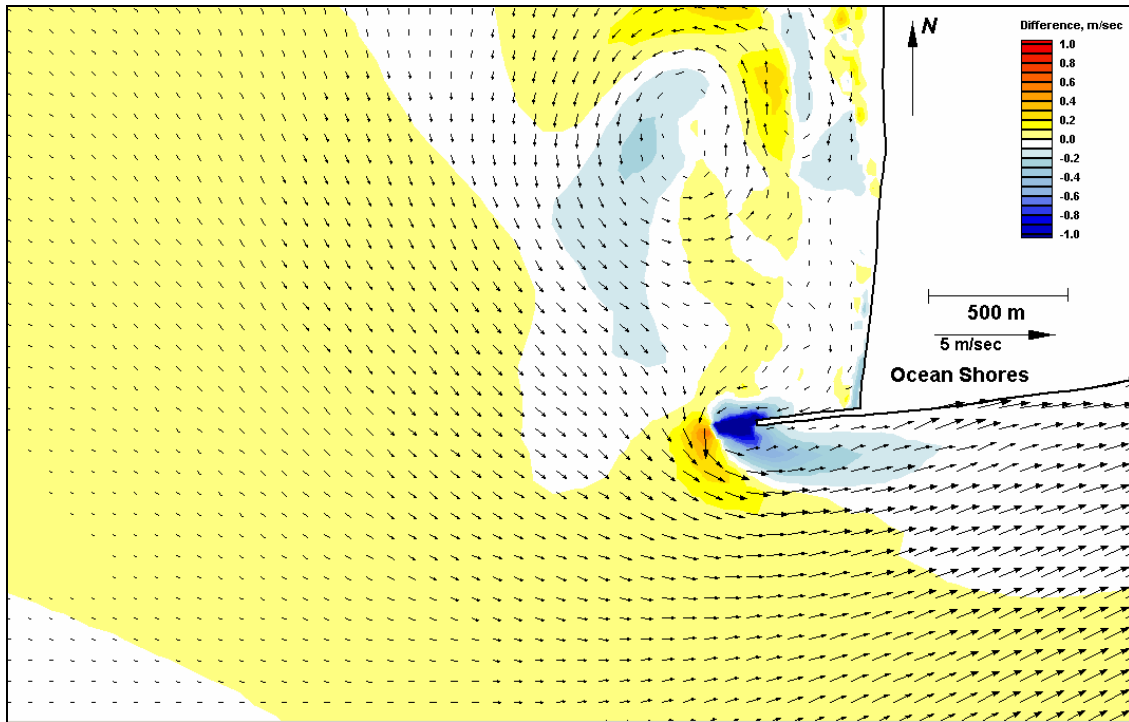
Figure E331. Difference map 143-140 for peak flood
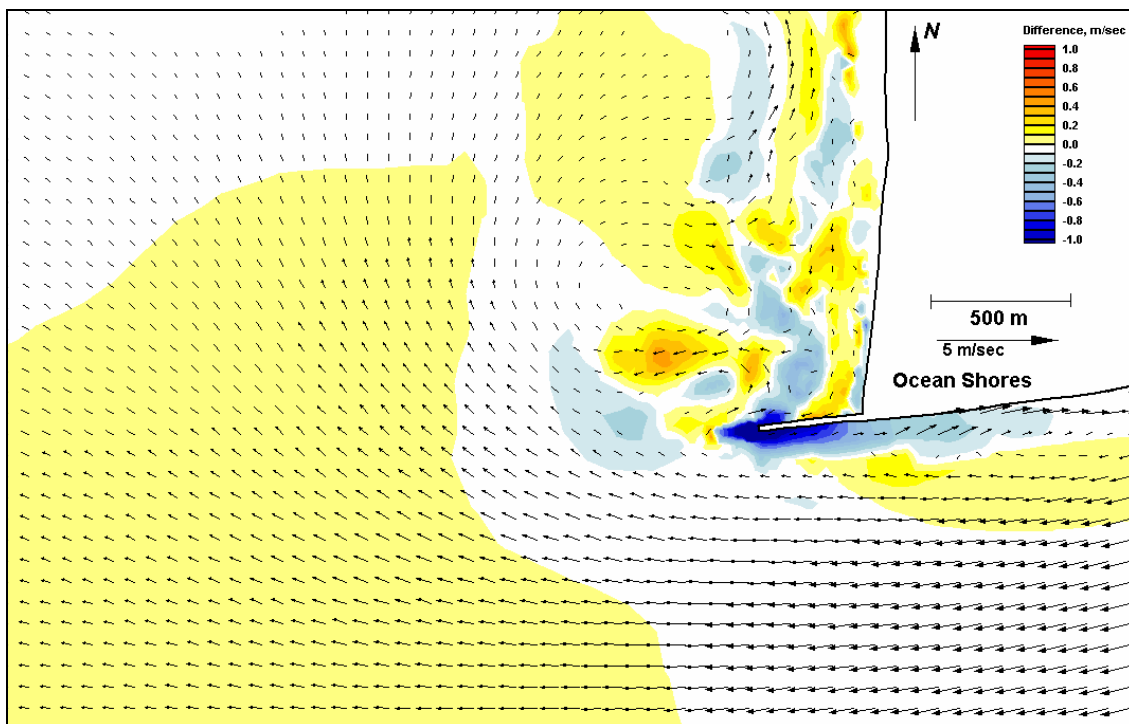
Figure E332. Difference map 143-140 for peak ebb
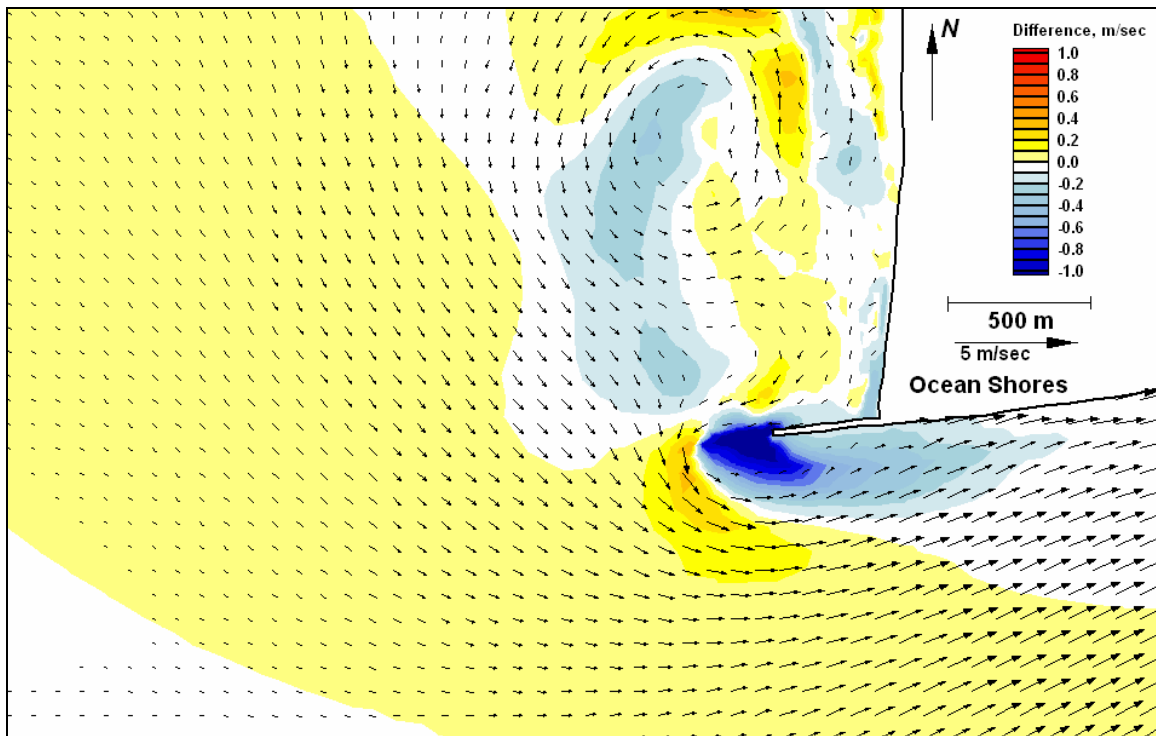
Figure E333. Difference map 144-140 for peak flood
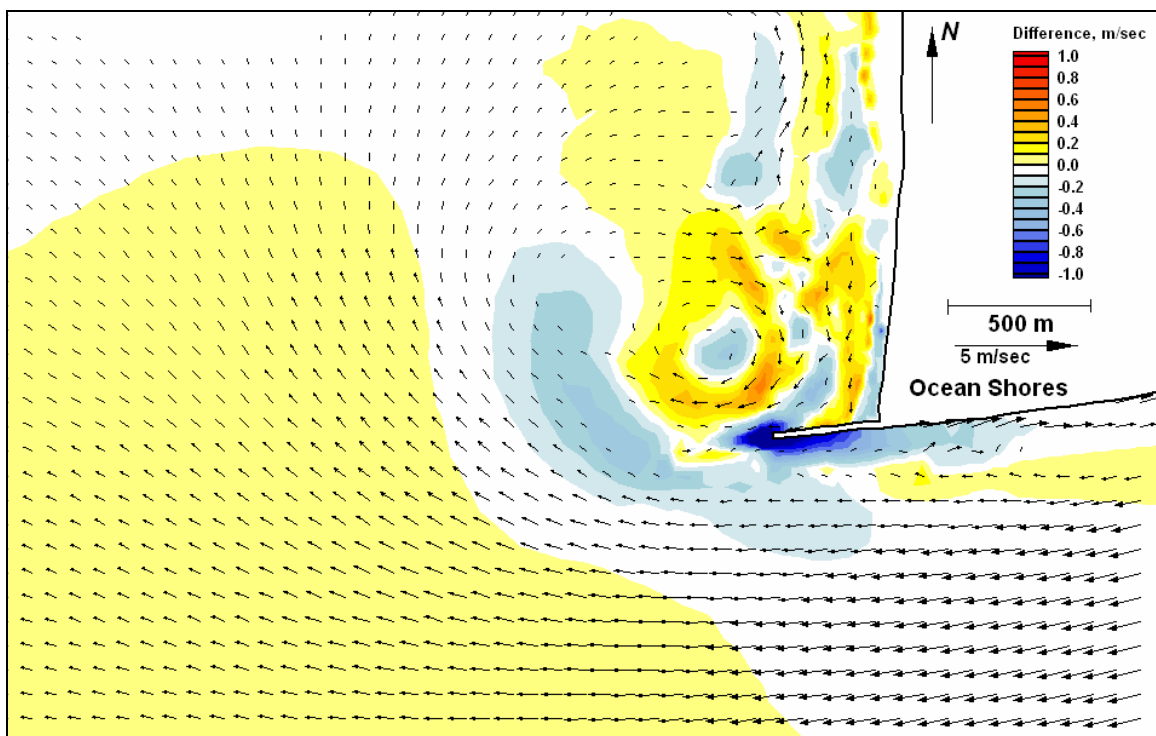
Figure E334. Difference map 144-140 for peak ebb
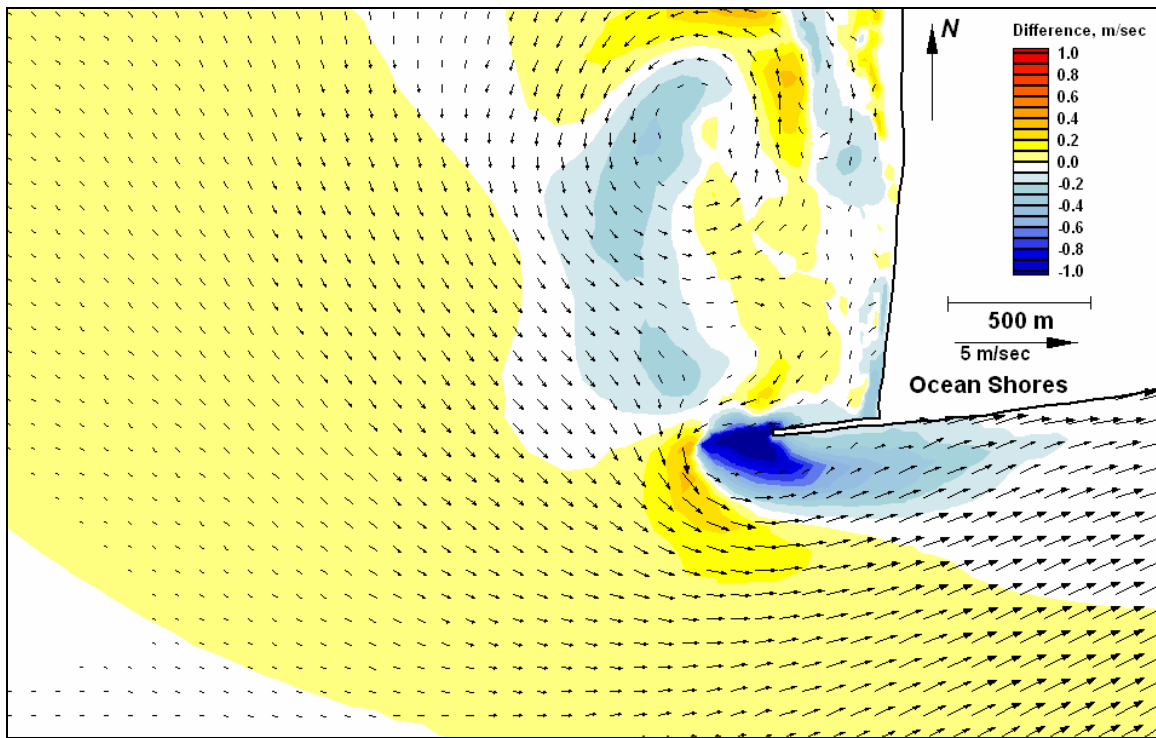
Figure E335. Difference map 145-140 for peak flood
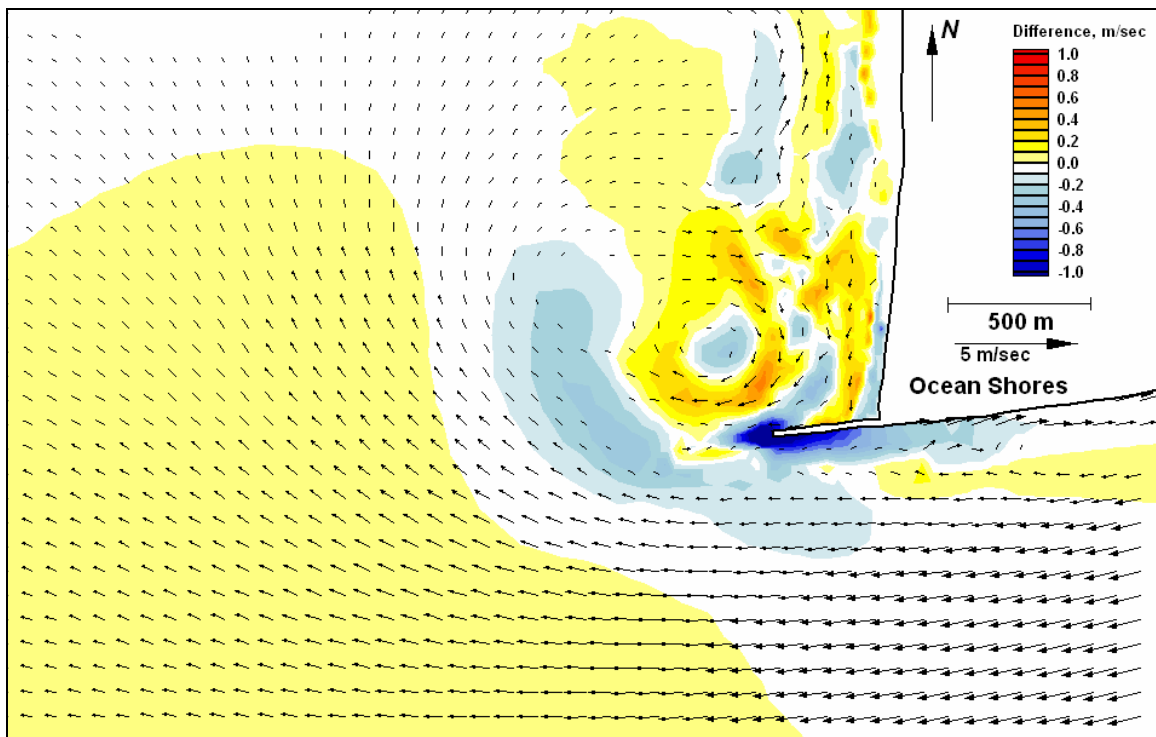
Figure E336. Difference map 145-140 for peak ebb
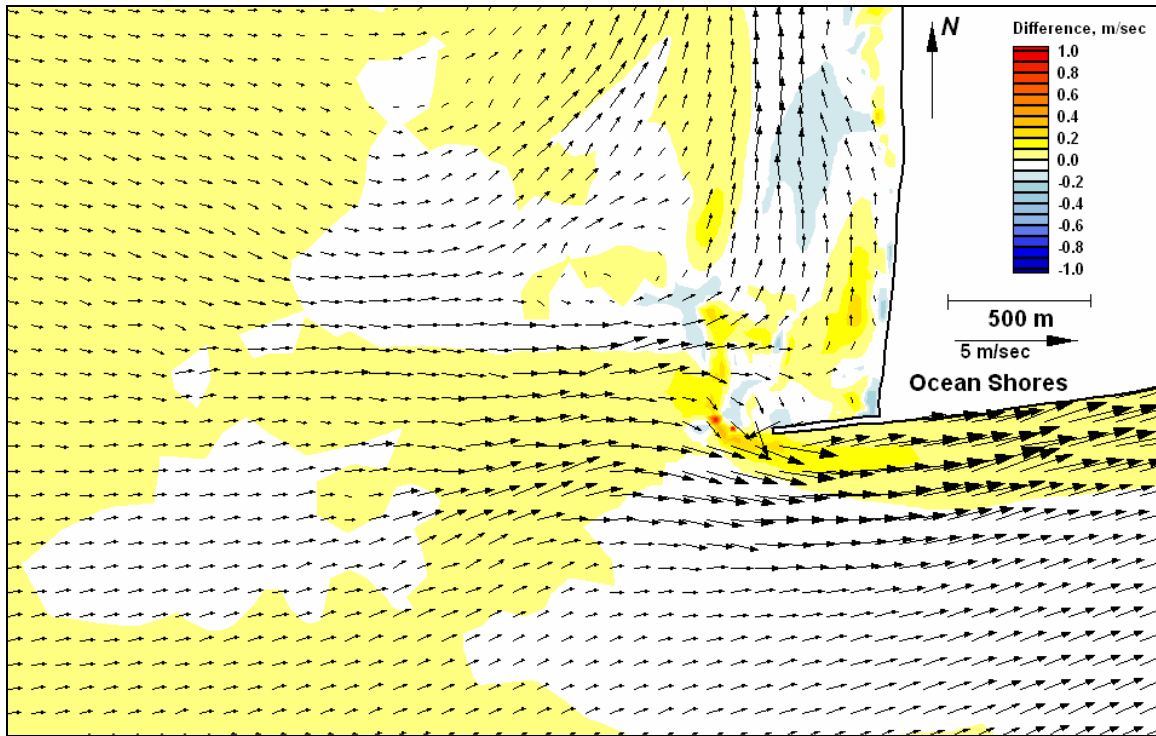
Figure E337. Difference map 147-146 for peak flood
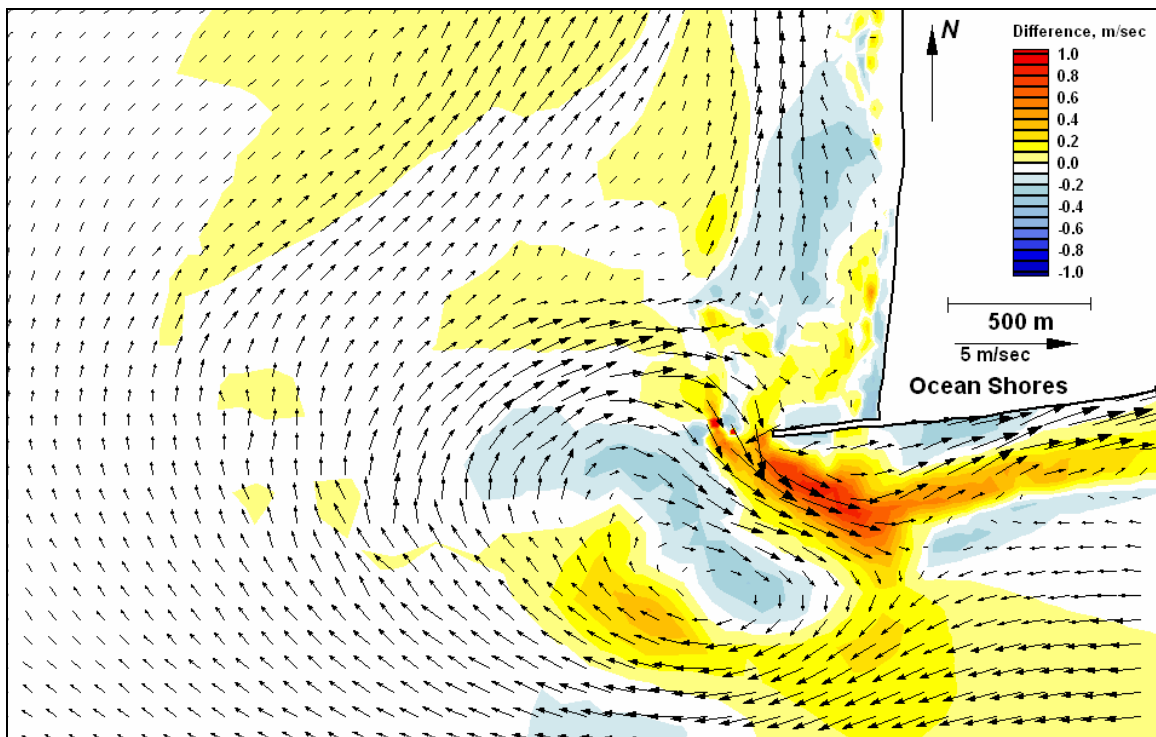
Figure E338. Difference map 147-146 for peak ebb

Appendix E   Tidal Circulation Simulation Results
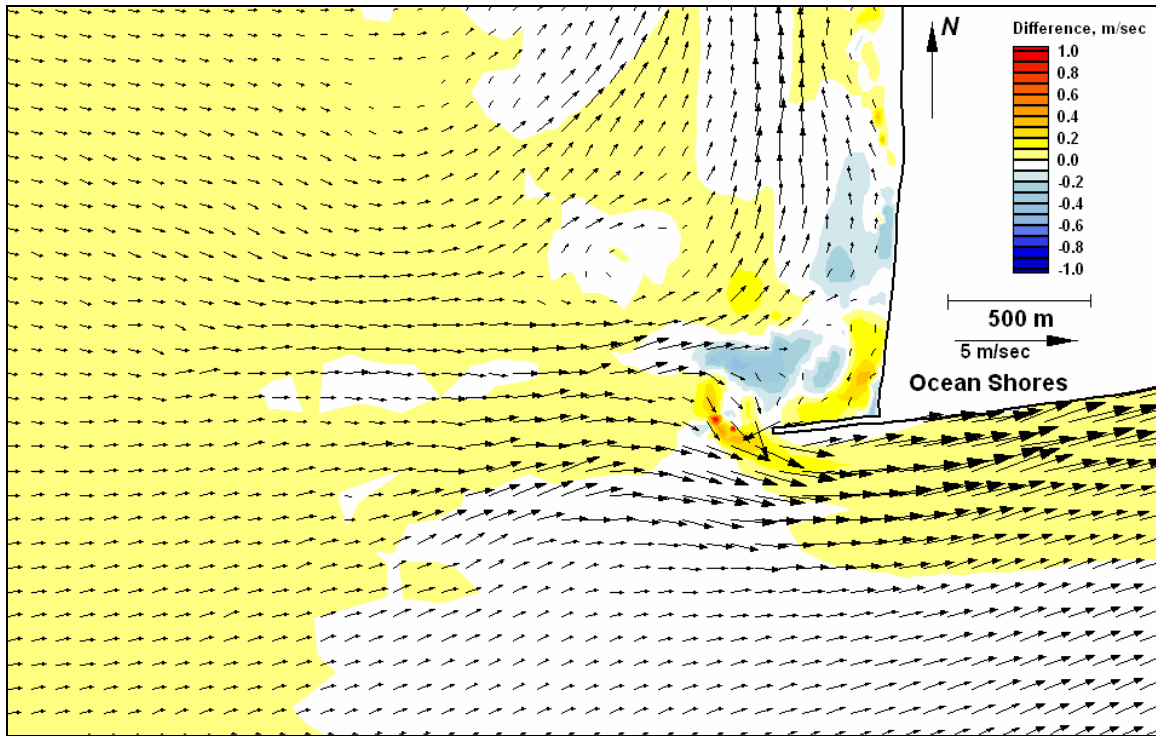
Figure E339. Difference map 148-146 for peak flood
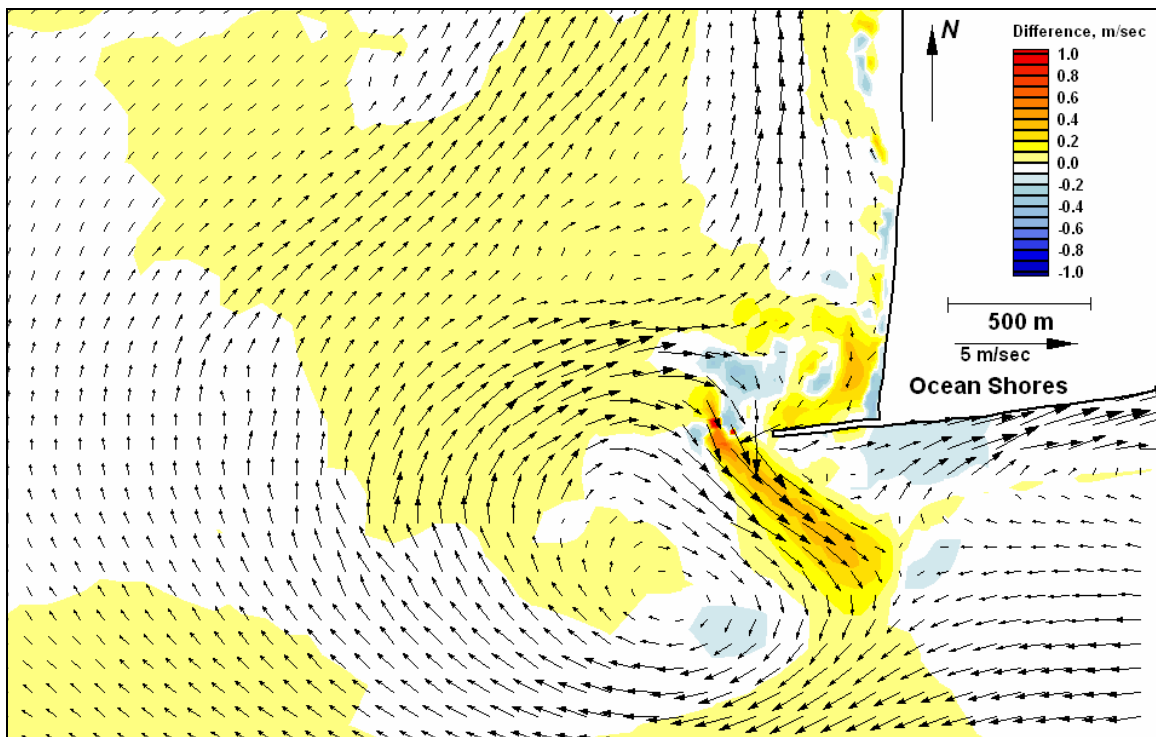
Figure E340. Difference map 148-146 for peak ebb
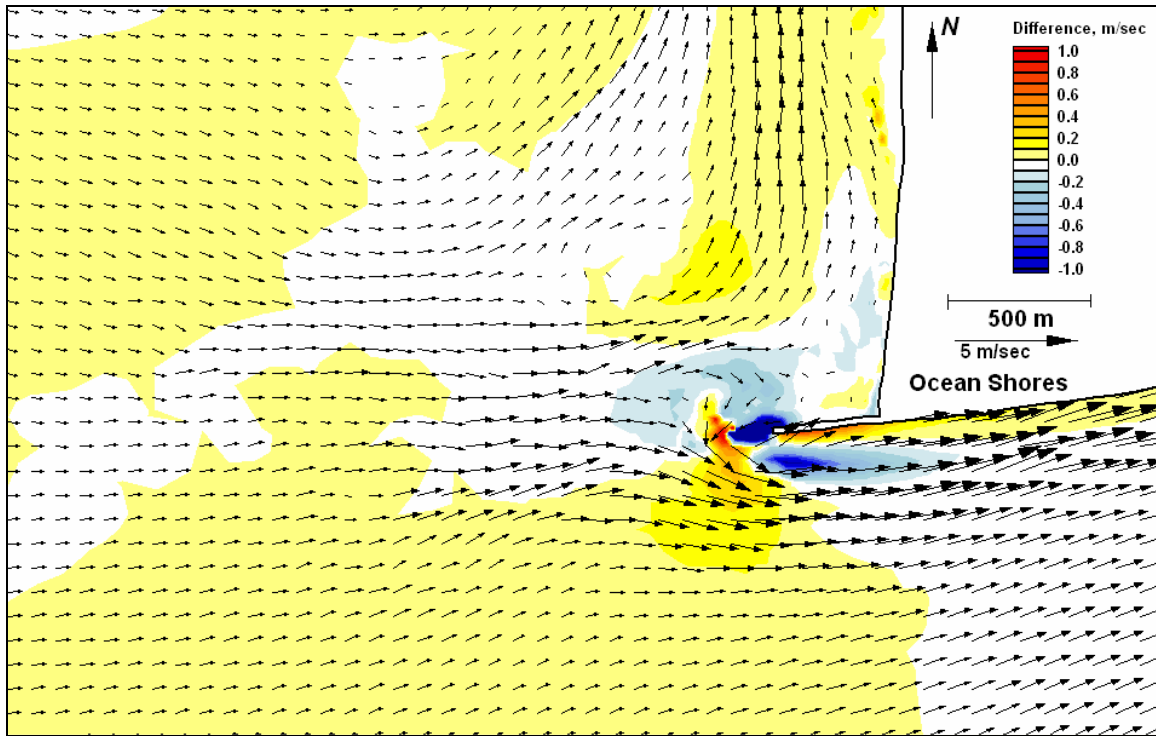
Figure E341. Difference map 149-146 for peak flood
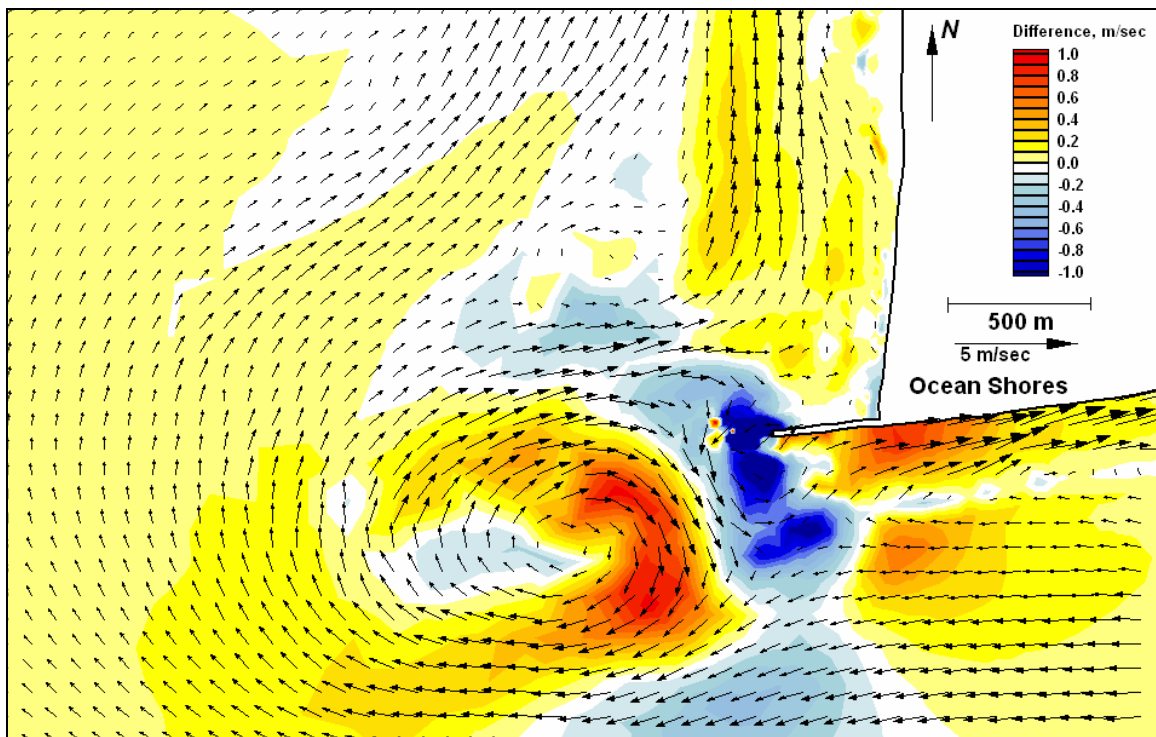
Figure E342. Difference map 149-146 for peak ebb

Appendix E   Tidal Circulation Simulation Results
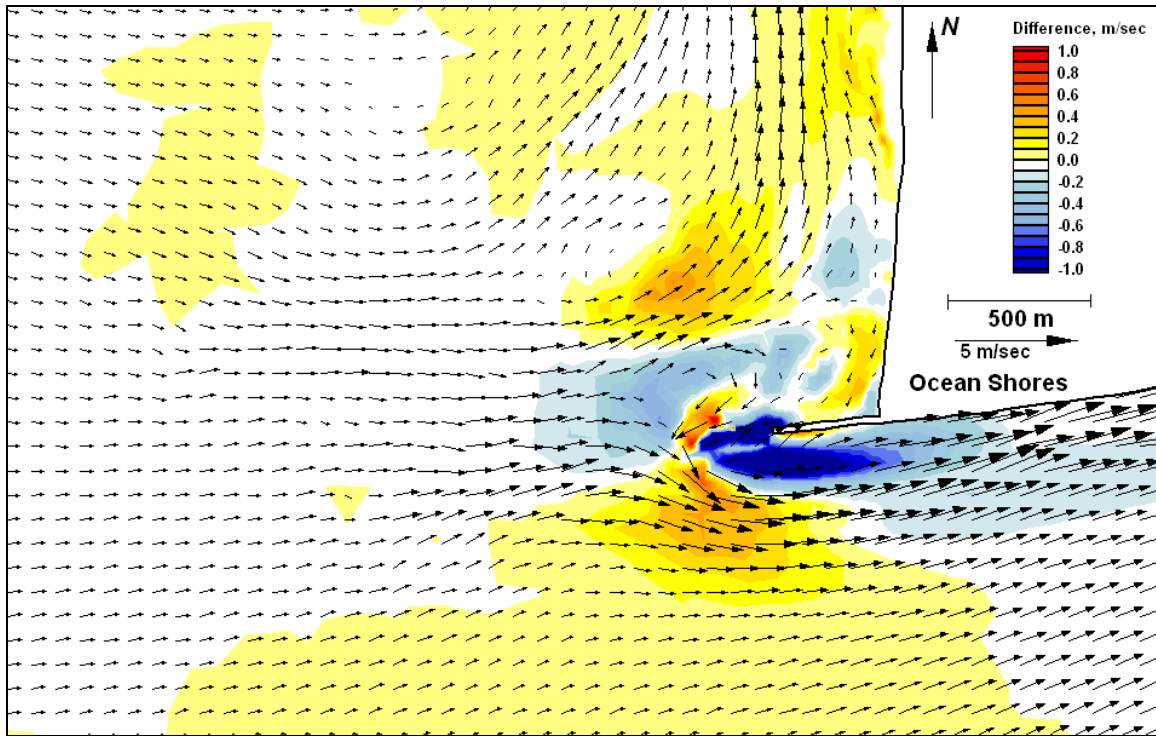
Figure E343. Difference map 150-146 for peak flood
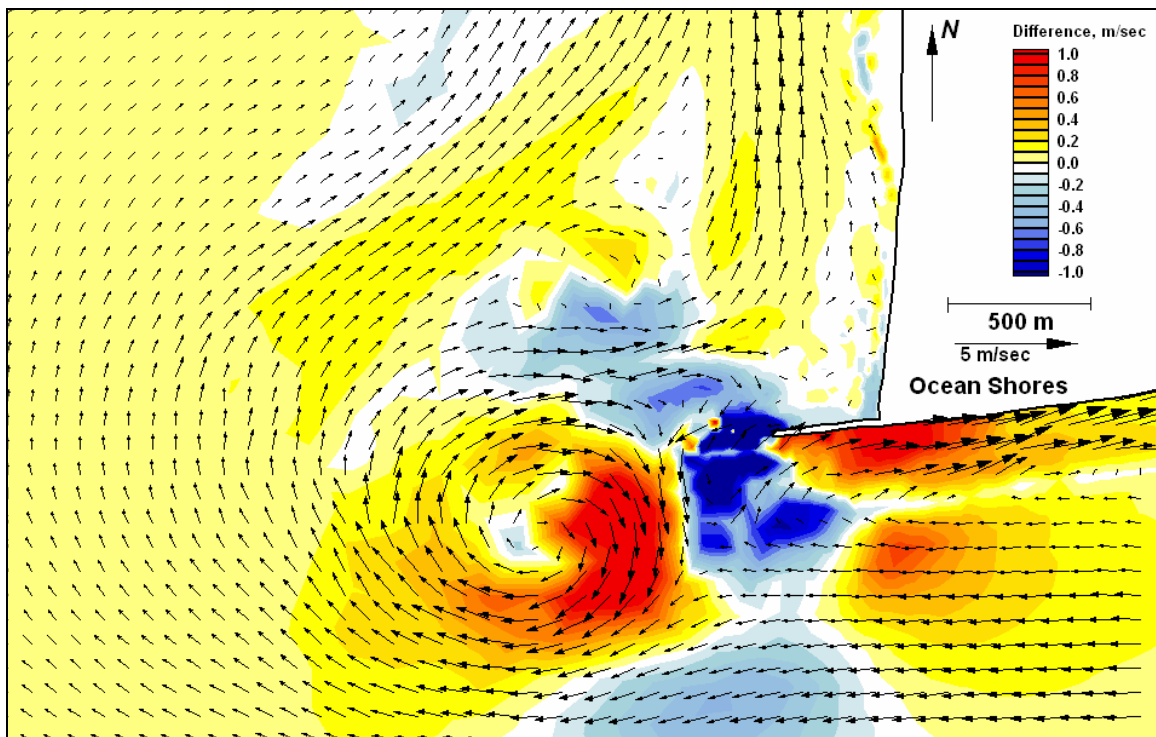
Figure E344. Difference map 150-146 for peak ebb
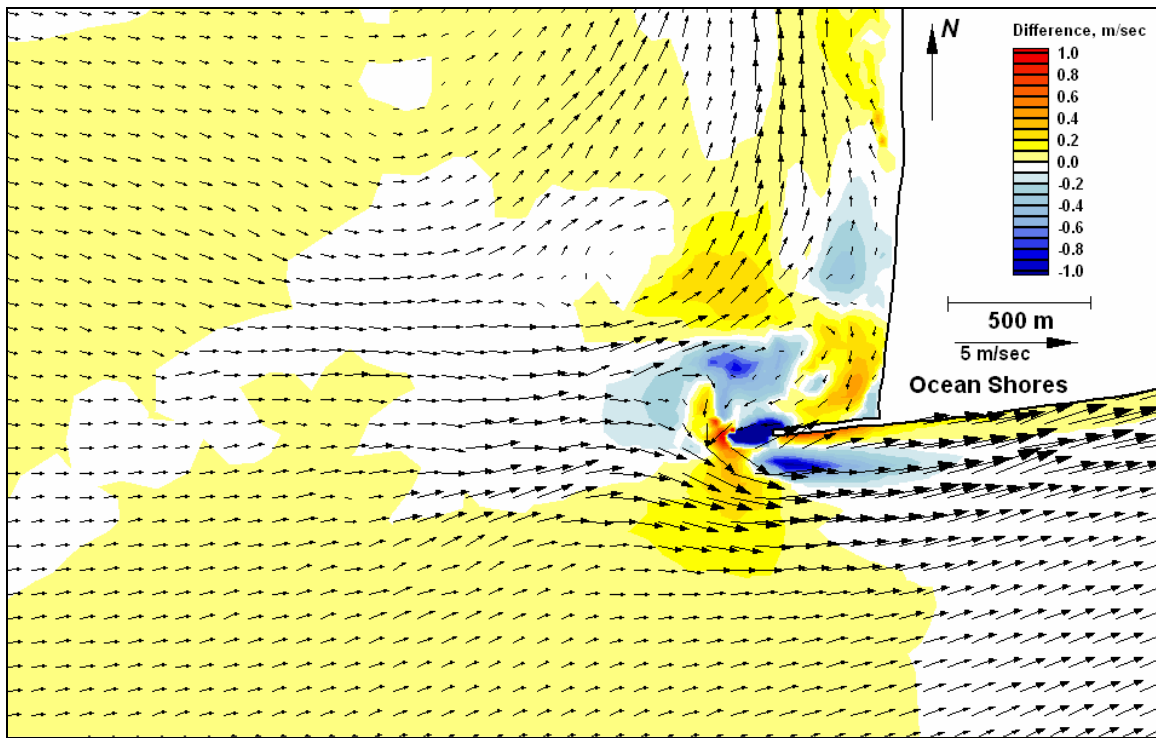
Figure E345. Difference map 151-146 for peak flood
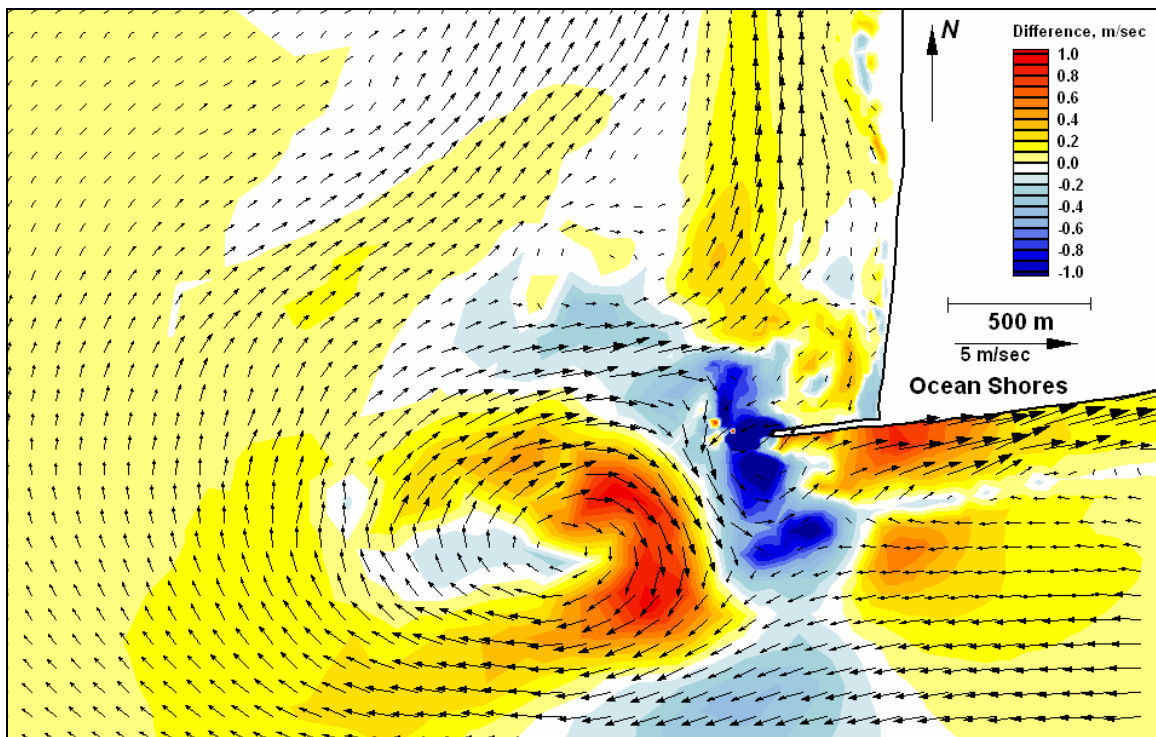
Figure E346. Difference map 151-146 for peak ebb

Appendix E   Tidal Circulation Simulation Results
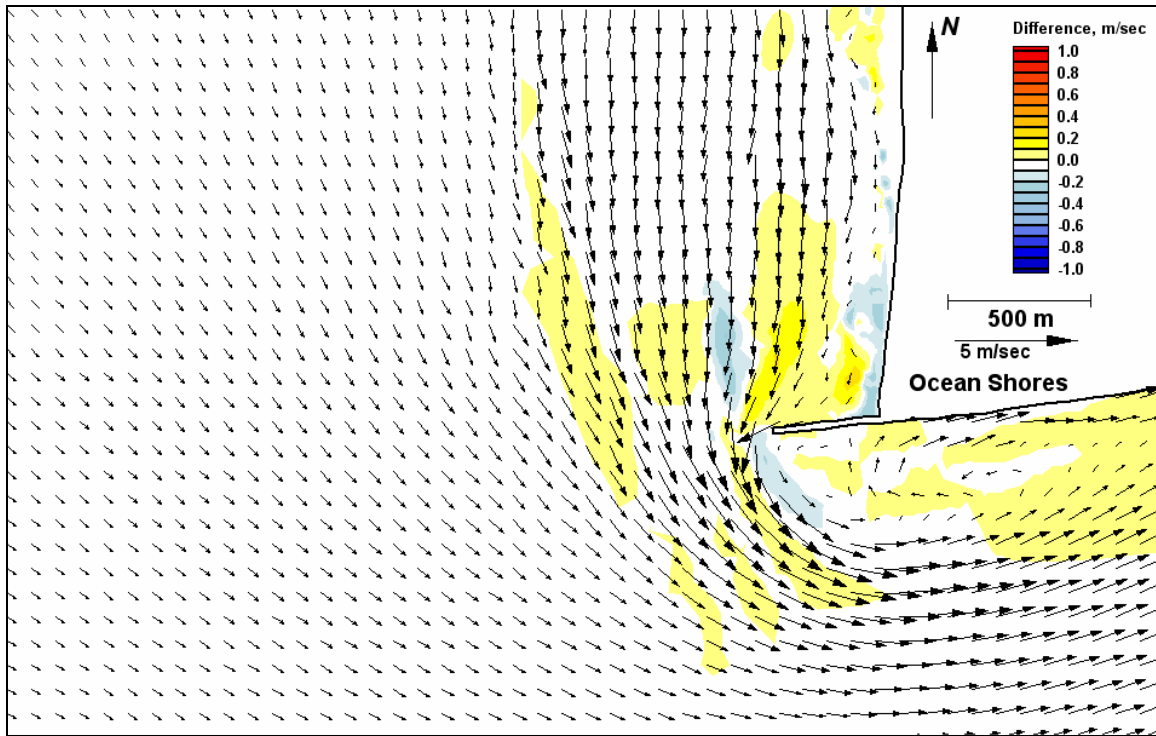
Figure E347. Difference map 153-152 for peak flood
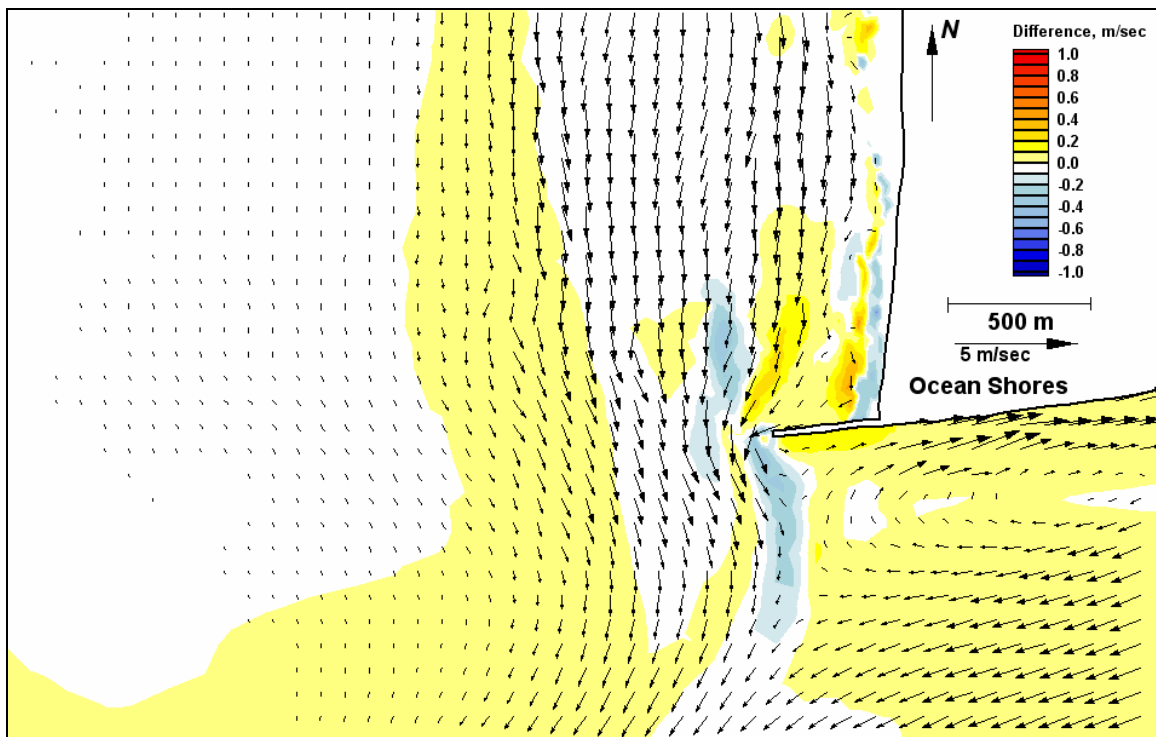
Figure E348. Difference map 153-152 for peak ebb
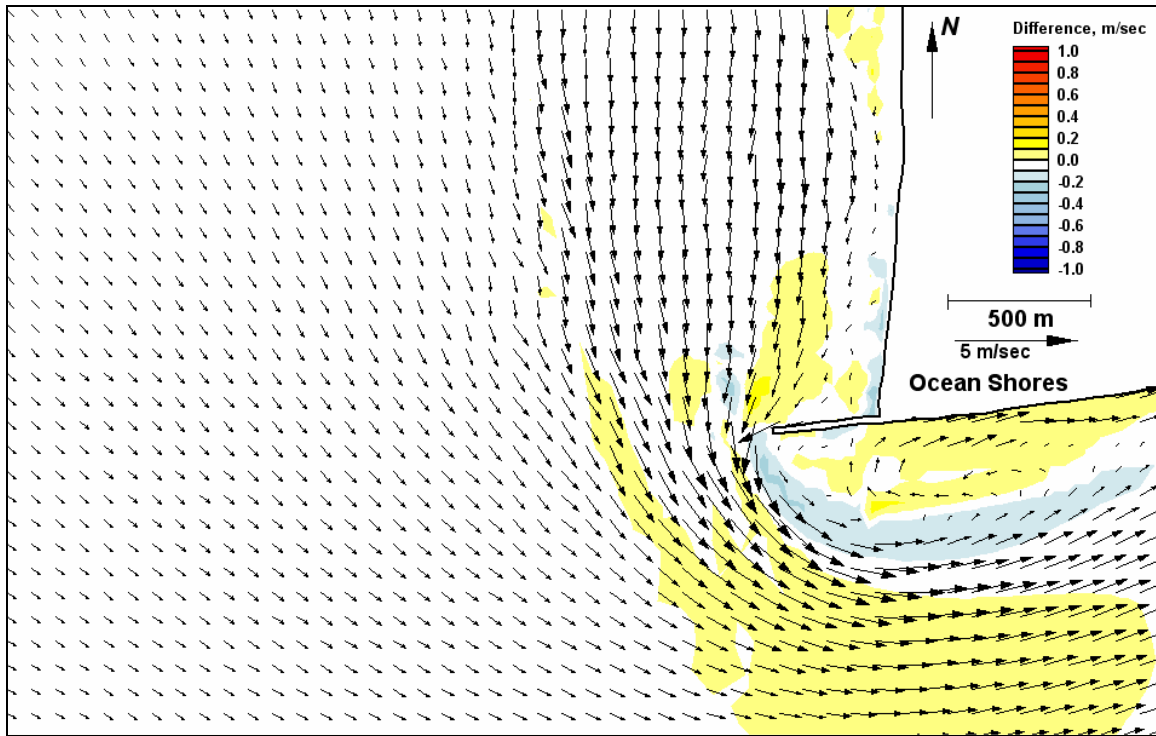
Figure E349. Difference map 154-152 for peak flood
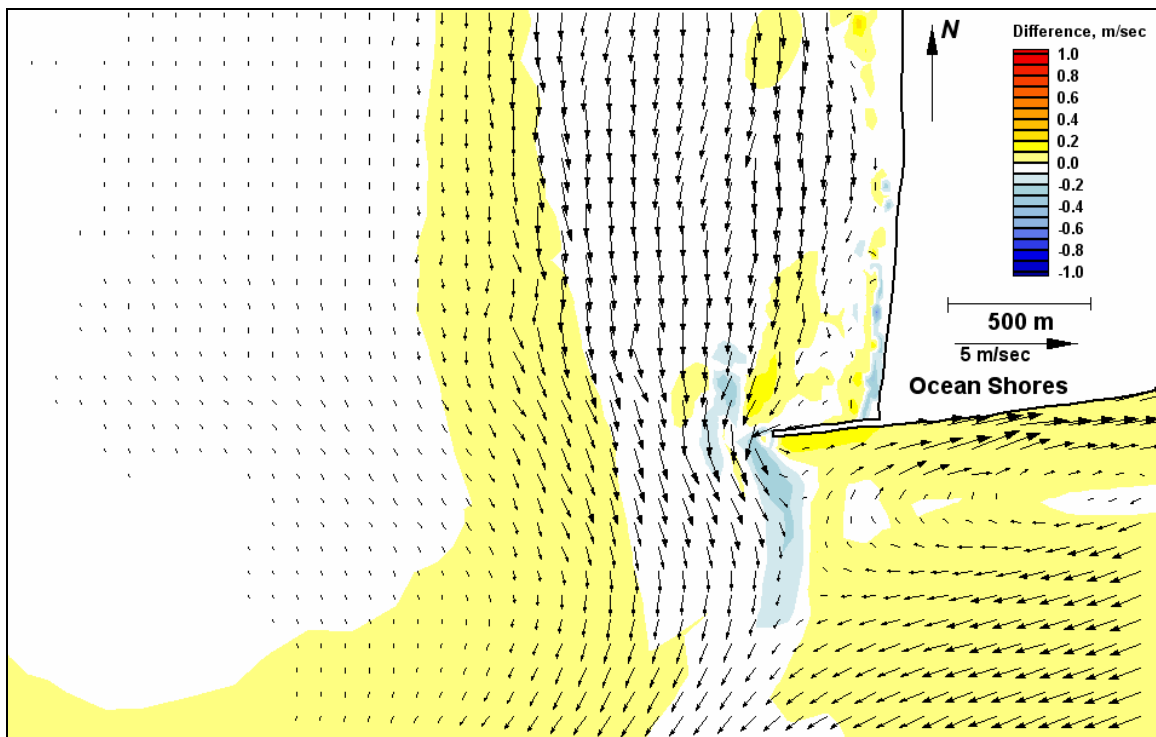
Figure E350. Difference map 154-152 for peak ebb

Appendix E   Tidal Circulation Simulation Results
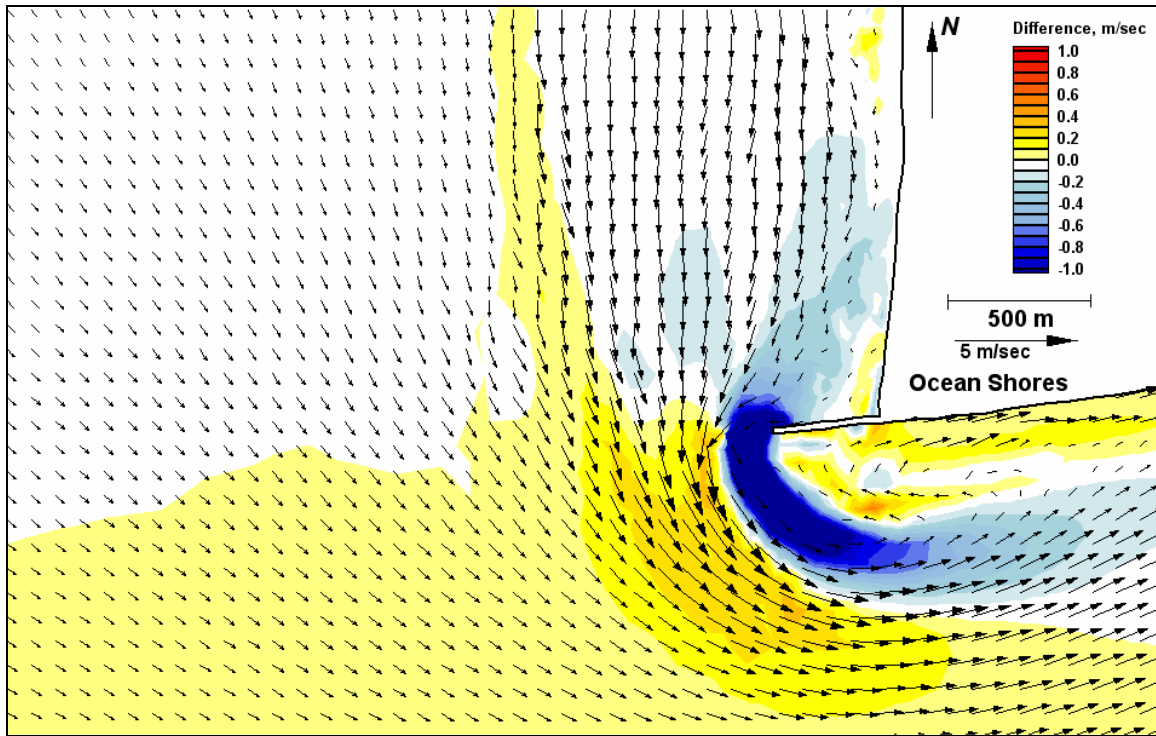
Figure E351. Difference map 155-152 for peak flood
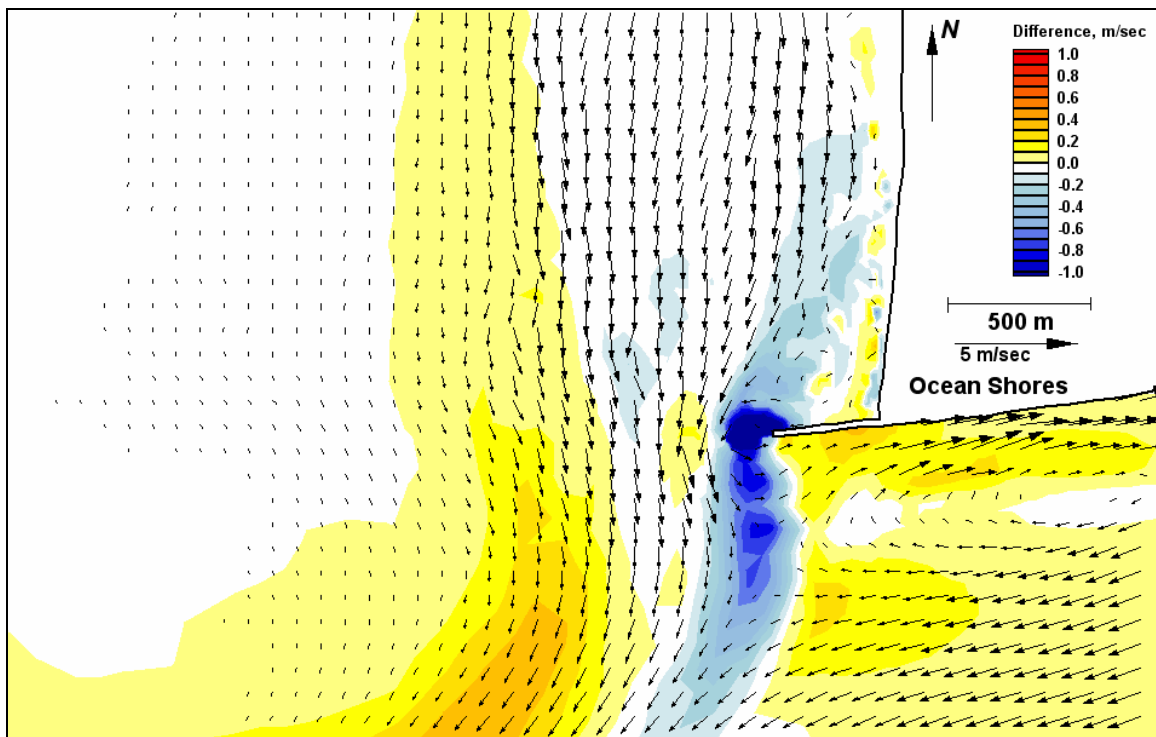
Figure E352. Difference map 155-152 for peak ebb
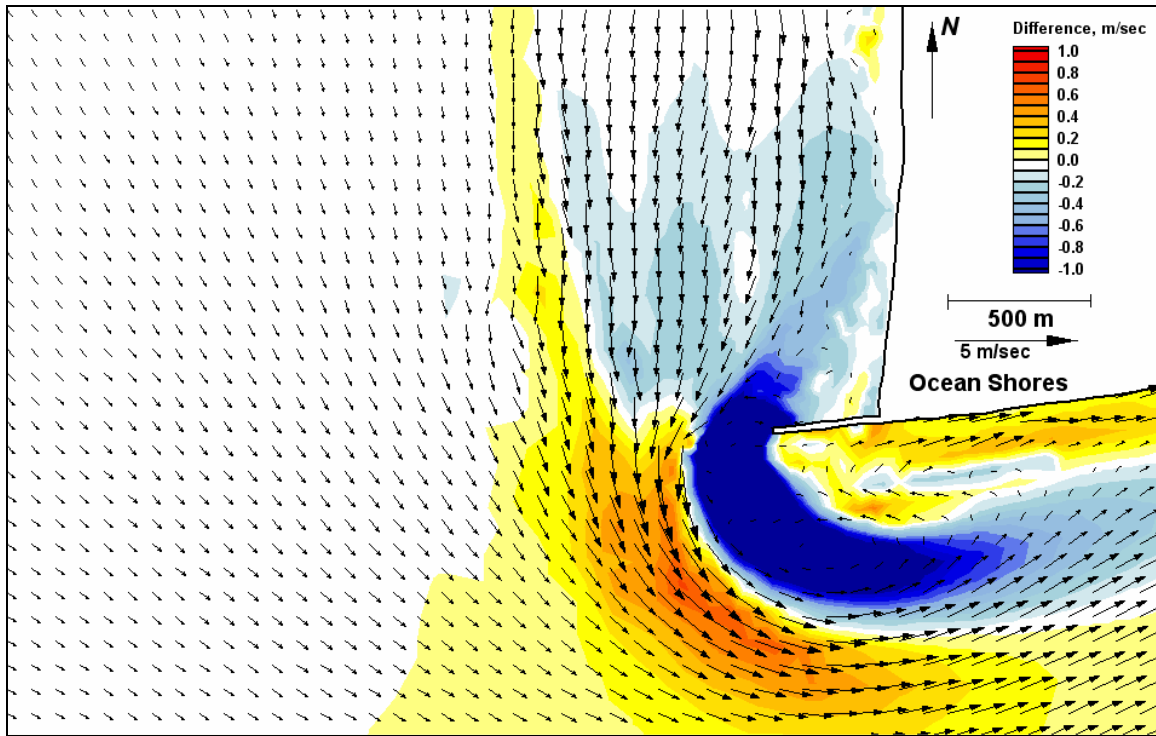
Figure E353. Difference map 156-152 for peak flood
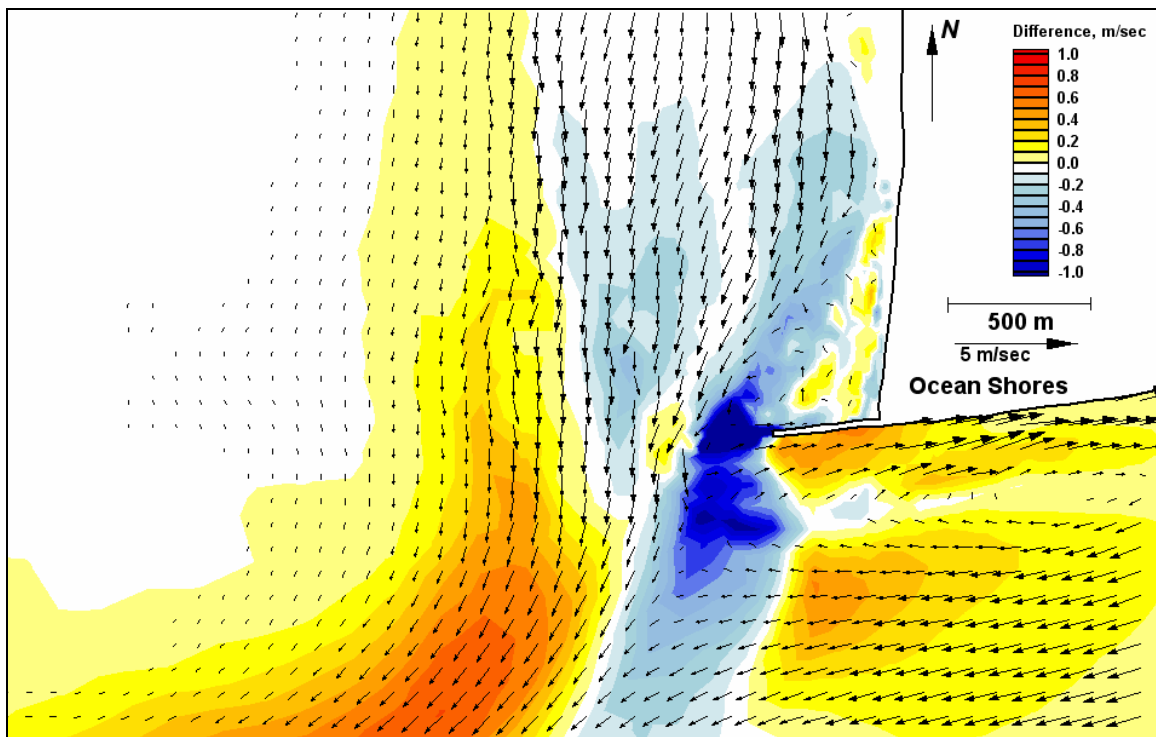
Figure E354. Difference map 156-152 for peak ebb
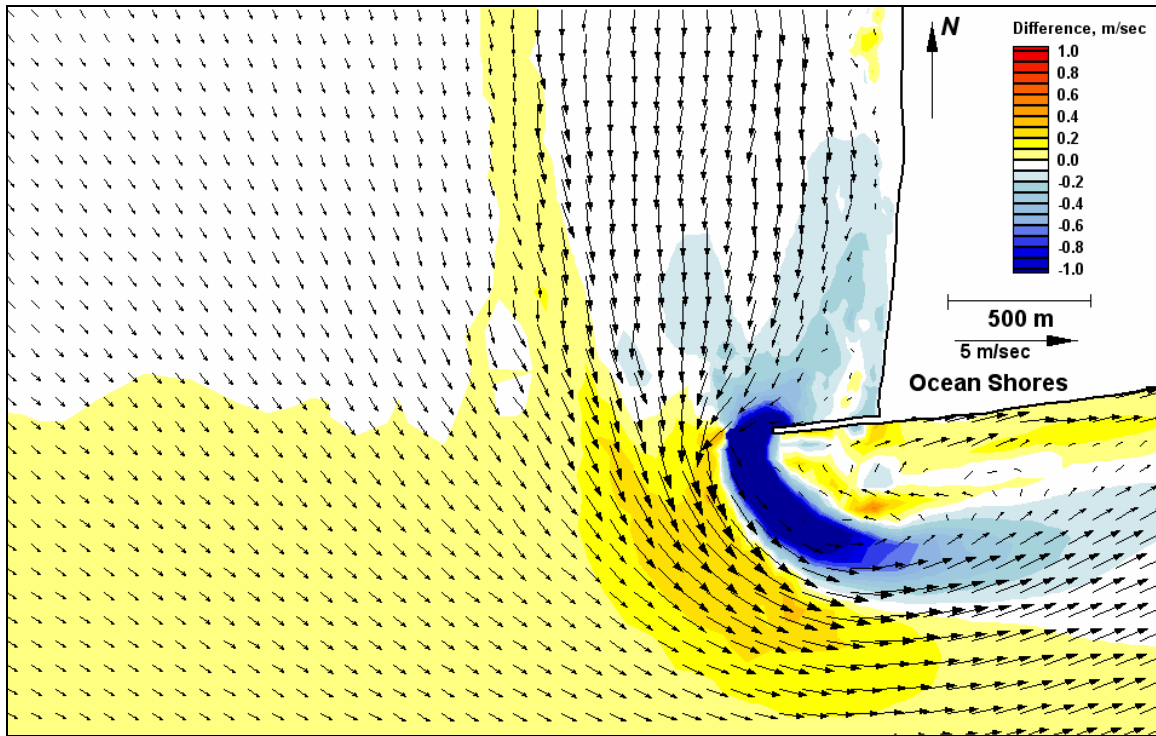
Figure E355. Difference map 157-152 for peak flood
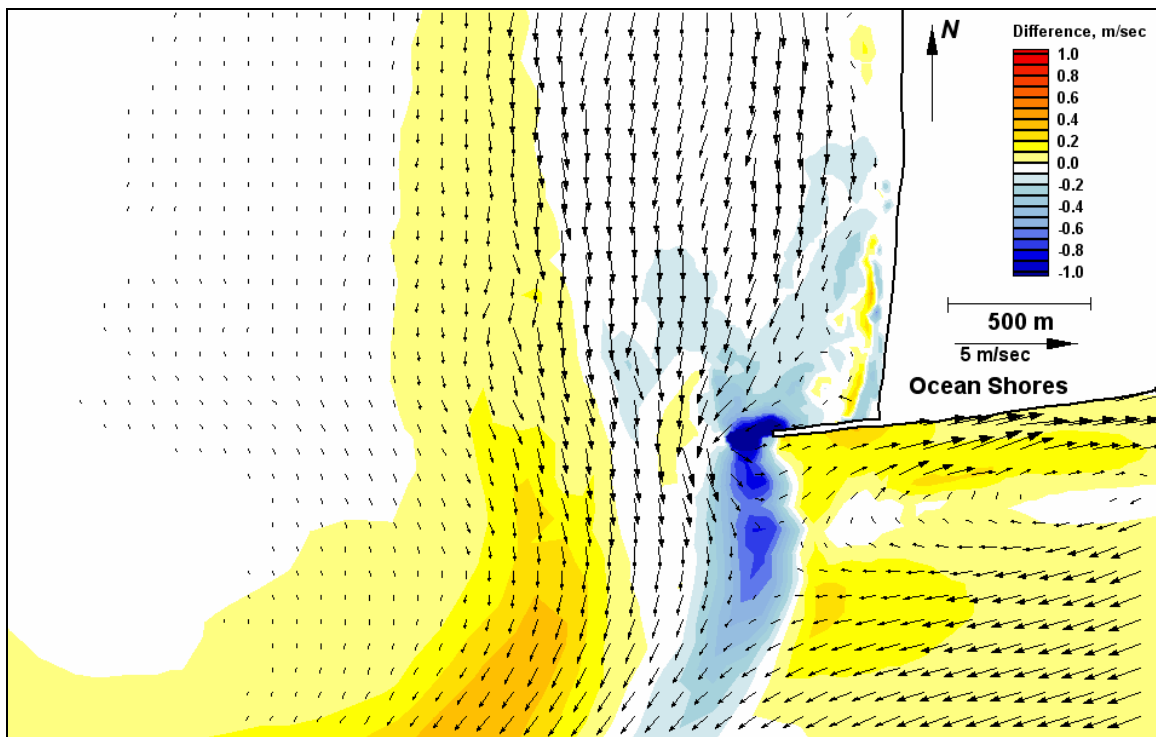
Figure E356. Difference map 157-152 for peak ebb
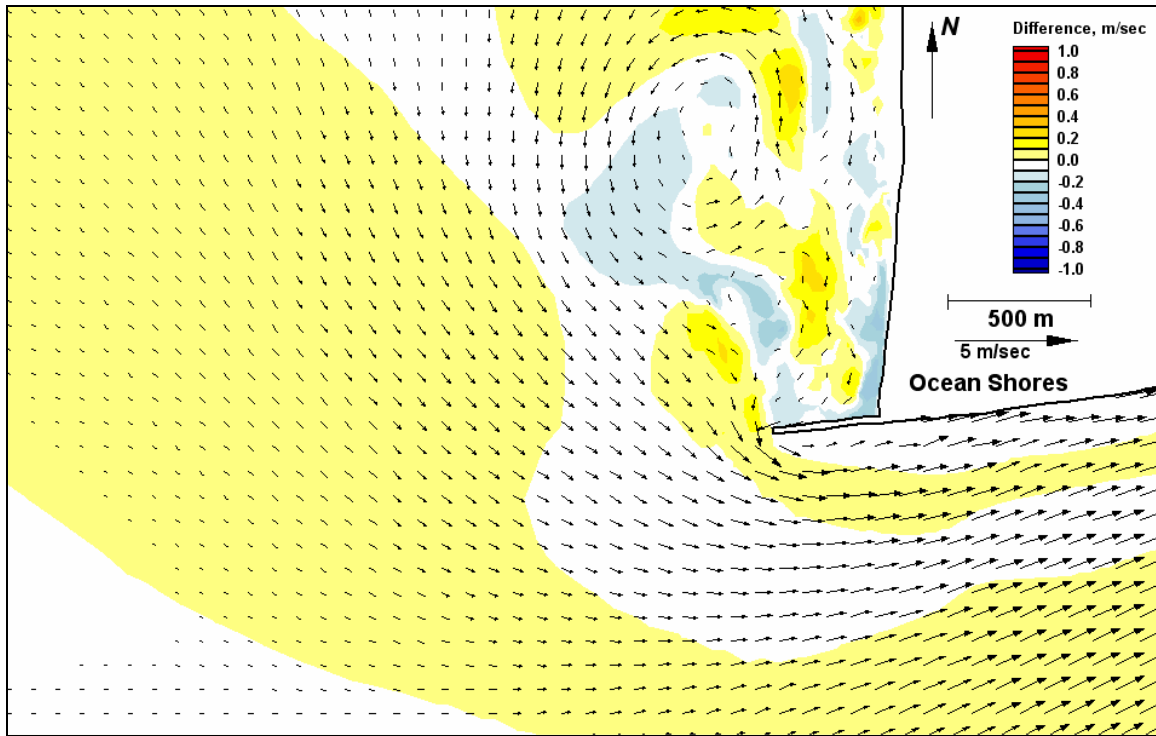
Figure E357. Difference map 159-158 for peak flood
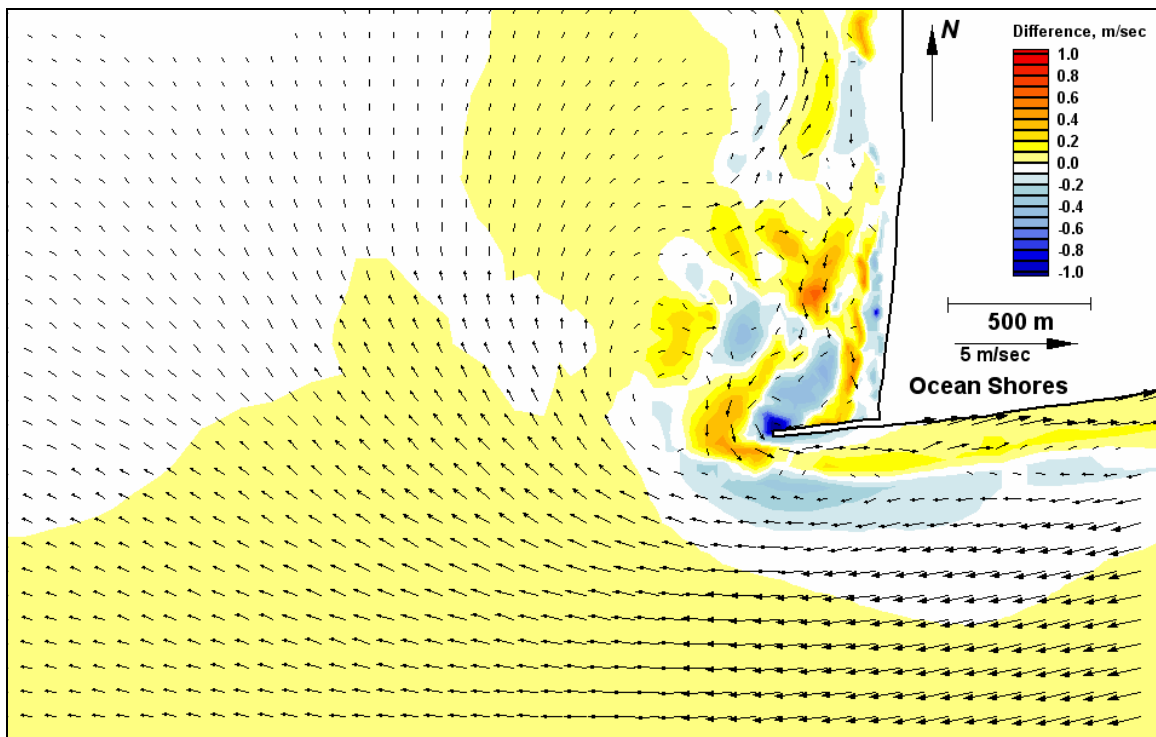
Figure E358. Difference map 159-158 for peak ebb

Appendix E   Tidal Circulation Simulation Results
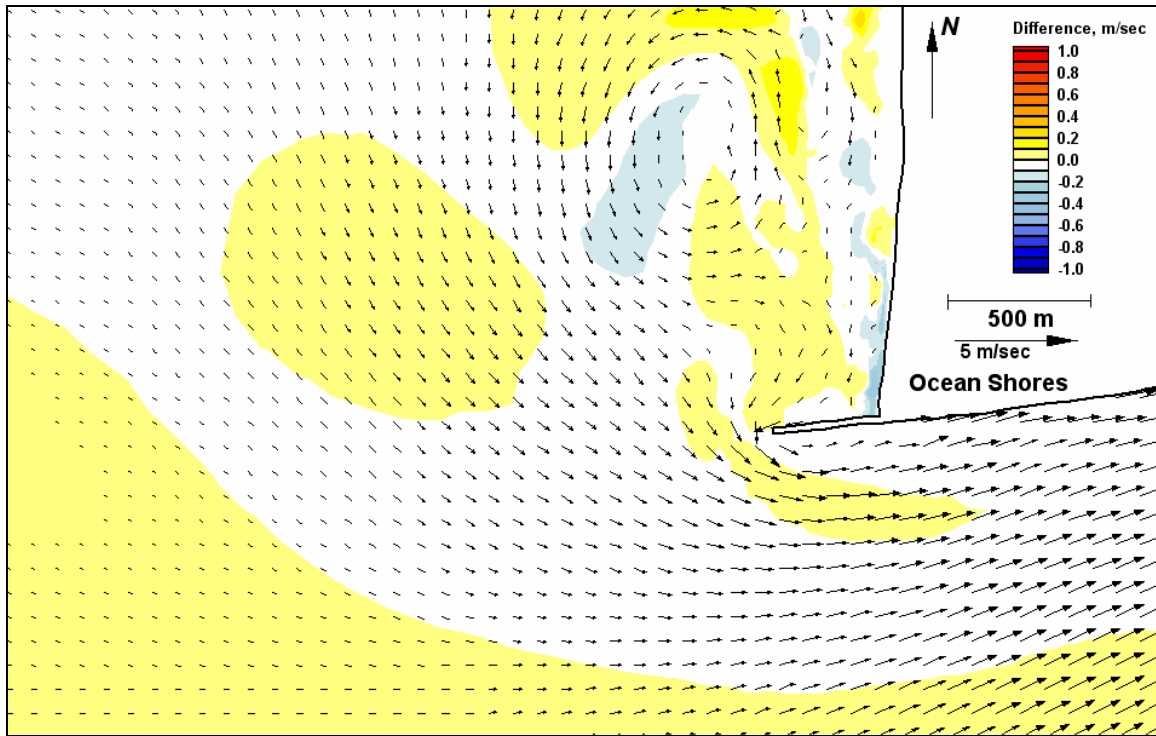
Figure E359. Difference map 160-158 for peak flood
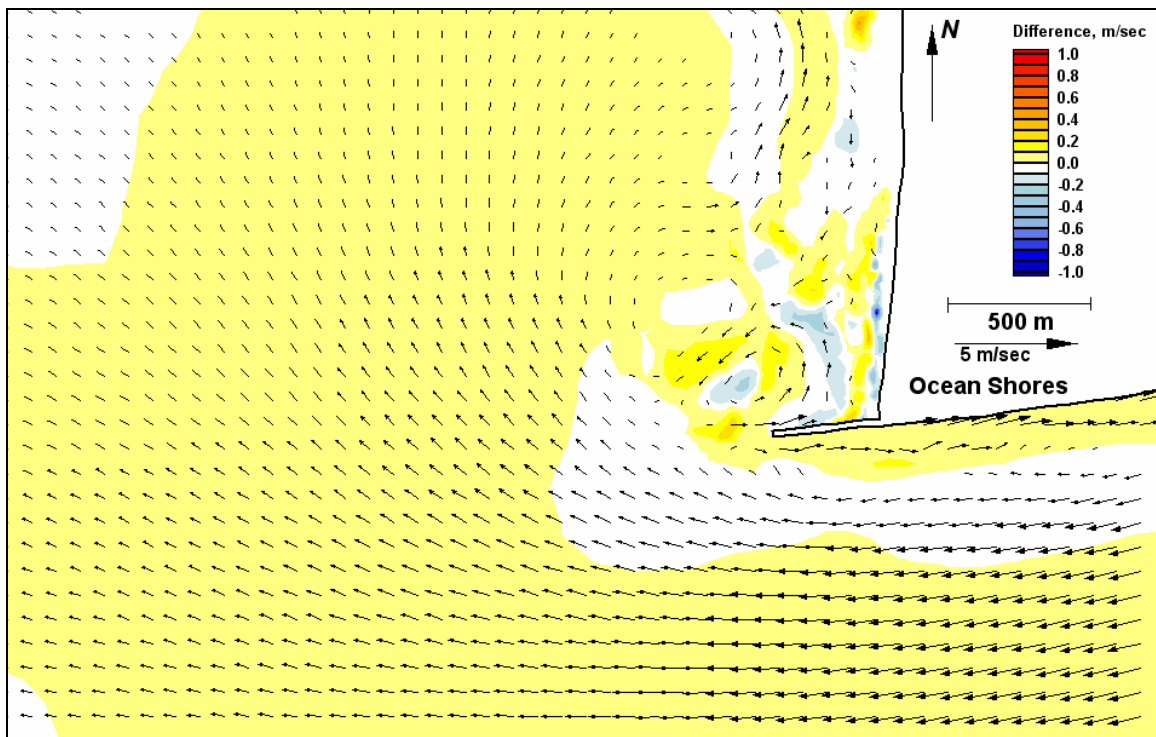
Figure E360. Difference map 160-158 for peak ebb
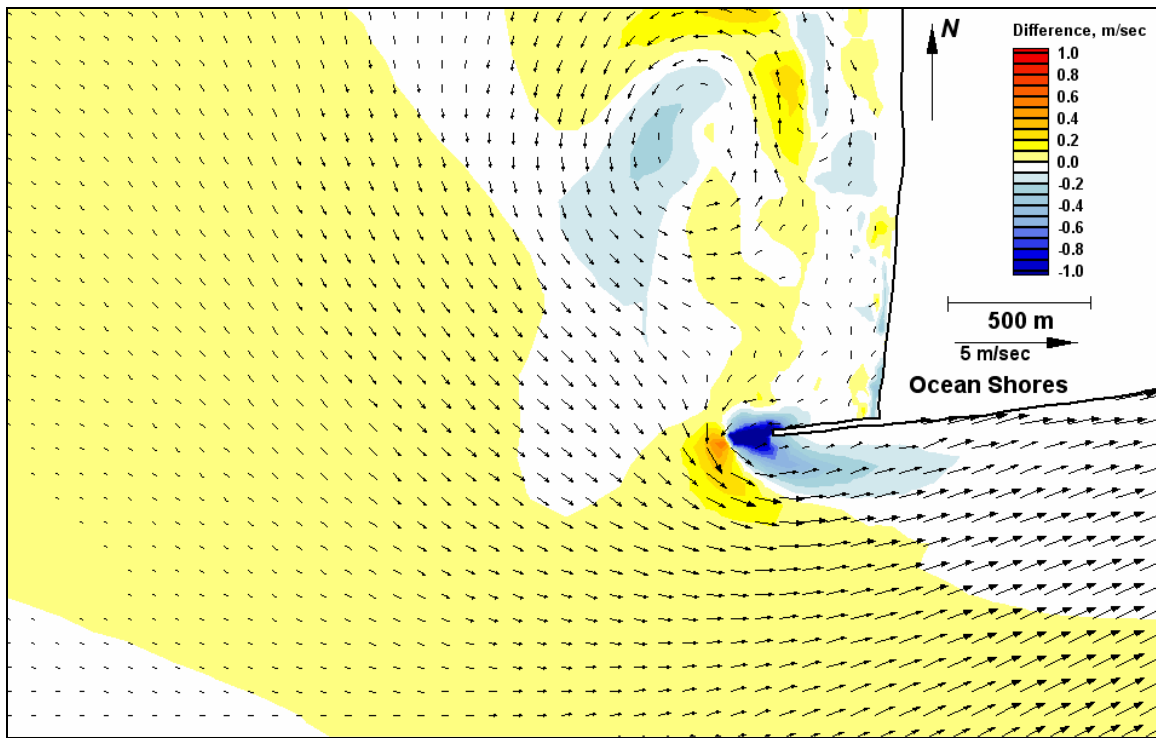
Figure E361. Difference map 161-158 for peak flood
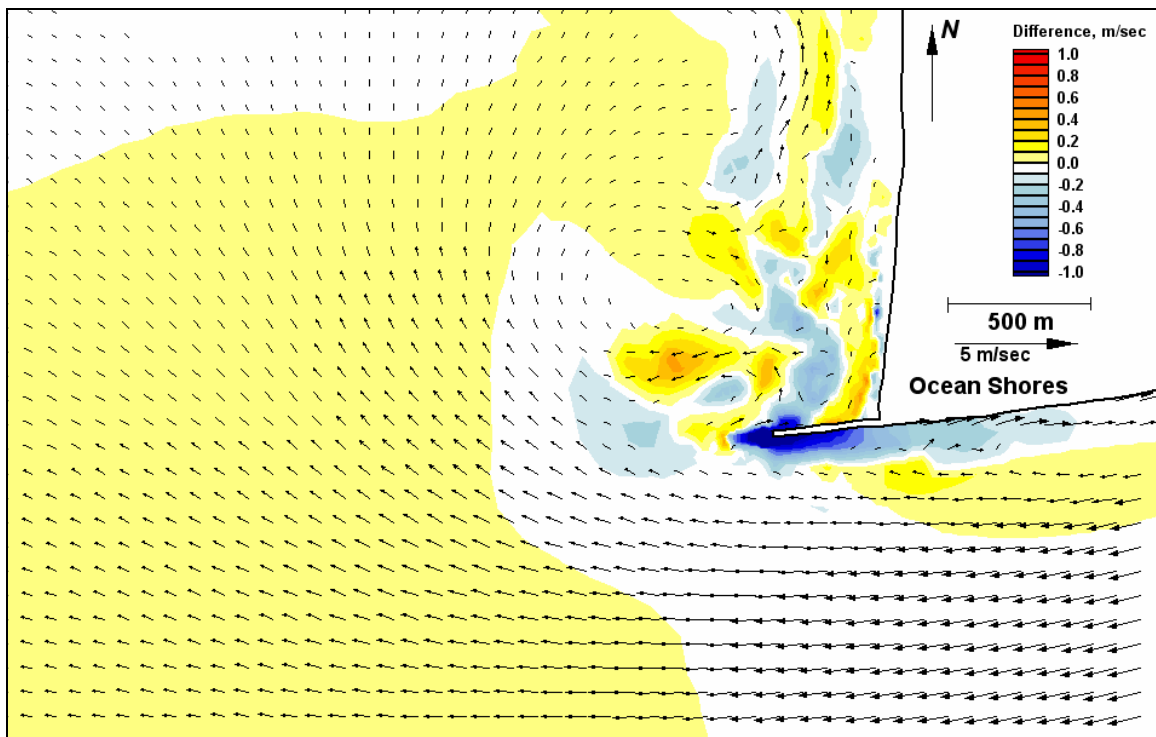
Figure E362. Difference map 161-158 for peak ebb

Appendix E   Tidal Circulation Simulation Results
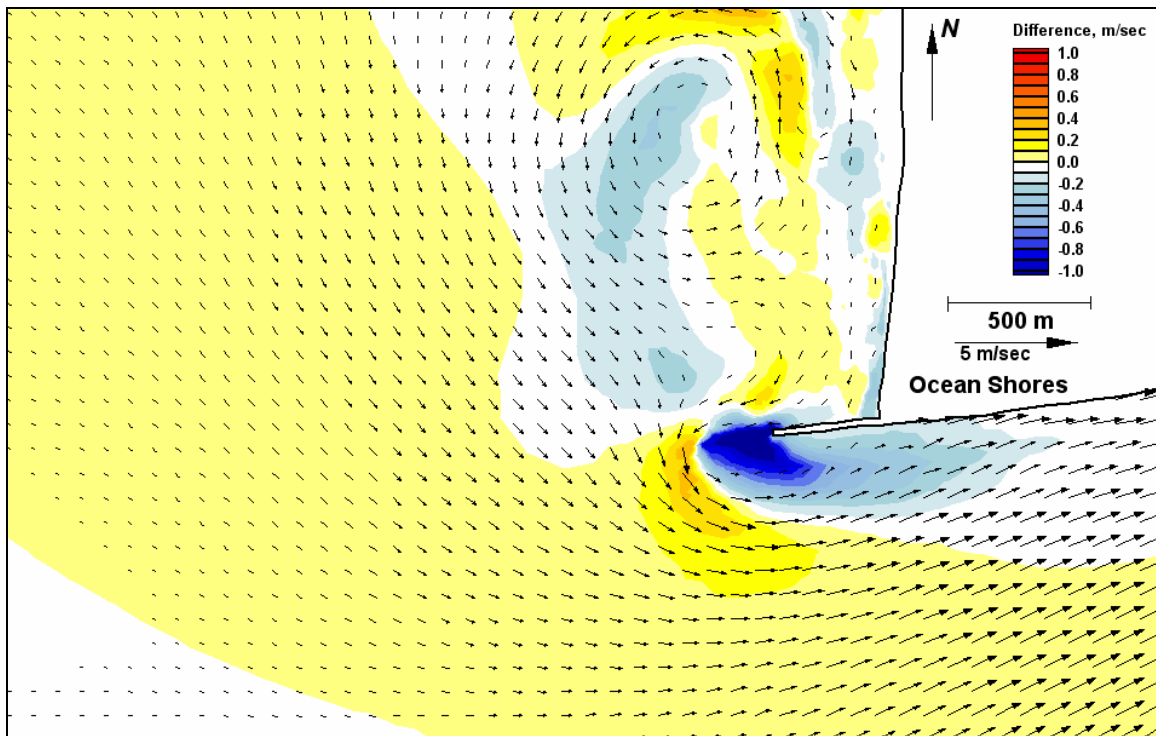
Figure E363. Difference map 162-158 for peak flood
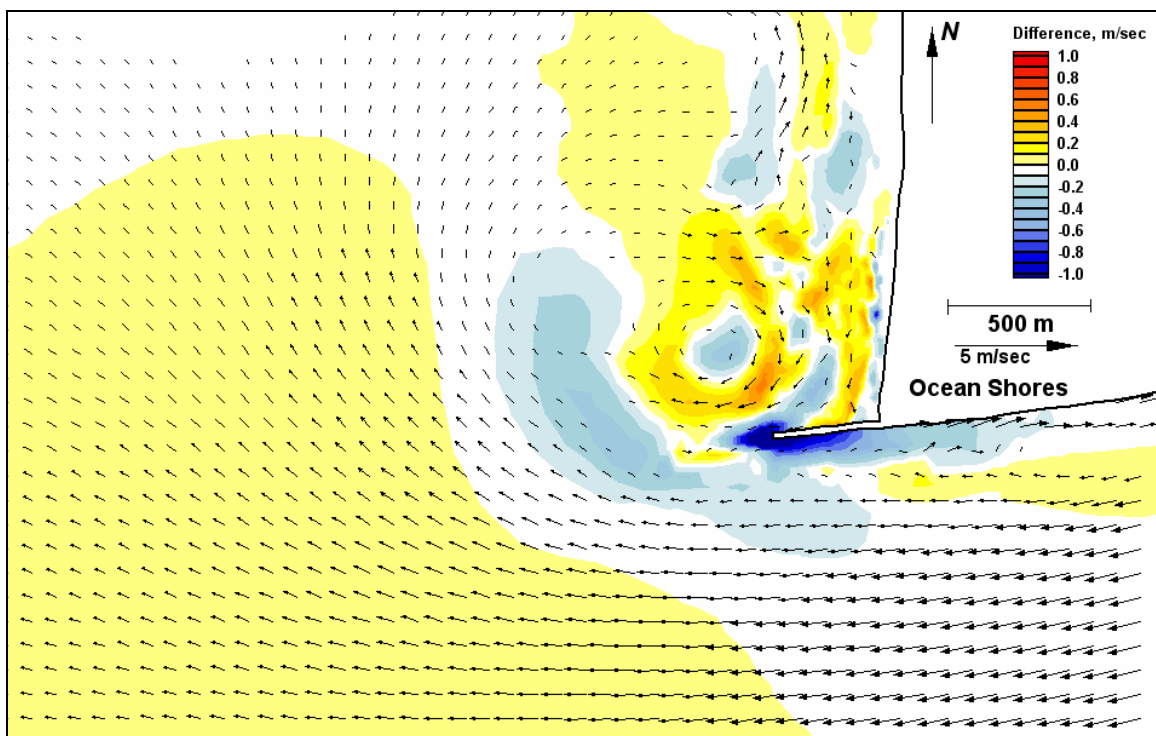
Figure E364. Difference map 162-158 for peak ebb
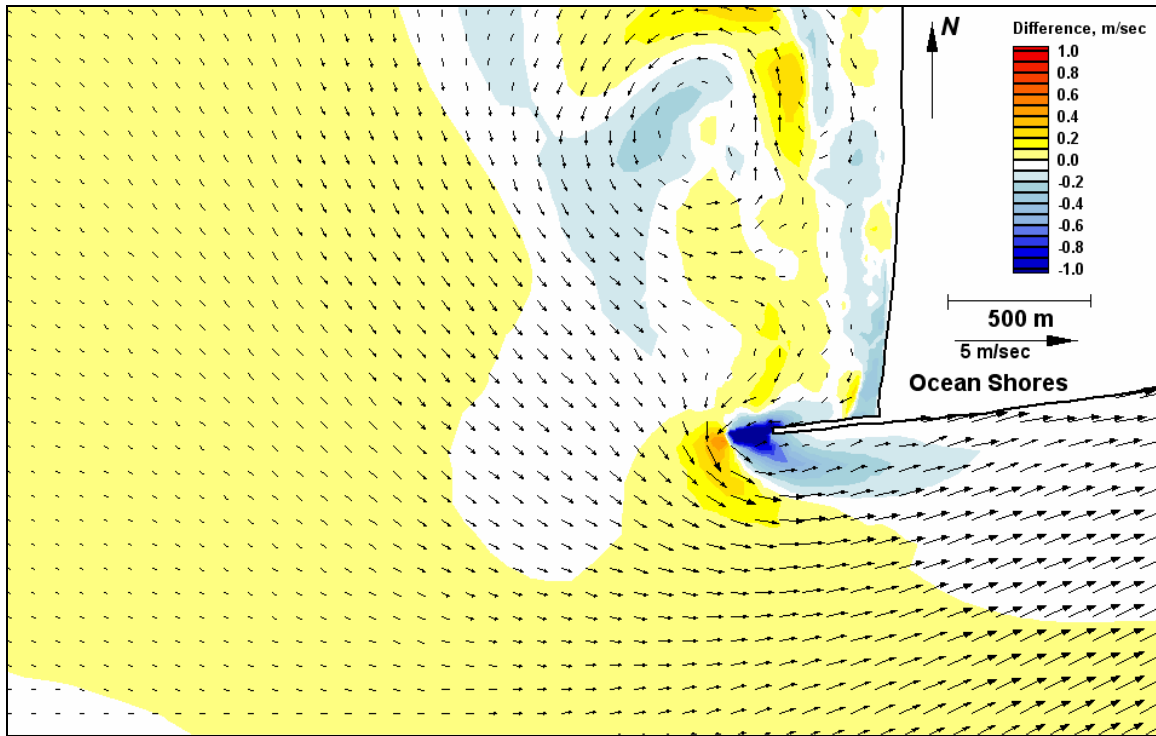
Figure E365. Difference map 163-158 for peak flood
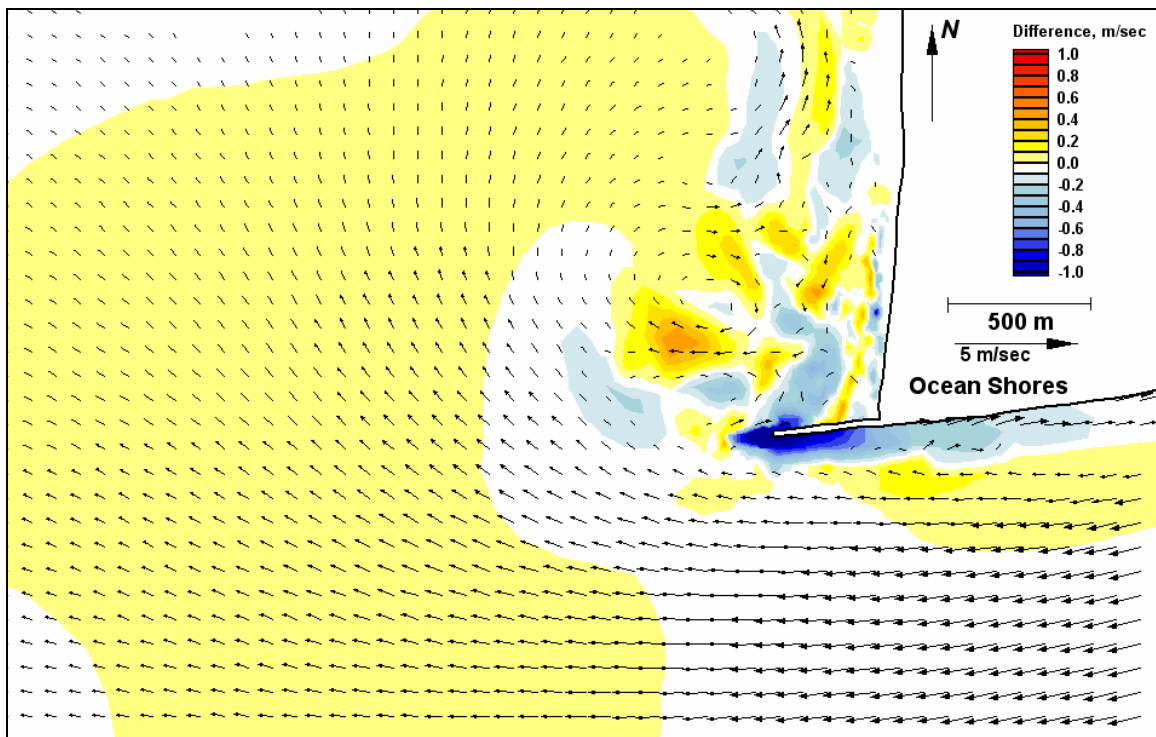
Figure E366. Difference map 163-158 for peak ebb

Appendix E   Tidal Circulation Simulation Results
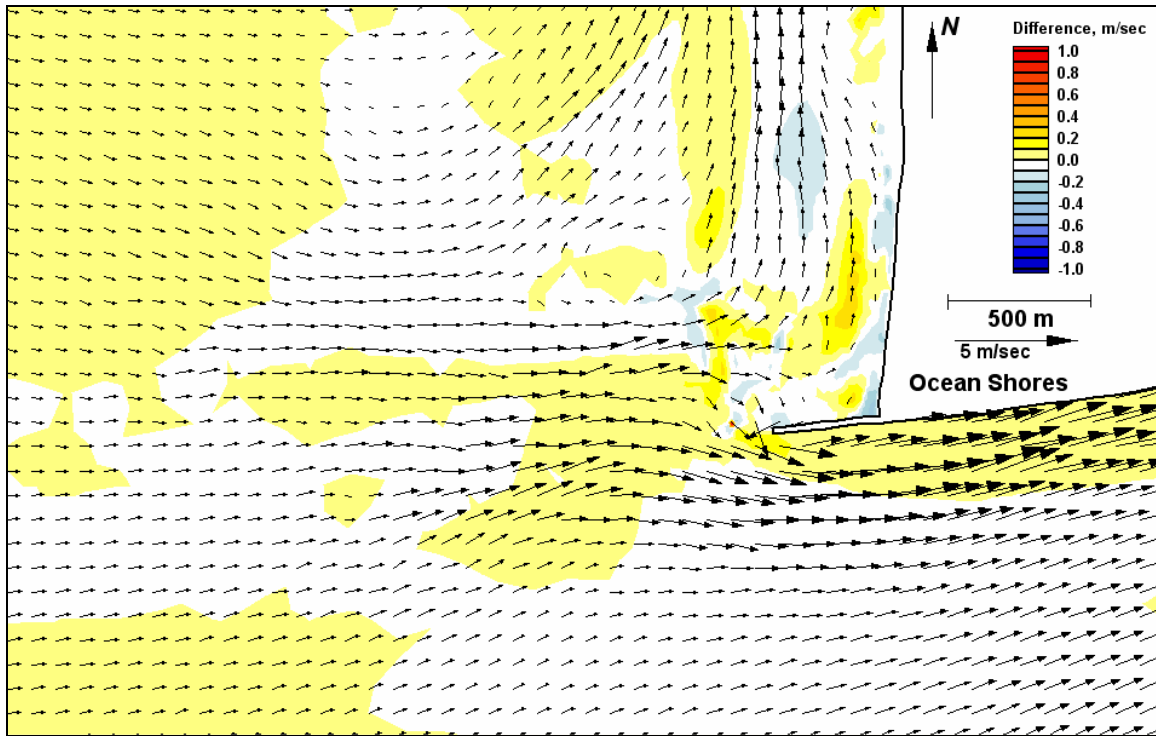
Figure E367. Difference map 165-164 for peak flood
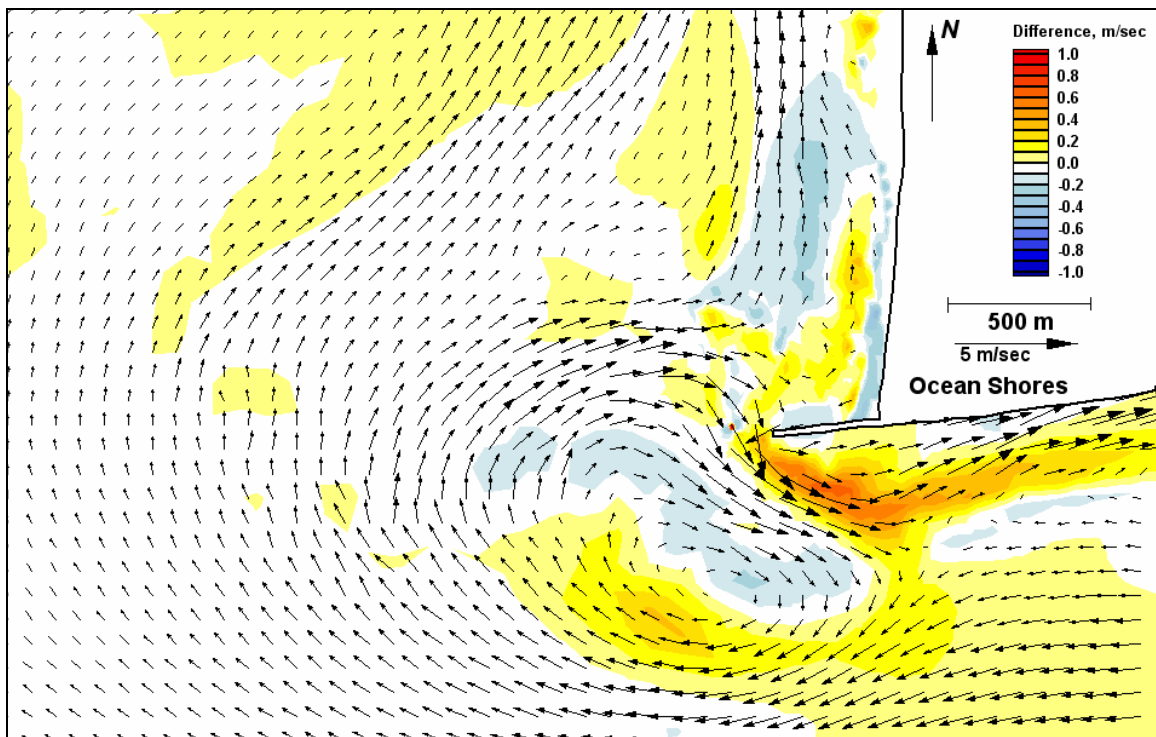
Figure E368. Difference map 165-164 for peak ebb
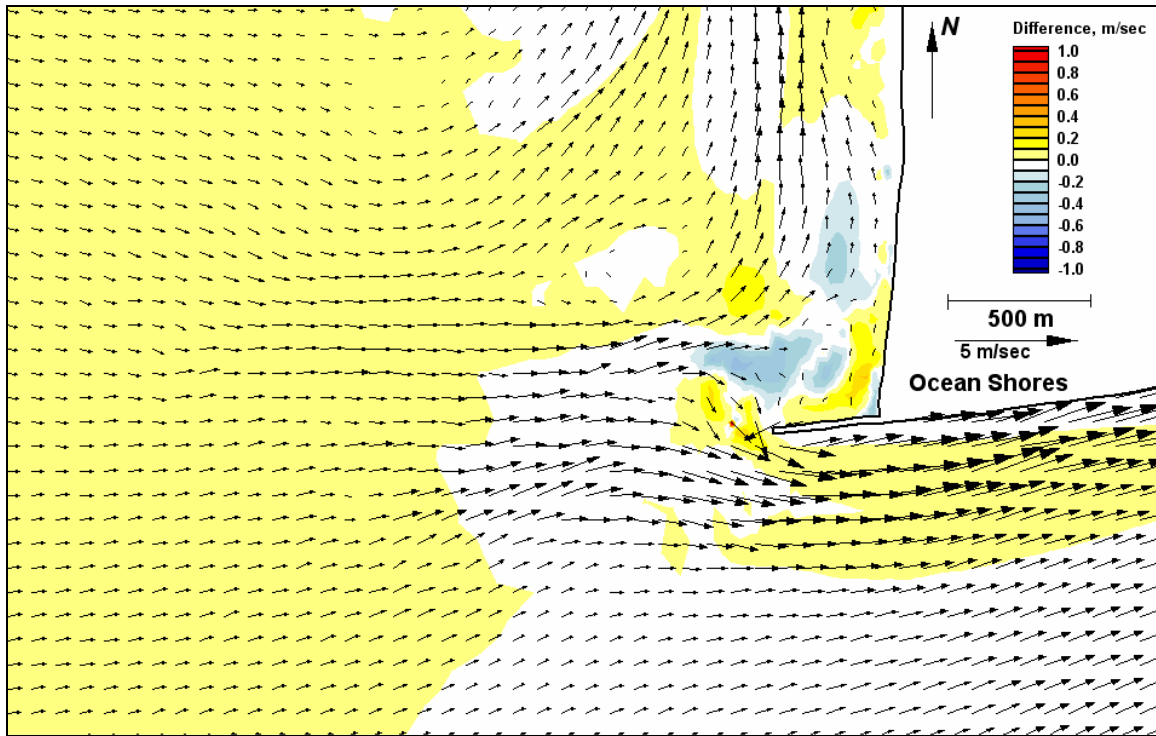
Figure E369. Difference map 166-164 for peak flood
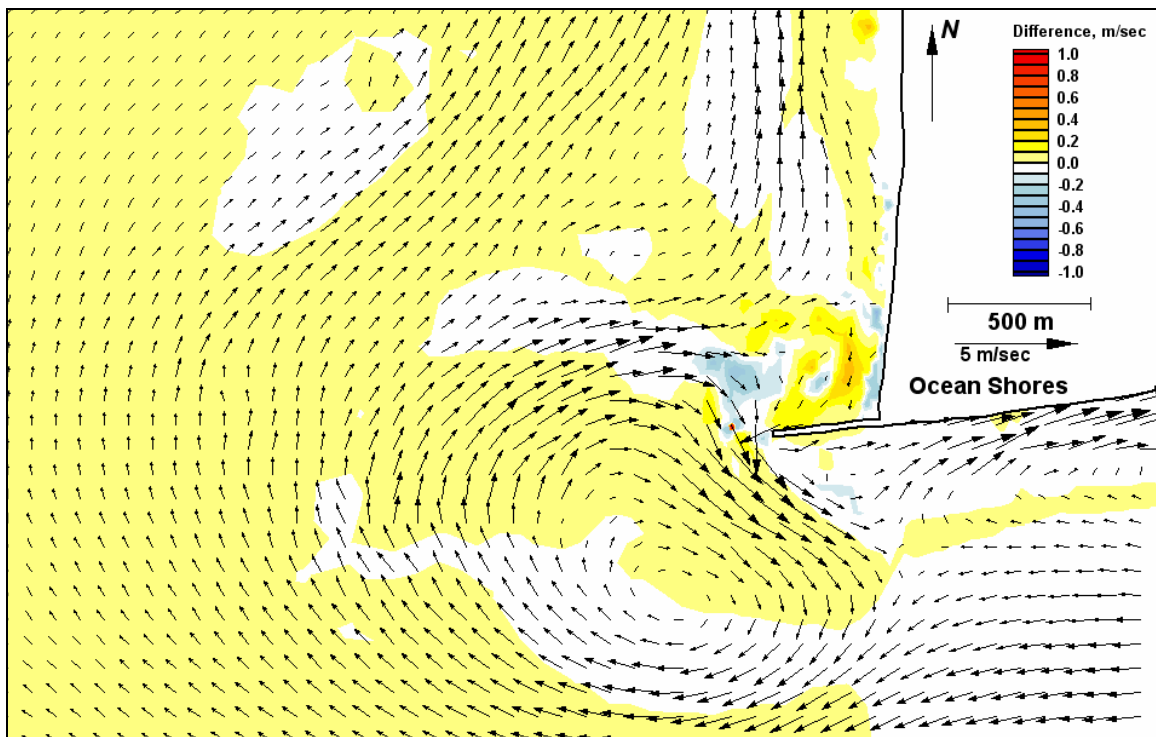
Figure E370. Difference map 166-164 for peak ebb
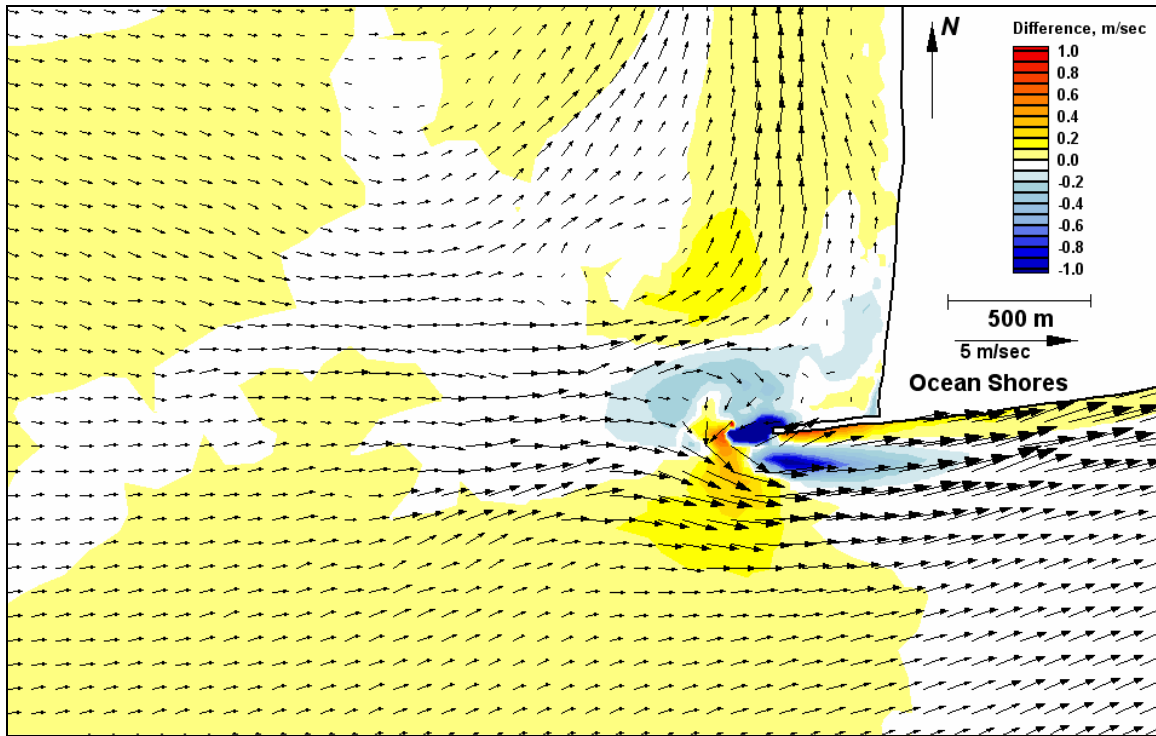
Figure E371. Difference map 167-164 for peak flood
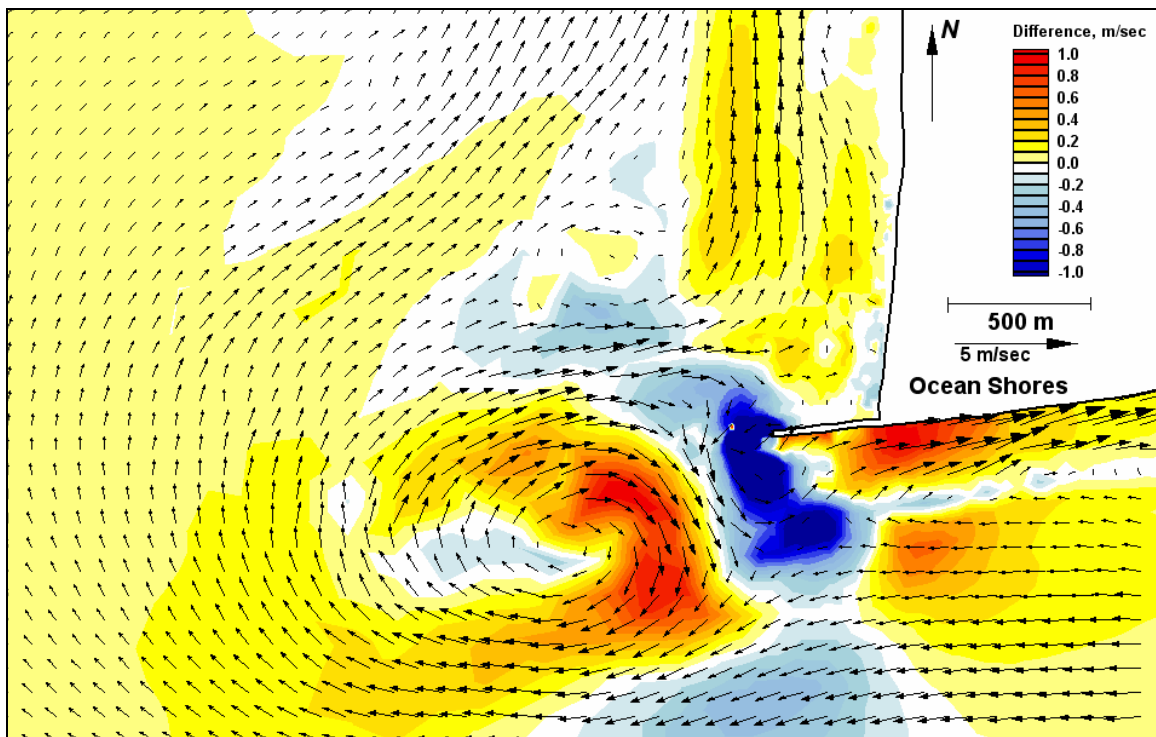
Figure E372. Difference map 167-164 for peak ebb
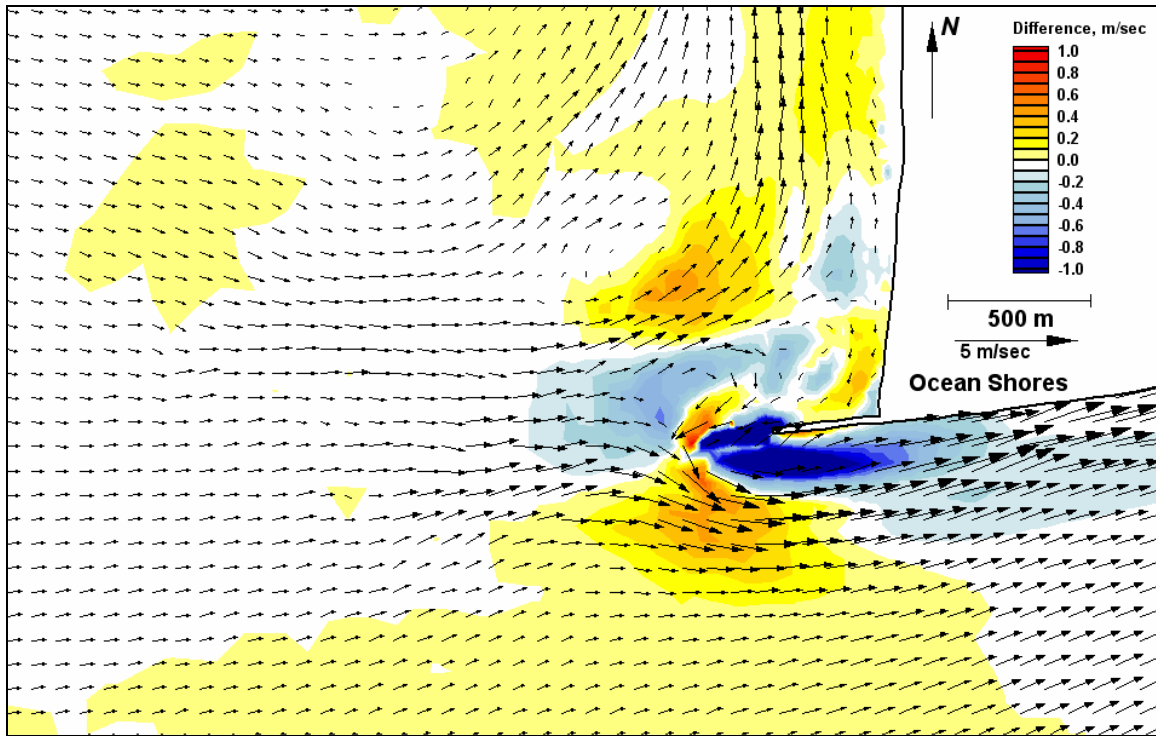
Figure E373. Difference map 168-164 for peak flood
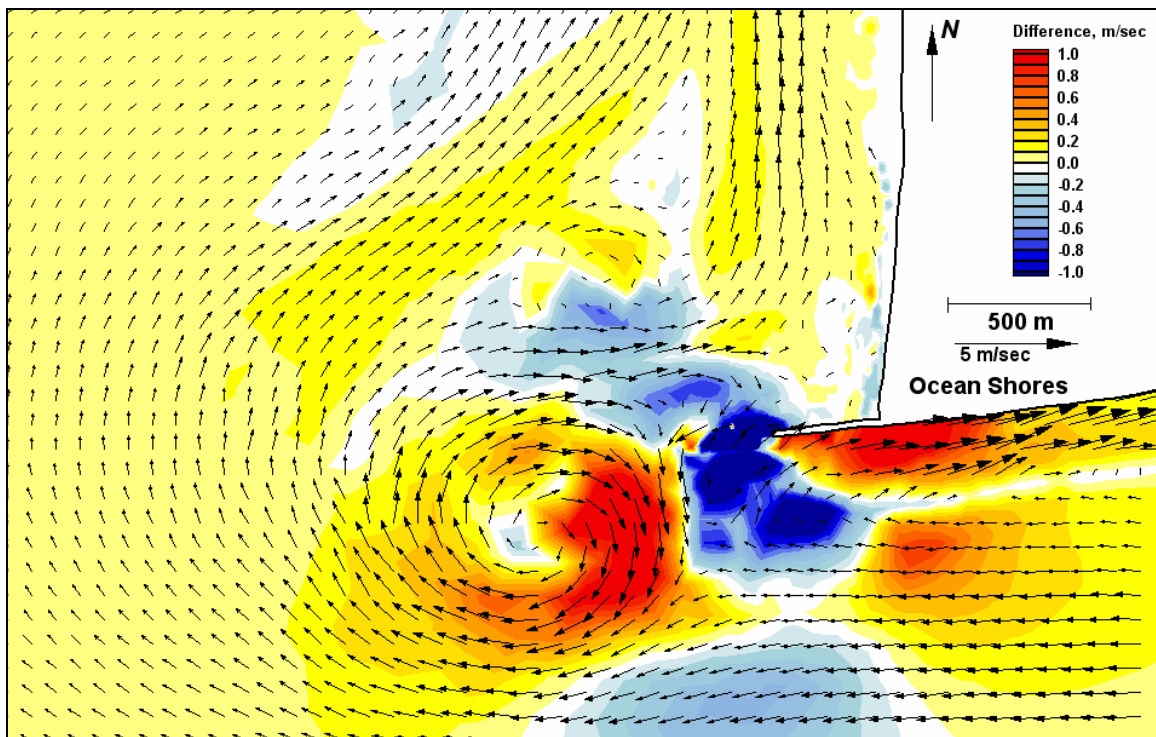
Figure E374. Difference map 168-164 for peak ebb

Appendix E   Tidal Circulation Simulation Results
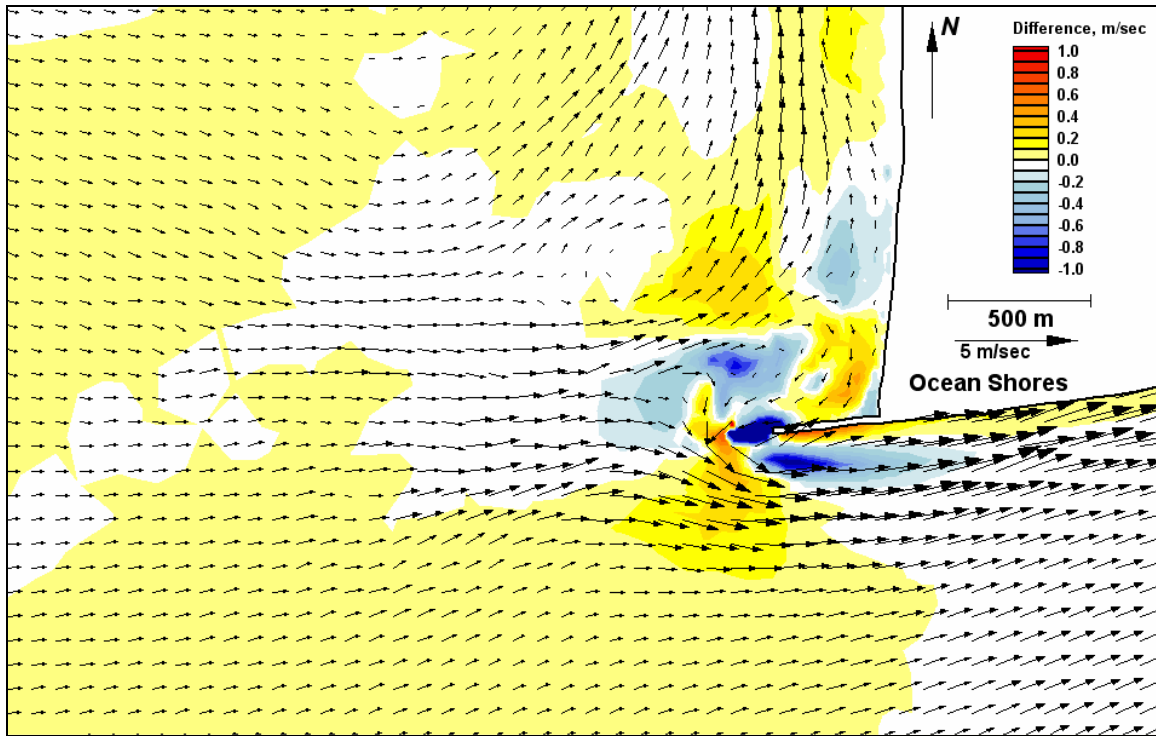
Figure E375. Difference map 169-164 for peak flood
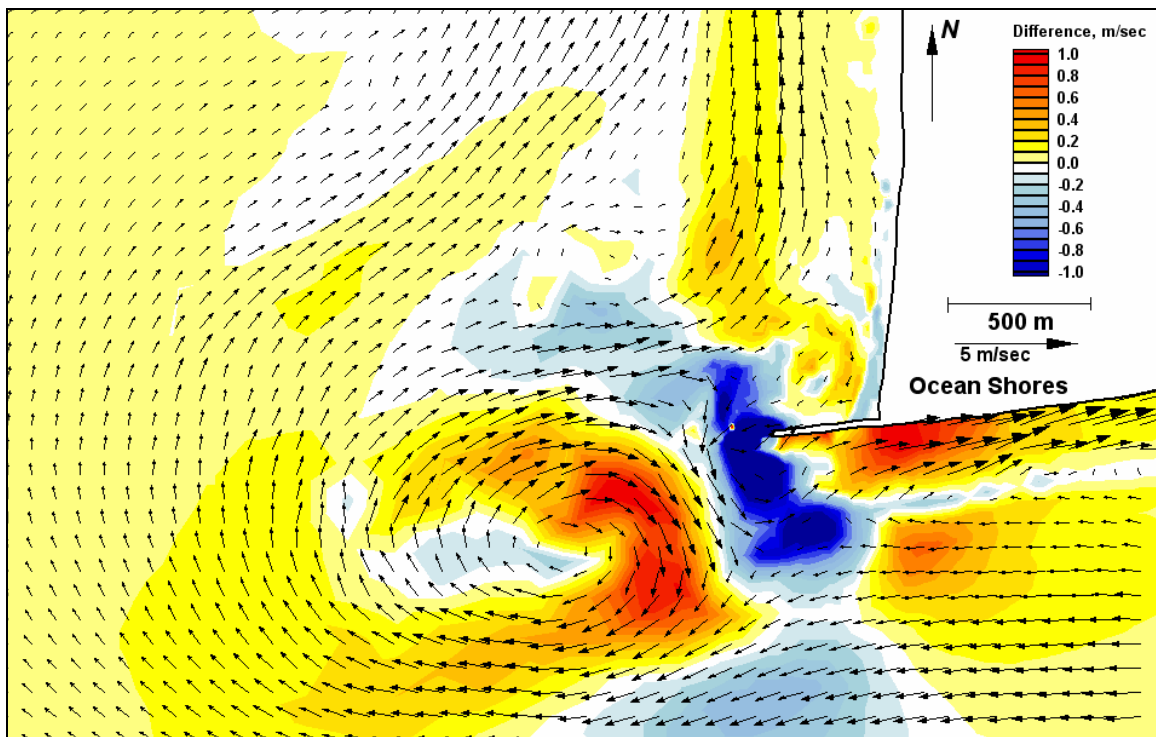
Figure E376. Difference map 169-164 for peak ebb

Time Series Plots of Velocity Components

Figure E377. Locations of calculation nodes
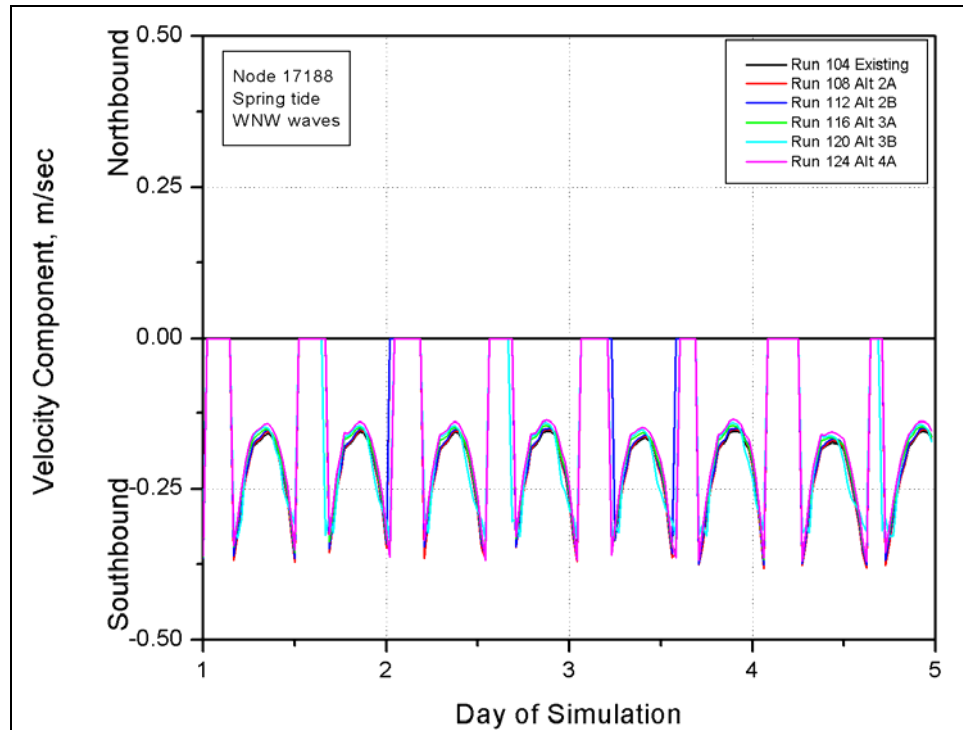
Figure E378.   North-south velocity component at node 17188 (spring tide, west-northwest waves)
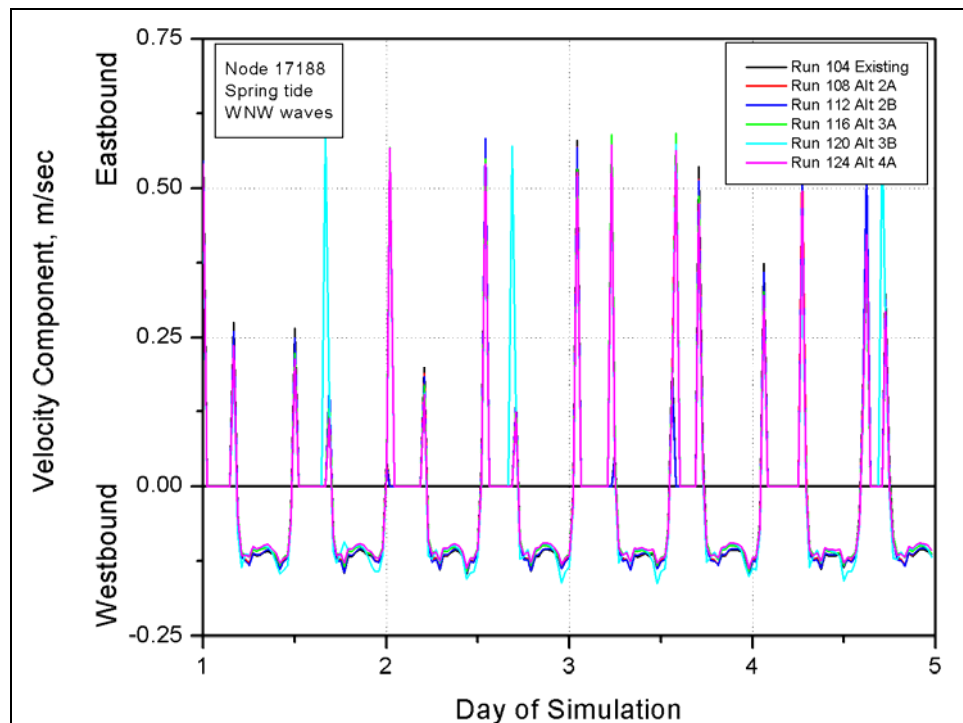
Figure E379.   East-west velocity component at node 17188 (spring tide, west-northwest waves)
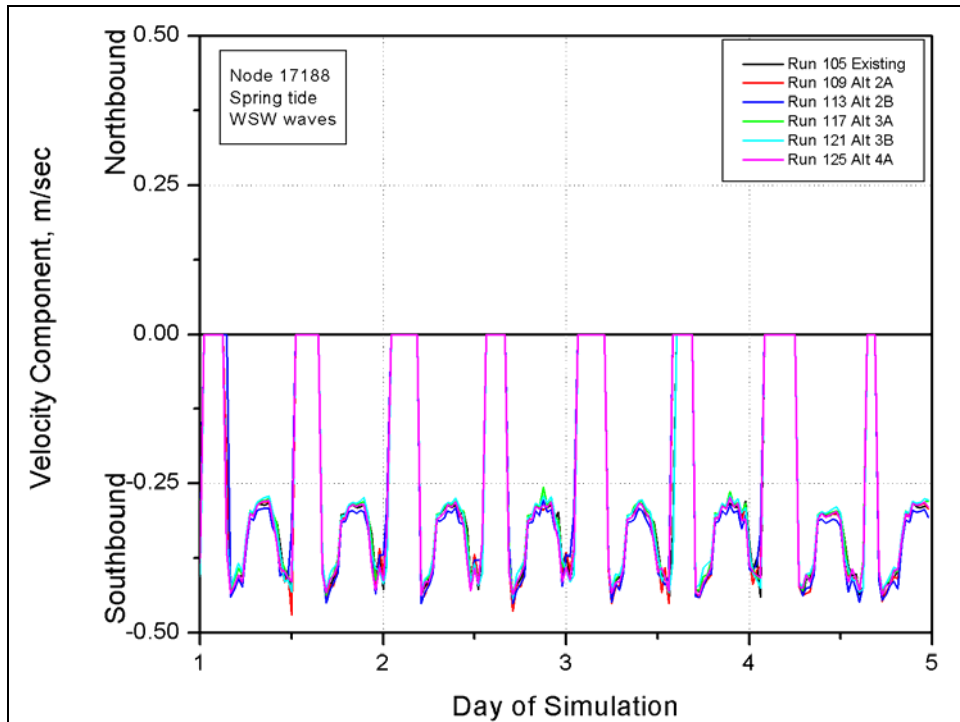
Figure E380.   North-south velocity component at node 17188 (spring tide, west-southwest waves)
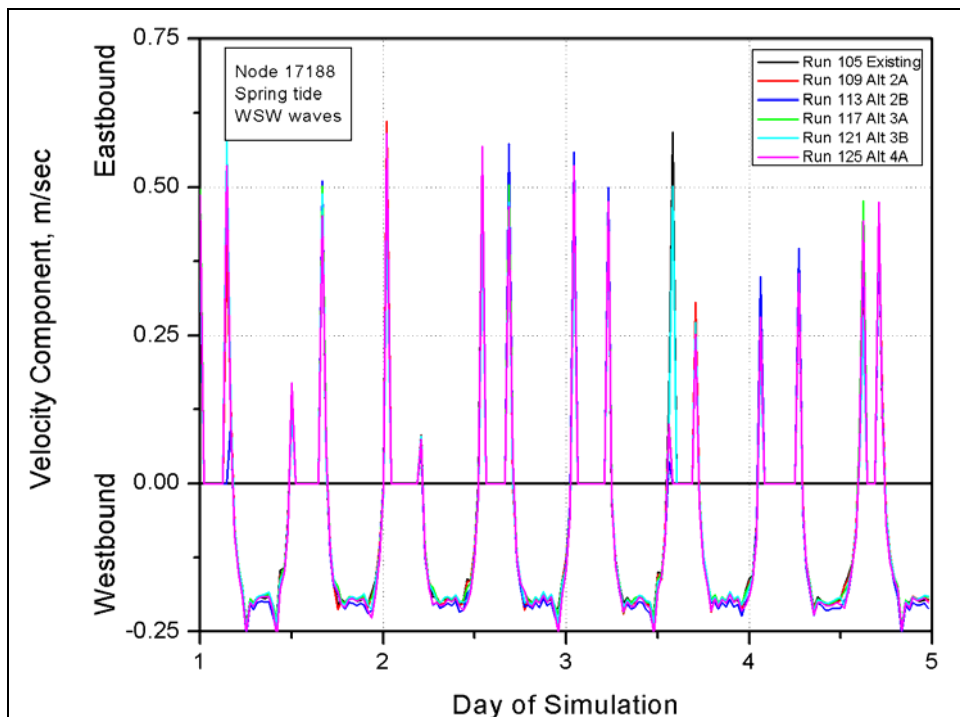
Figure E381.   East-west velocity component at node 17188 (spring tide, west-southwest waves)
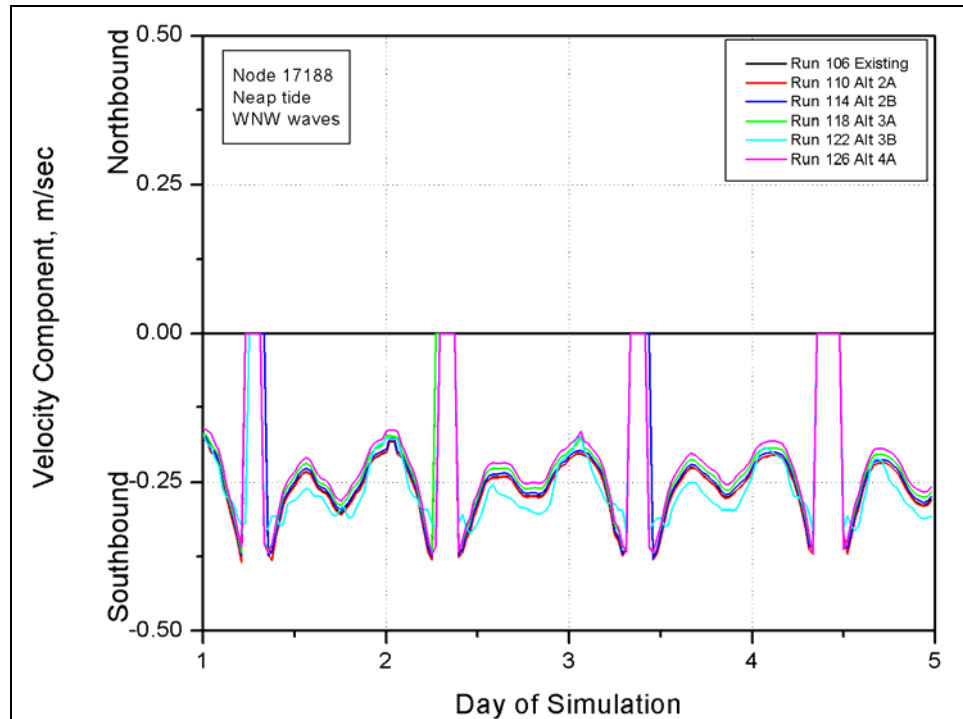
Figure E382.   North-south velocity component at node 17188 (neap tide, west-northwest waves)
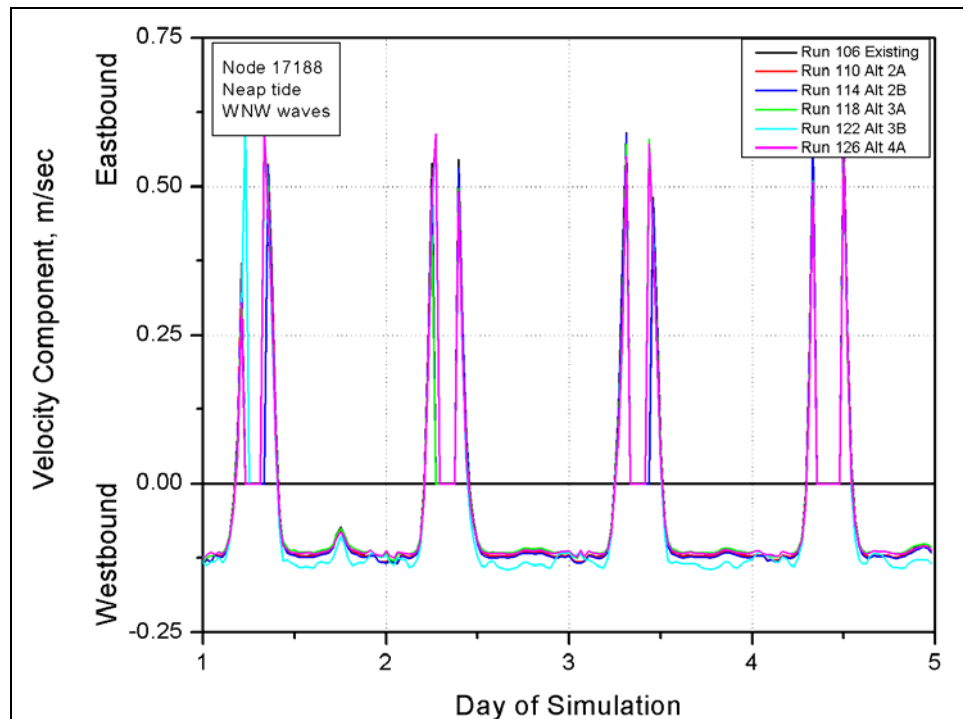
Figure E383.   East-west velocity component at node 17188 (neap tide, west-northwest waves)
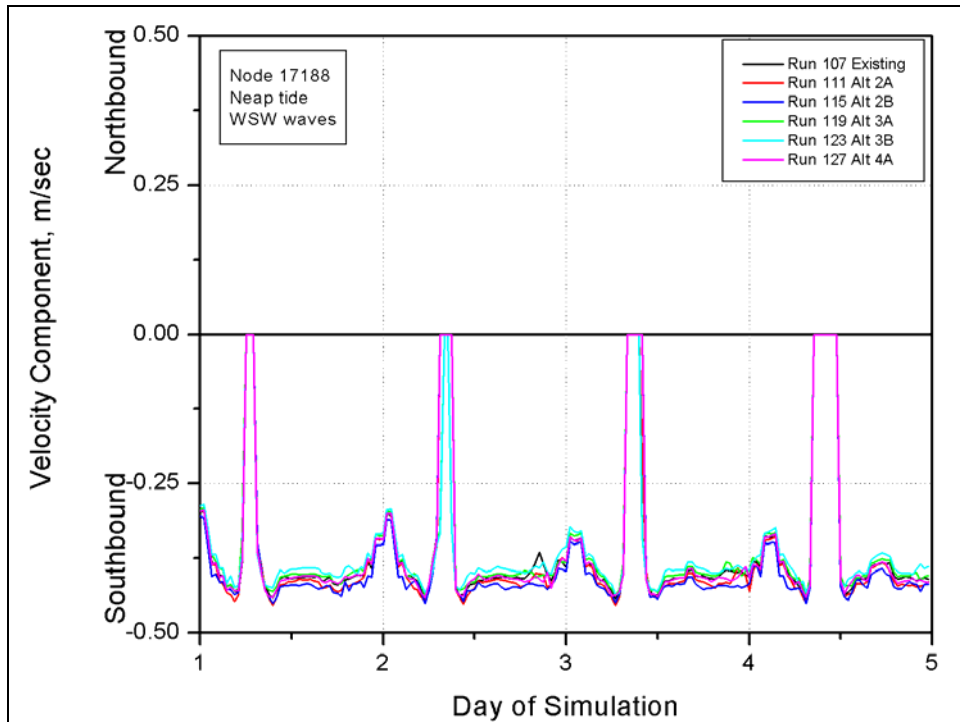
Figure E384.   North-south velocity component at node 17188 (neap tide, west-southwest waves)
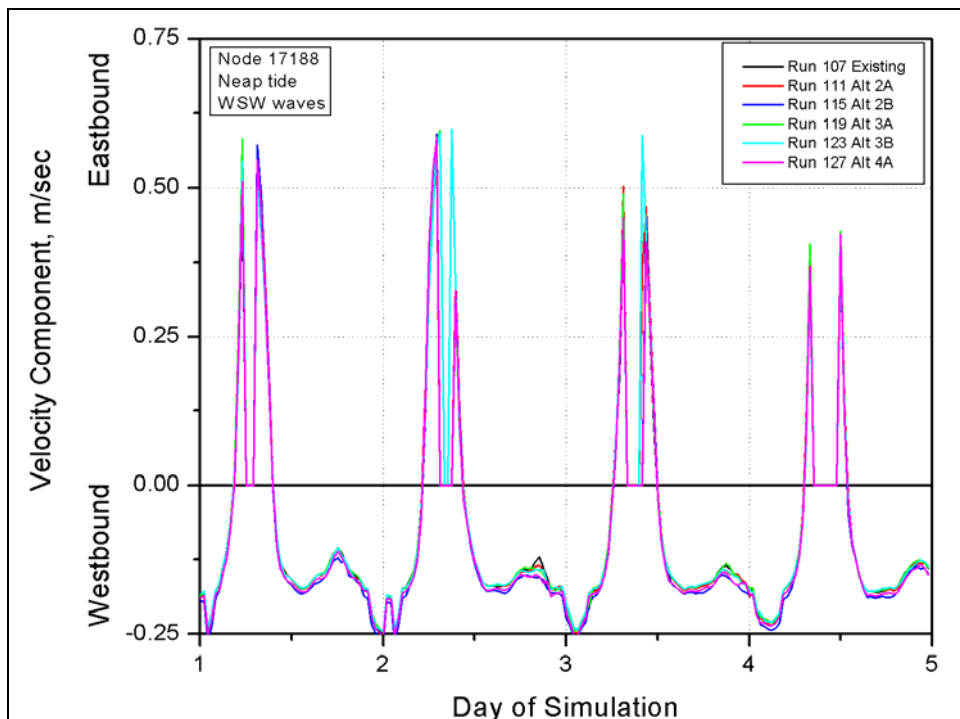
Figure E385.   East-west velocity component at node 17188 (neap tide, west-southwest waves)
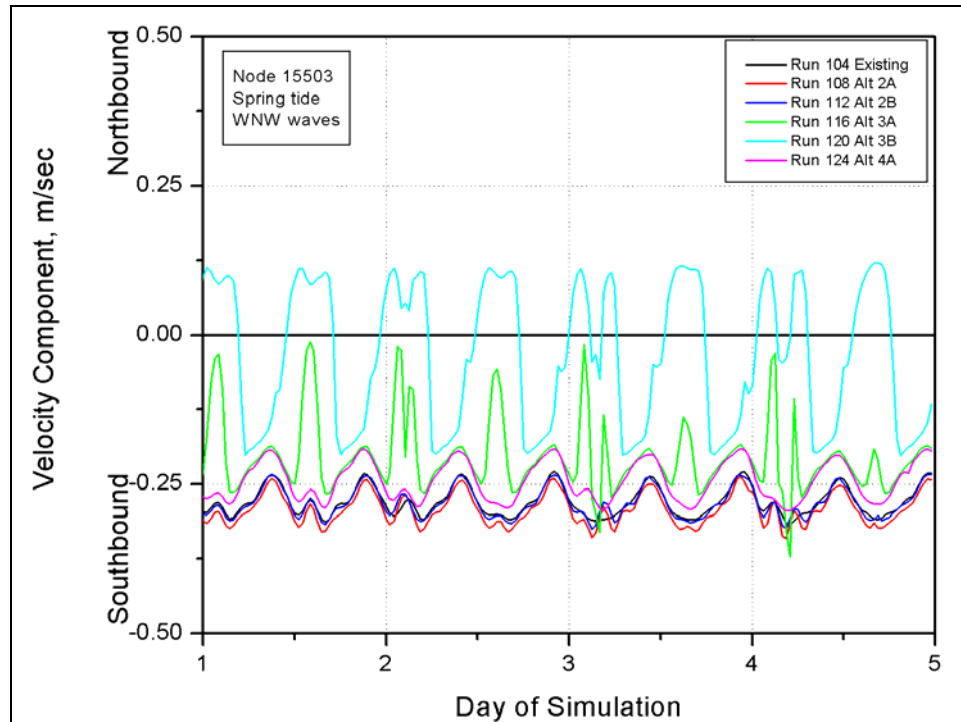
Figure E386.   North-south velocity component at node 15503 (spring tide, west-northwest waves)
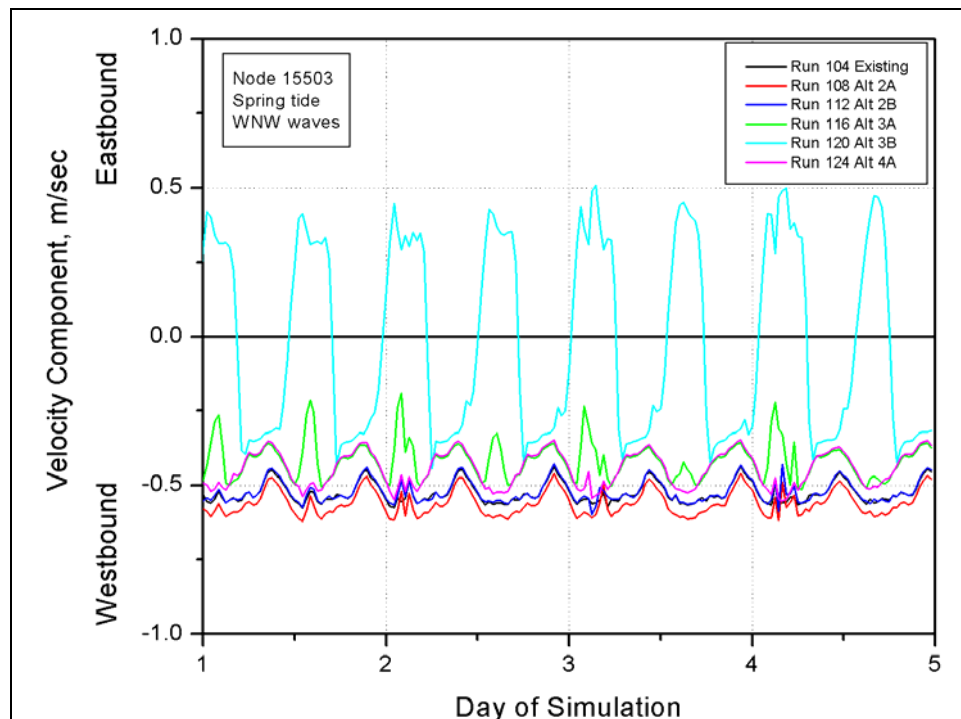
Figure E387.   East-west velocity component at node 15503 (spring tide, west-northwest waves)
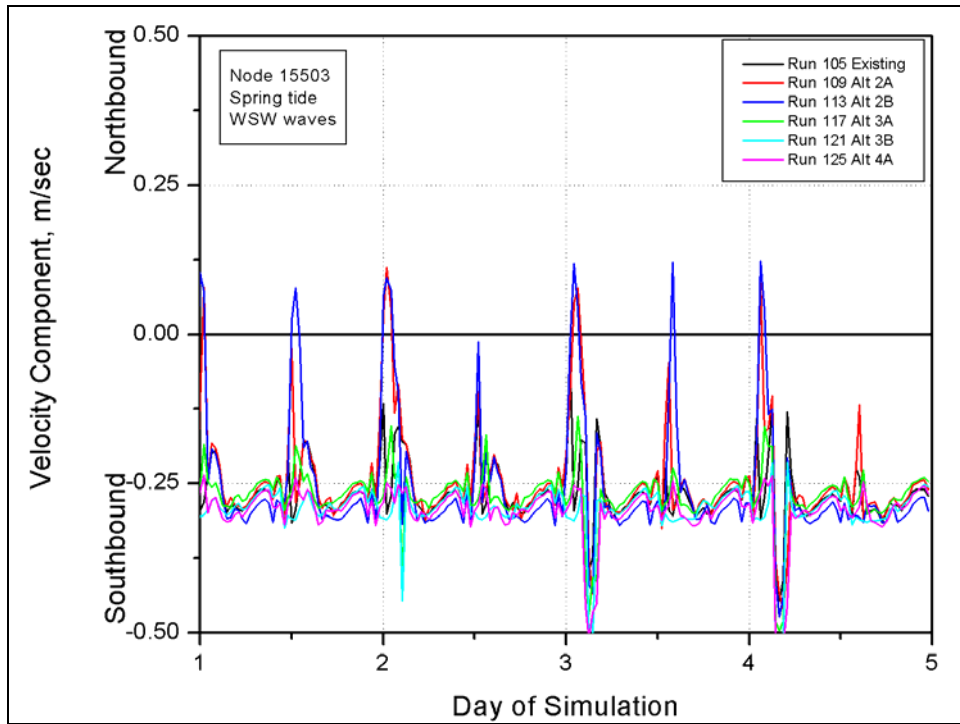
Figure E388.   North-south velocity component at node 15503 (spring tide, west-southwest waves)
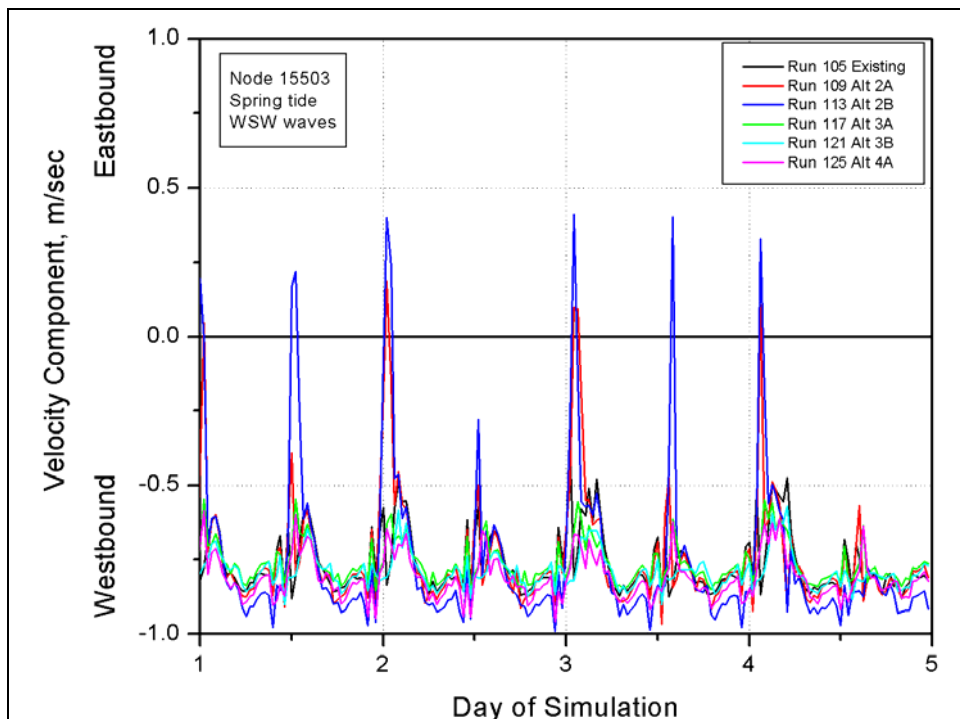
Figure E389.   East-west velocity component at node 15503 (spring tide, west-southwest waves)
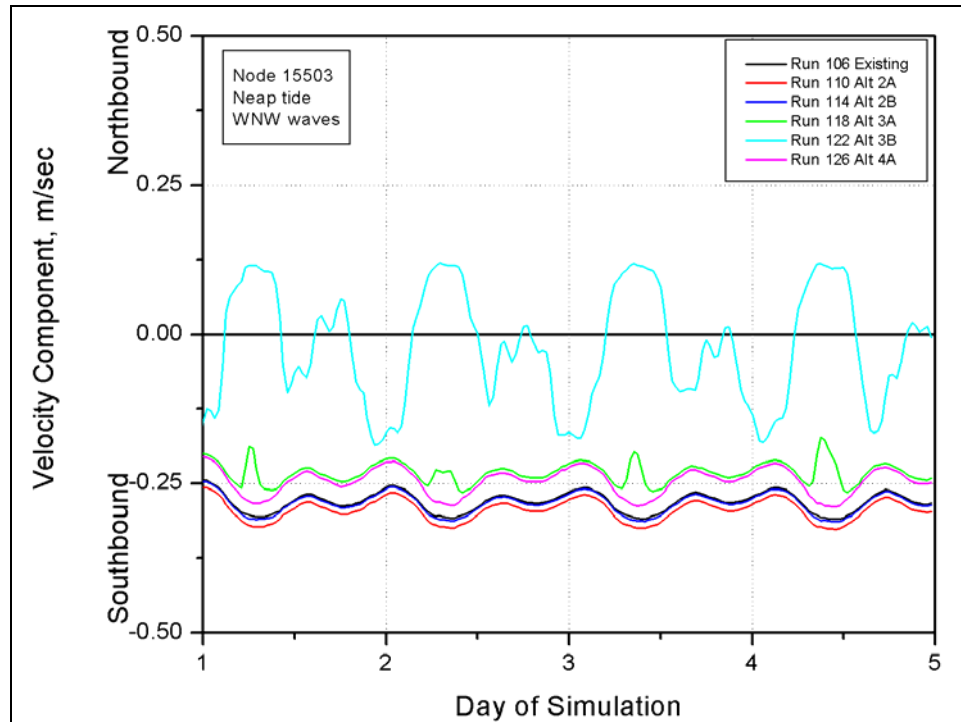
Figure E390. North-south velocity component at node 15503 (neap tide, west-northwest waves)
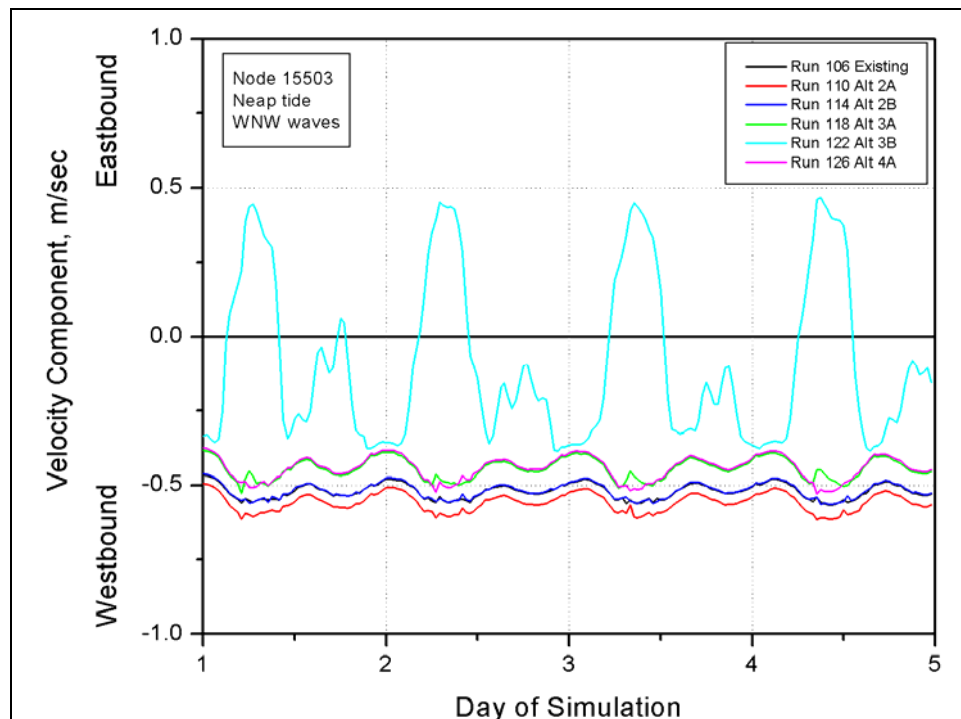
Figure E391. East-west velocity component at node 15503 (neap tide, west-northwest waves)
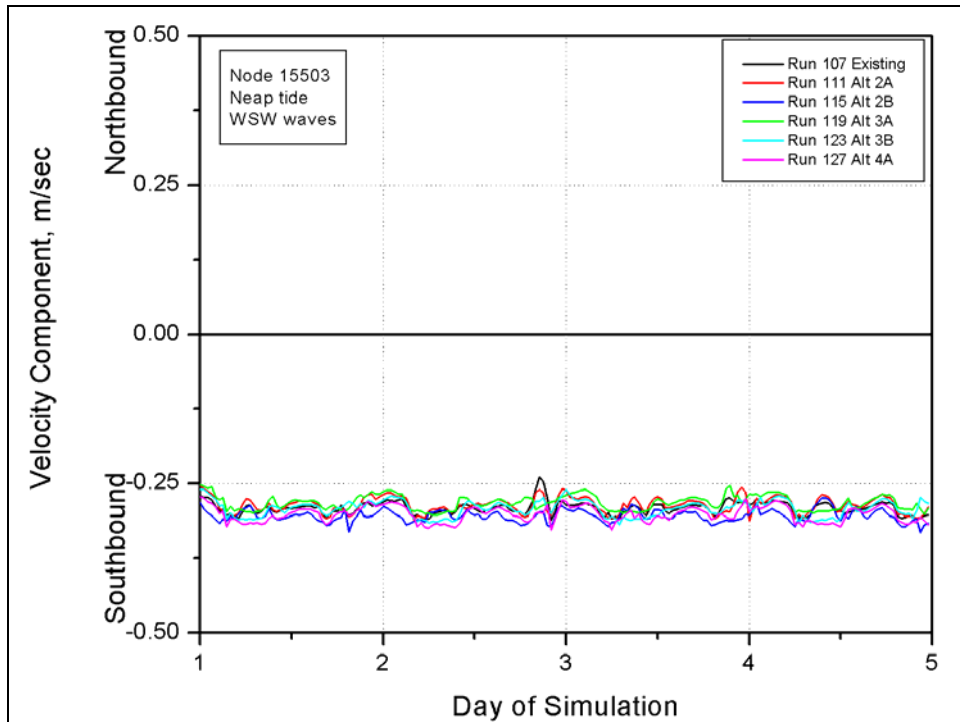
Figure E392.   North-south velocity component at node 15503 (neap tide, west-southwest waves)
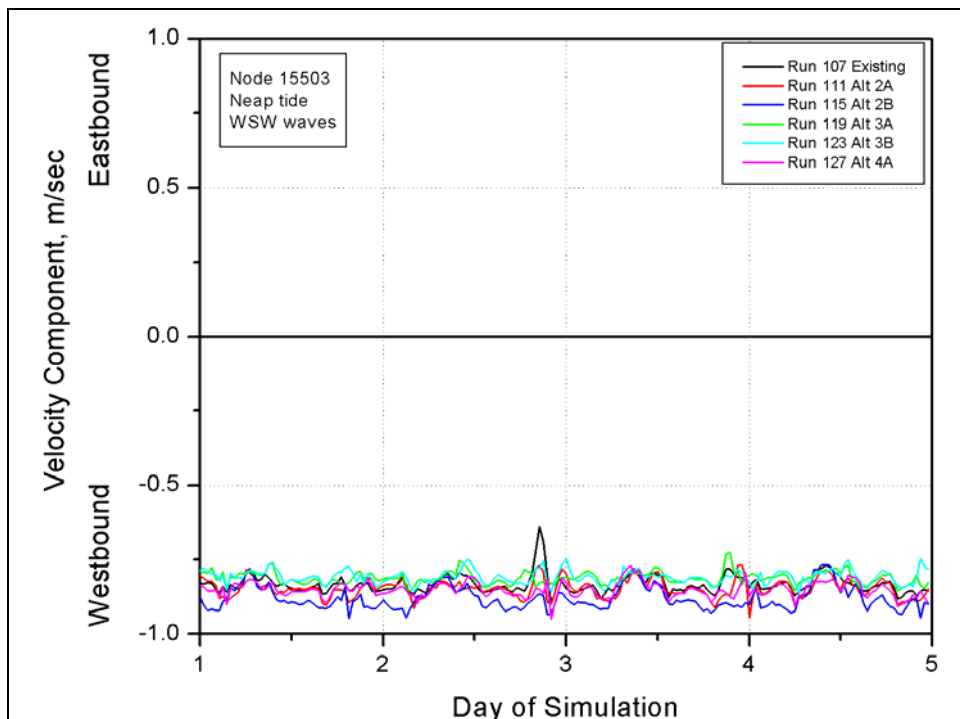
Figure E393.   East-west velocity component at node 15503 (neap tide, west-southwest waves)

Appendix E   Tidal Circulation Simulation Results
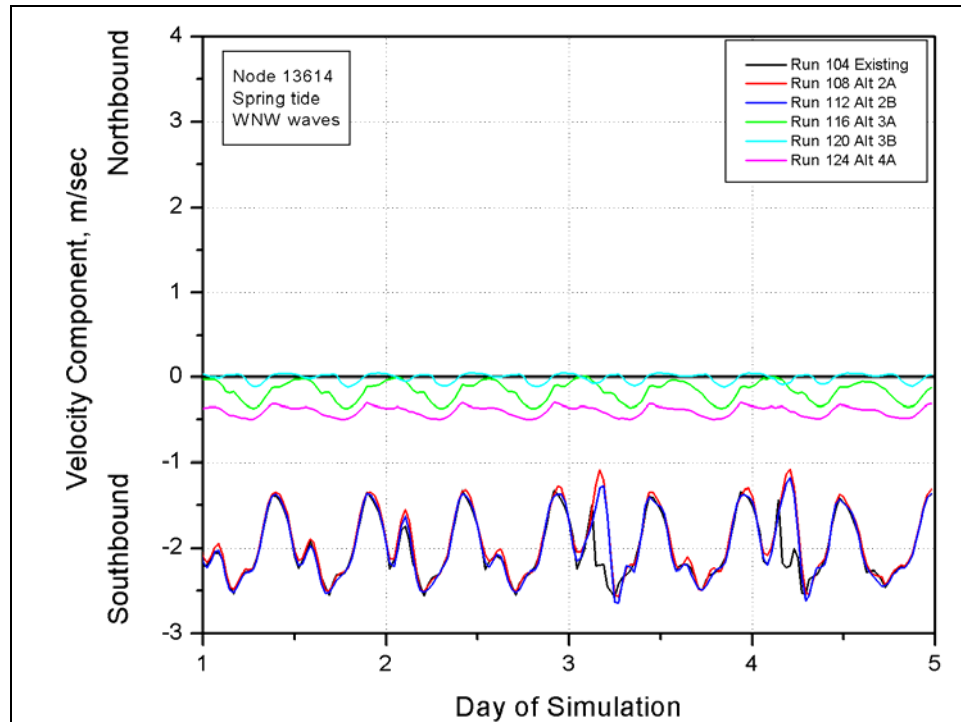
Figure E394. North-south velocity component at node 13614 (spring tide, west-northwest waves)
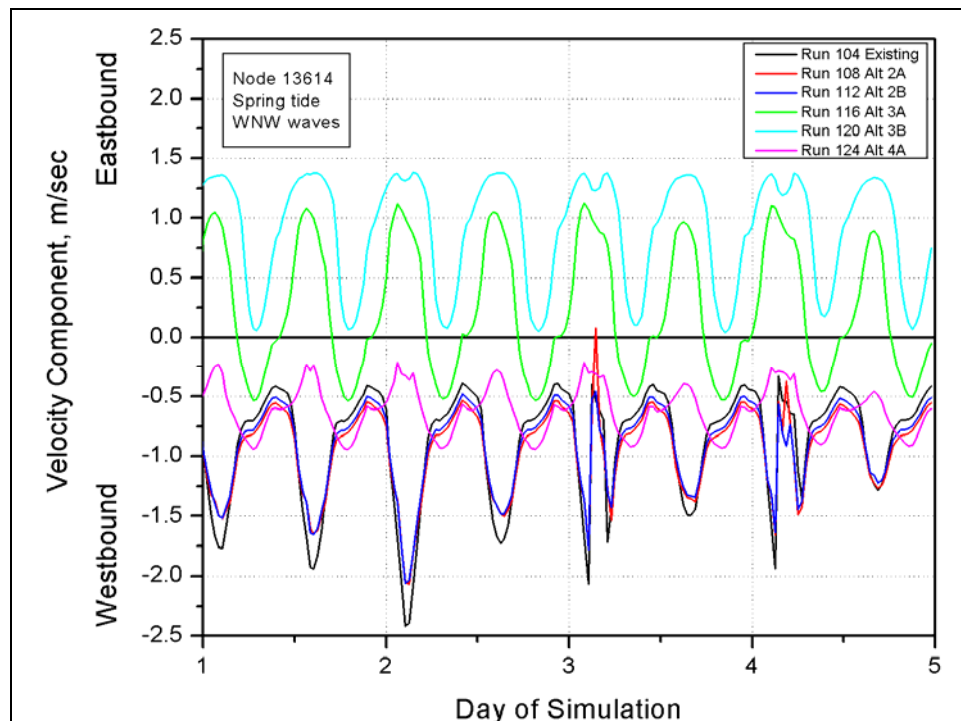
Figure E395. East-west velocity component at node 13614 (spring tide, west-northwest waves)
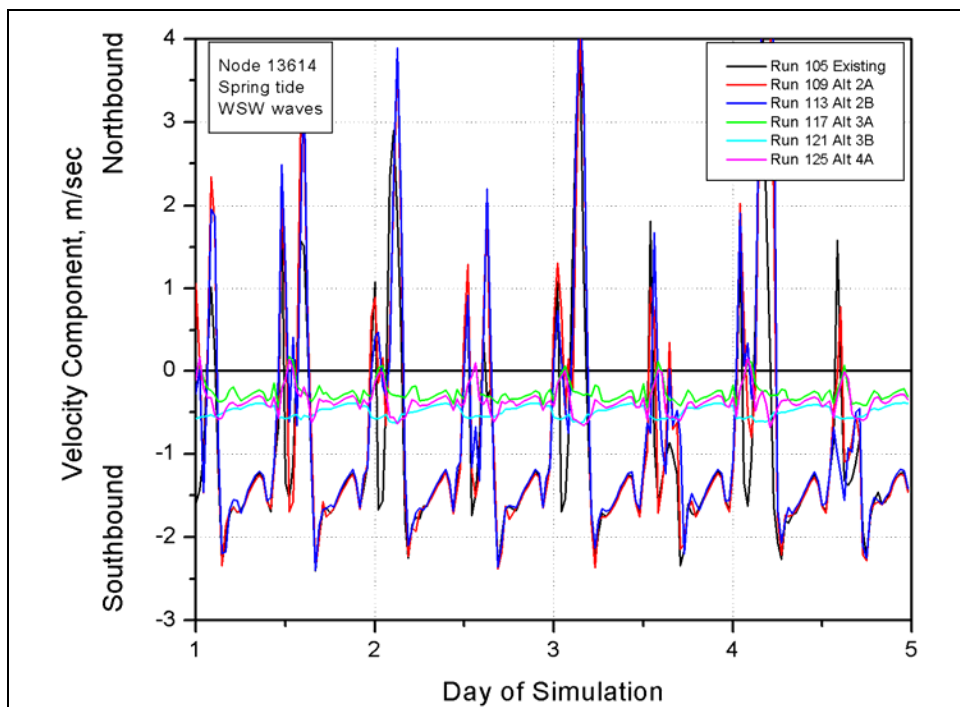
Figure E396.   North-south velocity component at node 13614 (spring tide, west-southwest waves)
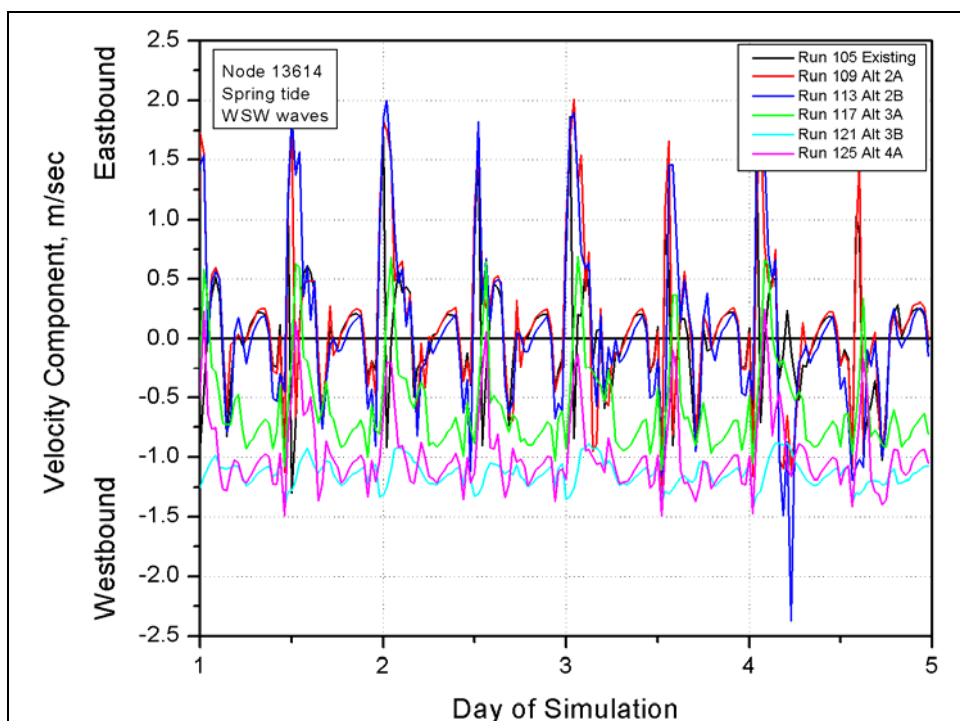
Figure E397.   East-west velocity component at node 13614 (spring tide, west-southwest waves)
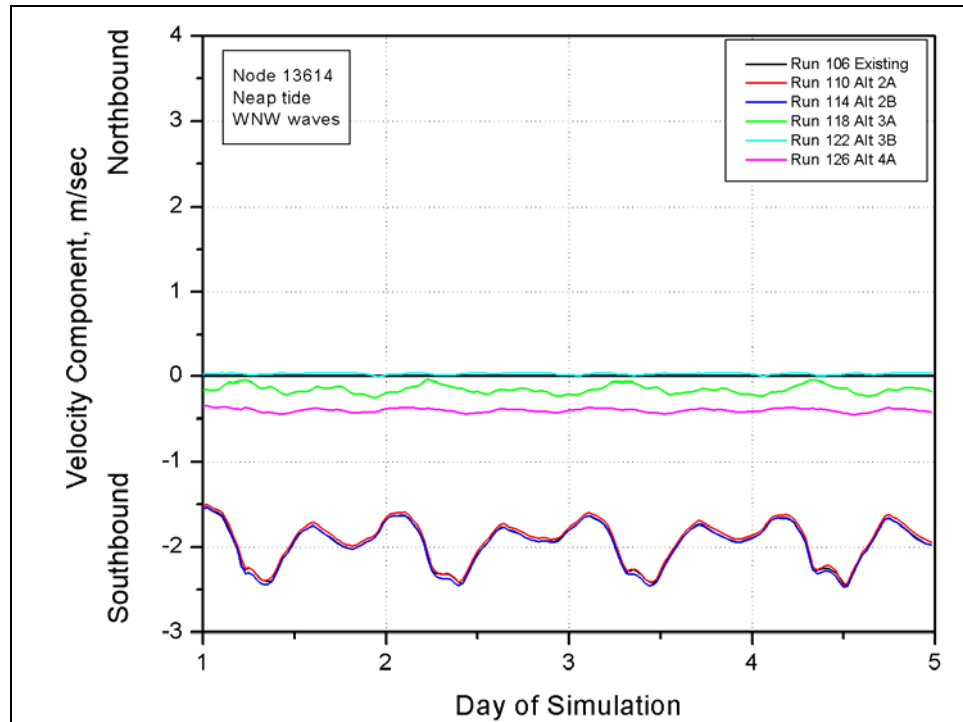
Figure E398. North-south velocity component at node 13614 (neap tide, west-northwest waves)
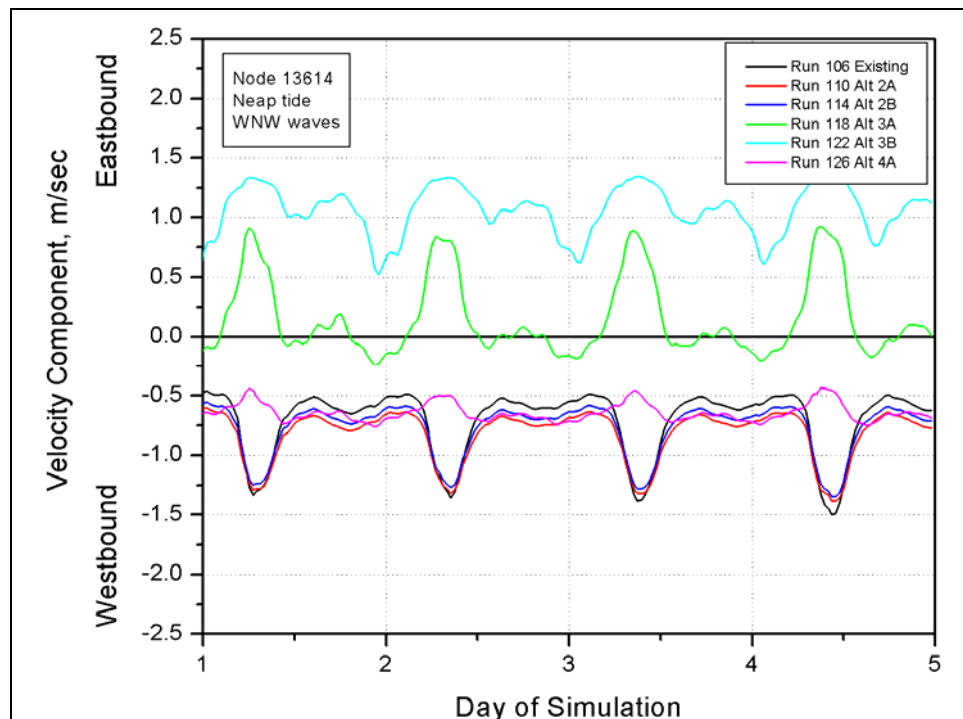
Figure E399. East-west velocity component at node 13614 (neap tide, west-northwest waves)
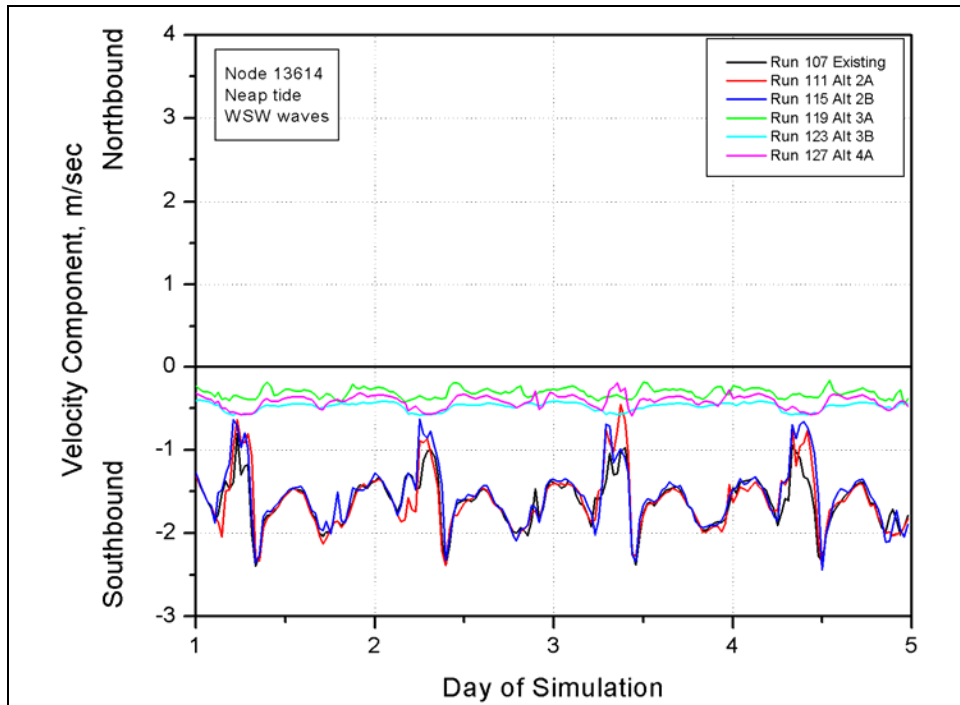
Figure E400.   North-south velocity component at node 13614 (neap tide, west-southwest waves)
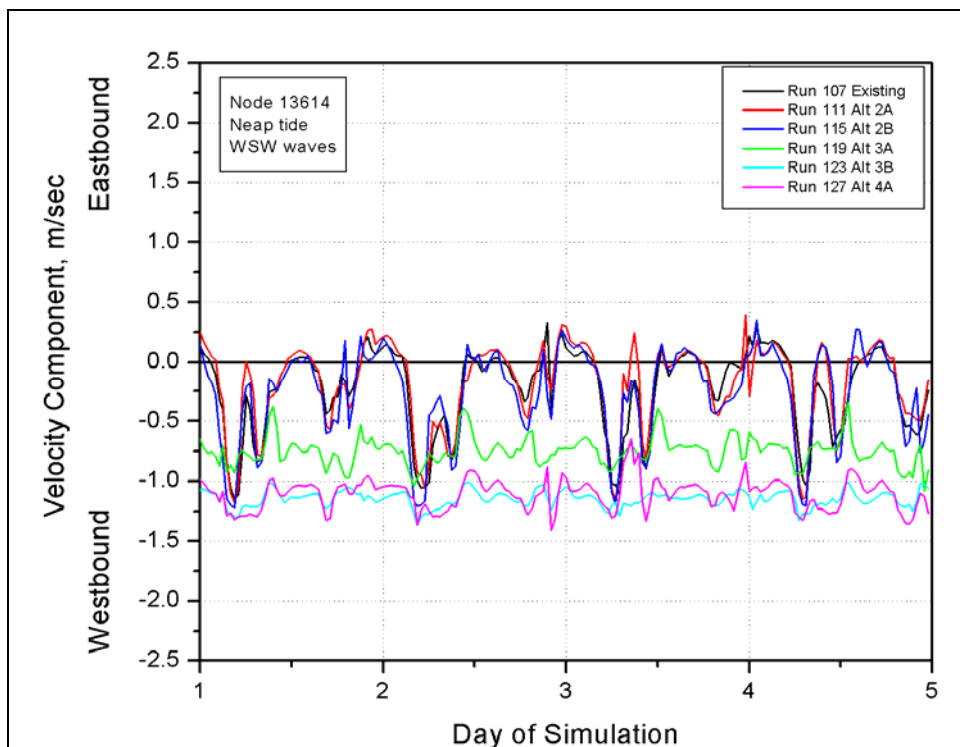
Figure E401.   East-west velocity component at node 13614 (neap tide, west-southwest waves)
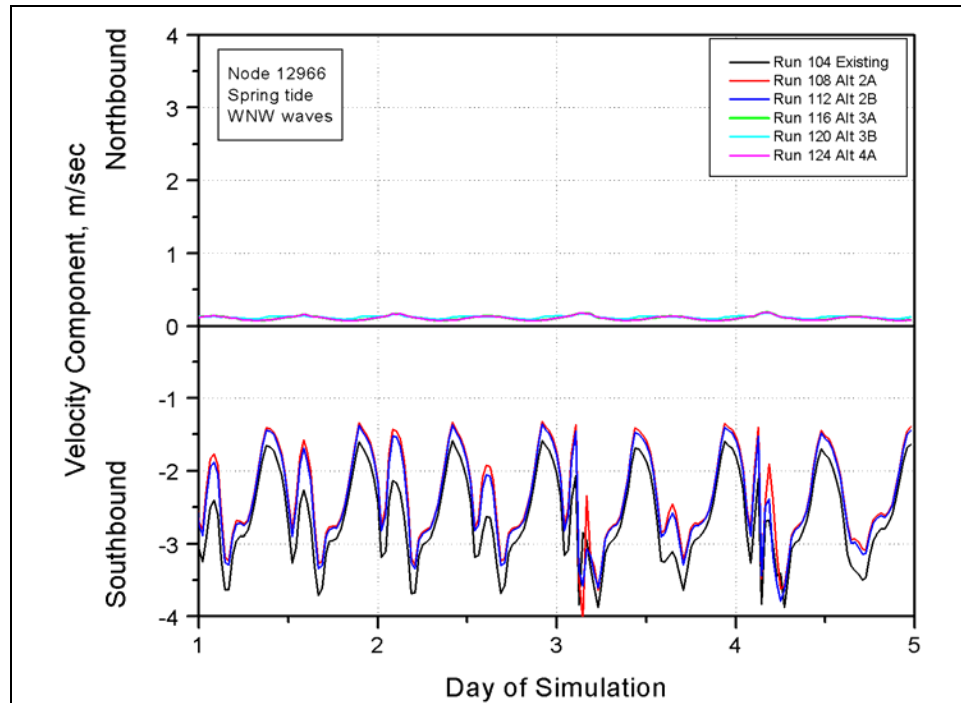
Figure E402.   North-south velocity component at node 12966 (spring tide, west-northwest waves)
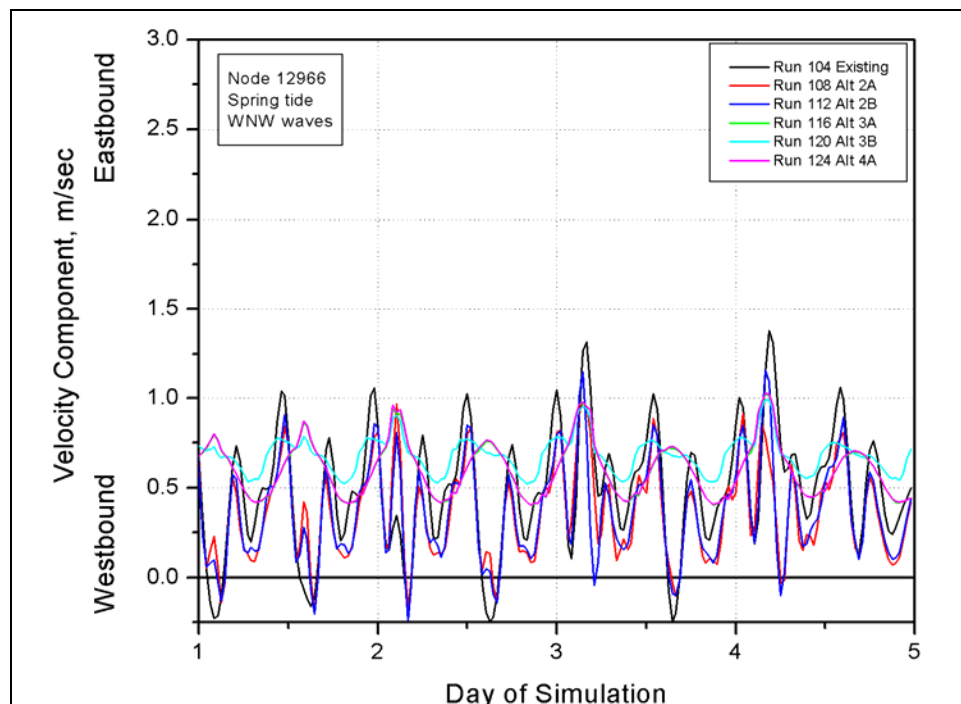
Figure E403.   East-west velocity component at node 12966 (spring tide, west-northwest waves)
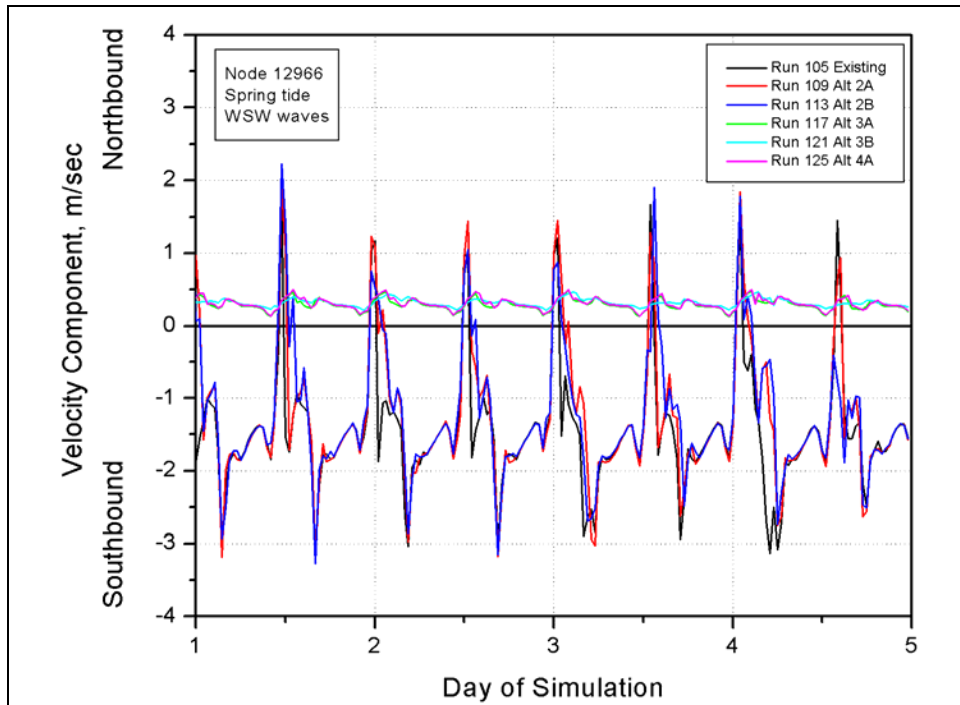
Figure E404. North-south velocity component at node 12966 (spring tide, west-southwest waves)
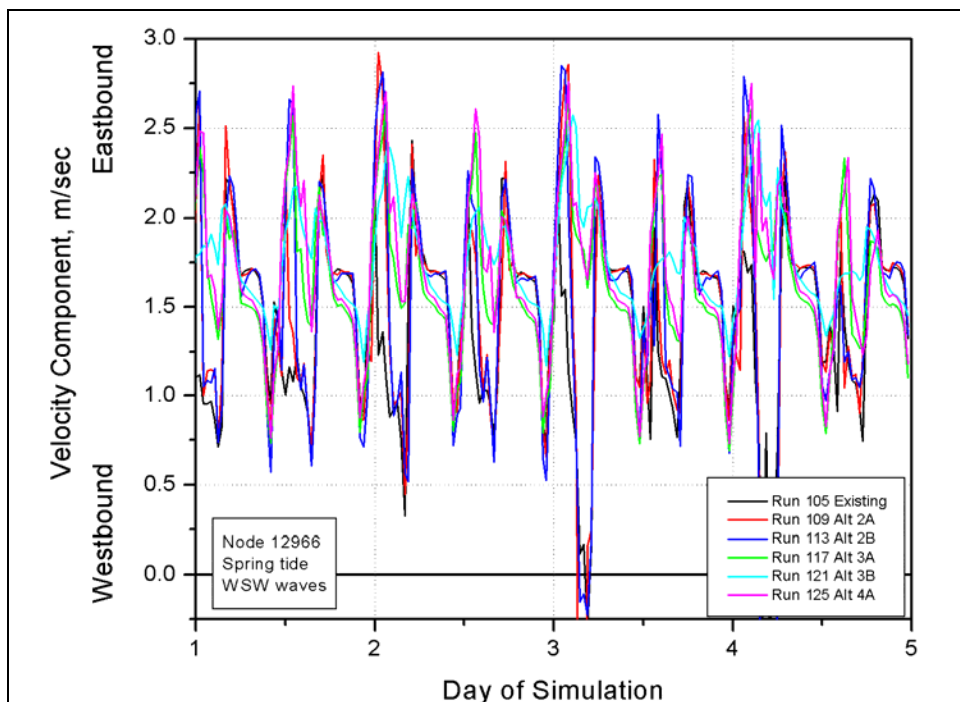
Figure E405. East-west velocity component at node 12966 (spring tide, west-southwest waves)
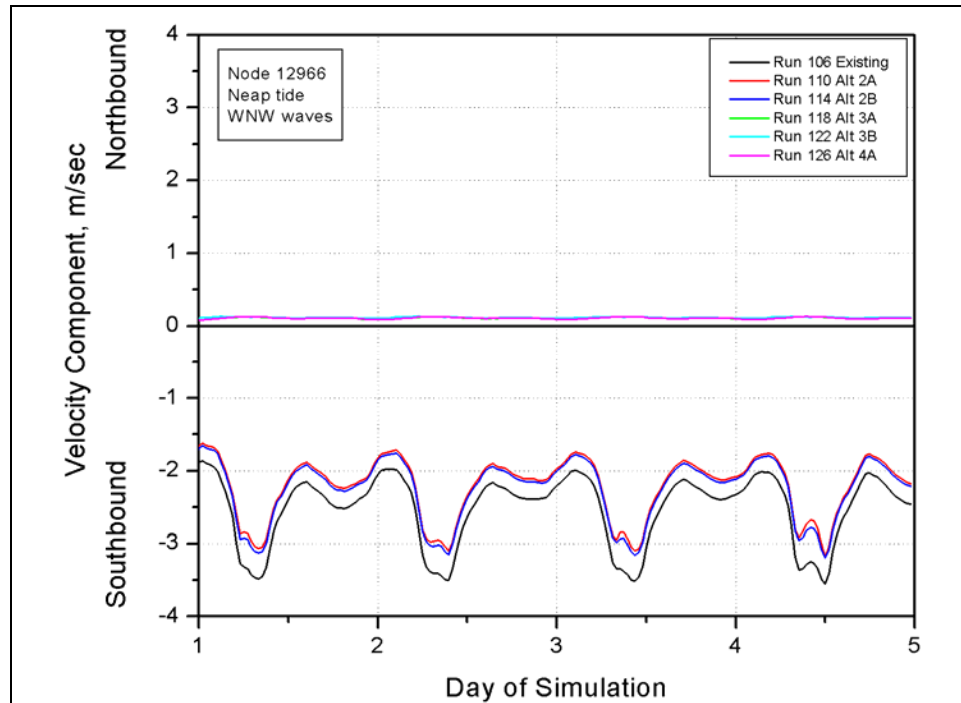
Figure E406.   North-south velocity component at node 12966 (neap tide, west-northwest waves)
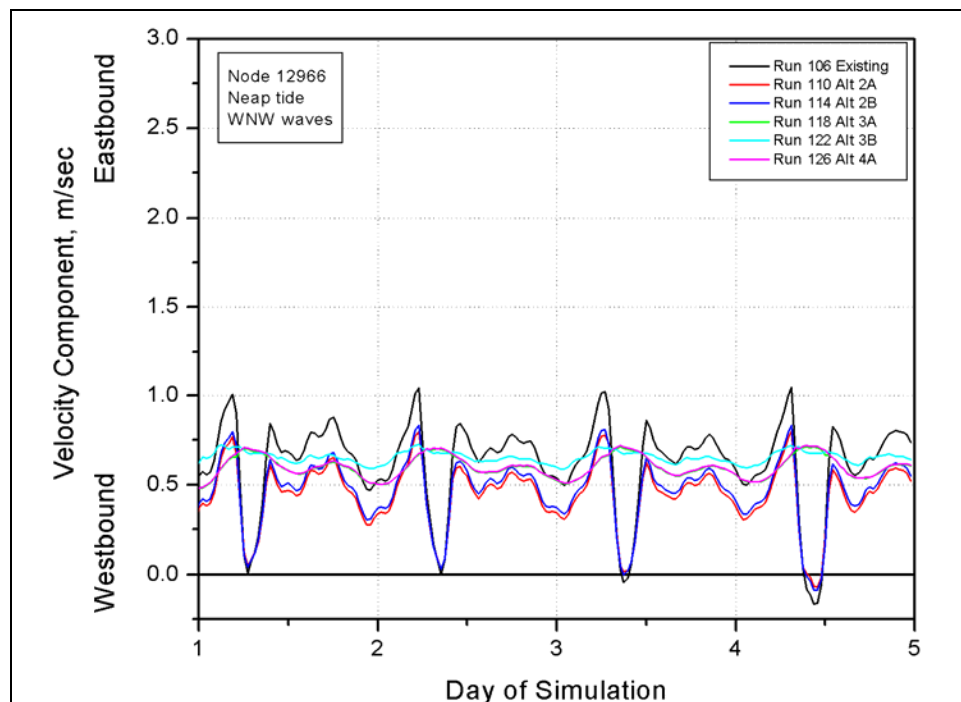
Figure E407.   East-west velocity component at node 12966 (neap tide, west-northwest waves)
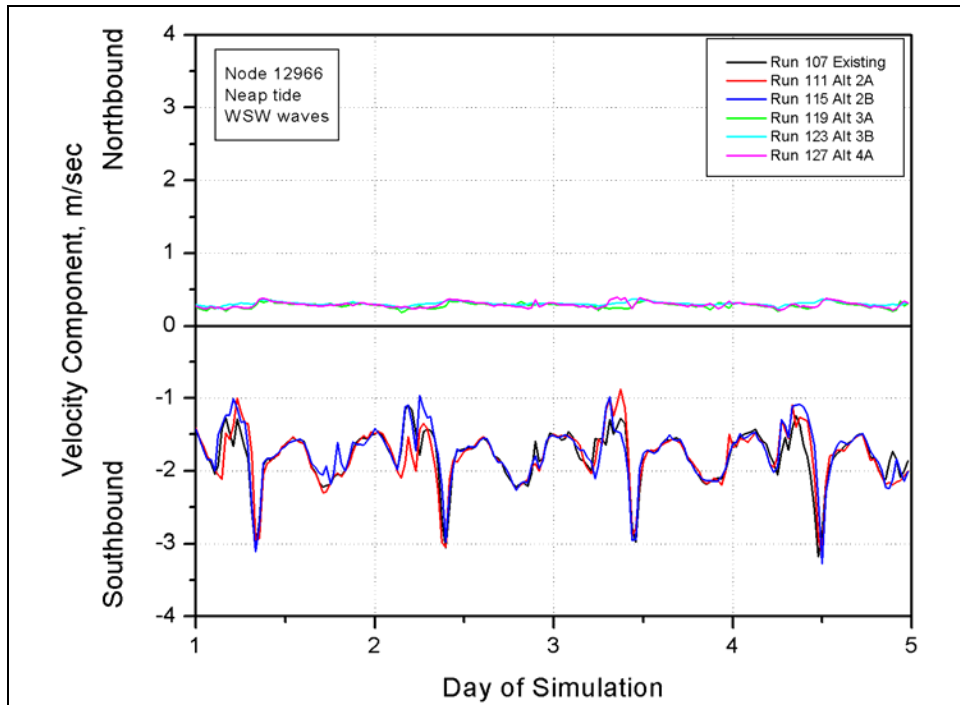
Figure E408.   North-south velocity component at node 12966 (neap tide, west-southwest waves)
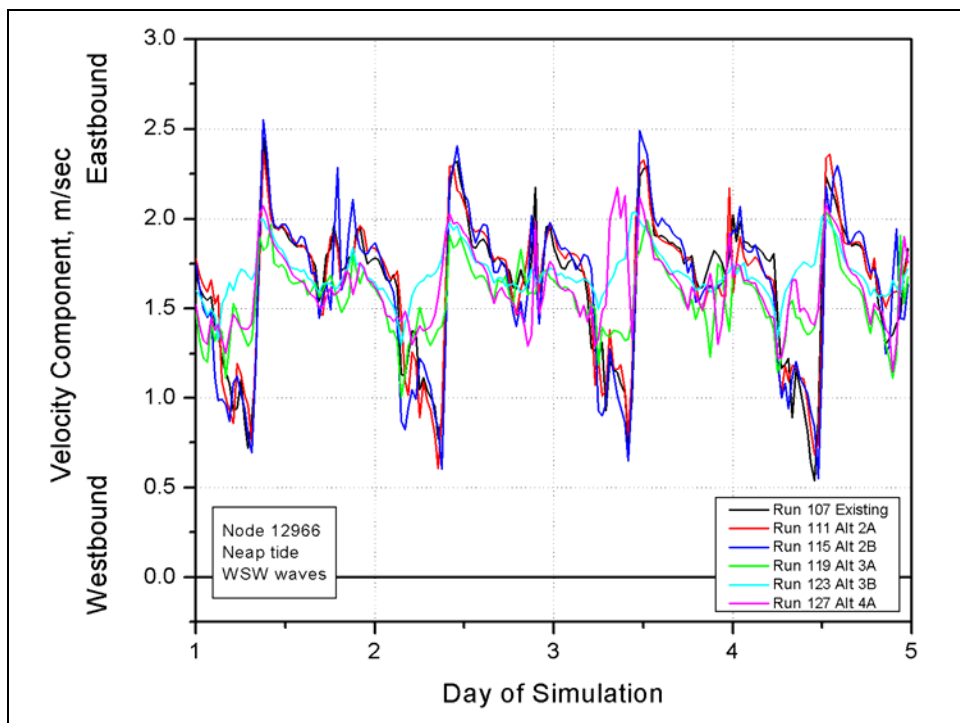
Figure E409.   East-west velocity component at node 12966 (neap tide, west-southwest waves)
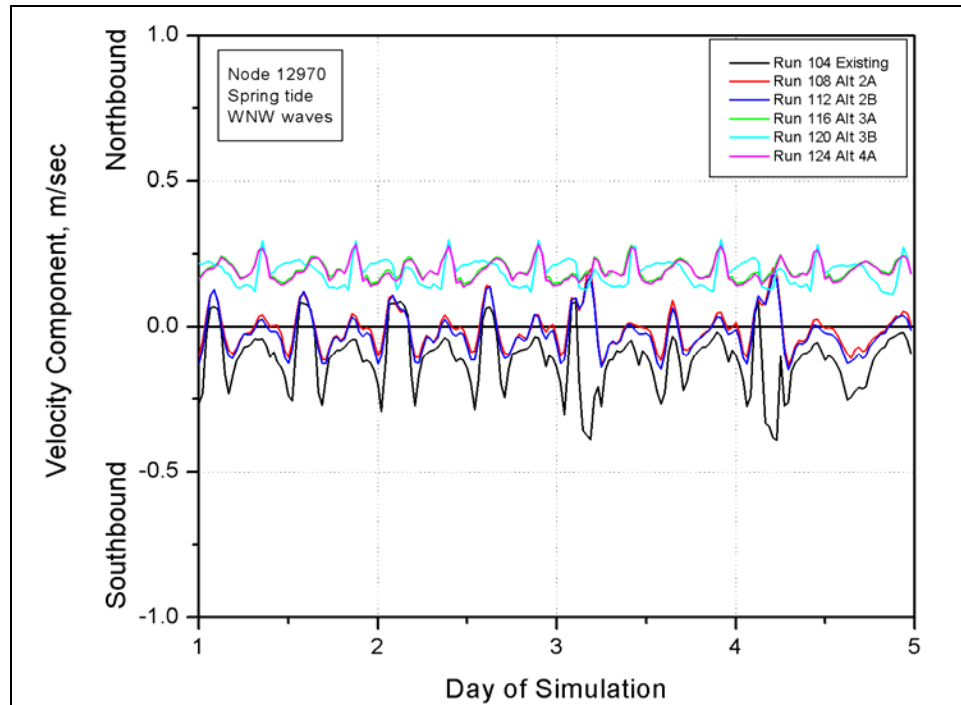
Figure E410.   North-south velocity component at node 12970 (spring tide, west-northwest waves)
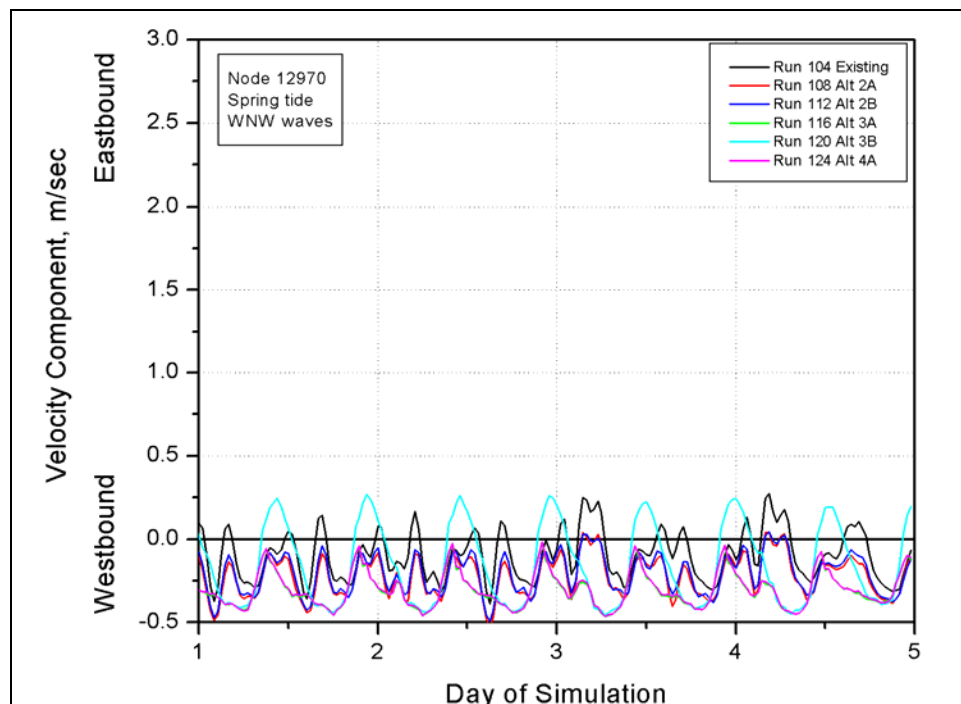
Figure E411.   East-west velocity component at node 12970 (spring tide, west-northwest waves)
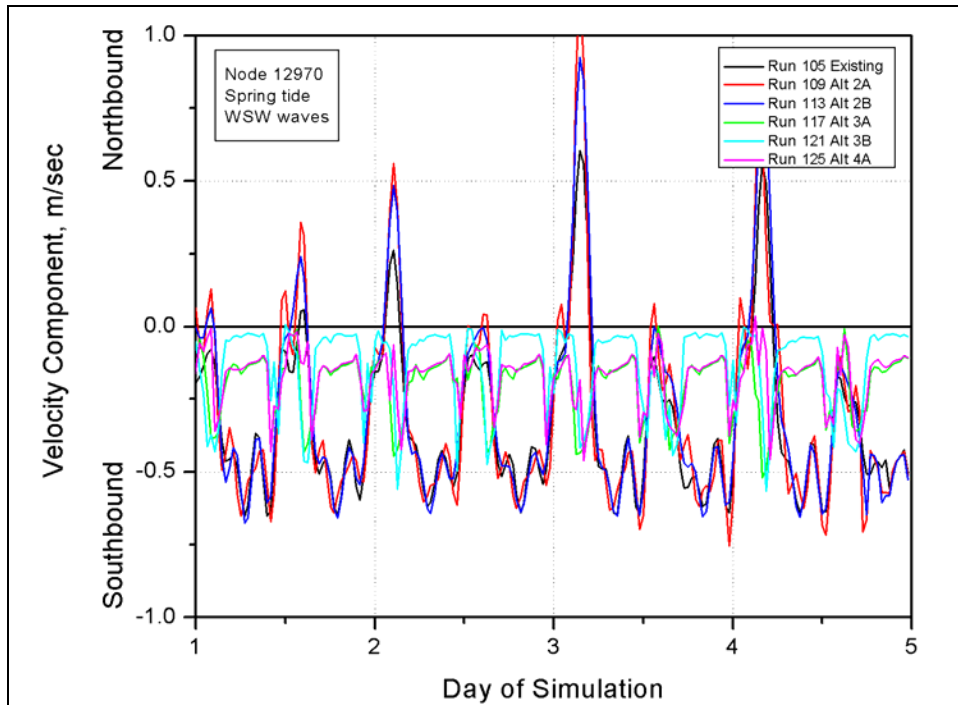
Figure E412.   North-south velocity component at node 12970 (spring tide, west-southwest waves)
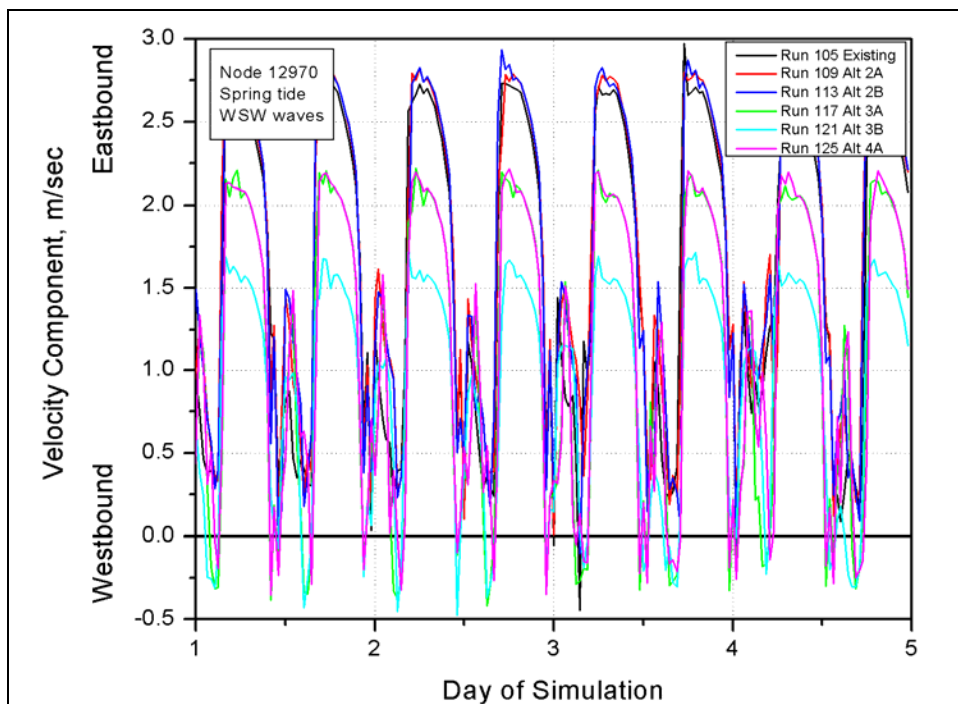
Figure E413.   East-west velocity component at node 12970 (spring tide, west-southwest waves)
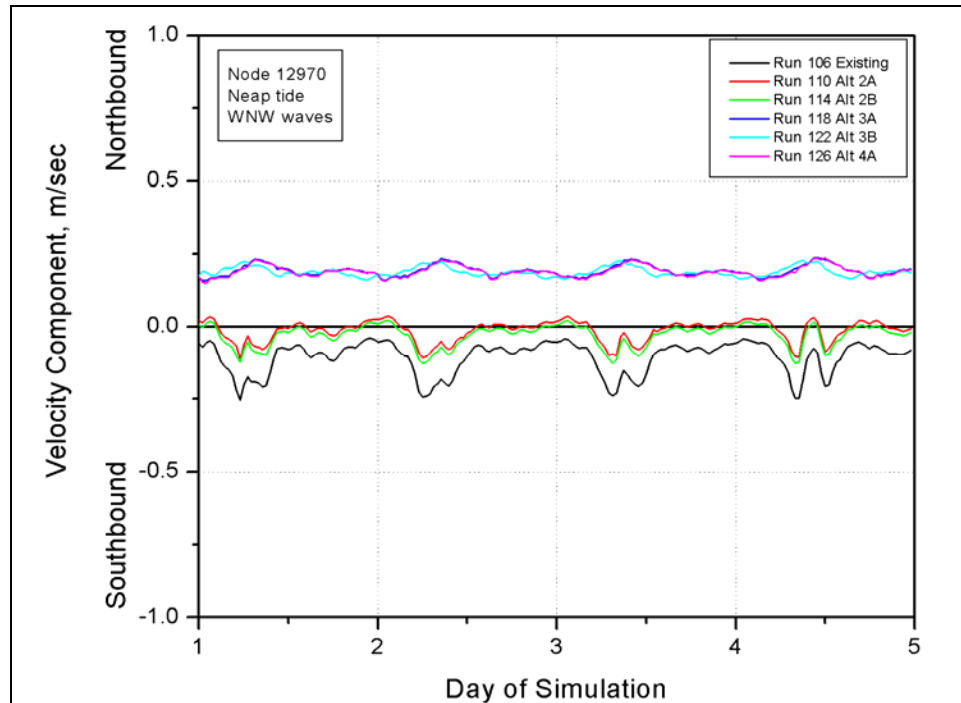
Figure E414.   North-south velocity component at node 12970 (neap tide, west-northwest waves)
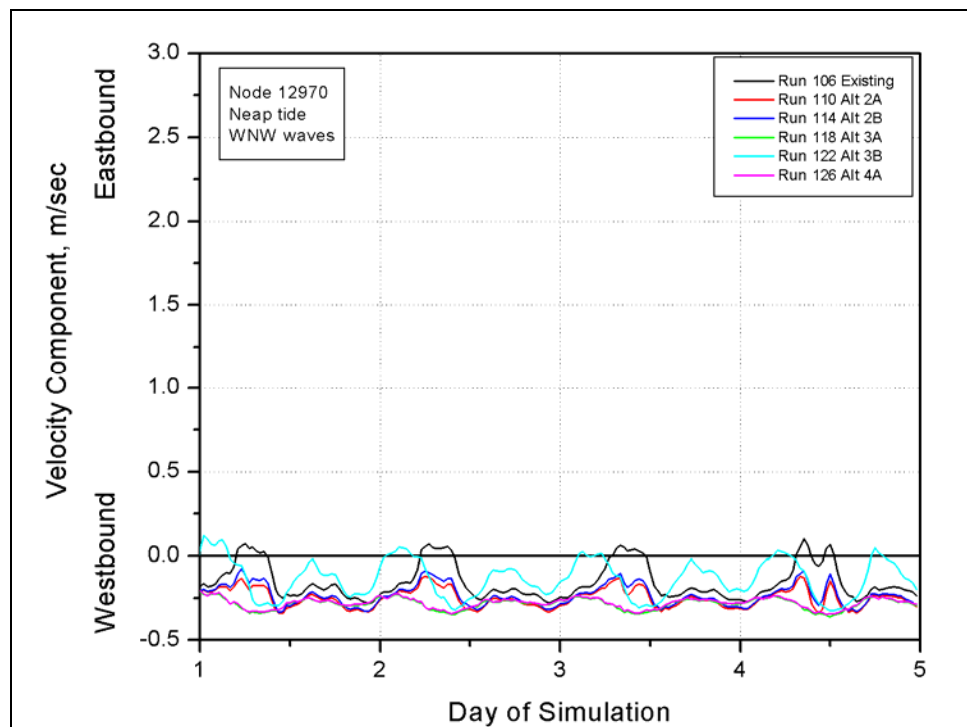
Figure E415.   East-west velocity component at node 12970 (neap tide, west-northwest waves)
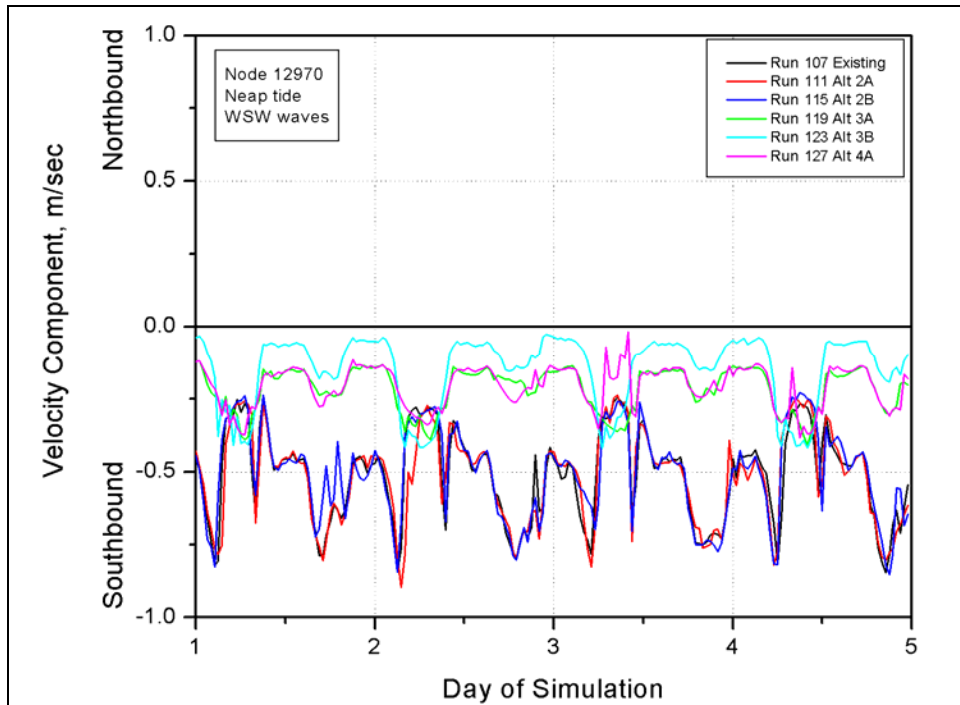
Figure E416.   North-south velocity component at node 12970 (neap tide, west-southwest waves)
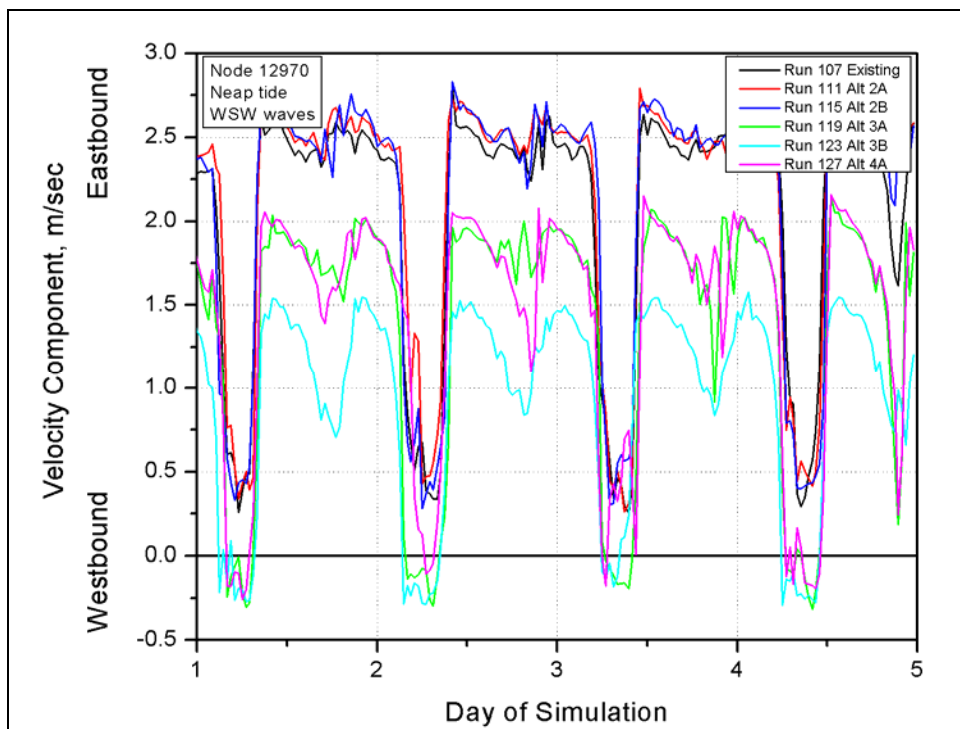
Figure E417.   East-west velocity component at node 12970 (neap tide, west-southwest waves)
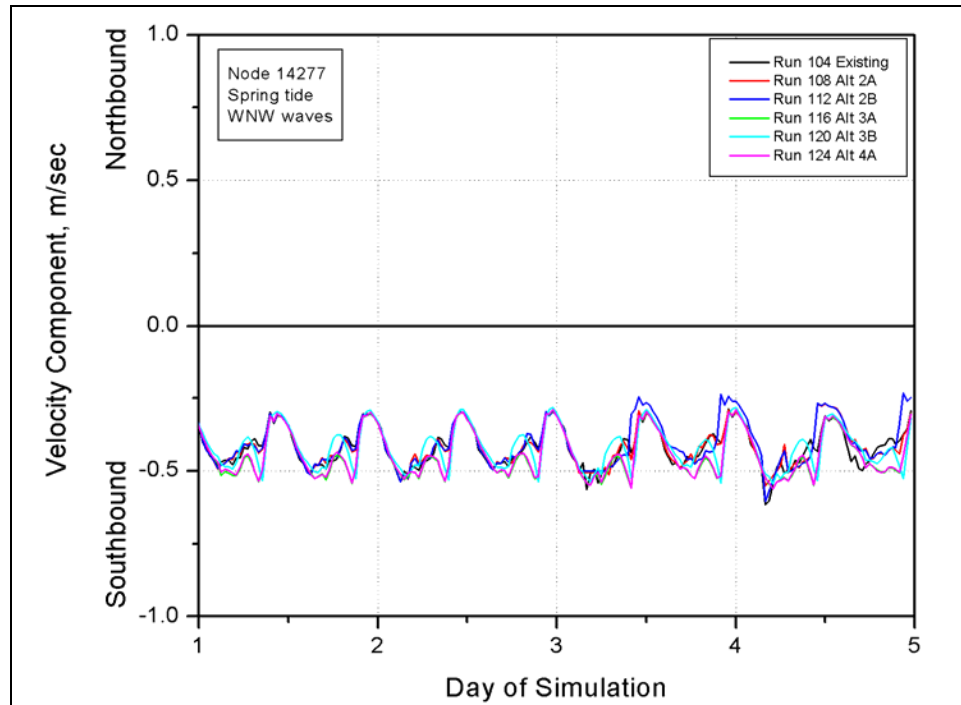
Figure E418.   North-south velocity component at node 14277 (spring tide, west-northwest waves)
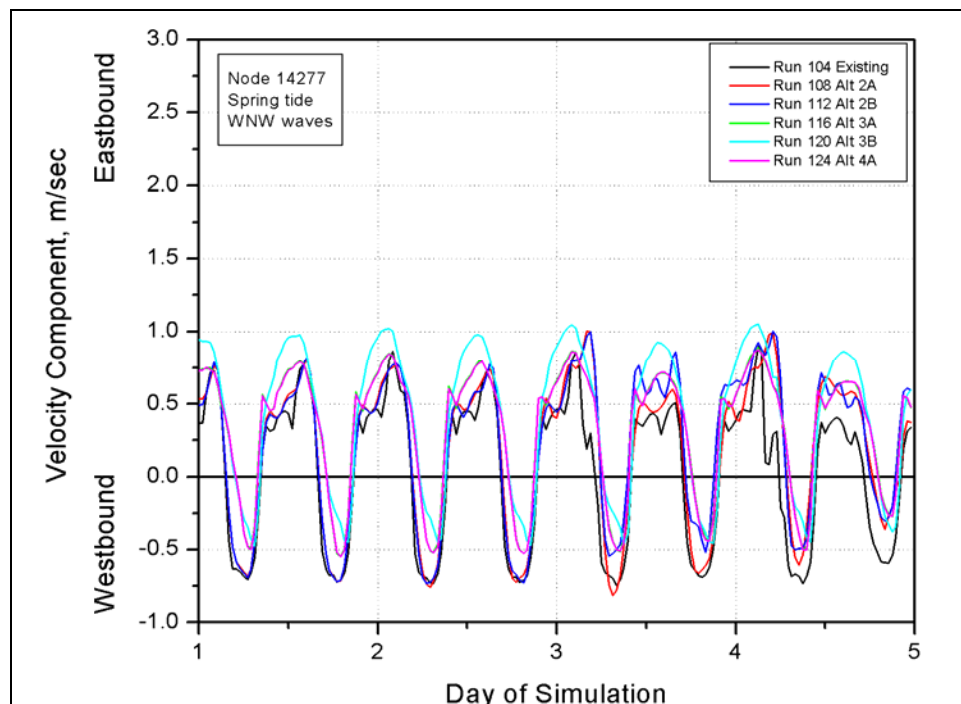
Figure E419.   East-west velocity component at node 14277 (spring tide, west-northwest waves)
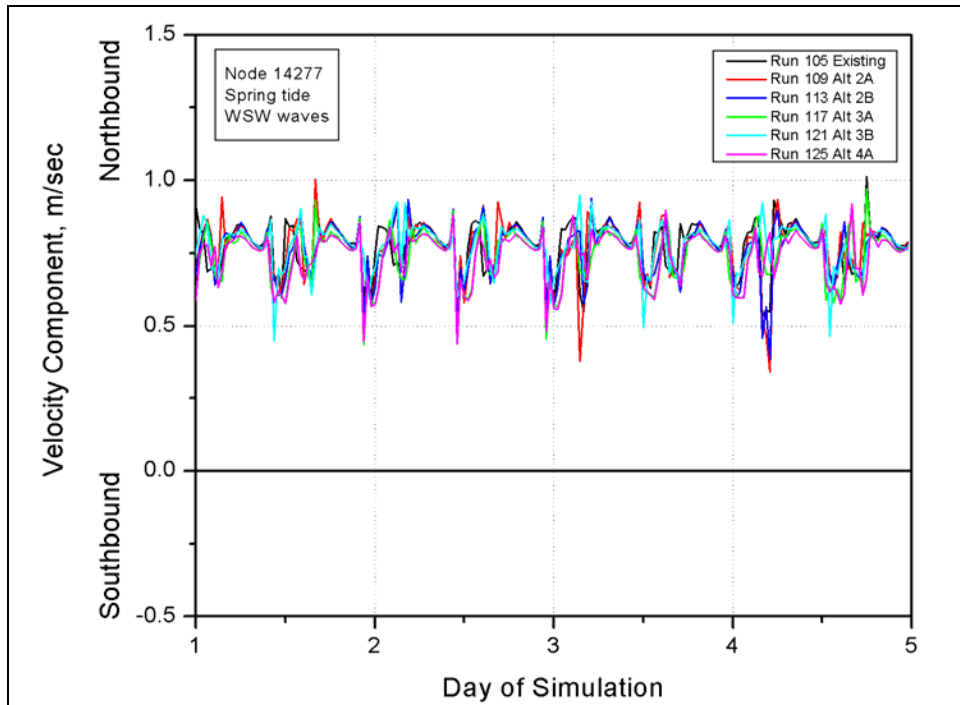
Figure E420.   North-south velocity component at node 14277 (spring tide, west-southwest waves)
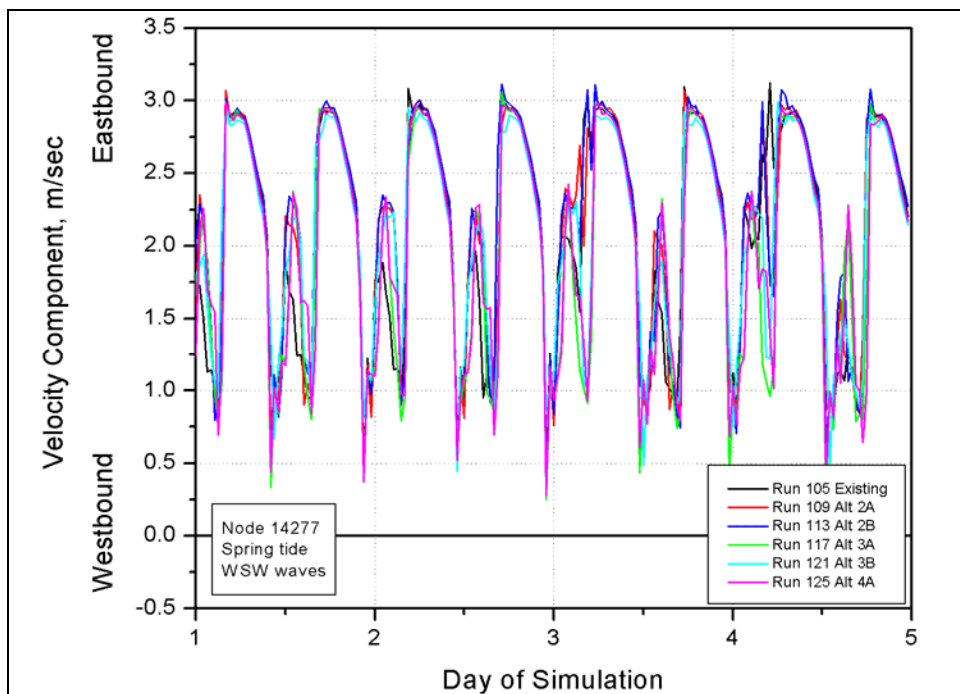
Figure E421.   East-west velocity component at node 14277 (spring tide, west-southwest waves)

Appendix E   Tidal Circulation Simulation Results
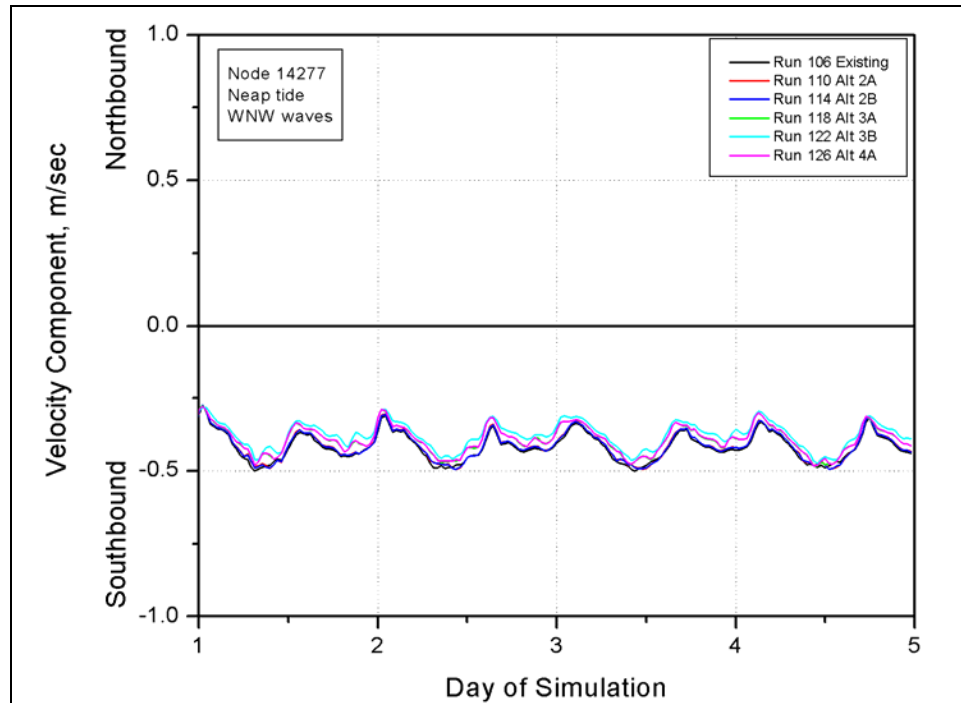
Figure E422. North-south velocity component at node 14277 (neap tide, west-northwest waves)
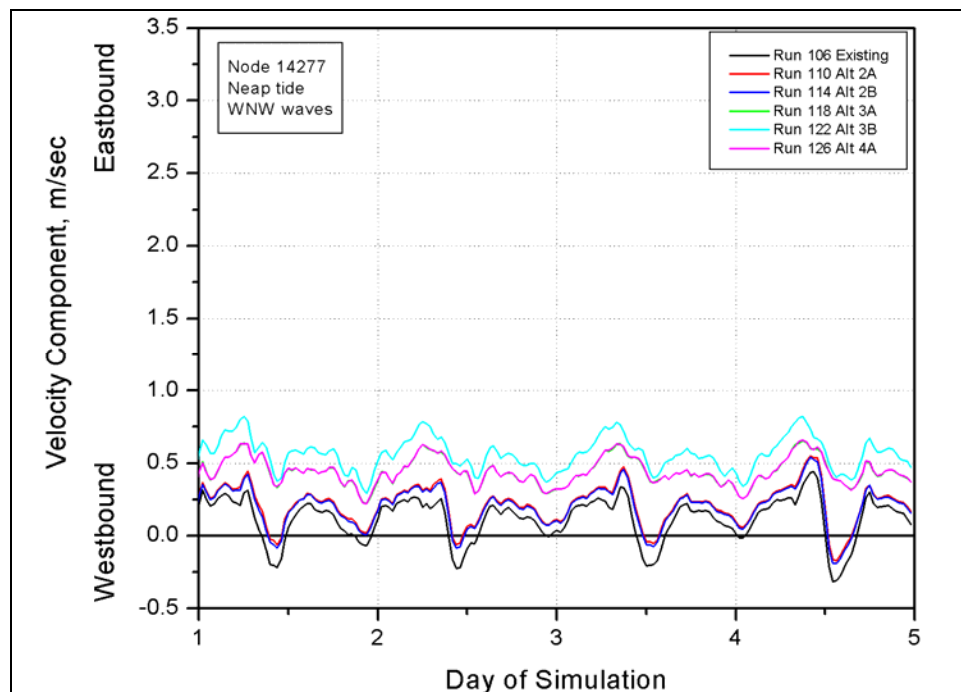
Figure E423. East-west velocity component at node 14277 (neap tide, west-northwest waves)
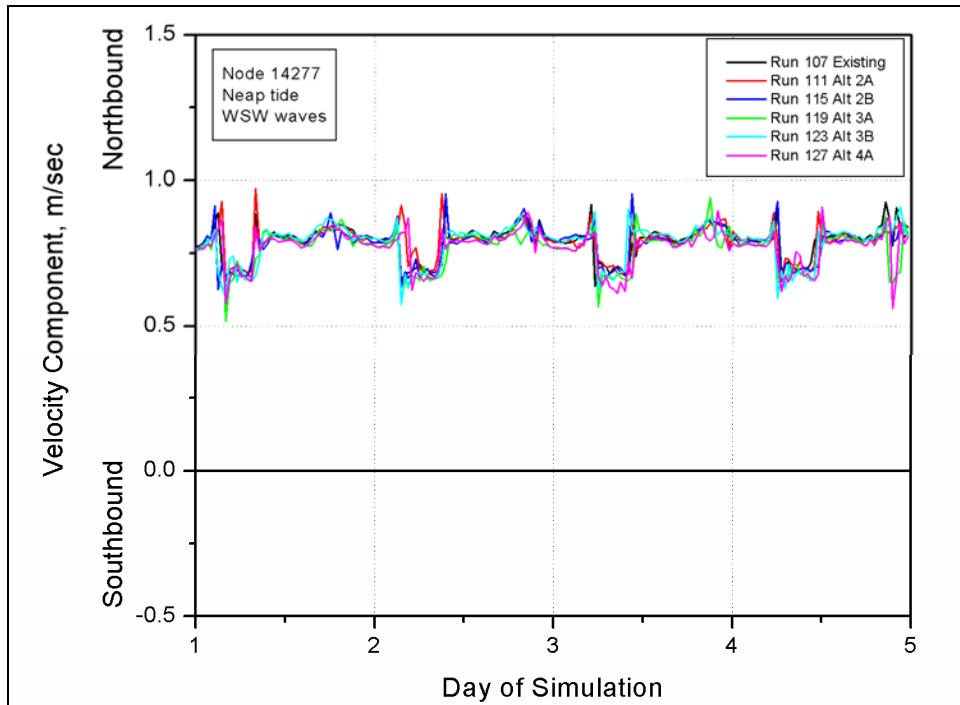
Figure E424.   North-south velocity component at node 14277 (neap tide, west-southwest waves)
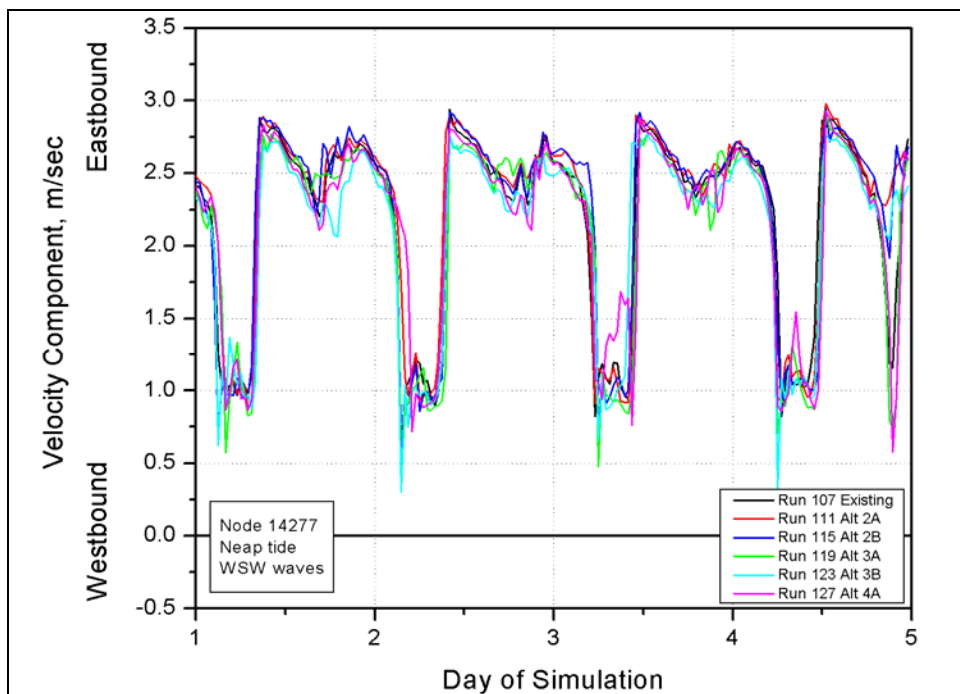
Figure E425.   East-west velocity component at node 14277 (neap tide, west-southwest waves)
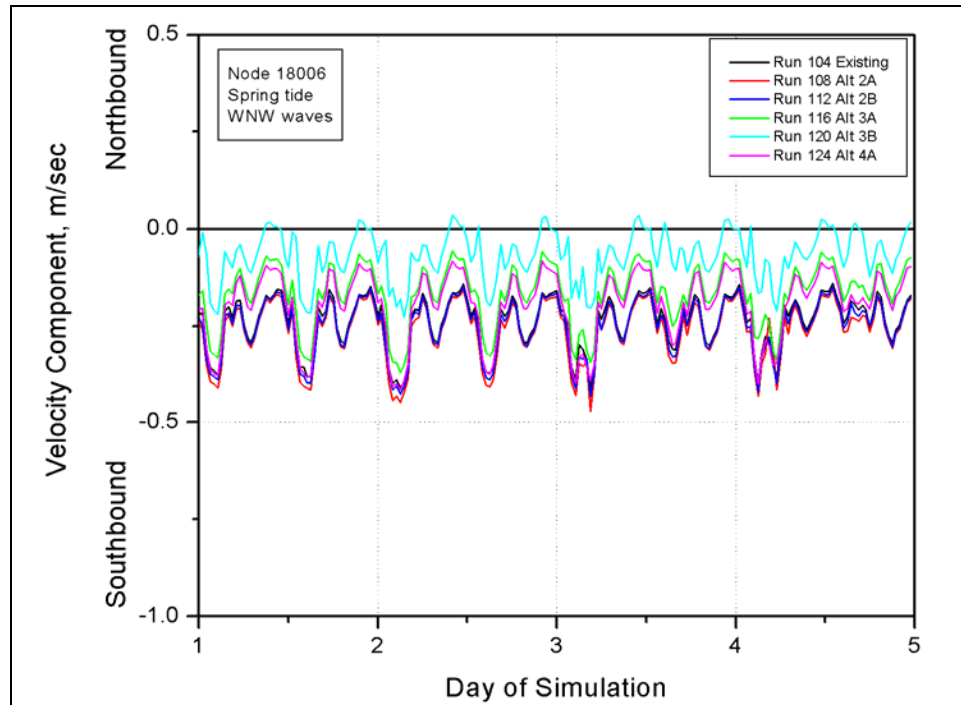
Figure E426.   North-south velocity component at node 18006 (spring tide, west-northwest waves)
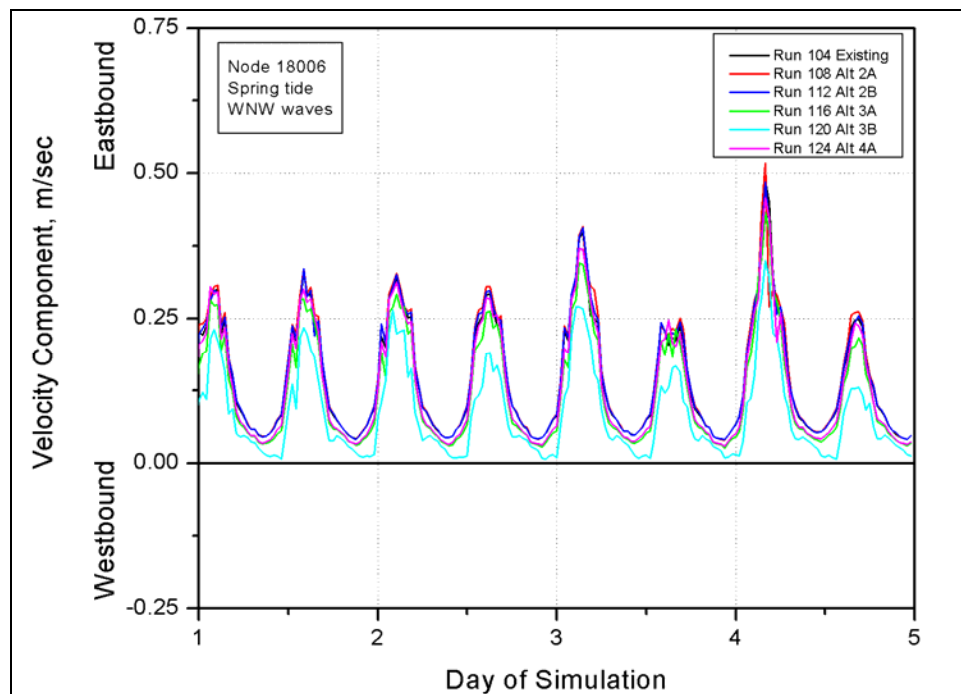
Figure E427.   East-west velocity component at node 18006 (spring tide, west-northwest waves)
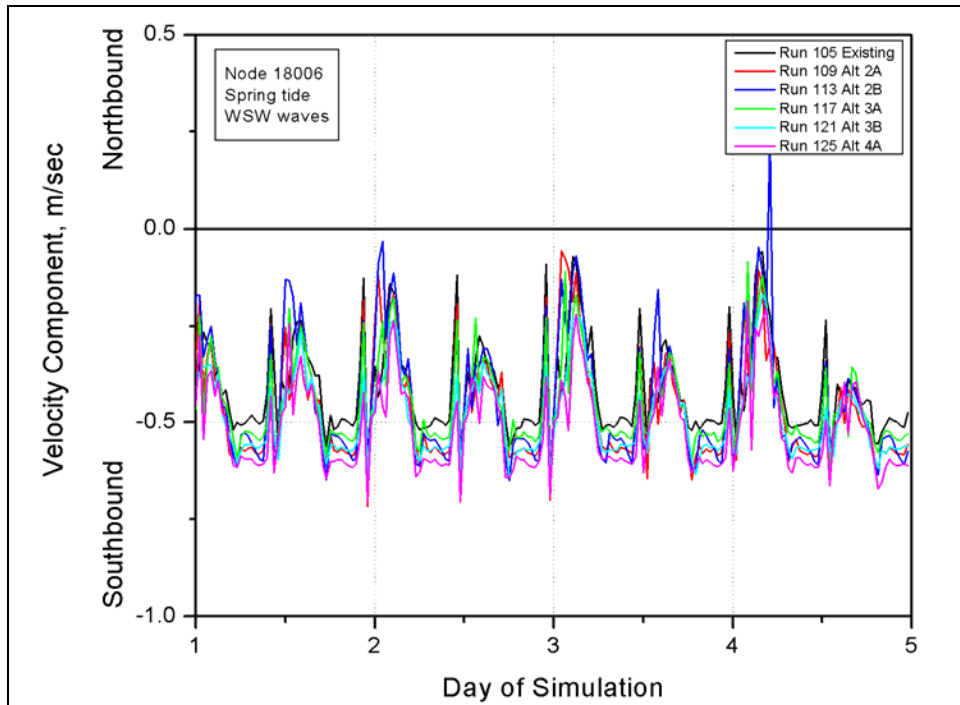
Figure E428.   North-south velocity component at node 18006 (spring tide, west-southwest waves)
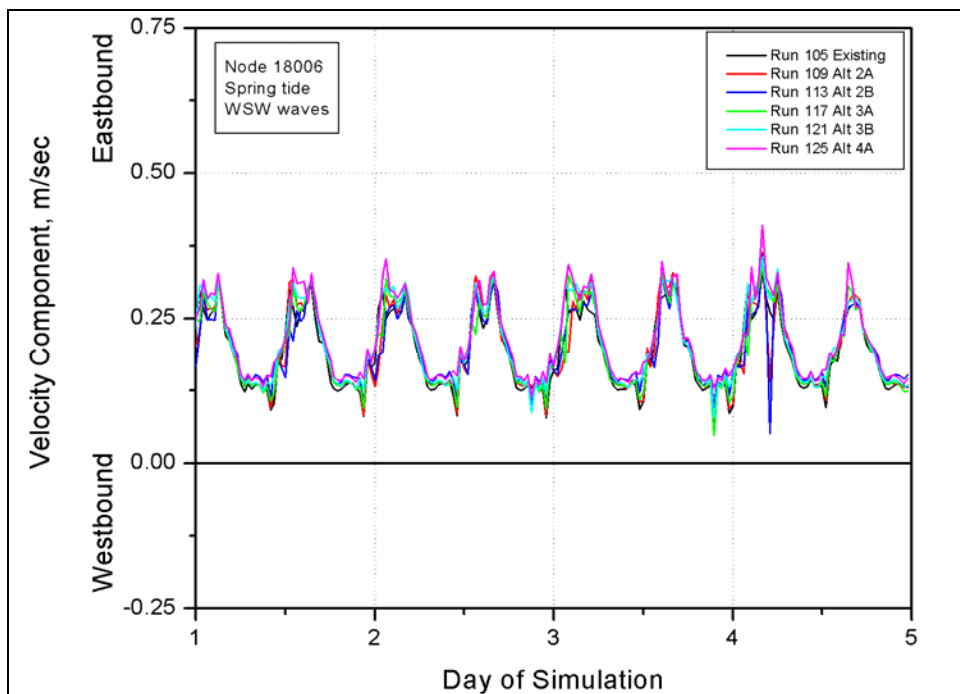
Figure E429.   East-west velocity component at node 18006 (spring tide, west-southwest waves)
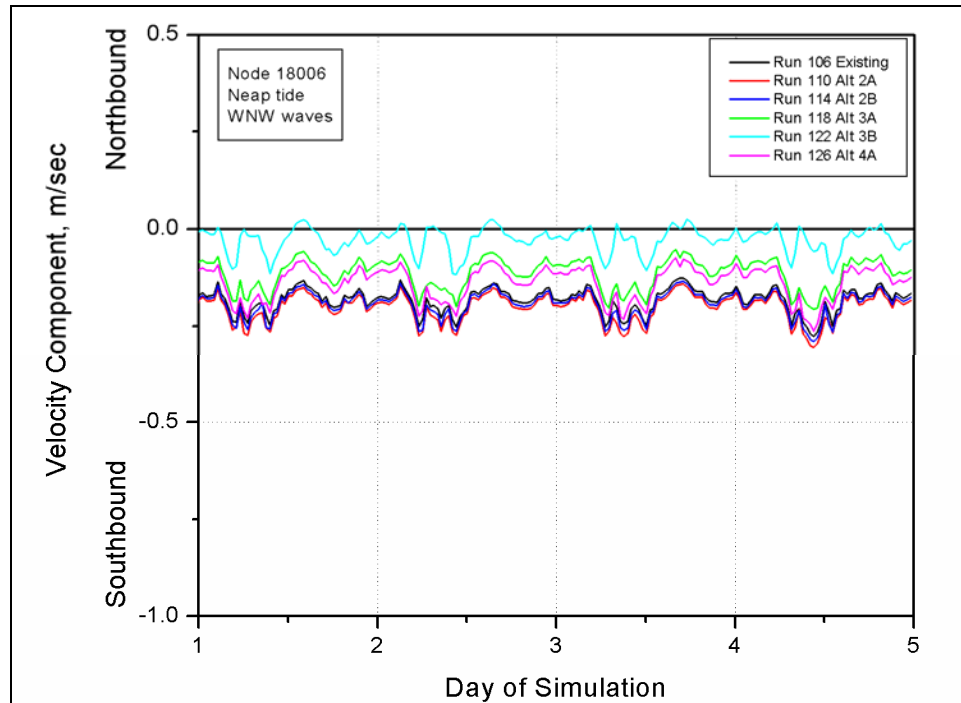
Figure E430.   North-south velocity component at node 18006 (neap tide, west-northwest waves)
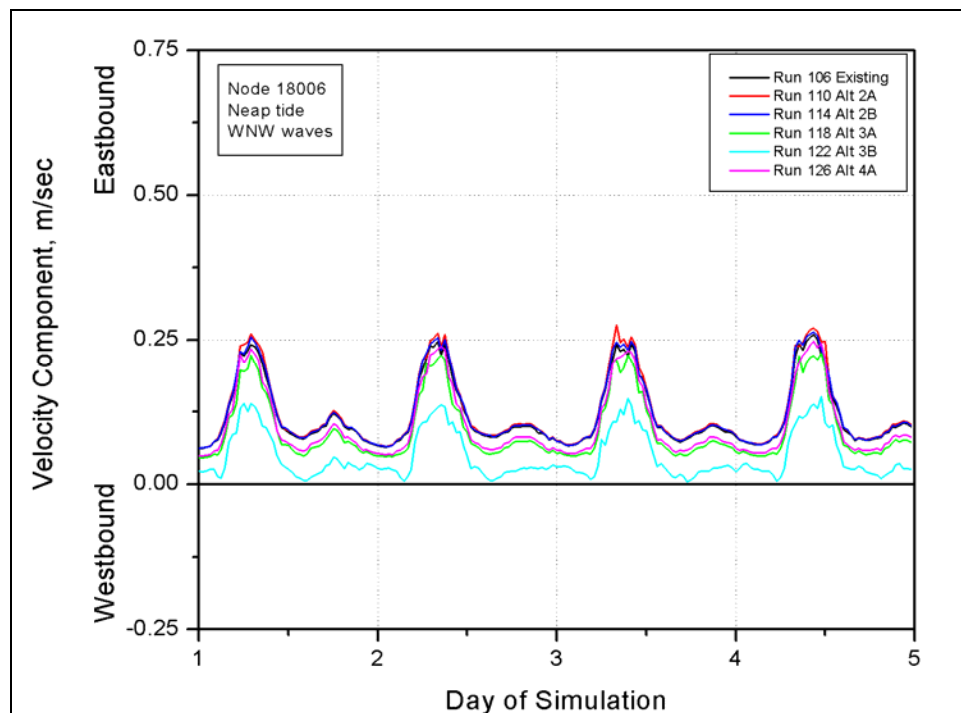
Figure E431.   East-west velocity component at node 18006 (neap tide, west-northwest waves)
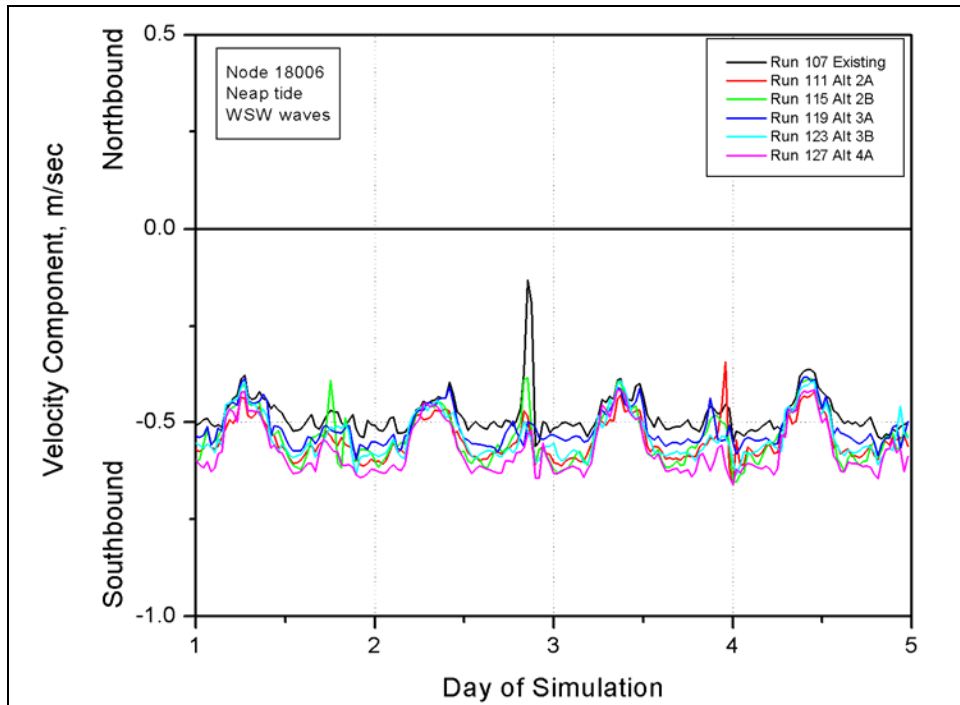
Figure E432.   North-south velocity component at node 18006 (neap tide, west-southwest waves)
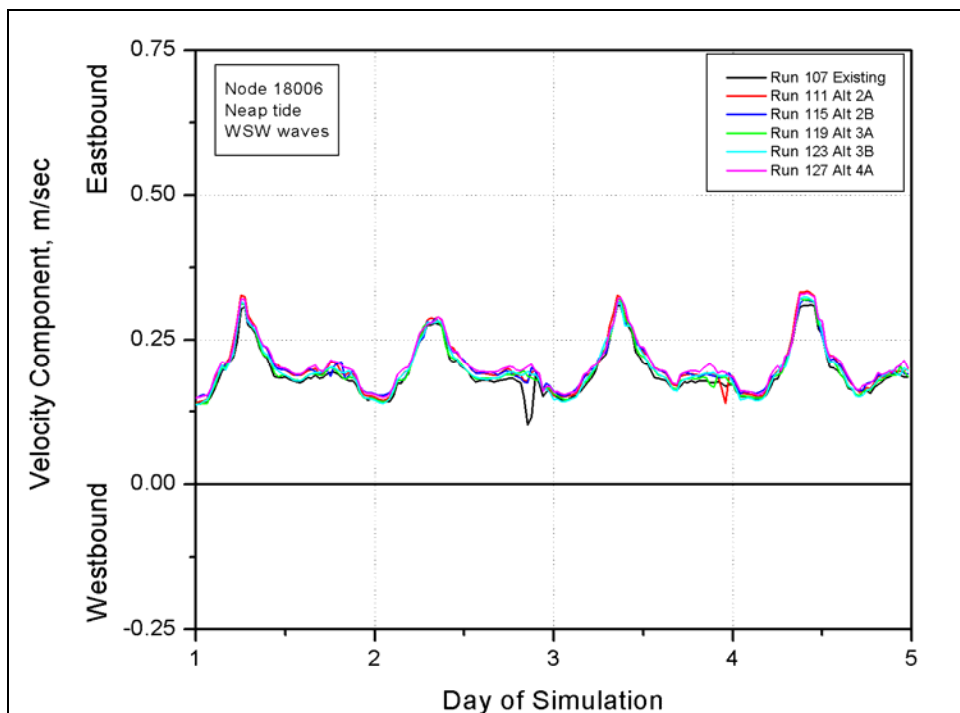
Figure E433.   East-west velocity component at node 18006 (neap tide, west-southwest waves)
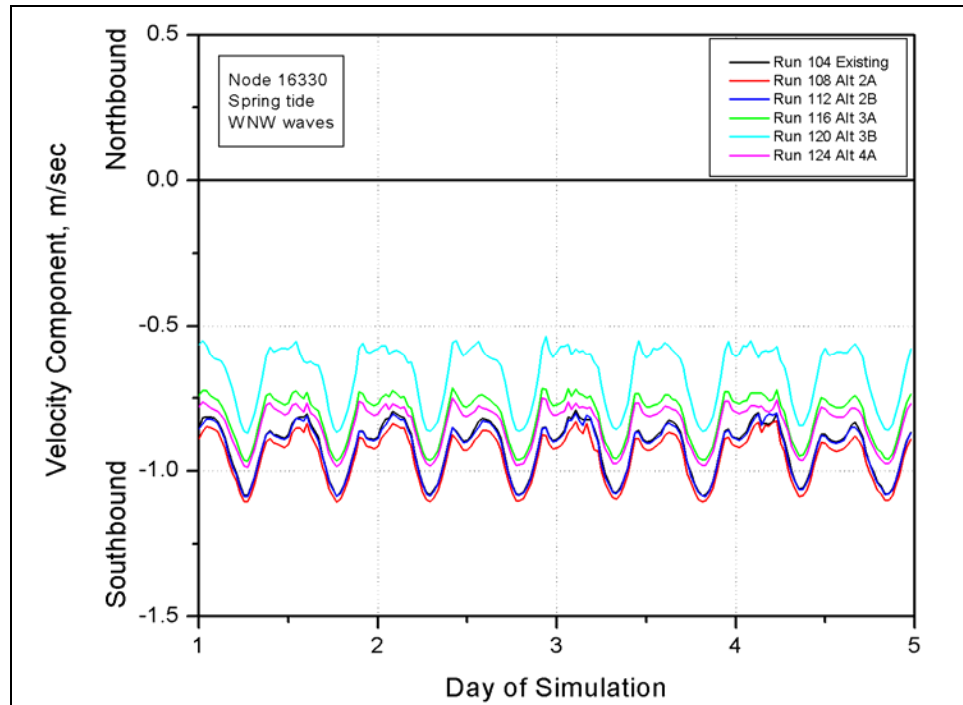
Figure E434.   North-south velocity component at node 16330 (spring tide, west-northwest waves)
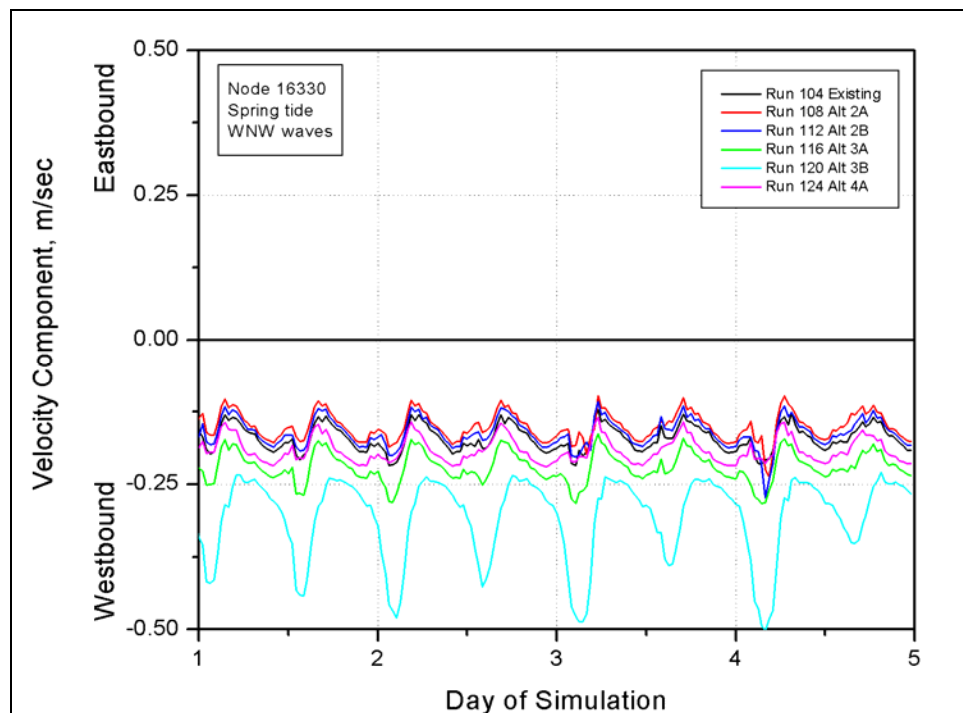
Figure E435.   East-west velocity component at node 16330 (spring tide, west-northwest waves)
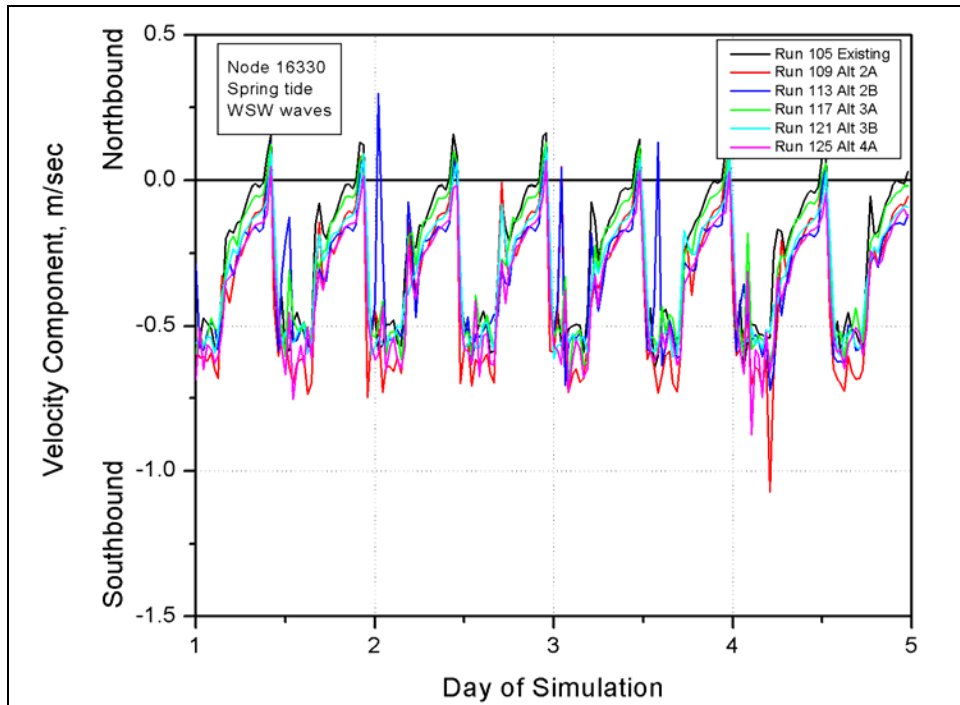
Figure E436.   North-south velocity component at node 16330 (spring tide, west-southwest waves)
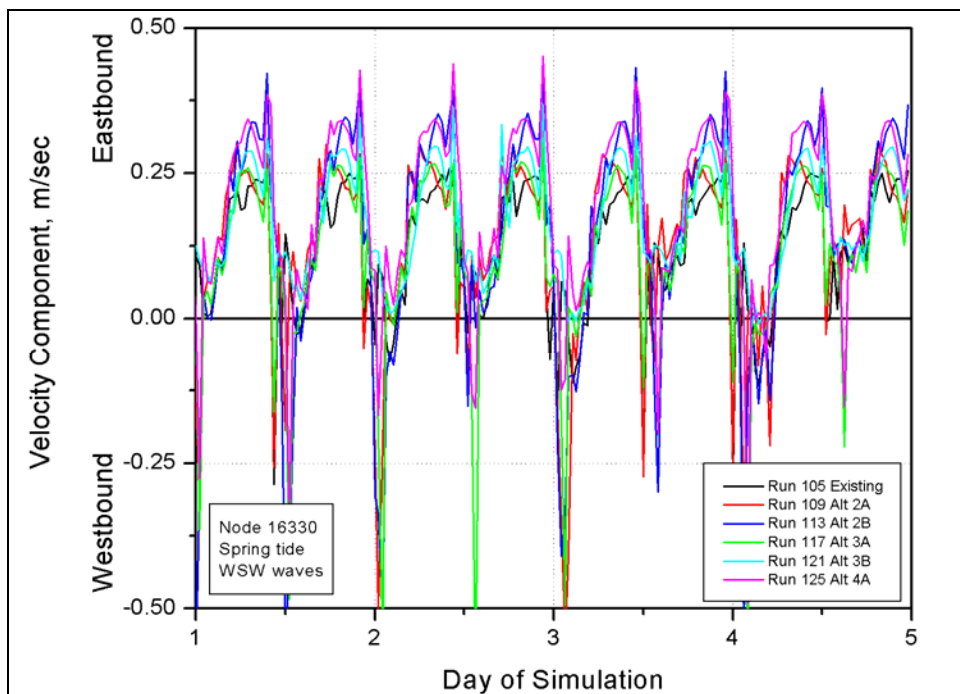
Figure E437.   East-west velocity component at node 16330 (spring tide, west-southwest waves)

Appendix E   Tidal Circulation Simulation Results
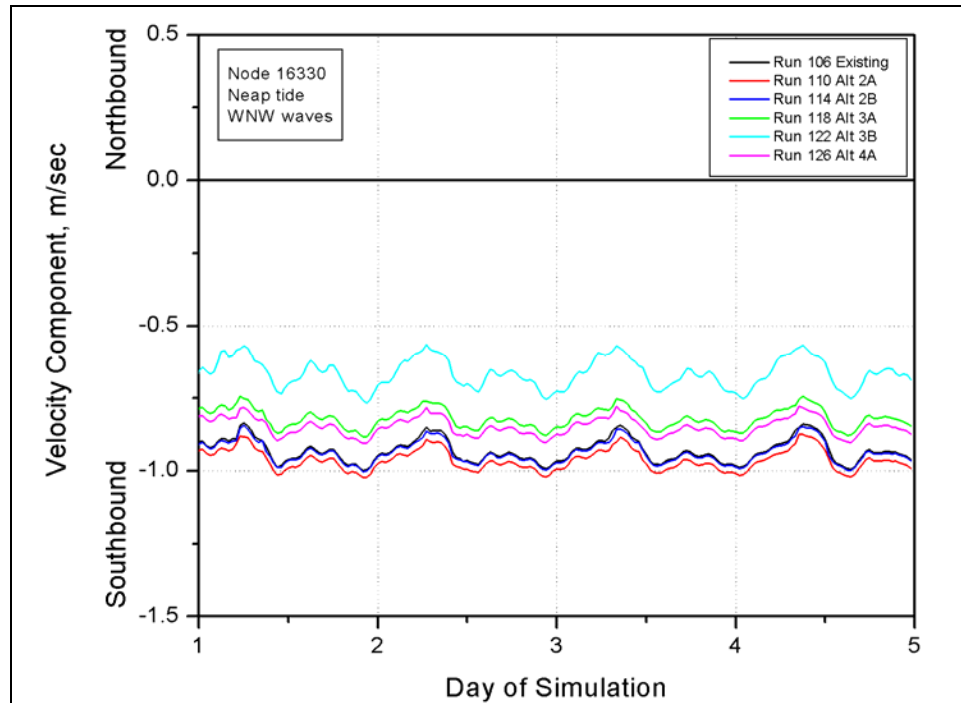
Figure E438.   North-south velocity component at node 16330 (neap tide, west-northwest waves)
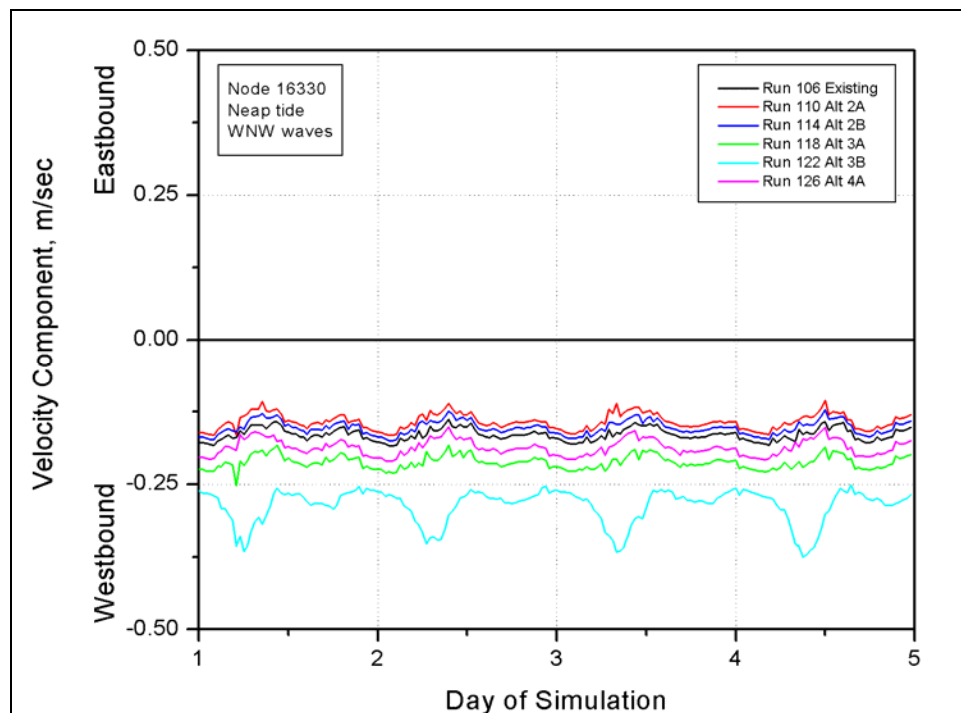
Figure E439.   East-west velocity component at node 16330 (neap tide, west-northwest waves)
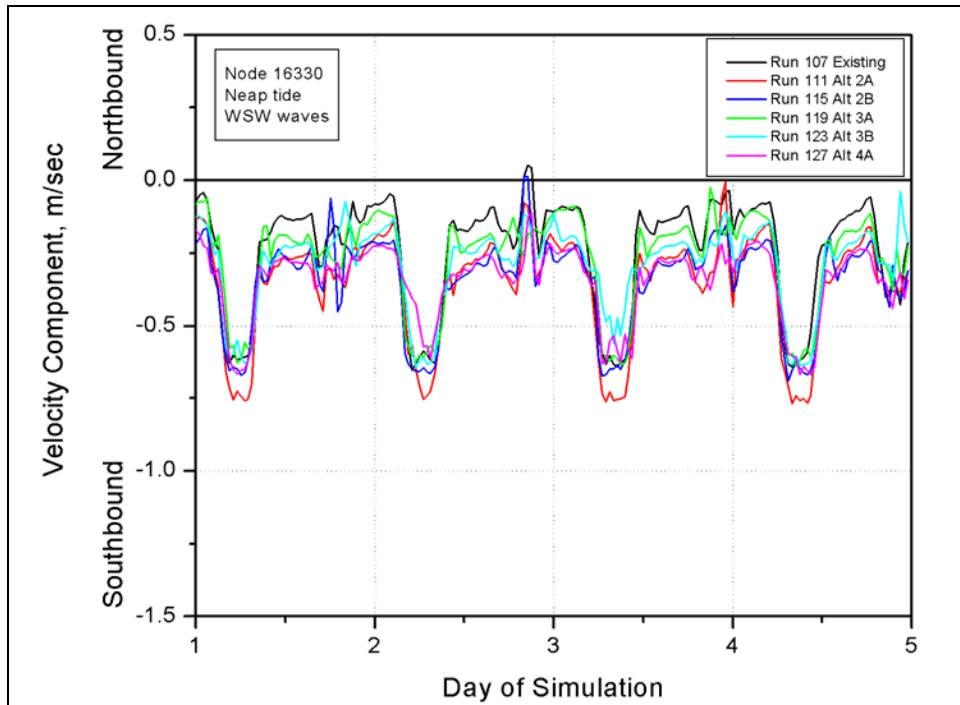
Figure E440.   North-south velocity component at node 16330 (neap tide, west-southwest waves)
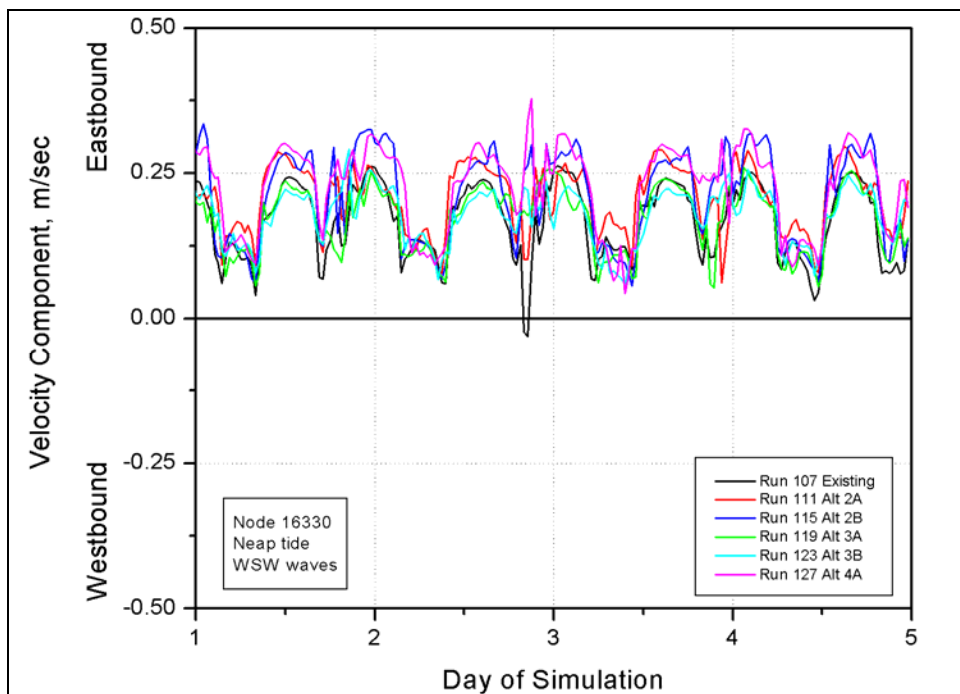
Figure E441.   East-west velocity component at node 16330 (neap tide, west-southwest waves)
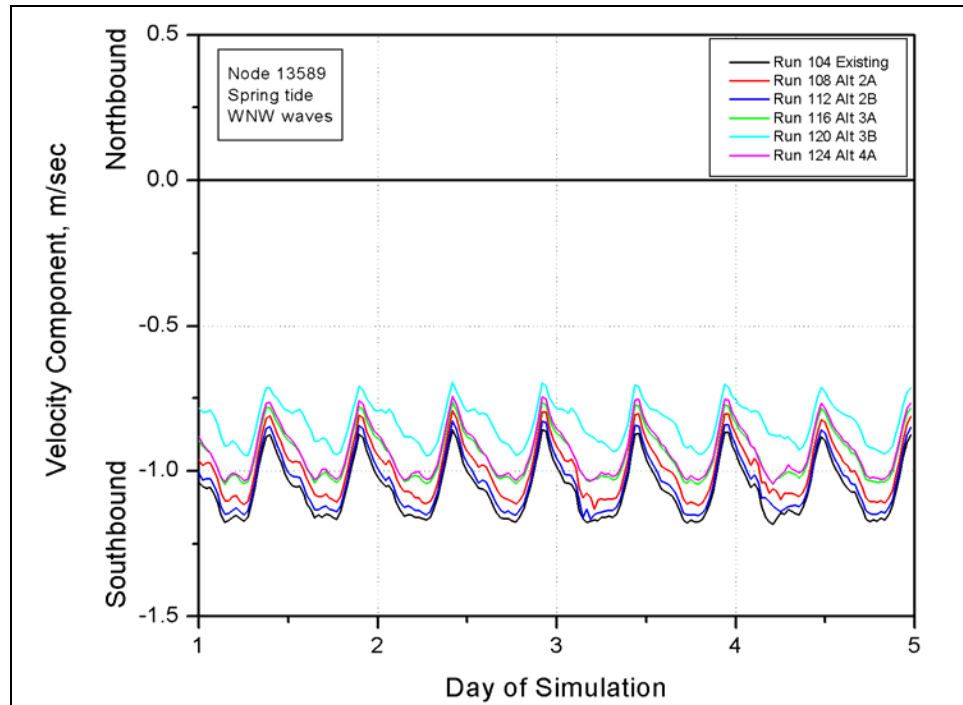
Figure E442.   North-south velocity component at node 13589 (spring tide, west-northwest waves)
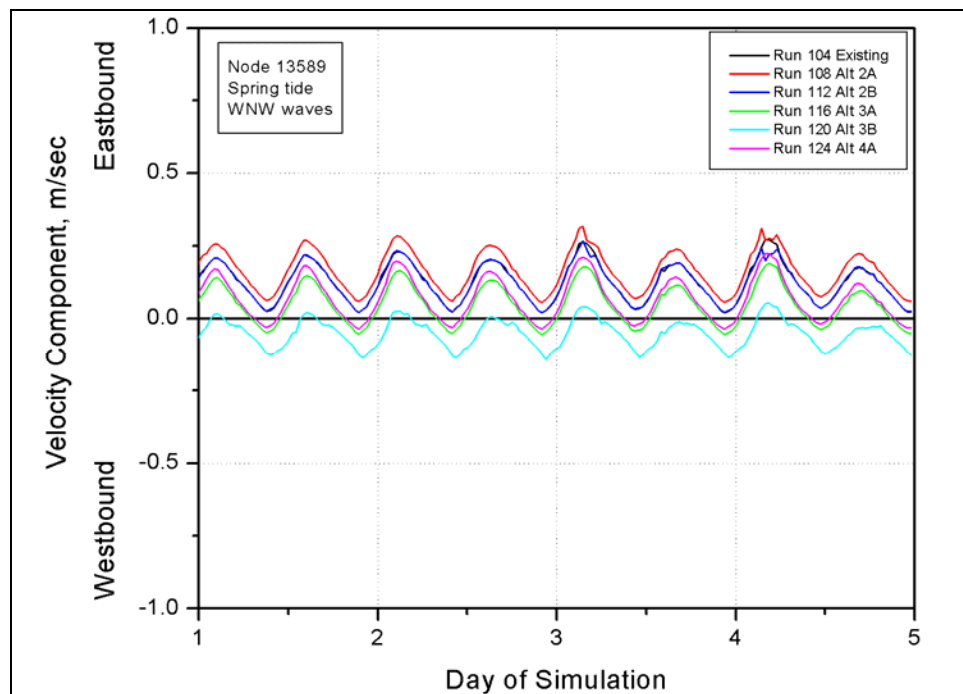
Figure E443.   East-west velocity component at node 13589 (spring tide, west-northwest waves)
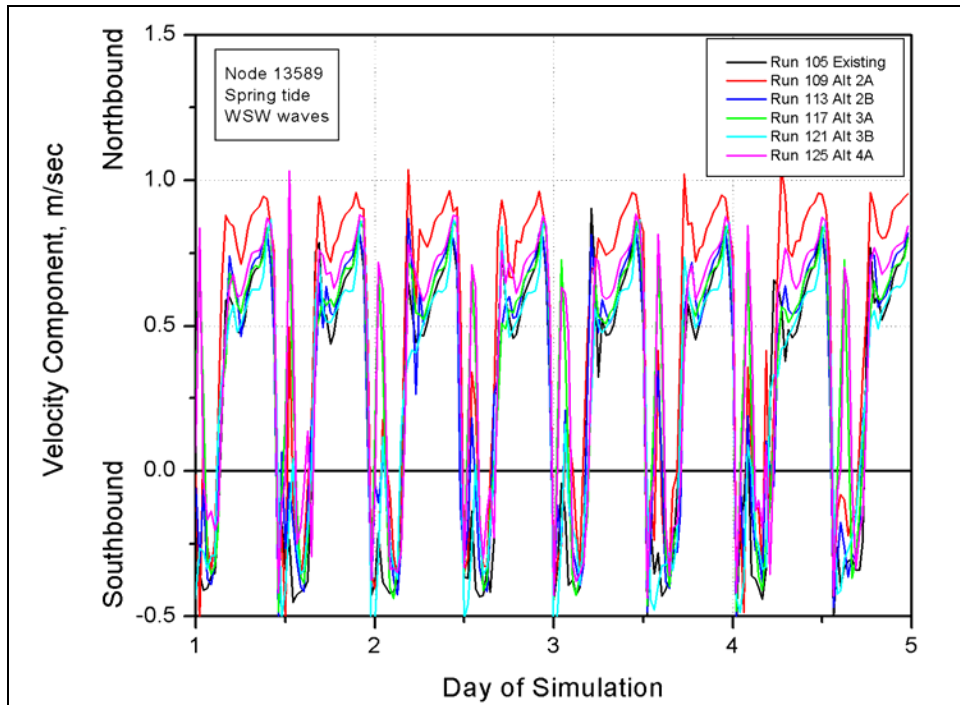
Figure E444.   North-south velocity component at node 13589 (spring tide, west-southwest waves)
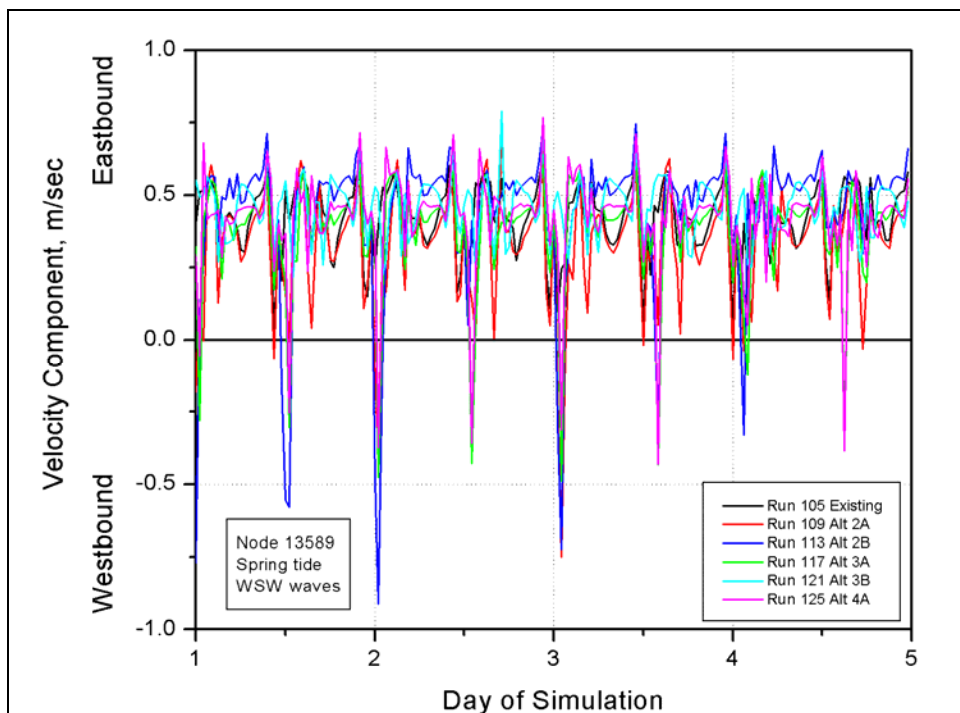
Figure E445.   East-west velocity component at node 13589 (spring tide, west-southwest waves)
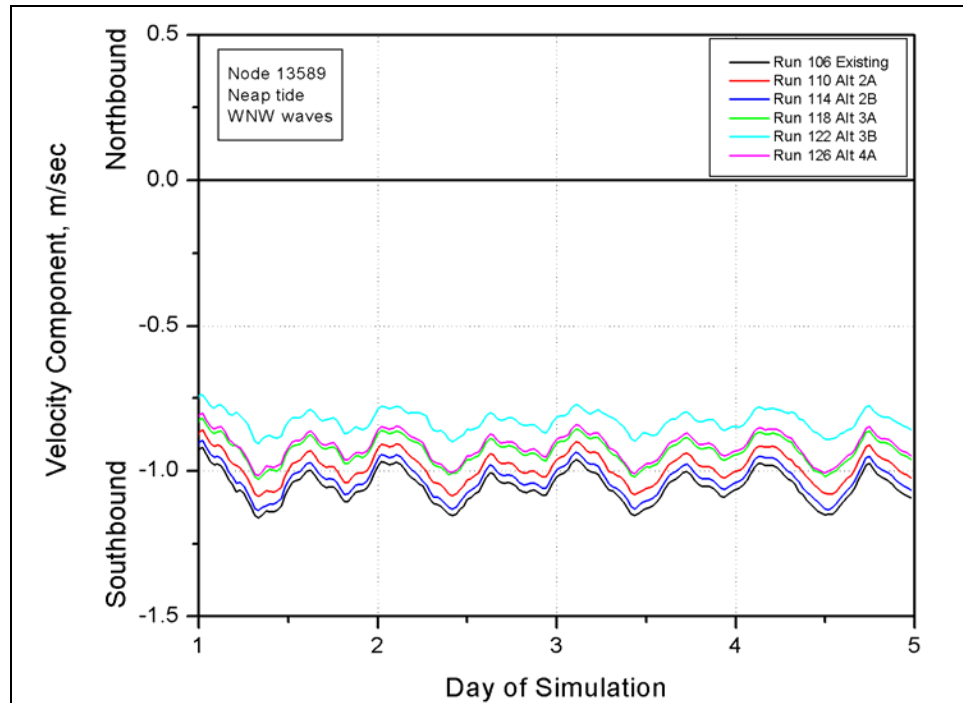
Figure E446.   North-south velocity component at node 13589 (neap tide, west-northwest waves)
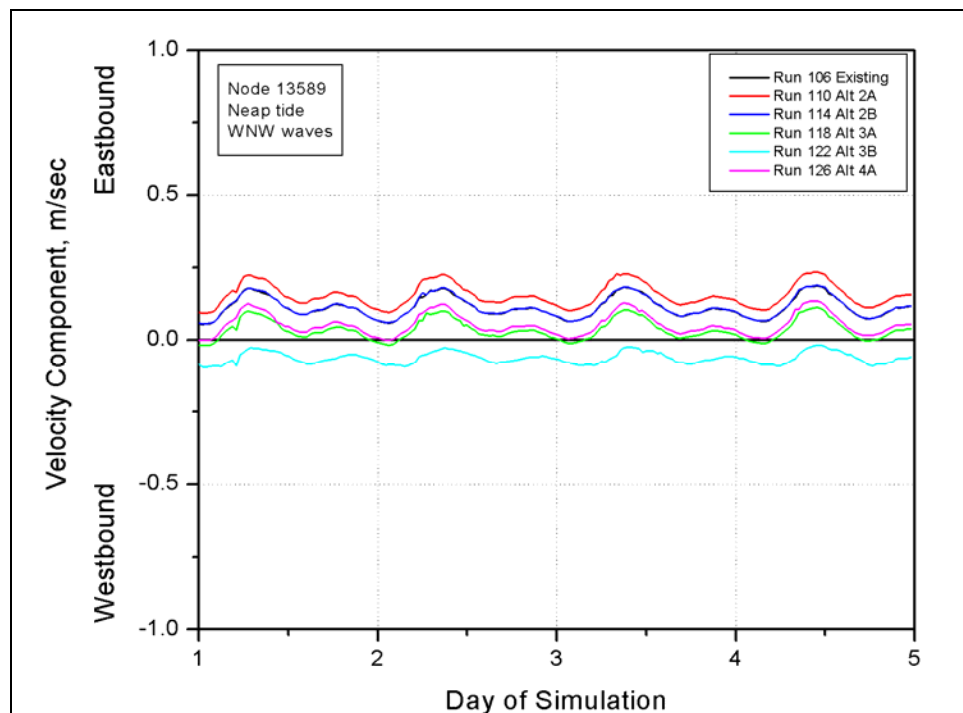
Figure E447.   East-west velocity component at node 13589 (neap tide, west-northwest waves)
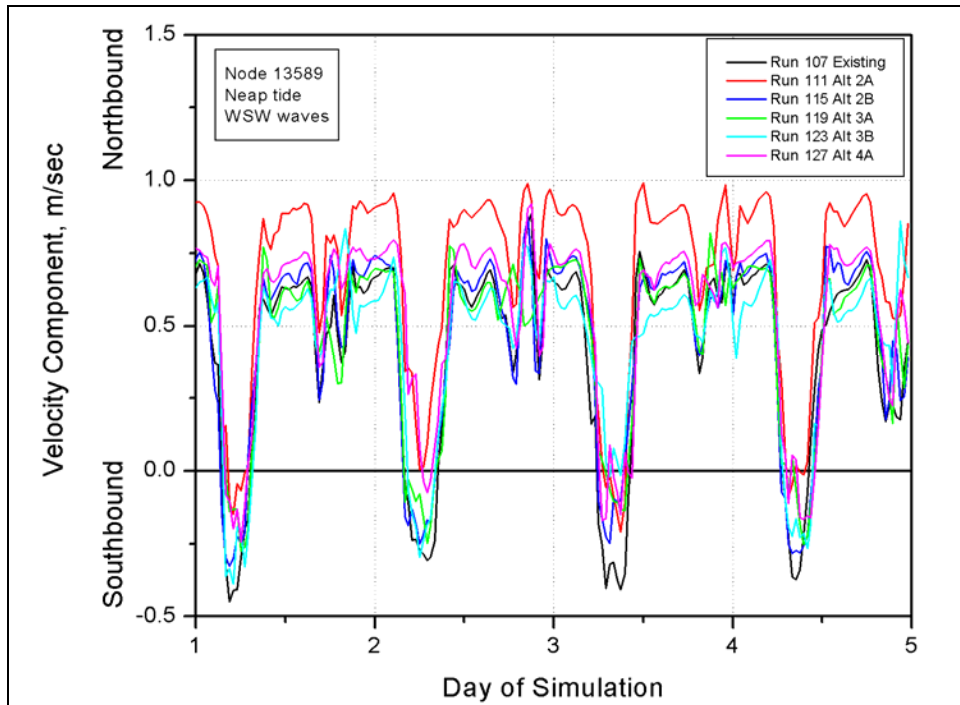
Figure E448.   North-south velocity component at node 13589 (neap tide, west-southwest waves)
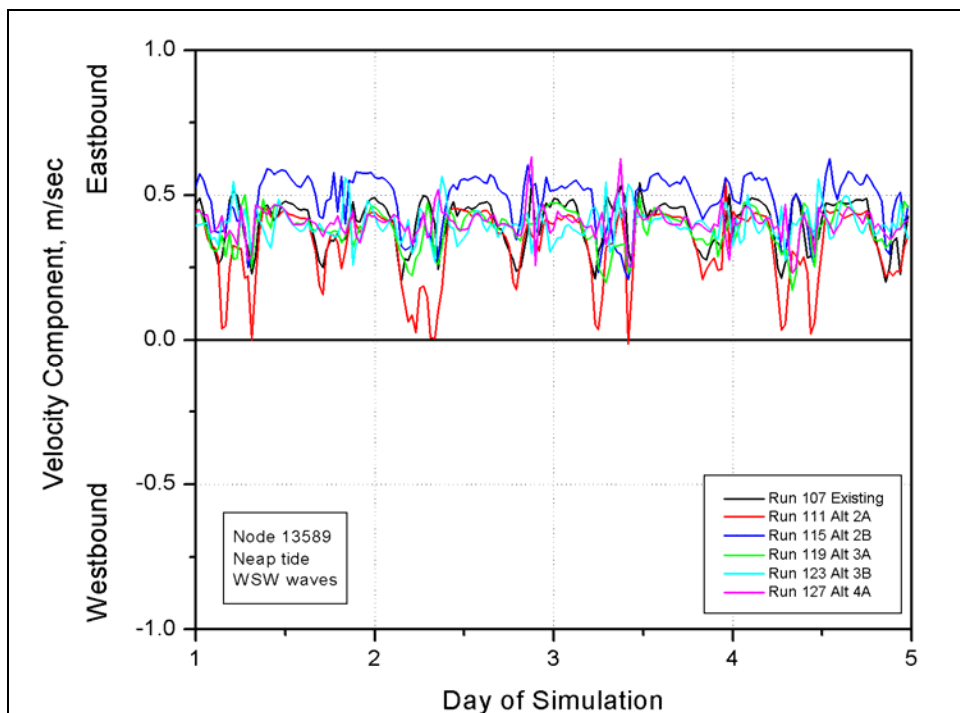
Figure E449.   East-west velocity component at node 13589 (neap tide, west-southwest waves)
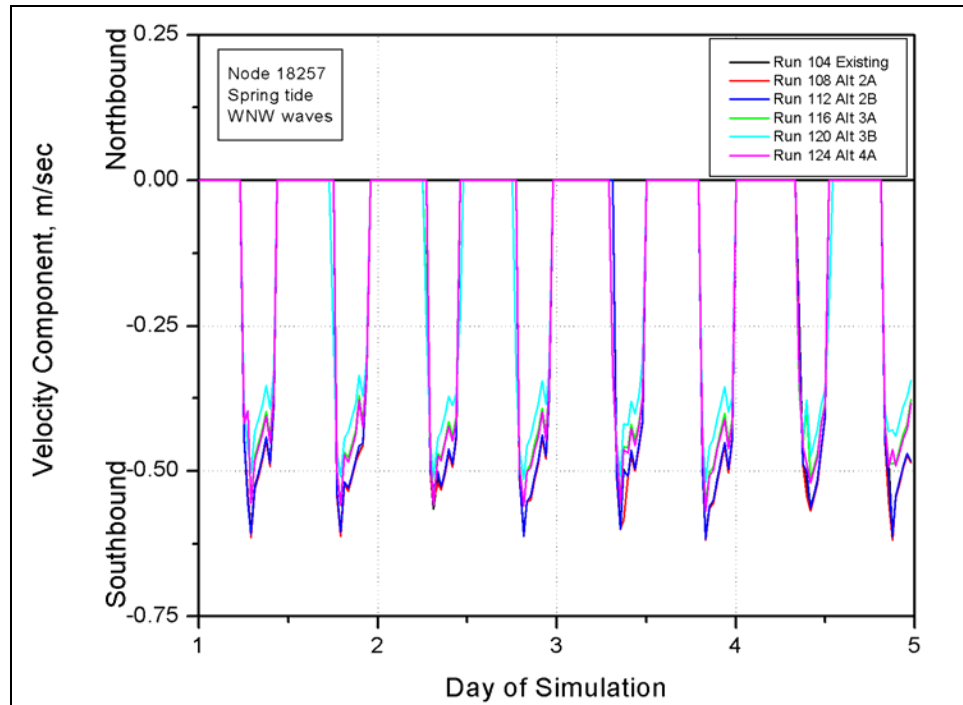
Figure E450.   North-south velocity component at node 18257 (spring tide, west-northwest waves)
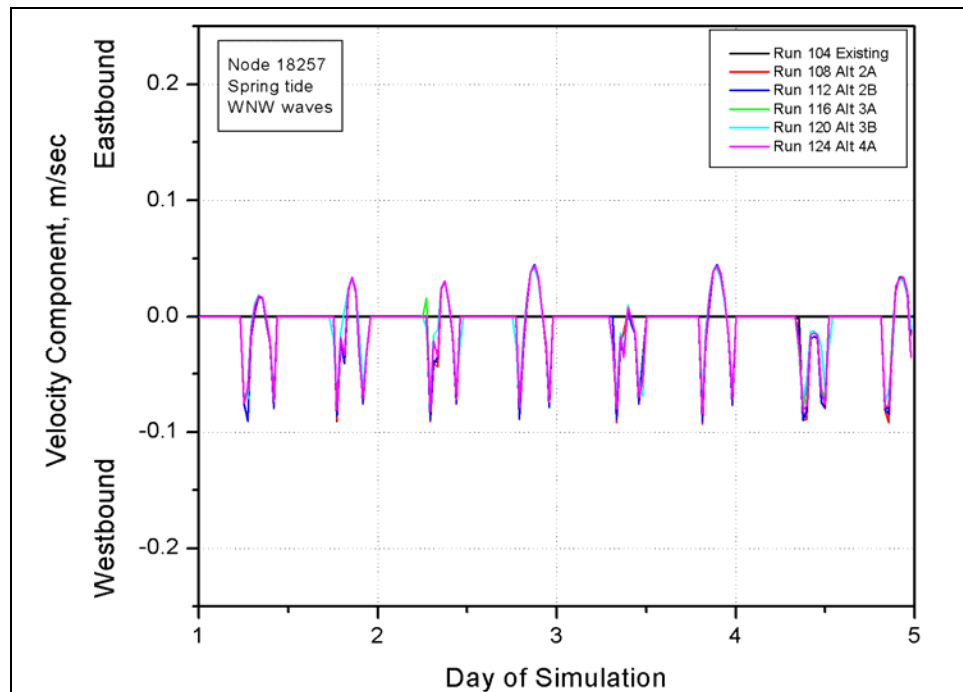
Figure E451.   East-west velocity component at node 18257 (spring tide, west-northwest waves)
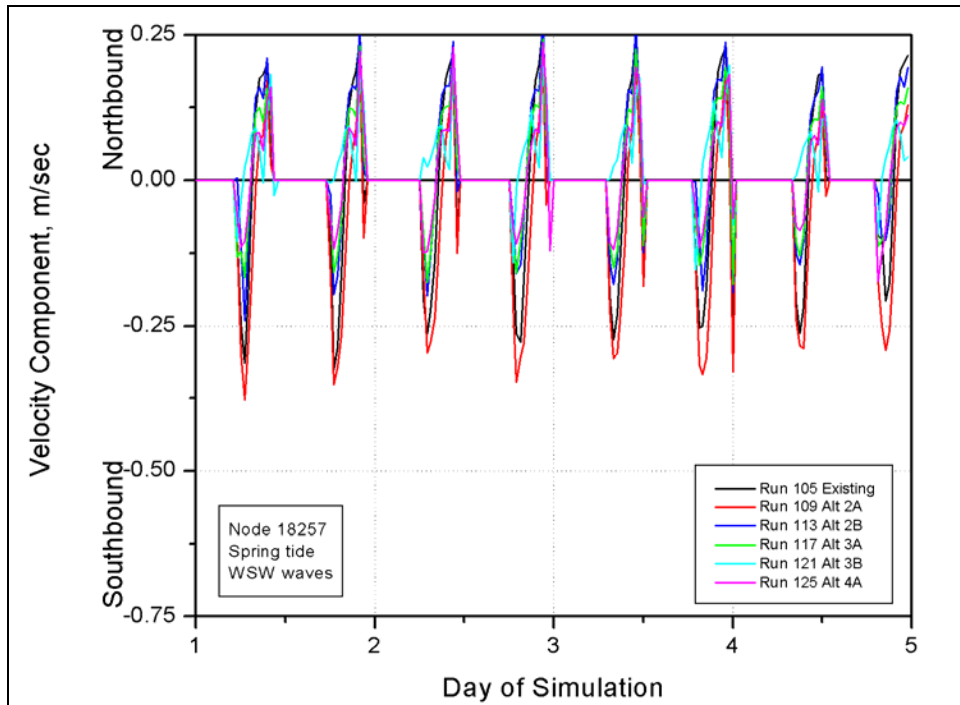
Figure E452.   North-south velocity component at node 18257 (spring tide, west-southwest waves)
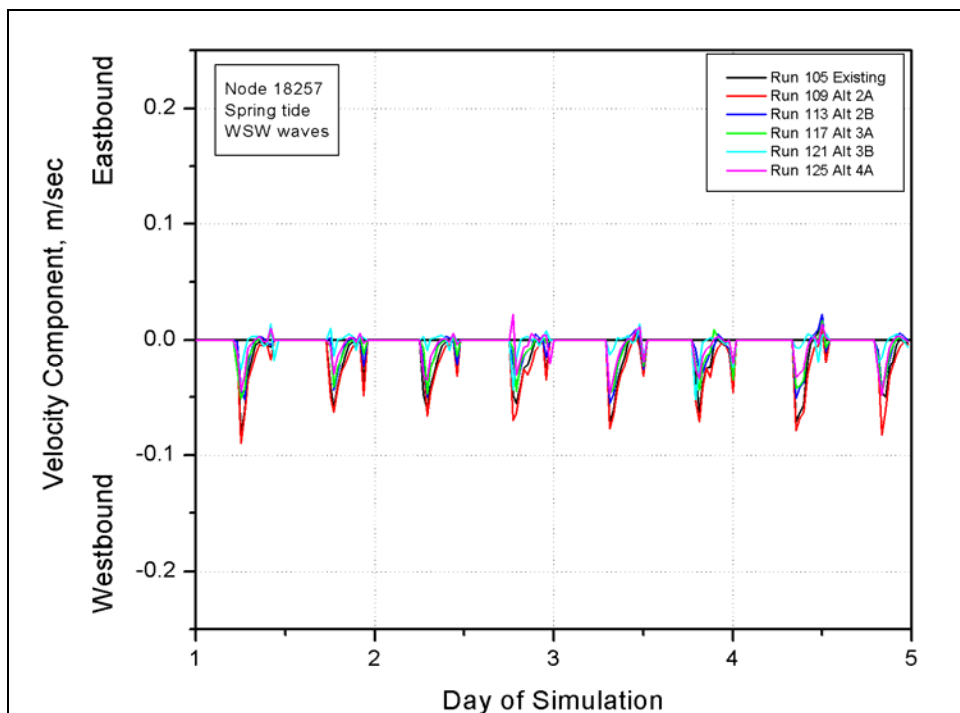
Figure E453.   East-west velocity component at node 18257 (spring tide, west-southwest waves)
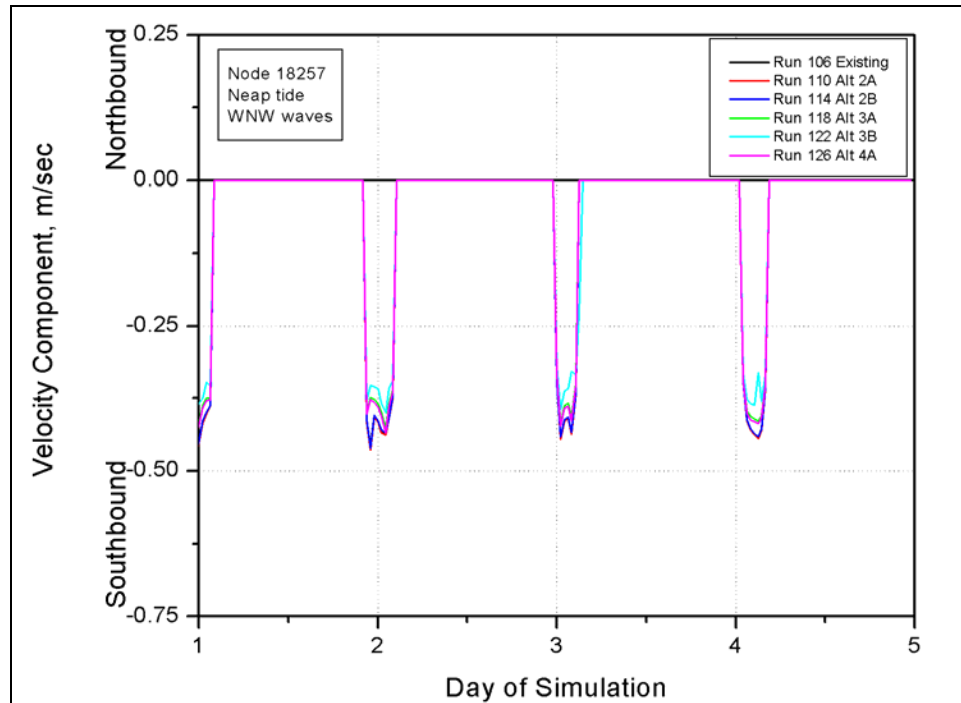
Figure E454. North-south velocity component at node 18257 (neap tide, west-northwest waves)
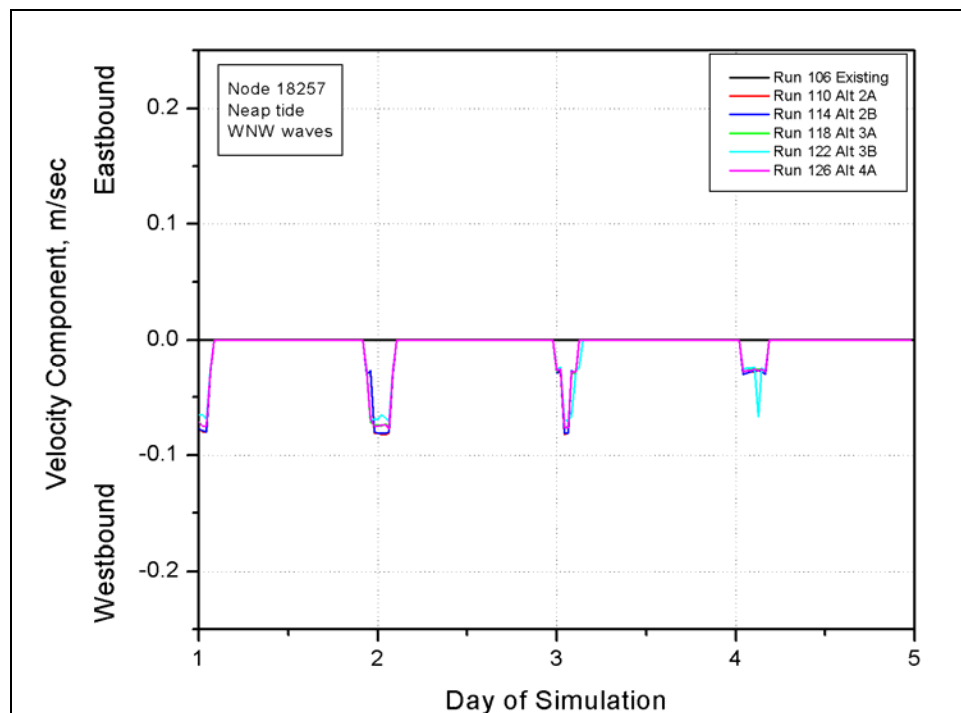
Figure E455. East-west velocity component at node 18257 (neap tide, west-northwest waves)
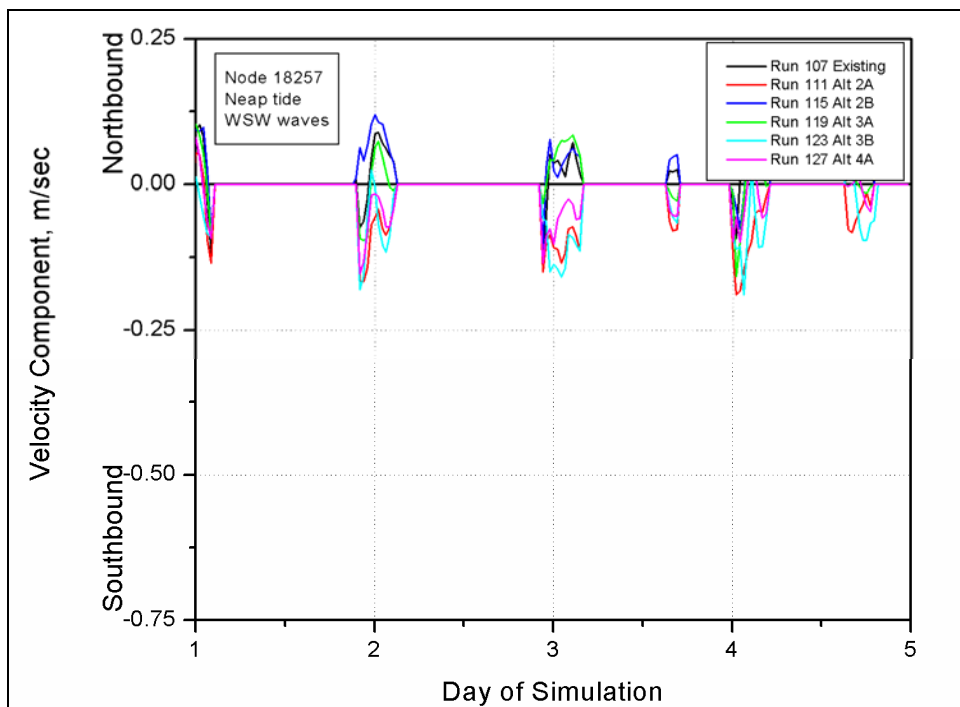
Figure E456.   North-south velocity component at node 18257 (neap tide, west-southwest waves)
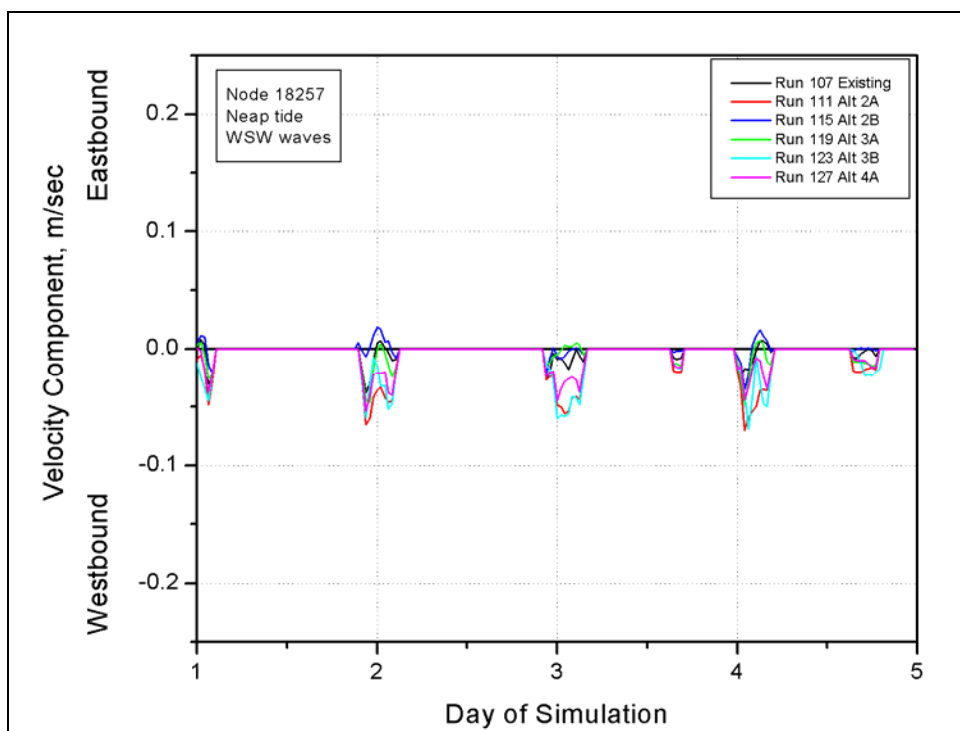
Figure E457.   East-west velocity component at node 18257 (neap tide, west-southwest waves)
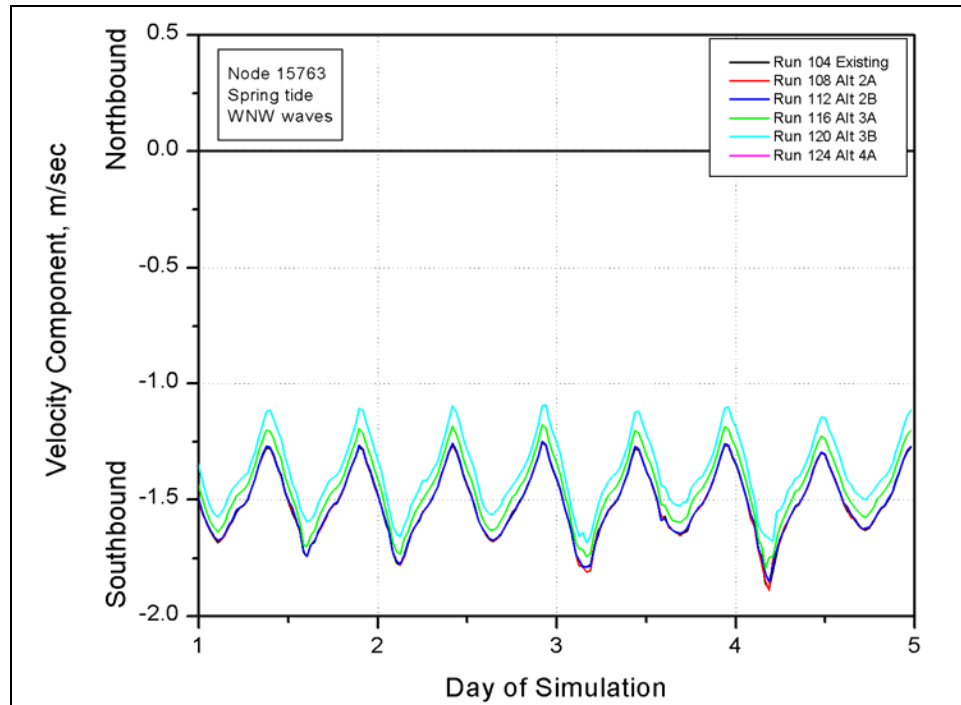
Figure E458.   North-south velocity component at node 15763 (spring tide, west-northwest waves)
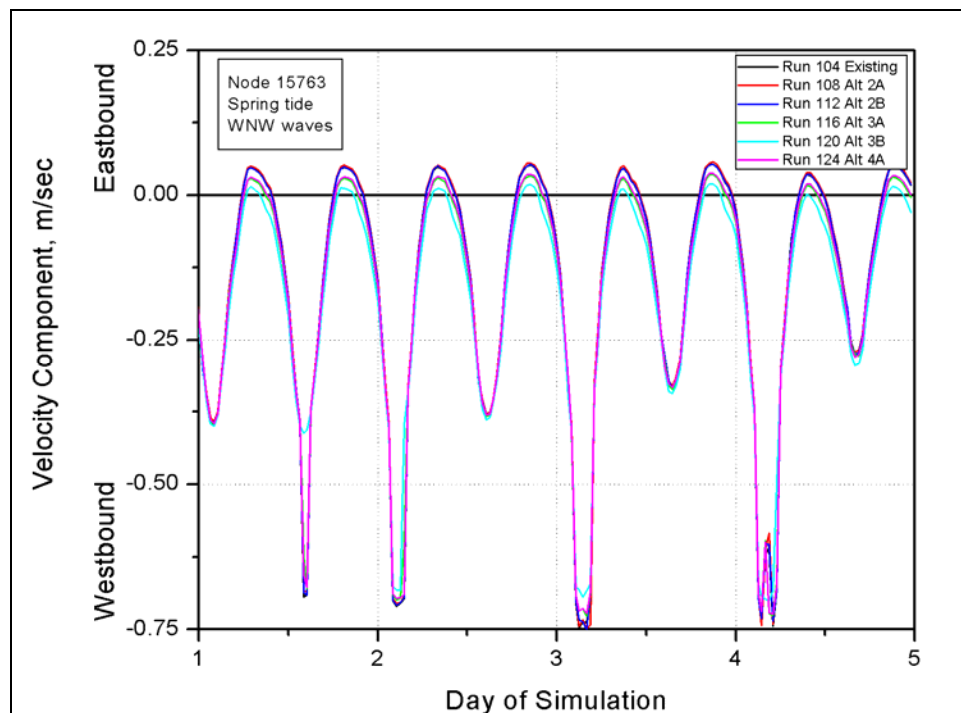
Figure E459.   East-west velocity component at node 15763 (spring tide, west-northwest waves)
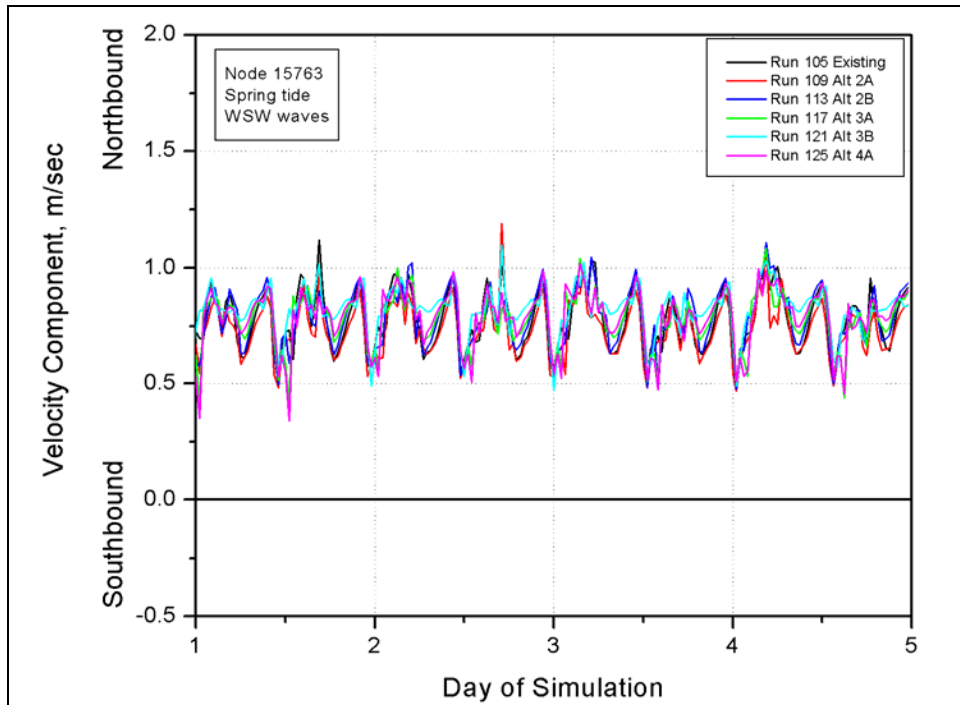
Figure E460.   North-south velocity component at node 15763 (spring tide, west-southwest waves)
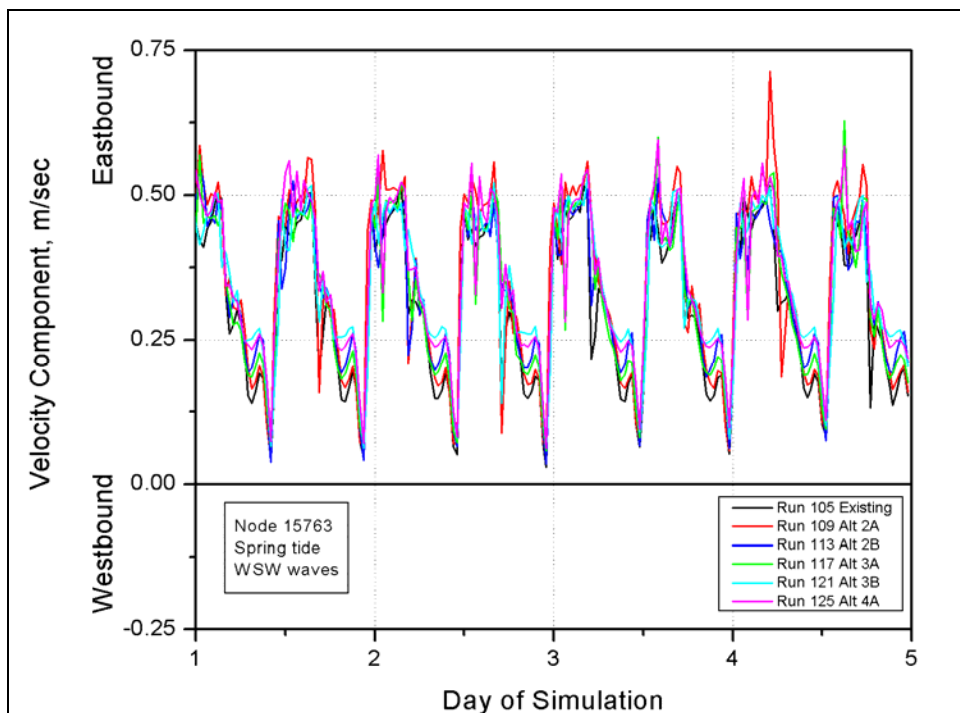
Figure E461.   East-west velocity component at node 15763 (spring tide, west-southwest waves)
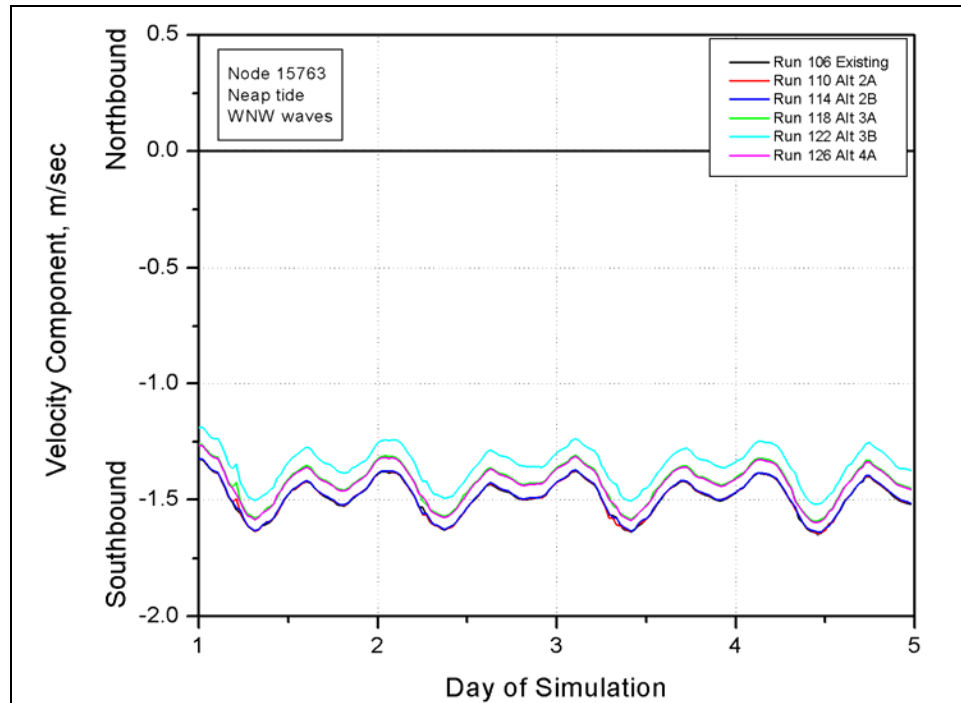
Figure E462. North-south velocity component at node 15763 (neap tide, west-northwest waves)
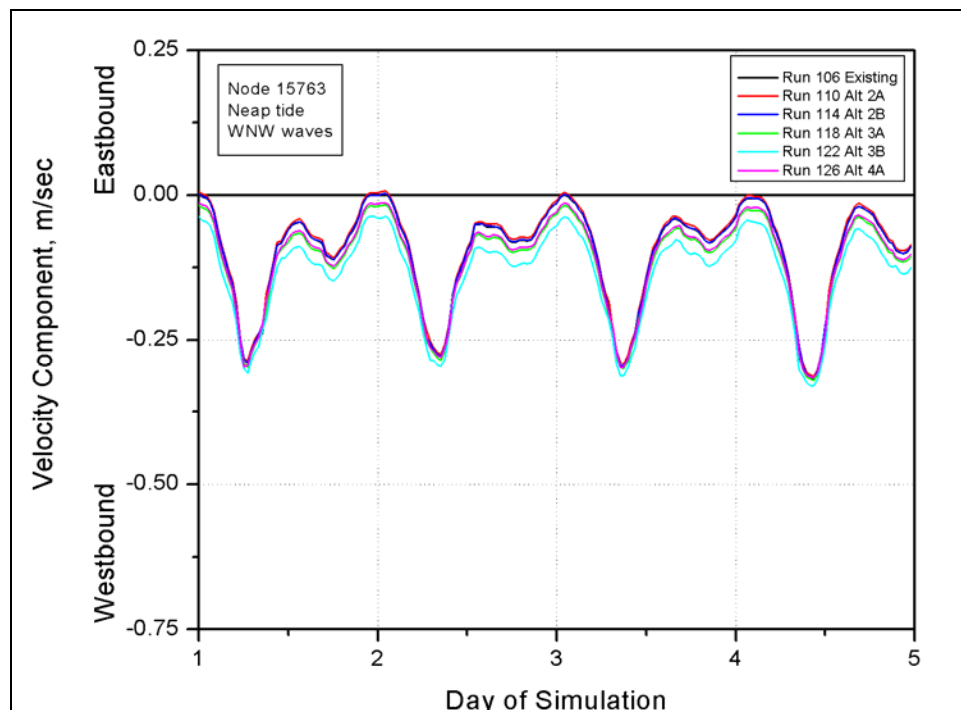
Figure E463. East-west velocity component at node 15763 (neap tide, west-northwest waves)
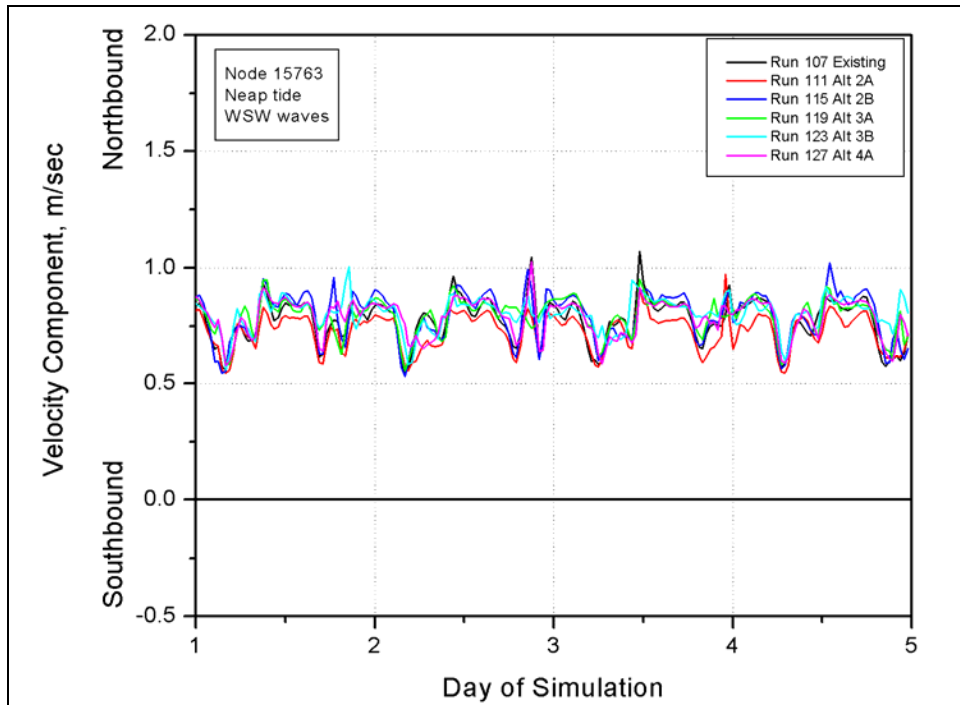
Figure E464.   North-south velocity component at node 15763 (neap tide, west-southwest waves)
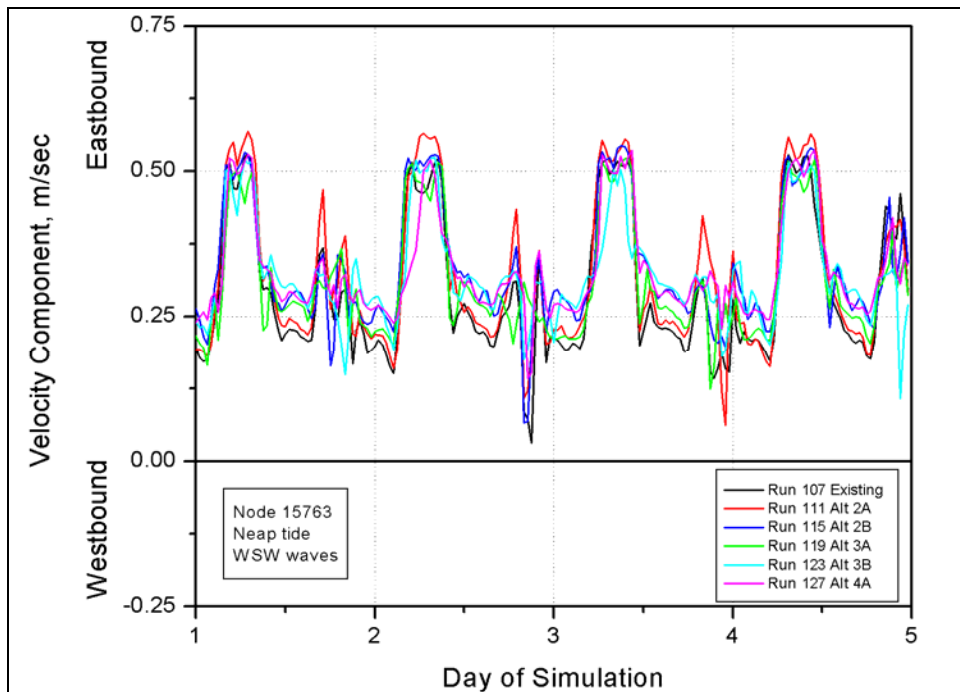
Figure E465.   East-west velocity component at node 15763 (neap tide, west-southwest waves)
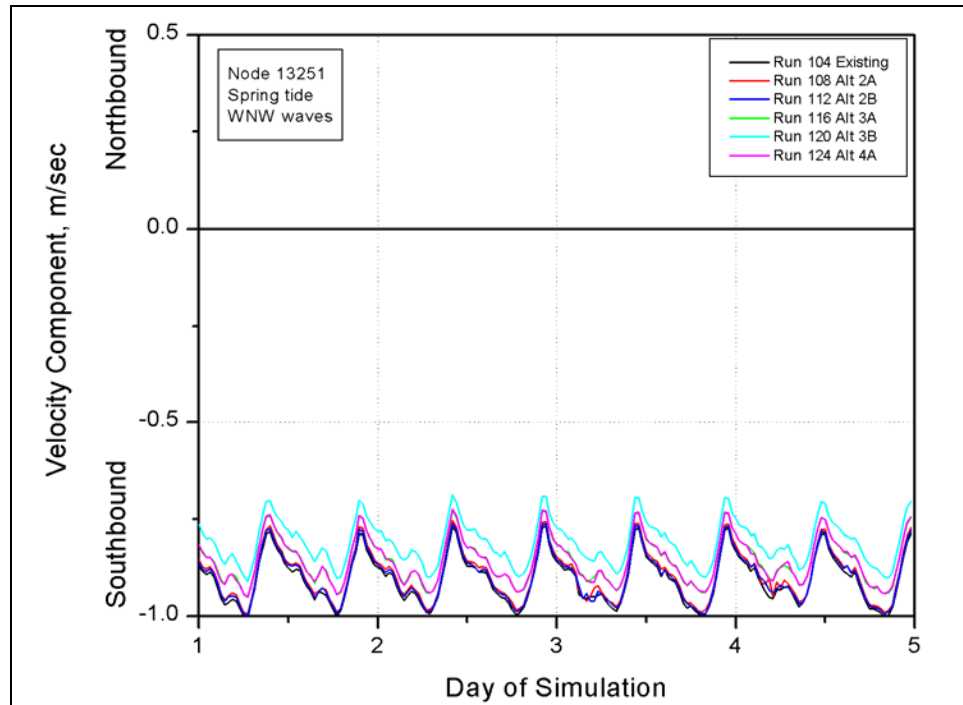
Figure E466. North-south velocity component at node 13251 (spring tide, west-northwest waves)
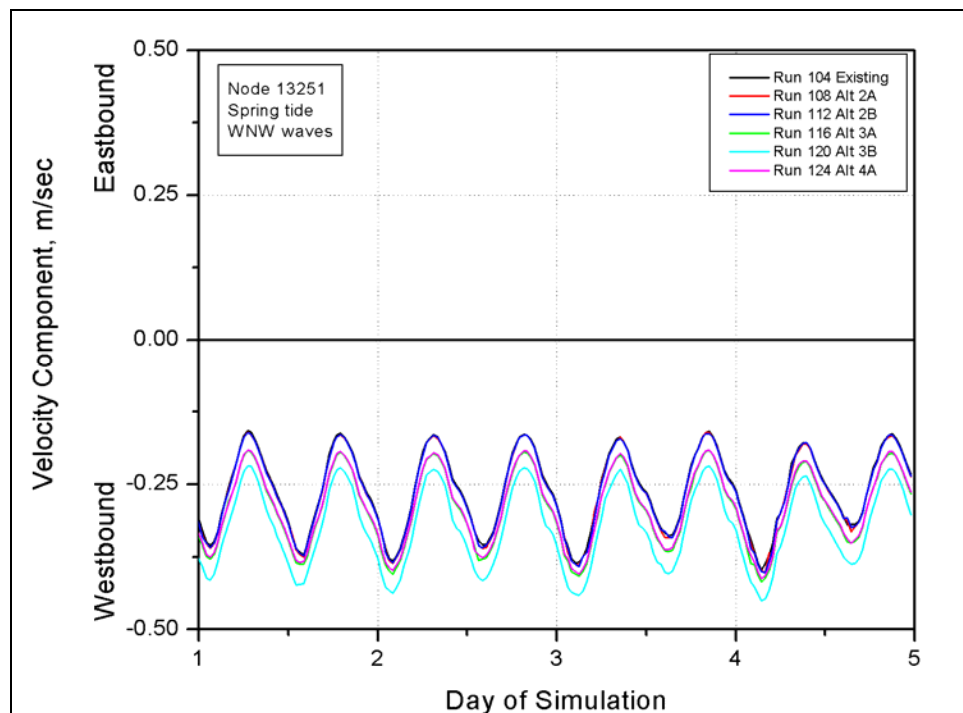
Figure E467. East-west velocity component at node 13251 (spring tide, west-northwest waves)
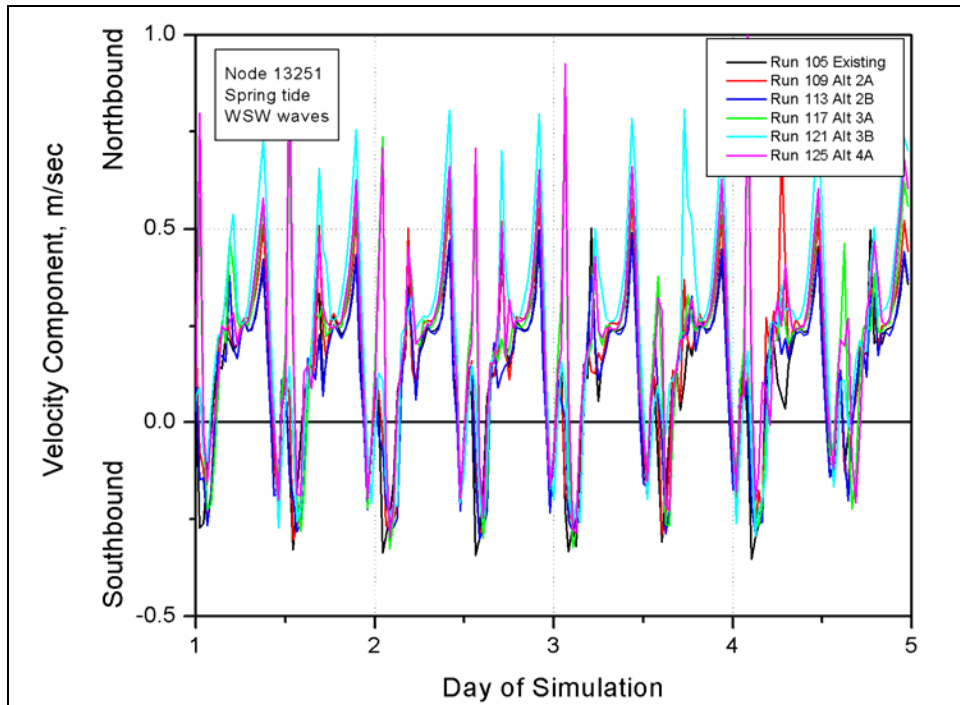
Figure E468.   North-south velocity component at node 13251 (spring tide, west-southwest waves)
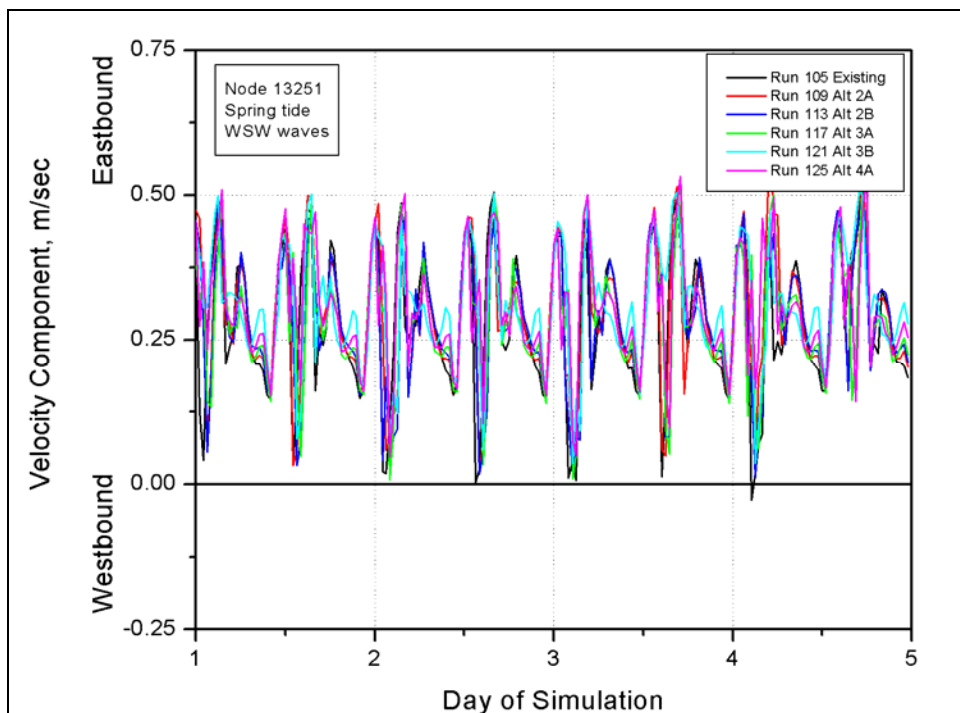
Figure E469.   East-west velocity component at node 13251 (spring tide, west-southwest waves)
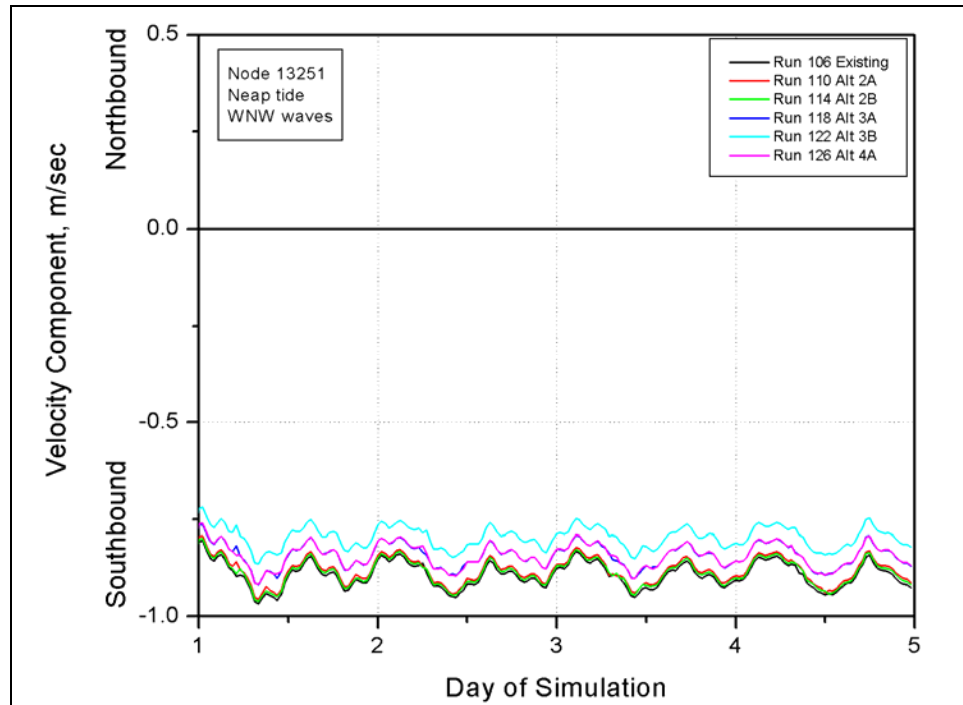
Figure E470.   North-south velocity component at node 13251 (neap tide, west-northwest waves)
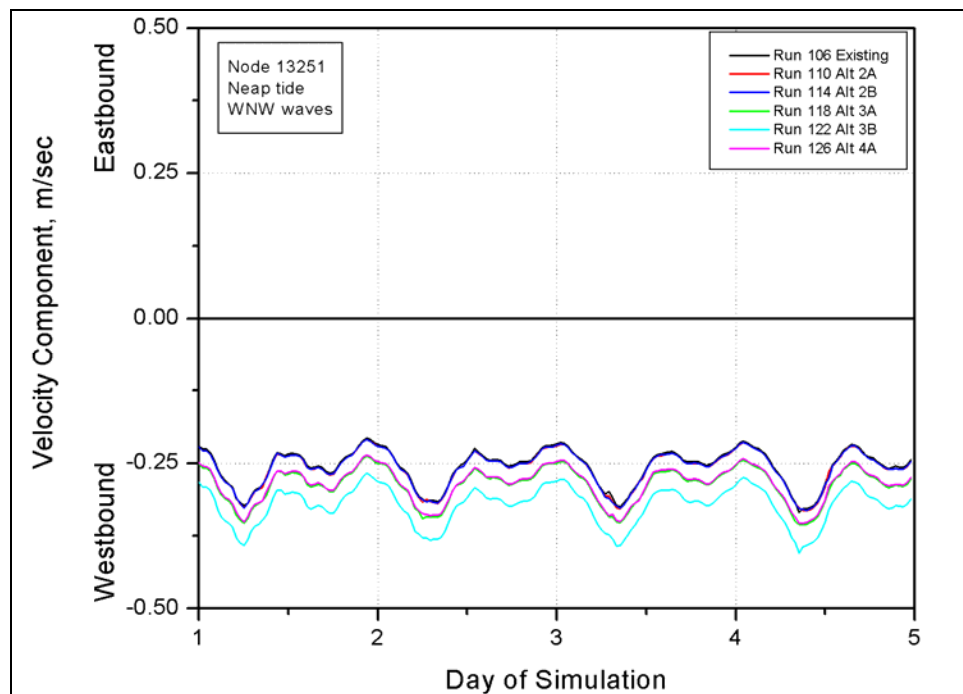
Figure E471.   East-west velocity component at node 13251 (neap tide, west-northwest waves)
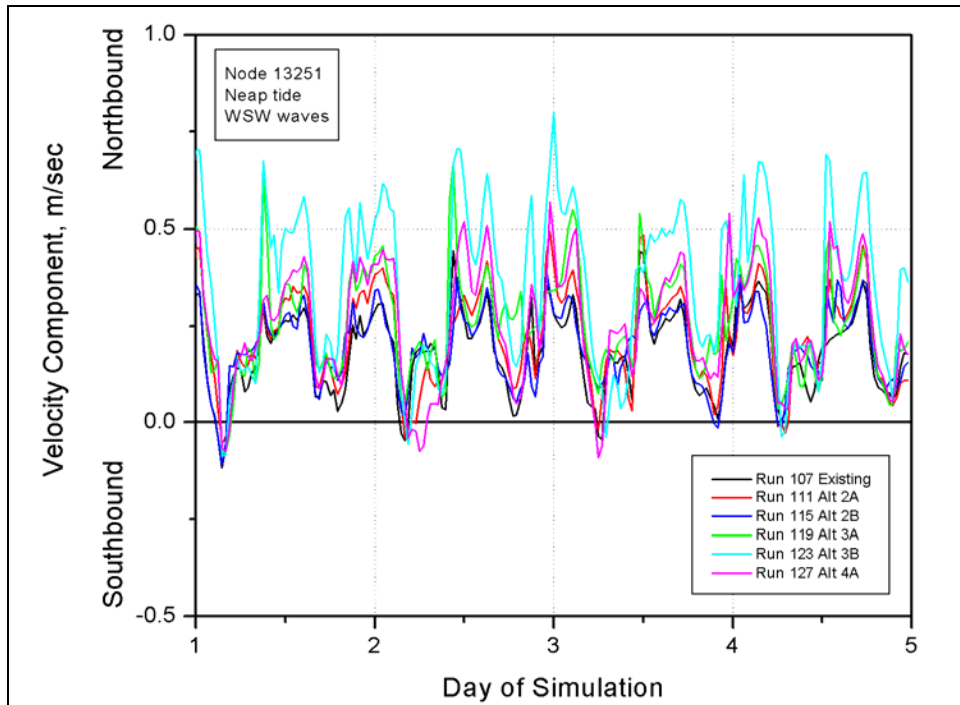
Figure E472.   North-south velocity component at node 13251 (neap tide, west-southwest waves)
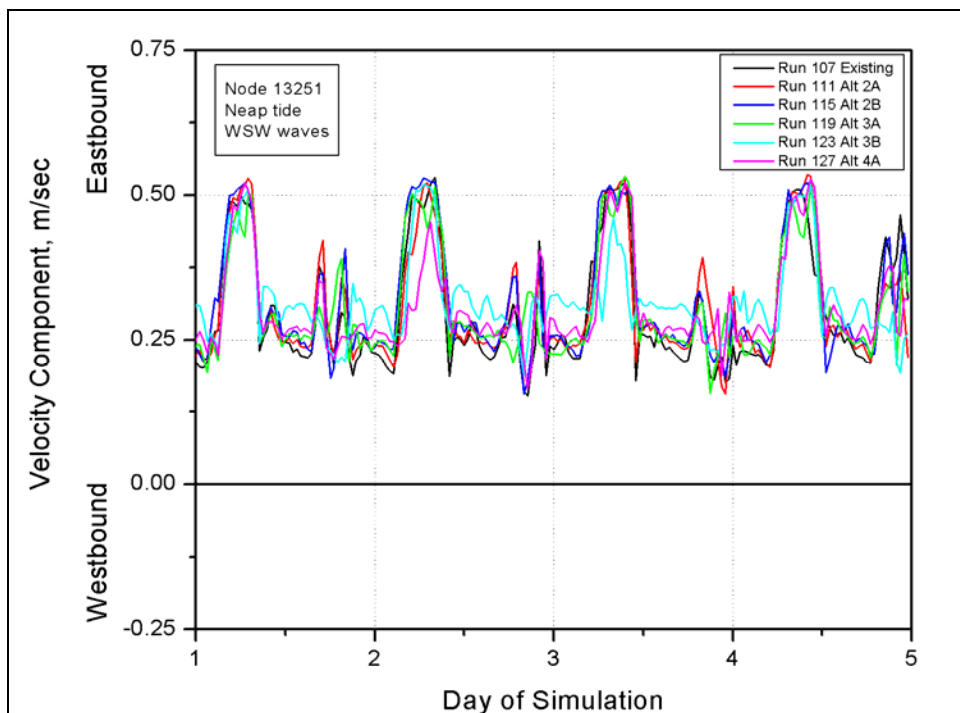
Figure E473.   East-west velocity component at node 13251 (neap tide, west-southwest waves)
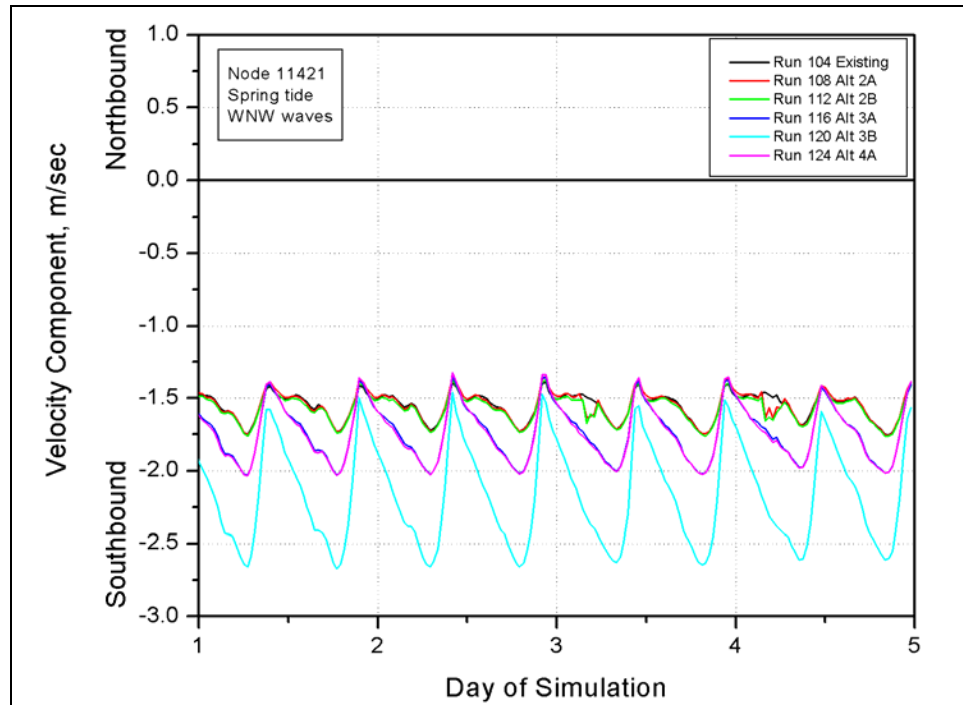
Figure E474. North-south velocity component at node 11421 (spring tide, west-northwest waves)
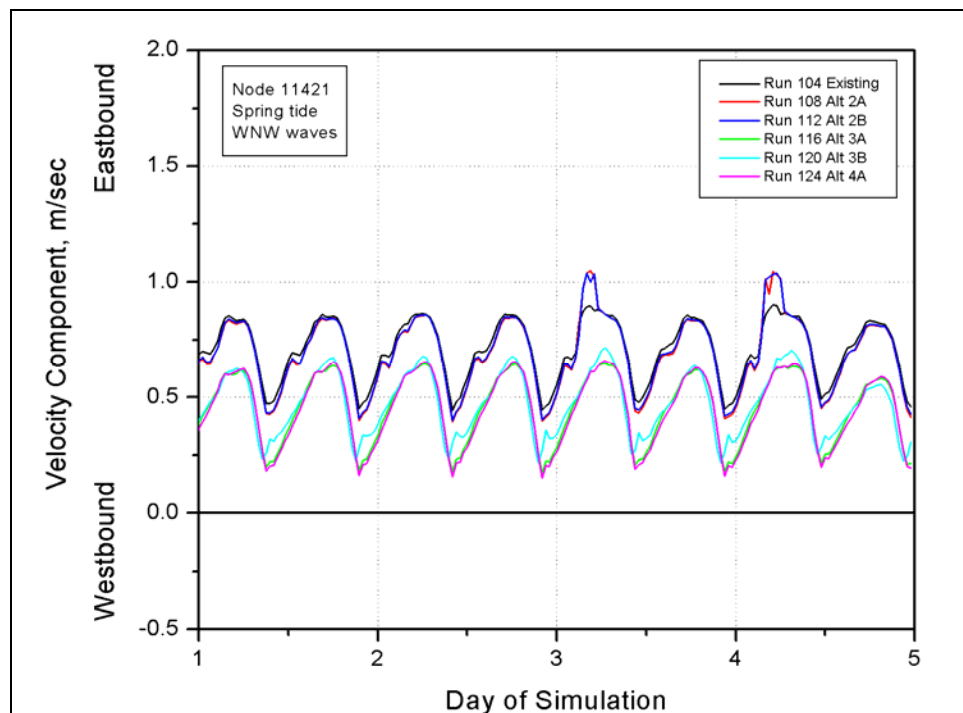
Figure E475. East-west velocity component at node 11421 (spring tide, west-northwest waves)
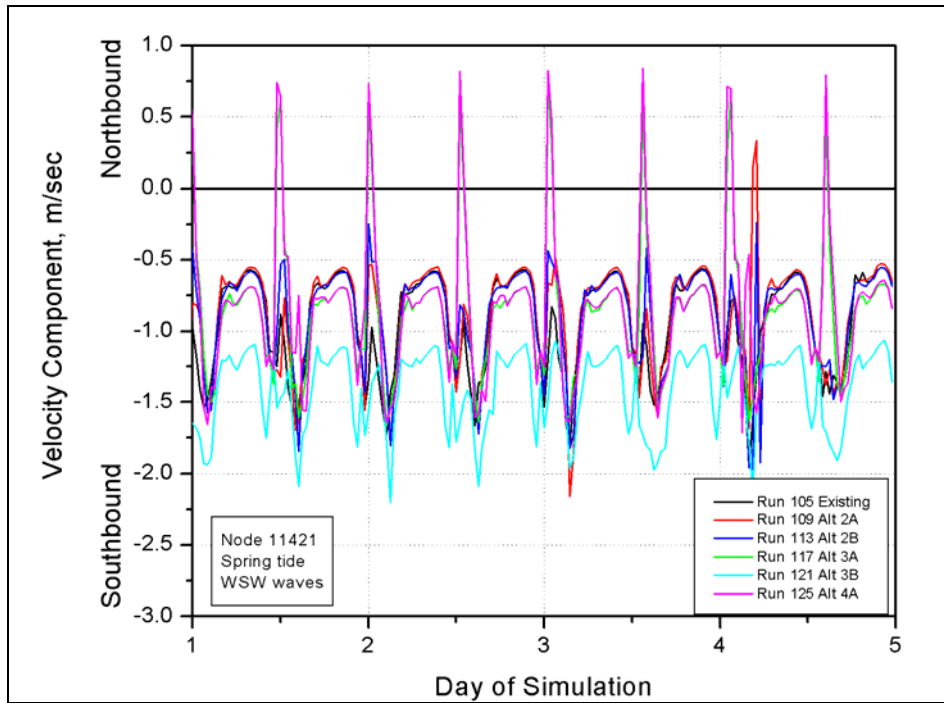
Figure E476.   North-south velocity component at node 11421 (spring tide, west-southwest waves)
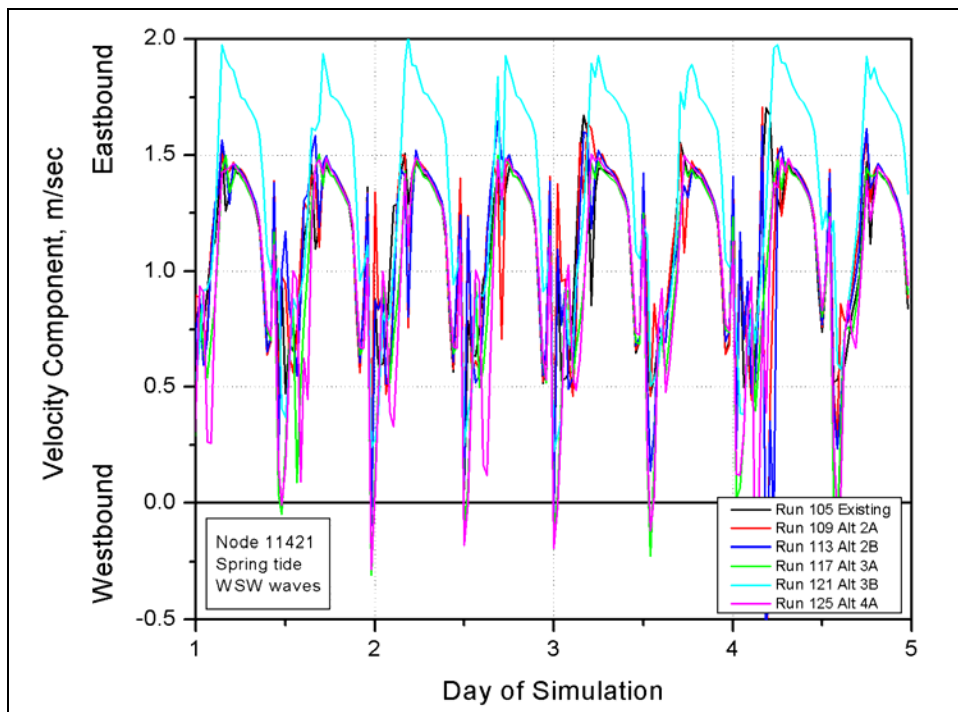
Figure E477.   East-west velocity component at node 11421 (spring tide, west-southwest waves)
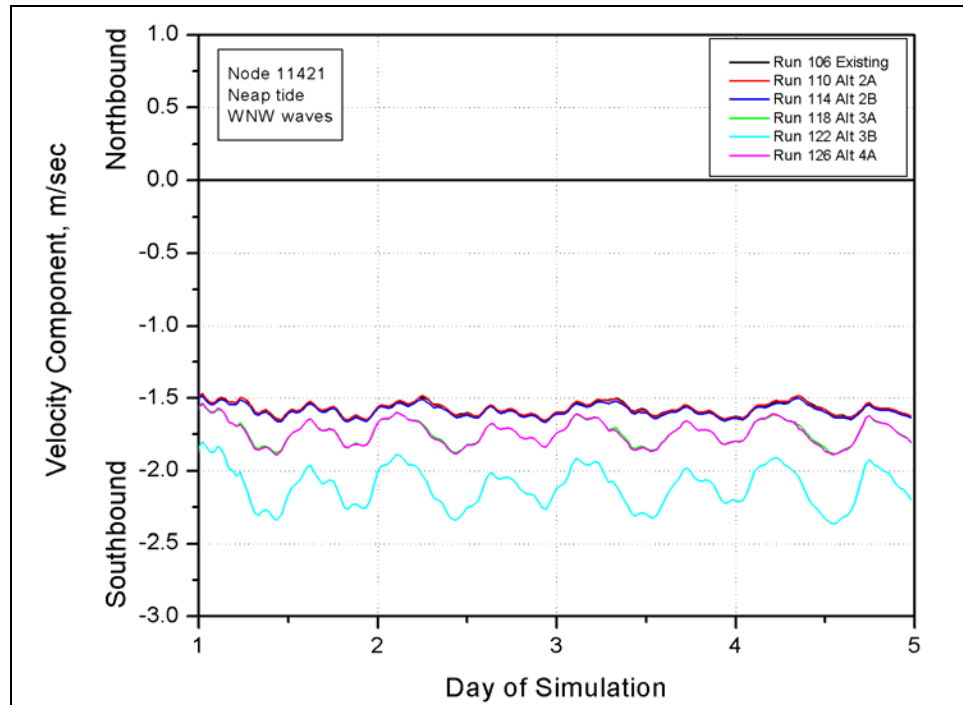
Figure E478.   North-south velocity component at node 11421 (neap tide, west-
northwest waves)
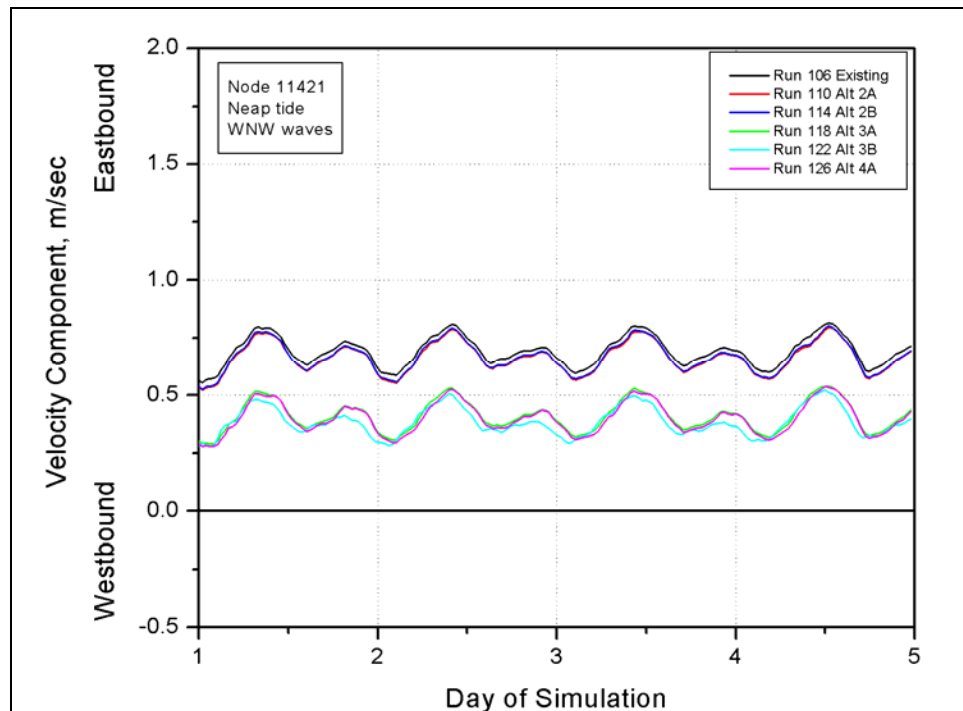
Figure E479.   East-west velocity component at node 11421 (neap tide, west-
northwest waves)
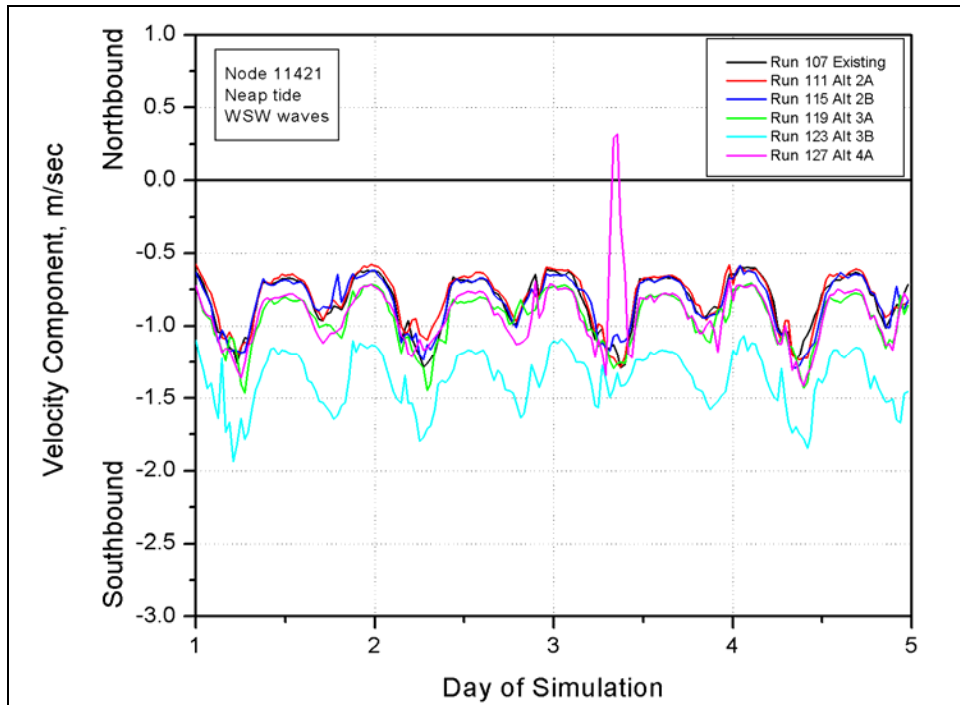
Figure E480.   North-south velocity component at node 11421 (neap tide, west-southwest waves)
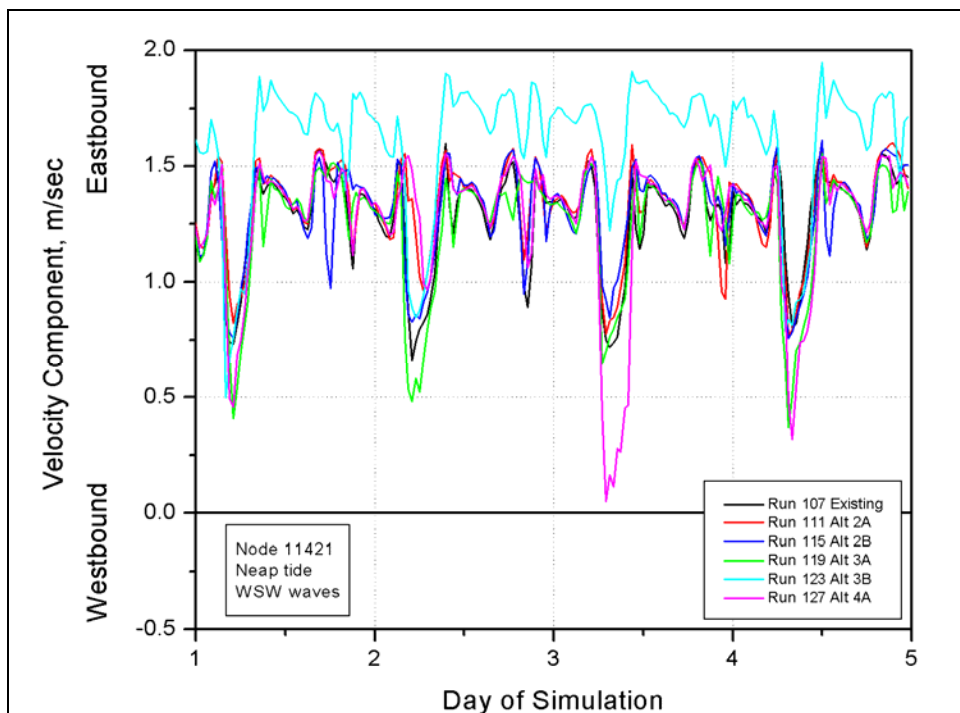
Figure E481.   East-west velocity component at node 11421 (neap tide, west-southwest waves)
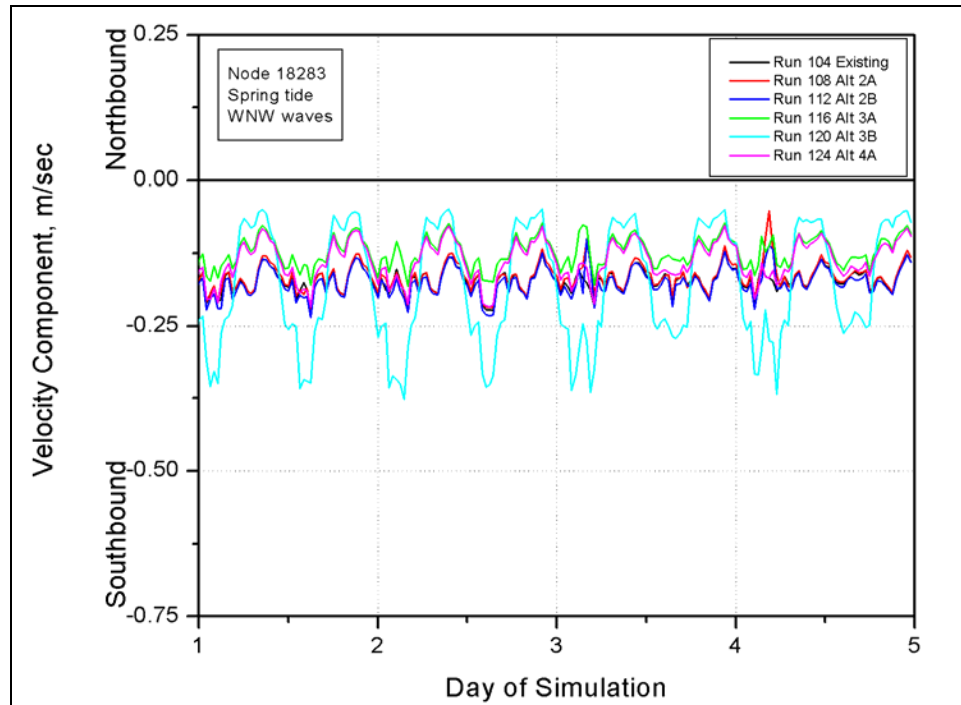
Figure E482.　North-south velocity component at node 18283 (spring tide, west-northwest waves)
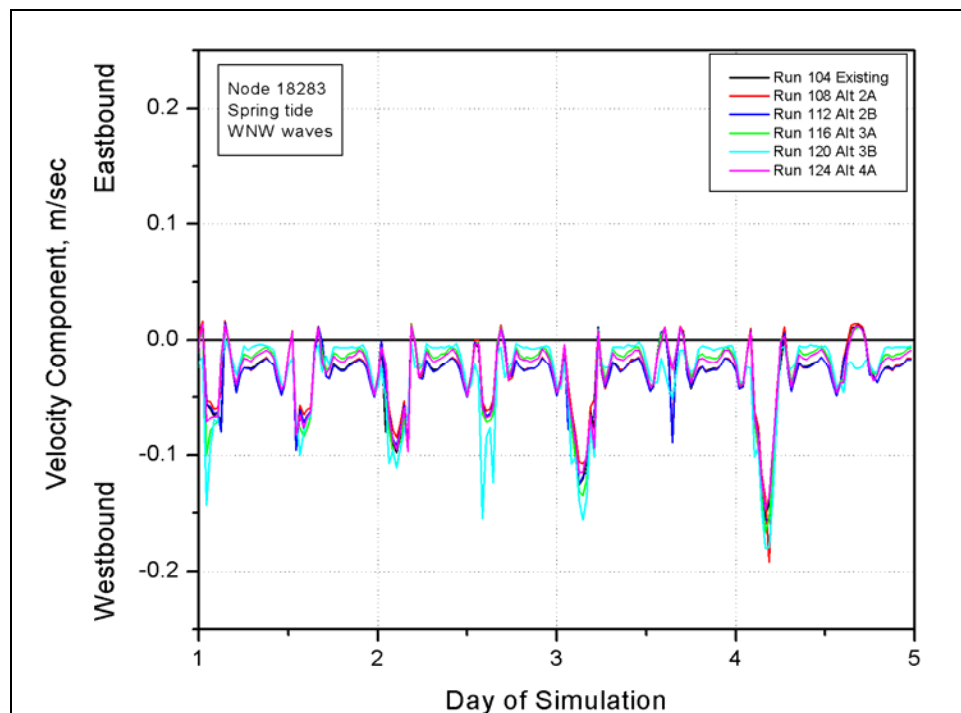
Figure E483.　East-west velocity component at node 18283 (spring tide, west-northwest waves)
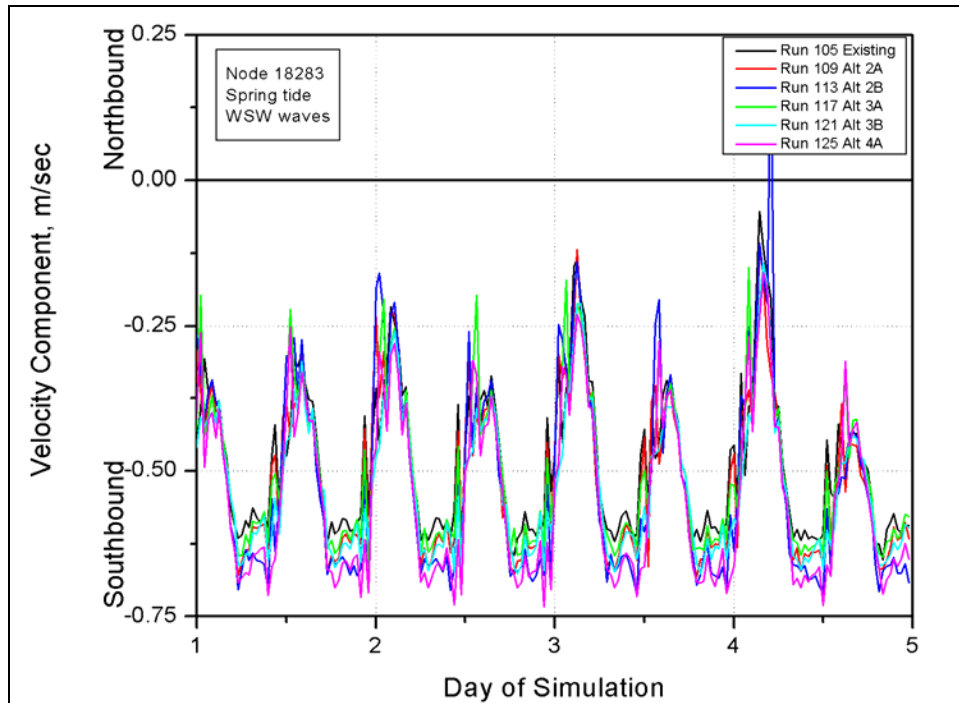
Figure E484.   North-south velocity component at node 18283 (spring tide, west-southwest waves)
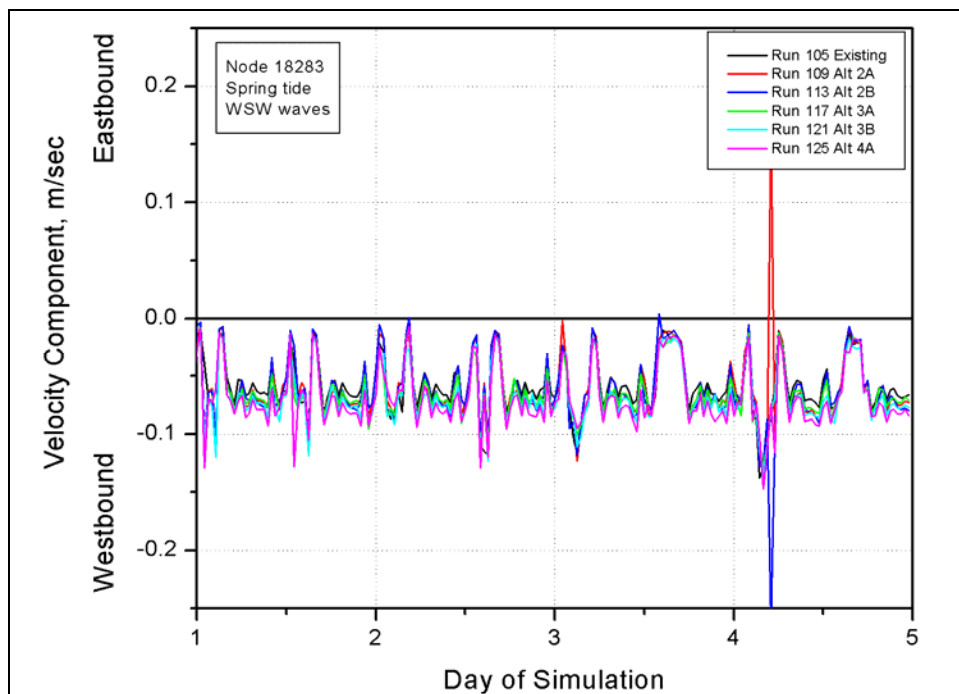
Figure E485.   East-west velocity component at node 18283 (spring tide, west-southwest waves)

Appendix E   Tidal Circulation Simulation Results
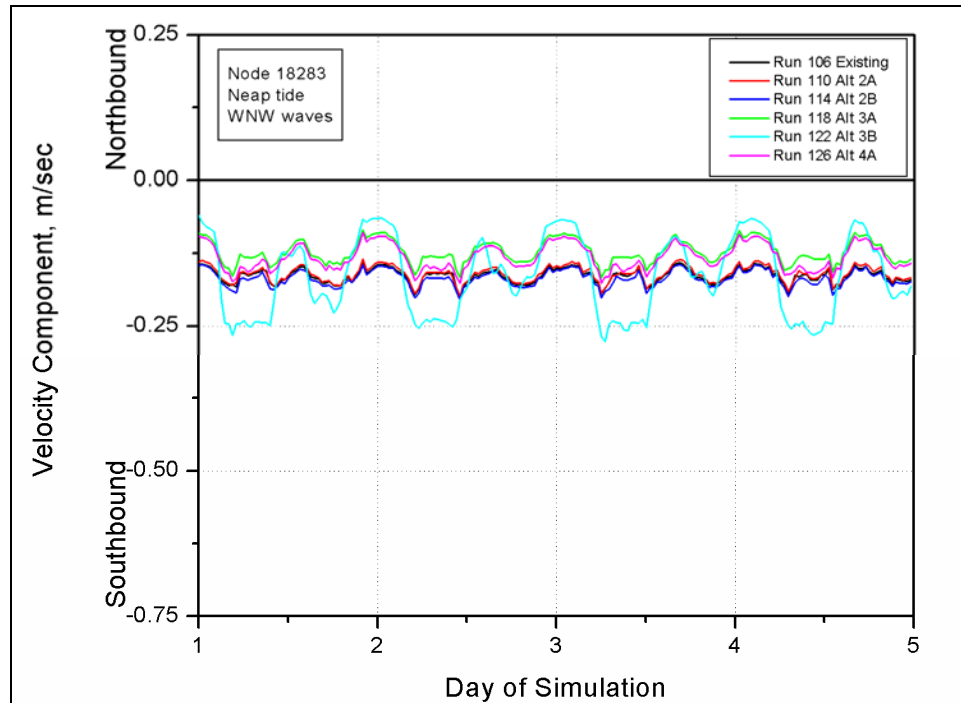
Figure E486.   North-south velocity component at node 18283 (neap tide, west-northwest waves)
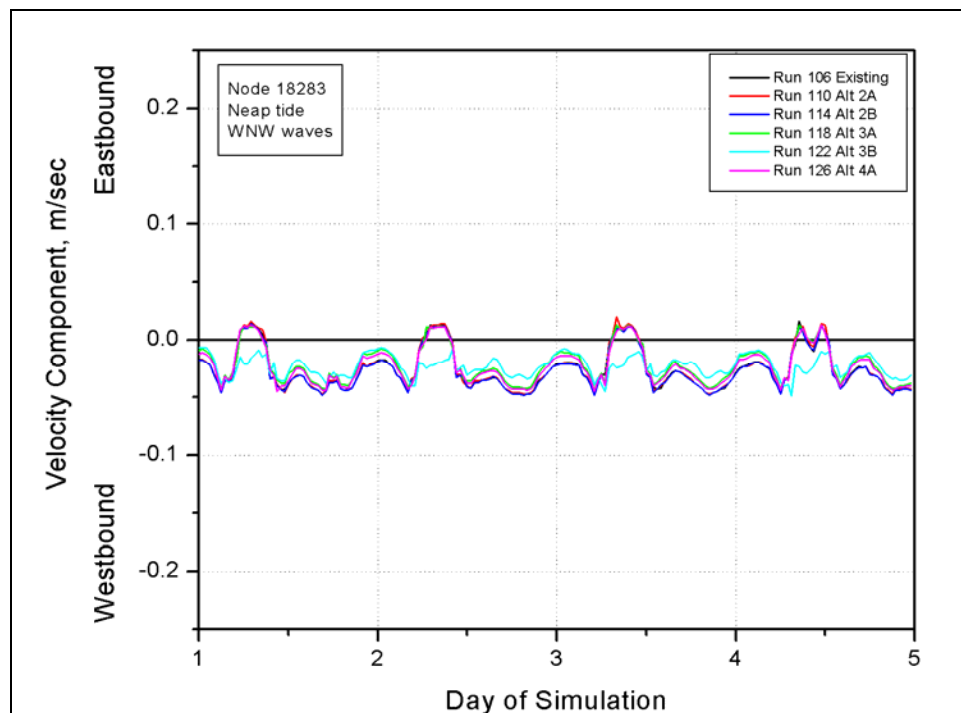
Figure E487.   East-west velocity component at node 18283 (neap tide, west-northwest waves)
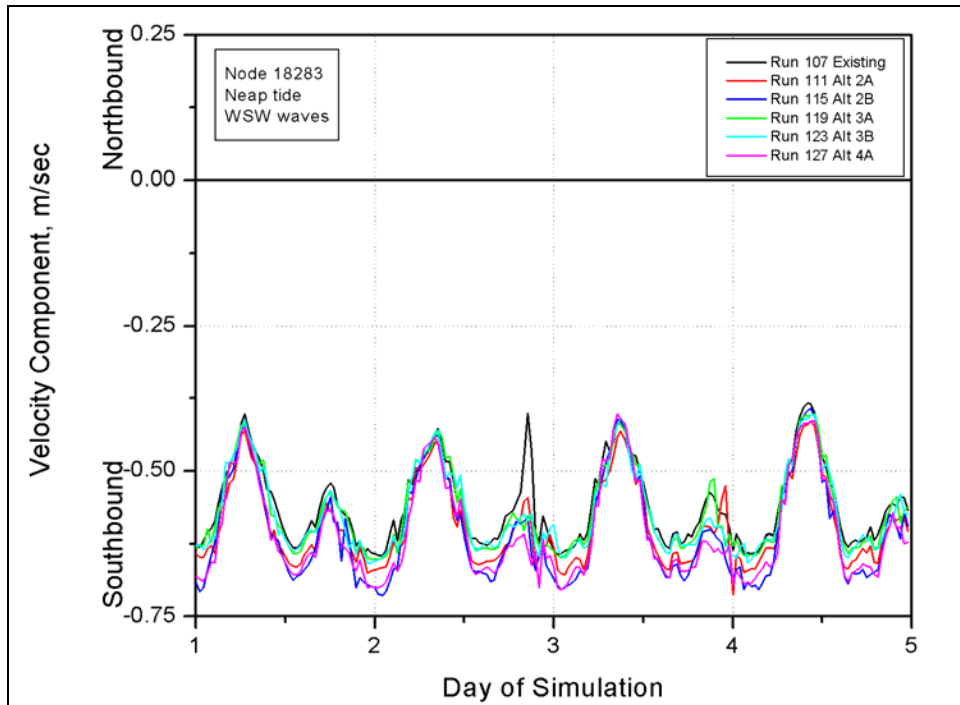
Figure E488.   North-south velocity component at node 18283 (neap tide, west-southwest waves)
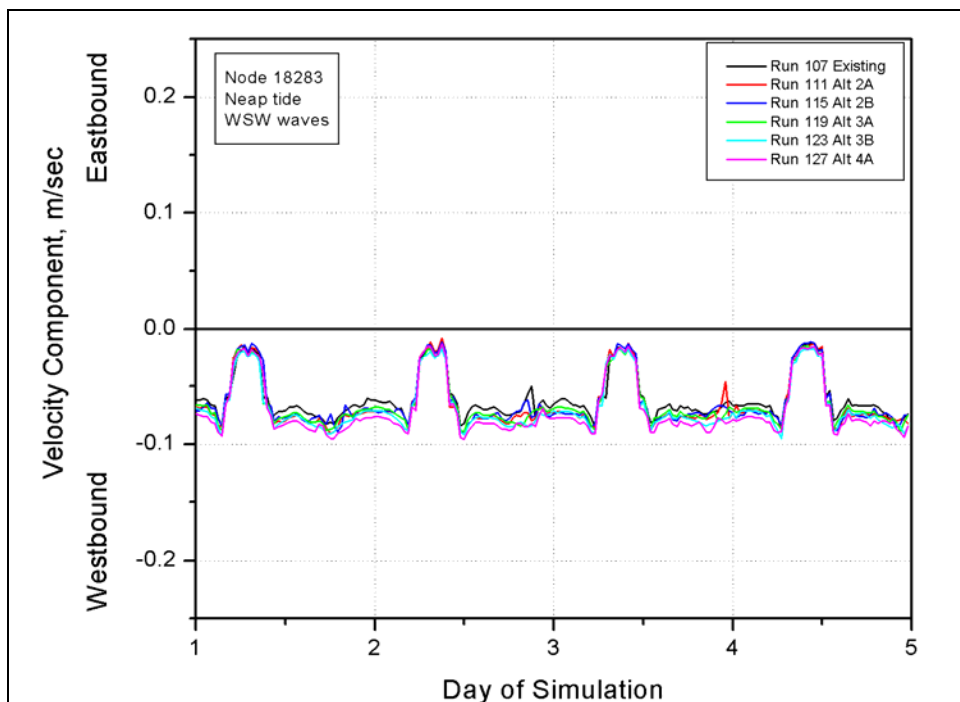
Figure E489.   East-west velocity component at node 18283 (neap tide, west-southwest waves)
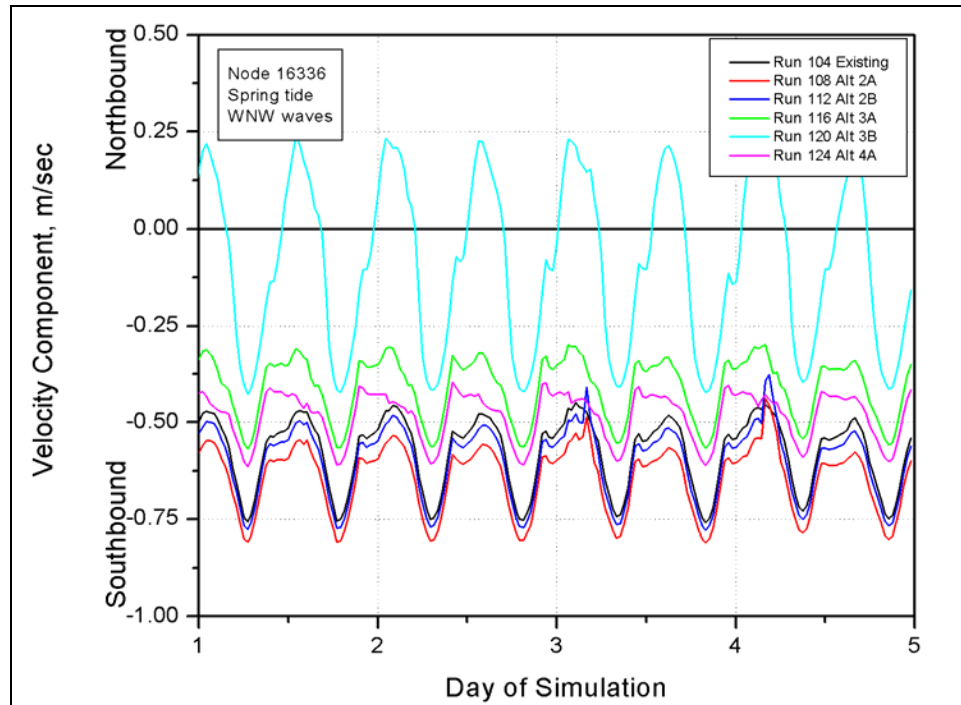
Figure E490. North-south velocity component at node 16336 (spring tide, west-northwest waves)
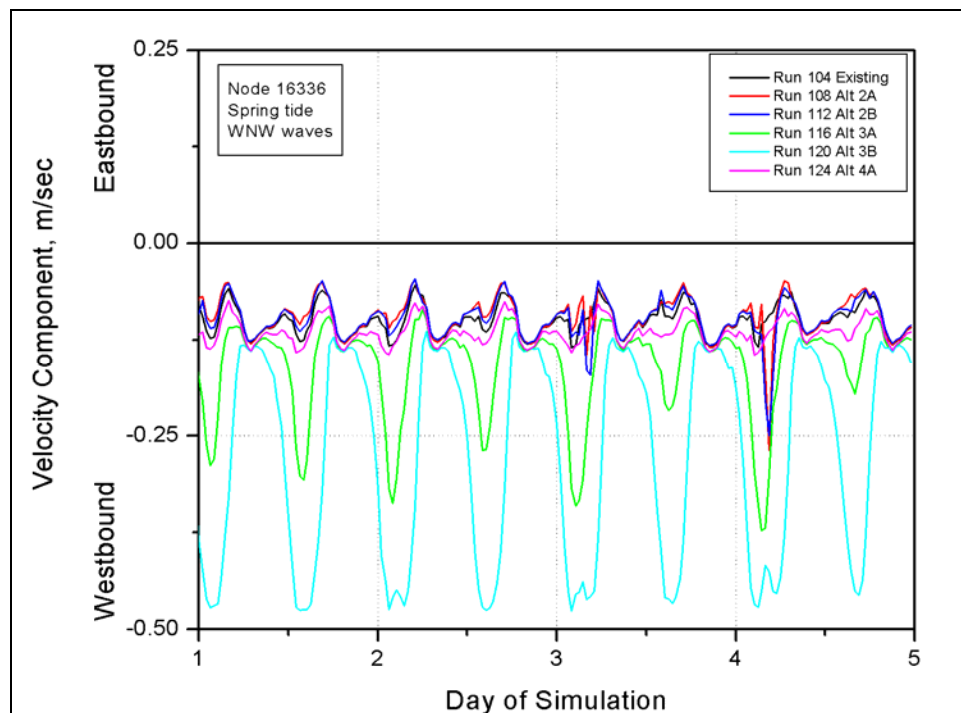
Figure E491. East-west velocity component at node 16336 (spring tide, west-northwest waves)
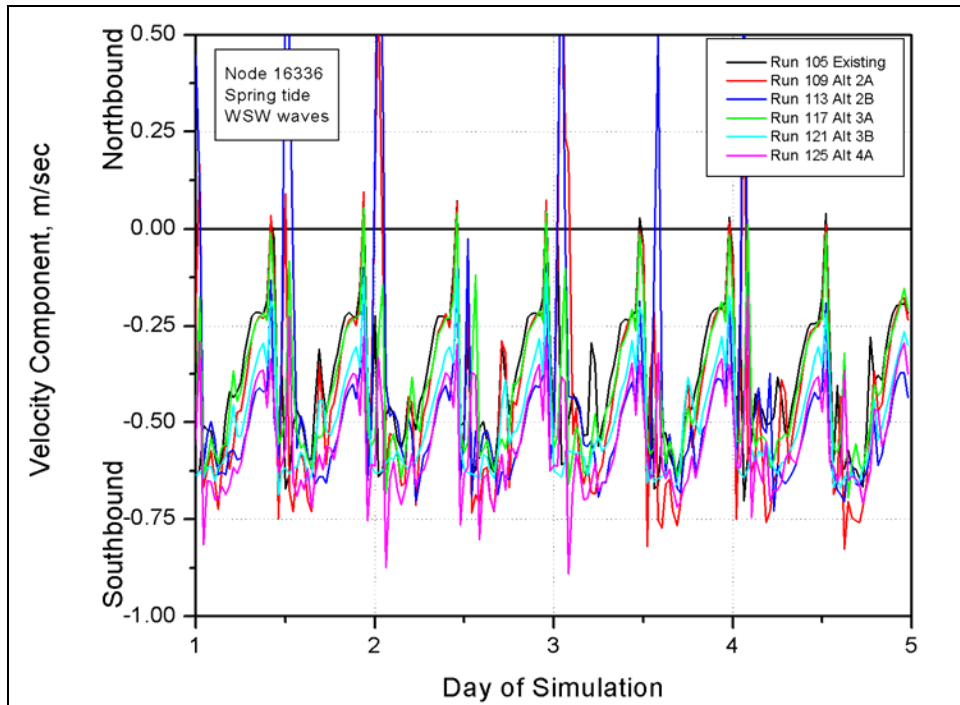
Figure E492.   North-south velocity component at node 16336 (spring tide, west-southwest waves)
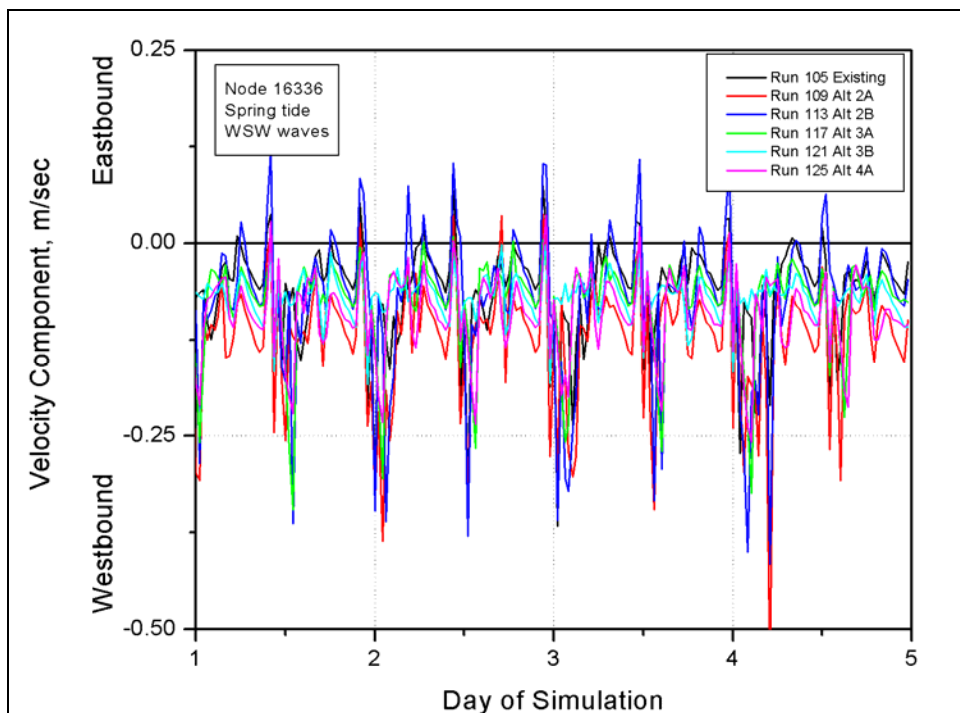
Figure E493.   East-west velocity component at node 16336 (spring tide, west-southwest waves)
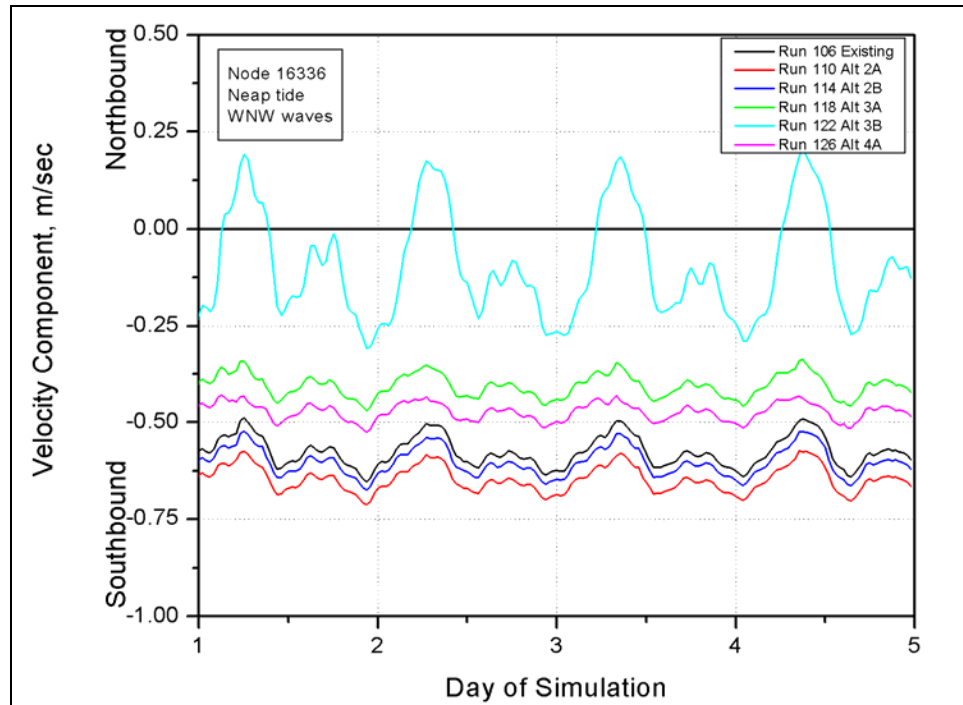
Figure E494.   North-south velocity component at node 16336 (neap tide, west-northwest waves)
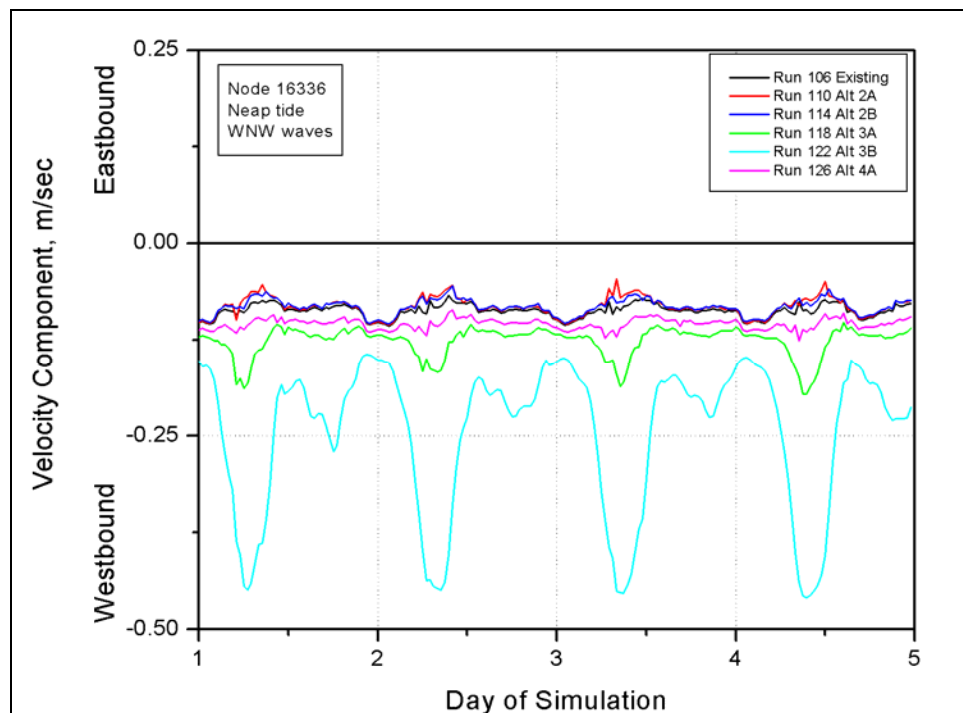
Figure E495.   East-west velocity component at node 16336 (neap tide, west-northwest waves)
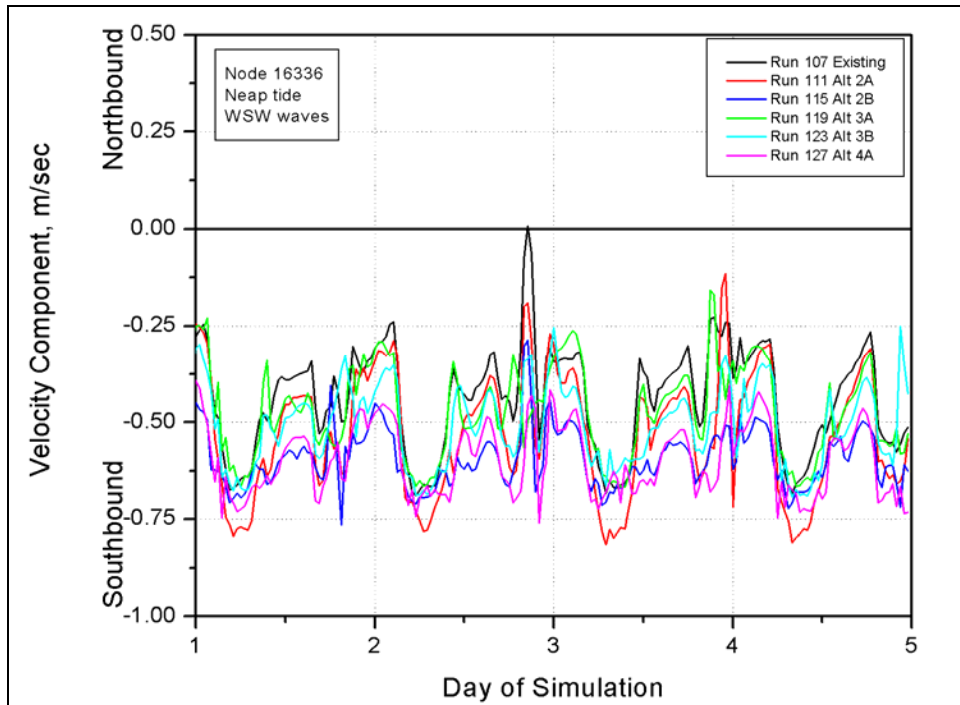
Figure E496.   North-south velocity component at node 16336 (neap tide, west-southwest waves)
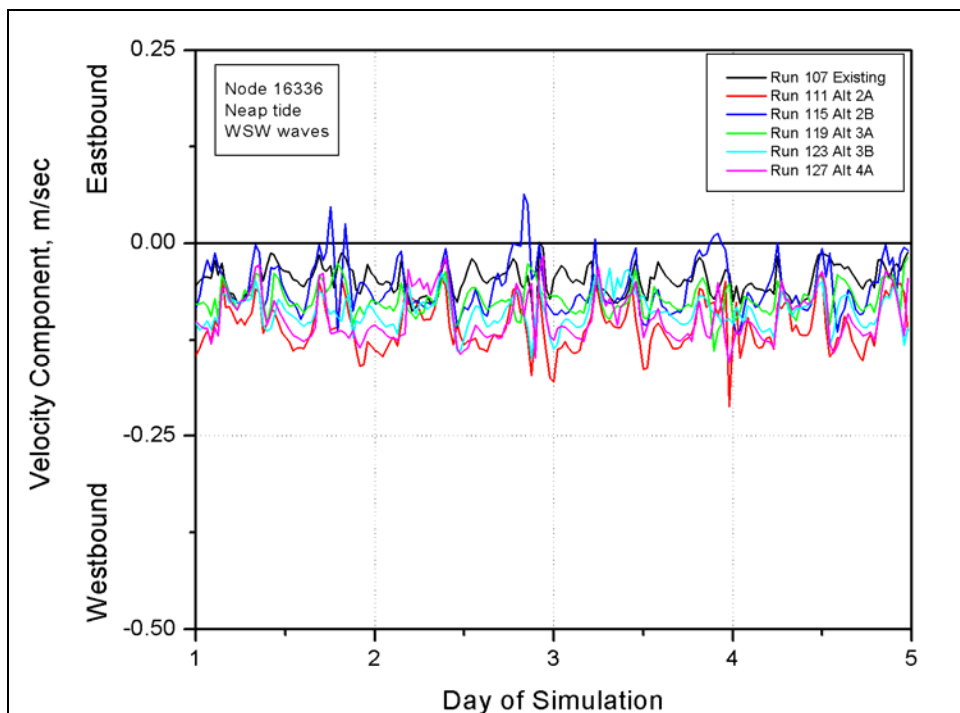
Figure E497.   East-west velocity component at node 16336 (neap tide, west-southwest waves)

Appendix E   Tidal Circulation Simulation Results
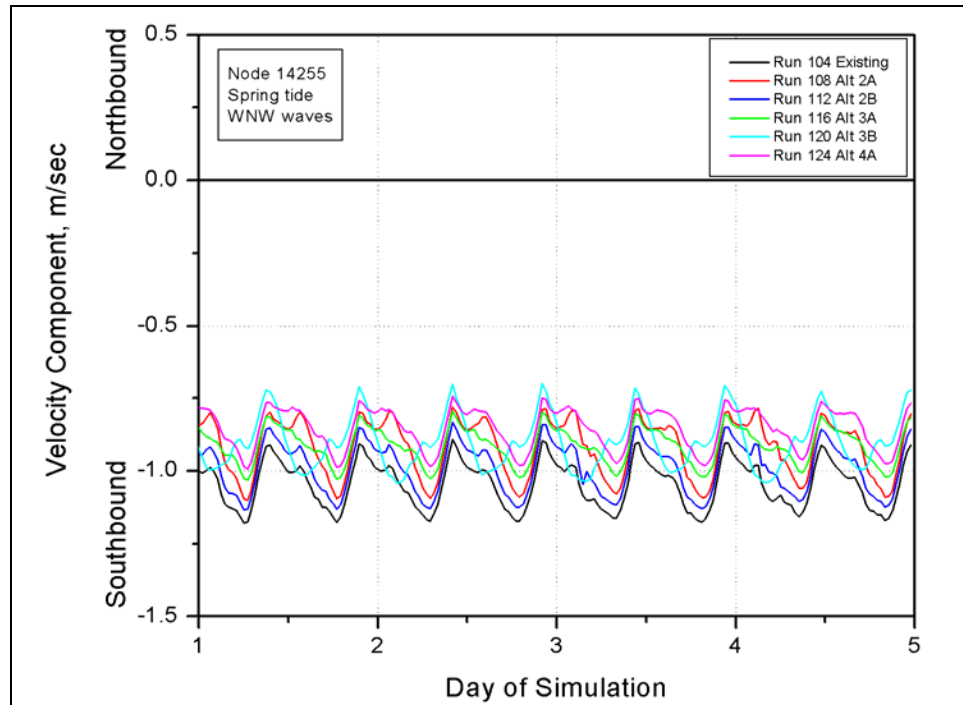
Figure E498.   North-south velocity component at node 14255 (spring tide, west-northwest waves)
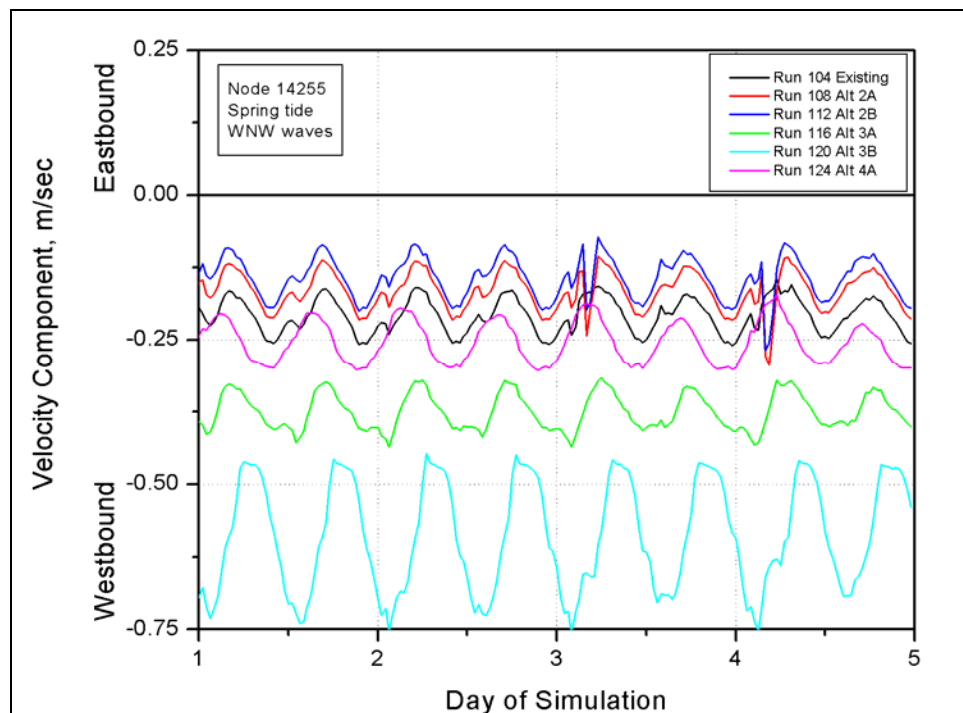
Figure E499.   East-west velocity component at node 14255 (spring tide, west-northwest waves)
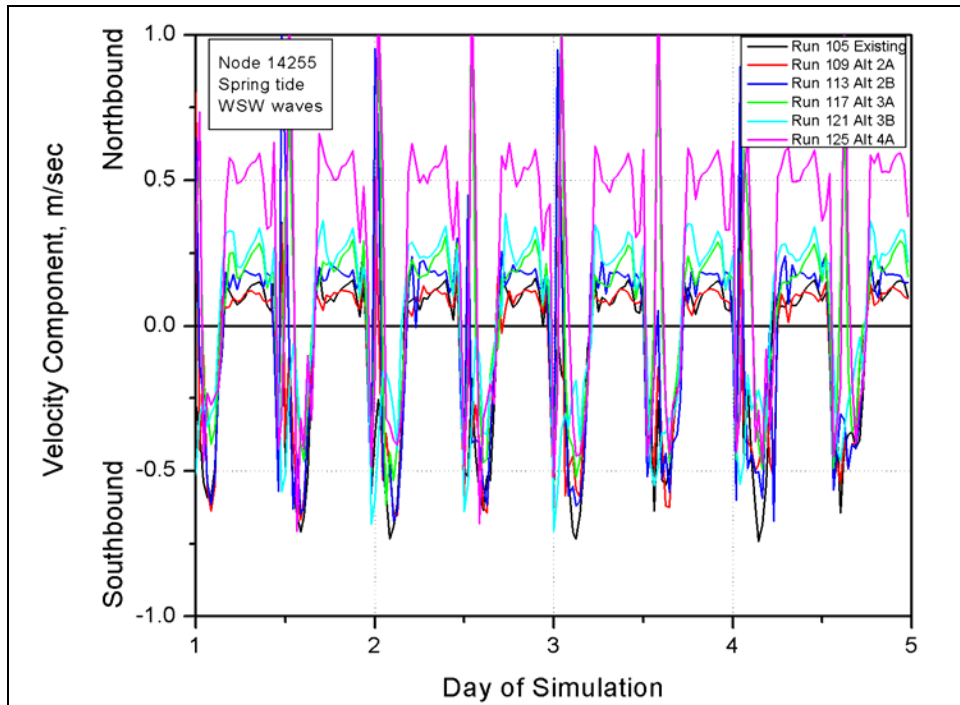
Figure E500.   North-south velocity component at node 14255 (spring tide, west-southwest waves)
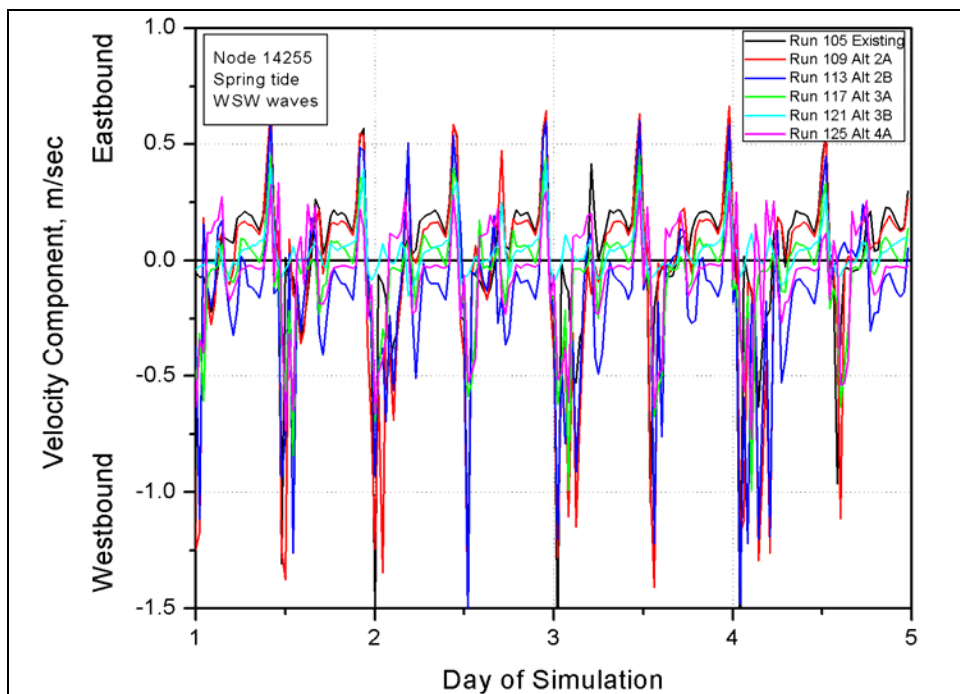
Figure E501.   East-west velocity component at node 14255 (spring tide, west-southwest waves)
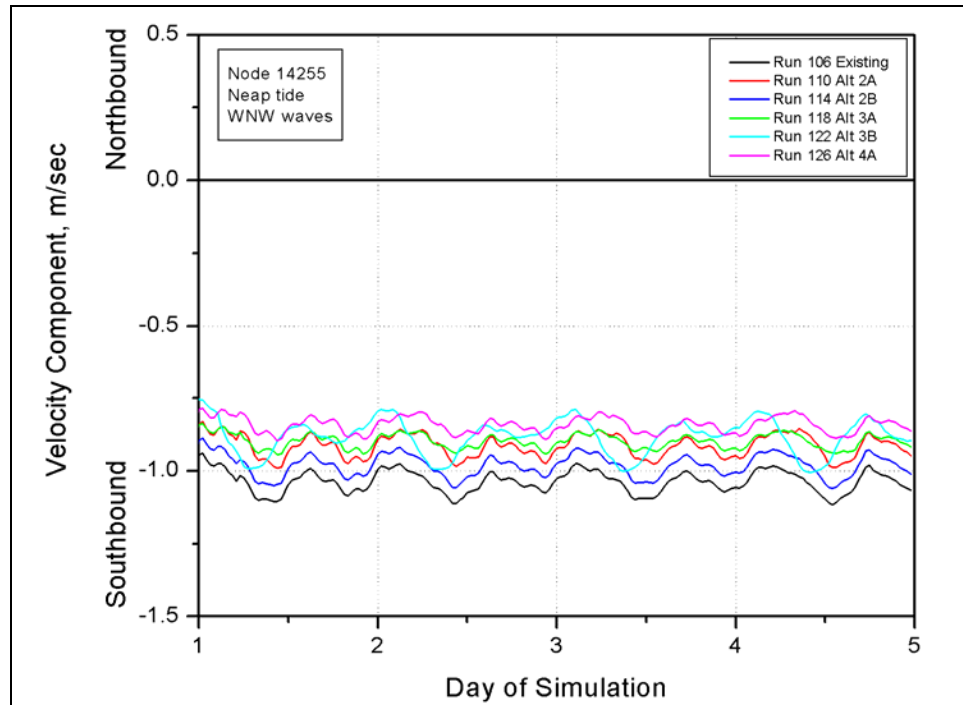
Figure E502.   North-south velocity component at node 14255 (neap tide, west-northwest waves)
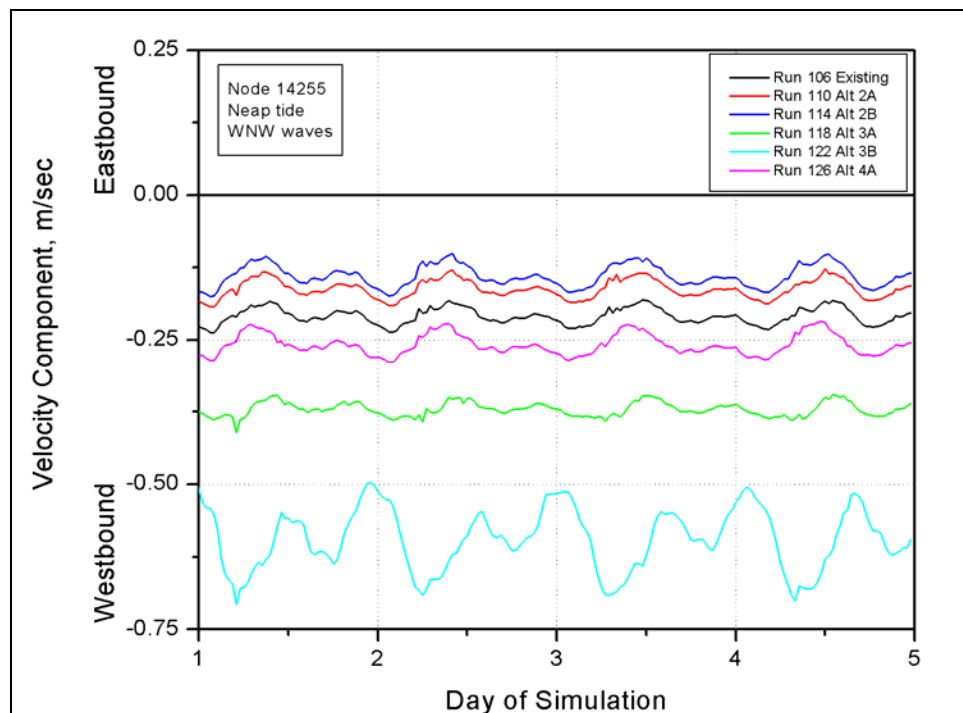
Figure E503.   East-west velocity component at node 14255 (neap tide, west-northwest waves)
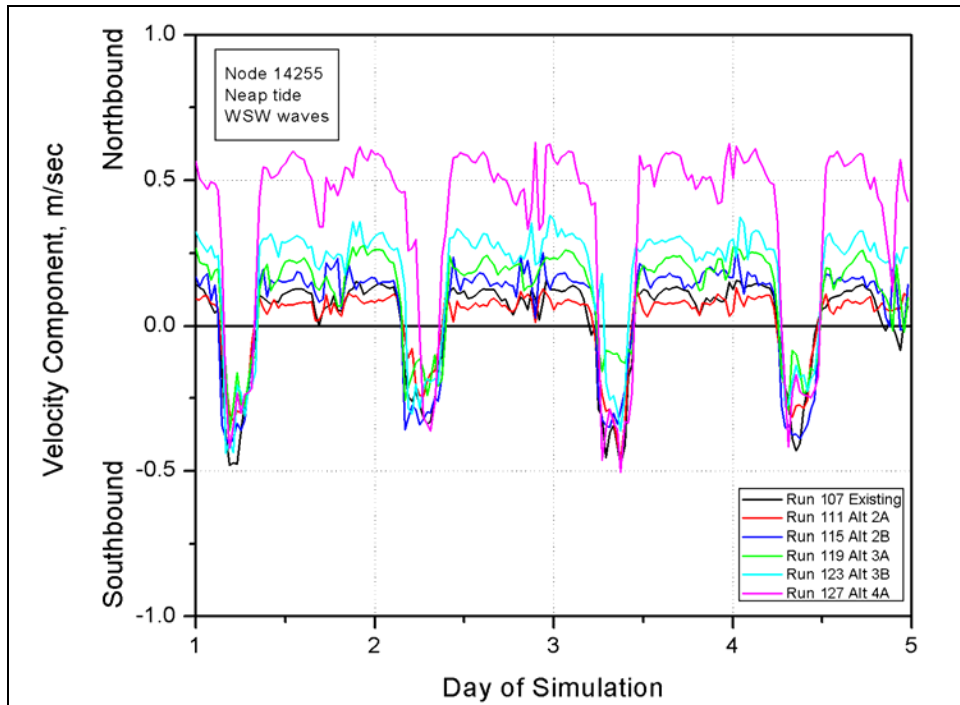
Figure E504.   North-south velocity component at node 14255 (neap tide, west-southwest waves)
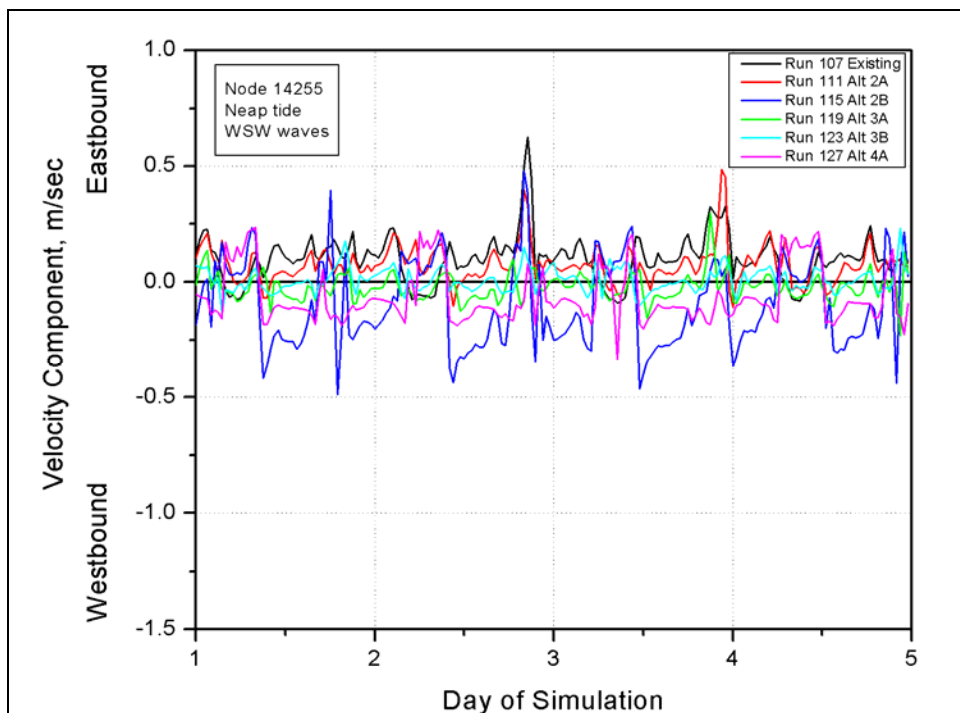
Figure E505.   East-west velocity component at node 14255 (neap tide, west-southwest waves)
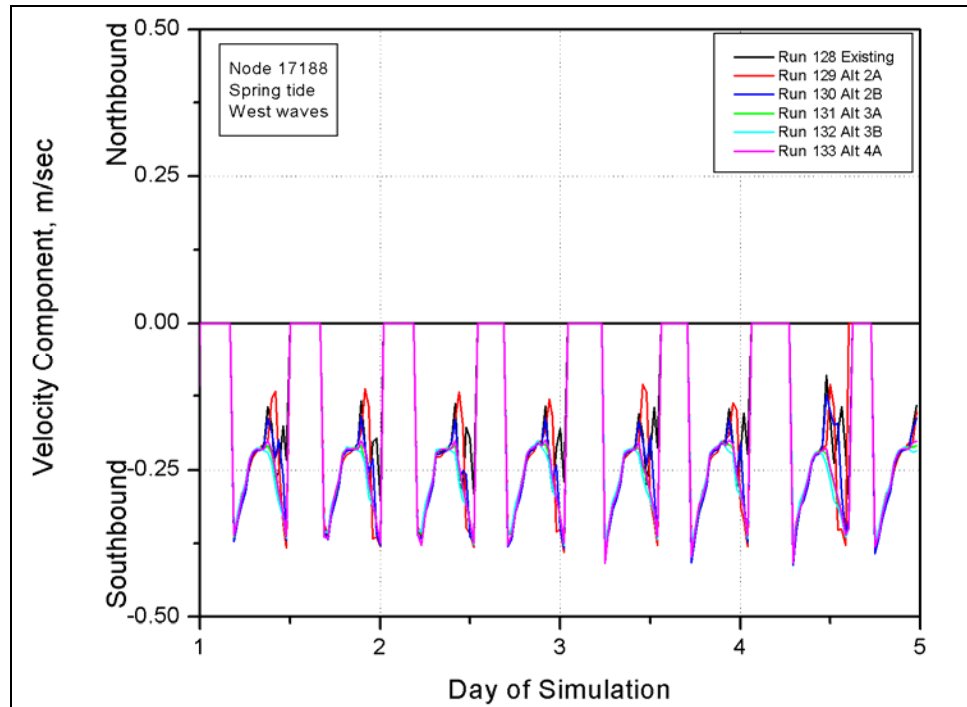
Figure E506.   North-south velocity component at node 17188 (spring tide, west waves)
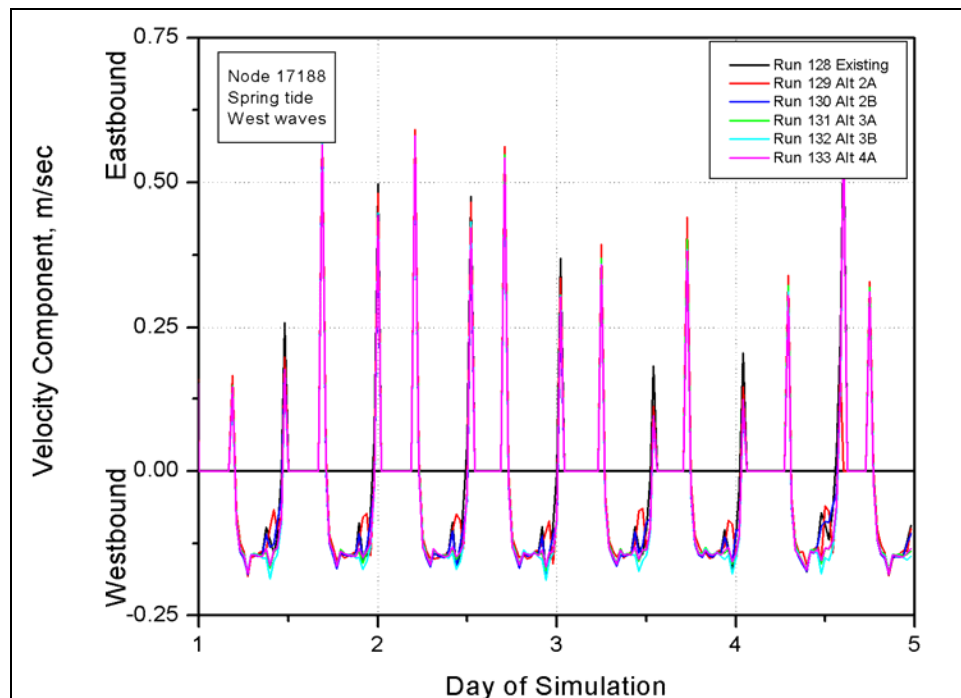
Figure E507.   East-west velocity component at node 17188 (spring tide, west waves)
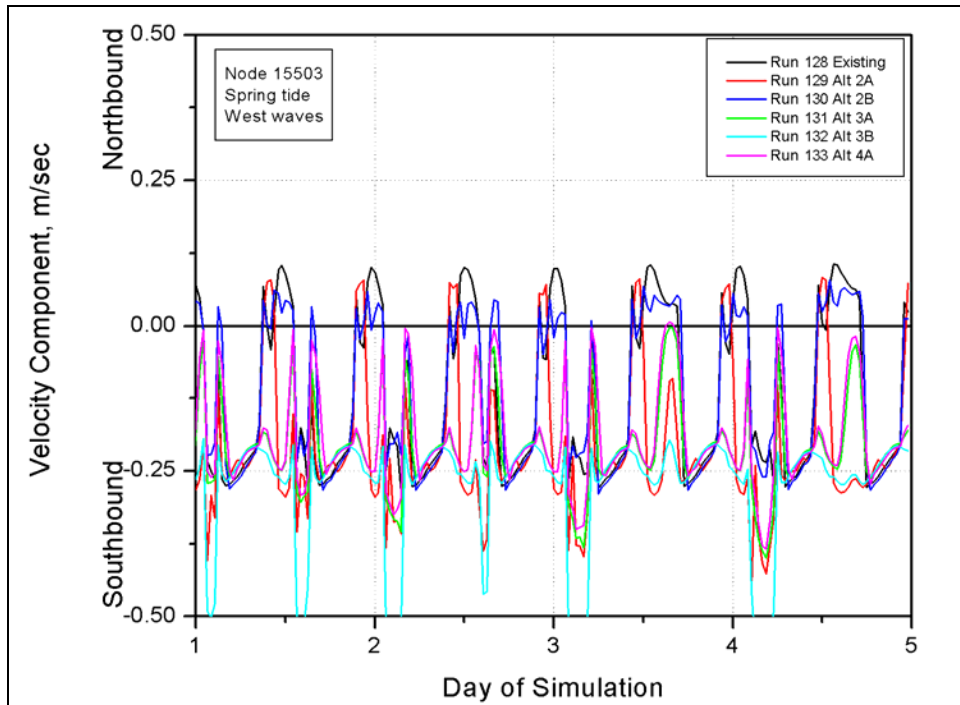
Figure E508.   North-south velocity component at node 15503 (spring tide, west waves)
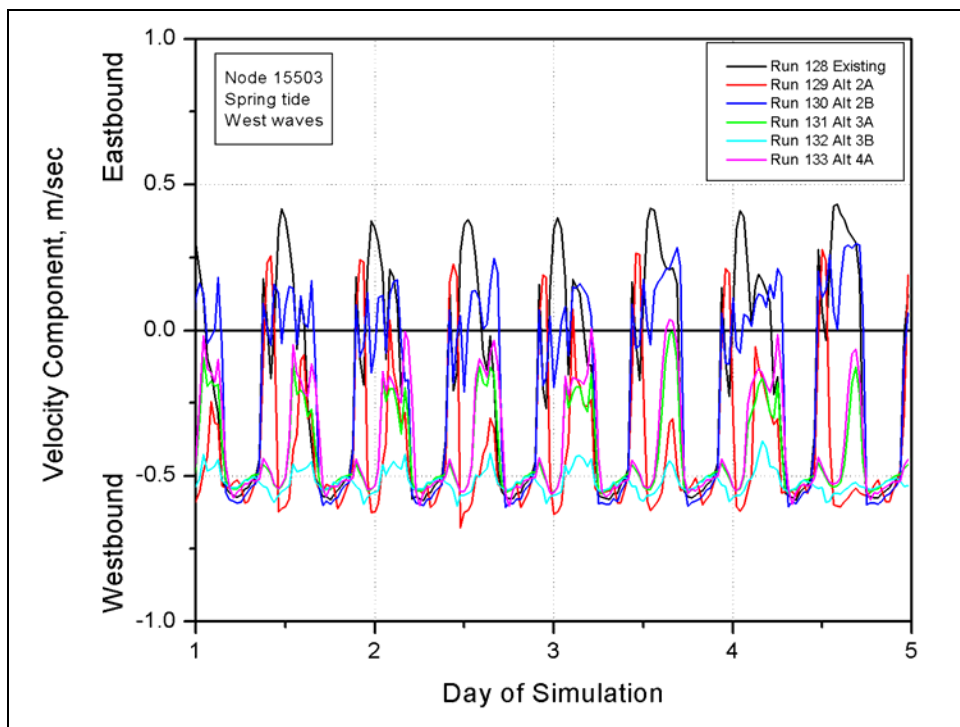
Figure E509.   East-west velocity component at node 15503 (spring tide, west waves)

Appendix E   Tidal Circulation Simulation Results
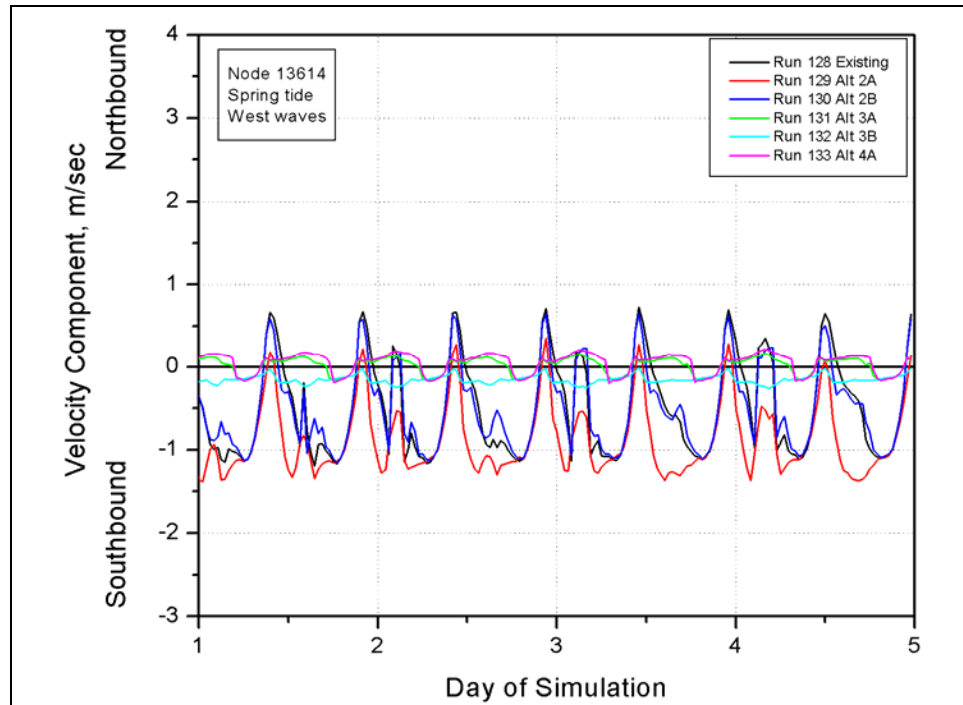
Figure E510.   North-south velocity component at node 13614 (spring tide, west waves)
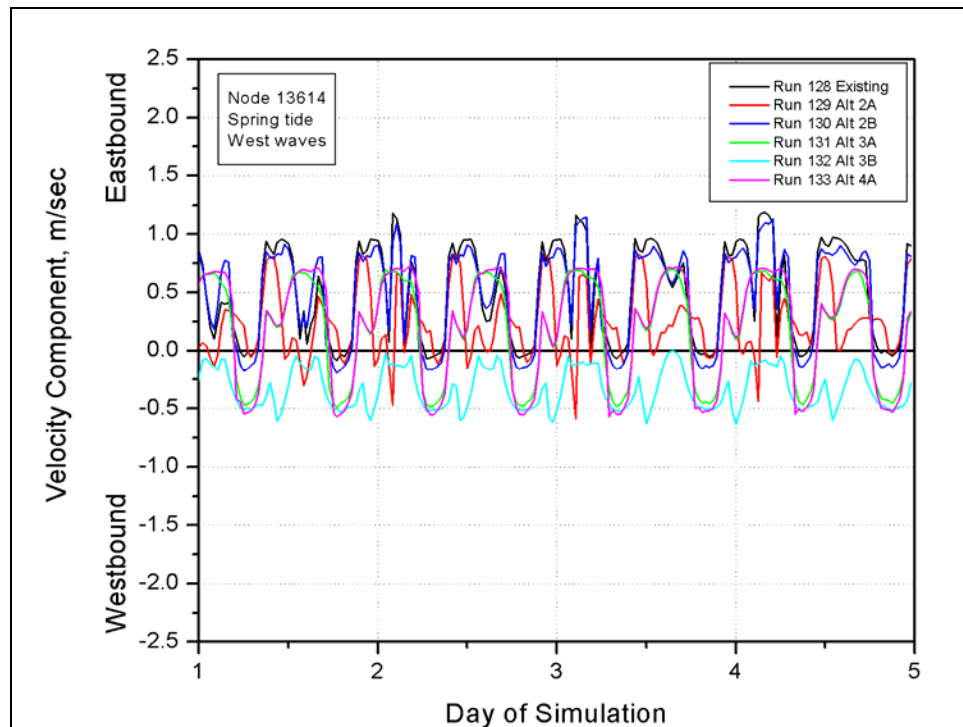
Figure E511.   East-west velocity component at node 13614 (spring tide, west waves)
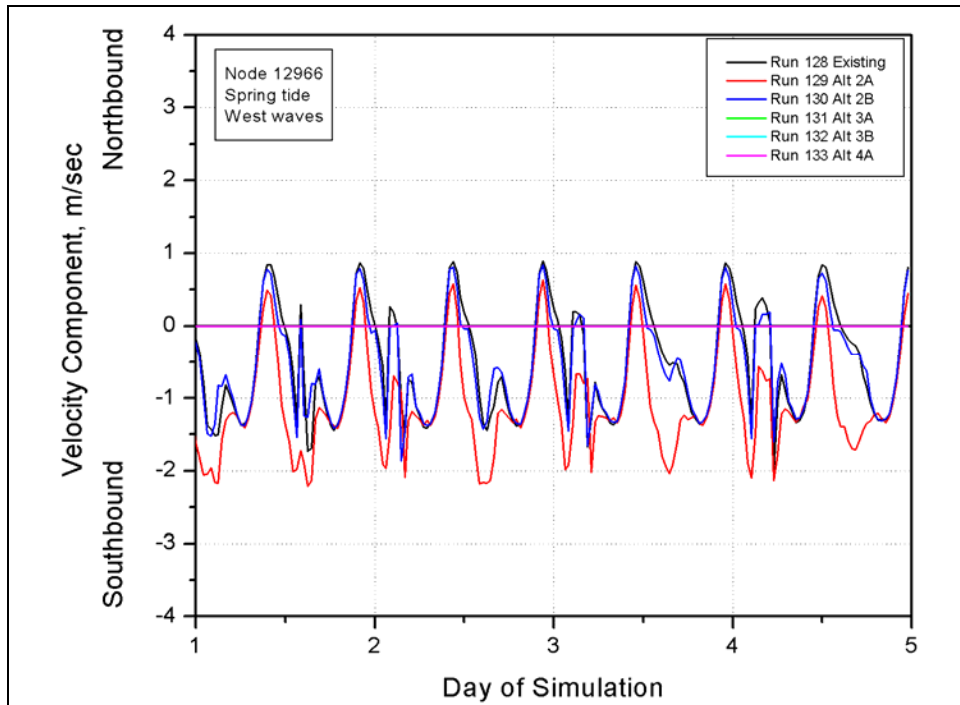
Figure E512. North-south velocity component at node 12966 (spring tide, west waves)
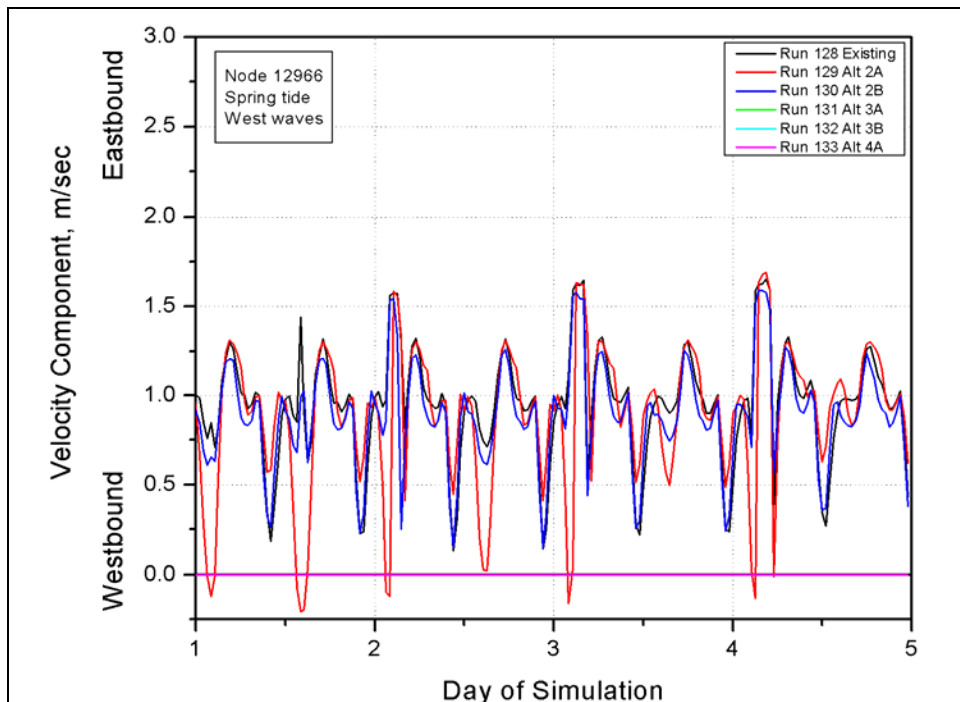
Figure E513. East-west velocity component at node 12966 (spring tide, west waves)
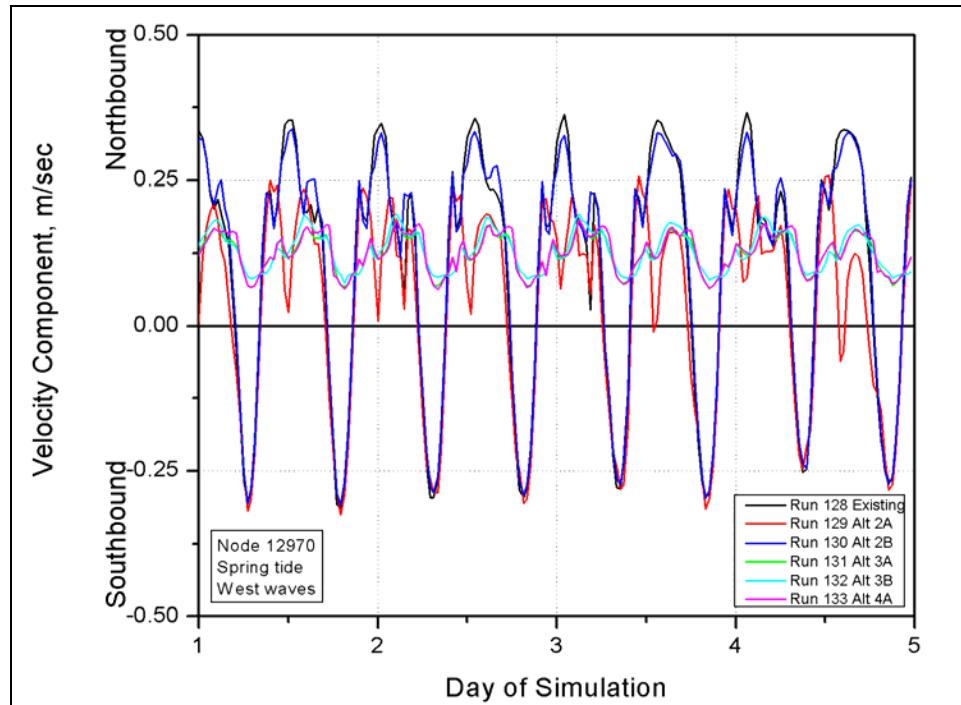
Figure E514.   North-south velocity component at node 12970 (spring tide, west waves)
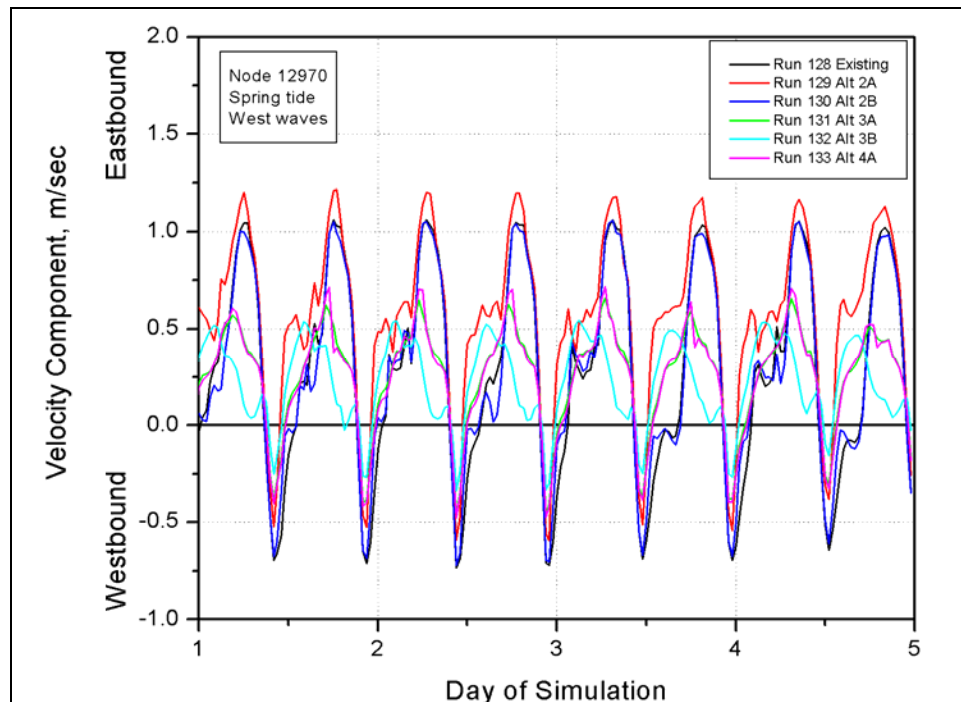
Figure E515.   East-west velocity component at node 12970 (spring tide, west waves)
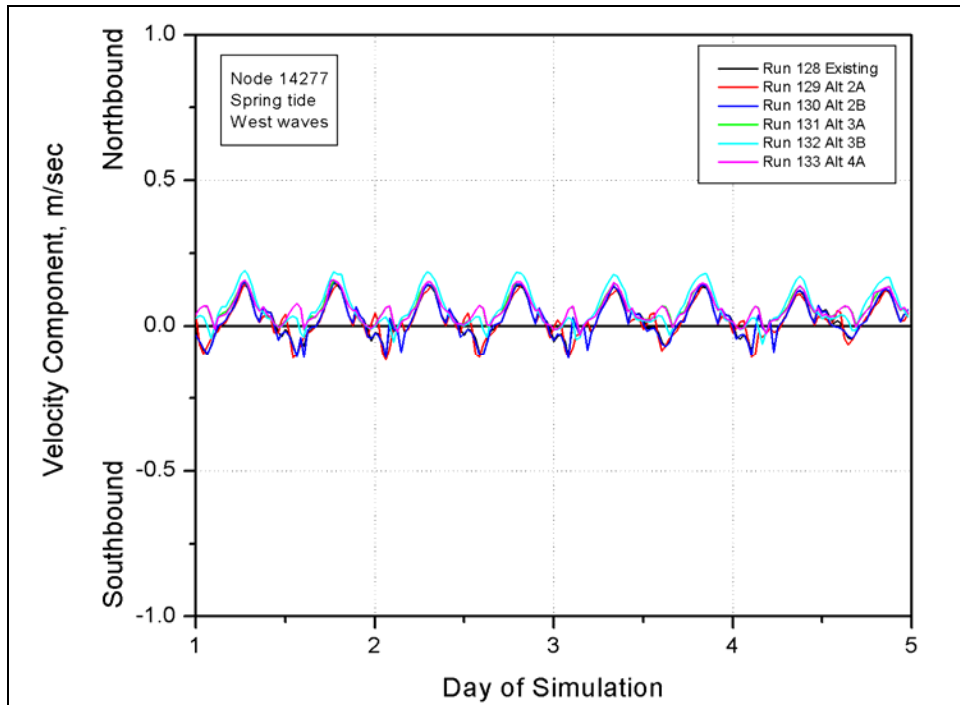
Figure E516. North-south velocity component at node 14277 (spring tide, west waves)
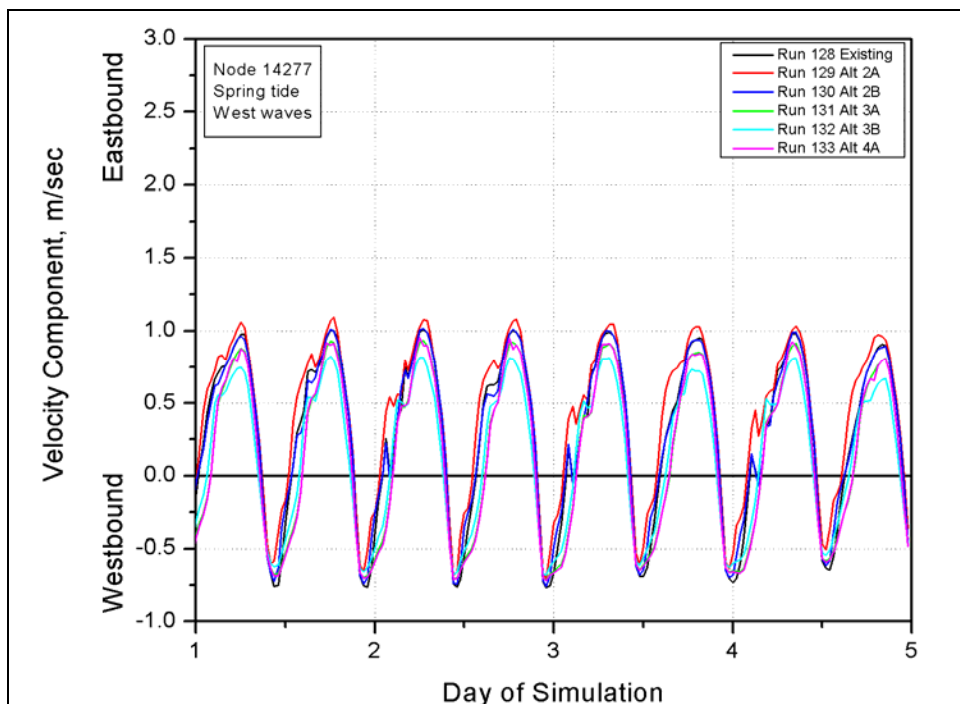
Figure E517. East-west velocity component at node 14277 (spring tide, west waves)
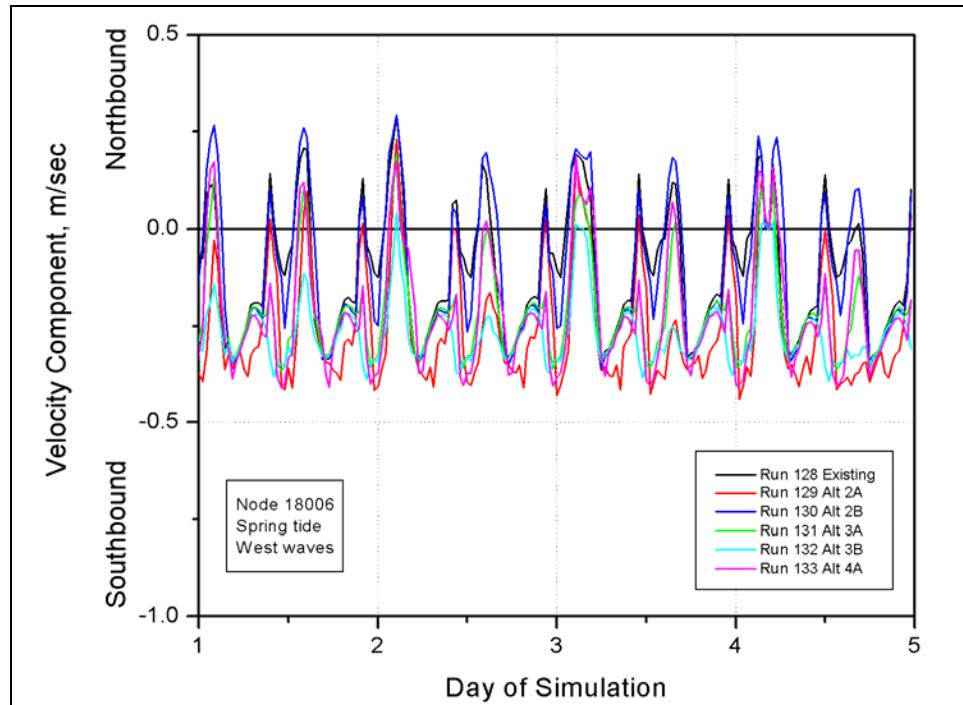
Figure E518.   North-south velocity component at node 18006 (spring tide, west waves)
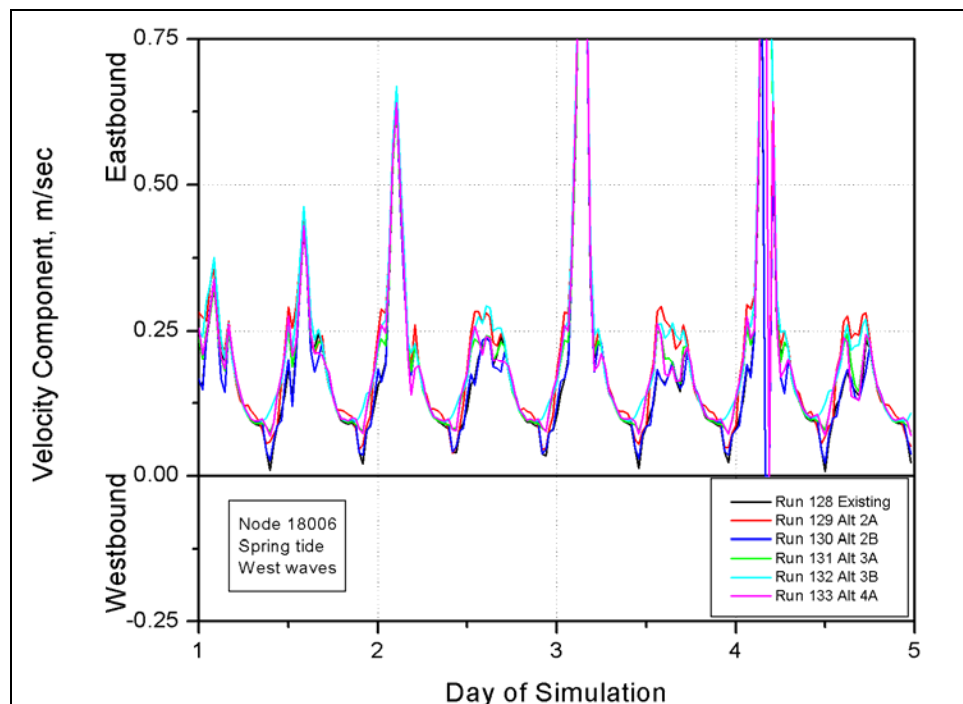
Figure E519.   East-west velocity component at node 18006 (spring tide, west waves)
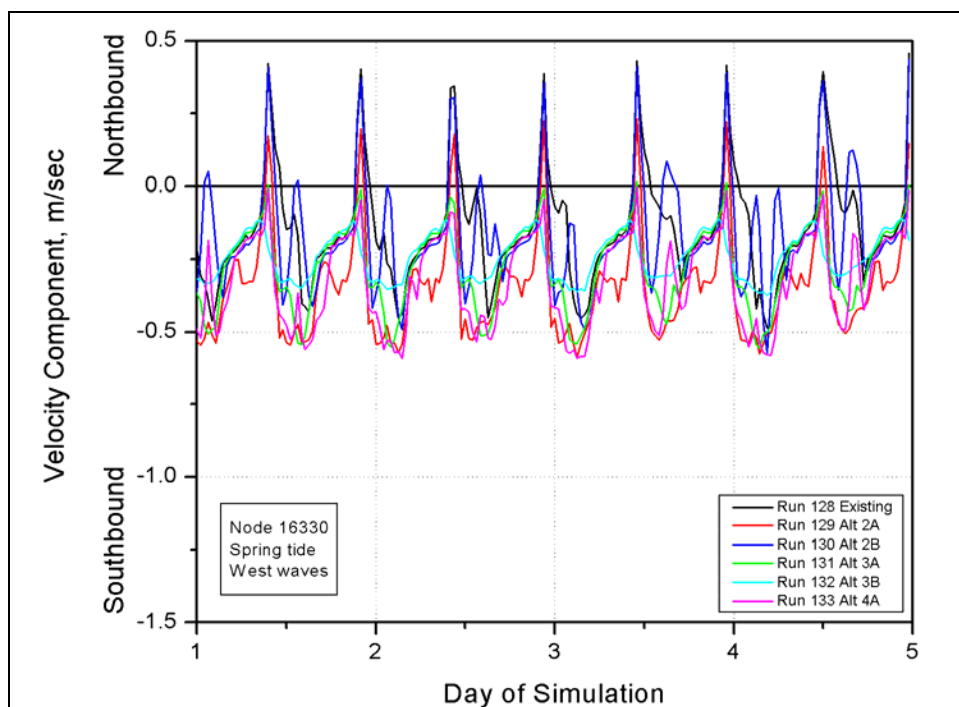
Figure E520.   North-south velocity component at node 16330 (spring tide, west waves)
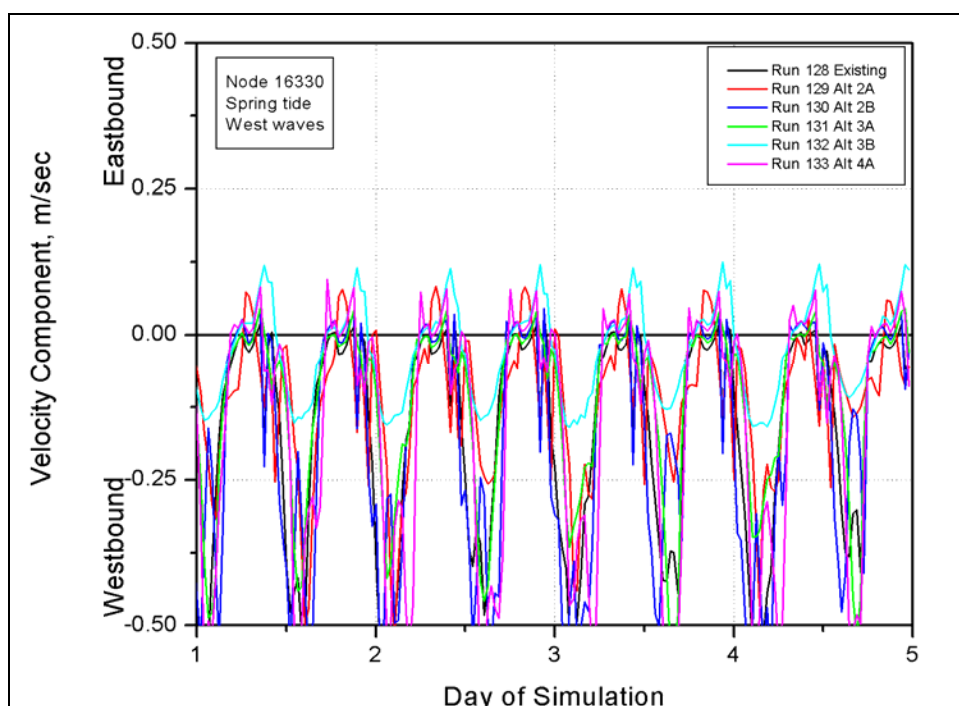
Figure E521.   East-west velocity component at node 16330 (spring tide, west waves)
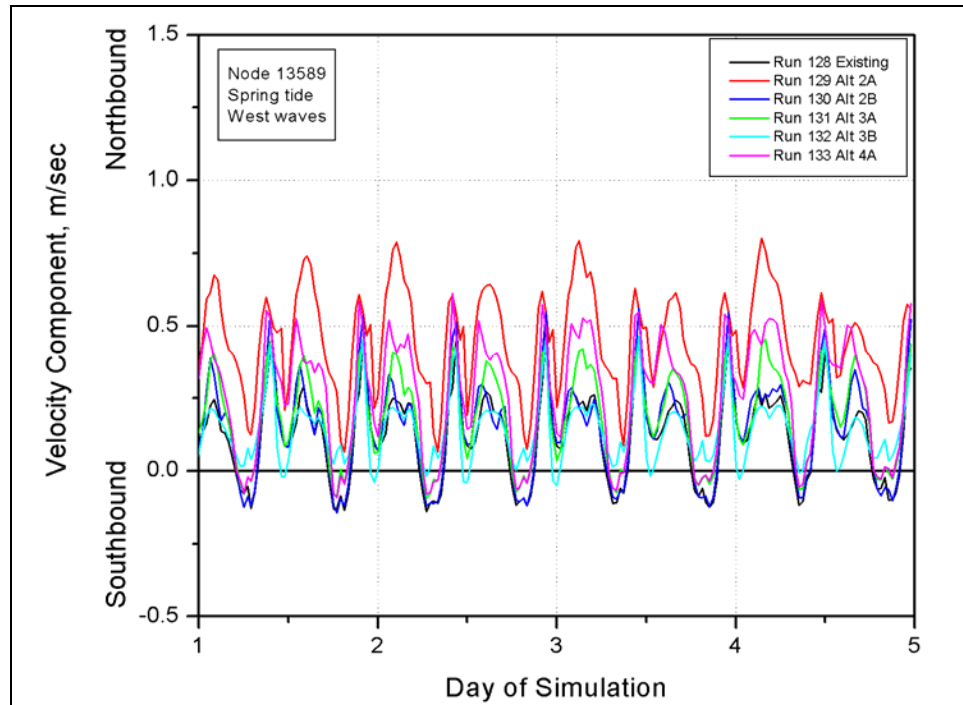
Figure E522.   North-south velocity component at node 13589 (spring tide, west waves)
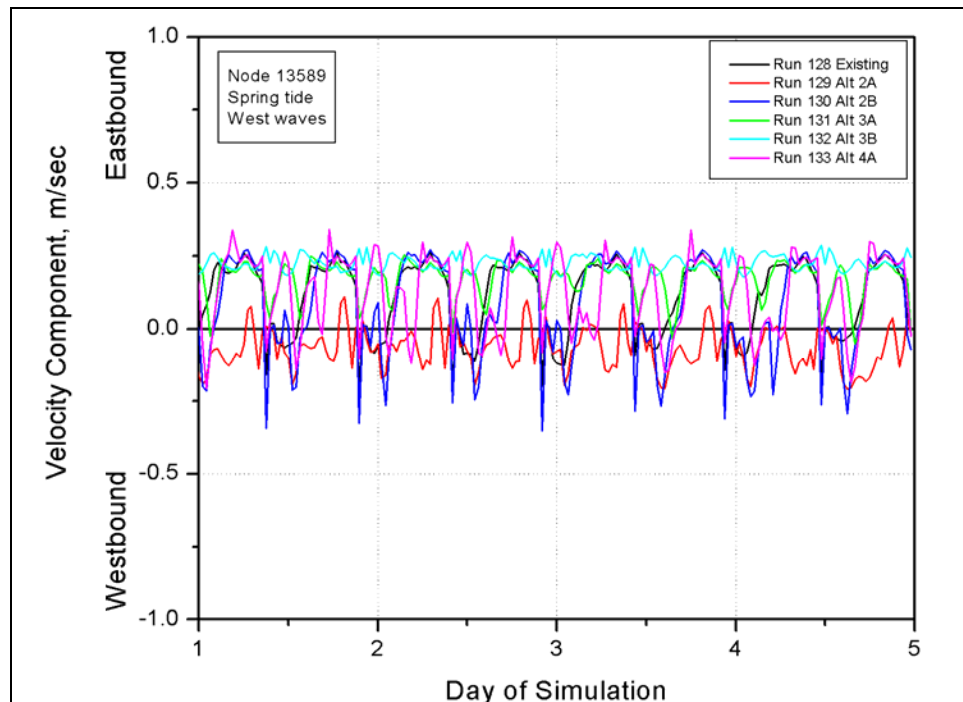
Figure E523.   East-west velocity component at node 13589 (spring tide, west waves)
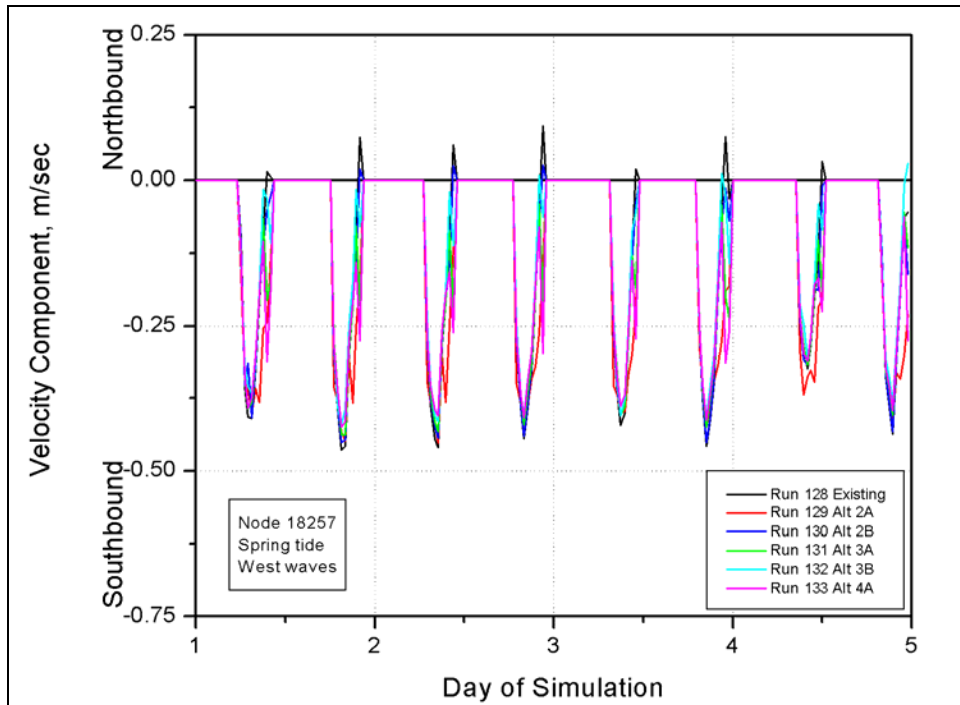
Figure E524.   North-south velocity component at node 18257 (spring tide, west waves)
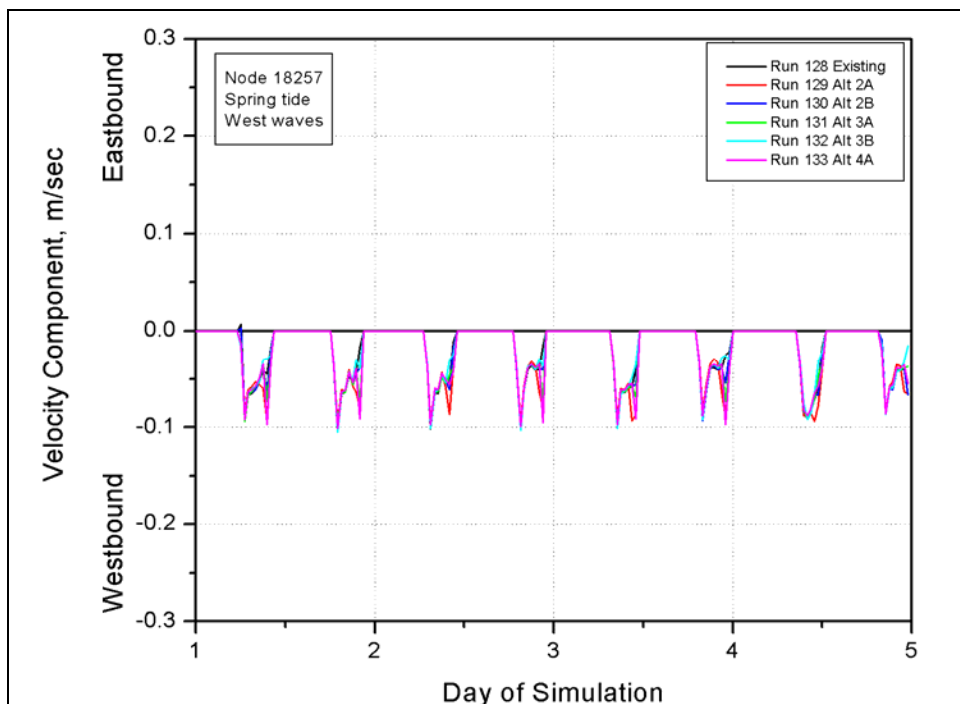
Figure E525.   East-west velocity component at node 18257 (spring tide, west waves)

Appendix E   Tidal Circulation Simulation Results
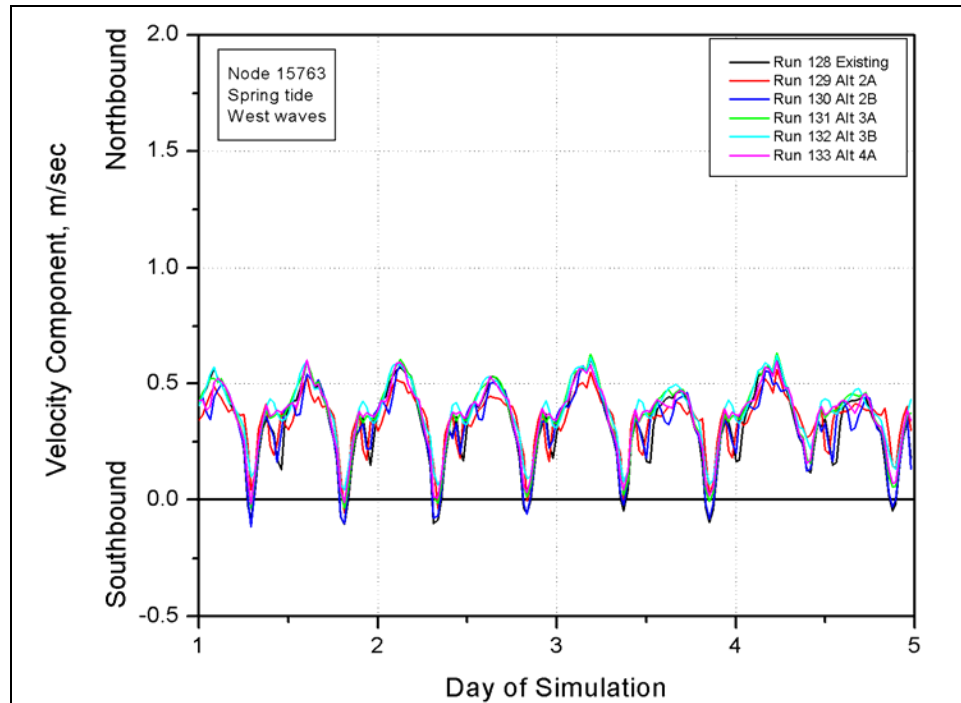
Figure E526.　North-south velocity component at node 15763 (spring tide, west waves)
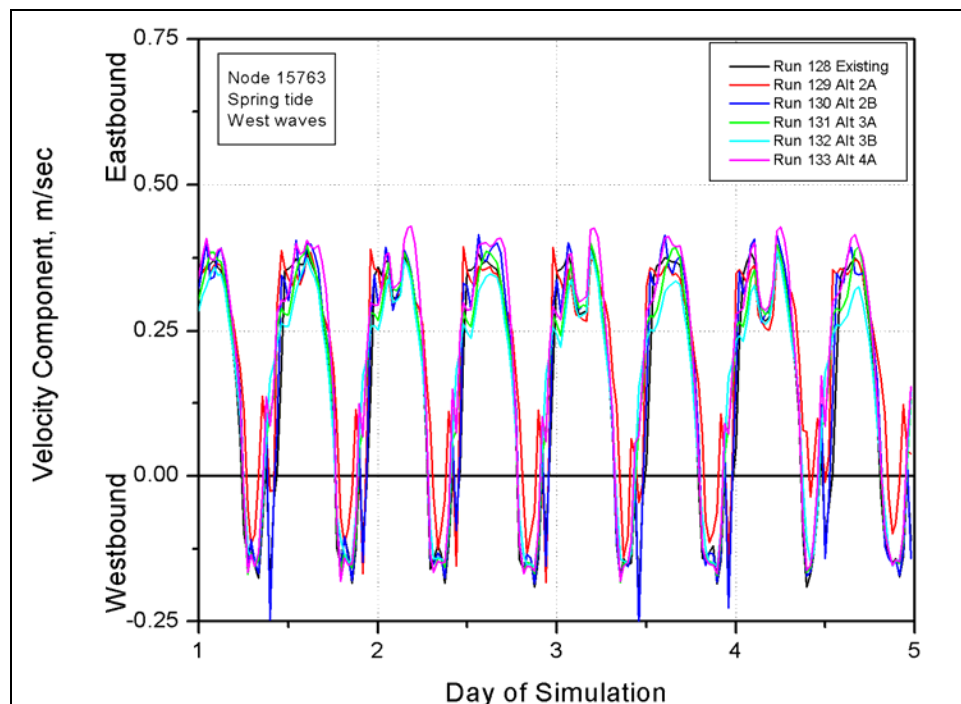
Figure E527.　East-west velocity component at node 15763 (spring tide, west waves)
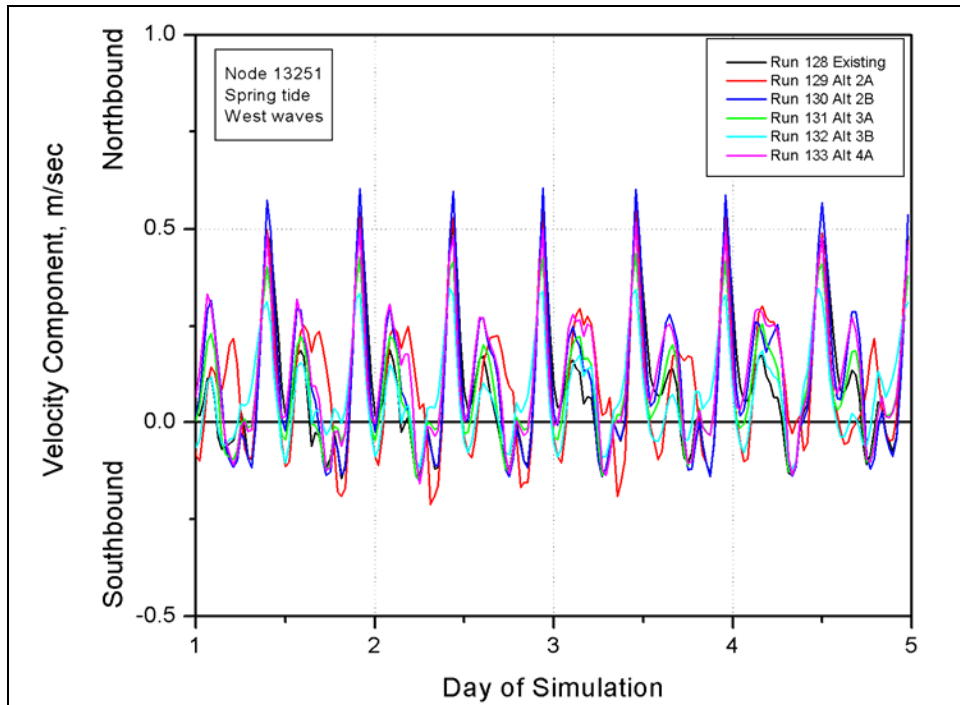
Figure E528. North-south velocity component at node 13251 (spring tide, west waves)
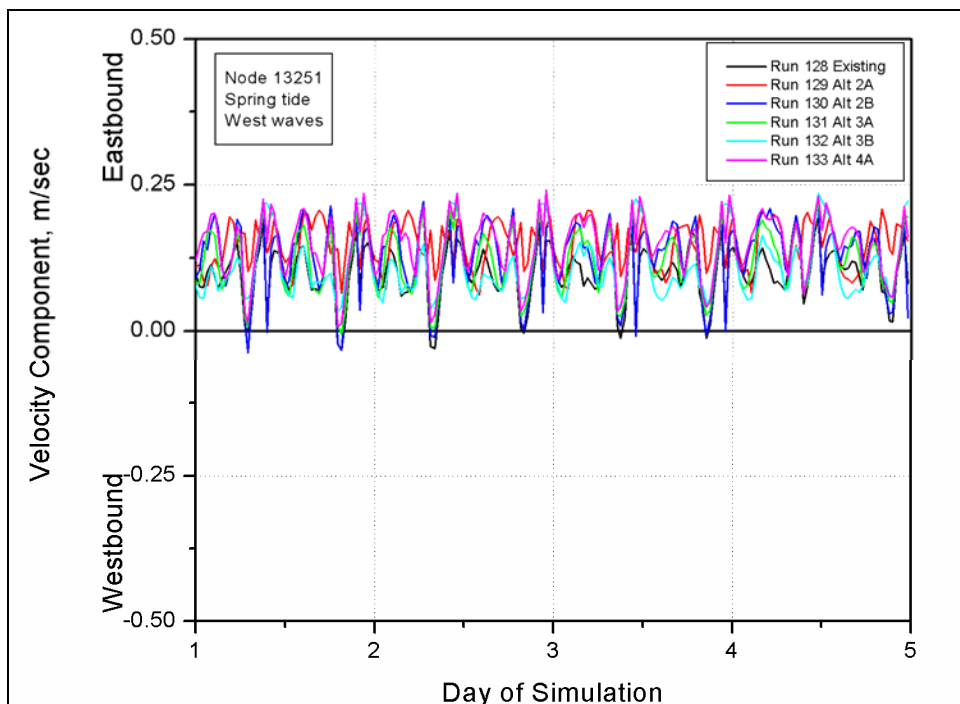
Figure E529. East-west velocity component at node 13251 (spring tide, west waves)

Appendix E   Tidal Circulation Simulation Results
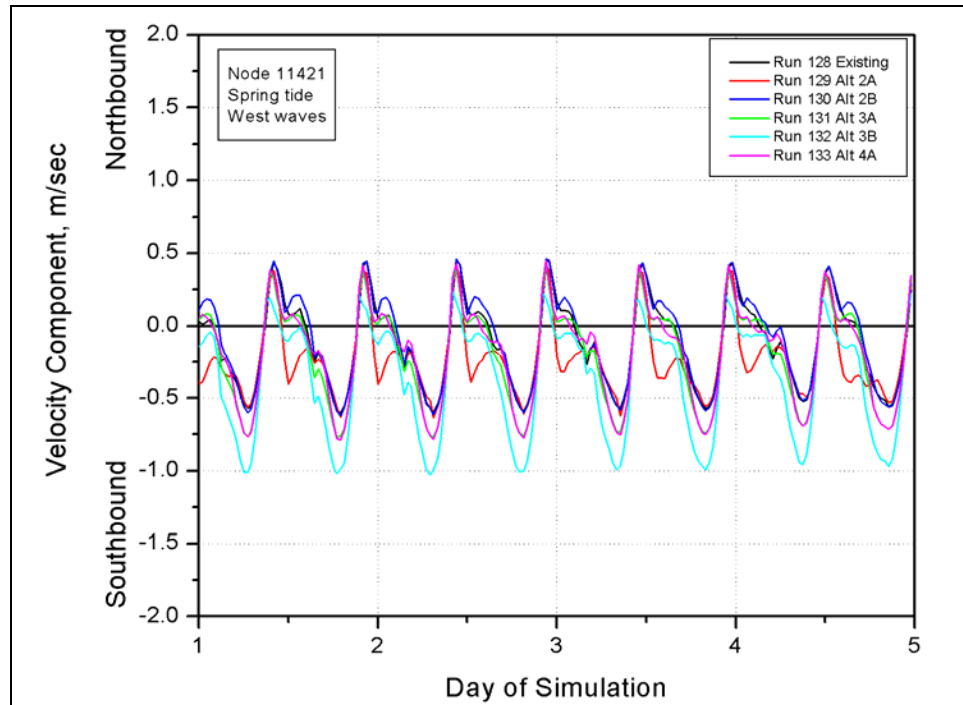
Figure E530. North-south velocity component at node 11421 (spring tide, west waves)
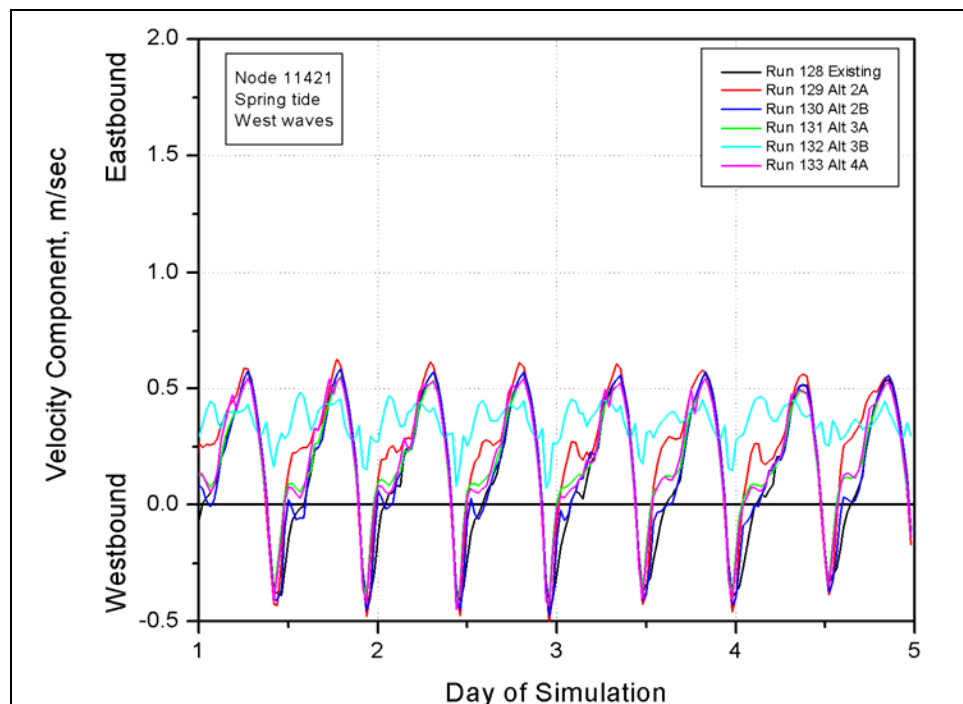
Figure E531. East-west velocity component at node 11421 (spring tide, west waves)
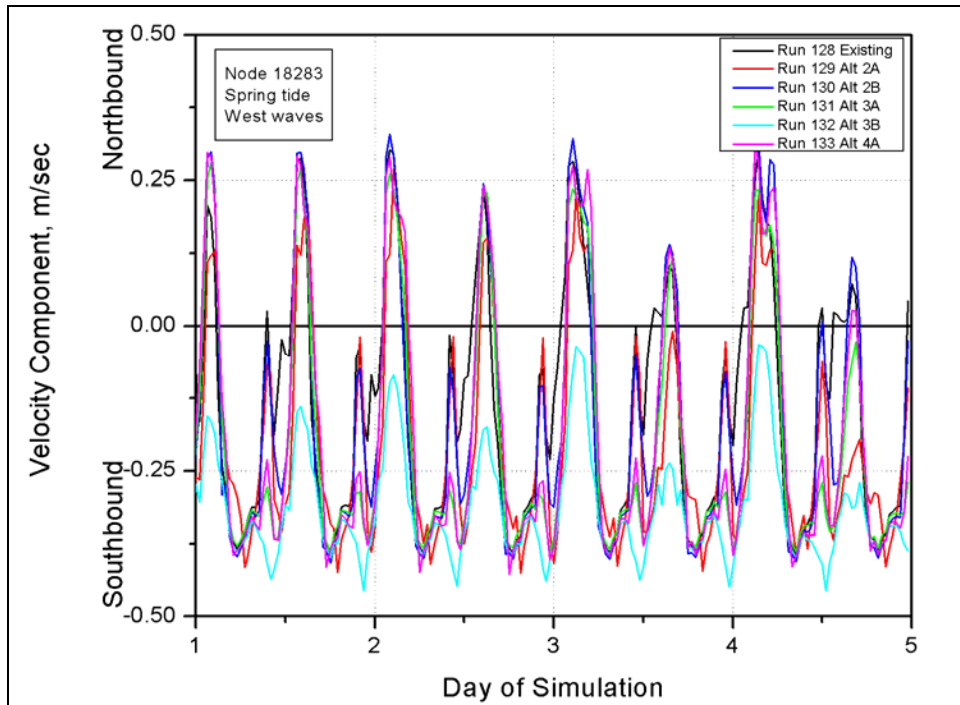
Figure E532. North-south velocity component at node 18283 (spring tide, west waves)
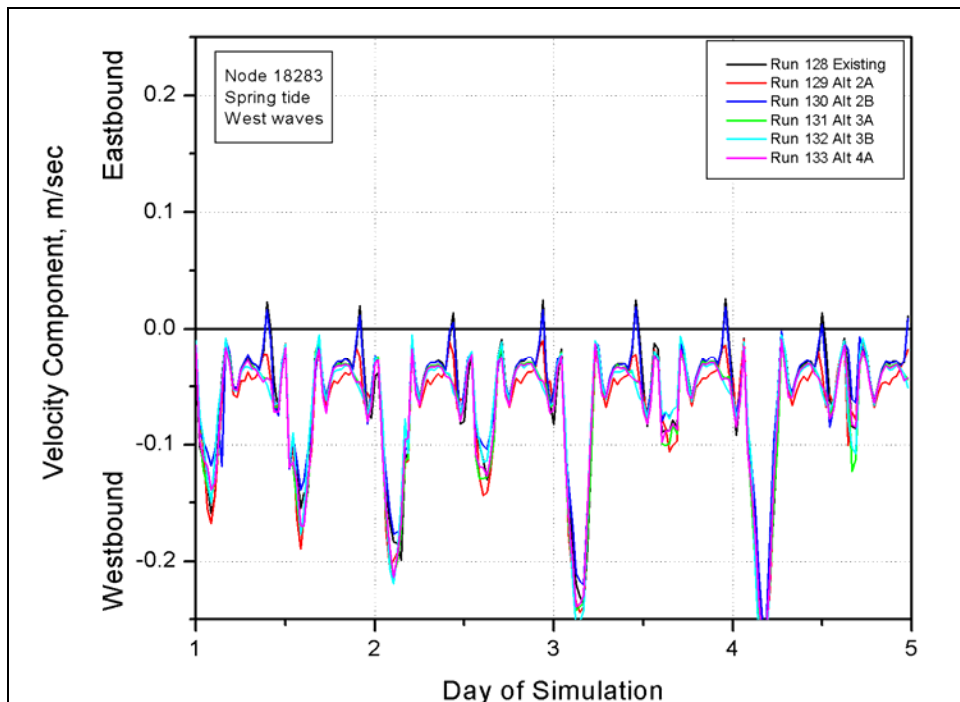
Figure E533. East-west velocity component at node 18283 (spring tide, west waves)

Appendix E   Tidal Circulation Simulation Results
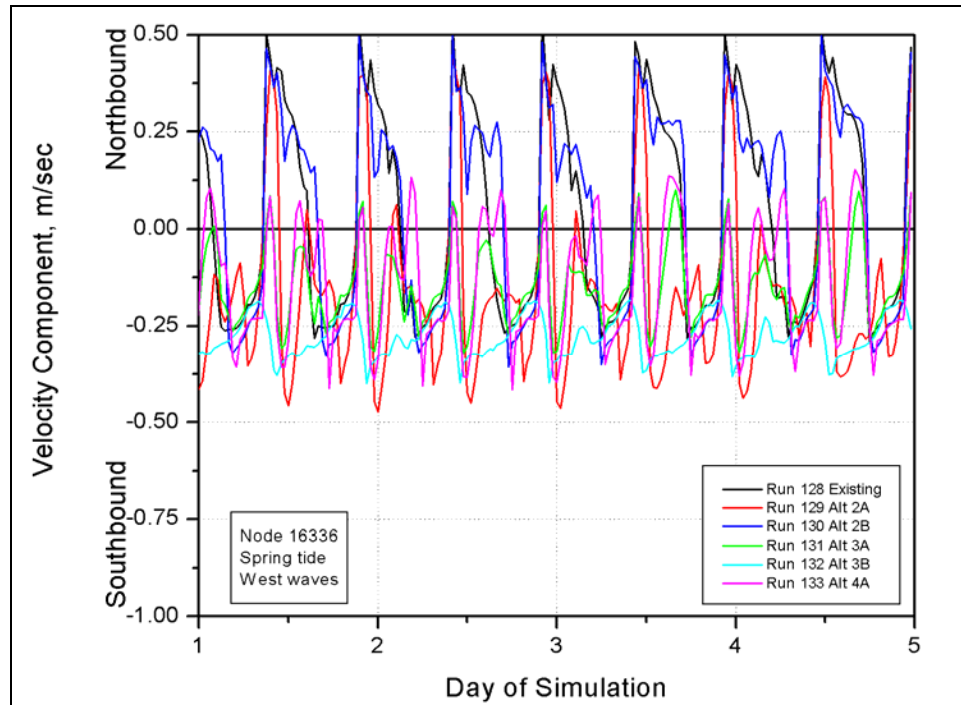
Figure E534.   North-south velocity component at node 16336 (spring tide, west waves)
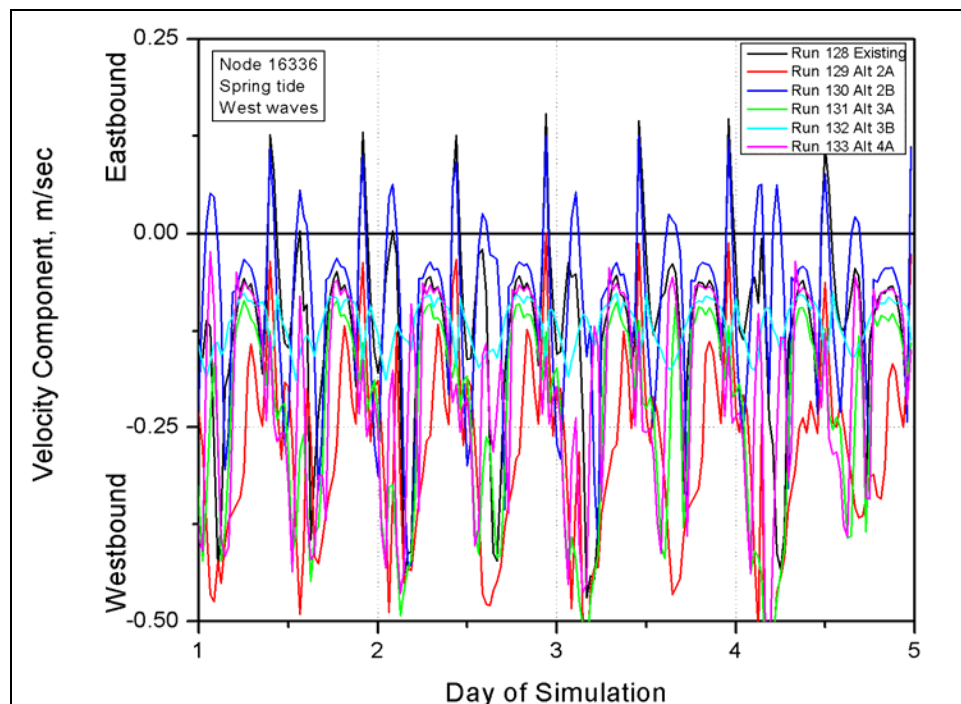
Figure E535.   East-west velocity component at node 16336 (spring tide, west waves)
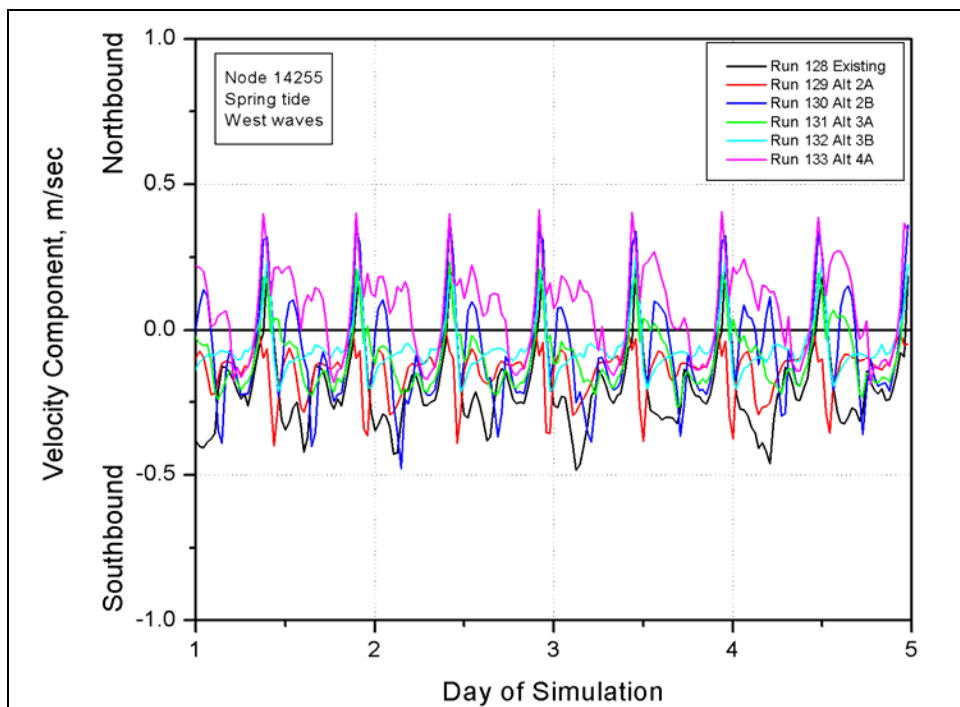
Figure E536. North-south velocity component at node 14255 (spring tide, west waves)
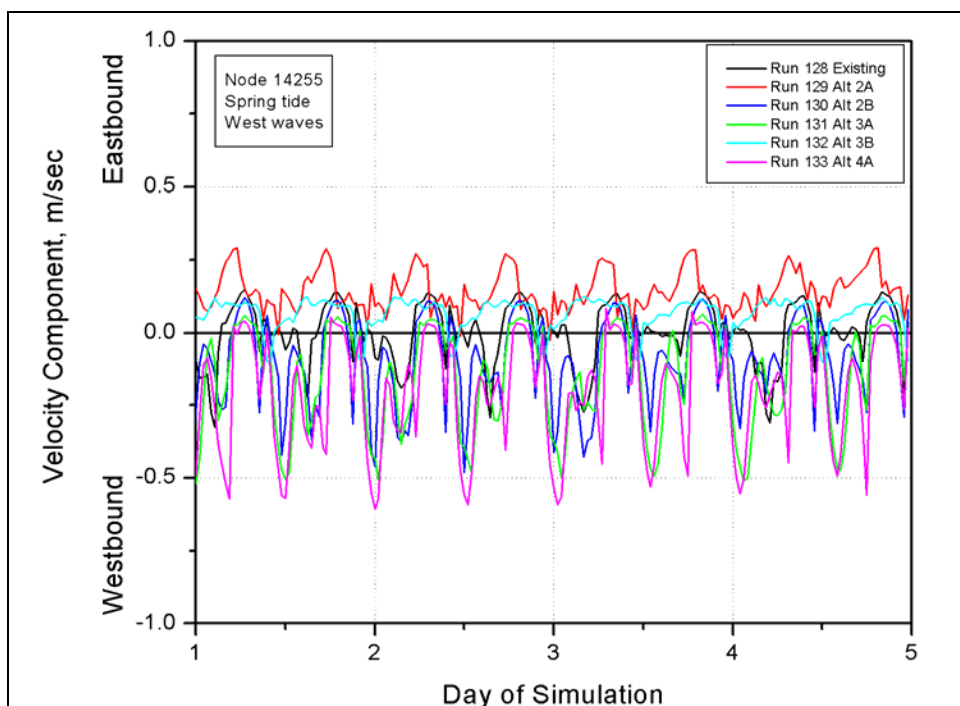
Figure E537. East-west velocity component at node 14255 (spring tide, west waves)

Appendix E   Tidal Circulation Simulation Results

Table E1
Steering Module Simulations, Definitions of Runs

Run	Alternative	Tide	Wave Direction	Wave Condition
104	Existing	Spring	west-northwest	5-m 13 sec
105	Existing	Spring	west-southwest	6-m 14 sec
106	Existing	Neap	west-northwest	5-m 13 sec
107	Existing	Neap	west-southwest	6-m 14 sec
108	Alt 2A	Spring	west-northwest	5-m 13 sec
109	Alt 2A	Spring	west-southwest	6-m 14 sec
110	Alt 2A	Neap	west-northwest	5-m 13 sec
111	Alt 2A	Neap	west-southwest	6-m 14 sec
112	Alt 2B	Spring	west-northwest	5-m 13 sec
113	Alt 2B	Spring	west-southwest	6-m 14 sec
114	Alt 2B	Neap	west-northwest	5-m 13 sec
115	Alt 2B	Neap	west-southwest	6-m 14 sec
116	Alt 3A	Spring	west-northwest	5-m 13 sec
117	Alt 3A	Spring	west-southwest	6-m 14 sec
118	Alt 3A	Neap	west-northwest	5-m 13 sec
119	Alt 3A	Neap	west-southwest	6-m 14 sec
120	Alt 3B	Spring	west-northwest	5-m 13 sec
121	Alt 3B	Spring	west-southwest	6-m 14 sec
122	Alt 3B	Neap	west-northwest	5-m 13 sec
123	Alt 3B	Neap	west-southwest	6-m 14 sec
124	Alt 4A	Spring	west-northwest	5-m 13 sec
125	Alt 4A	Spring	west-southwest	6-m 14 sec
126	Alt 4A	Neap	west-northwest	5-m 13 sec
127	Alt 4A	Neap	west-southwest	6-m 14 sec
128	Existing	Spring	west	2.5-m 10 sec
129	Alt 2A	Spring	west	2.5-m 10 sec
130	Alt 2B	Spring	west	2.5-m 10 sec
131	Alt3A	Spring	west	2.5-m 10 sec
132	Alt 3B	Spring	west	2.5-m 10 sec
133	Alt 4A	Spring	west	2.5-m 10 sec
134	Existing	Spring	west-northwest	5-year shoreline
135	Alt 2A	Spring	west-northwest	5-year shoreline
136	Alt 2B	Spring	west-northwest	5-year shoreline
137	Alt3A	Spring	west-northwest	5-year shoreline
138	Alt 3B	Spring	west-northwest	5-year shoreline
139	Alt 4A	Spring	west-northwest	5-year shoreline

(Continued)

Table E1
Steering Module Simulations, Definitions of Runs (Concluded)

Run	Alternative	Tide	Wave Direction	Wave Condition
140	Existing	Spring	west	5-year shoreline
141	Alt 2A	Spring	west	5-year shoreline
142	Alt 2B	Spring	west	5-year shoreline
143	Alt3A	Spring	west	5-year shoreline
144	Alt 3B	Spring	west	5-year shoreline
145	Alt 4A	Spring	west	5-year shoreline
146	Existing	Spring	west-southwest	5-year shoreline
147	Alt 2A	Spring	west-southwest	5-year shoreline
148	Alt 2B	Spring	west-southwest	5-year shoreline
149	Alt3A	Spring	west-southwest	5-year shoreline
150	Alt 3B	Spring	west-southwest	5-year shoreline
151	Alt 4A	Spring	west-southwest	5-year shoreline
152	Existing	Spring	west-northwest	30-year shoreline
153	Alt 2A	Spring	west-northwest	30-year shoreline
154	Alt 2B	Spring	west-northwest	30-year shoreline
155	Alt3A	Spring	west-northwest	30-year shoreline
156	Alt 3B	Spring	west-northwest	30-year shoreline
157	Alt 4A	Spring	west-northwest	30-year shoreline
158	Existing	Spring	west	30-year shoreline
159	Alt 2A	Spring	west	30-year shoreline
160	Alt 2B	Spring	west	30-year shoreline
161	Alt3A	Spring	west	30-year shoreline
162	Alt 3B	Spring	west	30-year shoreline
163	Alt 4A	Spring	west	30-year shoreline
164	Existing	Spring	west-southwest	30-year shoreline
165	Alt 2A	Spring	west-southwest	30-year shoreline
166	Alt 2B	Spring	west-southwest	30-year shoreline
167	Alt3A	Spring	west-southwest	30-year shoreline
168	Alt 3B	Spring	west-southwest	30-year shoreline
169	Alt 4A	Spring	west-southwest	30-year shoreline

Appendix F
Shoreline and Bathymetry Data[1]

This appendix contains information and documentation compiled as part of activities associated with morphologic analysis in Chapter 3 of Volume I.

Historical Aerial Photography

A sequence of aerial photography for the project site provides baseline qualitative information on the plan-view geomorphic response of an area to natural processes and engineering activities. The following 12 images illustrate the sequence of beach evolution at the Grays Harbor, WA, entrance between 1938 and 2001.

---

[1] This appendix was written by Jessica L. Baker and Mark R. Byrnes, Applied Coastal Research and Engineering, Mashpee, MA.

3 August 1938
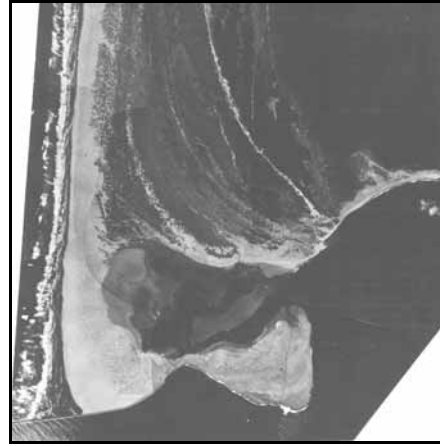
4 September 1943

4 April 1950

10 September 1964
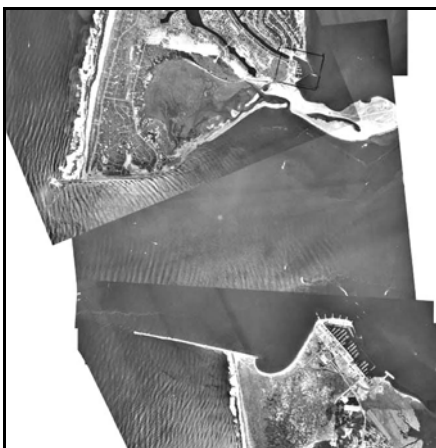
8 September 1976
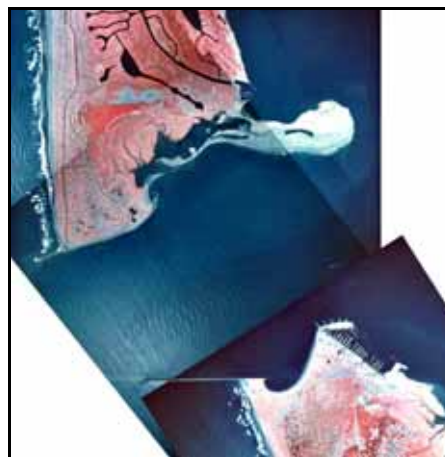
26 May 1983
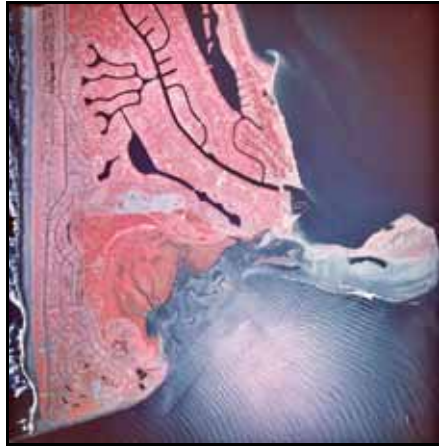
27 May 1984
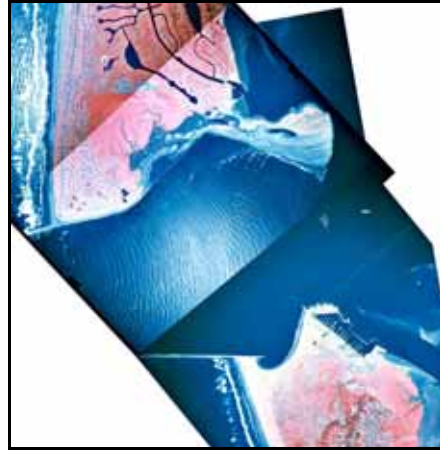
2 June 1987
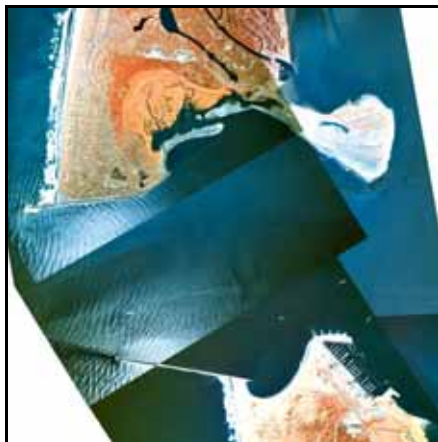
21 September 199
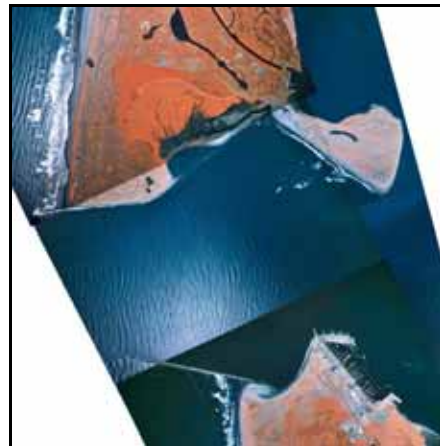
19 July 1994
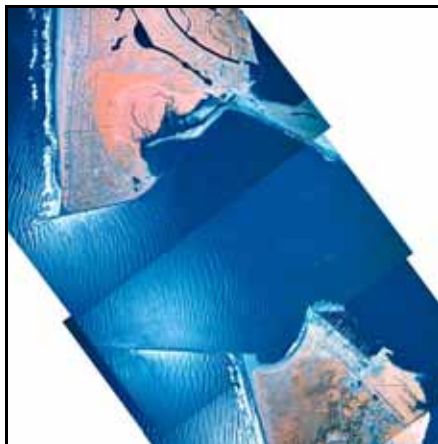
13 July 1996
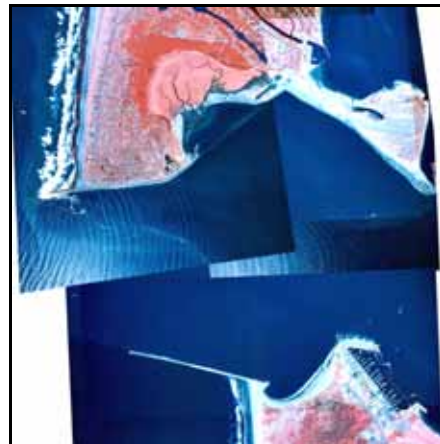
9 September 2001

Data Sources

Historical shoreline positions

Shoreline position data were compiled from U.S. Coast and Geodetic Survey (USC&GS, predecessor to the National Ocean Service (NOS)) hydrographic and topographic sheets, U.S. Army Engineer District, Seattle, field surveys, georeferenced aerial photography, LiDAR data, and Washington Department of Ecology (DOE) intertidal topographic surveys. Two sets of shoreline data were compiled; one set for a regional analysis of shoreline evolution along ocean beaches north and south of Grays Harbor, and another for a detailed analysis of the development of Damon Point.

Grays Harbor regional analysis

The data sets developed for a regional analysis of shoreline change at Grays Harbor include one shoreline for 1862 developed from a USC&GS hydrographic sheet (H-00809), two NOS topographic sheets, received in digital format from the DOE Coastal Monitoring and Analysis Program (CMAP) for the years 1886 and 1926/27; 30 Seattle District field survey maps, ranging in date from 1894 to 1980, scanned at U.S. Army Engineer Research and Development Center, Coastal and Hydraulics Laboratory (CHL) at a resolution of 300 dots per in. (dpi); six aerial photo-interpreted shorelines received in digital format from CMAP ranging from 1942 to 1999; one shoreline interpreted from LiDAR data for 1998; and three shorelines interpreted from aerial photography for August 1938, April 1950, and September 2001. Aerial photography for 1938 and 1950 was obtained in digital format from CHL. Aerial photography for 2001 was obtained from the Seattle District and scanned in-house at 400 dpi. All aerial photographs were registered with ground control data and high water shorelines were interpreted by Applied Coastal personnel. The August 1938 aerial photographic shoreline north of Grays Harbor was combined with the June 1938 Seattle District Field Survey south of Grays Harbor to produce a complete data set for the study area. Forty-two data sets were developed for documenting regional change (Table F1).

Table F1
Shoreline Source Data Characteristics

Date	Data Source	Comments
1862	USC&GS Hydrographic Survey 1:20,000 (H-00809)	High-water shoreline and mean low water line digitized from registered scanned map.
1886	USC&GS Topographic Sheet 1:10,000 (T-1701, project ph46b)	Developed by the Coastal Monitoring & Analysis Program (CMAP), Washington Department of Ecology, as part of the NOAA sponsored data rescue project.
October 1894	USACE Field Survey 1:24,000	Entrance to Grays Harbor, WA, showing proposed location of jetty for improving entrance. Data digitized from registered scanned map.
1898	USACE Field Survey 1:24,000	Grays Harbor, WA, U.S. Engineers Survey of 1898. High-water line extracted from point data provided by CMAP.
June 1900	USACE Field Survey 1:24,000 E-5-7-12	Improvement of Grays Harbor Bar and Entrance, WA, June 1900. Data digitized from registered scanned map.
June 1901	USACE Field Survey 1:24,000 E-5-7-5	Improvement of Grays Harbor Bar and Entrance, WA, June 1901. Data digitized from registered scanned map.
July 1903	USACE Field Survey 1:24,000 E-5-7-3	Improvement of Grays Harbor Bar and Entrance, WA, July 1903. Data digitized from registered scanned map.
August 1904	USACE Field Survey 1:24,000 E-5-7-7	Improvement of Grays Harbor and Bar Entrance, WA, August 1904. Data digitized from registered scanned map.
September 1906	USACE Field Survey 1:24,000 E-5-7-17	Improvement of Grays Harbor and Bar Entrance, WA, September 1906. Data digitized from registered scanned map.
May 1909	USACE Field Survey 1:24,000 E-5-7-11	Improvement of Grays Harbor Bar and Entrance, WA, May 1909. Data digitized from registered scanned map.
December 1914	USACE Field Survey 1:24,000 E-5-7-22	Grays Harbor and Bar Entrance WA, 5-10 December 1914. Data digitized from registered scanned map.
June 1916	USACE Field Survey 1:24,000	Grays Harbor Bar and Entrance, WA, June 1916. High water line extracted from point data provided by CMAP.
July 1921	USACE Field Survey 1:24,000 E-5-7-34	Grays Harbor Bar and Entrance, WA, July 1921. Data digitized from scanned map.
June 1922	USACE Field Survey 1:24,000 E-5-7-35	Grays Harbor Bar and Entrance, WA, June 1922. Data digitized from registered scanned map.

(Sheet 1 of 4)

Table F1
Shoreline Source Data Characteristics (Continued)

Date	Data Source	Comments
June 1923	USACE Field Survey 1:24,000 E-5-7-37	Grays Harbor Bar and Entrance, WA, June 1923. Data digitized from registered scanned map.
June 1925	USACE Field Survey 1:24,000 E-5-7-46	Grays Harbor Bar and Entrance, WA, June 1925. Data digitized from registered scanned map.
1926/1927	USC&GS Topographic Sheets T-4254 (1926), T-4305 (1927) (Ph-46c), 1:10,000	Developed by the Coastal Monitoring & Analysis Program (CMAP), Washington Department of Ecology, as part of the NOAA sponsored data rescue project.
August 1932	USACE Field Survey 1:24,000 E-5-7-82	Grays Harbor Bar and Entrance, WA, Condition, 9 August 1932. Data digitized from registered scanned map.
June 1936	USACE Field Survey 1:24,000 E-5-7-95	Grays Harbor Bar and Entrance, WA, Condition, June 1936. Data digitized from registered scanned map.
June 1938	USACE Field Survey 1:24,000, E-5-7-99;	Shoreline for outer coast in 1938 digitized from USACE Grays Harbor and Chehalis River, Washington Bar and Entrance Condition, June 1938.
August 1938	Black and White Aerial Photo Mosaics	Aerial mosaic is a composite of images 977-37 and 977-40 flown 8/3/38. Registration quality unclear due to lack of control points on the image. This data set combined with June 1938 to create a composite shoreline.
October 1940	USACE Field Survey 1:24,000, E-5-7-104	Grays Harbor and Chehalis River, Washington Bar and Entrance Condition. Data digitized from registered scanned map.
July 1942	US Air Force Photos	Developed by the Coastal Monitoring & Analysis Program (CMAP), Washington Department of Ecology, as part of the NOAA sponsored data rescue project.
September-October 1943	USACE Field Survey 1:24,000, E-5-7-111	Grays Harbor and Chehalis River, Washington Bar and Entrance Condition, September-October 1943. Data digitized from scanned map.
July 1944	USACE Field Survey 1:24,000, E-5-7-112	Grays Harbor and Chehalis River, Washington Bar and Entrance Condition, July 1944. Data digitized from scanned map.
September 1946	USACE Field Survey 1:24,000, E-5-7-115	Grays Harbor and Chehalis River, Washington Bar and Entrance Condition, September 1946. Data digitized from scanned map.
June 1948	USACE Field Survey 1:24,000, E-5-7-116	Grays Harbor and Chehalis River, Washington Bar and Entrance Condition, June 1948. Data digitized from registered scanned map.
April 1950	Rectified Aerial Photo	29 April 1950 mid-tide Aerial Photos. Photo numbers 974-2_5 through 974-2_9 and 974-3_10 through 974-3_20.

(Sheet 2 of 4)

Table F1
Shoreline Source Data Characteristics (Continued)

Date	Data Source	Comments
August 1953	USACE Field Survey 1:24,000, E-5-7-124	Grays Harbor and Chehalis River, Washington Bar and Entrance Condition, August 1953. Data digitized from scanned map.
August 1954	USACE Field Survey 1:24,000, E-5-7-125	Grays Harbor and Chehalis River, Washington Bar and Entrance Condition, August 1954. Data digitized from scanned map.
September 1956	USACE Field Survey 1:24,000, E-5-7-126	Grays Harbor and Chehalis River, Washington Bar and Entrance Condition, September 1956. Data digitized from scanned map.
August 1959	USACE Field Survey 1:24,000, E-5-7-128	Grays Harbor and Chehalis River, Washington Bar and Entrance Condition, August 1959. Data digitized from scanned map.
September 1965	USACE Field Survey 1:24,000, E-5-7-141	Grays Harbor Bar and Entrance Condition, September 1965. Data digitized from scanned map.
September 1968	USACE Field Survey 1:24,000, E-5-7-148	Grays Harbor and Chehalis River Washington Bar and Entrance Condition, September 1968. Data digitized from registered scanned map.
June 1974	Orthorectified Aerial Photography	Developed by the Coastal Monitoring & Analysis Program (CMAP), Washington Department of Ecology, as part of the NOAA sponsored data rescue project.
October 1975	USACE Field Survey 1:24,000, E-5-7-157	Grays Harbor and Chehalis River Washington Bar and Entrance Condition. Position of north jetty appears to be drawn incorrectly on map.
December 1980	USACE Field Survey 1:24,000, E-5-7-162	Grays Harbor and Chehalis River Washington Bar and Entrance Condition, December 1980. Position of south jetty appears to be drawn incorrectly.
June 1987	1987 orthophotos	Developed by the Coastal Monitoring & Analysis Program (CMAP), Washington Department of Ecology, as part of the NOAA sponsored data rescue project. Data were compared with 1987 scanned aerial photos. Damon Point shoreline edited to match registered aerial photo.
September 1995	Rectified Aerial Photo	Developed by the Coastal Monitoring & Analysis Program (CMAP), Washington Department of Ecology, as part of the NOAA sponsored data rescue project. Damon Point area was added on.
May 1997	Orthorectified Air Photography	Project OL-97 flown on 5/10/97. Developed by the Coastal Monitoring & Analysis Program (CMAP), Washington Department of Ecology. Compared with elevations of intertidal topography data collected with clammer on 18 August 1997 and 21 August 1997. The 1997 LiDAR shoreline developed at DOE also used for comparison.

(Sheet 3 of 4)

Table F1
Shoreline Source Data Characteristics (Concluded)

Date	Data Source	Comments
April 1998	LiDAR Data (2.75-m contour interpreted)	Developed by the Coastal Monitoring & Analysis Program (CMAP), Washington Department of Ecology, as part of the NOAA sponsored data rescue project. LiDAR data flown on 25 April – 27 April 1998. Elevation chosen by CMAP based on 1999 topographic data.
26 May 1999	Aerial Photography 1:12,000	Developed by the Coastal Monitoring & Analysis Program (CMAP), Washington Department of Ecology, as part of the NOAA sponsored data rescue project. Data were compared with May 1999 intertidal topography data.
September 2001	Registered Aerial Photography	Aerial photographs registered to Washington State Plane coordinate system. High water line interpreted from aerial photos. Intertidal topography collected for August 2001 on Ocean Shores and elevations compared with shoreline position.
		(Sheet 4 of 4)

The following images document historical shoreline position for the dates listed in Table F1 relative to orthorectified aerial photography obtained in May 1999. Jetty configurations for the survey date and present conditions are provided as a reference.

Appendix F   Shoreline and Bathymetry Data

Reconstructed to
+20 ft MLLW

Reconstructed to
+30 ft MLLW

1940
Shoreline

1942
Shoreline

1943
Shoreline

1944
Shoreline

Present Day Jetty

1940 Jetties

1942 Jetties

1943 Jetties

1944 Jetties

1500 0 1500 Feet

1999 Aerial Photo

Appendix F   Shoreline and Bathymetry Data

Appendix F   Shoreline and Bathymetry Data

Damon Point shoreline positions

Shoreline data sets were compiled to document the evolution of Damon Point between July 1921 and September 2001. July 1921 was chosen as the baseline or start date for analysis because it represents initiation of spit development after jetty construction. Jetty construction and changes in jetty elevation and length have been instrumental in the development of the spit,[1] thus including data prior to the first rehabilitation was important for understanding the evolution of the spit to structure changes. Data were developed from rectified aerial photography, Seattle District Field Surveys, and USC&GS topographic sheets (Table F2).

---

[1] Buijsman, M. C., Kaminsky, G. M., and Gelfenbaum, G. (2003). "Shoreline change associated with jetty construction, deterioration, and rehabilitation at Grays Harbor, Washington," *Shore and Beach* 71(1), 15-22.

Table F2
Damon Point Shoreline Source Data Characteristics

Date	Data Source	Comments
July 1921	USACE Field Survey 1:24,000 E-5-7-34	Grays Harbor Bar and Entrance, Washington, July 1921. Data digitized from scanned map.
1926/1927	USC&GS Topographic Sheets T-4254 (1926), T-4305 (1927) (Ph-46c) 1:10,000	Developed by the Coastal Monitoring & Analysis Program (CMAP), Washington Department of Ecology, as part of the NOAA sponsored data rescue project.
August 1938	Black and White Aerial Photo Mosaics	Composite of images 977-37 and 977-40 flown 8/3/38. Registration quality unclear due to lack of control points on the image. Position visually checked with jetty location and June 1938 USACE field survey map.
July 1942	U.S. Army Air Force Photos	Mosaics scanned and registered by the Coastal Monitoring & Analysis Program (CMAP), Washington Department of Ecology.
July 1944	USACE Field Survey 1:24,000 E-5-7-112	Grays Harbor and Chehalis River, Washington Bar and Entrance Condition, July 1944. Data digitized from registered scanned map.
September 1946	USACE Field Survey 1:24,000 E-5-7-115	Grays Harbor and Chehalis River, Washington Bar and Entrance Condition, September 1946. Data digitized from registered scanned map.
April 1950	Rectified Aerial Photo	29 April 1950 mid-tide Aerial Photos. Photo numbers 974-2_5 through 974-2_9 and 974-3_10 through 974-3_20.
September 1956	USACE Field Survey 1:24,000, E-5-7-126	Grays Harbor and Chehalis River, Washington Bar and Entrance Condition, September 1956. Data digitized from scanned map.
August 1959	USACE Field Survey 1:24,000 E-5-7-128	Grays Harbor and Chehalis River, Washington Bar and Entrance Condition, August 1959. Data digitized from registered scanned map.
September 1965	USACE Field Survey 1:24,000 E-5-7-141	Grays Harbor Bar and Entrance Condition, September 1965. Data digitized from scanned map.
April 1967	Orthorectified Air Photography	Project GH-67 flown 4/15/67. Developed by the Coastal Monitoring & Analysis Program (CMAP), Washington Department of Ecology.
June 1977	Orthorectified Air Photography	Project OL -77 flown 6/6/77 and 7/19/77. Developed by the Coastal Monitoring & Analysis Program (CMAP), Washington Department of Ecology.

(Continued)

Table F2 (Concluded)		
Date	**Data Source**	**Comments**
May 1981	Orthorectified Air Photography	Project OL-81 flown 5/28/81. Developed by the Coastal Monitoring & Analysis Program (CMAP), Washington Department of Ecology.
June 1985	Orthorectified Air Photography	Project OL-85 flown on 6/10/85. Developed by the Coastal Monitoring & Analysis Program (CMAP), Washington Department of Ecology.
August 1990	Orthorectified Air Photography	Project OL-90 flown on 8/4/90. Developed by the Coastal Monitoring & Analysis Program (CMAP), Washington Department of Ecology.
September 1995	Rectified Aerial Photo	Developed by the Coastal Monitoring & Analysis Program (CMAP), Washington Department of Ecology, as part of the NOAA sponsored data rescue project. Damon Point area was added on.
May 1997	Orthorectified Air Photography	Project OL-97 flown on 5/10/97. Developed by the Coastal Monitoring & Analysis Program (CMAP), Washington Department of Ecology.
May 1999	Aerial Photography 1:12,000	Developed by the Coastal Monitoring & Analysis Program (CMAP), Washington Department of Ecology, as part of the NOAA sponsored data rescue project. Aerial photography flown on 26 May 1999. Data were compared with May 1999 intertidal topography data.
September 2001	Rectified Infrared Aerial Photos	Image112-4 flown on 9/9/01.

Map registration and digitizing procedures

The Seattle District field survey maps were registered to the Washington State Plane South Coordinate System using Bentley's IRASC Image to Map module. Most of the older Seattle District field survey maps were drawn in a local coordinate system that did not have a geographic equivalent that could be referenced for registration. Additionally, the shape and position of the land surface in the Grays Harbor region resulted in control points being located primarily in the center of maps. The position of these control points enabled good registration for the north-south orientation, but prevented accurate registration for the east-west orientation. The best registration method available was to convert the local coordinate system into a Washington State Plane equivalent so that control could be gained across the entire map surface.

The positions of the local coordinate system tick marks were converted to Washington State Plane coordinates by registering the 1932 and 1940 maps. These maps were registered using control points obtained from the NGS on-line search and retrieval database for retrieving NGS benchmark data sheets. These maps were chosen for generating geographic coordinates for the local grid because they contained enough control points to be registered accurately using points across a large portion of both scanned maps. The local coordinate system grid was developed by digitizing tick marks from these registered maps. Tick-mark distances were verified for all registered maps, and control point locations and jetty positions were checked for positional accuracy. Using a combination of local coordinates derived from two maps, with calculated tick-mark distances and angles, the coordinate system for the area could be used for registering all remaining maps. The tick marks were used along with known control points to obtain control across the entire mapped area. All Seattle District field survey maps drawn in the local coordinate system were registered by this method. Maps not drawn in the local coordinate system were registered using tick marks plotted in geographic coordinates (latitude and longitude) and NGS control point locations. The best registration method determined for these maps included calculating an offset for the tick marks plotted on the map to translate from the original datum into the North American Datum 1983 (NAD 83). These tick marks were registered with available NGS control point locations to gain control across the entire mapped area. The root-mean-square (rms) error was recorded for each map registered, as shown in Table F3.

Table F3
RMS Horizontal Positional Error for USACE
Survey Maps Digitized at Applied Coastal

Map Date	RMS Error (± ft)
1894	19.69
1900	13.11
1901	37.97
1903	18.16
1904	34.12
1906	33.43
1909	27.99
1914	34.27
1921	14.27
1922	9.94
1923	50.13
1925	13.60
1927	8.36
1932	13.20
1936	23.71
1938	5.28
1940	9.61
1943	23.85
1944	29.14
1946	27.96
1948	8.53
1953	18.25
1954	17.69
1956	22.77
1959	19.34
1965	17.18
1968	27.15
1975	33.96
1980	8.75

Hydrographic sheet H-00809 was referenced to develop the 1862 shoreline. The best method determined for georeferencing this survey was to use the digital bathymetric data available from the GEOphysical DAta System (GEODAS) for hydrographic survey data CD[1]. Bathymetry soundings were downloaded from the CD, converted into Washington State Plane South feet, and input as control points to register the image. The RMS registration error was 38.5 ft by this method.

Aerial photographs were registered to the Washington State Plane Coordinate System by reference to identifiable landmarks. Landmarks were identified and generated from orthorectified imagery provided by the Seattle District. At least 12 control points were referenced to register each image.

Bathymetry data sources

Bathymetry data sets were compiled from NOS hydrographic surveys, Seattle District annual surveys, DOE nearshore bathymetry, and DOE intertidal topography. NOS hydrographic surveys were compiled for the years 1862 (H-00809), 1926/27 (H-04721, H-04728, H-04710), and 1955/56 (H-08250, H-08251, H-08252, H-08292, H-08293). The 1862, 1926/27 and 1955/56 data were extracted in digital format from the GEODAS CD[1]. Bathymetry data were projected into the Washington State Plane South Coordinate System, depth values converted to feet, and vertical adjustments made to convert from mean lower low water to North American Vertical Datum 1988 (NAVD 88). Seattle District historical survey data were digitized from first edition 1:24,000 annual condition surveys. Thirty survey maps were scanned at 300 dpi, georeferenced to the Washington State Plane South Coordinate System, and digitized. All data printed on survey maps were accessed to develop surfaces, including the interpreted contour lines, mean lower low water lines, and high-water lines. Methods for determining elevations for these lines are described in the following section titled "High Water Line Elevation." Digital annual survey data for 1987, 1993, 1996, 1999, and 2002 were provided by Seattle District personnel. Data were received in mean lower low water (mllw) meters and were converted to NAVD 88 ft. Data also were projected from Washington State Plane South meters to Washington State Plane South feet. High-water shorelines were included as landward boundaries for all surfaces and were assigned an elevation of 10.49 ft NAVD 88. If more than one data set was required to complete coverage of the study area, data were combined to create a composite bathymetric surface for that time period.

Nearshore bathymetry and intertidal topography data were available from the DOE in digital format for the years 1997 through 2001.[2] The North Beach area was surveyed in July 1999, July-August 2000, and August 2001; South Beach was surveyed in August-September 1999 and August 2000. Digital data were received in NAVD 88 meters; values were converted to feet. Intertidal topography data were available for August 1997 through August 2001. August

---

[1] National Geophysical Data Center. (1999). "Geophysical data system for hydrographic survey data," Volume 2, Version 4, National Ocean Service, U.S. Department of Commerce.
[2] Ruggeiro, P., and Voigt, B. (2000). "Beach monitoring in the Columbia River littoral cell, 1997-2000," Publication Number 00-06-026, Washington Department of Ecology, Olympia, WA.

1997 data were combined with the 1996 annual survey data to comprise the 1996/1997 bathymetry surface. August 2001 (North Beach) and September 2000 (South Beach) data were merged with 2001 annual survey data to comprise the 2000/2001 bathymetry surface. The following figures illustrate bathymetric survey coverages for defining sediment erosion and accretion trends.

1921 Data Coverage

1940 Data Coverage

Appendix F   Shoreline and Bathymetry Data

1975 Data Coverage

October 1975 Grays
Harbor Bar and
Entrance Condition
(USACE)

October 1975 HWL
(10.49 ft NAVD88)
(USACE)

October 1975 MLLW
(-1.51 ft NAVD88)
(USACE)

Present Day Channel

1975 Jetties

1987 Data Coverage

1987 Grays Harbor
Annual Bar and
Entrance Survey
(USACE)

1987 HWL
(10.49 ft NAVD88)
(Aerial Photos)

1987 MLLW
(-1.51 ft NAVD88)
(USACE)

Present Day Channel

Present Day Jetties

Appendix F   Shoreline and Bathymetry Data

1993 Data Coverage

- December 1993 Grays Harbor Bar and Entrance Annual Survey (USACE)
- August/September 1995 HWL (10.49 ft NAVD88) (Aerial Photos)
- December 1993 MLLW (-1.51 ft NAVD88) (USACE)
- Present Day Jetties
- Present Day Channel

Ocean Shores

Westport

N

4000   0   4000 Feet

1996/1997 Data Coverage

- 1996 Grays Harbor Bar and Entrance Annual Survey (USACE)
- 8/18/97 - 8/21/97 Intertidal Topography (USGS/ DOE CLAMMER Survey)
- May 1997 HWL (10.49 ft NAVD88) (Aerial Photos)
- Present Day Jetties
- Present Day Channel

Ocean Shores

Westport

N

4000   0   4000 Feet

1999 Data Coverage

1 1999 Annual Survey (USACE)

2 1999 Ocean Shores Nearshore Bathymetry (USGS/DOE Coastal Profiling System)

3 1999 Westport Nearshore Bathymetry (USGS/DOE Coastal Profiling System)

4 1999 Ocean Shores Intertidal Topography (USGS/DOE CLAMMER Survey)

5 1999 Westport Intertidal Topography (USGS/DOE CLAMMER Survey)

1999 High Water Line (10.49 ft NAVD) (Aerial Photo)

Present Day Jetties

Present Day Channel

2002 Data Coverage

1 2002 Annual Survey (USACE)

2 8/06/01 Nearshore Bathymetry (USGS/DOE Coastal Profiling System)

3 8/10/00-8/12/00 Nearshore Bathymetry (USGS/DOE Coastal Profiling System)

4 8/06/01 Intertidal Topography (USGS/DOE CLAMMER Survey)

5 9/25/00 Intertidal Topography (USGS/DOE CLAMMER Survey)

2001 High Water Line (10.49 ft NAVD) (09/08/01 Aerial Photo)

Present Day Jetties

Present Day Channel

Bathymetric surface data (1862 to 2002)

Grays Harbor Bathymetry 1862

Grays Harbor Bathymetry 1894

Grays Harbor Bathymetry 1900

Grays Harbor Bathymetry 1921

Grays Harbor Bathymetry 1940

Grays Harbor Bathymetry 1954/56

Grays Harbor Bathymetry
1965

Grays Harbor Bathymetry
1975

Appendix F   Shoreline and Bathymetry Data

Grays Harbor Bathymetry
1987

Grays Harbor Bathymetry
1993

Grays Harbor Bathymetry
1996

Grays Harbor Bathymetry
1999

　　　　Appendix F   Shoreline and Bathymetry Data

Grays Harbor Bathymetry 2002

Bathymetric change data set (1862 to 2002)

Grays Harbor Bathymetric Change 1921 to 1940

Grays Harbor Bathymetric Change 1940 to 1954/56

Grays Harbor Bathymetric Change 1921 to 1954/56

Grays Harbor Bathymetric Change 1900 to 1954/56

Grays Harbor Bathymetric Change 1954/56 to 1965

Grays Harbor Bathymetric Change 1965 to 1975

Grays Harbor Bathymetric Change 1975 to 1987

Grays Harbor Bathymetric Change 1954/56 to 1987

Appendix F   Shoreline and Bathymetry Data

Grays Harbor Bathymetric Change
1987 to 2002

Grays Harbor Bathymetric Change
1954/56 to 2002

High-water shoreline elevation estimation

Elevation of the high-water line was estimated by analyzing intertidal topographic data collected between 1997 and 2001 by the DOE. Two methods were employed to estimate shoreline elevation (in feet, NAVD 88). First, shoreline position data interpreted from aerial photography were overlaid on concurrent topography data to estimate average elevation of the high-water line. Collection dates of topographic data were chosen to most closely approximate the dates of interpreted shorelines. Topography elevations that fell within 10 ft (horizontal distance) of mapped shoreline position were compiled, and average elevation and standard deviation were calculated for the selected points (Table F4).

Individual calculations were made for the Ocean Shores and Westport data sets. For Ocean Shores (North Beach), three time periods were analyzed: August 1997, May 1999, and August 2001. Corresponding shoreline dates were May 1997, May 1999, and September 2001. Average elevation values along the shorelines ranged from 10.08 to 10.64 ft NAVD, with a standard deviation ranging from 0.91 to 1.48 ft. For the Westport data (South Beach), two time periods were evaluated (August 1997 and August 1999). The 1997 data had an average elevation of 13.32 ft, and the 1999 shoreline averaged 10.48 ft. The standard deviations were 1.12 and 1.25 ft, respectively.

Table F4			
Average Shoreline Elevations Extracted from Topography Data			
Shoreline Date	**Topography Date**	**Average elevation**	**Standard Deviation**
Ocean Shores			
5/10/1997	8/18/1997	10.15	1.06
5/26/1999	5/18/1999	10.08	1.48
8/6/2001	9/9/2001	10.64	0.91
Westport			
5/10/1997	8/21/1997	13.32	1.12
5/26/1999	8/26/1999	10.48	1.25

The second method determined average elevation of the berm crest by analyzing cross-sectional profiles from the topographic data. Four transect lines were selected along Ocean Shores beach (Figure F1) to represent variability along the shoreline. The August 2001 topography data were queried for extracting elevations along profile lines, and elevations were plotted to determine the shape of the beach and height of the berm crest (Figure F1). High-water shoreline elevations ranged from 10.14 to 11.29 ft.

Based on the information derived from these analyses, the high-water shoreline elevation was determined to be about 10.5 ft NAVD 88. The standard deviation indicates an average variability of 1.17 ft. This elevation is greater

than that chosen by the DOE for extracting a shoreline from 1997 and 1998 LiDAR data. The elevation determined by the DOE was 9 ft (2.75 m). The difference in average high-water shoreline elevations may be the result of different methods involved in extracting elevations or the different spatial extents of the data.
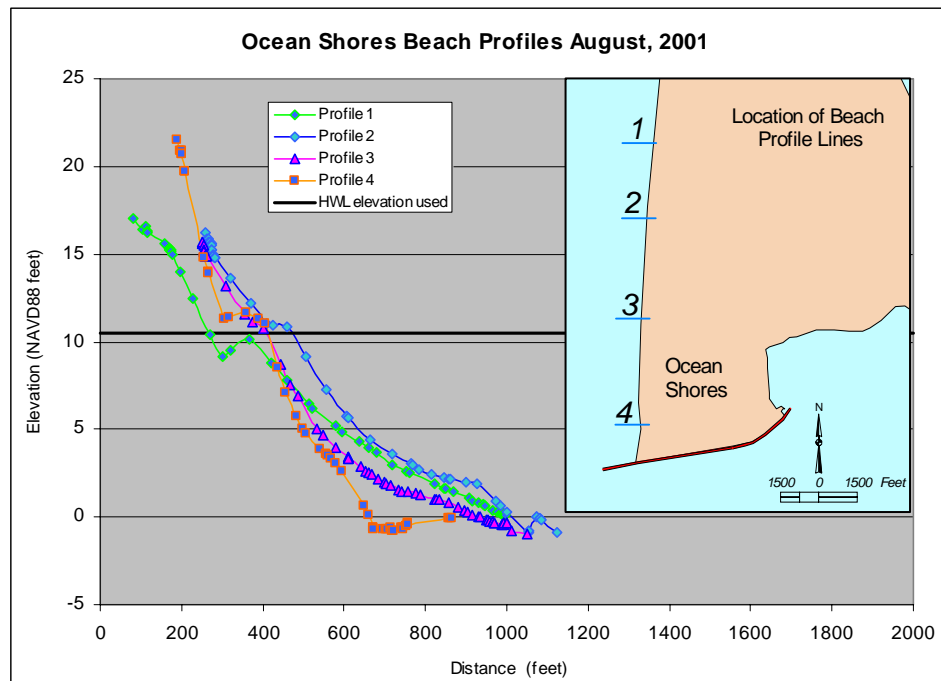
Figure F1. Elevation determination for high-water shoreline

MLLW reference elevation

Data sets lacking nearshore bathymetry or intertidal topography often included the mllw line as an intermediate contour between the high-water shoreline and offshore bathymetry data. Including the position of the mllw line in bathymetric surface comparisons is important for maintaining proper beach shape when interpolating from the high-water line to offshore bathymetry data and calculating volume changes within the nearshore region. For data sets developed from Seattle District field survey maps, the position of the mllw was digitized. The depth of the mllw line was determined to be 1.5 ft NAVD based upon elevation adjustment for tidal benchmark SD0042 (see section titled "Vertical Datum Adjustments"). This depth was verified by comparing nearshore bathymetry values with mllw lines for years where both data exist. The 1927 and 1956 NOS hydrographic survey data were selected for mllw depth verification. For each data set, a Triangulated Irregular Network (TIN) surface was created using nearshore bathymetry data, and the position of the mllw line was overlaid on the model surface to determine the average elevation at that position. Profiles were extracted along the shoreline to compare beach elevation

at the position of mllw. The average elevation associated with the mllw line was between -1 and -2 ft. Profiles from each data set are shown in Figure F2.
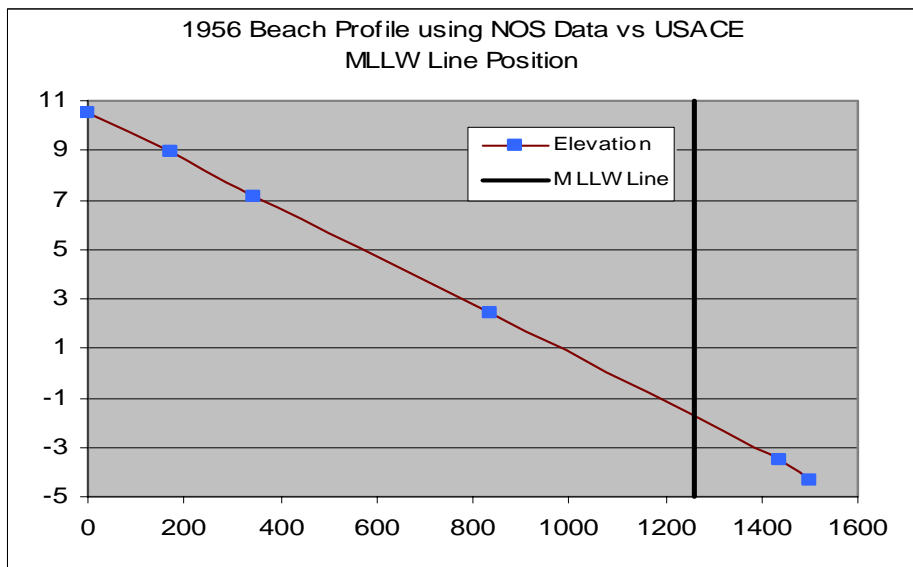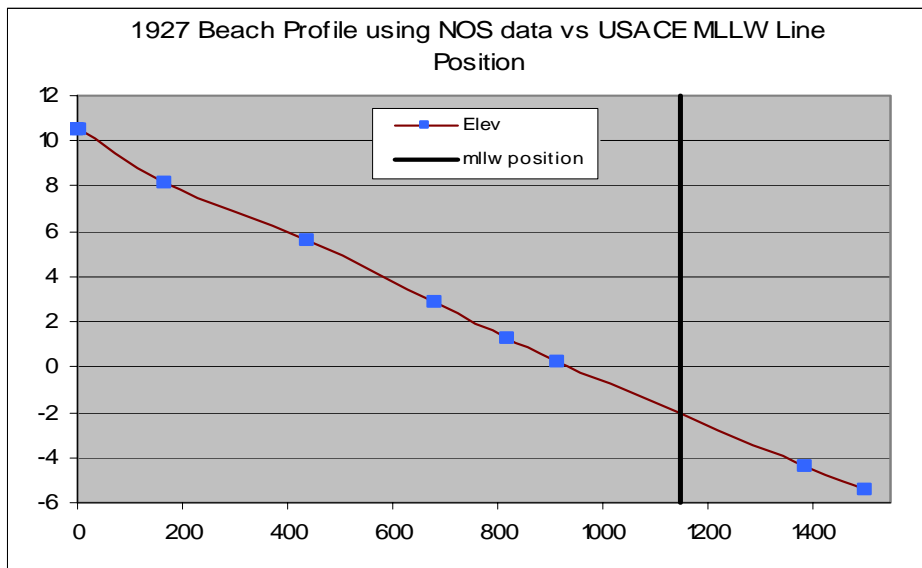
Figure F2. Relationship between mllw at base of a beach and nearshore water depths

Appendix F   Shoreline and Bathymetry Data

For recent data sets (e.g., 1987 and 1993) without available Seattle District mllw lines or nearshore bathymetry data, the position of the mllw line was determined using established relationships between the position of mllw and the position of the high-water line (hwl) on recent Seattle District field survey maps (Figure F3). The position of the mllw line for 1975 and 1980 Seattle District maps was approximately 550 ft seaward of the hwl. To verify the accuracy of this relationship, a mllw line was established 550 ft seaward of the hwl for the years 1999 and 2001. Two surfaces were created for each time period; one including nearshore bathymetry and intertidal topography with offshore data, and one using the hwl, mllw line, and offshore data. Cross sections were plotted along each surface to compare the beach shape obtained using each method. An example comparison for Profile 3 for the 2001 survey is shown in Figure F4.
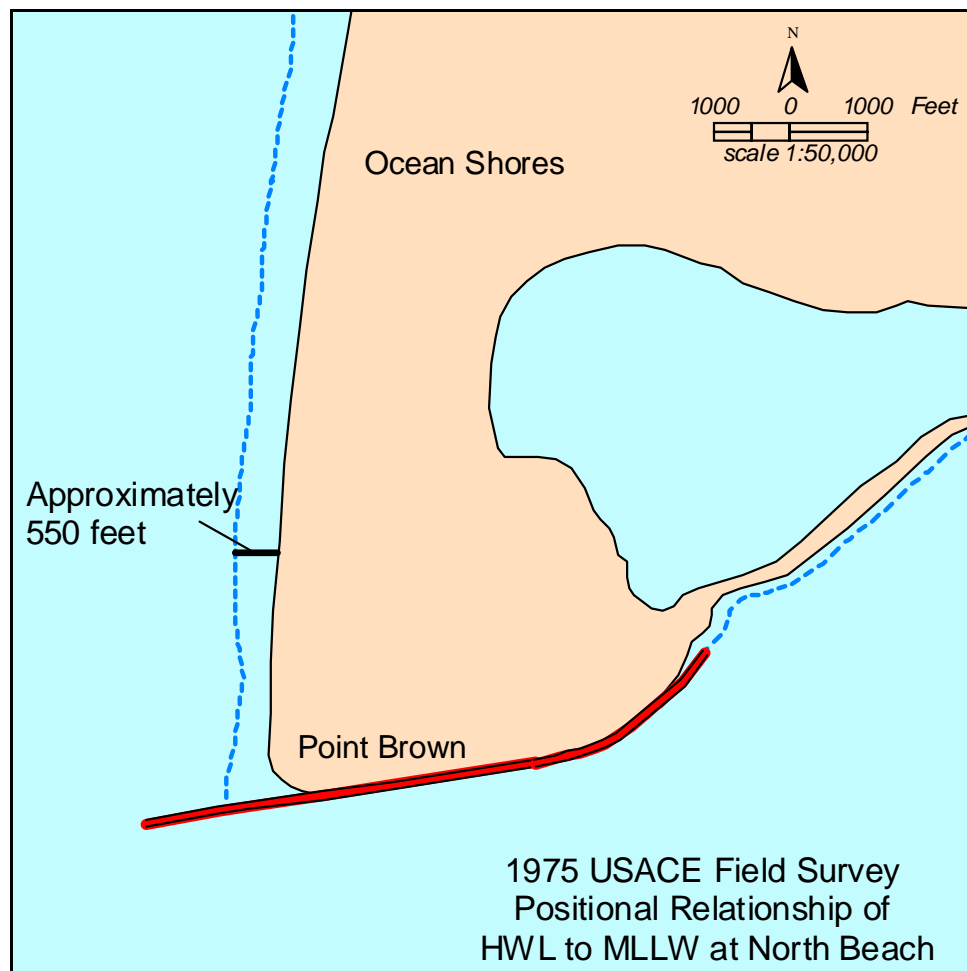
Figure F3. Distance relationship between mapped hwl and mllw for 1975 Seattle District Field Survey
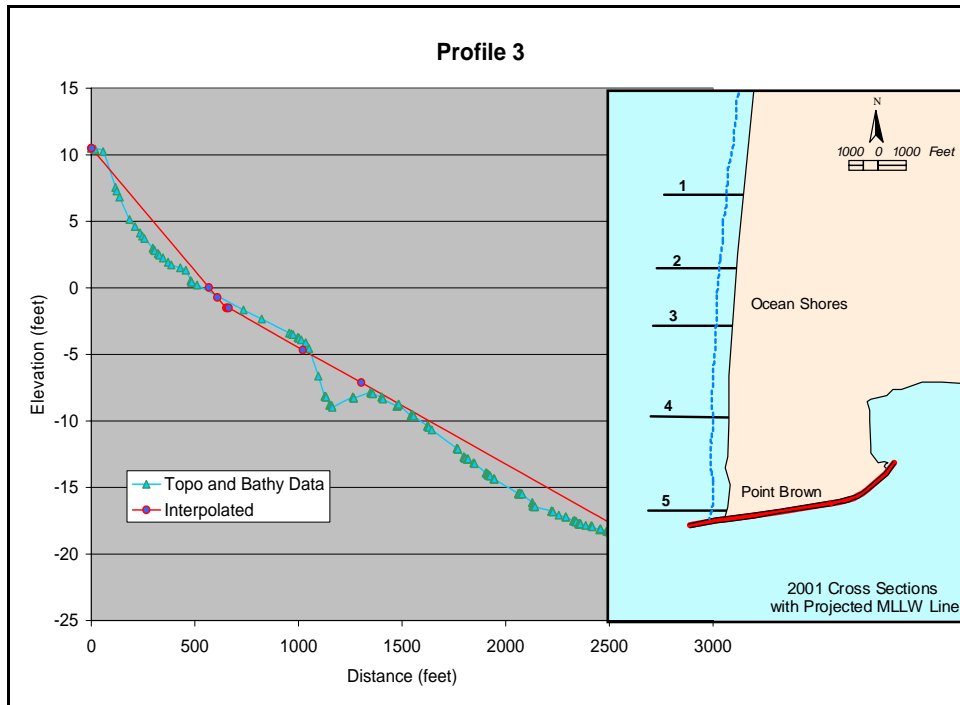
Figure F4. Comparison of measured profile elevations versus projected profile shape using hwl to mllw distance relationship with 2001 beach and nearshore survey data set

Vertical datum adjustments

All bathymetry data were adjusted to the NAVD 88 datum. Sea level rise during the study time period (1862 to 2002) was determined to be negligible in this region based on NOS water level records (Figure F5), so vertical adjustments were calculated for tidal datum differences only. NOS hydrographic surveys were adjusted according to vertical datum references found in the descriptive reports for each survey. Present day offset values for tidal benchmarks were obtained from the National Geodetic Survey (NGS) Web site (http://www.ngs.noaa.gov) and were used to make the adjustment for each data set. The tidal benchmark closest to the study area is SD0042 (Figure F6). For data sets inside the harbor where the benchmark used was unclear or unknown, the conversion from mean low water or mllw to NAVD 88 at SD0042 (-0.1 and -1.51 ft, respectively) served as a default. Adjustments for each NOS hydrographic survey used in this study are listed in Table F5.
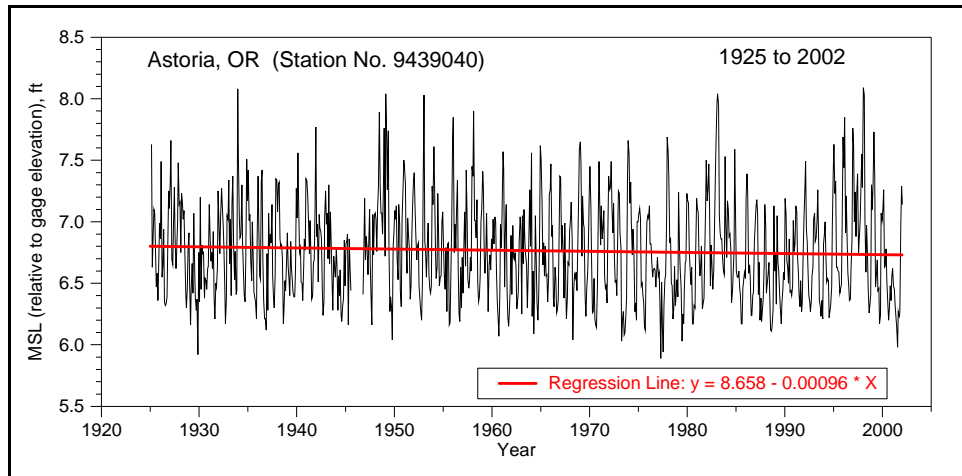
Figure F5. Water level change at Astoria, OR (mouth of the Columbia River), 1925 to 2002. Trends of change is about zero for period of record
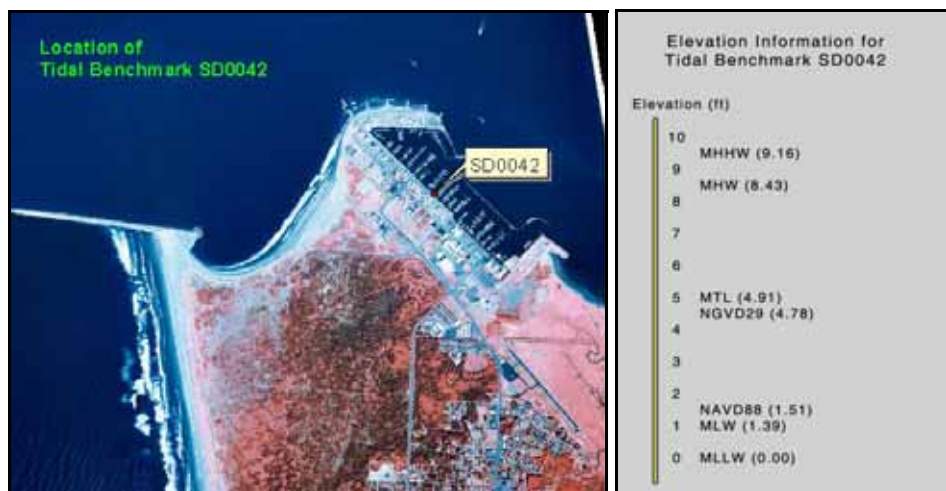
Figure F6. Location of tidal benchmark SD0042 and datum relationships

Table F5
Vertical Adjustments Made to Hydrographic Sheets

Survey	Date	Adjustment	Benchmark	Source
H-00809	1862	-0.1	SD0042	SD0042 assumed (conversion is MLW to NAVD 88).
H-04621	1926	-0.52	Ft. Stevens	H-04621 Descriptive Report.
H-04728	1927	-1.17	Pt. Grenville	H-04710 Descriptive Report.
H-04710	1927	-1.17	Pt. Grenville	H-04728 Descriptive Report.
H-08250	1956	-1.51	SD0042	H-08252 Descriptive Report.
H-08251	1956	-1.51	SD0042	H-08252 Descriptive Report.
H-08252	1955	-1.51	SD0042	H-08252 Descriptive Report.
H-08292	1956	-1.51	SD0042	H-08252 Descriptive Report.
H-08293	1956	-1.51	SD0042	H-08252 Descriptive Report.

All Seattle District survey maps also were adjusted to NAVD 88 from mllw using SD0042. For maps generated by the Seattle District prior to 1994, all data were adjusted by an additional -1.34 ft to convert from Seattle District mllw to NOS mllw. This adjustment was determined from the August 1953 survey, which described the difference between Seattle District and NOS mllw calculations (Figure F7). Confirmation of this offset was obtained through personal correspondence with Seattle District personnel, who indicated that -1.5 ft had been used previously as the adjustment from Seattle District mllw to NOS mllw for Seattle District surveys prior to 1994. In 1994, the Seattle District changed this practice, and the District mllw has since been the same as NOS mllw. Thus, all Seattle District data sets conducted after 1993 do not require a vertical adjustment for the old mllw datum difference.

NOTE:
SOUNDINGS ARE IN FEET AND REFER TO THE PLANE OF M.L.L.W. ESTABLISHED IN 1898 (CORPS OF ENGINEERS DATUM), WHICH IS 1.34 FEET LOWER THAN M.L.L.W. AS NOW ESTABLISHED BY U.S.C. & G.S.

Figure F7.   Vertical datum adjustment prior to 1994 as stated on Seattle District bar and entrance condition survey dated August 1953, File E-5-7-124

Bathymetric surface error and uncertainty estimates

Uncertainty estimates were calculated for the 1954/1956, 1987, and 2002 bathymetric surfaces using the methods outlined in Byrnes and Baker (2002).[1]

---

[1] Byrnes, M. R., and Baker, J. L. (2002). "Quantifying potential measurement errors and uncertainties associated with bathymetric change analysis," ERDC/CHL CHETN-IV-50, Coastal and Hydraulics Laboratory, U.S. Army Engineer Research and Development Center, Vicksburg, MS.

Twelve sets of line pairs were chosen to represent terrain variability across the study area. Line pairs were chosen that would accurately reflect the survey track line spacing and the irregularity of prominent geomorphic features in the region. An example of the line pairs examined for this analysis is displayed in Figure F8. Lines were adjusted slightly for each time period to overlay survey track lines for that year.

Bathymetry data were extracted along each line to calculate the variation in depth between the line pairs. Depths were extracted at 5-ft intervals along each line and the absolute value of the difference between points was averaged to calculate the potential uncertainty for each line pair (Figure F9). Uncertainty values for each pair were then grouped into similar geomorphic regions and averaged to estimate total uncertainty for each zone within the study area.

Four regions were defined within the study area for individual uncertainty calculations (Figure F10), including the Offshore/North Beach, Ebb Shoal, South Beach, and the Inlet Throat/South Jetty/Sand Island Shoal. Potential uncertainty was calculated for each of the different regions so that areas with highly variable topography (such as the Inlet Entrance) would not be averaged with areas of more regular topographic features (such as South Beach) when addressing uncertainties within volume change calculations for individual sediment budget polygons. Total surface uncertainty was then calculated for each time period using an area-weighted average of uncertainty for all zones.

The results of the uncertainty calculations are summarized below in Figures F11 through F14. Overall, the potential uncertainty calculations for each zone exhibit similar trends during every time period. The Offshore/North Beach and South Beach zones showed the lowest potential uncertainty for all time periods (i.e., little geomorphic variability), with the Ebb Shoal showing greater potential uncertainty and the Inlet Entrance/Sand Island Shoal/South Jetty region showing the greatest amount of potential uncertainty for each time period. These results were expected due to the topographic variability observed within each region. Temporal trends for these four regions were similar as well, with uncertainty generally decreasing from 1954 to 2002. One deviation from this general trend was observed in the 1987 surface, with South Beach showing a smaller amount of uncertainty than the 2002 surface (±0.4 and ±0.7 ft, respectively).

In all zones, the 1954/1956 surface showed greater potential uncertainty than the 2002 surface. The total surface uncertainty calculated for each time period also showed a consistent decline from 1954/1956-2002, decreasing from an average of ±1.5 ft for 1954/1956 to ±1.3 ft for 1987 to ±0.9 ft for 2002. Combining this information to estimate the impact of potential uncertainties associated with volume change calculations derived from these surfaces resulted in a rms variation of ±1.7 ft for the 1954/1956 to 2002 change surface and ±1.6 ft for the 1987 to 2002 change surface.
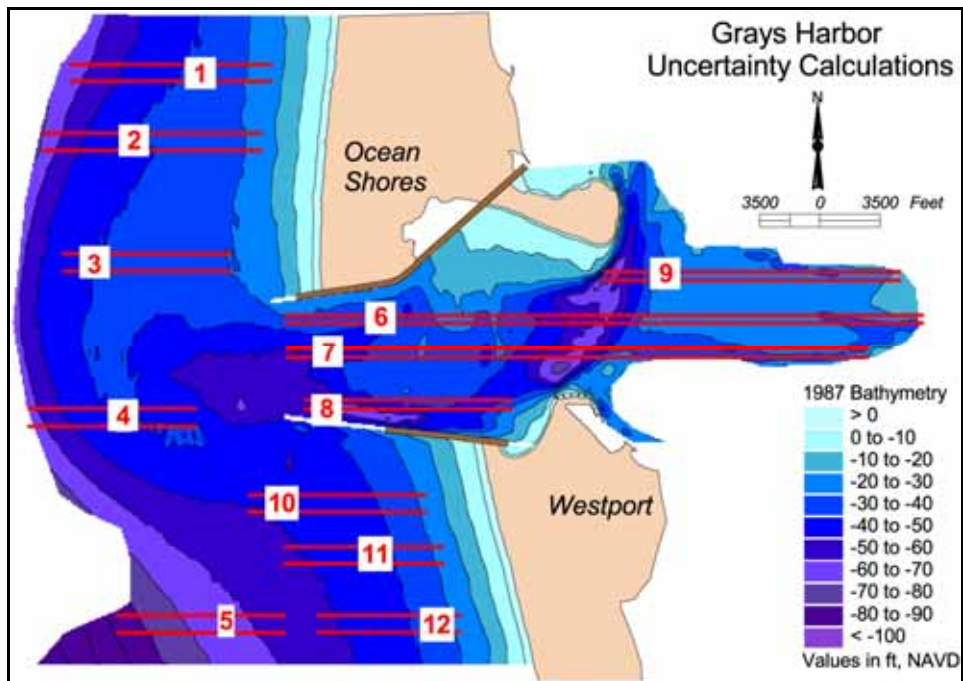
Figure F8.   Location of line pairs used to calculate potential uncertainty
             for bathymetric surfaces
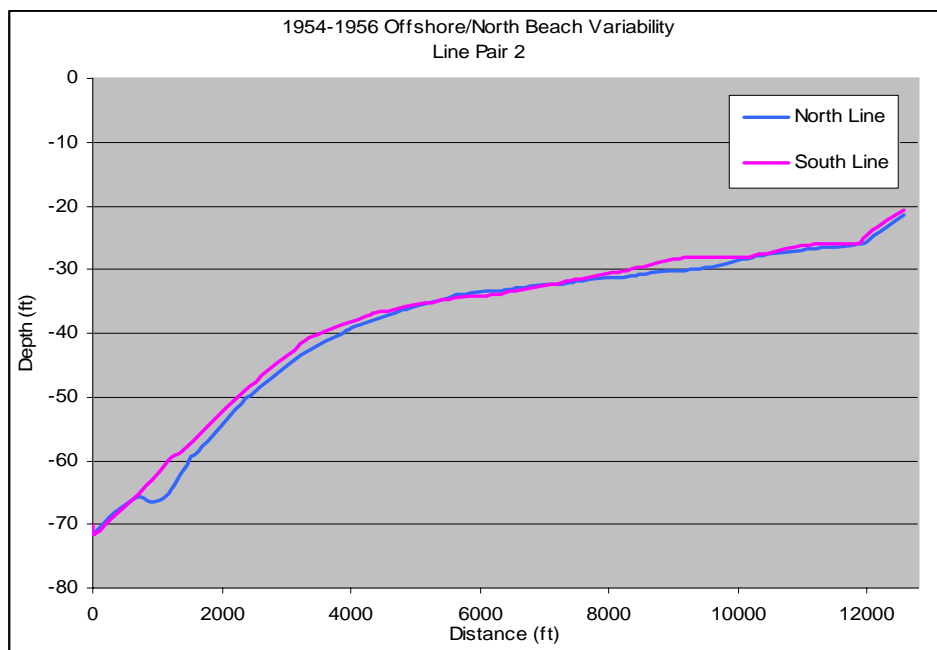
Figure F9.   Example of a cross-section line pair used to estimate potential
             uncertainty for 1954/1956 bathymetric survey data
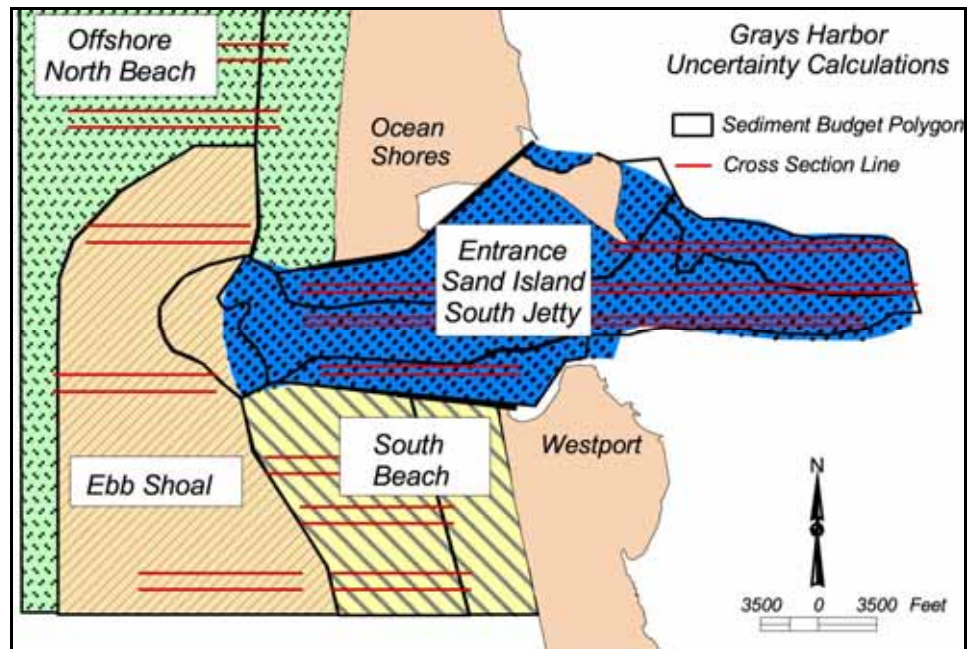
Figure F10. Uncertainty calculation polygons
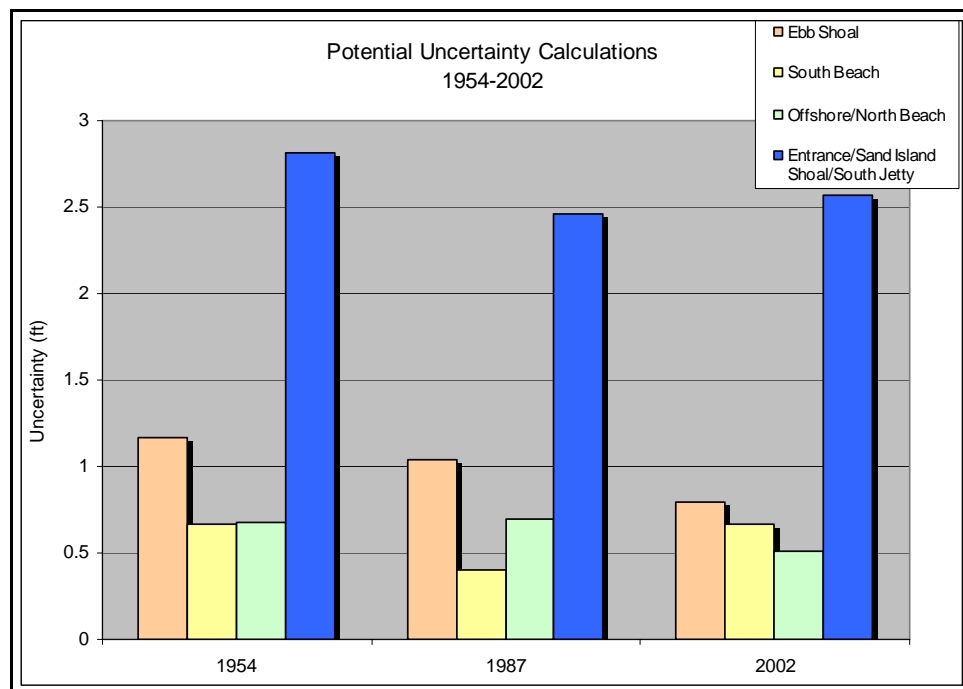
Figure F11. Average potential elevation uncertainty, 1954 to 2002

Table F6
1954/56 Uncertainty Calculations

Offshore/North Beach					Ebb Shoal			
Pair	Variability	Length (ft)	Variability x Length		Number	Variability	Length (ft)	Variability x Length
1	0.8	12,205	10048		3	0.5	9,820	5,368
2	0.5	12,085	6392		4	1.3	7,565	9,931
	Average Variability:		**0.68**		5	1.0	7,795	7,991
						Average Variability:		**1.17**

Inlet Entrance/South Jetty/Sand Island Shoal					South Beach			
Pair	Variability	Length (ft)	Variability x Length		Number	Variability	Length (ft)	Variability x Length
6	1.9	31,890	61,865		10	0.7	10,595	7,423
7	3.5	31,515	111,007		11	0.4	8,725	3,532
8	1.2	10,165	12,548		12	0.9	8,240	7,515
9	4.6	12,275	56,102			**Average Variability:**		**0.7**
	Average Variability:		**2.8**					

Average across the Surface:	**1.3**
Average (area weighted) across the Surface:	**1.5**
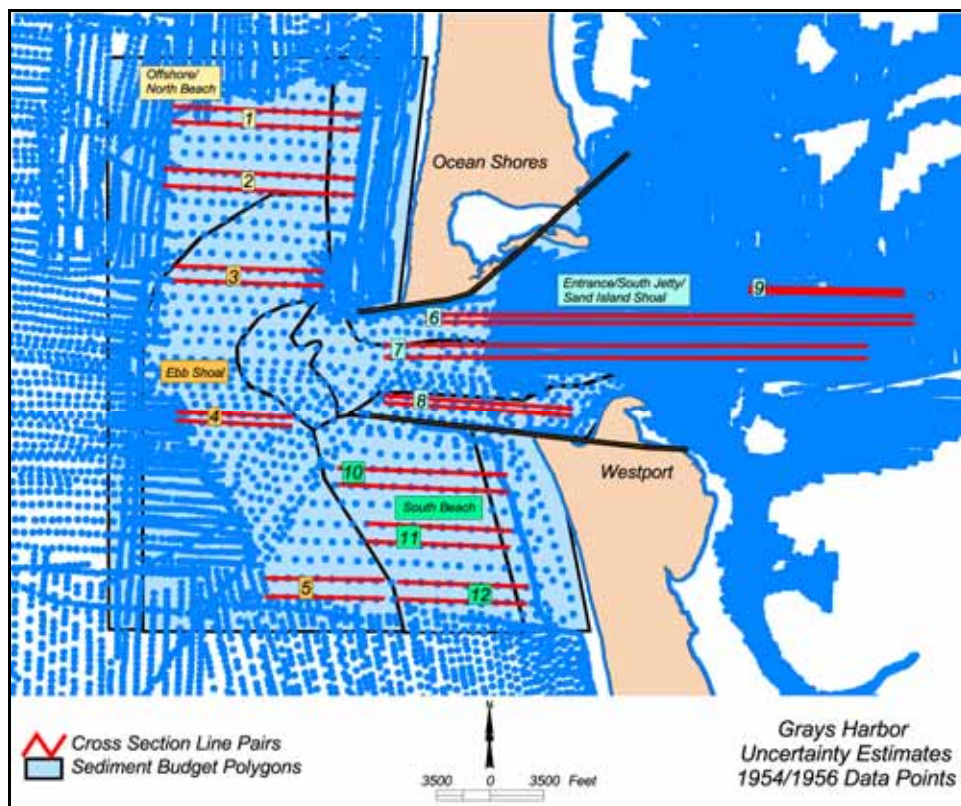
Figure F12.   Uncertainty calculations and line pairs for 1954/1956 bathymetry surface

Table F7
1987 Uncertainty Calculations

Offshore/North Beach					**Ebb Shoal**			
Pair	**Variability**	**Length (ft)**	**Variability x Length**		**Pair**	**Variability**	**Length (ft)**	**Variability x Length**
1	0.7	11,840	8463		3	0.5	9,890	4454
2	0.7	12,780	8749		4	1.5	9,830	15022
	Average Variability:		**0.7**		5	1.1	9,855	11194
						Average Variability:		**1.0**
Inlet Entrance/South Jetty/Sand Island Shoal					**South Beach**			
Pair	Variability	Length (ft)	Variability x Length		Pair	Variability	Length (ft)	Variability x Length
6	1.5	37,320	56,531		10	0.4	10,410	4,378
7	3.3	33,960	111,795		11	0.5	9,350	4,545
8	1.5	17,375	25,272		12	0.3	8,375	2,367
9	4.5	12,105	54,500			**Average Variability:**		**0.4**
	Average Variability:		**2.5**					
						Average across the Surface:		1.1
						Average (area-weighted) across the Surface:		1.3
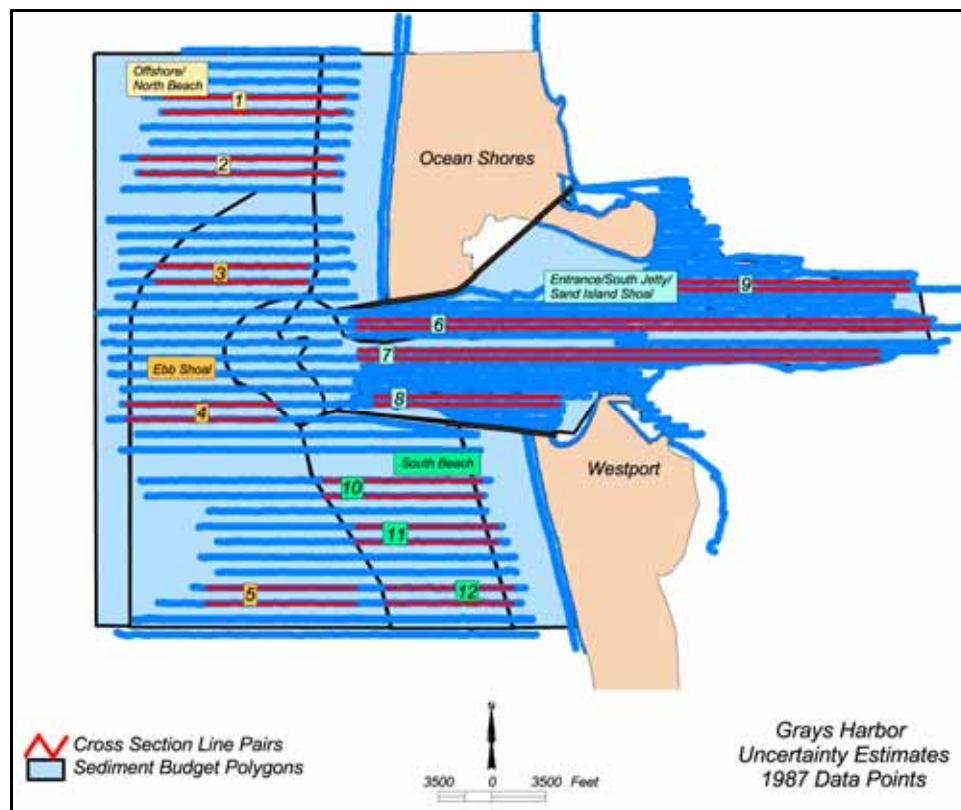
Figure F13. Uncertainty calculations and line pairs for 1987 bathymetry surface

Table F8
2002 Uncertainty Calculations

Offshore/North Beach					Ebb Shoal				
Pair	Variability	Length (ft)	Variability x Length		Pair	Variability	Length (ft)	Variability x Length
1	0.5	11,810	6,101		3	0.3	9,965	2,556
2	0.5	12,780	6,490		4	1.4	7,760	10,910
	Average Variability:		0.5		5	0.9	9,865	8,552
						Average Variability:		0.8

Inlet Entrance/South Jetty/Sand Island Shoal					South Beach				
Pair	Variability	Length (ft)	Variability x Length		Pair	Variability	Length (ft)	Variability x Length
6	2.6	37,285	96,980		10	1.0	10,430	10,373
7	2.6	34,005	88,746		11	0.4	9,305	3,644
8	3.4	17,245	58,690		12	0.5	8,385	4,602
9	1.5	16,130	24,375			Average Variability:		0.7
	Average Variability:		2.6					
					Average across the Surface:			1.1
					Average (area-weighted) across the Surface:			1.3
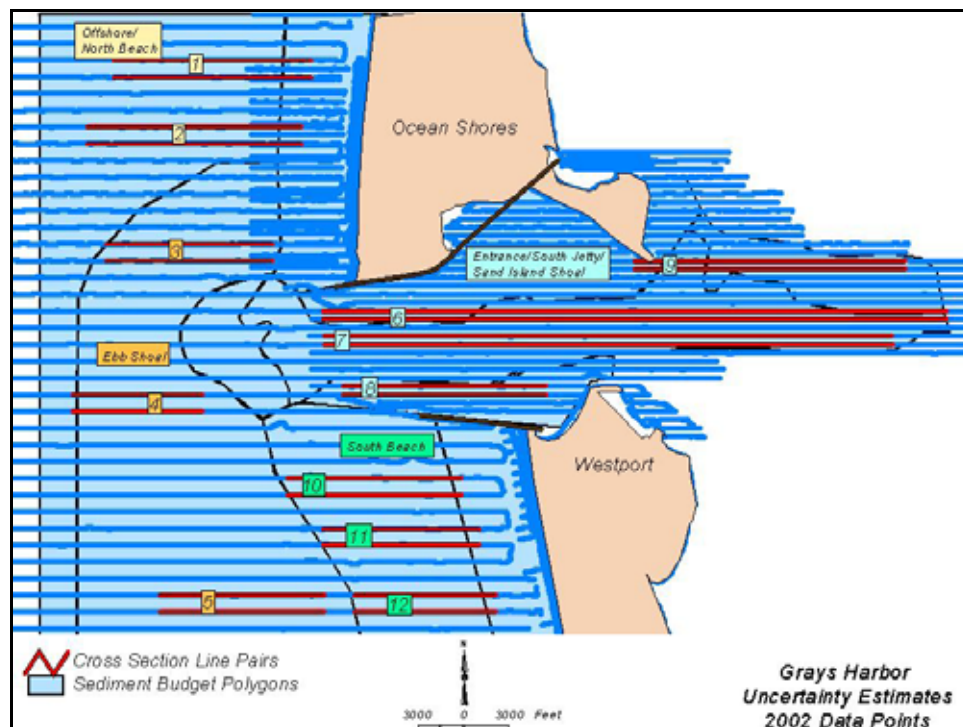
Figure F14. Uncertainty calculations and line pairs for 2002 bathymetry surface

Appendix G
Longshore Sand Transport Modeling and Shoreline Change Modeling with GENESIS-T: Seasonal Variation in Cross-shore Transport Distribution[1]

This appendix presents the development of a variable cross-shore transport budget for implementation in the GENESIS-T model (Hanson and Kraus 2000), a research version of the standard GENESIS model (Hanson and Kraus 1989). The sensitivity of the GENESIS-T model to the cross-shore sediment budget in space and time is evaluated. Estimates of the cross-shore transport patterns were predicted using a combination of the CoastL wave-current interaction model and computations of the potential sediment transport field using the van Rijn (1993) combined wave-current transport model described in Chapter 8 of the technical report. The analysis resulted in GENESIS-T simulations with a cross-shore sediment supply rate that varies both seasonally and spatially in accordance with the rip current patterns predicted by CoastL. Application of the GENESIS-T model to calculating longshore sand transport and modeling shoreline change is discussed in Chapter 6 of Volume I.

Cross-shore Transport Distribution in GENESIS-T

Incorporation of cross-shore transport rates to GENESIS-T is discussed in Chapter 6 of Volume I. In most applications, the cross-shore transport is represented by a constant longshore distribution of cross-shore transport. Net onshore transport represents a source of sediment, whereas offshore transport represents a sink for sediment. The distribution is input into GENESIS-T

---

[1] Written by Neil J. MacDonald, Philip D. Osborne, Maria Timpano, and David Katzev, Pacific International Engineering, PLLC, Edmonds, WA, and Ty V. Wamsley, Coastal and Hydraulics Laboratory, U.S. Army Engineer Research and Development Center, Vicksburg, MS.

through a file called bypass.dat, which contains cross-shore sediment transport rates in cubic model units/hour/model unit. The method of using a single bypassing file to model all alternatives will herein be defined as the Standard Bypassing Method or SBM. The CoastL simulations provided analysis of the patterns of on-offshore flows (i.e., rip cells) for each of the alternatives for a wide range of wave and tide forcing combinations. This information was incorporated into the GENESIS-T modeling through the development of bypassing files that characterize the seasonal variations in cross-shore sediment transport climate at the site.

The GENESIS-T simulations completed using the seasonally varying bypass files will herein be referred to as the Hybrid Bypassing Method, or HBM. The additional longshore transport and shoreline change modeling described in this appendix involved the calculation of sediment transport potentials, q_s, development and calibration of the hybrid bypassing files, completion of 5- and 30-year structural alternative simulations, and analysis of the results to determine changes in longshore transport and shoreline position.

Seasonal Variation of Sediment Transport Potential, q_s

The first step in the development of the seasonally varying bypass files (HBM) for Grays Harbor north jetty was the calculation of cross-shore rates q_s. This section describes how CoastL simulations, analysis of wave climatology, and the van Rijn (1993) combined wave-current sediment transport model were integrated to develop the required cross-shore q_s.

Coast-L modeling

Ninety-six distinct significant wave height H_s, period T_p, and azimuth direction (A_z) and tidal forcing combinations at the north jetty were simulated with the CoastL model (MacDonald 1998) as described in Chapter 8 of Volume I. These conditions are summarized in Table 8-3.

Calculation of q_s

The van Rijn (1993) combined wave-current sediment transport model was used to calculate q_s with the hydrodynamics simulated by CoastL. The transport calculations were performed using a program developed by Pacific International Engineering, PLLC, for this application. Inputs to the program include the finite-difference significant wave height and component velocity vectors at each location in the CoastL domain.

Figure G1 is an example illustrating the calculation of q from CoastL results. The sediment grain size distribution for the transport modeling had a d_{35} of 0.16 mm, a d_{50} of 0.20 mm, and d_{90} of 0.40 mm.
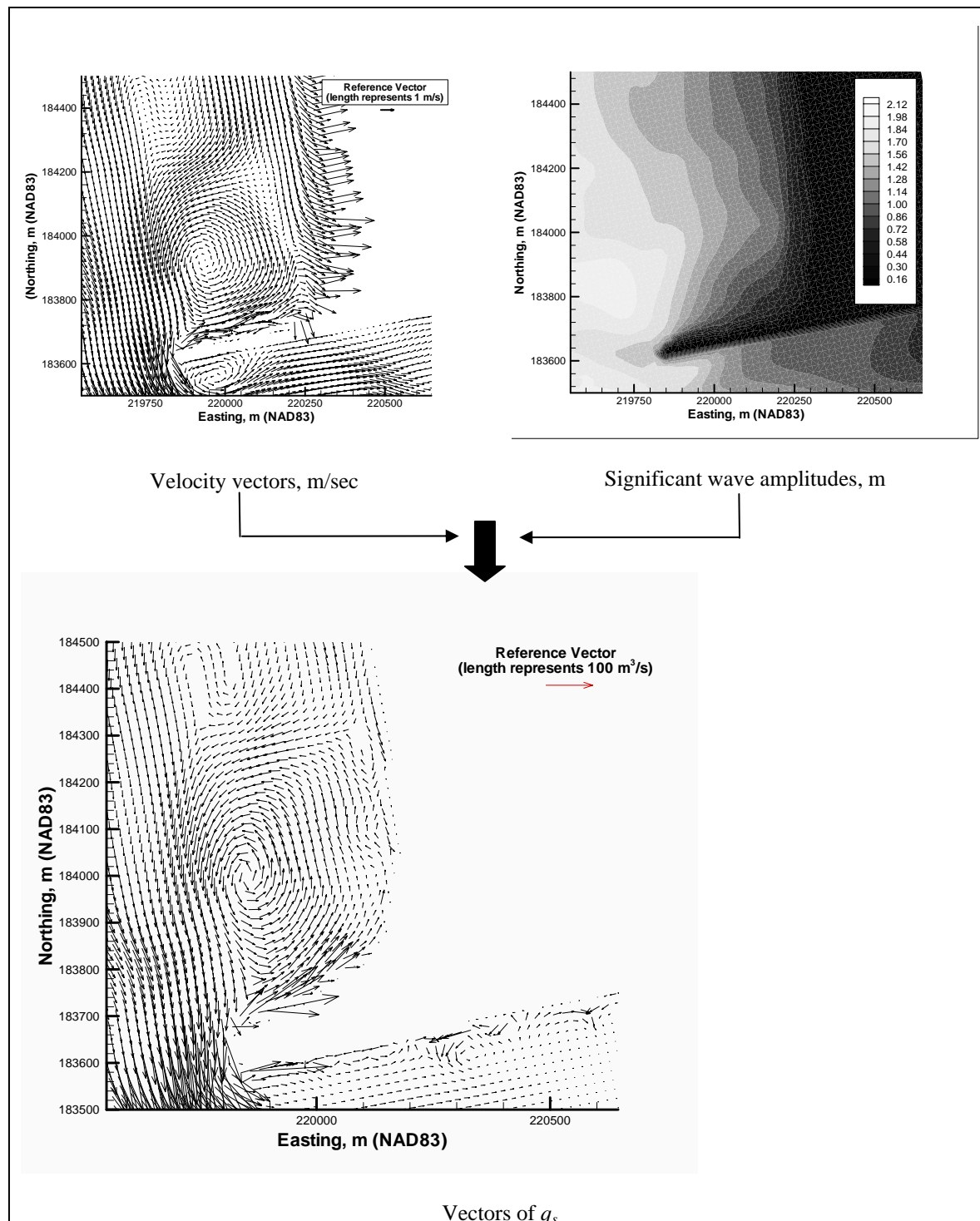
Figure G1. Example of significant wave height, H_s, and velocity vectors, (u,v), predicted by CoastL and calculated with van Rijn model for existing condition for H_s = 5 m, T_p = 13 sec, from A_z 300 deg for peak flood

Calculations of q_s were made for each alternative and for each of the 96 hydrodynamic combinations. Representative seasonal estimates of q_s (winter, spring, summer, and fall) were developed for each alternative by weighting the individual transport potentials for each combination with the joint seasonal frequency of occurrence. A joint seasonal frequency of occurrence distribution was determined for each of the wave height, period, and direction combinations in Table 8-3 from the CDIP buoy measurements for the period 1994 to 2002. Table G1 summarizes the results of this analysis. The methodology for calculating geospatially referenced seasonally characterized q_s is outlined in Figure G2.

Table G1
Seasonal Frequency of Occurrence of Wave Parameter Combinations at North Jetty, Grays Harbor

A_z Dir	H_s (m)	T_p (sec)	Winter (percent)	Spring (percent)	Summer (percent)	Fall (percent)
210	2	8	3.54	4.02	5.55	2.99
210	2	13	4.21	5.19	0.68	1.42
210	2	18	0.61	0.54	0.19	0.07
210	5	8	2.15	0.50	0.08	0.27
210	5	13	2.75	0.80	0.00	0.17
210	5	18	0.40	0.12	0.00	0.01
250	2	8	8.02	6.88	11.94	6.44
250	2	13	10.27	8.00	1.14	2.78
250	2	18	2.10	1.16	0.22	0.36
250	5	8	3.61	0.94	0.02	0.32
250	5	13	5.45	1.76	0.00	0.50
250	5	18	1.10	0.43	0.00	0.01
280	2	8	14.15	20.58	34.41	38.07
280	2	13	21.39	22.97	4.80	16.22
280	2	18	5.45	4.76	0.75	1.58
280	5	8	4.05	3.01	0.25	1.60
280	5	13	6.16	3.51	0.09	0.80
280	5	18	1.23	0.99	0.02	0.05
300	2	8	1.42	5.95	35.69	17.46
300	2	13	1.60	6.76	3.41	7.96
300	2	18	0.20	0.90	0.76	0.82
300	5	8	0.06	0.05	0.00	0.04
300	5	13	0.07	0.17	0.00	0.05
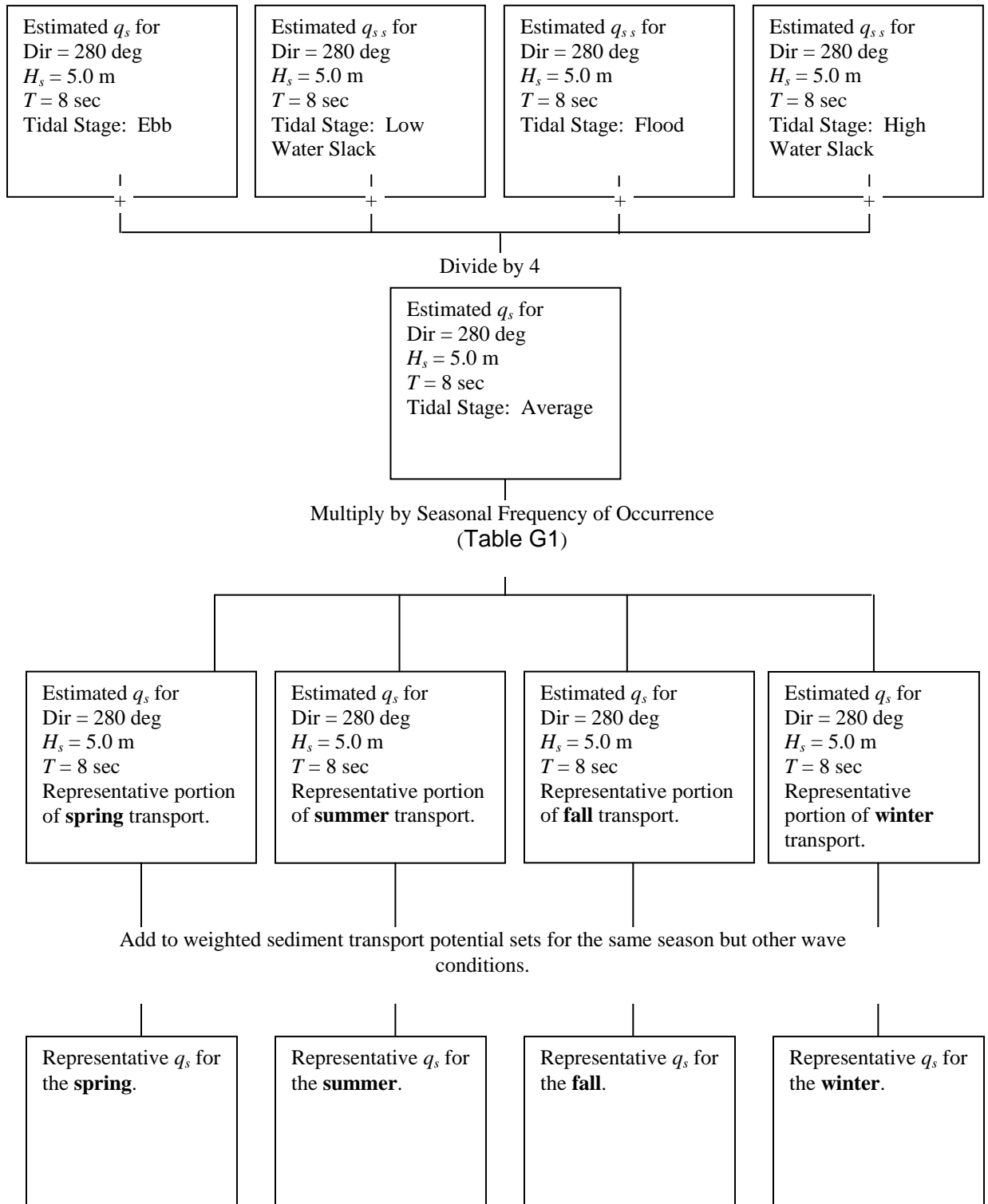
Figure G2. Method used to develop representative seasonal variations in q_s

Figures G3 through G7 show vector plots of representative, seasonally weighted transport potential for Alt 1. The results indicate subtle differences in magnitudes and directions of the q_s. Southbound q_s increase in magnitude at the northern extent of the grids between spring and summer. Also, a weak secondary rip is visible in the northeast corner of the spring plot. The q_s north of the main rip is slightly more northbound in the fall relative to the summer. The onshore transport is also larger in the fall. Figure G7 shows a comparison of q_s rates between winter and summer for Alt 1. Larger shore-perpendicular vectors occur near the north jetty in Figure G7 indicating significantly more onshore transport locally during the summer months. This local increase in onshore transport might be expected to lead to a local increase in shoreline advance during these months.
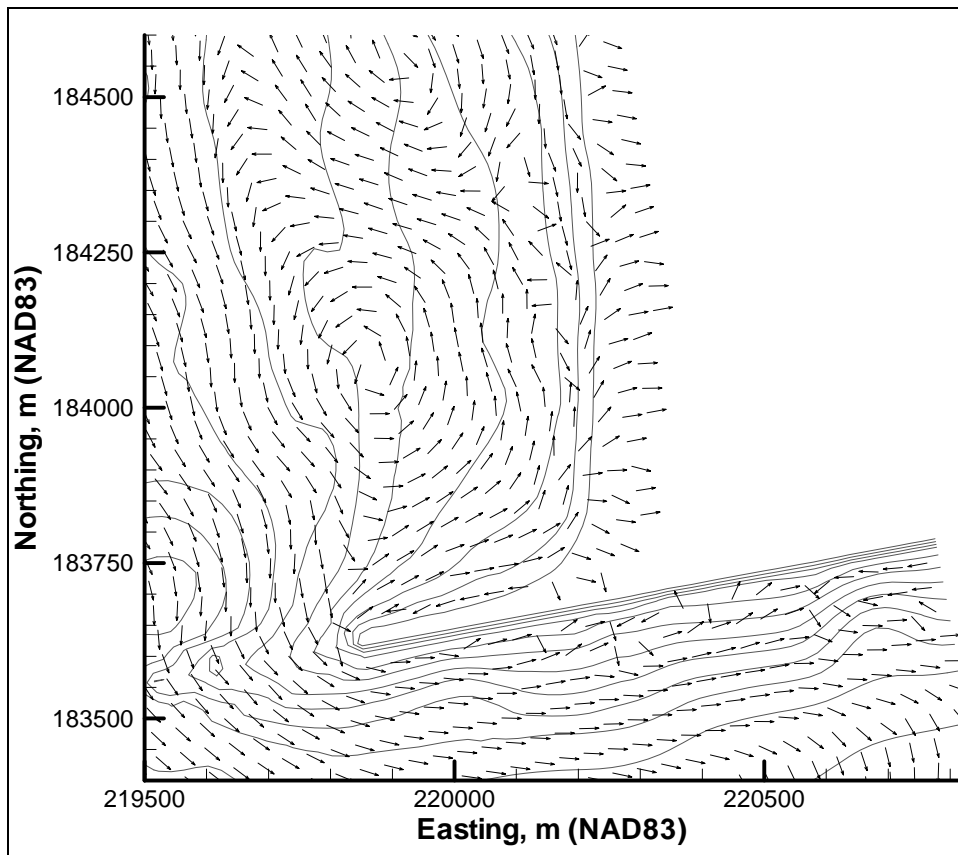
Figure G3. Transport vectors typical spring conditions, Alt 1
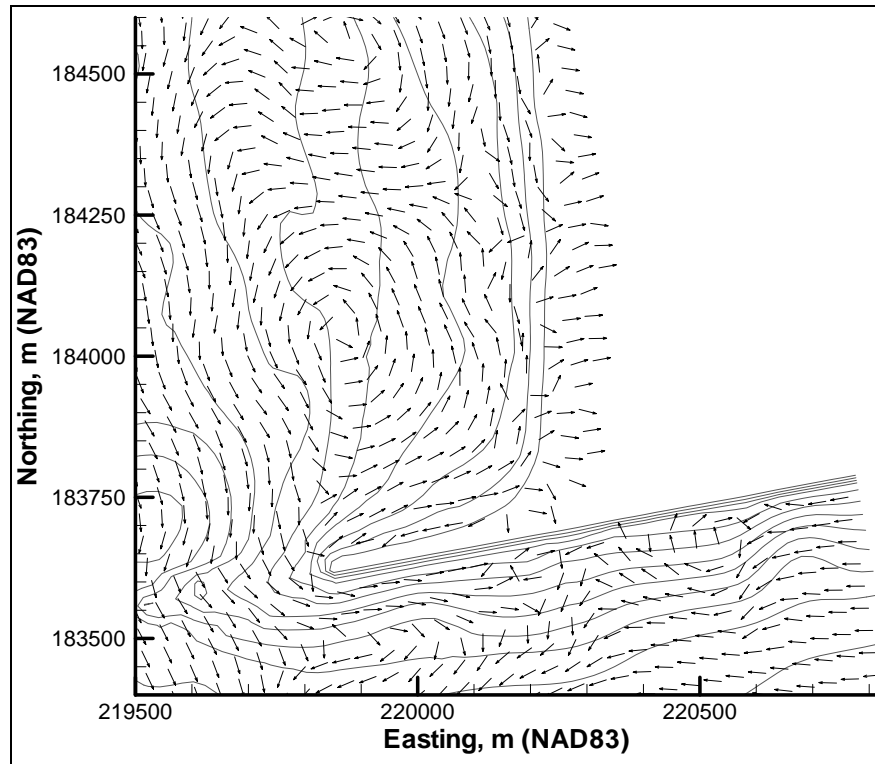
Figure G4. Transport vectors typical summer conditions, Alt 1
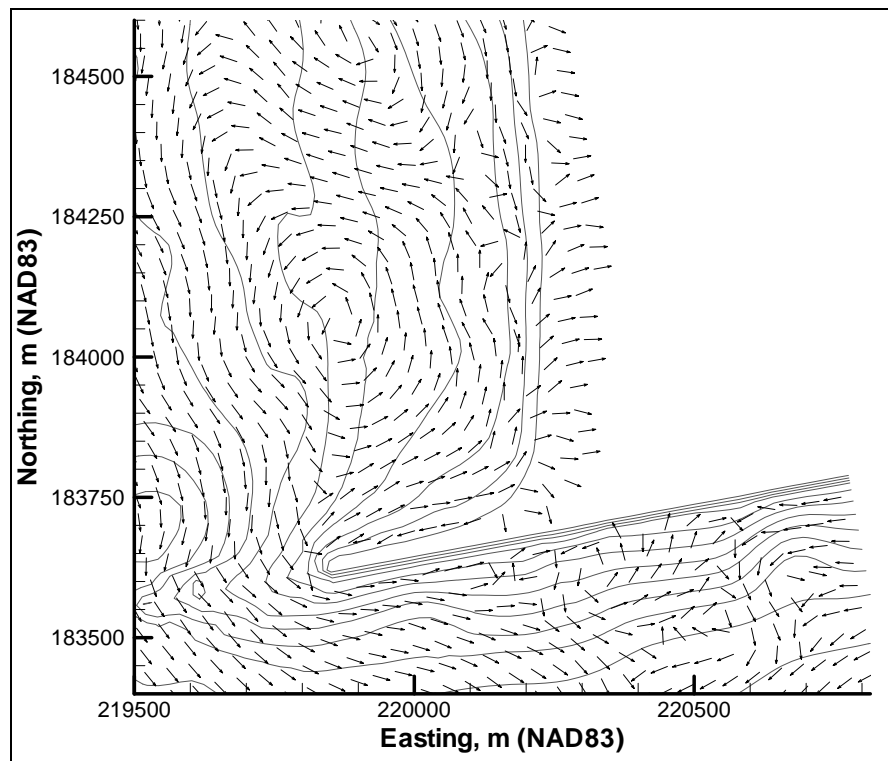
Figure G5. Transport vectors typical fall conditions, Alt 1
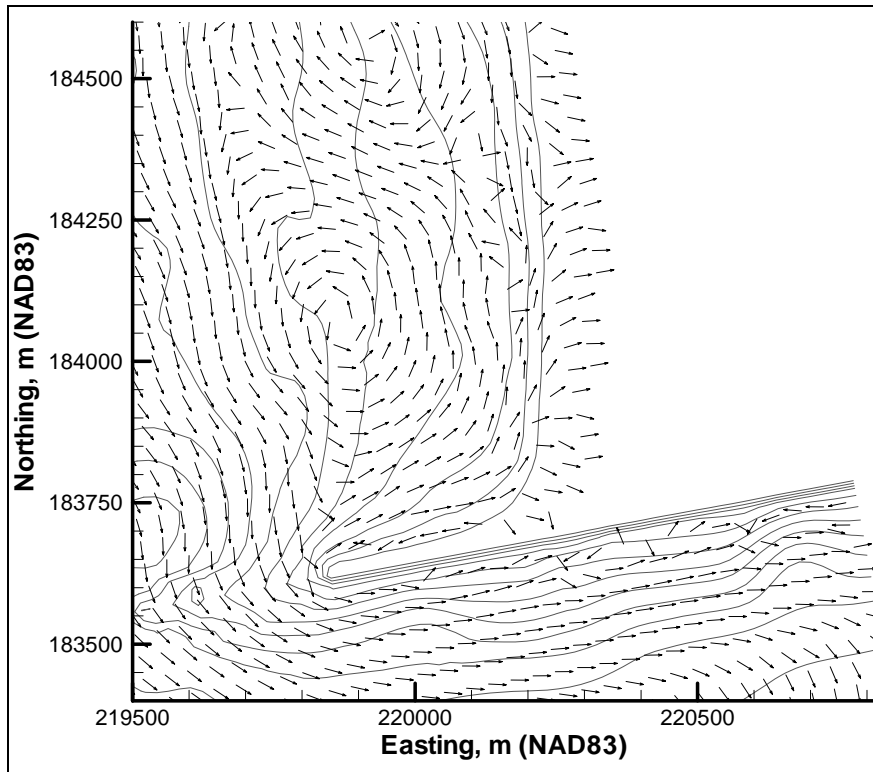
Figure G6. Transport vectors typical winter conditions, Alt 1
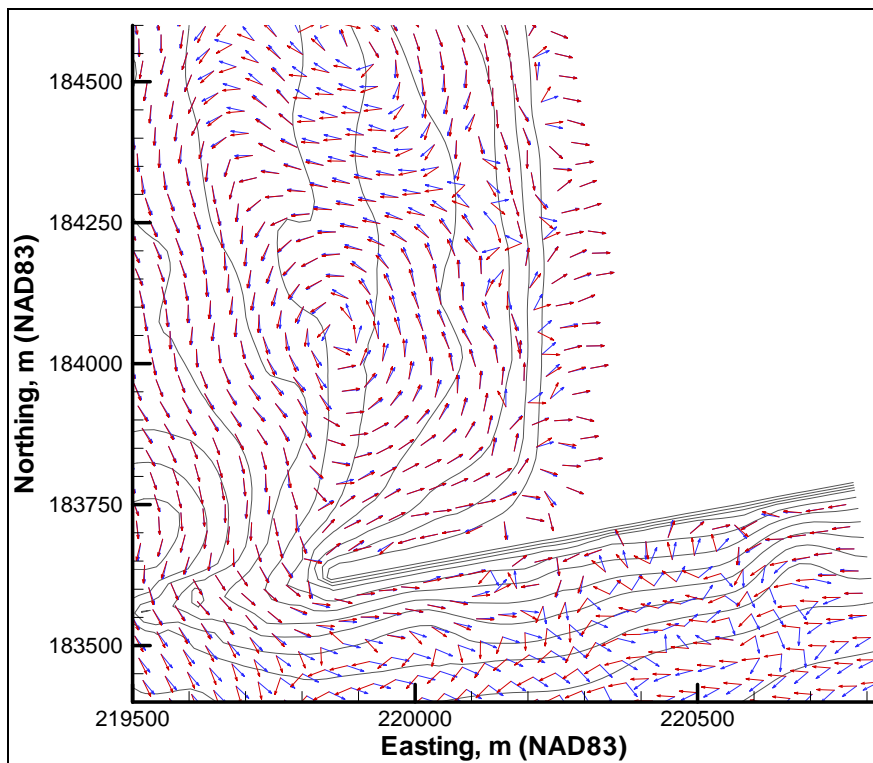
Figure G7. Comparison of summer (grey) and winter (black) q_s

Appendix G   Longshore Sand Transport Modeling and Shoreline Change Modeling with GENESIS-T

Figure G8 provides a comparison of the q_s vectors for Alt 2A and 2B. Differences in the potential sediment transport between the two jetty rehabilitation simulations are evident in the area to the south of the rip. Vectors for Alt 2A (red) vectors have a larger southbound component than those for Alt 2B. Northwest of the rip, the transport vectors indicate that more offshore transport potential for Alt 2A. The significant differences between the two Alt 2 plots indicates that a cross-shore transport function developed for Alt 1 would not be applicable to shoreline predictions for the alternatives.
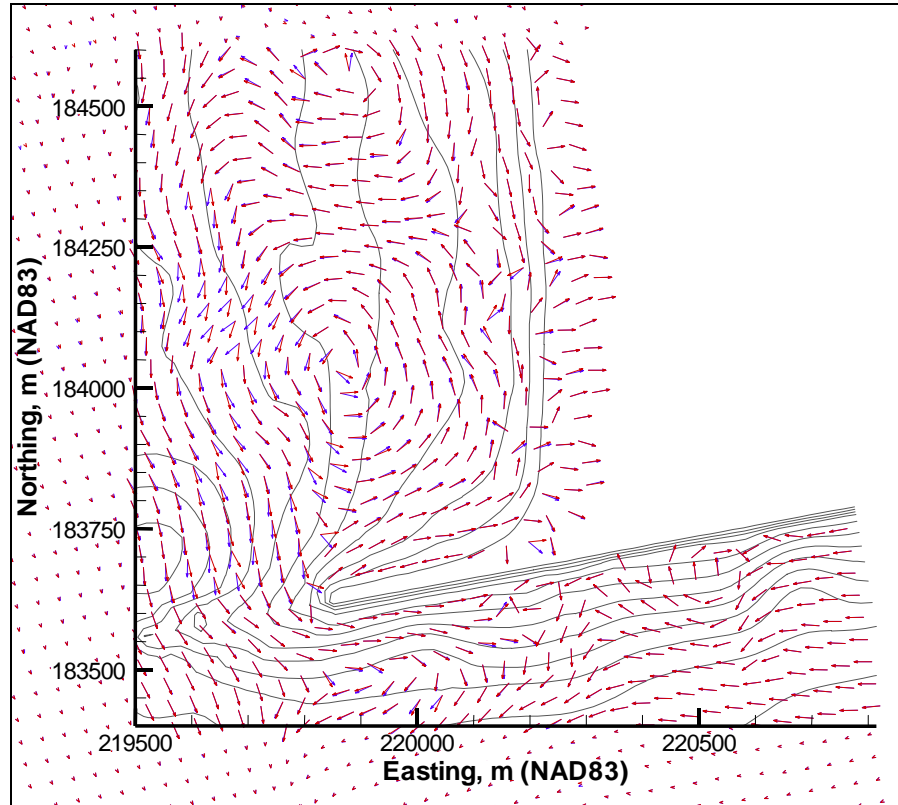
Figure G8. Characteristic summer q_s vectors for Alt 2A (blue) and 2B (red)

Seasonally varying cross-shore transport distribution function (HBM)

The seasonally varying long shore distribution of cross-shore transport is derived directly from the seasonal q_s. Vectors of q_s were extracted from each of the seasonal grids for each of the alternatives along the transect shown in Figure G9. The transect is parallel to the 1999 shoreline and traverses the major rip located north of the north jetty. The presence of the rip causes the direction of net transport to vary from onshore to offshore along the transect. Vectors of q_s inshore of the transect are dominated by longshore transport. The transect extends from the northing coordinate that corresponds with the origin of the GENESIS-T grid (183,705 m north, WA State Plane NAD83).
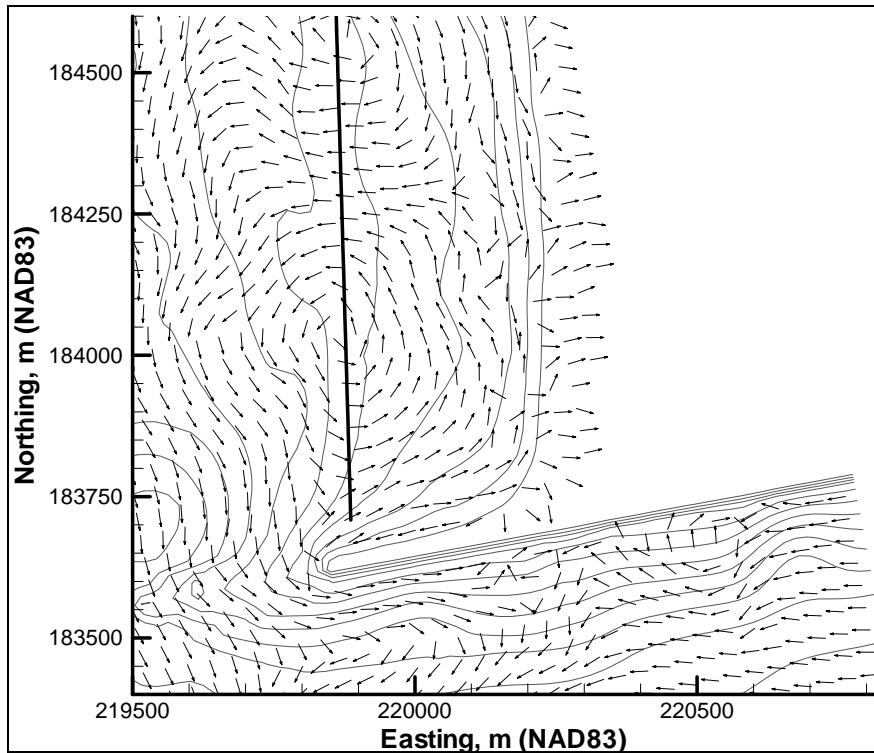
Figure G9. Alt 2A summer q_s vectors with data extraction transect (black line)

Only the easting components of the vectors were considered in the development of the hybrid cross-shore transport functions. The q_s vector components have true northing and easting directions, with the easting component taken as representative of cross-shore transport. The easting component was assumed despite the fact that the shoreline is at 2 deg to azimuth. The error caused by using the easting component of the transport vectors as opposed to ones corrected to be perpendicular to the shoreline was considered insignificant because a scaled relative magnitude of the vectors is applied to the development of the cross-shore transport functions.

Figure G10 shows the extracted vector components overlying the source vector plot for the Alt 2A grid representative of summer conditions. The vectors were extracted at 25-m intervals along the transect corresponding directly to the cell resolution in the GENESIS-T model. Vector components were extracted for each season and alternative, to develop cross-shore transport distribution functions that incorporate the spatial and temporal (seasonal) variations in the magnitude and position of the rip current.
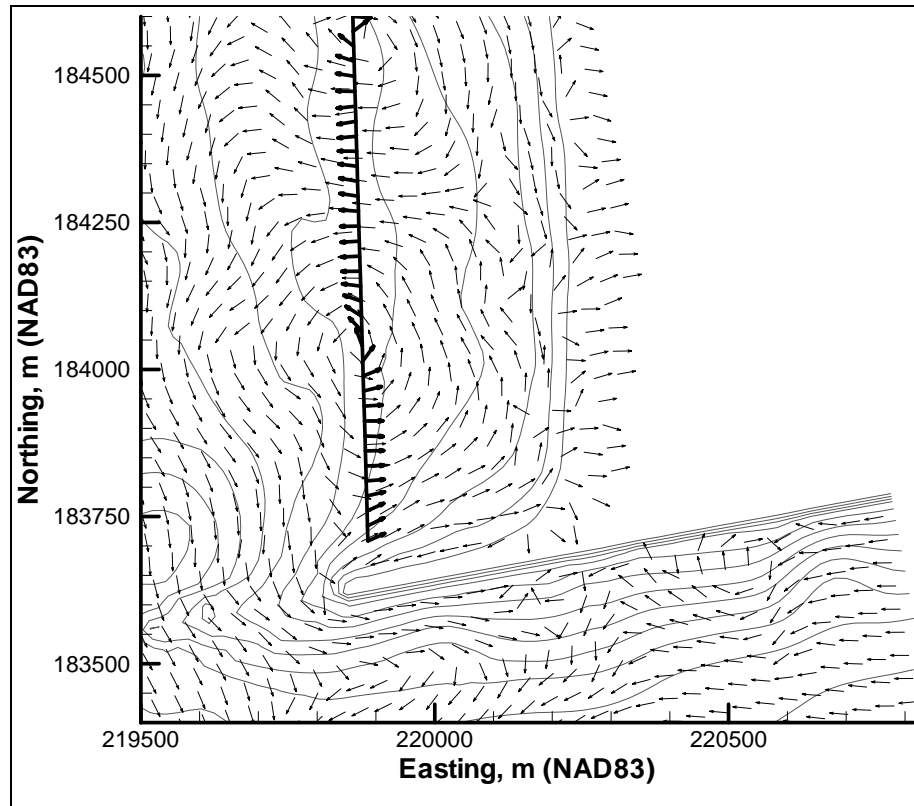
Figure G10.   Alt 2A summer q_s vectors with vectors extracted at 25-m
                     intervals for bypassing function creation (bold black)

Scaling of vector components

The cross-shore transport rates are represented in the GENESIS-T model in a cross-shore transport file with units of cubic meters per hour per meter of shoreline. The HBM rates were developed directly from the extracted q_s. The calculated cross-shore component of q_s was transferred into the required rates by scaling the calculated q_s. The rates in the cross-shore transport distribution file are typically two orders of magnitude lower than the calculated sediment transport rates.

In developing the hybrid cross-shore transport distribution functions, the net cross-shore transport rates, in cubic meters per hour, remained the same for the calibration and verification periods as with the standard cross-shore transport distribution functions (SBM). Rates 783,200 and 427,000 cu m/year were applied to the calibration and verification periods as determined by integrating the standard cross-shore transport distribution function (SBM). The SBM cross-shore transport distribution rates are based on sediment budget analysis as discussed in Chapter 6 and Chapter 3 of Volume I.

The SBM net cross-shore transport rates (in cubic meters per hour) determined the amount of scaling required to transform the calculated q_s into the rates required for the HBM. Beyond the boundaries of the CoastL domain, the sediment transport rates (in cubic meters per hour per meter) from the SBM were used without alteration. To match the SBM net cross-shore transport rates, two

procedures were needed to transform the extracted HBM easting vector components. Table G2 summarizes the transformation coefficients used for these two procedures.

The first procedure involved scaling all of the data so that the cross-shore transport rates are of a magnitude similar to those used with the SBM. The rates used for the SBM were calibrated and verified and were, therefore, assumed to be of the correct magnitudes. Second, a value was added to all of the easting vector components. This value is defined as the "shift coefficient" in Table G2. This was done so that a single value could be multiplied by all of the values used for the cross-shore transport distribution file. Without the shift, the required net cross-shore transport rate cannot be found without scaling the offshore and onshore components separately. Separate scaling was not done, because the CoastL results provide the relative transport magnitudes everywhere in the model domain. Separate scaling of the on/offshore values would negate the purpose of utilizing the CoastL results. Determination of appropriate shifting and scaling values were performed iteratively. The final values result in cross-shore transport distribution files that minimize the calibration/verification error, as well as contain cross-shore transport rates within the correct range of magnitudes. The determination of the shifting and scaling values was done separately for both the calibration and verification periods as the net cross-shore transport rates changed between the two simulation periods. The relative magnitudes of onshore and offshore transport were always maintained.

Table G2
Scaling and Shifting Coefficients Used to Transform Extracted q_s into Sediment Transport Rates for Cross-shore Transport Distribution Files

Time Period	Scale Coefficient	Shift Coefficient	Net Cross-shore Transport Rate (cu m/year)
Calibration	0.014940485	0.0484	783,200
Verification	0.011707395	0.0800	427,000

The scaling and shifting values were determined using the extracted q_s vectors for Alt 1 and applied to model calibration and verification. To create the other hybrid cross-shore transport distribution files, the verification transformations (scaling and shifting) were applied to the extracted q_s vectors for each of the other alternatives. This resulted in differences in the net cross-shore transport rates between the alternatives. These differences are summarized in Table G3.

The shape of the hybrid cross-shore transport distribution function for the verification period is shown in Figure G11. The scaled and shifted sediment transport rates produced from the Coast-L results are used for the first 800 m of the GENESIS-T model space. Beyond this point, the sediment transport rates from the SBM are used. The seasonal variations in cross-shore transport are evident in this figure, with the largest magnitude rates occurring in the fall and the smallest rates in the winter.

Table G3
Net Cross-shore Transport Rates for Each Alternative

Alternative	Net Cross-shore Transport Rate (cu m/year)
1	427,000
2A	447,900
2B	455,600
3A	428,100
3B	429,400
4	433,000
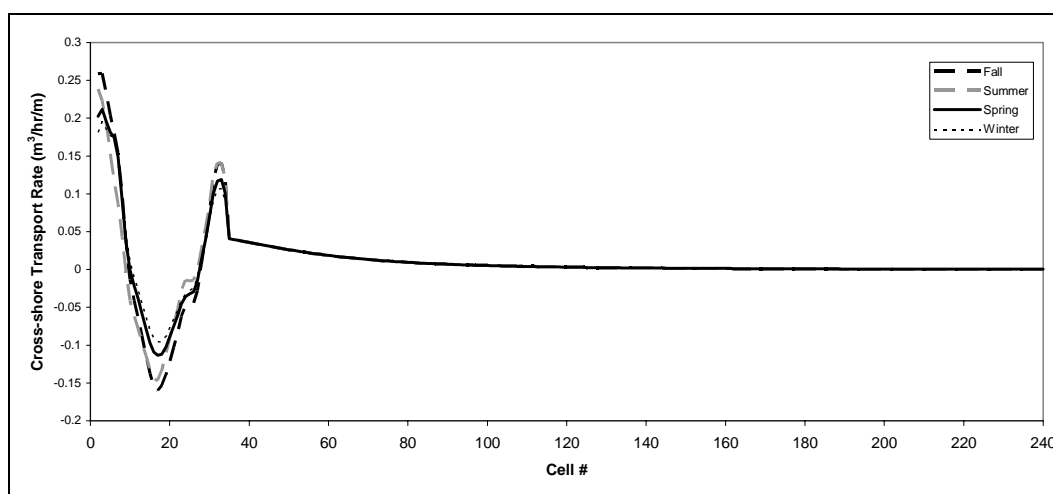
Figure G11. HBM function for verification runs

Preparation of bypassing files

The calibrated GENESIS-T model for the beach adjacent to the north jetty (North Beach) includes the SBM that specifies cross-shore sediment transport rates for every cell in the model in units of cubic meters per hour per meter. The SBM consists of a single cross-shore transport distribution that is used at every time-step in the simulation. In contrast, the HBM consists of four cross-shore transport distributions for every year of the simulation. Each distribution is a 240-cell array having the same length as the number of cells in the GENESIS-T domain. Each HBM distribution consists of seasonal scaled and shifted easting q_s vectors for those cells that occur within the CoastL model domain, and the SBM distribution is applied to cells that are beyond the CoastL domain. The four distributions in each year represent a season as defined in Table G4. Seasons were determined from the analysis of the wave climate as previously described. The season start- and end- dates are specified for each distribution for the HBM bypass file. An excerpt from the verification hybrid-bypassing file is provided in Figure G12.

Table G4	
Definition of Seasons Used to Develop Hybrid Bypassing Files	
Season	**Months Included:**
Winter	January, February, November, December
Spring	March, April
Summer	May, June, July, August
Fall	September, October

Results of GENESIS-T Modeling with HBM

The results of the GENESIS-T modeling performed with the HBM are summarized in this section. Detailed explanations of the north jetty, Grays Harbor GENESIS model setup are provided in Chapter 6 of the Volume I. With the exception of the bypass file, the simulations performed with the HBM used the same input and setup files as were employed for the modeling with the SBM as described in Chapter 6. Calibration of the GENESIS model for HBM simulations was performed through selection of scale and shift factors for the cross-shore transport distribution. Calibration of the other model parameters was completed for the SBM simulations and assumed applicable to the HBM simulations. The calibration parameters, K_1 and K_2, were not changed from those used for the SBM for the hybrid bypassing method simulations.

Model calibration

Calibration is the process of fine-tuning a model so that it can be used to accurately reproduce or predict changes in measured data over time. The skill of the fine-tuned model to accurately predict changes is verified by running the model over a different time period and comparing the results to data measurements for that time period. Calibration and verification of the GENESIS-T model were performed through comparison with planform shoreline measurements made in September 1976, August 1985, and August 1995.

The GENESIS-T model used at the north jetty, Grays Harbor was originally calibrated for use with the standard bypassing files. Additional calibration of the model for use with the HBM was completed through iterative adjustment of the scaling and shifting factors used to develop the cross-shore transport distribution function.

Calibration period, 1976 to 1985

Calibration of the HBM and GENESIS-T model was performed for the period 1 September 1976 and 31 August 1985. Figure G13 indicates that during this period the shoreline prograded seaward everywhere within the model domain. The average rate of shoreline progradation during this 9-year interval was approximately 17 ft/year. The shoreline advance was greatest further from the north jetty (left model boundary).

```
********************************************
BYPASS    DATA      Verification Bypassing File
BYPASS    DATA      Seasonal    for                    10 Years
********************************************
     850901        851031
   0.258935    0.259537    0.233796    0.204023    0.181122    0.154349    0.098558    0.037947   -0.012897   -0.040657
  -0.063469   -0.086902   -0.112083   -0.137187   -0.154097   -0.160104   -0.153738   -0.139523   -0.121911   -0.102814
  -0.083510   -0.061833   -0.048609   -0.046246   -0.043784   -0.028190    0.007161    0.039757    0.077627    0.117246
   0.138845    0.140878    0.121033    0.040826    0.039820    0.038806    0.037787    0.036766    0.035747    0.034732
   0.033725    0.032726    0.031740    0.030767    0.029810    0.028871    0.027949    0.027048    0.026168    0.025309
   0.024472    0.023658    0.022867    0.022099    0.021354    0.020632    0.019934    0.019258    0.018605    0.017974
   0.017365    0.016777    0.000000    0.015663    0.015136    0.014628    0.014139    0.013667    0.013214    0.012777
   0.012356    0.011952    0.011562    0.011187    0.010827    0.010479    0.010145    0.009824    0.009514    0.009216
   0.008929    0.008653    0.008387    0.008132    0.007885    0.007648    0.007419    0.007199    0.006986    0.006782
   0.006584    0.006394    0.006211    0.006034    0.005864    0.005699    0.005540    0.005387    0.005239    0.005096
   0.004958    0.004825    0.004696    0.004572    0.004452    0.004336    0.004223    0.004115    0.004009    0.003908
   0.003809    0.003714    0.003622    0.003533    0.003446    0.003362    0.003281    0.003203    0.003126    0.003052
   0.002981    0.002911    0.002844    0.002779    0.002715    0.002654    0.002594    0.002536    0.002479    0.002425
   0.002371    0.002320    0.002270    0.002221    0.002173    0.002127    0.002082    0.002039    0.001996    0.001955
   0.001915    0.001876    0.001838    0.001801    0.001765    0.001730    0.001695    0.001662    0.001629    0.001598
   0.001567    0.001537    0.001508    0.001479    0.001451    0.001424    0.001397    0.001371    0.001346    0.001322
   0.001298    0.001274    0.001251    0.001229    0.001207    0.001186    0.001165    0.001144    0.001124    0.001105
   0.001086    0.001067    0.001049    0.001031    0.001014    0.000997    0.000981    0.000964    0.000948    0.000933
   0.000918    0.000903    0.000888    0.000874    0.000860    0.000846    0.000833    0.000820    0.000807    0.000794
   0.000782    0.000770    0.000758    0.000747    0.000735    0.000724    0.000713    0.000703    0.000692    0.000682
   0.000672    0.000662    0.000652    0.000643    0.000634    0.000625    0.000616    0.000607    0.000598    0.000590
   0.000581    0.000573    0.000565    0.000557    0.000550    0.000542    0.000535    0.000527    0.000520    0.000513
   0.000506    0.000500    0.000493    0.000486    0.000480    0.000474    0.000467    0.000461    0.000455    0.000449
   0.000444    0.000438    0.000432    0.000427    0.000421    0.000416    0.000411    0.000406    0.000401    0.000396
     851101        860228
   0.180988    0.195788    0.185315    0.176734    0.173996    0.151343    0.096477    0.046689    0.011313   -0.010099
  -0.026775   -0.044261   -0.062756   -0.079456   -0.090642   -0.095481   -0.095861   -0.089096   -0.077618   -0.065421
  -0.054105   -0.041013   -0.032636   -0.028099   -0.024607   -0.009953    0.014361    0.039110    0.066650    0.091144
   0.105600    0.107041    0.090468    0.040826    0.039820    0.038806    0.037787    0.036766    0.035747    0.034732
   0.033725    0.032726    0.031740    0.030767    0.029810    0.028871    0.027949    0.027048    0.026168    0.025309
   0.024472    0.023658    0.022867    0.022099    0.021354    0.020632    0.019934    0.019258    0.018605    0.017974
   0.017365    0.016777    0.000000    0.015663    0.015136    0.014628    0.014139    0.013667    0.013214    0.012777
   0.012356    0.011952    0.011562    0.011187    0.010827    0.010479    0.010145    0.009824    0.009514    0.009216
   0.008929    0.008653    0.008387    0.008132    0.007885    0.007648    0.007419    0.007199    0.006986    0.006782
   0.006584    0.006394    0.006211    0.006034    0.005864    0.005699    0.005540    0.005387    0.005239    0.005096
   0.004958    0.004825    0.004696    0.004572    0.004452    0.004336    0.004223    0.004115    0.004009    0.003908
   0.003809    0.003714    0.003622    0.003533    0.003446    0.003362    0.003281    0.003203    0.003126    0.003052
   0.002981    0.002911    0.002844    0.002779    0.002715    0.002654    0.002594    0.002536    0.002479    0.002425
   0.002371    0.002320    0.002270    0.002221    0.002173    0.002127    0.002082    0.002039    0.001996    0.001955
   0.001915    0.001876    0.001838    0.001801    0.001765    0.001730    0.001695    0.001662    0.001629    0.001598
```

Figure G12. Excerpt from HBM bypass file for verification period
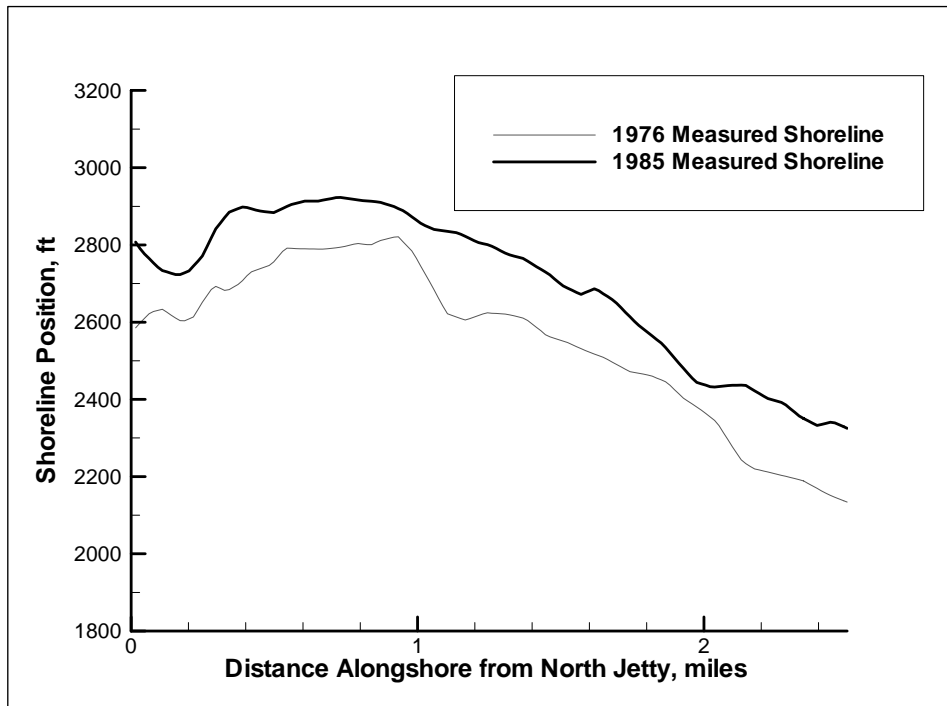
Figure G13. Measured shorelines, 1976 and 1985

With the exception of the bypass file, all other model inputs were the same as those applied with the SBM calibration. As a result, the differences between the model results from the HBM simulations and the SBM simulation results, discussed in Chapter 6, are directly attributable to the bypass file. A summary of the model inputs for the September 1976 to August 1985 calibration is provided in Table G5. The calibration coefficients, K_1 and K_2, were optimized for the SBM simulations.

Table G5
Summary of Model Input for Hybrid Bypassing Function

Input	Value
Calibration coefficient, K_1	0.10 (same as used for the SBM modeling)
Calibration coefficient, K_2	0.075 (same as used for the SBM modeling)
Median grain size, d_{50}	0.18 mm
Closure depth	40 ft
Average berm height	9.8 ft
Average annual cross-shore feeding	1.3 million cu yd
Average annual rip transport	148,000 cu yd
Bypassing file scale value	0.014940485
Bypassing file shift value	0.0484

The results of the GENESIS-T simulation performed for the calibration period with the HBM are shown in Figure G14. The predicted 1985 shoreline compares well with the measured shoreline, except at the north jetty. In this region the model predicts more accretion than was actually measured. The HBM also reproduces the indentation in the shoreline at the location of the rip that approximately matches the shape of the measured shoreline. The difference between the measured 1976 and 1985 shorelines indicate an average shoreline advance of 17 ft/year over the entire model domain (3.75 miles). The predicted results indicate an average shoreline advance of 15 ft/year over the model domain. The predicted rates are within 11.7 percent of the measured rates, indicating that the shoreline changes are reproduced well. The average absolute difference between the measured and predicted 1985 shorelines is 46.7 ft for the entire model domain, and 38.6 ft for the first 2.5 miles. This equates to an absolute error in the predicted shoreline of 5.2 ft/year, which is within the acceptable level of error associated with shoreline change models.
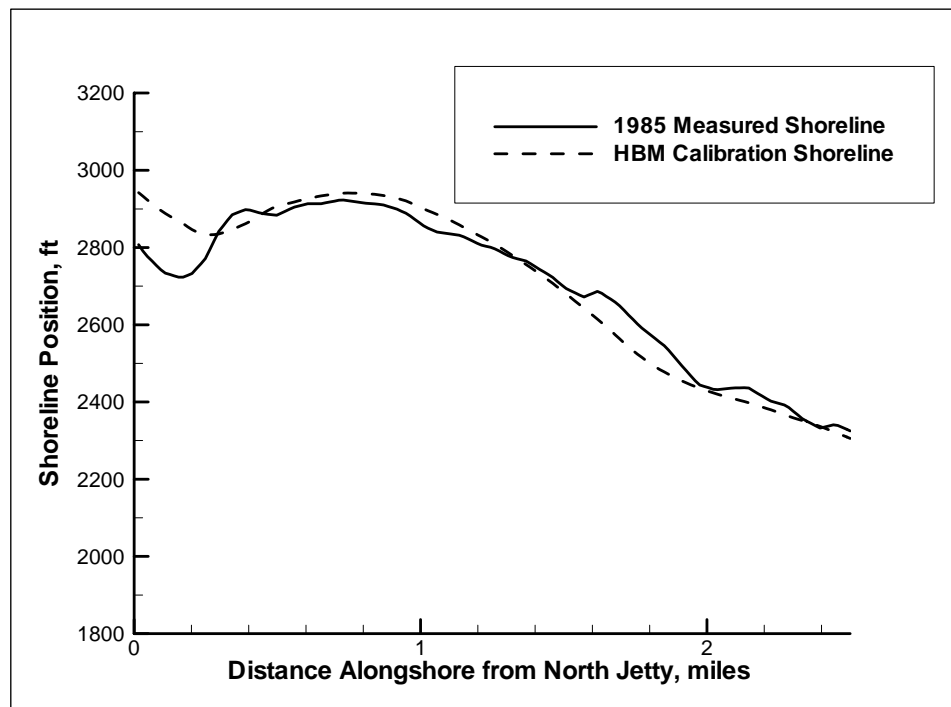
Figure G14. Measured and predicted 1985 shoreline

The calculated volume of sediment bypassing north jetty as a result of longshore transport during the calibration period is approximately 47,500 cu yd/year. The average annual volume of sediment lost to the inlet as a result of the rip was 148,000 cu yd/year. The net contribution to the inlet from the north beach is therefore approximately 195,500 cu yd/year. The net contribution from the inlet to the north beach, calculated as the average annual cross-shore feeding rate less the net contribution to the inlet, is approximately

1.1 million cu yd/year. This values falls within the error of the contribution of 1.3 million cu yd/year estimated by Kaminsky et al. (2000). The combined accuracy of the predicted shorelines, the calculated longshore sand transport rates, and cross-shore transport values indicate that the calibration was completed successfully.

Verification period, 1985 to 1995

Verification of the simulations using the HBM file was completed for the 10-year period between 1 September 1985 and 31 August 1995. As shown in Figure G15, the only significant shoreline change for this period occurred within the first mile north of the jetty where the average annual shoreline recession was 10 ft/year.
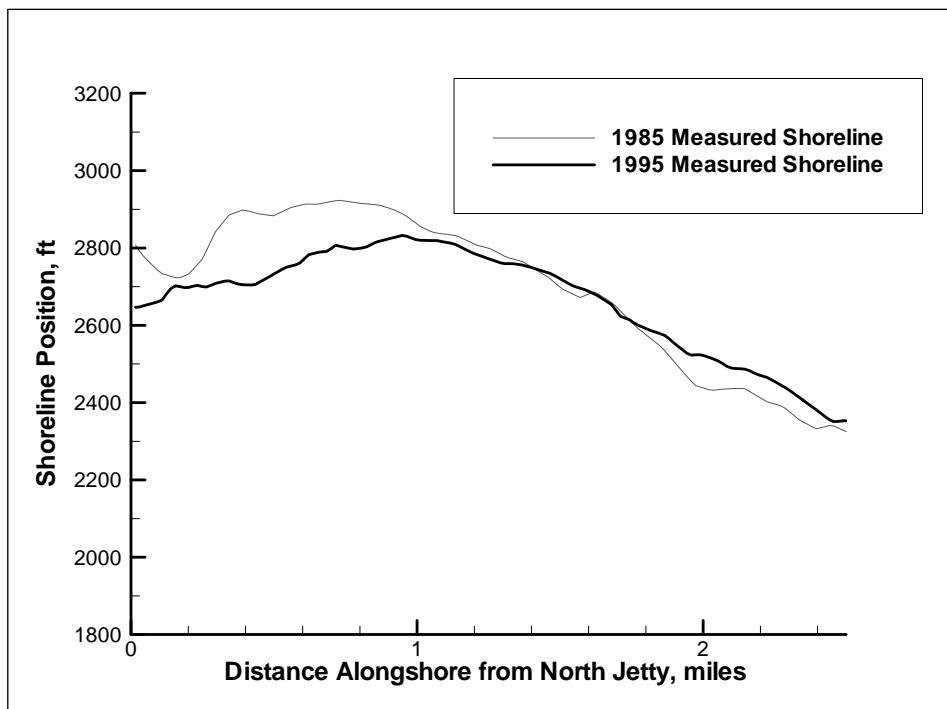
Figure G15.   Measured 1985 shoreline and modified measured 1995 shoreline SBM

With the exception of the rescaled bypass file, the same model inputs were utilized for the verification as for the calibration. The bypass file for the HBM was changed for the calibration period to account for the decreased sediment contribution from the deflating ebb shoal. During this period, the littoral feeding rate (onshore transport) was reduced to 900,000 cu yd/year. The HBM verification cross-shore transport distribution was altered to have the same net cross-shore transport as the SBM calibration distribution. Only the scaling and shifting values used to create the bypassing files were changed for the verification period (Table G6).

Table G6
Summary of Model Input for Hybrid Bypassing Function

Input	Value
Calibration coefficient, K_1	0.10 (same as used for the SBM modeling)
Calibration coefficient, K_2	0.075 (same as used for the SBM modeling)
Median grain size, d_{50}	0.18 mm
Closure depth	40 ft
Average berm height	9.8 ft
Average annual cross-shore feeding	0.9 million cu yd
Average annual rip transport	337,348 cu yd
Bypassing file scale value	0.014940485
Bypassing file shift value	0.0484

The results of the GENESIS-T simulation for the verification period with the hybrid bypassing function are shown in Figure G16. The predicted 1995 shoreline compares well with the measured shoreline, except within the first 0.13 miles north of the north jetty. The average absolute difference between the measured and predicted 1995 shorelines is 28.6 ft for the entire model domain, and 28.0 ft for the first 2.5 miles. The difference over the entire model domain equates to an error of 2.86 ft/year, which is within the level of error expected from the shoreline change model. The average absolute difference for the verification period is also 18.1 ft less than for the calibration period, indicating improved performance over the verification period.

Sensitivity to K_1 Values

It was found during the calibration and verification tests that the results of the GENESIS-T model were sensitive to the values of K_1, especially the amount of sediment bypassing the north jetty.

Results for the SBM model for six values of K_1 ranging from 0.08 to 0.2 are shown in Figure G17. The results indicate that the model has two different modes of response depending upon the selected value of K_1. The amount of sediment bypassing the jetty varies between an increase of approximately 30 percent for simulations with $K_1 < 0.1$ to a decrease of approximately 15 percent for simulations with $K_1 > 0.1$.

To investigate whether this impact was significant, GENESIS-T with the HBM was rerun over the calibration period 1976 to 1985, the 1985 to 1995 verification period and the 5-year prediction period. The results of these simulations are presented in the following sections.
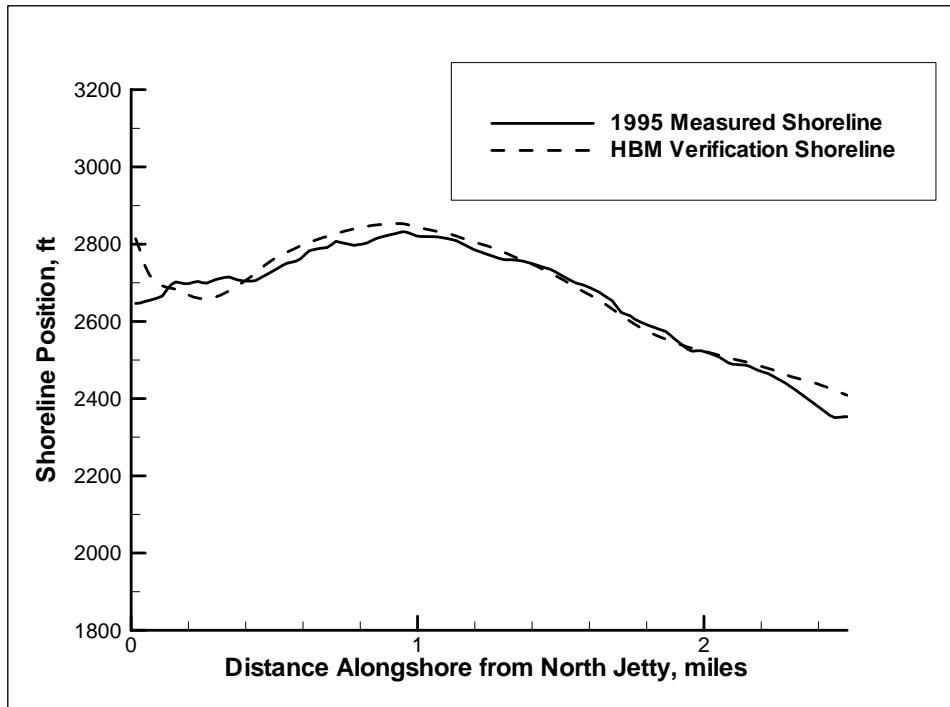
Figure G16. Measured and predicted 1995 shoreline (hybrid bypassing function)
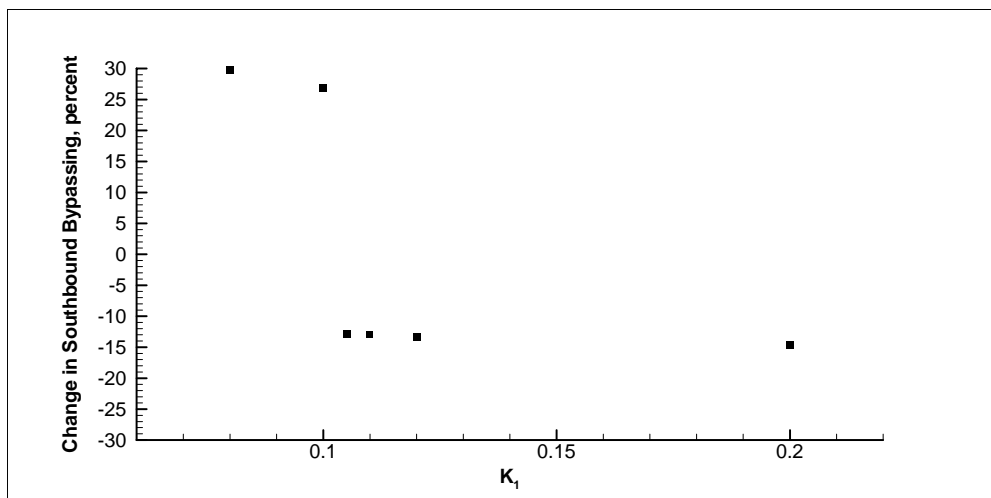
Figure G17. Change in southward bypassing as a function of K_1

Calibration period, 1976 to 1985

Calibration of the HBM and GENESIS-T model was performed for the period 1 September 1976 and 31 August 1985. The average rate of shoreline progradation during this 9-year interval was approximately 17 ft/year.

With the exception of the sediment transport calibration coefficient, K_1, all other model inputs were the same as those applied with the original HBM calibration. A summary of the model inputs for the September 1976 to August 1985 calibration is provided in Table G7.

Table G7 Summary of Model Input for Hybrid Bypassing Function	
Input	**Value**
Calibration coefficient, K_1	0.11
Calibration coefficient, K_2	0.075 (same value as that used for the SBM modeling)
Median grain size, d_{50}	0.18 mm
Closure depth	40 ft
Average berm height	9.8 ft
Average annual cross-shore feeding	1.3 million cu yd
Average annual rip transport	148,000 cu yd
Bypassing file scale value	0.014940485
Bypassing file shift value	0.0484

The results of the GENESIS-T simulation performed for the calibration period with the HBM are shown in Figure G18. The predicted 1985 shoreline position compares well with the measured shoreline, except at the north jetty. In this region, the model predicts more accretion than was measured. The model also predicts more recession than was observed at a distance 1.5 miles from north jetty. The average over-prediction in this region is approximately 138 ft (42 m) over the 9-year simulation period. The difference between the measured 1976 and 1985 shorelines yield an average shoreline advance of 17 ft/year over the entire model domain (3.75 miles). The predicted results produce an average shoreline advance of 13.5 ft/year over the model domain. The predicted rates are within 20 percent of the measured rates, indicating that the shoreline changes are reproduced well. The average absolute difference between the measured and predicted 1985 shorelines is 56.3 ft for the entire model domain and 45.3 ft for the first 2.5 miles. This equates to an absolute error in the predicted shoreline of 6.2 ft/year, which is within the acceptable level of error associated with shoreline change models for representing complex conditions.

The calibration performed with $K_1 = 0.10$ had less error in shoreline prediction over the entire model domain. However, the calibration simulation performed with $K_1 = 0.11$ resulted in an improvement in shoreline prediction next to the north jetty by an average of approximately 164 ft. It should be noted that the calibration of the HBM bypass file was completed only for a value of $K_1 = 0.10$; results of the simulations with $K_1 = 0.11$ would have been improved by recalibration of the bypass function for the new calibration coefficient.
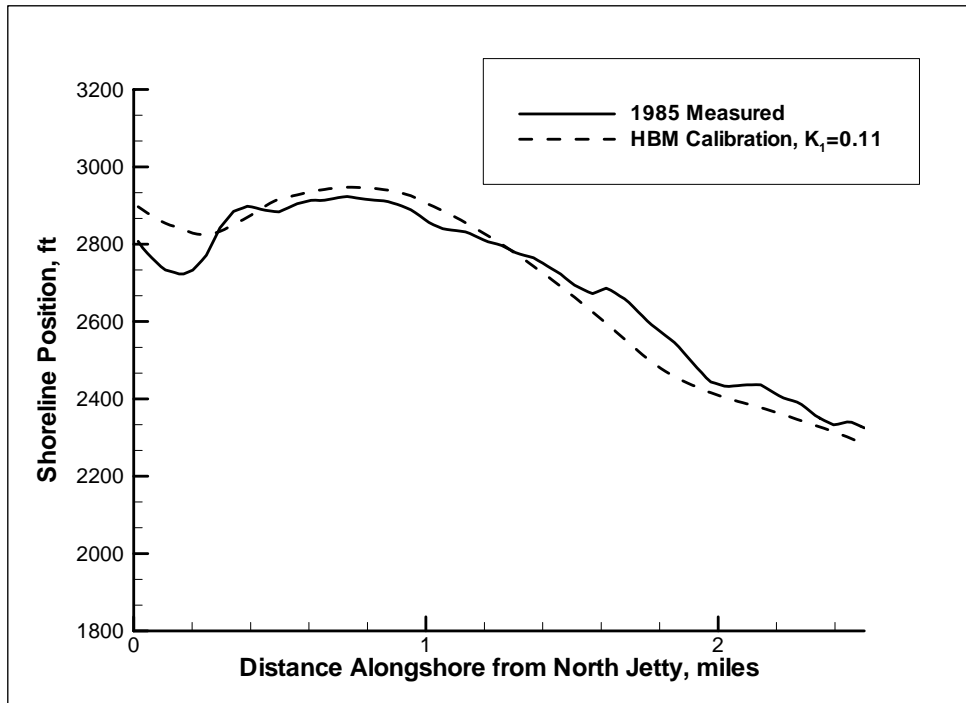
Figure G18. Measured and predicted 1985 shoreline

The calculated volume of sediment bypassing the north jetty as a result of longshore transport during the calibration period is approximately 42,700 cu yd/year. The average annual volume of sediment lost to the inlet as a result of the rip was 148,000 cu yd/year. The net contribution to the inlet from the north beach is therefore approximately 190,700 cu yd/year. The predicted net contribution to the inlet from the north beach is 4,800 cu yd/year less using a calibration $K_1 = 0.11$ than it is with $K_1 = 0.10$. The net contribution from the inlet to the north beach, calculated as the average annual cross-shore feeding rate less the net contribution to the inlet, is approximately 1.11 million cu yd/year. This value falls within the error of the contribution of 1.3 million cu yd/year estimated by Kaminsky et al. (2000). The combined accuracy of the predicted shorelines, the calculated longshore sand transport rates, and cross-shore transport values indicate that the calibration was completed successfully.

Verification period, 1985 to 1995

Verification of the simulations using the HBM file was completed for the 10-year period between 1 September 1985 and 31 August 1995. As stated previously, the only significant shoreline change for this period occurred within the first mile north of the jetty where the average annual shoreline retreat was 10 ft/year.

Only the calibration coefficient, K_1, differs between this simulation and the previous HBM verification simulation. The model inputs for the verification simulation performed with the altered calibration coefficient are shown in Table G8.

Table G8
Summary of Model Input for Hybrid Bypassing Function

Input	Value
Calibration coefficient, K_1	0.11
Calibration coefficient, K_2	0.075 (same as used for the SBM modeling)
Median grain size, d_{50}	0.18 mm
Closure depth	40 ft
Average berm height	9.8 ft
Average annual cross-shore feeding	0.9 million cu yd
Average annual rip transport	337,348 cu yd
Bypassing file scale value	0.014940485
Bypassing file shift value	0.0484

The results of the GENESIS-T simulation for the verification period with the HBM and $K_1 = 0.11$ are shown in Figure G19. The measured and predicted 1995 shorelines compare well. There is a better shoreline prediction within the first 0.13 miles of the jetty than that achieved using $K_1 = 0.10$. The average absolute difference between the measured and predicted 1995 shorelines is 23.7 ft for the entire model domain, and 29.0 ft for the first 2.5 miles. The difference over the entire model domain equates to an error of 2.37 ft/year, which is within the level of error expected from the shoreline change model. These model results show an improvement in accuracy of 21 percent in shoreline prediction over those with a calibration coefficient of $K_1 = 0.10$. The average absolute difference for the verification period is 32.6 ft less than that for the calibration period, which also shows improved performance over the verification period.
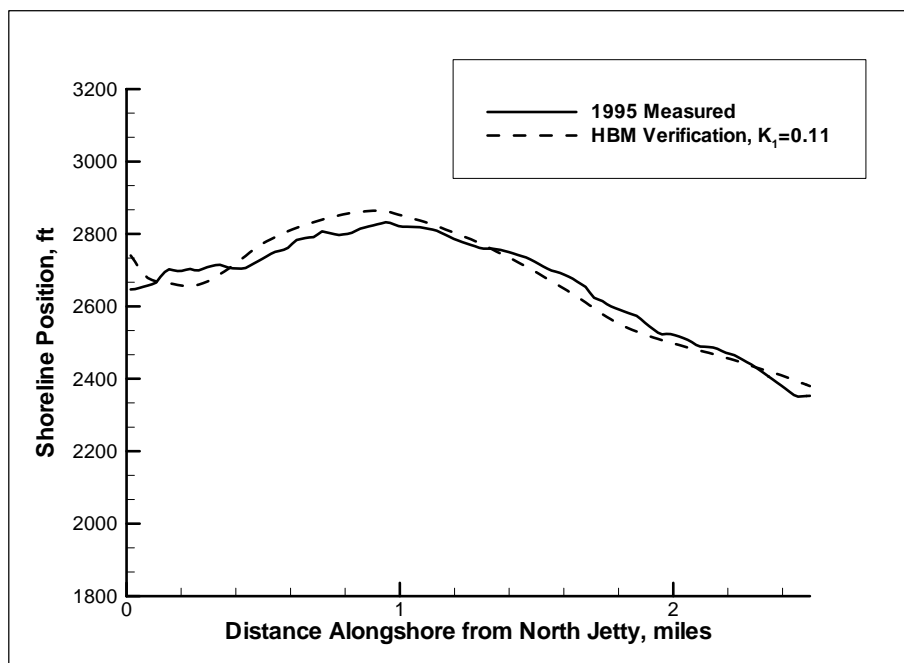
Figure G19.   Measured and predicted 1995 shoreline (hybrid bypassing function)

Discussion of effect of K_1

As is noted in Chapter 6 (Equations 6-1 and 6-2), the coefficients K_1 and K_2 are used to scale the standard CERC and wave-height gradient components of sediment transport, respectively. Increasing the value of K_1, while holding the value of K_2 constant, has the effect of lessening the relative importance of wave-height gradient. As is illustrated in Figure G20, this change has little impact on the without-project shoreline, except in the vicinity of the north jetty. The same conclusion, however, cannot be drawn from simulations with the structural alternatives in place. As is shown in Figure G21, the spur alternative is more sensitive to K_1 variation than is the existing condition. This occurs because the area behind the spur would have a larger variation in wave-height gradient and, therefore, a low value of K_1 would increase the relative importance of wave-height gradient in the transport computations. This sensitivity to K_1 was also found in simulations with the other alternatives.
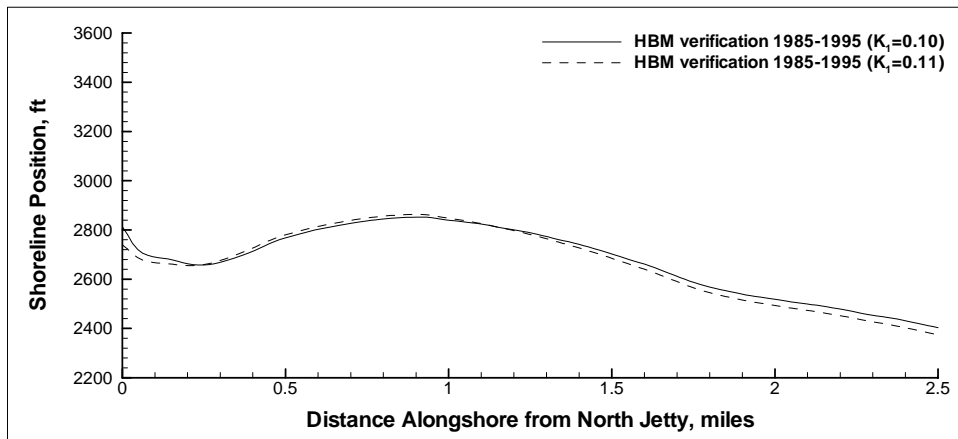
Figure G20.   Comparison of computed shoreline position for verification period 1985-1995 using HBM with different values of K_1
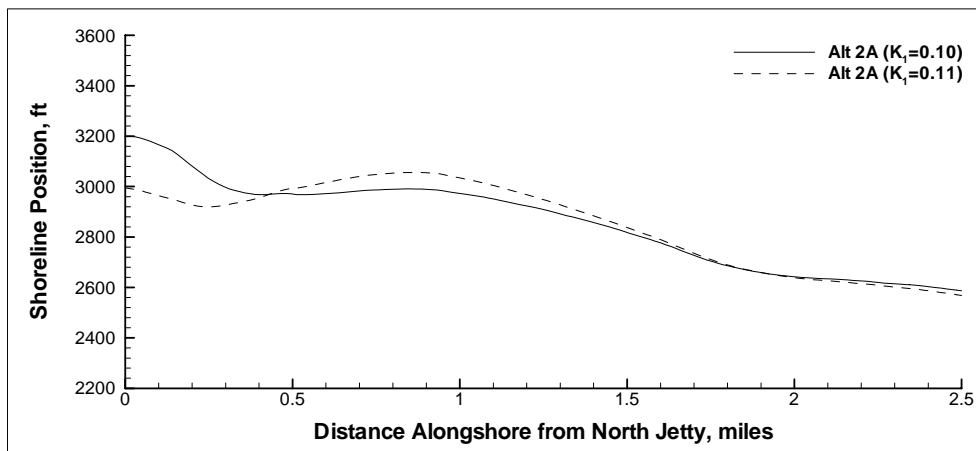
Figure G21.   Comparison of computed shoreline positions for 5-year simulations for Alt 2A using HBM with different values of K_1

Predicted Bypassing Using HBM

Sensitivity to value of K_1 is demonstrated by evaluation of the absolute southbound transport. With the lower value of K_1 (Figure G22), there is more variability in transport between the various alternatives in the first one-half mile north of the jetty. The results using the higher value of K_1 (Figure G23) show less variability in transport between the various alternatives, and generally lower bypassing volumes in the first one-half mile north of the jetty.
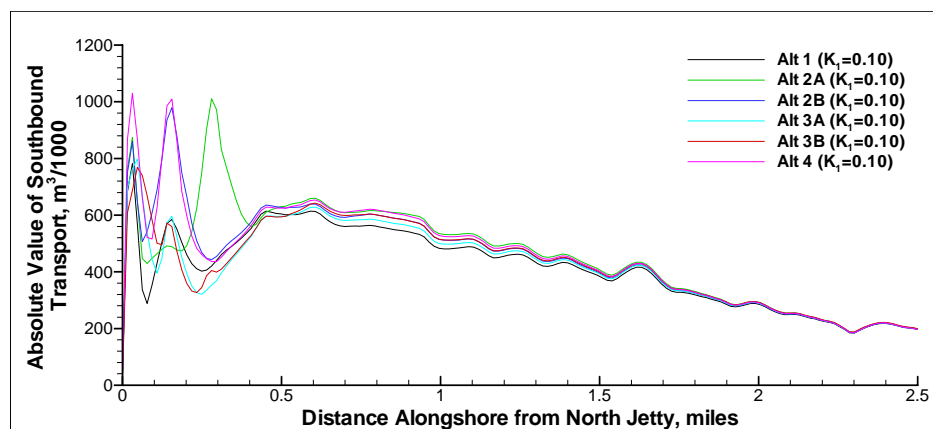
Figure G22.   Absolute southbound transport for each alternative for HBM ($K_1 = 0.10$)
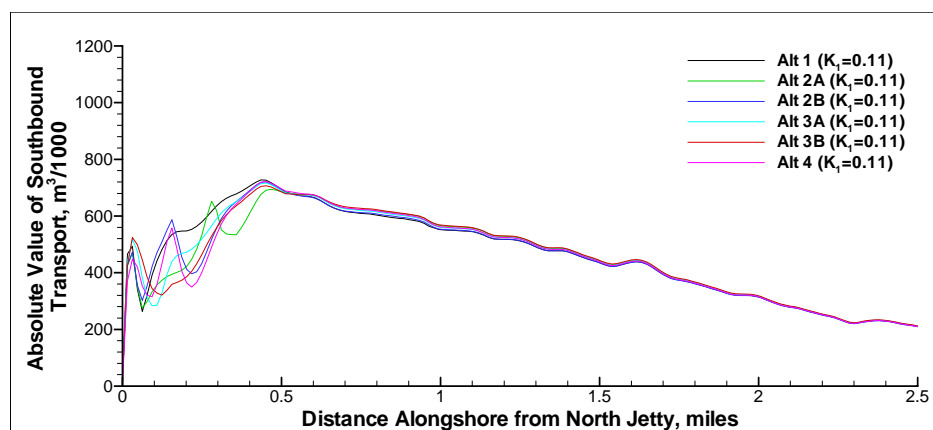
Figure G23.   Absolute southbound transport for each alternative for HBM ($K_1 = 0.11$)

Table G9 and G10 show the average southbound transport over the first one-half mile using the HBM with $K_1 = 0.10$ and $K_1 = 0.11$, respectively. The results using $K_1 = 0.10$ are inconsistent. For example, the long spur (Alt 2A) shows virtually the same increase in southward transport, as does the shorter spur (Alt 2B); the short jetty extension (Alt 3A) shows a slight decrease in southbound transport, whereas a longer extension (Alt 3B) produces a slight increase in southbound transport. The results for the HBM with $K_1 = 0.11$, however, show a more consistent and rational pattern of behavior. All alternatives show decreases in southward transport past the jetty. The longer spur (Alt 2A) has a reduction in southbound transport compared to the short spur (Alt 2B) that is roughly proportional to the ratio of the spur lengths. Similarly, the long jetty (Alt 3B) has a greater reduction in southbound transport than the short jetty (Alt 3A).

Table G9
Average Southbound Transport Over First 0.5 mile North of Jetty for HBM and $K_1 = 0.10$

Alternative	Annual Southbound Transport for First 0.5 mile	Change in Southbound Volume Relative to Alt 1	
	cu yd/year	cu yd/year	Percent
1	20,546,847	N/A	N/A
2A	25,531,516	4,984,668	24.26
2B	25,275,952	4,729,105	23.02
3A	20,304,886	-241,961	-1.18
3B	20,711,904	165,057	0.80
4	25,469,260	4,922,412	23.96

Table G10
Average Southbound Transport Over First 0.5 mile North of Jetty for HBM and $K_1 = 0.11$

Alternative	Annual Southbound Transport for First 0.5 mile	Change in Southbound Volume Relative to Alt 1	
	cu yd/year	cu yd/year	Percent
1	23,309,917	N/A	N/A
2A	20,356,156	-2,953,761	-12.67
2B	21,894,246	-1,415,671	-6.07
3A	21,676,350	-1,633,567	-7.01
3B	20,835,632	-2,474,285	-10.61
4	20,886,901	-2,423,016	-10.39

The results for the bypassing at the north jetty (calculated as the southward bypassing for the first cell) are shown in Table G11 and G12 for the HBM with $K_1 = 0.10$ and $K_1 = 0.11$, respectively. Both these sets of results show that the various alternatives reduce bypassing into the inlet. The ranking of the alternatives from most to least effective are the same in each case: Alt 4, Alt 3B, Alt 2A, Alt 3A, and Alt 2B.

Appendix G Longshore Sand Transport Modeling and Shoreline Change Modeling with GENESIS-T

Comparison of Table G11 and G12 suggests that the GENESIS-T model using $K_1 = 0.10$ may represent a conservative estimate of the effectiveness of the various alternatives. Since investigation of the effect of the value of K_1 indicates that the GENESIS-T model exhibits a bimodal behavior around $K_1 = 0.1$ (Figure G17), the results using $K_1 = 0.11$ may represent an upper bound on the expected effectiveness of the various alternatives.

Table G11
Southbound Transport Past North Jetty for HBM and $K_1 = 0.10$

Alternative	Annual Southbound Transport for First Cell	Change in Volume Passing North Jetty Relative to Alt 1	
	cu yd/year	cu yd/year	Percent
1	47,345.98	N/A	N/A
2A	33,482.24	-13,864	-29.28
2B	40,021.74	-7,324	-15.47
3A	36,621.20	-10,725	-22.65
3B	30,604.86	-16,741	-35.36
4	26,942.74	-20,403	-43.09

Table G12
Southbound Transport Past North Jetty for HBM and $K_1 = 0.11$

Alternative	Annual Southbound Transport for First Cell	Change in Volume Passing North Jetty Relative to Alt 1	
	cu yd/year	cu yd/year	Percent
1	44,207.02	N/A	N/A
2A	24,588.52	-19,619	-44.38
2B	26,158.00	-18,049	-40.83
3A	25,373.26	-18,834	-42.60
3B	15,433.22	-28,774	-65.09
4	14,386.90	-29,820	-67.46

Predicted 5-Year Shorelines Using HBM

The following section discusses the results of the HBM simulations for the five alternatives in terms of final shoreline position and change relative to Alt 1. Figures G24 and G25 show the final 5-year shoreline positions predicted for all five alternatives using K_1 values of 0.10 and 0.11, respectively. Both Figures G24 and G25 show small differences in shoreline position for each of the alternatives at distances greater than 0.5 mile north of the jetty, with the smaller differences shown for those predicted using a value of $K_1 = 0.11$. The final shorelines are shown in greater detail in Figures G26 and G27. Those predicted with $K_1 = 0.10$ have a maximum difference of 212 ft near the north jetty, whereas those with $K_1 = 0.11$ have a maximum difference of 79 ft. The results of the simulations performed with $K_1 = 0.11$ also indicate that less progradation occurs for all alternatives than is indicated from the results with $K_1 = 0.10$.
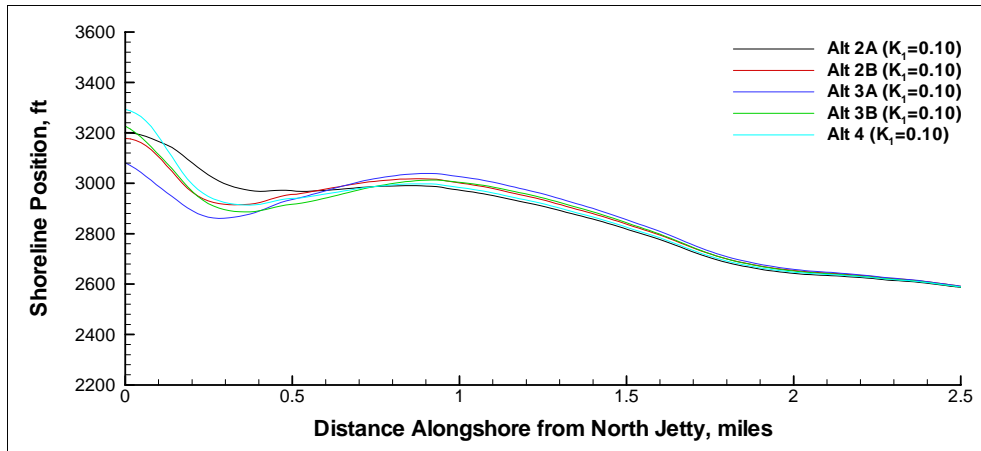
Figure G24. Final shoreline positions for 5-year simulations, $K_1 = 0.10$
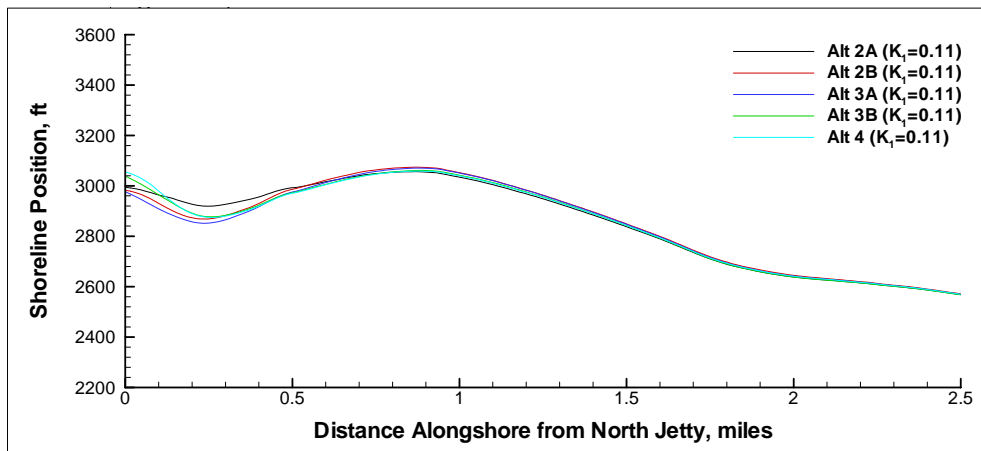
Figure G25. Final shoreline position for 5-year simulations, $K_1 = 0.11$
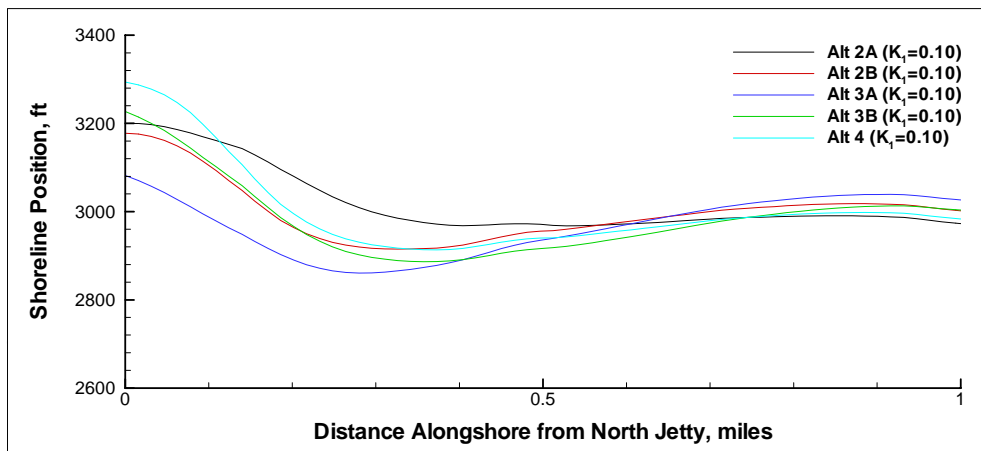
Figure G26. Final shoreline positions of 5-year simulations over first mile, $K_1 = 0.10$

Appendix G   Longshore Sand Transport Modeling and Shoreline Change Modeling with GENESIS-T
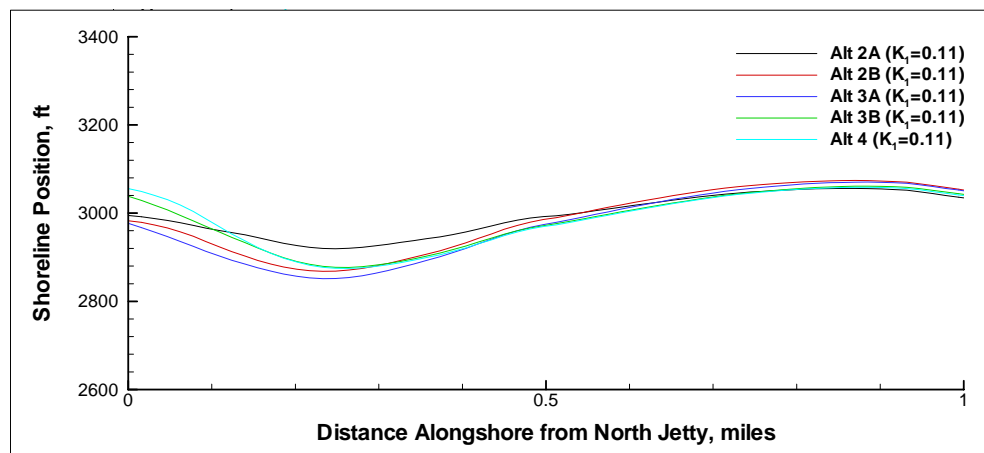
Figure G27. Final shoreline positions of 5-year simulations over first mile, $K_1 = 0.11$

The difference in shoreline position for each of the alternatives as compared to that predicted for Alt 1 using K_1 values of 0.10 and 0.11 are shown in Figures G28 and G29, respectively. Ranking of the shoreline progradation near the north jetty resulted in the same order for the various structural alternatives for both values of K_1; the largest to smallest increases were: Alt 4, Alt 3B, Alt 2A, Alt 2B and Alt 3A. Relative to Alt 1, the maximum shoreline progradation varied between 313 ft and 383 ft for $K_1 = 0.10$ and 153 ft and 171 ft for $K_1 = 0.11$.
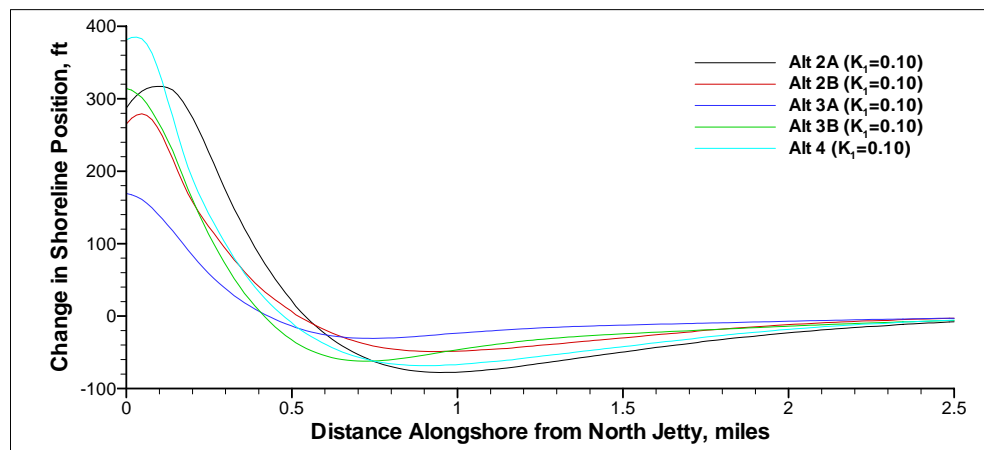
Figure G28. Change in shoreline position relative to Alt 1 for 5-year simulations, $K_1 = 0.10$
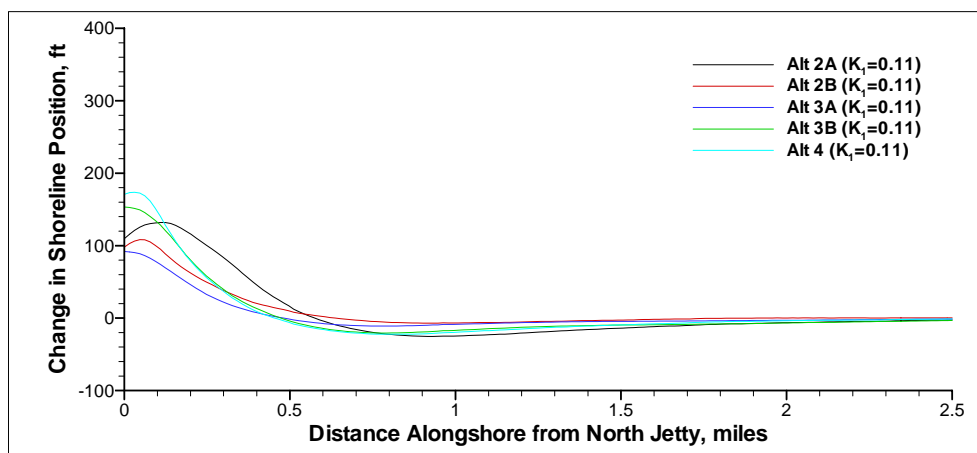
Figure G29.   Change in shoreline position relative to Alt 1 for 5-year simulations, $K_1 = 0.11$

The simulations using $K_1 = 0.10$ show greater shoreline progradation near the jetty and recession between 0.5 and 2.0 miles north of the jetty. The simulations using $K_1 = 0.11$ show a lesser progradation near the jetty and minimal recession north of 0.5 mile from the jetty. This suggests that, although the beach will build out near the north jetty, the beach angle further north will change little due to the presence of the alternatives for simulations using $K_1 = 0.11$.

Summary and Conclusions

The GENESIS-T model was applied to the shoreline north of Grays Harbor, WA, using a hybrid bypassing method that employed a spatially- and temporally-varying cross-shore transport function. The input for this function was computed from CoastL model simulation results and van Rijn sediment transport calculations (see Chapter 8).

Calibration and verification of the model using the same input parameters as those in the standard bypass method (see Chapter 6) was undertaken using data for the periods 1976 to 1985 and 1985 to 1995, respectively. During this process, it was found that the model results were sensitive to small variations in the value of the sediment transport calibration coefficient K_1. Analysis of the 5-year GENESIS-T model simulation results with the HBM suggests that the GENESIS-T model and $K_1 = 0.10$ may represent a conservative picture of the effectiveness of the various alternatives. Subsequent simulations were performed using two values of this coefficient, $K_1 = 0.10$ (used in the SBM simulations) and $K_1 = 0.11$.

Ranking of the sediment transport bypassing at the north jetty resulted in the same order for the various structural alternatives for both values of K_1; the largest to smallest decreases were: Alt 4, Alt 3B, Alt 2A, Alt 3A and Alt 2B. Relative to Alt 1, the decrease in volume passing varied between 15 and 43 percent for $K_1 = 0.10$ and 41 and 67 percent for $K_1 = 0.11$. The predicted average southbound transport over the first one-half mile north of the jetty was not found

to be similar in the two sets of model simulations. The results for the model simulations using $K_1 = 0.10$ did not show a consistent pattern, whereas the model simulations using $K_1 = 0.11$ showed that all alternatives resulted in decreases in southward transport.

Ranking of the shoreline progradation near the north jetty resulted in the same order for the various structural alternatives for both values of K_1; the largest to smallest increases were: Alt 4, Alt 3B, Alt 2A, Alt 2B, and Alt 3A. Relative to Alt 1, the maximum shoreline progradation varied between 313 and 383 ft for $K_1 = 0.10$ and 153 and 171 ft for $K_1 = 0.11$.

References

Hanson, H., and Kraus, N. C. (1989). "GENESIS: Generalized model for simulating shoreline change, Report 1: Technical reference," Technical Report CERC-89-19, Coastal Engineering Research Center, U.S. Army Engineer Waterways Experiment Station, Vicksburg, MS.

Hanson, H., and Kraus, N. C. (2000). "Representation of tombolos and sediment transport by tidal currents in the "GENESIS" model," *Proceedings 13th Annual National Conference on Beach Preservation Technology*, Florida Shore and Beach Preservation Association, Tallahassee, FL, 64-80.

Kaminsky, G. M., Buijsman, M. C., and Ruggiero, P. (2000). "Predicting shoreline change at decadal scale in the Pacific Northwest, USA," *Proceedings 27th Coastal Engineering Conference*, ASCE, 2,400-2,413.

MacDonald, N. J. (1998). "Numerical modelling of non-linear wave-induced nearshore circulation," Ph.D. diss., Department of Civil Engineering, University of Liverpool, United Kingdom, 566 pp.

van Rijn, L. C. (1993). *Principles of sediment transport in rivers, estuaries and coastal seas*. Aqua Publishers, Amsterdam, The Netherlands.

Appendix H
Governing Equations of Numerical Models for Circulation and Wave Transformation, and Sediment Transport

This appendix contains the governing equations and associated information for the tidal circulation, wave transformation, and nearshore circulation, numerical simulation models applied in Chapters 7 and 8 of Volume I. The formulae applied to sediment transport calculations in Chapter 4 and Chapter 8 are also presented, and their application is described.

Tidal Circulation Model

Water-surface elevation and currents were calculated by applying the hydrodynamic model Advanced CIRCulation (ADCIRC) (Luettich et al. 1992). ADCIRC is a two-dimensional (2-D), depth-integrated, finite-element hydrodynamic model. It was developed with the capability of operating over a wide range of element sizes. This flexibility in grid resolution over the computational domain allows for fine resolution in the project area and coarse resolution in areas distant from the region of interest. Grid flexibility is of particular importance to this project because the evaluation of structural alternatives requires the ability to resolve these structures in the model domain.

Model attributes include the following capabilities:

a. Simulating tidal circulation and storm-surge propagation over very large computational domains while simultaneously providing high resolution in areas of complex shoreline configuration and bathymetry. The targeted areas of interest include continental shelves, nearshore areas, and estuaries.

b. Representing all pertinent physics of the 2-D equations of motion. These include tidal potential, Coriolis, and all nonlinear terms of the governing equations.

c. Providing accurate and efficient computations over time periods ranging from months to years.

In two dimensions, the model is formulated with the depth-averaged shallow-water equations for conservation of mass and momentum. The formulation assumes that the water is incompressible, that hydrostatic pressure conditions exist, and that the Boussinesq approximation is valid. Applying the standard quadratic parameterization for bottom stress and neglecting baroclinic terms and lateral diffusion and dispersion, a set of conservation equations in primitive, nonconservative form, are incorporated in the model. If the wave field changes slowly in time, the radiation stress gradients can be included in the momentum balance (Luettich et al. 1992; Westerink et al. 1994; Luettich and Westerink 1999). In this case the momentum equations are modified from those given by Luettich, Westerink, and Scheffner (1992) to:

$$\frac{\partial \zeta}{\partial t} + \frac{\partial UH}{\partial x} + \frac{\partial VH}{\partial y} = 0 \tag{H1}$$

$$\frac{\partial U}{\partial t} + U\frac{\partial U}{\partial x} + V\frac{\partial U}{\partial x} - fV = -\frac{\partial}{\partial x}\left[\frac{p_s}{\rho_o} + g\left(\zeta - (\eta + \Upsilon)\right)\right]$$
$$+ \frac{1}{H}\left[\frac{\tau_{sx}}{\rho_o} - \frac{\tau_{bx}}{\rho_o}\right] + D_x - B_x + R_x \tag{H2}$$

$$\frac{\partial V}{\partial t} + U\frac{\partial V}{\partial x} + V\frac{\partial V}{\partial x} + fU = -\frac{\partial}{\partial y}\left[\frac{p_s}{\rho_o} + g\left(\zeta - (\eta + \Upsilon)\right)\right]$$
$$+ \frac{1}{H}\left(\frac{\tau_{sy}}{\rho_o} - \frac{\tau_{by}}{\rho_o}\right) + D_y - B_y + R_y \tag{H3}$$

where

$$\zeta \ = \ \text{free-surface elevation relative to the geoid}$$

$$t \ = \ \text{time}$$

$$U \text{ and } V \ = \ \text{depth-averaged horizontal velocities in the x- and y-directions, respectively}$$

$$x \text{ and } y \ = \ \text{horizontal, distance-based coordinates}$$

$$H = \zeta + h \ = \ \text{total water depth}$$

$$h \ = \ \text{depth relative to the geoid}$$

$$f = 2\Omega \sin \varphi \ = \ \text{Coriolis parameter}$$

$$\Omega \ = \ \text{angular speed of the Earth}$$

$$p_s \ = \ \text{atmospheric pressure at the free surface}$$

$$\rho_0 \ = \ \text{reference density of water}$$

$$g \quad = \quad \text{acceleration due to gravity}$$

$$\eta \quad = \quad \text{Newtonian tide potential and earth tide parameter}$$

$$\Upsilon \quad = \quad \text{self-attraction and load tide parameter}$$

D_x and D_y = momentum diffusion/dispersion terms in the x and y directions, respectively

B_x and B_y = baroclinic pressure gradient terms in the x and y directions, respectively

τ_{sx} and τ_{sy} = applied free surface stresses in the longitudinal and latitudinal directions, respectively

τ_{bx} and τ_{by} = bottom shear stress given by the expression $C_f(U^2 + V^2)^{1/2}/H$, where C_f = the bottom friction coefficient

$$R_x \equiv \frac{1}{\rho_o H}\left(\frac{\partial S_{xx}}{\partial x} + \frac{\partial S_{xy}}{\partial y}\right) \tag{H4}$$

and

$$R_y \equiv \frac{1}{\rho_o H}\left(\frac{\partial S_{xy}}{\partial x} + \frac{\partial S_{yy}}{\partial y}\right) \tag{H5}$$

where S_{xx}, S_{yy}, $S_{xy} = S_{yx}$ are the radiation stresses, computed from a short wave model. The stress gradients must be computed in a coordinate system that is oriented in the same direction as ADCIRC.

The momentum equations (Equations H2 and H3) are differentiated with respect to x and y and substituted into the time differentiated continuity equation (Equation H1) to develop the Generalized Wave Continuity Equation (GWCE). The ADCIRC-2DDI (2-D, depth-integrated) model solves the GWCE in conjunction with the primitive momentum equations given in Equations H2 and H3. The GWCE-based solution scheme eliminates several problems associated with finite-element programs that solve the primitive forms of the continuity and momentum equations, including spurious modes of oscillation and artificial damping of the tidal signal. Forcing functions include time-varying water-surface elevations, wind shear stresses, radiation stresses, atmospheric pressure gradients, and the Coriolis effect. Also, the study area can be described in ADCIRC with either a Cartesian (i.e., flat earth) or spherical coordinate system. This allows convenient linkage to the wave model, which requires a Cartesian system to describe a study area.

Wave Transformation Model

The STeady-state spectral WAVE model (STWAVE) (Resio 1987; Smith et al. 2001) computes nearshore wind-wave growth and propagation and was used to transform waves through Grays Harbor Entrance as part of the evaluation of project alternatives. STWAVE numerically solves the steady-state conservation of spectral action balance along backward-traced wave rays:

$$(C_{ga})_x \frac{\partial}{\partial x} \frac{C_a C_{ga} \cos(\mu - \alpha) E(f, \alpha)}{\omega_r}$$

$$+ (C_{ga})_y \frac{\partial}{\partial y} \frac{C_a C_{ga} \cos(\mu - \alpha) E(f, \alpha)}{\omega_r} = \sum \frac{S}{\omega_r} \tag{H6}$$

where

C_{ga}	=	absolute wave group celerity
x,y	=	spatial coordinates; as subscripts indicate x and y components
C_a	=	absolute wave celerity
μ	=	current direction
α	=	propagation direction of spectral component
E	=	spectral energy density
f	=	frequency of spectral component
ω_r	=	relative angular frequency (frequency relative to the current)
S	=	energy source/sink terms

The source terms include wind input, nonlinear wave-wave interactions, dissipation within the wave field, and surf-zone breaking. The terms on the left-hand side of Equation H6 represent wave propagation (refraction and shoaling), and the source terms on the right-hand side of the equation represent energy growth or decay in the spectrum.

The assumptions made in STWAVE are as follows:

a. Mild bottom slope and negligible wave reflection.

b. Spatially homogeneous offshore wave conditions.

c. Steady waves, currents, and winds.

d. Linear refraction and shoaling.

e. Depth-uniform current.

f. Negligible bottom friction.

STWAVE is a half-plane model, meaning that only waves propagating toward the coast are represented. Waves reflected from the coast or waves generated by winds blowing offshore are neglected. Wave breaking in the surf zone limits the maximum wave height based on the local water depth (ratio of maximum zero moment wave height to water depth cannot exceed 0.64) and wave steepness:

$$H_{mo_{max}} = 0.1 L \tanh kd \tag{H7}$$

where

$\quad H_{mo}$ = zero-moment wave height

$\quad L$ = wavelength

$\quad k$ = wave number

$\quad d$ = water depth

STWAVE is a finite-difference model and calculates wave spectra on a rectangular grid with square grid cells. The model outputs zero-moment wave height, peak wave period (T_p), mean wave direction (α_m), and radiation stress gradients (S_{xx}, S_{yy}, and S_{xy}) at all grid points and 2-D spectra at selected grid points.

Nearshore Circulation Model CoastL

CoastL is a nearshore circulation model developed by MacDonald (1998). The model is composed of two independent, but dynamically coupled modules; a combined refraction-diffraction wave model and a depth-averaged coastal flow model. Each module is solved at every time-step using the results of the other module from the previous time-step.

The wave model uses a wave-period averaged technique and so can be applied over areas ranging from tens of meters to tens of kilometers. Wave kinematics are determined from solution of the x and y wave number vector equations:

$$
\begin{aligned}
&\frac{\partial P}{\partial t} + \left(C_g \frac{P}{k} + U \right) \frac{\partial P}{\partial x} + \left(C_g \frac{Q}{k} + V \right) \frac{\partial P}{\partial y} + \frac{\omega_r G}{2d} \frac{\partial d}{\partial x} \\
&+ P \frac{\partial U}{\partial x} + Q \frac{\partial V}{\partial x} + C_g \left(\Delta_{xx} + \Delta_{xy} + \Pi_{xx} + \Pi_{xy} \right) = 0
\end{aligned}
\tag{H8}
$$

and

$$\frac{\partial Q}{\partial t}+\left(C_g\frac{P}{k}+U\right)\frac{\partial Q}{\partial x}+\left(C_g\frac{Q}{k}+V\right)\frac{\partial Q}{\partial y}+\frac{\omega_r G}{2d}\frac{\partial d}{\partial y}$$

$$+P\frac{\partial U}{\partial y}+Q\frac{\partial V}{\partial y}+C_g\left(\Delta_{yx}+\Delta_{yy}+\Pi_{yx}+\Pi_{yy}\right)=0 \tag{H9}$$

where

P and Q =   wave number vectors in the x- and y-directions, respectively

C_g =   wave group velocity

A =   wave amplitude (defined as one-half of the wave height)

G = $\dfrac{2kh}{\sinh 2kh}$

Δ_{ij} and Π_{ij} =   wave diffraction terms, defined as:

$$\Delta_{xx}=\frac{1}{2kA}\left(\frac{1}{A}\frac{\partial A}{\partial x}\frac{\partial^2 A}{\partial x^2}-\frac{\partial^3 A}{\partial x^3}\right)$$

$$\Delta_{xy}=\frac{1}{2kA}\left(\frac{1}{A}\frac{\partial A}{\partial x}\frac{\partial^2 A}{\partial y^2}-\frac{\partial^3 A}{\partial x\partial y^3}\right)$$

$$\Delta_{yx}=\frac{1}{2kA}\left(\frac{1}{A}\frac{\partial^2 A}{\partial x^2}\frac{\partial A}{\partial y}-\frac{\partial^3 A}{\partial x^2\partial y}\right)$$

$$\Delta_{yy}=\frac{1}{2kA}\left(\frac{1}{A}\frac{\partial A}{\partial y}\frac{\partial^2 A}{\partial y^2}-\frac{\partial^3 A}{\partial y^3}\right) \tag{H10}$$

$$\Pi_{xx}=\frac{1}{2AkCC_g}\left[\frac{\partial A}{\partial x}\frac{\partial CC_g}{\partial x}\left(\frac{1}{CC_g}\frac{\partial CC_g}{\partial x}+\frac{1}{A}\frac{\partial A}{\partial x}\right)-\frac{\partial A}{\partial x}\frac{\partial^2 CC_g}{\partial x^2}-\frac{\partial CC_g}{\partial x}\frac{\partial^2 A}{\partial x^2}\right]$$

$$\Pi_{xy}=\frac{1}{2AkCC_g}\left[\frac{\partial A}{\partial y}\frac{\partial CC_g}{\partial y}\left(\frac{1}{CC_g}\frac{\partial CC_g}{\partial x}+\frac{1}{A}\frac{\partial A}{\partial x}\right)-\frac{\partial A}{\partial y}\frac{\partial^2 CC_g}{\partial x\partial y}-\frac{\partial CC_g}{\partial y}\frac{\partial^2 A}{\partial x\partial y}\right]$$

$$\Pi_{yx}=\frac{1}{2AkCC_g}\left[\frac{\partial A}{\partial x}\frac{\partial CC_g}{\partial x}\left(\frac{1}{CC_g}\frac{\partial CC_g}{\partial y}+\frac{1}{A}\frac{\partial A}{\partial y}\right)-\frac{\partial A}{\partial x}\frac{\partial^2 CC_g}{\partial x\partial y}-\frac{\partial CC_g}{\partial x}\frac{\partial^2 A}{\partial x\partial y}\right]$$

$$\Pi_{yy}=\frac{1}{2AkCC_g}\left[\frac{\partial A}{\partial y}\frac{\partial CC_g}{\partial y}\left[\frac{1}{CC_g}\frac{\partial CC_g}{\partial y}+\frac{1}{A}\frac{\partial A}{\partial y}\right]-\frac{\partial A}{\partial y}\frac{\partial^2 CC_g}{\partial^2 y}-\frac{\partial CC_g}{\partial y}\frac{\partial^2 A}{\partial y^2}\right]$$

The wave amplitude is determined from solution of the conservation of wave energy equation:

$$\frac{\partial A}{\partial t} + \frac{1}{2A}\left\{\frac{\partial}{\partial x}\left[A^2\left(\frac{C_g}{k}P + U\right)\right] + \frac{\partial}{\partial y}\left[A^2\left(\frac{C_g}{k}Q + V\right)\right]\right\}$$
$$+ \frac{1}{\rho g A}\left[S_{xx}\frac{\partial U}{\partial x} + S_{xy}\left(\frac{\partial U}{\partial y} + \frac{\partial V}{\partial x}\right) + S_{yy}\frac{\partial V}{\partial y}\right] + C_A A^2 = -D_B \qquad \text{(H11)}$$

where

C_A = energy dissipation coefficient for wave friction

D_B = energy dissipation caused by wave breaking

The CoastL model equations were developed under the assumption of a steady, monochromatic wave field with mild spatial variability. Random wave effects have been included in the CoastL model through the energy dissipation from wave breaking. The wave propagation characteristics within the surf zone, and all characteristics outside the surf zone, are modeled as though the wave field was purely regular (i.e., a single direction, height, and frequency at each location in plan).

The approach used for the simulation of this random wave breaking is based on the work of Battjes and Janssen (1978). In this approach, the dependent variable in the energy conservation equation is taken as A_{rms}, and it is assumed that the wave height field is distributed according to a truncated-Rayleigh probability distribution that is discontinuous at the breaking wave height. The energy dissipation rate caused by random wave breaking is determined as:

$$D_B = \frac{1}{4}\frac{\rho g^{3/2}H_{rms}^3 Q_b}{d^{1/2}L}\left(\frac{-\ln Q_b}{1 - Q_b}\right)^{\frac{3}{2}} \qquad \text{(H12)}$$

where

Q_b = fraction of broken waves in a breaking wave field

H_{rms} = root-mean-square wave height

The fraction of broken waves is determined by solutions of:

$$Q_b = 3.2\left(\frac{H_{rms}}{H_b} - 0.312\right)^3 \qquad \text{(H13)}$$

where

$$H_b \quad = \quad \text{breaking wave height}$$

Full wave-current interaction between internally or externally imposed flow fields is included. The flow module computes the depth-averaged flows resulting from any combination of wave, wind and tidal forcing.

The flow equations used in CoastL are similar to those used in other 2-D hydrodynamic models. The free-surface displacement is calculated using the 2-D continuity equation:

$$\frac{\partial \zeta}{\partial t} + \frac{\partial}{\partial x}(dU) + \frac{\partial}{\partial y}(dV) = 0 \tag{H14}$$

The depth-averaged horizontal velocities are calculated from the horizontal momentum equations:

$$
\begin{aligned}
&\frac{\partial U}{\partial t} + U\frac{\partial U}{\partial x} + V\frac{\partial U}{\partial y} + \frac{1}{\rho d}\left(\frac{\partial S_{xx}}{\partial x} + \frac{\partial S_{xy}}{\partial y}\right) + g\frac{\partial \zeta}{\partial x} \\
&\quad - \frac{\partial}{\partial x}\left(\nu\frac{\partial U}{\partial x}\right) - \frac{\partial}{\partial y}\left(\nu\frac{\partial U}{\partial y}\right) + \frac{\tau_x}{\rho d} = 0
\end{aligned}
\tag{H15}
$$

and

$$
\begin{aligned}
&\frac{\partial V}{\partial t} + U\frac{\partial V}{\partial x} + V\frac{\partial V}{\partial y} + \frac{1}{\rho d}\left(\frac{\partial S_{xy}}{\partial x} + \frac{\partial S_{yy}}{\partial y}\right) + g\frac{\partial \zeta}{\partial y} \\
&\quad - \frac{\partial}{\partial x}\left(\nu\frac{\partial V}{\partial x}\right) - \frac{\partial}{\partial y}\left(\nu\frac{\partial V}{\partial y}\right) + \frac{\tau_y}{\rho d} = 0
\end{aligned}
\tag{H16}
$$

where the enhanced mean bottom shear stresses in the x- and y-directions, τ_x and τ_y are computed as

$$\tau_x = \rho C_f (\beta U + j\gamma V)|U|$$

$$\tau_y = \rho C_f (\beta V - j\gamma U)|U|$$

where

$$j = \begin{cases} -1 & \text{for waves on the right-hand-side of the current} \\ 1 & \text{for waves on the left-hand-side of the current} \end{cases}$$

β and γ =   shear stress enhancement factors to account for wave-current interaction effects in the directions parallel to and perpendicular to the current, respectively (MacDonald 1988).

C_f =   current-only friction factor

The turbulent eddy viscosity, ν, is used to quantify the degree of mixing in the flow. The CoastL model solves two transport equations to determine the turbulent kinetic energy, κ, and its dissipation rate, ε. The eddy viscosity is then calculated from:

$$\nu = M \kappa^{1/2} \min\left(C_D \frac{\kappa^{3/2}}{\varepsilon}, 2\,A \right) \tag{H17}$$

where $C_D = 0.225$. The turbulent kinetic energy and its dissipation rate are given by:

$$\frac{\partial \kappa}{\partial t} + U \frac{\partial \kappa}{\partial x} + V \frac{\partial \kappa}{\partial y} - \frac{\partial}{\partial x}\left(\frac{\nu}{\Gamma_\kappa} \frac{\partial \kappa}{\partial x} \right) - \frac{\partial}{\partial y}\left(\frac{\nu}{\Gamma_\kappa} \frac{\partial \kappa}{\partial y} \right) - P_\kappa + \varepsilon = 0 \tag{H18}$$

and

$$\frac{\partial \varepsilon}{\partial t} + U \frac{\partial \varepsilon}{\partial x} + V \frac{\partial \varepsilon}{\partial y} - \frac{\partial}{\partial x}\left(\frac{\nu}{\Gamma_\varepsilon} \frac{\partial \varepsilon}{\partial x} \right) - \frac{\partial}{\partial y}\left(\frac{\nu}{\Gamma_\varepsilon} \frac{\partial \varepsilon}{\partial y} \right) - P_\varepsilon + C_2 \frac{\varepsilon^2}{\kappa} = 0 \tag{H19}$$

where $\Gamma_\kappa = 1.0$, $\Gamma_\varepsilon = 1.3$ and $C_2 = 1.92$. The two production terms, P_κ and P_ε are calculated from:

$$P_\kappa = \frac{1}{\rho\,d}\left(D_B \;+\; D_F \right) \tag{H20}$$

and

$$P_\varepsilon = \frac{1}{4} C_2 \left(C_D \frac{\kappa}{A} \right)^2 \tag{H21}$$

where D_F is the energy dissipation caused by frictional dissipation from the waves and the currents.

Sediment Transport Equations

Bailard (Guza and Thornton) equation

The Bailard (1981) equation for total (bed load and suspended load) time-averaged immersed weight sediment transport rate, $\langle \vec{i}_t \rangle$, is given as:

$$\langle \vec{i}_t \rangle = \rho f_{wc} \frac{\varepsilon_B}{\tan\phi}\left[\left\langle |\vec{u}_t|^2 \vec{u}_t \right\rangle - \frac{\tan\beta}{\tan\phi}\left\langle |\vec{u}_t|^3 \right\rangle \hat{\mathbf{i}} \right] + \rho f_{wc} \frac{\varepsilon_s}{W}\left[|\vec{u}_t|^3 \vec{u}_t - \frac{\varepsilon_s}{W}\tan\beta \left\langle |\vec{u}_t|^5 \hat{\mathbf{i}} \right\rangle \right]$$

← Bed load → ← Suspended Load →

(H22)

where ρ is fluid density, f_{wc} is the combined wave-current friction factor following Madsen and Wikramanayake (1991), ε_B and ε_s are the suspended load and bed load efficiency factors (Bagnold 1966), respectively, $\tan\phi$ is the coefficient of dynamic friction, $\tan\beta$ is the local bottom slope, W is the sediment fall velocity (Ahrens 2000). Assuming the total velocity field, $\vec{u}_t$, may be decomposed into oscillatory (~) and mean (overbar) flows, and x (u-offshore) and y (v-longshore) directed components:

$$\vec{u}_t = \left(\widetilde{u} + \overline{u}\right)\hat{\mathbf{i}} + \left(\widetilde{v} + \overline{v}\right)\hat{\mathbf{j}}$$

(H23)

where $\hat{\mathbf{i}}$ and $\hat{\mathbf{j}}$ are unit vectors in the cross-shore and longshore directions.

Following Guza and Thornton (1985) substitution of Equation H23 into H22 yields the cross-shore and longshore transport rates, $\langle i_x \rangle$ and $\langle i_y \rangle$, respectively:

$$\langle i_x \rangle = \rho f_{wc} \frac{\varepsilon_B}{\tan\phi}\left[\left\langle \widetilde{u}^3 \right\rangle + \left\langle \widetilde{u}\widetilde{v}^2 \right\rangle + \left\langle \widetilde{u}^2 + \widetilde{v}^2 \right\rangle \overline{u} + 2\left\langle \widetilde{u}^2 \right\rangle \overline{u} \ldots$$

$$\ldots + 2\left\langle \widetilde{u}\widetilde{v} \right\rangle \overline{v} + \overline{u}\overline{v}^2 + \overline{u}^3 + \frac{\tan\beta}{\tan\phi}\left\langle |\vec{u}_t|^3 \right\rangle \right] \ldots$$

$$\ldots + \rho f_{wc} \frac{\varepsilon_s}{W}\left[\left\langle |\vec{u}_t|^3 \widetilde{u} \right\rangle + \left\langle |\vec{u}_t|^3 \overline{u} \right\rangle + \frac{\varepsilon_s}{W}\tan\beta \left\langle |\vec{u}_t|^5 \right\rangle \right]$$

(H24)

$$\langle i_y \rangle = \rho f_{wc} \frac{\varepsilon_B}{\tan\phi}\left[\langle \tilde{v}^3 \rangle + \langle \tilde{u}^2 \tilde{v} \rangle + \langle \tilde{u}^2 \tilde{v}^2 \rangle \overline{u} + 2\langle \tilde{v}^2 \rangle \overline{v} + 2\langle \tilde{u}\tilde{v} \rangle \overline{u}^2\overline{v} + \overline{v}^3 \right]....$$

$$...+ \rho f_{wc}\frac{\varepsilon_s}{W}\left[\left\langle \left|\overset{\scriptscriptstyle\rho}{u}_t\right|^3 \tilde{v}\right\rangle + \left\langle \left|\overset{\scriptscriptstyle\rho}{u}_t\right|^3 \right\rangle \overline{v} \right] \tag{H25}$$

in which $\left|\overset{\scriptscriptstyle\rho}{u}_t\right| = \left[\tilde{u}^2 + \tilde{v}^2 + \overline{u}^2 + \overline{v}^2 + 2(\tilde{u}\overline{u} + \tilde{v}\overline{v})\right]^{1/2}$

The volumetric transport rate Q, may be related to the immersed weight transport rate $\langle i \rangle$ by the following (e.g., Bailard 1982; King and Seymour 1989):

$$Q = \frac{\langle i \rangle}{(\rho_s - \rho)gN_o} \tag{H26}$$

where ρ_s = density of the sand grains, g = acceleration due to gravity, N_o = "at rest" volume concentration of sediment assumed here to be 0.6.

The wave friction factor in this case was estimated following Madsen and Wikramanayake (1991) as:

$$f_{wc} = \exp\left[5.2\left(\frac{A_b}{K_n}\right)^{-0.19} - 6.1\right] - 0.24\left(\frac{A_b}{K_n}\right)^{-1.2} \,, \quad \frac{A_b}{K_n} < 1000$$

$$\frac{1}{\sqrt{4f_{wc}}} + \log10\left(\frac{1}{\sqrt[4]{f_{wc}}}\right) = \log10\left(\frac{A_b}{K_n}\right) + 0.1 \,, \quad \frac{A_b}{K_n} > 1000 \tag{H27}$$

where A_b is orbital excursion amplitude, K_n is Nikuradse sand grain roughness (2.5 d_{50}).

Direct measurements of the near-bed velocity field from the Hydra ADV systems on the jetty tripods and beach pods were used to compute integrated sediment transport rates accounting for both waves and currents using the preceding equations.

Sensitivity analysis of Bailard equation

The Bailard equations contain a number of parameters that need to be selected or estimated based on knowledge of the site characteristics. The model includes the sediment grain size, the beach slope, bed load and suspended load efficiency factors, the friction factor, and the friction angle of the sediment. Although the friction factor was determined for each burst of data following the Madsen and Wikramanayake (1991) method, only grain-related roughness was accounted for because the bed form related roughness is not well known for the range of combined flows observed. A sensitivity analysis of each estimated parameter including the friction factor was conducted to estimate the influence of

uncertainty in the selection of parameter values on the cumulative net transport. The selected values and range of tested values are summarized in Table H1 and results of sensitivity calculations are summarized in Table H2.

The medium grain size d_{50} at Ocean Shores in the nearshore and shoreface regions varies between 180 and 330 microns (μm) with some localized areas of coarser and finer sediments. A size range of 150 to 250 μm was chosen to test transport model sensitivity and 200 μm was selected to represent d_{50} at the jetty tripods.

Table H1
Range and Selected Value of Parameters Tested in Sensitivity Analysis

Parameter	Minimum	Maximum	Selected Value
d_{50} (μm)	150	250	200
$\tan\beta$	0.0125	0.0250	0.0167
ε_b	0.15	0.25	0.21
ε_s	0.01	0.035	0.025
$\tan\phi$	0.38	0.75	0.63
f_{wc}	0.002	0.01	variable

Table H2
Sensitivity of Net Transport to Variations in Parameters in Bailard Formula

Parameter	Value	Cumulative Flux +North/-South m^3 m^{-1}	Cumulative Flux +East/-West m^3 m^{-1}	Sensitivity North-South	Sensitivity East-West
d_{50} (μm)	150	-92.5	-135.3		
	180	-82.3	-118.5	-0.53	-0.59
	250	-72.0	-101.7		
$\tan\beta$	0.0125	-82.0	-116.1		
	0.0167	-82.3	-118.5	-0.015	0.07
	0.0250	-81.5	-120.7		
ε_b	0.15	-75.1	-108.9		
	0.21	-82.3	-118.5	0.33	0.32
	0.25	-86.6	-124.7		
ε_s	0.01	-47.7	-68.3		
	0.025	-82.3	-118.5	0.77	0.76
	0.035	-104.7	-152.4		
$\tan\phi$	0.38	-97.5	-144.0		
	0.63	-82.3	-118.5	-0.41	-0.47
	0.75	-78.0	-111.5		
f_{wc}	0.002	-59.7	-90.3		
	Variable	-82.3	-118.5	0.87	0.87
	0.01	-199.0	-300.9		

Bed slopes in the lower intertidal region and outer nearshore near the north jetty range from 1:40 to 1:80 or less. The average nearshore slope near the north jetty is approximately 1:60.

Bailard (1981) suggests nominal values of 0.21 and 0.025 for ε_b and ε_s for the surf zone based on longshore transport data, whereas Bagnold (1966) suggested values of 0.11 to 0.15 for ε_b and 0.015 for ε_s for streamflow conditions. Seymour and King (1982) obtained a value of 0.12 for ε_b based on a comparison of the Bailard and Inman (1981) bed load model with beach volume change at Torrey Pines, CA. Bailard (1982) estimated values of 0.1 and 0.02 for ε_b and ε_s based on comparisons with beach volume changes at Torrey Pines but indicated broad confidence limits for these values of ε_b and ε_s due to the uncertainty in the data.

Bagnold (1966) suggested that the coefficient of dynamic friction, $\tan \phi$, varies over a factor of two between approximately 0.38 and 0.75 depending on the ratio of grain diameter to the dispersive shear. Bagnold (1966) further suggested that the static value of 0.63 should be adequate for sand-sized quartz grains under fluid transport.

Bailard (1982) selected a friction factor of 0.005 for use with the total load model based on an analysis of longshore current data at Silver Strand Beach, CA. Thornton and Guza (1982), on the other hand, found a value of 0.01 but with a relative uncertainty of +/-0.01 based on longshore current measurements at Torrey Pines (Bailard 1982). Calculations of f_{wc} for the present data set at sta OS 5 using the method of Madsen and Wikramanayake (1991) indicate variation between 0.003 and 0.03 and an average value of 0.007 for the period of deployment.

The Bailard model is relatively insensitive to variations in bed slope for the range of bed slopes relevant at north beach and north jetty. The north-south component of transport is marginally less sensitivity than the east-west component due to orientation of the shoreline.

The Bailard model is more than twice as sensitive to ε_s than ε_b. The efficiency factors and sediment size account for the greatest uncertainty in the model since other parameters have either a more restricted range or induce less sensitivity to results. Although the model exhibits relatively high sensitivity to $\tan \phi$, the range of uncertainty in this parameter is probably much less than the range tested since Bagnold based the overall range on a wide range of sediment sizes that included very coarse grains beyond the sizes present in this environment.

The model is also sensitive to uncertainty in the wave-current friction factor f_{wc}. Therefore, calculating a new friction factor for each time-step and allowing the parameter to vary as a function of relative roughness seemed the most appropriate way to minimize this uncertainty.

van Rijn equation

The van Rijn model (van Rijn 1993, 1989a, 1989b) is a total load model that computes the time varying bed-load transport and the time averaged (over a wave cycle) suspended load and combines them to obtain the total sediment transport rate. The following description is based on the original papers by van Rijn and material contained in Chapters 5 and 6 of Gailani et al. (2003). The method was developed for waves outside the surf zone with waves and currents at arbitrary angle. To compute the suspended load, van Rijn uses a near-bed reference concentration, c_a (kg/m^3), at reference elevation a, defined as:

$$c_a = 0.015 \rho_s \frac{d_{50}}{a} \frac{T_a^{1.5}}{D_*^{0.3}} \tag{H28}$$

where T_a is the dimensionless bed shear stress parameter at reference elevation and D_* is a dimensionless particle diameter. T_a and D_* are given by:

$$T_a = \frac{\left(\alpha_{cw} \mu_c \tau_c + \mu_{w,a} \tau_w \right) - \tau_{cr}}{\tau_{cr}} \tag{H29}$$

$$D_* = d_{50} \left[(s-1) g / v^2 \right]^{\frac{1}{3}} \tag{H30}$$

where α_{cw}, the wave current interaction coefficient, is a function of the bed roughness, wave boundary layer thickness, and water depth; μ_c, the current efficiency factor, is a function of bed roughness and grain-size distribution; $\mu_{w,a}$, the wave efficiency factor, is a function of the grain-size distribution and wave conditions; τ_c is the current related bed shear stress, τ_w is the wave related bed shear stress and τ_{cr} is the critical shear stress for the initiation of motion.

The vertical variation in c is estimated as a function of the of a current and wave related mixing coefficient, $\varepsilon_{s,cw}$, which is a function of the kinetic energy:

$$\frac{dc}{dz} = \frac{-(1-c)^5 c W_s}{\varepsilon_{s,cw} \left[1 + \left(\frac{c}{c_a} \right)^{0.8} - 2 \left(\frac{c}{c_a} \right)^{0.4} \right]} \tag{H31}$$

The time varying bed load (cubic mmeters per second) is estimated as:

$$\overset{\vee}{q}_b (t) = 0.25 \alpha d_{50} D_*^{-0.3} \left(\frac{\overset{\vee}{\tau}'_{b,cw}}{\rho} \right)^{0.5} \tag{H32}$$

where $\alpha = 1 - (H_s/h)^{0.5}$, and $\overline{\overset{\omega}{\tau}}_{b,cw}$ is the grain-related bed shear stress due to currents and waves. The computation of the preceding parameters is complex; the original references should be consulted to for a more detailed description.

Sediment transport at-a-point calculated from direct measurements

Near-bed direct measurements of velocity and suspended sediment concentration can be multiplied to obtain an at-a-point estimate of sediment flux that accounts for contributions due to both waves and currents as follows:

$$\langle q_s \rangle = \langle \overset{\rho}{u}_b c_b \rangle = \left\langle \left(\overline{u} + \widetilde{u} \right)\left(\overline{c} + \widetilde{c} \right) \right\rangle = \langle \overline{uc} \rangle + \langle \overline{u}\widetilde{c} \rangle + \langle \widetilde{u}\overline{c} \rangle + \langle \widetilde{u}\widetilde{c} \rangle \tag{H33}$$

and

$$\overset{\rho}{u}_t = \left(\widetilde{u} + \overline{u} \right)\hat{\mathbf{i}} + \left(\widetilde{v} + \overline{v} \right)\hat{\mathbf{j}} \tag{H34}$$

In this case $\overset{\varpi}{u}_t$ is determined from the Hydra Acoustic Doppler Velocimeter measurements, c_b is the near-bed concentration measured directly by the bottom OBS sensor, $<>$ indicates time averaging (1 burst, approximately 17 min). The method accounts for wave-current-suspended sediment coupling through the covariance term in the expansion (e.g., Jaffe, Sternberg, and Sallenger 1984; Osborne and Greenwood 1992a, 1992b) and provides some insight on the relative contributions of waves as opposed to steady currents to the net flux. The method does not account for vertical variations in velocity, concentration or the phase relationship between velocity and concentration. Therefore, the results should be considered more qualitative than quantitative.

Shear stresses and mobility within PSed

The critical shear stress of the parcel, τ_{cr} is determined using the Shields criterion, an analytic expression for which has been developed by Soulsby and Whitehouse (1997). This technique allows the prediction of the Shields parameter, θ_{cr} as a function of the dimensionless grain size, D_{gr}.

$$\theta_{cr} = \frac{0.30}{1 + 1.2 D_{gr}} + 0.055\left(1 - e^{-0.02 D_{gr}} \right) \tag{H35}$$

where

$$\theta_{cr} = \frac{\tau_{cr}}{(s-1)gD} \tag{H36}$$

or, conversely,

$$\tau_{cr} = \theta_{cr}(s-1)gD \tag{H37}$$

where τ_{cr} is the critical shear stress at which inception of motion occurs. The dimensionless grain size, D_{gr} is defined by:

$$D_{gr} = D \sqrt[3]{\frac{g(s-1)}{\upsilon^2}} \tag{H38}$$

The critical shear stress for sediment mobility τ_{cr} is the critical value of the skin friction shear stress, that frictional force acting on the sediment grains which controls sediment mobility. In addition to skin friction shear stress, there is also form drag shear stress that affects overall resistance of the flow. The form drag shear stress is determined by the presence of bed forms, whereas the skin friction

shear stress is independent of bed forms. The bed form calculations in PSed do not, therefore directly affect sediment mobility (M is calculated on the basis of skin friction); however, they can control the sediment transport regime.

Knowing, through the Shields relationship, the critical shear stress at which sediment transport will take place for a given grain size of sediment, τ_{cr}, and the shear stress acting at the bed, τ, one can calculate the mobility, M of the sediment.

$$M = \frac{\tau}{\tau_{cr}} \qquad\qquad\qquad\qquad\text{(H39)}$$

Consider a grain of sediment resting on the bed as the flow over it is steadily increased. This can be represented by increasing value of the sediment mobility, M as follows:

M=0   Under a zero-flow condition, the shear stresses acting on the particle are zero and hence the mobility, $M = 0$.

0<M<1   As the flow increases, the shear stress, τ acting on the grain of sediment will increase. However, the fluid forces will still be less than the inertial and interlocking restoring forces (represented by τ_{cr}). No movement of the grains.

M=1   At some point, the fluid shear will just be in balance with the critical shear stress for erosion ($M = 1$). As flow increases past this point, the grain will start to move along the bed: at first by 'saltating' or jumping along the bed (bed load). These jumps are caused by turbulence in the flow.

1<M<8   In this range, the size and mass of the grain is sufficient that it falls back to the bed quite quickly after each jump. As the amount of bed load increases, bed forms such as ripples and/or dunes develop. Bed form length is mainly a function of grain size while the height of the bed form is dependent on flow intensity.

8<M<14   As flow intensity increases, the bed forms start to reduce in height, the 'hang time' of the particles increases.

14<M<65   Sediment is now being swept higher into the flow field. The lift forces in this increasingly turbulent flow field are sufficient to keep the grain in suspension. The onset and characterization of suspended load is, in large part, controlled by the ratio of sediment fall velocity to the total shear velocity.

References

Ahrens, J. P. (2000). "A fall-velocity equation*," Journal of Waterway, Port, Coastal, and Ocean Engineering* 126(2), March/April, 99-102.

Bagnold, R. A. (1966). "An approach to the sediment transport problem from general physics," United States Geological Survey Professional Paper 422-I.

Bailard, J. A., and Inman, D. L. (1981). "An energetics bedload model for a plane sloping beach: local transport," *Journal of Geophysical Research* 86(C3), 2035-2043.

Bailard, J. A. (1981). "An energetics total load sediment transport model for a plane sloping beach," *Journal of Geophysical Research* 86, 10,938-10,954.

Bailard, J. A. (1982). "Modeling on-offshore sediment transport in the surfzone," *Proceeding, 18th Coastal Engineering Conference*, American Society of Civil Engineers (ASCE), 1,419-1,436.

Battjes, J. A., and Janssen, J. P. F .M. (1978). "Energy loss and set-up due to breaking of random waves," *Proceedings 16th Coastal Engineering Conference*, ASCE, 569-587.

Gailani, J. Z., et al. (2003). "Monitoring dredged material disposal at mouth of Columbia River, Washington/Oregon, USA," Technical Report ERDC/CHL TR-03-5, Coastal and Hydraulics Laboratoary, U.S. Army Engineer Research and Development Center, Vicksburg, MS.

Guza, R. T., and Thornton, E. B. (1985). "Velocity moments in nearshore," *Journal of Waterway, Port, Coastal, and Ocean Engineering* 111(2), 235-256.

Jaffe, B. E., Sternberg, R. W., and Sallenger, A. H. (1984). "The role of suspended sediment in shore-normal beach profile change," *Proceedings 19th Coastal Engineering Conference*, ASCE, 1,983-1,986.

King, Jr., D. B., and Seymour, R. J. (1989). "State of the art in oscillatory sediment transport models," in *Nearshore Sediment Transport*, R. J. Seymour (ed.) Plenum Press, New York, 371-385.

Luettich, R. A., Westerink, J. J., and Scheffner, N. W. (1992). "ADCIRC: An advanced three-dimensional circulation model for shelves, coasts, and estuaries; Report 1, Theory and methodology of ADCIRC-2DDI and ADCIRC-3DL," Technical Report DRP-92-6, U.S. Army Engineer Waterways Experiment Station, Vicksburg, MS.

Luettich, R. A., Jr., and Westerink, J .J. (1999). "Implementation of the wave radiation stress gradient as a forcing for the ADCIRC hydrodynamic model: Upgrades and documentation for ADCIRC Version 34.12," Contractor Report, Department of the Army, U.S. Army Engineer Waterways Experiment Station, Vicksburg, MS.

Madsen, O. S., and Wikramanayake, P. N. (1991). "Simple models for turbulent wave-current bottom boundary layer flow," Dredging Research Program Contract Report DRP-91-1, U.S. Army Engineer Research and Development Center, Vicksburg, MS.

MacDonald, N. J. (1998): *Numerical modelling of non-linear wave-induced nearshore circulation*. Ph D diss., Department of Civil Engineering, University of Liverpool, UK, 566 pp.

Osborne, P. D., and Greenwood, B. (1992a). "Frequency dependent cross-shore suspended sediment transport, 1: A non-barred shoreface," *Marine Geology* 106, 1-24.

Osborne, P. D., and Greenwood, B. (1992b). "Frequency dependent cross-shore suspended sediment transport 2: A barred shoreface," *Marine Geology* 106, 25-51.

Resio, D. T. (1987). "Shallow-water waves, Report I: Theory," *Journal of Waterway, Port, Coastal, and Ocean Engineering* 113(3), 264-281.

Seymour, R. J., and King, Jr., D. B. (1982). "Field comparisons of cross-shore transport models," *Journal of the Waterway, Port, Coastal, and Ocean Division* 108(WW2), 163-179.

Soulsby, R. L., and Whitehouse, R. J. S. W. (1997). "Threshold of sediment motion in coastal environments," *Proceeings Pacific Coasts and Ports '97*, University of Canterbury, New Zealand, 149-154.

Smith, J. M., Sherlock, A. R., and Resio, D.T. (2001). "STWAVE: Steady-state spectral wave model user's manual for STWAVE Version 3.0," Instruction Report ERDC/CHL IR-01-1, Coastal and Hydraulics Laboratory, U.S. Army Engineer Research and Development Center, Vicksburg, MS.

Thornton, E. B., and Guza, R. T. (1982). "Longshore currents and bed shear stress," *Proceedings Eirectional Wave Spectra Applications*, ASCE, 147-164.

van Rijn, L. C. (1989a). "Sediment transport, Part I: Bed load transport," *Journal of Hydraulic Engineering* 110(10), 1,431-1,456.

van Rijn, L. C. (1989b). "Sediment transport, Part II: Suspended load transport," *Journal. of Hydraulic Engineering* 110(11), 1,613-1,641.

van Rijn, L. C. (1993). *Principles of sediment transport in rivers, estuaries and coastal seas*. Aqua Publications, Amsterdam, The Netherlands.

Westerink, J. J., Blain, C. A., Luettich, R. A., Jr., and Scheffner, N. W. (1994). "ADCIRC: An advanced three-dimensional circulation model for shelves coasts and estuaries, Report 2: Users manual for ADCIRC-2DDI," Dredging Research Program Technical Report DRP-92-6, U.S. Army Engineer Waterways Experiment Station, Vicksburg, MS, 156 pp.

REPORT DOCUMENTATION PAGE

Public reporting burden for this collection of information is estimated to average 1 hour per response, including the time for reviewing instructions, searching existing data sources, gathering and maintaining the data needed, and completing and reviewing this collection of information. Send comments regarding this burden estimate or any other aspect of this collection of information, including suggestions for reducing this burden to Department of Defense, Washington Headquarters Services, Directorate for Information Operations and Reports (0704-0188), 1215 Jefferson Davis Highway, Suite 1204, Arlington, VA 22202-4302. Respondents should be aware that notwithstanding any other provision of law, no person shall be subject to any penalty for failing to comply with a collection of information if it does not display a currently valid OMB control number. **PLEASE DO NOT RETURN YOUR FORM TO THE ABOVE ADDRESS.**

1. REPORT DATE *(DD-MM-YYYY)*	2. REPORT TYPE	3. DATES COVERED *(From - To)*
June 2004	Final report	

4. TITLE AND SUBTITLE

North Jetty Performance and Entrance Navigation Channel Maintenance, Grays Harbor, Washington; Volume II: Appendices

5a. CONTRACT NUMBER

5b. GRANT NUMBER

5c. PROGRAM ELEMENT NUMBER

6. AUTHOR(S)

Nicholas C. Kraus, Hiram T. Arden, editors, with contributions by (in alphabetical order) Jessica L. Baker, Mark R. Byrnes, Mary A. Cialone, Julie A. Cohen, Michael H. Davies, David B. Hericks, David Katzev, Neil J. McDonald, Philip D. Osborne, Maria Timpano, Ty V. Wamsley, Donald L. Ward

5d. PROJECT NUMBER

5e. TASK NUMBER

5f. WORK UNIT NUMBER

7. PERFORMING ORGANIZATION NAME(S) AND ADDRESS(ES)

U.S. Army Engineer Research and Development Center
Coastal and Hydraulics Laboratory
3909 Halls Ferry Road, Vicksburg, MS 39180-6199

8. PERFORMING ORGANIZATION REPORT NUMBER

ERDC/CHL TR-03-12

9. SPONSORING / MONITORING AGENCY NAME(S) AND ADDRESS(ES)

U.S. Army Engineer District, Seattle
P.O. Box 3755, Seattle, WA 98124-3755

10. SPONSOR/MONITOR'S ACRONYM(S)

11. SPONSOR/MONITOR'S REPORT NUMBER(S)

12. DISTRIBUTION / AVAILABILITY STATEMENT
Approved for public release; distribution is unlimited.

13. SUPPLEMENTARY NOTES

14. ABSTRACT
This report documents a study performed for the U.S. Army Engineer District, Seattle, to identify and evaluate feasible methods for reducing annual maintenance dredging in the outer Federal navigation channel at Grays Harbor, WA, by modification of the north jetty. Main interest was in potential reduction of southward sand bypassing the north jetty and preservation of the jetty should the neighboring beach erode. Considerable information and predictive capability were generated concerning the behavior of the Federal navigation channel and adjacent coastal and inlet shorelines. The study was conducted as a coordinated multi-disciplinary approach involving field measurement, physical modeling of the hydrodynamics and potential sediment pathways, geomorphic analysis and sediment budget formulation, and numerical modeling of waves, circulation and sediment transport, including modeling of shoreline change and bypassing.
Numerous alternatives were considered and subjected to a screening process to identify feasible engineering and physically constructible alternatives within broad criteria. Six alternatives passed the screening and were evaluated. The alternatives concerned an innovative submerged spur that would be placed parallel to the shoreline along the north jetty, partial and full rehabilitation of the north jetty, and a combination of these alternatives with structures of different lengths.

(Continued)

15. SUBJECT TERMS
See reverse.

16. SECURITY CLASSIFICATION OF:

a. REPORT	b. ABSTRACT	c. THIS PAGE	17. LIMITATION OF ABSTRACT	18. NUMBER OF PAGES	19a. NAME OF RESPONSIBLE PERSON
UNCLASSIFIED	UNCLASSIFIED	UNCLASSIFIED		746	19b. TELEPHONE NUMBER *(include area code)*

14. ABSTRACT (continued)

The sediment-control alternatives were evaluated relative to the existing condition. The study revealed many wide-area processes controlling sedimentation in and around Grays Harbor. The scale of change in southward-directed bypassing of sediment expected to occur after construction of any of the evaluated alternatives was found to be small compared to the scale of transport at the Grays Harbor entrance from sources originating outside the entrance or by being reworked and redistributed within the entrance. Modification of the north jetty is one of relatively few options for controlling sedimentation in the outer navigation channel; others include channel realignment and modifications to the south jetty.

15. SUBJECT TERMS

Dredging
Channel maintenance
Field measurement
Grays Harbor, Washington
Jetty
Navigation channel
Numerical modeling
Physical modeling
Rip current
Sand bypassing
Sediment budget
Sediment transport